



STRUCTURES IN FIRE

SiF 2012

**PROCEEDINGS OF THE 7TH INTERNATIONAL
CONFERENCE ON STRUCTURES IN FIRE**

ZURICH, SWITZERLAND
6–8 June 2012



EDITORS: M. Fontana, A. Frangi, M. Knobloch

EMPA 
Materials Science & Technology

ETH
Eidgenössische Technische Hochschule Zürich
Swiss Federal Institute of Technology Zurich

STRUCTURES IN FIRE

SIF'2012

**7TH INTERNATIONAL CONFERENCE ON
STRUCTURES IN FIRE**

**ZURICH, SWITZERLAND
6 – 8 June 2012**

EDITORS

Mario Fontana, Andrea Frangi, Markus Knobloch

ORGANISATION

ETH Zurich, EMPA Dübendorf

STRUCTURES IN FIRE

First published in Switzerland in 2012 by ETH Zurich

All rights reserved. No part of this book may be reproduced or transmitted in any form or by any means, electronic or mechanical, including photocopying, recording or by any information storage and retrieval system, without permission in writing from the publisher.

DOI: 10.3929/ethz-a-007050197

Graphic Art Production, printed and bound by: ETH Zurich, 8092 Zurich

Distribution:
ETH Zurich, Institute of Structural Engineering, Zurich, Switzerland

Editors: Mario Fontana, Andrea Frangi, Markus Knobloch

SCIENTIFIC COMMITTEE

Chairman

Vila Real, Paulo – Portugal

Track Leader

Buchanan, Andy - New Zealand

Fontana, Mario – Switzerland

Franssen, Jean-Marc – Belgium

Kodur, Venkatesh – USA

Tan, Kang Hai – Singapore

Usmani, Asif - United Kingdom

Organising Committee

Fontana, Mario - Switzerland

Frangi, Andrea- Switzerland

Hugi, Erich - Switzerland

Knobloch, Markus – Switzerland

Steering Committee

Buchanan, Andy - New Zealand

Franssen, Jean-Marc - Belgium

Kodur, Venkatesh - USA

Vila Real, Paulo – Portugal

Reviewers

Ali, Faris - United Kingdom

AlJabri, Khalifa - Oman

Bailey, Colin - United Kingdom

Bhargava, Pradeep - India

Bisby, Luke - United Kingdom

Block, Florian - United Kingdom

Bradford, Mark - Australia

Burgess, Ian - United Kingdom

Craft, Steve - Canada

Dhima, Dhionis - France

Fragiacomo, Massimo - Italy

Frangi, Andrea - Switzerland

Gambarova, Pietro - Italy

Garlock, Maria - USA

Gillie, Martin - United Kingdom

Green, Mark - Canada

Han, Linhai - China

Horiguchi, Takshi - Japan

Huang, Zhaohui - United Kingdom

Izzuddin, Basam - United Kingdom

Janssens, Marc - USA

Joyeux , Daniel - France

Knobloch, Markus - Switzerland

Lamont, Susan - UAE

Lange, Jörg - Germany

Li, Guo Qiang - China

Lim, Linus - United Kingdom

Mensingher, Martin - Germany

Nadjai, Ali - United Kingdom

Outinen, Jyri - Finland

Phan, Long - USA

Plank, Roger - United Kingdom

Schaumann, Peter - Germany

Schmid, Joachim - Sweden

Taerwe, Luc - Belgium

Talamona, Didier - United Kingdom

Tonicello, Eric - Switzerland

Vassart, Olivier - Luxembourg

Wald, Frantisek - CzechRepublic

Wang, Yong C. - United Kingdom

Wu, Bo - China

Zaharia, Raul - Romania

Zhao, Bin - France

CONTENTS

Preface

Applications of Structural Fire Safety Engineering

APPLYING THE PEER PERFORMANCE BASED EARTHQUAKE ENGINEERING METHODOLOGY TO STRUCTURES IN FIRE <i>David Lange, Shaun Devaney and Asif S. Usmani</i>	3
APPLICATION OF STRUCTURAL FIRE ENGINEERING TO AN ITALIAN TALL OFFICE BUILDING <i>Emidio Nigro, Giuseppe Cefarelli, Anna Ferraro, Iolanda Del Prete, Domenico Sannino and Gaetano Manfredi</i>	13
POST-EARTHQUAKE STRUCTURAL DESIGN FOR FIRE - A NEW ZEALAND PERSPECTIVE <i>Gregory B. Baker, Peter C.R. Collier, Anthony K. Abu and Brent Houston</i>	23
PERFORMANCE-BASED FIRE SAFETY DESIGN OF SPECIAL STRUCTURES IN GERMANY <i>Jochen Zehfuss, Christoph Klinzmann and Karen Paliga</i>	33
EXPERIMENTAL AND NUMERICAL INVESTIGATION OF INCLINED GLAZING FACADE PERFORMANCE UNDER FIRE CONDITIONS <i>Michael Quinn, Ali Nadjai and Faris Ali</i>	43

Steel Structures

BEHAVIOUR OF COMPRESSED COLD FORMED STEEL ELEMENTS AT HIGH TEMPERATURES <i>Saulo J.C. Almeida, João Paulo C. Rodrigues and Jorge Munaiar Neto</i>	55
PARAMETRIC STUDY ON THE BEHAVIOUR OF STEEL COLUMNS EMBEDDED ON WALLS <i>António M. Correia, João P. Rodrigues and Paulo Vila Real</i>	65

BEHAVIOUR OF PROTECTED CELLULAR BEAMS HAVING DIFFERENT OPENING SHAPES IN FIRE CONDITIONS <i>Han Sanghoon, Klelia Petrou, El-Hadi Naili, Ali Nadjai and Faris Ali</i>	75
MATERIAL BEHAVIOUR OF HIGH STRENGTH STEEL S690 IN FIRE AND AFTER FIRE <i>Xuhong Qiang, Frans S.K. Bijlaard and Henk Kolstein</i>	85
CREEP BEHAVIOR OF ASTM A992 STEEL AT ELEVATED TEMPERATURES <i>Jinwoo Lee, Mohammed A. Morovat, Michael D. Engelhardt and Eric M. Taleff</i>	95
FIRE TESTS OF LOAD BEARING STEEL STUD WALLS EXPOSED TO REAL BUILDING FIRES <i>Anthony D. Ariyanayagam and Mahen Mahendran</i>	105
FULL SCALE FIRE TEST AND NUMERICAL SIMULATION OF A STEEL CONNECTION <i>Peter Schaumann, Thomas Kirsch and Florian Timmen</i>	115
THE BEHAVIOUR OF STEEL BEAMS WITH MOMENT-RESISTING BEAM-SPLICE CONNECTIONS IN FIRE <i>Takeo Hirashima, Mariati Taib, Bernice Wong and Ian Burgess</i>	125
A COMPONENT-BASED MODEL FOR MOMENT-RESISTING BEAM-SPLICE CONNECTIONS WITH HIGH-STRENGTH BOLTS AT ELEVATED TEMPERATURE <i>Mariati Taib, Ian Burgess and Takeo Hirashima</i>	135
EFFECT OF AGING ON RELIABILITY OF STEEL COLUMNS PROTECTED BY INTUMESCENT COATINGS TO NATURAL FIRES <i>Chao Zhang, Guo-Qiang Li and Yong-Chang Wang</i>	145
CONSIDERATION OF LOCAL INSTABILITIES IN BEAM FINITE ELEMENTS BY MEANS OF EFFECTIVE CONSTITUTIVE LAWS <i>Jean-Marc Franssen and Baptiste Cowez</i>	155
EXPERIMENTAL AND NUMERICAL TESTS ON BUILDING STEEL COLUMNS SUBJECTED TO FIRE <i>António M. Correia and João P. Rodrigues</i>	165
HIGH-TEMPERATURE CREEP BUCKLING PHENOMENON OF STEEL COLUMNS SUBJECTED TO FIRE <i>Mohammed A. Morovat, Michael D. Engelhardt, Todd A. Helwig and Eric M. Taleff</i>	175
LARGE SCALE TEST TO EXPLORE THERMAL EXPOSURE OF COLUMN EXPOSED TO LOCALIZED FIRE <i>Alexandra Byström, Johan Sjöström, Ulf Wickström and Milan Veljkovic</i>	185

INFLUENCE OF ASYMMETRICAL FIRE EXPOSURE ON THE STRUCTURAL BEHAVIOUR OF STEEL ELEMENTS <i>Peter Schaumann and Florian Tabeling</i>	195
NUMERICAL MODELLING OF LOAD BEARING LSF WALLS UNDER FIRE CONDITIONS <i>Poologanathan Keerthan and Mahen Mahendran</i>	205
STABILITY OF ALUMINIUM BEAMS IN CASE OF FIRE, EXPERIMENTS <i>O.R. (Ronald) van der Meulen, Frans Soetens and Johan Maljaars</i>	215
AN APPROACH FOR EVALUATING THE RESIDUAL STRENGTH OF FIRE EXPOSED BRIDGE GIRDERS <i>Esam M. Aziz and Venkatesh K. Kodur</i>	225

Composite Structures

SLENDER CONCRETE FILLED TUBULAR COLUMNS SUBJECTED TO FIRE. EXPERIMENTAL STUDIES AND FIRE DESIGN <i>Ana Espinos, Manuel L. Romero, Antonio Hospitaler, Carmen Ibañez, Ana Pascual and Vicente Moliner</i>	237
TESTING OF COMPOSITE SLAB-BEAM SYSTEMS AT ELEVATED TEMPERATURES <i>Trung T. Nguyen and Hai K. Tan</i>	247
EXPERIMENTAL STUDIES ON THE BEHAVIOUR OF HEADED STUD SHEAR CONNECTORS AT ELEVATED TEMPERATURES <i>Ling-Zhu Chen, Guo-Qiang Li and Shou-Chao Jiang</i>	257
BEHAVIOUR OF AXIALLY LOADED BOX COLUMNS FILLED WITH HIGH-STRENGTH SELF-COMPACTING CONCRETE AT ELEVATED TEMPERATURES <i>Cheng-Chih Chen, Wen-Chen Jau, Chien-Jung Chen, Yi-Chen Wu and Jheng-Yi Lin</i>	267
PERFORMANCE OF HOLLOW AND CONCRETE FILLED ELLIPTICAL STEEL COLUMNS SUBJECTED TO HYDROCARBON FIRE <i>Nathan Goodfellow, Faris Ali, Tom Scullion, Ali Nadjai and Tony McParland</i>	275
HIGH TEMPERATURE TESTS ON PARTIALLY ENCASED BEAMS <i>Paulo A.G. Piloto, Ana B.R. Gavilán, Luís M.R. Mesquita and Carlos Gonçalves</i>	285
EXPERIMENTAL AND NUMERICAL INVESTIGATION ON THE BEHAVIOUR OF A COMPOSITE FLOOR MADE OF CELLULAR BEAMS IN A FIRE SITUATION <i>Gisèle Bihina, Bin Zhao and Abdelhamid Bouchaïr</i>	295

EXPERIMENTAL AND NUMERICAL EVALUATION OF COMPOSITE FLOOR SLABS UNDER FIRE LOADING <i>Kristi L. Selden, Amit H. Varma and Erica C. Fischer</i>	305
 Timber Structures and Fire Protection Materials	
DESIGN OF POST-TENSIONED TIMBER BEAMS FOR FIRE RESISTANCE <i>Phillip M. Spellman, Anthony K. Abu, David M. Carradine, Peter J. Moss and Andrew H. Buchanan</i>	317
INFLUENCE OF SERVICE INSTALLATIONS FOR THE SEPARATION AND STRUCTURAL PERFORMANCE OF TIMBER ASSEMBLIES EXPOSED TO FIRE <i>Norman Werther, Michael Merk, René Stein and Stefan Winter</i>	327
FIRE PROTECTION BY MINERAL WOOL FOR TIMBER FRAME ASSEMBLIES <i>Alar Just and Joachim Schmid</i>	337
FIRE BEHAVIOUR OF FINGER-JOINTED TIMBER BOARDS <i>Michael Klippel, Andrea Frangi and Mario Fontana</i>	347
DESIGN MODEL FOR WOOD I-JOISTS IN WALL ASSEMBLIES EXPOSED TO FIRE <i>Joachim Schmid and Alar Just</i>	357
EXPERIMENTAL AND NUMERICAL ANALYSIS OF THE THERMO-MECHANICAL BEHAVIOUR OF STEEL-TO-TIMBER CONNECTIONS IN TENSION PERPENDICULAR TO THE GRAIN <i>Maxime Audebert, Dhionis Dhima, Abdelhamid Bouchaïr and Mustapha Taazount</i>	367
THE ADAPTATION OF DIANA FOR SIMULATING FIRE EXPOSED TIMBER STRUCTURES IN NATURAL FIRE CONDITIONS <i>Danny Hopkin</i>	377
FIRE INDUCED DESORPTION AND MIGRATION OF HYGROSCOPIC MOISTURE IN WOOD <i>Marjan Sedighi Gilani and Erich Hugi</i>	387
MODELLING THE FIRE PERFORMANCE OF STRUCTURAL TIMBER FLOORS <i>James W. O'Neill, Anthony K. Abu, David M. Carradine, Peter J. Moss and Andrew H. Buchanan</i>	397
EXPERIMENTAL AND NUMERICAL ANALYSIS OF THE THERMO-MECHANICAL BEHAVIOR OF STEEL-TO-TIMBER CONNECTIONS IN BENDING <i>Dhionis Dhima, Maxime Audebert, Abdelhamid Bouchaïr and Mustapha Taazount</i>	407

COMPARISON OF FIRE RESISTANCE OF TRADITIONAL SOLID JOIST LUMBER AND ENGINEERED I-JOISTS <i>Venkatesh Kodur, James Stein, Rustin Fike and Mahmood Tabbador</i>	417
PARAMETRIC STUDY OF MODELLING STRUCTURAL TIMBER IN FIRE WITH DIFFERENT SOFTWARE PACKAGES <i>Norman Werther, James W. O'Neill, Phillip M. Spellman, Anthony K. Abu, Peter J. Moss, Andrew H. Buchanan and Stefan Winter</i>	427
 Numerical Modelling	
A CONTINUUM-MECHANICAL MODEL FOR FE-SIMULATIONS OF STEEL CONSTRUCTIONS IN FIRE <i>Sebastian Hauswaldt, Manfred Korzen and Stefan Hartmann</i>	439
NUMERICAL MODELLING OF CREEP IN STRUCTURAL STEEL EXPOSED TO FIRE <i>James Lee and Martin Gillie</i>	449
DEVELOPMENT OF AN INTERFACE BETWEEN CFD AND FE SOFTWARE <i>Nicola Tondini, Olivier Vassart and Jean-Marc Franssen</i>	459
FINITE ELEMENT RELIABILITY ANALYSIS FOR STRUCTURAL SAFETY EVALUATION IN FIRE <i>Qianru Guo and Ann E. Jeffers</i>	469
MODELLING OF AN EARTHQUAKE DAMAGED RC FRAME SUBJECTED TO FIRE <i>Mariyana A. Ab-Kadir, Jian Zhang, Jian Jiang, Asif S. Usmani, Martin Gillie, Umesh K. Sharma and Pradeep Bhargava</i>	479
ANALYSIS OF UNPROTECTED CONCRETE FILLED STEEL TUBE COLUMNS IN FIRE <i>In-Rak Choi, Kyung-Soo Chung and Do-Hwan Kim</i>	489
MODELLING OF PROGRESSIVE FAILURE OF CONNECTIONS AND DUCTILITY DEMAND OF CONNECTIONS IN FIRE <i>Ruirui Sun, Ian W. Burgess, Zhaohui Huang and Gang Dong</i>	499
CHEMOPLASTIC MODELLING FOR CONCRETE AT HIGH TEMPERATURE <i>Rabah Hammoud, Rachid Boukhili and Ammar Yahia</i>	509

Concrete Structures and any other Topics

BEHAVIOURS OF SEISMIC DAMAGED RC COLUMNS IN POST-EARTHQUAKE FIRE
Bo Wu and Wei Xiong 521

A MULTIAXIAL CONCRETE MODEL FOR APPLICATIONS IN STRUCTURAL FIRE
 ENGINEERING
Thomas Gernay and Alain Millard 531

RELIABILITY ANALYSIS OF STEEL PERIMETER COLUMNS UNDER FIRE
Negar Elhami Khorasani, Maria E. Garlock and Paolo Gardoni 541

RESIDUAL FRACTURE ENERGY OF CONCRETE SUBJECT TO HIGH TEMPERATURES
Yu Jiangtao, Yu Kequan, Lu Zhoudao 551

RESIDUAL AND POST-COOLING STRESS-STRAIN CURVES FOR TRADITIONAL
 AND SELF-COMPACTING CONCRETE
Emmanuel Annerel and Luc Taerwe 561

COMPRESSIVE STRENGTH AND THERMAL EXPANSION PROPERTIES
 OF GEOPOLYMER CONCRETE AT ELEVATED TEMPERATURE
Shaikh F.U. Ahmed and Vanissorn Vimonsatit 571

DETERMINATION OF FIRE SPALLING OF CONCRETE – RELEVANCE OF DIFFERENT
 TEST METHODS
Robert Jansson and Lars Boström 581

THE INFLUENCE OF PORE PRESSURE ON THE APPARENT TENSILE STRENGTH OF
 CONCRETE
Roberto Felicetti, Francesco Lo Monte and Pierre Pimienta 589

RESTRAINT FORCES INDUCED IN REINFORCED CONCRETE COLUMNS SUBJECTED
 TO ECCENTRIC LOADS AT ELEVATED TEMPERATURES
Hai K. Tan and Thang T. Nguyen 599

AN APPROACH FOR ACCOUNT FOR TIE CONFIGURATION IN EVALUATING FIRE
 PERFORMANCE OF REINFORCED CONCRETE COLUMNS
Wasim Khaliq and Venkatesh Kodur 609

PERFORMANCE IN FIRE OF FIBRE REINFORCED POLYMER STRENGTHENED
 CONCRETE BEAMS AND COLUMNS: RECENT RESEARCH AND IMPLICATIONS
 FOR DESIGN
Mark F. Green, Kevin Hollingshead and Noureddine Bénichou 619

FIRE PERFORMANCE OF PRESTRESSED I-SHAPED BEAM WITH MULTIPLE OPENINGS <i>Shigeaki Baba, Shintaro Michikoshi, Shigehiro Sakamoto and Takeo Hirashima</i>	629
DEFORMATION CHARACTERISTICS OF TWO HIGHER STRENGTH CONCRETES EXPOSED TO ELEVATED TEMPERATURES AND MECHANICAL LOADS <i>Elin A. Jensen, Brittany L. Schuel and Meenakshi Joshi</i>	639
COMPARISON BETWEEN RESULTS OF NUMERICAL SIMULATIONS AND EXPERIMENTAL TESTS ON FRP RC SLABS IN FIRE SITUATION <i>Emidio Nigro, Giuseppe Cefarelli, Antonio Bilotta, Gaetano Manfredi and Edoardo Cosenza</i>	649
HIGH TEMPERATURE CREEP DEFORMATION AND FAILURE BEHAVIOUR OF PRESTRESSING STEEL <i>John Gales, Luke Bisby and Tim Stratford</i>	659
DIRECTIONAL DEPENDENCE OF DEFLECTIONS AND DAMAGES DURING FIRE TESTS OF POST-TENSIONED CONCRETE SLABS <i>Johan Sjöström, David Lange, Robert Jansson and Lars Boström</i>	669
VERIFICATION OF CODE FIRE RATINGS OF PRECAST PRESTRESSED CONCRETE SLABS <i>Jeong-Ki Min, Anthony K. Abu, Peter J. Moss, Rajesh P. Dhakal and Andrew H. Buchanan</i>	679
PUNCHING SHEAR STRENGTH OF R/C SLABS SUBJECTED TO FIRE <i>Patrick Bamonte, Miguel Fernández Ruiz and Aurelio Muttoni</i>	689
FIRE RESISTANCE OF HOLLOW CORE SLABS. INFLUENCE OF REINFORCEMENT ARRANGEMENT <i>Jose V. Aguado, Ana Espinos, Antonio Hospitaler, Javier Ortega and Manuel L. Romero</i>	699
FIRE RESISTANCE OF HOLLOW CORE FLOORS REGARDING SHEAR AND ANCHORAGE CAPACITY <i>Wim Jansze, Arnold Van Acker, Bruno Della Bella, Ronald Klein-Holte, Gösta Lindström, Andreas Nitsch, Jean-Paul Py, Fabienne Robert and Matthieu Scalliet</i>	709
TESTING OF FULL-SCALE RC FRAME UNDER SIMULATED FIRE FOLLOWING EARTHQUAKE <i>Umesh Kumar Sharma, Virendra Kumar, Bhupinder Singh, Pradeep Bhargava, Yogendra Singh, Praveen Kamath, Asif Usmani, Jose Torero, Martin Gillie and Pankaj Pankaj</i>	719
MECHANICAL PROPERTIES OF UNDAMAGED AND DAMAGED STEEL REBARS AT ELEVATED TEMPERATURES <i>Praveen Kamath, Umesh K. Sharma, Pradeep Bhargava, N.M. Bhandari and Asif Usmani</i>	729

STEEL RING-BASED RESTRAINT OF HSC EXPLOSIVE SPALLING IN HIGH-TEMPERATURE ENVIRONMENTS <i>Toru Tanibe, Mitsuo Ozawa, Ryota Kamada and Keitetsu Rokugo</i>	737
PREVENTIVE EFFECTS OF DIFFERENT TYPES OF FIBRES ON UFC SPALLING AT HIGH TEMPERATURES <i>Mitsuo Ozawa, Zhou Bo, Yuichi Uchida and Hiroaki Morimoto</i>	747
AN EXPERIMENTAL STUDY ON REINFORCED CONCRETE COLUMNS SUBJECTED TO ECCENTRIC LOADS AND AXIAL RESTRAINT AT ELEVATED TEMPERATURES <i>Thang T. Nguyen and Hai K. Tan</i>	757
FIRE PERFORMANCE OF RESTRAINED RC COLUMNS WITH TIME-DEPENDENT SIDESWAY <i>Bo Wu and Yiaomei Chen</i>	767
GLOBAL RESISTANCE FACTOR FOR CONCRETE SLABS EXPOSED TO FIRE <i>Ruben Van Coile, Robby Caspeelee and Luc Taerwe</i>	775
EVALUATING FIRE RESPONSE OF CONCRETE BEAM REINFORCED WITH FRP REBARS <i>Baolin Yu and Venkatesh Kodur</i>	785
HYBRID FIRE TESTING OF BUILDING STRUCTURES <i>Hossein Mostafaei</i>	795
ULTRASONIC PULSE VELOCITY INVESTIGATIONS ON CONCRETE SUBJECTED TO HIGH TEMPERATURE WITH THE USE OF CYLINDRICAL AND EXPONENTIAL TRANSDUCERS <i>Izabela Hager and H�el�ene Carr�e</i>	805
FIRE ANALYSIS OF A NEW STEEL BRIDGE <i>Eric Tonicello, Sylvain Desanghere, Olivier Vassart and Jean-Marc Franssen</i>	815
FIRE RESISTANCE OF SQUARE AND CIRCULAR CROSS-SECTION CONCRETE COLUMNS <i>Jo�o Paulo C. Rodrigues, Lu�s M. dos Santos Laim and Miguel C. Gon�alves</i>	823

Authors List

PREFACE

Structural fire safety is a key consideration in the design of buildings and is attracting world-wide attention. Significant advances in research have increased the knowledge on the structural behaviour in fire. Some areas like the behaviour of steel structures in fire are becoming well understood, while others like e.g. spalling of concrete need further studies, trends that are reflected by the contribution to this conference. To make full use of these innovations and advances gained, we need a forum for the dissemination of knowledge and exchange of ideas among academics, researchers, engineers, designers, construction companies and manufacturers working in the field of structural fire engineering.

The highly successful International Conference series on Structures in Fire is considered as a major forum for the exchange of knowledge among peers by the global structural fire engineering community. The Zurich conference is the 7th in the Structures in Fire (SiF) series with the first six being held in Copenhagen (2000), Christchurch (2002), Ottawa (2004), Aveiro (2006), Singapore (2008) and East Lansing (2010). The aim of this conference is to continue the successful conference series and provide a platform for the experts and practitioners from the global structural fire engineering community to participate present and discuss recent findings, innovations and developments on an international level.

This book constitutes the Proceedings of the Seventh International Conference of Structures in Fire (SiF 2012) and contains 83 selected papers to be presented in Zurich during June 6-8, 2012. The papers were selected in a severe review process and are subdivided into six themes and chapters including Applications of Structural Fire Engineering, Steel Structures, Composite Structures, Timber Structures and Fire Protection Materials, Numerical Modelling and Concrete Structures representing the work of authors from 24 different countries around the world.

This conference was organized by members of the Institute of Structural Engineering, ETH Zurich and the fire research unit at Empa with the help, support and cooperation of the members of the International Scientific Committees, in particular the support of Professors Paulo Vila Real (Chairman of the Scientific Committee), Andy Buchanan, Jean-Marc Franssen, Venkatesh Kodur, Kang Hai Tan and Asif Usmani. We thank all expert reviewers for the time and effort they spent on the task of selecting the best papers. Our sincere thanks to all authors – the quality of the book is just the corollary of the high standard of their contributions and research activity. Finally, we would like to appreciate the effort and extraordinary support provided by the staff of ETH.

Zurich, June 2012

Mario Fontana
Andrea Frangi
Markus Knobloch

**APPLICATIONS OF
STRUCTURAL FIRE SAFETY ENGINEERING**

APPLYING THE PEER PERFORMANCE BASED EARTHQUAKE ENGINEERING METHODOLOGY TO STRUCTURES IN FIRE

David Lange*, Shaun Devaney**, and Asif S. Usmani**

* SP Technical Research Institute of Sweden, Fire Technology;
email: david.lange@sp.se

** School of Engineering, the University of Edinburgh

Keywords: Structures in fire; performance based design; PEER; fire engineering.

Abstract *The Pacific Earthquake Engineering Research (PEER) Centre's Performance Based Earthquake Engineering (PBEE) framework is an established framework for performance based engineering for extreme loading. It is well documented and has achieved considerable interest applied to earthquake engineering of structures. The framework is based on a linear process which comprises the following stages: hazard analysis; structural analysis; loss analysis and finally decision making based on variables of interest, such as downtime or cost to repair. The strength of the framework is in its straightforward description, its clear flexibility and in the consideration of uncertainty at every stage of the analysis. The framework has potential applications to other forms of extreme loading; however in order for this to be achieved the 'mapping' of the different stages to the analysis of structures for other loading situations must be successful. Using a combination of simple analytical techniques and codified methods as well as random sampling techniques to develop a range of response records, the complete PEER framework is followed to illustrate its application to structural fire engineering.*

1 THE PEER FRAMEWORK

1.1 Introduction

The PEER PBEE (Pacific Earthquake Engineering Research centre Performance Based Earthquake Engineering) framework outputs a quantified measure of the performance of a system [1]. The framework is based across three calculation 'domains': the hazard domain; the structural system domain; and the loss domain. These domains are linked by so-called 'pinch variables': the severity of an event (Intensity Measure (IM)), the structural response to the event (Engineering Demand Parameters (EDPs)), and estimation of damage and resulting losses incurred (Damage Measures (DMs) and Decision Variables (DVs)). The framework is expressed as a triple integral, Equation 1; it is shown schematically in Figure 1, including the impact of uncertainty at every stage of the analysis.

$$g_{DV} = \int \int \int P[DV | DM] dP[DM | EDP] dP[EDP | IM] dg_{IM} \quad (1)$$

The diagram shows the triple integral equation (1) with three brackets below it. The first bracket, labeled 'Loss Domain', is under the term $P[DV | DM]$. The second bracket, labeled 'Structural System Domain', is under the term $dP[DM | EDP]$. The third bracket, labeled 'Hazard Domain', is under the term $dP[EDP | IM]$.

Implicit in the form of the equation is the assumption that each of the variables in the analysis is conditionally independent. The validity of this assumption is debatable even for earthquake engineering. However for structures in fire where the form of the structure and the features of the compartment or room of origin directly influence the definition of the fire scenario (unless only the most simple nominal fire models are used such as the British Standard fire curve) this is an even more critical assumption.

The framework is comprehensively reported in a number of references, for example Porter [2] provides a simple description of the framework and its components. Additional information may be found on the PEER website. Individual modules of the PEER framework are outlined in the following sections although for a more detailed description other references should be consulted. Examples of the PEER framework adapted to and applied to other extreme loading cases exist, for example applied to wind engineering [3]. Deierlein and Hamilton [4] have also proposed that the PEER framework may be applied to fire.

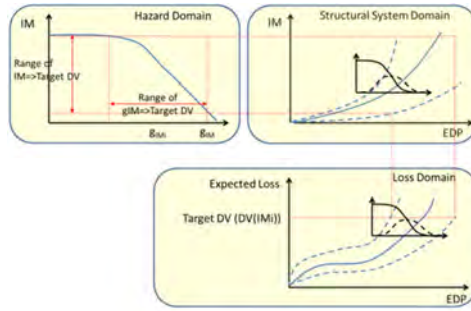


Figure 1 - schematic of the PEER framework: showing uncertainty associated with the modules which follow the hazard analysis

1.2 Hazard Domain

The hazard analysis results in the output of the intensity measure which is defined as a single or vector parameter that defines the event intensity and which quantifies the rate or probability of exceeding an intensity, $g(IM > im_i)$ per year. In PEER PBEE calculation of the intensity measure follows broadly the methodology employed in probabilistic seismic hazard analysis (PSHA), although where PSHA results in a rate of exceeding an intensity measure, the calculation required for the PEER framework results in a mean annual probability of exceedence.

In the resulting hazard curves the variable chosen to represent the intensity of the event is typically the peak ground acceleration; alternative variables may be used to measure the magnitude of an event including displacement, frequency, duration of the ground motion, etc. A sensitivity analysis should typically be carried out to investigate the sufficiency of IM's for alternative EDP's [5].

The intensity measure is illustrated by the hazard curve, which is defined by the frequency of exceeding a given intensity. This is equal to the probability of an IM im_i given that an earthquake has occurred, multiplied by the statistical rate of occurrence of an earthquake. For a single magnitude event the hazard curve is given by equation 2, r_n is the rate of occurrence of the event.

$$g_{IM_i} = r_n P(IM > im_i) \quad (2)$$

1.3 Structural System Domain

The structural analysis uses the records of perturbation from a database of earthquakes to determine

the response of the structure for each case. This may be the same set of records used in the hazard analysis, however it does not have to be so long as the resulting EDP can be expressed as a function of the IM. The output from the structural analysis is a probabilistic measure of the response of the structure which will be related to the damage analysis which follows in subsequent stages of the framework. For typical examples of the framework applied to earthquakes the EDP studied is the inter-storey drift and the DM evaluated could for example be damage to the non-structural walls. The structural analysis should reflect the response of the structure across the whole vector of the IM.

The EDP is expressed as a hazard curve, similar to the IM, defined as a vector parameter which again permits the quantification as a Poisson process of the rate of exceedance given the IM hazard curve.

$$g_{EDP} = \int P(EDP > edp_i | IM) dg_{IM} \quad (3)$$

Uncertainty in the response of the structure to a seismic event means that the structural response to a given IM has some probabilistic distribution associated with it and this may be included in the structural analysis to ensure that it is included in the EDP hazard curve.

The structural analysis often relies on a catalogue of earthquake records to determine the likely response given a peak ground acceleration (or other intensity measure) [6]. However the calculation of the structural response is based on the contents of entire records of earthquakes and not just the variable which is chosen to reflect the IM. By representing the intensity of the earthquake as a function of a single variable it follows that the distribution of the response of the structure is independent of any variation in the other variables which may be chosen to reflect the intensity and which may also affect the structure. This is a drawback of the framework. In applications of the framework the sensitivity of the EDP to the IM's is an important consideration when choosing the variable to represent the IM.

The structural analyses carried out to determine the probabilistic distribution of EDP for given IM's do not need to be deterministic and should normally include probabilistic aspects to describe uncertainty in the model such as material properties or other factors which may affect structural response.

1.4 Loss Domain

Loss analysis relies on the results of the damage analysis to derive consequence curves based on whether or not a damage state exists given the EDP hazard curve. The loss being considered may include, for example, down time or cost to repair. In PBEE consequence curves are used to provide an estimate of the annual impact of an earthquake for, e.g. budgetary reasons in order to allow developers to better assess the impact of performance based structural engineering decisions on their own project.

2. THE PEER FRAMEWORK ADAPTED TO STRUCTURAL FIRE ENGINEERING

For earthquake engineering as opposed to fire engineering, a relative wealth of independent records of earthquake events exists with libraries and databases of earthquakes in different regions being available. This is facilitated by the independence of the earthquake and the corresponding ground motion from the structure – the variables which are of interest in determining the ground motion intensity from the libraries of available data may be limited to only the distance from the fault line of the facility and the soil/ground conditions at the site. Conversely, nature of a structural fire is almost always dependent upon the form of the structure as well as its features. It may therefore be necessary to develop a suitable catalogue of fires bespoke to each structure, to determine the IM and the EDP's.

2.1 Hazard Domain

In examples of the PEER framework there are a number of different factors which may be taken as IM's, although typically peak ground acceleration seems to be used. In fire, several parameters have been historically considered to be measures of fires 'intensity'; duration, for example, as a measure of fire resistance implies that the duration of burning is a measure of the intensity. However when considered in the context of so-called real fires, the duration alone is insufficient and the fire severity may also be described in terms of parameters such as rate of increase in the temperature in a compartment, duration of

the steady burning phase, or peak temperature, etc; not to mention the impact of travelling fires

At this stage, peak temperature is taken as the IM, this was chosen based on ad-hoc analysis done during the writing of this paper and there is no suggestion that this is a fully adequate indicator of fire intensity. Future work should include studies to determine the most appropriate IM for EDP's of interest.

In order to derive the IM curve a procedure for probabilistic fire hazard analysis is mapped to the procedure for PSHA, as described below.

As mentioned, applications of the PEER framework may rely on a catalogue of representative earthquakes such as those described in [6] which are used to develop a set of characteristic responses to the loading. Work by Koo [7] details a methodology for developing a set of possible fire curves for a given compartment geometry based on a set of random input variables. Application of Koo's method provides a set of compartment fires of suitable number for stochastic purposes, but it is computationally intensive. Nevertheless, random sampling to derive a number of scenarios based on limitations of the compartment has been shown to be a suitable means of deriving a large bespoke catalogue of fires.

For this example, a parametric fire curve is used for the determination of the temperature within the compartment. This permits the variation of the fuel load, opening factor and the thermal inertia of the compartment linings when determining the compartment temperature. The output is simple and includes both a heating phase of almost non-predetermined duration and peak temperature and a linear cooling phase. The calculation required is deterministic within the Eurocodes and therefore at least one of the parameters needs to be varied in order to provide the necessary group of fire records for further analysis.

The fuel load and the actual opening factor have considerable uncertainty associated with them. Variability in the thermal inertia of the wall linings is arguably less uncertain and will be ignored here.

Eurocode 1 (EN 1991-1-2: 2002) [8] give basic data on the distribution of fire load densities for various occupancy classifications. Average fire loads are listed along with the 80% fractile fire load (Gumbel distribution). Using this data and the background documents to the Eurocodes allows for the construction of the entire distribution of fuel loads within a compartment [9], Figure 3.

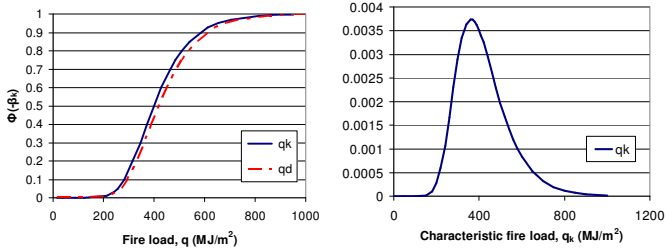


Figure 3 – CDF and PDF of the fire load in an office as a Gumbel distribution

Independent distributions also exist for the opening factor, for example the Joint Committee on Structural Safety (JCSS) probabilistic model code [10] gives an expression for a truncated log-normally distributed variable which is used as a modifier for the maximum opening factor. The Eurocode parametric fire seems to imply an opening factor which is equal to the maximum available, within certain limits, and the variation of opening factor with time or temperature is outside of the scope of the parametric fire model. Nevertheless, in order to more effectively capture the potential fire scenarios which may occur based on a parametric fire the maximum opening factor will be modified by the corresponding reduction factor obtained from the JCSS model code, Equation 4:

$$F = F_{\max} (1 - \xi) \quad (4)$$

Where F is the opening factor for calculation and F_{\max} is the maximum available opening factor based on the compartment geometry, ξ is a random log-normally distributed parameter with mean 0.2 and standard deviation 0.2 which is truncated at 1.

Using random sampling techniques, vectors of the opening factor (assuming compartment geometry)

and the fuel load are defined. Based on these vectors a sample library of fire records can be generated.

Having created the family of fires, the distribution of possible values of the peak compartment temperature is given by Equation 5 assuming that the distribution of the intensity measure may be approximated by an extreme value distribution. For this example, the cooling phase of the fire is ignored and peak compartment temperature is taken as the intensity measure.

$$p(T_{\max}) = \frac{ze^{-z}}{\beta}, \text{ where } z = e^{\frac{T_{\max} - \mu_{T_{\max}}}{\beta_{T_{\max}}}} \quad (5)$$

Where p is the probability density function, and, $\mu_{T_{\max}}$ and $\beta_{T_{\max}}$ are the mean and the shape factor of the distribution of peak compartment temperatures observed. Integrating this gives the probability of exceeding a given temperature given that a fire occurs.

The annual rate of exceeding the intensity measure is then given by the product of the annual rate of occurrence of a fire and $P(IM \geq im_i)$.

The structure to be used in the example is based on a sub-assembly from the SCI document 'Comparative Structure Cost of Modern Commercial buildings (Second Edition) [11]. The compartment is 15m by 15m and comprises 4 bays of the structure. Although the layout of the building as proposed in the SCI document is open plan, the compartment size is limited in this analysis for simplicity.

The total area of the compartment boundaries is assumed to be 612m². The height of the window openings is assumed to be 1.2m and the total area of openings is estimated to be 46.6m². The opening factor is varied according to the JCSS probabilistic model code. Using a medium fire growth rate corresponding with the fire growth rate of office buildings and the fuel load distribution as discussed above, a catalogue of parametric fires was developed based on 3000 random samples of fuel load and opening factor, Figure 5. Two extremes of fire scenario are also indicated in Figure 5 – a long-cool fire and a short-hot fire[12].

Recalling the assumption that the distribution of maximum compartment temperature can be described by an extreme value distribution the maximum compartment temperature, T_{\max} (°C), as intensity measure is plotted in Figure 6 below as well as the corresponding hazard curve, assuming the annual occurrence rate is 1/50 (although the natural fire safety concept or the JCSS propose alternative rates, the rate used is intended to be illustrative).

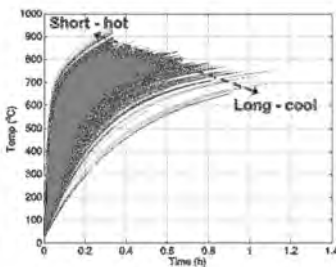


Figure 5 – Individual records of compartment temperature

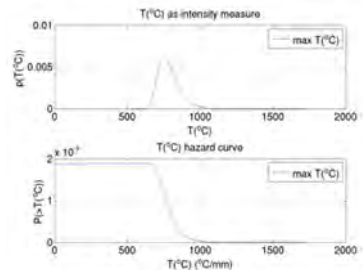


Figure 6 – Equivalent peak compartment temperature Intensity Measure and corresponding Hazard Curve

2.2 Structural System Domain

The temperature distribution through the depth of a section may be described as a thermal gradient, $T_{,z}$, and a uniform temperature increase, ΔT , using an idealized temperature distribution through the sections depth [13]. The effect of these two heating parameters on a structure may be described as a thermal force and a thermal moment [14]. These are both defined for in Equations 6 and 7 below.

$$N^T = EA\alpha\Delta T \quad (6)$$

$$M^T = E \frac{d^3}{12} \alpha T_{,z} \quad (7)$$

Where E is Young's modulus of elasticity, A is the area of the section, d is the depth of the section and α is the coefficient of thermal expansion. The value of both of these parameters is dependent upon the heat transfer through the section as well as upon the material properties of the section. The fire structure interaction model is based on an analysis of the section to determine the equivalent temperature increase and the equivalent through depth thermal gradient.

The stress distribution throughout the composite member is dependent on the structural form of the member, the temperature distribution through the member and the mechanical loading. The analysis procedure is simplified by dividing the cross section into horizontal slices. The stress and strain values are then calculated at the boundaries of these slices.

Heat transfer analysis in Steel is Carried out using a stepwise function, outlined in Eurocode 3 [15]. The heat transfer through concrete is a marginally more complicated matter. For the parametric fire curve chosen a 1-d finite difference heat transfer analysis is used.

Lamont et al. describe the response of a structure to a long-cool and a short-hot fire [12] (both of the extremes shown in Figure 5). The short-hot fire results in a higher peak temperature and, due to the short duration of the heating phase of the fire, a larger thermal gradient within the structure. This causes large thermal moments which induce bowing within a structure and a tensile force within, for example, a composite section. Correspondingly, a long-cool fire will have a much more uniform temperature distribution through a section. This will cause large compressive forces to develop within an element exposed to fire which must be accommodated by the surrounding structure. The result is a more uniform temperature throughout the depth of the composite section during a long cool fire as opposed to the steeper gradient of temperature through the depth of the short hot fire.

The response of the floor system to fire is based on the assumption that the floor system acts in a tensile membrane mechanism. The derivation of this is outlined in more detail in other articles [16], [17] however for this example a 2-dimensional variant is used as briefly discussed in [14]. In summary, the method is based on the steel within the floor system providing a catenary support to the applied loading, assuming that the ends are fully restrained against translation but not rotation and ignoring any capability of the concrete within the floor to provide any load resistance. This methodology has three stages: calculation of the temperature distribution through the depth of the member; calculation of the deflected shape of the member, based upon the gross cross-sectional area, and the stresses and strains in the reinforcing bars associated with this deflected shape and steel temperature; and calculation of the load carrying deflection and the internal and external work done to move from the thermal deflection to the required deflection, the internal work done is based on the steel reinforcement only and ignores any contribution from the concrete.

It is proposed to use the total deflection required to carry the load as the engineering demand parameter. This is analogous to an EDP commonly used for PEER PBEE: inter-storey drift.

Details of the structure are as follows: the assembly is a composite steel concrete section comprising a primary beam, UK section 305 x 165 x UB40 of 7.5m width, underneath a ribbed concrete deck with minimum thickness 70mm at the troughs and maximum thickness at the ribs of 130mm; reinforcing steel in the analysis is assumed to comprise of only the A193 anti-cracking mesh located at mid – height of the floor and, for the purposes of the 1-dimensional analysis, the width of the concrete portion acting compositely with the steel is assumed to be $\frac{1}{4}$ of the effective length, in accordance with Eurocode 4 [18].

The floor assembly is restrained at one end by the adjacent floor plate and structure in the adjacent bays and at the other end by a perimeter beam and column assembly.

In order to evaluate the engineering demand parameter and to derive the corresponding hazard curve,

the cumulative distributions of the engineering demand parameter are integrated with respect to the probability of exceedance of the intensity measure, equation 8.

$$g_{EDP_i} = \int P(EDP \geq edp_i | IM) dg_{IM} \quad (8)$$

Figure 8 shows the individual records of the EDP's for the sample of fires. This is the same set of fires which were used to derive the IM curve in the previous section. The left hand plot is the IM plotted against the annual probabilities of exceedance, and the right hand plot is the IM plotted against the EDP – the right hand plot shows all of the records of the EDP. Figure 8 also shows schematically an example of a discrete distribution of $P(EDP \geq edp_i | IM)$.

In order to determine the hazard curve for the EDP, the integral in Equation 21 is evaluated numerically. For the range of IM's, the density function $p(EDP)$ is estimated assuming that it is an extreme value distribution and the $P(EDP \geq edp_i | IM)$ is determined. This is then integrated with respect to $P(IM \geq im_i)$. Figure 9 shows the resulting hazard curve of the total deflection.

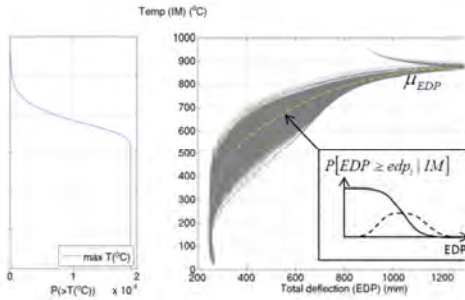


Figure 8 – Individual records of thermal deflection against compartment temperature (right hand graph) plotted alongside intensity measure hazard curves (left hand curve)

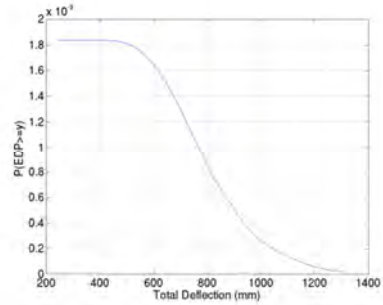


Figure 9 – Total deflection hazard curve

2.3 Loss Domain

The damage measures (DMs) provide a means to quantify the damage done to the structure. A fragility function was assumed based on the EDP to categorise the level of damage done to the composite beam caused by a given value of an EDP. In each case there are three levels of damage state, DM0, DM1 and DM2. The element is in DM0 when the level of the EDP is insufficient to cause any damage to the structure. The element enters DM1 when the EDP rises to a level where damage is caused to the element, but it is not beyond repair. DM2 applies when the EDP is such that the element is assumed to damage which may require its replacement or there is local collapse. In the future, when more information becomes available regarding potential losses resulting from structural damage and the damage states are more rigorously defined, additional damage states and real (as opposed to assumed) fragility functions may be included to give a more realistic and complete estimate of the losses.

For the definition of the damage states associated with thermal deflection of the floor, the residual deflection of the floor following fires is considered. It is observable in the reports of the Cardington tests [19] as well as other reported tests on pre-stressed and composite floor slabs in fire [20] that following heating up to $\frac{1}{4}$ of the total deflection observed at the end of heating was recovered. Since cooling is not explicitly included within the analysis, the final thermal deflection at the end of the heating phase of the fire is taken as being the final deformation for determination of the DM later. Since recovery of the deflection during cooling would intuitively lead to a relaxation of the tensile forces observed in the steel reinforcement and in any steel beams present this is a conservative assumption at this stage.

The deflection limit for DM1 is assumed to be 30mm, and the deflection limit for DM2 is assumed to

be 130mm. These are assumed values and are arbitrarily chosen. It is assumed that a deflection of up to 30mm may be addressed without the requirement for considerable structural repair work since it is less than 1/3 of the total depth of the concrete section including the ribs and is given as the recommended deflection limit in Eurocode 2. Anything over 130mm, which is equal to the total thickness of the concrete floor plate, is assumed to be irreparable and will require replacement. Standard deviations of both of these damage states are assumed to be 0.0001mm. These normally distributed variables are the conditional probabilities of the DM exceeding the damage state given a state of EDP, i.e. $P(DM|EDP)$.

The initial build cost for this part of the structure was calculated from the SCI document [11] and was then used to normalise the repair costs. The repair times have been estimated based on the repair work which is required. The repair times are normalised against the initial build time of the member, which is given as 5 days. Both the repair costs and the repair times have been assigned a lognormal distribution, the distributions of costs and repair times are summarised in Table 1 (for the lognormal distributions the mean values are given as a function of μ and σ , $mean = \exp(\mu + \sigma^2/2)$).

Table 1 – Summary of assumed DM1 damage states, assumed repair times and assumed repair costs

	μ	σ	Distribution type
Repair time (DM1)	1.120	0.3	Lognormal
Repair time (DM2)	2.403	0.3	Lognormal
Repair cost (DM1)	-1.311	0.3	Lognormal
Repair cost (DM2)	0.519	0.3	Lognormal

Figure 10 shows the cost consequence functions and repair time consequence functions associated with damage states of the reinforcement strain.

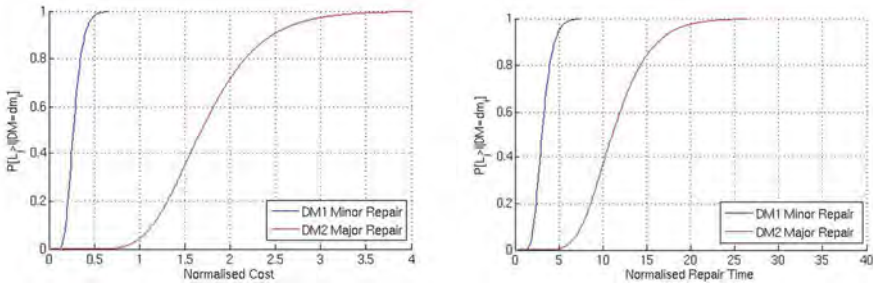


Figure 10 - Cost Consequence Functions and Downtime Consequence Functions associated with total deflection

The decision variables (DV) are the final outputs from the PEER framework. They are a quantification of the likely mean annual losses incurred as a result of an event leading to an unknown level of structural damage. Each DV is probabilistically related to a DM and each DM may have multiple DVs associated with it. The types of losses which may be measured as DVs are repair costs, repair times or casualties/injuries. The preceding analysis examined the effects of the fire on the structure only and because of this the repair costs and repair times have been calculated solely for the structure of the building. By integrating the DM resulting from an EDP with respect to the probability of the EDP occurring, as shown above, the frequency of exceeding a value of loss, or a period of downtime per year can be estimated. The integral to be evaluated is:

$$g_{DM_i} = \int P(DM \geq dm_i | EDP) dg_{EDP} \quad (9)$$

In order to evaluate equation 9, the probability of exceeding a given DM, $P(DM \geq dm_i | EDP)$ must be

determined. Recognising that DM1 is exclusive of DM2 but DM2 is not exclusive of DM1, for the stepwise DM described above, this is given by:

$$P(DM \geq dm_i | EDP) = P(DM1 | \overline{DM2}) \times P(dm_i(DM1)) + P(DM2) \times P(dm_i(DM2)) \quad (10)$$

Equation 9 may be evaluated numerically to obtain the annual costs and downtimes associated with EDP discussed, Figure 12. The annual frequency of incurring any loss is consistently set to 1.8×10^{-3} . This is the annual frequency of any of the events shown throughout the analysis for each of the stages of the framework and is the result of the initial probabilistic calculation of the likelihood of a structurally significant fire starting. It is the rate of drop off of the costs and downtime which are of interest.

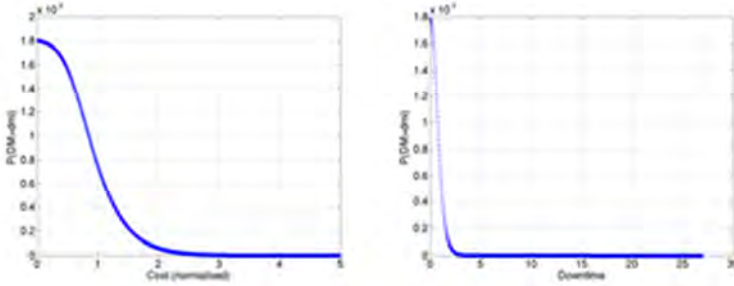


Figure 12 - Probabilistic annual repair cost and downtime associated with total deflection

3. DISCUSSION AND CONCLUSIONS

In the SCI publication, the cost for the structure is quoted as between £83 and £108/m² and the cost for protection between £12.70 and £32 /m². Based on the frequency of costs to repair exceeding the initial build costs, the owner may budget less than a tenth of a per cent per annum of the build costs to repair the structure whereas protection could add as much as 38% to the cost of the structure. This obviously ignores the cost of room fittings, services and furnishings – however in the event of a structurally significant fire these are very likely to require repair or replacement regardless of the provision of structural protection. This type of information may be used to influence decisions as to whether or not the structure should be protected, under the condition that it may be shown to sustain the applied load in fire for the duration of an analysis.

A number of assumptions have been made in the paper, in particular with reference to the reparability of fire damaged composite structures and the costs associated with this. There is little information in the literature and the majority of this is focussed on steel or concrete structures rather than composite construction. The material is also several years old and does not give any indication of the costs of repair. These are based in this paper upon the initial construction costs. Further information on damage states, the costs associated with the repair of fire damaged structures, as well as downtime associated with repair and the identification of alternative damage measures will most likely require a dialogue on this subject with industry.

An apparent disconnect between fire engineering and structural fire engineering provides reasonable justification at this time for the use of the parametric fire, however the impact of different fire models on the results of the framework should be considered in future research. The computational resources required to run numerous FE analyses to illustrate the application of the framework to Structural Fire Engineering have driven the authors to employ simpler analytical models in this paper although future iterations will consider different structural models which will allow the exploration of alternative EDPs

and DMs.

REFERENCES

- [1] "PEER: Pacific Earthquake Engineering Research Center," 2011. [Online]. Available: <http://peer.berkeley.edu/>. [Accessed: 03-Oct-2011].
- [2] K. A. Porter, "An Overview of PEER's Performance-Based Earthquake Engineering Methodology Keith A. Porter," in *Ninth International Conference on Applications of Statistics and Probability in Civil Engineering (ICASP9)*, 2003, no. 1995.
- [3] F. Petrini, M. Ciampoli, G. Augusti, and S. Università, "A probabilistic framework for Performance-Based Wind Engineering," *Wind Engineering*, 2009.
- [4] G. G. Deierlein and S. Hamilton, "Framework for Structural Fire Engineering and Design Methods," 2003.
- [5] J. W. Baker and C. A. Cornell, "PACIFIC EARTHQUAKE ENGINEERING Vector-Valued Ground Motion Intensity Measures for Probabilistic Seismic Demand Analysis," 2006.
- [6] G. G. Deierlein, H. Krawinkler, and C. A. Cornell, "A Framework for Performance-Based Earthquake Engineering," in *2003 Pacific Conference on Earthquake Engineering*, 2003.
- [7] "Forecasting fire development with sensor-linked simulation," 2010.
- [8] "BS EN 1991-1-2:2002. Eurocode 1: Actions on structures - Part 1-2: General actions-Actions on structures exposed to fire." BSI, 2002.
- [9] "IMPLEMENTATION OF EUROCODES - Handbook 5 - Design of Buildings for the Fire Situation," 2005.
- [10] "JCSS Probabilistic Model Code - Part 2: Load Models." The Joint Committee on Structural Safety, p. 73, 2001.
- [11] S. J. Hicks, R. M. Lawson, J. W. Rackham, and P. Fordham, *Comparative Structure Cost of Modern Commercial Buildings*, Second. Ascot, Berkshire: The Steel Construction Institute, 2004, p. 96.
- [12] S. Lamont, A. S. Usmani, and M. Gillie, "Behaviour of a small composite steel frame structure in a 'long-cool' and a 'short-hot' fire," *Fire Safety Journal*, vol. 39, no. 5, Jul. 2004.
- [13] A. S. Usmani, "Understanding the Response of Composite Structures to Fire," in *North American Steel Construction Conference*, 2003.
- [14] N. J. K. Cameron, "The Behaviour and Design of Composite Floor Systems in Fire," The University of Edinburgh, 2003.
- [15] "EN 1993-1-2:2005 Eurocode 3: Design of steel structures part 1.2 General rules - Structural Fire Design." 2005.
- [16] N. J. K. Cameron and A. S. Usmani, "New design method to determine the membrane capacity of laterally restrained composite floor slabs in fire Part 1: Theory and method," *The Structural Engineer*, no. October, pp. 28-33, 2005.
- [17] N. J. K. Cameron and A. S. Usmani, "A new design method to determine the membrane capacity of laterally restrained composite floor slabs in fire Part 2: Validation," *The Structural Engineer*, no. October, pp. 34-39, 2005.
- [18] "BS EN 1994-1-1:2004. Eurocode 4: Design of composite steel and concrete structures — Part 1-1: General rules and rules for buildings." BSI, p. 122, 2004.
- [19] "The behaviour of multi-storey steel framed buildings in fire," 1999.
- [20] L. . Ashton, "Fire Research Note No 54 – Prestressed concrete during and after fires, comparative tests on concrete floors in prestressed and reinforced concrete," 1953.

APPLICATION OF STRUCTURAL FIRE ENGINEERING TO AN ITALIAN TALL OFFICE BUILDING

Emidio Nigro*, Giuseppe Cefarelli*, Anna Ferraro*,

Iolanda Del Prete*, Domenico Sannino* and Gaetano Manfredi*,

* Department of Structural Engineering – University of Naples Federico II
e-mails: emidio.nigro@unina.it, giuseppe.cefarelli@unina.it, ferraroanna@gmail.com,
iolandadelprete@hotmail.it, mimmosannino@hotmail.it, gamanfre@unina.it

Keywords: Fire Safety Engineering, Sub-structure, Advance Calculation Models, Steel, Concrete.

Abstract. *Fire Safety Engineering (FSE) is a multi-discipline aimed to define the fire safety strategy for buildings in fire situation, in which structural stability and control of fire spread are achieved by providing active and/or passive fire protection system. In the following the main aspects of FSE for the structural safety checks in case of fire (Structural Fire Engineering) are shown with reference to Italian and European standards.*

FSE requires the choice of performance levels, the definition of design fire scenarios, the choice of fire models and generally advanced thermo-mechanical analyses. In the following the application of Structural Fire Engineering (namely the structural behaviour in fire situation) to an existing tall building will be described. This activity is still in progress; nevertheless, the paper provides enough information concerning the structural characteristics of the buildings, the choice of safety performance levels, the active and passive protection systems of the buildings, the identification of fire scenarios through Risk-Ranking approach and, finally, preliminary thermal and structural analyses.

1 INTRODUCTION

According to ISO/TR 13387-1 [1], the “Fire Safety Engineering” (FSE) is the application of engineering principles, rules and expert judgement based on a scientific assessment of the fire phenomena, the effects of fire and both the reaction and behaviour of peoples, in order to: save life, protect property and preserve the environment and heritage; quantify the hazards and risks of fire and its effects; evaluate analytically the optimum protective and prevention measures necessary to limit, within prescribed levels, the consequences of fire.

Current Italian and European codes ([2], [3], [4], [5]) allow the use of a performance approach through the concept of FSE. The temperature distribution within the elements and the mechanical and geometric nonlinear structural response are taken into account in the fire performance approach.

The Directive 89/106/CEE [6] on Construction Products of the European Community introduced the definition of the requirement of “safety in case of fire” in Europe, which is the base for the application of the FSE. This requirement, implemented in the National Codes of European member countries, is explained by achieving the following five objectives: the load-bearing capacity of the construction can be assumed for a specific period of time; the generation and spread of both fire and smoke within the works is limited; the spread of fire to neighbouring construction works must be limited; occupants have to be able to leave the works or be rescued by other means; the safety of rescue teams must be taken into consideration.

The FSE allows a more accurate adjustment of the safety measures at specific risk of the building through qualitative and quantitative criteria (namely acceptance criteria), which are agreed with the building approval authority and hence form an acceptable starting point for assessing the safety of a building design.

The European codes for structural fire safety are the “Fire Parts” of Structural Eurocodes.

In Italy, the new Technical Code for Constructions was published in 2008 [5]. For the first time in Italy, the fire action is introduced within the definition of the actions on constructions, as an “exceptional load”. The document defines the performance safety levels of buildings according to the safety objectives required by the Directive 89/106/CEE [6]. The Italian Technical Code for Constructions defines five safety performance levels depending on the importance of the building, which establish the damage level that can be accepted. These rules define the fire structural performance requirements and they refer to specific technical codes issued by the Italian Ministry of Interior for all activities under the control of the National Fire Brigades ([7], [8]).

2 CASE STUDY: TOWER OF AN EXISTING TALL BUILDING

In the following the application of Structural Fire Engineering (namely the structural behaviour in fire situation) to an existing tall building, intended for office use, is described. The tower, with 29-storeys, extends from a height of 11.45m to a height of 112.50m above sea level. The tower is characterised by reinforced concrete central cores and, from 30.00m above sea level, perimeter steel beams and columns. These latter are protected by several passive protection systems.

2.1 Building description: analysis of the structural characteristics

The tower is 101.00m high and has 29-storeys above the ground. The floor can be divided into four zones, named (see Figure 1a): 1) Lamellare, 2) Emicicli, 3) Nucleo, 4) Antinucleo. In particular the third and fourth zone, made of reinforced concrete, represent the bracing and seism-resistant structures of the Tower at each floor. Other stiffening reinforced concrete structures (Figure 1b) are: stairwells, omega wall and coupled columns. Until 30.00m above sea level the bracing structures are connected to a reinforced concrete framed structure, having large beams and columns, whereas, from 30.00m above sea level, for 25 storey, the bracing structures are connected to steel frames with interstorey equal to 3.30 m.

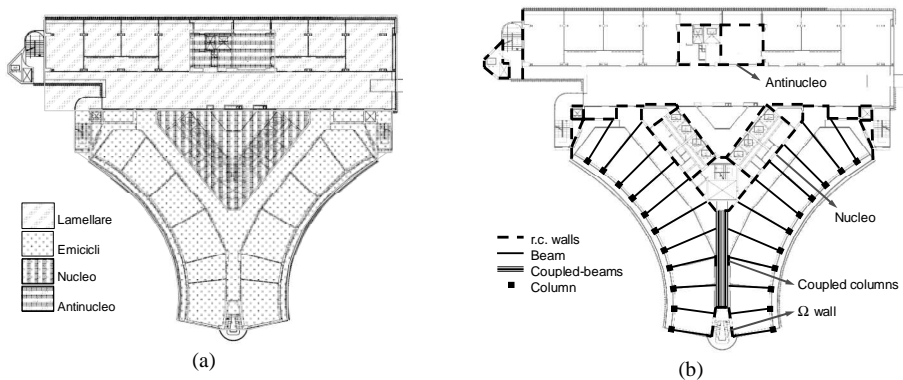


Figure 1 Tall office building: (a) Floor Map, (b) Structural elements

2.2 Choice of safety performance level

In the case study, the main objective of fire safety checks concerns the mechanical resistance and stability, in fire situation, of the tower. In agreement with the Fire Brigades and Owner, the safety

performance level required for the structure is assumed as: “maintaining the fire resistance requirements, which ensure the lack of partial and/or complete structural collapse, for the entire duration of the fire”.

In addition, with reference to some scenarios (the most probable fire scenarios which involve the effectiveness of active protection systems), a limited structural damage after the fire exposure has been also required.

2.3 Active and passive fire protection systems

The tower is equipped with several active protection systems: fire sprinklers system, fire hydrants and fire extinguishers. The building is not equipped with any smoke or heat evacuation systems. Each floor of the tower have 4 fire exits on external stairways and 1 fire exit on internal separated stairways equipped with 2 fire doors REI 120. Each floor can be divided in 3 fire compartments [9].

Both steel beams and columns are protected by gypsum boards.

2.4 Fire Scenarios and Fire models

The design fire scenario is a qualitative description of the fire development during the time, identifying key events that characterise the fire and differentiate it from other possible fires. It typically defines the ignition and fire growth process, the fully developed stage, decay stage together with the building environment and systems that will impact on the course of the fire.

In general, the number of distinguishable fire scenarios is too large to permit analysis of each one. In this case the choice of the design fire scenarios is carried out by Fire Risk Assessment. Really, the Fire Risk Assessment allows to individuate scenario structures of manageable size and allows to make the case that the estimation of fire risk based on these scenarios is a reasonable estimation of the total fire risk [10]. The Fire Risk Assessment takes into account the consequence and likelihood of the scenario. Key aspects of the process are: identification of a comprehensive set of possible fire scenarios; estimation of probability of occurrence of each fire scenario; estimation of the consequence of each fire scenario; estimation of the risk of each fire scenario (combination of the probability of a fire and a quantified measure of its consequence); ranking of the fire scenarios according to their risk.

The Fire Risk Assessment is performed through the event tree approach, according to ISO-16732 Guidelines. A fire scenario in an event tree is given by a time-sequence path from the initiating condition through a succession of intervening events to an end-event. Each fire scenario corresponds to a different branch of the event tree, and the branches collectively comprise or represent all fire scenarios. The following main events, that may affect the development of the fire, are considered: first aid suppression, alarm activation (smoke detectors), sprinklers activation, sprinklers suppression, barrier effectiveness.

In Figure 2 the event tree obtained combining the main events and the risk ranking are reported.

Probability of occurrence of each event and consequence value of each fire scenario is obtained both by direct estimation from available data ([11], [12], [13], [14]) and engineering judgment (see Figure 2).

The consequence value is expressed as a fraction of the economic value of the building. For each fire scenario the relative risk (R) is evaluated by multiplying the measure of the consequence (C) by the probability of occurrence of the scenario (P):

$$R = P \cdot C \quad (1)$$

The highest fire risk is for the **Scenario SS7a** for which: first aid suppression failed; alarm activation failed; sprinklers activation failed; barrier effectiveness. Therefore, fire scenario SS7a is a design fire scenario: the structure is required to “maintain the fire resistance requirements, which ensure the lack of partial and/or complete structural collapse, for the entire duration of the fire”.

Moreover, another design fire scenario is fire **Scenario SS5**, characterized by a higher probability of occurrence, for which limited damages are allowed for the structure.

Finally, secondary events that can be significant are: doors state (open or closed) and windows state (open or closed). The state of the secondary events will be considered inside the fire model as well as the location of fire ignition. The post-flashover fire is modelled by one-zone model, which assumes homogeneous temperature, density, internal energy and pressure of the gas in the compartment.

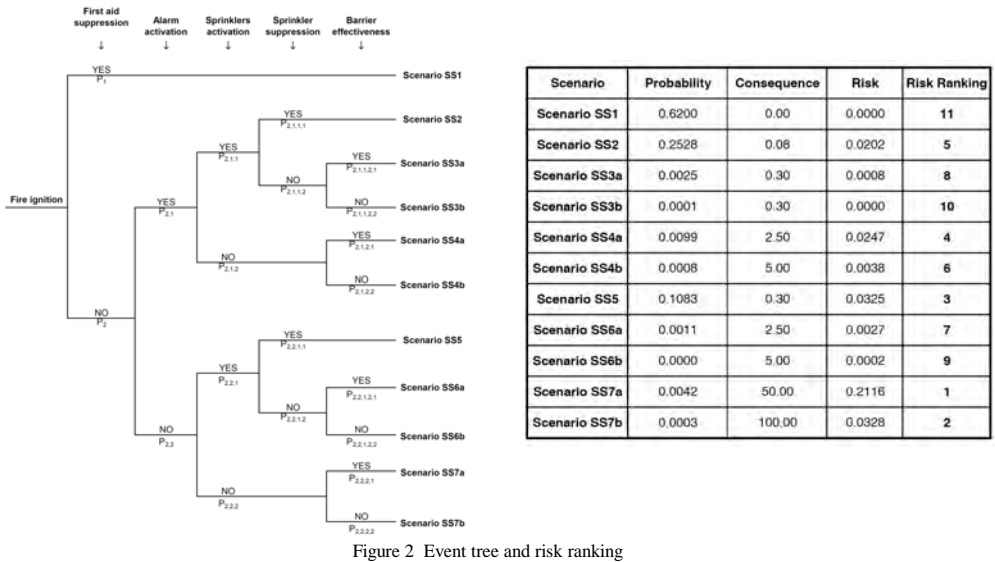


Figure 2 Event tree and risk ranking

2.5 Substructure identification by means of preliminary analyses

In the case study, due to the building’s large size, in order to reduce the computational time the *substructure analysis* is adopted, according to Eurocode suggestion. Several preliminary analyses allow to define the substructures limits and boundary conditions. The aim of the substructure analysis is to evaluate the structural fire response through the modelling of significant parts of the entire structure. The designer has the responsibility to choose the substructure in such a way that the hypotheses on the constant boundary conditions are reasonable and correspond at least to a good approximation of the real situation [15].

Preliminary analyses are carried out on a 25-storey plane frame extracted from the “Emicicli” zone (Figure 4); this simplification is possible because the RC slab is designed as simply supported by primary beams. In these preliminary analyses the structural members are considered without protection systems. The analyzed frame has been chosen in order to analyze structural members with the maximum degree of utilization at time $t = 0$ ($E_{d,ff}/R_{d,ff,0}$). All members (beam-column and beam-concrete wall) are connected by pinned joints.

The preliminary analyses are carried out adopting the standard time-temperature ISO834 [16], with the only purpose of defining the substructure, which should represent the global structural behaviour: really, ISO834 curve allows a direct comparison in term of fire resistance time. Two fire positions are considered (see Figure 3) in order to evaluate possible column’s buckling phenomenon due to fire scenarios localized on floors in which there is the change section of the columns.

The considered substructure (see Figure 5) is made by the beam and column exposed to fire and by the cold column above the compartment, which contributes to translational and rotational constraint of nodes of exposed structure. Regarding the boundary conditions, the part of structure above the cold column keeps stiffness, so it’s replaced by rigid restraint. Moreover, vertical displacements of cold column are allowed in order to transfer the loads from the above structure. Finally, the cold part of structure below the exposed compartment becomes stiffer than the heated part, so that it is replaced by rigid restraint. The comparison between thermo-mechanical behaviour of considered substructures and the 25-storey plane frame one (entire structure) allows to evaluate the validity of the substructure, for which the thermo-mechanical behaviour is analysed with reference to natural fire curves.

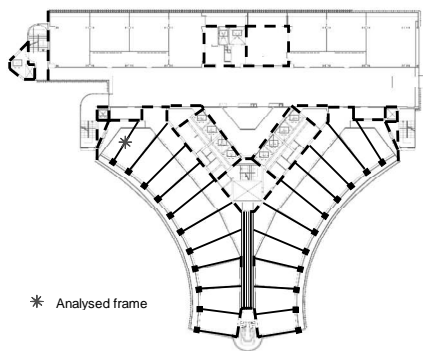


Figure 3 The analysed frame

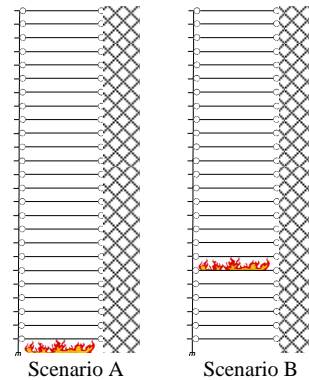


Figure 4 Fire scenarios: possible position along height

As previously said, post-flashover fire is modelled by one-zone model. Numerical fire analyses are performed by using the non linear software SAFIR2011 [16], developed at the University of Liege (Belgium). The fire resistance time reported in Figure 5 show that the substructures (one for each fire scenario) are able to represent the global structural behaviour. The results clearly show that columns are the weakest element in the structure: in fact failure occurs due to the columns failure. In the preliminary analyses, the latter are unprotected thin square hollow steel sections (350mmX350mmX12.5mm for Scenario A and 350mmX350mmX10mm for Scenario B), while a concrete coating protects steel beams (HE260B) by fire exposure. Column, loaded with constant axial force during fire exposure, fails mainly due to buckling, that clearly occurs for reduction of steel stiffness and strength produced by heating.

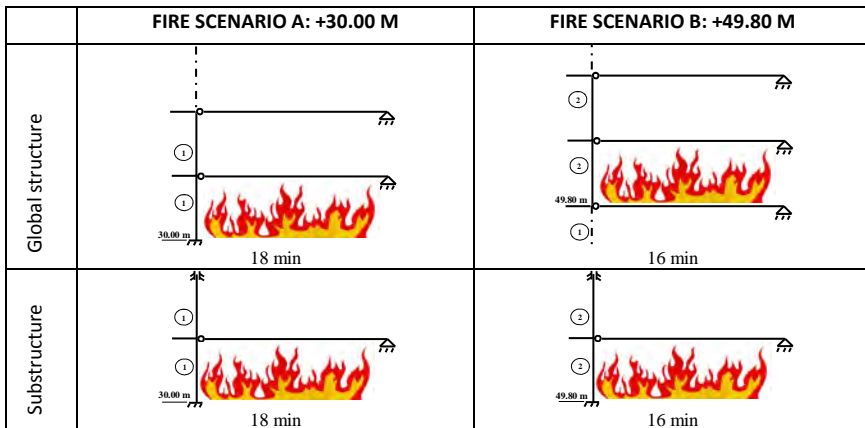


Figure 5 Analyses results.

Accordingly, analyses results on global structure (see Figure 6) show that the minimum fire resistance occurs when fire involves the thinnest column (fire scenario B). Really, the latter is characterized by a section factor (A_m/V) bigger than the thickest column: the highest section factor produces a fast thermal degradation of the thinnest column. As concerns the comparison between substructure and global structure (see Figure 7), approximately the same time of collapse is attained, because the stiffness of beams is not able to affect the axial force in the columns.

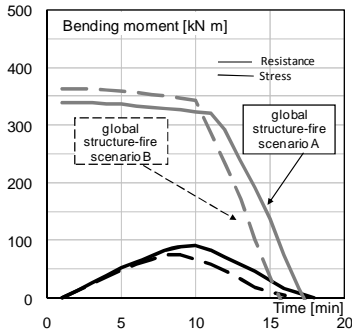


Figure 6 Acting bending moment and Resistance capacity to combined compression and flexure on the heated column of global structure – comparison between fire position A and B.

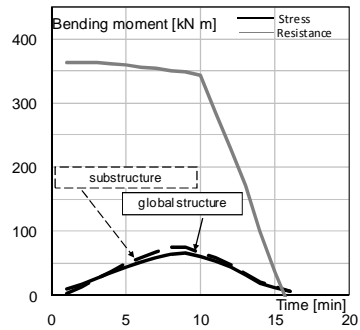


Figure 7 Comparison between global structure and substructure results – Fire position B.

2.6 Thermo-mechanical analyses with reference to the selected fire scenarios

Subsequent analyses are carried out on substructure characterized by the thinnest tubular columns (350mmx350mmx10mm) and HE260B beams (partially encased with concrete). Both steel beams and columns are protected by gypsum boards.

As previously said, the scenario with the highest risk is Scenario SS7a for which: first aid suppression failed; alarm activation failed; sprinkler activation failed; barrier effectiveness.

2.6.1 Fire Scenario SS7a - Fire model and structural behaviour

Fire curve (see Figure 9) is obtained by a one-zone model, deduced applying Ozone software [17]. Figure 8 shows the RHR curves obtained in accordance with EN1991-1-2 [2]. The characteristic fire load densities Q [MJ/m²] is assumed equal to 1000MJ/m² and 750MJ/m². The latter, according to office use for the building, is obtained multiplying the reference value 511 MJ/m² (80% Fractile as given in Table E.4 of EN1991-1-2 [2]) by the ratio “compartment area/rooms area”.

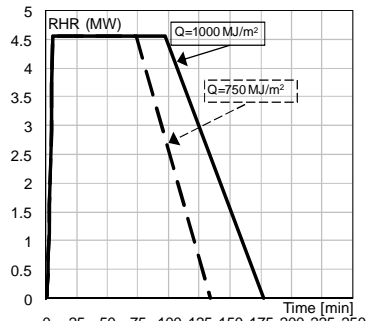


Figure 8 Rate of Heat Release curves

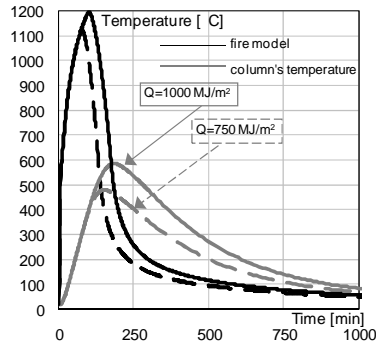


Figure 9 Comparison between fire curve and column temperature

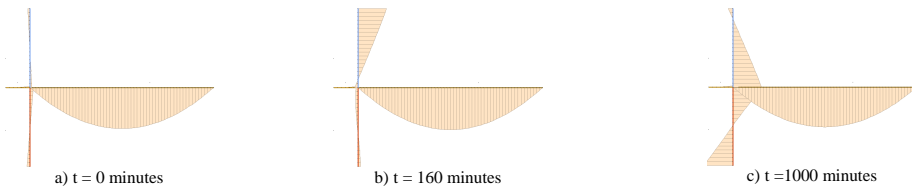


Figure 10 Bending moment during thermal transient ($Q=1000 \text{ MJ/m}^2$)

Heated column suffers indirect actions during fire exposure (Figure 10) such as bending moment due to beam's prevented thermal expansion and displacement of the top of heated column. Nevertheless, when the effect of beam's prevented thermal expansion is maximum (about 160 minutes, as shown in Figures 14 and 18) displacement and bending moment at the top of the column reduces. As shown in Figure 10 b), the higher stiffness of cold column produces a high bending moment on cold column top. The higher bending moment on heated column, at the end of the thermal transient, is due to stiffness recover during the cooling phase. Comparison between normal stress and yielding stress, during fire exposure time, shows that no significant plastic strains occur in heated column (see Figures 12 and 16).

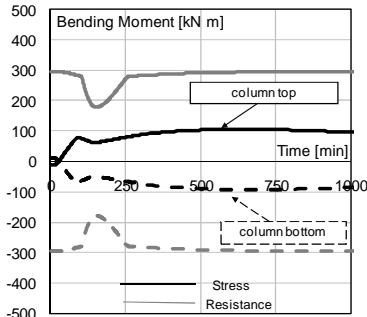


Figure 11 Bending moments and Resistance capacity to combined compression and flexure on heated column ($Q=750 \text{ MJ/m}^2$)

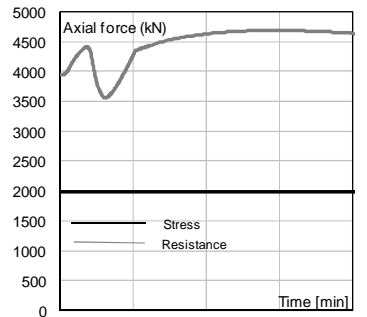


Figure 13 Axial force and Resistance capacity to combined compression and flexure on heated column ($Q=750 \text{ MJ/m}^2$)

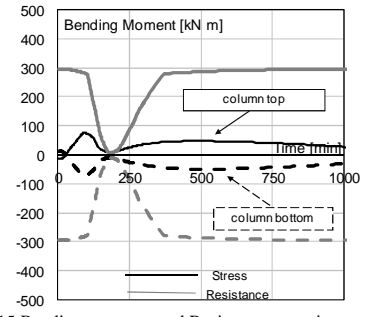


Figure 15 Bending moments and Resistance capacity to combined compression and flexure on heated column ($Q=1000 \text{ MJ/m}^2$)

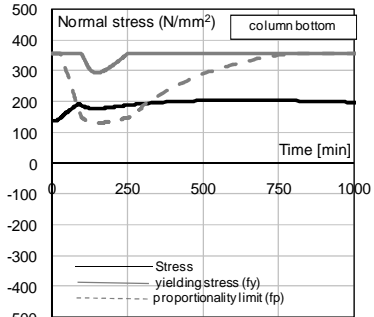


Figure 12 Comparison between normal stress, proportionality limit and yielding stress in heated column ($Q=750 \text{ MJ/m}^2$)

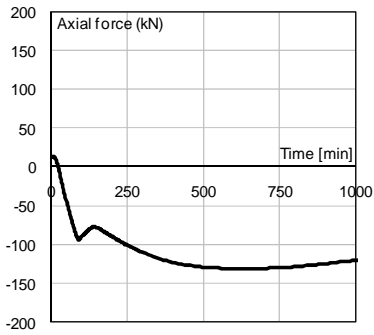


Figure 14 Axial force in heated beam ($Q=750 \text{ MJ/m}^2$)

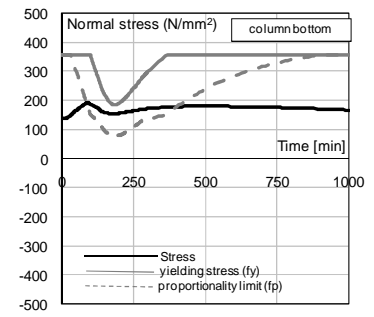


Figure 16 Comparison between normal stress, proportionality limit and yielding stress in heated column ($Q=1000 \text{ MJ/m}^2$)

Comparison between stress and resistance in heated column, when the load density is considered equal to 750 MJ/m^2 , shows that bending moment and axial force are less than resistance capacity to combined compression and flexure (see Figures 11 and 13).

When the load density is considered equal to 1000 MJ/m^2 , column is very close to collapse condition (see Figures 15 and 17), but failure doesn't occur.

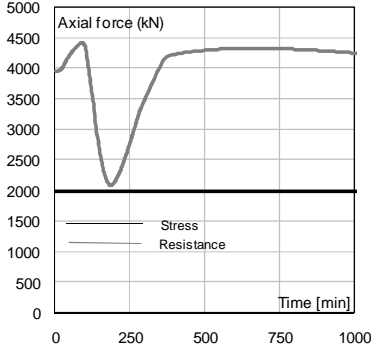


Figure 17 Axial force and Resistance capacity to combined compression and flexure in heated column ($Q=1000 \text{ MJ/m}^2$)

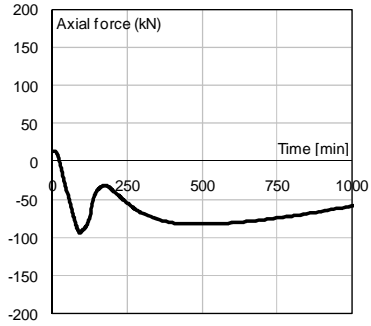


Figure 18 Axial force in heated beam ($Q=1000 \text{ MJ/m}^2$)

2.6.2 Fire Scenario SS5 - Fire model and structural behaviour

Fire scenario SS5 is considered in order to evaluate the effect of the sprinkler activation on the structure. As shown in Figure 19 the fire is extinguished and the heat release rate decreases to zero after some decreasing time [18]. The load density considered is equal to 1000 MJ/m^2 . Therefore, in the following is considered the most conservative event in which the fire is simply controlled by the extinguishing agent, the increase of heat release rate is stopped and the fire continues to burn at a constant rate [18] (see Figure 19). In the case in which the fire is controlled by the sprinkler system, the duration of the fire is obtained by an equivalence of the area under curve between this scenario and the ones in which the sprinkler system fails.

2.6.3 Fire Scenario SS6a - Fire model and structural behaviour

Thermal behaviour is very similar to the case in which sprinkler activation fails. In fact, comparison between fire scenarios SS7a and SS6a shows that column's temperature achieves approximately the same temperatures, as shown in Figure 20. Therefore, approximately the same structural behaviour is attained.

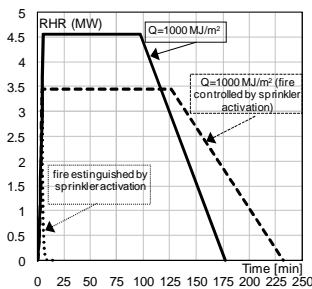


Figure 19 Rate of Heat Release curves

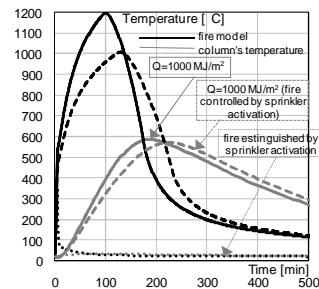


Figure 20 Comparison between fire curve and column temperature

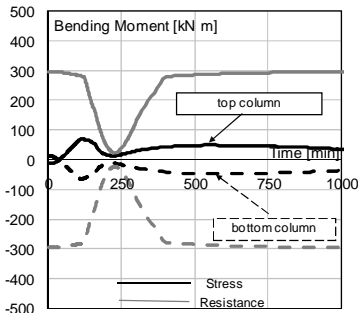


Figure 21 Bending moments and Resistance capacity to combined compression and flexure on heated column ($Q=1000 \text{ MJ/m}^2$)

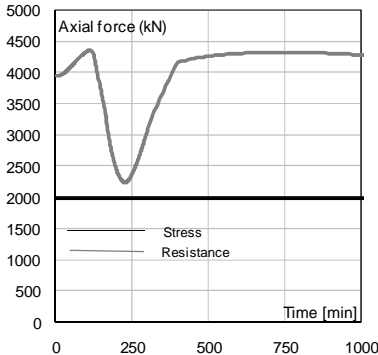


Figure 23 Bending stress and Resistance capacity to combined compression and flexure on heated column ($Q=1000 \text{ MJ/m}^2$)

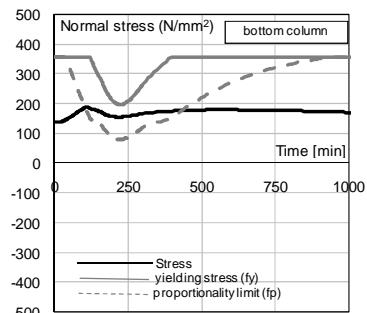


Figure 22 Comparison between normal stress, proportionality limit and yielding stress in heated column ($Q=1000 \text{ MJ/m}^2$)

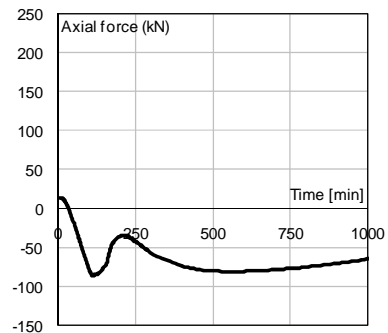


Figure 24 Axial force in heated beam ($Q=1000 \text{ MJ/m}^2$)

4 CONCLUSIONS

This paper is devoted to the application of Structural Fire Engineering (according to Italian and European Codes) to a tower of an existing tall building. The tower, with use office, is 101.00m high and has 29-storeys above the ground; the main structure is realised with a reinforced concrete central core and perimeter steel beams and columns.

In the presented case study, the objective of fire safety assessment concerns the mechanical resistance and stability in fire situation of the tower. In agreement with Fire Brigade and building's Owner, the performance level assumed for fire safety check of the structure is: "maintaining of the fire resistance requirements, which ensure the lack of partial and/or complete structural collapse, for the entire duration of the fire". In addition, only with reference to the most probable fire scenarios, a limited structural damage after the fire exposure is also required.

The identification of design fire scenarios is carried out by means of Fire Risk Assessment, applying the event tree approach according to ISO-16732 Guidelines. A fire scenario is given by a time-sequence path from the initiating condition through a succession of intervening events to an end-event. Each fire scenario corresponds to a different branch of the event tree, and the branches collectively comprise or represent all fire scenarios. The main events taken into account in the risk assessment, affecting the fire development, are: first aid suppression; alarm activation (smoke detectors); sprinklers activation; sprinklers suppression; barrier effectiveness. Moreover, the following secondary events can be significant: doors state; windows state. The latter are taken into account inside the fire model as well as the location of fire ignition.

The fire development is modelled by one-zone model, which assumes homogeneous temperature, density, internal energy and pressure of the gas in the compartment, implemented in Ozone software.

In order to evaluate the structural fire safety, Italian and European Codes allow the global structural analysis, the analysis of part of the structure (substructure analysis) and the analysis of a member (single member analysis). In this case study, due to the building's large size, in order to reduce the computational time the substructure analysis is adopted. The static scheme of building analysed allows to define simple substructures able to represent the global structural behaviour. It should be noted that the structural static scheme doesn't produce significant indirect actions on column.

Analyses results of the most probable fire scenario (SS7a) show that, when the load density is considered equal to 1000 MJ/m^2 , column is very close to collapse condition, but failure doesn't occur. The case in which the fire is controlled by the extinguishing agent is considered. In this case, the increase of heat release rate is stopped and the fire continues to burn at a constant rate. Analysis result shows that structural behaviour is similar to the case in which sprinkler activation fails. In fact, the comparison between fire scenarios SS7a and SS6a shows that structural element achieves approximately the same temperatures.

REFERENCES

- [1] ISO/TR 13387, *Fire safety engineering*. 1999.
- [2] EN 1991-1-2, *Eurocode 1. Actions on structures - Part 1-2: General actions - actions on structures exposed to fire*, November 2002.
- [3] EN 1992-1-2, *Eurocode 2. Design of concrete structures - Part 1-2: General Rules – Structural Fire Design*. March 2004.
- [4] EN 1993-1-2, *Eurocode 3. Design of steel structures - Part 1-2: General rules - Structural fire design*, April 2005.
- [5] Ministry of Infrastructure and Transport (Italian Government) Decree 14/02/2008. *Technical Code for the Constructions*.
- [6] Construction Product Directive, 89/106/CEE, Construction of European Community, December 1988.
- [7] Ministry of Interior (Italian Government). Decree 09/03/2007, *Prestazioni di resistenza al fuoco delle costruzioni nelle attività soggette al controllo del Corpo nazionale dei vigili del fuoco*.
- [8] Ministry of Interior (Italian Government) Decree 09/05/2007, *Direttive per l'attuazione dell'approccio ingegneristico alla sicurezza antincendio*.
- [9] Nigro E., Ferraro A., Cefarelli C., Del Prete I., Manfredi G. *Fire Safety Engineering per gli edifici alti: scelta della sottostruttura*; XXIII Congresso C.T.A. Ischia (Na) 2011
- [10] ISO/DS 16732: "*Fire safety engineering – Guidance on fire risk assessment*", Draft 2010.
- [11] NFPA. *Operation of fire Protection Systems - a Special Edition of the Fire Protection Handbook*. One Batterymarch Park, Quincy, Massachusetts 02269. 2003.
- [12] Hall, J.R. U.S. Experience with Sprinklers and other Fire Extinguishing Equipment. Fire Analysis and Research Division National Fire Protection Association, February 2010.
- [13] Nystedt F. *Verifying Fire Safety Design in Sprinklered Buildings*. Department of Fire Safety Engineering and Systems Safety, Lund University, Sweden, Report 3150, Lund 2011.
- [14] Hasofer A. M., Beck V. R., and Bennetts I. D. *Risk Analysis in Building Fire Safety Engineering*. Oxford: Elsevier Ltd., 2007.
- [15] Franssen J.M., Zaharia R. *Design of Steel Structures Subjected to Fire*, Les Éditions de l'Université de Liège. 2005.
- [16] Franssen J.-M. *SAFIR. A Thermal/Structural Program Modelling Structures under Fire*. Engineering Journal, A.I.S.C., Vol 42, No. 3 (2005), 143-158.
- [17] Cadorin J.F., Franssen J.M., and Pintea D. *The design Fire Tool Ozone V2.2 – Theoretical Description and Validation on experimental Fire tests*, Rapport interne SPEC/2001_01 University of Liege
- [18] Staffansson L., *Selecting Design Fire*, Report 7032 Lund 2010

POST-EARTHQUAKE STRUCTURAL DESIGN FOR FIRE – A NEW ZEALAND PERSPECTIVE

Gregory B. Baker*, Peter C.R. Collier*, Anthony K. Abu** and Brent J. Houston***

* BRANZ Ltd, Porirua City, New Zealand
e-mails: greg.baker@branz.co.nz, peter.collier@branz.co.nz

** University of Canterbury, Christchurch, New Zealand
e-mail: tony.abu@canterbury.ac.nz

*** Guardian Alarms, Christchurch, New Zealand
e-mail: brent@guardianalarms.co.nz

Keywords: Post-earthquake fires, Fire protection systems, Structural design, Fire sprinklers, Passive fire protection.

Abstract. *On Tuesday 22 February 2011, a 6.3 magnitude earthquake struck Christchurch, New Zealand's second largest city. The 'earthquake' was in fact an aftershock to an earlier 7.1 magnitude earthquake that had occurred on Saturday 4 September 2010. There were a number of key differences between the two events that meant they had dramatically different results for Christchurch and its inhabitants. The 22 February 2011 event resulted in one of New Zealand's worst natural disasters on record, with 185 fatalities occurring and hundreds more being injured. In addition, a large number of buildings either collapsed or were damaged to the point where they needed to be totally demolished. Since the initial earthquake in September 2010, a large amount of building-related research has been initiated in New Zealand to investigate the impact of the series of seismic events – the major focus of these research projects has been on seismic, structural and geotechnical engineering matters. One project, however, conducted jointly by the University of Canterbury, the Fire Protection Association of New Zealand and BRANZ, has focused on the performance of fire protection systems in the earthquakes and the effectiveness of the systems in the event of post-earthquake fires occurring. Fortunately, very few fires actually broke out following the series of earthquake events in Christchurch, but fire after earthquakes still has significant implications for the built environment in New Zealand, and the collaborative research has provided some invaluable insight into the potential threat posed by post-earthquake fires in buildings. As well as summarising the damage caused to fire protection systems, this paper discusses the flow-on effect for designing structures to withstand post-earthquake fires. One of the underlying issues that will be explored is the existing regulatory framework in New Zealand whereby structural earthquake design and structural design for fire are treated as discrete design scenarios.*

1 INTRODUCTION

When earthquakes occur, there are usually three key statistics quoted in the news media to characterise the event, namely the magnitude, the location (often referred to as the epicentre) and the depth of the earthquake below the earth's surface. It is generally the case that, the greater the magnitude, the closer the proximity of the epicentre, and the shallower the earthquake, then the greater the damage to buildings. The time of day that the earthquake occurs is also often quoted in news reports. While the former three parameters have a direct bearing on the damage that buildings will sustain and, indirectly, injuries and fatalities, the timing of an earthquake can have a dramatic bearing on the number of casualties.

The focus of this paper is the initial earthquake in the series, which occurred at 4.35 am on Saturday 4 September 2010, and a subsequent major aftershock, which occurred at 12.51 pm on Tuesday 22 February 2011. The September 2010 event had a magnitude of 7.1 and was centred 40 km to the west of the Christchurch central business district (CBD), near the rural town of Darfield, at a depth of 10 km. The aftershock in February 2011 had a magnitude of 6.3 and was centred 10 km south-east of the CBD near the port suburb of Lyttelton, at a depth of 5 km [1].

1.1 Darfield earthquake – September 2010

The key difference between the two seismic events was the proximity to the CBD area and, to a lesser extent, the depth of the earthquakes, which had a dramatic effect on the level of ground shaking that occurred. Earthquake ground shaking is measured in terms of acceleration, which is expressed as a proportion of the gravitational acceleration, g . In the September 2010 event, the impact was widespread and severe, but no major modern buildings collapsed and there was no loss of life. There was substantial damage to unreinforced masonry buildings in the CBD area, with the major hazard being falling masonry, but because of the time of day the earthquake occurred, there was no loss of life [1].

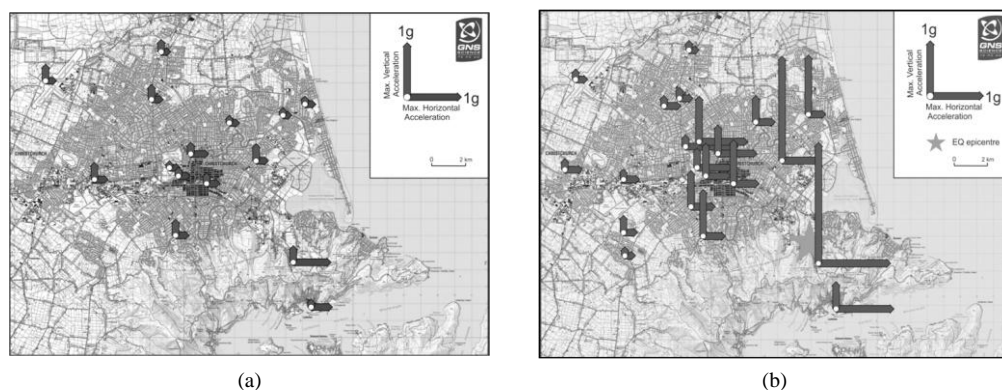


Figure 1. Peak ground accelerations: (a) September 2010; (b) February 2011 (courtesy GNS Science).

Figure 1(a) shows the horizontal and vertical peak ground accelerations (PGAs), which were recorded by a network of accelerometer measuring stations in and around Christchurch, for the September 2010 event. In the CBD area (shaded black in the centre of Fig. 1(a)), the PGAs are approximately 0.2–0.3 g .

1.2 Lyttelton aftershock – February 2011

In the February 2011 aftershock, severe damage occurred to buildings in the CBD and in eastern and southern suburbs. A large proportion of modern commercial buildings in the CBD area were significantly damaged, and many (older) unreinforced masonry buildings collapsed. At least two multi-storey buildings collapsed, and precast concrete stairs collapsed in at least four modern multi-storey buildings [1].

The vertical PGAs in the epicentral area were in the range 1.8–2.2 g – amongst the highest ever recorded in an urban area. The relatively short duration of the aftershock moderated the PGAs in the CBD area, where the vertical PGAs were in the range 0.5–0.8 g , as shown in Fig. 1(b). The horizontal PGAs near the epicentre exceeded 1.6 g , and in the CBD were between 0.4–0.7 g [1].

1.3 Seismic design

In a structural engineering context, buildings are designed to resist a combination of actions such as self-weight (dead), superimposed (live), snow, wind and earthquake loads. When these design actions are dominated by seismic forces, the building design is known as ‘seismic design’. Seismic loading is a low-likelihood/high-consequence scenario, and it is therefore uneconomic to design buildings for the maximum likely ground motion. Generally, therefore, buildings are designed to respond inelastically to

the ground motion but allowing sufficient ductility to prevent collapse [2]. Essentially this design approach seeks to prevent structural collapse, but accepting that significant, even irreparable, damage is likely to occur [1].

In New Zealand, buildings are designed in accordance with the seismic loadings standard [3], which is cited in the compliance document for New Zealand Building Code (NZBC) clause B1 *Structure* [4], using the limit state design method. The ultimate limit state (ULS) is achieved when there is a very low risk of: 1) structural collapse; 2) failure of parts or elements of the building that would be life threatening; or 3) failure of parts or elements whose function is critical for safe evacuation [5]. The annual probability of exceedance [6] for the ULS for a normal use building is 1/500 (500-year return period), i.e. these buildings are designed for earthquake ground shaking intensities expected to occur, on average, not more than once every 500 years [1]. For important buildings such as hospitals and the like, the corresponding threshold is 1/2500.

In Fig. 2, the elastic design spectrum (horizontal) from the seismic loadings standard [3] are shown for both a 1/500 and a 1/2500 event for the ULS, as well as spectral accelerations (horizontal) for the February 2011 event from four measuring stations around the perimeter of the CBD area. It can be seen from Fig. 2 that, for normal use buildings in particular, the ground accelerations in and around the CBD exceeded the level required by the NZBC. The specific requirements in the seismic loadings standard to design for vertical acceleration are less stringent than the horizontal action. With regard to period, typical commercial/industrial buildings would be in the range 0.5–1.5 s.

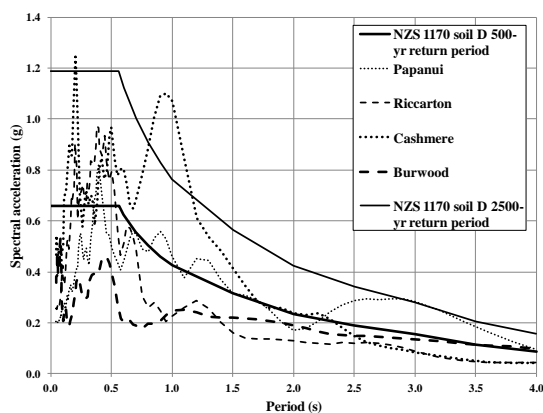


Figure 2. Design spectrum and recorded accelerations – February 2011 (recorded data courtesy GNS Science).

2 POST-EARTHQUAKE FIRES

Large fires in urban areas following earthquake are relatively rare events. The two largest post-earthquake fires in urban areas of the 20th century occurred in San Francisco, US, in 1906 and Kanto, Japan, in 1923 [7,8]. The 1906 San Francisco earthquake was magnitude 7.9, and there was a death toll of more than 3000 people. Eighty percent of the damage was due to fire, amounting to a burnt area of 12.2 km² and 28,000 buildings. In the 1923 Kanto earthquake, the magnitude 8.2 event resulted in 140,000 fatalities and a burnt area of 38.3 km² [7].

2.1 Northridge and Kobe earthquakes

In the later part of the 20th century, significant research has occurred in response to the post-earthquake fires that resulted from the 1994 Northridge (California), US, earthquake, as well as the Kobe (also known as the Great Hanshin or Great Hanshin-Awaji), Japan, earthquake in 1995 [7–13]. The two

earthquakes had a number of similarities such as magnitude, ground motions, affected population, time of day and season – the post-earthquake fire losses were quite different, however [9]. The Northridge earthquake was magnitude 6.7, and approximately 110 earthquake-related fires were reported, but relatively small post-earthquake fire losses occurred. The Kobe earthquake was magnitude 6.9, and approximately 200 (109 in Kobe City and 96 in cities other than Kobe) earthquake-related fires broke out, but the resulting damage was much more extensive [9–11].

In the Northridge earthquake, the majority of the earthquake-related fires occurred in the epicentral area of the San Fernando Valley [9,12]. Initially, the principal cause related to gas leaks [10,12], but subsequently, the major cause of ignition was electrical arcing as a result of short circuits [9]. In the Kobe earthquake, 43 percent of the total number of earthquake-related fires broke out within the first quarter hour and a further 42 percent in the next 4-hour period, with the balance of 15 percent over the remaining hours up until 24 hours after the event. In the initial quarter-hour period, the primary cause of ignition was due to gas leakage, but in subsequent hours, the primary cause of ignition was electrical as the electricity reticulation system was restored.

In the Northridge earthquake, between 1500 [13] and 3000 [9] leaks occurred to underground water reticulation pipes, while pump stations and storage tanks also sustained damage. This resulted in a shortage of firefighting water following the earthquake. Water tenders made up the shortfall, and also water was drawn from domestic swimming pools [9]. In the Kobe area, firefighting water was primarily supplied from the city water system. Seismic shut-off valves at reservoirs, for the purpose of conserving firefighting water in the event of earthquake, operated effectively, but approximately 2000 breaks in the reticulation system hampered the use of this water. The city also had approximately 1000 underground cisterns for disaster firefighting – in combination, these systems provided firefighting water for only 2–3 hours [9].

In the Northridge earthquake, virtually all earthquake-related fires were confined to the building of fire origin with only three instances of building-to-building fire spread in mobile-home parks [12]. All fires were brought under control within several hours of the earthquake [9]. The combination of light prevailing winds, building construction, building separation and Fire Service intervention were all contributory factors [12]. In contrast, in Kobe, major conflagrations occurred, and fires spread extensively. The response of the Fire Service was hampered by extreme traffic congestion, collapsed houses and buildings, and rubble in the streets, meaning that many areas had no vehicular access. Fire spread was via radiant heat and flame impingement between buildings, but because the wind was calm, the advance of fire fronts was slow. These factors, combined with the lack of firefighting water, resulted in damage to approximately 5000 buildings over a total estimated area of 1 km² [9].

3 PERFORMANCE OF FIRE PROTECTION SYSTEMS IN CHRISTCHURCH EARTHQUAKES

The recent earthquake series in Christchurch, New Zealand, has provided an opportunity to investigate the seismic resilience of fire protection systems. A collaborative research project involving the University of Canterbury, the Fire Protection Association of New Zealand (FPANZ) and BRANZ was therefore initiated in 2011 to investigate the performance of fire protection systems in the recent earthquake events. Although no significant fires occurred after the September 2010 and February 2011 earthquakes, very useful information was able to be gathered. In this context, the term ‘active fire protection’ relates to detectors, alarms and fire sprinkler systems, while ‘passive fire protection’ relates to items such as fire-rated compartmentation systems, fire doors, fire-stopping systems, fire-rated coatings on structural elements and the like.

3.1 Active fire protection systems

In the aftermath of both the September 2010 and February 2011 earthquakes, inspections of active fire protection systems were conducted in affected buildings in and around the city of Christchurch. With

regard to fire sprinkler systems, there are two main issues relevant to post-earthquake performance – whether the water supply had been disrupted and whether systems have been damaged.

In the Christchurch CBD, some sprinkler systems were required to have dual supplies due to the building height as a requirement of the automatic fire sprinkler standard [14] of the day. In most cases, the second supply was an additional independent connection to the mains water supply. In the September 2010 earthquake, water supply to the CBD area was temporarily disrupted but restored within a relatively short period of time. In the February 2011 event, however, the mains water supply to the CBD area suffered significant disruption. The most seriously affected central area (the ‘red zone’) was evacuated and more than a year later is still unoccupied as demolition work continues, and the water supply has not been restored. In commercial/industrial areas surrounding the red zone, the mains water supply took days or weeks to be restored.

In areas of the city away from the CBD and in surrounding rural areas, water tanks are often either the only water supply or form part of a dual water supply for fire sprinkler systems. Up until the 1980s, these tanks were mostly of concrete construction, and they generally performed well in the earthquakes.



Figure 3. Timber stave water tanks: (a) typical tank c. 1980s; (b) collapsed tank; (c) damaged tank (courtesy FPANZ).

In the 1980s and 1990s, the construction method was mostly timber stave tanks, with an example shown in Fig. 3(a). A significant number of the timber stave tanks were damaged and a number suffered catastrophic failures. In Fig. 3(b), a timber stave tank has collapsed, while in Fig. 3(c), the tank has moved sufficiently to pinch the bladder in the tank and release all the water.

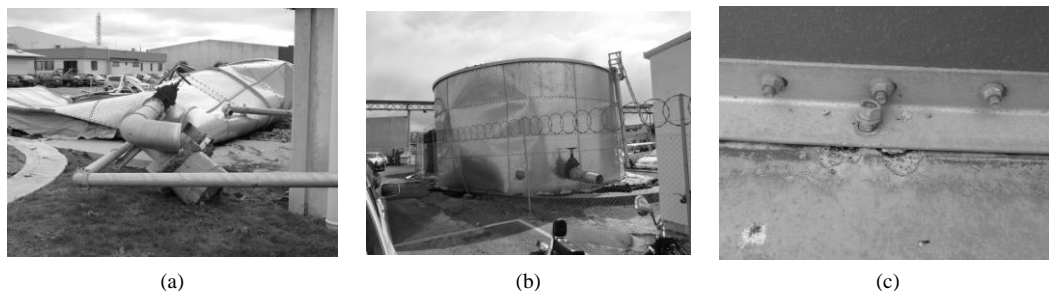


Figure 4. Steel water tanks: (a) collapsed tank; (b) damaged tank; (c) failed base fixings (courtesy FPANZ).

In the late 1990s, steel panel tanks became the norm. The performance of these tanks in the earthquakes was similar to the earlier timber stave tanks, with a collapsed steel tank shown in Fig. 4(a), a damaged tank in Fig. 4(b) and failed base fixings in Fig. 4(c).

A range of damage to fire sprinkler systems was observed following the 2010 and 2011 earthquakes in Christchurch. Some fire sprinkler systems require a booster pump to boost either the town’s main reticulation or tank supplies. In a number of cases, the basements where these pumps are generally housed

were flooded, and the pumps were rendered inoperable. In Fig. 5(a), the water level is shown in the foreground on a column, which submerged the booster pump system in the background.



(a)



(b)

Figure 5. Sprinkler system damage: (a) flooded basement; (b) collapsed ceiling (courtesy FPANZ).

Figure 5(b) shows a suspended ceiling where the lining has collapsed – in a number of cases, damage to sprinkler systems was observed where non-structural components and systems had collapsed, but in the centre of Fig. 5(b), the sprinkler head has actually remained operable.

In a number of cases, the roof cross-bracing in low-rise commercial buildings caused damage to sprinkler fittings. Figure 6(a) shows sprinkler heads that have been sheared off as steel angle cross-bracing has moved backwards and forwards in response to the cyclic earthquake ground motion, while Fig. 6(b) shows damage to sprinkler pipework due to vertical movement of steel cross-bracing ‘pounding’ the pipework.



(a)



(b)

Figure 6. Sprinkler component damage: (a) sprinkler heads sheared off; (b) pipe work damage (courtesy FPANZ).



(a)



(b)

Figure 7. Sprinkler systems: (a) pipework support; (b) collapsed racking system (courtesy FPANZ).

The 1996 edition of the automatic fire sprinkler systems standard introduced requirements for seismic design of sprinkler systems, and as a result, modern pipe systems performed well in the 2010/2011 earthquakes, as shown in Fig. 7(a). A number of racking systems collapsed in the earthquakes, and where in-rack sprinkler systems were present, these also suffered damage, as shown in Fig. 7(b).

Whereas only some types of commercial/industrial buildings require sprinkler systems, the vast majority require a fire alarm system. The most obvious issue identified during the course of the research related to alarm system cable routing. It was apparent that very little, if any, attention had been paid to the consequences of seismic movement of buildings when installing fire alarm cabling. Damage was observed where cabling passed through holes in or around cut edges of structural and secondary steelwork. Another example of damage to alarm cabling was where cyclic movement of building elements such as concrete tilt-up wall panels crushed cabling, as shown in Fig. 8.



Figure 8. Crushed alarm cabling (courtesy FPANZ).

Although very few fires actually occurred in both the September 2010 and February 2011 earthquakes, 600 and 450+ ‘fire’ notifications respectively were received from fire protection systems connected to the NZ Fire Service. (Note: the actual number of fire alarm notifications in February 2011 was probably significantly higher, but the serious damage affected the alarm transportation network.) These figures related to systems signalling a ‘fire’ condition, but the instances of other off-normal notifications from the respective systems increased this number to approximately 10,000.

3.2 Passive fire protection systems

Following the February 2011 earthquake, a series of inspections of passive fire protection systems in buildings were carried out. In some buildings, the damage had been so extensive that the passive fire protection was destroyed. The focus of the investigation was on damage in the low-to-medium range, i.e. where the building was structurally safe but where damage to passive fire protection had occurred, so that the impact of earthquake actions on passive fire protection could be quantified.

Fire doors were one area of focus for the site inspections, with a range of damage being observed. In Fig. 9(a), the gap down the door jamb has increased from 2–3 mm originally to 4–16 mm after the earthquake, while Fig. 9(b) shows damage to the fire-rated lining at the head of the door and Fig. 9(c) shows a 7 mm gap between the lining and door frame.

In a number of instances, damage to fire-rated walls was observed, as shown in Fig. 10. Figure 10(a) shows fire-rated lining having separated from the framing, Fig. 10(b) shows a wall-to-wall internal corner junction where a 15 mm gap has opened up in a fire-rated escape stairwell, and Fig. 10(c) shows the underside of a precast concrete stair where the junction to the fire-rated wall beneath has been crushed by earthquake-induced motion.

Inspection of concrete tilt-up wall panels in low-rise industrial buildings showed separation of fire-rated sealant joints, as shown in Fig. 11(a)–(c), increasing the risk of fire spread to neighbouring properties.

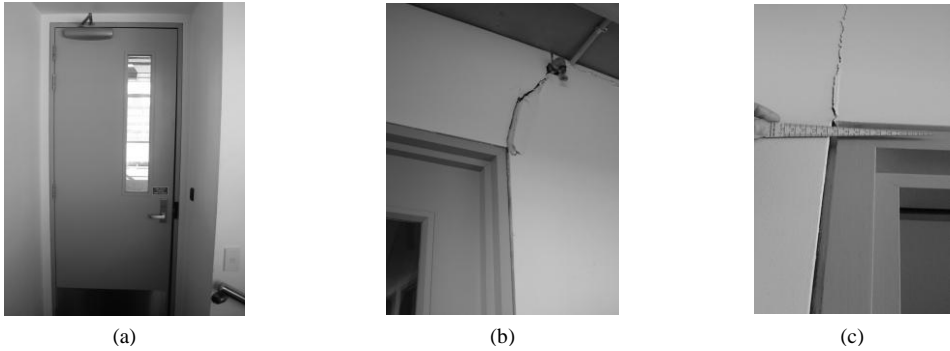


Figure 9. Fire door damage: (a) gap around door leaf; (b) diagonal crack; (c) gap between frame and lining.

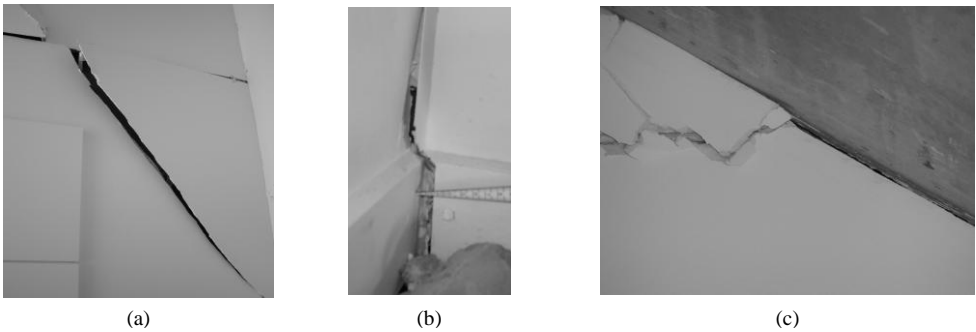


Figure 10. Compartmentation damage: (a) fire-rated wall; (b) stairwell; (c) stair soffit.

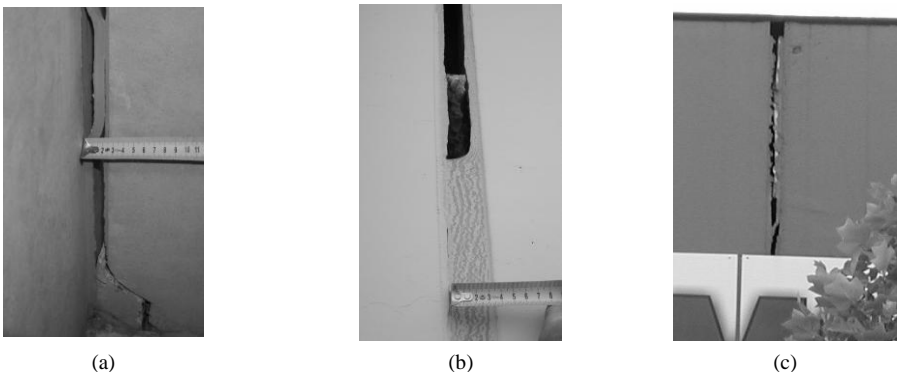


Figure 11. External walls: (a) wall corner junction; (b) wall panel butt joint; (c) wall panel butt joint.

4 STRUCTURAL DESIGN FOR FIRE

In New Zealand, there is a heavy reliance on fire sprinklers as part of the fire safety strategy in buildings. Based on very high levels of historic reliability [15] and comprehensive procedures for design, certification, inspections and maintenance, dispensations are given to the level of passive fire protection

systems when fire sprinklers are present. In many situations, a 50 percent reduction is permitted, for example, if a 2-hour fire resistance rating is required without sprinklers, a 1-hour rating is permitted when sprinklers are present [16].

In the February 2011 earthquake in particular, the municipal water supply was seriously disrupted. At the same time, approximately 40 percent of water tanks for supplying sprinkler systems were damaged – primarily timber stave and steel tanks of large diameter and volume. This would have meant that, if post-earthquake fires had broken out, the majority of sprinkler systems would have had no water supply, and the systems would have been largely ineffective.

The fire dynamics of post-earthquake fires is also likely to be different to typical fires in that the fuel is likely to be spread over a wider area, item-to-item fire spread is likely to be more rapid and glazing is likely to have been broken by the earthquake, thus providing additional ventilation. At the same time, compartmentation is likely to have been breached, thus allowing the fire to spread more rapidly to involve fuel that otherwise would not become involved so soon. In addition, there is likely to be a significantly reduced Fire Service response.

These factors in combination mean that earthquake-induced fires are likely to grow more quickly to high levels of heat output, i.e. have a greater severity, and have a longer duration. Where reductions in passive fire resistance ratings have also occurred, based on sprinkler systems being present, structural elements are likely to have to endure fire exposures that are of greater severity and for significantly longer periods of time than the elements were designed to withstand.

At the same time, it is also likely that passive fire protection to the member has been damaged. For reinforced concrete sections, the concrete cover, which provides passive fire protection to the steel reinforcing bars, is likely to have been badly damaged, exposing reinforcing, particularly in plastic hinge zones. For structural steel members, examples were observed during inspections where protective coatings had been damaged by earthquake-induced movement. In a general sense, structural elements in buildings that have been subjected to a design-level earthquake are going to have suffered significant damage, which weakens the members. This means that the structure of buildings is more vulnerable to fire-induced collapse than would be the case in non-earthquake fires.

The recommendation is that changes to two aspects of current practice be considered by the building regulator:

1. A sliding scale of reduction in fire resistance ratings when sprinklers are present be applied, i.e. a 50 percent reduction in areas of lowest seismic risk, up to 0 percent in areas of highest seismic risk.
2. Design fire scenarios, commensurate with the seismic zoning, where compartmentation has failed and egress routes compromised, thus becoming more onerous from an evacuation perspective, become mandatory

5 CONCLUSIONS

The fact that no significant fires occurred after the September 2010 and February 2011 earthquakes was due to a number of factors such as the time of day (reduced ignition sources from cooking), the time of year of the February earthquake being summertime (no ignition sources from space heating), and the low level of reticulated gas in Christchurch. Active fire protection systems still have an important role to play in post-earthquake fire safety. Therefore, in addition to the recommendations presented in Section 4 relating to structural design for fire, a number of relevant conclusions can still be drawn about the post-earthquake performance of active fire protection systems, based on the research reported in this paper:

1. Alternative strategies need to be considered to ensure the sprinkler water supply from in situ tanks is more reliable in the event of earthquakes and consideration needs to be given to retrospective upgrading based on individual risk assessment.
2. Alternatives to dual mains supply for existing sprinkler systems need to be considered (now not permitted by the 2007 edition of the automatic fire sprinkler standard).
3. Fire pump systems need to be installed so as to minimise the risk from basements flooding.

4. Trade practice with regard to routing of fire alarm cabling needs to be improved.
5. The seismic resilience of non-structural components and systems generally needs to be reviewed.

REFERENCES

- [1] New Zealand Government, “Technical Investigation into the Structural Performance of Buildings in Christchurch – Final Report”, Department of Building and Housing (DBH), Wellington, New Zealand, 2012.
- [2] Dhakal, R.P., “Report to the Canterbury Earthquake Royal Commission – Structural Design for Earthquake Resistance: Past, Present and Future”, University of Canterbury, Christchurch, New Zealand, 2011.
- [3] NZS 1170.5:2004, “Structural Design Actions Part 5: Earthquake Actions – New Zealand”, Standards New Zealand (SNZ), Wellington, New Zealand, 2004.
- [4] New Zealand Government, “Compliance Document for New Zealand Building Code Clause B1 Structure (Amendment 11)”, DBH, Wellington, New Zealand, 2011.
- [5] NZS 1170.5 Supp 1:2004, “Structural Design Actions Part 5: Earthquake Actions – New Zealand – Commentary”, SNZ, Wellington, New Zealand, 2004.
- [6] AS/NZS 1170.0:2002, “Australian/New Zealand Standard – Structural Design Actions Part 0: General Principles”, SNZ, Wellington, New Zealand, 2002.
- [7] Scawthorn, C., “Fire Following Earthquake”, *Fire Safety Science – Proceedings of the First International Symposium*, IAFSS, 971–979, 1984.
- [8] Borden, F.W., “The 1994 Northridge Earthquake and the Fires that Followed”, Thirteenth Meeting of the UJNR Panel on Fire Research and Safety, Vol. 2, NISTIR 6030, K.A. Beall (ed.), National Institute of Standards and Technology (NIST), Gaithersburg, MD, US, 303–312, 1997.
- [9] Scawthorn, C., “Fires Following the Northridge and Kobe Earthquakes”, Thirteenth Meeting of the UJNR Panel on Fire Research and Safety, Vol. 2, NISTIR 6030, K.A. Beall (ed.), NIST, Gaithersburg, MD, US, 325–334, 1997.
- [10] Sekizawa, A., “Post-Earthquake Fire and Performance of Firefighting Activity in the Early Stages in the 1995 Great Hashin Earthquake”, *Fire Safety Science – Proceedings of the Fifth International Symposium*, IAFSS, 971–982, 1996.
- [11] Hokugo, A., “The Performance of Fire Protection of Buildings Against the Fires Following the Great Hanshin-Awaji Earthquake”, Thirteenth Meeting of the UJNR Panel on Fire Research and Safety, Vol. 2, NISTIR 6030, K.A. Beall (ed.), NIST, Gaithersburg, MD, US, 313–323, 1997.
- [12] Evans, D.D, Walton, W.D., and Mowrer, F.W., “Progress Report on Fires Following the Northridge Earthquake”, Thirteenth Meeting of the UJNR Panel on Fire Research and Safety, Vol. 2, NISTIR 6030, K.A. Beall (ed.), NIST, Gaithersburg, MD, US, 273–281, 1997.
- [13] Ballantyne, D.B. and Crouse, C.B., “Reliability and Restoration of Water Supply Systems for Fire Suppression and Drinking Water Following Earthquakes”, NIST GCR 97-730, NIST, Gaithersburg, MD, US, 1997.
- [14] NZS 4541:2007, “Automatic Fire Sprinkler Standard”, SNZ, Wellington, New Zealand, 2007.
- [15] Marriott, H.W., *Fire A Century of Automatic Sprinkler Protection in Australia and New Zealand 1886–1986 (2nd ed.)*, Australian Fire Protection Association, Melbourne, Victoria, Australia, 90, 1988.
- [16] New Zealand Government, “Compliance Document for New Zealand Building Code Clauses C1, C2, C3, C4 Fire Safety (Amendment 9)”, DBH, Wellington, New Zealand, 109, 2011.

PERFORMANCE-BASED FIRE SAFETY DESIGN OF SPECIAL STRUCTURES IN GERMANY

Jochen Zehfuß*, Christoph Klinzmann* and Karen Paliga*

* hhpberlin – Ingenieure für Brandschutz GmbH
e-mails: j.zehfuss@hhpberlin.de, c.klinzmann@hhpberlin.de, k.paliga@hhpberlin.de

Keywords: Natural Fires, Global structural behaviour, Steel, thermal and mechanical analysis, non-linear material properties.

Abstract. *The objective of this article is the illustration of the calculation of natural fires and fire resistance of structural members based on the Eurocodes of two types of special structures, in this case a railway bridge and two airplane hangars. The railway bridge has a width of nearly 70 meters and consists of steel beams and a massive concrete slab that are supported by massive columns and walls and for that reason can be compared to a tunnel. The load-bearing structure of the roof of the hangars is made of steel and is supported by steel columns. The choice of a fire scenario on the safe side is crucial for the design process of the unprotected steel structure.*

1 INTRODUCTION

Improvements in performance-based design allow for a more realistic and cost effective fire safety design of structures. Within the year 2012, the fire parts of the Eurocodes and the included methods for the calculation of natural fires and the resistance to fire of structural members are introduced into the German building laws. For that reason the application of these methods is generally permitted by the authorities having jurisdiction (AHJ) and it can be assumed that they will become more and more important in years to come. The usage of natural fires is the largest opportunity for cost-savings in the design of structural fire protection due to the differences between standardized temperature time curves and natural fires. This is even more important with large special structures made of steel due to the high resistance required of the structural members of such structures in Germany.

The structural analysis of fire protection for the entire structure finds one's way into the constructive design of buildings. Under specific conditions it is possible to design unprotected steel constructions with sufficient fire resistance.

Thereby simplified or general calculation methods of the according European standards for structural fire safety design can be used, depending on application case. To adopt this method of calculation finite element analysis is required, which considers nonlinear material properties and nonlinear thermal loads in structural elements. In this contribution the application of these methods using the FE-program ANSYS shall be described by means of two types of realistic building projects.

2 GENERAL PROCEDURE

The first step in fire safety design is the definition of design fires in the form of heat-release-time curves specially adapted to the building in question and the relevant fire scenarios. Subsequently, the effects of a design fire on a building and its load bearing structure are evaluated using simulation models, depending on the complexity of the building with zone or CFD-models. The temperatures calculated in these analyses are the basis of the simplified and advanced calculation methods of the Eurocodes.

In Germany the fire safety design of large railway structures like tunnels and stations can rely on special pre-defined design fires that were developed by the German railway services on the basis of Eurocode 1-1-2 [1] and the specific geometric properties and fire loads of typical train cars.

Design fires for buildings like airplane hangars are not standardized in Germany and have to be derived for the special case. Similar to the design fires for train cars, the special geometric properties (like width and height of airplanes) are taken into account.

3 PROJECT EXAMPLE: TRAIN STATION “OSTKREUZ” IN BERLIN

3.1 Description of the Construction

The building in consideration is a crossing station in the city of Berlin, where the S-Bahn and long distance train lines intersect on two levels (see figure 1). The platform and the tracks supports of the upper level are made from steel girder grids supporting a concrete slab. The girders are single span beams carried by solid supports and supporting walls. The width of the superstructure is approx. 70 m and has almost the dimension of a tunnel. It spans the lower part of the station that is divided into several segments. Here the passenger waiting areas for the long distance trains are located.

A burning train located directly below the superstructure carrier represents the worst case fire scenario. The main task for the fire safety design of the superstructure was to prove that the steel parts of the structure withstand the effects of a fire long enough without loss of load carrying capacity and to devoid fire protection measures such as covering or coating.



Figure 1. Crossing station in Berlin with overlapping platforms (Source: Deutsche Bahn)

The heat generation on the platform level was to be simulated using a CFD simulation on the basis of a fire scenario of a train on fire. The calculated temperatures were used as input variable for the thermal analysis simulating the warming of the supporting structure.

In a subsequent mechanical analysis the structural behaviour was calculated taking into account the warming of the structure and the resulting thermal strain and stresses. The thermal and mechanical analysis, conducted with the help of ANSYS, is based on the advanced calculating procedures of Eurocode 1 Part 1-2 [1] and Eurocode 3 Part 1-2 [2].

3.2 Fire Scenarios and Design Fires

By means of a CFD simulation (computational fluid dynamics) the determination of temperature over the period of the fire is calculated using the program FDS [3].

The simulation model includes the lower platform with the relevant surrounding components. The top of the model area is formed by the superstructure of the rails and passenger bridges and consist of steel carrier parts and concrete slabs. A typical train car with the corresponding geometric dimensions and fire loads has been used as the source of the fire for the platform model. Fig. 2 shows the characteristics of the heat release rate for the scheduled fire scenario.

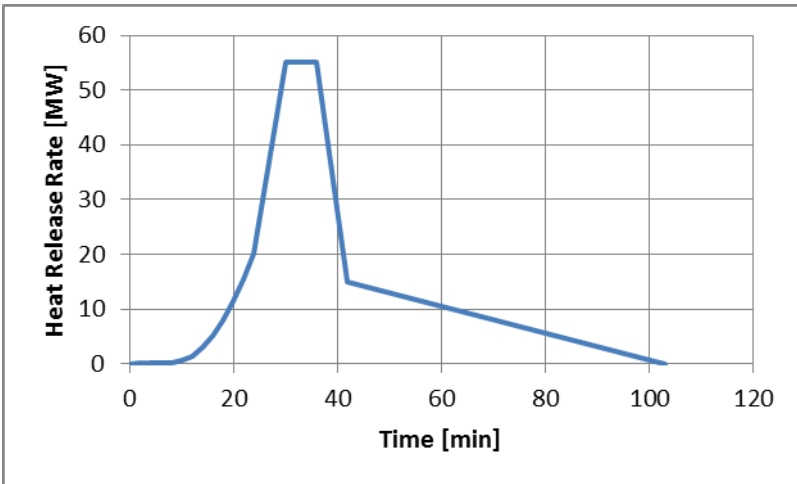


Figure 2. Characteristics of the applied heat release rate [4]

From the evaluation of the individual results of the CFD simulation the maximum time-temperature-curve was filtered out and used as a natural fire time-curve for the thermal analysis of the structure. In Fig. 3 the relevant time-temperature-curve of the train fire is shown. This time-temperature curve has been measured at the open carriage door one metre above the roof of the car.

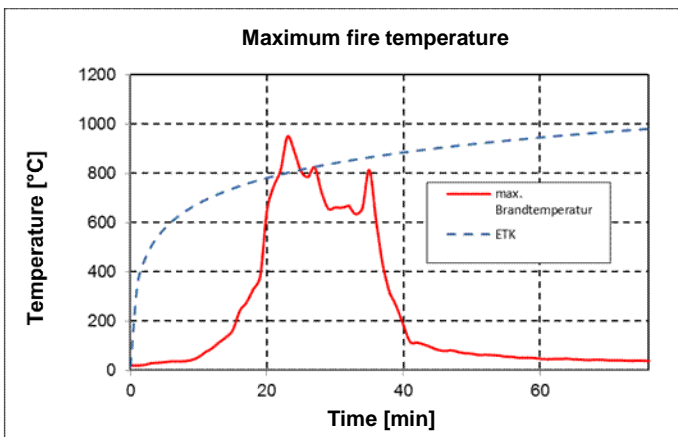


Figure 3. Development of the maximum fire temperature

The time period during which temperatures $> 200\text{ }^{\circ}\text{C}$ act on the structure, is approx. 25 minutes. At the time of the maximum impact $950\text{ }^{\circ}\text{C}$ are reached for a short time. For comparison, the uniform-temperature-time-curve (UTTC) is also shown in Fig 3. It is clearly to be seen that the influence of the fire room temperature due to the natural fire is much lower. The peak of the natural fire curve exceeds the course of the UTTC briefly and reaches its maximum earlier than the standard fire curve, but for the duration of the entire fire the UTTC is significantly greater than the relevant natural fire curve of simulated train fire.

3.3 Model of the Construction

The structure of the station bridge consists of single-spanned elements from one supporting wall to the other that form a support for the rails and the platform. Since the single-spanned girder grids are not mutually coupled and thus have no static interactions, they can be considered individually in terms of the thermal loads. The girder grid with the largest static load was chosen for the fire calculation and was considered as relevant for the evaluation of the fire resistance for the entire station structure. Fig. 4 shows the three-dimensional structural model of a girder grid which is 28 m long and 17 m wide. The longitudinal beams consist of hollow box sections with an average height of 1.50 m. The cross members between the side rails are made up of HEA profiles. Their arrangement is interrupted in the middle of the grid, because here the staircases of the platform are situated. The concrete slab that is designed as a composite panel is located on the girder grid. The thickness of the slab is very low, so the static effect could be neglected and is therefore not included in the model for the mechanical analysis.

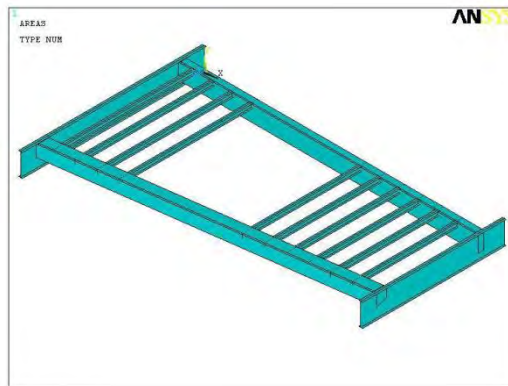


Figure 4. Three-dimensional model of the steel girder grid of the platform level

The fire scenario of the train is situated on the lower platform below the girder and is orientated parallel to the cross members. In this way the direct impact of the fire occurs only on one side of the girder grid and heats only certain parts of the structure. Since the floor plan of the girder grid is trapezoidal, the beam section with the long cross-carrier dimensions was used for the calculation (in the image from the left upper section of the grate to the stair hole of the slab).

3.4 Thermal Analysis

The thermal analysis was performed with the FE program ANSYS. Fig. 5 shows the temperature-time-curve in the cross-section of a cross beam.

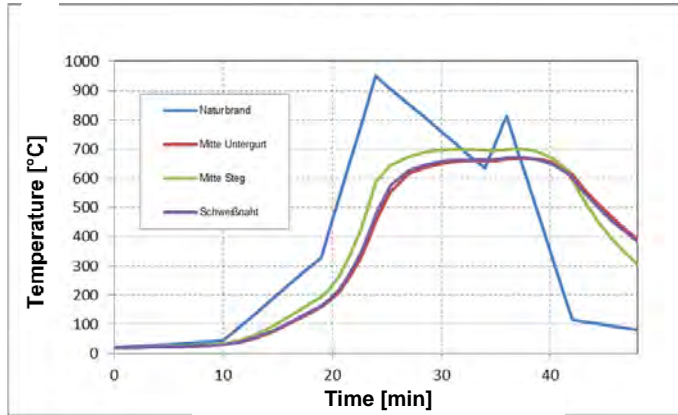


Figure 5. Temperature-time-curve of a selected cross section

The component temperatures measured were applied as thermal loads to the elements of the 3D model. It was assumed that the temperatures over the height of the beams are uniform, so that equal values for bottom, rib and upper flanges could be used.

3.5 Mechanical Analysis

The mechanical analysis examined the load bearing and deformation behaviour of the construction. The temperatures acting on the structure over the duration of the fire, as well as the mechanical loads and the non-linear temperature-dependent material properties were taken into account.

For the description of the failure state of a loaded structure, it is necessary to define failure criteria. Steel and reinforced concrete construction parts, consisting of ductile materials, do not generally fail by a brittle fracture. The failure of these components is introduced by a rapid growth of deformations. During an international research project in Cardington, where the load behaviour of steel composite structures was investigated in 1: 1 scale, a failure criterion of a maximum deflection of $u_{crit} = l / 20$ was defined [6].

In fire tests conducted according to [5] on statically determined storage components stressed wholly or mainly by bending, failure is defined by the so-called Ryan Robertson criterion of the permissible deflection speed. Ryan and Robertson noted in [7] after numerous fire tests on members of steel and reinforced concrete construction subjected to bending that after reaching the critical speed of deflection, failure occurs by sudden growth of the deflections.

$$\Delta f / \Delta t = l^2 / (9000 \cdot h) \quad (1)$$

with:

- Δf Deflection interval [cm] during a time interval of 1 min,
- Δt Time interval of 1 min,
- l Effective span of the element [cm],
- h Static height of the element [cm].

The two aforementioned failure criteria were used in assessing the fire resistance of the construction of the train station. When one of the two criteria is reached, it is assumed that the integrity of the load-bearing structure is exhausted.

Fig. 6 shows the vertical deformation of the loaded cross member over the period of fire exposure. It is clearly visible how the course of the deformations corresponds with the natural fire curve of the thermal load (fig. 5). At the end of the fire, the influences of the temperatures on the load-bearing structure are getting smaller and the deformations are reduced.

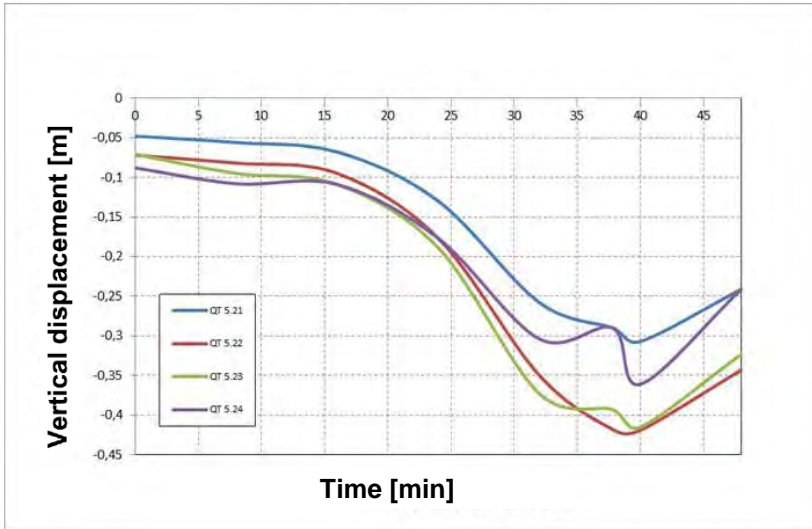


Figure 6. Deformation of the cross-members during the time of the fire

The calculations showed that the failure criteria of the distortion were met over the entire period of stress. In the early stages of the fire, great stress is applied on the structure by the heating of the steel without decreasing its strength. As a result, the internal stresses rise, caused by the obstruction of the free formability. When 300 °C are reached, the bending stiffness and strength of the steel begin to decrease so that the resistance of the structural member is reduced and deformations increase subsequently.

The results of the simulation show that the girder grid made from unprotected steel resists a natural train fire with temperatures above 900 °C and does not fail in the event of a fire. No fire protection measures such as insulating surface protection for the steel are required.

4 PROJECT EXAMPLE: AIRCRAFT HANGAR

4.1 Description of the Construction

The hangar discussed here has the outer dimensions of 83.40 m width and 77.60 m depth and thus an inner area of approximately 6,472 m². The hangar has a horizontally orientated roof, which is supported by an external two truss girders on steel supports that are located on the outside. A secondary internal load-bearing system is attached below the main load-bearing elements. The hangar has a medium interior height of approximately 18.10 m, the height of the lower edge of the secondary load bearing structure is 15.25 m.

4.2 Safety Objectives

Alike to the train station, the main objective that has to be fulfilled by the fire safety design of the construction was a sufficient structural safety in case of fire. As a basis of the analysis, the definition of a design fire and fire scenarios is very important. The largest airplane that will be maintained in the hangar case will be a Boeing B747, which has a maximum height of approx. 10 m at the top of the cabin.

The results from CFD-Simulations should be used for the structural fire design of the steel structure according to the simplified calculation procedures of Eurocode 3 (columns and roof structure). The objective was to use the least possible amount of fire protection measures.

4.3 Fire Scenarios

Various aircrafts are to be serviced in the hangar. To demonstrate the stability of the load bearing structure of the roof, it is the worst case to assume that the fire occurs as high as possible in the building.

The following scenarios were used:

- Scenario 1: fire in the cabin of a B747-400 with participation of part of the wings (plastics and kerosene fire), fire surface 100 m², fires in a height of approx. 6 m.
- Scenario 2: cabin fire in a B747-400 in the upper-deck (plastics) without participation of the wings, fire area 50 m², fires in a height of approx. 8 m.
- Scenario 3: local fire, for example larger car or a similar major technical device or storage good, fire area 10 m², fires at a height of 4.0 m.

4.4 Design Fires

To ensure design fires on the safe side, the relevant input parameters must be adopted conservatively, so that all relevant fire events are covered.

With regard to the course of the heat release rate, it is assumed that the fire does not extinguish after the depletion of the fire load but will remain at the maximum rate of the heat release. For that reason, only the nature of the fire load, but not the amount is significant for the fire safety design.

The safety objectives in the building will be proven when a stationary state, i.e. a balance of the energy supplied by the fire and the energy dissipated by the smoke and heat exhaust measures is reached. In all fire scenarios extinguishing measures, for example, by the extinguishing system or the airport fire brigade, are not considered to have a direct effect on the heat release rate. They are accounted for conservatively by the partial factor $\gamma_{fi,HRR}$ according to [1].

Due to the fact that a fire develops higher temperatures if it burns with a high heat release rate concentrated in a small area and on the other hand a higher smoke gas production occurs in a larger fire area, the realistic fire areas mentioned above are chosen for the aircraft fire scenarios.

According to the literature such as the [7], area-specific heat release rates of between 150 kW/m² and 500 kW/m² are realistic. In individual cases also values over 600 kW/m² can occur especially in plastics and lubricants. This adds up to the following design fires for the defined fire scenarios (partial safety factors in accordance with [1]):

- Scenario 1 (Fire in cabin + wing): $q' = 600 \text{ kW/m}^2$
 $Q'_{\text{max}} [\text{kW}] = 600 \text{ kW/m}^2 * 100 \text{ m}^2 * 1,075 = 64500 \text{ kW}$ after approx. 930 s
- Scenario 2 (Fire in upper-deck cabin): $q' = 450 \text{ kW/m}^2$
 $Q'_{\text{max}} [\text{kW}] = 450 \text{ kW/m}^2 * 50 \text{ m}^2 * 1,075 = 24187.5 \text{ kW}$ after approx. 720 s
- Scenario 3 (Local fire at support): $q' = 500 \text{ kW/m}^2$
 $Q'_{\text{max}} [\text{kW}] = 500 \text{ kW/m}^2 * 10 \text{ m}^2 * 1,075 = 5375 \text{ kW}$

The illustration in figure 6 shows an example for the curve progressions of the heat release over time.

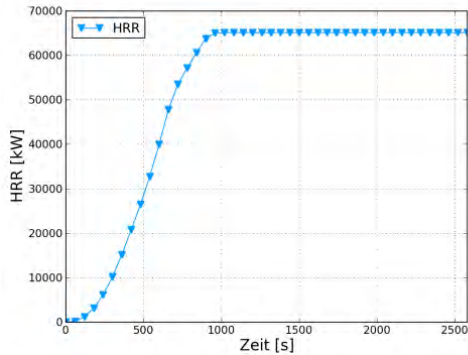


Figure 6. Time sequence of heat release rate (HRR) in the fire scenario 1 ("aircraft fire")

The specification of the source of a fire is required for fire simulations. The calculations are based on a mixed load of fire, which consists of 33% wood, 33% polystyrene, and 33% polyurethane and thus is based by 2/3 on plastics. Regarding the existing flammable substances in the hangar and airplanes this could to be regarded as conservative.

The mean value of the heat of combustion of the fuel mixture was derived from the specific parameters of the individual substances to be approximately 27 MJ/kg.

Due to the relation between the heat release q' , the mass flow m' and the heat of combustion H ($m' = q'/H$) a higher heat of combustion leads to a lower mass flow in case a heat release rate was specified. Thus this leads to a lower production of smoke gas, so that this value specified is considered to be conservative.

The results of the fire simulations carried out have proven to be decisive for the roof structure. Because of the height and the width of an aircrafts and their necessary distance to the steel columns of the building, there was no relevant increase in temperature in their vicinity during the fire simulations. Since no fire scenario could be ruled out, the effects of a localized fire event in the immediate vicinity of the columns were analysed. The temperatures resulting from such a fire were calculated with a Plume-model in accordance with Heskestad (see [1]) using a maximum heat release rate of 5 MW. To produce temperatures on the safe side this fire was applied only from a ceiling height of 4 m upwards, up to this level a flame temperature of 900 °C according to Heskestad was used.

4.5 Fire Safety Design

In a next step, a thermal analysis in 3-D was undertaken for the steel columns using the temperatures evolving from the localized fire as thermal load. Here, segments of a height of 2 metres were assumed to receive the same thermal load. It was taken into account that the components were protected by a protective coating up to a height of 8 m.

In a next step, a thermal analysis in 3-D was undertaken for the steel columns using the temperatures evolving from the localized fire as thermal load. Here, segments of a height of 2 metres were assumed to receive the same thermal load. It was taken into account that the components were protected by a protective coating up to a height of 8 m.

A thermal analysis for the structure of the roof was not necessary, since the temperatures recorded in the CFD simulation were only at about 400 °C. This temperature is well below the critical temperature of steel, as a result a fire safety design was only required for the columns. This design was carried out using the simplified calculation procedures on resistance level of Eurocodes 3 part 1-2. This was done in the most unfavourable area of the components regarding the internal forces and thermal loads. A fire safety design was not necessary for all stiffening components because they were protected from a critical warming by protective coatings.

5 CONCLUSION

The application of computational design methods of the Eurocodes for complete or partial structures can only be performed with powerful FEM programs that are able to depict and calculate the non-linearities of material build-ups and design loads. The heat generation in the cross section of the components is done by FEM programs as well. Usually a thermal analysis of two-dimensional models is of sufficient accuracy due to the material properties of steel that lead to quick uniform temperatures.

Depending on the complexity of the analysed structures the simplified or general calculation methods of the Eurocode. In the first case, the internal force in the fire case can be calculated using simple standard software, in the latter case more complex 3-D mechanical analysis is required.

With the rapid development and the increasing capacity of the computer coupled analysis of 3-D models will be possible in the future. Further research in these areas will extend the possibilities of the design of constructions, reduce the cost of planning the implementation of a project, and shorten the time for the realisation of buildings by the reduced structural fire protection at the same level of safety.

REFERENCES

- [1] DIN EN 1991-1-2: Eurocode 1: Einwirkungen auf Tragwerke. Teil 1-2: Allgemeine Einwirkungen - Brandeinwirkungen auf Tragwerke. Deutsche Fassung EN 1991-1-2:2010.
- [2] DIN EN 1993-1-2: Eurocode 3: Bemessung und Konstruktion von Stahlbauten. Teil 1-2: Allgemeine Regeln - Tragwerksbemessung für den Brandfall. Deutsche Fassung EN 1993-1-2:2005 + AC:2005.
- [3] McGrattan, K. B. a. o.: Fire Dynamics Simulator (Version 5) – User’s Guide. National Institute of Standards and Technology, Gaithersburg, October 2010.
- [4] Institut für Brandtechnologie GmbH: Gutachten Nr. G071201, Entwicklung eines numerischen Brandmodells zum DB-Bemessungsbrand für S-Bahn-Fahrzeuge, Leverkusen, 30.01.2008
- [5] DIN 4102-2: Brandverhalten von Baustoffen und Bauteilen, Bauteile – Begriffe, Anforderungen und Prüfungen, September 1977.
- [6] Twilt, L et al.: Design tools for the behaviour of multi-storey steel framed buildings exposed to natural fire conditions. Cardington (2) final report, TNO report 2003-CVB-R0088, Final Report Agreement 7210-PA, PB, PC, PD-112, 2002.
- [7] Ryan, J. V.; Robertson, A. F.: Proposed Criteria for Defining Load Failure of Beams, Floors and Roof Constructions During Fire Tests. Journal of research of the National Bureau of Standards, Vol. 63C, No. 2, 1959
- [8] vfdb-Leitfaden „Ingenieurmethoden des Brandschutzes“, vfdb, Technischer Bericht TB 04/01, Mai 2009

EXPERIMENTAL AND NUMERICAL INVESTIGATION OF INCLINED GLAZING FACADE PERFORMANCE UNDER FIRE CONDITIONS

Michael Quinn*, Ali Nadjai* and Faris Ali**

FireSERT, University of Ulster, Northern Ireland
e-mails: Quinn-M27@email.ulster.ac.uk, a.nadjai@ulster.ac.uk

** FireSERT, University of Ulster, Northern Ireland
f.ali@ulster.ac.uk

Keywords: Fire Tests, Glazing Facade, Finite Element.

Abstract. *Breakage and fallout of glazing systems create openings in an enclosure that affect the fire growth and the development of post flashover flames emerging outside of the openings. The behaviour of glazing is the result of its thermally induced stress response to the heat fluxes from the fire in an enclosure. The objective of this research is to carry out realistic experimental testing incorporating current glazing products & construction techniques. In recent times glazed façade layouts have evolved into more adventurous shapes and layouts, which necessitates the analysis of their performance as a result of localized fires. It is also envisaged that other environmental conditions such as wind will be included as a test parameter. These experimental tests will be cognisant of recent advances in glazing design and manufacture which have seen a move away from traditional single or double glazed units toward a higher specification unit with two or more glass panes held together by a special fire resisting resin.*

1 INTRODUCTION

Having reviewed previous tall building fires, history has shown that fires in high rise buildings are rare events, however when they do occur they generally have major consequences. It is known that many of these fires spread from floor to floor due to weaknesses which exist in the external glazing facade. This has become more prevalent as building design has evolved.

Data from previous scaled compartment glazing tests conducted at FireSERT on traditional single and double glazed units [1] will be used for comparative purposes with results of modern glazed unit tests to be carried out. This paper will also discuss Finite Element Analysis (F.E.A) validation exercises completed on [1] using TNO Diana.

The second unique and useful resource available at FireSERT is temperature data obtained from the window openings of the full scale office compartment test conducted by FireSERT [2]. This paper will discuss some preliminary F.E.A. analysis exercises completed using the data from [2]

Phase 1 – Ulster Fire resistance experimental tests: Six different Pyroguard glazing specimens of two different thicknesses (7.2 & 11.4mm) were tested following the ISO 834 fire curve. (Figure 1 & Table 1) These tests act as benchmarking as to the expected initial behaviour of the glazing material when subjected to the ISO 834.

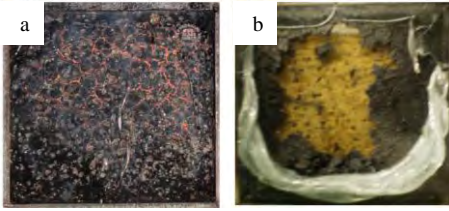


Figure 1. Test 5. No fireside (a), fireside (b).

Table 1. Electric furnace test landmarks.

Test	Specimen	1st Crack (secs)	1st Crack (°C)
1	7.2mm	305	463
2	11.4mm	324	469
3	7.2mm	305	403
4	7.2mm	482	480
5	11.4mm	240	410
6	11.4mm	256	366

Also completed was some F.E.A using TNO Diana as a comparison to the experimental findings. The numerical model outputs displayed in Figures 2 and 3 are a representation of a sample tested in the electric furnace. The maximum stresses generated within the numerical model were within the shaded edges of glass both at the top and bottom of the model. These maximum stresses were generated at approximately 243 seconds (Figure 4). These numerical model results show similarities with 5 of the 6 electric furnace tests' first crack times from Table 1 above, especially Test No. 5. It is noted that this model was completed for exploratory purposes.

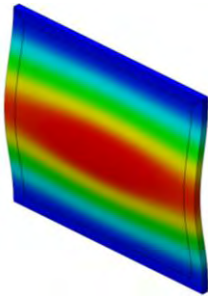


Figure 2. Electric furnace model displacement at 243s

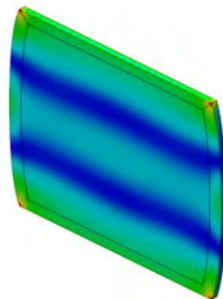


Figure 3. Electric furnace model stresses at 243s

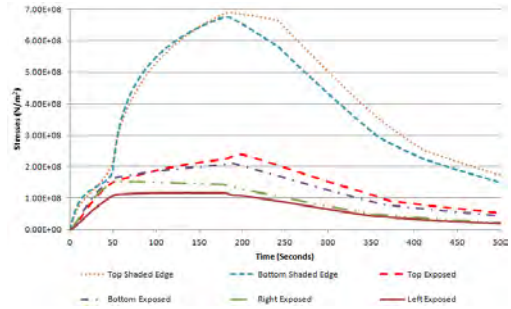


Figure 4. Electric furnace model stresses

Phase 2 -Finite Element Analysis - Ulster Scaled Compartment Tests: As set out above, a large amount of previous research into the performance of glazing systems at elevated temperatures has been conducted worldwide by people such as [3] and [4]. Another such program of research was that conducted at FireSERT by [1]. This research entailed a number of experimental tests within a scaled compartment. Variables within the tests included: fire size, fire location and glazing type (single and double). The data accumulated during these tests has never before been utilized for the purposes of numerical analysis. The single glazing model constructed within the TNO Diana software is a replica of the single glazing tested by [1]. The temperature data applied to the numerical model is that obtained from the numerous exposed and shaded thermocouples attached to the tested glazing assembly. Temperature curves were applied to the exposed glass, the shaded glass, and the exposed timber frame. The timber frame surrounding the model was constrained against movement during the numerical analysis process.

The purpose of creating and running this numerical model is to establish whether the TNO Diana software has the capability to represent accurately the behaviour of such glazed assemblies subject to the

elevated temperatures of a real life fire scenario. Having run the model the outputs provided by the software are quite extensive. The outputs of most interest to this research are the model temperature profiles, stress contours and model deformations. The graphical illustration below (Figure 5) is a comparison between the temperatures recorded at a specific location on the glazing during the experiment and that same location in the numerical model. Therefore it can be seen from Figure 5, that the numerical model is thermally calibrated with the experimental glazing temperature data. Figure 6 below is a graphical illustration of the evolution of stresses within the exposed glass in the top glazed section of the assembly. Also shown below in Figure 7 is an illustration of the model stress contours at the point of critical stress in the overall glazing assembly (i.e. 2025 seconds).

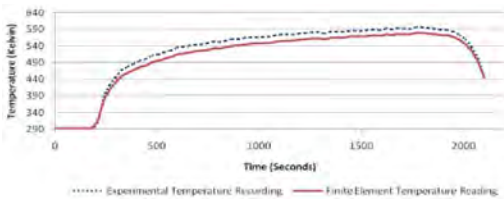


Figure 5. Experiment & finite element thermal calibration

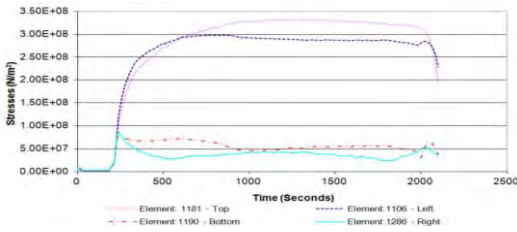


Figure 6. Model 1: Finite element pane 1 stress evolution

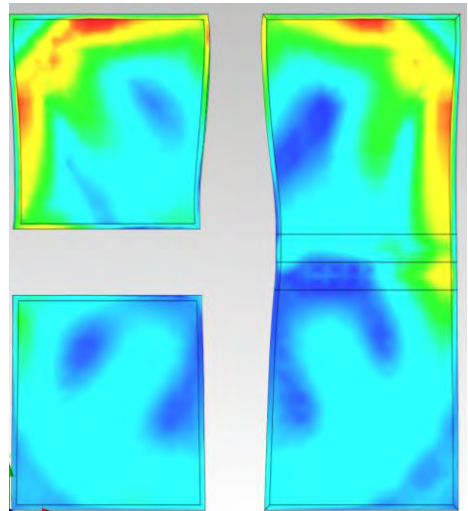


Figure 7. Model 1: Overall glazing stress contours at point of failure (2025 sec)

Figure 8 is a graphical illustration of the temperature and maximum stress evolution of pane 1 together on a single graph for convenience purposes. Following this in Figure 9 are the model deformations; most notable are the curvatures experienced within the numerical model at the time of critical stress (i.e. 2025 seconds).

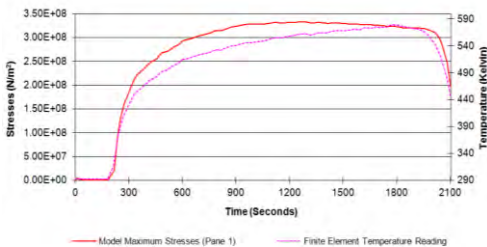


Figure 8. Model 1: Finite element temperature & maximum stress evolution

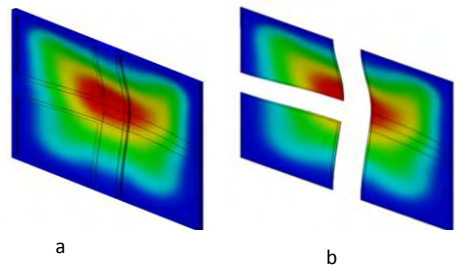


Figure 9. Model 1: deformation/ curvature at point of failure (2025 sec) incl. timber frame(a) no timber frame(b)

As an assessment and validation exercise, variables of the above model (model 1) were also produced using the Diana software. The top glazed panel from model 1 was tested as a standalone item (model 2). The same temperature curves were applied to both the exposed glass and timber frame and the shaded glazing areas of model 2 as per model 1 previously. This model's timber frame was constrained against movement in a similar manner to model 1. This model was initiated in an effort to determine the variability in performance from model 1 above given the absence of the remainder of the glazed assembly around the top panel in this case. (Figure 10).

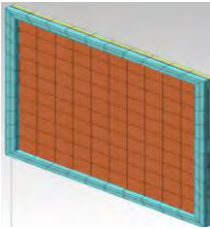


Figure 10. Model 2: Top panel model

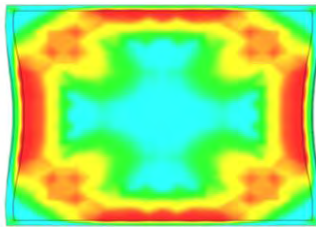


Figure 11. Model 2: Glazing stress contours at point of failure (1967 sec)

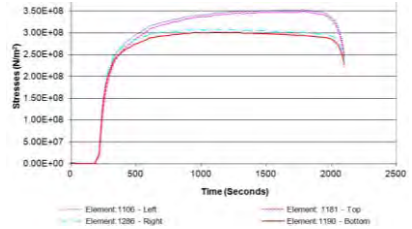


Figure 12. Model 2: Finite element stress evolution

Shown above in Figure 11 is an illustration of the model stress contours at the point of critical stress in the model. (i.e. 1967 seconds). Figure 12 is a graphical illustration of the evolution of stresses within the exposed glass in the model. Figure 13 is a graphical illustration of the temperature and maximum stress evolution within the model on a single graph for convenience purposes. Following this in Figures 14 are the model deformations; most notable are the curvatures experienced within the numerical model at the time of critical stress (i.e. 1967 seconds).

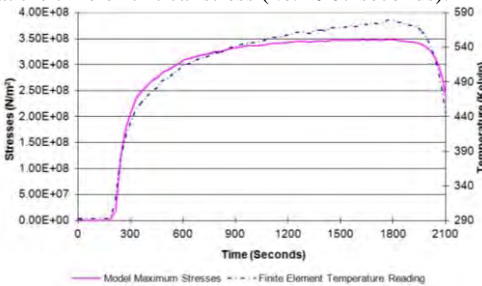


Figure 13. Model 2: Finite element temperature & maximum stress evolution

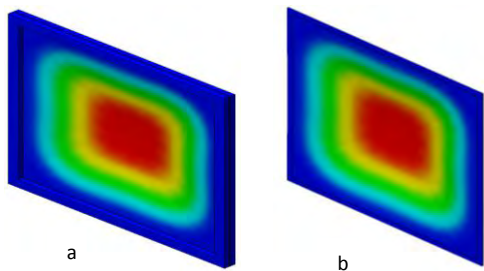


Figure 14. Model 2: deformation/ curvature at point of failure (1967 sec) - incl. timber frame (a) no timber frame (b)

The next model produced (model 3) differed from models 1 & 2 above. In the previous model (model 2) the timber frame and the shaded glazing (which had a temperature curve applied to it) within the frame played a part in the model. However in model 3 both were removed with only the exposed glass being present. The edges of the model (now the exposed glass) were constrained against movement in the same way as the previous models. This model was initiated in an effort to determine the variability in performance from model 2 above, given the absence of the shaded area of glass and timber frame in this case.

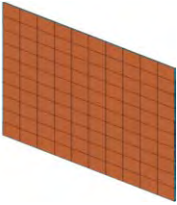


Figure 15. Model 3:
Top panel model

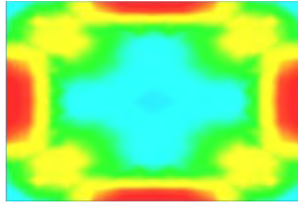


Figure 16. Model 3: Glazing stress contours at point of failure (1808 sec)

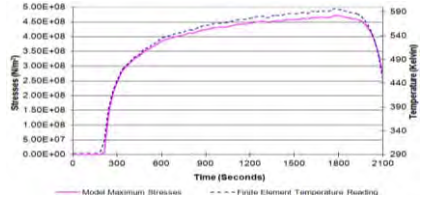


Figure 17. Model 3: Finite element temperature & maximum stress evolution

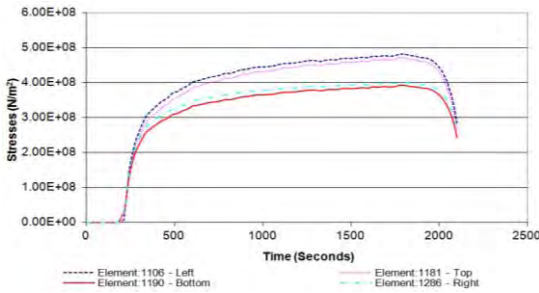


Figure 18. Model 3: Finite element stress evolution

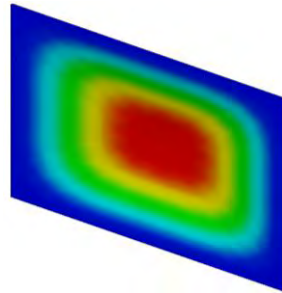


Figure 19. Model 3: deformation/curvature at point of failure (1808 sec)

In the same way as the previous model results outlined above. The pictures and graphical illustrations above; Figures 15-19 give an understanding of the variable stress distributions in each model as time passes. Figure 20 and Table 2 summarise the numerical analysis outcomes further. It is clear from the table that the maximum stresses were generated in model 3. The evolution of stresses in this model are such, due to the fact that the model consisted solely of heated glass which was constrained against movement on the four perimeter edges. Although the constraint mechanism around each of the 3 models was consistent, models 1 & 2 also contained sections of cooler glass and heated timber, which surrounded the exposed areas of glass. These surrounding elements and the fact that they would have allowed greater movement and expansion of the exposed glass has an undoubted effect on the respective models overall performance.

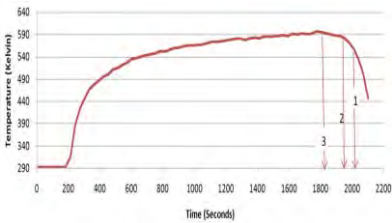


Figure 20. Finite element landmarks

Table 2. Finite element landmarks

Model	Time (secs)	Temp (K)	Temp (°C)	Stress (N/m ²)
1-Assembly	2025	534	261	3.05E+08
2-Top Panel (incl. shading)	1967	562	289	3.38E+08
3-Top Panel (no shading)	1808	595	322	4.71E+08

Phase 3: Finite Element Analysis – Ulster Full Scale Office Compartment Test: As set out above, an innovative fire safety research project was conducted by [2]. This project entailed the completion of a full scale office compartment fire test (Figure 21). During the evolution of the burn, a large amount of data was recorded. The data which is of particular interest to the area of glazing performance in fire are the temperatures recorded by the thermocouples which were strategically placed in the window openings of the office compartment. In all there were three thermocouples placed within the window opening (top, middle, and bottom). Figure 22 is a graphical illustration of the window opening thermocouple readings mentioned above.



Figure 21. Window opening thermocouples.

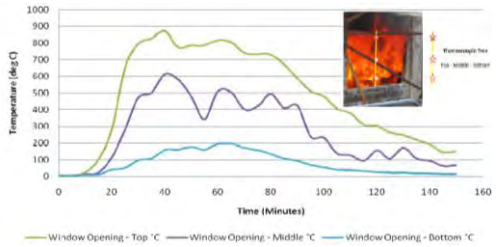


Figure 22. Window opening thermocouple recordings

Figure 21 also provides an illustration of the severity of the actual full scale office fire as it evolves. Of particular interest is the flame lapping through the window opening to external. These temperature recordings are of enormous value as they provide actual temperature data from window openings in a full size office compartment fire scenario. This data has been used in some preliminary finite element analysis exercises to date, and will continue to form an integral part of the research project as it progresses. Figure 23 is a graphical illustration of the thermal calibration of the numerical model with the fire test window opening thermocouple recordings. Figure 24 is the results output for the model glass surface temperatures at 23 minutes, which was the time of glazing failure within the numerical model.

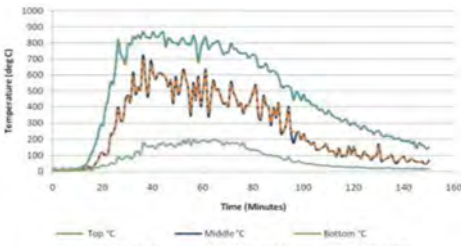


Figure 23. Numerical model thermal calibration.

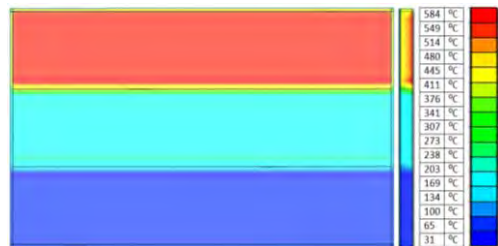


Figure 24. Glass surface temperature distribution @ 23 mins.

Figures 25 and 26 give an indication of the temperatures on the exposed and unexposed sides of the glass panel and also the temperatures present in the shaded rim of the glazing panel at each of 4 the stress landmarks to follow as set in Figures 27 to 30 and Figures 31 to 34.

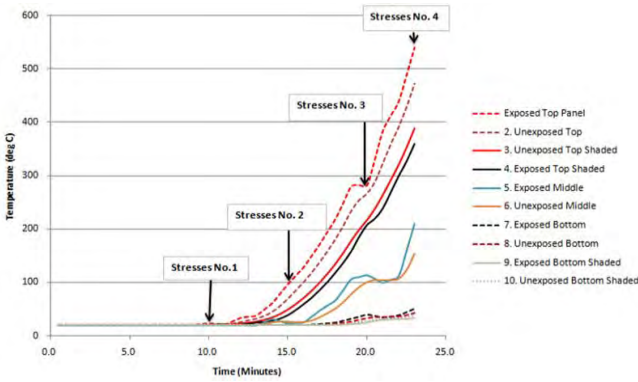


Figure 25. Numerical model temperature evolution incl. stress landmarks.

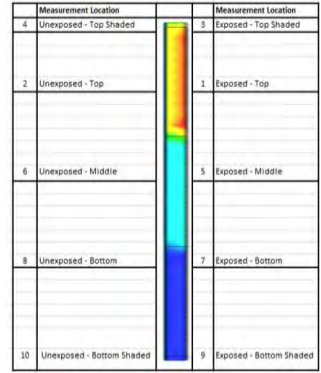


Figure 26. Edge temperature distribution.

The first model stresses to be viewed are those of the above mentioned model when it was positioned in an absolute vertical position. Figures 27 illustrates the evolution of stresses on the numerical model from the: a) 10th, b) 15th, c) 20th until glazing failure in the d) 23rd minute.

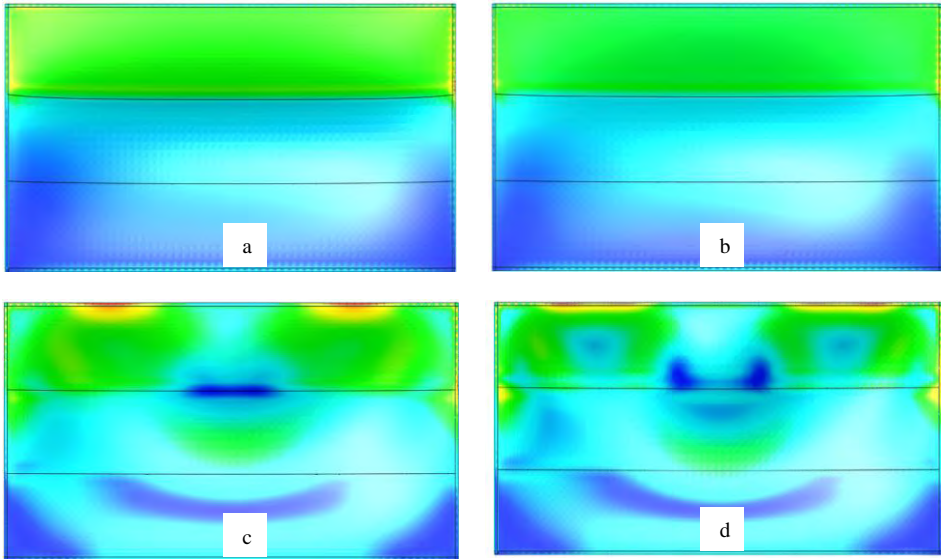


Figure 27. Stress contours 10, 15, 20 & 23 minutes.

The next model stresses to be viewed are those of the above mentioned model when it was positioned at an angle of 15° off the vertical, to represent an inclined glazed panel. Figures 28 illustrates the evolution of stresses on the numerical model from the: a) 10th, b) 15th, c) 20th until glazing failure in the d) 23rd minute.

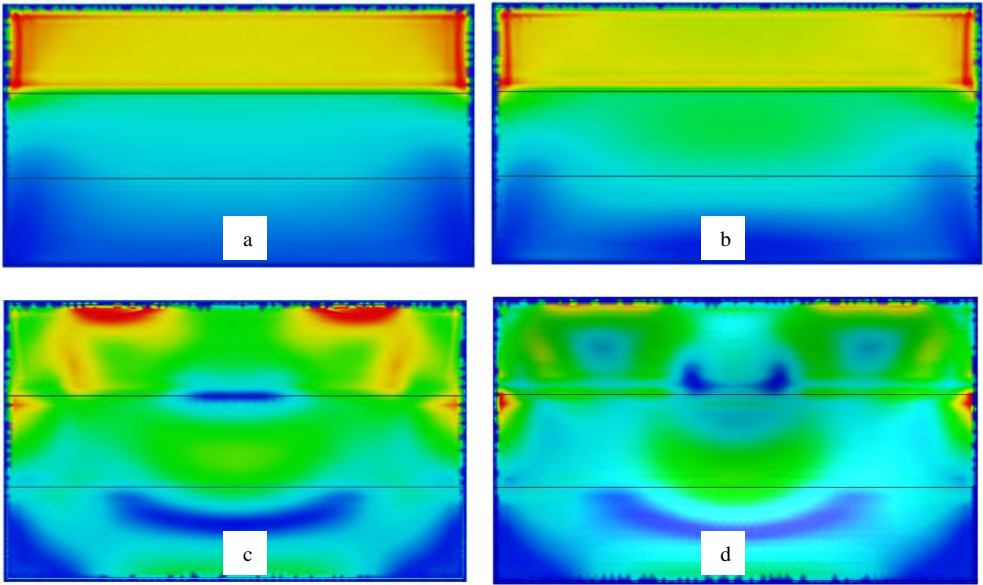


Figure 28. Stress contours 10,15, 20 & 23 minutes.

It is clear that there is little difference in the stress patterns in Figures 28 above for this model at 15° off the vertical, when compared against the absolute vertical model in Figures 27. The evolution of stresses for each scenario is set out in Figure 31. Also set out in Figures 29-30 are displacement output pictures for each scenario (vertical & inclined). Figure 32 is a graphical illustration of displacement evolution for each scenario.

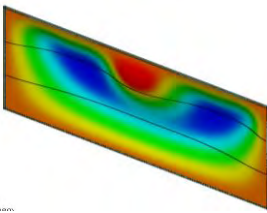


Figure 29. Vertical displacement curvature (23mins).

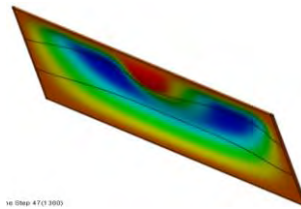


Figure 30. Inclined displacement curvature (23mins).

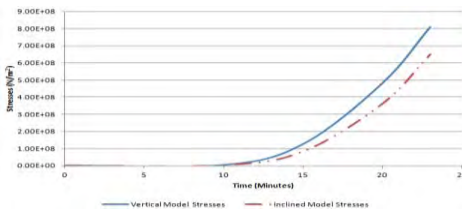


Figure 31. Stress evolution variability.

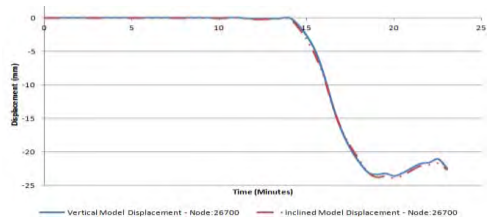


Figure 32. Displacement evolution variability.

It is clear that for failure of the inclined glazing model to occur similar thermal stresses were required as to that of the vertical model. As this numerical study evolves further, the effects of inclination angle and resultant gravity forces will be examined in depth.

To summarise the above numerical simulation outputs, as expected the maximum stresses were generated in the areas of the glazing panel which were subjected to the most excessive temperatures. Particular attention is also drawn in this scenario, as before, to the effect the presence of a shaded perimeter of glass has on the overall performance of the glazing panel at elevated temperatures. It can be seen from a review of the stress result outputs that the area of contact between the heated glass and the shaded rim is of particular importance and will require further more detailed research, both experimentally and numerically as part of this research project. The importance and impact of gravitational forces on the inclined numerical model cannot be ignored and will be monitored fully in future inclined glazing numerical models.

As with the numerical modelling undertaken using the experimental test data from [1], the numerical modelling discussed above using the data from the full scale office compartment fire test by [2] is preliminary and will be advanced upon as time progresses throughout the time span of this research project.

Phase 4: Localized fire tests on inclined glazed facades: An important factor to be considered in materials testing is the effect of localized fire and thermal radiation. This is particularly relevant with inclined glazed facades, which are becoming more popular with building designers; hence the need to investigate the effect variable inclination angle has on glazing performance under fire conditions.

As shown above a preliminary numerical analysis exercise has been conducted using the data from [2] on an inclined glazed panel at 15° off the vertical. The results of this numerical exercise were then compared with an identical glazed panel positioned vertically.

The next step in this research project will be to carry out experimental testing on inclined glazing panels, using realistic fire loading and replicating environmental conditions which may be expected in a real life fire scenario.

In these tests 3, Pyroguard 30 minute integrity only glazing specimens of 7.2mm thickness and overall dimensions of 1m (w) x 1.5m (h) will be tested. Test recordings taken will include thermocouple, strain gauge and Gordon gauge heat flux readings.

It is noted that inclined fire tests have been conducted previously on other building elements and materials by [5]. Also the properties of fire plumes from window openings to building facades have been previously studied by [6].

Following completion of these experiments a detailed numerical parametric analysis exercise will be completed using the TNO Diana F.E.A. software. Similar numerical case studies such as this were previously conducted by [7]. The data and facilities available at FireSERT will assist in advancing the knowledge which exists on inclined glazing façade performance in fire conditions.

2 CONCLUSION

- 1- Upon review of both the fire resistance experimental tests and the preliminary numerical analysis exercises conducted, (Phase 1) it is clear that the maximum stresses are generated at the shaded edge of the glazing samples.
- 2- The numerical analysis exercise which followed using the test set up and recorded data from [1] (Phase 2) again uncovered this phenomenon of edge stress generation.
- 3- Upon review of the numerical analysis models; 1, 2 and 3 of Phase 2, some interesting results were uncovered:
 - All three models experience the creation of off-plane curvature during the numerical analysis process. (Figures 9, 14 & 19)
 - The presence of both the timber frame and shaded perimeter of glass in models 1 and 2 result in the creation of a curvature at the edges of both models (Figures 7 & 11). This

curvature is not present in model 3 (Figure 16), due to the absence of a timber frame and shaded perimeter in this model.

- The most severe stresses were generated in model 3, mainly due to complete model exposure to the heating process, and the total resistance to movement which existed in this model due to the absence of any shaded glass or timber frame.
- 4- The data recorded in the full scale office compartment fire test conducted at Ulster [2] has only been used minimally to date but shall form an integral element of this research as it gives an indication of actual temperatures to be expected in a real office fire scenario.
 - 5- The preliminary numerical analysis exercises conducted using [2] - Phase 3, demonstrate similar tendencies as before with regard to the location maximum stresses.
 - 6- The importance and impact of gravitational forces on the inclined numerical model in Phase 3 cannot be ignored and will be monitored fully in future inclined glazing numerical models.
 - 7- The inclined glazing facade tests to be carried out in due course will ultimately form the core of the research project and assist in advancing the knowledge which currently exists on inclined glazing façade performance under fire conditions.

REFERENCES

- [1] Shields, J., Silcock, G.W.H. & Flood, M. 2002, "Performance of a Single Glazing Assembly Exposed to a Fire in the Centre of an Enclosure", *Fire and Materials*, , no. 26, pp. 51-75.
- [2] Nadjai, A., Bailey, C.G., Vassart, O., Han, S., Zhao, B., Hawes, M., Franssen, J.M. & Simms, W.I. 2011, "Full-scale fire test on a composite floor slab incorporating long span cellular steel beams", *The Structural Engineer*, vol. 89, no. 21, pp. 18-25.
- [3] Xie, Q., Zhang, H., Wan, Y., Zhang, Q. & Cheng, X. 2008, "Full Scale Experimental Study on Crack & fall Out of Toughened Glass with Different Thicknesses", *Fire and Materials*, , no. 32, pp. 293-306.
- [4] Joshi, A.A. & Pagni, P.J. 1990, *Thermal Analysis of Compartment Fire on Window Glass*, NIST, USA.
- [5] Oka, Y., Imazeki, O. & Sugawa, O. 2010, "Temperature profile of ceiling jet flow along an inclined unconfined ceiling", *Fire Safety Journal*, vol. 45, no. 4, pp. 221-227.
- [6] Tang, F., Hu, L.H., Delichatsios, M.A., Lu, K.H. & Zhu, W. 2012, "Experimental study on flame height and temperature profile of buoyant window spill plume from an under-ventilated compartment fire", *International Journal of Heat and Mass Transfer*, vol. 55, no. 1-3, pp. 93-101.
- [7] Pope, N.D. & Bailey, C.G. 2007, "Development of a Gaussian glass breakage model within a fire field model", *Fire Safety Journal*, vol. 42, no. 5, pp. 366-376.

STEEL STRUCTURES

BEHAVIOUR OF COMPRESSED COLD FORMED STEEL ELEMENTS AT HIGH TEMPERATURES

Saulo J. C. Almeida*, João Paulo C. Rodrigues** and Jorge Munaiar Neto*

* Engineering School of Sao Carlos, University of Sao Paulo, Sao Carlos, Brazil
e-mails: saulojca@sc.usp.br, jmunaiar@sc.usp.br

** University of Coimbra, Coimbra, Portugal
e-mail: jpaulocr@dec.uc.pt

Keywords: Cold formed steel, column, fire, restraining.

Abstract. *This paper presents the results of an experimental investigation on the behaviour of compressed cold formed steel elements at high temperatures. The objectives of the work were to gain an insight into the mechanical behaviour of these elements at high temperatures considering the influence of the restraining to thermal elongation and to provide some experimental results for detailed numerical studies. Three types of cross-sections, C, I and 2R and two types of end-supports, semi-rigid and pin-ended, were investigated. A load level of 30% of the design value of buckling load at ambient temperature was applied during the tests. From this experimental investigation it has been observed that the influence of the thermal restraining was different for each type of cross-section. The behaviour of the columns at high temperatures was not significantly affected by the geometric imperfections and columns nominally identical showed a similar deformed shape and ultimate strength.*

1 INTRODUCTION

Cold formed steel members are increasingly being used as load bearing members. However, fire performance of cold formed steel structures is not well understood. Recent research works have been carried out in order to establish simplified design methods for cold-formed steel members at high temperatures, based on the design methods of EN1993 - 1.3 [1] or EN1993 - 1.2 [2]. However, until today no consensus has been reached about the use of these design methods. According to [3] the low number of experimental results available in the literature does not permit to use the EN1993 - 1.3 or EN1993 - 1.2 procedures for designing cold formed steel elements at high temperatures. Nowadays tests are conducted in order to better understand the structural behaviour of these elements in fire and provide experimental data.

In the present work was investigated the behaviour of compressed cold-formed steel elements at high temperatures considering the influence of the restraining to thermal elongation. It is known that when a steel column is subjected to fire the restraining forces will increase due to the restraining thermal elongation provided by the building surrounding structure [4]. Thus, in order to better understand the structural behaviour of cold formed steel columns at high temperatures as well as to predict the restraining forces generated in these elements, it is important to consider the restraining to the thermal elongation.

2 EXPERIMENTAL STUDY

2.1 Test Set-up

Figure 1 shows the general layout of a test system used to investigate the fire resistance of building columns erected at University of Coimbra, Portugal. This test system was composed by a 3D restraining frame (1) which allows simulating three levels of axial restraining of the surrounding structure. Using this steel frame was possible to study the influence of the restraining to thermal elongation on the behaviour of the building columns subjected to fire.

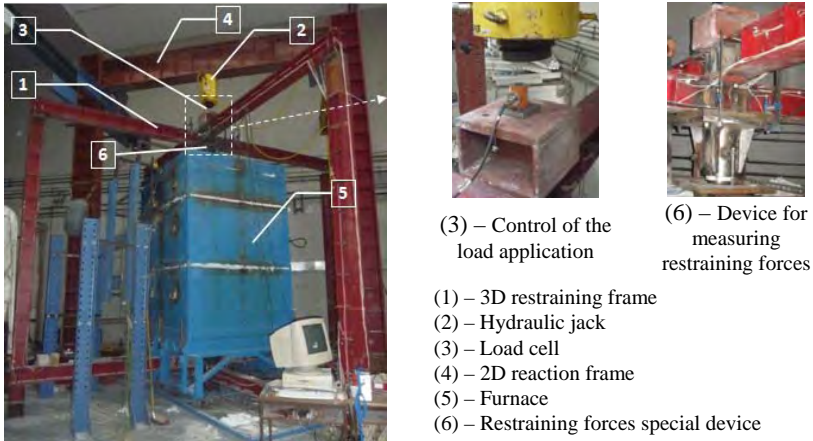


Figure 1. Test Set-up.

The restraining system was composed by four columns, two upper beams and two lower beams which were arranged in an orthogonal system. The connection between the beams and columns were done by screws at the bottom and threaded rods at the top which allows transmitting a serviceability applied by a hydraulic jack (2) to the testing columns. A load cell (3) positioned between the top flange of the upper beam of the 2D restraining frame (1) and the hydraulic jack controlled the load that was being applied. The hydraulic jack was fixed to an external 2D reaction frame (4).

A special device (6) was designed to measure the restraining forces in the test columns (figure 2 (a) and (b)). This device comprised a hollow high-strength steel cylinder, which was rigidly connected to the upper beams of the restraining system. In this hollow high-strength steel cylinder entered a massive steel cylinder which was connected on the top of the test column. The lateral surface of this massive cylinder was Teflon (PTFE) lined in order to reduce the friction between the hollow and massive cylinders. Inside the hollow steel cylinder was located a load cell for measuring the restraining forces. The compression of this load cell was done by the massive cylinder due to the thermal elongation of the column in test.



Figure 2 – (a) Scheme of the device for measuring the restraining forces (b) Fabrication of the device (C) column's pinned support

The thermal action was imposed by a modular electric furnace (5) composed by two modules of 1m and another of 0.5m high. The modules were superimposed one another forming a chamber of 1.5x1.5m x 2.5m around the test specimen. The heating curve tried to follow the ISO834 fire curve.

The temperature inside the furnace was measured with plate thermometers. The temperatures in the specimen were registered with type K thermocouples on four sections distributed along the height of the test column allowing not only knowing the distribution of temperatures on the cross-section but also in column's height (figure 3).

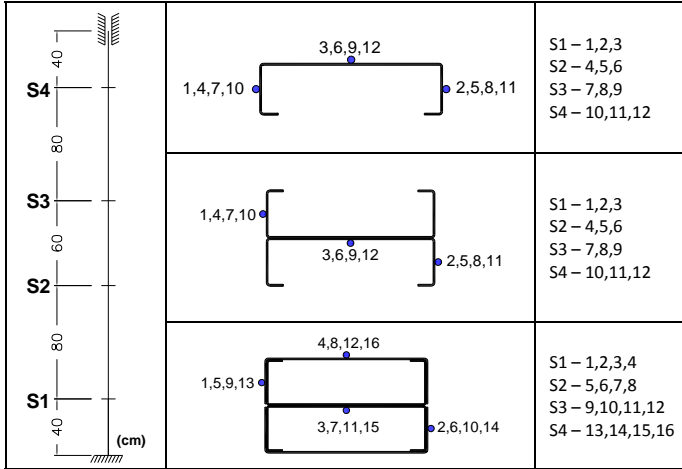


Figure 3. Thermocouples distribution in the column's cross-sections

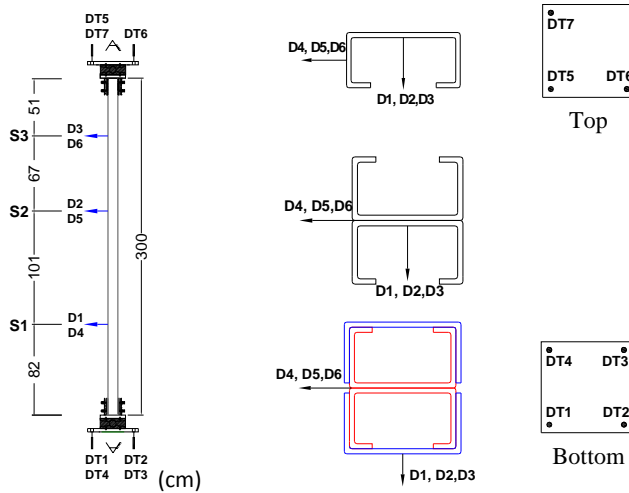


Figure 4. Displacement transducers location

To measure the column longitudinal displacements and end rotations seven displacement transducers were used, three at the top and four at the bottom. The transducers were arranged orthogonally allowing not only measuring the axial displacements but also the end rotations of the columns ends.

Six cable displacement transducers were placed along the height of the columns for measuring the lateral deflection, three in the direction of the minor axis and three in the direction of the major axis (Figure 4).

2.2 Test specimens and test programme

A total of eighteen transient fire tests were performed on 3m tall columns with C, I and 2R sections (Figure 5). The basic sections used to form the I and 2R section were lipped and unlipped channels, 150x43x15x1.5 and 153x43x1.5, respectively. Nine tests on semi-rigid and nine on pin-ended columns were carried out. Figure 6 shows the screw distribution used to compose the I and 2R sections.

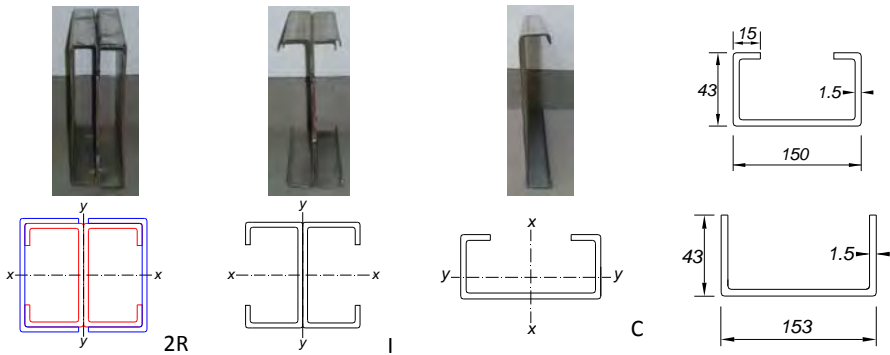


Figure 5. Cross sections (dimensions in mm)

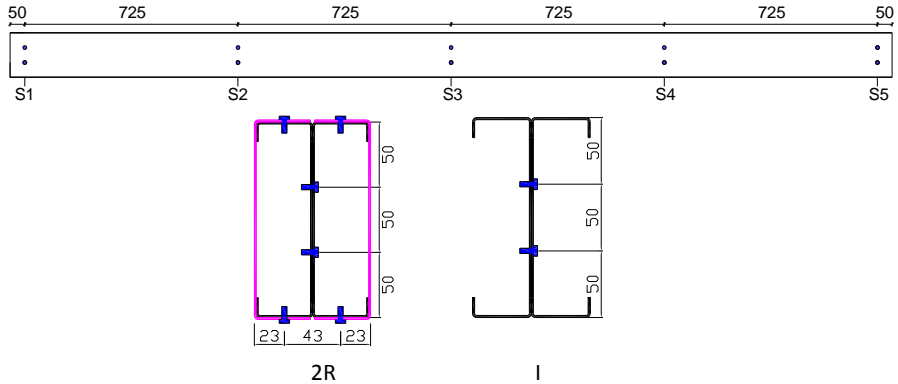


Figure 6. Screw distribution (dimensions in mm)

The steel grade was the S280 GD+ with minimum yield strength of 280 N/mm^2 .

Table 1 present the test plan of the fire tests on the compressed cold-formed steel elements.

All the tests were carried out for an axial restraining of the restraining frame of 7 kN/mm and a load level of 30% of the design value of the buckling load of the columns at room temperature determined according to EN 1993 -1.3 [1].

Table 1 – Test specimens

Cross-section type	(C)	(I)	(2R)
End-supports	Semi-rigid and pin-ended		
Number of tests	3 / parameter combination		
Global slenderness	96	77	50
Initial Load (kN)	10	38	60

2.3 Test procedure

The test specimen was first placed at the supports in the centre of the 3D restraining frame. Then the serviceability load was applied to the column. During the load application the threaded rods that connected the upper beams to the columns of the 3D restraining frame were totally free allowing with this the total transfer of the applied load to the test column. When the desired value of the serviceability load was reached the nuts of the threaded rods were tightened to provide the restraining to thermal elongation of the column in test. After this the furnace was finally switched on and the heating started.

As the temperature increasing the restraining forces on the test columns start increasing up to a maximum due to the restraining to thermal elongation after which started decreasing due to the degradation of the mechanical properties of the steel. The test was finished when the restraining forces reach again the value of initial applied load.

Figure 7 shows an illustrative scheme of the test system with the specimen mounted on the centre of the 3D restraining frame.

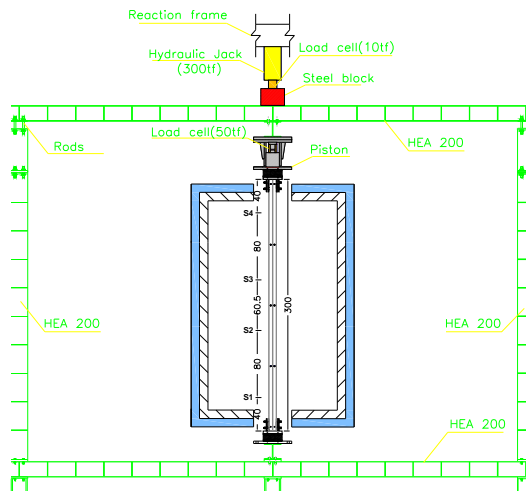


Figure 7. Scheme of the test system with the specimen

3 RESULTS

3.1 Furnace Temperatures

In all fire tests the set point heating curve of the furnace was regulated to the ISO 834 fire curve. However, as shown in figure 8, it was difficult to reproduce this curve in the early stages of the test due to lack of power of the electric furnace used. Only after 6 minutes of test the furnace temperature

followed quite well the ISO 834 fire curve. A uniformity of temperatures in the three modules of the furnace was registered (Figure 8).

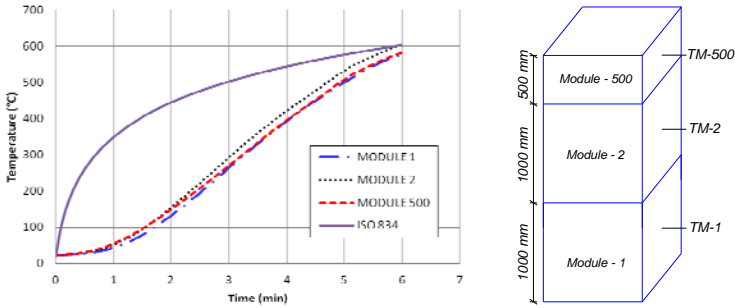
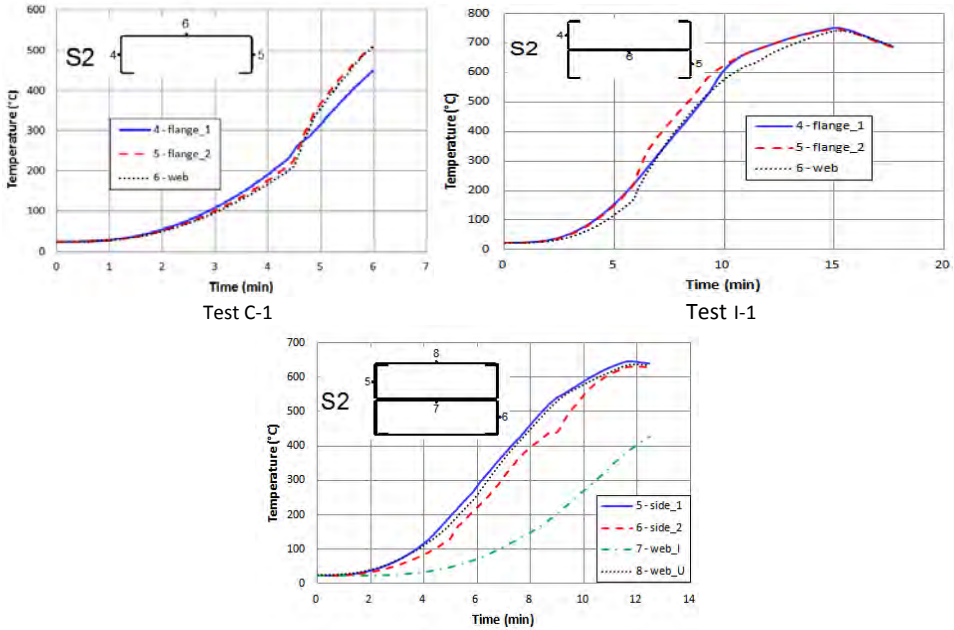


Figure 8. Temperature in the furnace

3.2 Thermal behavior of the specimens

From figure 9, it can be observed that the temperature distribution on the boundary of the cross-section was approximately uniform during the major part of the time for tested columns. In general, for the C and I cross-sections the temperatures of the flanges and the web were very close and for 2R cross-section the difference among the temperatures of the points located on the boundary was also small. For the 2R cross-sections the temperature on inside thermocouples was smaller than the temperatures on the outside thermocouples. This is justified by the fact that the 2R is a closed cross-section not subjected to gas convection and protected against the furnace radiation.



Test 2R-1

Figure 9. Temperature vs time for the section S2

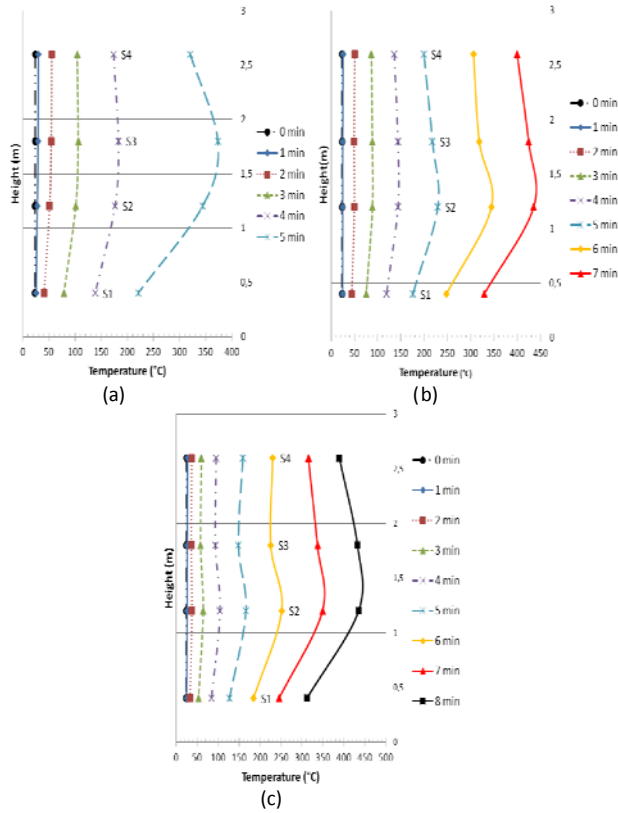


Figure 10. Temperature distribution along the length
 (a) test C-1, (b) test I-1 and (c) test 2R-1

The temperature distribution on column’s height was not uniform and a thermal gradient was observed (figure 10). The maximum temperature was registered at column’s mid-height and this may have influenced the failure mode of the columns.

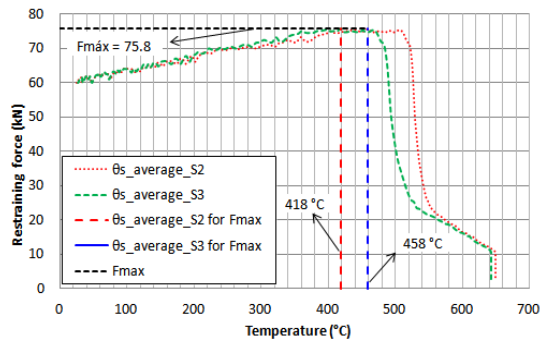


Figure 11. Restraining forces in function of steel temperature for S2 and S3 cross-sections (test 2R-2) – semi-rigid end joints

In Figure 11, it can be observed for a 2R test column, with semi-rigid end joints, that whichever was the chosen section to calculate the average temperature there may be slight differences on the temperatures corresponding to the maximum restraining forces and the instant when the restraining forces reach again the value of the initial applied load (critical temperature). For the case of the test column 2R-2, selecting the cross-sections S2 or S3, a difference of about 40°C was registered.

3.3 Structural behavior of the specimens

The development of the axial restraining forces in function of the temperature, for each type of cross-section tested, is shown in figure 12. For the C cross-section the restraining forces increased up to 3.21 times while for I and 2R cross-sections increased up to 1.58 and 1.26 times the initial applied load, respectively. These results are for semi-rigid end joint columns.

Qualitatively the buckling behaviour of the columns at high temperatures also showed differences. According to figure 12 after losing stability, the restraining forces for the C sections decreased rapidly with the temperature. On the other hand, for I and 2R section, the rate of decreasing of the restraining forces with the temperature was smoother. This suggests that columns with I and 2R cross-sections did not lose their bearing capacity immediately after reaching the maximum restraining forces and the failure temperature is greater than the buckling temperature.

However, quantitatively the post-critical behaviour at high temperatures of the investigated elements was not so significant. Both the numerical differences between the failure temperature (critical temperature) and buckling temperature and between the instant of time corresponding to the failure and buckling temperatures were short (figure 13).

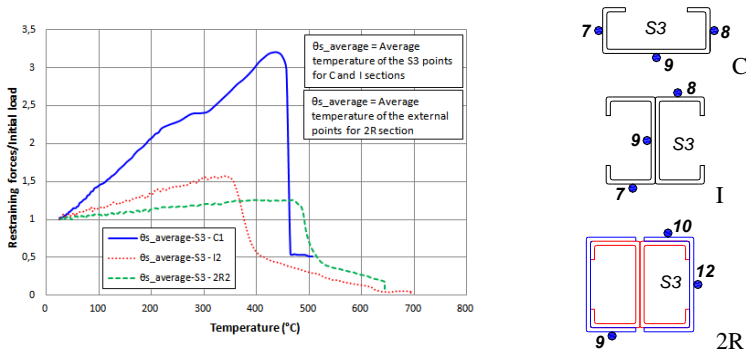
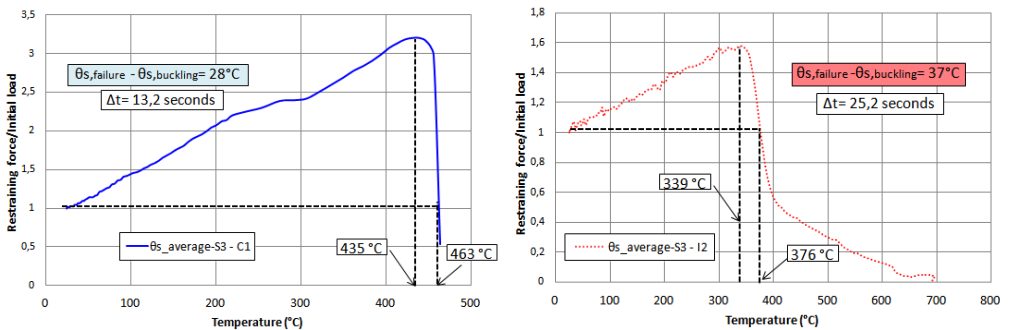


Figure 12. Restraining forces in function of the mean steel temperature of column's cross-section 3 – tests C1, I2 and 2R2 – semi-rigid end joints



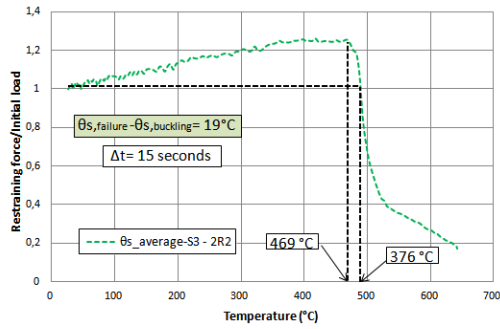


Figure 13. Differences between buckling and failure temperature for column's cross-section 3 – tests C1, I2 and 2R2 – semi-rigid end joints

3.4 Failure Modes

Figure 14 shows an I - cross-section column after test. It can be observed the global and local buckling especially on the flanges of the column at mid height cross-section.



Figure 14. I - cross-section column inside the furnace after test

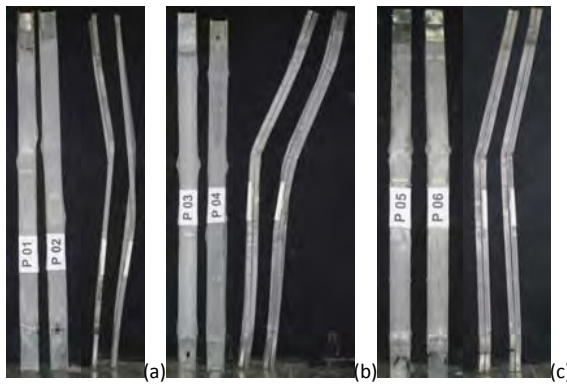


Figure 15. Failure mode of the test columns: (a) C (b) I and (c) 2R cross-sections

In figure 15 is presented the deformed shape of the specimens after test. It should be highlighted that this deformed shape was only observed after test. Due to the characteristics of the test system and mainly of the furnace it was impossible to register / photograph the failure mode of the specimens when the buckling started.

Since the elevated temperature failure mode involved local and global buckling by flexural bending, it is difficult to asseverate what was the predominant failure mode for each test. However, it does appear that for the lipped channels, the final shapes of the specimen indicate local buckling as predominant. For I and 2R sections, it does appear that global mode was predominant and the local crush at the middle was consequence of the bending of the column. During the tests, for the lipped channels tests was heard an abrupt noise indicating the failure whereas for I and 2R tests it does not happen.

5 CONCLUSIONS

This paper presented the results of an experimental investigation into the behaviour of compressed cold-formed steel elements under high temperatures. A total of 12 fire resistance tests were carried out. From the experimental results the following conclusions may be drawn:

- The results indicate that the behaviour of the columns at high temperatures was not significantly affected by the geometric imperfections.
- Furthermore, indicate that the testing device was suitable for determining the buckling loads of the columns. Identical columns showed similar deformed shapes and buckling loads.
- For the heating conditions of the tests, totally engulfment of the columns, the results indicate that the failure temperature should be determined on sections near column's mid-height. From the test results the temperature distribution along the height showed the maximum near this part of the columns.
- The influence of the restraining to the thermal elongation on the development of the restraining forces was less for I and 2R than for C cross-sections.
- The results indicate that the critical temperature can be considered as the failure temperature.

ACKNOWLEDGEMENTS

The authors gratefully acknowledge to the Portuguese cold-formed steel profile maker PERFISA S.A. (www.perfisa.net) and the Portuguese Foundation for Science and Technology – FCT (www.fct.mctes.pt) for their support.

REFERENCES

- [1] EN 1993-1-3: 2006 - Design of Steel Structures. Part 1-3: General rules – Supplementary rules for cold-formed members and sheeting, European Committee for Standardization, Brussels.
- [2] EN 1993-1-2: 2005 - Design of Steel Structures. Part 1-2: General rules – Structural Fire Design, European committee for standardization, Brussels.
- [3] Heva, Y. B., “Behaviour and design of cold-formed steel compression members at elevated temperatures”, PhD thesis, Queensland University of Technology, 2009.
- [4] Wang, Y. C. *Steel and Composite Structures - Behaviour and Design for Fire Safety*. Spon Press, London, 2002.

PARAMETRIC STUDY ON THE BEHAVIOUR OF STEEL COLUMNS EMBEDDED ON WALLS

António M. Correia*, **João P. Rodrigues**** and **Paulo Vila Real*****

* ISISE – Institute for Sustainability and Innovation on Structural Engineering
Polytechnic Institute of Coimbra, Portugal
e-mail: antonio.correia@isec.pt

** ISISE – Institute for Sustainability and Innovation on Structural Engineering
University of Coimbra, Portugal
e-mail: jpaulocr@dec.uc.pt

*** University of Aveiro, Portugal.
e-mail: pvreal@ua.pt

Keywords: steel, columns, fire, walls, restraining.

Abstract. *This paper presents a study on the fire behaviour of H steel columns embedded on walls with restrained thermal elongation. Based on a set of experimental tests on H steel columns, a finite element model was developed, taking into account the interaction of the column with the walls. It was possible, with this study, to observe and understand the typical behaviour of steel beam-columns with huge thermal gradients within the cross-section. In the scope of this work, the failure of the columns was observed to occur by bending, due to the thermal bowing phenomenon, instead of buckling.*

1 INTRODUCTION

The behaviour of building steel columns in contact with walls, in fire situation, is considerably different from the one observed in isolated steel columns [1, 2, 3]. The different temperatures attained in the flanges of the steel cross-section, lead to different thermal stresses and strains in the heated and unheated sides, and a bending moment is generated, causing a bow deflected shape towards the hot side, and then to the cold side. This leads to a shift of the effective centroid of the section and an inversion of bending moments. For the purpose of studying this behaviour of steel columns, a special experimental set-up was constructed in the University of Coimbra, and a set of full-scale tests was carried out. These tests were used to calibrate a numerical model, used in a parametric study, which is presented in this study.

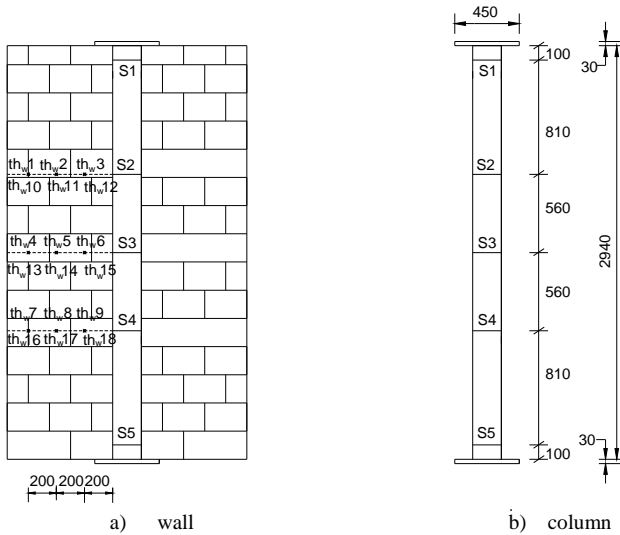
2 EXPERIMENTAL TESTS

The system comprises a restraining frame (figure 1) with the function of simulating the surrounding structure to the columns under test. HEA 160 and HEA200 steel columns, isolated and embedded on walls were tested experimentally. The columns on this system can be tested under a load that tried to simulate the applied load on the columns in real situations. The stiffness of the surrounding structure was obtained with different beams of the restraining frame.



a) columns embedded on walls b) bare columns
Figure 1. Experimental Set-up

Figure 2 and 3 describe the cases studied. The specimens were made of HEA160 and HEA200 profiles, 3m height, with end steel plates of dimensions 450mm x 450mm x 30mm, all of steel grade S355.



a) wall b) column
Figure 2. Scheme of the specimens embedded on walls

The reference “Exx” indicates the tests carried out on columns embedded in walls while the reference “Iyy” indicates the tests carried out on isolated steel columns.

Walls with a thickness nearly the same or smaller than the columns width were considered. The walls thicknesses were chosen according to the commercial dimensions of the bricks.

Two different orientations of the steel profile in relation to the wall surface were considered: web parallel and perpendicular to the walls surface. The reason for this choice is that a different behaviour was expected, since in the two cases, bending occurred around minor or major axis of the cross sections.

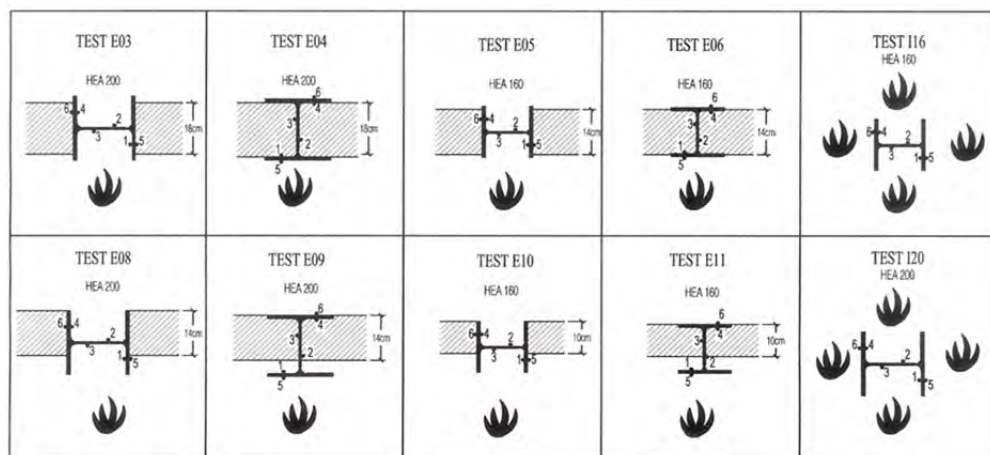


Figure 3. Experimental studied cases and location of thermocouples.

3 NUMERICAL SIMULATIONS

3.1 Numerical model

A thorough numerical modelling of the experimental tests (figure 4), considering a geometrical and material non-linear analysis, with imperfections was carried out. The target parameters of this study were the slenderness of the columns, the load level (50 and 70% of the buckling load at ambient temperature, according to EN1993-1-1(2005) [4]), the stiffness of the surrounding structure (two values) and the thickness of the building walls for the case of columns embedded on walls. Both in the experimental tests and in the numerical simulations of the steel columns embedded on walls, the thermal action was considered following the ISO 834 standard curve, and acting only on one side of the specimens. Moreover, two orientations of the cross-section were tested (with the web perpendicular to the wall and parallel to the wall surface leading to thermal gradients along the web or along the flanges).

The results of these simulations, allowed the assessment of the restraining forces developed during the tests, and the assessment of the thermal gradients observed in the cross-sections.

Table 1 presents the plan of the numerical simulations.

Table 1. Plan of the numerical models.

Test	Steel profile	Orientation in relation to the wall surface	Thickness of the walls	P_0 (kN) LL 70%	P_0 (kN) LL 50%	λ_{z-z} (minor axis)	λ_{y-y} (major axis)	Relevant axis / Slenderness
E03	HEA 200	parallel	180	1088	777	42.2	25.4	zz / 42.2
E04	HEA 200	perpendicular	180	1088	777	42.2	25.4	yy / 25.4
E05	HEA 160	parallel	140	704	503	52.8	32.0	zz / 52.8
E06	HEA 160	perpendicular	140	704	503	52.8	32.0	yy / 32.0
E08	HEA 200	parallel	140	1088	777	42.2	25.4	zz / 42.2
E09	HEA 200	perpendicular	140	1088	777	42.2	25.4	yy / 25.4
E10	HEA 160	parallel	100	704	503	52.8	32.0	zz / 52.8
E11	HEA 160	perpendicular	100	704	503	52.8	32.0	yy / 32.0
I16	HEA 160	no walls	-	704	503	52.8	32.0	zz / 52.8
I20	HEA 200	no walls	-	1088	777	42.2	25.4	zz / 42.2

The values of the slenderness λ were determined using the following formula:

$$\lambda = \frac{L_0}{\sqrt{\frac{I}{A}}} \quad (1)$$

in which I is the second moment of area of the steel cross-section, A is the area of the cross-section, and L_0 is the buckling length of the columns, calculated by:

$$L_0 = 0.7 \times L \quad (2)$$

in which L is the real length of the column, which is 3m for all tests.

The last column of table 1 indicates the relevant axis, around which buckling of the columns occurs. Considering that the walls prevent the buckling of the column in its plane, the relevant buckling axis when the profile is oriented with the web perpendicular to the wall is y - y , while when the web is parallel to the wall is z - z .

A numerical model was built with solid elements from the ABAQUS library of finite elements (Figure 4). The elements chosen for the columns were the C3D20RT while for the rest of the surrounding structure were the C3D8RT. The C3D8RT is an 8-node while the C3D20RT is a 20 node linear finite element with reduced integration, an hourglass control solid element and a first-order (linear) interpolation. These elements have one integration point, three degrees-of-freedom per node corresponding to translations and six stress components in each element output.

The finite element mesh was generated automatically by the ABAQUS program and the size of the finite elements was 30 mm in the specimen, walls and upper beams of the restraining frame and 100mm in the columns of the restraining frame.

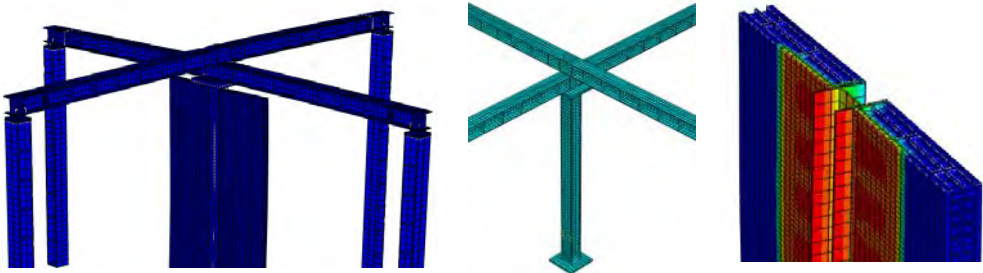


Figure 4. Three-dimensional model and finite element mesh for the restraining frame and specimen

The thermal and mechanical properties at high temperatures of the concrete were defined according to EN1993-1-2(2005) [5]. For the bricks the properties were not considered varying with temperature due to a lack of data available in the literature. Values used in the software Ozone, from the University of Liège, were adopted.

The thermal action was applied following the standard ISO 834. For the radiation and convection, a sensitivity analysis was performed. The adopted values were the ones which provided a better correlation with the experimental results, in the calibration of the model. On the un-exposed side, a convection coefficient of $4 \text{ Wm}^2/\text{°C}$ and emissivity coefficients of 0.7 for the concrete and 0.8 for the steel, and on the exposed side a convection coefficient of $25 \text{ Wm}^2/\text{°C}$ and an emissivity of 0.7 were used for both materials.

The numerical simulations were performed using a coupled-temperature displacement type of analysis, in which thermal and structural calculations are performed at the same time.

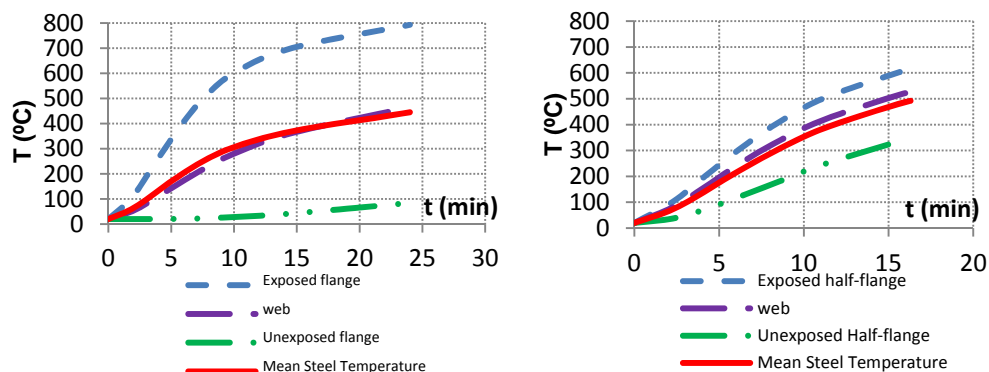
Interactions between different parts of the model were in most cases “tie-constraint” of type master-slave, except between the upper beams and peripheral columns, in which a several step procedure was adopted to apply directly the applied load to the specimen.

Geometrical imperfections were considered as initial eccentricities in two orthogonal directions.

3 ANALYSIS

3.1 Temperatures

From figure 5 it may be observed the great thermal gradient within the steel profiles in the case of the column perpendicular to the walls (E11) and in the case of the web parallel to the walls (E10)



a) with the web perpendicular to the wall (Test E11)

b) with the web parallel to the wall (Test E10)

Figure 5. Thermal gradients in columns embedded on walls

Tables 2 and 3 depict in a more detailed way the temperatures attained in the several parts of the steel profiles, for the same cases. Temperatures in the exposed flange or half-flanges were purposefully plotted for instants of time at which they experimented temperatures of 100°C intervals.

Table 2. Temperatures on test E11

t(min)	Exposed flange	Web	Unexposed flange	Mean steel temperature
0.0	20	20	20	20
1.8	100	49	20	57.5
3.2	200	87	20	105
4.5	300	127	20	152
5.9	400	170	21	200
7.6	500	220	23	252
10	600	280	28	306
14.6	700	362	42	369
24	793	465	84	445

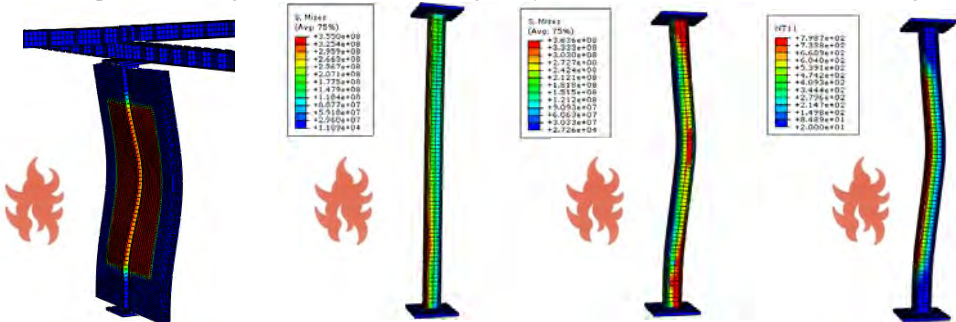
Table 3. Temperatures in test E10

t(min)	Exposed half-flange	Web	Unexposed half-flange	Mean steel temperature
0	20	20	20	20
2.25	100	80	37	71.8
4.16	200	159	72	141.9
6.1	300	244	119	218.4
8.3	400	329	174	297.8
11.1	500	417	245	383.9
15.5	600	513	333	478.5
16.3	614	526	347	492.2

3.2 Von Misses stresses

In figure 6, the failure mechanism of a steel column embedded on walls is presented. The behaviour of this column, with a thermal gradient in the direction of the web is known as “thermal bowing”. In the beginning of the fire, since the left flange is hotter, it will undergo greater thermal expansion, leading the column to bend towards the side of the fire. Due to the fact that the ends of the column are restrained, a bending moment is generated. With the increase of the temperatures, the Young’s modulus and the yield stress will reduce, and the effective centroid will move towards the cold side. This will create an additional bending moment, which is opposite to the thermal moment, and will cause the column to bend to the opposite side, *i.e.*, the cold side of the column. In figure 6 b), the Von Misses stresses are depicted at

the inversion instant ($t=3.8$ min), and in figure 6 c), the formation of three plastic hinges is observed on bottom, top and mid-height of the column, although only a small extent of the column is hot (figure 6 c).



a) Column after test b)VMS at instant $t=3.8$ min c)VMS at instant $t=24$ min d) NT at instant $t=24$ min

Figure 6. Evolution of the Von Misses stresses (VMS) and nodal temperatures (NT) in a steel column embedded on walls, with the web perpendicular to the wall (Test E11)

Figures 7, 8 and 9, depict the evolution of temperatures (in $^{\circ}\text{C}$) and axial stresses (in Pa), in three sections (bottom, mid-height and top) along the height of the column in test E11. It may be observed the inversion in the axial stresses at time 3.8 minutes. Yield stress (355 Mpa) was reached in the three sections, at time 24 minutes.

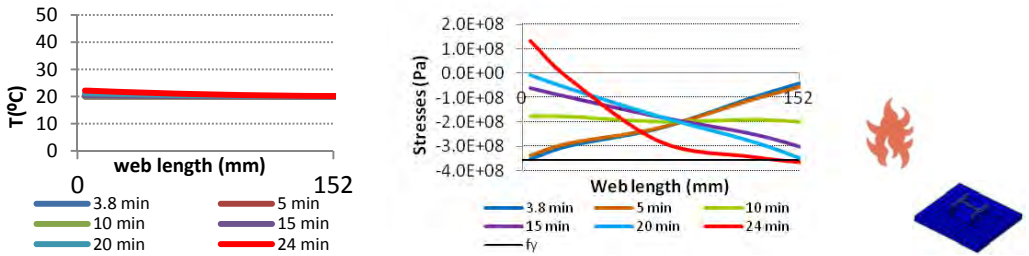


Figure 7. Temperatures and axial strains on the base section of a column embedded on walls subjected to fire (Test E11)

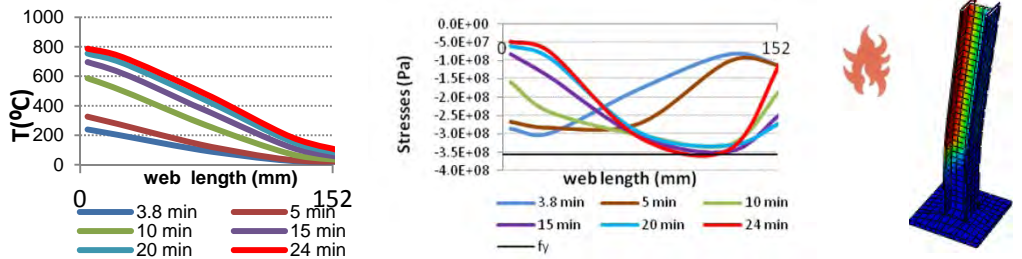


Figure 8. Temperatures and axial strains at mid-height, 1.5m from the base of a column embedded on walls subjected to fire (Test E11)

In figure 9, full plastification of the web and the cold flange is observed, despite of the very low temperatures attained in the section.

It was possible to observe the inversion of axial stresses, in some sections from compression to tension, and sudden variation in the axial stresses, in sections with very low temperatures.

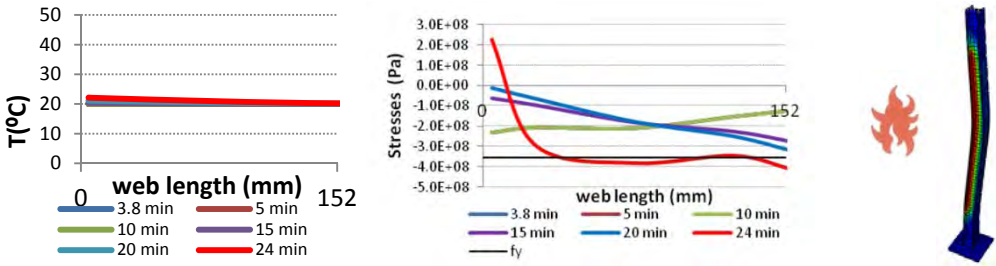


Figure 9. Temperatures and axial strains at the top section of a column embedded on walls subjected to fire (Test E11)

4 STRUCTURAL ANALYSIS

For the assessment of the structural behaviour of a steel column in contact with walls, two approaches are applicable: either considering a reduced cross-section in the heated part of the profile or considering plastic stress diagrams, with the yield stress reduced with temperature dependent coefficients defined in EN 1993-1-2 (2005).

4.1 Reduced cross-section

4.1.1 Column with the web perpendicular to the walls

In this case, the real behaviour of the column may be calculated considering a reduced area of the heated flange, using the reduction factors of the effective yield strength relative to yield strength at 20°C, as a function of the temperature of the exposed flange. The yield stress is uniform along this area (figure 10).

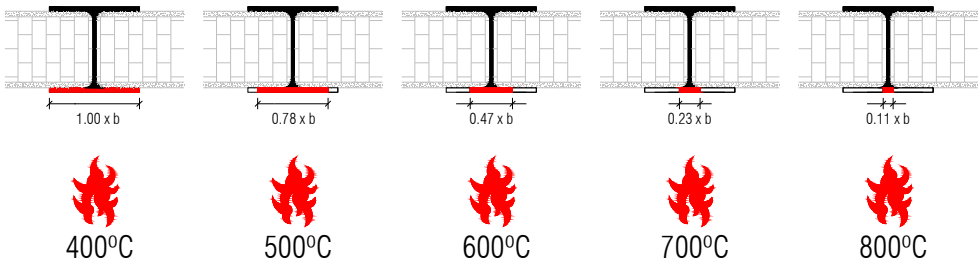


Figure 10. Analysis of the plastic resistance of a steel column embedded on walls, for the case of the web perpendicular to the walls (thermal gradient along the web).

4.1.2 Column with the web parallel to the walls

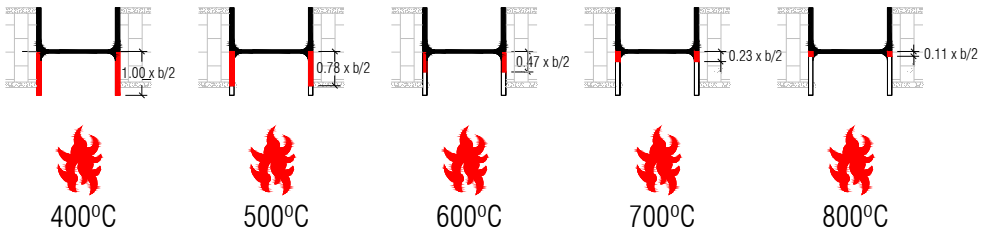


Figure 11. Analysis of the plastic resistance of a steel column embedded on walls, for the case of the web parallel to the walls (thermal gradient along the flanges)

For this case, an hybrid cross-section is now to be considered for the analysis, using the same reduction factors, applied to the half-flanges exposed to fire (figure 11).

Table 4. Reduction factors of the effective yield strength relative to yield strength at 20°C, as a function of the temperature (EN 1993-1-2-2005)

Temperature (°C)	20-400	500	600	700	800	900	1000
$k_{y,\theta}$	1	0.78	0.47	0.23	0.11	0.06	0.04

4.2 Reduced yield stress

4.2.1 Column with the web perpendicular to the walls

In this case, a reduction of the yield stress is applied in the heated flange. In figure 12 a) pure compression is depicted, and in figure 12 b) pure bending occurs, depending on the position of the plastic neutral axis (x is the distance of the plastic neutral axis to the geometric centroid).

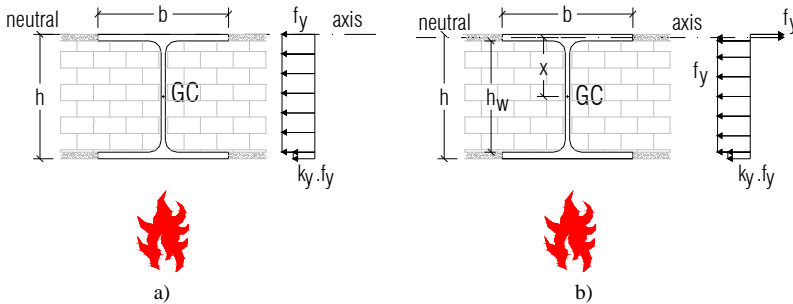


Figure 12. Stress diagrams for non-uniformly heated steel columns, in case of a column with the web perpendicular to the walls (thermal gradient along the web)

4.2.2 Column with the web parallel to the walls

In this case, the reduction of the yield stress is applied to the heated half-flange. Likewise, in figure 13 a) $M/M_{pl}=0$ and N/N_{pl} is maximum, and in figure 13 b) $N/N_{pl}=0$ and M/M_{pl} is maximum. The position of the plastic neutral axis (for the situation depicted in figure 13 b) is calculated under the condition that resultant compression equals resultant of tension in the hybrid cross-section.

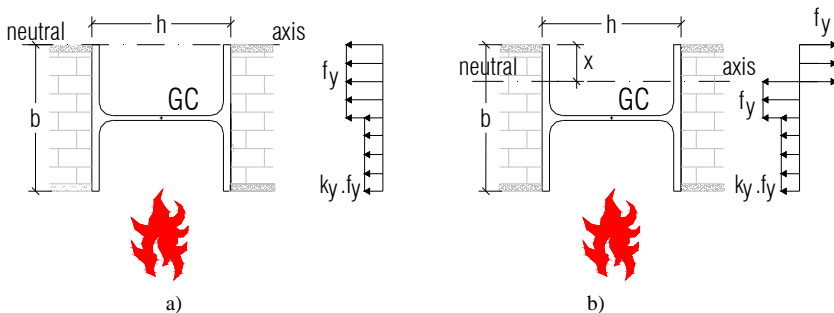


Figure 13. Stress diagrams for non-uniformly heated steel columns, in case of a column with the web parallel to the walls (thermal gradient along the flange)

5 PARAMETRIC STUDY

In the scope of this research, a parametric study was performed, to assess the influence of the thickness of the walls, the load level and the stiffness of the surrounding structure.

5.1 Influence of the thickness of the walls

In figure 14 a) and b), the behaviour of eight tests is presented, for the cases of the web perpendicular and parallel to the wall, respectively. The evolution of the axial force, related to the initial applied load, allow the definition of the critical time, which is considered as the time, from the beginning of the fire, at which the axial force, after increasing and reaching a peak, decreases and equals the initial load, *i.e.*, $P/P_0=1$.

In these graphs, the thick lines stand for thick walls, and the thin lines stand for thin walls.

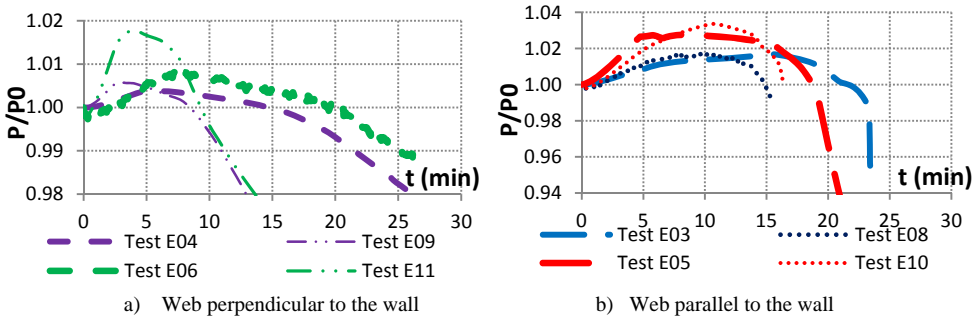


Figure 14. Evolution of axial forces for the columns embedded on walls, with a load level of 70%

It is observed in both graphs, that the thicker walls provide greater fire resistances. In case of the web perpendicular to the walls, the difference is greater than with the web parallel to the walls. The peak is also greater for the thin walls, especially in the case of the web perpendicular to the wall. Moreover, it is observed that the failure of the columns is more gentle in this case, than with the web parallel to the walls, in which failure is more abrupt.

5.2 Influence of the Load level

The load level is also expected to play an important role in the fire resistance of these columns. In figure 15, load levels of 70% and 50% of the buckling load at ambient temperature are analysed for tests E05, E08, E10 and E11. Continuous lines stand for load level 70% and dashed lines stand for load level 50%.

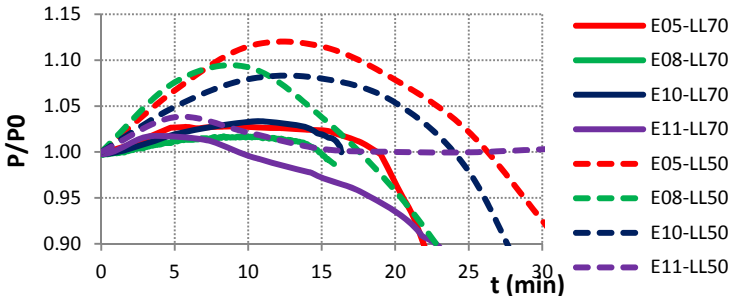


Figure 15. Evolution of axial forces for the columns embedded on walls, for different load levels, 70% and 50% of the design buckling load at room temperature

It was concluded that the dashed lines seem to have been stretched to the right side, for all tested cases meaning that for the load level 50%, the fire resistance is greater.

5.3 Influence of the stiffness of the surrounding structure

The influence of the stiffness of the surrounding structure is depicted in figure 16. Two values of the stiffness of the surrounding structure were considered (7kN/mm obtained with upper beams in the restraining frame made of HEA200, and 13kN/mm when these beams were HEB300). Only two tests were considered (E05 and E10), and the results show that the higher stiffness of the structure, the greater the fire resistance.

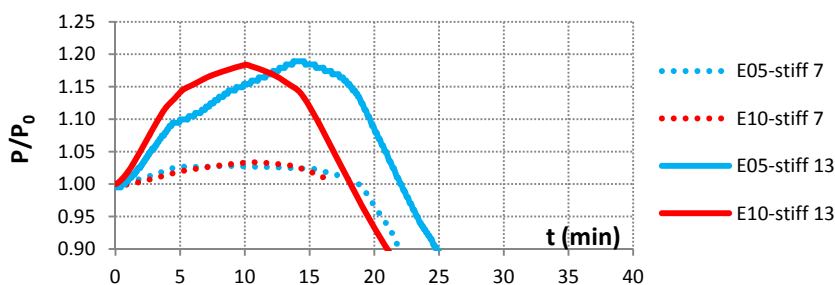


Figure 16. Evolution of axial forces for the columns embedded on walls, for different values of the stiffness of the surrounding structure

This may be explained by the fact that associated with the axial stiffness, is a rotational stiffness, which plays a favourable role in the fire resistance of the columns.

6 CONCLUSIONS

The main conclusions of this research concern the failure mechanism of steel columns embedded on walls, under great thermal gradients. In all cases, columns in contact with walls presented lower temperatures and higher fire resistances than bare steel columns.

The load level, the thickness of the walls and the stiffness of the adjacent structure have proved to have great influence on the critical temperatures and times.

It was possible to analyze the stress-strain state of several sections of these columns, in fire.

Two approaches of considering future designing procedures for these columns were presented: either considering plastic stress diagrams, with the yield stress reduced with temperature dependent coefficients defined in EN 1993-1-2 (2005), or considering a reduced cross-section in the heated part of the cross-section. The aim of this study is to provide data to sustain future axial force – bending moment interaction diagrams on the fire behaviour of this type of columns.

REFERENCES

- [1] Garlock, M. E. M., Quiel, S. E., (2006), “Combined axial load and moment capacity of fire-exposed beam-columns with thermal gradients”, Proc. 4th International Workshop for Structures in Fire (SIF '06), Vol. I, University of Aveiro, Portugal, pp 187-198.
- [2] Knobloch M., Somaini D., Pauli J. and Fontana M., “Numerical Analysis of the Cross-Sectional Capacity of Structural Steel Members in Fire”, *Structures on Fire – Proceedings of the Sixth International Conference*, V. Kodur, J.-M. Franssen (eds.), DEStech Publications, Lancaster, 19-26, 2010.
- [3] Knobloch, M., Fontana, M. and Frangi A., “Steel beam-columns subjected to fire”, *Steel Construction – Design and Research*, 1(1), 51-58, 2008
- [4] EN 1993-1-1 (2005). “Eurocode 3 - Design of steel structures - Part 1.1: General Rules and rules for buildings”. CEN, Brussels.
- [5] EN 1993-1-2 (2005). “Eurocode 3 - Design of steel structures - Part 1.2: General Rules - Structural fire design”. CEN, Brussels.

BEHAVIOUR OF PROTECTED CELLULAR BEAMS HAVING DIFFERENT OPENING SHAPES IN FIRE CONDITIONS.

Han Sanghoon*, Klelia Petrou**, El-Hadi Naili**, Ali Nadjai**, Faris Ali**

*Korea Ship and Offshore Research Institute, Pusan National University, Korea
e-mail: hans1@pusan.ac.kr

**School of Art, Design and the Built Environment, FireSERT, University of Ulster, Northern Ireland, UK
e-mails: kleliamixmix@hotmail.com, eha-naili@email.ulster.ac.uk, a.nadjai@ulster.ac.uk, f.ali@ulster.ac.uk

Keywords: Cellular Beams, Intumescent Coating, Fire Resistance.

Abstract. *The growing popularity of the use of Cellular steel Beams in composite floors comes at the same time as an increasing attention to the fire safety engineering design. In fire, the temperature distribution across a composite member is non-uniform, since the web and bottom flange have thin cross-sections and a greater exposed perimeter than the top flange. The deterioration of the material properties of the web will therefore become an important effect on the overall performance of the member in the event of fire. Fire resistance and protection of Cellular-Beams has been very controversial concerning their behaviour in elevated temperatures, the fire protection material and the required thickness. This paper describes an experimental and numerical study at elevated temperatures on the behaviour of unprotected and protected Cellular steel Beams having different size of openings.*

1 INTRODUCTION

Cellular Beams give architectural flexibility of open large spaces forming compartments as it is possible to achieve long spans. This structural element is currently being widely used in multi-storey buildings, commercial and industrial buildings, warehouses and portal frames, in the UK and Europe. There are structural steel Beams that are deeper than normal roller sections, having openings into their web. They are produced by modern automated fabrication processes and can be competitive for the construction of both floor and roof systems. The openings in the web can be of various shapes such as rectangular, castellated, circular, and elongated [1-3].

The openings in the web allow the passage of technical installations, as cables, pipes and ducts. The increased section depth results in added strength without additional material, leading to reduce the total weight of steel work.

Their widespread use of Cellular Beams has prompted several investigations concerning their structural behaviour. In fire, the degradation of strength and stiffness of unprotected steel sections exposed to elevated temperatures can result to early structural collapse. The fire resistance of Cellular Beams has been very controversial in the recent years, considering the fire protection material and the required thickness.

The most common fire protection material used for Cellular Beams is the intumescent coatings, giving the advantage of allowing the passage of technical services as it can be applied without blocking the holes in the web. Intumescent coating are applied on steel structural elements at the specific thickness necessary to protect the structural element, minimising the wastage and hence cost. They can be applied

in the fabricator's shop or on the completed structure on the construction site. In addition, ensures that the steel work is fully fire protected throughout the construction phase [4].

Intumescent coatings contain a mixture of chemical ingredient, reactive in fire conditions producing an insulating layer of carbonaceous char. They can be swelling to between 5 and 50 times their original applied thickness, so that 1mm film can produce up to 5cm of char [5]. The char contains air vacuoles in a carbon based matrix, which effectively surrounds and insulated the steel substrate from the rapid temperature increase that will occur to an unprotected steel section [5].

The use of intumescent coating extends the loadbearing capacity of the steel structure. The stability of a building, having intumescent coating protected steel structural elements, in case of fire depends on the thickness of the coating, the depth and insulation properties of the char produced of it [5-6].

2 EXPERIMENTAL TEST PROGRAMME

The experimental work is a continuation of the research fire test programme funded by the EPSRC and conducted at the University of Ulster, FireSERT Laboratory [1, 2].

The tests carried out on six full-scale composite Cellular Beams, protected and unprotected, of 4.5 meters span length. The Cellular Beams were fabricated from standard hot-rolled steel sections, subjected to one or two point loading, using three different geometries [1-3].

2.1 Specimen Details

The following types of Beams have been tested:

- a) Beam 1: An asymmetric composite Cellular Beam, having large web opening, was produced on the basis of UB 356x171x57 as a top tee section and of UB610x305x179 as a bottom tee section having finished depth of 555x171/305ACBx118kg/m (figure 1). The diameter of cells was 375mm at 600mm centres.
- b) Beam 2: A symmetrical composite Cellular Beam, having two large web openings, was produced on the basis of UB 457x191x74, having a finished depth of 550x191CB74 kg/m (figure1). The cells diameter was 335mm at 600mm centres.
- c) Beam 3: An asymmetrical composite Cellular Beam, having multiple circular web openings, was produced on the basis of UB 356x171x57 as a top tee section and of UB 457x191x74 as a bottom tee section having finished depth of 555x171/191ACBx 65.5 kg/m (figure 1). The cells diameter was 375mm at 600mm centres.

The Cellular Beams were S355 steel grade. In all six tests was used a 150mm thick x 1100mm wide concrete slab, of normal weight concrete, grade 35N/mm². The reinforcement consisted of welded wire mesh A142 of 460N/mm² yield strength. The interaction between slab and Beam was ensured in all specimens with shear connectors of 19mm diameter studs at height 95mm. They have been equally distributed in one row with a distance of 150mm over the Beam length. The steel deck was Multideck 50 -V2 of strength 350N/mm², having 0.9mm thickness. Concrete compressive strength was determined at different stages of time: after 2 weeks, 28 days and during the testing days giving an average of 35N/mm² using a compressive strength calibrated machine at the University of Ulster. The geometry data of Cellular Beams are presented in Table 1.



Figure 1: Cellular Beams geometry

Table 1: Cellular Beam Geometry Data

Geometry	Beam1	Beam 2	Beam 3
Span (mm)	4500	4500	4500
Top flange: width /thickness	172/13	190/14.5	172/13
Top tee depth (mm)	255	275	255
Bottom flange: width/ thickness	307/23.6	190/14.5	190/14.5
Bottom tee depth(mm)	300	275	300
Web thickness: top/bottom (mm)	8/14	9/9	8/9
Overall depth (mm)	555	550	555
Cell diameter(mm)	375	335	375
Cell Spacing	600	600	600

2.2 Mechanical and Thermal Loading

Beam 1 was tested under two-points loading and the other 2 Beams were tested under one point loading; both ends of the Beams were simply-supported. The Beams were designed at ambient temperature in order to determine the failure load. The loading was considered nearly equal to 30% of the

ultimate load found from the pre-design at cold conditions and by taken into account the previous tests conducted at University of Ulster as reference [1].

In order to evaluate the deflection limit for the protected Cellular Beams the applied loading in protected and unprotected composite Cellular Beam tests were kept the same. The applied load for Beam 1 was 200kN and 150kN for Beam 2 and Beam 3.

The six fire tests, protected and unprotected composite Cellular Beams were conducted in the furnace of FireSERT facilities, of university of Ulster. The fire load was represented by the standard ISO 834 fire curve. Exposed to fire was the lower side of the composite slab and the steel section.

2.3 Temperature Distribution and Deflection

Temperatures distribution on the composite Cellular Beams were recorded by 33 thermocouples disposed at various location along the Cellular Beam in different zone (figure 2) and by 10 thermocouples disposed along the composite slab. Deflections and axial displacements were recorded using 5 Linear Differential Transducers LVDT's, placed in different location on the unexposed concrete slab.

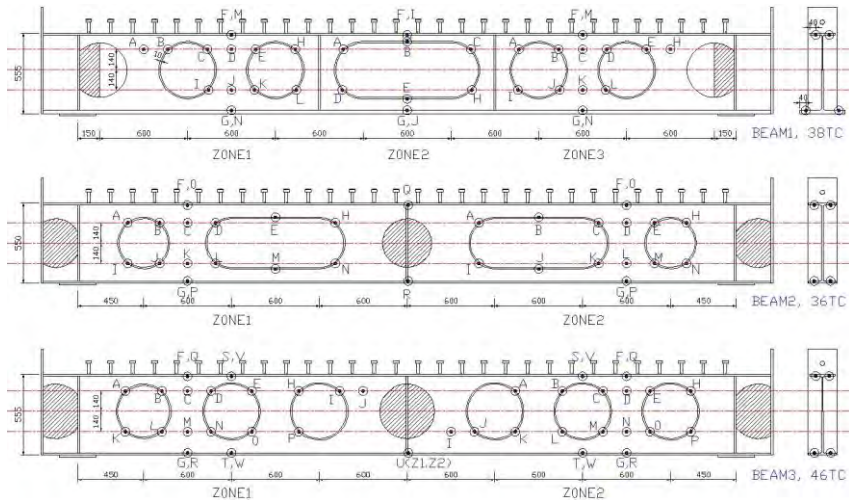


Figure 2: Thermocouples locations

3 EXPERIMENTAL RESULTS

The maximum recorded temperatures on the protected composite Cellular Beams were in the bottom web of the steel sections. At time 66 minutes when the furnace test stopped the maximum temperatures were 787°C, 837°C, 798°C for Beam 1, Beam 2 and Beam 3 respectively. The results of the temperatures distribution through the steel sections are presented in Figure 3 and Figure 4. On Figure 4 is also presented a comparison of the temperatures distribution of the protected and unprotected Beam 3. The protected composite Cellular Beams failed in longer time than the unprotected and the recorded deflection at failure time was less than the unprotected.

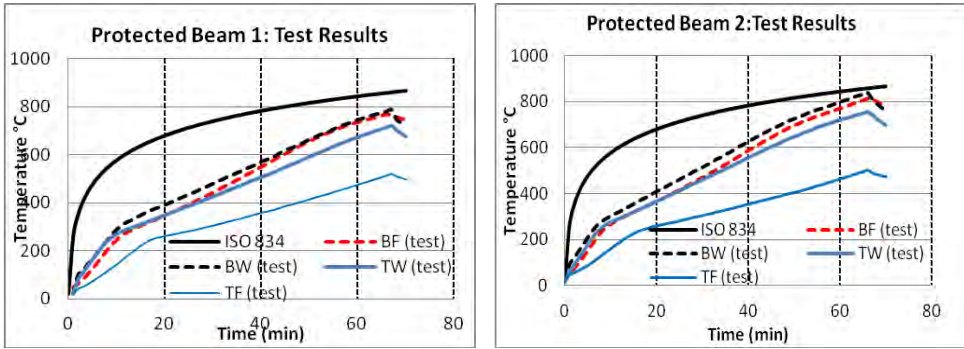


Figure 3: Temperatures distribution of Cellular Beams 1 and 2

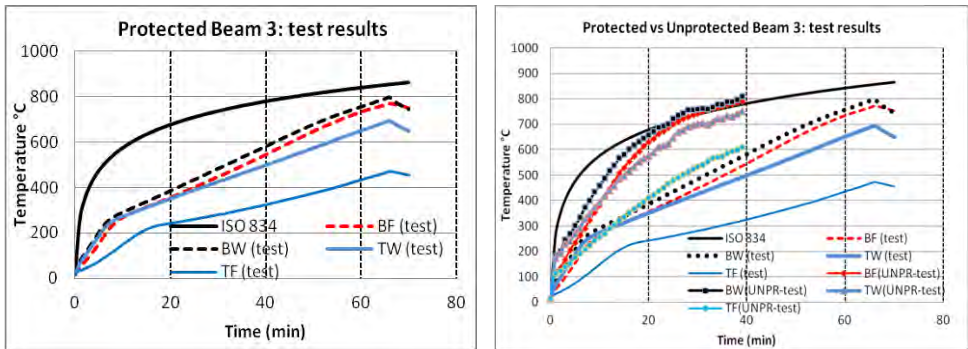


Figure 4: Temperatures distributions of Cellular Beam 3 (left), comparison protected and unprotected Beam 3 (right)

Figure 5 shows pictures taken after the test on Cellular Beam 2 after the furnace test showing the carbonaceous char and the deflection of the Beam web.



Figure 5: Protected Cellular Beam 2 after the test

4 NUMERICAL ANALYSIS

Eurocode 3, EN 1993-1-2, provides an equation for calculating the temperature increase $\Delta\theta_{a,t}$ of a protected steel member, in the case of uniform temperature distribution in a cross-section [7].

$$\Delta\theta_{a,t} = \left[\frac{\lambda_{p,t}/d_p}{c_a\rho_a} \times \frac{A_p}{V} \times \left(\frac{1}{1 + \Phi/3} \right) \times (\theta_t - \theta_{a,t}) \Delta t \right] - [(e^{\Phi/10} - 1)\Delta\theta_t] \quad (1)$$

Where: $\Phi = \frac{c_p\rho_p}{c_a\rho_a} \times d_p \times \frac{A_p}{V}$, $\Delta\theta_{a,t} \geq 0$ and $\Delta t \leq 30s$

In equation 1, θ_t is the gas temperature, $\theta_{a,t}$ is the steel temperature, A_p/V is the section factor of the protected steel section, d_p fire protection material thickness, c_a , ρ_a , the specific heat and density of steel, c_p , ρ_p specific heat and density of the protection material and $\lambda_{p,t}$ the effective thermal conductivity of the fire protection material at time t .

Intumescent coating is a thermal reactive material; consequently, its effective thermal conductivity does not have a fixed relationship with temperature. Thus, the fire exposure of intumescent coating is important [8]. In the paper of X.H *et al* [9] the effective thermal conductivity of intumescent coating was computed using the inverse solution of equation 1 and experimental data from a test series of ten specimens[8-9]. This approach is being taken from DD ENV1331-4:2002 [10].

The steel temperatures of protected steel section exposed to ISO 834 curve were calculated using equation 2. The thermal effective conductivity was taken as computed in papers X.H *et al* [9] and R.P.K *et al* [8]. The material properties of the intumescent coating are presented in Table 2.

During the tests conducted, in the University of Ulster, on the three protected composite Cellular Beams, it was observed that the thickness of the thin film of the applied intumescent coating was changing with the exposed temperature. This is the characteristic of intumescent coatings, forming a thick char surrounding and insulating the steel Cellular Beam from fire. Based on these observations the fire protection thickness and thermal properties materials were calibrated for to be used in the calculations of the steel temperatures using equation 1.

Table 2: Intumescent coating properties

Fire Protection	Density kg/m ³	Specific Heat J/kgK
Intuscement Coating	1300	1000

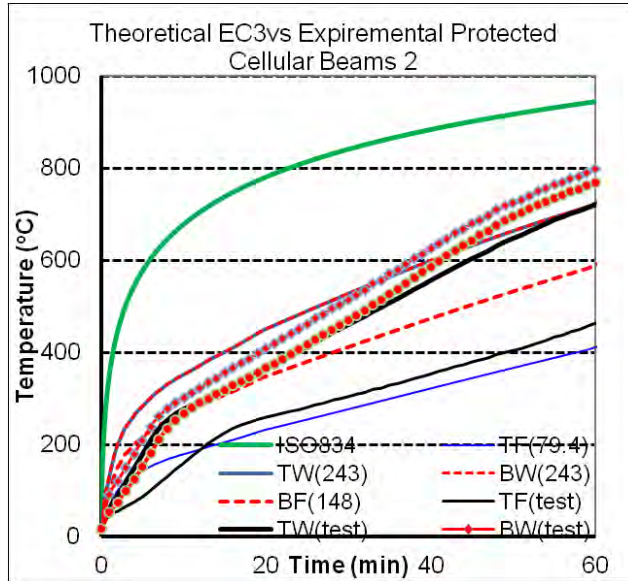


Figure 6: EC3 and experimental steel section temperatures of protected Cellular Beam 3

From Figure 6 it can be concluded that the calculated protected steel section temperatures, Eurocode 3, is in a relative good agreement with the experimental results. The Eurocode 3 calculations gives the top and bottom web of protected Cellular Beam2 to have the higher temperatures, 723°C at 60 minutes of fire exposure, than the other section parts. Although, the experimental results shows that the bottom web has the higher temperature, 798°C at 60 minutes exposure. The reason for this difference is the geometry of the Cellular Beam 2.

5 FINITE ELEMENT MODELING

The composite slab and Cellular Beam sections were modelled, in the finite element software Diana, using solid-brick elements and heating elements in order to add a temperature depended mesh on the structural mesh. The steel deck, and the reinforcement mesh, within the concrete were included to the model. For more accurately models with the fire tests the Beams were split into different areas.

The composite Cellular Beam 2, with two elongated web openings, fire load was represented by different time/temperature curves according to the average thermocouple reading recorded in the protected furnace tests for the bottom flange, bottom web, top web, top flange, the bottom layer of steel decking and concrete slab.

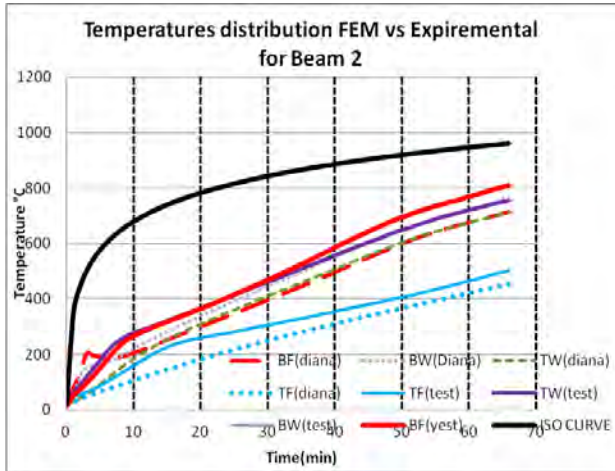


Figure 7: Experimental protected steel temperatures with FEM results

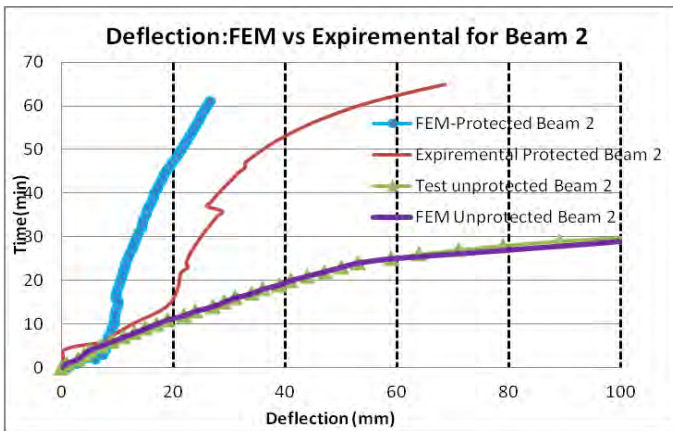


Figure 8: Deflection of Beam 2 compared with protected and unprotected test results

As demonstrated on the above Figure 7 the temperatures distribution given by the finite element model is in a good agreement with the experimental results for the protected composite Cellular Beam 2.

In Figure 8 are showed the deflection results from the finite element analysis software Diana, the experimental results for the protected and unprotected composite Cellular Beam 2. The protected Cellular Beams deformation is less crucial than the unprotected. Also, the results from the finite element model give a relative good estimation of the experimental results for the protected Cellular Beam 2. However, with further calibrations finite element models can achieve better results.

5 CONCLUSIONS

Intumescent coatings are the most effective fire protection material for steel Cellular Beams. The experimental results of the furnace tests of unprotected and protected composite Cellular Beams have demonstrated that the recorded temperatures on the protected steel sections are less than the unprotected

steel sections. Also, the deformation of the protected composite Cellular Beams is less crucial than the unprotected.

Further investigation on the behaviour of protected composite Cellular Beams having longer span, different geometry and different web openings could be proceed using finite element software. Although, several factors used for the finite element analysis should be calibrated for better results.

The simplified analysis presented in Figure 6 will be used in the finite element model and compare with the experimental as next step forward.

The failure mechanism in the protected composite Cellular Beam 2 is Vierendeel bending combined with web post buckling as shown in Figure 5.

REFERENCES

- [1] A. Nadjai, H. Sanghoon, Private Communication “*Full-scale fire test on composite floor with long span Cellular steel Beams*”, Northern Ireland: Report Ref. Numbe: EU-FireSert2010, University of Ulster 2010.
- [2] A. Nadjai, O. Vassart, F. Ali, D. Talamona, A. Allan, M. Hawes “*Performance of Cellular Composite Floor Beams at Elevated Temperatures*”, *Fire Safety Journal* 42(2007), 489-497
- [3] E. Naili, A. Nadjai, S. Han, F. Ali, S. Choi “*Experimental and Numerical Modelling of Cellular Beams with circular and elongated web openings at elevated temperatures*” *Journal of Structural Fire Engineering* 24(2011), 288-300
- [4] V. Y. B. Wong, I. W. Burgess, R. J. Plank “*Experimental and analytical investigations of the behaviour of protected composite floor Beams with web openings in fire*”, *Proceedings of Structures In Fire, SIF 2010*, 366-373.
- [5] H. van de Weijert “*Protecting structural steel*” *Fire Safety Engineering*, (2001) 16-19,
- [6] P. Morris “*Test of Strength*” *Fire Safety Engineering*, (2005) 17-20,
- [7] R. P. Krishnamoorthy, C. G. Bailey “*Temperature distribution of intumescent coated steel framed connection at elevated temperature*”, *NISCC*(2009), 572-579
- [8] Committee of European Normalisation CEN (1995) *Eurocode 3: design of steel structures, part 1-2: general rules-structural fire design*, ENV 1993-1-2. British Standards Institution, London
- [9] X. Dai, Y. Wang, C. Bailey “*A simple Method to Predict Temperatures on Steel Joints with Partial Intumescent Coating Fire Protection*”, *Fire Technology*, 46(2010), 19-35,
- [10] Committee of European Normalisation CEN “*Test methods for determining the contribution to the fire resistance of structural members-part 4: applied protection to steel members*”, DD ENC 13381-4 (2002) (E). British Standards Institution, London.

MATERIAL BEHAVIOUR OF HIGH STRENGTH STEEL S690 IN FIRE AND AFTER FIRE

Xuhong Qiang*, Frans S.K. Bijlaard* and Henk Kolstein*

* Structural and Building Engineering, Department of Design and Construction, Faculty of Civil Engineering and Geosciences, Delft University of Technology, 2600GA Delft, the Netherlands
e-mails: X.Qiang@tudelft.nl, F.S.K.Bijlaard@tudelft.nl, M.H.Kolstein@tudelft.nl

Keywords: High strength steel, S690, Material behaviour, In fire, After fire.

Abstract. *In order to reveal material behaviour of high strength structural steel S690 both in fire and after fire, an experimental research has been carried out. The elastic modulus, yield strength and ultimate strength of S690 in fire and after fire were presented herein. The comparison with current European, American, British and Australian design standards of steel structures showed that the material behaviour of high strength steel S690 in fire was different from that of mild steels, and the current leading design standards were not applicable to high strength steel S690. This paper highlights the necessity of employing unique elevated-temperature and post-fire material behaviour of high strength steel S690 to conduct safe fire-resistance design and accurate evaluation after fire for steel structures with S690. Moreover, the residual material behaviour of high strength steel S690 after fire was found promising for its reuse, and some recommendations were proposed for its reuse after fire.*

1 INTRODUCTION

Compared to mild steel, high strength steel offers higher performance in tensile stress, yield stress, bending, weld ability and corrosion resistance. In Europe the cost of building a structure usually depends more on fabrication, transportation and erection than on the price of raw material. In the construction of steel structures high strength steel allows less material to be used, which reduces the volume of weld metals and correspondingly the time of welding. Further, less material has to be transported and the lighter weight simplifies the erection of structures. In some structural applications the light weight plays an important role, because the payload can be increased or the running expense can be decreased, such as cranes and vehicles. What is more, an increasing international concern on environment protection results in more attention on saving energy and raw materials. Hence the practical application of high strength steel in constructions has received some attention and is gaining more and more popularity due to its cost-effective and environmental-friendly benefits. At present in some significant structures and landmark constructions high strength steels have been employed, such as New York Freedom Tower, Beijing Bird's Nest Olympic Stadium and French cable-stayed road-bridge Millau Viaduct.

Due to numerous unpredictable fire hazards happen almost every day all over the world, structural fire safety is currently one of the critical considerations in the design of high-rise buildings which are usually made of steel. As a basis of evaluating fire performance of steel structures, the material behaviour of steels in fire is significant. Since 911 World Trade Centre Tragedy, the material behaviour of steels has been paid more attention and investigated, however the previous researches mainly focused on mild steels. For high strength steels, the elevated-temperature material behaviour of S460 and BISPLATE 80 has been reported in literature; no quantitative research result has been found for high strength steel S690 in fire. Therefore there is a need in investigating the material behaviour of S690 at elevated temperatures to fill in the research blank.

Provided collapse does not occur when a steel structure is exposed to fire, the steel members begin to cool once the fire starts to decay and the atmosphere temperature begins to decrease. Residual forces and deformations redevelop in steel structures during the cooling phase and after cooling down, which might be more dangerous conditions than in fire. Whether the steel structures once exposed to fire should be removed, repaired or reused directly, a reliable evaluation is needed. However, as a critical basis of evaluating the performance of steel structures after fire, the material behaviour of steels after fire is not well documented in literature, neither mild steels nor high strength steels. In current leading design standards, only British standard BS5950 [1] has some assumptions for the reuse of mild steels (S235, S275 and S355) after fire, but not for high strength steels.

In order to keep pace with the application of high strength steel S690 in practice, an experimental investigation on material behaviour of HSS S690 in fire and after fire has been conducted. This paper presents the experimental results, including the deterioration of elastic modulus, yield strength, ultimate strength of S690 at various fire temperatures and the residual material properties after cooling down from various fire temperatures. For the tests in fire, both steady state tensile tests and transient state tensile tests were conducted and compared. For the tests after fire, tensile tests were undertaken on specimens at ambient temperature after cooling down from fire temperatures up to 1000 °C. The deterioration of material behaviour of S690 in fire is represented by reduction factor while the residual factor is representative of the residual material behaviour of S690 after fire. The obtained reduction factors of material behaviour of S690 in fire were compared with the recommendations of current European, American, Australian and British design standards. Based on the residual factors of material behaviour of S690 after fire obtained herein, some recommendations were proposed for the reuse of steel members made of HSS S690 after being exposed to fire. Further, some specific predictive equations based on experimental results were developed to evaluate the material behaviour of HSS S690 in fire and after fire.

2 EXPERIMENTAL STUDY

2.1 Test material and specimen

Table 1. Chemical composition of HSS S690QL material (%).

C	Si	Mn	P	S	Cr	Cu	Mo
0.160	0.210	0.850	0.012	0.001	0.350	0.030	0.200
N	Nb	Ni	Ti	V	Al-g	B-g	Zr
0.0026	0.025	0.050	0.006	0	0.093	0.0024	0

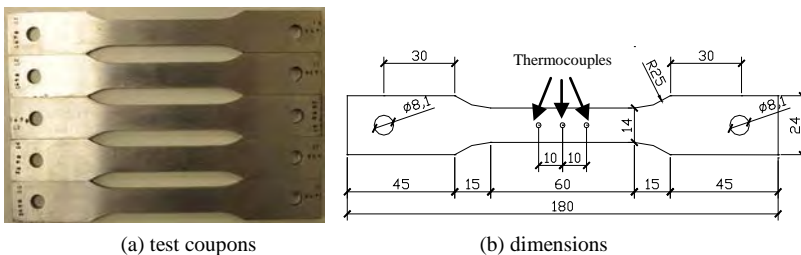


Figure 1. Tensile test coupon and dimensions.

All test specimens were cut from a S690QL steel sheet with a nominal thickness of 5mm. S690QL is a high strength structural steel produced in compliance with EN 10025-6 [2]. The material is heat-treated

using the quenched and tempered process and has good bending and welding properties. *S690QL* is the grade designation abbreviation of this steel, where *S* means structural steel, *690* is its minimum yield strength, *Q* means quenching and tempering, and *L* means low notch toughness testing temperature. The chemical composition of the tested high strength steel S690 was shown in Table 1. The shapes and dimensions of the specimens were prepared in accordance with EN 10002-5 [3] and ASTM standard E21-09 [4], as shown in Figure 1.

2.2 Test set-up

The tensile tests in fire were conducted using a Gleeble 3800 System, which is a fully integrated digital closed loop control thermal and mechanical testing system, as shown in Figure 2. The direct resistance heating system of the Gleeble 3800 can heat specimens or can hold steady-state equilibrium temperatures. Gleeble 3800 has a digital control system, which provides all the signals necessary to control thermal and mechanical test variables simultaneously through the digital closed-loop thermal and mechanical servo systems. In this study, 3 pairs of thermocouples provided signals for accurate feedback control of specimen temperatures, see Figure 1. The air temperature inside the furnace was obtained by Gleeble 3800 System. The Gleeble 3800 mechanical system is an integrated hydraulic servo system capable of exerting as much as 10 tons in tension. A non-contact laser extensometer was used to measure the strain of the specimens. The experimental process was controlled by some predefined programming options using QuikSim Software. All the data obtained from the tests were recorded by a computer and could be monitored during testing. To obtain the post-fire material behaviour, the heating of the specimens were conducted in a temperature-controllable electrical furnace, as shown in Figure 3, after cooling down the tensile tests were conducted on specimens at ambient temperature using the Gleeble 3800 System.



Figure 2. Gleeble 3800 system.



Figure 3. Temperature-controllable furnace.

2.3 Test method and procedure

To assess the material behaviour of steels under fire conditions, the commonly used method is to conduct tensile tests either in steady state or transient state. In order to compare the difference between these two methods on high strength steel, both steady state test method and transient state test method were conducted to study the material behaviour in fire. For the residual material behaviour after fire only steady state test method was employed.

2.3.1 Steady state test in fire

In steady state test, the specimen was heated up to a specified temperature then loaded until it failed while maintaining the same temperature. The heating rate used herein was 50°C/min, and the preselected temperatures were 100°C, 200°C, 300°C, 400°C, 500°C, 550°C, 600°C and 700°C. After reaching the preselected temperature, approximately 10mins was required for the temperature to stabilize, to ensure a uniform temperature within the central part of the specimen. And then tensile load was applied to the

specimen until failure. In the steady state tests, strain-control was employed. The strain rate used herein was 0.005/min, which satisfied the requirement of ASTM Standard E21-09 [4]. In order to compare the elevated temperature effect on material behaviour of S690, tensile tests were conducted at ambient temperature as well.

2.3.2 Transient state test in fire

In transient state tests, the specimen was under some constant tensile load while the temperature rose until failure occurred. The used tensile stress levels were preselected; they were 100, 200, 250, 300, 400, 500, 600, 650, 700, 800, 850 and 900MPa. The heating rate in all transient state tests was 10°C/min. The total strain and temperature of the specimen during the whole test procedure were recorded. The thermal elongation of specimen were subtracted from the total strain, and then the strains of specimen at various temperatures could be obtained. Under some constant stress level the strain-temperature curves obtained from transient-state tests can be transferred to stress-strain curves at various elevated temperatures, by the method which Maljaars et al. [5] and Outinen [6] used in their previous researches.

2.3.3 Post-fire tensile test

In the temperature-controllable furnace the specimens were heated from ambient temperature to a pre-selected temperature under heating rate of 10°C/min. 13 elevated temperatures were selected in this study, i.e. 100°C, 200°C, 300°C, 400°C, 500°C, 600°C, 650°C, 700°C, 750°C, 800°C, 850°C, 900°C and 1000°C. After reaching each pre-selected elevated temperature, approximately 10mins holding time was required for the uniform temperature achieved in the whole specimen. And then the specimens were cooled to ambient temperature, after which tensile tests were applied to them at ambient temperature in the Gleeble 3800 System. All the tensile tests were conducted at ambient temperature until failure, and the air temperature inside the rig was obtained by Gleeble 3800 System. In the tensile tests, strain-control was used and the strain rate used herein was 0.005/min, which satisfied the requirement of ASTM Standard E21-09 [4].

3 EXPERIMENTAL RESULTS AND DISCUSSIONS

3.1 Elastic modulus

Under fire condition the elastic modulus of steel is determined from the stress-strain curve at the corresponding temperature, based on the tangent modulus of the initial elastic linear curve. Similarly, the elastic modulus of post-fire steel is also obtained from the stress-strain curve of steel after cooling down from certain elevated temperature. The deterioration of elastic modulus at elevated temperatures is represented by reduction factor at corresponding temperature; while the post-fire material properties of steel are representative by residual factors. Reduction factor of elastic modulus is determined from the ratio of elastic modulus at some elevated temperature E_{θ} to that at ambient temperature E_{20} ; residual factor is calculated as the ratio of the elastic modulus after cooling down from some elevated temperature $E_{p\theta}$ to that at ambient temperature without being exposed to fire E_{20} . In European, American, British and Australian design standards, reduction factors are recommended for fire-resistance design and evaluation of steel structures because of their simplicity. Therefore the reduction factors of elastic modulus E_{θ}/E_{20} for S690 at various fire temperatures and the residual factors of elastic modulus $E_{p\theta}/E_{20}$ after fire were obtained and presented in Figure 4. The recommendations of some current leading design were included for comparison. In Figure 4 the residual factor of S690 after fire was indicated, the others were reduction factors.

It can be seen that for the prediction of elastic modulus of S690, the current European design standard EC3 [7] and American design standard AISC [8] are generally conservative, and the prediction of Australian design standard AS 4100 [9] is non-conservative.

In addition it can be seen when S690 is cooled down after exposed to elevated temperatures below 600°C, it can regain more than 90% of its elastic modulus. But beyond 600°C, there is a considerable

degradation of its post-fire elastic modulus. It is interesting to note that even being exposed to fire temperatures up to 1000°C, HSS S690 can regain at least 60% of its nominal elastic modulus.

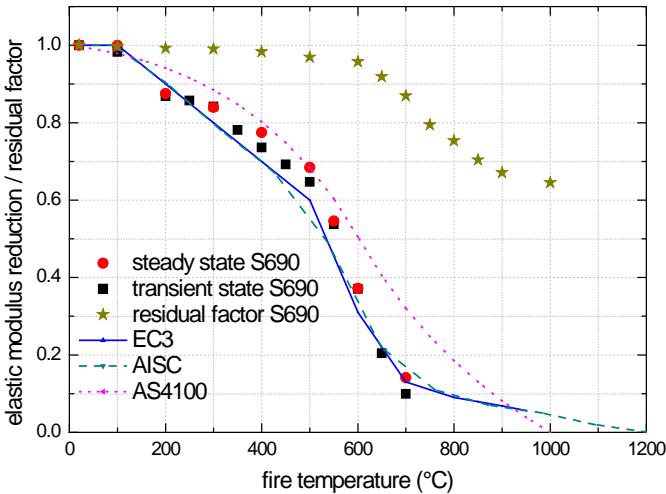


Figure 4. Reduction and residual factors of elastic modulus in fire and after fire.

3.2 Yield strength

In current design standards for steel structures, the reduction factors of yield strength recommended by EC3 are based on the strain level of 2.0%, and in BS 5950 different reduction factors are given based on three strain levels 0.5%, 1.5% and 2.0%. The yield strength at elevated temperatures studied herein was defined based on the total strain of 2.0%, to agree with the normally used method in literature and current leading design standards. The reduction factors of yield strength in fire were calculated by the ratio of yield strength at elevated temperatures $f_{y\theta}$ to that at ambient temperature f_{y20} . Similarly, the yield strength residual factors after fire were calculated as the ratio of yield strength after cooling down from elevated temperatures $f_{yp\theta}$ to that at ambient temperature f_{y20} . The yield strength reduction factors and residual factors of HSS S690 obtained from this experimental study were presented in Figure 5, where the recommendations of current leading design standards were shown for comparison. In addition the yield strength reduction factors of mild steels (i.e. S235 and S355) and S420M reported by Makelainen et al. were also included as reference. In Figure 5, the residual factor of S690 after fire was indicated in legend, the others were reduction factors.

It is confirmed that the recommendations of EC3 [7], BS 5950 [1] and AISC [8] are very accurate for the yield strength reduction factors of mild steels S235 and S355, however not the case for S420M and S690. When used to predict the yield strength reduction factor of HSS S690, the recommendations of EC3 [7], AISC [8] and BS5950 [1] are non-conservative, AS 4100 [9] is conservative from 400°C to 550°C but not the case for other temperatures, while ASCE [10] is conservative from 300°C to 550°C but not the case for other temperatures. Therefore it is proved that none of the current leading design standards is applicable to predict the yield strength reduction factors of HSS S690 in fire.

It is interesting to note when S690 is cooled down after exposed to elevated temperatures below 600°C, it can regain almost 100% of its nominal yield strength. But beyond 600°C, there is a considerable degradation of its post-fire yield strength. This is positive for the reuse of high strength steel structures or components after fire. For safe consideration, a conservative suggestion is recommended to use 90% of its nominal yield strength for post-fire S690 if it is exposed to fire temperatures below 600° C. Therefore if structural members made of HSS S690 are exposed to fire temperature below 600° C and their distortions remain within the tolerances for straightness and shape, they are reusable after fire.

In addition, it is worthwhile to mention that the residual yield strength of HSS S690 after fire is different from that of mild steels. In British design standard BS 5950 [1], it recommends that for S235 and S275 at least 90% of the mechanical strength is regained irrespective of the temperatures attained (even after heating to above 1000° C); for S355 it can be assumed that at least 75% of the strength is regained on cooling from temperatures above 600° C. Hence, it is apparent that the residual yield strength of structural steels after fire is dependent on steel grade.

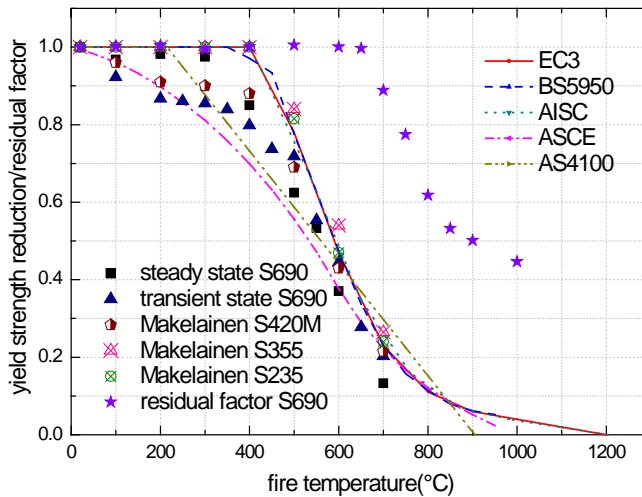


Figure 5. Reduction and residual factors of yield strength in fire and after fire.

3.3 Ultimate strength

The ultimate strength reduction factors were calculated based on the ratio of ultimate strength at a particular elevated temperature $f_{u\theta}$ to that at ambient temperature f_{u20} . Similarly, the residual factors of ultimate strengths after fire were calculated as the ratio of ultimate strength after cooling down from elevated temperature $f_{up\theta}$ to that at ambient temperature f_{u20} . The ultimate strengths reduction factors of HSS S690 at elevated temperatures and residual factors after fire obtained herein were compared with the recommendations of American design standard AISC [8], and the available research result for BISPLATE 80 from Chen et al. [11] was also included as reference, as shown in Figure 6. The ultimate strength residual factor of S690 after fire was indicated in legend, the others were reduction factors.

The reduction factors of ultimate strength for S690 are below the recommendations of AISC [8]. In AISC the recommendations for ultimate strength reduction factors obtained mainly from mild steels are uniform for all steel grades, which are proved not safe for evaluating HSS S690 under fire condition.

Similar to elastic modulus and yield strength, it can be seen when S690 is cooled down after exposed to elevated temperatures below 600°C, it can regain much more than 90% of its nominal ultimate strength. But beyond 600°C, there is a considerable degradation of its post-fire residual ultimate strength. For safe consideration, a conservative suggestion is recommended to use 90% of the nominal ultimate strength for HSS S690 after fire if it is exposed to fire temperatures below 600° C.

It is interesting to note that, similar to yield strength, the residual ultimate strength of HSS S690 after fire is different from that of mild steels. It means the residual ultimate strength of structural steels after fire is also dependent on steel grade.

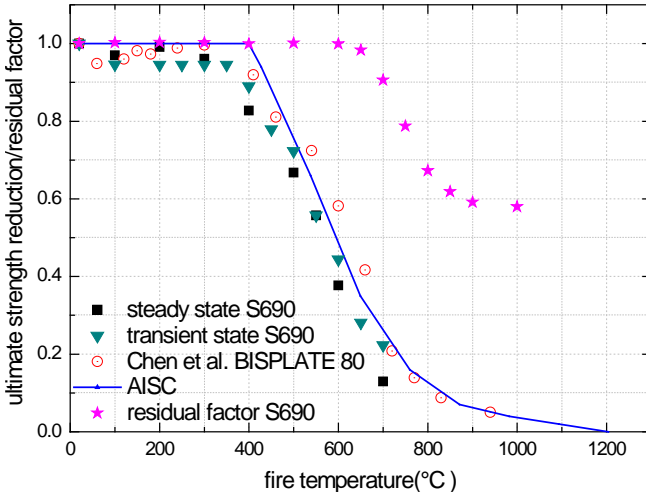


Figure 6. Reduction and residual factors of ultimate strength in fire and after fire.

4 PREDICTIVE EQUATIONS

As discussed above, the material behaviour of high strength steel S690 in fire and after fire is different from that of mild steels. Therefore some specific predictive equations were introduced herein to assess the deteriorations of material behaviour of HSS S690 in fire and after fire, in order to offer accurate choice for structural engineers to conduct safe fire-resistance design and accurate post-fire evaluation of steel structures with S690. As fire temperature was the main reason causing the deterioration of material properties of steel, the equations were developed as a function of the elevated temperature θ , which specimens have been exposed to.

4.1 Material behaviour of S690 in fire

The predictive equations proposed for presenting the deteriorations of material behaviour of HSS S690 in fire agree well with the experimental results, more details can be found in another research paper [12], here only the predictive equations were introduced.

4.1.1 Elastic modulus

$$20 \leq \theta \leq 200, \quad \frac{E_{\theta}}{E_{20}} = -5.986 \times 10^{-6} \theta^2 + 6.058 \times 10^{-4} \theta + 0.9903 \quad (1a)$$

$$200 < \theta \leq 700, \frac{E_{\theta}}{E_{20}} = -1.709 \times 10^{-9} \theta^3 - 9.914 \times 10^{-7} \theta^2 + 4.991 \times 10^{-4} \theta + 0.8226 \quad (1b)$$

4.1.2 Yield strength

Since the deviations between yield strength reduction factors of S690 under steady state fire condition and that under transient state fire condition were not small, two sets of equations were developed to predict the deterioration of yield strength of S690 exposed to fire. Equations 2 were proposed to evaluate the yield strength reduction factors of S690 under steady state fire condition, while Equations 3 were worked out to describe the yield strength reduction factors of S690 under transient state fire condition.

$$20 \leq \theta \leq 300, \frac{f_{y\theta}}{f_{y20}} = -6.038 \times 10^{-5} \theta + 0.9906 \quad (2a)$$

$$300 < \theta \leq 700, \frac{f_{y\theta}}{f_{y20}} = 7.355 \times 10^{-9} \theta^3 - 1.31 \times 10^{-5} \theta^2 + 5.185 \times 10^{-3} \theta + 0.4003 \quad (2b)$$

$$20 \leq \theta \leq 450, \frac{f_{y\theta}}{f_{y20}} = -9.492 \times 10^{-9} \theta^3 + 6.776 \times 10^{-6} \theta^2 - 1.785 \times 10^{-3} \theta + 1.036 \quad (3a)$$

$$450 < \theta \leq 700, \frac{f_{y\theta}}{f_{y20}} = 6.126 \times 10^{-8} \theta^3 - 1.077 \times 10^{-4} \theta^2 + 5.999 \times 10^{-2} \theta - 10.02 \quad (3b)$$

4.1.3 Ultimate strength

$$20 \leq \theta \leq 700, \frac{f_{u\theta}}{f_{u20}} = 1.959 \times 10^{-11} \theta^4 - 3.024 \times 10^{-8} \theta^3 + 1.232 \times 10^{-5} \theta^2 - 1.757 \times 10^{-3} \theta + 1.033 \quad (4)$$

4.2 Material behaviour of S690 after fire

The predictive equations proposed for evaluating the residual material behaviour of HSS S690 after fire were shown below. Good agreements between the predictive equations and experimental results were proved exist previously [13].

4.2.1 Elastic modulus

$$20 \leq \theta \leq 600, \frac{E_{p\theta}}{E_{20}} = -1.52 \times 10^{-10} \theta^3 + 2.70 \times 10^{-8} \theta^2 - 3.35 \times 10^{-5} \theta + 1 \quad (5a)$$

$$600 < \theta \leq 1000, \frac{E_{p\theta}}{E_{20}} = 6.27 \times 10^{-9} \theta^3 - 1.38 \times 10^{-5} \theta^2 + 8.95 \times 10^{-3} \theta - 0.806 \quad (5b)$$

4.2.2 Yield strength

$$20 \leq \theta < 650, \quad \frac{f_{y\theta}}{f_{y20}} = 1.0 - \frac{(\theta - 20)^{1.584}}{9957\theta} \quad (6a)$$

$$650 \leq \theta \leq 1000, \quad \frac{f_{y\theta}}{f_{y20}} = 1.80 \times 10^{-8} \theta^3 - 4.03 \times 10^{-5} \theta^2 + 2.74 \times 10^{-2} \theta - 4.711 \quad (6b)$$

4.2.3 Ultimate strength

$$20 \leq \theta \leq 600, \quad \frac{f_{u\theta}}{f_{u20}} = 1.000 \quad (7a)$$

$$600 < \theta \leq 1000, \quad \frac{f_{u\theta}}{f_{u20}} = -1.24 \times 10^{-10} \theta^4 + 4.13 \times 10^{-7} \theta^3 - 5.077 \times 10^{-4} \theta^2 + 0.271\theta - 52.21 \quad (7b)$$

5 CONCLUSION

This paper presents an experimental study on the material behaviour of high strength steel S690 at elevated temperatures and after being exposed to fire. The elastic modulus, yield strength and ultimate strength of S690 at elevated temperatures up to 700°C were reported herein. The comparison of HSS S690 with S420M and mild steels proved that the deterioration of material behaviour of structural steels in fire was dependent on steel grades. Hence the recommendations of current leading design standards on the material behaviour of steels in fire, which were mainly obtained from mild steels, are not applicable to high strength structural steels. It is highlighted that some specific statements for material behaviour of high strength structural steels in fire are necessary in the current leading design standards. Further, some unique predictive equations were worked out based on the experimental results to describe the deterioration of S690 in fire. Moreover, the residual elastic modulus, yield strength and ultimate strength of S690 after cooling down from fire temperatures up to 1000°C were presented as well. The recovery ability of mechanical properties of HSS S690 after cooling down from fire is promising. Its residual material behaviour after fire is almost not affected until being exposed to fire temperatures beyond 600°C. This is very positive for the reuse of steel structures or members made of HSS S690 after being exposed to fire. For safe consideration, a conservative suggestion is recommended to use 90% of the nominal material behaviour for HSS S690 after fire, if the fire temperature is below 600° C. To evaluate the residual material behaviour of S690 after cooling down from fire temperatures beyond 600° C up to 1000° C, some predictive equations were proposed to accurately determine elastic modulus, yield strength and ultimate strength. The research results described herein can be used by structural engineers to conduct safe fire-resistance design of steel structures with HSS S690 and accurate evaluation of high strength steel structures after being exposed to fire, as well as supports other related research about fire performance of steel structures with high strength steel S690.

REFERENCES

- [1] Institution BS. *BS 5950, Structural use of steelwork in building, Part 8: Code of practice for fire resistant design*, London, 1998.
- [2] CEN, *European Standard EN 10025-6, Hot rolled products of structural steels - Part 6: Technical delivery conditions for flat products of high yield strength structural steels in the quenched and tempered condition*, Brussels, 2009.
- [3] CEN, *European Standard EN 10002-5, Metallic materials-Tensile testing-Part 5: Method of testing at elevated temperature*, Brussels, 1992.
- [4] ASTM, *E21-09, Standard test methods for elevated temperature tension tests of metallic materials*, West Conshohocken, 2009.
- [5] Maljaars J., Twilt L., and Soetens F. , “Flexural buckling of fire exposed aluminium columns” *Fire Safety Journal*, 44, 711–717, 2009.
- [6] Outinen, J., “Mechanical properties of structural steels at high temperatures and after cooling down” , *PhD thesis*, Helsinki, Finland: Helsinki Univ. of Technology, 2007.
- [7] European Committee for Standardization (CEN), *EN 1993-1-2, Eurocode 3 - Design of steel structures Part 1-2: General rules - Structural fire design*, Brussels, 2005.
- [8] American Institution of Steel Construction (AISC), *Specification for structural steel buildings*, Chicago, 2005.
- [9] Australian Standards (AS) , *AS 4100, Steel structures*, Sydney, 1998.
- [10] American Society of Civil Engineering (ASCE), *Structural fire protection*, New York, 1992.
- [11] Chen J., Young B., and Uy B., “Behavior of high strength structural steel at elevated temperatures”, *J Struct Eng-ASCE*, 132, 1948-1954, 2006.
- [12] Qiang, X., Bijlaard, F.S.K. and Kolstein, M.H., “Predictive equations for high strength structural steel S690 exposed to fire” , *Advances in Steel Concrete Composite and Hybrid Structures - Proceedings of the 10th International Conference*, R. Liew (ed.), ASCCS, Singapore (2- 4/07), 2012. (in press)
- [13] Qiang, X., Bijlaard, F.S.K. and Kolstein, M.H., “Post-fire mechanical properties of high strength structural steels S460 and S690” , *Engineering Structures*, 35, 1-10, 2012.

CREEP BEHAVIOR OF ASTM A992 STEEL AT ELEVATED TEMPERATURES

Jinwoo Lee*, Mohammed A. Morovat *, Michael D. Engelhardt * and Eric M. Taleff**

* Ferguson Structural Engineering Laboratory, Department of Civil, Architectural and Environmental Engineering, University of Texas at Austin

e-mails: jinwoo@utexas.edu, morovatma@mail.utexas.edu, mde@mail.utexas.edu

** Department of Mechanical Engineering, University of Texas at Austin

e-mail: taleff@mail.utexas.edu

Keywords: Creep, Fire, ASTM A992 Steel, Elevated Temperatures, Material Creep Model.

Abstract. *This paper presents highlights of an extensive testing program recently completed to evaluate the creep response of ASTM A992 steel under a wide range of temperatures and stress levels. Creep tests were performed in which the steel was subjected to constant temperature and engineering stress, with the response measured in terms of engineering strain versus time. Temperatures from 400 °C to 1000 °C were considered in the creep tests. Applied stresses were fractions of the yield and tensile strengths obtained from tension tests at the specific temperature. Test results are then compared against existing material creep models for structural steel. The experimental results clearly indicate that material creep is significant within the time, temperature, and stress regimes expected in a building fire and demonstrate the need for a more reliable creep model for steel for structural-fire engineering analysis.*

1 INTRODUCTION

Predicting the response of steel structures to fire requires information on the mechanical properties of steel at elevated temperature, including creep behavior. An accurate knowledge of time-dependent mechanical properties of steel at high temperatures is an integral part of predicting the response of steel members subjected to fire, especially those elements whose behavior is controlled by buckling failure modes [1].

A comprehensive review of the literature on high-temperature mechanical behavior of structural steel reveals that there is very little experimental creep data on structural steels used in building construction for the temperature and stress regimes of interest in structural-fire engineering applications. Furthermore, there appears to be virtually no data for ASTM A992 steel, the most common grade of structural steel used in the US building construction practice. The specified minimum yield and tensile strength of A992 steel is 50 ksi and 65 ksi, respectively.

This paper presents some results of an extensive testing program on the phenomenon of high-temperature creep of ASTM A992 steel. The experimental creep data is then compared to several models for predicting creep, to assess the accuracy and limitations of creep models.

2 CREEP OF STEEL AT ELEVATED TEMPERATURES

2.1 Creep phenomenon

The term *creep* refers to time-dependent strain response of materials, or more generally to time- and rate-dependent stress-strain response. At normal temperatures, the stress-strain response of steel shows only a very mild dependence on loading rate and virtually no dependence on time, for typical loading

rates seen in buildings. Therefore, creep effects are normally neglected in the analysis and design of steel structures at normal temperatures. However, as temperature increases, steel exhibits increasingly significant creep effects. Creep tests on materials are commonly conducted by subjecting the material to constant stress and temperature, and then measuring strain as a function of time. A typical creep curve is often divided into the three phases of primary, secondary and tertiary creep. In the primary stage, the curve is nonlinear and typically exhibits a decreasing creep strain rate with increase in time. In the secondary stage, the creep strain rate is almost constant, and this stage is often referred to as steady-state creep. In the tertiary stage, the creep strain rate increases with time. For steel, the shape of the curve, the magnitude of the creep strain, and the time scale are highly dependent on temperature and stress level.

2.2 Literature on high-temperature creep

The creep behavior of steel at elevated temperatures has been studied and reported by several researchers [2, 3, 4, 5, 6, 7, 8, 9, 10]. One of the simplest and most widely used creep models is the Norton-Bailey model, also known as the creep power law [2, 3]. Although the Norton-Bailey law is capable of modeling primary creep, it can define the steady-state or secondary stage of creep more accurately. One of the widely used creep models in structural-fire applications proposed by Fields and Fields [6] incorporates a power law and represents creep strain, ϵ_c , in the form of a Norton-Bailey equation as follows:

$$\epsilon_c = at^b \sigma^c \quad (1)$$

In this equation, t is time and σ is stress. The parameters a , b and c are temperature-dependent material properties. Fields and Fields [6] derived equations for these temperature-dependent material properties for ASTM A36 steel. The model developed by Fields and Fields [6] is capable of predicting creep in the temperature range of 350 °C to 600 °C and for creep strains up to 6-percent. The validity of this creep model will be discussed in more detail in the following sections of this paper.

Another creep model commonly used for structural-fire engineering applications is the one developed by Harmathy [5]. Harmathy appears to be one of the first investigators who attempted to develop a creep formula for structural steels subjected to fire exposure. Harmathy [5] proposed a creep model based on experiments on several structural and prestressing steels including ASTM A36. His model attempts to predict creep strains in both the primary and secondary stages of creep. The model proposed by Harmathy represents creep strain, ϵ_c , for steel as follows:

$$\epsilon_c \approx (3Z\epsilon_{c_0}^2)^{1/3} \theta^{1/3} + Z\theta \quad \text{when } \frac{d\sigma}{dt} = 0 \quad \text{and } \theta = \int_0^t te^{-Q_c/RT} dt \quad (2)$$

In this equation, θ is the temperature-compensated time in Dorn's creep theory [4], Z is the slope of the secondary part of the creep curve, also known as the Zener-Hollomon parameter [8], and ϵ_{c_0} is the intercept obtained by extending the straight-line section (secondary part) of the $\epsilon_c(\theta)$ curve to the ϵ_c axis. The parameters ϵ_{c_0} , and Z are stress-dependent material parameters.

Although models developed by Fields and Fields [6] and Harmathy [5] are referenced by many investigators in the field of structural-fire engineering, their predictions of creep strain for some applied stress levels and temperatures are quite different. This difference in creep predictions will be discussed in the following sections.

The last creep model considered in this paper is the one developed by Batsoulas [7]. The significant feature of this creep model, shown in Equation 3, is that it can describe the primary, secondary and tertiary stages of the creep curve.

$$\epsilon_c = \frac{e^{at}}{a\eta + K} \left[1 - e^{-\left(a + \frac{K}{\eta}\right)t} \right] \sigma \quad (3)$$

In this equation, t is time and σ is stress. The parameters a , η and K are temperature-dependent material properties.

3 EXPERIMENTAL CREEP OF ASTM A992 STEEL AT HIGH TEMPERATURES

3.1 Equipment and specimens

An extensive series of creep tests were conducted on tension coupons made of samples of ASTM A992 steel. A 22 kips (100 kN) capacity MTS 810 test frame with water cooled wedges was used to conduct the tests. The heating system consisted of an electric furnace, the furnace temperature controller, and the data acquisition system for recording and monitoring coupon temperatures.

An MTS Model 653 furnace (Figure 1) was used as the heating device. The furnace generates heat using electrical coils, and is separated into upper, middle and lower heating zones that can be individually controlled using an MTS Model 409.83 temperature controller. Three thermocouples are located inside the furnace to measure the furnace air temperature.

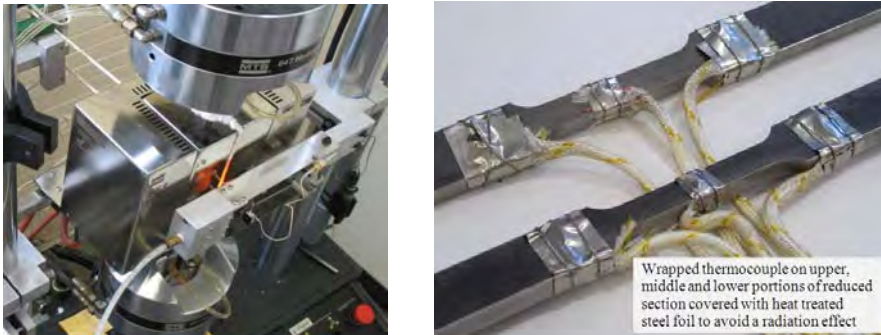
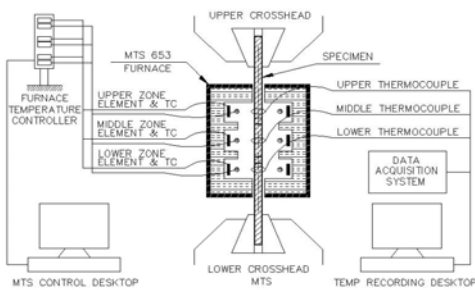
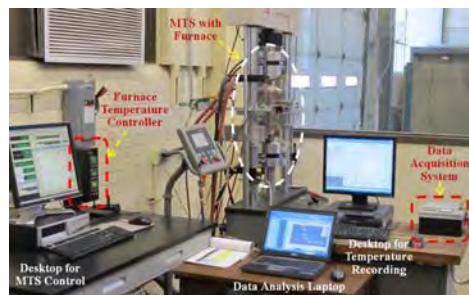


Figure 1. High-temperature testing device and thermocouples on coupon prior to testing

Coupon temperatures were monitored and controlled using a separate data recording system as shown in Figure 2. Three K-type thermocouple wires were used to measure the surface temperature of the specimen at different locations along the gauge length of the coupon. The researchers found that considerable experience was required in the control of the three zones of the furnace in order to achieve uniform temperature along the gauge length of the coupon, and in order to achieve the target temperature of the steel. However, using temperature control strategies developed through experience, it was possible to keep temperature differences between the actual temperature of a specimen and a target temperature within ± 3 °C for temperatures below 1000 °C.



(a) Schematic diagram of heating system



(b) General view of the experimental set-up

Figure 2. Test set-up consisting of the test machine and heating system.

An MTS Model 632.54E-11 air-cooled high-temperature extensometer with 1-in. gauge length (with limit strain of -5 to +10%) was used to measure strain. In order to capture the entire stress-strain relationship, throughout the course of the tests, the 1-in. gauge-length extensometer was reset when it approached the 10% limit. The resetting procedure is described in detail in Lee [11].

All specimens were cut from the flanges of a single W4×13 section made from ASTM A992 structural steel. The dimensions of the specimens are shown in Figure 3. The cross sectional area of each coupon was approximately 0.17 in². The coupons were prepared so that their longitudinal dimension was along the rolling direction of the wide flange member. The result of a chemical analysis of the steel used in this research is presented in Table 1.

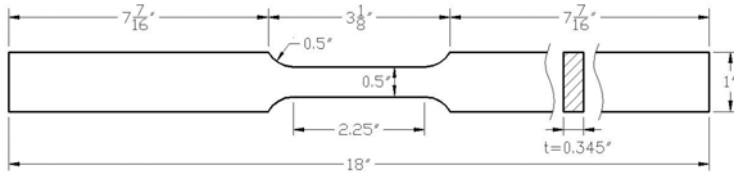


Figure 3. Dimensions of the coupon specimens.

Table 1. Chemical Composition of the Tested Specimens (Weight %).

Coupon	C	Mn	Cu	Si	Cr	Ni	Mo	S	Nb	P	Sn
Flanges	0.08	0.91	0.24	0.23	0.10	0.09	0.026	0.025	0.014	0.011	0.01

3.2 Testing procedure

All tests were steady-state temperature tests, in which the specimens were heated up to a specified temperature and then loaded while maintaining the same temperature. During the initial heating process, the load was maintained at zero to allow free expansion of the specimen.

Two types of tests were conducted as part of this research. The first type of test was a tension test in which the specimen was heated to the target temperature under no load, and then loaded to failure. These tests were conducted under displacement control, in which a crosshead displacement rate was maintained at a constant value of 0.01 in./min throughout a test. Tension tests were conducted at 20°C, and then at temperatures of 100 to 1000 °C, in increments of 100 °C. The purpose of the tension tests was to establish the basic stress-strain curves for the material at various temperatures, and to establish values of yield strength and ultimate tensile strength at each temperature. Results for selected temperatures are listed in Table 2. The yield strength values reported in this table are based on a 0.2-percent strain offset definition.

Table 2. Yield and tensile strengths of ASTM A992 steel

Temp (°C)	20	400	500	600	700	800	900	1000
Yield Strength (ksi)	51.8	35.4	29.0	18.8	9.0	5.3	4.5	2.8
Tensile Strength (ksi)	68.3	60.0	39.0	18.9	9.7	6.1	5.3	3.3

The second type of test conducted in this research, and the main objective of the experimental program, was the creep test. For these tests, the coupons were heated to the target temperature under no load. Load was then applied to the coupon, and held at a constant level, usually for a period of two hours. The initial application of the load, from zero to the target value was done rapidly, typically in less than 2 seconds, to minimize the influence of creep in the initial loading process. Creep tests were conducted at temperatures of 400 to 1000 °C, in increments of 100 °C. The application of a constant load resulted in

the application of a constant engineering stress (load divided by initial cross-sectional area). Note that the term “stress” as used in this paper refers to engineering stress. For each temperature, creep tests were run at four levels of constant load, in order to achieve constant stress levels that corresponded to 50, 75, and 90 percent of the yield strength and 90 percent of the tensile strength of the material at the specified temperature, as reported in Table 2. For example at 500 °C, the measured yield and tensile strength were 29.0 ksi and 39.0 ksi, respectively (Table 2). Thus, the corresponding stress levels used for the creep tests were 14.5 ksi, 21.7 ksi, 26.1 ksi, and 35.1 ksi, corresponding approximately to 50, 75, and 90 percent of 29.0 ksi and 90 percent of 39.0 ksi.

3.3 Tensile creep curves

Selected results of creep tests are shown in Figures 4 through 10 for materials from the flanges of the W4×13 section. Figure 11 shows a photo of the coupons after testing. The full data are reported in Lee [11]. These figures show the measured strain versus time response the coupons of ASTM A992 steel while being exposed to specified constant stresses and temperatures. The strain plotted in these figures includes the strain measured while increasing the load from zero to the target values, and the strain measured while at constant load. Thus, the curves include both instantaneous strain and creep strain. At higher temperatures, say at about 600 °C and above, the instantaneous strain during initial load application was very small compared to the subsequent creep strain.

As can be observed from these figures, at low to moderate stress levels, creep becomes significant at about 500 °C while at high stress, the creep strains are large even at 400 °C. Interestingly, curves at temperatures above 700 °C corresponding to moderate and high level of stresses indicate that the steel material almost immediately enters the tertiary stage of creep, with a rapid increase in creep strain over a short time interval. Moreover, as can be seen in Figures 8 and 9, at moderate stress levels, the coupon actually fractured in the time frame of less than 2 hours, a phenomenon known as *stress rupture* or *creep rupture*.

The data plotted in Figures 4 through 10 suggest that creep strains can be quite significant for temperatures, stress levels, and time durations that might be expected in a typical building fire. For example, at a steel temperature of 700 °C and a stress level under 10 ksi, creep strains on the order of 2-percent are achieved in less than 45 minutes. This suggests that ignoring creep may lead to highly inaccurate predictions of structural response for some classes of structure-fire problems.

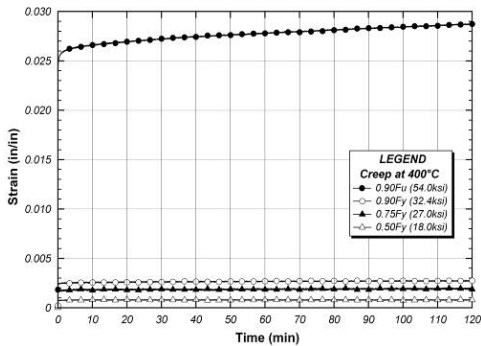


Figure 4. Creep curves at 400 °C.

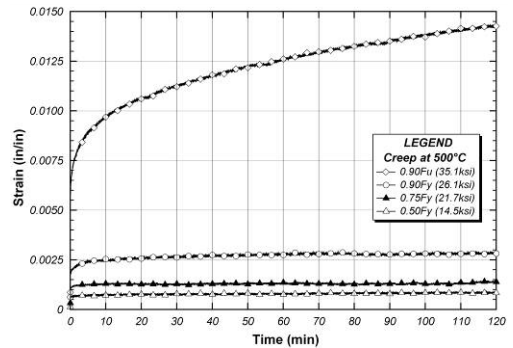


Figure 5. Creep curves at 500 °C.

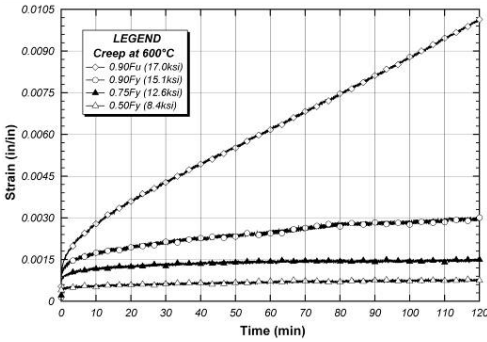


Figure 6. Creep curves at 600 °C.

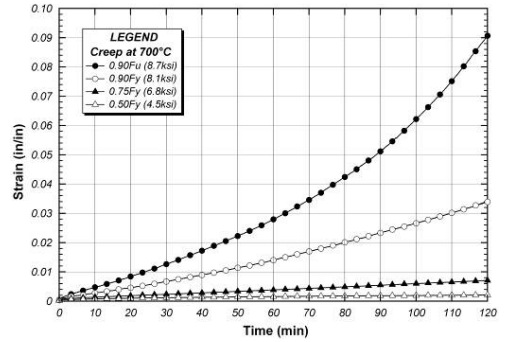


Figure 7. Creep curves at 700 °C.

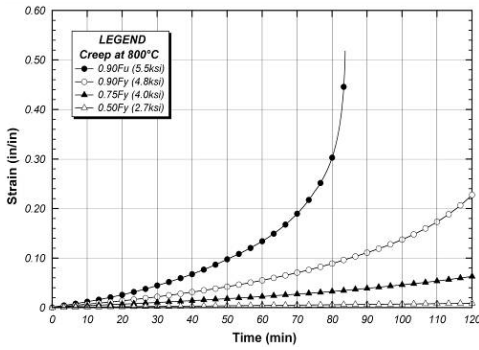


Figure 8. Creep curves at 800 °C.

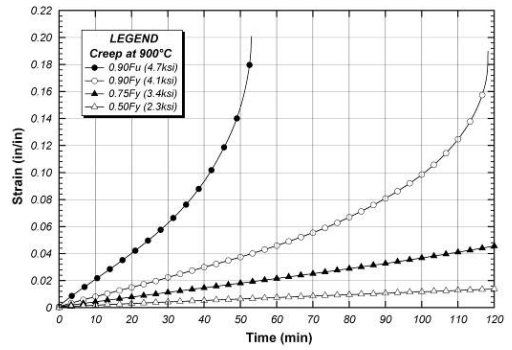


Figure 9. Creep curves at 900 °C.

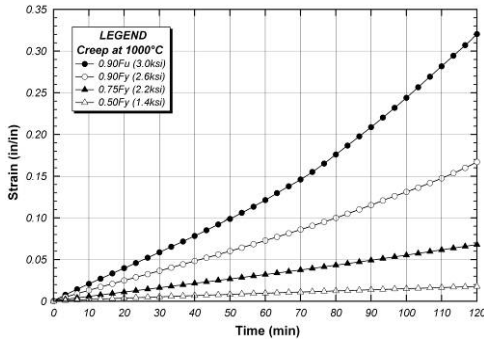


Figure 10. Creep curves at 1000 °C.



Figure 11. Coupons after creep testing

4 ANALYTICAL CREEP OF ASTM A992 STEEL AT HIGH TEMPERATURES

As part of this research investigation, an attempt was made to develop a model that could predict strain versus time for ASTM A992 steel for various stresses and temperatures. The model, which was fit to the experimental data, is shown in Table 3 and presented in Figure 12. The model includes both an initial instantaneous strain term, which is independent of time, and a time dependent creep strain term. The initial strain term includes both time-independent elastic and plastic strains. The creep strain term is written in the form of a double power law. This form of the creep strain permits capturing all three stages of creep: primary, secondary and tertiary.

Table 3. Suggested creep model.

Stage	Time Range	Suggested Creep Model (400°C ≤ T ≤ 1000°C)
Initial	t = t ₀	$\epsilon_i = \epsilon_e + \epsilon_p = \begin{cases} \frac{\sigma}{E} & : \sigma \leq F_y \\ \frac{F_y}{E} + \frac{\sigma - F_y}{E_p} & : F_y < \sigma \leq F_u \end{cases}$ <p>E = 41,348 - 37.12 T, E_p = 2,700 - 2.57 T</p>
Creep	t ₀ < t ≤ t _r , t ₃	ε _c = ε _i + A ₁ t ^{n₁} + A ₂ t ^{n₂}

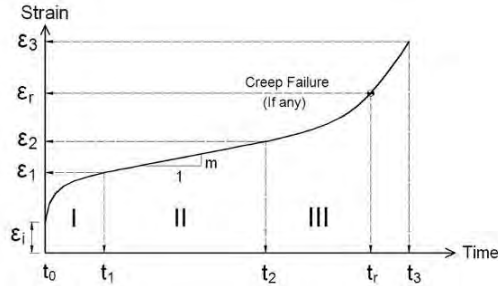


Figure 12. Suggested creep model for ASTM A992 steel.

The parameters in the suggested creep model obtained through the process of curve fitting to the creep test results of ASTM A992 steel are summarized in Table 4. It should be noted that these parameters are functions of both stress and temperature.

Table 4. Parameters used in the suggested creep model

Temp. (°C)	σ (ksi)	t ₃ (min)	A ₁	n ₁	A ₂	n ₂	
400	0.50F _y	17.7	120	1.00E-04	0.050	-	-
	0.75F _y	26.6	120	7.50E-04	0.045	-	-
	0.90F _y	31.9	120	1.25E-03	0.040	-	-
	0.90F _u	54.0	120	1.25E-02	0.052	-	-
500	0.50F _y	14.5	120	5.00E-05	0.310	-	-
	0.75F _y	21.7	120	2.50E-04	0.120	-	-
	0.90F _y	26.0	120	1.00E-03	0.120	-	-
	0.90F _u	35.3	120	2.00E-03	0.300	-	-
600	0.50F _y	8.4	120	4.00E-05	0.440	-	-
	0.75F _y	12.6	120	3.00E-04	0.230	-	-
	0.90F _y	15.1	120	4.00E-04	0.355	-	-
	0.90F _u	17.0	120	5.00E-04	0.544	1.00E-07	2.100
700	0.50F _y	4.5	120	1.50E-04	0.525	-	-
	0.75F _y	6.8	120	2.00E-04	0.665	3.00E-08	2.310
	0.90F _y	8.1	120	3.00E-04	0.880	3.00E-08	2.720
	0.90F _u	8.7	120	4.00E-04	0.950	3.00E-08	3.000
800	0.50F _y	2.7	120	1.50E-04	0.770	2.00E-07	1.980
	0.75F _y	4.0	120	6.00E-04	0.800	2.00E-07	2.520
	0.90F _y	4.8	120	8.00E-04	1.000	2.00E-11	4.720
	0.90F _u	5.5	84	8.00E-04	1.170	2.00E-11	5.200

900	0.50F _y	2.3	120	2.00E-04	0.865	2.00E-07	1.770
	0.75F _y	3.4	120	5.00E-04	0.890	2.00E-07	2.250
	0.90F _y	4.1	118	1.00E-03	0.920	2.00E-18	8.100
	0.90F _u	4.8	53	1.50E-03	1.100	2.00E-18	9.630
1000	0.50F _y	1.5	120	3.00E-04	0.830	2.00E-07	1.880
	0.75F _y	2.2	120	6.00E-04	0.950	2.00E-07	2.280
	0.90F _y	2.6	120	2.00E-03	0.860	2.00E-08	3.050
	0.90F _u	2.9	120	2.00E-03	0.980	2.00E-08	3.230

5 EVALUATION OF MATERIAL CREEP MODELS

In this section, the experimental creep results along with the suggested creep model are compared against the creep material models by Fields and Fields [6], by Harmathy [5] and by Batsoulas [7]. The creep material models by Fields and Fields and by Harmathy were developed for ASTM A36 steel (specified $F_y = 36$ ksi). It appears that the Batsoulas model was also developed for steels similar to ASTM A36. Since the material under consideration here, ASTM A992, has a larger strength than ASTM A36, the application of these models to A992 steel is unclear. However, in an attempt to provide a basis for comparison, the models by Fields and Fields, by Harmathy, and by Batsoulas were modified to account for the strength difference between A36 and A992. The primary modification made was that the stress value used in the models was modified by the ratio of 36/50. Thus, for example, if the applied stress in a test on A992 steel was 30 ksi, the stress value used in the A36 creep models was entered as $30 \text{ ksi} \times (36/50) = 21.6 \text{ ksi}$. Further, it should be noted that the computed model predictions all included both the instantaneous strain and the creep strain for all models except Harmathy. A full description of how the models by Fields and Fields, by Harmathy, and by Batsoulas were interpreted and modified for comparison with this experimental creep data is described in Lee [11].

Predictions from material creep models are compared with experimental results in Figures 13 through 18. Several observations can be made from these figures. First, it can be observed that the suggested model (Tables 3 and 4) matches the experiments quite well. This, of course, is no surprise since the model parameters were fit to match the experimental data. More importantly, however, the form of the suggested model can capture all three stages of creep quite well. For example, at lower temperatures and stress levels, the strain versus time response is dominated by primary and secondary creep. However, at higher temperatures, the response is dominated by tertiary creep, even for short time periods. The form of the suggested model can reasonably capture this wide range of creep responses. The specific parameters of the model (Table 4) were chosen to fit this data, and it is unclear how well these parameters would predict creep for other steels, even other samples of A992 with somewhat different values of yield stress. Nonetheless, if the proper parameters can be determined through testing, the form of the suggested model is quite versatile in modeling the full range of creep behavior.

It can also be observed that the predictions by Fields and Fields, by Harmathy, and by Batsoulas do not in general agree with the test results, and in some cases, are grossly different. Most of these discrepancies likely reside in the limitations in the scope of such creep models. As noted above, these models were developed for a lower strength steel (A36), and so their application to A992, even with the adjustments described above, is unclear. Further, the models were intended for specific temperatures and strains. For example, the Fields and Fields models were based on experiments that were conducted in the temperature range of 350 °C to 650 °C. Further, the maximum creep strain reached during the experiments was about 6%. Therefore, caution should be observed in extrapolating strain values for temperatures above 650 °C and for strain values higher than 6%. It should also be added that the creep models by Fields and Fields [6] and by Harmathy [5] are suitable for predicting creep strains in the primary and secondary stages of creep. As a result they can not capture tertiary creep behaviors observed at temperatures above 700 °C. All in all, observations like these clearly show the need for more reliable creep models for structural steel at elevated temperatures.

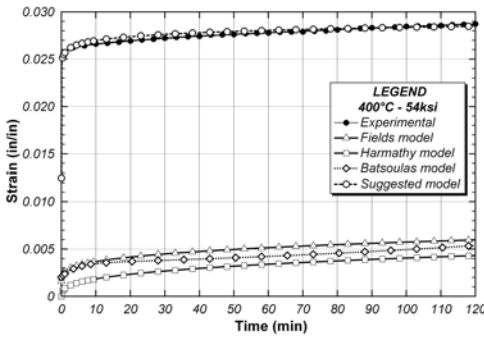


Figure 13. Creep model comparison at 400 °C.

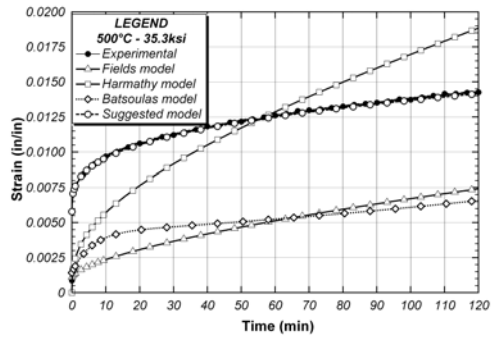


Figure 14. Creep model comparison at 500 °C.

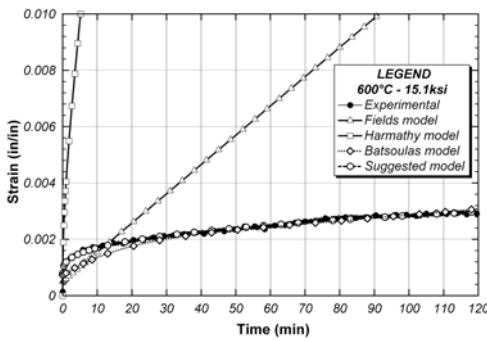


Figure 15. Creep model comparison at 600 °C.

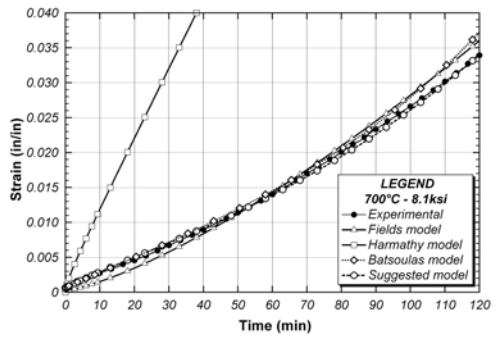


Figure 16. Creep model comparison at 700 °C.

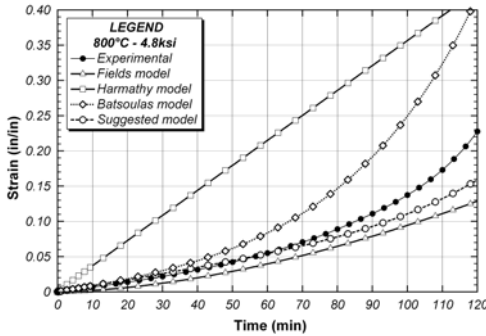


Figure 17. Creep model comparison at 800 °C.

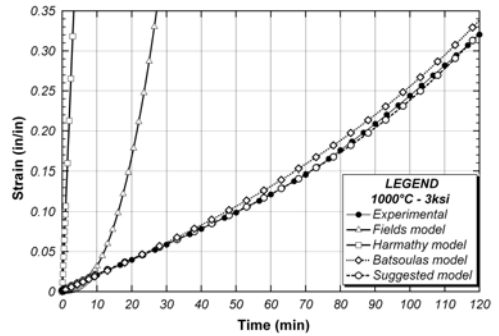


Figure 18. Creep model comparison at 1000 °C.

5 CONCLUSIONS

This paper has presented representative results of on-going research on the time-dependent or creep behavior of structural steel. Creep behavior has been presented as strain-time curves at constant stresses and temperatures for ASTM A992 structural steel. A material creep model was suggested for A992 steel based on these tests. The suggested material creep model, as well as models reported in the literature, was compared with the experimental creep data.

Several conclusions can be made from this work. First, the test data shows creep strains can be quite significant for temperatures, stress levels, and time durations representative of building structures exposed to fire. This suggests that ignoring creep may lead to highly inaccurate predictions of structural response for some classes of structure-fire problems. Secondly, existing creep models may provide poor predictions when compared to experimental data. Interpretation of creep models is difficult, and it is unclear how far they can be interpolated or extrapolated beyond the specific steels, temperature ranges and stress levels for which the model parameters were fit to experimental data. Thus, the fundamental conclusion of the authors is that the ability to accurately model creep in structural-fire engineering problems, at present, is quite poor. Considering the potential importance of creep in structural-fire engineering analysis, considerable work is needed to develop more robust and accurate creep models for steel.

6 ACKNOWLEDGMENTS

The research reported herein was conducted as part of a research project on *Creep Buckling of Steel Columns Subjected to Fire* supported by the National Science Foundation (NSF Award 0927819). The support of the National Science Foundation and of the former NSF Program Director M.P. Singh is gratefully acknowledged. The authors also gratefully acknowledge Gerdau-Ameristeel for donating materials for this research. The authors thank Matthew Gomez of Gerdau-Ameristeel for his support of this research.

REFERENCES

- [1] Morovat M.A., Lee J., Engelhardt M.D., Helwig T.A. and Taleff E.M., "Analysis of Creep Buckling of Steel Columns Subjected to Fire", *Proceedings, Structures Congress, ASCE*, Las Vegas, April 14-16, 2011.
- [2] Norton F.H., *The Creep of Steel at High Temperatures*, McGraw-Hill Inc., New York, 1929.
- [3] Bailey R.W., "Creep of Steel under Simple and Compound Stress", *Engineering*, 148, 121, 528-529, 1929.
- [4] Dorn J.E., "Some Fundamental Experiments on High Temperature Creep", *Journal of the Mechanics and Physics of Solids*, 3(2), 85-116, 1955.
- [5] Harmathy T.Z., "A Comprehensive Creep Model", *Journal of Basic Engineering, Trans. ASME*, 89(3), 496- , 1967.
- [6] Fields B.A. and Fields R.J., *Elevated Temperature Deformation of Structural Steel*, Report NISTIR 88-3899, NIST, Gaithersburg, MD, 1989.
- [7] Batsoulas N.D., "Prediction of Metallic Materials Relaxation at Elevated Temperature", *Steel Research*, 74(3), 176-180, 2003.
- [8] Zener C. and Hollomon J.H., "Effect of Strain Rate on the Plastic Flow of Steel", *Journal of Applied Physics*, 15, 22- , 1944.
- [9] Freudenthal A.M., *The Inelastic Behavior of Engineering Materials and Structures*, John Wiley & Sons Inc., New York, 1950.
- [10] Shanley F.R., *Weight-Strength Analysis of Aircraft Structures*, McGraw-Hill Inc., New York, 1952.
- [11] Lee, J., "Elevated Temperature Properties of steel for Structural Fire Engineering Analysis." Ph.D. Dissertation, Department of Civil, Architectural and Environmental Engineering, University of Texas at Austin, 2012.

FIRE TESTS OF LOAD BEARING STEEL STUD WALLS EXPOSED TO REAL BUILDING FIRES

Anthony D. Ariyanayagam and Mahen Mahendran

PhD Researcher and Professor, Science and Engineering Faculty, Queensland University of Technology, Australia.

e-mail: a.ariyanayagam@qut.edu.au, e-mail: m.mahendran@qut.edu.au

Keywords: Light gauge steel frames, Load bearing steel stud walls, Real building fires, Fire rating, Cold-formed steel structures, Full scale tests.

Abstract. *Fire resistance has become an important part in structural design due to the ever increasing loss of properties and lives every year. Conventionally the fire rating of load bearing Light gauge Steel Frame (LSF) walls is determined using standard fire tests based on the time-temperature curve given in ISO 834 [1]. Full scale fire testing based on this standard time-temperature curve originated from the application of wood burning furnaces in the early 1900s and it is questionable whether it truly represents the fuel loads in modern buildings. Hence a detailed fire research study into the performance of LSF walls was undertaken using real design fires based on Eurocode parametric curves [2] and Barnett's 'BFD' curves [3]. This paper presents the development of these real fire curves and the results of full scale experimental study into the structural and fire behaviour of load bearing LSF stud wall systems.*

1 INTRODUCTION

In recent times, LSF stud wall systems are extensively used in residential, industrial and commercial buildings as primary load bearing components. Although they have been used widely, their behaviour in real fires is not fully understood, especially in relation to fire resistance. The fire resistance of LSF stud walls has been traditionally determined using the standard fire tests specified in ISO 834 [1]. Fire Resistance Rating (FRR) should be sufficient in a fire event, for safe evacuation, fire service intervention and for rescue activities. Recent researches [4-6] have shown that the actual FRR of building elements exposed to real building fires is significantly less than that obtained from standard fire tests. Based on a series of Cardington fire tests, Lennon and Moore [4] suggested that the standard fire exposure would severely underestimate the severity of the fire in terms of maximum temperature and duration. Jones [5] has also shown that the actual fire resistance of building elements exposed to real building fires can be significantly less than the FRR obtained from exposing them to standard time-temperature curve [1].

Fire testing of LSF wall systems is generally based on the standard time-temperature curve given in ISO 834 [1], which originated based on wood burning. In reality, modern residential and commercial buildings also incorporate synthetic foams, fabrics and thermoplastic materials. Bwalya et al.'s [7] recent fire load survey of Canadian residential dwellings showed that although the cellulosic material takes up the highest contribution, plastics occupy 13 to 39% by weight and contribute 20 to 48% to the fuel load. This shows a significant contribution from synthetic plastic materials to the fire loads in residential dwellings. During a fire, these thermoplastic materials melt and flow to the floor and burn faster with higher heat release rates resulting in more severe fires than standard fires. Therefore building structural elements may not ensure safe evacuation, or offer the required life safety for occupants and fire rescuers.

The experimental time-temperature curve should cover most of the potential fires in buildings. However, the present standard time-temperature curve [1] may not meet this requirement. This was shown by many researchers [4-6] using compartment tests, where the maximum temperature of a natural

fire exceeded the standard ISO curve within a short period of time from ignition. Also the shape of the curve strongly relates to the behaviour of an element during a fire. The natural building fire has a decay phase, whereas the ISO curve [1] rises continuously. This may be conservative for long duration, average temperature rise fires, but not for short duration, very hot fires. Also there is some concern nowadays about the importance of the behaviour of structural elements in the decay (cooling) phase of a building fire. Guo and Bailey [8] showed that significant structural damage can occur during the cooling phase. Standard fire tests will give good comparative results for building systems tested under identical conditions, and also valuable basic data, but do not provide accurate FRR for buildings which have a high fire severity. In a real fire, the growth, fully developed burning and decay phases depend on aspects such as the total fuel load present in the room, fuel type and configuration, ventilation openings and thermal properties of compartment lining materials. To overcome the current limitations in fire resistance of LSF walls, a research project is currently under way at the Queensland University of Technology (QUT). The main objective of this project is to undertake both experimental and numerical studies of LSF stud wall systems to develop a better understanding of the behaviour of these wall panels under realistic fire conditions. This paper presents the details of the development of realistic fire curves based on Eurocode parametric curves [2] and Barnett's 'BFD' curves [3] and the results of full scale fire tests of five LSF stud wall systems. The test variables included fire scenario, LSF wall panels and load ratio.

2 NON-STANDARD DESIGN FIRES

Fire behaviour prediction models representing the behaviour of a fire are of two types; pre-flashover and post-flashover models. The post-flashover fire scenario models are important in the analysis and design of the building fire safety systems whereas the pre-flashover fires mainly focus on the life safety of building occupants, especially the toxic gas production and fire spread. Several equations and computer models have been developed by researchers [3,9,10,15,16] to simulate the post-flashover time-temperature profiles. These fire profiles can be either probabilistic or deterministic models. The probabilistic models are based on previously captured compartment and real fire events while deterministic models utilise scientific principles to predict the fire behaviour with time. The fire profiles were obtained and validated for different types of fuels and ventilation conditions. Also most of the fire profile equations have limitations in-built within them and their range of application is limited and needs extensive calculations to derive a suitable time-temperature profile. For computer models more reliable and detailed measurement data from large-scale fire tests are needed for validation. Hence it is very difficult to envisage the time-temperature profile of a compartment fire. Also it is clear that a predefined standard fire curve in [1] to suit the real building fires is unrealistic and the design fires have to be determined based on the fuel load, ventilation openings and thermal properties of wall lining materials in a compartment. Therefore in order to investigate the structural and thermal behaviour of LSF wall panels under real building fire conditions, the time-temperature profiles recommended in Eurocode 1 Part 1-2 [2] known as the parametric curve and Barnett's 'BFD' [3] curve were selected.

Eurocode parametric curve allows a time-temperature relationship to be developed for a combination of the above mentioned parameters. The rate of temperature rise and peak temperatures in the Eurocode parametric curves are well above those in the ISO fire curve [1] in most situations for the same time period. But the decay rates are linear and very fast, leading to shorter fire durations. Pope and Bailey [11] also states that Eurocode parametric curve under-predicts the temperatures in the decay phase and the linear time-temperature relationship in the decay phase is not acceptable. Barnett [3] on the other hand states that the parametric curves are unrealistic as they do not take the shape of a fully developed fire, and recommends that the 'BFD' curve is much closer to the real fire time-temperature distribution. Barnett's 'BFD' [3] curve uses a single log-normal equation to represent both the growth and decay phases of a fire and has been developed using curve fitting to a wide range of experimental test results (142 natural fire tests with a range of fuels and different enclosure materials). The 'BFD Curve' is a good replacement for the standard time-temperature curve as it takes the shape of the natural fire curve and fits the results of actual fire tests closer than other methods. It requires only three factors; the maximum gas temperature,

the time at which it occurred and a shape constant. Hence in order to study the structural and thermal behaviour of LSF walls under natural decay phase of a fire, Barnett's 'BFD' curve is also considered.

3 DEVELOPMENT OF REAL BUILDING DESIGN FIRES

As mentioned earlier, design fires are determined based on three parameters, namely; fuel load, ventilation openings and thermal properties of wall lining materials. Of these the fuel load density values depend on geographic locations, type of building and room use. Many varying values have been recommended by researchers and in codes of practice. It is uncertain which mean value and the percentile are to be selected in determining the time-temperature fire curve representing a more realistic fire scenario for residential buildings. Hence this question was raised with many academics, researchers and experts in the field of fire engineering, whose common recommendations and suggestion are to select a realistic value from the available literature that is justifiable to the present building environment than using a value obtained 20 years ago. Also there is no definitive value for a type of building and the fuel load density value alone does not provide a realistic time-temperature curve. Instead parameters such as composition of fuel load and heat release rates are also important in obtaining a more accurate curve together with ventilation opening sizes and thermal properties of wall lining materials. However for design purposes it is obvious to select the worst case fire scenario, which reflects the actual fire growth in a modern building. Therefore an average value of 780 MJ/m² was selected from Eurocode 1 Part 1-2 [2], which is very close to the Bwalya et al.'s [7] recent survey results (807 MJ/m²) obtained for Canadian residential buildings. As recommended by most researchers, an 80th percentile value of 948 MJ/m² was selected for design purposes. Hence the design variable fuel load density based on floor area for residential building is 1138 MJ/m², taking in to account the combustion ($m = 0.8$), fire activation risks for compartment area ($\delta_1 = 1.5$) and type of occupancy ($\delta_2 = 1$) given in Eurocode 1 Part 1.2 [2].

Design fuel load density in a room is primarily made up of both permanent and variable fuel loads. Permanent fuel loads includes built-in combustible materials such as wall and floor finishes and other permanently installed equipment. The National Fire Protection Association (NFPA) in its NFPA 557 [12] has proposed a value of 130 MJ/m² for permanent fuel load density in buildings with non-combustible construction. Hence the design fuel load density for residential buildings is determined as 1268 MJ/m².

The compartment boundary of enclosure materials for this research is chosen to be with light gauge steel partitions lined with gypsum plasterboards and rock fibre insulations for walls and ceiling, and with concrete floor slab to represent a typical single storey residential building. The thermal inertia (b) for the compartment enclosure materials was calculated using Equation 1 as given in Eurocode 1 Part 1.2 [2].

$$b = \sqrt{\rho c \lambda} \quad [J / m^2 s^{1/2} K] \quad (1)$$

Properties of 16 mm thick Firestop^(R) Gypsum plasterboard at ambient (20°C) temperature (Firestop^(R) manufactured by Boral Plasterboards, Australia) are: Density (ρ) – 729 kg/m³, Specific heat (c) – 950 J/kgK and Thermal conductivity (λ) - 0.25 W/mK. These values were recommended by Keerthan and Mahendran [13] based on their experimental and numerical studies of gypsum plasterboards, which led to a value (b) of 416 J/m²s^{1/2}K. The values of 'b' for rock fibre insulation and concrete floor are 145 J/m²s^{1/2}K [13] and ($b = 1899$ J/m²s^{1/2}K) [14], respectively. To account for different fire scenarios, two different fire compartments having light gauge steel frame walls and ceiling panels with and without rock fibre insulations and concrete floor were selected in this research, where Compartment – A walls and ceilings are lined with gypsum plasterboards and Compartment – B consists of rock fibre insulation sandwiched between these two plasterboards. Based on the 'b' values above, the compartment thermal inertia for enclosure surface with different layers of materials was calculated using the equations given in Eurocode 1 Part 1.2 [2]. Table 1 shows the values used to develop the design real fire curves namely: fuel load density ($q_{f,a}$), ventilation factor (O) and thermal inertia (b) of the compartment. The compartment geometry considered was based on the dimensions of 3600 (L) x 2400 (W) x 2400 (H) mm. Opening factors 0.08 and 0.03 m^{1/2} were chosen to represent a rapid fire and a long-drawn-out fire for LSF walls.

Using these parameters three Eurocode parametric curves [2] were developed as shown in Figure 1. Fire curves EU1-(0.08) and EU2-(0.03) were considered to be the most appropriate curves as they represent a rapid fire (EU1) and a prolonged fire (EU2), respectively. They also come within the acceptable fire durations of about 60 minutes and 4 hours, respectively, for experimental purposes.

Table 1. Fire compartment characteristics

Design Parameters	Compartment - A		Compartment - B
Opening factor - O ($m^{1/2}$)	0.08	0.03	0.03
Design fuel load density - $q_{f,d}$ (MJ/m^2)	1268	1268	1268
Compartment Thermal Inertia - b ($J/m^2s^{1/2}K$)	715	702	585

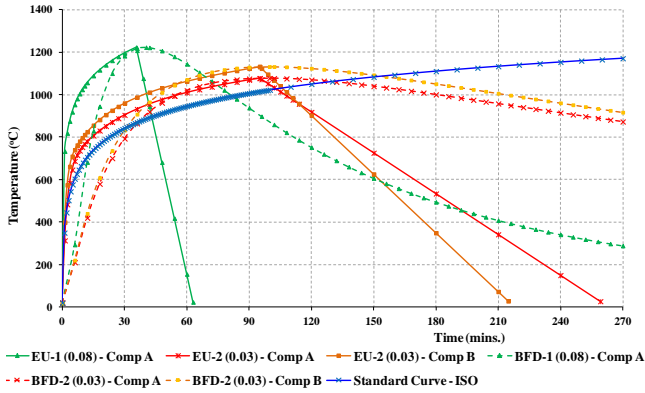


Figure 1. Real design fire time-temperature curves.

The ‘BFD’ curves [3] were also drawn for the same parameters as for the Eurocode parametric curves. In comparison, the peak temperature values of Barnett’s [3] BFD curve are much less, but the shape of the curve fits well with the natural fire curve. The ‘BFD’ curve [3] calculates the maximum temperature from the equation recommended by Law [9] based on many experimental fires. This equation may not incorporate the modern materials such as thermoplastics and synthetic foams. Therefore it was decided to use the maximum temperature of the Eurocode parametric curve [2] for the ‘BFD’ curve. In developing the ‘BFD’ curves for opening factors 0.03 and 0.08 $m^{1/2}$, the time to reach the maximum temperature (t_m) was obtained from the Eurocode parametric curve equations as prescribed by the authors of the ‘BFD’ curve [15]. The Eurocode parametric curve does not include the pre-flashover phase and the time to reach the maximum temperature in Eurocode [2] (t_{max}) excludes the pre-flashover phase. However, ‘BFD’ curve [3] is a natural fire curve, which incorporates both pre-flashover and post-flashover phases. Hence the time to flashover point has to be added to t_{max} (Eurocode) to obtain t_m (BFD). The time to flashover was calculated based on Walton and Thomas’s [16] expression for the critical value of heat release rate and fire growth rates specified in ISO 834 [1]. This way of modifying the original ‘BFD’ curves appears to be a reasonable solution to derive more realistic time-temperature curves for design. The ‘modified BFD’ curves and the Eurocode parametric curves [2] are shown in Figure 1.

4 EXPERIMENTAL STUDIES

4.1 Test specimens

Test program consisted of fire tests of five LSF stud wall panels of 2100 mm width and 2400 mm height (LSF1 to LSF5). The wall panels consisted of four cold-formed steel lipped channel sections (90 x 40 x 15 x 1.15 mm) spaced at 600 mm and tracks (top and bottom) made of channel sections (92 x 50 x

1.15 mm). They were fabricated from 1.15 mm galvanized steel sheets with a minimum yield strength of 500 MPa. Test specimens LSF1 and LSF2 were lined with two layers of 16 mm thickness Firestop^(R) gypsum plasterboards on either side of the studs. The first (base) layer of plasterboard consist of three pieces (150 x 2400, 1200 x 2400 and 750 x 2400 mm) to accommodate two vertical joints in Studs 1 and 3 (Figure 2). The second (face) layer where exists has two equal pieces (2100 x 1200 mm) fixed horizontally. Test specimens LSF3 and LSF4 were lined with single layer of plasterboard (16 mm thick) and LSF5 was built with 25 mm rock fibre insulation sandwiched between two 16 mm plasterboards on both sides of the steel frame. Table 2 gives the details of the load bearing LSF stud wall test specimens.

Table 2. Details of test specimen configurations.

Test	LSF Wall Configuration	Fire Profile	Load Ratio	Insulation Type
LSF1		EU2-(0.03) - Comp A	0.2 (15 kN/Stud)	-
LSF2		BFD2-(0.03) - Comp A	0.2 (15 kN/Stud)	-
LSF3		EU1-(0.08) - Comp A	0.2 (15 kN/Stud)	-
LSF4		BFD1-(0.08) - Comp A	0.2 (15 kN/Stud)	-
LSF5		BFD2-(0.03) - Comp B	0.4 (30 kN/Stud)	Rock fibre

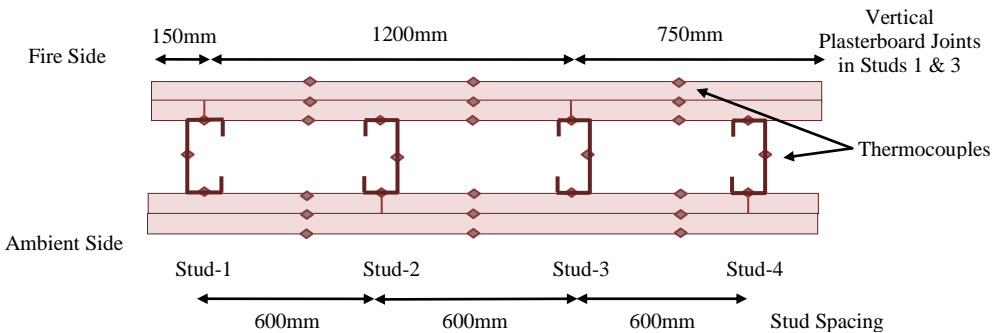


Figure 2. Typical arrangement of thermocouples for LSF wall specimen.

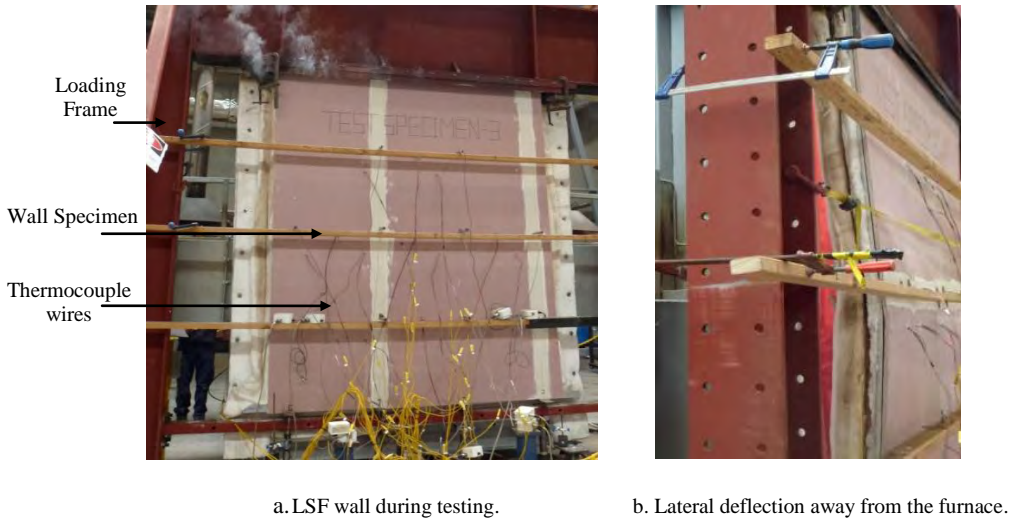
D-Type self drilling 16 mm long flat head screws were used to fix the studs to top and bottom tracks. Also D-Type self drilling 25 and 45 mm long bugle head screws were used to fix the first and second layers of plasterboards. The first plasterboard was screwed at 200 mm spacing along the edge studs where plasterboard joints exist and 300 mm spacing along the intermediate studs. S-Type 75 mm long bugle head screws at 300 mm centres were used to fix the second plasterboard for the insulation sandwiched wall panels. The plasterboard joints were sealed with two coats of plaster-based jointing compound and 50 mm wide paper type joint tape. Type-K cable thermocouples were used to measure the temperature development in the wall specimens. The stud and plasterboard surface temperatures were measured at three levels; 0.25H, 0.5H and 0.75H along the stud, where 'H' is the height of the wall panel of 2400 mm (Figure 2). The thermocouple wires on the studs were connected to their hot and cold flanges and web.

4.2 Test set-up and procedure

Fire tests on LSF stud wall systems were conducted using the propane gas furnace. Four thermocouples monitor the furnace temperatures in the fire chamber during the fire test. These temperatures were used to control the fuel and air supply to the chamber to obtain the required time-temperature fire curve. The test specimen was placed in the loading frame, where the bottom track rested

on the loading plates and the top track was clamped to the loading frame. The test specimen was placed to align the centroids of the studs with those of the loading plates and hydraulic ramps. Each loading plate was connected to individual hydraulic ramps and a single pump was used to apply the required axial load. A pressure transducer was connected to the hydraulic pump to record the applied pressure (load).

An axial compression load of 15 kN was applied to each stud in Test Specimens LSF1 – LSF4 by the hydraulic pump. The load was based on 0.2 times the ultimate capacity of each stud at ambient temperature obtained by Kolarkar [17], ie. load ratio of 0.2. An axial load of 30 kN (load ratio = 0.4) was applied to LSF5. These loads were applied at the room temperature and maintained during the fire test. The axial shortening of each stud and the out-of-plane movements of the wall specimen at 600, 1200 and 1800 mm heights were measured using displacement transducers. During the fire test the temperatures and displacements were recorded at 10 s intervals using a Labview data logger (Figure 3).



a. LSF wall during testing.

b. Lateral deflection away from the furnace.

Figure 3. Fire testing of LSF wall specimen.

4.3 Results and Discussions

The proposed real design fire curves in Figure 1 were achieved reasonably well (within 50°C) in all the tests as shown in Figures 4b, 5b and 6 except in Test LSF4 (within 100°C). The structural failure of studs occurred instead of insulation or integrity failure in all the tests except Test specimen LSF1 that did not fail. In all the tests, the stud that had the vertical small strip of plasterboard (150 x 2400 mm) joint (Stud 1) was subjected to more heat flow due to the opening up of joints, except in LSF2 Stud 2. In specimen LSF2, a partial collapse of plasterboard attached to Stud 1 and 2 initiated the failure. Table 3 compares the failure times and critical stud temperatures when the Eurocode parametric and 'BFD' curves were used together with the results from the standard fire tests performed by Kolarkar [17] and Gunalan [18].

Gunalan's [18] numerical studies for different LSF wall configurations showed that the stud failure is merely dependent on its hot flange temperature and not on its configuration. The effect of using different type of insulations and arrangement is simply to delay the time to reach that critical hot flange temperature in the LSF wall stud. These critical stud hot flange (HF) temperatures proposed by Gunalan [18] are also given in Table 3. The failure times shown in Table 3 were based on the time when the oil pressure in the hydraulic ramps could not be conserved, ie. the initial point of a rapid unloading phase noticed in the data logger. The stud hot flange (HF) temperature at this failure time was recorded as the critical HF temperature.

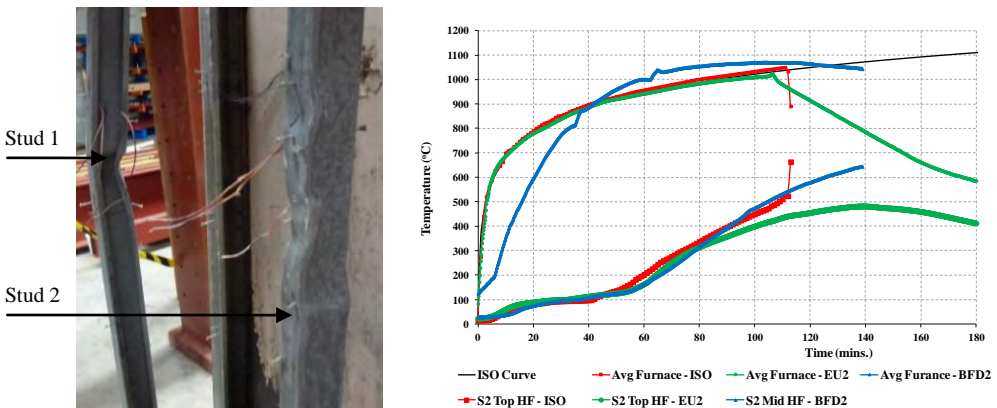
Table 3. Failure times and critical stud hot flange (HF) temperatures.

LSF Configuration		Fire Curve	Failure Time	Critical Max. Stud HF (°C)	FEA Failure HF Temp (°C)[18]
Double layers of Plasterboard (LR=0.2)	LSF1*	EU2-(0.03)	-	481	
	LSF2	BFD2-(0.03)	139 mins	645	626
	Kolarkar [17]	ISO Curve	111 mins	663	
Single layer of Plasterboard (LR=0.2)	LSF3	EU1-(0.08)	28 mins	561	
	LSF4	BFD1-(0.08)	39 mins	630	611
	Kolarkar [17]	ISO Curve	53 mins	550	
Composite panel (LR=0.4)	LSF5	BFD2-(0.03)	118 mins	527	510
	Gunalan [18]	ISO Curve	134 mins	523	

Note: * No Failure ; HF – Hot Flange; LR – Load Ratio

4.3.1 Test specimens LSF1 and LSF2 – Double layers of gypsum plasterboard

Test specimen LSF 1 was exposed to the furnace heat for a period of 180 minutes and did not fail under any failure criteria. Hence the furnace was turned off after 180 mins since the furnace temperature was in the fire decay phase and the maximum stud temperature is below 500°C. During the test the furnace temperature was nearly 75 to 100°C less than the target temperature profile of EU2-(0.03), which is identical to standard fire in the fire growth period up to 105 minutes and then followed the specified decay rate (see Figure 4b). The failure time of 111 minutes in the standard fire test (Table 3) indicates that EU2 curve with the decay phase was less severe than the standard test. The stud hot flange temperature reached 481°C at 140th minute during the decay phase. As seen in Figure 4b, it was gradually increasing for 35 minutes even during the decay phase. Hence the studs could have failed during the decay period, if they had reached the critical hot flange temperature. If the intended higher EU2-(0.03) curve shown in Figure 1 was achieved, the stud failure might have occurred during the decay phase. Visual inspection of the tested specimen revealed that the face layer plasterboards (Pb1) has severely calcinated and partially collapsed in the middle. The second layer of plasterboards (Pb2) was partially calcinated but was intact and offering protection to the studs. The central stud (Stud 2) displayed some local buckling waves in the hot flange (HF) and web (W) near the top (0.5 H to 0.75 H). The ambient side plasterboards (Pb3 and Pb4) were in fairly good condition.



a. Failure pattern - LSF2

b. Average furnace & stud hot flange temperatures – LSF1, LSF2 & ISO.

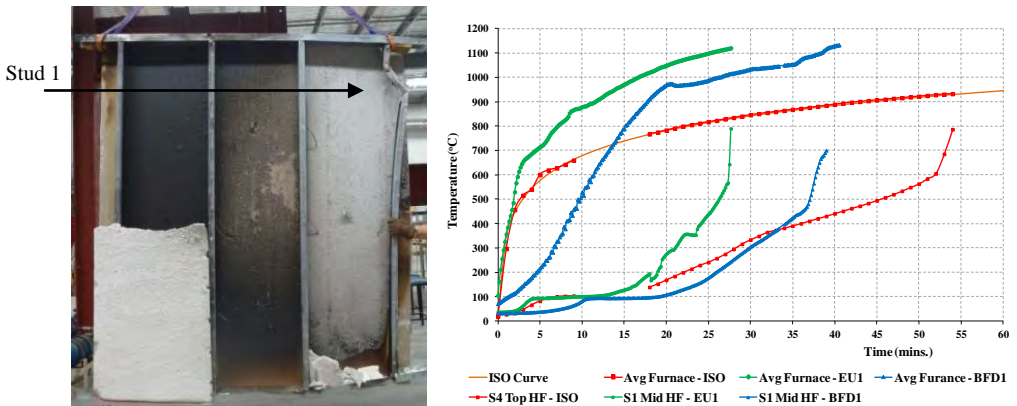
Figure 4. Test specimens LSF1 and LSF2

Test specimen LSF2 was exposed to the Barnett’s ‘BFD’ curve for 139 minutes until it could no longer maintain the applied load. The initial lateral deflection was towards the furnace and it reversed after 120 min. After the test, the exposed plasterboard Pb1 had totally collapsed while a portion of Pb2 had also fallen off between Studs 1 and 2. The ambient side plasterboards were not calcinated although they had cracked horizontally at the plasterboard (Pb4) joint due to bending away from the furnace at failure (Figure 3b). In Studs 1 and 2 local buckling waves were observed near the mid-height of the wall. Test specimen LSF2 failed when the hot flange temperature reached 645°C, which is similar to Kolarkar’s [17] and Gunalan’s [18] temperatures (663°C) and (626°C). Kolarkar’s [17] test wall for standard fire curve failed by flexural buckling about the minor axis due to plasterboard fall-off, whereas LSF2 failed by flexural buckling about the major axis in Studs 1 and 2 with some local buckling (see Figure 4a).

4.3.2 Test specimens LSF3 and LSF4 – Single layer of gypsum plasterboard

Test specimen LSF3 structurally failed after 28 minutes of EU1-(0.08) fire curve exposure. Visual inspection after the test showed that the exposed plasterboard (Pb1) strip over Stud 1 had fallen off. This strip of plasterboard (150 x 2400 mm) was fixed only along one edge to Stud 1. The Stud 1 hot flange time-temperatures profile also confirmed this, where rapid temperatures rise of nearly 250°C was noticeable within a minute as shown in Figure 5b. Due to the fall-off of this plasterboard strip, Stud 1 lost its lateral support and failed by minor axis flexural buckling as shown in Figure 5a. Local buckling waves were also noticeable in the hot flange of Stud 2. The ambient side temperatures were well below the insulation failure criteria temperature of 180°C and were seen to be partially calcinated.

Test specimen LSF4 exposed to the ‘BFD1-(0.08)’ curve failed after 39 minutes. Similar to LSF3, the plasterboard strip attached to Stud 1 had fallen off, resulting in its minor axis flexural buckling.



a. Failure pattern - LSF3.

b. Avg furnace & stud hot flange temperatures – LSF3, LSF4 & ISO.

Figure 5. Test specimens LSF3 and LSF4.

In all three tests, the failure occurred in the stud which had the vertical plasterboard strip (150 x 2400 mm) joint, and partial collapse of this plasterboard initiated the failure. This is clearly noticeable with a rapid temperature rise in the stud hot flange (HF) temperatures. Kolarkar’s [17] standard fire test also showed the same failure mode. Figure 5b shows the stud hot flange temperatures at failure together with the average furnace temperature profiles. The stud failure temperature of LSF4 (630°C) under the ‘BFD’ curve differs from those for the Eurocode parametric (561°C) and standard curves (550°C) (see Table 3). This is possibly due to the plasterboard fall-off at different temperatures resulting in a rapid temperature rise in the studs and causing them to fail earlier than in the standard fire test (Table 3). A rapid temperature rise can be seen in the stud hot flange under EU1 fire curve (see Figure 5b). In BFD1 and ISO curves the stud temperature rise is gradual compared to EU1 fire test due to its rapid temperature rise and higher temperatures than in other tests. This suggests that in BFD1 and ISO fire tests the plasterboard

has partially collapsed, but a portion of the plasterboard was still intact and protected the stud further. Also the temperature that initiated the plasterboard fall-off was different in each test. In BFD1 fire test it was about 450°C, and for EU1 and ISO fire tests this temperature was about 550 and 600°C, respectively (Figure 5b). These values were taken as the starting point of the rapid stud hot flange temperature rise in Figure 5b. In the BFD1 fire test the furnace temperature was much higher than the standard curve and was also maintained at higher temperatures than in the case of other two fire curves. This higher heat flow might have caused the plasterboard to partially collapse at a lower temperature. This is because the plasterboard calcinates and shrinks rapidly at high temperatures and rapid temperature rise situations. Similar observation was made by Gerlich [19] where the plasterboard collapsed earlier during a severe fire than during an ISO fire test [1]. Gunalan's [18] FEA prediction of critical stud temperature (611°C) was based on the presence of lateral (plasterboard) support throughout the test. Therefore due to the early shrinkage and cracking of plasterboard, studs could fail by minor axis flexural buckling much earlier than predicted by FEA. Hence it appears that the plasterboard fall-off time depends on the rate of temperature rise, peak temperatures experienced and their duration.

4.3.3 Test specimen LSF5 – Composite panel (External Insulation)

Test specimen LSF5 failed structurally after 118 minutes exposure to the 'BFD2-(0.03)' curve. The initial lateral deflection was towards the furnace, and near failure it started to reverse its direction away from the furnace. The fire exposed plasterboard (Pb1) fell off after 100 minutes as seen in the temperature profile in Figure 6a. Also after 118 minutes the second layer (Pb2) attached to Studs 1 and 2 must have partially collapsed as seen in the stud hot flange temperature profile in Figure 6b. This has occurred earlier than in the standard fire tests. This caused Studs 1 and 2 to fail by minor axis buckling as no lateral restraints were available to prevent it. Hence this also indicates that the plasterboard fall-off depends on the type of fire curve used in the tests. Further experimental and numerical studies are in progress to fully investigate the behaviour of LSF wall panels under various realistic design fires.

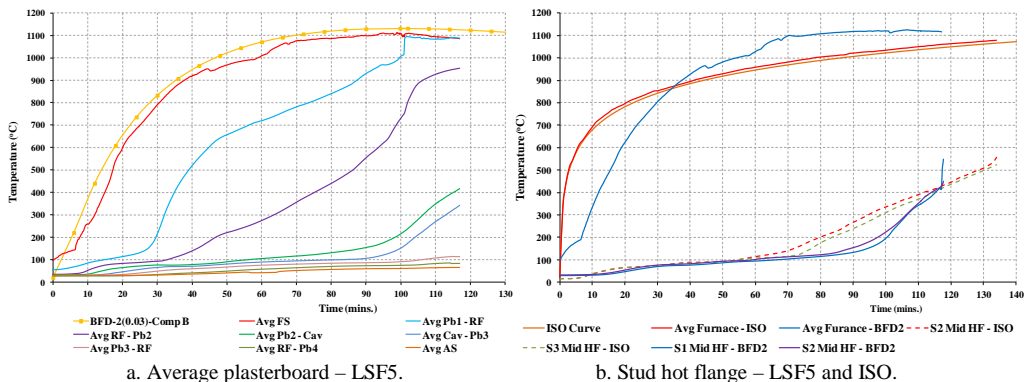


Figure 6. Experimental time-temperature profiles (F–Fire side, RF–Rock fibre & AS–Ambient side).

5 CONCLUSION

This paper has described an experimental study of the structural and thermal performances of load bearing LSF wall panels under realistic design fires. This study has shown that the plasterboard fall-off depends on the rate of temperature rise and the peak temperature during a fire test. This is important in the use of single plasterboard lined walls where the plasterboard fall-off will expose the load bearing wall studs and thus result in low fire resistance rating. Also it has been shown that the LSF wall studs could fail during the decay period if the stud temperatures reach the critical failure temperature. Further research is in progress to understand the behaviour of LSF wall panels under real design fires since the

use of thermoplastics materials in modern buildings has increased the rate of temperature rise and peak temperatures during a building fire than indicated by the standard fire curve.

6 ACKNOWLEDGEMENTS

The authors wish to thank Australian Research Council for the financial support to this project, QUT for providing testing facilities and Boral Plasterboard for providing the required plasterboards.

REFERENCES

- [1] ISO 834-1, Fire Resistance Tests – Elements of Buildings Construction, Part-1 General Requirements, International Organization for Standardization, Switzerland, 1999.
- [2] EN 1991-1-2, Eurocode 1: Actions on structures. Part1-2: General Actions – Actions on structures exposed to fire, Brussels: European Committee for Standardization, Germany, 2002.
- [3] Barnett C. R., “BFD curve: A New Empirical Model for Fire Compartment of Temperatures”, *Fire Safety Journal*, 37(2002), 437-463, 2002.
- [4] Lennon T. and Moore D., “The Natural Fire Safety Concept – Full-scale Tests at Cardington”, *Fire Safety Journal*, 38(2003), 623-643, 2003.
- [5] Jones B.H., “Performance of Gypsum Plasterboard Assemblies Exposed to Real Building Fires”, *Fire Engineering Research Report - University of Canterbury*, New Zealand, 2002.
- [6] Abecassis-Empis C., Reszka P., Steinhaus T., Cowlard A., Biteau H., Welch S. and Rein G., “Dalmarnock Fire Test One”, *Experimental Thermal & Fluid Science*, 32, 1334-1343, 2008.
- [7] Bwalya A.C., Lougheed G.S.D., Kashef A. and Saber H.H., “Survey Results of Combustible Contents and Floor Areas in Canadian Dwellings”, *Fire Technology*, 32(2), 120-136, 2008.
- [8] Guo S. and Bailey C.G., “Experimental Behaviour of Composite Slabs during Heating and Cooling Fire Stages”, *Engineering Structures*, 33(2), 563-571, 2011.
- [9] Law M., “Design of Fire Protection of Buildings”, *The Structural Engineer*. 61A(1), 1983.
- [10] Zhongcheng Ma. And Makelainen Pentti., “Parametric Temperature-Time Curves of Medium Compartment Fires for Structural Design”, *Fire Safety Journal*, 34(2000), 361-375, 2000.
- [11] Pope N.D. and Bailey C.G., “Quantitative Comparison of FDS and Parametric Fire Curves with Post-Flashover Compartment Fire Test Data”, *Fire Safety Journal*, 41(2006), 99-110, 2006.
- [12] NFPA 557, Standard for Determinations of Fire Load for Use in Structural Fire Protection Design – 2012 Edition, National Fire Protection Association, Quincy, USA, 2012.
- [13] Keerthan P. and Mahendran M., “Numerical Modelling of non-load bearing LSF walls under fire conditions”, *Journal of Fire Sciences*, In press, 2012.
- [14] Buchanan A.H., *Structural Design for Fire Safety*, John Wiley & Sons Ltd, Chichester, 2001.
- [15] Barnett C.R. and Clifton G.C., “Examples of Fire Engineering Design for Steel Members, using a Standard Curve Versus a New Parametric Curve”, *Fire and Materials*, 28, 309-322.
- [16] Walton W.D., and Thomas P.H., “Estimating Temperatures in Compartment Fires”, Chapter 3-6, *SFPE Handbook of Fire Protection Engineering*, Society of Fire Protection Engineers, USA.
- [17] Kolarkar P.N., “Fire Performance of Plasterboard Lined Steel Stud Walls”, *PhD Thesis-Queensland University of Technology*, Brisbane, Australia, 2010.
- [18] Gunalan S., “Structural Behaviour and Design of Cold-formed Steel Wall Systems under Fire Conditions”, *PhD Thesis-Queensland University of Technology*, Brisbane, Australia, 2011.
- [19] Gerlich J.T., “Design of Load Bearing Light Steel Frame Walls for Fire Resistance”, *Fire Engineering Research Report – University of Canterbury*, New Zealand, 1995.

FULL SCALE FIRE TEST AND NUMERICAL SIMULATION OF A STEEL CONNECTION

Peter Schaumann*, Thomas Kirsch* and Florian Timmen**

* Institute for Steel Construction, Leibniz Universitaet Hannover
e-mails: stahlbau@stahl.uni-hannover.de, kirsch@stahl.uni-hannover.de

** Ingenieurbuero Dr. Binnewies
e-mail: timmen@dr-ing-binnewies.de

Keywords: Connection, End Plate, High Strength Bolts, Fire Test, Intumescent Coating

Abstract. *This paper presents an investigation in the behaviour of extended end plate connections in fire. A full scale fire test on this type of connection has been conducted including fire protection by intumescent coating, ISO-fire-load and moments induced by weight loads. In addition to the experimental investigation, a thermal finite element model for calculation of connection temperatures has been developed taking into account the behaviour of the intumescent coating. From parametric studies with this model, a simplified calculation method for prediction of component temperatures has been developed. Finally, the results of thermal calculations have been used to investigate the mechanical behaviour of the connection using two different methods. The first one represents an application of the component method for elevated temperatures and the second one is a finite element simulation. The state of work for both methods is presented.*

1 INTRODUCTION

In recent years, a global approach in calculating the fire behaviour of buildings taking into account the whole structure with nonlinear material performance and geometry has become suitable for practical application. In this kind of simulation, structural members are not considered separately but interacting with each other, as real connection behaviour can be taken into account using moment-rotation-relationships. As there are no regulations on how to determine these relationships in fire, a recent research project deals with the development of moment-rotation-relationships for different connection dimensions and different times in fire. The actual state of work of this project is presented in this paper.

The behaviour of connections in fire may be divided into its thermal and its mechanical behaviour. The calculation of thermal behaviour of unprotected connections is relatively simple as there are already normative regulations for material properties and interactions suitable in finite element simulations in the Eurocode [1]. Even a simple temperature calculation method for unprotected connections is offered. An investigation in the usability of these methods has been conducted by Anderson and Gillie in [2]. Temperatures in unprotected steel members increase rapidly. For this reason in most cases it is not possible to reach 30 minutes of fire resistance, which in many cases is a minimum requirement. To overcome this disadvantage of steel members and connections without fully embedding them into spray applied plaster or encasing them with fire protection board, different solutions have been investigated in the recent years. One opportunity is the partial embedding of connections into the concrete slab. Some investigations are presented in [3].

Another increasingly popular possibility to protect steel structures from high temperatures, while keeping their slim appearance, is the use of intumescent coatings. As numerical simulation methods for this fire protection material are not well developed yet, it is difficult to predict temperatures of connections protected by intumescent coatings. A first investigation in this topic with three tests on

unloaded fin plate connections has been conducted by Wald et. al. in [4]. Dai et. al. described 14 composite connection tests in [5]. All specimens were unloaded and some were protected by an intumescent coating. As both investigations were mainly focused on the question whether bolts may be left unprotected, no numerical investigation of the connections temperature field was published.

After the thermal analysis of the connection, the mechanical response can be determined. Many investigations have been conducted in the recent years. In this context, Dai et. al. published experimental results of steel frames within different types of connections in [6]. As a full frame was tested, the connected beam caused compression forces by thermal expansion and tensile forces by catenary action.

An experimental programme and preliminary numerical investigations on flush end plate connections at different temperatures have been described by Haremza et. al. in [7]. Aim of the research project was the simulation of failure of a column below a tested connection and thus the robustness of the whole structure in fire. As the investigation aimed at open car parks, the steel structures were left unprotected as common for those types of structures.

The probably most extensive investigation in connection behaviour in fire was conducted at the University of Sheffield, where a large number of types of connections were tested. The test setup consisted of a short part of a column fixed in a furnace and connected to a short part of a beam, loaded by tensile and shear forces. Tests have been conducted for different constant temperatures and different ratios of shear and tension. Test results for end plate connections have been published in [8]. Based on those test results the authors have conducted finite element calculations published in [9].

As those investigations in the mechanical behaviour of connections are based on constantly elevated temperatures or in some cases on transient temperature fields of unprotected steel structures exposed to ISO 834 fire curve, there has been no investigation in the connection behaviour with realistic fire protection yet. In this paper, an experimental test and numerical models of an end plate connection between a steel beam and column including an intumescent coating for fire protection is presented.

2 FIRE TEST ON A CONNECTION PROTECTED BY INTUMESCENT COATING

2.1 Test setup and connection detail

The test setup comprises a connection of two beams, consisting of IPE 330 sections, to an internal HE 220 B column. The connection is realised by an end plate and six high strength bolts. The end plate of 15 mm thickness, 160 mm width and 420 mm height extends the top flange of the beam by 70 mm. The connection detail is shown in Figure 1.

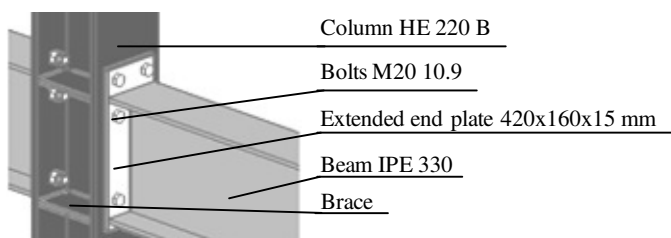


Figure 1. Scheme of tested connection.

The connection and the members are protected by intumescent coating for the fire resistance class R 30 to ensure a realistic fire protection. The measured average thickness of the painting is 1 mm. The thermal load is defined to ISO 834 fire curve.

Table 1. Yield strength and tensile strength of components of tested connection.

	Beam	Column	End plate	Bolts
Yield stress [MPa]	326	336	314	996
Tensile strength [MPa]	443	465	447	1107

The steel sections for column and beams as well as the end plate and additional braces inside the column are made of steel grade S235 steel. The bolts have been designed as M20 grade 10.9 high strength bolts. As yield stress of steel members always differs from the normative minimum yield stress, material properties of the components are determined by material tests. Results are shown in Table 1.

The test specimen is loaded by a constant bending moment of 38.1 kNm, leading to a load ratio of $\mu_{fi}=0.5$. The moment is realised by steel plates located on top of a load structure as depicted in Figure 2.

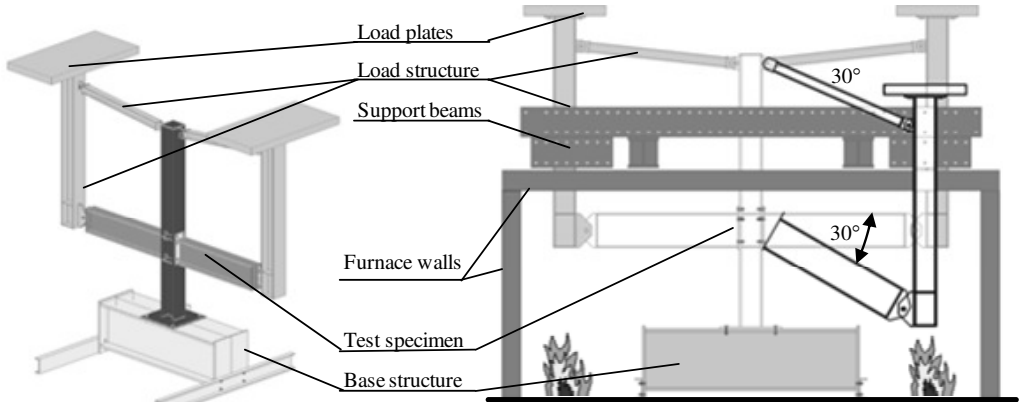


Figure 2. Scheme of test setup.

As shown in Figure 2, the load structure is connected to the specimen beam ends to induce the vertical loads. It is also connected to the top of the specimen column to keep the load structure in a vertical direction. Parts of the load structure and the whole base structure are located inside the furnace. To prevent them from failure, they are protected by thick layers of rockwool. The test setup is designed to allow a connection rotation of 30°. During the test, gas and steel temperatures are measured by numerous thermocouples. Deflections of the beams are determined by potentiometers and thickness of intumescent coating is measured during the fire, using a furnace camera and small steel bars used as visual gauges.

2.2 Results of fire test

The temperatures of the connection are lower than expected and so the R 30 protected connection reaches a fire resistance of 71 minutes. The specimen was recorded by a video camera during the test. This is visualised by images at different times in Figure 3.

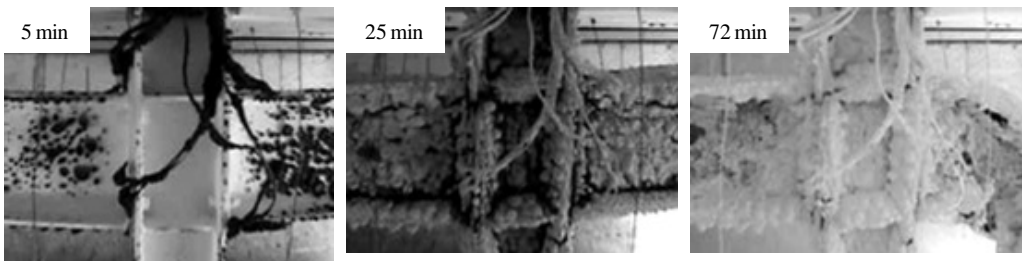


Figure 3. Tested connection during fire test.

As can be seen, the intumescent painting starts to inflate at exposed positions in the first 5 minutes. After 10 minutes the reaction is finished in most positions and the intumescent coating nearly reaches its full isolation capacity. As the colour of the full coating is black in this period, leading to a limited quality of photographs, this is not displayed in Figure 3. Between 10 and 50 min of fire exposure the thickness

increases only marginal. The colour of the coating skin changes from black to white in this period. After about 55 min the coating starts to fall off locally. After 72 minutes the connection has failed.

Figure 4 illustrates the connection after the intumescent coating foam is removed from the specimen. Obviously, the connection component “lower flange in compression” failed at the right connection.



Figure 4. Tested connection before and after fire test.

Although the burners are shut down after failure of the connection on the right side, the deflection of the beam on the left side increases significantly during the following 10 minutes. Afterwards the deflection stops and failure does not occur. This indicates the approaching collapse, which can be indicated as a combination of lower flange buckling and bending failure of the end plate.

As mentioned before the connection behaviour is measured by several techniques. The gas temperature is measured by 8 thermocouples. All measured gas temperatures follow approximately the ISO 834 fire curve. The transient temperature field of the steel structure is measured by 21 thermocouples. The temperatures at five different locations are plotted in Figure 5 versus time.

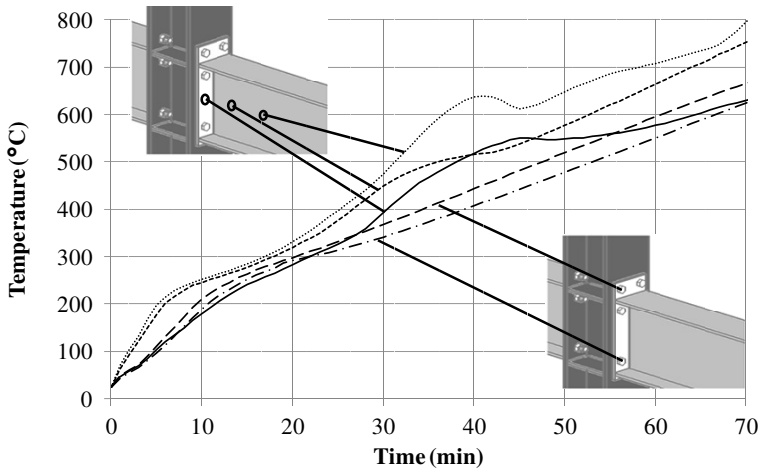


Figure 5. Temperatures in components beam, end plate and bolts of the tested connection.

The general shape of all temperature curves is bilinear. Until a steel temperature of 200°C is reached, the temperatures increase rapidly. Afterwards the temperatures rise slower as the intumescent coating is activated. As shown in Figure 5 as well, temperatures are getting lower with less distance between thermocouples and the connection. The reason for this might be found in the more compact shape of the connection compared to the beam. Between minutes 30 and 45 two of the thermocouples show disproportional high temperatures with a peak up to 650°C in one case. The reason has been found by photographs, which show that the intumescent coating does inflate with delay at those positions.

In addition to the thermal results, the behaviour of the intumescent coating is investigated using visual gauges in combination with the furnace camera. By measuring the length of the uncovered part of the

gauge, it is possible to determine the coating thickness during the test. Results are depicted in Figure 6. It can be seen that thickness of the intumescent coating starts to increase after 4 minutes. After 20 minutes the coating is fully inflated leading to a thickness of about 30 mm.

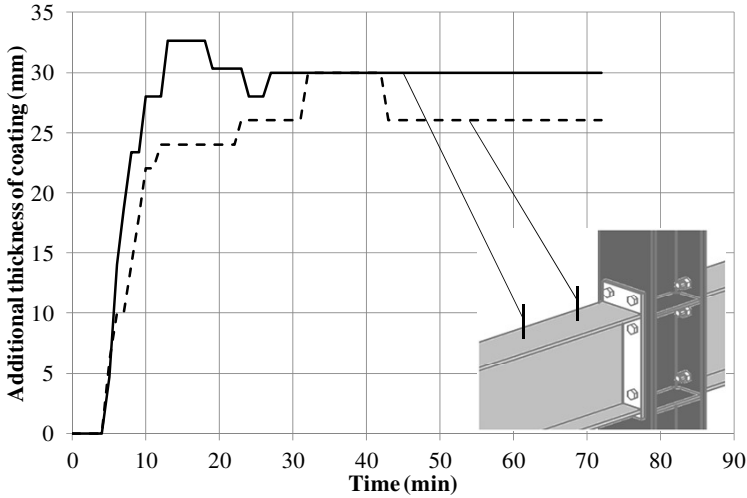


Figure 6. Additional coating thickness at different positions during the test.

Finally, the displacement of the beam ends is measured during the test using potentiometers. As depicted in Figure 7 deflections are rather low during the first 60 minutes of the test. Between 60 and 70 minutes the deflections increase exponentially, reaching a value of 100 mm at 70 minutes. During the last 2 minutes of the test, deflections of beam 2 increase very fast. Failure is determined to 71 minutes and 39 seconds, when deflections reach the measuring limit of the potentiometers. The deflections of the second beam are still increasing after the end of the test. After another ten minutes the deflections stop due to the cooling of the connection.

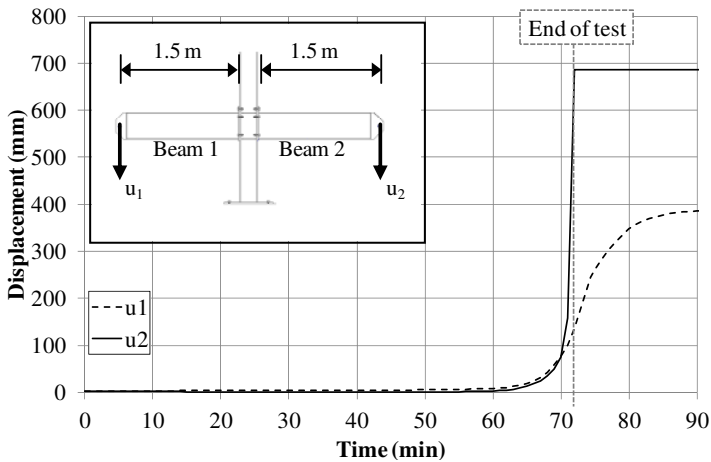


Figure 7. Displacement of beam ends during the test.

3 CALCULATION OF CONNECTION TEMPERATURES

3.1 Setup and validation of thermal finite element simulation

Based on the test setup a thermal finite element model in Abaqus [10] is developed to determine the transient temperature field of the connection. As Figure 8 depicts, two symmetry conditions are used in the model. The geometry of the intumescent coating is modelled constantly with dimensions of the fully inflated protection of 30 mm thickness. Differences between model and real geometry are considered in the material properties.

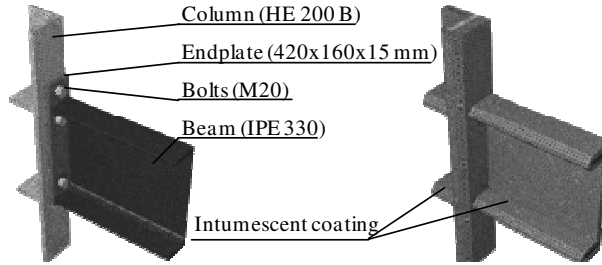


Figure 8. Connection model in Abaqus [10] for thermal analysis (without (left) and with (right) intumescent coating).

Thermal material properties of structural steel and bolts are used according to Eurocode [1]. Thermal interaction properties as $\epsilon_m=0.8$ and $\alpha_c=25 \text{ W}/(\text{m}^2\text{K})$ are taken into account according to [11].

The coating is simulated using a material model developed by the authors and presented in [12] in detail. The material model is based on proportion between gas pores and basic material (paint) inside the coating that can be determined by the measured coating thickness versus time or temperature. Superposing the behaviour of the gas inside the pores, which is approximated to the behaviour of air, and the behaviour of the basic material (paint) in accordance with their proportion, the resulting behaviour of the protection foam can be determined. Finally, the calculated behaviour, which consists mainly of thermal conductivity and specific heat, has to be adapted for the coating geometry in the model, which is determined as constant over time.

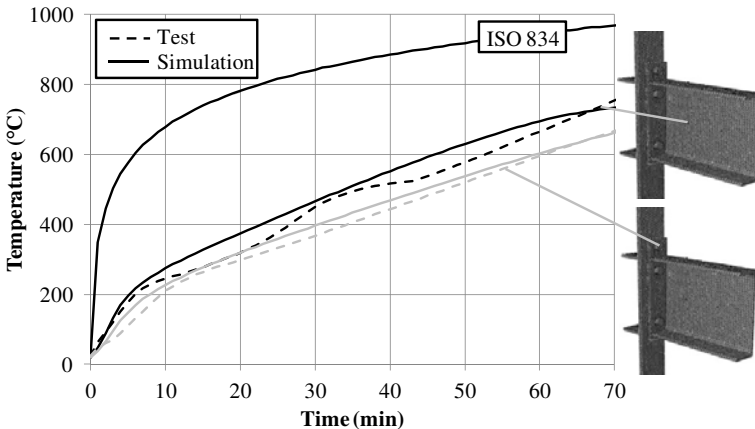


Figure 9. Measured and simulated temperature curves at several locations.

As Figure 9 illustrates for two positions, the calculated and the measured temperatures are correlating very well. Generally the measured temperatures are a few degrees lower than the calculated. For the further thermocouples, comparison between test and calculation lead to similar correlations.

3.2 Parametric studies and simple calculation method for connection temperatures

Extensive parametric studies including more than 70 simulations are conducted using the validated thermal finite element model. The conducted parametric studies imply different beam, column and bolt sizes as well as different end plate dimensions. The parameters are based on typified connections for end plate connections with extended end plates according to [13] as they are used in Germany. In [13] optimised end plate and bolt sizes are defined for many beams. Thickness of the intumescent coating is adapted to the minimum thickness for the connected beam to achieve the fire resistance of R30 or R60 according to the product information.

Using the parametric study the average temperatures for the structural components of the connection according to [14], which includes “Column web in tension” (K3), “Column flange in bending” (K4), “End plate in bending” (K5), “Beam web in compression” (K7) and “Bolts in tension” (K10), have been calculated at different times (30, 60 and 90 min) during ISO fire.

It has been found that component temperatures depend on several parameters. Obviously, the coating thickness has a main influence on the component temperatures. The coating thickness depends on the achieved fire resistance class and also on the size of the beam. For this reason the component temperatures depend on size and achieved fire resistance class of the beam. An additional factor which influences the temperature of most components is the size of the connected column. For this reason the section factor $(A/V)_{col}$ of the connected column has been defined as the third parameter. Finally, the temperatures of some components are slightly influenced, if large bolts of size M24 or higher are used. It has to be mentioned that end plate dimensions of connections according to [13] are optimised for different bolt sizes. For this reason the end plate dimensions increase with increasing bolt sizes, leading to a reduction of temperatures. Consequently, temperatures do not depend on bolt sizes directly, but indirectly over adapted end plate sizes.

The simplified calculation method for temperature calculation of extended end plate connections according to [13], which has been validated against parametric studies is described by the following equation in combination with Table 2.

$$\theta_{K,RC,t} = F_{1,K,RC,t} + F_{2,K,RC} \cdot h_{beam} + F_{3,K,RC} \cdot (A/V)_{col} \quad (^\circ C) \tag{1}$$

with: h_{beam} : Height of connected beam (mm)
 $(A/V)_{col}$: Section factor of connected column $((A/V)_{col} \leq (A/V)_{beam})$ (m⁻¹)

The results of the simplified calculation for the component “end plate” are shown in Figure 10 for connections to an HE 220 B column. Temperatures calculated by Abaqus [10] and with the simplified method correlate very well, while the simplified method is slightly conservative.

Table 2. Factors for simplified temperature calculation method.

Resistance class of coating (RC)	Component (K)	Bolt size	F _{1,K,RC,30}	F _{1,K,RC,60}	F _{1,K,RC,90}	F _{2,K,RC}	F _{3,K,RC}
R30	K3	All	420	635	820	0.2	0.7
	K4, K5, K10	M16 / M20	400	615	800	0.1	0.7
	K4, K5, K10	M24	380	595	780	0.1	0.7
	K4, K5, K10	M27 / M30	360	575	760	0.1	0.7
	K7	All	650	890	990	0	0
R60	K3	All	100	220	340	0.2	0.7
	K4, K5, K10	M16 / M20	100	220	340	0.2	0.7
	K4, K5, K10	M24	95	210	330	0.2	0.7
	K4, K5, K10	M27 / M30	90	200	320	0.2	0.7
	K7	All	370	570	720	0	0

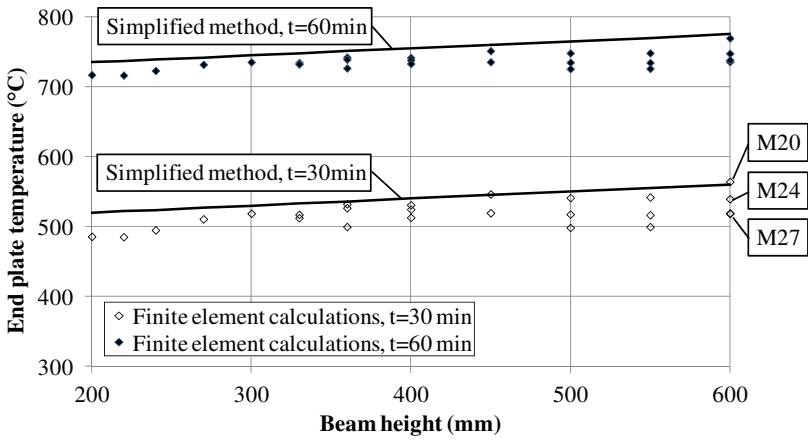


Figure 10. Temperatures of end plate versus beam height for HE 220 B column and R30 coating.

4 INVESTIGATIONS IN THE MECHANICAL CONNECTION BEHAVIOUR

4.1 Adaption of component method

A simplified calculation method for predicting the connection behaviour is the adaption of the component method according to [14] for elevated temperatures. The adaption is performed by determining the temperatures for any component at several times during fire exposure, using the thermal finite element model validated against experimental data. Afterwards yield stress (structural steel elements) or tensile strength (bolts), listed in Table 1, are reduced using reduction factors according to [1]. In Figure 11 the load capacity of the different connection components during fire exposure is depicted.

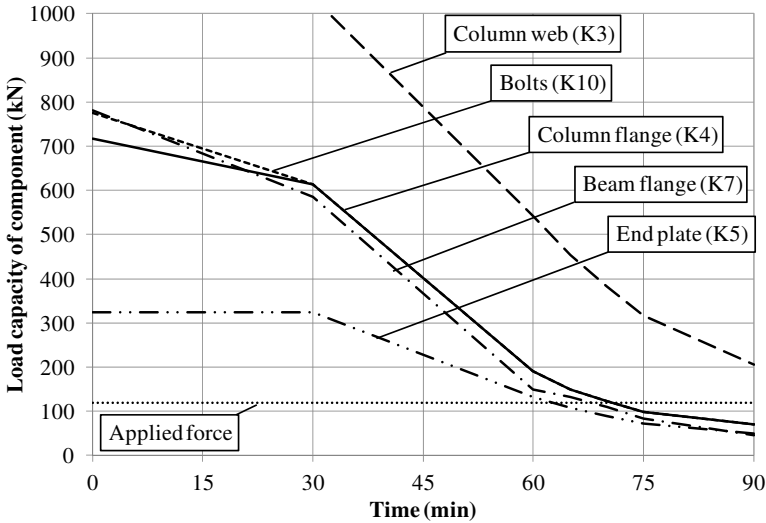


Figure 11. Load capacity of different connection components during fire.

In addition, the applied load is depicted. This load is determined by dividing the applied moment by distance between tensile (K3, K4, K5, K10) and compression (K7) components. As the applied moment is constant during fire exposure, the resulting load of 119.3 kN is constant as well. As can be seen, the end plate has been designed to be the failing component at ambient temperatures. The temperatures of all components increase during the test and thus the load capacities decrease. At 63 minutes the load capacity of the component “end plate” is decreasing below the applied load which would lead to a failure of this component and thus connection failure. As described before the failure of the test specimen occurs after 71 minutes due to buckling of the lower flange in beam 2. So the calculated time of failure shows good correlation with the measured time of failure.

The determined failing component (“end plate”) is not correct, compared to the experimental results. However, the load capacities of components “beam flange” and “end plate” are very close and the end plate is calculated to fail less than 5 min after the first component. Furthermore the second connection in the test continued deflecting after the test indicating the approaching failure of end plate and beam flange.

For this reason the adapted component method is validated at least for the components “end plate” and “beam flange” to foresee the failure time in fire with slightly conservative results.

4.2 Finite element simulation

The simplified method is not able to describe the connections moment-rotation-behaviour in fire and cannot be validated for different geometries. Therefore an additional numerical analysis is prepared using the finite element software Abaqus [10]. The model is based on nonlinear material properties that have been tested and validated in [9], overcoming challenges as fractures and large strains.

Results of the present state of work are satisfying regarding end plate bending and global failure. Bending of the end plate, which occurs in beam 2 in the test, is well reproduced by the numerical model. In the numerical model failure occurs due to fracture of the bolts after 69 min. So there are significant differences between simulated and test results. As a reason for this may be the missing buckling of the lower flange for the reason of an ideal geometry, the finite element model is currently improved to be able to take buckling into account.

5 CONCLUSIONS

In this paper, state of work of an ongoing research project on the fire behaviour of extended end plate connections, protected by an intumescent coating, is described. Aim of the research is to determine the moment-rotation-relationship of the connections at different times in fire.

For this reason, a full scale fire test on an extended end plate connection between two steel beams and an internal steel column, both protected by an intumescent coating, has been conducted. The measured data, including steel temperatures, coating thickness and deflections are described in detail.

Based on the test results a thermal finite element simulation, including new material properties for intumescent coatings has been developed and validated. The numerical model is used to conduct parametric studies on thermal behaviour of the connection with variable beam, column and connection geometry. The study leads to a simplified method for calculation of component temperatures of extended end plate connections protected by an intumescent coating.

Based on the results of the thermal investigations, two methods to investigate the mechanical response of the connection are presented. First, the component method is adapted to fire situation and validated against the experimental results. The adaption is able to determine the load capacity of components and thus the moment capacity of the connection in fire. Additionally, a finite element model of the mechanical behaviour in fire is presented briefly. As differences between finite element simulation and test results are still substantial, the model will be optimised.

6 ACKNOWLEDGEMENTS

The authors would like to thank the companies GOLDBECK and RÜTGERS ORGANICS for their help preparing the test specimen and applying the intumescent coating. The IGF-Project No. 16586 N from FOSTA is funded by the German “Federal Ministry of Economics and Technology” via AiF. The authors express their profound gratitude.



Federal Ministry
of Economics
and Technology

REFERENCES

- [1] Eurocode 3-1-2, *Design of steel structures – Part 1-2: General rules – Structural fire design*, German Version EN 1993-1-2:2005 + AC:2009, Beuth Verlag, Berlin, 2010.
- [2] Anderson K., Gillie M., “Investigation into methods for predicting connection temperatures”, *Applications of Structural Fire Engineering – Proceedings of International Conference, Prague 19 February 2009*, F. Wald, P. Kallerova, J. Chloubka (eds.), Czech Technical University, Prague, 332-337, 2009.
- [3] Chloubka J., Wald F., Sokol Z., “End plate connection partially imbedded in concrete slab“, *Eurosteel 2011 - 6th European Conference on Steel and Composite Structures*, Dunai L. et al. (eds.), ECCS European Convention for Constructional Steelwork, Belgium, 1533-1538, 2011.
- [4] Wald, F. S., Strejcek, M., Ticha, A., “On bolted connections with intumescent coatings”, *Fourth International Workshop on Structures in Fire*, Portugal, 371-378, 2006.
- [5] Dai, X. H., Wang, Y. C., Bailey, C. G., “Temperature developments in partially protected steel-concrete composite joints using intumescent coating”, *Fifth International Conference Structures in Fire*, Singapore, 172-183, 2008.
- [6] Dai, X. H., Wang, Y. C., Bailey, C. G., “An experimental study of the structural behavior of joints in restrained steel frames in fires”, *Applications of Structural Fire Engineering – Proceedings of International Conference, Prague 19 February 2009*, F. Wald, P. Kallerova, J. Chloubka (eds.), Czech Technical University, Prague, 350-355, 2009.
- [7] Haremza C., Santiago A., da Silva L. S., “Behaviour of heated composite joints”, *Applications of Structural Fire Engineering – Proceedings of International Conference, Prague 29 April 2011*, F. Wald, K. Horová, J. Jirku (eds.), Czech Technical University, Prague, 231-236, 2011.
- [8] Yu H., Burgess I. W., Davison J. B., Plank R. J., “Experimental investigation of the behavior of flush endplate connections in fire”, *Structures in Fire – Proceedings of 5th International Conference*, K. Tan, V. Kodur, T. Tan (eds.), Nanyang Technological University, Singapore, 150-157, 2008.
- [9] Schaumann P., Kirsch T., “Fracture Simulation in a steel connection in fire”, *Applications of Structural Fire Engineering – Proceedings of International Conference, Prague 29 April 2011*, F. Wald, K. Horová, J. Jirku (eds.), Czech Technical University, Prague, 213-218, 2011.
- [10] ABAQUS. Abaqus/Standard Version 6.10. Pawtucket: Hibbit, Karlsson & Sorensen, Inc. 2011.
- [11] Eurocode 1-1-2, *Actions on structures – Part 1-2: General actions – Actions on structures exposed to fire*, German Version EN 1991-1-2:2002 + AC:2009, Beuth Verlag, Berlin, 2010.
- [12] Schaumann, P., Kirsch, T., Kressin, H., „Full scale fire test and numerical simulation of a steel concrete composite connection“, accepted for *10th International Conference on Advances in Steel Concrete Composite and Hybrid Structures (ASCCS)*, Singapore, 2nd-4th July, 2012.
- [13] DSTV, “Typified connections in steel building construction” (German title: “Typisierte Anschlüsse im Stahlhochbau”), volume 2, Stahlbau-Verlagsgesellschaft mbH, Duesseldorf, 2000.
- [14] Eurocode 3-1-8, *Design of steel structures – Part 1-8: Design of joints*, German Version EN 1993-1-8:2005 + AC:2009, Beuth Verlag, Berlin, 2010.

THE BEHAVIOUR OF STEEL BEAMS WITH MOMENT-RESISTING BEAM-SPLICE CONNECTIONS IN FIRE

Takeo Hirashima*, Mariati Taib**, Bernice Wong*** and Ian Burgess**

* Chiba University, Division of Architecture and Urban Science, Japan
e-mail: hirashima@faculty.chiba-u.jp

** University of Sheffield, Dept. of Civil and Structural Engineering, UK
emails: m.taib@sheffield.ac.uk, ian.burgess@sheffield.ac.uk

*** Ramboll SAFE Ltd, London, UK
e-mail: Bernice.Wong@ramboll.co.uk

Keywords: Fire, Moment-resisting beam-splice connections, Critical temperature, FE simulation

Abstract. *Splice connections within a beam which is rigidly connected to columns at its ends are generally designed to be stronger than the connected beam sections, so that the resistance of the whole beam in the fire limit state is calculated as for an undivided span, with three plastic hinges. In the case of a fire, the critical load-carrying mechanism of the connection may change from bolt friction to bolt bearing. Strength loss at elevated temperature is larger for the HSFGB bolts than that of the steel plates or the connected beams. In this study, a series of loaded fire tests, imitating the action of continuous beams with internal splice connections, was carried out in order to obtain temperature distributions, deflection behaviour, variations of thermal stress and the critical temperatures of the beams. It was also useful to observe the deformation ductility of the components of the connection. FE simulations were also carried out to rationalise the behaviour.*

1 INTRODUCTION

Beam-to-beam connections with splice plates and high strength friction grip (HSFG) bolts have become common for field connections of the central sections of beams in rigid steel frames which have beam-to-column connections with full penetration welds. The beam splice connections are generally designed to be stronger than the connected beams, so that the resistance of the beam, in either the ambient-temperature Ultimate Limit State or the Fire Limit State, is calculated as for an undivided span with three plastic hinges [1]. In the case of a fire, it is possible that the critical load-carrying function of the bolts in the connection may change from friction to bearing. Therefore, the connection may have the problem that strength loss at elevated temperature is larger for the HSFGB bolts than for the steel plates or the connected beams [1, 2]. However, this type of connection has high mass, and therefore high heat capacity, so that the temperatures of the connection components may be lower than those of the connected beams. Moreover, some experimental reports [3, 4] indicate that the rotational capacity of bolted connections considerably improves at elevated temperature, because the deformation ductility of its components increases. These are significant points where steel structures are designed for structural fire resistance on the basis of plastic design principles. Research on common beam-column connections (flush or flexible endplate, web cleat, fin plate *etc*) in fire is increasing, and some reports have studied the influence of their structural behaviour on overall frame performance in fire. Most previous studies on beam splice connections in fire have been limited to their performance in isolation. In this paper the behaviour of full-strength beam splice connections in steel frames in fire is discussed on the basis of these tests and FE simulations.

2 TESTS AND FINITE ELEMENT SIMULATIONS

2.1 Test setup

Load-bearing fire tests, imitating the action of continuous beams with beam splice connections, were carried out, and instrumented to obtain temperature distributions, deflections and variations of thermal stress of the beams, and also to observe the deformation ductility of the components of the connection [5]. As shown in Table 1, the test parameters were the connection details, the (constant) load and the fire protection. The standard specimen in these tests was Specimen 3. A fully-moment-resisting connection was defined [6] as one whose bearing resistance was more than 1.15 times the plastic moment of the beam. The constant load applied to the beam (except for Specimen 4) was near to the design permanent load of the continuous beam. With fire protection of Type A (see Table 1), the thickness of insulation material differs between loading point and the support point to prevent the shear failure at the section (see Figure 5).

Figure 1 shows the experimental setup. The steel grade of the rolled I-beam and splice plates is SN400B in accordance with JIS G-3136. The section of the I-beam is RH-350x175x7x11 (height: 350mm, width: 175mm, web thickness: 7mm, flange thickness: 11mm, fillet radius: 14mm). Figure 2 shows the detail of the moment-resisting beam-splice connections. The grade of the HSFG bolt is F10T, and the pre-tension of the high strength hexagon bolts, is in accordance with JIS B 1186 for friction grip joints. The bolt shank diameter is 16 mm and bolt hole diameter is 17 mm. The thicknesses of the splice plates for the flanges and web are 9 mm and 6 mm respectively. All lap joints are double shear. The fire protection material is ceramic fibre blanket, with a fire resistance rating of about one hour for a thickness 12.5 mm. The ALC board which forms the ceiling of the furnace is not structurally connected to the beam.

The tests were carried out in a loading frame and furnace for horizontal elements at General Building Research Corporation of Japan. The temperature of the furnace was controlled to follow the ISO 834 standard fire [12]. The total length of the beam specimens was 7.0 m, and the distance between supports was 4.2 m, with a heated length of 4.7 m. Lehigh mechanisms were used in order to prevent lateral buckling of the beam. Constant loads were applied near to mid-span of the beam as two point loads, and controlled loads were applied near the ends of the cantilevers in order to fix the beam against rotation at its supports. The rotational fixity of the supported span of the beam was controlled from the difference of the values between transducers Dh1 and Dh2 at the supports. During the tests, the initial setting of these loads at the ends of the cantilevers before heating were mistakenly set at 1.25 times the theoretical value for a beam with fixed ends. The initial slope at support was therefore not actually zero, but about 2.29×10^{-3} radians, and this initial value was kept during the fire tests.

Table 1. Test parameters.

Specimen	Connection type	Constant load	Fire protection
No.1	Without connection		
No.2	Semi-moment-resisting connection $jM_u/M_p=0.73$ (Flange: 4 bolts, Web: 4 bolts)	122 [kN] x 2 $(M_c + M_e)/2M_p=0.48$	<u>Type A:</u> Ceramic fiber blanket, Thickness: 12.5mm (mid-span, connections, supports)
No.3	Full-moment-resisting connection $jM_u/M_p=1.18$ (Flange: 8 bolts, Web: 4 bolts)	61.0 [kN] x 2 $(M_c + M_e)/2M_p=0.24$	Thickness: 25mm (between the loading point and the connection)
No.4		122 [kN] x 2 $(M_c + M_e)/2M_p=0.48$	<u>Type B:</u> Ceramic fiber blanket, Thickness: 12.5mm.
No.5			

jM_u : design resistance of the connection, M_p : design plastic moment resistance of the beam,
 M_c : bending moment at the middle span, M_e : bending moment at the supports.

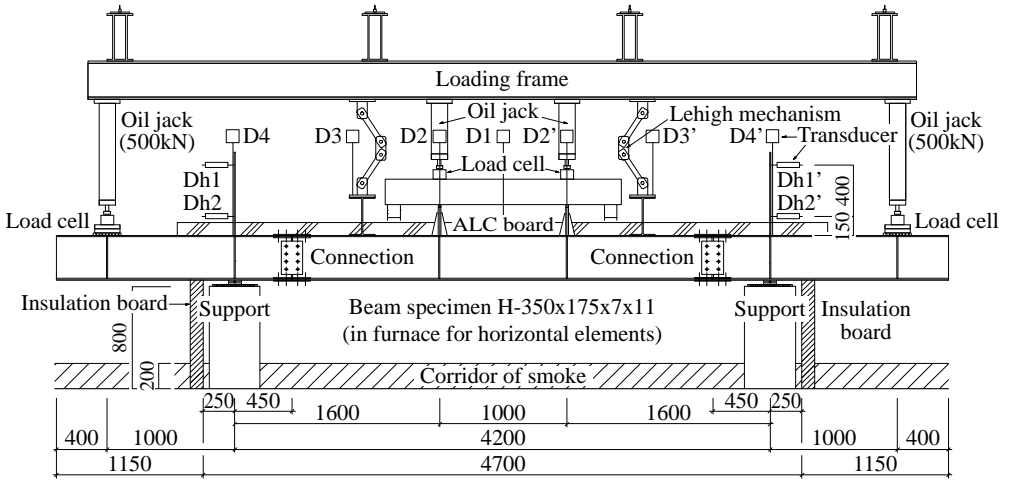


Figure 1. The test setup. (Unit: mm)

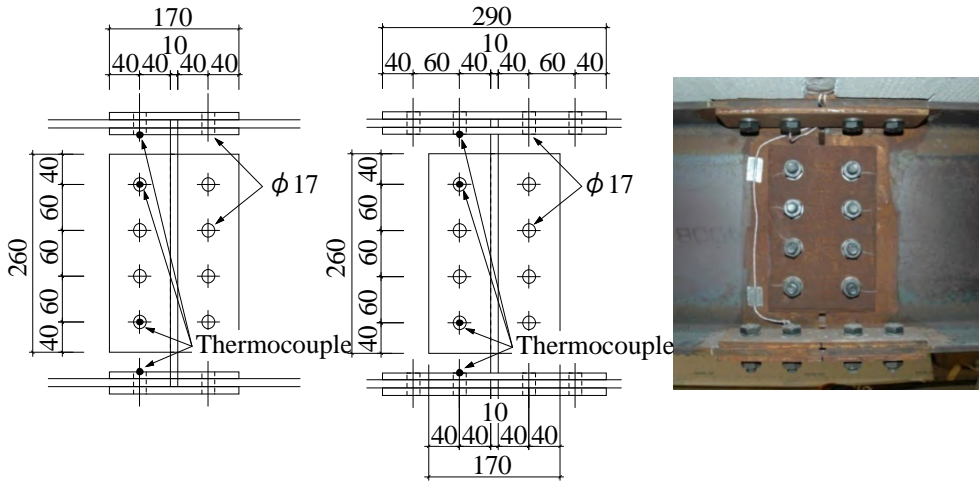


Figure 2. Moment-resisting beam-splice connections. (left: Specimen 2, right: Specimens 3-5, Unit: mm)

2.2 FE Modelling

Geometrically non-linear finite element simulations were carried out using ABAQUS [7] with non-linear material properties. Figure 3 shows the FE model, using the inherent symmetry of the test specimen to model one half only. The part at the end of the beam is virtually rigid, and rotation here is fixed by three roller supports. The I-beam, splice plates and bolts are created using solid elements. An explicit dynamic analysis is carried out for the analysis of members with discontinuous parts. Interaction between the plate surfaces at the bolted connections are defined as “hard contact” with the kinematic contact method [7]. The frictional slip resistance between the splice plates and beam due to the tension in the HSFG bolts is not taken into consideration in this simulation.

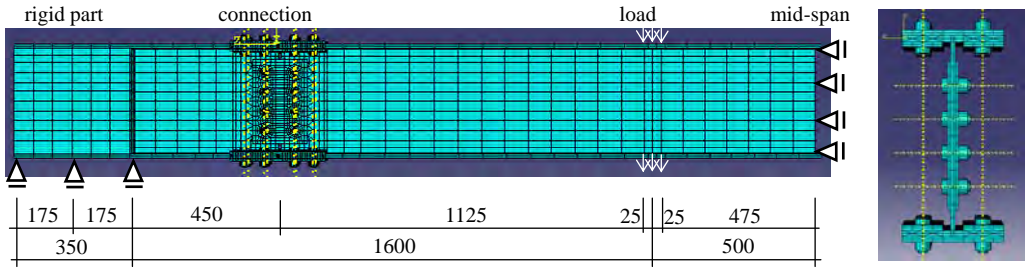


Figure 3. FE model. (Specimens 3-5)

2.3 Stress-strain relationship of the materials for FE simulations

Figures 4(a) and 4(b) show the stress-strain relationships of the steel plates and bolts which were used in FE simulations. The design strength of Grade SN400B is 235 N/mm^2 . The mechanical properties, in terms of the 0.2% offset proof stress, the stress at 1% strain and the tensile strength, of SN400B at elevated temperatures, are given by mean values from tensile test results of 23 samples at temperatures ranging from ambient to 800°C [8]. Elastic modulus values at elevated temperatures are assumed to accord with EC3 [2]. The stress-strain relationships of SN400B are given by a tetra-linear model, and the strain at tensile strength is 15%. Strain hardening of the carbon steel decreases above 500°C . The design tensile strength of an F10T bolt is 980 N/mm^2 . The mechanical properties of F10T-M16 bolts at elevated temperatures are given from the results of tensile tests and lap joint tests [9] on specimen using the same grade, diameter and factory of origin. The stress-strain relationships of F10T bolts are given by a tri-linear model. Figures 4(a) and 4(b) indicate that the reduction factor is less for HSFG bolts than for normal structural steel. The reduction factors for both the steel plate and bolts between 400°C and 800°C are similar to the values given by EC3.

In the lap joint tests, the bolts in shear reached their maximum shear resistance at a displacement of about a quarter of the diameter; the shear resistance then reduced linearly to zero for cases above 500°C [9]. However, the post-peak-behaviour of bolts in shear is not taken into consideration in this simulation.

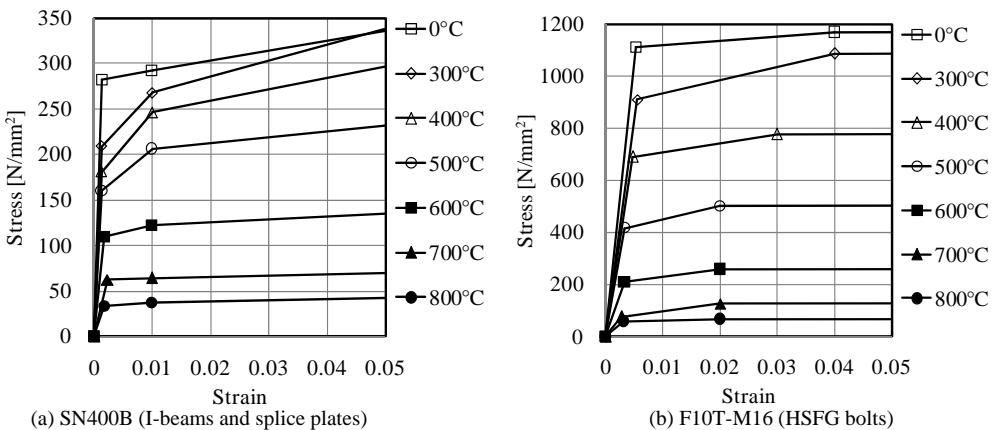


Figure 4. Stress-strain relationships of the steel plates and bolts.

2.4 Temperature of specimens covered with fire protection subjected to ISO 834 fire heating.

Steel temperature was measured with type K Chromel-Almel thermocouples which were arranged at 34 points on the surfaces of the beam and bolts. The measurement points on the beams were at mid-span (6 points), connections (12 points, on bolt heads; see Figure 2), at the supports (12 points) and the high-shear zone (4 points, only on the web) between the loading point and the connection where the thicker insulation was installed to prevent shear failure of the beams, as shown in Figure 5. The input data on steel temperatures for FE simulation was based on the test results. In this paper, examples from the results of Tests 1 and 3 were described. Figure 6 shows a comparison of the temperature distributions at 60 minutes after ignition between Specimen 1 (without connection) and Specimen 3, with a fully-moment-resisting connection. Although the fire protection and heating method were same in these tests, the temperature at the connection position was higher for Test 1 than for Test 3, because moment-resisting beam-splice connections have a relatively high heat capacity. The mean temperature at the connection part of Specimen 3 (367°C at 60 minutes) was 70-80 % of that for Specimen 1 (504°C at 60 minutes). As shown in Figures 7(a) and 7(b), the steel temperature was higher for the bottom flange than for the top flange at mid-span and at the connection, and the difference of temperatures was about 150°C. The temperature distribution was uniform between the bottom flange and the lower part of the web. As shown in Figure 7(c), the temperature of the bottom flange at the support was lower than in other parts, because the supports prevented heat flux to the bottom flange. In Test 1, heating was stopped at 81 minutes. The temperature data after 81 minutes was calculated for FE simulation using the slope of the time-temperature curve at 81 minutes. This approach was also adopted for the other tests. In Test 3, heating was stopped at 102 minutes. As shown in Figure 8, the time-temperature relationship of Test 3 was similar to that for Test 1. However, in Test 3, steel temperatures were distinctly lower for the connection than for the mid-span. While strength loss at elevated temperature was larger for HSFG bolts than for the connected beams and plates, the bolt temperatures were lower than for the connected beams.

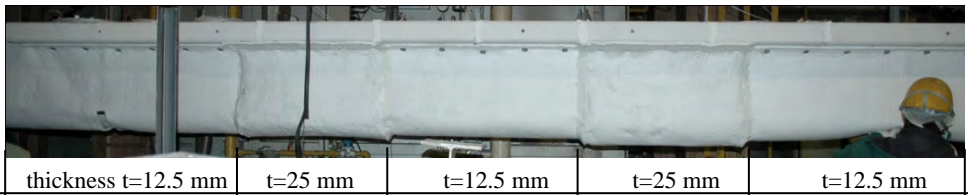


Figure 5. Type-A fire protection to prevent shear failure of the beam (Specimen 1-4).

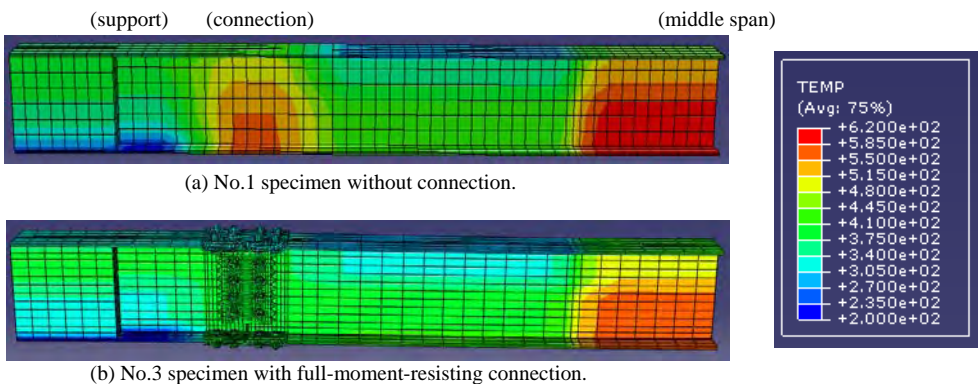


Figure 6. Comparison of temperature distributions at 60 minutes after ignition.

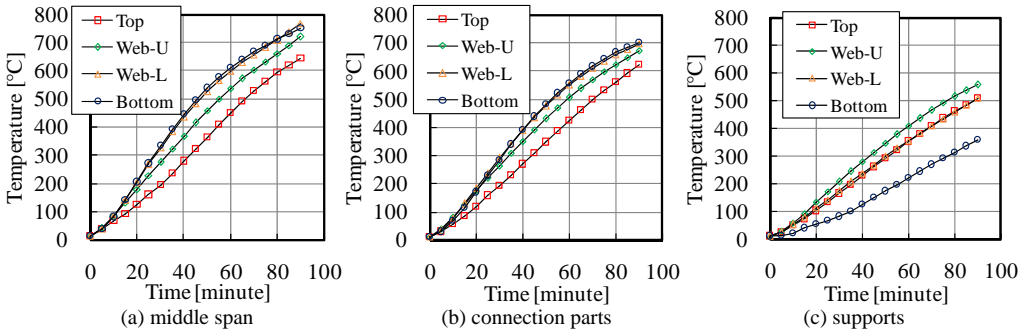


Figure 7. Steel temperatures of No.1 specimen without connection.

(Legends: Top: top-flange, Web-U: upper part of web, Web-L: lower part of web, Bottom: bottom-flange)

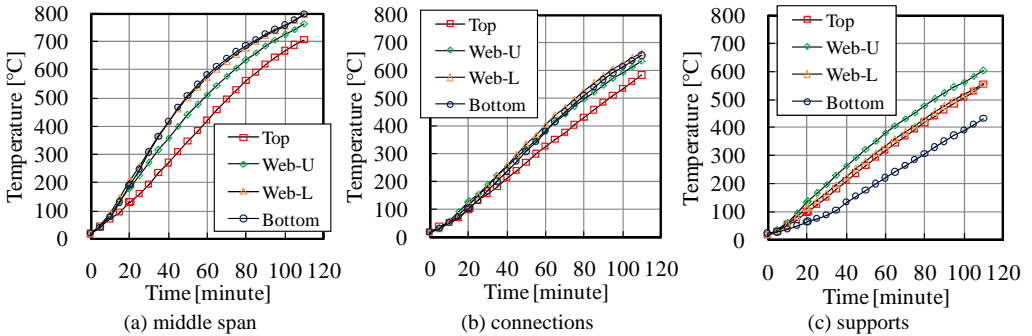


Figure 8. Steel temperatures of Specimen 3 with full-moment-resisting connection.

3 RESULTS AND DISCUSSIONS

3.1 Deflection at the mid-span of beams

Figure 9 shows deflections at mid-span of the beams, and comparison of the test results with results calculated from FE analysis (legend “FEA”). Specimen 1, without connection (Test 1) lost load-bearing capacity at 81 minutes, and the fire resistance time was the shortest of all the test results. In Test 1, not only shear deformation at the connection but also torsion was observed. Torsion was not observed in the other tests which included connections. The reason for this apparent anomaly is that in Specimen 1 the temperature at the zone which was connected in the other tests was the highest (see Figures 6-8), and that the overall torsional stiffness is lower for the beam without connections. The results from FEA 1 agree with the result of Test 1, even though torsion was not taken into consideration in the FEA. Specimen 2, with semi-moment-resisting connections (Test 2) lost its load-bearing capacity at 88 minutes, and the bolts through its top flange failed. The ISO834 [12] fire resistance criterion of limiting beam deflection was 126 mm, and the bolt failure occurred after the deflection had passed this value. As shown in Figure 9, a reduction of the deflection rate appears in both the test (70 mm) and FEA (80 mm) results for Test 2, because at these points the bottom flanges at the connection came into contact, which increased the flexural rigidity and strength of the connection. Specimen 3, with a fully-moment-resisting connection had a fire resistance of 102 minutes, which was considerably longer than Specimen 1. In the case of Test 3 the bolts did not fail, although there was some shear deformation of the bolts. The result of FEA 3 agrees with the result of Test 3. The fire resistance time of Test 4 was the longest, because the constant

load was half that of Test 3. The deflection given by FEA 4 was less than the Test 4 result after 100 minutes, when the mean temperature at the mid-span of the beam was above 700°C. Specimen 5, with Type B fire protection (Test 5) lost its load-bearing capacity at 83 minutes, and shear deformation was observed between the loading points and the inside of the connection. On the other hand, deformation at the connection, for example deformation of the bolt in shear, was not developed in Test 5. The deflection given by FEA 5 was greater than the Test 5 result after 75 minutes. During the early stages of the fire, up to 60 minutes, deflections of all beams were comparatively low because of the rotational restraint at the ends of the supported span, and the beam deflection was not affected by the connections. Moment-resisting beam-splice connections (Tests 2, 3, 4) have sufficient load-carrying capacity up to large deflections in fire.

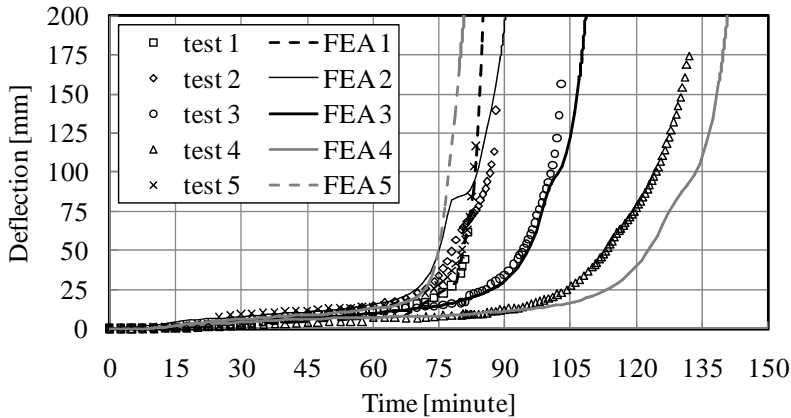


Figure 9. Deflection at the mid-span of beams.

3.2 Deformation of the beam with moment-resisting beam-splice connections

Figures 10 and 11 show an example of deformation of the beam with moment-resisting beam-splice connections subjected to vertical load and fire heating. The beam deflects largely due to rotation at the connections. Both figures show the compressive contact between the bottom flanges of the beams as rotation of the connection developed, but the bolts do not fail because their ductility in shear increases at high temperature. Figure 10 shows large shear deformation of a bolt at high temperature. Previous papers [9-11] also reported that bolts in shear do not easily fail at large shear deformations above 500°C. Its ductility at high temperature may improve the rotational capacity of the bolted connection. The figures show diagonal tension adjacent to the connection and thus a “truss analogy” as a mechanism of shear transfer. Therefore, the resistance near the connection may be related not only to bending resistance but also to shear resistance. However it is considered that the failure mode was plastic collapse of the beam and its connections due to bending moment, because rotation of the connections was very large. In Test 2, for semi-moment-resisting connections, complete bending fracture at the connection was observed, because web buckling due to diagonal compression was not observed and the bolts through the top flange failed. FE simulations were approximately able to represent the global aspect of deformation of the specimens with connections. Distributions of strain at the connection, given by FE simulation, were similar to those of the test specimens. In Tests 3 and 4, for fully-moment-resisting connections, deformations due to both bolts in shear and plate yielding were developed before plate bearing reached its resistance, and bolts did not fail. In Test 2, however, the bolts did fail. These results were in agreement with the test results.



Figure 10. Deformation of Specimen 3, a connection and bottom-flange bolt, after test.

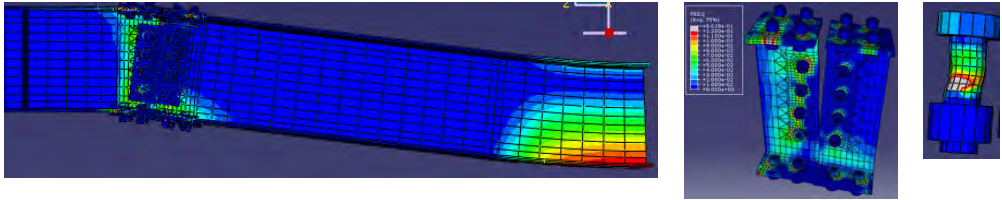
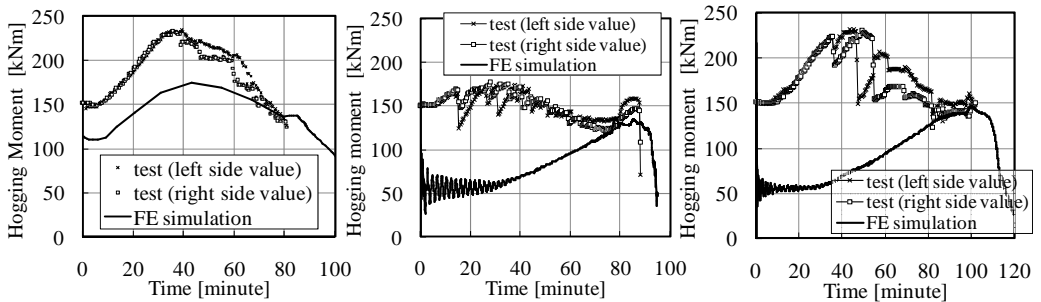


Figure 11. Distribution of equivalent plastic strain in Specimen 3 at 108 minutes by FE simulation.

3.3 Hogging moments at the ends of the beams

Figures 12 (a)-(c) show variation of hogging moment at the ends of the beams under the rotational fixity at their ends. The hogging moments in the tests were measured by the load cells installed at the ends of the specimens (see Figure 1). The hogging moment from FE simulation was given by the reactions at the supports (see Figure 3). As shown in Figure 12 (a), the hogging moments at the ends of the beam increase during the early stages of fire, up to about 40 minutes in these tests, because the thermal expansions across the height of the beam (see Figure 6 and 7), which would normally cause much of the deflection of the beam, are countered by the restraint to rotation at its ends which apply a hogging moment. After this hogging moment has reached the resistance of the beam, it decreases due to reduction of the steel's resistance. The difference of the initial value between tests and FEA results was caused by the mistake in the loading in the tests. The initial value for Specimen 1 from FEA agrees with the theoretical value. In Tests 2 and 3, FE simulations using a frictionless model cannot demonstrate the development of the hogging moment before the occurrence of slip between the splices and the connected beams. However, the FE simulations can predict the bending moment distribution of the beam at the limit state stage.



(a) Without connection (No.1) (b) Semi-moment connection (No.2) (c) Full-moment connection (No.3)

Figure 12. Hogging moment at the ends of the beams

3.4 Critical temperatures of steel beams with moment-resisting beam-splice connections

Table 2 shows critical temperature, fire resistance times and the collapse modes of the beams. The fire resistance time from both test and FEA results was given using the ISO 834 criterion [12]. The critical temperatures from test and FEA results were mean temperatures of the section at mid-span of the beam at the fire resistance time. Failure modes were determined from the deformation of the specimens. On the other hand, the critical temperatures of continuous steel beams can also be approximated on the basis of the theory of simple plastic design [1, 2]. An approximation to the critical temperature of a simple plastic collapse model was given by AIJ recommendation [1]. The resistance of a connection was calculated using the strength of the bolts and the mean temperature at the connection. Both results by FEA and the simple plastic collapse model approximately agree with test results.

Table 2. Critical temperatures, fire resistance times and collapse modes of the beams

Specimen	Test results	FEA Results	Simple plastic collapse model
No.1	671°C, 81min., S-mode	690°C, 84min., S-mode	671°C, S-mode
No.2	706°C, 88min., M-mode	698°C, 85min., M-mode	681°C, M-mode
No.3	731°C, 102min., M-mode	746°C, 105min., M-mode	731°C, M-mode
No.4	822°C, 128min., M-mode	852°C, 136min., M-mode	826°C, M-mode
No.5	682°C, 83min., S-mode	661°C, 78min., S-mode	619°C, S-mode

(M-mode: Plastic collapse of the beam and connections, S-mode: Shear failure of the beam.)

3.5 Influence of axial restraint to the beam

Rotational restraint at the ends of a beam increases the fire resistance time of the beam, whereas axial restraint to a beam may decrease its fire resistance time, because its axial thermal stress is developed by restraint to its thermal expansion, and can cause buckling of the beam. However, it was difficult to carry out the testing, applying axial restraint to the beam. In the FE simulations, the influence of axial restraint at the ends of the beams was capable of being considered by changing the boundary conditions at the end of the model from roller support to pin support (see Figure 3).

As shown in Figures 13 (a)-(c), the FE simulations indicate that axial restraint to the beam increases its deflection when exposed to fire heating. The influence was most noticeable in the case of semi-moment-resisting connections. However, axial restraint to the beam does not affect its load-bearing capacity at the final limit stage. Deflection at 60 minutes was less for the beam with fully-moment-resisting connections than for the beam without connections in the presence of axial restraint, because the development of deflection may be delayed by slip at the connection.

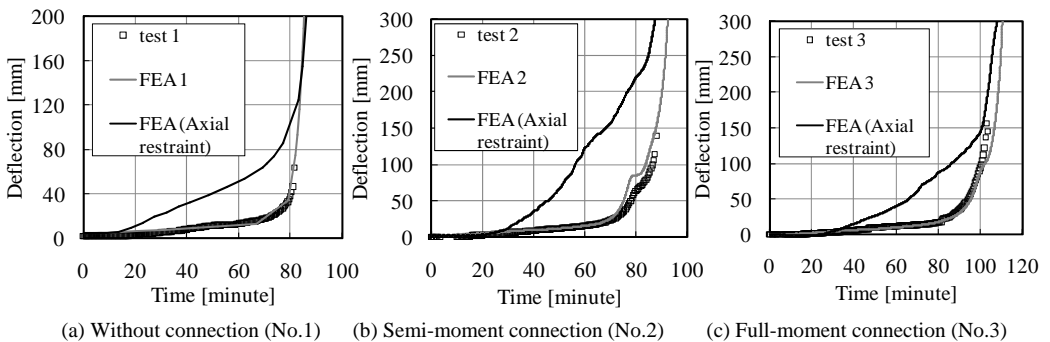


Figure 13. Influence of axial restraint on deflection of the beam

4 CONCLUSIONS

Moment-resisting beam-splice connections have sufficient load-carrying capacity up to large deflections in fire. The ductility of bolts in shear increases considerably at high temperatures. FE analysis can approximate well the deflection behaviour of a steel beam with splice connections. The analysis using a frictionless model cannot demonstrate the development of hogging moment at the ends of a beam before the occurrence of slip between the splice plates and the connected beams. However, the analysis can predict the bending moment distribution of the beam at the limit state. The critical temperature of a steel beam with beam-splice connections was well approximated by a simple plastic collapse model, assuming plastic hinges at the connections. This means that the connections can reach their maximum resistance at the limit state. The results of FE analysis also show these collapse modes. Axial restraint to the beam increased its deflection when exposed to fire heating, and the deflection was larger for weak connections than for fully-moment-resisting connections. However, the normal compression force in a beam due to thermal stress disappears at the limit state, and its critical temperature does not depend on the axial restraint.

ACKNOWLEDGEMENTS

The tests were carried out in a research project on "Method for approximating the fire resistance of connections in building structures" at the General Building Research Corporation of Japan. The authors thank Messrs. Koji Toyoda, Shigeki Tasaka, Masatomo Yoshida, Hideaki Masuda and Kazunori Harada for allowing us to use the test results.

REFERENCES

- [1] Architectural Institute of Japan, "Recommendation for fire resistant design of steel structures", 1st edition 1999, 2nd edition 2008. (in Japanese)
- [2] CEN, EN 1993-1-2. Eurocode 3: Design of steel structures Part 1-2: General rules - Structural fire design, British standards Institution, 2005.
- [3] Lawson R. M., "Behaviour of steel beam-to-column connections in fire", *Structural Engineer*, 68 (14), 263-271, 1990.
- [4] Al-Jabri K.S., Burgess I.W., Lennon T. and Plank R.J., "Moment-rotation-temperature curve for semi-rigid joints", *Journal of Constructional Steel Research*, 61, 281-303, 2005.
- [5] Hirashima T., Toyoda K., Yatagai A., Esaki Y., Tasaka S., Yoshida M., Masuda H. and Harada K., "Experimental Study on Fire Resistance of H-shaped Steel Beams with High Strength Bolted Joints", *J. Struct. Constr. Eng.*, AIJ, Vol.75 No.658, 2257-2265, 2010. (in Japanese)
- [6] Architectural Institute of Japan, "Recommendation for design of connections in steel structures", 2001. (in Japanese)
- [7] ABAQUS Analysis User's Manual Version 6.9, ABAQUS Inc., 2009.
- [8] Architectural Institute of Japan, "Guide book for fire-resistive performance of structural materials", 1st edition 2004, 2nd edition 2009. (in Japanese)
- [9] Hirashima T., Hamada N., Ozaki F., Ave T. and Uesugi H., "Experimental Study on Shear Deformation behavior of High Strength Bolts at Elevated Temperature", *J. Struct. Constr. Eng.*, AIJ, No.621, 175-180, 2007. (in Japanese)
- [10] Hirashima T. and Uesugi H., "Experimental Study on Shear Strength of Friction-Type High-Tension Bolted Joints at Elevated Temperature", *Proceedings of the 6th Asia-Oceania Symposium on Fire Science and Technology*, Daegu, Korea, 272-284, 2004.
- [11] Hongxia Y., Burgess I.W., Davison J.B. and Plank R.J., "Experimental investigation of the behaviour of fin plate connections in fire", *Proceedings of ICSCS 2007*, 541-548, 2007.
- [12] ISO/TC92/SC2, ISO 834-1: 1999(E), "Fire-resistance tests - Elements of building construction - Part 1: General requirements", 1999.

A COMPONENT-BASED MODEL FOR MOMENT-RESISTING BEAM-SPLICE CONNECTIONS WITH HIGH-STRENGTH BOLTS AT ELEVATED TEMPERATURE

Mariati Taib*, Ian Burgess* and Takeo Hirashima**

* University of Sheffield, Department of Civil and Structural Engineering, UK
e-mails: m.taib@sheffield.ac.uk, ian.burgess@sheffield.ac.uk

** Chiba University, Department of Architecture and Urban Science, Japan
e-mail: hirashima@faculty.chiba-u.jp

Keywords: Connections, Beam-splices, Component-based modelling, Moment-resisting frames, Fire

Abstract. *This paper is concerned with the generation of a proposed model for moment-resisting beam-splice connections in the framework of a component-based method. The model is composed of an assembly of extensional springs and rigid links, so that the spring components represent specific contributions from the connection's main zones of structural action. The temperature-dependent properties of the equivalent component springs are governed by the weakest component, for any given bolt row. The proposed model is validated, utilising the finite element software Vulcan, against results from an experimental programme on spliced beams, conducted in Japan. The tests included two different arrangements at the beam splices, which create partial-strength and full-strength connections. The model is shown to be capable of simulating the connection behaviour, and gives close agreement with the tests, thus demonstrating the applicability of this method for beam-splice connection. The research extends the applicability of component modelling as an efficient computational tool to predict connection response in fire.*

1 INTRODUCTION

Steel moment-resisting framed buildings are assumed to develop their ductility through the development of yielding in their beam-column connections. Many engineers believe that it is possible to withstand large deformations without significant degradation in strength, and without the development of instability and collapse. However, evidence of unforeseen connection failures in different types of hazard (earthquake, blast and fire) has challenged this paradigm, raising questions about the adequacy of moment-resisting connection design in building code provisions. Even before the destructive fires in the WTC7 building, and following the Northridge and Kobe earthquakes, substantial effort was being made to represent the realistic behaviour of such connections. The framing system type identified in these catastrophic events is widely utilised in the USA and Japan, where it provides a popular solution for buildings in highly seismic regions. This is known as a "column-tree" system [1], and needs to utilise its beam-splices as major elements in design. The beam-splices act as ductile 'fuses', and limit the magnitudes of the internal forces, including bending moments, which can be developed in the frame, which makes them an ideal type of connection in both fire and earthquake scenarios. Depending on the bending strength and rotational stiffness of these splices, the structural frame can behave either as 'rigid' or semi-rigid'. Semi-rigidity can be beneficial at high temperature, when redistribution of forces from beams to other structural members is critical, influencing the survival time of the whole framing system. This paper adopts the widely recognised component-based approach to characterise the moment-resisting connection behaviour of beam-to-beam-splices in fire. This method is capable of capturing the key

features of the overall connection interaction in a realistic manner, based on the underlying mechanics, coupled with evidence from experimental data.

In extreme events, very high demands for local and global deformation are imposed on structural elements, connections and details. Connections between members, in particular, are anticipated to be the regions where the material is exposed to inelastic deformations, which consequently influence local ductility requirements and frame performance. The beam-splices, as the key elements in column tree systems, need to be designed appropriately in order not to compromise the strength of the beams. The beam-splice connections most often used are either welded, field-bolted or a mixture of bolted and welded elements. However, the advantages of using column-tree systems can be fully utilised using fully bolted splices. Thus, this analysis concentrates on the bolted connections. Plate splices, shown in Figure 1, can be either single- or double-plated, the arrangement being repeated on each side of the joint. The use of double plates in general reduces the number of bolts and shortens the lengths of plate splices. The web splices normally employ double plates to stiffen the web out-of-plane and utilise the double-shear capacity of the bolts. The design philosophy [2] for this type of connection is that the flange splices are designed to resist most of the applied moment. The web splice carries transverse shear, distributed equally between the bolts. Additionally, any axial force in the beam is divided equally between the flanges.

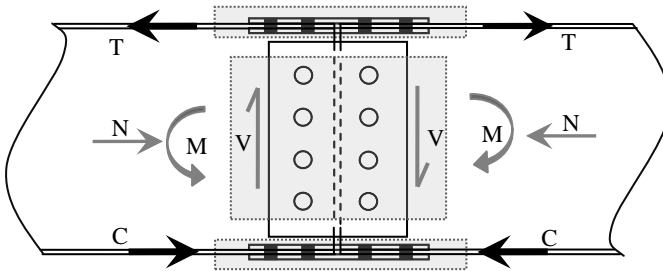


Figure 1. Forces in splice connection

Connections in general should possess the characteristics of both strength and ductility, which in this context refers to the ability to articulate plastically at some stage of the loading cycle without failure, and this is governed by the ductilities of their parts. The ductility of a joint reflects to the length of the yield plateau in its moment-rotation response, which is provided mainly by its capacity for plate yielding and bearing deformation at its bolt holes. Failure criteria are introduced for each individual component to facilitate the simulation of its behaviour at different temperatures, including final fracture. The design procedure classifies failure modes into 'ductile' and 'brittle', and attempts to ensure that ductile failure modes will precede the brittle ones. In this study only the dominant failure modes (bearing of plates and bolt shear) are considered on the basis of previous test results and researches [3,4].

2 MECHANICAL MODEL DEVELOPMENT

In developing the mechanical model of a connection, a comprehensive understanding of the general behaviour of the connection is necessary. Evaluation of the key aspects can be described by assuming their idealised load transfer mechanisms. For splice connections, the utilisation of friction grip bolts can transfer force, initially through frictional resistance and subsequently through bearing stresses. It is assumed in this research that the bolts are subjected to forces acting through their centroids. In the initial stage of loading, the bolts, which are presumed to be installed centrally, do not carry any force. The load is solely transferred by frictional resistance at the contact surfaces of the plates. When the load exceeds the frictional resistance, large relative displacement occurs, and the bolt comes into contact with the bolt hole edges. This displacement is caused by a finite slip, ranging from zero to two hole clearances. The positions of the bolts in their respective holes during the assembly process define their slip ranges. The bolts positioned furthest away from centre of rotation usually come into contact with the hole walls first,

and are therefore described as the critical bolts. These then deform plastically, either by bolt shear or plate bearing, and eventually fracture. Overall, the connection behaves elastically with increasing load until the stress in either the bolt or the plates reaches the yield strength of the material. Beyond this stage, the maximum resistance of the aggregate bolt-row characteristic is controlled by that of its weakest component. Thus, the post-yield failure characteristic follows the dominant component. It should be noted that the initial frictional resistance diminishes somewhat when slip occurs in a bolt row.

Commonly used beam-splice connections consist of splice plates, which are lapped across the two connected beams and bolted to either side of the web and flanges. In a component model framework, the active zones for splice connection cover the region where the two members are interconnected and where the set of physical components mechanically fasten the connected elements, as shown in Figure 2. Characterisation of these active zones is based on the force transfer across a bolted double-splice butt joint between in-line connected members. Within each zone, several sources of deformation can be identified, which are simple elemental parts (known as “components”) which in this case refer to the frictional, bearing and shearing resistance of the connected plates and bolts. The characteristics of these individual components are subsequently defined by nonlinear-force-deformation relationships, derived from their mechanical behaviour.

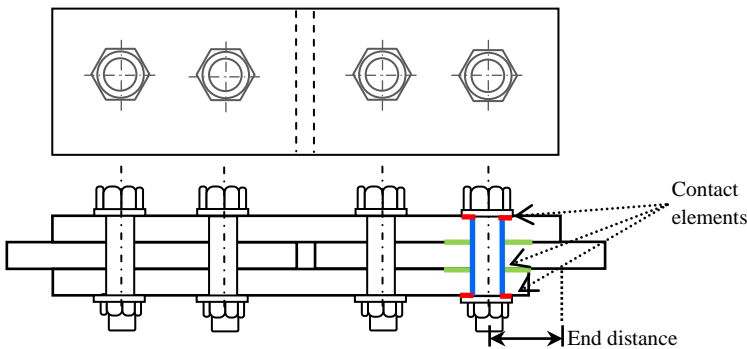


Figure 2. A bolted double-splice butt joint.

2.1 Plate bearing

As the applied force increases, the maximum concentration of stress develops in the vicinity of the bolt hole. Consequently, local yielding of the plates at the hole edge allows for stress redistribution and ultimately bearing failure to occur. The plate bearing characteristic tends to be stiff up to the initiation of yield, beyond which there is a long plateau until the considerable plastic range is exceeded. Elongation of the bolt hole is largely influenced by the ductility of the plate material and its geometry (thickness t and end distance e_2). Ultimate failure is controlled by the end distance of the plate, and treats both bearing and tear-out as single limit state. This failure mode in a connection generally shows signs of distress through permanent plastic deformation, but tends to be non-catastrophic in contrast to the more brittle shearing failure. Based on a detailed investigation of a single-bolt lapped plate connection, Rex and Easterling [5] concluded that the initial stiffness associated with a plate in bearing depends on three primary stiffness values; bending (K_b), shearing (K_v) and bearing (K_{br}). On the basis of a parametric study Sarraj [3] distinguished two cases of bearing; small end distance and large end distance. The plate strength $F_{b,rd}$, formulated as in Table 1, represents the bearing component by normalised force-displacement relationship using predefined curve-fit values.

2.2 Bolt shear

This criterion is adopted to simulate the effect when the critical shear cross section of a bolt becomes fully plastic. When the equivalent plastic stress exceeds the true yield stress of the bolt, then the residual cross section of the bolt is gradually deemed to fracture. Bolt shear is generally considered to be an

undesirable failure mode, because it does not involve enough ductility to ensure a simultaneous plastic distribution of the forces taken by the bolts [4], and can therefore allow progressive failure. It is assumed here that the shear resistance decreases to zero at a displacement equal to the bolt diameter, d_b . The ‘down-hill’ part of the force-displacement curve is defined simply on the basis of the residual connected bolt area. The temperature-dependent bolt shearing strength, $F_{v,Rd}$ given in Table 1, is subsequently applied to a modified Ramberg-Osgood [5] expression for bolt shear deformation.

Table 1. Design resistance for bearing and shearing

Failure modes	Load Resistance	
	Tension	Compression
Plate Bearing	For all sizes of bolt:	For bolts up to M20:
	$F_{b,Rd} = \frac{e_2}{d_b} \times f_u \times d_b \times t$	$F_{b,Rd} = 0.92 \times \frac{e_2}{d_b} \times f_u \times d_b \times t$
Bolt in shear	$F_{v,Rd} = k_{f,v,b} \times f_{u,b} \times A$	

2.3 Friction

The friction component involves two mating surfaces, and the magnitude of its force depends on the friction coefficients, the normal force and the number of friction surfaces [6]. A rational representation of this characteristic is defined through the pre- and post-slip behaviour of connection. The initial stiffness of the pre-slip region is determined fairly arbitrarily, approximately when the friction force reaching its peak at 10% of the bolt-hole clearance. The friction resistance then persists as a plateau until the bolt makes positive contact with bolt hole edge. This post-slip resistance subsequently degrades slowly with movement until no frictional force remains on the connection. Since the friction force is controlled by the normal force between the plate surfaces caused by bolt tension, and this is assumed to be generally based on elastic bolt behaviour, the reduction of friction characteristics with temperature is assumed to depend on the elastic modulus reduction factor.

3 PROPOSED COMPONENT-BASED MODEL

Application of the component-based method generally involves characterisation of the nonlinear component ‘springs’, which are then assembled into two-noded connection elements. The nonlinear structural analysis then iteratively establishes equilibrium subject to the internal compatibility within the spring elements, coupled with the stiffness and deformations of individual components. Sarraj[3] first developed a component-based model for fin-plate connections based on a numerical investigation of single lap-joint connections. The lap-joint zone consists of three fundamental components placed in series in each bolt row; the fin-plate in bearing, the bolt in shearing, and the beam web in bearing. These component models include a friction spring in parallel with this basic spring assembly. Yu [4] verified the component model against the results from experiments performed at the University of Sheffield, with the modification of an additional spring at the location of the beam’s bottom flange. In this research, the basis of Sarraj’s active components is adopted, with some modification for use with moment-resisting beam-splice connections. An idealised representation of the double-splice butt connection is shown in Figure 3(a). When the connection is loaded either in tension or compression, the contact achieved by closing the gap activates one or other series of three components. The equivalent characteristic of the active series follows the failure characteristics of its weakest individual component. To include the effect of material weakening with increasing temperature, reduction factors based on EC3 [7] have been adopted. These temperature-dependent characteristics have subsequently been incorporated into the nonlinear finite element program *Vulcan* to assess realistic connection response within frame analysis.

The arrangement of a bolt row of the beam-splice connection is shown in Figure 3(b). Essentially, the springs are in series, with stiffness $k_{lap,n}$ representing a web bolt row with a single bolt either side of the gap. The indices ‘lap’ refer to a single lap joint which consists of individual components of the plate in

bearing and the bolt in shear. In parallel to the bolt springs, a friction spring is included with stiffness $k_{slip,n}$. The upper and lower beam flange springs, $k_{bf, upper/lower}$ account for positive compressive contact between the beam flanges.

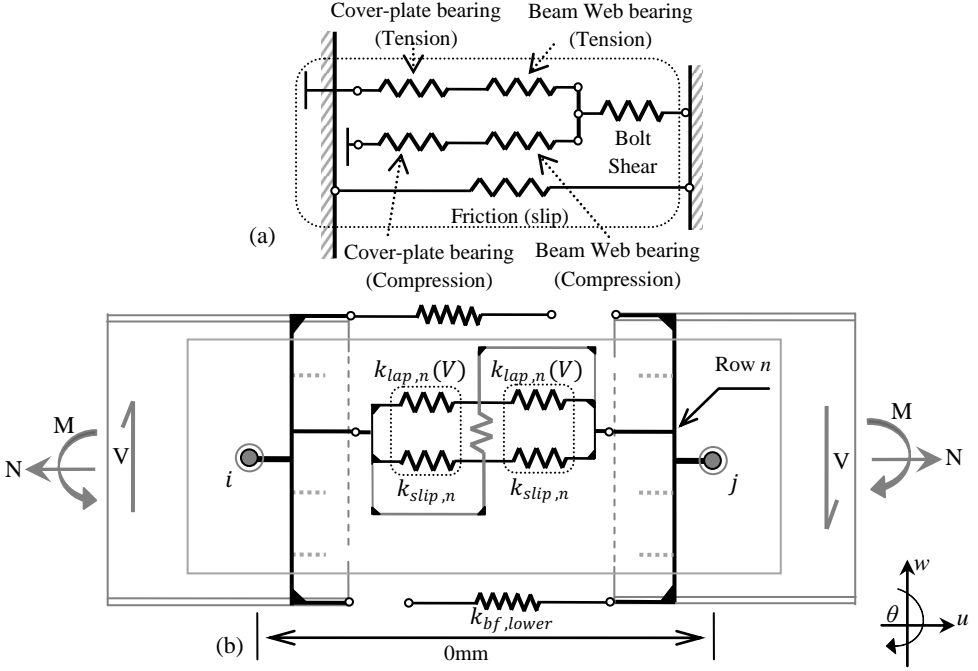


Figure 3. Component-based model for (a) Butt splice joint (b) single bolt row.

4 IMPLEMENTATION IN *Vulcan*

The implementation of the joint element in *Vulcan* is modelled as an assembly of bolt rows which each contain the basic component springs, with no physical length in between the rigid links. Referring to the splice connection shown in Figure 1, each spring in Figure 4 represents the equivalent bolt row assemblies at the positions of the beam flanges $k_{bf, n}$ and web $k_{w, n}$, arranged in parallel. Prior to lower beam flange contact, the connection is assumed to rotate and deform with the applied load at the centre-line of the beam. After contact is established, bearing on the beam flange results in an increased stiffness and capacity. The nonlinear bolt-row springs are subjected to axial and shear forces according to their relative positions. In order to consider the complicated load-reversal at high temperatures, the force transitions are applied using the Masing Rule [8] relative to positive contact between the bolt and plate.

The component method is formulated according to the principles of nonlinear stiffness analysis in order to incorporate it in *Vulcan*. The nonlinear behaviour of each individual connection component is resolved iteratively. The connection stiffness matrix k_c relates the incremental forces ΔF to the incremental displacements Δu of the connection in an equation of the form:

$$\Delta F = k_c \Delta u \quad (1)$$

In *Vulcan* the nonlinear incremental stiffness matrix is a function of the internal forces and displacements developed during a load step. An iteration scheme is employed which updates the stiffness matrix continuously, using the previously calculated incremental displacements as a datum. The next

incremental load or temperature is calculated if convergence is reached. Otherwise, the incremental displacement is reduced until equilibrium is reached.

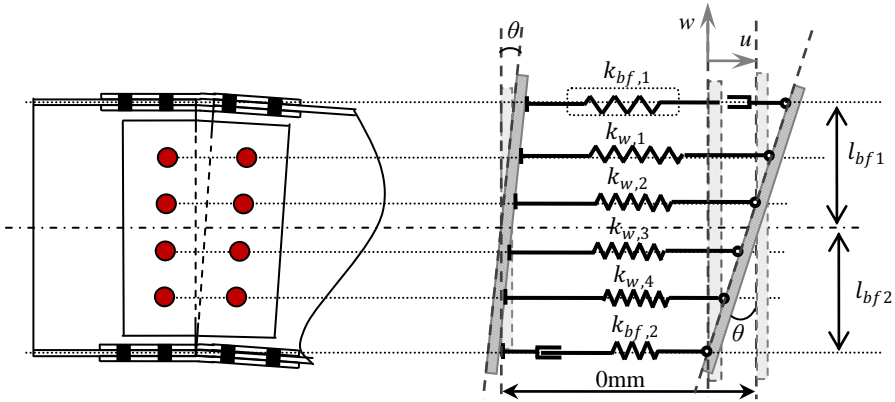


Figure 4. Component based model arrangement in *Vulcan*. (Note that u_i is the relative mean displacement across the whole connection).

5 EXPERIMENTAL SETUP

An experimental study [9], in which I-section steel beams incorporating high-strength bolted splice joints were subjected to increasing temperatures, was investigated. The experiments had investigated both the temperature distributions within the connected zones of the beams and the structural behaviour of the moment-resisting connections at high temperatures. Four specimens using beam-splice connections with varying details and loading were tested. However, only three tests with the more significant arrangements are studied here, since the objective of this study is to understand the influence of fire on moment-resisting connection response. Details of the selected specimens are given in Table 2.

Table 2. Test detailing for different arrangement.

Specimen	Connection type of moment resisting connection	Number of HSFGB bolts		Constant load P_c (kN)	Fire protection
		Flange	Web		
No. 2	Partial-strength $\frac{M_u}{M_p} = 0.73$	4	8	121.9 kN	12.5mm ceramic fibre blanket.
No. 3	Full-strength $\frac{M_u}{M_p} = 1.18$	8	8	61.0 kN	In region e, a double layer was applied.
No. 4		8	8		

A schematic setup of a test is given in Figure 5, showing half of the symmetric test setup. The span between supports was 4.2m. The load P_c was applied mainly through two jacks near mid-span with the loads given in Table 2. Two additional jacks P_e at the ends of the cantilevers (Position *a*) were used to maintain zero rotation at the supports throughout the test. In order to control lateral buckling and twisting of the beam during heating, a stabilising system was set up at the point of contraflexure (indicated at *e*). The connection detail is shown in Figure 5(b). The distinction between the partial-strength (Test 2) and full-strength (Test 3 and 4) connections is based on the number of bolts at the beam flanges.

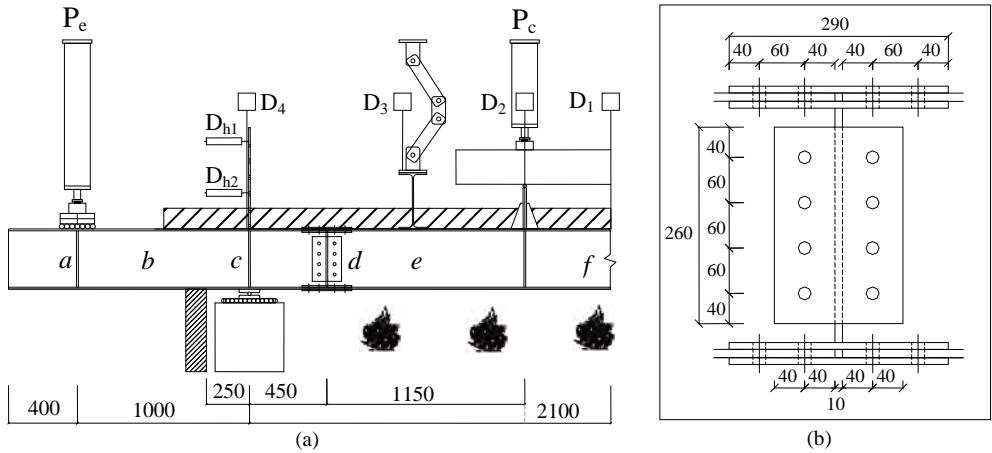


Figure 5. (a) One half of the symmetric test setup (b) Connection details.

5.1 Material properties

Details of the material properties and section of the structural member are given in Table 3. The yield and ultimate stresses were measured from tensile coupon tests from the test specimens; nominal grades were SN 400B for the beam and F10T for the bolts, according to the Japanese Industrial Standard (JIS). The degradation of strength of the structural members was based on the reduction factors defined from the experimental results depicted in Figures 6(a) for SN 400B and 6(b) for F10T. These are compared with recommendations of EC3 [7]. It can be observed that the experimental reduction curve employed is more pronounced in the early heating stage, whilst at higher temperatures it follows closely the EC3 curve.

Table 3. Section properties of structural members.

	Sections	Dimensions(mm)	Yield Stress, f_y (N/mm ²)	Tensile strength, f_u (N/mm ²)	Elongation (%)
Beam	I-section steel beam	350 x 175 x 7x 11	308	446	31
Cover Plates	Flange (Test 2)	170 x 175 x 9.0 170 x 70 x 9.0	393	456	28
	Web (Test 2)	260 x 170 x 6.0 *			
	Flange (Tests 3 & 4)	290 x 175 x 9.0 290 x 70 x 9.0			
	Web (Tests 3 & 4)	260 x 170 x 6.0 *			
Bolt	Flange	16 x 60	1043	1083	19
	Web	16 x 55	1019	1057	19

* Coupon tests were only performed on 9mm plate; assumed the same for 6mm plate.

5.2 Temperature distribution

The furnace fire curve, together with the effect of fire protection in some zones, resulted in a differential temperature distribution along the beam. The thermal gradients across the beam depth, however, were caused by the 100mm thick ALC (autoclaved lightweight concrete) panel, supported on the upper flange, which caused about 160°C temperature difference between the bottom and top flanges at 60 minutes. To represent the shielding and heat-sink effects of a normal-weight concrete slab on the top flange temperature in more realistic construction, a ceramic fibre blanket (130 kg/m³ at 12.5mm thickness), with fire resistance rating of about 1 hour, was used to provide some insulation to the top flange of the beam. This fire protection varied along the beam in the zones denoted as a to f in Figure 5.

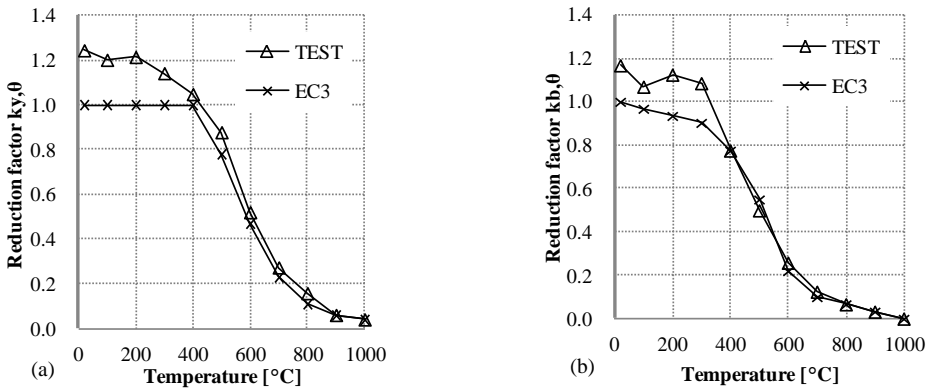


Figure 6. Strength reduction factors for a) SN 400B b) F10T steels.

6 COMPONENT MODEL VERIFICATION

The component model of the connection has been incorporated into *Vulcan* to represent the beam-to-beam test setup, with the real boundary conditions of the test. In the model, full rotational restraint is provided at the support to simulate the constant zero rotation which is maintained during the tests. An “axis of symmetry” boundary condition is applied at the right-hand end of the model (Position f), to represent the mirror-image arrangement of the right-hand half of the beam arrangement. The three tests conducted are examined here in terms of the deflection at mid-span, and the distribution of bending moment at several main positions along the beam, with respect to temperature increase. The plotted results are arranged in two columns in Figure 7, with the graphs in the left-hand column representing mid-span deflection and the right-hand column the bending moment diagram. The temperature axis shows the mean temperature in the section at the mid-span of the beam. In these graphs the dotted lines indicate the test results while the full lines are the analytical results using the component models for the splice connections.

6.1 Deflection at mid-span

In general, very reasonable agreement can be seen between the tests and the analytical models using the component elements in terms of the mid-span deflection (Figure 7(a)). The component models generally exhibit a similar loading pattern, with large deformation forming a plastic hinge, which eventually fails in a ‘runaway’ stage. The bending moment is carried mainly by the flanges, and so the number of bolts in each flange splice is a major influence on the connection strength. The term ‘failure’ in this model can be defined as either the occurrence of beam failure by runaway, or the fracture of any component the connection. In the early heating stage, the forces in the bolts are transferred mainly by frictional resistance until the slip resistance is exceeded. In Test 2, a significant rotation caused a very obvious bearing contact of lower beam flanges at a beam temperature of 713.5°C. In this test the failure of the beam caused considerable shearing deformation of the bolts in the beam upper flange, followed by large bearing deformation of the beam web’s tension zone. With increased numbers of bolts in the beam flanges (Test 3), the failure of the beam was delayed slightly to the higher temperature of 725.5°C. After positive contact between the lower beam flanges was made, at high rotation, they experienced a high compressive force which subsequently generated higher bolt deformation in the upper beam flange due to this lowering of the centre of rotation at the connection. The beam specimen in Test 4 failed at a critical temperature of 818°C, at only half the loading of the standard test. This arrangement experienced a much larger beam mid-span deflection because of the higher temperature, and the connection components were more highly deformed.

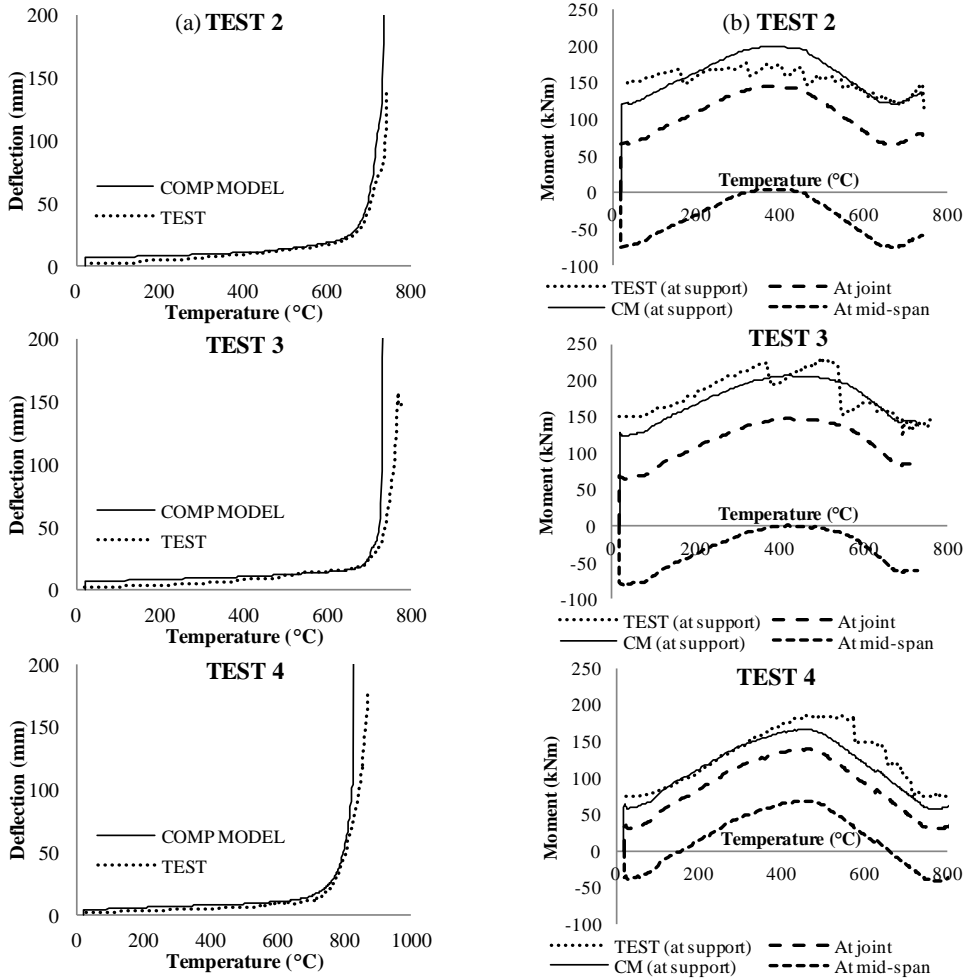


Figure 7. (a) Deflection at mid-span (b) Bending moment variation at different positions.

6.2 Moment distribution

The variation of bending moment at three different positions (support, joint and mid-span) along the beam span is depicted in Figure 7(b) for each of the three tests. The fixed-end bending moment at the support location (Position c) is directly compared with the test measurement. The analytical results at the other positions provide a general view of the change of bending moment at the joint and mid-span during the transient heating. The discrepancy shown between the analytical and test results for Tests 2 and 3 at the support was due mainly to an error during the initial setting up of these experiments, which caused the initial moment to be 25% larger than the theoretical value of 120.8kNm. This accounts for the difference between the test results and component model. This also contributes to the small difference in deflection at ambient temperature. During the tests, it was intended to keep the beam rotation at the support constant at zero, using the loading jack P_e . However, it was later observed that this initial rotation had actually been approximately 0.0023 radian, and this value was used throughout the fire tests. Essentially, hogging moment is added across the span during heating in order to counteract thermal bowing caused by the thermal gradient across the beam cross-section. As the thermal gradient reduces, this additional hogging moment decreases.

7 CONCLUSION

A practical model for beam-splice connections when analysing the global behaviour of frames in fire has been developed, which has been shown to give good comparison with the experimental data from three large-scale furnace tests. It is observed that the rotational behaviour and moment capacity of the connection depend essentially on its detailing, particularly on the numbers of high-strength bolts used and the frictional resistance which they generate. The partial-strength connection model of Test 2 managed to achieve a fairly similar fire resistance, in terms of both temperature and time, to the full-strength Test 3. The full-strength connection (Tests 3 and 4) is not the critical part of the beam at ambient temperature, and plastic hinges should occur in the I-section instead. The use of high strength friction grip bolts dominates the load path of the splice connection, by generating frictional resistance through the specified tensions in the bolts. However, at high temperature, the contact pressures of the bolts are reduced, causing a reduction of the friction resistance; it has been assumed here that the bolts remain in elastic tension, and so the reduction of friction is controlled by the steel modulus reduction factor. This is clearly a simplification of a combination of factors which affect the frictional resistance, but seems adequate. When frictional resistance has sufficiently dissipated, the bolts begin to function as bearing bolts, and this may allow the connection to become the critical part of the beam. The component-based model shows that the way the frictional resistance degrades at elevated temperatures highly influences the overall response of the splice connection, compared with its ambient-temperature performance. The component-based methodology provides sufficient flexibility to allow realistic modelling of such interactions between individual components within connections of this type.

ACKNOWLEDGEMENT

The authors gratefully acknowledged sponsorship and support of the first author by the Malaysian Government for this research.

REFERENCES

- [1] Astaneh, A., "Seismic Design of Steel Column-Tree-Moment-Resisting Frames", Steel TIPS Report, Structural Steel Education Council, 1998.
- [2] BCSA, The British Constructional Steelwork Association, "Joints in Steel Construction: Moment Connection", The Steel Construction Institute, 2002.
- [3] Sarraj, M., "The Behaviour of Steel Fin-Plate Connections in Fire", PhD Thesis, University of Sheffield, 2006.
- [4] Yu, H., Burgess, I.W., Davison, J.B., Plank, R.J., "Experimental Investigation of the Behaviour of Fin-Plate Connections in Fire", *Journal of Constructional Steel Research*, 65(3), 723-736, 2009.
- [5] Rex, C.O., Easterling, S.W., "Behaviour and Modelling of a Bolt Bearing on a Single Plate" *Journal of Structural Engineering*, ASCE 129(6), 792-800, 2003.
- [6] European Committee for Standardisation, "Eurocode 3; Design of Steel Structures, Part 1.8: Design of Joints", UK: British Standard Institution, 2005.
- [7] European Committee for Standardisation, "Eurocode 3; Design of Steel Structures, Part 1.2: General rules-Structural Fire Design", UK: British Standard Institution, 2005.
- [8] Masing, G., "Zur Heynschen Theorie der Verfestigung der Metalle durch verborgen elastische Spannungen, *Wiss Veröffentl aus dem Siemens-Konzern*", 31, 231-239, 1923. (In German)
- [9] Hirashima, T., Toyoda, K., Yatagai, A., Esaki, Y., Tasaka, S., Yoshida, M., Harada, K., "Experimental Study on Fire Resistance of H-Shaped Steel Beams with High Strength Bolted Joints", *Journal of Structural and Construction Engineering*, 75(658), 2257-2265, 2010-12. (In Japanese)

EFFECT OF AGING ON RELIABILITY OF STEEL COLUMNS PROTECTED BY INTUMESCENT COATINGS TO NATURAL FIRES

Chao Zhang*, Guo-Qiang Li** and Yong-Chang Wang***

* College of Civil Engineering, Tongji University, 1239 Siping Road, Shanghai 200092, China
e-mails: 08_chao_zhang@tongji.edu.cn

** Sate Key Laboratory for Disaster Reduction in Civil Engineering, 1239 Siping Road, Tongji University, Shanghai 200092, China
e-mail: gqli@tongji.edu.cn

*** School of Mechanical, Aerospace and Civil Engineering, The University of Manchester, PO Box 88, Manchester, M60 1QD, UK
e-mail: yong.wang@manchester.ac.uk

Keywords: Fire, Steel structures, Reliability, Aging effect, Failure probability.

Abstract. *This paper investigates the aging effect on reliability of steel columns protected by intumescent coatings subjected to natural fires. Post-flashover fire is considered and time equivalent is adopted to model the fire behavior. The maximum steel temperature in natural fire is calculated by a recently developed formula. The thermal insulation property of intumescent coating is assessed by using the concept of constant thermal resistance. Previous test data on aging effect on thermal insulation property of intumescent coatings are used. Monte Carlo simulation method is used to calculate the fail probability and reliability index. The study finds that aging has effect of decreasing the reliability index of steel columns protected by intumescent coatings. That decrease effect increases with aging year increases. The decrease is more serious for cases with high load ratio μ_0 than for cases with low μ_0 . For the investigated cases with low load ratio ($\mu_0 \leq 0.3$), the amount of the decrease of reliability index $\Delta\beta$ due to aging effect is less than 0.2 (the corresponding increase in failure probability ΔP_{fail} is less than 3 %; and for the investigated cases with high load ratio ($\mu_0 > 0.3$), the maximum $\Delta\beta$ is about 0.24 (the corresponding maximum ΔP_{fail} is about 9 %). However, the ratio of failure probability change is large.*

1 INTRODUCTION

Intumescent coatings, by their advantages like attractive appearance, potential for off-site application and practically taking no space, are now the dominant passive fire protection materials used in industrial and public steel buildings [1]. The coatings, which usually are composed of inorganic components contained in a polymer matrix, are inert at low temperatures and will expand and degrade to provide a charred layer of low conductivity materials at temperatures of approximately 280 to 350 oC [2]. The charred layer, which acts as thermal barrier, will prevent heat transfer to underlying substrate. In practice, when specifying coating fire protection for steel structure, it assumes that the coating is correctly applied and its performance meets the fire protection needs without degradation over time. However, since the organic components of intumescent coating, it should be expected that the fire protection function of intumescent coating over time would not be as reliable as when freshly applied [3].

This paper presents a study on reliability of steel columns protected by intumescent coatings to natural fires. State-of-the-art knowledge in current researches on structural fire engineering has been used in our study. MCS is adopted for probabilistic analysis.

2 DETERMINISTIC APPROACHES

2.1 Fire modeling

The behavior of a real fire is complex, which depends on many parameters such as sprinkler, fire load, combustion, ventilation, compartment size and geometry, and thermal properties of compartment boundaries [4]. So far, with increase in complexity, empirical correlations (e.g. nominal fire curves and parameter fire curve [5]), zone models (e.g. one-zone models for post-flashover fires and two-zone models for pre-flashover fires [6]), and sophisticated CFD models (e.g. Fire Dynamic Simulation [7]) have been developed to model the fire behavior. Also, stochastic models have been developed for compartment fires [8].

In practice, the concept of equivalent fire severity, commonly referred as time equivalent, had been developed to relate real fires with the simply standard fire. In our investigation, the formula recommended by EC1 [4] is used for evaluating the equivalent fire severity. The formula is based on maximum temperature method which defines the equivalent fire severity as the time of exposure to the standard fire that would result in the same maximum temperature in a protected steel member as would occur in a realistic fire, and is given in a simply form that

$$t_{eq} = q_f k_b w_f \quad (1)$$

where, t_{eq} is the equivalent standard fire duration time; q_f is the floor fire load density; k_b is the conversion factor to account for the thermal properties of the enclosure; and w_f is the ventilation factor, for small compartments without horizontal vents

$$w_f = \left(\frac{A_v \sqrt{h_{eq}}}{A_t} \right)^{-1/2} \frac{A_f}{A_t} = O^{-1/2} \frac{A_f}{A_t} \quad (2)$$

where, A_v , A_f , A_t are the summed area of the vents, the floor area and the total enclosure area, respectively; h_{eq} is the weighted average of vent heights on all walls; and O is opening factor.

2.2 Steel temperature calculation

The temperature of steel members exposed to fire is usually determined with a 1D condensed heat transfer model [9, 10]. At present, various formulae are provided by fire codes in different countries for calculating the temperature of insulated steel members in fire [9]. In deriving those formulae by different technologies like separation of variables, laplace transform and green's function approach, the standard fire curve is always adopted to represent the fire environment [10]. The current formulae, which are based on the standard fire, might give unacceptable results for calculation in natural fires [10]. Besides, the current formulae are developed as "simplified" methods that their applications are limited to situations where the properties of the insulation materials are or can be treated as constant or temperature-independent [10]. The temperature of steel members in a fire can also be determined by advanced CFD simulations [11], or by solving the heat balance equation for modified one zone compartment fire model with considering the heat sink effect of steel members [12].

When evaluating the load capacity of a steel member in fire, the maximum temperature it reached is the critical parameter being considered. In our investigation, the maximum temperature of insulated steel members subjected to natural fires is calculated by using a recently developed simply closed-form expression given by [13]

$$T_{s \max} = -0.0024\Delta^2 + 2.528\Delta + 0.96 \quad (3)$$

where

$$\Delta = \frac{q_f k_b w_f}{40} \left(\frac{A_f / V}{d_i / \lambda_i} \right)^{0.77} \quad (4)$$

here A_f/V is the section factor of the member, in which A_f is the appropriate area of the fire insulation material per unit length, and V is the volume of the steel per unit length; d_i is the insulation thickness; and λ_i is the conductivity of the insulation.

2.3 Buckling temperature of steel columns

In the past decades, many researchers had studied the robust behaviour of steel columns in fire conditions experimentally and numerically [14-17]. Also, simple calculation approaches had been developed for predicting the critical temperature of steel columns [18,19].

The simple model developed by Franssen et al. [18] is adopted by EC3 [20] for calculating the buckling resistance of axially loaded steel column in fire, which is given by

$$N_{b,T} = \chi_T A f_{yT} \quad (5)$$

where

$$\chi_T = \frac{1}{\varphi_T + \sqrt{\varphi_T^2 - \bar{\lambda}_T^2}} \quad (6)$$

$$\varphi_T = \frac{1}{2} (1 + \alpha \bar{\lambda}_T + \bar{\lambda}_T^2) \quad (7)$$

$$\alpha = 0.65 \sqrt{\frac{235}{f_{y20}}} \quad (8)$$

$$\bar{\lambda}_T = \bar{\lambda}_{20} \sqrt{\frac{k_{yT}}{k_{E,T}}} = \sqrt{\frac{A f_{yT}}{P_{E,T}}} \quad (9)$$

where, A is steel cross section area; $f_{yT} = k_{yT} f_{y20}$ is high temperature yield strength, in which k_{yT} is the reduction factor for the yield strength of steel at the steel temperature T and f_{y20} is the yield strength of steel at room temperature; $\bar{\lambda}_T$ and $\bar{\lambda}_{20}$ are non-dimensional slenderness ratio at high and room temperatures, respectively; $k_{E,T}$ is the reduction factor for elastic modulus of steel at the steel temperature T ; $P_{E,T}$ is Euler buckling load at high temperature; and 0.65 in Eq. 8 is the severity factor at fire condition.

From Eq. 5, we can get the buckling temperature of steel column by solving

$$\frac{P_T}{N_{b,T}} = 1 \quad (10)$$

where P_T is the column service load at fire condition.

In EC3 [20], a closed-form equation has also been presented for calculating the buckling temperature of steel column in fire, that

$$T_b = 39.19 \ln \left(\frac{1}{0.9674 \mu_0^{3.833}} - 1 \right) + 482 \quad (11)$$

where $\mu_0 = P_T/N_{b,0}$ is utilization factor, in which $N_{b,0}$ is the column buckling resistance at room temperature. μ_0 must not be taken less than 0.013.

2.4 Thermal resistance of intumescent coatings

Unlike the conventional fireproofing materials (e.g. concrete, gypsum, SFRMs) whose thermal properties are temperature-dependent only, the performance of intumescent coatings under fire is complex that they will behave differently according to the applied heating condition, coating thickness, and protected structures [21]. As a result, the traditional standard test methods are not applicable to measure the thermal properties of intumescent coatings [22].

In practice, effective thermal conductivity or equivalent thermal resistance is usually adopted to characterize the thermal insulation property of intumescent coatings. Till now, many researchers had developed procedures to estimate the effective thermal conductivity of intumescent coatings [22]. In DD ENV13381-4:2002, the inverse equation of the EC3 [20] equation for calculating the temperature of insulated steel members to fire is presented to extract the effective thermal conductivity of intumescent

coatings. In our study, the simple approach proposed by [22] is adopted to assess the thermal insulation property of intumescent coatings.

At present, little work has been conducted to investigate the effects of aging on thermal insulation property of intumescent coatings subjected to fire. Wang et al. [3] reported some test data on this issue, which will be adopted in our study.

3 PROBABILISTIC APPROACH

3.1 Parameter uncertainties

Characterization of parameter uncertainties is of fundamental importance in a probabilistic approach. In modeling a post-flashover fire, the major source of parameter uncertainties is associated with the prescription of fire load, vent, and thermal inertia of the compartment boundary. Based on fire load surveys in different countries, several probabilistic models (e.g. Lognormal distribution [23, 24] and Gumbel type I distribution [25]) had been derived to characterize the distribution of fire load densities. In probabilistic codes, mean and COV of fire load density in different occupancies are given. For example, in Eurocode [5], the fire load density in office building has a mean of 420 MJ/m² and a COV of 0.3, and in JCSS probabilistic model code [26], the fire load density in office building has a mean of 600 MJ/m² and a COV of 0.3.

When calculating opening factor in deterministic approach, it is assumed that ordinary window glass is immediately destroyed when fire breaks out. However, in many conditions it is possible that some of the openings are partially or fully closed in fire conditions. In JCSS probabilistic model [26], a random parameter ζ is defined to consider the uncertainty of openings in fire conditions. The parameter is described by a truncated lognormal distribution with a mean of 0.2 and a COV of 1. Correspondingly, the effective opening factor in fire conditions is given by

$$O_{eff} = O(1 - \zeta) \quad (12)$$

In compartment fire modelling [4], when calculating heat transfer from fire environment to compartment boundary, the semi-infinite solid assumption is adopted, or in other words the fire temperature is assumed to be not affected by the thickness of the compartment boundary. Therefore, only the uncertainty in evaluating thermal inertia of the compartment boundary is considered. In the following studies, compartment boundaries are assumed to be constructed from normal weight concrete (NWC) only. In [27], the thermal inertia of NWC is described by a normal distribution with a mean of 2014 Ws^{1/2}/m²K and a COV of 0.09.

Intumescent coatings are reactive materials that they will swell under heating conditions. Li et al. [22] proposed a simple procedure to assess the thermal insulation property of intumescent coatings by using the concept of constant thermal resistance derived at a critical temperature of 550 oC. Due to different chemical components and complex intumescent behavior, the thermal insulation property of different type of intumescent coatings might be different significantly. As a result, although a number of studies on intumescent coatings have been reported in literature, available data to characterized the thermal insulation property of intumescent coatings is limited. In [28], the thermal conductivity of traditional fire protection materials and the thickness of the protection are both described by lognormal distribution. According to the definition of thermal resistance, which is the ratio of protection thickness to thermal conductivity, from probabilistic theory we know if protection thickness and thermal conductivity both follow lognormal distribution, then thermal resistance also follows lognormal distribution. As a result, in our study the constant thermal resistance of intumescent coatings is assumed to follow lognormal distribution with COV of 0.3.

Table 1 gives the statistics of uncertain parameters. The distributions of yield strength and elastic modulus of steel at room temperature are assumed to be normal. The COVs for yield strength and elastic modulus used in [28] are adopted. The distributions of the dimensions of the steel columns are also assumed to be normal. The distribution of column service load is assumed to be normal.

Table 1. Statistics of uncertain parameters

Parameters	Unit	PDF	Mean	COV
q_f	MJ/m ²	Lognormal	100-600	0.3
W	m	Deterministic	3.6/4.8	-
D	m	Deterministic	4.8/6.0	-
H	m	Deterministic	2.7/3.6	-
b	Ws ^{1/2} /m ² K	Normal	2014	0.09
W_o	m	Deterministic	3/4.5	-
H_o	m	Deterministic	1.5/1.8	-
ζ	-	Lognormal	0.2	1
d_i/k_i	Km ² /W	Lognormal	Rcon	0.3
B_s	mm	Normal	Nominal	0.05
H_s	mm	Normal	Nominal	0.05
t_w	Mm	Normal	Nominal	0.05
t_f	mm	Normal	Nominal	0.05
l_c	mm	Normal	2.5/3.5	0.05
f_{y20}	Mpa	Normal	235	0.063
E_{20}	Mpa	Normal	2.05e5	0.045
P_T	N	Normal	$\mu_0 * N_{b,0}$	0.3

3.2 Professional factor for maximum steel temperature

Professional factor is used to account for model error in calculation approaches, which is defined as the ratio of measured and predicted results.

The professional factor or model error for Eq. 3, PF1, is characterized by using test data reported by Konicek and Lie [29], and Kirby et al. [30], which has a mean of 0.955 and a COV of 0.014, and can be best described by lognormal distribution as shown in Fig. 1.

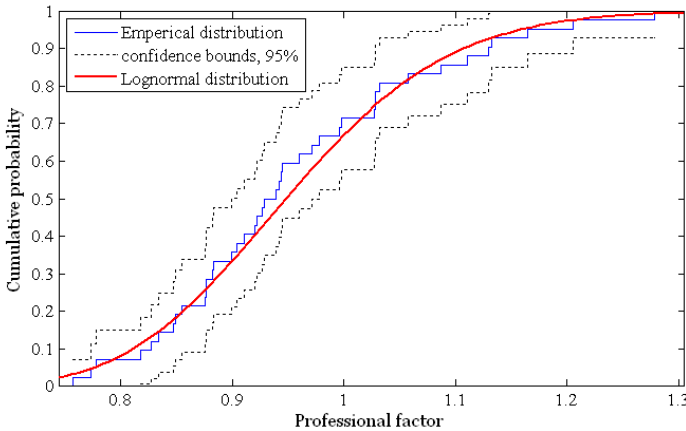


Figure 1. Probabilistic property for professional factor of Eq. 3

3.3 Professional factor for steel buckling temperature

Eq. 11 is adopted to predict the buckling temperature of steel column in fire. In [31], the professional factor for Eq. 11, PF2, are characterized by using test data reported in literature. Fig. 2 shows the professional factor with respect to utilization factor. The professional factor for Eq. 11 has a mean of 0.949 and a COV of 0.016, and can be best described by the extreme value distribution as shown in Fig. 3.

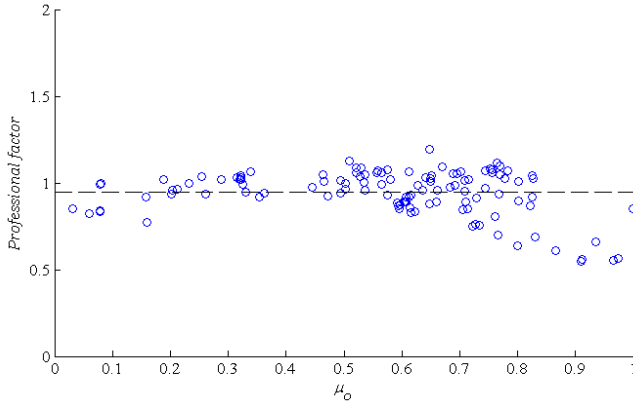


Figure 2. Professional factor for Eq. 11

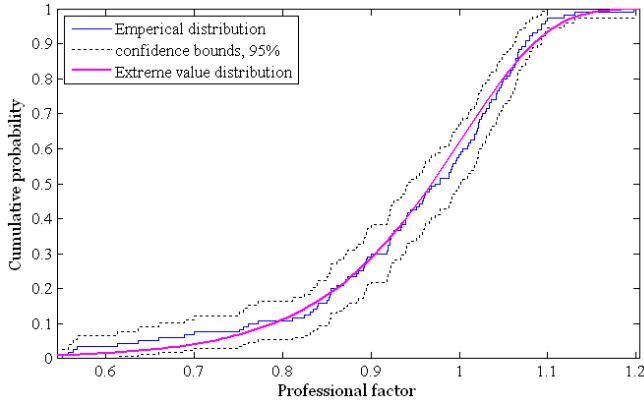


Figure 3: Probabilistic property for professional factor of Eq. 11

4 RELIABILITY ANALYSIS

4.1 Performance function

When exposed to fire, the steel columns will survive if the maximum temperatures they reached are less than their buckling temperatures. The performance function for reliability analysis of steel columns in fire is given by

$$G(\mathbf{X}) = R - S = T_b - T_{s \max} \quad (19)$$

4.2 Investigated cases

Table 2 gives the investigated cases considered in reliability analysis. Two fire compartments are considered and labeled as “Comp1” and “Comp2”, respectively. “Comp1” is 3.6 m width, 4.8 m depth and 3.0 m height, and has a window of 3.0 m width and 1.5 m height. “Comp2” is 4.8 m width, 6.0 m depth and 3.6 m height, and has a window of 4.5 m width and 1.8 m height. The two compartments both have fire doors which are assumed to be closed in fire condition.

Table 2. Investigated cases in reliability analysis

Label	Comp.	Sec.	λ_{20}	Coat.	Label	Comp.	Sec.	λ_{20}	Coat.
Case 1	Comp1	S1	50.2	C1	Case 7	Comp2	S1	68.9	C1
Case 2	Comp1	S1	50.2	C2	Case 8	Comp2	S1	68.9	C2
Case 3	Comp1	S2	32.9	C1	Case 9	Comp2	S2	46.1	C1
Case 4	Comp1	S2	32.9	C2	Case 10	Comp2	S2	46.1	C2
Case 5	Comp1	S3	24.8	C1	Case 11	Comp2	S3	35.0	C1
Case 6	Comp1	S3	24.8	C2	Case 12	Comp2	S3	35.0	C2

In each case, the design floor fire load density, q_f , ranges from 100 to 600 MJ/m² with increment of 100 MJ/m². The investigated q_f covers the range of type fire compartments given in JCSS model [27].

Three different steel cross sections are considered and labeled as “S1”, “S2” and “S3”, respectively. “S1” is H200×200×8×12, “S2” is H300×300×10×15, and “S3” is H400×400×15×20. In “Comp1” the column length is 2.5 m and in “Comp2” the column length is 3.5 m. The columns are pinned-pinned, and four sides exposed to fire. The nominal values of steel yield strength and elastic modulus are 235 MPa and 205000 MPa, respectively. The considered slenderness ratio ranges from 24.8 to 68.9 (along weak axis).

In each case, the utilization factor or load ratio, μ_0 , ranges from 0.1 to 0.6. In normal design, load ratios ranging from 0.3 to 0.6 are usually adopted. The probability of coincidence of a fire with maximum values of live load, snow, wind, or earthquake loads is negligible, and a structure is likely to be loaded to only a fraction of the design live load when a fire occurs [32]. Considering the combination of dead and live loads, and assuming the live load in fire condition is half of the design live load, then the lower and upper limit of load ratio in fire condition are 0.15 and 0.6 for normal design with load ratios ranging from 0.3 to 0.6. As a result, the considered load ratios cover the typical values in fire designs.

Two fire protections using intumescent coating are considered and are labeled as “C1” and “C2”, respectively. The coating thickness for “C1” is 1 mm and for “C2” is 2 mm. The performance of the intumescent coatings in different design fires are assumed to be the same as that in standard fire, and the insulation properties of the coatings are assumed to be equal to the values reported in [3,22]. Fig. 4 shows the constant thermal resistance of the coatings [22].

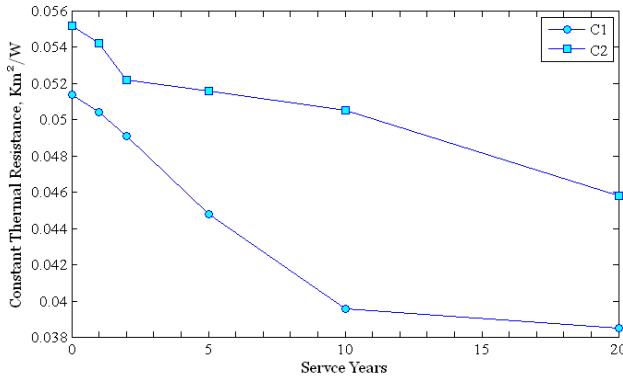


Figure 4: Constant thermal resistance for intumescent coatings in different service years reported in [22](Units in Km²/W)

4.3 Monte Carlo Simulations

Fig. 5 shows the flowchart for Monte Carlo simulations. For each loop, maximum steel temperature calculated by Eq. 3 (multiply by profession factor, PF1) is compared with buckling temperature of steel column calculated by Eq. 11 (multiply by profession factor, PF2). The number of simulations, N , is taken

as 1,000,000. Sensitive study shows that using more simulation loops, e.g. 2,000,000, 5,000,000, yields similar results.

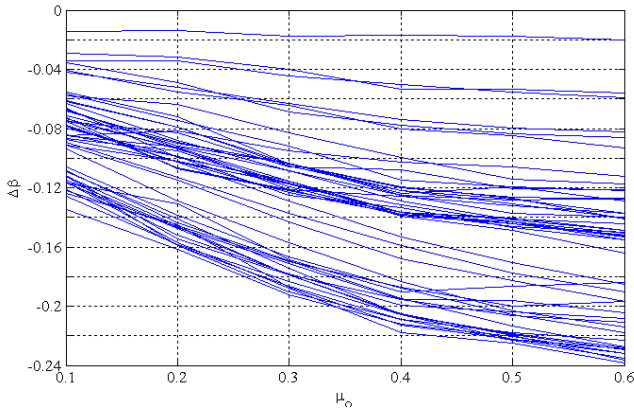


Figure 5: Difference among reliability index for 0 and 20 service years with respect to μ_0

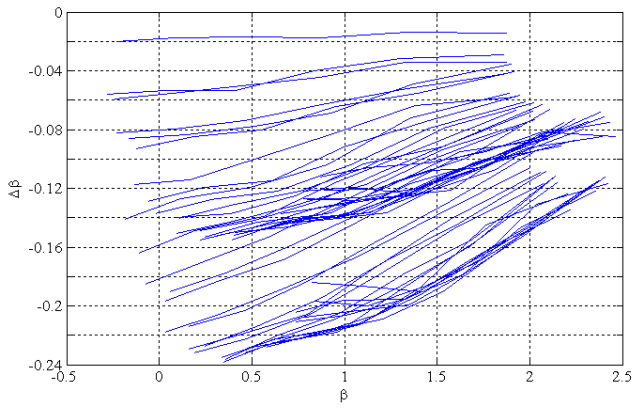


Figure 6: Difference among reliability index for 0 and 20 service years with respect to β at 0 aging year

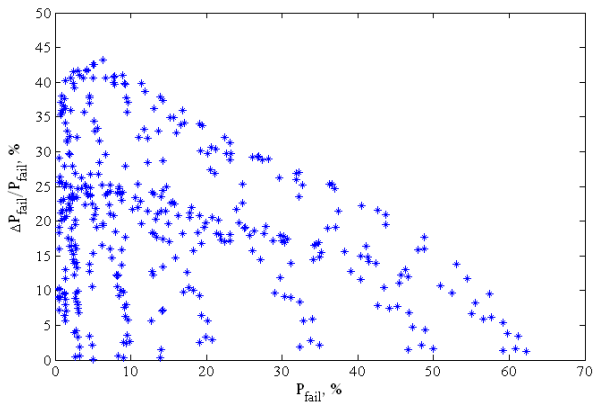


Figure 6: Difference among reliability index for 0 and 20 service years with respect to β at 0 aging year

4.4 Results

As shown in Figs 5 and 6, the reliability index, β , decreases with load ratio, μ_0 , increases. With service year increases, due to aging effect of intumescent coating, β decreases. The aging effect on β is comparatively more serious for cases with big β or high μ_0 than for cases with small β or low μ_0 .

For cases with $\beta \geq 1.5$ or $\mu_0 \leq 0.3$, the amount of the decrease of β due to aging effect, $\Delta\beta$, is less than 0.2 (the corresponding increase in failure probability, ΔP_{fail} , is less than 3%). For cases with $\beta < 1.5$ or $\mu_0 > 0.3$, the maximum is about 0.24 (the corresponding maximum ΔP_{fail} is about 9%). However, the ratio of failure probability change is large (can be about 45 %), as shown in Fig. 7.

5 CONCLUSION

Intumescent coatings are now the dominant passive fire protection materials used in engineering. Due to its organic components, intumescent coating has aging problems. The reliability of structures protected by intumescent coatings should be investigated. Based on the results of this study, the following conclusions can be drawn:

- Aging has effect of decreasing the reliability index, β , of steel columns protected by intumescent coatings. That decrease effect increases with aging year increases. The decrease of is more serious for cases with high μ_0 than for cases with low μ_0 .
- For the investigated cases with low load ratio ($\mu_0 \leq 0.3$), the amount of the decrease of due to aging effect, $\Delta\beta$, is less than 0.2 (the corresponding increase in failure probability, ΔP_{fail} , is less than 3%); and for the investigated cases with high load ratio ($\mu_0 > 0.3$), the maximum $\Delta\beta$ is about 0.24 (the corresponding maximum ΔP_{fail} is about 9%). However, the ratio of failure probability change is large (can be about 45 %).
- Limited by test data on thermal insulation properties of intumescent coating with aging effects, the study has only considered steel columns protected by two different thickness of coatings. Also, many assumptions have been made on the coating properties. Further studies using different coatings with various thickness are needed to obtain a general conclusion on the aging effect on reliability of intumescent coating protected steel columns in fire conditions.

REFERENCES

- [1] Fire resistance of steel-framed buildings, 2006 edition. Corus Construction and Industrial, 2006.
- [2] S Bourbigot, S Duquesne, JM Leroy. Modeling of heat transfer of a polypropylene-based intumescent system during combustion. Journal of Fire Sciences, 1999;17:42-56.
- [3] LL Wang, YC Wang, GQ Li. Experimental study of aging effects on insulative properties of intumescent coating for steel elements. Proceedings of the Sixth International Conference on Structures in Fire, MI, USA, 2010, pp.735-42.
- [4] D. Drysdale. An introduction to fire dynamics, 2nd edition. John Wiley and Sons, 1999.
- [5] EC1-1-2. Eurocode 1: Actions on structures - Part 1-2: General actions - Actions on structures exposed to fire. British Standards Institution (BSI), 2002.
- [6] JF Cadorin, JM Franssen. A tool to design steel elements submitted to compartment fires - OZone V2. Part 1: pre- and post-flashover compartment fire model, Fire Safety Journal, 2003;38:395-427.
- [7] K McGrattan, R McDermott, S Hostikka, J Floyd. Fire Dynamics Simulator (Version 5) User's Guide. NIST Special Publication 1019-5, National Institute of Standards and Technology (NIST), 2010.
- [8] V Bertola, E Cafaro. Deterministic-stochastic approach to compartment fire modeling. Proceedings of the Royal Society A, 2009;465:1029-41.
- [9] GQ Li, C Zhang. Thermal response to fire of uniformly insulated steel members: background and verification of the formulation recommended by chinese code CECS200. Advanced Steel Construction, 2010;6:788-802.

- [10] C Zhang, GQ Li, YC Wang. Sensitivity Study on Using Different Formulae for Calculating the Temperature of Insulated Steel Members in Natural Fires. *Fire Technology*, 2012;48:343-66.
- [11] C Zhang, GQ Li. Thermal response of steel columns exposed to localized fires - numerical simulation and comparison with experimental results. *Journal of Structural Fire Engineering*, 2011;2:311-7.
- [12] C Zhang, GQ Li. A new model for temperature calculation of steel members in post-flashover fires. *Advanced Steel Construction (Revision)*.
- [13] GQ Li, C Zhang. Simple approach for calculating maximum temperature of insulated steel members in natural-fires. *Journal of Constructional Steel Research*, 2012;71:104-10.
- [14] GQ Li, PJ Wang, YC Wang. Behaviour and design of restrained steel column in fire, Part 1: Fire test. *Journal of Constructional Steel Research*, 2010;66:1138-47.
- [15] YC Wang. Postbuckling behavior of axially restrained and axially loaded steel columns under fire conditions. *Journal of Structural Engineering*, 2004;130:371-80.
- [16] JM Franssen. Failure temperature of a system comprising a restrained column submitted to fire. *Fire Safety Journal*, 2000;34:191-207.
- [17] GQ Li, C Zhang. Creep effect on buckling of axially restrained steel columns in real fires. *Journal of Constructional Steel Research*. 2012;71:182-8.
- [18] JM Franssen, JB Schleich, LG Cajot, W Azpiazu. A simple model for the fire resistance of axially-loaded members - comparison with experimental results. *Journal of Constructional Steel Research*, 1996;37:175-204.
- [19] PJ Wang, GQ Li, YC Wang. Behaviour and design of restrained steel column in fire, Part 3: Practical design method. *Journal of Constructional Steel Research*, 2010;66:1422-30.
- [20] EN 1993-1-2, Eurocode 3: Design of Steel Structures - Part 1-2: General Rules - Structural Fire Design, British Standard Institution, London, 2005.
- [21] JF Yuan, YC Wang. Prediction of intumescent coating performance under cone calorimeter - a mathematical approach to performance based design. *Proceedings of the fifth international conference on structures in fire (SiF'08)*, 2008, Singapore, pp.713-24.
- [22] GQ Li, C Zhang, GB Lou, YC Wang, LL Wang. Assess the fire resistance of intumescent coatings by equivalent constant thermal resistance. *Fire Technology*, 2012;48:529-46.
- [23] SJ Melink. The distribution of fire load. *Fire Safety Journal*, 1993;20:83-8.
- [24] C Chauvoye, B Zhao, J Klein, M Fontana. Fire load survey and statistical analysis. *Fire Safety Science - Proceedings of the Ninth International Symposium*, 2008, pp.991-1002.
- [25] JB Schleich, LG Cajot, M Pierre. Valorisation project-Natural fire safety concept, final report. EUR 20349, Brussel 2002.
- [26] JCSS (Joint Committee on Structural Safety). Probabilistic model code, Part II- Load models. 2001.
- [27] S Iqbal, RS Harichandran. Reliability-based design specifications for simply supported steel beams exposed to fire. *Proceedings of the 10th International Conference on Structural Safety and Reliability*, Osaka, Japan, 2009.
- [28] S Iqbal, RS Harichandran. Capacity reduction and fire load factors for LRFD of steel columns exposed to fire. *Fire Safety Journal*, 2011, doi:10.1016/j.firesaf.2011.02.005.
- [29] L Konicek, TT Lie. Fire tests on protected steel columns under different fire severities. *Fire Study No.34*, Division of Building Research, National Research Council of Canada, 1974.
- [30] BR Kirby, DE Wainman, LN Tomlinson, TR Kay, BN Peacock. Natural fires in large scale compartments - a British Steel technical, fire research station collaborative project, British Steel, 1994.
- [31] C Zhang, GQ Li, YC Wang. Buckling Temperature of Axially Loaded Steel Columns in Fire. *Journal of Constructional Steel Research*. (Accepted).
- [32] BR Ellingwood. Load combination requirements for fire-resistant structural design. *Journal of Fire Protection Engineering*, 2005;14:43-61.

CONSIDERATION OF LOCAL INSTABILITIES IN BEAM FINITE ELEMENTS BY MEANS OF EFFECTIVE CONSTITUTIVE LAWS

Jean-Marc Franssen* and Baptiste Cowez*

* University of Liège, Belgium
e-mails: jm.franssen@ulg.ac.be, bcowez@doct.ulg.ac.be

Keywords: Structures in fire, Bernoulli, Beam finite Elements, Slender cross-section.

Abstract. *In the fire situation, Bernoulli beam finite elements are the workhorse used in the general calculation model for simulating the behaviour of the structure. Such finite elements treat all sections as class 1 (stocky) sections whatever the slenderness of the plates that make the section, allowing the development of a full plastic stress distribution in the section which leads to complete plastic redistribution in the structure. This type of element is thus not adapted for modelling structures that contain slender sections of class 2, 3 or 4. This document presents a new approach to take into account local instabilities using beam finite elements. The new approach is based on an effective constitutive law of steel. The effective law is not symmetrical with respect to tension and compression because, in tension, the stress-strain relationship is not modified whereas, in compression, the stress-strain relationship is modified.*

1 INTRODUCTION

The use of slender steel sections has increased in recent years because they provide excellent strength to weight ratio; this trend has also been favored by the development of higher steel grades. A major issue with slender sections is local buckling that may occur in compression zones of the elements made of slender plates, in the flange under compression for elements in bending, in both flanges and also in the web for elements in compression. In the fire situation, Bernoulli beam finite elements are the workhorse used in the general calculation model for simulating the behavior of the structure. The problem is that such finite elements treat all sections as class 1 (stocky) sections whatever the slenderness of the plates that make the section, allowing the development of a full plastic stress distribution in the section which leads to complete plastic redistribution in the structure. This type of element is thus not adapted for modeling structures that contain slender sections of class 2, 3 or 4.

2 EXISTING SOLUTIONS

To take local instabilities into account in a precise manner, the designer is left with no other choice than to use shell finite elements that can represent the local buckling phenomena. These elements are yet very expensive already for modeling single construction members, let alone for modeling complete structures.

It is thus desirable to use cheaper beam elements modified to take local buckling into account. The approach that is most often used is based on the concept of effective width [1,2]; the width of the plates is reduced in such a way that the plastic capacity of the reduced section is equal to the capacity of the slender plate under local buckling. This approach has first been proposed and has been used for analytical analyses. Yet, because the effective width depends on the stress level which in turn depends on the effective width, this procedure is iterative, which is already a serious complication when it comes to analyzing the situation of a single member under a defined loading.

If this approach has to be applied in beam finite elements used in transient or step-by-step analyses of complete structures, the additional level of iteration on the effective width leads to a severe modification, not only in the formulation of the finite element, but also in the formulation of the solution strategies of the code. Moreover, convergence problems may occur because it is not possible to derive the real tangent stiffness matrix of the elements.

One possible approximation is to assume that the stress has reached the yield strength in all compression zones and to perform the complete simulation with the minimum values of the effective width, thus eliminating the additional iteration level and requiring no modification of the code; only the definition of the sections is modified by the user. This procedure yet leads to incorrect value of the stiffness from the very early stage of initial loading as well as during all the simulation because excessive reduction of width has been imposed. This is all the more true in a structure subjected to fire because thermal restrains make it difficult to determine a priori where the compression and tension zones will exist in the structure. Moreover, different zones may change from tension to compression and vice versa, possibly several times, during the course of the simulation as thermal restraint develops, then are relieved by plasticity or, by the large displacements which generally develop at failure. It has to be mentioned that some authors proposed a strain-based approach to determine the effective width [3].

Other studies have been carried on modified beam finite elements in adding a complementary local displacement field on a classical beam element [4] but it also leads to a severe modification of the finite element formulation.

3 NEW PROPOSAL

It is here proposed to take local instabilities in beam type elements into account by means of effective constitutive laws of steel. The effective law has to be derived with the same objective as the effective width: the plastic capacity obtained with the effective law in the full section is equal to the capacity of the slender plate with the real material under local buckling. Figure 1 shows the difference between the effective width approach and the new proposal.

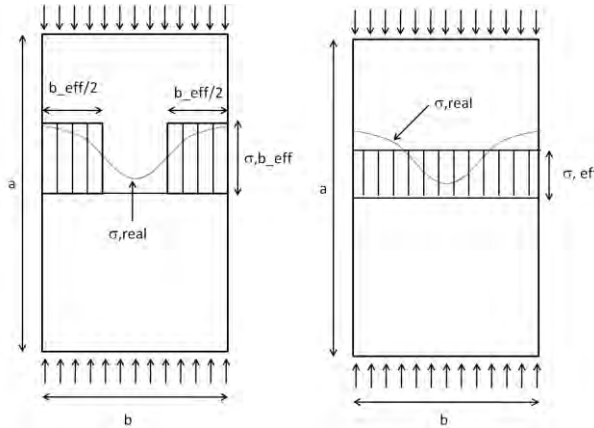


Figure 1. Difference between effective width method and proposed effective stress method

Because local buckling develops only in compression, the stress-strain relationship needs to be modified only in compression and remains untouched in tension, which leads to a non-symmetrical law with respect to compression-tension.

The tangent modulus at the origin of the law is not modified (which comes from the fact that low compression stresses do not produce local instabilities), but the development of local instabilities is reflected by a reduction of the limit of proportionality and of the effective yield strength.

The effective stress-strain relationship in compression should depend on the slenderness and on the boundary conditions of the plates, either supported on four sides as the web or supported on three sides as the flanges, and possibly also on the steel grade, but these conditions are known at the time of creating the model and can easily be entered by the user as new material properties. The material law should also depend on the temperature, but this is already the case for the real law considered up to now and there is nothing new here.

The method used in this research to determine the effective stress-strain diagram is based on the simulation of isolated plates modelled in SAFIR [5] with shell elements, simply supported on three or four sides and subjected to progressive imposed shortening in one direction. The simulations are performed first at ambient temperature and then at various elevated temperatures. From each simulation of a plate, the effective strain at any time is considered as the shortening of the plate divided by initial length of the plate, see Eq. (1), whereas the effective stress is considered as the reaction force applied on the edge of the plate divided by the sectional area of the plate, see Eq. (2). From the obtained effective stress-effective strain curve, the effective yield strength and effective proportionality limit can be determined depending on the relevant parameters.

$$\varepsilon_{eff} = \frac{\Delta L}{L_i} \quad (1)$$

$$\sigma_{eff} = \frac{R}{bt} \quad (2)$$

Figure 2, for example, shows an effective stress-strain diagram obtained for an isolated 150 x 75 mm plate, 8 mm thick which leads to a slenderness ratio of $75 / 8 = 9.375$, simply supported on three sides at a temperature of 500°C. Only the limit of proportionality and the effective yield strength have been reduced in the adapted material law called “User Steel” at that stage of the research work but the figure shows that the value of the characteristic strains (here taken as 2% and 15%) should also be adapted in the future.

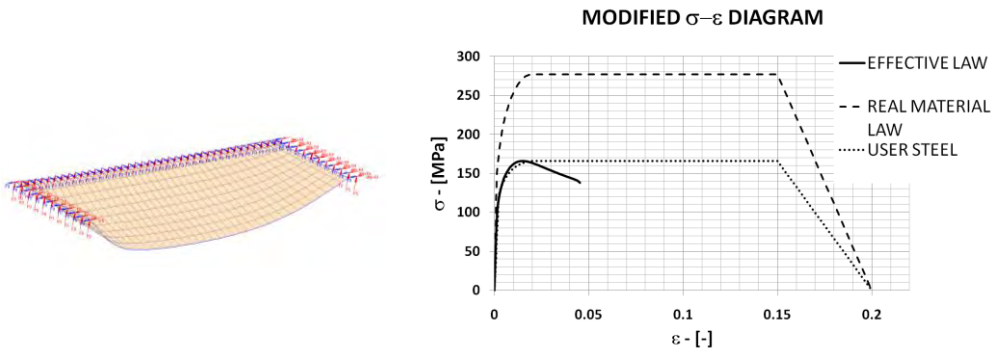


Figure 2. Modified stress-strain diagram for an isolated compressed plate at 500°C

When the tables that give the values of the parameters of the effective law (limit of proportionality, effective yield strength and characteristic strains) at various values of the temperature and slenderness will be established for all steel grades and for both boundary conditions, a simple adaptation of the subroutine at the material level can be made and easily introduced in any computer code. The user will only have to introduce a different material model for the web and for the flanges, to give the slenderness of the plate as a new material property, and the software will automatically take care of the temperature, of the stress level and of the direction of the stress, tension or compression. This procedure can be used also for analyses of structures at room temperature. It has to be underlined that, compared to existing methods, there is no stepwise variation of the behavior at the interface between the four classes; in fact,

there is no need to define the class because the adaptation of the material model is a continuous function of the slenderness. The limit of this approach is that it cannot capture local buckling produced by shear forces, but this is also the case for the effective width approach.

4 PARAMETRICAL STUDY ON PLATES

The main difficulty of this research resides in the determination of the parameters that will influence the modified stress-strain diagram and selection of the appropriate values for these parameters. This section explains how some of the most significant parameters were determined.

4.1 Dimensions of the plates

The present study is based on the elastic theory of plates [6,7]. For a rectangular plate simply supported on four sides, from this theory, the stress in the plate at any point (x, y) can be described by Eq. (3) and Eq.(4):

$$\frac{D}{t} \left(\frac{\partial^4 w}{\partial x^4} + 2 \frac{\partial^4 w}{\partial x^2 \partial y^2} + \frac{\partial^4 w}{\partial y^4} \right) = \sigma_{xx} \frac{\partial^2 w}{\partial x^2} \quad (3)$$

$$w(x, y) = w_0 \sin\left(\frac{m\pi x}{a}\right) \sin\left(\frac{n\pi y}{b}\right) \quad (4)$$

where $D = Et^3 / [12(1-\nu)]$ is the flexural stiffness, t is the thickness of the plate, m and n are the number of half-buckling waves in the length- and in the width-direction, w_0 is the amplitude of the initial imperfection. This equation leads to a reduction factor k in the critical stress of a uniaxially compressed plate.

$$\sigma_{cr} = \frac{D\pi^2}{tb^2} \left(\frac{mb}{a} + \frac{n^2 a}{mb} \right)^2 = \frac{D\pi^2}{tb^2} \left(\frac{m}{r} + \frac{n^2 r}{m} \right)^2 = \frac{D\pi^2}{tb^2} k^2 \quad (5)$$

In the last member of this equation, ratio a/b has been replaced by r . Considering the web of an I-beam as a long plate simply supported on four sides, the minimal buckling stress appears with a single half-buckling wave on the width of the plate ($n=1$) and it is possible to determine the value of m that minimises the critical stress for a given value of r .

$$\frac{d\sigma_{cr}}{dm} = 2 \left(\frac{m}{r} + \frac{r}{m} \right) \left(\frac{1}{r} - \frac{r}{m^2} \right) = 0 \quad (6)$$

$$m^4 - r^4 = 0 \quad (7)$$

This condition implies that the minimal critical stress appears for an integer value of the length-to-width ratio of the plate and that, if the plate is infinitely long, the plate buckles into an integer number of square cells of dimensions $b \times b$.

According to this result, square plates simply supported on four sides are used in this research to determine the effective stress-strain diagram of webs.

In order to determine the effective material law in half flanges, to model plates, simply supported on three edges, the same theory has been applied with an initial shape deformation described in Eq.(8), which leads to another value of m that minimises the critical stress as described in Eq. (9).

$$w(x, y) = w_0 \sin\left(\frac{m\pi x}{a}\right) \sin\left(\frac{n\pi y}{2b}\right) \quad (8)$$

$$m = \frac{a}{2b} \quad (9)$$

This condition implies that the minimal critical stress appears for an integer value of the length-to-width ratio of the plate and that, if the plate is infinitely long, the plate buckles into an integer number of rectangular cells of dimensions $b \times 2b$.

In accordance to this result, such rectangular plates simply supported on three edges are used in this research to determine the effective stress-strain diagram of flanges.

Figure 3 shows the influence of the geometric aspect ratio of the plate is shown here for a 75 mm wide plate supported on three sides with a varying length from 75 mm to 150 mm at a temperature of 500 °C (thickness = 8 mm and initial imperfection = 1.5 mm). As it can be seen on this figure, the critical stress appears for a plate of dimensions $b \times 2b$ with a single half-buckling wave $m = 1$. It is also shown that the same critical stress is obtained for a plate of dimensions $b \times 4b$ with two half-buckling waves $m = 2$ as expected.

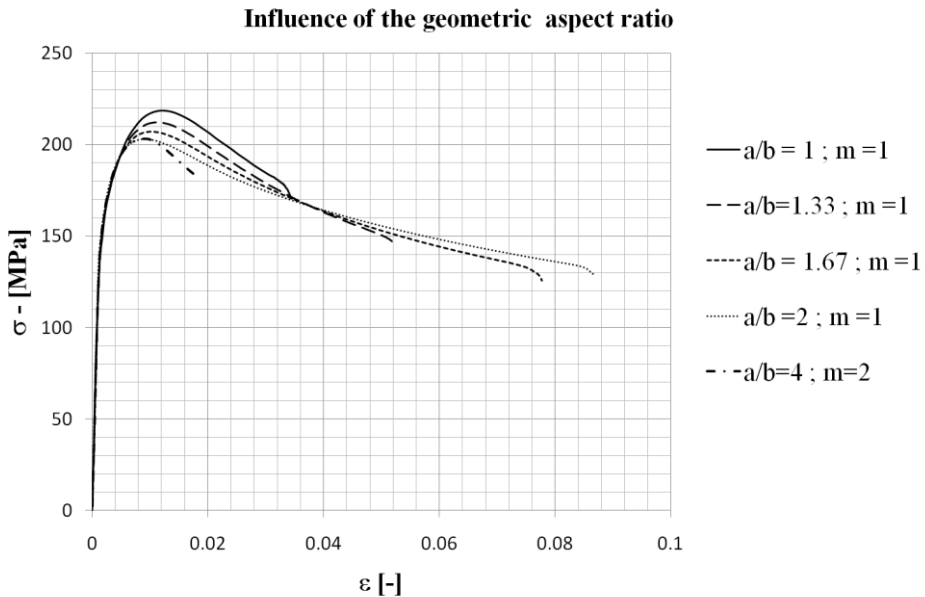


Figure 3. Influence of length-to-width ratio

4.2 Initial imperfection

A wide range of plates has been tested to see the influence of the amplitude of the initial imperfection on the stiffness, the proportionality limit and the yield strength. The dimensions of the tested plate for which the results are plotted are given in Table 1. The amplitude of the initial imperfection varies from 0.05 mm to 1.5 mm with an increment of 0.05 mm at each step.

Table 1. Dimensions of the tested plates for initial imperfection study.

Supported edges	Length [mm]	Width [mm]	Thickness [mm]	T[°C]	w0 [mm]
3	150	75	8	500	0.05 – 1.5

As it can be seen on Figure 4, the amplitude of the initial imperfection has a major influence on the effective yield strength but it does not influence as much the effective limit of proportionality and the stiffness. Similar results have been observed for plates simply supported on four sides.

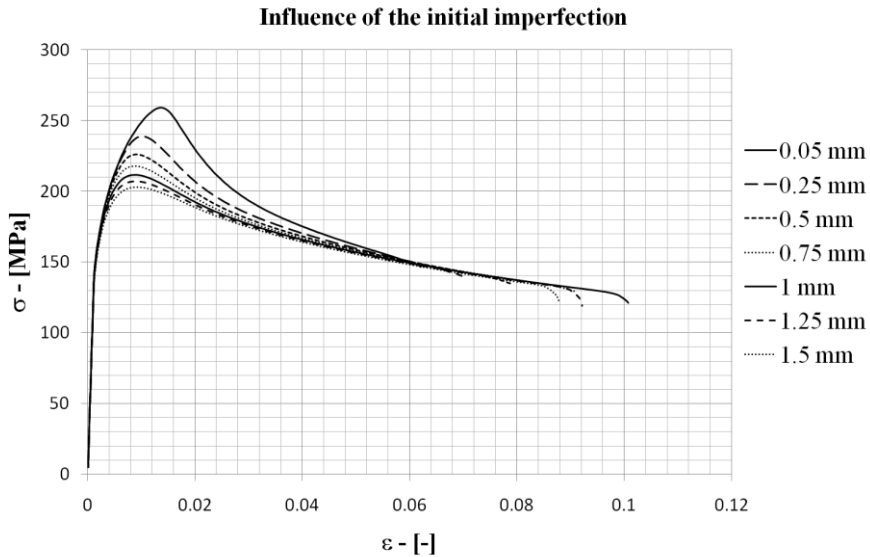


Figure 4. Influence of the initial imperfection

At this time, the amplitude of the initial imperfection has been taken as recommended by the Eurocode 3 part 1-5 [8] (min ($a/200$; $b/200$) for webs, $b/50$ for flanges = 1.5mm in this case) in the shell F.E. model. In the future, results obtained from experimental tests will be compared to the shell model to calibrate and adapt the amplitude of the initial imperfection.

4.3 Slenderness ratio

The influence of the slenderness of the plate is shown here in a $150 \times 75 \text{ mm}^2$ with an initial imperfection of 1.5 mm (as recommended by the Eurocode), with thickness varying from 4 to 10 mm at a temperature of 500 °C.

Figure 5 shows that the slenderness ratio b/t has almost no influence on the stiffness of the plate. With an increasing thickness, an increase of the proportionality limit and of the yield strength is observed

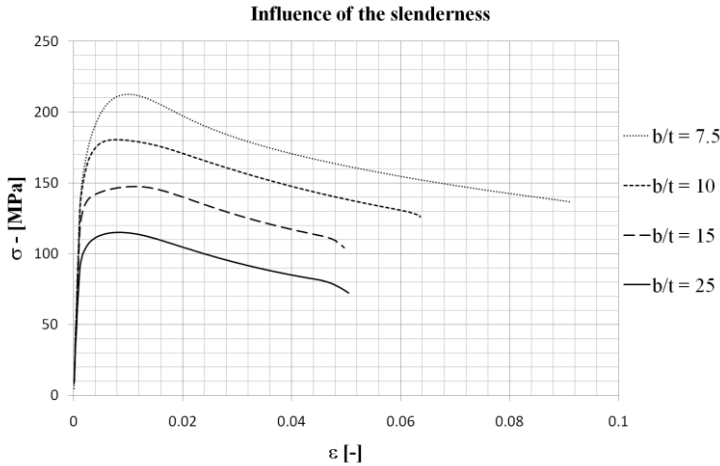


Figure 5. Influence of the slenderness on the effective law

4.4 Conclusions

From the preliminary analyses presented in this section 4, the effective stiffness of the new material will be the same as the real stiffness of steel. The effective yield strength and limit of proportionality will be determined for different slenderness of the plate (probably varying the dimensions of the plate for constant values of the plate thickness) but the aspect ratio of the plates will remain constant (one value for plates supported on 3 sides and one value for plates supported on 4 sides).

The analyses will first be made for initial geometrical imperfections as recommended by Eurocode 3 Part 1-5 but these values will be questioned on the base of comparisons with experimental test results when available because it is expected that the initial imperfection may influence the value of the effective yield strength.

5 EXAMPLE

As a feasibility study of the new proposal the results obtained with different methods for a 6-meters span laterally restrained I-beam subjected to bending at ambient and elevated temperature have been compared. The dimensions of the member are presented in Table 2. Table 3 gives the yield strength and of the limit of proportionality for normal steel at 20 and 500°C.

Table 2. Dimensions of the analysed member.

h_{web} [mm]	t_{web} [mm]	b_{flange} [mm]	t_{flange} [mm]	f_y [MPa]	Span [mm]
300	5	150	5	355	6000

Table 3. Yield strength and proportionality limit for normal steel at different temperature.

T [°C]	f_y [MPa]	f_p [MPa]
20	355	355
500	276.9	127.8

Tables 4 and 5 show the effective yield strength and the effective limit of proportionality obtained for the flanges and the web respectively of the chosen profile. Steel materials corresponding to these values

are used in the compression zones of the new beam F.E. model shown in Figure 6 whereas normal steel (STEEL_EN) is used in the zones in tension. This is because, at that stage, a material that is non-symmetrical with respect to compression and tension has not yet been developed. In the future, only one material would be used for both flanges and one material for the entire web.

Table 4. Dimensions and results of the isolated plate for the flange (USER_STEEL_FL)

Supported edges	Length [mm]	Width [mm]	Thickness [mm]	T□ [°C]	fy,eff [MPa]	fp,eff [MPa]
3	150	75	5	20	269.8	269.8
3	150	75	5	500	147.3	126.7

Table 5. Dimensions and results of the isolated plate for the web (USER_STEEL_WB)

Supported edges	Length [mm]	Width [mm]	Thickness [mm]	T□ [°C]	fy,eff [MPa]	fp,eff [MPa]
4	300	300	5	20	188	188
4	300	300	5	500	94	43

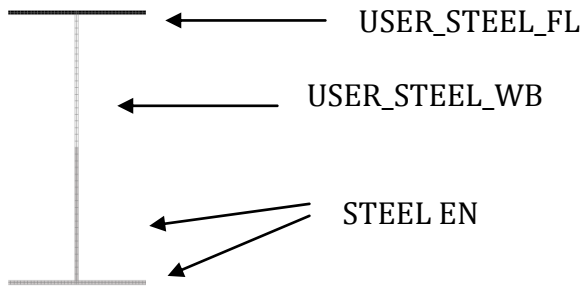


Figure 6. New steel material is used in the compression zones

Figure 7 shows the failure mode obtained with the shell F.E. model. In this figure, which is a zoom on the central part of the beam, it can be seen that local buckling appears in the flanges in compression and in the top of the web.

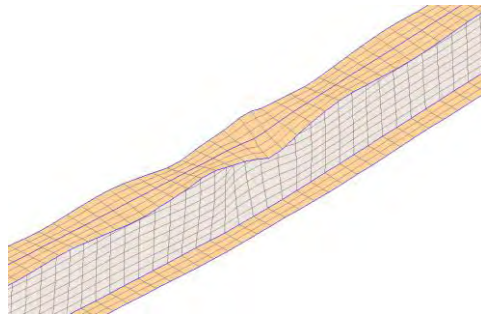


Figure 7. Failure obtained with shell F.E.

Figure 8 shows the comparisons of the results obtained from different analyses in the beam with simply supported ends subjected to an increasing uniformly distributed load at ambient temperature. As it can be seen on this figure, the classic Bernoulli beam F.E. cannot capture the correct behavior of the beam (assumed to be represented by the shell F.E) and gives unsafe results as expected. The effective cross section method cannot match the correct behavior; it gives results which are too much on the safe side

and the stiffness is underestimated since the earliest steps of the loading. This could be an issue in statically indeterminate structures comprising several members. The new method still slightly underestimates the ultimate load capacity but by a much smaller extent.

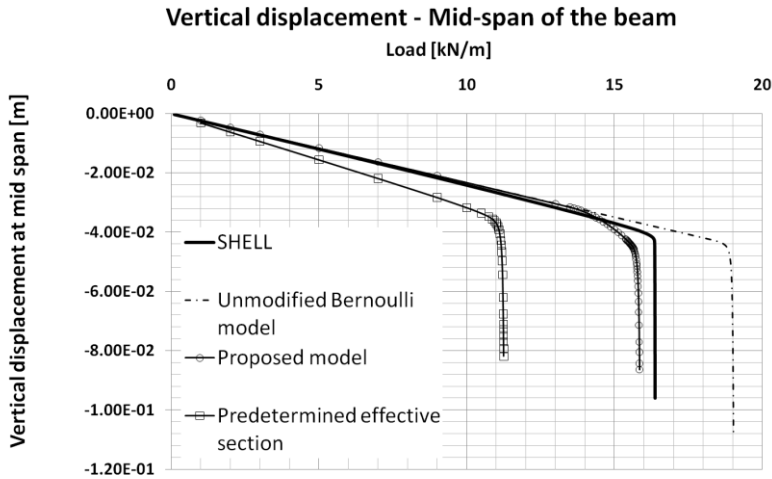


Figure 8. Results for different methods at ambient temperature

Figure 9 shows the results for the same beam loaded but at a temperature of 500°C. Also here, the new method gives safe results and the stiffness decreases earlier than the shell F.E.

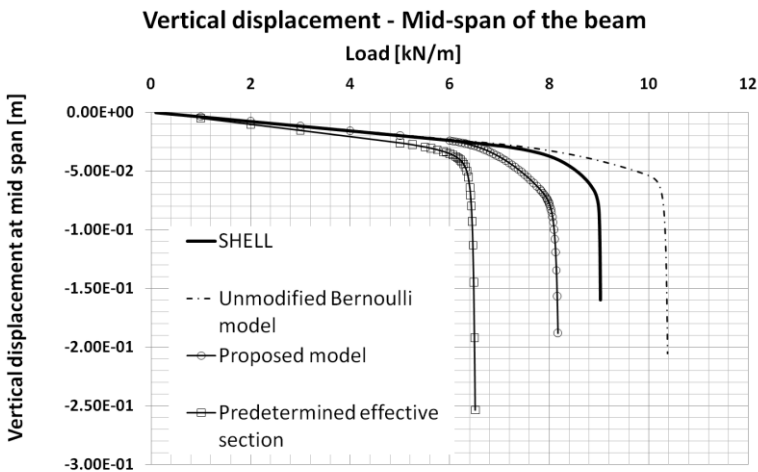


Figure 9. Results for different methods at elevated temperature

6 CONCLUSIONS

The perspective of the above described model is to give an alternative to the use of very expensive shell elements to simulate slender cross-section members in which local instabilities may occur. Preliminary investigations and feasibility studies are promising although. As it can be seen in Table 6, the number of degree of freedom is drastically reduced with the new model. This leads to substantially reduced computation time.

Table 6. Number of DoF and calculation time for different methods

Element Type	DoF [-]	Relative computation time [s]
Shell F.E.	14586	100
Beam F.E. USER_STEEL	359 (-97.5%)	11.7

Another advantage with this new model is the facility to construct a model with beam finite elements in comparison with models based on shell finite elements.

The modified constitutive law of the new steel material can still be improved in order to offer a better accuracy regarding the differences observed with the results obtained with the shell F.E.

REFERENCES

- [1] EN 1993-1-3. “Eurocode 3 – Design of steel structures – Part 1–3: General rules – supplementary rules for cold-formed members and sheeting”, *European Committee for Standardization, European Prestandard*, Brussels, 2006.
- [2] Bambach, M.R., Rasmussen, K.J.R., “Effective Widths of Unstiffened Elements with Stress Gradient”, *Journal of Structural Engineering*, Vol.130, No.10, 1611-1619, 2004
- [3] Knobloch, Fontana, M. “Strain-based approach to local buckling of steel sections subjected to fire”, *Journal of Constructional Steel Research*, Vol. 62, 44-67. 2006,
- [4] Degée, H., “Stability and non-linear behavior of thin-walled members and structures”, *International Journal of Structural Stability and Dynamics*”, Vol.7, No.2, 213-241, 2007.
- [5] Franssen, J.-M., “SAFIR, A thermal/Structural Program for Modelling Structures under Fire”, *Eng J A.I.S.C.*, 42, 143-158, 2005
- [6] Jones, R.M., *Buckling of bars, plates and shells*, Bull Ridge Publishing, Blacksburg, Virginia, 2006.
- [7] Rees, D. *Mechanics of Optimal Structural Design : Minimum Weight Structures*, John Wiley & Sons Ltd, United Kingdom, 2009.
- [8] EN 1993-1-5. “Eurocode 3 – Design of steel structures – Part 1–5: Plated structural elements”, *European Committee for Standardization, European Prestandard*, Brussels, 2003.

EXPERIMENTAL AND NUMERICAL TESTS ON BUILDING STEEL COLUMNS SUBJECTED TO FIRE

António M. Correia * and João P. Rodrigues **

* ISISE – Institute for Sustainability and Innovation on Structural Engineering
Polytechnic Institute of Coimbra, Portugal
e-mail: antonio.correia@isec.pt

** ISISE – Institute for Sustainability and Innovation on Structural Engineering;
University of Coimbra, ISISE, Portugal
e-mail: jpaulocr@dec.uc.pt

Keywords: experimental, numerical, tests, steel, columns, fire.

Abstract. *The present paper presents a thorough study on the fire behaviour of isolated steel columns with restrained thermal elongation. Based on a set of experimental tests on steel columns with restrained thermal elongation, a numerical model used for finite element simulations was developed using the advanced calculation commercial code ABAQUS, taking into account the interaction of the column with the surrounding building structure. A parametric study was carried out, in order to provide data for future development of a new simplified calculation method for fire design of HEA steel columns with restrained thermal elongation. It was concluded in this study that the axial and rotational restraints, considered acting together, have a minor influence on the reduction of the fire resistance and critical temperature of the columns.*

1 INTRODUCTION

Although the EN1993-1-2 (2005) [1] states that indirect actions such as the restraint to thermal elongation in structural elements should be considered in fire design, the simplified calculation methods proposed for fire design of steel columns do not take into account the restraint to its thermal elongation provoked by the building surrounding structure.

The behaviour of building steel columns subjected to fire has been widely studied both experimentally and numerically [2, 3, 4 and 5]. However, in several other studies on this issue, the interaction of the column with the adjacent building structure was not properly considered. With the aim of taking into account both axial and rotational restraint in the columns in case of fire, a new experimental set-up was constructed in the University of Coimbra, and a set of twelve full-scale tests on steel columns was carried out. These tests were used to calibrate a numerical model, used in a parametric study, which intend to lead to future proposals for new simplified design methods for steel columns in fire situation.

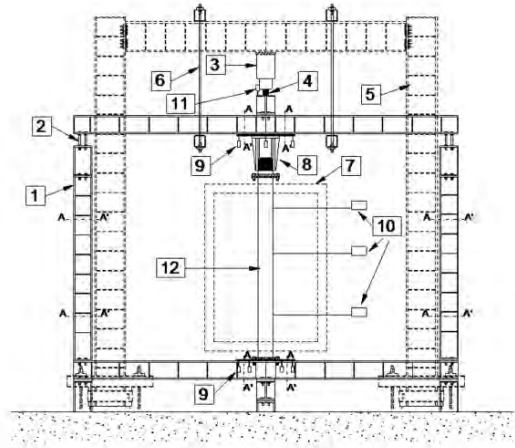
2 EXPERIMENTAL TESTS

2.1 Test Set-up and specimens

The numerical models were calibrated with results from fire resistance tests on steel columns with restrained thermal elongation carried out at the Laboratory of Testing Materials and Structures of the University of Coimbra [6]. A new experimental system was specially conceived and constructed for fire resistance tests on columns with restrained thermal elongation (figure 1).



a) view



b) scheme

Figure 1. Test set-up

This system comprises a 3D restraining frame of variable stiffness (1) with the function of simulating the stiffness of the surrounding structure to the column subjected to fire. The use of a three-dimensional frame allowed to take into account not only the axial stiffness but also the rotational stiffness, such as observed in real structures.

The restraining frame was composed by four columns, two upper beams and two lower beams, placed orthogonally. The beams of this frame were steel profiles HEB300, grade S355. The connections between these structural elements were performed with four M24 bolts, grade 8.8, except the connections between columns and the upper beams where threaded rods M27, grade 8.8, were used (2). Different hole positions in the flanges of the beams of this frame, allowed the assembly of the columns with different spans, giving thus different values of stiffness of the surrounding structure. The tested values of the axial stiffness of this restraining frame were 13, 45 and 128 kN/mm.

The columns were subjected to a constant compressive load that tried to simulate the serviceability load of the column when inserted in a real building structure. This load was 70% and 30% of the design value of buckling load at room temperature calculated according to EN1993-1-1 (2005) [7]. This load was applied by a hydraulic jack of 3MN (3) and was controlled by a load cell of 1MN between the upper beam of the restraining frame and the hydraulic jack (4). The hydraulic jack was placed in a reaction frame (5).

The thermal action was applied by a modular electric furnace (7) following approximately the standard ISO 834 fire curve. The furnace was composed of two modules of 1m and one module of 0.5m height, placed on top of each other forming a chamber around the column of about 1.5m x 1.5m x 2.5m.

A special device was built to allow accurate measurement and record of the restraining forces generated by the surrounding structure, during the heating process (8). It consists of a hollow and stiff cylinder, rigidly connected to the upper beams of the 3D restraining frame. On the top of the specimen, a massive cylinder rigidly connected, entered into the hollow cylinder and compressed a load cell of 3MN. This load cell measured the restraining forces generated in the column during the fire resistance test. The lateral surface of the massive cylinder was Teflon lined in order to reduce the friction with the external void cylinder.

The test column was placed in the centre of the three-dimensional restraining frame and was properly fitted to it, in each end plate, with four M24 bolts, class 8.8.

The test columns were made with HEA 160 and HEA 200 bare steel columns, 3m tall, steel grade S355. All specimens were instrumented with three type K thermocouples per section in 5 sections along the height of the column (figure 2).

In order to conduct the load applied on top of the beams, totally to the testing column, a special procedure was used: first unscrew the nuts of the threaded rods (2) that connect the columns with the upper beams of the 3D restraining frame, then apply the load, and after that screw the nuts of the threaded rods in order to provide the necessary restraining forces to the column.

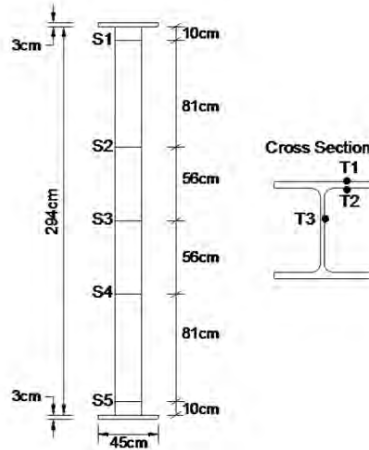


Figure 2. Test column with the thermocouples.

2.2 Test plan

Table 1 presents the plan of the fire resistance tests used for the calibration of the numerical models. Two steel cross-sections, HEA200 and HEA160, two load levels (LL), 30% and 70% of the buckling load at ambient temperature (P_0), and three values of the stiffness of surrounding structure ($K_{A,S}$), 13, 45 and 128 kN/mm, were tested.

It should be pointed out that the slenderness of the columns was calculated considering the length of the testing column, including the device in the top of it, used to measure the restraining forces, *i.e.*, 3.6m, and a buckling length of $0.7l_c$.

Table 1. Plan of the experimental tests

Test reference	Steel Profile	P_0 (kN)	$K_{A,S}$ (kN/mm)	f_{syd}
K13-LL70- λ 50.6	HEA 200	1000 (70%)	13	364
K13-LL70- λ 63.3	HEA 160	621 (70%)	13	399
K13-LL30- λ 50.6	HEA 200	428 (30%)	13	375
K13-LL30- λ 63.3	HEA 160	266 (30%)	13	399
K45-LL70- λ 63.3	HEA 160	621 (70%)	45	399
K45-LL30- λ 63.3	HEA 160	266 (30%)	45	385
K45-LL70- λ 50.6	HEA 200	1000(70%)	45	360
K45-LL30- λ 50.6	HEA 200	428 (30%)	45	364
K128-LL30- λ 50.6	HEA 200	428 (30%)	128	412
K128-LL30- λ 63.3	HEA 160	266 (30%)	128	395
K128-LL70- λ 50.6	HEA 200	1000 (70%)	128	412
K128-LL70- λ 63.3	HEA 160	621 (70%)	128	395

The reference K13-LL70- λ x indicates a column tested with an axial stiffness of the surrounding structure of 13 kN/mm, a load level (LL) of 70% and a slenderness (λ) of “x”.

3 NUMERICAL SIMULATIONS

3.1 Numerical model

A thorough numerical simulation of the experimental tests described in the previous section, as well as several other cases, with a geometrical and material non-linear analysis with imperfections, was carried out.

The numerical model was generated with three-dimensioned solid elements C3D8RT and C3D20RT from the ABAQUS (ABAQUS, 2005) program library. The C3D8RT and C3D20RT are defined as hexahedral 8 node and 20 node linear brick with reduced integration, an hourglass control solid element and a first-order (linear) interpolation element, with 3 degrees of freedom per node, referring to translations in the 3 directions X, Y and Z (global coordinates). These finite elements have one integration point, three degrees-of-freedom per node, corresponding to translations and six stress components in each element output. The hourglass control was introduced in the element to suppress spurious modes.

The finite element mesh was generated automatically by the ABAQUS program and the size of finite element was approximate 30mm for the specimen and 50mm for the surrounding structure.

The structural analysis was coupled temperature-displacement type, in which thermal and mechanical responses are performed together at the same time.

The temperatures used in the numerical simulations for calibration of the numerical models were the gas temperatures registered in the experimental tests. In the further numerical simulations, used to develop the simplified calculation method for fire design of steel columns, were used the ISO 834 standard fire curve. Thermal action was thus applied in the gas in the vicinity of the surfaces of the structural elements. Radiation was considered with emissivity coefficient $\varepsilon=0.8$ for steel with “radiant to ambient” surfaces. Convection was considered with convection $\alpha_c=25W/m^2\text{ }^\circ\text{C}$ with “surface film condition” surfaces. The thermal action in the tests for the calibrations of the model was considered with different temperatures at different heights according to the modules of the electrical furnace.

Constraints between different parts of the model were considered tie constraint, with interfaces of master-slave type.

The nonlinear geometry parameter (*NLGEOM=ON) was set to deal with the geometric non-linear analysis, namely with the large displacement analysis.

The mechanical properties of the steel at room temperature were determined experimentally in tensile tests in steel coupons. The thermal and mechanical properties of the steel at high temperatures given in EN 1993-1-2 (2005) [1] were considered in the numerical simulations.

The thermal action was applied on the test column, at different heights, according with the data taken from the furnace. It was observed in the tests a great temperature gradient along the vertical direction, in the gas inside the furnace. In such a way to reproduce as faithfully as possible the test conditions, different gas temperatures were applied in the gas in the vicinity of the column at different heights, with the corresponding coefficients of radiation and convection. The column was partitioned into two parts of 1m height, and one part 0.5m height, according to the furnace dimensions. The temperature used in the simulations were the ones recorded in the tests for each of the mentioned modules (figures 3 a) b) and c)).

The axial forces developed during the tests were determined with the stresses in the finite elements of the cylinder on top of the column. This cylinder was modeled exactly as in the experimental tests and was used only in the numerical simulations to calibrate the model (figure 3 e)).

The load was applied on top of the upper beam, in several points, to prevent excessive deformation of the upper flange (figure 3 f)).

Interaction between most of the surfaces was type “master-slave” with “tie-constraint” (figure 3 d)), except in the connections between the upper beams and peripheral columns.

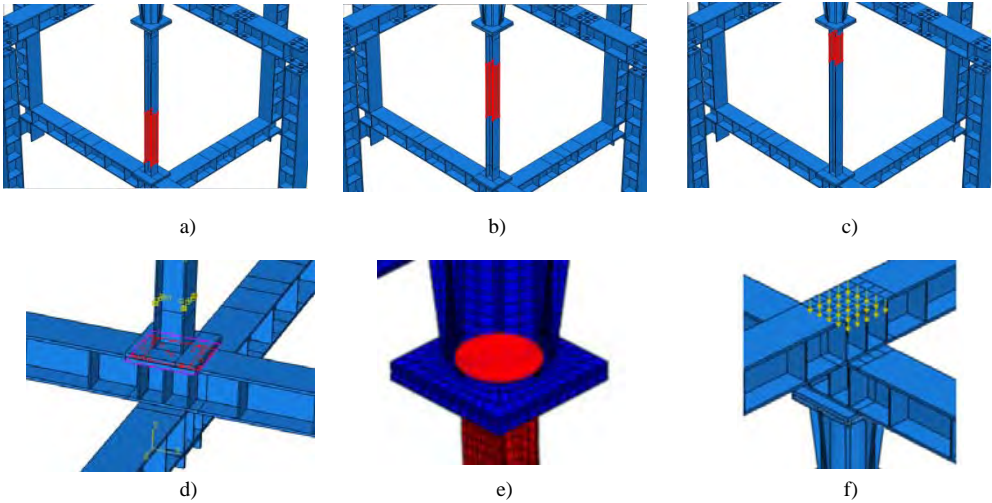


Figure 3. Numerical models

Geometrical imperfections were considered as initial eccentricity of the load and bow out-of-straightness of $l_c/1000$ at mid-height of the column. Eccentricities of $l_c/1000$ were also considered in the position of the column.

The test procedure used in the tests for transferring totally the initial applied load to the testing columns was reproduced in the numerical simulations using different time steps (figure. 4).

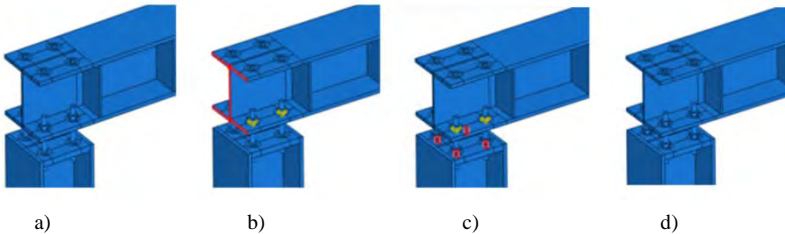


Figure 4. Procedure used in the numerical simulations to simulate the application of the initial applied load

In the first step, there was no constraint between the upper beams and peripheral columns of the restraining frame (figure 4 a)). The upper beams could descend in vertical movement of translation guided by a top constraint allowing only vertical displacement, as a slide (figure 4 b)). This was necessary due to the fact that geometrical imperfections were considered as an initial eccentricity and out-of-straightness of the column axis. In the second step, considering a tie constraint between the threaded rods and the end plate of the columns, to simulate the screw of the nuts, the thermal load was applied (figure 4 c) and d)). With this procedure, the initial load was exactly the load applied on top of the beams, in the center of the frame.

Table 2 summarizes the plan of the numerical simulations carried out, which comprises more than 60 numerical simulations. As in the experimental tests, HEA bare steel columns were simulated. In this numerical model the columns were considered in the restraining frame without the cylinder with the load cell.

Table 2. Plan of the numerical simulations

Test reference	$K_{A,S}$ (kN/mm)	α_A	β_R	l_c (m)	λ	LL (%)	P_0 (kN)
Ki-LL30- λ 35.1		0.03	1.08	2.50	35.1		495.7
Ki-LL30- λ 50.6		0.04	1.55	3.60	50.6	30	428.5
Ki-LL30- λ 65.4		0.05	2.00	4.65	65.4		359.5
Ki-LL30- λ 80.1		0.07	2.45	5.70	80.1		293.5
Ki-LL30- λ 90		0.07	2.75	6.40	90.0		254.8
Ki-LL50- λ 35.1		0.10	1.25	2.50	35.1		826.1
Ki-LL50- λ 50.6	$i=13, 45,$	0.14	1.80	3.60	50.6	50	714.2
Ki-LL50- λ 65.4	128 and ∞	0.19	2.33	4.65	65.4		599.1
Ki-LL50- λ 80.1		0.23	2.86	5.70	80.1		489.1
Ki-LL50- λ 90		0.26	3.21	6.40	90.0		424.6
Ki-LL70- λ 35.1		0.28	1.75	2.50	35.1		1156.6
Ki-LL70- λ 50.6		0.41	2.52	3.60	50.6	70	998.8
Ki-LL70- λ 65.4		0.53	3.25	4.65	65.4		838.8
Ki-LL70- λ 80.1		0.65	3.98	5.70	80.1		684.8
Ki-LL70- λ 90		0.73	4.47	6.40	90.0		594.5

In this table, the first column indicates the references of the numerical tests that are similar to the ones used in the experimental tests (table 1). The reference Ki-LL30- λ 35.1 indicates a column tested with an axial stiffness of the surrounding structure i ($i=13, 45, 128$ and ∞ kN/mm), a load level (LL) of 30% and a slenderness (λ) of 35.1.

It should also be pointed out that the modelling of the columns was performed at this stage without the device in the top of it, used to measure the restraining forces, and the slenderness of the columns was calculated considering the length of the column of 3.0m, and a buckling length of $0.7l_c$.

The initial applied load P_0 is again a percentage of the design value of the buckling load at room temperature calculated according to EN 1993-1-1 (2005) [7].

The non-dimensional axial restraint ratio α_A of the column is defined by a relation between the axial stiffness of the surrounding structure $K_{A,S}$ and the elastic axial stiffness of the column $K_{A,C}$:

$$\alpha_A = \frac{K_{A,S}}{K_{A,C}} \quad (1)$$

where

$$K_{A,C} = \frac{A_C \cdot E_s}{l_c} \quad (2)$$

in which A_C is the cross-sectional area of the column, E_s is the Young's modulus of the steel at room temperature and l_c is the column length.

The non-dimensional rotational restraint ratio β_R is defined by the relation between the structure rotational stiffness $K_{R,S}$ and the elastic rotational stiffness of the column $K_{R,C}$:

$$\beta_R = \frac{K_{R,S}}{K_{R,C}} \quad (3)$$

where

$$K_{R,C} = \frac{4 \cdot E_s \cdot J_C}{l_c} \quad (4)$$

in which J_C is the moment of inertia of the column cross-section around its minor axis.

The rotational stiffness of the structure $K_{R,S}$ was determined numerically with ABAQUS, considering the whole experimental system. Figure 5 presents the simulated cases summarized in Table 3.

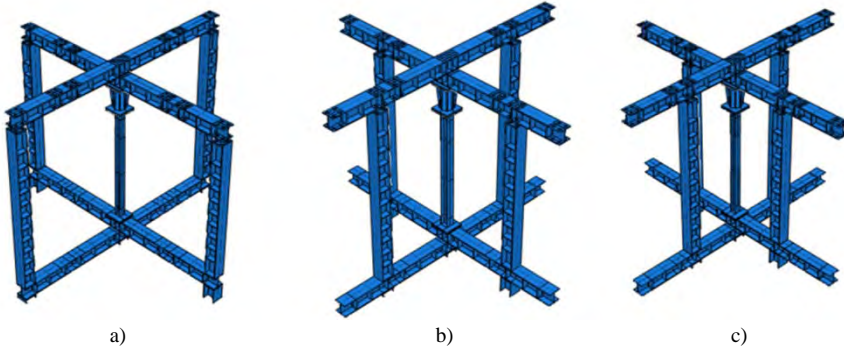


Figure 5. Test model of the 3D restraining frame for the different stiffness of the surrounding structure

Table 3. Axial and rotational stiffness of the surrounding structure

Case study	Span of the beams (m)	$K_{A,S}$ (kN/m)	$K_{R,S}$ (kNm/rad)
Fig. 5 (a)	3	13100	4827.5
Fig. 5 (b)	2	45000	5622
Fig. 5 (c)	1.5	128350	7844

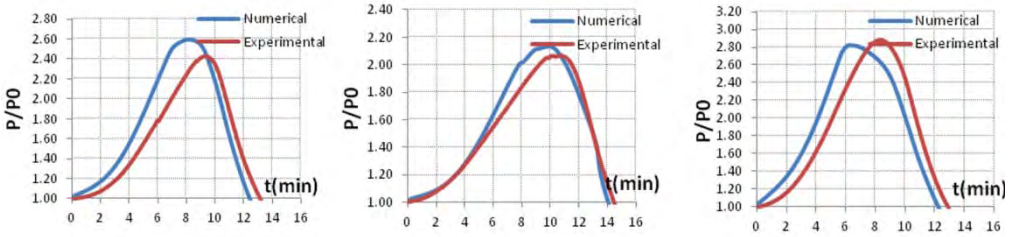
3.2 Calibration of the numerical model

The calibration of the numerical model consisted in testing several values of the emissivity coefficients for steel and fire, taking as reference the measured temperatures in the columns obtained in the experimental tests. The thermal action was applied in the gas in the vicinity of the steel column, and the convection and radiation performed by the coupled temperature-displacement analysis of ABAQUS. The adopted values for the emissivity were $\varepsilon_m=0.8$ for steel and $\varepsilon_f=0.8$ for the fire, and a convection coefficient factor of $\alpha_c=25W/m^2\text{ }^\circ\text{C}$, leading to very close temperatures to the ones obtained experimentally.

Table 4 – Comparison of results between experimental and numerical tests for isolated steel bare columns

Steel Profile	λ	Load (kN) (LL)	$K_{A,S}$ (kN/mm)	t_{crit} experimental (min)	t_{crit} numerical (min)	T_{crit} experimental ($^\circ\text{C}$)	T_{crit} numerical ($^\circ\text{C}$)
HEA	50	1000 (70%)	13	11.6	11.1	445	464
HEA	63	621 (70%)	13	10.6	8.5	428	453
HEA	50	428 (30%)	13	14.6	13.6	494	556
HEA	63	266 (30%)	13	13.6	12.9	545	560
HEA	63	621 (70%)	45	10.3	9.8	416	446
HEA	63	266 (30%)	45	13.2	12.4	511	556
HEA	50	1000 (70%)	45	11.4	11.1	433	442
HEA	50	428 (30%)	45	14.6	14.1	543	541
HEA	50	428 (30%)	128	14.3	13.4	538	553
HEA	63	266 (30%)	128	12.9	12.3	499	549
HEA	50	1000 (70%)	128	11.8	11.3	457	454
HEA	63	621 (70%)	128	9.6	10.1	404	437

Table 4 presents a comparison of critical times and critical temperatures for both the experimental tests and the numerical simulations of these 12 tests, used for the calibration of the model. Critical times were defined as the instant of time taken from the beginning of the test to the moment at which the restraining forces, after increasing, decrease up to the initial value. In the numerical simulations, the axial forces were calculated with the axial stresses on the top plate of the column. Critical temperatures were considered as the mean temperatures in the whole specimen, at that instant of time.



a) K45-LL30- λ 63.3 b) K45-LL30- λ 50.6 c) K128-LL30- λ 63.3

Figure 6. Evolution of axial forces for experimental tests and numerical simulations

In Figure 6, the comparison of the evolution of restraining forces as a function of time is presented. It can be observed a good agreement between the experimental tests and the numerical simulations.

4 RESULTS

For the purpose of developing a simplified calculation method for the assessment of the fire resistance of steel columns, a parametric study was carried out, covering different values of the main parameters involved, such as the slenderness of the column, the load level and the stiffness of the surrounding structure. In figures 7 and 8 the critical temperatures and critical times, are plotted for the different load levels and stiffness of the surrounding structure, as a function of the slenderness. The critical temperature is defined as the mean steel temperature of the column when the restraining forces after increasing and reaching a peak, reach again the value of the initial applied load. The definition of critical time is similar however now in terms of time.

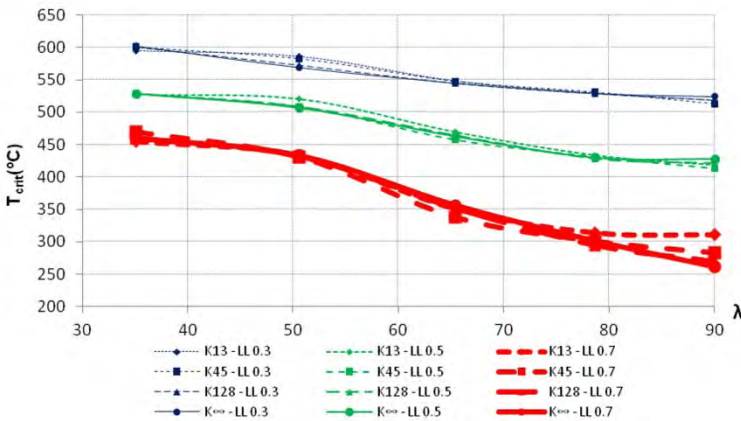


Figure 7. Critical temperatures for different values of the load level and axial stiffness of the surrounding structure as a function of the slenderness

From Figure 7, it is observed a reduction of the critical temperatures with the increasing of the slenderness of the columns. However, the reduction is more notorious for columns tested with the higher load level. The analysis of the two graphs, referring to different values of axial restraint, leads to the conclusion that the stiffness of the surrounding structure does not influence the critical temperatures.

From Figure 8, it can be said that the conclusions drawn for the critical temperatures are valid as well for the critical times. The great influence of the load level in reducing the fire resistance of the columns is clearly evident.

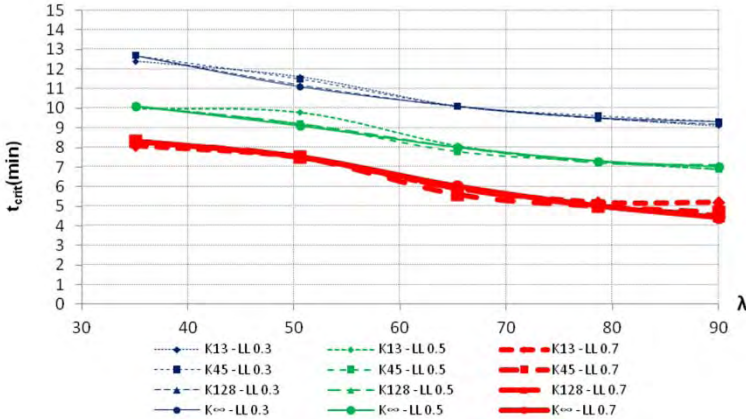


Figure 8. Critical temperatures for different values of the load level and axial stiffness of the surrounding structure as a function of the slenderness

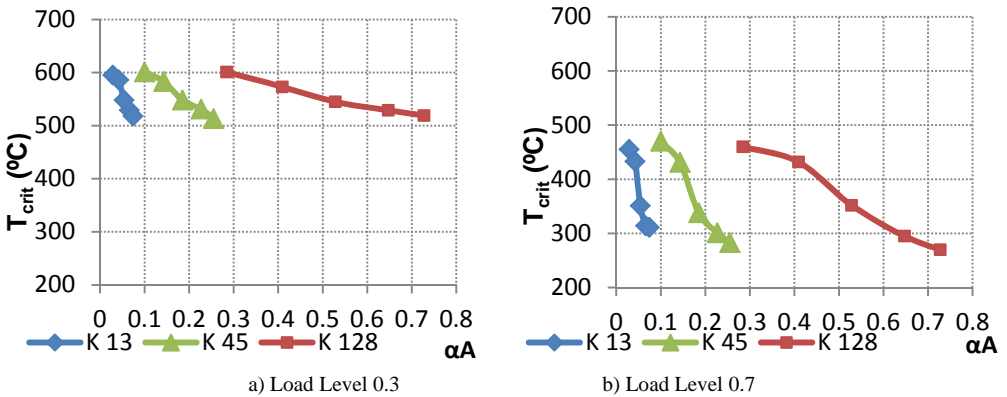


Figure 9. Critical temperatures as a function of the non-dimensional axial restraint ratio for different axial stiffness of the surrounding structure and load levels

Figure 9 a) and b) represents the critical temperatures in the steel columns, as a function of the non-dimensional axial restraint ratio for different load levels. The analysis of each graph, corresponding to a specific value of load level, leads to the conclusion that the critical temperatures are always between a certain range of temperatures, regardless of the stiffness of the surrounding structure. For the load level 0.3, the critical temperatures are within the range 500°C to 600°C, for the three values of stiffness of the structure 13, 45 and 128 kN/mm. For a load level of 0.7, the range of the critical temperatures is now

between 275°C to 450°C, and still the same for the three different values of stiffness of the surrounding structure.

6 CONCLUSION

The main conclusion of this research contradicts the general idea that in real structures higher stiffness leads to a reduction in the critical temperatures and fire resistance of the steel columns. Usually, in real buildings, associated to an increase of the axial restraint corresponds, to an increase of the rotational restraint. While the first leads to a reduction, the second leads to an increase in the critical temperature and fire resistance of the columns. In these tests, the reduction in the critical temperatures with the increase of the stiffness of the surrounding structure was negligible. This fact leads to the conclusion that the value of the restraint to thermal elongation has not a major influence in the fire behaviour of the column. An analytical formulation for the assessment of the fire resistance of steel columns in buildings may consider the columns fully restrained, because the fire resistance and critical temperatures are practically independent of the value of this restraint. The conclusions here presented are valid for the range of slenderness between 35 to 90, and load levels between 0.3 to 0.7, with any value of restraint from 13kN/mm up to fully restrained columns.

The load level was the most important parameter involved. Increasing the load level, leads to a great reduction of the critical temperatures and critical times of the columns.

The slenderness of the columns was also proven to have great influence on the critical temperatures and times.

The conclusion of this study, that the influence of the surrounding structure may have a negligible influence in the fire resistance of a steel column in a real structure of a building, was already stated by Franssen [8].

ACKNOWLEDGEMENTS

Special thanks are due to the support of the Portuguese Foundation for Science and Technology, under the framework of the projects REEQ 499/2001 and the PhD scholarship SFRH/BD/21939/2005.

REFERENCES

- [1] EN 1993-1-2 (2005). “Eurocode 3 - Design of steel structures - Part 1.2: General Rule - Structural fire design”. CEN, Brussels.
- [2] Ali F. and O’Connor D., “Structural Performance of rotationally restrained steel columns in fire”, Fire Safety Journal 36, 679-691, 2001
- [3] Burgess I.W., Olawale A.O., Plank R.J. “Failure of Steel Columns in Fire”. Fire Safety Journal, vol. 18, 183-201, 1992
- [4] Huang Z.F., Tan K.H. “Structural response of restrained steel columns at elevated temperatures. . Part 2: FE simulation with focus on experimental secondary effects”. Engineering Structures 29, 2036-2047, 2007
- [5] Burgess I.W., Najjar S.R. (1994). “A Simple Approach to the Behaviour of Steel Columns in Fire”. Journal of Constructional Steel Research 31, 115-134.
- [6] Correia A. M., Rodrigues J. P. “Fire resistance of steel columns with restrained thermal elongation”. Fire Safety Journal, vol. 50 (2012) 1-11.
- [7] EN 1993-1-1 (2005). “Eurocode 3 - Design of steel structures - Part 1.1: General Rules and rules for buildings”. CEN, Brussels.
- [8] Franssen J.M. “Failure temperature of a system comprising a restrained column submitted to fire”. Fire safety journal 34, 191-207, 2000.

HIGH-TEMPERATURE CREEP BUCKLING PHENOMENON OF STEEL COLUMNS SUBJECTED TO FIRE

Mohammed A. Morovat*, Michael D. Engelhardt*, Todd A. Helwig* and Eric M. Taleff**

* Ferguson Structural Engineering Laboratory, Department of Civil, Architectural and Environmental Engineering, The University of Texas at Austin
e-mails: morovatma@mail.utexas.edu, mde@mail.utexas.edu, thelwig@mail.utexas.edu

** Department of Mechanical Engineering, The University of Texas at Austin
e-mail: taleff@mail.utexas.edu

Keywords: Creep Buckling, Fire, Steel Columns, Elevated Temperatures, Time-Dependent Tangent Modulus.

Abstract. *This paper presents highlights of on-going research, which aims at developing analytical, computational and experimental predictions of the phenomenon of creep buckling in steel columns subjected to fire. Analytical solutions using the concept of time-dependent tangent modulus are developed to model time-dependent buckling behavior of steel columns at elevated temperatures. Results from computational creep buckling studies using Abaqus are also presented, and compared with analytical predictions. Material creep data on ASTM A992 steel is also presented in the paper and compared to existing creep models for structural steel. Both analytical and computational methods utilize material creep models for structural steel developed by Harmathy, by Fields and Fields, and by the authors. Predictions from this study are also compared against those from Eurocode 3 and the AISC Specification.*

1 INTRODUCTION

Successful implementation of performance-based structural-fire safety philosophy in designing steel structures depends on accurate predictions of thermal and structural response to fire. An important aspect of such predictions is the ability to evaluate strength of columns at elevated temperatures. Columns are critical structural elements, and failure of columns can lead to collapse of structures. One of the critical factors affecting the strength of steel columns at elevated temperatures is the influence of material creep. Under fire conditions, steel columns can exhibit creep buckling, a phenomenon in which the critical buckling load for a column depends not only on slenderness and temperature, but also on duration of applied load. This paper presents highlights of on-going research on the phenomenon of high-temperature creep buckling of steel columns.

2 CREEP OF STEEL AT ELEVATED TEMPERATURES

2.1 Background on creep

It is generally accepted that for ductile materials like steel, plastic strain is a function of shear stress and time at any specific temperature. Therefore, for design purposes, it is usually assumed that the total plastic strain at a constant temperature can be broken into a *time-independent component* or *slip* and a *time-dependent component* or *creep*. For typical loading rates seen in buildings, the inelastic response of steel at room temperature shows a very mild dependence on loading rate and virtually no dependence on

time. Therefore, time effects are normally neglected in the analysis and design of steel structures at ambient temperature. However, as temperature increases, steel exhibits increasingly significant creep effects. Creep tests, either in tension or compression, are usually conducted by subjecting a material to constant load, hence constant engineering stress at a specific temperature, and then measuring engineering strain as a function of time. A typical creep curve is often divided into the three stages of primary, secondary and tertiary creep. In the primary stage, the curve is nonlinear and typically exhibits a decreasing creep strain rate with increase in time. In the secondary stage, the creep strain rate is almost constant, and this stage is often referred to as steady-state creep. In the tertiary stage, the creep strain rate increases with time in an unstable manner. For steel, the shape of the curve, the magnitude of the creep strain and the time scale are greatly affected by both the temperature and the stress level.

Experimental and empirical models have been developed to predict creep strain of steel at elevated temperatures [1, 2, 3, 4, 5, 6]. One of the simplest and most widely used creep models is the Norton-Bailey model, also known as the creep power law [1, 2]. It should be noted that although the Norton-Bailey law is capable of modeling primary creep, it can define the steady-state or secondary stage of creep more accurately. One of the widely used creep models in structural-fire engineering applications proposed by Fields and Fields [5] incorporates a power law and represents creep strain, ϵ_c , in the form of a Norton-Bailey equation as follows:

$$\epsilon_c = at^b \sigma^c \quad (1)$$

In this equation, t is time and σ is stress. The parameters a , b and c are temperature-dependent material properties. Fields and Fields [5] derived equations for these temperature-dependent material properties for ASTM A36 steel. The model developed by Fields and Fields [5] is capable of predicting creep in the temperature range of 350 °C to 600 °C and for creep strains up to 6-percent. For initial studies of creep buckling of steel columns at elevated temperatures, one of the creep models used by the authors was the Fields and Fields [5] model. The application of this creep model together with observations will be discussed in more detail in the following sections of this paper.

Another creep model used by the authors in their study of creep buckling phenomenon at high temperatures is the one developed by Harmathy [4]. Harmathy [4] appears to be one of the first investigators who attempted at developing creep formula for structural steels at elevated temperatures. Harmathy proposed a creep model based on experiments on several structural and prestressing steels including ASTM A36. His model attempts to predict creep strains in both the primary and secondary stages of creep using the concept of activation energy for creep, Q_c . The model proposed by Harmathy [4] represents creep strain, ϵ_c , for steel as follows:

$$\epsilon_c \approx (3Z\epsilon_{c0}^2)^{1/3} \theta^{1/3} + Z\theta \quad \text{when} \quad \frac{d\sigma}{dt} = 0 \quad \text{and} \quad \theta = \int_0^t te^{-Q_c/RT} dt \quad (2)$$

In this equation, θ is the temperature-compensated time in Dorn's creep theory [3], Z is the slope of the secondary part of the creep curve (ϵ_c versus θ), also known as the Zener-Hollomon parameter [6], and ϵ_{c0} is the intercept obtained by extending the straight-line section (secondary part) of the $\epsilon_c(\theta)$ curve to the ϵ_c axis. The parameters ϵ_{c0} , and Z are stress-dependent material parameters.

Although models developed by Fields and Fields [5] and Harmathy [4] are referenced by many investigators in the field of structural-fire engineering, their predictions of creep strain for some applied stress levels and temperatures are quite different. As an example, predictions from these two models for ASTM A36 steel are compared and plotted in figure 1 for an applied stress of 23 ksi at 500 °C. As can be observed from this plot, the differences in the two models are significant. This difference in creep predictions and its impact on creep buckling behavior will be discussed in the following sections and emphasized throughout this paper.

2.2 Creep of ASTM A992 steel at elevated temperatures

In this section, representative results of a comprehensive material creep investigation of ASTM A992 steel at elevated temperatures are presented and discussed. In addition, these experimental creep results are compared against the creep material models by Fields and Fields [5] and by Harmathy [4] to verify the accuracy and reliability of their predictions. As mentioned in the previous section, creep tests are usually conducted by subjecting the material to constant stress and temperature, and then measuring strain as a function of time.

Such tests are commonly referred to as steady state tests, in which the specimens are heated up to a specified temperature and then loaded to the desired stress while maintaining the same temperature. It should be also mentioned that during the initial heating process, the load is maintained at zero to allow free expansion of the specimen. As far as the steel material is concerned, almost all specimens were cut from the web and flanges of a W4×13 section made from ASTM A992 structural steel. Some specimens were also cut from the web of a W30×99 section which is also of ASTM A992 steel.

Representative results of creep tests on ASTM A992 steel are shown in figure 2 for materials from the webs of the W4×13 ($F_y = 60$ ksi) and the W30×99 ($F_y = 62$ ksi) sections. This figure simply shows the measured creep strain versus time response of ASTM A992 steel after being exposed to specified constant stresses at 500 °C and 700 °C. As can be observed from figure 2, it is clear that creep effects are highly significant in the stress-strain response of structural steel at temperatures on the order of 500 °C to 700 °C; temperatures that can be expected in steel members during a fire. It should be specifically noted that some of the curves in figures 2(a) and 2(b) show very large creep strains in the time frame of one to two-hours, which may be considered a representative time frame for a compartment fire. Interestingly, curves at 700 °C indicate that the material from the web almost immediately enters the tertiary stage of creep, with a rapid increase in creep strain over a short time interval. In the case of the W4×13 web material, the coupon actually fractured approximately after 44 minutes, a phenomenon known as *stress rupture* or *creep fracture*.

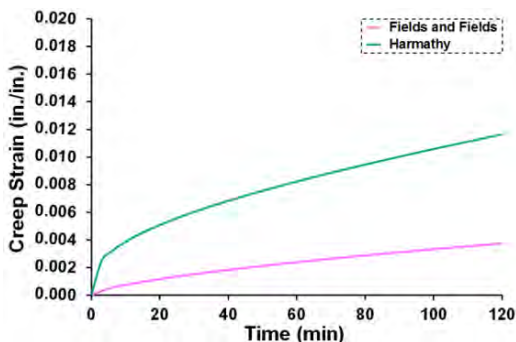
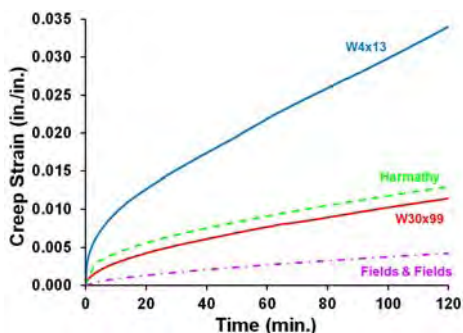
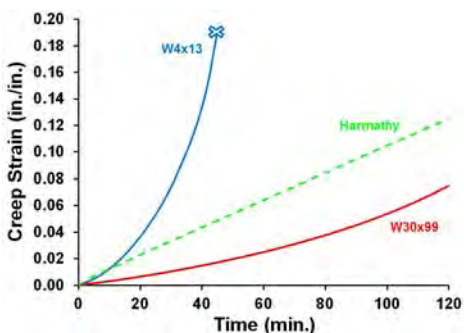


Figure 1. Comparison between Fields and Fields [5] and Harmathy [4] models at 23 ksi and 500 °C.



(a) Constant stress of 40 ksi at 500 °C.



(b) Constant stress of 10 ksi at 700 °C.

Figure 2. Verification of material creep models against the web materials of W4×13 and W30×99.

Figures 2(a) and 2(b) also compare experimental results from the web material of the W4×13 sections and the web material of the W30×99 section. As is clear, there is appreciable difference in material creep response between the two specimens that are both ASTM A992 steel. This observation suggests that there may be large variability in creep response for a particular grade of steel, and this variability should be considered in any attempt at developing *general* material creep models for structural steel at elevated temperatures. Note that some of this variability may be due to experimental error resulting from factors such as non-uniform temperature distribution over the gage-length of the steel coupons, inaccuracies involved in temperature and strain measurements, inaccuracies in maintaining constant stress, etc.

Predictions from material creep models are also compared with experimental results in figures 2(a) and 2(b). As can be seen in these figures, there is not generally a very good agreement between material creep model predictions and experimental creep results. It should be noted that in order to compare the experimental material creep predictions to those from Fields and Fields [5] and Harmathy [4] models, corrections must be made due to the difference in materials. As mentioned before, these two material creep models are developed for ASTM A36 steel, not for ASTM A992 steel. A suggested methodology to make this correction is to adjust for the stress values considering the difference in yield strength of materials in consideration [7]. Since ASTM A36 steel has lower yield strength than that of ASTM A992 steel, the stress values should be reduced in creep equations (a reduction factor equal to the ratio of 36 ksi to 60 ksi has been considered). Therefore, some of the discrepancies observed in figure 2 are due to such stress adjustments. Moreover, in order to draw any conclusion on inconsistencies observed in figure 2, limitations in the scope of creep models and approximations involved have to be carefully considered. It should also be added that the creep models by Fields and Fields [5] and by Harmathy [4] are suitable for predicting creep strains in the primary and secondary stages of creep. As a result, they cannot capture tertiary creep behaviors observed at 700 °C as can be seen in figure 2(b). All in all, observations like these clearly indicate the need for more reliable creep models for structural steel at elevated temperatures.

As part of the comprehensive material creep investigation of structural steel at elevated temperatures, equations in the form of a double power-law have been developed to describe creep of ASTM A992 steel at elevated temperatures. Equation (3) represents the general form of such creep equations. Like in equation (1), the parameters a , b , c , d , e and f are temperature-dependent material properties.

$$\epsilon_c = a t^b \sigma^c + d t^e \sigma^f \quad (3)$$

One of the most important features of equation (3) is that it represents a double-curvature function, which makes it capable of modeling the entire creep curve that is also double-curvature in nature. As mentioned before, creep models by Fields and Fields [5] and by Harmathy [4] being single-curvature functions cannot model the three stages of the creep curve, specifically the tertiary part. Another advantage of the double power-law equation is its ability to relate creep strain and time using just one single continuous equation. Since the main goal here is to develop equations to predict the time-dependent tangent modulus, the smoothness of the proposed stress-strain law is important, since the tangent modulus is the derivative of the stress-strain curve [8]. Application of this model to predict creep buckling of steel columns will be presented and discussed in the following sections of this paper.

3 CREEP BUCKLING OF STEEL COLUMNS AT ELEVATED TEMPERATURES

3.1 Background on creep buckling

The term *creep buckling*, as used herein, refers to the phenomenon in which the critical buckling load for a column depends not only on slenderness and temperature of the column, but also on the duration of applied load. Since creep effects are not significant at room temperature, the buckling load for a steel column of given effective slenderness KL/r at room temperature is independent of the duration of applied load. As temperature increases, the initial buckling load (at time zero) decreases, due to the decrease in material strength, modulus and proportional limit. Consequently, the buckling capacity at initial application of load depends only on temperature. But, as temperature increases and material creep

becomes significant, the buckling load depends not only on temperature, but also on the duration of load application.

3.2 Creep buckling analysis of steel columns

To better evaluate the potential importance of creep buckling in structural-fire engineering applications, preliminary creep buckling analyses have been conducted by the authors. These analyses, analytical and computational, attempt to predict the elevated-temperature creep buckling strength of a pin ended steel column. For these analyses, a W12×120 section made of ASTM A36 steel is considered. Moreover, the effective slenderness ratio is kept constant by considering only one single column length of 240 inches.

For the analytical creep buckling studies, the concept of time-dependent tangent modulus proposed by Shanley [9] is utilized, along with the creep material models developed by Harmathy [4] and by Fields and Fields [5], both for ASTM A36 steel. This analytical method basically uses the Euler buckling equation and replaces Young's Modulus, E , with the tangent modulus, E_T , which is a function of time, stress and temperature. In order to calculate the time-dependent tangent modulus, the isochronous stress-strain curves need to be constructed. Simply put, isochronous stress-strain curves are constant-time stress-strain curves derived from creep curves. The slope of the tangent to the isochronous stress-strain curve at any stress and time value is the time-dependent tangent modulus. Since the material creep equation by Fields and Fields [5] has a simple form, it can be used to explain the procedure of constructing isochronous stress-strain curves and evaluating time-dependent tangent moduli correspondingly. At a specific time, equation (1) can be rewritten as follows,

$$\varepsilon_c = a_0 \sigma^c \quad (4)$$

where a_0 is equal to $a t^b$ and is constant. In fact, since a_0 is dependent on a , b and t , it is both temperature and time dependent. It can also be inferred from equation (4) that each constant-time, stress-creep strain curve is conceptually equivalent to a time-independent stress-plastic strain curve, here with the power law representation [8]. As a result, the total strain which is the sum of elastic and inelastic (in this case creep) strains can be written as,

$$\varepsilon = \sigma/E + a_0 \sigma^c \quad (5)$$

Equation (5) therefore represents the isochronous stress-strain curves based on the creep model by Fields and Fields [5] (see also figure 3). Consequently, equation (5) can be used to derive an expression for time-dependent tangent modulus. In other words, using the differential form of equation (5) and considering the tangent to be the slope of the stress-strain curve

($d\sigma/d\varepsilon$), a mathematical expression relating tangent modulus to stress can be derived as follows (see also figure 4),

$$E_T = \frac{E}{1 + [a_0 c \sigma^{(c-1)}] E} \quad (6)$$

in which, E is the temperature-dependent Young's modulus and E_T is the tangent modulus, here a function of both time and temperature. Since $E_T / E = P_{cr} / P_E$, equation (6) yields an equation for creep buckling which is shown as equation (7).

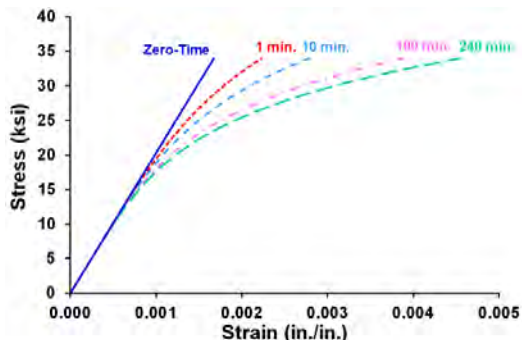


Figure 3. Representative isochronous stress-strain curves at 400 °C, based on equation (5).

$$P_{cr} = \frac{P_E}{1 + [a_c \sigma^{(c-1)}] E} \quad (7)$$

P_E is the Euler buckling load at elevated temperatures in equation (7). At buckling, $\sigma = \sigma_{cr} = P_{cr} / A$, therefore equation (7) can be rewritten as follows,

$$P_{cr} + \left[\frac{a_c c E}{A^{(c-1)}} \right] P_{cr}^c = P_E \quad (8)$$

in which A is the cross sectional area of the column. Equation (8) can be solved iteratively to get the P_{cr} as a function of time at a constant temperature. Sample solutions of equation (8) applied to a 240-inch long $W12 \times 120$ column are plotted in figure 5.

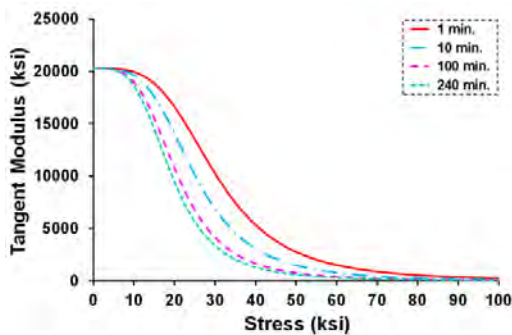
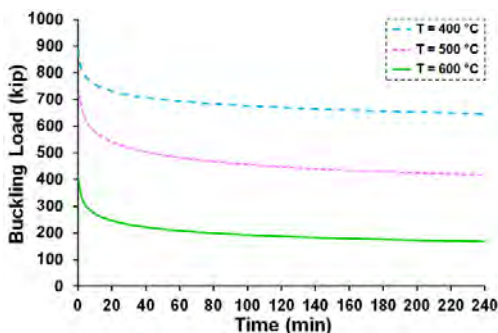
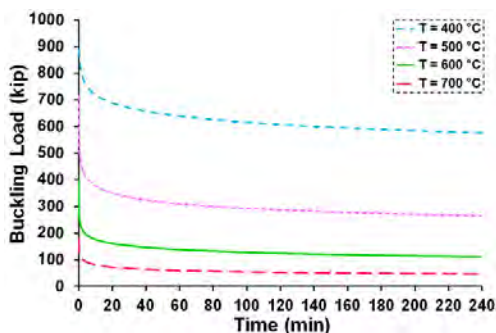


Figure 4. Representative isochronous tangent modulus-stress curves at 400 °C, based on equation (6).



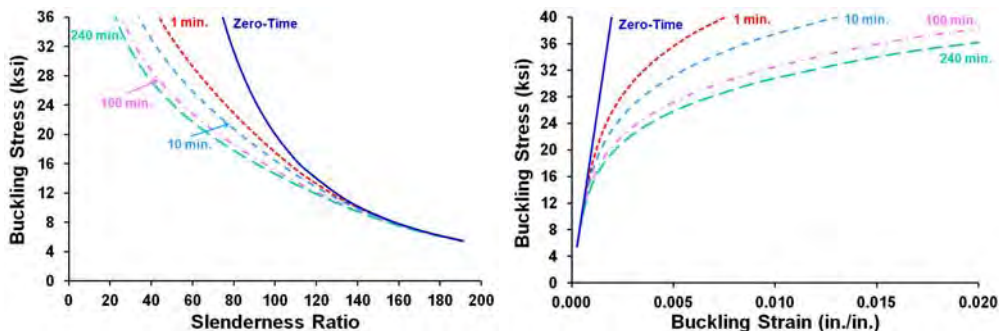
(a) Using Fields and Fields' creep model.



(b) Using Harmathy's creep model.

Figure 5. Analytical creep buckling curves using time-dependent tangent modulus method.

Using equation (8) for several column lengths, creep buckling curves can be constructed in the conventional form of column curves represented by buckling stresses versus effective slenderness ratios. In other words, time-dependent effects on column strength can be represented by isochronous column curves as shown in figure 6(a). In this figure, the Zero-time curve represents the Euler buckling curve or elastic buckling phenomenon. As can be observed from figure 6(a), the elastic buckling phenomenon of steel columns at elevated temperatures is time-independent. Moreover, it is really possible to construct column curves as plots of critical stress against the term, $\pi^2 / (KL/r)^2$, which can be thought of as the *critical or buckling strain* ($\sigma_{cr} = \epsilon_{cr} E_T$). This form of column curves, as shown in figure 6(b), indicates a close relation between the stress-strain behavior and the column strength. To be more specific, the curves in figure 6(b) would be true representations of isochronous stress-strain curves in compression provided that secant modulus instead of tangent modulus were used in evaluating steel column strength at elevated temperatures [9].



(a) Isochronous column curves. (b) Column curves as critical stress-strain curves.
 Figure 6. Analytical creep buckling curves plotted in the conventional form of column curves.

As a final note on the analytical formulation, it should be added that this method disregards any initial imperfections and assumes a perfectly straight column. Moreover, this method predicts the Euler buckling load as the zero-time buckling load at any given temperature. To be more specific, this method only considers time-dependent inelasticity and ignores time-independent inelasticity due to the applied load at time zero. To have a more sensible model, a cap was placed on the maximum predicted buckling strength to reflect the effects of inelasticity and initial crookedness at time zero. This limit is the result of load-deflection analysis on Abaqus assuming an initial imperfection of $L/1000$ and including material inelasticity.

As a next step, computational predictions of creep buckling are developed using Abaqus. In order to simulate creep buckling on Abaqus, first, temperature is increased to the desired level, and then a fraction of the zero-time buckling load is applied to the column. No material creep is considered in these two steps. Next, the column is allowed to creep over the time period of 50 hours under the sustained load. Finally, the time-to-buckle due to creep is estimated. It should be pointed out here that to get the zero-time buckling load, an inelastic load-deflection analysis has to be performed. This has been done in Abaqus by using a nonlinear analysis scheme called Riks Analysis. Moreover, to model initial geometric imperfections, an Eigen-value buckling analysis is performed. The initial shape of the column is taken as

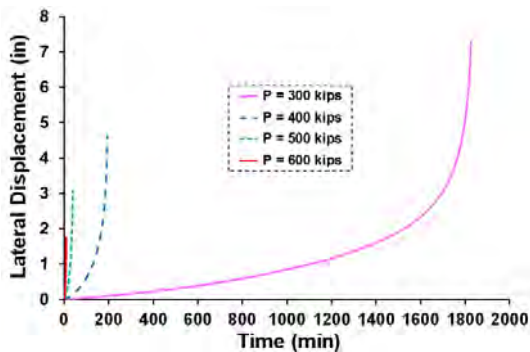


Figure 7. Lateral deflections due to creep at 500 °C and $\Delta_0 = L/1000$.

the shape of the first buckling mode, and the magnitude of the imperfection is chosen as a fraction of the column length. As far as material modeling is concerned, the inelastic material model at elevated temperatures is defined according to Eurocode 3 [10], and the creep material model is the one proposed by Fields and Fields [5], explained in the previous section. 3D hexahedral eight-node linear brick elements, C3D8R, have been utilized to model the columns on Abaqus.

As an example, the results of creep buckling simulations for the temperature of 500 °C and an initial out-of-straightness of $L/1000$ are presented in figure 7 as plots of creep deflection versus time at different load levels. Figure 7 clearly shows that the rate of change of deflection with time increases very slowly at the beginning and then increases more rapidly until the column no longer can support its load. The time at which the displacement-time curves become nearly vertical is taken as the failure time or time-to-buckle

in this study. Curves like the ones presented in figure 7 can be used to construct time-dependent column buckling curves, examples of which are shown in figure 8 for three different temperatures.

Creep buckling predictions from analytical and computational methods are compared at 600 °C and presented in figure 9. The analytical predictions are for a perfect column, while the computational one is for a column with $L/1000$ initial crookedness. As can be seen in figure 9, these three curves follow the same trend after about 10 minutes. The difference between these predictions after 10 minutes is related to the difference in predictions of the material models and inclusion of time-independent inelasticity in the computational method. The initial differences prior to about 10-minutes may possibly be related to the effect of initial imperfection on the zero-time buckling load. These differences may also be related to the fact that Harmathy's and Fields' and Fields' models consider primary creep quite differently, especially at high levels of stress as shown in figure 1. Of special interest are the predictions from the double power-law model, which is developed using experimental creep data on ASTM A992 steel in this study. Firstly, as already discussed, corrections are needed in order to use this creep model to predict creep buckling behavior of a column made of ASTM A36 steel. Secondly, due to its double-curvature nature, the double power-law model is predicting the effect of primary creep more accurately compared to the model by Fields and Field [5]. Rather than the initial part of the creep buckling curve, it can be seen a general agreement between the predictions of these two models since for the range of buckling stresses for this column, ASTM A992 steel does not get into the tertiary part at 600 °C.

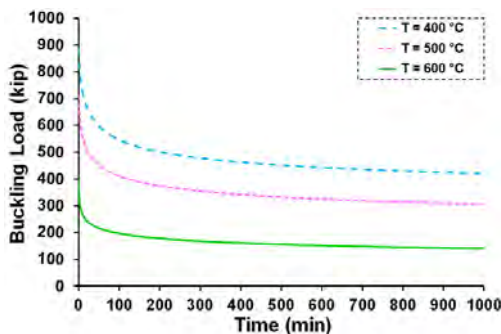


Figure 8. Computational creep buckling curves with $\Delta_0 = L/1000$.

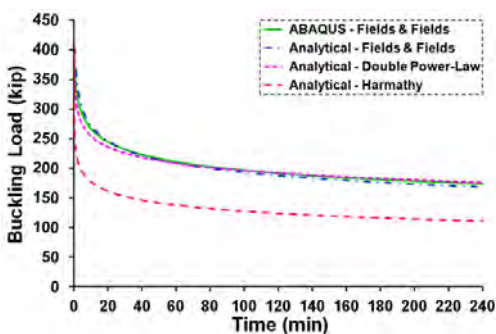


Figure 9. Comparison between analytical and computational creep buckling predictions at 600 °C

4 COMPARISON WITH AISC AND EUROCODE 3 PREDICTIONS

In this section results obtained from analytical and computational creep buckling analyses presented in the previous sections will be compared with the corresponding elevated temperature column strength predictions of AISC [11] and Eurocode 3 [10].

It should be pointed out here that formula to predict column strength at high temperatures in Appendix 4 of the 2011 edition of the *AISC Specification for Structural Steel Buildings* are based on work by Takagi and Deierlein [12]. Both the Eurocode 3 [10] column strength formula and that proposed by Takagi and Deierlein [12] predict column strength as a function of temperature, but do not consider duration of load and temperature exposure; i.e., they do not consider creep buckling effects. These formulas are based on computational studies using elevated-temperature stress-strain curves for steel that do not explicitly include creep effects, and are verified against high-temperature column buckling experiments that also did not explicitly consider time dependent effects on buckling.

Figure 10 depicts the comparison of creep buckling predictions from Abaqus and time-dependent tangent modulus with the ones from Eurocode 3 [10] and AISC [11]. Generally speaking, it can be observed that code-based predictions underestimate buckling strength of this column for relatively short

load durations, at higher temperatures such as 600 and 700 °C. The problem with code-based predictions of buckling becomes more evident when analytical creep buckling predictions using Harmathy’s material creep model are compared against code-based ones, as shown in figures 10(b), 10(c) and 10(d). It is also interesting to note that as temperatures get higher, analytical and computational buckling predictions using the Fields and Fields material creep model get closer, suggesting that the effect of creep is perhaps more important in overall inelastic buckling behavior at higher temperatures. Observations like these clearly show the significance of the need for more reliable creep data for structural steel.

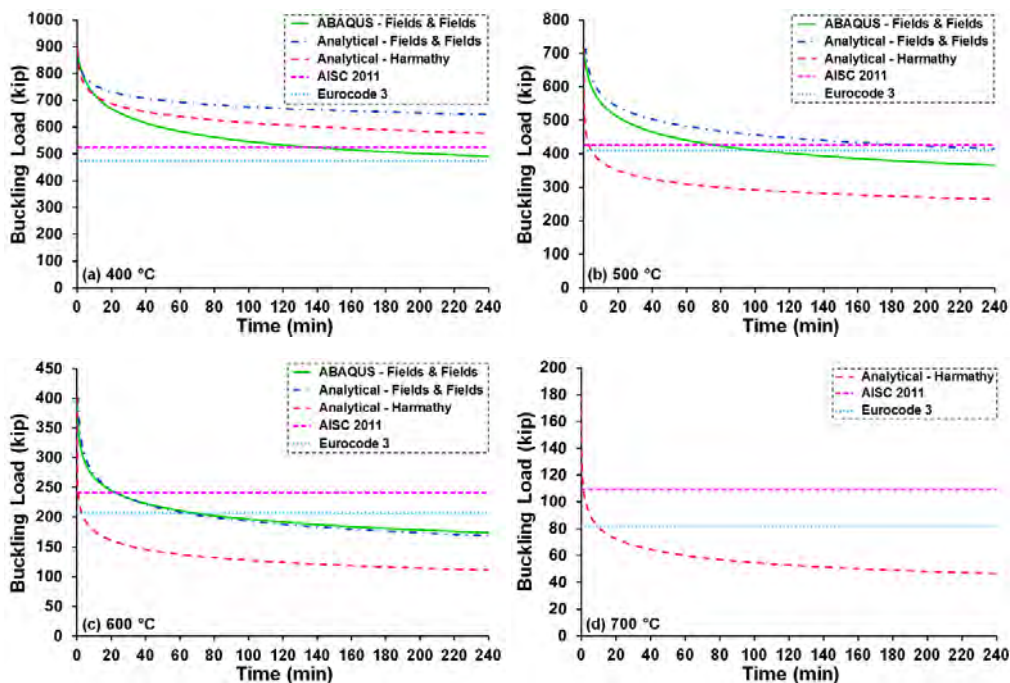


Figure 10. Comparison between computational and analytical creep buckling predictions with code-based buckling predictions.

5 CONCLUSION

This paper has presented some results of on-going research on the time-dependent buckling behavior of steel columns subjected to fire. Studies were conducted using a 3D finite element model incorporating both geometric and material nonlinearities. Analytical solutions were also developed to consider material creep effects on the overall time-dependent buckling. Predictions from this study were also compared against those from Eurocode 3 and the AISC Specification.

It is clear from results presented in this paper that material creep is significant within the time, temperature, and stress regimes expected in a building fire and that having an accurate knowledge of material creep is essential in predicting column buckling behavior at elevated temperatures. There is clearly a need for more extensive and reliable creep data for structural steel. In addition, results show that neglecting creep effects can lead to erroneous and potentially unsafe predictions of the strength of steel columns subjected to fire.

6 ACKNOWLEDGMENT

The research reported herein was conducted as part of a research project on *Creep Buckling of Steel Columns Subjected to Fire* supported by the National Science Foundation (NSF Award 0927819). The support of the National Science Foundation and of the former NSF Program Director M.P. Singh is gratefully acknowledged. The authors also gratefully acknowledge Gerdau-Ameristeel for donating materials for this research. The authors thank Matthew Gomez of Gerdau-Ameristeel for his support of this research.

REFERENCES

- [1] Norton F.H., *The Creep of Steel at High Temperatures*, McGraw-Hill Inc., New York, 1929.
- [2] Bailey R.W., “Creep of Steel under Simple and Compound Stress”, *Engineering*, 148, 121, 528-529, 1929.
- [3] Dorn J.E., “Some Fundamental Experiments on High Temperature Creep”, *Journal of the Mechanics and Physics of Solids*, 3(2), 85-116, 1955.
- [4] Harmathy T.Z., “A Comprehensive Creep Model”, *Journal of Basic Engineering, Trans. ASME*, 89(3), 496-502, 1967.
- [5] Fields B.A. and Fields R.J., *Elevated Temperature Deformation of Structural Steel*, Report NISTIR 88-3899, NIST, Gaithersburg, MD, 1989.
- [6] Zener C. and Hollomon J.H., “Effect of Strain Rate on the Plastic Flow of Steel”, *Journal of Applied Physics*, 15, 22-32, 1944.
- [7] Luecke, W.E. et al., *Federal Building and Fire Safety Investigation of the World Trade Center Disaster – Mechanical Properties of Structural Steels (Draft)*, Report NIST NCSTAR 1-3D, National Institute of Standards and Technology, Gaithersburg, MD, 2005.
- [8] Morovat M.A., Lee J., Hu, G. and Engelhardt M.D., “Tangent Modulus of ASTM A992 Steel at Elevated Temperatures”, *Structures in Fire – Proceedings of the Sixth International Conference*, East Lansing, June 2-4, 2010.
- [9] Shanley F.R., *Weight-Strength Analysis of Aircraft Structures*, McGraw-Hill Inc., New York, 1952.
- [10] Eurocode 3, *Design of Steel Structures. Part 1-2: General rules. Structural Fire Design*, EN 1993-1-2 European Committee for Standardization, CEN, 2006.
- [11] American Institute of Steel Construction (AISC), *Specification for Structural Steel Buildings*, Standard ANSI/AISC 360-11, Chicago, 2011.
- [12] Takagi, J. And Deierlein, G.G., “Strength Design Criteria for Steel Members at Elevated Temperatures”, *Journal of Constructional Steel Research*, 63, 1036-1050, 2007.

LARGE SCALE TEST TO EXPLORE THERMAL EXPOSURE OF COLUMN EXPOSED TO LOCALIZED FIRE

Alexandra Byström*, Johan Sjöström**, Ulf Wickström* ** and Milan Veljkovic*

* Luleå University of Technology, LTU, Sweden
e-mails: alexandra.bystrom@ltu.se, Milan.Veljkovic@ltu.se.

** Technical Research Institute of Sweden, SP
e-mails: Johan.Sjostrom@sp.se, Ulf.Wickstrom@sp.se

Keywords: Localized fire, Plate thermometer, steel column, adiabatic surface temperature.

Abstract. *A localized fire is a fire in a compartment which is unlikely to reach flash-over or a uniform temperature distribution. Designing for localized fires are generally more difficult than for a typical room fire both because of the complexity of the problem as well as the lack of experimental data. We reports on a full scale test on a steel column exposed to a localized fire. The setup is a 6 meters hollow circular column, $\varnothing=200$ mm with a steel thickness of 10 mm. The unloaded column was hanging centrally above different pool fires. We report temperatures of gas and steel as well as those measured by plate thermometer of the somewhat asymmetric fires. The results are compared with estimates based on Eurocode 1991-1-2 which in all cases studied overestimates the thermal impact for this setup.*

1 INTRODUCTION

In large in-door enclosures like air terminals a fully developed fire with high uniform temperatures is unlikely. Still, an intense fire could locally expose structures to severe thermal conditions although the mean temperature in the enclosure is low. Thus structural elements must be designed to resist fire also in large compartments. Usually structures are designed to resist the standard fire according to EN 1363-1 for a specified time. Alternatively, parametric fires as specified in the Eurocode (EN 1991-1-2 - Annex A) could be applied but all these design fires are intended for relatively small spaces where flashover with very high and uniform temperatures can develop. We may instead assume localized fires, as specified in EN 1991-1-2 - Annex C, to consider fire exposure effects. These are dominated by the incident radiation and depends on the magnitude and dimensions of the flames and the thermal exposure could be relatively small despite high local fire gas temperatures. Furthermore, only parts of a structural element will be affected that may reduce the structural effects on load-bearing elements in comparison to a uniform exposure. Asymmetric fires may on the other hand make the exposure more severe. More detailed analyses allow for taking into account more relevant temperature levels as well as variations along structures to avoid over design of fire protection measures while still obtaining reliable and safe solutions.

Very little experimental data from full scale fires are available in the literature. This work summarizes full-scale experiments on a steel column exposed to various pool fires in a large room. All the experimental data can be downloaded from the SP website [1]. For design purposes data on localized fire can be determined by plume theories [2, 3] which has been implemented models of Eurocode 1 [4,5].

2 BACKGROUND

The heat transfer from the flame and hot gases to a surface consists of three main components, absorbed radiation, emitted radiation and convective heat transfer.

$$\dot{q}_{tot}^{\bullet} = \dot{q}_{abs}^{\bullet} - \dot{q}_{emi}^{\bullet} + \dot{q}_{con}^{\bullet} \quad (1)$$

The absorbed radiation heat \dot{q}_{abs}^{\bullet} depends on the incident radiation and the absorptivity of the surface, which equals the emissivity of the surface, ε_s . Thus

$$\dot{q}_{abs}^{\bullet} = \varepsilon_s \cdot \dot{q}_{inc}^{\bullet} \quad (2)$$

The incident radiation inside the flame depends on the flame temperature and flame emissivity ε_{fl} , which in turn depends on the flame thickness d and absorption coefficient k in the following manner:

$$\dot{q}_{inc}^{\bullet} = \varepsilon_{fl} \cdot \sigma \cdot T_{fl}^4 = (1 - e^{-kd}) \cdot \sigma \cdot T_{fl}^4 \quad (4)$$

For gas species k depends on wavelength but as the bulk of the radiation from flames and smoke layers emanates from soot it is treated as an effective absorption wavelength independent coefficient.

The emitted heat depends only on the surface temperature and the surface emissivity:

$$\dot{q}_{emi}^{\bullet} = \varepsilon_s \cdot \sigma \cdot T_s^4 \quad (5)$$

Thus the total heat transfer by radiation may be written as

$$\dot{q}_{rad}^{\bullet} = \varepsilon_s \cdot \sigma (\varepsilon_{fl} \cdot T_{fl}^4 - T_s^4) \quad (6)$$

The heat transfer by convection is generally assumed to be linear with respect to the temperature difference between the surface- and gas temperatures. The proportionality constant is the convection heat transfer coefficient, h_c . For adjacent fires the gas temperature = temperature of flames and hot gases T_{fl} :

$$\dot{q}_{con}^{\bullet} = h_c \cdot (T_{fl} - T_s) \quad (7)$$

The total heat transfer to the column exposed to the surrounded fire can be expressed as:

$$\dot{q}_{tot}^{\bullet} = \varepsilon_s \cdot \sigma (\varepsilon_{fl} \cdot T_{fl}^4 - T_s^4) + h_c \cdot (T_{fl} - T_s) \quad (8)$$

2.1 Thermal action, according to the EN 1991-1-2

According to the EN 1991-1-2 [4] the localized fire is a fire where flash-over is unlikely to occur and which involves only a limited area of the fire load in the compartment. Height of flames must be considered. It depends on burning source size and heat release rate, figure 1, and can be calculated using

$$L_f = -1.02 \cdot D + 0.0148 \cdot Q^{2/5}, \quad (9)$$

where D (m) is the flame thickness and Q (W) heat release rate. The latter, according to the EN 1991-1-2, is based on the time t_{α} need to reach a rate of heat release of 1 MW.

$$Q = 10^6 \left(\frac{t}{t_{\alpha}} \right)^2 \quad (10)$$

For the ultra-fast fire spread, which in our setup can be considered, t_{α} equals 75 seconds. Instead of equation 10 the following equation for the heat release rate was used, which considers the mass loss rate, the heat of combustion for the evaporated gases, ΔH_c , and the combustion efficiency, χ .

$$Q = \frac{dm}{dt} \cdot \Delta H_c \cdot \chi \cdot 10^6 = \frac{dm}{dt} \cdot \Delta H_{eff} \cdot 10^6 \quad (11)$$

Where the mass burning rate dm/dt has been taken from experimental data, ΔH_c from reference [6] and $\chi = 0.7$ based on the high soot production from heptane and diesel.

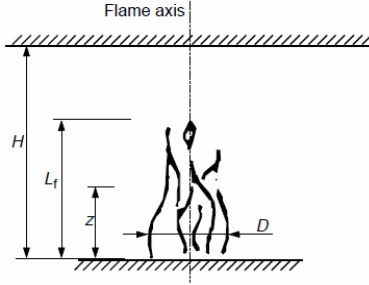


Figure 1. Some flame properties [2].

When the flame is not impacting the ceiling of a compartment ($L_f < H$, figure 1) or in case of fire in open space, the temperature $\Theta_{(z)}$ in the plume along the symmetrical vertical flame axis is given by:

$$\Theta_{(z)} = 20 + 0.25 \cdot Q_c^{2/3} \cdot (z - z_0)^{-5/3} \leq 900, \quad (12)$$

$$z_0 = -1.02 \cdot D + 0.00524 \cdot Q^{2/5} \quad (13)$$

Where z_0 is the virtual origin. Q_c , the convection part of the energy release is set to 70% of the total release according to Eurocode. There is no equation in the Eurocode for $\Theta_{(z)} > 900$. We therefore assume a linear relation for the lowest regions from the height where 900 °C is reached to 1200 °C at the surface (which is a much lower value than what can be extrapolated from equation (12) at $z = 0$).

$$\Theta_{(z)} = - \frac{300 \cdot z}{\left(\frac{900 - 20}{0.25 \cdot Q_c^{2/3}} \right)^{-3/5} + z_0} + 1200 \quad (14)$$

Equations (9), (12) and (13) can be recognized as Heskestad plume equations [2]. Equation (12) is also found in reference [2] with the difference that it can be used when $L_f < z$ (see figure 1) or not inside the plume. In case of $L_f > z$ McCaffrey [3] has been studying plume temperature.

On the fire exposed surfaces the net heat flux

$$\dot{q}_{net} = \dot{q}_{net,c} + \dot{q}_{net,r} \quad (15)$$

The net radiative heat flux component per unit surface area is determined by:

$$\dot{q}_{net,r} = \Phi \cdot \varepsilon_s \cdot \varepsilon_{fl} \cdot \sigma (T_r^4 - T_s^4) \quad (16)$$

Where in our case configuration/view factor, Φ , can be considered 1 and flame emissivity ε_{fl} suggested as 1. Surface emissivity ε_s exposed to the heat should be considered as 0.8. The net convective heat flux component per unit surface area expressed as equation (7), where h_c should be set to 25 (W/m²). Equation (16) is different from equation (6) in that the flame emissivity is included also for the emitted radiation. Naturally the flame emissivity is completely irrelevant for the emitted radiation but

for thick sooty flames, where emissivities are close to one it makes a marginal difference. However, for cleaner fuels, like methanol, this is not valid.

The steel is considered as a lumped heat capacity and we use a one-dimensional model for the heat absorption. The final expression for the steel/surface temperature increase at time step i , with a duration of Δt , can, according to EN 1991-1-2 [4], be expressed as:

$$\dot{q}_{net}^i = 0.8 \cdot \sigma [T_r^4 - (T_s^i)^4] + 25(T_g - T_s^i) \quad (17)$$

$$T_s^{i+1} = T_s^i + \frac{\dot{q}_{net}^i \cdot SF \cdot \Delta t}{\rho \cdot c} \quad (18)$$

ρ is density, c specific heat and the section factor, SF =cross sectional area/volume for a column section.

2.2 Previous work

A series of test on a steel beam in a Room Corner test room (according to ISO 9705) has previously been conducted [7]. The beam was hanging 20 cm from the ceiling and a gas burner was placed in the corner and under the beam. The result shows a very large difference in the temperatures probed by small thermocouples and plate thermometers. The PTs are much less sensitive to convection as they have a lower convective heat transfer coefficient relative the small thermocouples and will therefore adjust to temperatures dependent on the incident radiation to the specimen surface.

3 EXPERIMENTAL SETUP

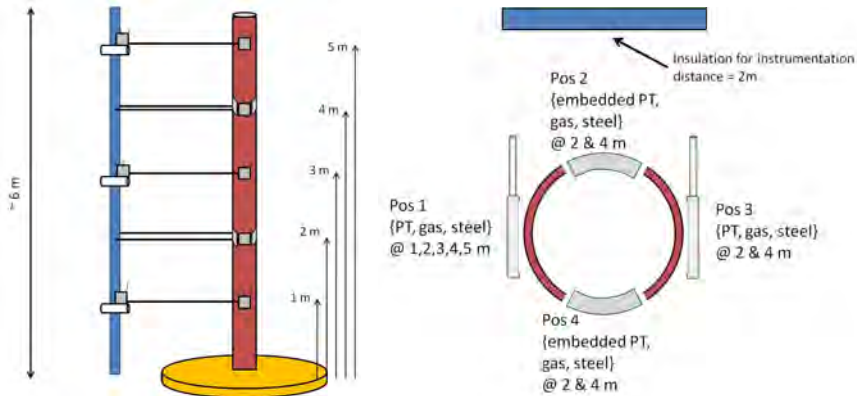


Figure 2. Left: experimental setup seen from position 1. The grey squares indicate plate thermometers. Right: cross section of the column from top view showing the different instrumentations in the different positions.

The experiments were carried out in the large fire hall of SP, 20 x 20 x 20 m in size. A full size (6 m tall, 200 mm wide and 10 mm thick) circular unprotected steel column was exposed to circular pool fires with various burning area. The column was un-loaded as load-bearing capacity of the steel column was not the topic of this experimental study and its interior was empty. The column was hanging centrally, 20 cm over the fuel container in the middle of the fire hall under the main exhaust hood. The lower and upper ends of the column were sealed and the column was fixed at the upper end to two well insulated beams.



Figure 3. Thermocouples and PT setup.

Along one position of the column (position 1) gas temperatures, steel temperatures and temperatures recorded by plate thermometers (PT) were measured at heights of 1, 2, 3, 4 and 5 meters along the column, as indicated in figure 1 below. Thus, the instruments at e.g. 2 meters along the column are situated 2.2 meters above the fuel surface. Gas temperatures were measured using welded 0.25 mm thermocouples. Steel temperatures were measured with thermocouples fixed about 1 mm into the steel structures. The plate thermometers were standard plate thermometers as used in furnace testing according to EN 1363-1 but mounted a few cm from the steel surface. In two positions, $\pm 90^\circ$ from position 1, curved PTs were mounted inside the steel column on height 2 and 4 together with gas thermocouples, see figure 3. Opposite to position 1 gas and steel temperatures were measured together with PTs at 2 and 4 meters height.

Three experiments were performed. Diesel, and heptane were burned using a pool diameter of 1.1 m. An additional diesel fire was also run with a pool diameter of 1.9 m. The fuel container was placed on a balance to probe the mass loss rate. Two meters from the column was a vertical stone wool insulation board, 6 m high and 1.2 m wide to protect instrumentation anchors and data collection.

Table 1 displays the calculated fuel characteristics according to the Eurocode described above.

Table 1. Fuel characteristics, mass loss rate, heat of combustion (ΔH_c), Heat release rate (HRR) and flame height.

Fuel	Mass loss rate (kg/sec)	ΔH_c [1], (MJ/kg)	HRR (MW), eq. (14)	Flame height (m), eq. (12)
Heptane	0.051	44.6	1.6	3.3
Diesel, diameter 1.1 m	0.032	44.4	1	2.6
Diesel, diameter 1.9 m	0.107	44.4	3.3	4.1

4 RESULTS AND DISCUSSIONS

4.1 Results from the experiments

Even though no sideways draught could be noticed before the experiments the flames were clearly tilted towards position 1. Figure 4 shows a series of pictures from the smaller diesel fire of diameter 1.1 m. Flames are flickering to a height between 2 and 3.5 m and above 1 m the flame is preferentially in position 1.

Increasing the pool diameter to 1.9 m increased the size of the flames considerably. The height was constantly over 4 m, sometimes reaching well over 5 m. A movie of the larger fire can be viewed from SP's web page [1]. Some temperatures along position 1 are presented in figure 5. It is quite evident that the small 0.25 mm thermocouples and the PTs display essentially the same temperatures.

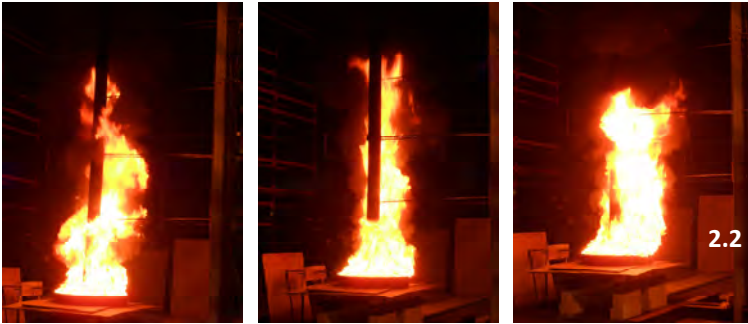


Figure 4. The flame from diesel $\varnothing = 1.1$ m. The flames are tilted towards position 1.

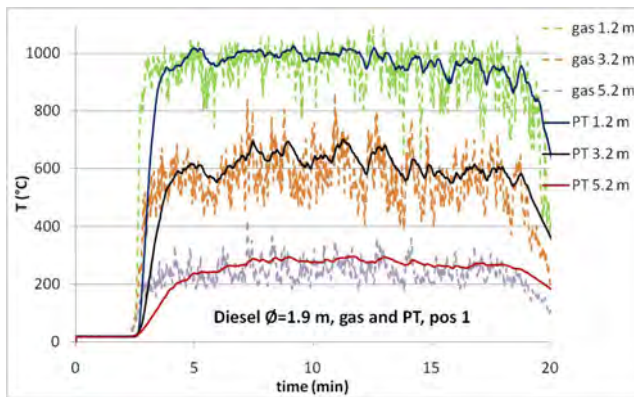


Figure 5. Measured gas and PT temperatures in position 1 for the larger diesel fire. The fuel was ignited after 2 minutes.

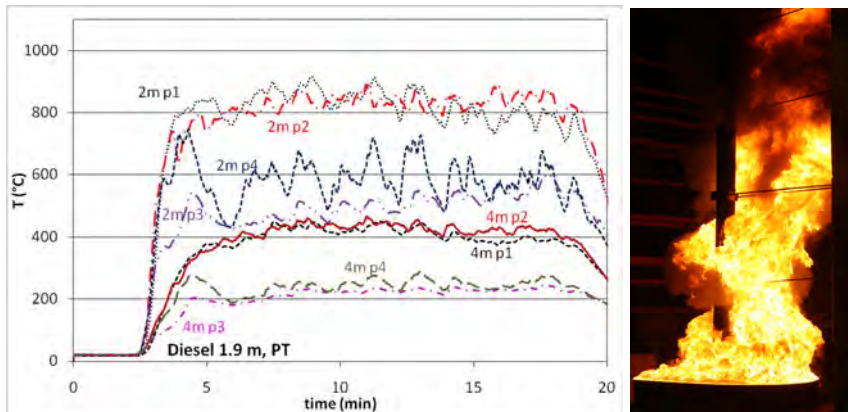


Figure 6. Left: PT temperatures at 2.2 and 4.2 m height in all positions for the larger diesel fire ($\varnothing = 1.9$ m). “2m p4” indicate 2 meters height at position 4. Right: a photo of the same fire with >4 m flames and a characteristic asymmetry.

This asymmetric fire load naturally has consequences on the steel temperatures. From the movie [1] one can observe the curvature of the column due to uneven thermal expansion. The recorded steel temperatures are shown in figure 7. The hottest region is close to the fire source and the steel reaches almost 800 °C at 1 m height after about 15 minutes of fire. The temperature decreases with height. At 2 m the difference between position 1 and 3 (opposite each other) is very big. After 8 minutes of fire the difference is 250 °C. Analysing the shapes of the curves it is clear that heat is transferred to the colder region of the column which evens out these differences. Given a thermal diffusivity of $\sim 10^{-5} \text{ m}^2/\text{s}$ (which yields a characteristic diffusion time of two hours over half the circumference) conduction alone could not be responsible for this heat transfer. A large portion must also be due to radiative exchange between the inside surfaces of the column.

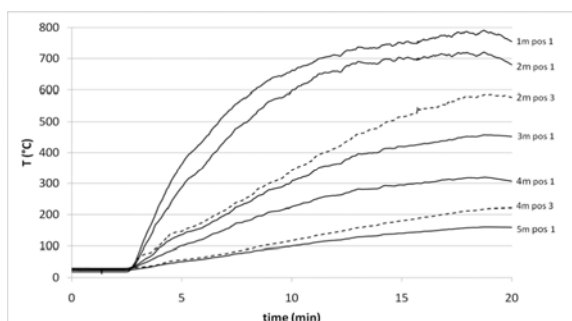


Figure 7. Steel temperatures for the larger diesel fire. Solid and dashed lines represent position 1 and 3, respectively.

4.2 Comparison between experimental data and the data according to EN 1991-1-2

The gas temperature estimated using the EN 1991-1-2 at different heights and fuels can be seen in table 2. Once again, the asymmetry of the flame induces a big span in the measured temperatures. However, it is worth noticing that at each height and for each fuel the Eurocode estimation exceeds the highest measured value.

Table 2. Gas temperatures after 10 minutes of fire. * The measured gas temperatures from position 1 if only one number is given. At heights where temperatures were probed around the column values are given in intervals.

Fuel	Height of TC (m)	T_{gas} , (°C),*	T_{gas} EN 1991-1-2, (°C)
Heptane	1.2	900	1056
	2.2	300-650	937
	3.2	500	563
	4.2	150-280	343
	5.2	180	238
Diesel, diameter 1.1 m	1.2	800	1011
	2.2	250-500	695
	3.2	250	364
	4.2	110-150	233
	5.2	120	167
Diesel, diameter 1.9 m	1.2	950	1078
	2.2	480-800	978
	3.2	640	782
	4.2	220-400	492
	5.2	250	346

This difference in temperatures is also reflected when comparing the calculated steel temperatures. The Eurocode estimations lead to values exceeding the actual impact on the column that has been measured during experiment. Figures 8-13 show the comparison of the measured steel temperature and calculated according to the EN 1991-1-2 [4, 5]. The emissivity of the flame is assumed equal 1. Note that Eurocode over estimates the steel temperatures. But just by assuming the flame emissivity less than 1 depending on the flame thickness and absorption coefficient (4) give values of the steel temperature closer to measured temperatures. The flame thickness is then assumed equal $d / 2$ and the absorption coefficient 0.35 m^{-1} .

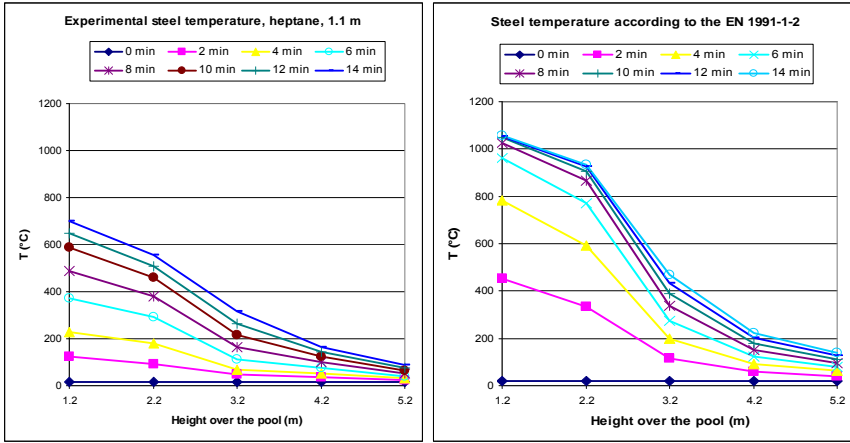


Figure 8. Measured (left) and calculated (right) steel temperature according to the EN 1991-1-2. Heptane. 1.1 m.

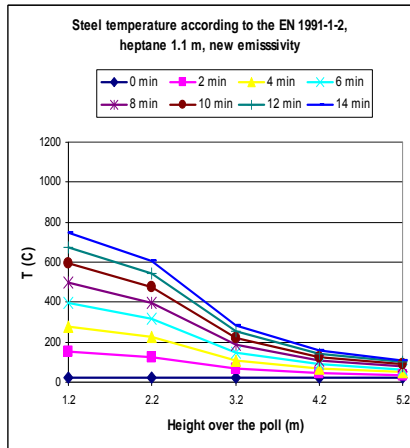


Figure 9. Calculated steel temperature according to the EN 1991-1-2 using a lower emissivity. Heptane 1.1 m.

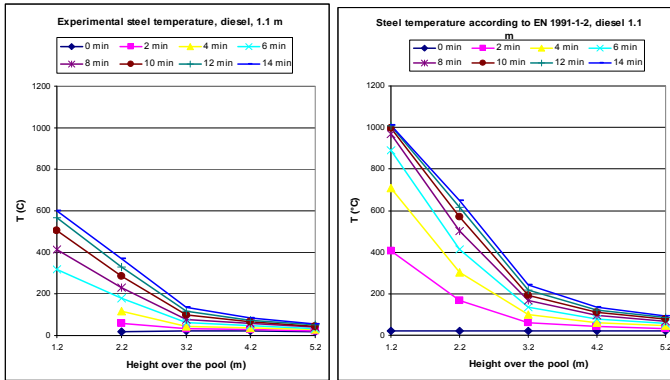


Figure 10. Measured (left) and calculated (right) steel temperature according to the EN 1991-1-2. Diesel. 1.1 m.

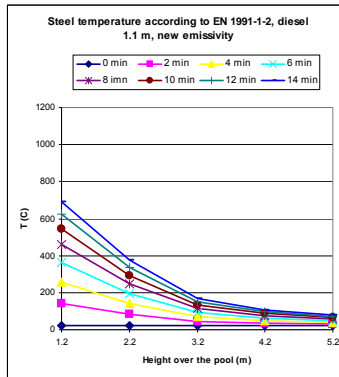


Figure 11. Calculated steel temperature according to the EN 1991-1-2 using a lower emissivity. Diesel 1.1 m.

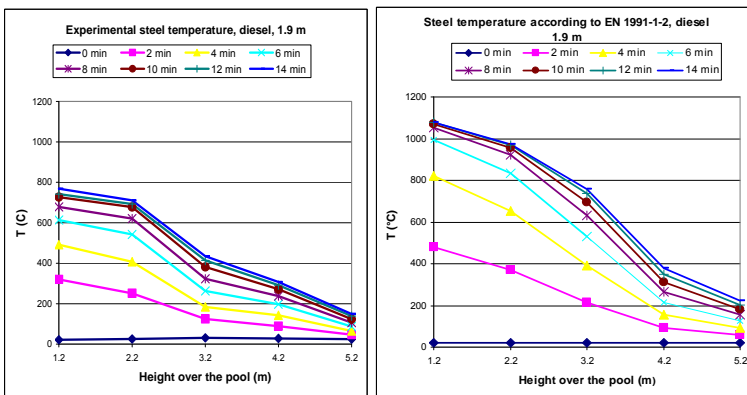


Figure 12. Measured steel temperature (on the left), calculated steel temperature according to the EN 1991-1-2 (on the right). Diesel with diameter of container 1.9 m.

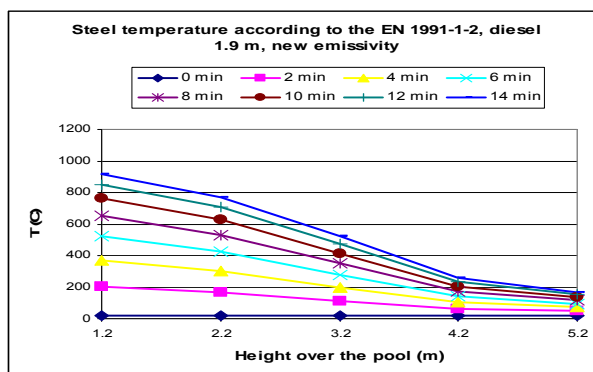


Figure 13. Calculated steel temperature according to the EN 1991-1-2 using a lower emissivity. Diesel. 1.9 m.

5 CONCLUSIONS AND FUTURE WORK.

A general conclusion of these experiments is that the Eurocode recommendations overestimate the thermal exposure and thereby the steel temperatures by several hundred degrees. Thus there is a great potential to reduce the fire resistance requirements for structures which are designed to resist localized fires. However, a detailed knowledge of the flame emissivity improves the agreement considerably.

In the experiments reported here the PTs showed about the same temperatures as the thermocouples in contrast to experiences from beams exposed to a propane fire as reported by Wickström, Jansson and Tuovinen [7]. They reported great differences between PT and TC measured temperatures. The small measured differences in this study are likely to depend on high gas velocities and high flame emissivities.

In the test reported here the flames tilted considerable which made the thermal exposure asymmetric. Large parts of the column were at times engulfed in flames only on one side. This reduces the temperature but may in practice have harmful effects on the load-bearing capacity of a column as it introduces eccentric loading. The total effects of asymmetric thermal exposure on the load-bearing need further studies including structural analyses.

The authors gratefully acknowledge the financial support provided by The Swedish fire research board, Brandforsk, Sweden.

REFERENCES

- [1] http://www.sp.se/en/index/services/localized_fire/Sidor/default.aspx
- [2] Heskestad, G. "Fire Plumes", *SFPE Handbook of Fire Protection Engineering*, 2nd edition, National Fire Protection Association, Quincy, MA 1995.
- [3] McCaffrey, B.J. "Purely Buoyant Diffusion Flames: Some Experimental Results". *Fire Safety Journal*, vol 3, pp 107-121, 1980.
- [4] Eurocode 1: Actions on Structures- Part 1-2: General actions- Actions on Structures exposed to Fire, 2002.
- [5] Franssen J.M. and Real P.V. "Fire Design of Steel Structures.". 2010.
- [6] Iqbal N. and Salley M. H. "Fire Dynamics Tools (FDT): Quantitative Fire Hazard Analysis Methods for the U.S. Nuclear Regulatory Commission Fire Protection Inspection Program." *Final Report*, Washington, DC, 2004.
- [7] U. Wickström, R. Jansson and H. Tuovinen, SP Report 2009:19.

INFLUENCE OF ASYMMETRICAL FIRE EXPOSURE ON THE STRUCTURAL BEHAVIOUR OF STEEL ELEMENTS

Peter Schaumann*, Florian Tabelaing*

* Institute for Steel Construction, Leibniz Universitaet Hannover
e-mails: stahlbau@stahl.uni-hannover.de, tabelaing@stahl.uni-hannover.de

Keywords: Stability, Thermal Gradient, Buckling, Thermal Expansion

Abstract. *This paper presents numerical investigations of stability behaviour of steel elements directly connected to plane space-enclosing elements in fire. In the fire situation these load bearing components are heated from three sides. Due to this asymmetrical heating, thermal induced strains may lead to a different buckling mode compared to heating from all sides. For this purpose, a numerical model of a representative steel column exposed to ISO 834 fire curve is developed to compare the fire resistances of both heatings. Additional parametric studies extend the results to a practical range of compressive members.*

1 INTRODUCTION

The research work presented came about in the context of a joint research project which addresses the fire resistance of steel members protected by intumescent coating where parts of the cross-sections are covered by adjacent space-enclosing members. Consequently, the cross-sections are exposed to fire on three sides only. This leads to an asymmetrical temperature distribution in the cross-section. The main research approach is to investigate the heating of the steel members by tests and simulation while the mechanical response is scrutinized by numerical methods.

Usually, a uniform temperature distribution over the cross-section is assumed in structural fire design of steel elements. This simplification enables comparably simple calculation methods for the heating of steel sections in case of fire. Suitable formulae are given in Eurocode 3 Part 1-2 [1] for instance. However, for steel elements adjusted to space-closing elements, this assumption is not valid due to a non-uniform temperature distribution caused by an asymmetric heating.

Space-enclosing may be realised by trapezoidal or sandwich plates as they are used, e.g. in industrial buildings. Figure 1 shows examples for space-enclosing elements directly connected to load bearing elements.

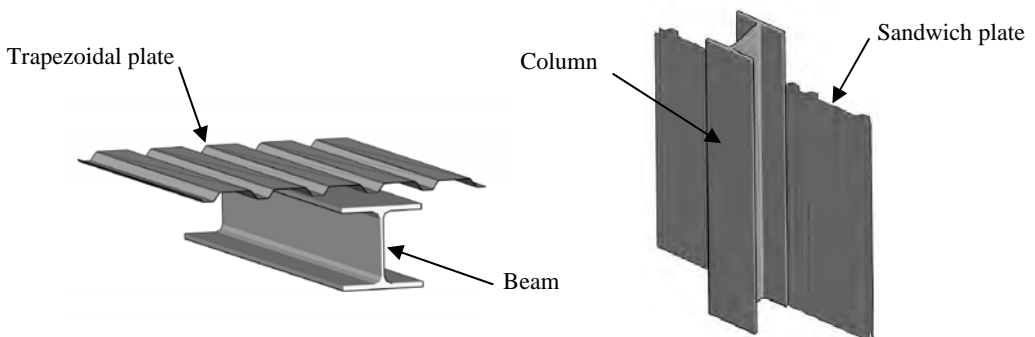


Figure 1 – Beam and column connected to space-enclosing elements

In case of fire, this assembly causes an asymmetrical heating from three sides leading to lower average temperatures in the cross-section in comparison to heating from all sides. On the other hand, the asymmetrical heating may induce a thermal gradient in the cross-section. If a thermal gradient arises, steel elements get additional thermal induced curvatures having negative effects on the stability performance.

Thus, the main issue of this paper is to investigate whether the positive effect of the lower average temperature or the negative effect of the temperature gradient is governing the performance of structural steel elements. In comparison to a fire exposure from four sides different fire resistance times may occur. For this reason, numerical simulations on the stability behaviour of unprotected steel columns directly connected to space-enclosing elements are presented. Fire protection by intumescent coating is not considered in these investigations.

2 NUMERICAL SIMULATIONS

The numerical simulations are performed using the finite-element software Abaqus [2] in a sequentially coupled thermal-stress analysis. First, the temperature field is calculated in a pure heat transfer analysis. Based on this a mechanical calculation is performed to determine the structural response. This approach assumes that increasing temperatures influence the mechanical response, whereas the mechanical response has no influence on the temperatures within the cross-section.

Both for the thermal calculation and the mechanical analysis a three-dimensional model is developed. The model is discretised using 8 node solid elements with linear shape functions.

In the thermal analysis ISO 834 fire curve is applied to the fire exposed surfaces as thermal boundary condition for convection and radiation heat transfer. The corresponding coefficients and thermal material parameters are set according to EN 1993-1-2 [1]. Heat flux due to thermal conduction from the heated space-enclosing element to the load bearing element is neglected. This assumption leads to higher induced thermal gradients and consequently to higher thermal curvatures and is therefore conservative.

Based on the thermal analysis, the mechanical simulation is performed taking into account geometrical and material non-linearities. The material non-linearities include the consideration of temperature dependent non-linear stress-strain relationship according to EN 1993-1-2 [1]. The geometrical non-linearities result from the consideration of precise kinematic relationship and allow accounting of P- Δ -effects. Within the mechanical model, initial structural and geometrical imperfections are considered as well. The geometrical imperfections are generated by the first buckling mode shape of an eigenvalue analysis multiplied by an amplification factor equal to 1/500. The structural imperfections are applied as a linear initial stress according to [4].

3 INVESTIGATIONS ON THE STABILITY PERFORMANCE OF STEEL ELEMENTS

As mentioned before, the investigations are conducted with an unprotected steel column. The stability performance in consideration of a uniform and non-uniform temperature distribution in the cross-section is investigated in detail. In particular, the effect of thermal induced curvatures on the structural performance is analysed. For this reason, a numerical model of a representative steel column is developed.

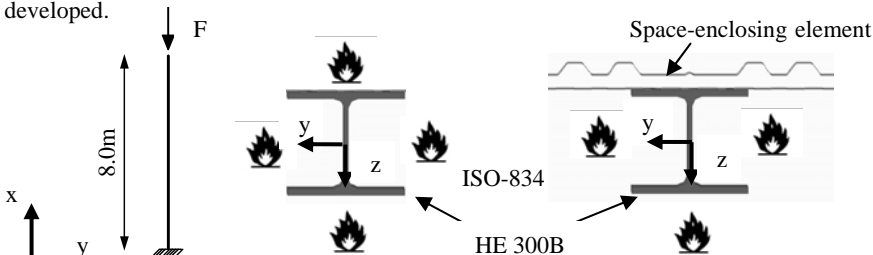


Figure 2 – System and fire exposure cross-sections

The investigated column represents Euler Case I. The column is 8.0 m high and consists of a HE 300 B profile. Figure 2 illustrates the static system and the two different assemblies investigated. The first case represents a freestanding column heated from all sides. The second one is connected directly to a space-enclosing element and consequently, heated only from three sides. The temperature distributions at point of failure are presented in Figure 3 by using symmetrical conditions.

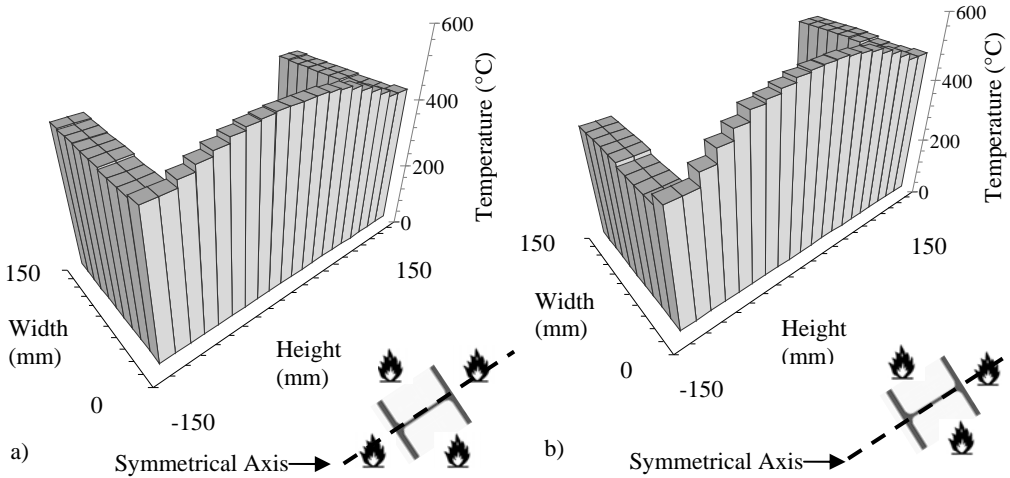


Figure 3 – Cross-sectional temperature distribution (HE 300 B) for a) four- and b) three sides fire exposure at failure

Fire exposure from all sides leads to a nearly uniform temperature distribution in the cross-section. The temperature distribution is symmetrical and only a small thermal gradient due to the lower mass of the web occurs. In contrast, a fire exposure from three sides leads to a non-uniform and asymmetrical temperature distribution. The thermal gradient between the flanges amounts to 100 K. A slightly nonlinear gradient due to the lower mass of the web is induced to the web as well.

The effective stiffness of the cross-section directly corresponds to the temperature distribution due to the temperature-dependent reduction of the Young's modulus k_E according to [1]. Hence, a difference in the mechanical response between both cases is expected.

In the following, coupled thermal-stress calculations based on the temperature fields are described. In these analyses, an initial load of 300 kN is applied on top of the column. This corresponds to a load ratio of $\mu = 0.5$ at room temperature conditions. The load orientation is strictly vertical and does not follow rotational deformations of the column. Structural imperfections, which mean initial stresses, are considered as well and geometrical imperfections are applied to the minor axis. This is reasonable because failure of the column is expected around the minor axis.

The calculation stops, if the load bearing capacity of the column is reached, e.g. due to instability, failure of equilibrium or failure of material. In this manner, fire resistance times can be calculated. This method corresponds to level 3 according to the Eurocodes. Figure 4 shows the different behaviour of an asymmetrically heated column. While a column exposed to fire on all four sides shows lateral deflections around the minor axis as expected, deformations around both major and minor axis are detected for the asymmetrical heated column.

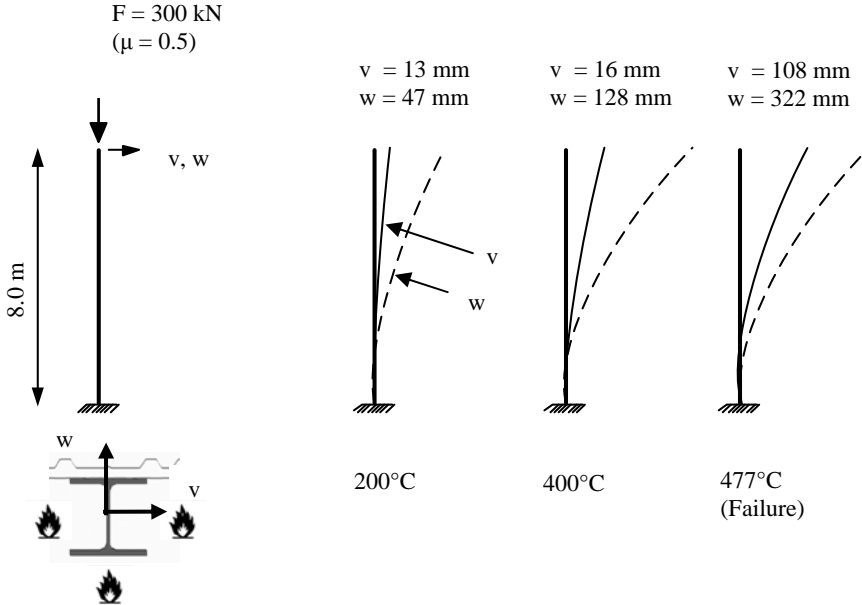


Figure 4 – Deformation of a column exposed to fire from three sides at different temperatures of the heated flange

A fire exposure on four sides leads to failure when an average steel temperature of about 430°C is reached. Branching occurs and the deflections around the minor axis increase to a high value. This phenomenon can be identified in Figure 5 precisely. Deflections around the major axis do not occur in this case. The cross-sectional distribution of longitudinal stresses at failure is depicted in Figure 6. The stress distribution attunes as expected and constitutes a bending moment considering P-Δ effects.

Compared to this, an asymmetric fire exposure leads to large deflections both around the major and minor axis as mentioned before (compare Figure 5). The main reason for this is the thermal induced curvature which results from the thermal gradient.

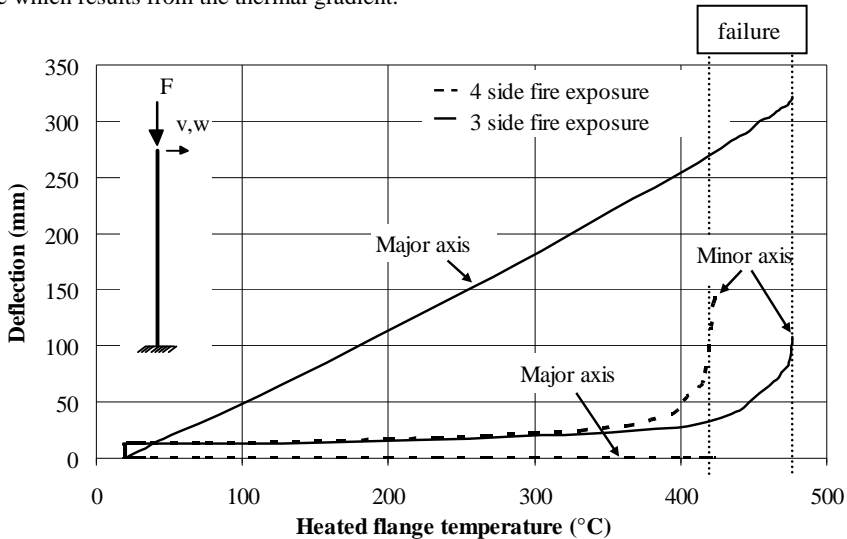


Figure 5 - Lateral deflection of the column versus temperature

The deflection of the column around the major axis increases dramatically until the load bearing capacity is reached. The thermal gradient mainly induces these deflections around the major axis of the column. These deflections influence the P- Δ effects significantly and lead to much higher stresses in the cross-section. However, buckling still does not occur around the major axis, as the resistance of the cross-section around the major axis is much higher than around the minor axis. Consequently, the P- Δ effects around the major axis do not reach such an amount, that a buckling problem around the minor axis becomes a buckling problem around the major axis. Furthermore, it is indicated that stresses around both major and minor axis are activated for three side fire exposure. The stresses which result from bending around the major axis are strongly increased. In addition, the stiffness of the flanges becomes smaller due to the fact, that the proportional limit is reached. As the buckling resistance around the minor axis is represented by the flanges particularly, branching finally occurs around this axis.

Due to the quite different structural behaviour, caused from a three-side fire exposed column, a higher fire resistance is reached. This circumstance is owed to the lower average temperature of this column. Both columns fail due to buckling around the minor axis, whereas the stiffness of the three side fire exposed column decreases later due to the lower average temperature.

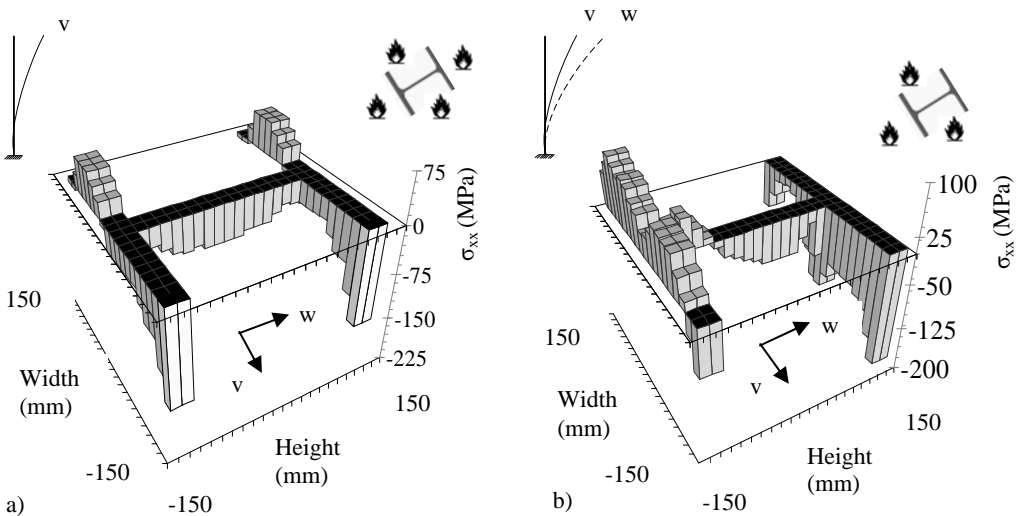


Figure 6 – Cross-sectional stress distribution at failure for a) four- and b) three side fire exposure

The above described investigations show that a three side fire exposure influences the buckling performance significantly due to thermal induced curvatures. A thermal gradient in the cross-section is responsible for this circumstance. In addition, the fire exposure from three sides leads to an asymmetrical distribution of stiffness as well. The stiffness of the heated parts in the cross-section decreases due to high temperatures. As a consequence, the centroid of the cross-section is shifted compared to the initial condition. Regarding the axial load applied to the column, an eccentricity between load and centroid arises. Consequently, an additional bending moment occurs. This fact is considered in the previous investigations as well, but it has to be noted, that this effect appears in the opposite direction than the thermal induced curvatures. While the asymmetrical distribution of the stiffness leads to shifting of the centroid towards the cooler flange and consequently generates deflections in direction of the heated flange, the thermal induced curvatures constrain the column in the direction of the cooler flange. To investigate the impacts of these different effects on the fire resistance, analysis disregarding and regarding thermal induced strains are presented in the following.

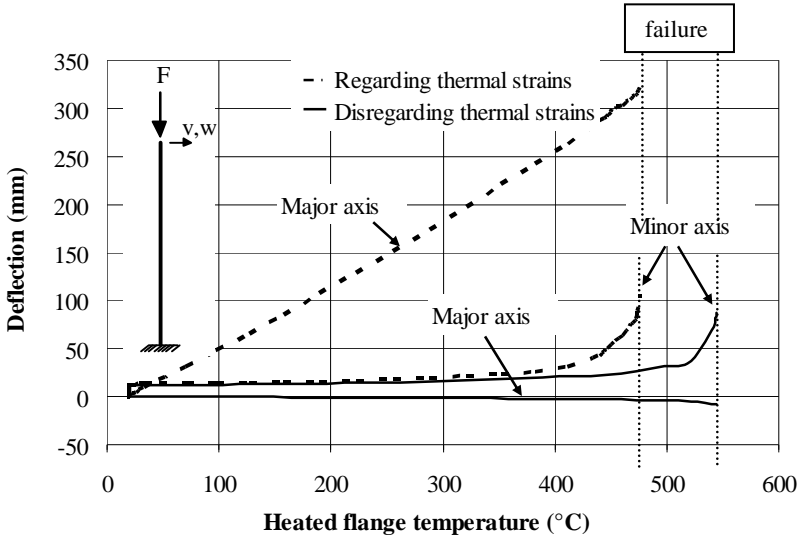


Figure 7 – Lateral deflection of a three side fire exposed column versus temperature

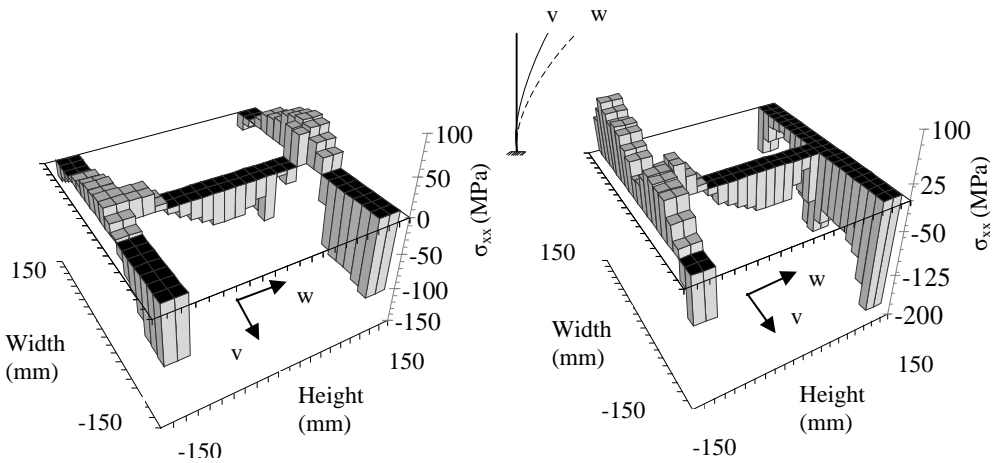


Figure 8 - Cross-sectional stress distribution at failure for three side fire exposure by a) disregarding and b) regarding thermal strains

Figure 7 illustrates, that ignoring thermal strains leads to overestimation of the fire resistance. The aforementioned effect, which results in quite different deflections, can be identified explicitly. As the column deflects into the direction of the cooler flange by regarding thermal induced strains, the eccentricity due to the shifting of centroid leads to deformations into opposite direction. These deflections are very small compared to the thermal induced deflections. The stress distribution at point of failure is depicted in Figure 8. This distribution is similar to the stress distribution which results from a four side fire exposure (compare Figure 6a). Consequently, large P-Δ effects do not occur. Hence, a higher fire resistance is reached due to the lower average temperature caused by three side fire exposure.

4 PARAMETER STUDY

The investigations described before show the quite different stability performance of unprotected steel columns with four- and three side fire exposure. These investigations are performed with a HE 300 B profile and a length of 8.0 m. To extend the prescribed phenomena to other conditions, some parametric studies are carried out in the following. A range of non-dimensional slenderness, different load levels and profiles used in building practice are investigated. It has to be mentioned that different profiles with a similar A/V-ratio are chosen to ensure similar temperatures in the cross-section. The slenderness ratio is determined for room temperature conditions, taking into account the buckling length according to Euler Case I. Further parameters remain unaffected in these calculations. These analyses are performed for both three- and four side fire exposure to compare both cases afterwards.

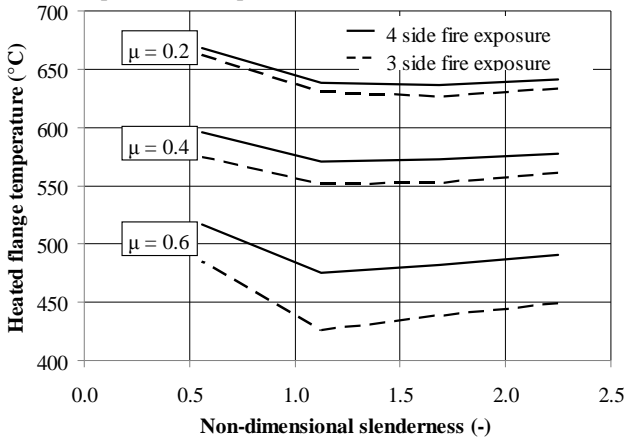


Figure 9 – Critical temperatures of the heated flange for full- and three side fire exposure versus slenderness

Figure 9 shows critical temperatures of the heated flange for three- and four side fire exposure, taking into account different slenderness ratios and load ratios. Obviously, a four side fire exposure leads to a higher critical temperature compared to a fire exposure from three sides in all cases. While the critical temperature of both cases is similar for low load levels, the influence of a three side fire exposure increases and leads to a significantly lower critical temperature for high load levels. This is due to the much higher P-Δ effects and consequently higher stresses in the cross-section.

In the following, these findings shall be checked for different cross-sections. For this reason, two

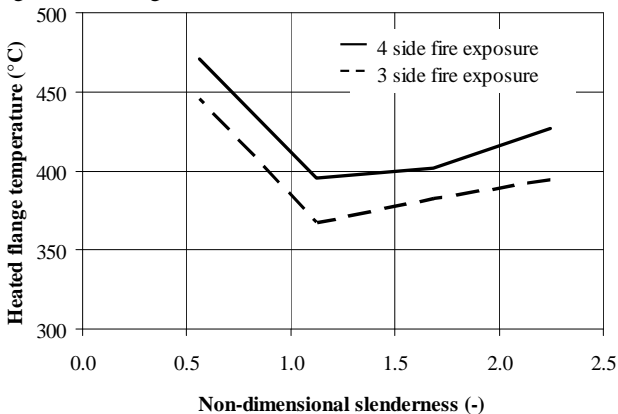


Figure 10 - Critical temperatures of the heated flange for four- and three side fire exposure versus slenderness for a HE 100M profile and load ratio $\mu = 0.6$

different profiles (HE 100M and HE 450A) are modelled, taking into account a load level of $\mu = 0.6$ and different slenderness ratios.

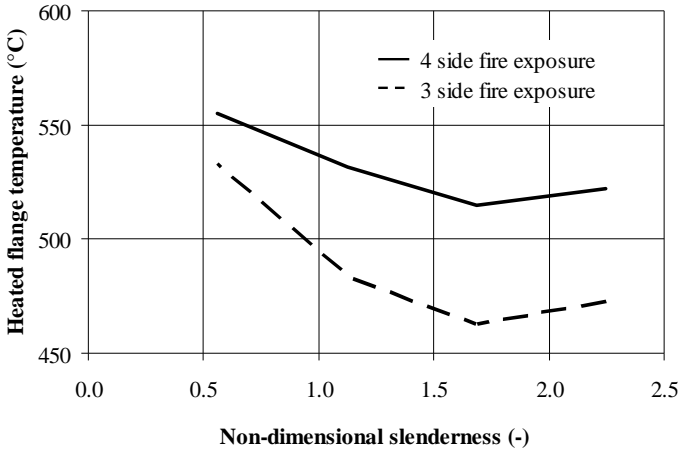


Figure 11 - Critical temperatures of the heated flange for four- and three side fire exposure versus slenderness for a HE 450A profile and load ratio $\mu = 0.6$

The figures above show that the stability performance is quite similar to the previous investigations. Again, a higher critical temperature for a full side fire exposure is reached. A fire exposure from three sides leads to a significantly lower fire resistance due to the effects discussed in chapter 3. Summing up, all investigation confirm the hypothesis that a three side fire exposure leads to a lower fire resistance.

5 CONCLUSION

In this paper numerical simulations on the stability performance of structural steel elements adjusted to space-enclosing elements are presented. The behaviour of a representative unprotected steel column, taking into account four- and three side fire exposure is investigated in detail. The conducted simulations show the significantly different structural behaviour in case of fire. A four side fire exposure leads to the expected buckling mode around the minor axis. In contrast, a three side fire exposure induces large deflections around the major axis which increase the $P-\Delta$ effect substantially. The asymmetrical stress distribution in the cross-section leads to asymmetrical stiffness of the column. As a consequence, the column fails due to buckling around the minor axis. Several slenderness ratios, load levels and cross-sections are investigated in parametric studies, to extend the findings to a practical range.

In conclusion, the results of this paper show, that the lower average temperature in the cross-section governs the stability performance of structural steel elements. Thermal induced curvatures cause large deflections, but $P-\Delta$ effects do not lead to failure. As a consequence, a four side fire exposure leads to lower fire resistances compared to fire exposure from three sides. In this context, the design method of Eurocode 3, which assumes an equal temperature distribution in the cross-section, is applicable for the regarded special kind of fire exposed columns and leads to conservative results.

6 ACKNOWLEDGEMENT

The results have been produced during the German research project „Optimierter Einsatz intumeszierender Anstriche im Stahlbau“ (IGF 17200 N). The project IGF 17200 N from DAST was funded by the “Federal Ministry of Economics and Technology” via AiF.

The authors would like to thank Timur Stickel for his technical input and assistance in performing numerical simulations. This is gratefully acknowledged.

REFERENCES

- [1] DIN EN 1993-1-2: Eurocode 3: Design of steel structures – Teil 1-2: General rules – Structural fire design; EN 1993-1-2:2005, Deutsches Institut für Normung, Beuth Verlag, Berlin, 2006.
- [2] ABAQUS. Abaqus/Standard Version 6.10. Pawtucket: Hibbit, Karlsson & Sorensen, Inc. 2011.
- [3] ECCS-CECM-EKS, Publication No. 33, Ultimate Limit state Calculation of Sway Frames with Rigid Joints, Brüssel, 1984.
- [4] P. Schaumann: Contribution to the computation of fire-exposed steel members and frames (in German: Zur Berechnung stählerner Bauteile und Rahmentragwerke unter Brandbeanspruchung) PhD thesis, Institut für konstruktiven Ingenieurbau der Ruhr-Universität Bochum, 1984.

NUMERICAL MODELLING OF LOAD BEARING LSF WALLS UNDER FIRE CONDITIONS

Poologanathan Keerthan and Mahen Mahendran

Post-doctoral Research Associate and Professor, Science and Engineering Faculty, QUT, Australia.
e-mails: keeds123@qut.edu.au, m.mahendran@qut.edu.au

Keywords: Load Bearing LSF Walls, Finite Element Analysis (FEA), Gypsum Plasterboard, Insulation, Cold-formed Steel Studs, Thermal Performance, Standard Fire, Real Design Fire.

Abstract. *Fire safety of light gauge cold-formed steel frame (LSF) stud walls is significant in the design of buildings. In this research, finite element thermal models of both the traditional LSF wall panels with cavity insulation and the new LSF composite wall panels were developed to simulate their thermal behaviour under standard and real design fire conditions. Suitable thermal properties were proposed for plasterboards and insulations based on laboratory tests and literature review. The developed models were then validated by comparing their results with available fire test results. This paper presents the details of the developed finite element models of load bearing LSF wall panels and the thermal analysis results. It shows that finite element models can be used to simulate the thermal behaviour of load bearing LSF walls with varying configurations of insulations and plasterboards. Failure times of load bearing LSF walls were also predicted based on the results from finite element thermal analyses.*

1 INTRODUCTION

In recent times, LSF wall and floor systems are increasingly used in low-rise and multi-storey buildings, but without a full understanding of their fire performance. Currently LSF wall and floor systems are made of cold-formed thin-walled steel lipped channel sections and gypsum plasterboards. Under fire conditions, cold-formed thin-walled steel stud and joist sections heat up quickly resulting in fast reduction in their strength and stiffness. Therefore they are commonly used in structural wall and floor systems with plasterboard linings on both sides used as fire protection.

Cavity insulated LSF walls are often used for the purpose of climate control in exterior and party walls and acoustic benefits. However, they are also required to be fire rated. Hence many researchers investigated the fire resistance ratings of LSF wall systems with different types of insulations in the wall cavities. Sultan [1] conducted full scale fire resistance tests on non-load bearing gypsum board wall assemblies and found that when rockwool was used as cavity insulation the fire resistance rating increased by 54% over the non-insulated wall assemblies while cellulose fibre cavity insulation reduced the fire resistance rating. Kodur and Sultan [2] conducted 14 full-scale fire tests of load bearing LSF wall panels and found that the insulation type, number of gypsum board layers and stud-spacing have a significant influence on the fire resistance of steel wall assemblies. They also found that LSF wall assembly without insulation provides higher fire resistance compared to cavity insulated LSF wall assembly. Feng et al. [3] conducted eight small-scale fire tests of non-load bearing wall panels to investigate the thermal performance of cold-formed steel channel sections under standard fire conditions. They found that the thermal performance of these steel channel wall panels was not affected by the type of insulation and that the thermal performance of wall panels improved with the use of cavity insulation.

In summary, past research has provided varying results about the benefits of cavity insulation to the fire rating of LSF wall systems. Extensive research has been undertaken on the fire performance of LSF walls with various configurations in the USA and Canada. However, only limited research has been

undertaken on the fire performance of LSF wall systems used in Australia. Kolarkar and Mahendran [4] developed a new composite LSF wall panel system in which a thin insulation layer was used externally between plasterboards instead of the conventional cavity insulation located within the stud space. Since the new composite LSF wall panels have an external insulation layer between the plasterboards, they also provide climate control and acoustic benefits. Figure 1 shows the new composite LSF wall system [4].

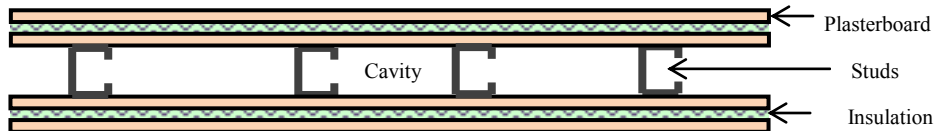


Figure 1. New composite LSF wall panel [4].

Kolarkar and Mahendran [4] found that composite LSF wall panels provided a better quality thermal envelope than the cavity insulated LSF wall panels. Kolarkar [5] conducted a series of fire tests to investigate the thermal performance of load bearing LSF wall panels made of the new composite panels under standard fire conditions. However, numerical studies of the thermal performance of these load bearing LSF wall panels have not been conducted. Hence they were performed to investigate the thermal performance of the new load bearing LSF wall panels under standard and realistic design fire conditions. The numerical analyses also included the traditional LSF wall systems with and without cavity insulation to investigate the differences in their thermal performances. This paper presents the details of the numerical study of the thermal performance of load bearing LSF wall panels under fire conditions. It includes the details of finite element models of load bearing LSF wall panels, the thermal analysis results under standard and real design fire conditions, and their comparisons with experimental results.

2 THERMAL PROPERTIES OF GYPSUM PLASTERBOARD, INSULATION MATERIALS AND STEEL

2.1 Gypsum Plasterboard

In order to develop suitable finite element models of Australian gypsum plasterboard, thermal properties of gypsum plasterboard were summarized based on a series of experimental results [6] and past research [7,8]. These proposed thermal properties were used in the finite element models (SAFIR) [9]. Figure 2(a) shows the proposed thermal conductivity of gypsum plasterboard. In order to include the effect of ablation, the thermal conductivity of plasterboard was modified to 0.80 W/m/K at 1000°C.

Past research showed some discrepancy in relation to the second dehydration reaction. However, it is concluded that the first and second dehydrations occur at 100 to 150°C and 150 to 200°C, respectively, based on our experiments [6]. Decomposition of Calcium Carbonate occurs at 670°C, which is similar to Wakili et al.'s [10] observation. These outcomes including the third peak to simulate the effect of decomposition of Calcium Carbonate were used in the proposed specific heat versus temperature curves. At about 400°C, an exothermic reaction occurs, in which the molecular structure of the soluble crystal restructures into a lower insoluble energy state (Figure 2b). This observation is similar to Manzello et al.'s [11] findings. Figure 2(b) also shows the proposed specific heat values as a function of temperature and compares them with test and other researchers' specific heat values [7,8] while Figure 2(c) shows the relative density values as a function of temperature and compares them with test and other researchers' relative density values [7,8,12]. Further details of the proposed thermal properties of plasterboards are given in [6]. The specific volumetric enthalpy of gypsum plasterboard is given by the area under the specific heat multiplied by the density versus temperature curve as shown in Equation (1). The proposed specific volumetric enthalpy values were used as input to SAFIR [9] in our thermal analyses.

$$E(T) = \int_{T_a}^T C_p(T) \rho(T) dT \quad (1)$$

where $E(T)$ is the specific volumetric enthalpy in J/m^3 at temperature T , $C_p(T)$ is the specific heat ($J/(kg^\circ C)$) and $\rho(T)$ is the density (kg/m^3) at temperature T , and T_A is the ambient temperature. Keerthan and Mahendran [6] recommended a convective coefficient (h) of $25 W/m^2/K$ for the exposed side of plasterboard and $10 W/m^2/K$ for its unexposed side. They recommended 0.9 as emissivity of plasterboard for both exposed and unexposed surfaces. When the proposed thermal properties were used as input to SAFIR, the time-temperature profiles agreed well with Kolarkar's [5] fire test results.

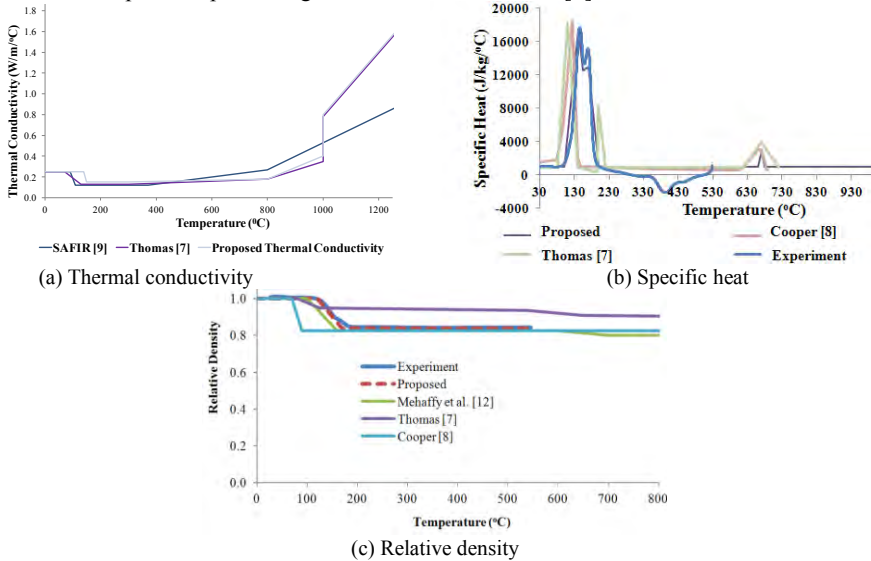


Figure 2. Proposed thermal properties of plasterboard.

2.2 Insulation Materials

The new composite LSF wall system was developed with glass fibre or rockwool or cellulose fibre insulation sandwiched between the plasterboard layers. Glass wool is formed from molten glass (silicate) fibres and is currently the most commonly used insulation in Australia, particularly in residential construction. Rockwool insulation typically provides much higher levels of insulation being formed from basalt or iron ore blast furnace slag to provide higher density. In order to develop suitable finite element models of composite panels, thermal properties of insulation were summarized based on our experimental results and past research work [13-15]. When the proposed thermal conductivity and specific heat values of rockwool, glass fibre and cellulose fibre were used as input to the numerical models based on SAFIR [9], the time-temperature profiles agreed well with fire test results from Kolarkar [5]. Figure 3 shows proposed thermal conductivities of insulations. Further details of the proposed thermal properties of insulation materials and the specific heat test procedure used in the testing of plasterboard and insulation are reported in Keerthan and Mahendran [16].

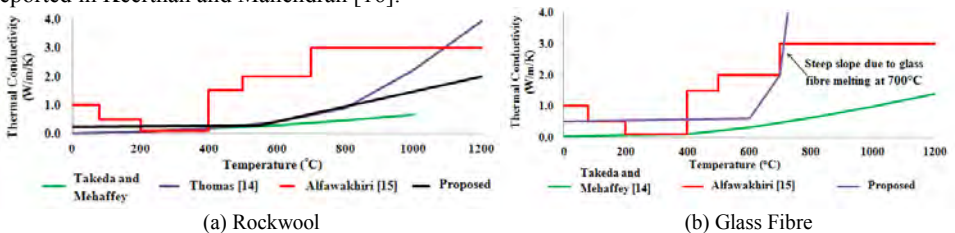


Figure 3. Proposed thermal conductivity of insulation.

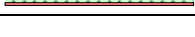
2.3 Steel

The temperature increase of a steel member is a function of its thermal conductivity and specific heat of steel. The precision in the determination of thermal properties of steel, such as specific heat and thermal conductivity, has little influence on the thermal modelling of LSF walls under fire conditions since steel framing plays a minor role in the overall heat transfer mechanism of the LSF wall assembly [15]. The properties of steel within the SAFIR code are obtained from those given in Eurocodes [17].

3 EXPERIMENTAL STUDIES OF THE THERMAL BEHAVIOUR OF LOAD BEARING LSF WALL PANELS

In order to investigate the thermal performance of load bearing LSF wall panels, 10 fire tests of full scale panels of dimensions 2400 mm x 2100 mm were conducted by Kolarkar [5] and Gunalan [18]. The wall assemblies typically consisted of four commonly used cold-formed steel lipped channel section studs (90x40x15mm) spaced at 600 mm. The studs were fabricated from galvanized steel sheets (G500) having a nominal base metal thickness of 1.15 mm and a minimum yield strength of 500 MPa. Test specimens were built by lining the test frames with one or two layers of gypsum plasterboards manufactured by Boral Plasterboard under the product name of Firestop. All the plasterboards used were 1200 mm in width and 2400 mm in height with a thickness of 16 mm and a mass of 13 kg/m². There were three groups of wall specimens made of (1) no insulation (2) cavity insulation and (3) external insulation (composite panels). Three insulation materials, glass fibre, rockwool and cellulose fibre were used. Tests were conducted using the standard fire curve given in AS 1530.4 [19]. One face of the test specimens was exposed to heat in a propane-fired vertical gas furnace. Time-temperature profiles at various locations across the specimen thickness were measured during the tests using thermocouples. Table 1 shows the failure times of test specimens. Kolarkar [5] provides a full description of these tests while this section provides their important details and some results. Experimental studies showed that LSF walls with external insulation provided a greater fire protection than those with cavity insulation. The composite panel with rockwool insulation (Test Specimen 7) failed earlier due to the lack of space for thermal expansion. Its failure time was predicted as 153 minutes based on finite element analyses [18].

Table 1. Failure times of LSF wall test specimens [5,18].

Test No.	Configuration	Load Ratio	Insulation	Failure Time (min)
1		0.2	None	53
2		0.2	None	111
3		0.2	Glass Fibre (Cavity)	101
4		0.2	Rock Fibre (Cavity)	107
5		0.2	Cellulose Fibre (Cavity)	110
6		0.2	Glass Fibre (External)	118
7		0.2	Rock Fibre (External)	136*
8		0.2	Cellulose Fibre (External)	124
9		0.4	Glass Fibre (External)	108
10		0.4	Rock Fibre (External)	134

4 NUMERICAL STUDIES OF THE THERMAL BEHAVIOUR OF LOAD BEARING LSF WALL PANELS

4.1 General

This section presents the details of the numerical studies into the thermal behaviour of the tested load bearing LSF wall panels and their results. Recently many numerical heat transfer models have been developed [9,15]. There are also many general finite element packages that can be used for thermal analyses. The finite element model employed in this study to predict the thermal behaviour of load bearing LSF wall panels was based on SAFIR [9]. SAFIR is a special purpose finite element program for the analysis of structures under ambient and elevated temperature conditions. In this research the GID software was used to create the input file for the models as well as analysing the model output results.

4.2 Thermal boundary conditions and material properties

The heat flux at the boundary will be calculated from the temperature of the fire curve T_g and the temperature on the surface T_s according to Equation (2).

$$q = h(T_g - T_s) + \sigma\varepsilon(T_g^4 - T_s^4) \quad (2)$$

where q is the total heat flux, ε is the relative emissivity, σ is the Stefan–Boltzmann constant ($5.67E-08\text{W/m}^2/\text{K}^4$), T_g and T_s are the gas and surface temperatures, respectively. For fire exposure to the standard cellulosic curve, $T_g = 345\log(8t+1)+20$. Convective heat transfer coefficient (h) is approximately $25\text{W/m}^2/\text{K}$ on the fire exposed side, and it is $10\text{W/m}^2/\text{K}$ on the unexposed side. Emissivity of 0.9 was used for both exposed and unexposed surfaces. Default thermal properties (specific heat and thermal conductivity) for both Type X and Type C gypsum plasterboards within SAFIR are based on Cooper's [8] research. However, the proposed thermal properties in Section 2 were used in this research. In order to investigate the thermal performance of load bearing LSF walls, finite element models of Kolarkar's [5] test wall panels were developed. Figure 4 shows the finite element models of Test Specimen 7. Here three voids were created to transfer the heat through radiation and convection. Elements surrounding an internal void were assigned in the counter clockwise direction. The developed finite element models were validated using the results obtained from fire tests of load bearing LSF walls in [5].

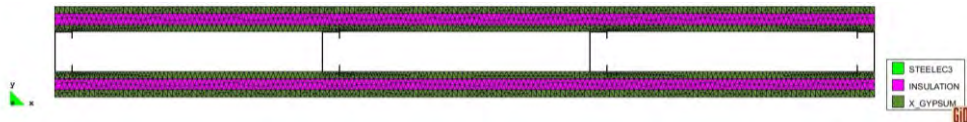


Figure 4. Finite element modelling of LSF wall panel.

4.3 Validation of finite element models of LSF walls using fire test results

It is necessary to validate the developed finite element models for the thermal analyses of load bearing LSF walls. This was achieved by comparing the time-temperature profiles with the corresponding fire test results of load bearing LSF walls [5]. Figures 5 (a) to (d) and Figure 6 show the finite element analysis (FEA) results in the form of temperature versus time for selected load bearing LSF wall specimens and compare them with corresponding test results [5]. The average temperature profiles of the studs were considered in the comparison of test and FEA results. These figures indicate that the developed finite element models predict the time-temperature profiles of load bearing LSF walls with good accuracy. Comparisons were also made for other LSF wall specimens and a similar level of agreement between FEA and test results was obtained in all the tests.

Finite element analyses clearly show that the temperature gradients across the steel studs and associated thermal bowing effects are larger when cavity insulation is used in comparison to other cases (Figure 5(c)). Hence it is considered that the use of cavity insulation is detrimental to the fire rating of walls as also shown by fire tests. Figure 5(d) shows that the new composite LSF wall panels using

external insulation lead to reduced temperatures in steel studs at any given time and a more uniform temperature distribution across their cross-sections, thus producing minimum early lateral deformation (thermal bowing). For example, the results show that in Specimen 4 with rockwool cavity insulation the hot (HF) and cold flange (CF) temperatures are 590°C and 227°C after 100 minutes while in Specimen 7 with rockwool external insulation they are 293°C and 192°C (Figures 5 (c) and (d)). Hence it is clear that the use of external insulation is able to provide much greater thermal protection to LSF steel studs than cavity insulation. All of these findings thus confirm the observations made in Kolarkar’s fire tests [5]. It is noted that load bearing LSF walls exposed to fires are affected by processes not described by heat transfer such as ablation of plasterboard and insulation, migration of moisture vapours and penetration of cool ambient air or hot furnace gases into the cavity. These processes were taken into account through the use of suitable thermal conductivity values for plasterboard and insulations (Section 2).

In summary, the comparisons between FEA and fire test results reported here have established the validity of the finite element models in simulating the thermal behaviour of full scale load bearing LSF walls and the accuracy of the values used for relative emissivity, convective coefficient and other thermal properties. The results from FEA also produced valuable time-temperature data and an improved understanding of the thermal performance of load bearing LSF wall panels using cavity and external insulations. Figure 7 shows the temperature distributions across the cross-section of Test Specimens 2 and 7 (Rockwool external insulation).

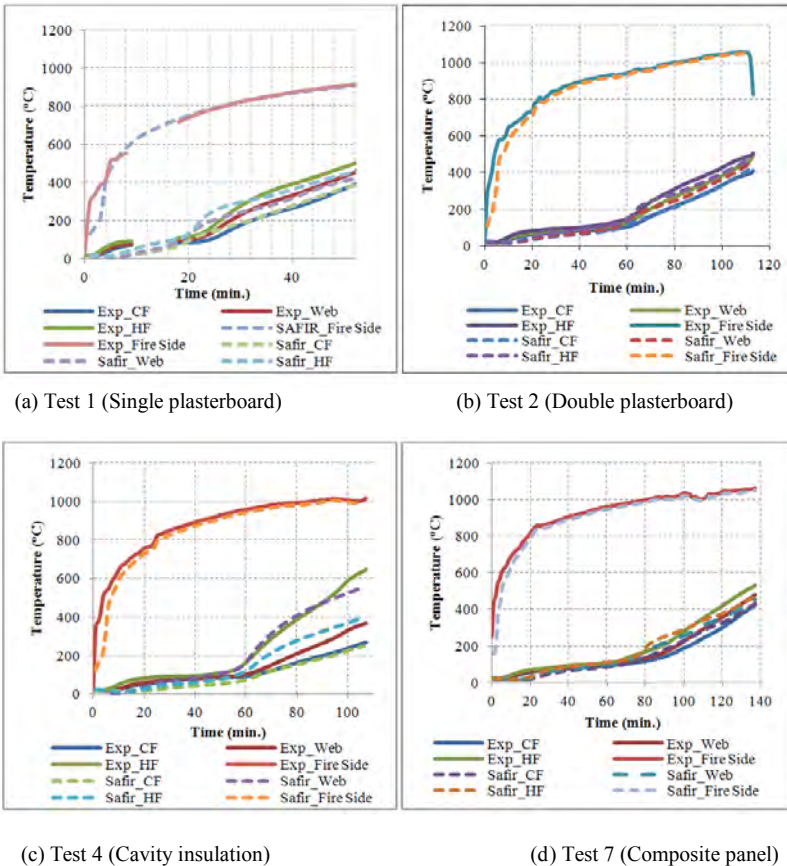


Figure 5. Time-temperature profiles of test specimens (Steel stud).

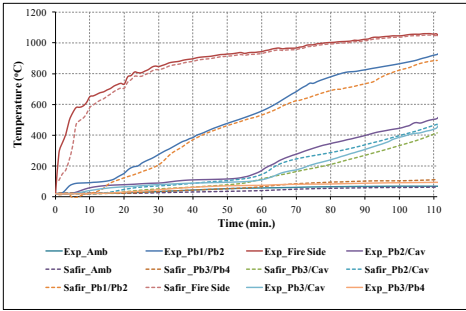


Figure 6. Time-temperature profiles of Test Specimen 2 (Plasterboard).

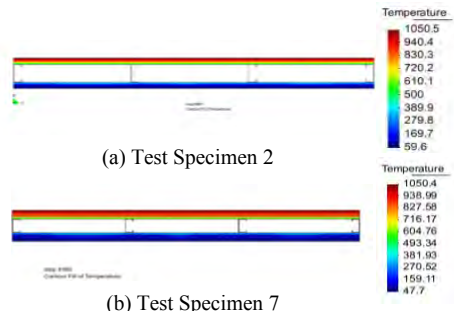


Figure 7. Temperature distributions of LSF walls under standard fire conditions.

5 EFFECT OF VARIOUS PARAMETERS ON THERMAL BEHAVIOUR OF LOAD BEARING LSF WALL PANLES USING NUMERICAL STUDIES

5.1 Geometry of cold-formed steel stud section and stud depth

In order to investigate the effect of the geometry of cold-formed steel stud sections on the thermal behaviour of load bearing LSF walls, further finite element analyses were conducted. In this study LSF wall panels made of 90x40x15x1.15 LiteSteel Beams (LSB) and 90x40x15x1.15 Lipped Channel Sections (LCS) (Test Specimen 2) with double plasterboards on both sides of steel studs were considered. The LSB is a cold-formed steel hollow flange channel beam produced using a patented manufacturing process involving simultaneous cold-forming and dual electric resistance welding. Figure 8 shows the time-temperature profiles of LSB and LCS wall panels while Figure 9 shows their temperature distributions. Figure 8 indicates that the geometry of the cold-formed steel stud section does not have a significant effect on the time-temperature distributions in LSF wall panels. Further finite element analyses were conducted to investigate the effect of stud depth on the thermal behaviour of LSF walls. They also indicate that the depth of the cold-formed steel member does not have a significant effect on the time-temperature distributions in LSF wall panel systems.

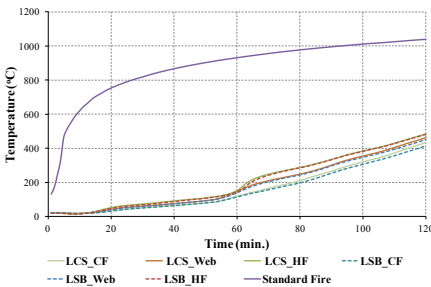


Figure 8. Effect of stud section geometry on the thermal performance.

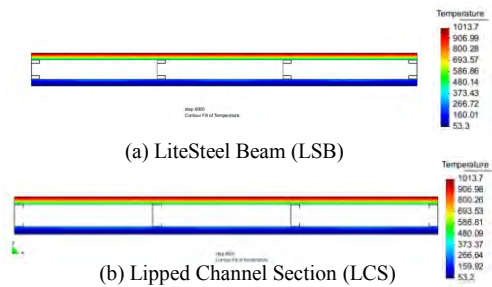


Figure 9. Temperature distributions of LSF walls under standard fire conditions.

5.2 Real design fire curves

The standard time-temperature curve does not represent the modern accessories in typical residential and commercial buildings, where they incorporate both traditional wooden furniture and modern items such as cushion furniture, mattresses, fabric coated partitions and many other items that make use of thermoplastic materials. Therefore finite element analyses were performed using the recently developed realistic design fire curves [20] based on the parametric curves in Eurocode 1 Part 1-2 [21]. They were

conducted using the finite element model described in Section 4 and the proposed thermal properties in Section 2. Figure 10 shows the FEA results in the form of temperature versus time for Test Specimen 2 (Double plasterboards) under the real design curve (EU-0.03) and compares them with corresponding test results [20]. EU-0.03 fire curve represents an opening factor of 0.03. This comparison shows a good agreement between the test and FEA results, and thus allows the use of finite element models for LSF wall panels under other real design fire curves.

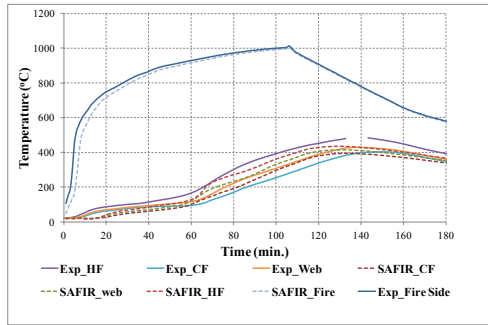


Figure 10. Time-Temperature Profiles of Test Specimen 2 under Real Design Fire Curve (EU-0.03).

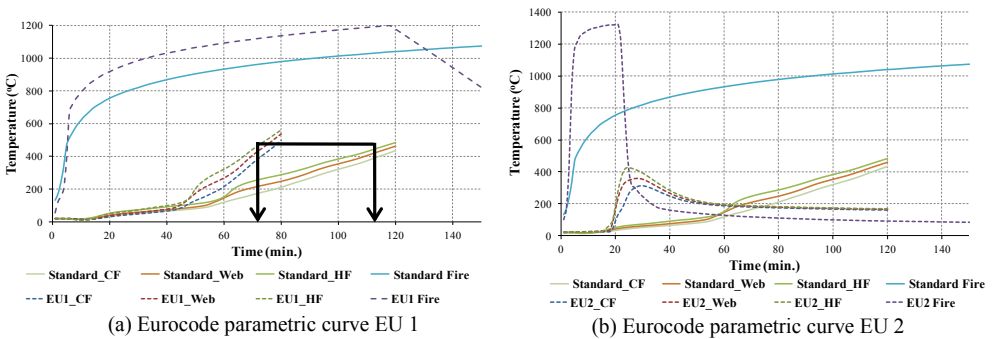


Figure 11. Time - temperature profile of Test Specimen 2 under real design fire curves (EU1 and EU2).

Two Eurocode parametric curves (EU1 and EU2) were also considered in the numerical studies reported in this section. EU1 and EU2 curves represent the opening factors of 0.02 (EU1) and 0.12 (EU2) as they cover the entire range, and are conservative. Also EU1 (0.02) and EU2 (0.12) would be the ideal time-temperature curves for this investigation of load bearing LSF wall panels for real building fires as they include a rapid (EU2) and a prolonged (EU1) fire curve falling between the two extremes. Figure 11 shows these two Eurocode parametric curves developed for dwellings based on a fuel load density of 1138 MJ/m² [20,21]. Figures 11 (a) and (b) show the finite element analysis results in the form of temperature versus time for a load bearing LSF wall panel (Test Specimen 2) under these two real design fire curves [21] and compare them with those under standard fire conditions. Figure 11 (a) shows that the LSF steel stud temperatures under real design fires [hot (HF) & cold (CF) flanges, web] are considerably increased in comparison to LSF wall studs under standard fires. This means that the failure time (fire resistance rating) decreases from 111 to 73 minutes based on a limiting temperature of 500°C, ie. 35% reduction. Figure 11 (a) shows that the time-temperature profiles of load bearing LSF wall panels under the real design fire curve - EU1 are much higher than those under the standard fire curve while Figure 11 (b) shows that the time-temperature profiles of load bearing LSF wall panels under the real design fire curve - EU2 are lower than those under the standard fire curve. It is clear from Figure 11 (a) that real

design fires such as EU1 can cause severe damage to LSF wall panels protected by two plasterboards than standard fires. However, real design fires such as EU2 will not cause severe damage to these wall panels than standard fires (Figure 11 (b)).

Hopkin et al. [22] stated that thermal properties of gypsum plasterboard depends on heating rate and can result in inaccuracies when they were used in the simulation of temperature development under natural fire conditions. The likely cause of this is the relationship between heating rate and other behaviours such as moisture flow, ablation and cracking. Hence detailed experimental and numerical studies will be undertaken to investigate the effect of rapid real fires on the thermal performance of LSF wall panels.

6 CONCLUSIONS

This paper has presented the details of a numerical study on the thermal performance of load bearing LSF wall panels that included both the conventional cavity insulated and the new composite panel walls. It included the details of the developed finite element models of load bearing LSF wall panels, the thermal analysis results from SAFIR under standard fire conditions and their comparisons with fire test results obtained by Kolarkar [5]. A good comparison with fire test results showed that accurate finite element models can be developed and used to simulate the thermal behaviour of full scale load bearing LSF wall panels with varying configurations of cavity and external insulations and plasterboards. For this purpose the proposed thermal properties of plasterboard, insulation materials and steel given in this paper should be used. Experimental and numerical studies showed that the use of cavity insulation was detrimental to the fire rating of walls. It not only led to higher temperatures in the steel studs, but also to larger temperature gradients across their depth and increased thermal bowing effects. In contrast, the use of external insulation led to lower temperatures and a more uniform temperature distribution in the steel stud cross-sections at any given time, thus providing greater thermal protection to the walls. Finite element analysis results showed that the shape and depth of the cold-formed steel stud cross-sections did not have a significant effect on the temperature distributions in load bearing LSF wall panels. The use of real design fire conditions based on Eurocode parametric curves in the numerical studies showed that some real building fires can cause severe damage to LSF wall panels than the standard fire specified in various fire codes while other real building fires are not as severe as the standard fire.

7 ACKNOWLEDGEMENTS

The authors wish to thank Australian Research Council for the financial support to this project, Queensland University of Technology for providing testing facilities and technical support, and Boral Plasterboard for providing the required plasterboards.

REFERENCES

- [1] Sultan, M. A., "Effect of Insulation in the Wall Cavity on the Fire Resistance Rating of Full-Scale Asymmetrical (1 x 2) Gypsum Board Protected Wall Assemblies", *Proceedings of the International Conference on Fire Research and Engineering*, Orlando, MA, 545-550, 1995.
- [2] Kodur, V.R. and Sultan, M.A., "Factors Governing Fire Resistance of Load Bearing Steel Stud Walls", *Proc. of the 5th AOSFST International Conference*, Newcastle, Australia, pp.1-2, 2001.
- [3] Feng, M., Wang, Y.C. and Davies, J.M., "Thermal Performance of Cold-formed Thin-walled Steel Panel Systems in Fire", *Fire Safety Journal*, 38(4), 365-394, 2003.
- [4] Kolarkar, P. and Mahendran, M., "Thermal Performance of Plasterboard Lined Steel Stud Walls", *Proc. of the 19th International Specialty Conference on Cold-Formed Steel Structures*, St. Louis, Missouri, USA, 517-530, 2008.

- [5] Kolarkar, P., Structural and Thermal Performance of Cold-formed Steel Stud Wall Systems under Fire Conditions, PhD Thesis, Queensland University of Technology, Brisbane, Australia, 2010.
- [6] Keerthan, P. and Mahendran, M., “Numerical Studies of Gypsum Plasterboards under Fire Conditions”, *Research Report, Queensland University of Technology*, Brisbane, Australia, 2010.
- [7] Thomas G., “Modelling Thermal Performance of Gypsum Plasterboard-lined Light Timber Frame Walls using SAFIR and TASEF”, *Fire and Materials*, 34(8), 385-406, 2010.
- [8] Cooper, L.Y., “The Thermal Response of Gypsum-Panel/Steel Stud Wall Systems Exposed to Fire Environments – A Simulation for the use in Zone-Type Fire Models”, *NIST Report NISTIR 6027, Building and Fire Research Laboratory*, NIST, Gaithersburg, USA, 1997.
- [9] Franssen J.-M., “SAFIR. A Thermal/Structural Program Modelling Structures under Fire”, *Engineering Journal*, A.I.S.C., 42 (3), 143-158, 2005.
- [10] Wakili, K.G., Hugi, E., Wullschleger, L. and Frank, T.H., “Gypsum Board in Fire—Modelling and Experimental Validation”, *Journal of Fire Sciences*, 25(3), 267–282, 2007.
- [11] Manzello, S.L., Richard, G.G., Scott, R.K. and David B.L., “Influence of Gypsum Board Type on Real Fire Performance of Partition Assemblies”, *Fire and Materials*, 31(7), 425-442, 2007.
- [12] Mehaffey, J.R., Cuerrier, P., and Carisse, G., “A Model for Predicting Heat Transfer through Gypsum-Board/Wood-Stud Walls Exposed to Fire”, *Fire and Materials*, 18(5), 297-305, 1994.
- [13] Takeda, H. and Mehaffey, J.R., “Wall 2D: A Model for Predicting Heat Transfer Through Wood-Stud Wall Exposed to Fire”, *Fire and Material*, 22(3), 133-140, 1998.
- [14] Thomas, G.C., “Fire Resistance of Light Timber Framed Walls and Floors”, *Fire Engineering Research Report 97/7, University of Canterbury*, Christchurch, New Zealand, 1997.
- [15] Alfawakhiri, F., “Behaviour of Cold-Formed Steel-Frames Walls and Floors in Standard Fire Resistance Tests”, PhD Thesis, Dept. of Civil and Environmental Eng., Carleton University, Canada, 2001.
- [16] Keerthan P. and Mahendran M., “Numerical Modelling of non-load bearing LSF walls under fire conditions”, *Journal of Fire Sciences*, In press, 2012.
- [17] EN 1993-1-2 Eurocode 3: Design of steel structures - Part 1-2: General Rules - Structural Fire Design, European Committee for Standardization, Brussels, 1995.
- [18] Gunalan, S., “Structural Behaviour and Design of Cold-formed Steel Wall Systems under Fire Conditions”, PhD Thesis, Queensland University of Technology, Brisbane, Australia, 2011.
- [19] Standards Australia (SA), AS 1530.4 Methods for Fire Tests on Building Materials, components and structures, Sydney, Australia, 2005.
- [20] Ariyanayagm, A., “Structural and Thermal Behaviour of Light Gauge Steel Frame Wall Panels Exposed to Real Fires”, *PhD Report, QUT*, Brisbane, Australia, 2010.
- [21] EN 1991-1-2, Eurocode 1: Actions on structures. Part1-2: General Actions – Actions on structures exposed to fire, Burssels: European Committee for Standardization, Germany, 2002.
- [22] Hopkin, D.J., Lennon, T., Rimawi, J.E., and Silberschmidt, V.V., “Numerical Study of Gypsum Plasterboard Behaviour under Standard and Natural Fire Conditions”, *Fire and Materials*, 36(2), 107-126, 2012.

STABILITY OF ALUMINIUM BEAMS IN CASE OF FIRE, EXPERIMENTS

O. R. (Ronald) van der Meulen*, Frans Soetens** and Johan Maljaars***

*Materials innovation institute (M2i), Eindhoven University of Technology, TNO
r.vandermeulen@m2i.nl / private@vandermill.eu

** Eindhoven University of Technology
f.soetens@tue.nl

*** TNO
e-mail: johan.maljaars@tno.nl

Keywords: Aluminium, Moment gradient, Rotation capacity, Local buckling, Creep, Experiments

Abstract. *Fire is often the dominant design criterion for aluminium Structures. Present design rules neglect both the decrease in susceptibility to local buckling and the effects of creep that are intrinsic to aluminium and may therefore either under or over predict the temperature of failure depending on the load and exposure period. As part of a larger research program aimed at remedying this situation, the present paper reports the results of an experimental study on 28 aluminium SHS members with varied cross-sections, temperature(-gradient)s and heating rates loaded in bending. The experimental setup is novel itself and employs an electric heating tube or “sock” on the inside of the specimen as well as heated supports and load application point, delivering a high degree of control of temperature in time and a consistent temperature in space.*

1 INTRODUCTION

Fire is often the dominant design criterion for lightweight aluminium structures such as helicopter platforms and atria. In aluminium constructions, direct contact to the flames is generally prevented by designing structures to be far from potential sources of heat, insulation or active cooling measures. Relatively modest temperature rises still require careful design using accurate design rules as over half the strength of aluminium is lost in the temperature range of approximately 175-300°C. Present design rules are inspired by steel standards and neglect aluminium's decrease in susceptibility to local buckling that is intrinsic to it as a consequence of its stiffness declining much more slowly with temperature than its strength [1]. This positive effect is counteracted by the action of creep, which is the continued straining of a material under a load that remains constant. The rate of creep is a function of both temperature and load. Experiments presented in the present paper indicate a significant reduction in carrying capacity of especially ductile sections subjected to bending at a temperature of approximately 300°C.

The aim of the paper is to provide experimental data that investigates the effect of elevated temperatures on the local buckling behaviour of beams subjected to bending with a varying moment in the length direction. Columns were already considered in an earlier study[2],

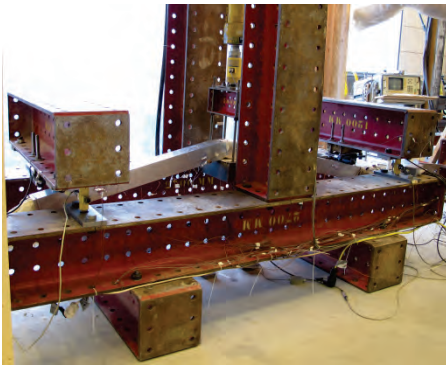
Two different types of experiments were performed on a total of 28 aluminium AA6060-T66 beams: For the first type, termed the *steady state* test, the specimen is heated to, and then kept at, a predetermined temperature. Then the beam is subjected to an increasing deformation at the centre of the 3-point bending setup and the resulting force and rotations are measured. This type of test might be less well suited for aluminium structures as it does not reproduce well the effects of creep in a real fire. The second type of experiment, The *transient state* test, seeks to remedy this by first applying a load between 45-75% of the room temperature strength $F_{0,2}$, and then increasing the temperature at a rate corresponding

to either a 30 or 120 minute fire, at $10^{\circ}\text{C}/\text{min}$ and $2.5^{\circ}\text{C}/\text{min}$, respectively. This mimics the action of a real fire on an insulated aluminium structure where a static load in the same range is always present and the structure is slowly heating up.

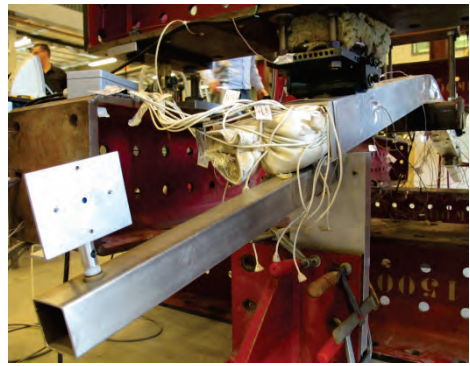
2 DESCRIPTION OF THE SETUP

The profiles were heated from within by means of a purpose made “heating sock” constructed from a ceramic welding blanket with 8 electric resistance heater strips attached to the sides and stuffed with ceramic insulation wool. A 2 cm layer of insulation was also applied to the outside of the specimens to increase the maximum temperature and reduce (spatial) temperature variation.

Placing the heating system inside the specimen simplified the support and load application point in the setup. Moreover it facilitated sensor placement and improved temperature consistency. All experiments were performed on the 3-point bending setup as depicted in fig. 1a.



(a) Total Experimental setup.



(b) Detail showing rotation sensor,(square on the left) heated roll support, heating sock with electric leads and a protective casing for the laser displacement sensor measuring the support deflection (aluminium column with clamps)

Figure 1 Experimental Setup. No insulation was applied to the outside for this room temperature experiment.

The specimens were freely supported and a deflection or constant load was applied at centre span via a steel saddle. Both the saddle and the supports were electrically heated to the same profile as the specimen to minimize heat loss and temperature differences in the length and cross-section of the beam. Temperatures were measured at 32 locations by type T class a thermocouples. A computer PI-algorithm was used to continuously control the electric heater power directed to the individual sides of the specimen, the supports and the saddle.

The setup was designed to limit and/or dissipate heat flowing to the reaction frame to allow for accurate measurements. The load application saddle at centre span was fitted with a 1 cm layer of calcium silicate plate insulation to further reduce temperature differences in the part of the beam with the maximum moment.

Reaction forces to the roll-supports were also measured to verify symmetry. The heated support-rolls were attached to large steel profiles by 6 cm long stainless steel threaded rods. These steel profiles acted as radiators, limiting temperature changes at the 2 load cells at either end (4 reaction load cells in total). The

steel profiles could be easily moved to change the length between the supports and thus the gradient of the moment.

3 MATERIAL PROPERTIES

An extensive study to the material properties of aluminium alloy AA6060-T66 was performed by [4]. This includes data on the creep behaviour of the material. This data will be used to reproduce the experiments presented in the present paper in a future finite element analysis. In order to compare experiments performed at different temperatures, all results are normalized to their respective moment $M_{0.2,\theta}$, force $F_{0.2,\theta}$ and rotation $\varphi_{0.2,\theta}$ at the 0.2% proof stress $f_{0.2,\theta}$ at the given temperature. These quantities were calculated from:

$$M_{0.2,\theta} = W_{el} f_{0.2,\theta}$$

$$F_{0.2,\theta} = 4 M_{0.2,\theta} / (L - D)$$

$$\varphi_{0.2,\theta} = \frac{f_{0.2,\theta}}{E_{0.2,\theta}} \left(\frac{L+D}{H-t} \right)$$

where W_{el} is the elastic section modulus, L is the length between the supports and D is the length of constant moment at the load application. (Equal to the length of the load application insulation plate) The Young's modulus of aluminium alloy AA6060-T66 at elevated temperatures was measured by [3] and for the specific beams used in the experiments by the author. All these measurements correspond well with the tabulated stiffness values of Eurocode [4], and these are used therefore. Measurements on the 0.2% proof stress $f_{0.2,\theta}$ were also performed on a Gleeble 3800 thermo mechanical simulator. Values found were higher than the lower bound values of [4]. The values are plotted in figure 2 together with fitted equations for each different thickness of aluminium as used in the experiments independently. Figure 3 shows an example of the stress-strain curves obtained and clearly shows the effect of creep; well before the onset of necking the stress-strain curves is decreasing. Curve-fits represent LSE fits to the general shape of equation as proposed by Kandare [5], which was found to be in excellent agreement with available data:

$$f_{0.2,\theta} = \frac{f_{0.2,\theta=0}}{2} - \frac{f_{0.2,\theta=0}}{2} \tanh[C_1(\theta - \theta_{50\%})]$$

where $f_{0.2,\theta=0}$ is the fictitious value of the 0.2% proof stress at 0°C, introduced to have the Kandare equation pass through $f_{0.2}$ at 20°C. Its value is defined by

$$f_{0.2,\theta=0} = f_{0.2,\theta} \frac{1 - \tanh[C_1(20 - \theta_{50\%})]}{2}$$

The values $\theta_{50\%}$ and C_1 are curve-fitting constants. $\theta_{50\%}$ indicated the temperature where the 0.2% proof stress is reduced by 50% from its room temperature value. In Table 1, these parameters may be found.

Table 1 Curve-fitted parameters for Kandare equation for 0.2% proof stress as a function of temperature. R^2 is the residual sum of squares.

	$f_{0.2}$ (N/mm ²)	$f_{0.2,\theta=0}$ (N/mm ²)	$\theta_{50\%}$ (°C)	C_1 (1/°C)	R^2
van der Meulen 3 mm	256.0	262.4	239.7	$8.4490 \cdot 10^{-3}$	0.9947
van der Meulen 4 mm	217.3	230.8	215.6	$7.2640 \cdot 10^{-3}$	0.9990
van der Meulen 5 mm	222.5	224.4	255.0	$1.0140 \cdot 10^{-3}$	0.9930
Maljaars	206.3	217.5	224.7	$7.2500 \cdot 10^{-3}$	0.9835

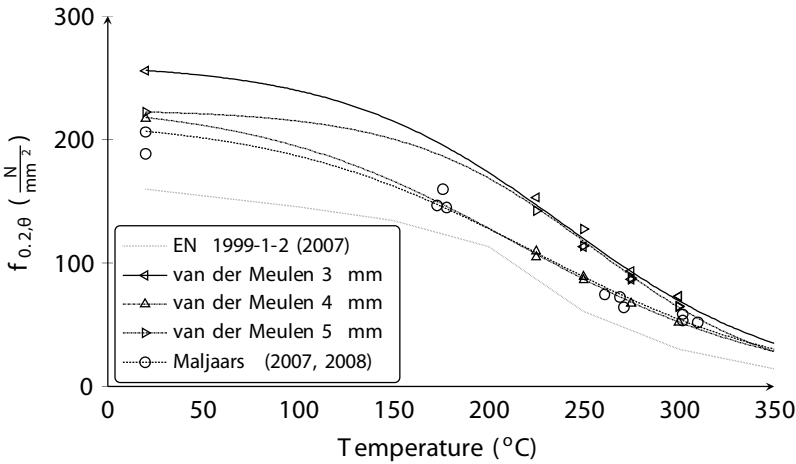


Figure 2. 0.2% proof stress $f_{0.2,\theta}$ of steady state tests as a function of temperature along with fitted equations

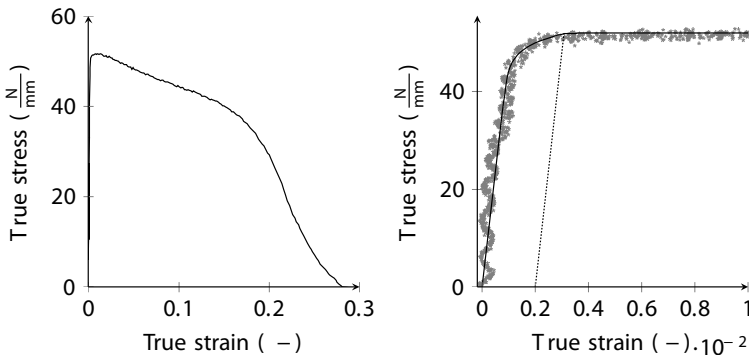


Figure 3. Example of stress-strain curves as obtained in tensile test at elevated temperature. Necking did not occur before a true strain of 0.15. The results of 141A/B at 300°C are shown.

4 EXPERIMENTAL PROGRAM

In total 28 different aluminium square hollow sections were subjected to bending tests. Three different nominal thickness values were used with identical nominal outer dimensions. Per thickness, all sections are originating from the same manufacturing batch. Both material and geometric properties are consistent therefore. Geometric properties were measured and are defined in figure 4, The values for the different variables are given in tables 2 and 3, for constant temperature and constant load experiments, respectively.

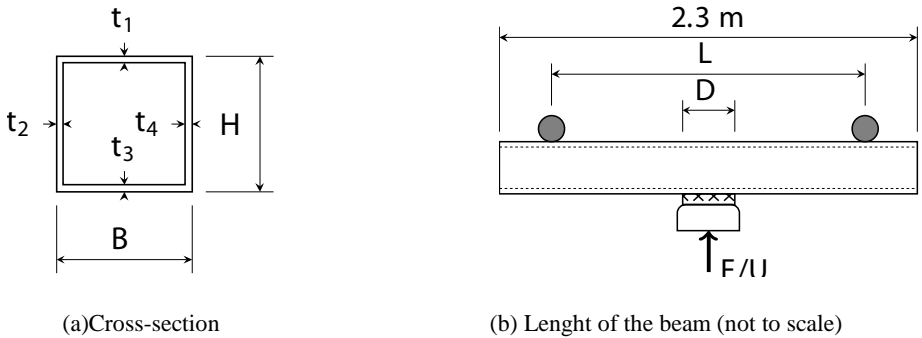


Figure 4. Cross-sectional properties definition

Table 2. Constant temperature test properties. Double temperatures indicate an applied linear gradient over the height of the beam, the highest temperature is at the tensile flange.

Name	$M_{0.2}$ kN	$\varphi_{0.2}$ rad·10 ²	t_1 mm	t_2 mm	t_3 mm	t_4 mm	H mm	B mm	D mm	L m	Temperature °C
135A	9.60	8.11	2.90	3.04	2.99	2.90	99.94	99.93	151.0	2.0	20
131B	9.75	8.12	3.05	3.00	3.00	2.89	99.91	99.96	150.0	2.0	20
134A	4.49	4.87	2.90	3.03	3.01	2.89	99.92	99.94	152.0	2.0	250
133A	2.60	3.24	2.90	3.00	2.98	2.91	99.85	99.86	149.0	2.0	300
134B	5.38	5.58	2.91	3.06	2.98	2.89	99.94	99.95	150.0	2.0	229-250
135B	3.98	4.46	2.90	3.04	2.98	2.89	99.92	99.94	150.0	2.0	262-300
144B	10.31	6.97	3.95	3.93	4.10	4.12	99.94	99.90	145.0	2.0	20
141B	4.14	3.57	4.08	4.12	3.96	3.90	99.99	99.91	146.0	2.0	250
145A	4.14	3.57	4.12	3.96	3.90	4.09	99.99	99.91	146.0	1.0	250
141A	2.49	2.46	4.08	4.12	3.96	3.90	99.99	99.91	146.0	2.0	300
145B	4.91	4.09	4.12	3.98	3.92	4.25	99.90	99.96	150.0	2.0	229-250
143A	3.30	3.05	4.11	3.95	3.90	4.09	99.90	99.95	150.5	2.0	273-300
151B	12.13	7.19	4.81	4.75	4.82	4.88	100.03	100.01	151.5	2.0	20
154B	6.49	4.95	4.74	4.83	4.86	4.79	100.01	100.02	157.5	2.0	250
154A	6.48	2.64	4.74	4.82	4.85	4.79	100.00	100.03	150.0	1.0	250
151A	4.29	3.74	4.79	4.75	4.83	4.86	100.03	100.01	152.0	2.0	300
153A	7.33	5.37	4.73	4.82	4.86	4.79	100.01	100.03	151.0	2.0	231-300
152A	6.21	4.8	4.82	4.85	4.80	4.73	99.99	99.95	152.0	2.0	256-300

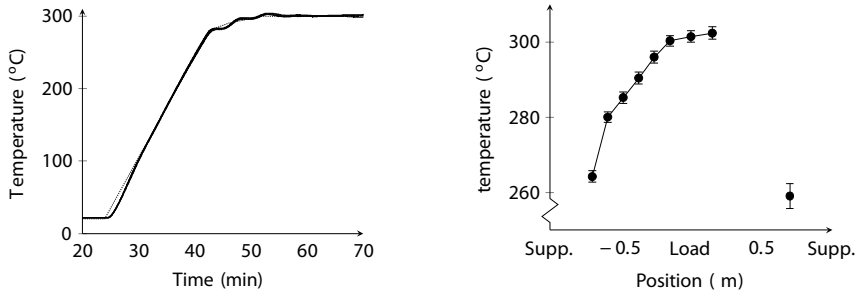
Table 3. Constant load, increasing temperature geometric properties

Name	$F_{0.2}$ kN	$\varphi_{0.2}$ rad·10 ²	t_1 mm	t_2 mm	t_3 mm	t_4 mm	H mm	B mm	D mm	L m	$F/F_{0.2}$ -	Rate °C/min
132A	17.9	8.11	2.90	3.01	3.00	2.90	99.92	99.92	148.0	2	0.458	10
131A	17.8	8.11	2.91	3.04	2.98	2.89	99.92	99.93	149.5	2	0.628	10
132B	17.8	8.11	2.90	3.01	2.99	2.89	99.92	99.90	148.0	2	0.459	2.5
142A	19.2	6.98	3.96	3.92	4.08	4.09	99.94	99.90	149.0	2	0.531	10
143B	19.1	6.98	4.11	3.95	3.90	4.09	99.90	99.95	150.0	2	0.739	10
142B	19.2	6.98	3.96	3.92	4.08	4.09	99.94	99.90	149.0	2	0.538	2.5
144A	35.9	3.73	3.96	3.91	4.10	4.12	99.95	99.90	150.0	1	0.558	10
152B	22.6	7.18	4.83	4.86	4.79	4.72	100.00	99.96	147.0	2	0.588	10
153B	22.6	7.19	4.74	4.82	4.86	4.80	100.00	100.03	150.0	2	0.782	10
155A	22.5	7.19	4.79	4.73	4.83	4.86	100.02	99.99	150.0	2	0.565	2.5

5 EXPERIMENTAL RESULTS

5.1 Temperature distribution

The setup was able to control the temperature of the beam very accurately and according to a constant or increasing temperature profile. This is illustrated in figure 5a. An example temperature distribution along the length of the beam is given in figure 5b. It may be observed that towards the ends of the beam the temperature is lower, but the centre section, where buckling occurs, it is at a constant temperature. Error markers reflect the maximum combined error of the measurement system and thermocouples and the variation in time during the time that the force in the beam is above 90% of the ultimate force as measured. (And the temperature is held constant.)



(a) Temperature profile, 4 indistinguishable lines depict the temperature of the 4 sides of the specimen at centre span. 1 (dashed) line indicates the desired and programmed profile.

(b) Temperature distribution along the length of the beam. The temperature of the beam is controlled by the temperature at centre span

Figure 5 Temperature distribution as measured.

5.2 load/Temperature - rotation plots

5.2.1 Steady state tests

In this section a summary of the data obtained in the experiments is offered. In figure 6 on the left hand side. The normalized moment is shown as a function of the normalized rotation. The normalization was performed using the values quoted in table 2 and 3. For both the 3 and 4 *mm* sections, the constant temperature experiments show that the normalized moment is increased from its room temperature value to a higher value at 250°C. It is noted that the absolute strength and moment decreases with temperature, but less than 0.2% proof stress. This is in line with the expected increase in stability against local buckling. For the 5 *mm* thick specimens, such an increase is not observed and a considerable decrease is observed instead. This might be caused by the fact that an increase in stability does not lead to a higher normalized maximum moment for this relatively stocky cross section (The 3, 4 and 5 *mm* beams are of cross-sectional class 4, 3 and 2, respectively). A decrease in maximum strength due to creep is possible, lowering the maximum normalized moment instead. Further research is required however.

5.2.2 Transient state tests

On the right hand side of figure 6, the normalized rotation as a function of the steadily increased temperature is shown. These figures show expected results, and serve as a calibration and verification of the finite element simulations to be performed. The graphs show that for higher loads the temperature where runaway failure occurs is lower. Also lowering the heating rate leads to an increase in creep and a lowering of the failure temperature. This is because the specimen is subjected to high temperatures for a longer time.

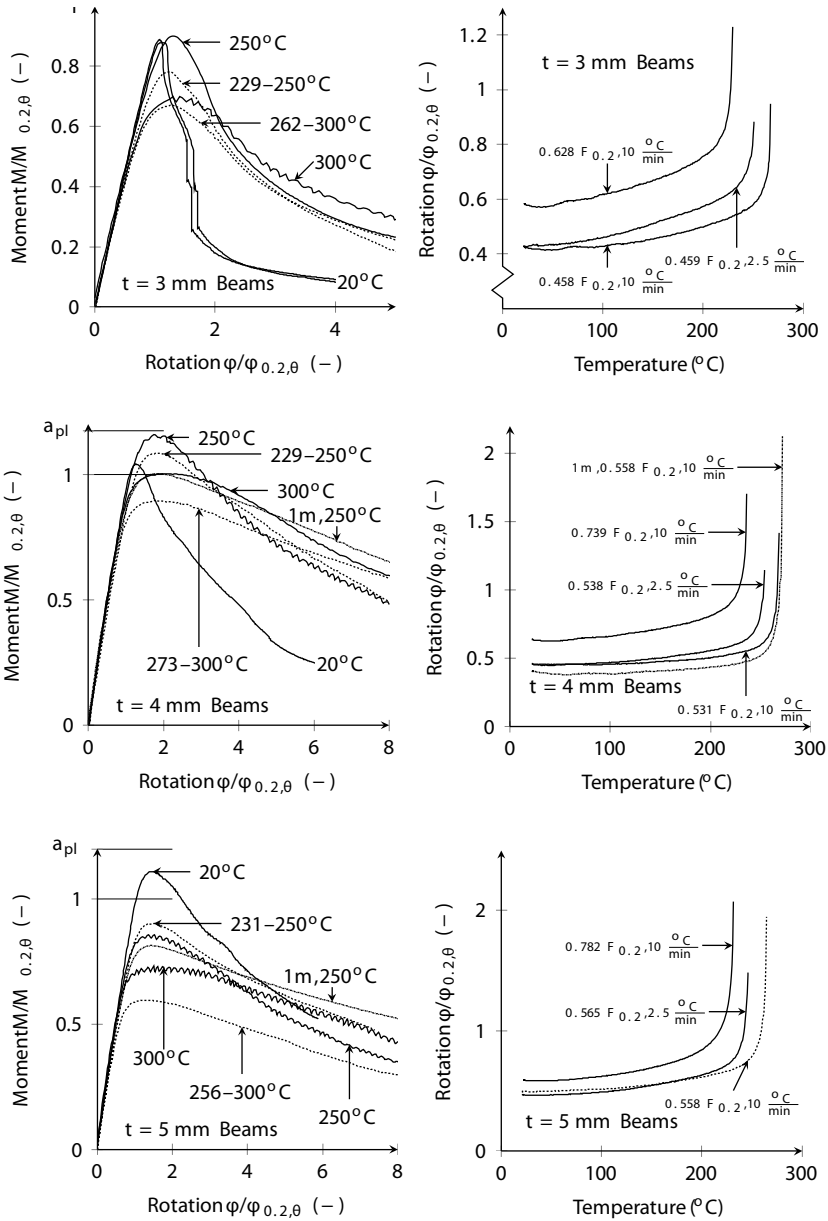


Figure 6. Summarized test data from experiments performed. $a_{pl} = W_{pl}/W_{el}$

6 CONCLUSIONS

An experimental study was presented to the strength and stability of aluminium beams subjected to three point bending at elevated and ambient temperatures. An in-depth analysis of the results and finite element simulations using advanced creep models remain to be performed, but from the experimental evidence obtained it seems clear that a lower reduction for local buckling is required for slender sections at temperatures up to approximately 250°C, as they become less susceptible to local buckling because their 0.2% proof stress is reduced more rapidly with temperature than their stiffness. This may be exploited in more accurate design rules. For stocky sections this may not be the case. For higher temperatures an unexpectedly large decrease in normalized strength is encountered. This is attributed to creep and warrants a closer investigation as it may prove to be unconservative as compared to present design rules.

REFERENCES

- [1] van der Meulen, O. R.; Maljaars, J. & Soetens, F., 'Cross-sectional classification of aluminium beams subjected to fire', *Heron* 55(3/4), 285-302,2010
- [2] Maljaars, J.; Soetens, F. & Snijder, H. H., 'Local buckling of aluminium structures exposed to fire. Part 1: Tests', *Thin-Walled Structures* 47(11), 1404-1417,2009
- [3] Maljaars, J.; Soetens, F. & Katgerman, L., 'Constitutive model for aluminum alloys exposed to fire conditions', *Metallurgical and Materials Transactions A: Physical Metallurgy and Materials Science* 39(4), 778-789.1-2, E. 1999.,2008
- [4] Eurocode 9: Design of aluminium structures - Part 1-2: Structural fire design, European Committee for Standardization, Brussels, Belgium,2007
- [5] Kandare, E.; Feih, S.; Kootsookos, A.; Mathys, Z.; Lattimer, B. Y. & Mouritz, A. P., 'Creep-based life prediction modelling of aluminium in fire', *Materials Science and Engineering: A* 527(4-5), 1185-1193.,2010

ACKNOWLEDGEMENT

This research was carried out under project number M81.1.108306 in the framework of the Research Program of the Materials innovation institute M2i (www.m2i.nl).

AN APPROACH FOR EVALUATING THE RESIDUAL STRENGTH OF FIRE EXPOSED BRIDGE GIRDERS

Esam M. Aziz*, Venkatesh K. Kodur*

* Department of Civil and Environmental Engineering, Michigan State University, USA
e-mails: azizesam@msu.edu, kodur@egr.msu.edu

Keywords: Bridge fires, residual strength, steel girders, finite element analysis, fire resistance.

Abstract. *This paper presents an approach for evaluating the residual strength of fire exposed steel bridge girders. For developing this approach, a set of numerical studies is carried out on typical steel girders using the finite element computer program ANSYS. The analysis is performed in two stages, namely during exposure to fire and then after cooling of the bridge girder. In the first stage of analysis, thermal and structural response of the bridge girder is traced under specified fire exposure and loading conditions. In the second stage (after the bridge girder cools down), the girder was loaded to failure to evaluate the residual capacity of the girder. Results from numerical studies indicate that the maximum fire temperature (and associated temperature in steel) is the most critical factor that influence the residual strength of fire exposed bridge girders. A girder exposed to typical external fire conditions, with maximum fire temperatures reaching 600-700 °C, retains about 70 to 80% of its strength on cooling. On the other hand, a steel bridge girder exposed to hydrocarbon fire with maximum temperature of about 1100 °C loses most of its strength during heating phase of the fire and experiences failure.*

1 INTRODUCTION

In recent years there have been numerous fires in bridges and some of these fires resulted in the collapse of steel girders [1,2]. Thus, fire hazard in bridges can result in significant economic and public losses. Following the fires, traffic on fire damaged bridge (routes) is usually hard to detour and significantly affect the traffic quality in the region. In many cases, fires in bridges burn-out quickly or are extinguished through fire fighting. Thus structure members, in most cases, might retain much of their capacity after exposure to a fire, depending on the severity of the fire, fire duration, geometry and materials used in construction. However, a quick assessment of residual capacity of fire exposed structural members is necessary before routing the traffic on the bridges. Such an assessment also helps in developing strategies for retrofitting structural members in bridges.

The residual capacity of fire exposed bridge girder depends on numerous factors which include fire scenario, permanent degradation of material properties (strength and stiffness), and existence of residual deformations [3].

A review of literature indicates that there is lack of information on the post-fire strength assessment of bridge girders [4]. But, there are limited studies on the residual strength of fire exposed building elements. These studies considered the effect of reversible material properties (thermal and mechanical) in evaluating residual strength of structural members [5,6,7]. However, this information from building elements might not be directly applicable to bridge girders due to different fire scenarios, loading, boundary conditions, failure limit state and sectional properties encountered in bridge fires. This paper presents the development of a numerical approach for evaluating residual strength of fire exposed steel bridge girders.

2 FINITE ELEMENT MODEL

2.1 General

To evaluate the residual strength of fire exposed steel girders, a numerical study is carried out using the finite element computer program ANSYS [8]. This program is capable of handling coupled and uncoupled thermo-mechanical problems. For the analysis, a typical steel bridge girder comprising of different structural components, namely steel girder, reinforced concrete slab, and lateral supports, is selected. Two sets of discretization models were developed for undertaking thermal and mechanical (strength) analysis. Results from thermal analysis are applied as a thermal-body-load on the structural model, uniformly along the girder span. The mechanical analysis is carried out in two stages, namely during fire exposure and after cooling of the girder. High temperature thermal and mechanical properties of steel and concrete, in both heating and cooling phase, are incorporated in the analysis. Strength limit state was adopted for defining failure and the failure is said to occur when the girder is unable to resist the applied load effects.

2.2 Discretization for thermal analysis

For undertaking heat transfer analysis a composite steel-concrete girder, comprising of steel girder and concrete slab, is discretized in to SOLID70 elements. This SOLID70 is a 3-D element with three-dimensional thermal conduction capability and has eight nodes with a single degree of freedom, namely temperature, at each node. This element is applicable to three-dimensional, steady-state or transient thermal analysis. The external surface areas of the SOLID70 elements that are exposed to fire from three sides, were used to simulate the surface effect of convection and radiation that occur from the ambient air to the steel girder. The discretization adopted for thermal analysis is shown in Fig. 1.

The girder-slab assembly segment AB, that is shown in Fig. 1(b), was meshed with SOLID70 elements. Both (heat) convection and radiation loads were applied at the exposed surface areas of the solid element. A convection coefficient of $\alpha_c = 50 \text{ W/(m}^2\text{°C)}$ and $\alpha_c = 35 \text{ W/(m}^2\text{°C)}$ was used in the thermal analysis under hydrocarbon and external fire respectively and this is based on Eurocode 1 [9] recommendations. Depending on the exposure boundaries, different values of effective emissivity factor were used as per Eurocode 1 [9]. Effective emissivity factor of 0.7 was used for the bottom and side surfaces of the bottom flange of the girder. For the side surfaces of the web, an emissivity factor of 0.5 was used, while a factor of 0.3 was used for top flange and the bottom of the slab. This variation in emissivity factor is to reflect the fact that the web, top flange and slab will experience slightly less radiation due to the effect of larger depth of the girder. Stefan-Boltzmann radiation constant of $5.67 \times 10^{-8} \text{ W/(m}^2\text{°C)}$ was applied in the thermal analysis.

The temperature (T) obtained at various points in the girder, via finite element analysis, were averaged at every time step by taking the arithmetic mean of the temperatures at several points for each component (flange, web or slab portion) of the composite section as shown in Fig. 1(c).

2.3 Discretization for structural analysis

For structural analysis, the bridge girder is discretized with two elements, namely SHELL181 element for the bottom flange, web, top flange and bearing stiffeners, and a SOLID65 element for the concrete slab. SHELL181 element has four nodes with six degrees of freedom per node, three translations in x, y, and z directions and three rotations about x, y, and z-axes. This element can capture local buckling of flange and web and also lateral torsional buckling of the girder and therefore is well-suited for large rotation, large strain and nonlinear problems. SOLID65 has eight nodes with three degrees of freedom; namely three translations in x, y, and z directions. This element can be used for three-dimensional modeling of solids with or without reinforcement and it is capable of accounting for cracking of concrete in tension, crushing of concrete in compression, creep and large strains. The output from the thermal analysis (temperatures) can be applied as a thermal-body-load on the structural model to

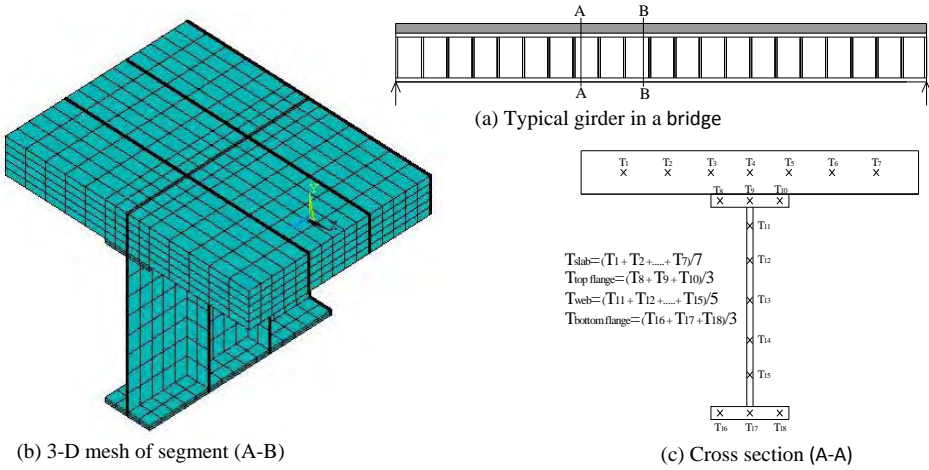


Figure 1. 3-D discretization of girder cross-section for thermal analysis

evaluate the mechanical response of steel-concrete composite girder. The 3-D structural model and the meshing adopted in the analysis is shown in Fig. 2(a).

To simulate the boundary conditions in the structural model, the support conditions (of the girder) were applied on multi-line nodes at the lower face of the bottom flange as shown in Fig. 2(b). This boundary condition reflects practical scenario, reduces stress concentration at the boundary nodes, and improves the convergence of the (finite element) solution. Also, to consider continuity effect of the concrete slab, the slab was restrained from lateral movement.

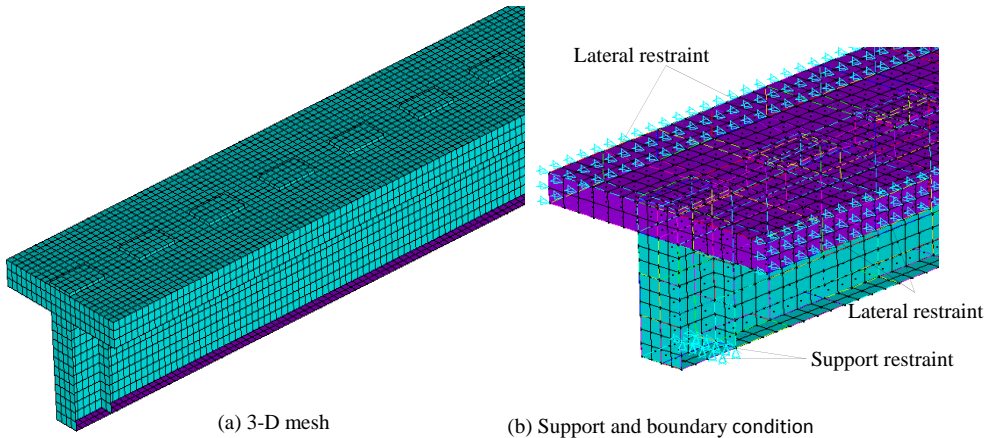


Figure 2. 3-D discretization of bridge girder for structural analysis

2.4 High temperature material properties

The progression of temperatures in the steel girder, under fire exposure, depends on the fire scenario and thermal properties of constituent materials, namely thermal conductivity, specific heat and thermal expansion, which vary as a function of temperature. The mechanical properties of steel and concrete that

are critical for residual strength assessment of fire exposed bridge girder are yield strength and modulus of elasticity of steel which vary with temperature. Further, variation of these properties are different in heating phase as compared to cooling phase.

During heating phase, the temperature dependent thermal and mechanical properties of steel and concrete are assumed to follow as that of Eurocode 2 and 3 provisions [10,11]. After cooling of the fire exposed girder, the residual yield strength of steel at room temperature is assumed to be reduced by $0.3 \text{ MPa}/^\circ\text{C}$, when steel temperatures reached beyond 600°C [2]. The residual compressive strength of concrete after cooling is assumed to be 10% less than the strength attained at the maximum temperature. This assumption is according to Eurocode 4 provisions [7]. However, all the thermal properties of steel and concrete including; thermal expansion, thermal conductivity and specific heat are assumed to be fully reversible during the decay phase.

3 MODEL VALIDATION

There is lack of fire test data on the response of bridge girders under fire conditions. Therefore, the validation of the above developed ANSYS model was carried out on a steel beam-concrete slab assembly (4.5 m span), typical to that in buildings, tested by British Steel Corporation under ISO 834 fire exposure [12]. The validation process during fire exposure phase included comparison of both thermal and structural response predictions from the analysis with that reported in the fire test. The steel beam in this case was not insulated. The analysis was carried out with the same mesh discretization and high temperature properties as discussed above.

Fig. 3 shows a comparison of predicted steel temperatures (by the finite element model) with that measured in the fire test. It can be seen that the top flange of the beam experienced much lower temperatures as compared to bottom flange. This is due to the “heat-sink” effect of concrete slab that dissipate the temperature in the top flange because of lower thermal conductivity and higher thermal capacity of concrete as compared to steel. The web temperatures are slightly higher than that in the bottom flange and this is due to the fact that thickness of the web is much lower than that of the flanges. Overall, predicted temperatures from the analysis compare well with measured data from the test. The slight differences can be attributed to variation of the heat transfer parameters, such as emissivity and convection coefficients, used in the analysis as compared to actual values encountered in the test (furnace) [13].

The comparison of mid-span deflections predicted by ANSYS model and those measured in the test is shown in Fig. 4. It can be seen that the mid-span deflection gradually increases with time at the early stages of fire (up to 10 minutes). These initial deflections are mainly due to high temperature gradients that develop across the top and bottom flanges of the steel section and the slight reduction in elastic modulus of steel resulting from increased temperatures in the girder. After 10 minutes, the rate of deflection increases slightly due to spread of plasticity that result from faster strength and stiffness degradation of steel as a result of high temperatures. At about 21 minutes, when the bottom flange and web temperatures at this point exceed 600°C , the mid-span deflection increases rapidly due to the effects of high temperature creep. The failure of the girder occurs in about 23 minutes through the formation of plastic hinge at the mid-span section.

Overall, predictions from the ANSYS match well with the reported test data. The slight variation in deflections can be attributed to minor variations in idealization adopted in the analysis, such as span length that is exposed to fire. While the entire span (4.5 m) was exposed to fire in the finite element model, only 4m span of the assembly was exposed to fire during the test and the support region were outside the furnace as reported by British Steel. It can be seen that ANSYS model can predict the time to failure with a good acceptability. For instance the predicted failure time was 22.5 minutes, as compared to 23 minutes in the test considering deflection limit state as the governing failure criterion.

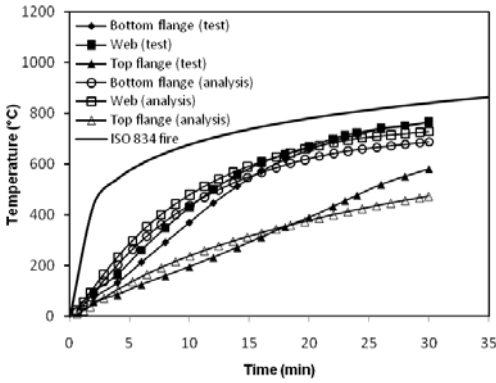


Figure 3. Comparison of predicted and measured cross sectional temperatures in beam-slab assembly

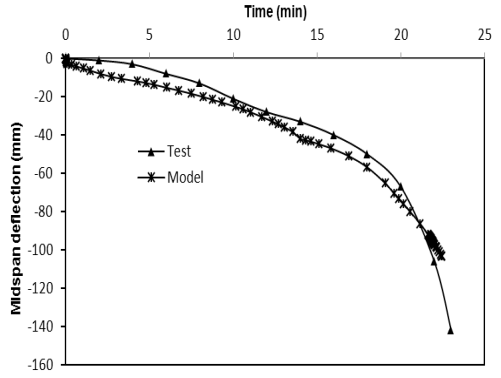


Figure 4. Comparison of predicted and measured mid-span deflection in beam-slab assembly

4 CASE STUDY

The validated finite element model was applied to evaluate the residual capacity of the fire exposed steel-concrete composite bridge girder.

4.1 Selection of bridge girder

To evaluate the residual strength of a typical fire exposed bridge girder, a simply supported steel bridge girder was selected for analysis [13]. The steel bridge comprises of five hot rolled steel girders of W33x141 supporting a reinforced concrete slab of 200 mm thickness. The steel girder is assumed to be in full composite action with slab and to be laterally supported by transverse diaphragms at the mid span, as well as at both ends, to prevent lateral movement as shown in Fig. 5. The bridge girder is 12.2 m in span length and has two expansion joints at its ends with a width of 36 mm. The girders are fabricated from Grade 50 steel (yield strength of 350 MPa), while the concrete used in slab has a compressive strength of 30 MPa.

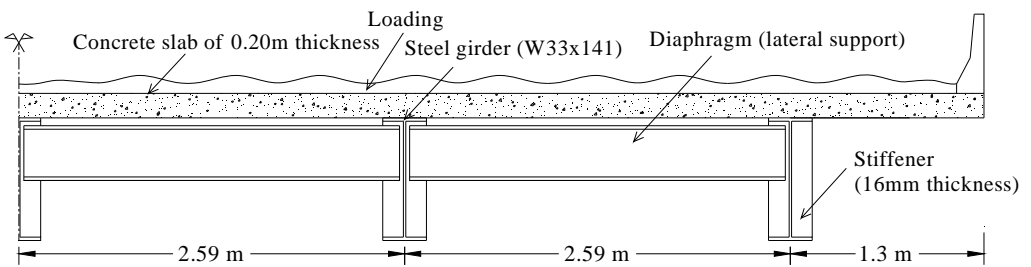


Figure 5. Transverse section of the bridge girder near the supports

4.2 Methodology

The numerical analysis is carried out in two stages namely, during fire exposure, and following the cooling of the girder. Prior to undertaking fire response analysis, the load carrying capacity of the bridge girder is evaluated by gradually incrementing the load on the girder till failure is attained. For this analysis, the room temperature mechanical properties for both steel and concrete were considered. In the

first stage of analysis, the bridge girder was analyzed by exposing the bridge girder to a given fire scenario and load level. In this stage high temperature material properties for both concrete and steel, considering the change in material properties in the cooling phase, is considered. Results from the analysis is utilized to evaluate the state of bridge girder to see if there is failure. Following the cooling down of the bridge girder, if there was no failure, second stage of analysis was carried out wherein the bridge girder was loaded incrementally to failure and the structural response of the girder was traced.

4.3 Fire and loading scenarios

For the analysis, three fire scenarios namely, hydrocarbon fire, moderate design fire, and external design fire were considered to study the effect of fire severity on the residual capacity of bridge girder. In Case 1, the bridge girder was exposed to hydrocarbon fire, while in Case 2, a design fire exposure was considered with peak temperature reaching to 800°C, followed by a 60 minutes steady state burning and then entering decay (cooling) phase. In Case 3 an external design fire with maximum temperature of 680 °C and a 45 minutes steady state burn-out prior to decay phase was used. The time-temperature curves representing Cases 1, 2, and 3 are shown in Fig. 6.

The structural analysis on the bridge girder was carried out under an applied loading comprising of dead load plus 30% live load. The self-weight of the girder section (2.0 kN/m) and that contributed from the tributary area of the concrete slab and wearing surface of the deck (22.5 kN/m) were considered in the dead load according to AASHTO provisions [14]. For the live load, a uniformly distributed load (9.3 kN/m) representing 0.3 times the live load was applied.

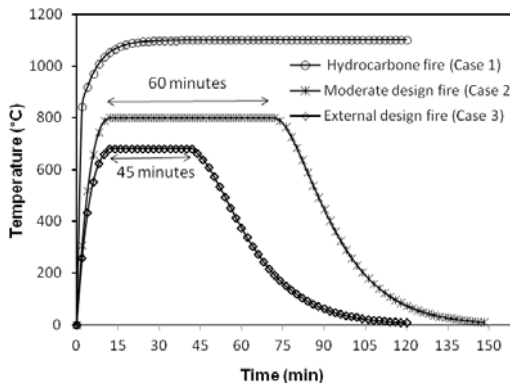


Figure 6. Time-temperature curves for different fire scenarios used in analysis

5 RESULTS AND DISCUSSION

Results from ANSYS thermal analysis are plotted in Fig. 7 to show the temperature distribution in the steel-concrete composite girder as a function of time for Cases 1, 2, and 3. It can be seen in Fig. 7 that the top flange temperature in all three cases is much lower as compared to the bottom flange. This is mainly due to the insulating effect of the concrete slab that dissipates heat from the top flange to the concrete slab. Also, the temperatures in the web are slightly higher as compared to that in bottom flange and this is because the web is much more slender (lower thickness) than the flanges and this produces rapid rise in web temperatures. But after the steady state period and entering the decay phase, the web temperatures decrease at a faster rate than the bottom flange temperature due to lower thickness of the web as compared to the flange. In the cooling phase, the top flange loses heat slower as compared to the web and bottom flange. This is because of the presence of the concrete slab that gains and dissipates heat

slowly due to lower thermal conductivity and higher specific heat of concrete. Therefore, it takes long time for the concrete and top flange to cool down.

The large difference in temperatures between the web and mid-depth of the slab leads to significant thermal gradients across the girder-slab cross section. This thermal gradient is influenced by the fire scenario (fire severity). For example, at 15 minutes the thermal gradient is 950°C in Case 1, as compared to 580°C in Case 2 and 480°C in Case 3. In general, higher thermal gradients produce higher thermal strains at the bottom of the steel girder (and in web), as compared to that in concrete slab. Thus, a significant curvature (thermal bowing) is developed in the girder, resulting in high thermal stresses even in a statically determinate girder (unrestrained girder). The developed curvature at the initial stage of fire exposure is independent of applied load because this curvature results mostly from the thermal gradient effect. Therefore, the curvature, resulting from the thermal gradients, alone contributes to the deflection at the early stage of fire exposure. Once steel temperatures exceed 400°C, girder deflections increase significantly due to degradation of mechanical properties (elastic modulus) of steel.

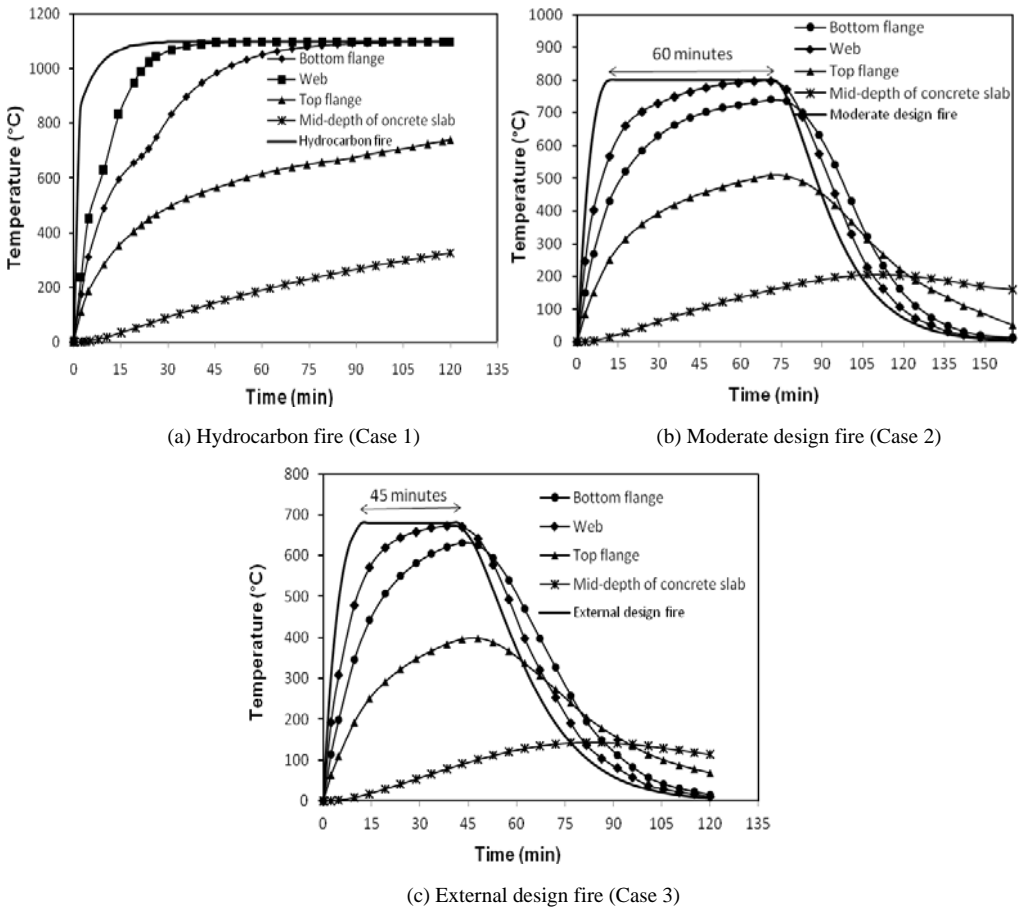


Figure 7. Temperatures progression in a bridge girder subjected to different fire scenarios

The structural response of typical bridge girder during fire exposure is illustrated in Fig. 8, wherein mid-span deflection of the girder is plotted as a function of fire exposure time. These deflection curves are plotted for the three fire exposure cases that are considered in the analysis. The general trend of the deflection progression can be grouped in to different stages. At the early stage of the fire exposure, the mid-span deflection increases due to significant thermal gradients along the cross section of the girder. During the intermediate stage of fire exposure, mid-span deflection increases linearly up to occurrences of first yielding, which depend on the temperature progression in the girder cross section. Therefore the time at which yielding occurs is different in different fire exposure cases. After steel temperatures exceed 400 °C during the heating phase of fire exposure, the deflections increase with time at a faster rate due to spread of plasticity and deterioration in strength and stiffness properties of steel and concrete. During the steady state burning (when fire temperatures remain constant), the progression of mid-span deflection slows down significantly due to steady state temperature in the girder (steel) section. However, in Case 1 the mid-span deflection increased continuously till failure since this is under severe fire exposure (hydrocarbon fire) scenario. Towards final stages of fire exposure (in the cooling phase), the mid-span deflections in Cases 2 and 3 decreased since the girder temperature reduced significantly. This is due to recovery of strength and stiffness properties of steel and concrete due to cooling phase of fire.

The effect of fire scenario on performance of the bridge girder can be illustrated by comparing results from Cases 1, 2, and 3 as shown in Fig. 8. In Cases 2 and 3, the bridge girder survived burn-out conditions under moderate design fire and external design fire scenario; however the girder failed at 20 minutes under hydrocarbon fire exposure (Case 1). This can be attributed to the fact that the fires in Cases 2 and 3 are less severe as compared to hydrocarbon fire in Case 1. For instance, the maximum fire temperature attained in hydrocarbon fire is about 1100°C, (Case 1) as compared to 680°C in the case of external design fire (Case 3) and 800°C in the case of moderate design fire (Case 2). Also, the heating rate at early stages is much higher in a hydrocarbon fire, than under external or moderate design fires, and this produces higher thermal gradients in the section. This differentiation in peak fire temperature and heating rate between these two fire scenarios lead to slower deterioration in strength and stiffness properties in steel and concrete under Cases 2 and 3, as compared to Case 1. As a result, bridge girder sustained the applied load for the entire fire duration under external and moderate fire exposure scenarios (Case 2 and Case 3).

A summary of the analysis results, including the post-fire residual capacity of the bridge girder under different fire scenarios are presented in Table 1. The residual capacity (strength) of bridge girder exposed

Table 1. Residual analysis results of fire exposed bridge girder

Case	Fire scenario	Max. fire temperature	Max. steel temperature	Room temperature capacity load (kN)	Residual capacity load (kN)	% of original capacity
Case 1	Hydrocarbon fire	1100°C	1000°C	4270	Failure under fire	---
Case 2	Moderate fire	800°C	795°C	4270	2974	70%
Case 3	External fire	680°C	670°C	4270	3579	84%

to maximum fire temperature of 800°C (in Case 2) is about 70% of the room temperature capacity, as compared to 84% residual capacity under fire scenario with 600°C peak (fire) temperature (Case 3). This is due to higher temperatures reached in the steel section in Case 2, as compared to Case 3. Therefore, steel (girder) in the case of Case 2 lost about 20% of its room temperature (yield) strength and stiffness permanently, which occurred mainly due to steel temperatures exceeding 600°C. As a result, the steel girder in Case 2 regained less stiffness and strength after cooling down to room temperature as compared

to that of girder in Case 3. This resulted in permanent residual strains (deformations), which can be seen in Fig 9, and this reflects the level of plasticity reached by the girder during fire exposure. The residual deformation is higher in Case 2, as compared to Case 1, since the steel temperature in Case 2 reached 800°C as compared to 680°C in Case 3. Furthermore, the concrete slab in Case 2 also lost some of its strength due to spread of temperature in the slab which reached about 500°C as compared to that in Case 3.

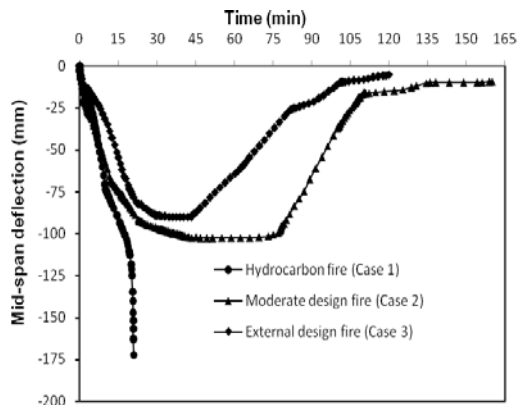


Figure 8. Effect of fire severity on the flexural response of bridge girder during fire exposure

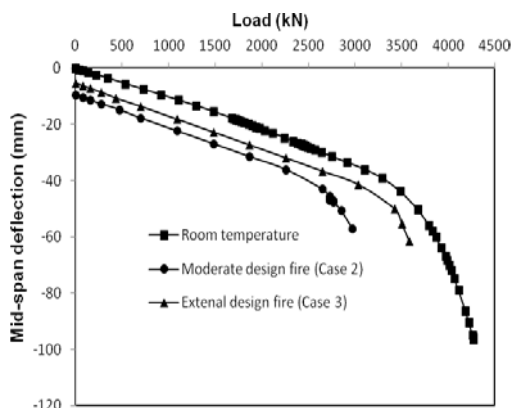


Figure 9. Effect of fire severity on the residual capacity of fire exposed bridge girder

6 CONCLUSIONS

A nonlinear finite element analysis was applied to evaluate the residual capacity of fire exposed steel bridge girders. Based on the results of analysis the following conclusions can be drawn:

1. ANSYS can successfully be applied to evaluate the response of fire exposed bridge girders. The thermal response can be simulated using SOLID70 elements, while structural response can be simulated using SHELL181 and SOLID65 elements.
2. Type of fire exposure and fire severity has significant influence on the resulting residual capacity of fire exposed steel bridge girders.
3. A bridge girder when exposed to external design fire with maximum fire temperature of 680 °C, has a residual capacity of about 84% as compared to 70% when exposed to moderate design fire with a maximum fire temperature reaching 800°C.
4. A steel bridge girder experiences failure under fire conditions when the maximum fire temperatures is around 1100°C, as in the case of typical hydrocarbon fires.

ACKNOWLEDGEMENTS

This material is based upon work supported by the National Science Foundation under Grant No. CMMI-1068621 and the authors wish to acknowledge NSF's support. Any opinions, findings, conclusions, or recommendations expressed in this paper are those of the authors and do not necessarily reflect the views of the NSF.

REFERENCES

- [1] National Steel Bridge Alliance. *Steel Bridge News*. Chicago, USA, 2010.

- [2] Astaneh-Asl A., Noble C. R., Son J., Wemhoff A.P., Thomas M.P., and McMichael L.D. *Fire Protection of Steel Bridges and the Case of the MacArthur Maze Fire Collapse*. Proc. of the ASCE TCLEE Conf. pp. 1-12, 2009.
- [3] Franssen J. M., Kodur V. “*Residual Load Bearing Capacity of Structures Exposed to Fire.*” *Proceeding of the 2001 Structures Congress and Exposition*. Washington DC, USA, 2001.
- [4] Kodur V., Gu L., Garlock M. E.. “*Review and Assessment of Fire Hazard in Bridges.*” *Proceedings of the TRB Annual Meeting*, Washington D.C, USA, 2010.
- [5] Kirby B. R., Lapwood D. G. & Thomson G. “*The Reinstatement of Fire Damaged Steel and Iron Framed Structures.*” ISBN 0 900206 46 2, B.S.C, Swiden Laboratories. UK, 1986.
- [6] Franssen J.-M. “*Etude du compartement au feu des structures mixtes acier beton.*” These de doctorat, collection de la F.S.A., N°111, Univ. de Liege, 1987.
- [7] European Committee for Standardization (CEN). EN 1994-1-2: 2005 Eurocode 4: “*Design of Composite Steel and Concrete Structures*. Part 1.2 General Rules-Structural Fire Design,” CEN, Brussels, Belgium, 2005.
- [8] ANSYS. *ANSYS metaphysics*. Version 11.0 SP1. ANSYS Inc. Canonsburg, PA, USA, 2007.
- [9] European Committee for Standardization (CEN). EN 1991-1-2: 2002. Eurocode 1: “*Actions on Structures*. Part 1.2 General Action-Action on Structures Exposed to Fire,” CEN, Brussels, Belgium, 2002.
- [10] European Committee for Standardization (CEN). EN 1992-1-2: 2004 Eurocode 2: “*Design of Concrete Structures*. Part 1.2 General Rules-Structural Fire Design,” CEN, Brussels, Belgium, 2004.
- [11] European Committee for Standardization (CEN). EN 1993-1-2: 2005 Eurocode 3: “*Design of Steel Structures*. Part 1.2 General Rules-Structural Fire Design,” CEN, Brussels, Belgium, 2005.
- [12] Compendium of UK. “*Standard Fire Test Data for Unprotected Steel-2.*” Published by British Steel Technical and Swinden Laboratories, Rotherham, UK, 1989.
- [13] Kodur V., Aziz E. M. “*Evaluating Fire Resistance of Steel Girders in Bridges.*” *Proceeding of the 6th Steel Structures ISSS Conference*. Sioul, Korea, 2011.
- [14] AASHTO. “*LFRD Bridge design specifications.*” AASHTO, Washington D.C, USA, 2009.

COMPOSITE STRUCTURES

SLENDER CONCRETE FILLED TUBULAR COLUMNS SUBJECTED TO FIRE. EXPERIMENTAL STUDIES AND FIRE DESIGN

Ana Espinos*, Manuel L. Romero*, Antonio Hospitaler*, Carmen Ibañez*, Ana Pascual* and Vicente Moliner**

* Instituto de Ciencia y Tecnología del Hormigón, Universitat Politècnica de València, Valencia, Spain
e-mails: aespinos@mes.upv.es, mromero@mes.upv.es, ahospitaler@cst.upv.es, caribus@upvnet.upv.es, anpaspal@aaa.upv.es

** Centro Técnico del Fuego, AIDICO, Valencia, Spain
e-mail: vicente.moliner@aidico.es

Keywords: Concrete filled steel tubular column, Fire, High strength concrete, Steel fibres.

Abstract. *The results of an experimental research on the fire behaviour of slender concrete filled circular hollow section columns are presented in this paper. In total, the testing program included 14 columns tested under concentric load and 24 columns tested under eccentric load, with eccentricities of 20 and 50 mm. The influence of important parameters affecting the fire behaviour of the columns such as the concrete grade (C30 and C90), load level (20% and 40%) and type of concrete filling (plain, bar reinforced and steel fibre reinforced concrete) was investigated. In particular, the performance of high strength concrete at elevated temperatures and the effect of the addition of reinforcing bars or steel fibres were observed. Based on the experimental results, the current provisions of EN1994-1-2 for the fire design of concrete filled steel tubular columns were studied and discussed.*

1 INTRODUCTION

Concrete filled tubular (CFT) columns make use of the combined action of steel and concrete showing an ideal structural performance. While the steel tube confines the concrete core enhancing its compressive strength, the concrete core prevents the steel tube wall from local buckling. In addition, CFT columns can reach high fire resistance times without the need of external protection [1-2].

In recent years, the use of high strength concrete (HSC) as infilling in CFT columns has increased, becoming an alternative to normal strength concrete (NSC) in room temperature design. Nevertheless, the performance of HSC at elevated temperatures is not well established. It is known that HSC behaves differently from NSC at elevated temperatures [3], and in some situations spalling can occur affecting its behaviour, as it leads to a explosive deterioration of the material due to the development of high internal pore pressures [4]. It is therefore important to evaluate the convenience of using HSC as infilling in hollow steel columns as spalling can affect their fire resistance. While the fire behaviour of normal strength CFT columns has been deeply investigated for years [5-11] and numerous experimental programs have been carried out worldwide for both slender and non-slender columns [12-16], specific experimental research on slender high strength CFT columns is required, since only a reduced number of results can be found in the literature. Lu et al. [17] studied the fire resistance of high strength concrete filled steel tubular stub columns, but did not study slender columns. Only Hass et al. [18], Han et al. [19] and Kodur & Latour [20] have performed some tests combining HSC and slender CFT columns. Nevertheless, more results are needed to investigate the influence of the main factors affecting the fire behaviour of high strength CFT columns.

This paper presents the results from an experimental research on the fire resistance of slender axially loaded CFT columns. The influence of parameters such as the concrete grade (C30 and C90), load level (20% and 40%; 60% in some cases), type of concrete (plain, bar reinforced and steel fibre reinforced concrete) and load eccentricity was investigated.

2 EXPERIMENTAL INVESTIGATION

In this experimental research, 14 fire tests were carried out on normal and high strength concrete-filled tubular columns under concentric axial load and another 24 columns were tested under eccentric loads, with eccentricities of 20 and 50 mm. The tests were carried out in the fire laboratory of AIDICO (Instituto Tecnológico de la Construcción) in Valencia, Spain. The aim of the experimental program was to investigate the effects of four parameters on the fire behaviour of CFT columns: concrete strength (f_c), type of concrete infill (plain, reinforced and steel fibre reinforced concrete, hereafter referred to as C, RC, FC respectively), load level (μ) and load eccentricity (e).

The column specimens were 3180 mm long, having all of them a relative slenderness at room temperature higher than 0.5. All the columns had an outer diameter of 159 mm and steel tube wall thickness of 6 mm. For each column, two ventilation holes of 15 mm diameter were drilled in the steel tube wall and located at 100 mm from each column end. Steel end plates of dimensions 300×300×15 mm were welded to the column ends. All the columns were tested under pinned-fixed (P-F) boundary conditions. The specimens were filled with concrete mixes of 30 MPa (NSC) and 90 MPa (HSC).

The tests were carried out in a 5×3 m furnace equipped with a hydraulic jack with a maximum capacity of 1000 kN. The columns were placed vertically inside the furnace, fixed at the bottom end and pinned at the top end. Once the load was applied, it was kept constant and the gas burners were then activated, following the standard ISO-834 fire curve with unrestrained column elongation.

In order to register the temperature evolution within the cross-section during the fire tests, a set of five thermocouples were located in the mid-length section of the columns. The axial elongation of the columns was measured by means of a LVDT located outside the furnace. Figure 1 presents some details of the experimental setup.

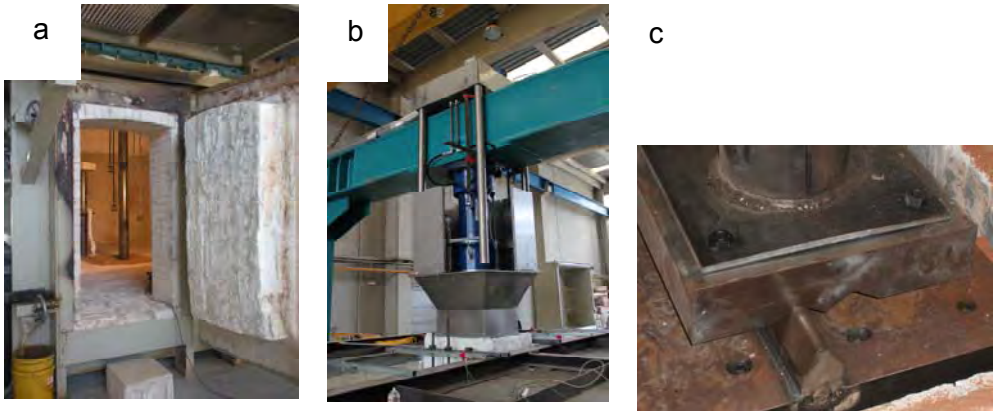


Figure 1. Test setup: a) Specimen inside the furnace, b) Hydraulic jack, c) “Knife” bearing.

The tested specimens with their particular characteristics and resulting fire resistance measured in minutes are listed in Table 1. In this table, the tested specimens can be identified in this table as follows: NXXX-T-L-FF-EE-MM (e.g. C159-6-3-30-00-20), where N stands for type of concrete (C = plain concrete, RC = reinforced concrete and FC = fibre reinforced concrete), XXX is the steel tube outer

diameter in mm, T the steel tube wall thickness in mm, L the nominal length of the column in meters, FF the nominal concrete strength in MPa, EE is the load eccentricity in millimetres and MM is the load level in % of the maximum capacity at room temperature.

Table 1. Test properties and results.

Test No.	Name	f_c (MPa)	f_y (MPa)	e (mm)	μ (%)	Load (kN)	t (min)
1	C159-6-3-30-00-20	35.75	337.8	00	20	198	42
2	C159-6-3-30-00-40	28.55	337.8	00	40	396	25
3	C159-6-3-30-00-60	34.05	337.8	00	60	594	14
4	C159-6-3-90-00-20	70.6	341.45	00	20	335	38
5	C159-6-3-90-00-40	68.7	341.45	00	40	670	11
6	RC159-6-3-30-00-20	23.9	337.8	00	20	229	43
7	RC159-6-3-30-00-40	30	337.8	00	40	458	30
8	RC159-6-3-30-00-60	33.7	337.8	00	60	687	13
9	RC159-6-3-90-00-20	68.7	337.8	00	20	343	65
10	RC159-6-3-90-00-40	77	337.8	00	40	720	19
11	FC159-6-3-30-00-20	28.3	337.8	00	20	198	37
12	FC159-6-3-30-00-40	26.7	334.4	00	40	396	22
13	FC159-6-3-90-00-20	93.1	337.8	00	20	335	36
14	FC159-6-3-90-00-40	89.9	334.4	00	40	670	16
15	C159-6-3-30-20-20	35.83	---	20	20	169	32
16	C159-6-3-30-20-40	42.17	332.031	20	40	337	16
17	C159-6-3-90-20-20	73.70	332.031	20	20	272	34
18	C159-6-3-90-20-40	74.64	343.628	20	40	544	11
19	C159-6-3-30-50-20	30.50	---	50	20	126	30
20	C159-6-3-30-50-40	38.25	365.651	50	40	253	23
21	C159-6-3-90-50-20	79.13	365.651	50	20	194	30
22	C159-6-3-90-50-40	98.32	365.651	50	40	388	16
23	RC159-6-3-30-20-20	39	357.221	20	20	180	48
24	RC159-6-3-30-20-40	40.38	357.221	20	40	360	24
25	RC159-6-3-90-20-20	93.67	357.221	20	20	264	48
26	RC159-6-3-90-20-40	96	386.376	20	40	528	23
27	RC159-6-3-30-50-20	31	386.376	50	20	140	39
28	RC159-6-3-30-50-40	39.50	386.376	50	40	280	20
29	RC159-6-3-90-50-20	92.97	315.221	50	20	204	40
30	RC159-6-3-90-50-40	91.87	315.221	50	40	407	16
31	FC159-6-3-30-20-20	34.67	315.221	20	20	169	31
32	FC159-6-3-30-20-40	31.50	337.767	20	40	337	17
33	FC159-6-3-90-20-20	87.12	337.767	20	20	272	23
34	FC159-6-3-90-20-40	83.04	337.767	20	40	544	13
35	FC159-6-3-30-50-20	33.00	318.638	50	20	126	30
36	FC159-6-3-30-50-40	37.65	318.638	50	40	253	19
37	FC159-6-3-90-50-20	96.99	318.638	50	20	194	29
38	FC159-6-3-90-50-40	92.78	326.394	50	40	388	15

The cold formed circular steel hollow section columns used in the experimental program used S275JR steel grade, nevertheless the real strength (f_y) of the empty tubes was obtained by performing the corresponding coupon tests, and is summarized in Table 1. The mean value of the steel modulus of elasticity was 210 GPa according to the European standards. Concrete mixtures of normal (30 MPa) and high strength concrete (90 MPa) were used for the column infill. In order to determine the compressive

strength of concrete, sets of concrete cylinders were prepared and cured in standard conditions during 28 days. All cylinder samples were tested on the same day as the column fire test. The cylinder compressive strength of all the tested specimens can be found in Table 1. The reinforced concrete (RC) specimens had an arrangement of four longitudinal reinforcing bars of 12 mm diameter and 6 mm stirrups with 30 cm spacing. The geometrical reinforcement ratio was close to a 2.5%. The steel fiber reinforced (FC) specimens had a proportion of 40 Kg/m³ high strength Dramix 40/60 steel fibers. More details on the experimental program carried out by the authors can be found in [21].

3 ANALYSIS OF TEST RESULTS

3.1 Centrally loaded columns

Figure 2 shows the evolution of the axial elongation versus the fire exposure time, for all the columns subjected to concentric axial load. As expected, for both normal and high strength concrete, and for all type of reinforcements, the higher the axial load level applied, the lower the fire resistance resulted.

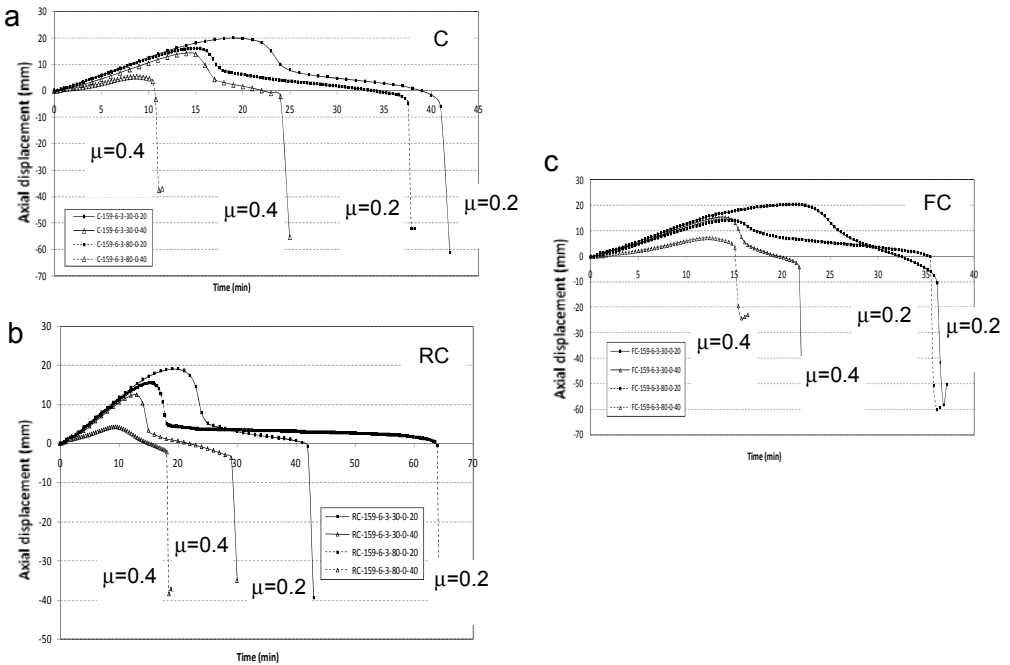


Figure 2. Axial displacement versus time curves for centrally loaded columns: a) C, b) RC, c) FC.

From Figure 2a all the column specimens filled with plain concrete can be compared. It can be observed that for a certain load level, the fire resistance was lower for the HSC filled specimens, although it is important to clarify that for the same load level, the HSC cases were subjected to a higher axial load. It can be observed in Figure 3a that the specimen with a $\mu=0.4$ and filled with HSC (C159-6-3-90-00-40) had a different behaviour, where the part of the curve corresponding to the contribution of the concrete core was not found (see [11] for a complete description of the typical failure mode of CFT columns under fire). This fact was also observed in the RC and FC specimens (Figures 2b and 2c) with the same load level and concrete strength combination. In all these cases the failure occurred before the load could be transferred to the concrete core, since its great magnitude made the column fail when the steel tube was

still sustaining the whole applied load. In general, for the cases which used reinforcing bars (RC), plotted in Figure 2b, the FRR was higher compared to those filled with plain concrete, resulting specially improved for the RC159-6-3-90-00-20 (65 min). It is worth noting that all bar reinforced specimens were tested under a higher axial load (for the same load level) than their plain concrete counterparts, since their maximum capacity at room temperature was also higher.

However, filling the columns with steel fibre reinforced concrete did not improve their fire resistance, as can be seen in Figure 2c. In fact, while the axial load applied to these columns was the same than that of their plain concrete counterparts, a lower fire resistance was obtained in some of the cases. An explanation can be found in the temperature curves obtained from the thermocouples (not shown in this paper for simplicity), where a higher temperature was registered in the concrete for the FC specimens, which can be due to the lower moisture content in the fibre reinforced concrete which affects directly to the heating up of the column during the early stages of the fire tests. Only for the column specimen with a higher axial load level and high strength concrete (FC159-6-3-90-00-40) a small increment was observed.

3.2 Eccentrically loaded columns

For those columns subjected to eccentric loads, the results are plotted in Figures 3 to 5 in terms of the evolution of the axial displacement of the top end of the column along the fire exposure time.

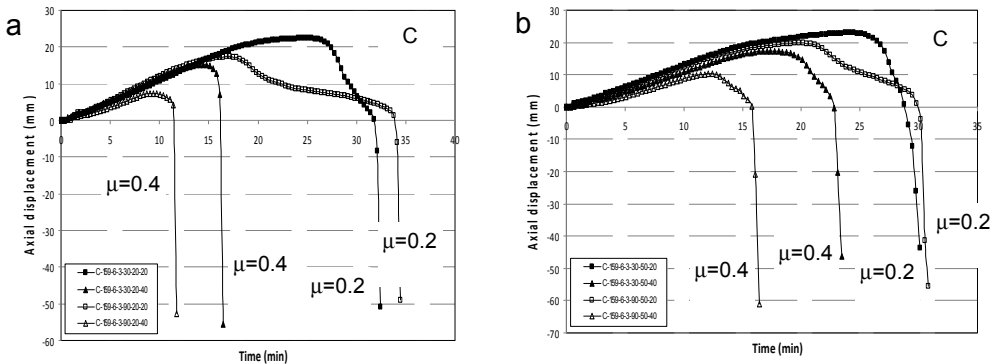


Figure 3. Axial displacement versus time curves for eccentrically loaded columns filled with plain concrete (C): a) $e = 20$ mm, b) $e = 50$ mm.

Obviously, for a certain type of concrete filling, as the load eccentricity was increased, the fire resistance time decreased, except in those cases where the moisture content or the concrete strength was found higher in the specimen with the higher eccentricity, producing the opposite effect (see tests 5-18-22).

The fire resistance of the HSC specimens was found lower than that of the NSC specimens for the higher load levels (40%), where in most cases the failure occurred before the load was transferred to the concrete core, thus not taking advantage of its contribution to sustain the applied load. Nevertheless, for a 20% load level, the difference was not so clear, the HSC specimens producing the same or higher fire resistance times with a higher axial load applied (except for tests 31 and 33).

From Figures 3 and 4, it can be inferred that the addition of reinforcing bars produced a benefit in the fire resistance, helping in some cases to avoid a premature failure of the column (see tests 24-26 versus 16-18), since the reinforcing bars improved the resistance of the concrete areas into tension, allowing the concrete to sustain the load for a certain time.

From Figure 5 it becomes clear that no special benefit was obtained though the addition of steel fibres, which leads to the same conclusion that was obtained for the centrally loaded specimens.

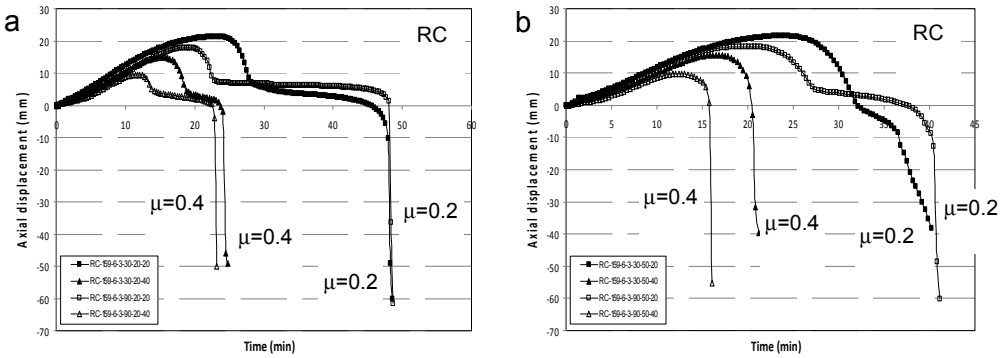


Figure 4. Axial displacement versus time curves for eccentrically loaded columns filled with bar reinforced concrete (RC): a) $e = 20$ mm, b) $e = 50$ mm.

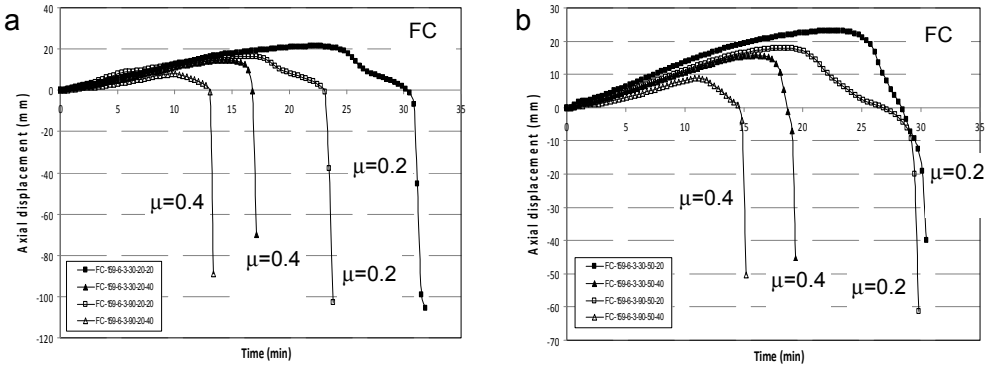


Figure 5. Axial displacement versus time curves for eccentrically loaded columns filled with fiber-reinforced concrete (FC): a) $e = 20$ mm, b) $e = 50$ mm.

Therefore, it can be concluded that for slender CFT columns no special benefit in the fire resistance is found through the addition of steel fibers, while the use of reinforcing bars can improve the fire performance of these columns under both concentric and eccentric loads, in some cases modifying their failure mode and allowing the contribution of the concrete core to sustain the load.

Regarding the use of high strength concrete, no particularities were encountered in the corresponding fire tests, without finding any evidences of the phenomenon of spalling, since in this type of columns the concrete core is protected from a direct exposure to the fire by means of the steel tube.

4 STUDY AND DISCUSSION OF EUROCODE 4

4.1 Centrally loaded columns

In this section, the test results will be employed to study and discuss the current provisions of EN1994-1-2 [22]. This standard provides a method for calculating the fire resistance of CFT columns subjected to concentric and eccentric axial loads in its Annex H. The field of application of the method is C20/25-C40/50, so only columns with concrete cubic strength under 50 MPa can be calculated,

nevertheless the application of the method for HSC specimens will be intended here in order to check its validity in this range of concrete strengths.

There is also a general simple calculation model for composite columns present in EN1994-1-2 (Clause 4.3.5.1), nevertheless the values of the reduction coefficients depending on the effect of the thermal stresses are not specified in the code for CFT columns. In the absence of predefined values, a common approach in practice is to take them as equal to unity [23]. Both methods will be studied here, where EC4 stands for the general method in Clause 4.3.5.1 and EC4(H) refers to the Annex H.

All the tested specimens were compared with the predictions of the two approaches from EN1994-1-2 [22]. The buckling resistance of the columns at the time of test failure was obtained, and summarized in Table 2 for concentric load. The errors were computed as the test value divided by the prediction.

Table 2. Comparison of the buckling resistance at the time of failure between EC4 and tests, concentric load.

a) Normal strength concrete (NSC)					
Column specimen	Axial load (kN)				
	TEST	EC4	TEST/EC4	EC4(H)	TEST/EC4(H)
C159-6-3-30-0-20	198	257.58	0.77	241.54	0.82
C159-6-3-30-0-40	396	490.40	0.81	507.36	0.78
C159-6-3-30-0-60	594	706.38	0.84	705.94	0.84
RC159-6-3-30-0-20	229	352.83	0.65	283.74	0.81
RC159-6-3-30-0-40	458	391.31	1.17	353.42	1.30
RC159-6-3-30-0-60	687	1146.18	0.60	1030.35	0.67
FC159-6-3-30-0-20	198	267.94	0.74	293.99	0.67
FC159-6-3-30-0-40	396	360.74	1.10	418.47	0.95
		Mean	0.83		0.85
		Std. dev.	0.20		0.20

b) High strength concrete (HSC)					
Column specimen	Axial load (kN)				
	TEST	EC4	TEST/EC4	EC4(H)	TEST/EC4(H)
C159-6-3-90-0-20	335	355.13	0.94	382.93	0.87
C159-6-3-90-0-40	670	1122.35	0.60	1128.86	0.59
RC159-6-3-90-0-20	343	328.45	1.04	234.35	1.46
RC159-6-3-90-0-40	720	727.01	0.99	736.38	0.98
FC159-6-3-90-0-20	335	443.12	0.76	541.05	0.62
FC159-6-3-90-0-40	670	1155.09	0.58	1263.36	0.53
		Mean	0.82		0.84
		Std. dev.	0.20		0.35

It was found that the two simplified models (general method and Annex H) produced unsafe results, for both normal and high strength concrete with a mean value of the error under 0.85 and high dispersion of results, which demonstrates that the code does not produce accurate results for slender columns loaded in axial compression. This result confirms the findings of previous investigations carried out by Aribert et al. [24] and Espinos et al. [11, 25], who found that EN1994-1-2 simple calculation model leads to buckling load values which result unsafe for high column slenderness under concentric loads.

4.2 Eccentrically loaded columns

With regard to the eccentrically loaded columns, a comparison between the test results and the application of the simple calculation model can be found in Table 3. For eccentric loads, a method is given in Section H.4 from Annex H of EN1994-1-2 [22], where the buckling resistance is calculated as for columns without eccentricity, and afterwards two correction coefficients are used, as a function of the

percentage of reinforcement (φ_s) and the load eccentricity (φ_δ), which are given by Figures H.1 and H.2 from the referred Annex.

Table 3. Comparison of the buckling resistance at the time of failure between EC4 and tests, eccentric load.

a) Normal strength concrete (NSC)					
Column specimen	Axial load (kN)				
	TEST	EC4	TEST/EC4	EC4(H)	TEST/EC4(H)
C159-6-3-30-20-20	169	103.91	1.63	124.47	1.36
C159-6-3-30-20-40	337	161.62	2.09	179.99	1.87
C159-6-3-30-50-20	126	57.45	2.19	57.81	2.18
C159-6-3-30-50-40	253	90.45	2.80	100.67	2.51
RC159-6-3-30-20-20	180	203.10	0.89	157.18	1.15
RC159-6-3-30-20-40	360	312.35	1.15	366.61	0.98
RC159-6-3-30-50-20	140	162.25	0.86	156.01	0.90
RC159-6-3-30-50-40	280	320.25	0.87	347.41	0.81
FC159-6-3-30-20-20	169	73.67	2.29	68.91	2.45
FC159-6-3-30-20-40	337	146.52	2.30	153.51	2.20
FC159-6-3-30-50-20	126	55.95	2.25	55.75	2.26
FC159-6-3-30-50-40	253	113.02	2.24	120.11	2.11
	Mean		1.80		1.73
	Std. dev.		0.68		0.65

b) High strength concrete (HSC)					
Column specimen	Axial load (kN)				
	TEST	EC4	TEST/EC4	EC4(H)	TEST/EC4(H)
C159-6-3-90-20-20	272	131.45	2.07	178.78	1.52
C159-6-3-90-20-40	544	334.41	1.63	343.14	1.59
C159-6-3-90-50-20	194	99.16	1.96	125.74	1.54
C159-6-3-90-50-40	388	205.16	1.89	258.54	1.50
RC159-6-3-90-20-20	264	262.63	1.01	236.70	1.12
RC159-6-3-90-20-40	528	416.67	1.27	440.69	1.20
RC159-6-3-90-50-20	204	226.92	0.90	240.05	0.85
RC159-6-3-90-50-40	407	491.24	0.83	556.02	0.73
FC159-6-3-90-20-20	272	159.84	1.70	214.41	1.27
FC159-6-3-90-20-40	544	283.98	1.92	338.43	1.61
FC159-6-3-90-50-20	194	108.21	1.79	140.52	1.38
FC159-6-3-90-50-40	388	218.53	1.78	259.01	1.50
	Mean		1.56		1.32
	Std. dev.		0.44		0.29

For all the eccentric columns analysed in this paper, their buckling resistance at the time of failure were obtained under the two approaches explained above (Clause 4.3.5.1 and Annex H) as if they were subjected to concentric axial loads, and afterwards these loads were corrected by means of the two coefficients (φ_s and φ_δ) in order to obtain the corresponding buckling resistance under eccentric loads.

As can be seen in Table 3, for eccentrically loaded columns the two methods from EN1994-1-2 produced safe results (average value over 1 for both approaches), but with high errors and elevated dispersion of results. Similar results were obtained under the two approaches (EC4 and EC4(H)), although with a lower average error and dispersion for the high strength concrete filled specimens. All the exposed above suggests that the current simple calculation model from EN1994-1-2 [22] should be revised for both concentric and eccentric loads, and its applicability extended to higher concrete grades.

5 CONCLUSIONS

Through the investigation of the results of the fire testing program presented here, a series of conclusions on the fire behaviour of slender CFT columns were obtained.

In HSC filled columns no sudden failure was found which could be attributed to the brittle nature of such type of concrete, probably due to the reduced duration of the fire tests and the reduced size of the section, which did not allow the development of high enough pore pressures inside the concrete.

The use of steel fibres did not show an increase in the fire resistance of normal or high strength concrete filled columns, since the failure in most of the tests was mainly due to the hollow steel column premature buckling, the concrete filling only helping to delay the heating of the column but not contributing to sustain the load. Nevertheless, an improvement was found when adding reinforcing bars, under both concentric and eccentric loads.

The current provisions of EN1994-1-2 were compared with the results of this series of fire tests, revealing that the method results unsafe for concentric loads when the slenderness of the columns is elevated (over 0.5 in all the cases studied), whereas under eccentric loads it turns to the safe side, but producing elevated errors and dispersion of results. Therefore, it is suggested here that the current simple calculation model in EN1994-1-2 should be improved in the future by means of test results and realistic numerical models.

6 ACKNOWLEDGEMENTS

The authors wish to express their sincere gratitude to the Spanish Ministry of Science and Innovation for help provided through project BIA 2009_09411, and to the European Community for the FEDER funds.

REFERENCES

- [1] Twilt L., Hass R., Klingsch W., Edwards M. and Dutta D., *Design guide for structural hollow section columns exposed to fire*, Comité International pour le Développement et l'Etude de la Construction Tubulaire (CIDECT), Cologne, Germany, 1996.
- [2] Wang Y. and Kodur V., "Research toward use of unprotected steel structures", *Journal of Structural Engineering*, 126(12), 1442-1450, 2000.
- [3] Schaumann P., Kodur V. and Bahr O., "Fire behaviour of hollow structural section steel columns filled with high strength concrete", *Journal of Constructional Steel Research*, 65(8-9), 1794-1802, 2009.
- [4] Ali F., Nadjai A. and Choi S., "Numerical and experimental investigation of the behavior of high strength concrete columns in fire", *Engineering Structures*, 32(5), 1236-1243, 2010.
- [5] Lie T.T., "Fire resistance of circular steel columns filled with bar-reinforced concrete", *Journal of Structural Engineering-ASCE*, 120(5), 1489-1509, 1994.
- [6] Zha X.X., "FE analysis of fire resistance of concrete filled CHS columns", *Journal of Constructional Steel Research*, 59, 769-779, 2003.
- [7] Renaud C., Aribert J.M. and Zhao B., "Advanced numerical model for the fire behaviour of composite columns with hollow steel section", *Steel and Composite Structures*, 3(2), 75-95, 2003.
- [8] Yin J., Zha X.X. and Li L.Y., "Fire resistance of axially loaded concrete filled steel tube columns", *Journal of Constructional Steel Research*, 62(7), 723-729, 2006.
- [9] Ding J. and Wang Y.C., "Realistic modelling of thermal and structural behaviour of unprotected concrete filled tubular columns in fire", *Journal of Constructional Steel Research*, 64, 1086-1102, 2008.

- [10] Hong S. and Varma A.H., “Analytical modeling of the standard fire behavior of loaded CFT columns”, *Journal of Constructional Steel Research*, 65, 54-69, 2009.
- [11] Espinos A., Romero M. and Hospitaler A., “Advanced model for predicting the fire response of concrete filled tubular columns”, *Journal of Constructional Steel Research*, 66(8-9), 1030-1046, 2010.
- [12] Lie T.T. and Chabot M., *Experimental studies on the fire resistance of hollow steel columns filled with plain concrete. Internal report No. 611*, Institute for Re-search in Construction, National Research Council of Canada (NRCC), Ottawa, Canada, 1992.
- [13] Chabot M. and Lie T.T., *Experimental studies on the fire resistance of hollow steel columns filled with bar-reinforced concrete. Internal report No. 628*, Institute for Research in Construction, National Research Council of Canada (NRCC), Ottawa, Canada, 1992.
- [14] Kordina K. and Klingsch W., *Fire resistance of composite columns of concrete filled hollow sections. CIDECT Research Project 15C1/C2-83/27*, Comité International pour le Développement et l'Etude de la Construction Tubulaire, Cologne, Germany, 1983.
- [15] Park S., Chung K. and Choi S., “A study on failure prediction and design equation of concrete filled square steel tube columns under fire condition”, *International Journal of Steel Structures*, 7(3), 183-191, 2007.
- [16] Park S., Choi S. and Chung K., “A study on the fire-resistance of concrete-filled steel square tube columns without fire protection under constant central axial loads”, *Steel and Composite Structures*, 8(6), 491-510, 2008.
- [17] Lu H., Zhao X. and Han L., “Fire behaviour of high strength self-consolidating concrete filled steel tubular stub columns”, *Journal of Constructional Steel Research*, 65(10-11), 1995-2010, 2009.
- [18] Hass R., Ameler J. and Zies H., *Fire Resistance of Hollow Section Composite Columns with High Strength Concrete Filling. CIDECT Research Project 15P-12/00*, Comité International pour le Développement et l'Etude de la Construction Tubulaire, Brunswick, Germany, 2000.
- [19] Han L., Zhao X., Yang Y. and Feng J., “Experimental study and calculation of fire resistance of concrete-filled hollow steel columns”, *Journal of Structural Engineering*, 129(3), 346-356, 2003.
- [20] Kodur V.K.R. and Latour J.C., *Experimental studies on the fire resistance of hollow steel columns filled with high-strength concrete*, Institute for Research in Construction, National Research Council of Canada (NRCC), Ottawa, Canada, 2005.
- [21] Romero M.L., Moliner V., Espinos A., Ibañez C. and Hospitaler A., “Fire behavior of axially loaded slender high strength concrete-filled tubular columns”, *Journal of Constructional Steel Research*, 67(12), 1953-1965, 2011.
- [22] EN 1994-1-2, *Eurocode 4: Design of composite steel and concrete structures. Part 1-2: General rules - Structural fire design*, Comité Européen de Normalisation (CEN), Brussels, Belgium, 2005.
- [23] Lennon T., Moore D.B., Wang Y.C. and Bailey C.G., *Designers' guide to EN 1991-1-2, EN 1992-1-2, EN 1993-1-2 and EN 1994-1-2*, Thomas Telford Limited, 2007.
- [24] Aribert J.M., Renaud C., Zhao B., “Simplified fire design for composite hollow-section columns”, *Structures & Buildings*, 161, 325-336, 2008.
- [25] Espinos A., Gardner L., Romero M. and Hospitaler A., “Fire behaviour of concrete filled elliptical steel columns”, *Thin-Walled Structures*, 49(2), 239-255, 2011.

TESTING OF COMPOSITE SLAB-BEAM SYSTEMS AT ELEVATED TEMPERATURES

Trung T. Nguyen*, Hai K. Tan*

* School of Civil and Environmental Engineering, Nanyang Technological Univ., Singapore
e-mails: nguyentt@ntu.edu.sg, CKHTAN@ntu.edu.sg

Keywords: Tensile membrane action, Slab-beam systems, Slab-beam assemblies, Concrete slabs, Fire.

Abstract. *This paper presents the results of experimental investigations on structural behaviour of composite slab-beam systems in simulated fire condition. Two ¼ scale composite slab-beam systems, 3.15m by 3.15m in plan, were tested in fire. One of the two slabs had no interior beams, while the other had two unprotected interior steel beams. The tests were to examine the effects of protected deformed edge beams and unprotected interior beams on the behaviour of the floor assemblies in fire. The results show that the continuity of reinforcement over supporting beams and the presence of interior beams can reduce deflection and greatly enhance the load-bearing capacity of the slab-beam systems. However, the presence of edge beams may lead to some failure modes which are different to those of isolated slabs.*

1 INTRODUCTION

Large-scale fire tests as well as some well-publicised actual building fires over the past two decades showed that composite steel framed buildings possess superior fire performance by mobilizing tensile membrane action (TMA) in composite slabs at large displacements. A number of studies on tensile membrane behaviour have been conducted [1-3]. A design concept for steel-framed buildings using composite construction was subsequently developed in UK, viz. the P288 design guide [4], which allowed structural engineers to take advantage of TMA to minimize fire protection cost to interior steel beams. Although previous studies are very valuable towards a greater understanding of structural fire engineering, most studies only focused on isolated slab behaviour itself, and not on the behaviour of overall floor assemblies.

In recognition of this shortcoming, researchers recently concentrate on testing of the overall floor assemblies. In 2008, a single composite floor slab panel with two unprotected secondary beams was subjected to a 120-minute ISO 834 standard fire in France [5]. The main aim of this test was to assess the fire resistance of partially protected floors using the P288 design concept. Also, to assess the suitability of such rules in Germany, Stadler et al. [6] conducted two large scale fire tests. They found that tensile membrane forces change considerably when taking the edge beams into account. Zhang et al. [7] conducted four composite slabs with a size of 5.23m x 3.72m each under ISO834 standard fire. Based on the test observations, they developed a new method to estimate the tensile membrane capacity of reinforced concrete slabs in fire. In 2010, a research on thin composite floor assemblies under fire loading [8] was conducted in the United States. The authors concluded that it is not recommended to remove the fire protection from the interior beams of thin lightweight composite slabs.

However, there is still a lack of experimental works on composite slab-beam systems in fire. Some important aspects of the system behaviour such as the effects of deflections of fire-protected edge beams and stiffness of the edge beams on TMA have not been investigated experimentally. Most notably, it is not clear whether deflections of the protected edge beams will impair the mobilization of TMA in the slabs. Thus, to ascertain the usefulness of P288 design rules in Singapore, further research is required to address the above issues. These give the impetus for the current research.

The objective of the current research is to explore the structural behaviour of composite slabs incorporating realistic behaviour of protected edge beams under fire conditions. This paper presents the experimental work on two one-fourth scale composite floor assemblies tested in fire. The aims are to examine the effects of deformed edge beams and unprotected interior beams on the behaviour of the floor assemblies.

2 TEST SETUP

The configuration of the test setup is shown in Fig. 1. A specimen including steel beams, four columns and concrete slab was totally enclosed in an electrical furnace and heated from the bottom surface. All gaps between the furnace and the specimen were filled up by thermal superwool blankets to reduce heat loss.

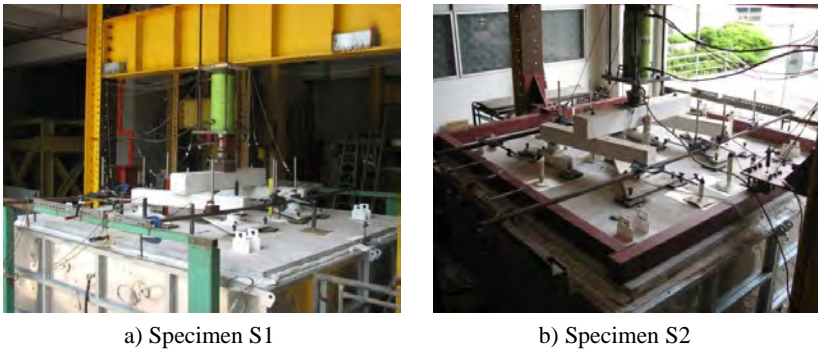


Fig. 1 Test setup

2.1 Heating facility

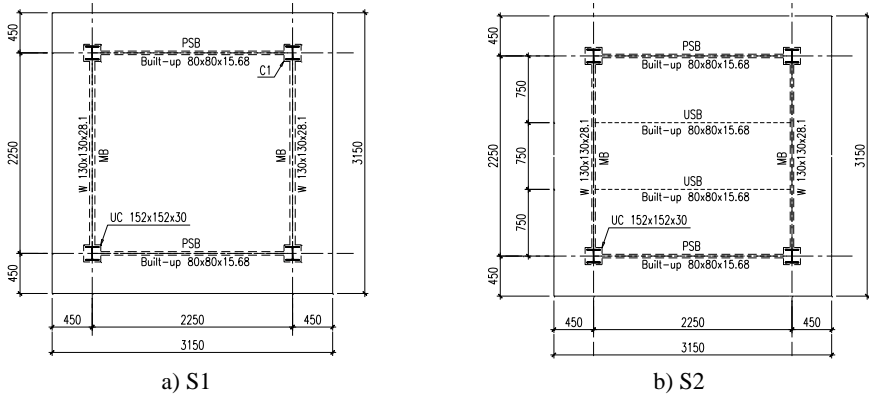
An electric furnace of dimensions 3m long by 3m wide by 0.75m high was setup at Nanyang Technological University (NTU). The dimensions of the furnace were dictated by the space constraint of the fire laboratory.

Due to the huge dimensions of the furnace, it is impossible to have adequate power supply to follow the ISO 834 fire curve. From the trial test conducted by the authors, when there was no specimen, the furnace temperature enabled to reach 1000°C within 50 minutes giving a heating rate of about 20°C/min. This rate is within the practical range for steel sections as prescribed in BS 5950.

2.2 Design of test specimens

The dimensions of the specimens were in turn limited by those of the electric furnace. Thus, the slab dimensions were scaled down by ¼ from a prototype floor which was designed for gravity loading in accordance with BS EN1993-1-1 and BS EN 1994-1-1. The other parameters such as the beam size, reinforcement ratio, and ratio of flexural stiffness of the beams to that of the slab were selected in such a way to replicate the relationships typically present in conventional design of composite floors.

One of two slabs had no interior beams, and was denoted as slab **S1**, while the other had two unprotected intermediate beams, denoted as slab **S2**. Both specimens had an aspect ratio of 1.0 with an overhang of 0.45m in both directions (Fig. 2). S2 was considered as a flexural restrained slab, with an all round beam system at a distance of 0.45m from the vertical supports (Fig. 1b). Here, it is assumed that for slab S1 reinforcement continuity over the all-round supporting protected edge beams and 0.45m wide neighbouring slabs provide little flexural restraint since only one layer of shrinkage reinforcement was present in the slabs. It should be noted that both slabs did not have inplane restraint to thermal expansion. Further tests are being prepared in NTU to investigate the effect of inplane restraint on TMA generated by surrounding ‘cool’ slabs.



MB: main beam; PSB: protected secondary beam; USB: unprotected interior beam

Fig. 2 Structural layouts of specimens

Due to one-fourth scale, there was no standardized steel decking suitable for the slabs. To protect heating elements from concrete spalling, a 2.0 mm-thick steel sheet with small holes drilled was cast with the slabs. The contribution of this sheet to the load bearing capacity of the slabs was negligible since the unprotected steel sheet was de-bonded from the lightly reinforced concrete slabs as observed in many previous tests in the past.

The concrete slab thickness was 55mm. Shrinkage reinforcement mesh with a grid size of 80mm x 80mm and a diameter of 3 mm was placed within the slab, 30 mm from the top. This resulted in a reinforcement ratio of 0.16%. The mesh had a yield strength of 543 MPa. The specimens were cast using ready-mixed concrete with aggregate size ranging from 5 to 10mm. The desirable compressive strength was 30 MPa. Concrete cylinders were tested at 28 days giving a characteristic strength f_{ck} of 36.3 MPa and a calculated elastic modulus E_{cm} of 34.4 GPa.

Material and geometrical properties of the I-section steel beams are given in Table 1. The beams were designed for full-shear composite action using 40 mm long, 13 mm diameter headed shear studs with a spacing of 80mm so that no unexpected failure occurred due to shear. A common type of steel joints, i.e. flexible end plates, was used for beam-to-beam and beam-to-column connections.

Table 1 Details of steel beams

	Depth h (mm)	Width b_f (mm)	Thickness		Yield stress f_y (MPa)	Elastic modulus E_s (MPa)
			Web t_w (mm)	Flange t_f (mm)		
Main beam (MB)	127	127	6.96	10.77	302	197500
Secondary beams (PSB & USB)	80	80	9.01	9.14	435	206900

This research applied the principle of fire protection for members from the P288 design guide. Thus all the edge beams and columns were protected for 60 minutes without applying additional fire-proofing to the slabs and interior beams.

2.3 Loading system and boundary condition

The concentrated force from a 50-ton hydraulic jack was distributed equally to twelve-point loads by means of a twelve-point loading system designed to simulate uniformly distributed loads (Figs. 3 & 4). In between steel plates and steel rods, ball and socket joints were used to maintain verticality of the loading system when the slab deformed excessively.



Fig. 3 Loading system

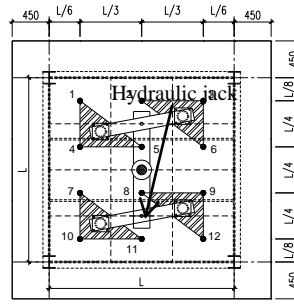


Fig. 4 Locations of loading points



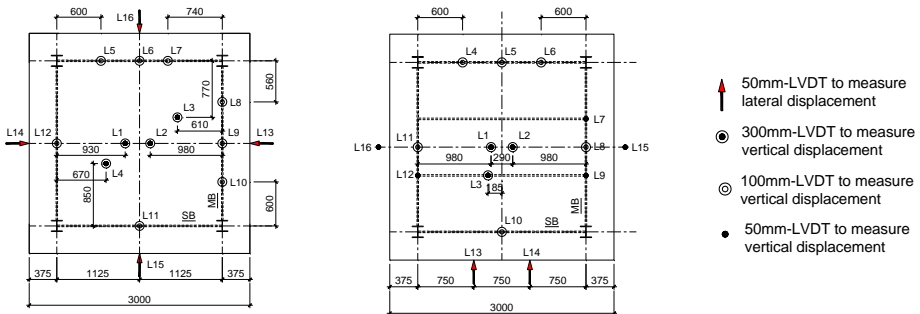
Fig. 5 Supporting column

The floor assemblies enclosed inside the furnace were connected to four supporting circular columns. In turn, these columns were located outside the furnace and connected to the strong floor by pinned connections (Fig. 5). The deliberately designed pin-ended columns allowed the specimens to move horizontally without any degree of restraint. Besides, the use of these columns simplified the test setup.

2.4 Acquisition of deformation and temperature

Sixteen linear variable differential transducers (LVDTs) were used to measure the vertical and horizontal deformations of the slabs and the beams as shown in Fig. 6.

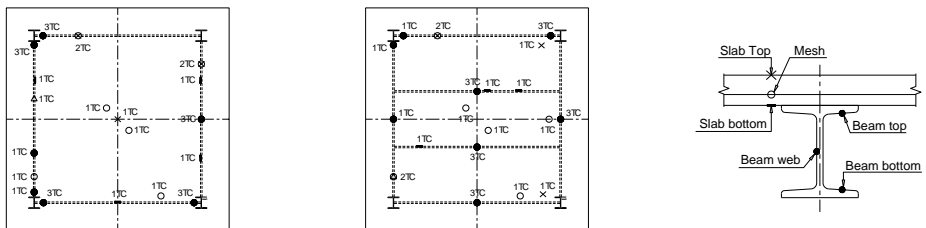
A total of 31 K-type thermocouples were used to capture temperatures of the beams and slabs. For each member, at least 3 positions were measured to check for temperature uniformity (Fig. 7). Furnace air temperature was monitored by 4 thermocouples connecting to two side heating panels and two interior positions of the furnace.



a) Specimen S1

b) Specimen S2

Fig. 6 Arrangement of LVDTs



a) Specimen S1

b) Specimen S2

c) Thermocouples in section

Fig. 7 Arrangement of thermocouples

2.5 Test procedure

Transient-state heating was used in the tests. First, the specimens were loaded up to a predetermined value by a hydraulic jack. The same uniform load was applied for all specimens. Second, at the heating stage, the specimens were heated while the load was manually maintained to be constant. The furnace temperature was increased until the specimens failed.

3 EXPERIMENTAL OBSERVATIONS

All figures below show the test results at the heating stage because at the end of the loading stage, the slab deflections were very small, i.e. 2.5 mm for S1 and 2.7mm for S2.

3.1 Temperature distributions

Fig. 8 shows average air temperature inside the furnace. Up to 45 minutes of the fire, in both tests the temperature development was consistent with only a small deviation of 74 °C at the maximum temperature of 909 °C for slab S1. As the temperature increased, slab S1 which allowed curling of slab corners upwards experienced greater heat loss compared to slab S2. Therefore, after 45 minutes, in S2 test the temperature was greater than that in S1 test. Consequently, temperature at the reinforcing mesh in S2 test was significantly higher than that in S1 test.

Between 0 and 40 minutes, temperatures at the steel mesh and on the unexposed face of the slabs increased at a very slow rate, only from 23°C to 100°C (Fig. 9). This was because the release of moisture inside the concrete slab slowed down the increase of slab temperature. When free water in concrete almost evaporated, the temperature increased at a much faster rate.

Fig. 9 indicates that the removal of fire protection from interior beams seemed to have no influence on the temperature distribution of the slabs.

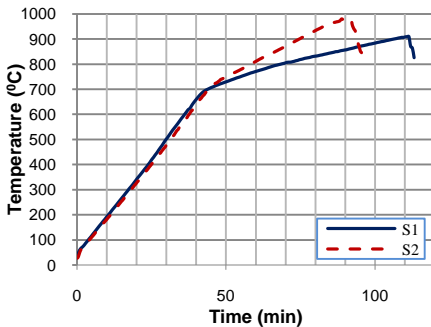


Fig. 8 Distribution of furnace temperature

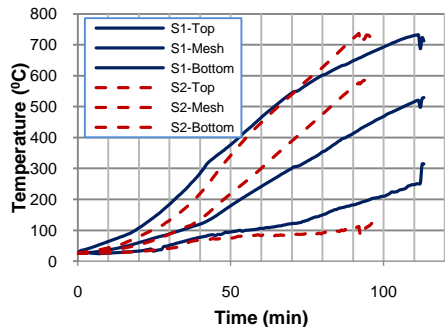


Fig. 9 Distribution of slab temperatures

A comparison of thermocouple temperatures at different locations on the slab but at the same cross sectional height, i.e. at the reinforcing mesh, at the bottom and the top surfaces of the slabs, has been conducted. As expected, the results confirm that temperature only varied across the slab thickness but did not vary much on the plan dimensions of the slab. Once again, this gives credibility and confidence to the fire test set-up.

3.2 Comparison of slab deflections

Fig. 10 shows the load-temperature relationships and theoretical yield loads of two slabs at ambient temperature. The test load was chosen so that the value of loading would correspond to a load ratio of 1.97 for slab S1 and 0.43 for slab S2 over the yield loads. This is because although both slabs were subjected to the same uniform loads, the yield load of S2 with two interior beams was greater than S1 at ambient temperature. However, in S1 test, due to oil leak in the hydraulic jack, it was not possible to keep the applied load constant during the heating process. In S2 test, the load was maintained as expected.

Fig. 10 indicates the decrease of yield line load versus temperature. While it is easy to calculate this value for slab S1, it is impossible to do so for slab S2 as it was difficult to find out exactly when the interior beams did not have contribution to the yield load. Therefore, it was assumed that at 400°C the beams would produce no resistance to the yield load. It means that from 400°C onwards, the yield load was assumed to be calculated based on structural configuration without the interior beams. As a result, there was a significant reduction of S2 yield load at 400°C.

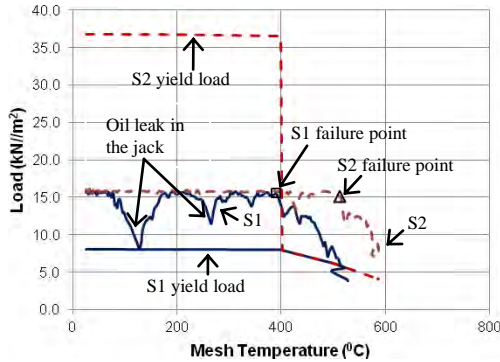


Fig. 10 Load-mesh temperature relationships

Figs. 11 & 12 show the comparison of mid-span slab deflections against steel mesh temperature and time. It is obvious that the continuity of reinforcement over supports and the presence of interior beams can significantly reduce the deflection and enhance the load-bearing capacity of the slabs. However, at this time of writing it is not yet possible to separately quantify the individual beneficial contribution from flexural restraint and interior beams. Further tests will be conducted to assess this effect experimentally.

As can be seen in Fig. 11, the mechanical load has little effect on the response of the structure in spite of the oil leak of the hydraulic jack in slab S1. Thus, it can be concluded that the temperature differential between the top and bottom surfaces of slabs (thermal bowing) as well as strength degradation and stiffness deterioration of concrete and reinforcement can lead to large displacements.

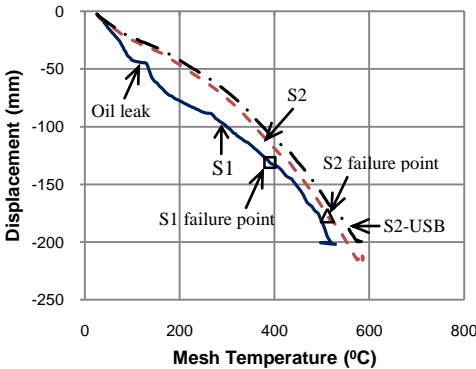


Fig. 11 Deflection-Temperature relationships

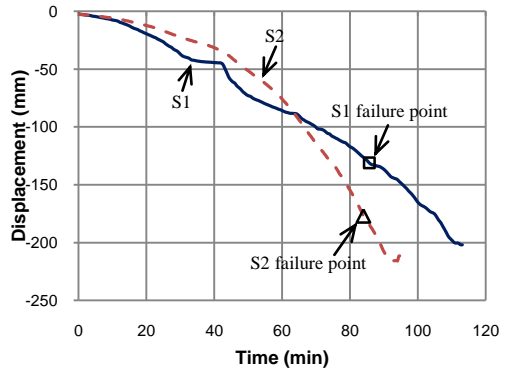


Fig. 12 Deflection-Time relationships

The deflection of the interior beam in test S2, denoted as S2-USB, is also plotted in Fig. 11. As expected, the beam had a deflection very close to that of the slab. A small discrepancy was due to the position of S2-USB not exactly at the centre of slab S2.

Table 2 summarizes the test results. It is apparent that TMA greatly enhanced the load-bearing capacity of the two slabs. The enhancement factors, defined in this paper as the ratio of the test load over the yield load at the temperature where failure occurred, are 1.96 for slab S1 and 2.55 for slab S2.

Table 2 Details of test results

	$P_{yield,20}$ kN/m^2	Time min	Mesh temperature, θ $^{\circ}C$	P_{test} kN/m^2	$P_{yield,\theta}$ kN/m^2	$P_{test}/P_{yield,\theta}$	Displacement mm	w/d
S1	8.02	85.8	390.5	15.62	7.97	1.96	131	3.28
S2	36.77	84.0	511.7	15.13	5.93	2.55	177	4.43

$P_{yield,20}$: yield load at room temperature; $P_{yield,\theta}$: yield load at temperature θ ; P_{test} : test load.

3.3 Behaviour of steel frames

3.3.1 Steel beam systems

Fig. 13 shows the temperature profiles at the bottom flanges of MB, PSB and USB (defined in Fig. 2), while the deflection profiles of these beams are plotted in Fig. 14.

All the beams had a similar trend in deflection. Up to 25 minutes into heating or about 200^oC, the beams deflected downwards at a slower rate due to thermal bowing. This was followed by a constant rate up to 400^oC because the beams were fire protected by intumescent paint. When temperatures at bottom flanges of the beams reached 550^oC, after 50 minutes of the fire, the beams deflected at a very rapid rate. From this point onwards, strength and stiffness of the beams also significantly reduced.

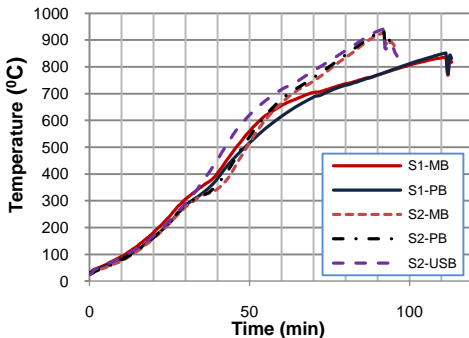


Fig. 13 Temperature at bottom flange of beams

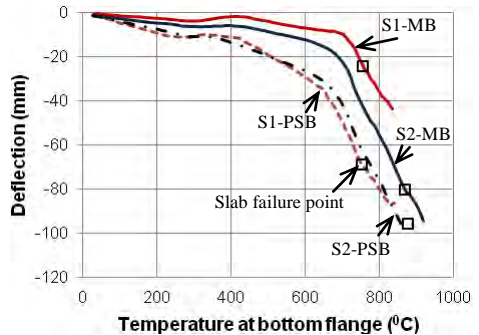


Fig. 14 Mid-span deflection of beams

At a similar temperature, beam S1-PSB had a slightly greater deflection than S2-PSB because of the difference in load path from the slabs to the beams. At initial heating stage, in slab S1, mechanical load was transferred directly to the protected edge beams, while in slab S2, load was transferred via unprotected secondary beams to the edge beams. But at high temperature, the load transfer mechanism of the two slabs became the same since the unprotected secondary beams lost their stiffness and strength from 400^oC onwards.

The discrepancy in the deflections of beams S1-MB and S2-MB was much more obvious. One of the reasons is the load path as explained above. Another reason is due to restrained thermal expansion of unprotected interior beams. High normal forces were generated within the interior beams due to partial restrained thermal elongation provided by the edge beams, leading to out-of plane bending moment for the main beams. Therefore, beam S2-MB had a greater deflection than that of beam S1-MB at a similar temperature.

Local buckling of the beam bottom flanges was not observed in the two tests. This could be due to discontinuity of the steel beams, allowing them to expand separately to some extent through the flexible end plate connections.

3.3.2 Steel columns & Connections



Fig. 15 Deflected shape of column – S1



Fig. 16 Deflected shape of column – S2

Figs. 15 & 16 show the deformed shape of protected steel columns after cooling. As can be seen, the columns were subjected to biaxial bending moments due to pulling forces of the edge beams at large deflections. Buckling was observed in the column flanges in test S2, but it was not detected in test S1. This is possibly due to greater bending moments generated in the main beams of slab S2.

Although both beam-to-beam and beam-to-column connections were designed within a common range in practice, none of the connections failed or fractured during the heating or cooling phase.

3.4 Development of crack patterns

Cracking noises were heard from both tests approximately from 10 to 15 minutes at the beginning of the heating process. At approximately 7 minutes, diagonal cracks were observed at the beam-to-column joints. These cracks continued to grow and opened up through the slab thickness. These corner cracks ran at an angle ranging from 30 to 45 degree to the slab edges as shown in Figs. 17 & 18. Water vapour was emitted from the cracks at this time. These cracks were possibly due to torsional effect of slab corners.

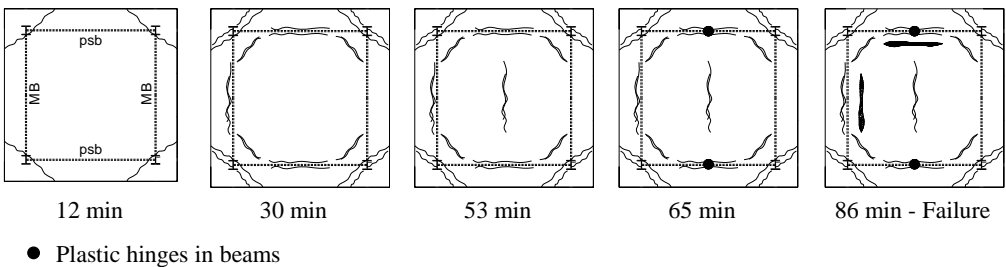


Fig. 17 Slab S1

After the appearance of corner cracks, additional cracks formed around the protected edge beams of the slabs. However, the sequence was different between the two tests. In test S1, cracks appeared simultaneously along the interior length of edge beams, followed by cracks at the slab centre. In test S2, more severe cracks were observed first above MB, then in the vicinity of PSB. Cracks along USB appeared near the end of the fire test. This sequence can be attributed to the difference in the load path from the slabs to the protected edge beams.

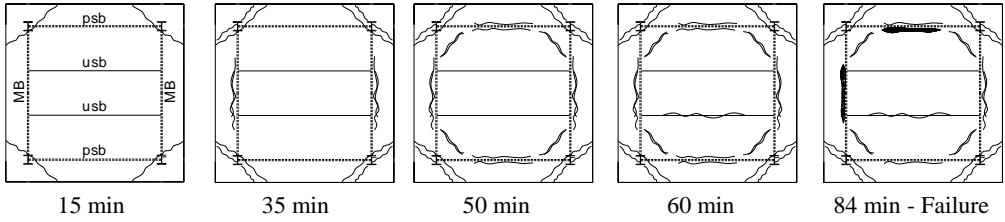


Fig. 18 Slab S2

3.5 Failure modes

For slab S1, concrete cracks occurred around the column locations. However, the test was continued since there was no obvious failure. At approximately 65 minutes, the protected secondary beams experienced very large deflection due to loss of fire-protection on the bottom flanges. Folding in single-curvature occurred by formation of plastic hinges in the secondary edge beams. At 86 minutes into S1 test, a loud sound was heard due to fracture of reinforcement. Two full-depth cracks were observed; one close to the main beam and one directly above the secondary beam. Heating was stopped at this time because the integrity failure criterion was violated. There was no cooling test afterwards.

For slab S2, concrete failure also occurred around the columns. The test ended when fracture of reinforcement occurred and full-depth cracks appeared close to the edge beams. However, no folding mechanism was observed. It seems that if the slab is continuous and flexurally restrained around all four edges, folding in single-curvature is unlikely to occur. This deduction will need to be confirmed by further tests.



a) Folding mechanism



b) Deformed shape



c) Fracture of reinforcement

Fig. 19 Slab S1



a) Deformed shape



b) Fracture of reinforcement



c) After cooling

Fig. 20 Slab S2

These mentioned failure modes are different from those stipulated in the SCI P288 design guide [5]. In this design guide, only two failure modes are considered, which include fracture of mesh reinforcement across the short span at the slab centre and compressive failure of the concrete at the slab corners.

However, in the authors' tests, no fracture of reinforcement at the mid span of the slabs was found. Therefore, the observed failure modes in the tests should be incorporated into the P288.

4 CONCLUSIONS

The objective of the current research is to study the structural behaviour of slab incorporating protected edge beams in fire. This paper presented the experimental results, comparisons and evaluations of two tested composite slab-beam-column systems. The observations and comparisons indicate that:

- (1) The continuity of reinforcement over supporting beams and the presence of interior beams can reduce deflection and greatly enhance the load-bearing capacity of the slab-beam systems. The enhancement factors are 1.96 for slab S1 and 2.55 for slab S2.
- (2) The presence of interior beams changes the behaviour of the slab-beam systems since it affects the load path from the slabs to the edge beams. Consequently, the development of crack pattern is also affected.
- (3) For slabs with an aspect ratio of 1.0, peripheral compressive rings exist irrespective of the presence of interior beams.
- (4) Failure modes of the floor assemblies are different from isolated slab panels. They include: (a) concrete failure around the column locations; (b) fracture of reinforcement close to the protected edge beams; (c) folding in single-curvature by formation of plastic hinges in the secondary edge beams.
- (5) No fracture of reinforcement at the mid span of the slabs was observed. It is unlike the failure modes indicated in the P288 design guide.

ACKNOWLEDGMENT

The research presented in this paper was funded by Agency for Science, Technology and Research (A*Star Singapore). The financial support of A*Star is gratefully acknowledged.

REFERENCES

- [1] Foster SJ, Bailey CG, Burgess IW, Plank RJ. "Experimental behaviour of concrete floor slabs at large displacements". *Engineering Structures*. 2004;26:1231-47.
- [2] Bailey CG, Toh WS. "Small-scale concrete slab tests at ambient and elevated temperatures". *Engineering Structures*. 2007;29:2775-91.
- [3] Huang Z, Burgess IW, Plank RJ. "Modeling membrane action of concrete slabs in composite buildings in fire. I: Theoretical development". *Journal of Structural Engineering*. 2003;129:1093-102.
- [4] Newman GM, Robinson JT, Bailey CG. "Fire Safe Design: A new Approach to Multi-Story Steel-Framed Buildings". Berkshire, UK: The Steel Construction Institute; 2006.
- [5] Zhao B, Roosefid M, Vassart O. "Full scale test of a steel and concrete composite floor exposed to ISO fire". *Proceedings of the Fifth International Conference on Structures in Fire (SiF'08)*. Singapore: Nanyang Technological University; 2008. p. 539-50.
- [6] Stadler M, Mensinger M, Schaumann P, Sothmann J. "Munich Fire Tests on Membrane Action of Composite Slabs in Fire". *Application of Structural Fire Design*. Prague, Czech Republic 2011.
- [7] Zhang N-S, Li G-Q, Lou G-B, Jiang S-C, Hao K-C. "Experimental study on full scale composite floor slabs under fire condition". *Application of Structural Fire Engineering*. Prague, Czech Republic 2009. p. 502-11.
- [8] Wellman E, Varma A, Fike R, Kodur V. *Experimental Evaluation of Thin Composite Floor Assemblies under Fire Loading*. *Journal of Structural Engineering*. 2011:1002-12.

EXPERIMENTAL STUDIES ON THE BEHAVIOUR OF HEADED STUD SHEAR CONNECTORS AT ELEVATED TEMPERATURES

Ling-Zhu Chen^a, Guo-Qiang Li^b, Shou-Chao Jiang^b

a) Department of Building Engineering, Tongji University, Shanghai
e-mail: 2lingzhuchen@tongji.edu.cn

b) State Key Laboratory for Disaster Reduction in Civil Engineering, Tongji University, Shanghai
e-mails: gqli@tongji.edu.cn, scjiang@tongji.edu.cn

Keywords: Structural Behaviour, Headed Stud Shear Connectors, Elevated Temperatures.

Abstract. *The steel-concrete composite beam has been widely used nowadays in buildings and bridges. In the composite beams, headed stud shear connectors are commonly used to transfer longitudinal shear forces across the steel-concrete interface. The behaviour of shear connectors under elevated temperatures is of great importance in the performance of composite beams in fire. Totally, 24 push-out tests were carried out in Tongji University to investigate the temperature distribution, failure mechanism, degradation of shear capacity of stud shear connectors with temperature, and the force-slip relationship of stud shear connectors at high temperatures. It was observed in the test that the predominant mode of failure for the solid slabs and profiled slabs with the corrugation of the deck run parallel to the steel beam was headed stud shear failure while the predominant mode of failure for the profiled slabs with the corrugation of the deck run perpendicular to the steel beam was concrete cracking failure at low temperatures and then turned to stud shear failure at high temperatures. Also, the ultimate load in solid slabs was generally higher than that in the profiled slabs. The ultimate load and stiffness decreased with increasing temperature for all slabs. Furthermore, the proposed equations to calculate the shear strength of studs at elevated temperatures were compared with existing test results. It was found that the calculation formula specified in the Eurocode EN 1994-1-2 to calculate the shear strength at elevated temperatures is reasonable and able to predict the shear strength of stud shear connectors at elevated temperatures.*

1 INTRODUCTION

The steel-concrete composite beam has been widely used nowadays in buildings for its economical and technical advantages. Composite steel-concrete beams usually comprise a structural steel section and a concrete slab. In the composite beams, headed stud shear connectors are commonly used to transfer longitudinal shear forces across the steel-concrete interface and limit the longitudinal slip and separation between the steel beam and concrete slab. The behaviour of shear connectors under elevated temperatures is of great importance in the performance of composite beams in fire. Much experimental and numerical research [1,2,3] has been done to investigate the performance of headed stud shear connectors at ambient temperature. The push-out test is commonly adopted to obtain the structural behaviour of shear connectors instead of full-scale composite beam test, since it is more convenient and economic than the composite beam test and it has been verified to be able to provide the relevant properties for shear connectors with acceptable accuracy although there is some difference of stress state between the push-out specimen and beam.

Shear connectors subject to tensile-bending-shear composite stress due to the deformation difference between the steel beam and concrete slab at ambient temperature. So, the failure mechanism is very complicate. However, the failure mechanism is more complicate at elevated temperatures due to the thermal stress caused by the non-uniform temperature distribution across the section. Little research on the performance of headed stud shear connectors in fire could be found at present. In 1995, Zhao and Kruppa[4] conducted a series of push-out tests to determine the shear capacity and load-slip relationship of headed studs and angled connectors, subject to the standard ISO fire, in conjunction with solid slabs and composite slabs with both trapezoidal and re-entrant profiled steel sheet. All specimens were heated until collapse while the load was constant and different load levels were considered in the test. It was observed that the collapse of specimens with flat concrete slab and composite slab with re-entrant profiled steel sheet was always caused by the shearing off of headed studs just at the level of the flange, while the mode of failure for the specimen with composite slab with trapezoidal steel sheet was the shearing of studs accompanied by shearing off of the concrete rib. The mode of failure with angle connectors was the shearing off of pins used for fixing the connectors in the steel flange. Based on these experimental results, the empirical equations to calculate the shear resistance of shear connectors at elevated temperatures were achieved, which were applied in the Eurocode EN 1994-1-2[5]. The formulas to determine the load-slip relationship of shear connectors at elevated temperatures were also derived. In 2009, Sengkwan Choi et al[6] also did some experimental research on the structural behaviour of headed stud shear connectors with solid slabs, employing modified push-out test instrument which comprised one steel beam and only one concrete slab. All specimens were loaded to failure after they were heated to specified temperatures. The shear failure at the weld-collar interface was consistently observed. The equation to evaluate the strength of the stud was proposed. The mechanical properties of studs both in and after fire were studied by Imagawa et al[7] with experiments. It was found that the fatigue strength of the stud after fire in case of the furnace temperature was 700 °C showed remarkable decrease due to the undesirable slip behaviour. In 2011, Mirza et al[8] conducted 8 push-out tests on headed stud shear connectors with solid slabs and composite slabs. It was observed that the ultimate load in solid slabs was generally higher than the profiled slabs, while the profiled slab achieved greater ductility than the solid slab. The formulas to determine the degradation of the shear resistance with temperature were presented.

Although there are already several equations to calculate the shear resistance degradation with temperature of shear connectors, they were mostly proposed by researchers only based on the test result obtained by them which is limited. So, the accuracy of these equations needs to be further verified with more test result. Also, the behaviour of studs in profiled slabs with the corrugation of the deck run parallel to the steel beam, which was usually the main beam, has not been well studied.

2 EXPERIMENTAL INVESTIGATION

2.1 Objectives

The properties of shear connectors most relevant to composite design are the shear capacity and load-slip characteristic at the interface. In general, 24 push-out tests were carried out in the Structure Fire Resistance Laboratory at Tongji University. The test series are primarily designed to investigate the temperature distribution, failure mechanism, degradation of shear capacity of stud shear connectors at elevated temperatures, and the force-slip relationship of stud shear connectors at high temperatures which is the basis of the shear connection design in composite beams.

2.2 Test specimens and test set-up

All specimens were designed based on the recommendations in Eurocode EN 1994-1-1[9]. However, some modification has been made due to furnace limitation. Each push-out specimen (Fig.1 (a), (b), (c)) consisted of a welded H type steel beam, two rectangular concrete slabs and two studs. Different types of concrete slabs including the flat concrete slab, composite slab with profiled steel sheet perpendicular to

the steel beam, and composite slab with profiled steel sheet parallel to the steel beam were considered in the test. The details of specimens were shown in Table 1.

All studs were of the same dimension and welded to steel beam at the centre of the beam. The diameter of the studs was taken as 19mm, and the height was 100mm. The commercial concrete was used, and nine coupons (three were cubic and other six were prismatic) were casted at the same time to obtain the strength of the concrete. The cubic compressive strength of concrete after 28 days curing period was an average of 38.5 N/mm² and the elastic modulus was an average of 2.84×10⁴ N/mm². The rebar with the diameter of 10 mm was put in the slab and the arrangement was shown in Fig.1. The measured strength of steel plate and reinforcement was listed in Table 2. The overall instrumentation arrangement of the test was shown in Fig.2. The relative displacement between the top of steel beam and concrete slab and absolute displacement of steel beam and concrete slab were recorded respectively with displacement gauges (Fig.3). K-type thermocouples were installed to measure temperature developments of the flanges and web in the steel beam, locations at 15mm, 25mm depths of the headed studs and locations at 15mm, 50mm, 100mm depths of the concrete slabs from the fire exposed surface as shown in Fig.3.

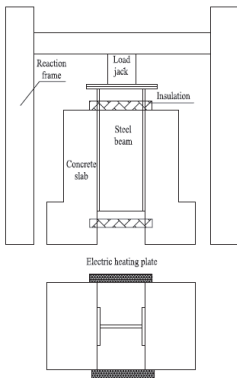
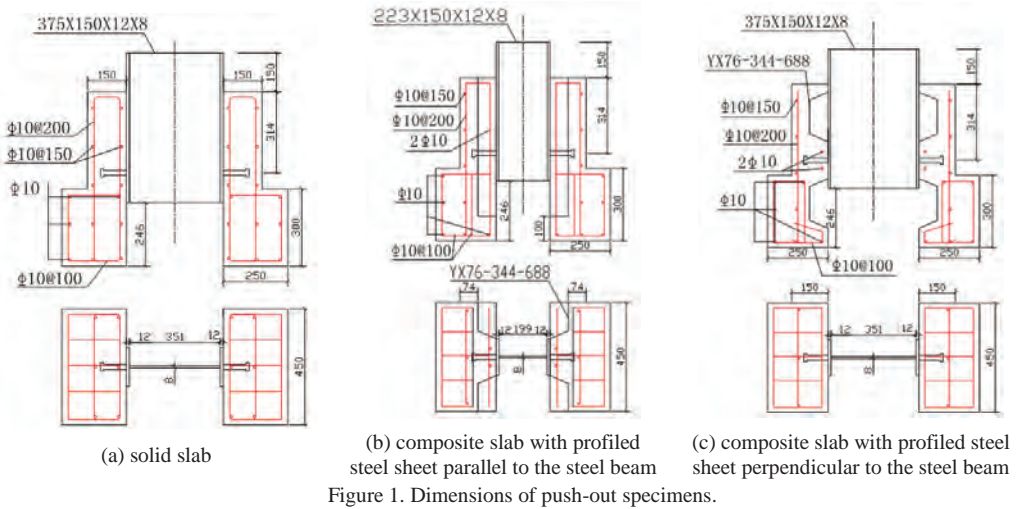


Figure 2. Arrangement of the instrument.

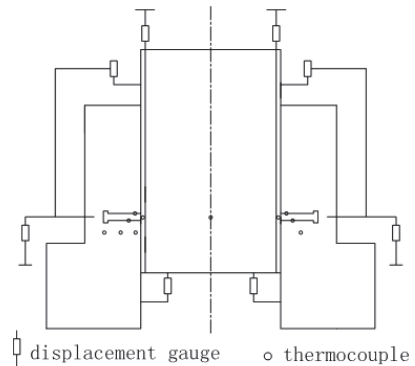


Figure 3. Locations of thermocouples and displacement gauge.

Table 1. Details of push-out specimens.

Specimen number	Slab type	Temperatures (°C)	Number
F-P-20	Solid slab	20	2
F-P-400		400	2
F-P-500		500	2
F-P-600		600	2
F-YP-20		20	2
F-YP-400	Composite slab with the deck parallel to the steel beam	400	2
F-YP-500		500	2
F-YP-600		600	2
F-YC-20	Composite slab with the deck perpendicular to the steel beam	20	2
F-YC-400		400	2
F-YC-500		500	2
F-YC-600		600	2

Table 2. Measured strength of components in tests.

Component	Dimension (mm)	Material	Yield strength (N/mm^2)	Ultimate tensile strength (N/mm^2)
Steel flange	12	Q235B	241.0	346.2
Steel web	8	Q235B	244.1	339.9
Rebar	10	HRB335	345.8	462.1

2.3 Test procedures

The push-out specimens were pre-loaded at about 30% of the ultimate load at ambient temperature to ensure the arrangements were in right state and the load was loaded along the axis of the cross section. After the pre-load process, they were heated to a given temperature, in which the temperature measured at the basis of stud was considered (10mm from the flange of the steel beam). Then the load was loaded until the failure of the specimen. The reason why the temperature of the stud at 10mm from the flange of the steel beam was taken into consideration was as follows. First, the temperature distribution of the stud in the longitudinal direction is un-uniform; the temperature at some points should be taken to represent the temperature of the stud. On the other hand, the stress state at the basis of the stud is the most severe, and it was observed in the previous experiments that the shear failure always occurred at the weld-collar interface. So, the bottom part of the stud plays an important role in the shear bearing capacity of the whole stud. In addition, the temperature of the stud below 10mm from the flange of the steel beam is close and the arrangement of the thermocouples at 10mm would cause little affect on the behaviour of connectors. Therefore, it is reasonable to adopt the temperature of the stud at 10mm from the flange of the steel beam as the temperature of the stud.

3 RESULTS AND DISCUSSION

Concerning the headed studs with solid slabs, it was observed in the tests that the collapse of specimen was always caused by the shearing off of headed studs just above the weld collar as shown in Fig.4(a). This is also the case for the headed studs with composite slabs with the corrugation of the deck run parallel to the steel beam as shown in Fig.4(b). However, when the corrugation of the deck run perpendicular to the steel beam, the mode of failure is no longer the same and the shearing off of concrete ribs were observed at low temperatures while the failure mode turned to stud shear failure at high temperatures as shown in Fig.5. That is probably because the temperature of the concrete was lower than that of stud resulting relatively higher strength of concrete at high temperatures. But the limit of this change needs further research. Test results were listed in Table 3.

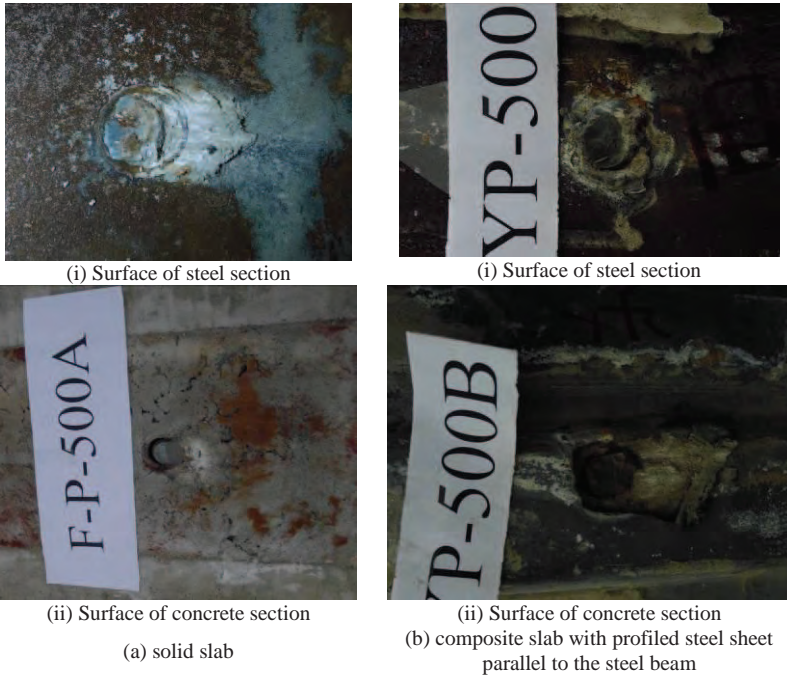


Figure 4. Typical failure mode of stud shear connector after push-out test.

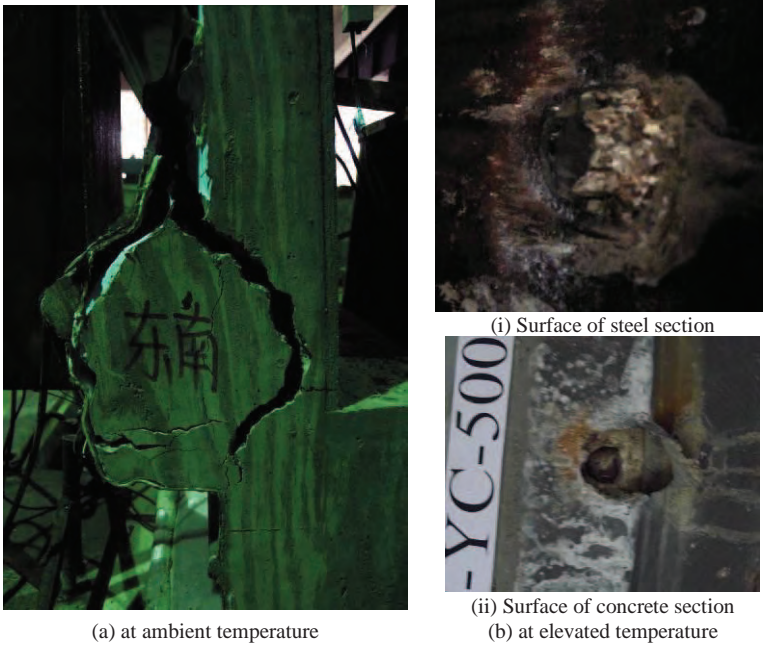


Figure 5. Failure mode of stud shear connector in composite slab with deck perpendicular to the steel beam observed from the test.

Table 3. Summaries of test results.

Specimen number	Measured temperature (°C)	Ultimate shear load (KN)	Average (KN)	Failure mode
F-P-20	1	20	280	Stud failure
	2	20	230.4	Stud failure
F-P-400	1	400	203.6	Stud failure
	2	400	188.8	Stud failure
F-P-500	1	500	150.8	Stud failure
	2	500	133.7	Stud failure
F-P-600	1	600	87.3	Stud failure
	2	600	102.9	Stud failure
F-YP-20	1	20	197	Separation between the deck and concrete, stud failure
	2	20	202	Separation between the deck and concrete, stud failure
F-YP-400	1	400	175.8	Stud failure
	2	400	190.5	Stud failure
F-YP-500	1	500	140.8	Stud failure
	2	500	107.4	Stud failure
F-YP-600	1	600	108.5	Stud failure
	2	580	85.4	Stud failure
F-YC-20	1	20	138.4	Concrete failure
	2	20	128.8	Concrete failure
F-YC-400	1	400	109.7	Concrete failure
	2	350	142.5	Weld failure
F-YC-500	1	500	141.3	Stud failure
	2	500	108	Stud failure
F-YC-600	1	580	79.1	Stud failure
	2	585	84.1	Stud failure

3.1 Temperature distribution

It was apparent that the temperature distribution of the concrete slab was un-uniform. The temperature development curves of steel beam, shear connector and concrete slab with time were shown in Fig.6. Since the temperature of the furnace did not increase according to the standard ISO834 curve and the rate of the temperature heated with electricity was relatively low, the temperature distribution of the concrete slab and shear connector in test was not the same with that in the standard experiment of composite beams at elevated temperatures.

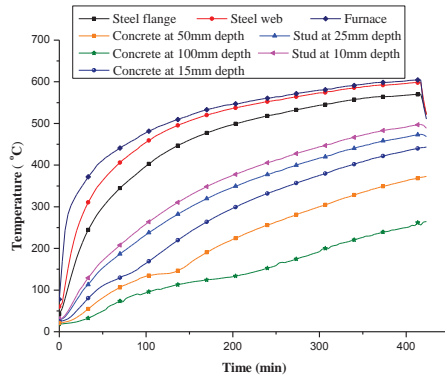


Figure 6. Measured temperature development.

3.2 Load-slip relationship

The load-slip relationship for solid slab, composite slab with profiled steel sheet perpendicular to the steel beam, and composite slab with profiled steel sheet parallel to the steel beam under elevated temperatures is illustrated respectively in Fig.7(a), (b) and (c). It was observed that the ultimate load and stiffness decreased with increasing temperature for all slabs. The failure mode of F-YC-400-2 was weld failure due to the defect of the weld between the steel beam and stud.

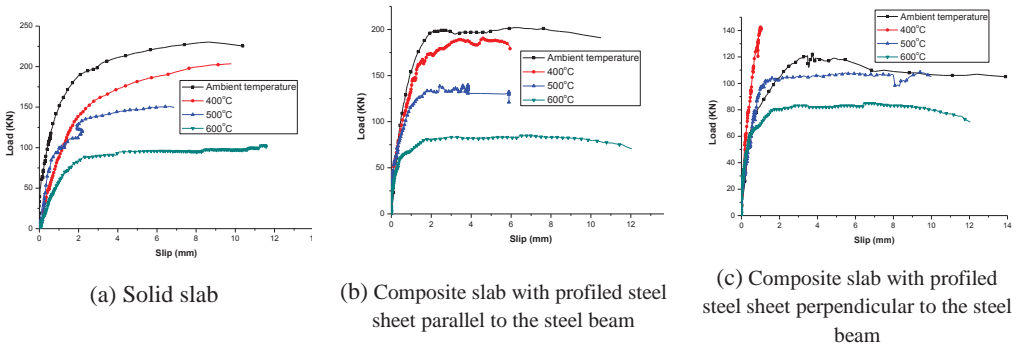


Figure 7. Load-slip relationship of headed studs at elevated temperatures.

3.3 Ultimate load

The ultimate load for all studs can be determined from Fig.7. Fig.8 illustrates the ultimate shear load reduces significantly according to temperature.

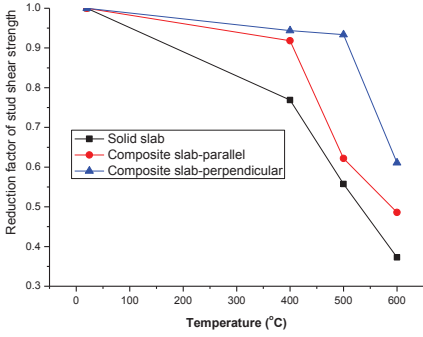


Figure 8. Ultimate shear load versus temperature.

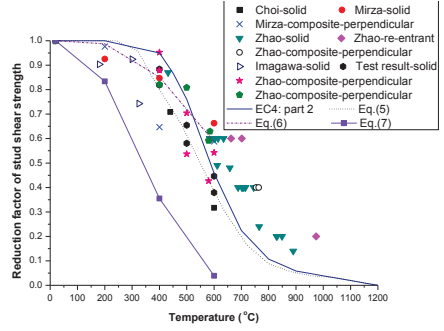


Figure 9. Comparison between existing test results.

3.4 Proposed equations

The proposed equations to calculate the degradation of shear resistance with temperature were listed as follows.

3.4.1 Equations in EN 1994-1-2

The shear resistance of shear connectors at high temperatures was taken as the minor of the results obtained with Eq. (3) and Eq. (4).

$$\left\{ \begin{aligned} Q_d &= \frac{0.8 f_u \pi d^2 / 4}{\gamma_v} & (1) \\ Q_d &= \frac{0.29 \alpha d^2 \sqrt{E_c f_{ck}}}{\gamma_v} & (2) \end{aligned} \right.$$

$$\left\{ \begin{aligned} Q_{dT} &= 0.8 k_{u\theta} Q_d & \text{with } Q_d \text{ as obtained from equation (1)} & (3) \\ Q_{dT} &= k_{c\theta} Q_d & \text{with } Q_d \text{ as obtained from equation (2)} & (4) \end{aligned} \right.$$

where, α is the factor considering the effect of the stud height, when $3 \leq h/d \leq 4$, $\alpha = 0.2[(h/d) + 1] \leq 1.0$; when $h/d > 4$, $\alpha = 1$; d is the diameter of the shank of the stud (mm); h is the overall nominal height of the stud (mm); f_u is the specified ultimate tensile strength of the material of the stud but not greater than 500 N/mm²; E_c is the elastic modulus of concrete (N/mm²); f_{ck} is the characteristic value of the cylinder compressive strength of concrete at 28 days; γ_v is the partial factor, generally taken as 1.0 at elevated temperatures; $k_{u\theta}$ is the reduction factor for the ultimate tensile strength of structural steel at elevated temperatures, the temperature of the stud connectors may be taken as 80% of the temperature of the upper flange of the beam; $k_{c\theta}$ is the reduction factor for the compressive strength of concrete at elevated temperatures, the temperature of the concrete may be taken as 40% of the temperature of the upper flange of the beam.

3.4.2 Equations by Choi

Eq.(5) was proposed by Choi to evaluate the shear strength of stud at elevated temperatures, in which the ultimate capacity of stud at a slip of 5mm was calculated. That was because the consideration of the acceptable connector ductility in composite plastic design was in a form of 5mm available slip.

$$Q_{uT} = f_u k_{u\theta} \pi d^2 / 4 \quad (5)$$

3.4.3 Equations by Mirza

Mirza presented that the ultimate shear load which relates to different temperatures at the 4mm slip for shear connectors with the solid slab and profiled slab could be determined from Eq (6) and (7) respectively.

$$Q_{uT} = -0.0003T^2 + 0.0525T + 186.67 \quad \text{for } 0^\circ\text{C} \leq T \leq 600^\circ\text{C} \quad (6)$$

$$Q_{uT} = 4 \times 10^{-7} T^3 - 0.0004T^2 + 0.034T + 38.721 \quad \text{for } 0^\circ\text{C} \leq T \leq 600^\circ\text{C} \quad (7)$$

3.4.4 Comparison

The Eq.(3), Eq.(4) and Eq.(5) are proposed based on the empirical equations to determine the shear resistance of stud at ambient temperature, while Eq.(6), Eq.(7) are directly derived from experimental result with curve-fitting. Although the equations to calculate the shear resistance of stud at room temperature were also developed with empirical method, The Eq.(3), Eq.(4) and Eq.(5) seemed to be more reasonable since the degradation of the shear resistance of the stud is caused by the strength and stiffness degradation of the steel and concrete materials. Also, a plenty of existing research achievements on the behaviour of studs at room temperature could be used. The comparison of these equations with the push-out tests result at elevated temperatures conducted by Zhao and Kruppa, Sengkwan Choi, Imagawa and Mirza was illustrated in Fig.9. It can be observed that Eq.(3), Eq.(4) is able to predict the shear strength of stud shear connectors at elevated temperatures with acceptable accuracy, while Eq.(7) is too conservative.

4 CONCLUSION

Tests conducted in this paper were designed to investigate the structural behaviour of headed stud shear connectors at elevated temperatures. In general, 24 push-out tests were carried out in Tongji University. Different types of concrete slabs including the flat concrete slab, composite slab with profiled steel sheet perpendicular to the steel beam, and composite slab with profiled steel sheet parallel to the steel beam were considered in the test. An electric furnace was applied to heat the specimens. Temperature development was measured across the section and the stud shank and the relative displacement between the steel beam and concrete slab were continually recorded. Furthermore, the comparison between the proposed equations which were proposed to calculate the shear strength retention properties of the stud with existing test results was made.

The main conclusions are summarized as follows:

1 The predominant mode of failure for the solid slabs and profiled slabs with the corrugation of the deck run parallel to the steel beam was headed stud shear connection failure while the predominant mode of failure for the profiled slabs with the corrugation of the deck run perpendicular to the steel beam was concrete cracking failure.

2 The ultimate load in solid slabs was generally higher than the profiled slabs. The ultimate load and stiffness decreased with increasing temperature for all slabs.

3 The calculation formula specified in the Eurocode EN 1994-1-2 to calculate the shear strength at elevated temperatures is reasonable and able to predict the shear strength of stud shear connectors at elevated temperatures with acceptable accuracy.

5 ACKNOWLEDGEMENT

The work reported herein above is financially supported by the National Natural Science Foundation of China by the contract 51120185001. The support is gratefully acknowledged.

REFERENCES

- [1] Viest I.M., "Investigation of Stud Shear Connectors for Composite Concrete and Steel T-Beams", *Journal of the American Concrete Institute*, 27(8):875-891, 1956.
- [2] Ollgaard J.G., Slutter R.G., Fisher J.W., "Shear Strength of Stud Connectors in Lightweight and Normal-Weight Concrete", *Engineering Journal*, 8(2):55-64, 1971.
- [3] Lam D., El-Lobody E., "Behaviour of Headed Stud Shear Connectors in Composite Beam", *Journal of Structural Engineering*, 131(1):96-107, 2005.
- [4] Zhao B., Kruppa J., Property and Service Performance: Fire Resistance of Composite Slabs with Profiled Steel Sheet and of Composite Steel Concrete Beams, Part 2: Composite Beams, Luxembourg, 1997.
- [5] Eurocode4: Design of Composite Steel and Concrete Structures, Part 1-2: General rules-Structural fire design, British standard, 2005.
- [6] Choi S.K., Han S.H., Kim S.B., Nadjai A., Faris A. and Choi J.Y., "Performance of Shear Studs in Fire", *Application of Structural Fire Engineering-Proceedings of International Conference*, Prague, 490-495, 2009.
- [7] Imagawa Y., Ohyama o., Kurita a., "Mechanical Properties of Stud in and after Fire", *Proceedings of Society of Civil Engineers*, 65(2):384-394, 2009.
- [8] Mirza O., Uy B. and Krezo S., "Experimental Studies on the Behaviour of Headed Stud Shear Connectors for Composite Steel Concrete Beams under Elevated Temperatures", *Advances in Steel and Aluminium Structures-7th International Conference on Steel and Aluminium Structures*, Lau H.H (ed.), Research Publishing Services, Malaysia, 467-473, 2011.
- [9] Eurocode4: Design of Composite Steel and Concrete Structures, Part 1-1: General rules and rules for buildings, British standard, 2001.

BEHAVIOUR OF AXIALLY LOADED BOX COLUMNS FILLED WITH HIGH-STRENGTH SELF-COMPACTING CONCRETE AT ELEVATED TEMPERATURES

Cheng-Chih Chen*, Wen-Chen Jau*, Chien-Jung Chen**, Yi-Chen Wu*
and Jheng-Yi Lin*

* National Chiao Tung University, Dept of Civil Engineering, Taiwan, ROC
e-mails: chrischen@mail.nctu.edu.tw, jau@mail.nctu.edu.tw, ycw715@hotmail.com,
jylin.cv97g@nctu.edu.tw

** Architecture and Building Research Institute, Ministry of the Interior, Taiwan, ROC
e-mail: john@abri.gov.tw

Keywords: Concrete, Box column, Fire, Axial deformation.

Abstract. *This study aims to investigate experimentally the behaviour of large-scale concrete-filled steel box columns subjected to axial load at elevated temperatures. Three specimens were filled with high-strength self-compacting concrete. During the ISO standard fire test, axial compression force, corresponding to 64%, 63.6% and 35.8% of the calculated compression strength of the columns, was applied to the specimens. Test results indicated that fire protection can enhance fire resistance rating. During the fire test, sound of the concrete bursting was continued heard. But the fire induced spalling of concrete did not cause immediate failure of the column due to the confinement provided by structural steel plate. The failure mode of the concrete-filled box columns was the bulge of the steel plate and crushing of the outer concrete. The load ratio is a major variable affecting the axial deformation for the concrete-filled box column.*

1 INTRODUCTION

Hollow structural steel sections or pipes that are filled with structural concrete are often used to enhance the column strength and stiffness. The use of concrete-filled tube columns leads to several advantages such as possessing excellent strength and stiffness compared with steel or reinforced concrete columns, using steel tube to replace formwork and simplifying the construction process, and providing confinement for the concrete through the use of steel tube. However, to be used for medium- and high-rise buildings, concrete-filled box columns are frequently designed instead of the concrete-filled tube columns because the concrete-filled box columns can provide greater strength than concrete-filled tube columns do. A steel box column is fabricated by welding four structural steel plates through the complete joint penetration weld or partial penetration weld.

In addition to analytical and numerical work [1-3], experimental work on the behaviour of the concrete-filled tube columns has been conducted by a number of researchers [1,2,4-10]. The test specimens included various test variables such as size of the cross section, shape of the steel tube, thickness of the fire protection, load ratio, load eccentricity, concrete strength, type of the concrete material, and fire duration time, etc. Moreover, the specimens tested in the literature were mostly small-scale. Although the behaviour of the concrete-filled tube columns in fire has been extensively studied, experimental work carried out for large-scale concrete-filled box columns is very few due to the limitation of the test equipment. Furthermore, the behaviour of the concrete-filled box columns at elevated temperature is not yet well established.

The structural steel used in the concrete-filled box columns possesses high strength and ductility, but with higher thermal conductivity, and the strength will be significantly decrease at elevated temperature. Concrete has good compression strength, and low thermal conductivity, and has better fire resistance than the steel. The concrete-filled box columns must subject to axial compression, and the structural behaviour and thermal response is complex at elevated temperature. The purpose of this study is to investigate experimentally the behaviour of the large-scale concrete-filled box columns subjected to axial load at elevated temperatures.

2 EXPERIMENTAL STUDIES

The experimental program was conducted to study the fire resistance of three concrete-filled steel box columns. Specimens were axially loaded and subjected to fire to explore the axial deformation, axial stiffness, and mode of failure.

2.1 Test specimens

The experiment consisted of fire tests on three large-scale concrete-filled box column (CFBC) specimens, filled with high-strength self-compacting concrete which the thermal properties has been studied as presented in the literature [11-13]. Specimen designation is tabulated in Table 1. The cross section of the specimens was 500 mm square and the length was 4350 mm. The structural steel box column was 500 mm square and 22 mm thick. As depicted in figure 1, the box column was fabricated by welding four steel plates through completely joint penetration weld and ultrasonic test was performed to confirm the welding quality. The average tensile strength of the steel plate was 372 MPa. Self-compacting concrete was used to fill the box column. The average concrete compressive strength was 59.7 MPa (for specimen CFBC-1) and 66.0 MPa (for specimens CFBC-2 and CFBC-3) when the specimens were tested. Two of the specimens, CFBC-1 and CFBC-2, had been sprayed with fire protection for two hours fire resistance rating. The average thickness of the fire protection was 15.3 and 14.3 mm for specimens CFBC-1 and CFBC-2, respectively.

Table 1. Specimen designation.

Specimen	CFBC-1	CFBC-2	CFBC-3
Tensile strength of the structural steel (MPa)	372	372	372
Concrete compressive strength (MPa)	59.7	66.0	66.0
Thickness of fire protection (mm)	15.3	14.3	-
Axial compression force (kN)	15,190	15,680	8,820

2.2 Instrumentations and test apparatus

In order to measure the temperature distribution of the specimens, type-K thermocouples were installed at four sections of the columns as indicated in figure 2 which also depicts the numbering of the thermocouples. The fire test was carried out on a fire test furnace as shown in figure 3. The furnace was programmed to execute the specified fire time-temperature curve.

2.3 Test procedure

ISO-834 [14] standard fire time-temperature curve was followed for the fire test. During the ISO standard fire test, axial compression force, corresponding to 64%, 63.6% and 35.8% of the calculated compression strength of the specimens based on the material strengths, was applied to three specimens CFBC-1 to CFBC-3, respectively, to study their behaviour and failure in fire. The axial compression force was 15,190, 15,680 and 8,820 kN for three specimens, respectively.

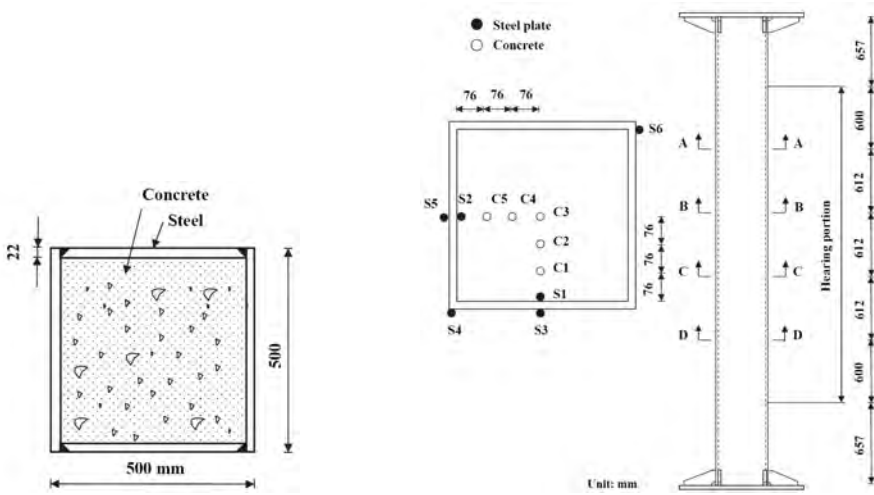


Figure 1. Cross section of the specimens. Figure 2. Location and numbering of thermocouples.

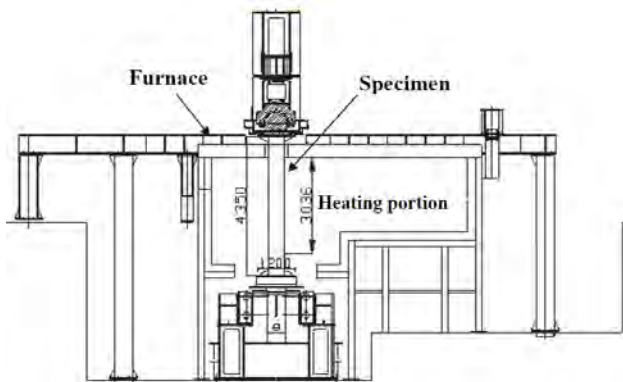


Figure 3. Sketch of the furnace and test setup.

3 RESULTS AND DISCUSSION

3.1 Specimen behaviour

Test results indicated that two specimens with two hours fire protection, specimens CFBC-1 and CFBC-2, can reach two hours fire resistance rating. During the specimen tested at elevated temperature, sound of the concrete bursting was continued heard which did not cause immediate failure of the specimen.

Specimen CFBC-1, with two hours fire protection, was subjected to two hours standard fire test and the highest temperature in the concrete was only 93°C while that in the structural steel was 287°C. The average temperature in the steel was 256°C. Figure 4 shows the measured temperatures as a function of time at cross section A. The elongation of this specimen was 3.8 mm. Figure 5 presents the specimen appearance after the test. Further, in order to explore the effect of the temperature on the specimen's structural behaviour, axial compression test was carried out again after the specimen had been cooled

down. The axial load-axial deformation curve illustrated that the axial stiffness of the specimen was recovered and the specimen behaved linearly elastic within the range of the design load, as indicated in figure 6.

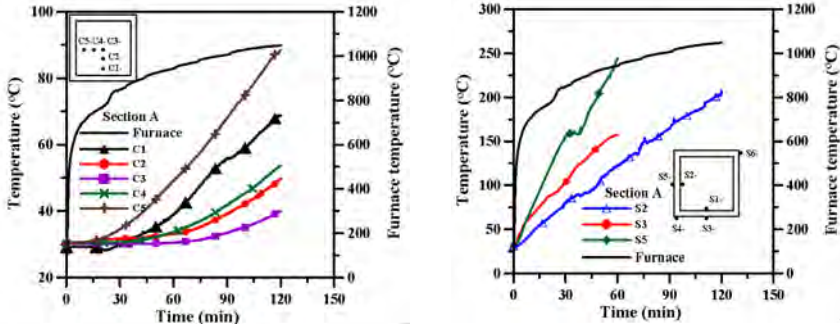


Figure 4. Measured temperatures at cross section A of Spec. CFBC-1.

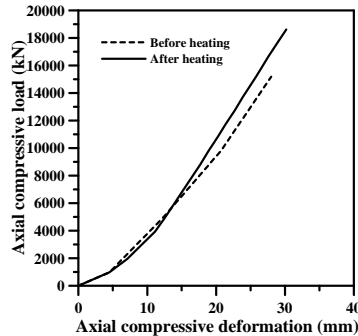


Figure 5. Spec. CFBC-1 at conclusion of the test. Figure 6. Axial deformation of Spec. CFBC-1 before and after fire.

Test results of specimen CFBC-2 demonstrated typical column behaviour that the column elongated, reached maximum elongation, compressed and finally failed while subjected to elevated temperature. Specimen CFBC-2 failed at 179 minutes and the highest temperature in the concrete reached 146°C while that in the steel was 512°C. Figure 7 presents the measured temperatures for specimen CFBC-2. Specimen CFBC-2 reached to the maximum elongation of 4.0 mm. The final failure mode was the bulge of the column steel plate and concrete crushing, as shown in figure 8.

Specimen CFBC-3 was tested without fire protection. As presented in figure 9, the highest concrete temperature was 470°C. The highest steel temperature reached 847°C and the average temperature in the steel was 758°C. The axial compressive load applied to this specimen was only 35.8% of the compression strength of the column which was even less than concrete strength in the ambient temperature. However, owing to the concrete bursting, specimen CFBC-3 failed at 43 minutes with maximum elongation of 17.3 mm. As demonstrated in figure 10, the bulge of the column steel plate occurred at several locations were also observed. After the specimen cooled down, the steel plate was flame cut, and the crushed concrete inside the steel plate was noticed.

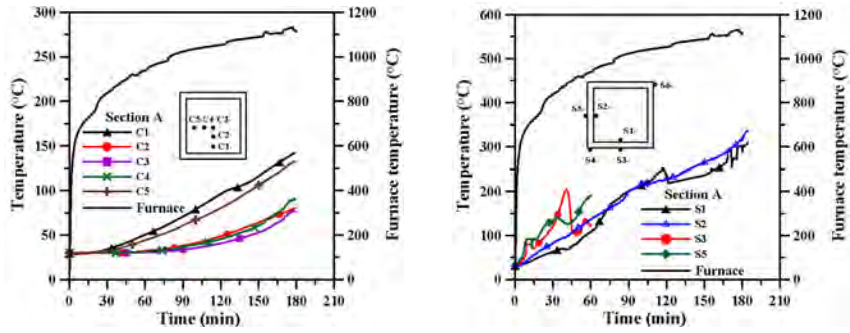


Figure 7. Measured temperatures at cross section A of Spec. CFBC-2.



Figure 8. Appearance of Spec. CFBC-2 at conclusion of the test.

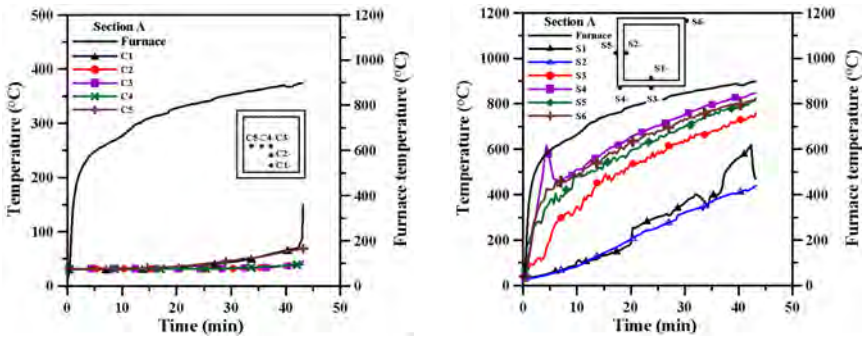


Figure 9. Measured temperatures at cross section A of Spec. CFBC-3.



Figure 10. Appearance of Spec. CFBC-3 at conclusion of the test.

Figure 11 presents the axial deformation versus fire time relations for three specimens and the distinct behaviour of specimen CFBC-3 was indicated. It is noted that the load ratio is a major variable affecting the axial deformation for the column. Structural steel plates provided the confinement for concrete exposure and prevented immediate failure of the column. Acceptable fire resistance of the concrete-filled box columns was also observed.

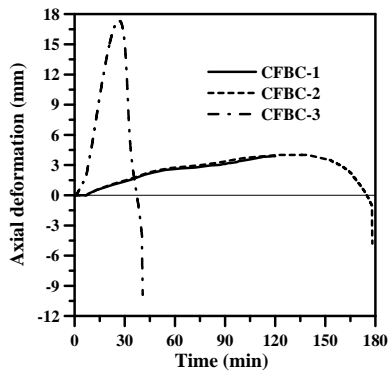


Figure 11. Axial deformation versus fire time.

3.2 Test results

As indicated in figures 4 and 7, temperatures at inner portion of the concrete rose slowly as compared to outer portion of the concrete. Unlike the behaviour observed from reinforced concrete columns that the rate of temperature rose in concrete slows down around 100°C due to the evaporation of water in concrete, no distinct temperature plateau was observed in these tests. This can be primarily attributed to the fact that the concrete was fully confined by the structural steel plates. Table 2 summarizes the test results, including the structural behaviour and thermal response for all three specimens. It is noted that the maximum axial elongation of specimen CFBC-3 during the fire duration was 17.3 mm which indicated an axial strain of 0.0057. Owing to lack of the shear studs for structural steel plate, this axial strain might imply the bond loss between steel plate and the concrete.

Table 2. Test results.

Specimen	CFBC-1	CFBC-2	CFBC-3
Fire duration time*/fire resistance time (min)	120*	179	43
Max. axial elongation (mm)	3.8	4.0	17.3
Time at max. axial elongation (min)	114	125	27
At conclusion of the test:			
Average temperature in steel (°C)	256.0	390.9	758.2
Max. temperature in steel (°C)	286.7	512.0	847.4
Average temperature in concrete at a depth of 76 mm (°C)	84.6	129.1	266.8
Max. temperature in concrete at a depth of 76 mm (°C)	93.4	145.5	470.2
Average temperature in concrete at a depth of 152 mm (°C)	52.7	80.7	201.9
Max. temperature in concrete at a depth of 152 mm (°C)	58.2	92.5	484.1
Average temperature in concrete at the center of column (°C)	38.6	73.6	112.5
Max. temperature in concrete at the center of column (°C)	41.7	76.5	249.4

4 CONCLUSIONS

The following conclusions can be drawn from the results of this research.

- (1) Fire protection sprayed for the concrete-filled box columns significantly enhance the fire resistance.
- (2) For specimen CFBC-1 with fire protection did not fail within two hour fire exposure, axial compression test was performed after the specimen had been cooled down. The axial stiffness of the specimen was recovered and the specimen behaved linearly elastic within the range of the design load.
- (3) The failure mode of the concrete-filled box columns was the bulge of the steel plate and crushing of the outer concrete. Structural steel plates provided the confinement for concrete fire induced spalling and prevented immediate failure of the column.
- (4) No distinct temperature plateau around 100°C in concrete due to the evaporation of water in concrete was observed in these tests owing to the fact that the concrete was fully confined by the structural steel plates.

ACKNOWLEDGEMENTS

This research was financially supported by the Architecture and Building Research Institute, Ministry of the Interior and National Science Council of the Republic of China, Taiwan and the support is gratefully acknowledged.

REFERENCES

- [1] Lu, H., Zhao, X. L., and Han, L. H., "Fire behaviour of high strength self-consolidating concrete filled steel tubular stub columns", *Journal of Constructional Steel Research*, 65, 1995-2010, 2009.
- [2] Lie, T. T., and Irwin, R. J., "Fire resistance of rectangular steel columns filled with bar-reinforced concrete", *Journal of Structural Engineering*, ASCE, 121(5), 797-805, 1995.
- [3] Yang, H., Han, L. H., Wang, Y. C., "Effects of heating and loading histories on post-fire cooling behaviour of concrete-filled steel tubular columns", *Journal of Constructional Steel Research*, 64(5), 556-570, 2007.
- [4] Han, L. H., and Huo, J. S., "Concrete-filled hollow structural steel columns after exposure to ISO-834 fire standard", *Journal of Structural Engineering*, 129(1), 68-78, 2003.

- [5] Han, L. H., Yang, Y. F., and Xu, L., "An experimental study and calculation on the fire resistance of concrete-filled SHS and RHS columns", *Journal of Constructional Steel Research*, 59(4), 427-452, 2003.
- [6] Han, L. H., Zhao, X. L., Yang, Y. F., and Feng J. B., "Experimental study and calculation of fire resistance of concrete-filled hollow steel columns", *Journal of Structural Engineering*, 129(3), 346-356, 2003.
- [7] Kim, D. K., Choi, S. M., Kim, J. H., Chung, K. S., and Park, S. H., "Experimental study on fire resistance of concrete-filled steel tube column under constant axial loads", *Steel Structures*, 5(4), 305-313, 2005.
- [8] Kodur, V. K. R., "Performance of high strength concrete-filled steel columns exposed to fire", *Canadian Journal of Civil Engineering*, 25, 975-981, 1998.
- [9] Lie, T. T., and Chabot, M., "Experimental studies on the fire resistance of hollow steel columns filled with plain concrete", *Internal Report No 611*, National Research Council of Canada, 1992.
- [10] Sakumoto, Y., Okada, T., Yoshida, M., and Tasaka, S., "Fire resistance of concrete-filled fire-resistant steel-tube columns", *Journal of Materials in Civil Engineering*, 6(2), 169-184, 1994.
- [11] Kodur, V. K. R., and Sultan, M. A., "Effect of temperature on thermal properties of high-strength concrete", *Journal of Materials in Civil Engineering*, 15(2), 101-107, 2003.
- [12] Wu, B., Su, X. P., Li, H., and Yuan, J., "Effect of high temperature on residual mechanical properties of confined and unconfined high-strength concrete", *ACI Materials Journal*, 99(4), 399-407, 2002.
- [13] Noumowé, A., Carré, H., Daoud, A., and Toutanji, H., "High-strength self-compacting concrete exposed to fire test", *Journal of Materials in Civil Engineering*, 18(6), 754-758, 2006.
- [14] ISO, "Fire resistance tests-elements of building construction, Part 1, General requirements", International Standard ISO 834, Geneva, 1999.

PERFORMANCE OF HOLLOW AND CONCRETE FILLED ELLIPTICAL STEEL COLUMNS SUBJECTED TO HYDROCARBON FIRE

Nathan Goodfellow*, Faris Ali*, Tom Scullion*, Ali Nadjai*, and Tony McParland**

* FireSERT, School of the Built Environment, University of Ulster, United Kingdom
e-mails: : n.goodfellow@ulster.ac.uk, f.ali@ulster.ac.uk, scullion-t@email.ulster.ac.uk,
a.nadjai@ulster.ac.uk

** Jeremy Gardner Associates, Howard House, 1-3 Brunswick Street, BT2 7GE, UK
TMcParland@jgafire.com

Keywords: Elliptical, Columns, Fire, Hydrocarbon, Steel, Concrete, FEM.

Abstract. *This paper presents the outcomes of the first ever conducted experimental research to investigate the performance of elliptical hollow and concrete filled steel columns subjected to severe hydrocarbon fire. The test programme involved 6 columns of a 200x100x8mm oval section yielding a slenderness $\lambda = 51$ and tested under the severe hydrocarbon fire curve. The 1800mm columns were tested under loadings ratios ranging between 0.2 and 0.6 of the ultimate strength determined using EC2, EC3 and EC4. Three columns were concrete filled and three columns had hollow sections. The paper presents the results of the fire tests including measured displacements, and failure time. The tests have shown that the concrete filled sections have demonstrated an improved fire resistance when compared to the hollow sections under the low loading ratios. A finite element study was performed and a model for the EHS was built. The finite element model showed an excellent agreement with the tests results for failure time, axial displacements and failure modes.*

1 INTRODUCTION

Within the construction industry there is a growing trend in the use of elliptical hollow and concrete filled steel columns in buildings due to their aesthetically pleasing shape compared to rectangular and circular hollow sections. There are also the added advantages when adopting the filled sections as they increase the load carrying capacity of the hollow section as well as preventing spalling from occurring as the concrete is totally encased. There is however limited research carried out on the performance of the elliptical columns under fire conditions. In recent years, research has investigated the performance of other types of hollow sections (circular, rectangular and square) under fire conditions. Han et. al. [1, 2] carried out tests on square and circular concrete filled columns with and without fire protection under different axial loadings. The research also involved tests on sections filled with self-consolidating concrete. A research carried out by Kodur [3] investigated the performance of concrete filled square and circular columns under fire. It is important to indicate that there has been some research carried out on the performance of stub elliptical columns by Chan and Gardner [4] and Lam and Testo [5] for concrete filled sections. However, these studies were carried out under normal temperatures. Although, there has been a limited research carried out on hollow elliptical columns in fire [6, 7] there is no experimental research performed on concrete filled elliptical sections under fire situations. This paper presents the results of a test programme to investigate the performance of elliptical steel columns in fire. The tests involved six columns (three hollow and three concrete filled) tested under three loading ratios of 0.2, 0.4 and 0.6 of the ultimate strength. All the columns have been subjected to the hydrocarbon fire curve

shown in Figure 1. The ultimate strength of the columns has been calculated using EC2 [8], EC3 [9] and EC4 [10].

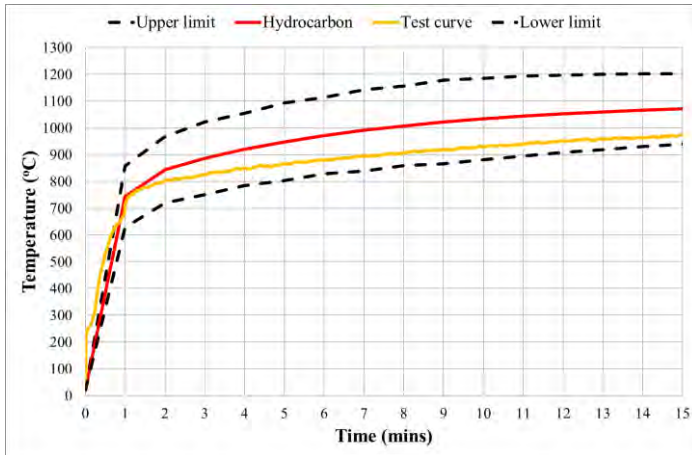


Figure 1. Hydrocarbon fire curve with test curve

2 TESTING PROGRAMME

The columns have been tested at the FireSERT research facilities at the University of Ulster. The test programme involved testing 1800 mm steel columns with an oval section 200x100x8mm (EHS-A) and slenderness $\lambda = 51$. The columns were tested under loadings levels of 0.2, 0.4 and 0.6 of the EC3 ultimate strength for both the hollow (EHS-A) and concrete filled (ECFS-A) sections giving a total of 6 tests. The columns were pin ended at the top and bottom. This was achieved using half-moon steel bearings at each end. To reduce the friction at the supports, graphite paper was incorporated between the two steel surfaces. In determining the ultimate loading of the concrete filled sections, three 100x100x100mm cube were cast during the filling process. The cubes were cured and tested after 28 days from the date of the casting giving an average compressive strength of 28N/mm². The columns were filled with concrete where a vibration poker was used during casting.

2.1 Test Methodology

The loading was imposed gradually on the columns in ten equal steps to allow the column to settle under each load step and get a stabilised reading for the axial displacement. Once the load level was reached the burner was ignited and the column was subjected to the hydrocarbon fire curve. The column is deemed to have failed once the axial displacement has passed beyond the starting (before heating) point.

2.2 Test Instrumentation

Thermocouples were located throughout the length of the columns measuring the temperature at sections located at 250mm from the top, at the midpoint of the column, and at 250mm from the bottom of the column. At each of these levels, four thermocouples were placed around the outer edge of the elliptical section as shown in Figure 2. In the case of the concrete filled sections an additional three thermocouples were embedded in the section at (mid-height of the column) during the casting process before the concrete has been given time to set (Figure 2).

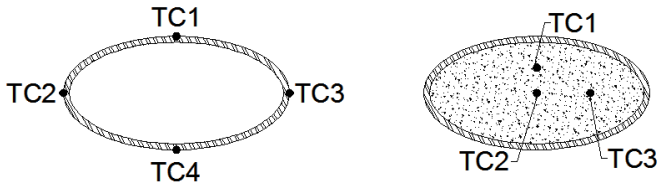


Figure 2. Thermocouple locations.

Four linear variable displacement transducers (LVDT's) were used to measure the axial displacements. Two at the top of the column and two at the bottom of the column and the average value was calculated. In order to accurately measure the lateral displacements of the columns, quartz rods were used due to their low thermal expansion coefficient. They were placed through the side of the furnace unto the surface of the column with the other end contacted to an LVDT outside the furnace.

3 TEST RESULTS

3.1 Elliptical Hollow Columns

The data gathered from the tests were used to plot the curves representing the development of the axial displacements with time as shown in Figure 3. The results for columns EHS-A show that increasing the load ratio reduced the time for failure from 15mins for 0.2 loading, to 10mins for 0.4 loading and 8mins for 0.6 loading. It can also be noticed that the axial displacement increases linearly as the time increases. Once the columns have reached their peak the deformation starts to decrease in slow rates. After that a rapid decrease in the displacement rate takes place until failure. This can be observed more clearly in the load levels of 0.6 of the ultimate loading as there is 30 seconds between the peak deformation and the columns failing where as it takes the 0.2 loaded sections between 1min 30secs to 2mins.

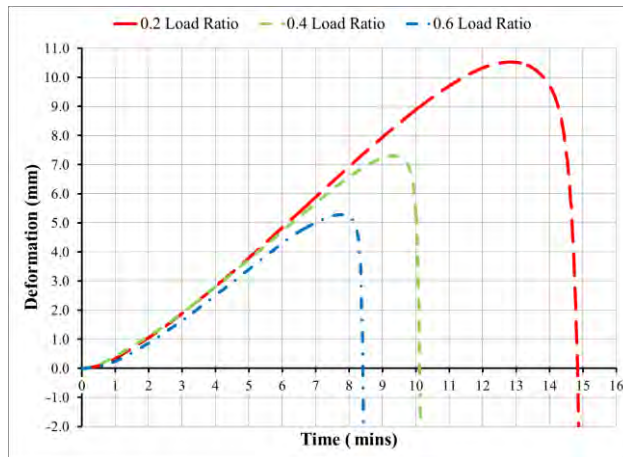


Figure 3. Time v axial displacement for unfilled EHS-A.

All the columns failed by overall buckling mode accompanied by localised buckling as shown in Figure 4.



Figure 4. Failure mode of elliptical hollow column.

3.2 Concrete filled columns

The three concrete filled columns were tested 28 days after casting using the same testing methodology as for the hollow sections with the introduction of vent holes in the top and bottom of the column in order to prevent the build-up of steam pressure within the section under heating as per EC4. In all the tests the concrete temperature was measured in 3 locations at the concrete core and at half distance between the concrete core and the steel wall from both sides as shown in Figure 3. The results from the tests indicate that the concrete temperature shows no significant increase if compared with the increase in the steel temperature as shown in Figure 5. This means that during heating, the steel expanded faster than the concrete core. Therefore, the applied load was resisted by the steel skin and not by the concrete core during most of the fire test period.

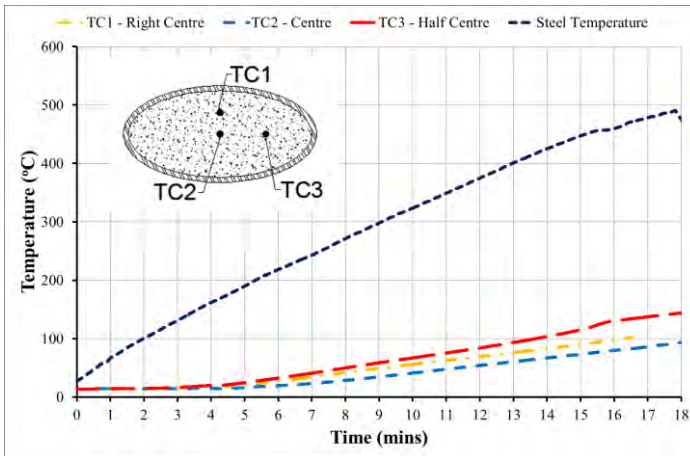


Figure 5. Concrete and steel temperatures in concrete filled column.

The axial displacements obtained during the testing show that failure time of the ECFS-A (Figure 6) has decreased with the increase in the loading level from 16mins for 0.2 loading, to 12mins for 0.4 loading and 8mins for 0.6 loading.

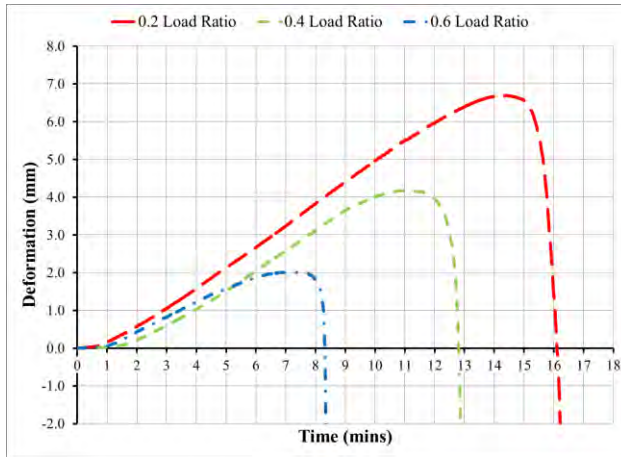


Figure 6. Time v axial displacements for concrete filled ECFS-A.

The failure modes of the concrete filled columns (Figure 7) were similar to those of the hollow sections with overall buckling accompanied by localised buckling occurring in some of the steel columns.



Figure 7. Failure mode of the concrete filled elliptical column.

4 TEST SUMMARY

The summary of the results in Table 1 and 2 indicate that the infilling of the elliptical sections has increased the fire resistance of the section under low loadings. It is noted that there is an increase in 0.2 and 0.4 load ratios. However, for the 0.6 loading the failure occurred approximately at the same time. There is also a decrease in the amount of axial deformation if the hollow section is filled with concrete due to the concrete steel interface which produces a friction force due to the expanding steel and the concrete not expanding.

Table 1. Summary of test results for elliptical hollow columns.

Section	Slenderness	Load Ratio	Load (kN)	Time of Failure (mins)
EHS-A.0.2	50.85	0.2	208	14
EHS-A.0.4		0.4	417	10
EHS-A.0.6		0.6	625	8

Table 2. Summary of test results for concrete filled elliptical columns.

Section	Slenderness	Load Ratio	Load (kN)	Time of Failure (mins)
ECFS-A.0.2	50.85	0.2	249	16
ECFS-A.0.4		0.4	497	12
ECFS-A.0.6		0.6	746	8

5 FINITE ELEMENT MODEL

A 3-D finite element model was created using TNO Diana [11] for the EHS-A. The model was built using 20 node iso-parametric brick element, CHX60, and the boundary heated element, BQ4HT, which is a four-node iso-parametric quadrilateral element was used to describe boundaries in three-dimensional general potential flow analysis. The final model consists of 38845 nodes and 10445 elements that represent the structural and temperature elements as shown in Figure 8.

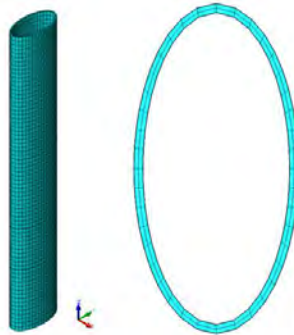


Figure 8. FEM created for the elliptical hollow sections.

The non-linear properties of the steel at high temperatures were taken from EC3 [12]. The results from the finite element analysis are shown in Figure 9 for the EHS-A section. The results show an excellent agreement between the time of failure and maximum axial deformation with slight divergence when the load ratio is reduced to 0.2 of the ultimate capacity.

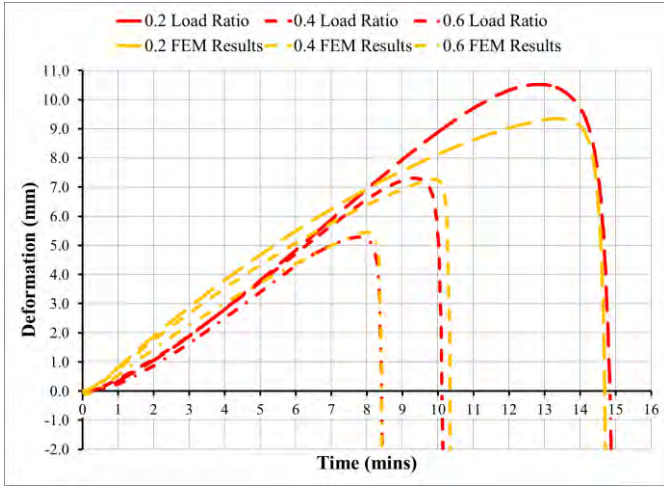


Figure 9. Time v Deflection for test results and FEM for EHS-A.

The failure mechanism that was observed in the testing was generally by overall buckling of the elliptical columns accompanied by local buckling. The FE model has also shown an excellent capability of predicting the mode of failure including the local and the overall buckling. Figure 10 shows that the model was successful in predicting the location of the local buckling failure to be at the same position as in the tests.

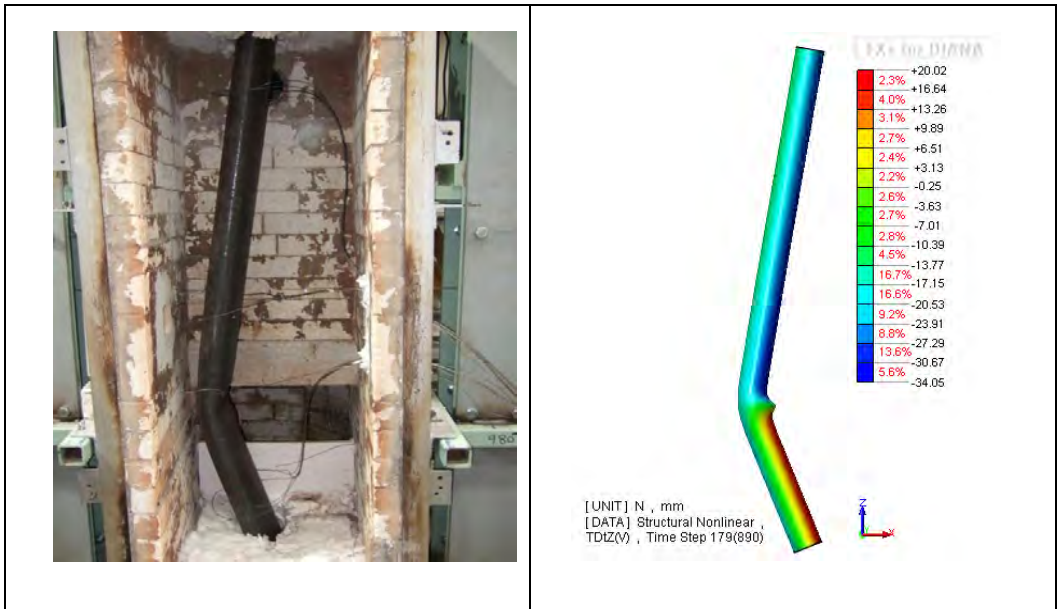


Figure 10. Comparison of failure modes of the test and FEM for EHS-A

6 CONCLUSIONS

Resulting from the testing programme the following conclusions can be drawn:

- In general, filling the elliptical hollow sections with concrete has improved the fire resistance of columns subject to low loadings.
- The maximum axial displacement in the concrete filled sections was less if compared to the hollow sections due to the restraining factor on the concrete/steel interface.
- Failure of the tested columns was by combination of overall and localised buckling occurring in the steel section.
- Failure time decreases more as the loading level is increased; for both of the hollow and concrete filled columns
- The hollow sections' failure was more instantaneous when compared to the concrete filled sections which showed a plateau stage before failing, increasing the time to failure.
- The FEM model results are in excellent agreement with the test results sections with regards to failure times, axial deformation and failure modes.

7 ACKNOWLEDGEMENTS

The authors would like to thank the EPSRC (Engineering and Physical Sciences Research Council) UK for providing the funding grant EP/H048782/1 for this research.

REFERENCES

- [1] Han LH., Zhao XL., Yang YF. and Feng JB., "Experimental study and calculation of fire resistance of concrete-filled hollow steel columns", *Journal of Structural Engineering*, ASCE, 346-356, 2003.
- [2] Han LH. and Yao GH., "Experimental behaviour of thin-walled hollow structural steel (HSS) columns filled with self-consolidating concrete (SCC)", *Thin-Walled Structures*, 42 (9), 1357-1377, 2004.
- [3] Kodur V., "Performance-based fire resistance design of concrete-filled steel columns", *Journal of Constructional Steel Research*, 51, 21-36, 1999.
- [4] Chan T.M. and Gardner L., "Compressive resistance of hot-rolled elliptical hollow sections", *Engineering Structures*, 30, 522-532, 2008.
- [5] Lam D. and Testo N., "Structural design of concrete filled steel elliptical hollow sections", *Composite Construction VI*, Colorado, USA, 2008.
- [6] Scullion T., Ali F. and Nadjai A., "Effect of axial restraint on the performance of Elliptical Hollow Section steel columns, in hydrocarbon fire", *Engineering Structures*, 33, 3155-3161, 2011.
- [7] Scullion T, Ali F, Nadjai A., "Experimental study on performance of elliptical section steel columns under hydrocarbon fire", *Journal of Constructional Steel*, 67(6), 986-91, 2011.
- [8] BS EN 1992-1-1, "Eurocode 2, Design of concrete structures, General rules and rules for buildings", 2004.
- [9] EN 1993-1-1, "Eurocode 3, Design of steel structures, General rules and rules for buildings", 2005.
- [10] EN 1994-1-1, "Eurocode 4, Design of composite steel and concrete structures, General rules and rules for buildings", 2004.
- [11] TNO Building and Construction research, "DIANA Finite Element Analysis user manuals", Release 9.4.3, Delft, 2011.

- [12] BS EN 1993-1-2, “Eurocode 3, Design of steel structures, General rules, Structural fire design. 2005.

HIGH TEMPERATURE TESTS ON PARTIALLY ENCASED BEAMS

Paulo A. G. Piloto*, Ana B. R. Gavilán**, Luís M. R. Mesquita* and Carlos Gonçalves*

* IDMEC, Polytechnic Institute of Bragança, Portugal
e-mails: ppiloto@ipb.pt, lmesquita@ipb.pt, carlosajgoncalves@gmail.com

** University of Salamanca, Spain
e-mail: aramos@usal.es

Keywords: Partially encased beams, High temperature, Experimental tests, Bending resistance.

Abstract. *Partially encased beams (PEB) are composite steel and concrete elements that present several advantages with respect to steel bare elements. This paper presents a set of experimental tests developed using two different beam lengths and two different shear conditions between stirrups and web (W – welded and NW – not welded), at high temperature (200, 400, 600 °C) and room temperature. The composite section was built-up with IPE100 steel profile and reinforced concrete between flanges. The deformed shape mode and the bending resistance were compared for different temperature levels and stirrup shear conditions (W and NW). The behaviour of PEB was also compared with bare steel at room temperature. Most of the beams attained the ultimate limit state by lateral torsional buckling (LTB), with exception for those tested at 600 °C, which collapsed by the formation of a plastic hinge (PH).*

1 INTRODUCTION

PEB have been widely tested at room temperature, but only a small number of testes are reported under fire or under high temperature. The most relevant tests were developed by Kindmann et al [1], proving the importance of the reinforced concrete between flanges for bending resistance. Lindner and Budassis in 2000 [2] developed a new design proposal for lateral torsional buckling. Maquoi et al [3], improved the knowledge on the elastic critical moment and on the lateral torsional buckling resistant moment. Makamura et al. [4], tested 3 partially encased girders with longitudinal and transversal rebars (W and NW) to flanges, concluding that bending strength of the PEB was almost two times higher than conventional bare steel girders and specimens with rebar not welded to flanges presented a decrease of 15 % for maximum load bearing when compared to the welded rebar (W) specimens.

PEC (partially encased columns) were also tested at room and elevated temperatures. Hunaiti et al. [5], analysed the behaviour of 19 PEC without additional shear connectors, and tested those fabricated with shear connectors and batten plates for different loading conditions. All columns presented full composite action and similar strength, regardless of the type of additional steel. Stefan Winter and Jörg Lange [6], determined the ultimate load of 8 PEC at room temperature using high strength-steel. Authors developed some full scale tests under fire conditions and concluded for equal ultimate load for both materials. Brent and Robert [7], investigated the behaviour of PEC, comparing the performance of High Strength Concrete (HSC) and Normal Strength Concrete (NSC), evaluating the ultimate load and failure mode. Authors verified that PEC with HSC had more brittle failure mode than NSC, concluding that introducing steel fibres and reducing spaces between stirrups would improve ductility. A. Correia and João P. Rodrigues [8], studied the effect of load level and thermal elongation restraint on 3.0 m length PEC, built with HEA 160 and HEA 200, under fire conditions. They concluded that the surrounding stiffness had a major influence on fire element behaviour for lower load levels. The increasing of the surrounding stiffness is responsible for reducing critical time. Critical time remains practically unchanged for higher load levels.

A small number of 15 experiments were already developed on PEB under fire conditions (small series) to determine fire resistance, reported by authors in a previous work [9]. This current work intends to present high temperature tests for medium and large series, using the same cross section type with two different lengths, three different temperature levels of 200, 400 and 600 °C, calculating bending resistance.

2 SPECIMENS

PEB were prepared by filling the space between the flanges of a steel IPE100 profile, using reinforced concrete (RC). Partially encased sections achieve higher fire resistance when compared to bare steel sections. The increase in fire resistance is due to the encased material, reducing the exposed steel surface area, introducing concrete which has a low thermal conductivity. Higher fire resistance can also be achieved by increasing the amount of reinforcement to compensate for the reduction of steel strength in case of fire, as reported by several researchers.

Two different shear configurations for stirrups were used, both represented in figure 1. According to EN1994-1-1 [10], this composite steel and concrete section is classified as class 1.

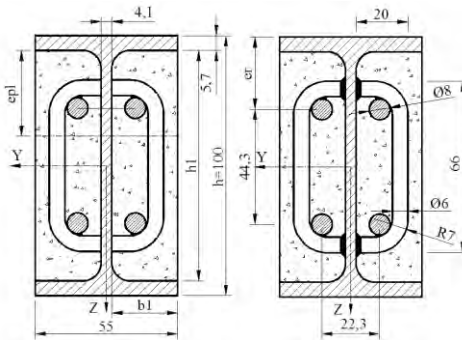


Figure 1. Cross section geometry

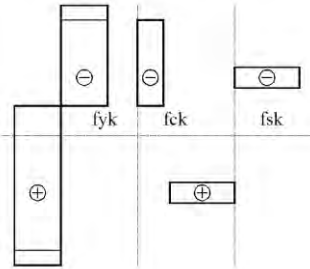


Figure 2. Plastic stress distribution in cross section

The plastic neutral axis is referenced to “epI”, reinforced concrete block dimensions are represented by “b1” and “h1”, while “er” represents the relative position for reinforcement.

According to EN1994-1-2 [11], member analysis under fire conditions may be verified using either tabulated data, simplified or advanced calculation methods. Tabulated data refers only to composite beams rather than PEB, depends on load level, and is only valid for standard fire exposure and simple supporting conditions. A simple calculation method may be used to determine fire resistance of PEB without shear connection to the concrete slab. The rules for composite beams may be applied to PEB, assuming no mechanical resistance of the reinforced concrete slab, and establishing reduced effective areas of the cross section. An advanced calculation method may also be used to analyse partially encased beams. These models may include separate calculation programs for temperature and displacement.

In order to define load level dependence for partially encased sections at room temperature, the plastic moment was calculated using characteristic values for material properties, assuming certain hypotheses based on stress field distribution, see figure 2 and eq. 1, [2].

The plastic moment at room temperature was calculated, assuming that the effective area of the steel profile may be stressed in compression and tension, up to its characteristic yield strength (f_{yk}); the effective area of longitudinal reinforcement (A_s) may be stressed to their characteristic yield strength (f_{sk}) in tension and compression, and the effective area of concrete in compression may be stressed up to the characteristic value of concrete cylinder compressive strength f_{ck} , constant over the compressive part of concrete. The contribution of IPE100 bare steel to the plastic moment is equal to 80%, while the contribution of RC to the plastic moment represents 20%.

$$M_{pl} = W_{pl,y} \cdot f_{yk} - 2 \cdot f_{yk} \cdot t_w \cdot (0.5h_1 - e_{pl})^2 / 2 + f_{ck} \cdot 2 \cdot b_1 \cdot e_{pl} (0.5h_1 - 0.5e_{pl}) + 2 \cdot A_r \cdot (f_{sk} - f_{ck}) (h - 2 \cdot e_r) \quad (1)$$

The shear resistance was also verified at room temperature. The contribution of web encasement to shear may be taken into account if stirrups are fully welded to the web, otherwise shear reinforcement should not be considered. The distribution of the total shear resistance into steel resistance and RC resistance may be assumed to be in the same proportion as it is for bending resistance, [10]. The design resistance for bending and shear were determined by 14.8 kNm and 102 kN. These limits helped to decide about the capacity of the hydraulic jack to be used.

PEB were made of IPE100 with steel S275 JR, using C20 encased concrete with siliceous aggregates. Four longitudinal steel B500 rebar were used with diameter of 8 mm. Stirrups were designed with B500 rebar with a diameter of 6 mm, spaced every 167 mm. Stirrups were also partially welded to the longitudinal steel reinforcement, as represented in figure 1.

3 EXPERIMENTS

Twenty PEB and two bare steel beams were tested under four-point bending. Tests were grouped in eight series to determine bending resistance at different temperature levels. Two series were prepared to analyse the behaviour of stirrups not welded to the web (NW), four series were prepared for high temperature levels using welded stirrups (W) and two series were defined to be tested at room temperature. Two slenderness ratio were considered, using beams with $L_t=2.5$ m and $L_t=4.0$ m. Three tests were defined for high temperature series, with exception for series 7 and 8, see table 1.

Table 1. List of partially encased beams to be tested (specimens).

Series	Specimen	Length L_s [m]	Stirrups [W/NW]	Temp. [°C]	Max. impe. [mm]
1	B/2.4-01	2.4	W	400	2
	B/2.4-02				2
	B/2.4-03				2
2	B/2.4-04	2.4	W	200	1
	B/2.4-05				2
	B/2.4-06				1
3	B/2.4-07	2.4	NW	400	1
	B/2.4-08				1
	B/2.4-09				1
4	B/3.9-01	3.9	W	400	2
	B/3.9-02				5
	B/3.9-03				3
5	B/3.9-04	3.9	W	600	2
	B/3.9-05				2
	B/3.9-06				5
6	B/3.9-07	3.9	NW	400	5
	B/3.9-08				5
	B/3.9-09				2
7	B/3.9-11	3.9	W	room	2
	B/3.9-12				5
8	B/3.9-11A	3.9	W	room	1
	B/3.9-12A				3

Table 1 identifies each PEB tested, the length between supports (L_s), the shear condition for stirrups, the maximum temperature used during heating and the maximum geometric imperfection. The initial out-of-straightness was measured using a laser beam.

Specimens were tested using a steel portal frame, see figure 3. Room temperature tests were developed in one single stage, using small increments of load, while high temperature tests were developed in two stages. The first stage was used for heating the beam along the length “Lf”, using a constant heating rate and a dwell time for constant temperature. During the second stage, temperature was kept constant and load was slowly increased.

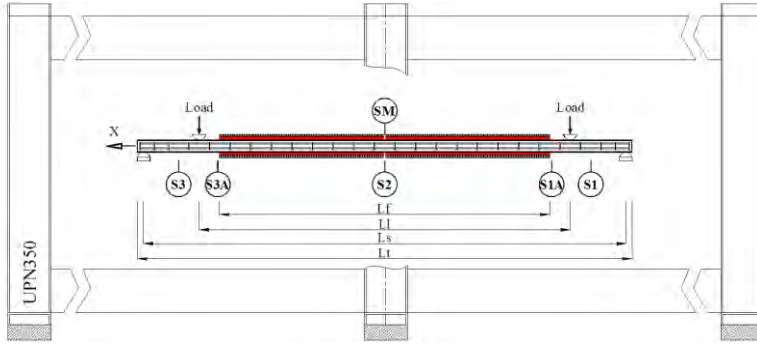


Figure 3. Testing conditions and main cross sections.

Five different cross sections were defined to measure temperature (S1, S1A, S2, S3A and S3), in case of high temperature tests and one cross section was used to measure strain (SM at room temperature), displacements (vertical Z_G , lateral Y_G) and cross section rotation θ_G .

Table 2 defines the lengths for medium and large test series.

Table 2. Lengths defined for each beam (specimen).

Specimen	Total length	Length supports	Length load	Heating length
	Lt [m]	Ls [m]	Ll [m]	Lf [m]
B/2.4	2.5	2.4	1.5	1.3
B/3.9	4.0	3.9	3.0	2.8

Two fork supports were applied on each four-point bending test. Restraint against Y/Z displacement and restraint against X rotation was considered at each support. A special interface was developed to apply vertical load, introducing a certain level of restraint against X rotation but allowing for lateral displacement Y. Teflon was used to reduce friction between the beam and the hydraulic jack. see figure 4.



Figure 4. Testing supports with load cell (left) and load applied by the hydraulic jacks (right).

The distance between load and support was kept constant for large and medium series. The length of specimens to be heated was shorter than the length between supports. This effect may be negligible

because bending moment is reduced in the region nearest the supports and will not be affected by heating. Free thermal elongation was allowed before adjusting both supports and starting with each test.

3.1 Materials

Each material was characterized according to international standards [12] for hot rolled and cold formed steel, see table 3. Three samples were collected from the web of steel hot rolled profile and two more samples were collected from steel reinforcement.

Table 3. Tensile tests for hot rolled and cold formed steel.

Properties	Steel profile		Steel reinforcement	
	Average	Std. Deviation	Average	Std. Deviation
E [GPa]	197.901	2.948	203.294	2.110
R _{p,0.2%} [MPa]	300.738	6.720	524.993	3.521
ReH [MPa] (f _{yk}) (f _{sk})	302.466	5.749	531.508	7.908
ReL [MPa]	300.856	4.028	520.825	4.068
Rm [MPa] (fu)	431.252	5.020	626.574	11.539
At [%]	41.584	0.231	25.155	0.495

E- Elastic modulus, R_{p,0.2%}- proof strength for 0.2%, ReH- upper yield strength, ReL- lower yield strength, Rm- tensile strength, At- total extension at the moment of fracture.

Concrete was made with Portland cement, sand and siliceous aggregates. The concrete composition was prepared according to table 4. Aggregates (gravel and sand) were characterized by the sieving method and tested according to international standard [13] to determine particle size dimension. Due to the small size of the steel section and considering the offset dimension for the concrete cover of the stirrups, the concrete was made up with small-sized aggregates. The percentage of aggregates with diameters between 4-6 mm was 90%, while the percentage of sand with diameters between 0.063-0.5 mm was 80%. The aggregate dimensions limit the value of the compressive resistance of concrete as concluded by Keru et al, [14]. The high level of permeability at elevated temperature was responsible for decreasing pore pressure. This fact justifies the absence of explosive spalling.

Table 4. Mix proportions of concrete.

Component for	1 [m ³] concrete
Sand	1322.7 [kg]
Aggregates	451.1 [kg]
Water	198 [l]
Cement	466.7 [kg]
Water / Cement	45 %

Table 5 shows the results for the compressive strength of concrete, using three compressive tests for cubic samples (f_{ck,cube}) and three compressive tests for cylindrical samples (f_{ck}).

Table 5. Compressive tests results for concrete.

Properties	Cure [days]	Average	Std. Deviation
f _{ck,cube} [MPa]	29	21.45	1.03
f _{ck} [MPa]	29	20.36	0.30

An increase of 100% on the compressive strength of concrete would lead to an increase of 2% in the bending resistance of PEB at room temperature. This means that this section type is not sensitive to the value of the compressive strength of concrete.

3.2 Instrumentation

PEB were prepared to be tested at room temperature, measuring strain in central section (SM). Figure 5 represents the location for strain gauges, over steel flange and web, in hot rolled section (SM-WS and SM-OS) and over concrete (SM-RC1 and SM-RC2). Whereas perfect bond was considered between concrete and reinforcement, concrete strain was measured on steel reinforcement; for the latter measurement, rebars were machined 1 mm in depth and 15 mm in length, in respect to the dimensions of the electrical strain gauge. Five strain gauges (HBM reference 1-LY11-3/120) were used. All strain gauges were protected with gloss and special viscous putty (HBM reference Ak22) against moisture, water and mechanical damage.

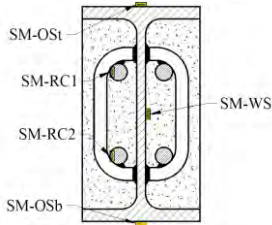


Figure 5. Strain gauge positions for steel and concrete.

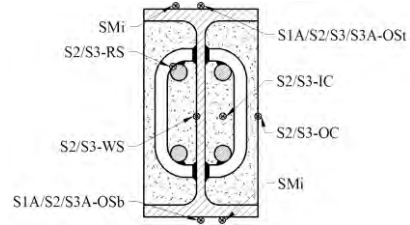


Figure 6. Thermocouple positions for all cross sections

PEB were also prepared to be tested at high temperatures, using thermocouples type K positioned along the length of each element, according to figure 6. Thermocouples were positioned in place, using the spot welding machine. For the concrete temperature measurements, positions Si-IC and Si-OC, thermocouples were welded to a small steel washer, wrapped in concrete.

3.3 Testing procedures

Tests developed at room temperature used quasi-static load increments, based on load cell readings. Load was applied with two synchronized hydraulic jacks. Strain, displacement and cross section rotation were determined at central section (SM). Transversal and lateral displacements (Z_G , Y_G) as well as cross section rotation were based on three wire potentiometric displacement transducers. Some important force events were recorded for each test. The force value for plastic moment (F_{Mpl}) was determined using the intersection method between two straight lines drawn from linear and non-linear interaction. The load event for transversal displacement equal to $L/30$ was also determined ($F_{L/30}$) and the maximum load level for the asymptotic behaviour of the transversal displacement was identified by (F_u).

Tests developed at elevated temperature used electro-ceramic heating device to increase and sustain temperature during loading. A heating rate of 800 °C/hour was applied, which lead to heating periods of 15, 30 and 45 minutes. An insulation ceramic mat was applied to increase heating efficiency. Supports were adjusted and load was applied after temperature stabilization (60, 90 and 120 minutes after the start of heating). The same procedure was used to measure transversal and lateral displacement, as well as, cross section rotation. Load events were also recorded as well and temperature measurements in the main cross section.

4 RESULTS

Four-point bending tests were performed to evaluate bending resistance of PEB at high and room temperature. Bending resistance was also compared to bare steel beams, using the same cross section for steel. Two different beam lengths were tested (medium and large series). Two different conditions were tested for stirrups (W and NW) at elevated temperature (400 °C). Several performance criteria were defined to compare the effect of different conditions. Force events were defined when the cross section became plastic (F_{Mpl}), when the transversal displacement reached $L/30$ ($F_{L/30}$) and when force reached its

maximum value (F_u). Temperature evolution in time was represented for certain periods of time and temperature distribution over each beam length was also represented.

4.1 Bending resistance of PEB (medium series)

The medium series includes results of PEB with $L_s=2.4$ m. All tested beams reached lateral torsional buckling as deformed shape mode. Figures 7-12 present the results for PEB with welded stirrups.

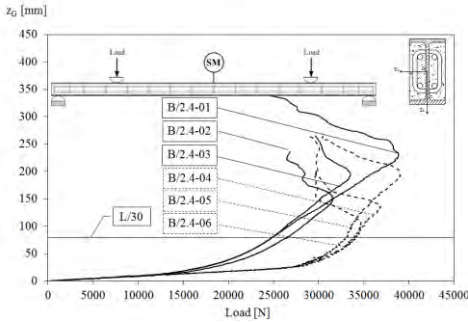


Figure 7. Deflection behaviour at mid span for series 1/2.

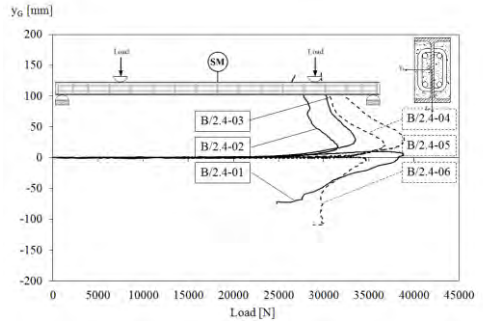


Figure 8. Lateral displacement for series 1/2.

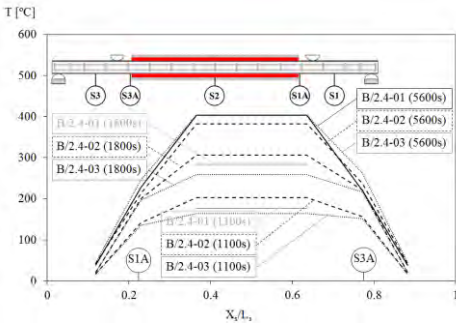


Figure 9. Temp. distribution and evolution for series 1.

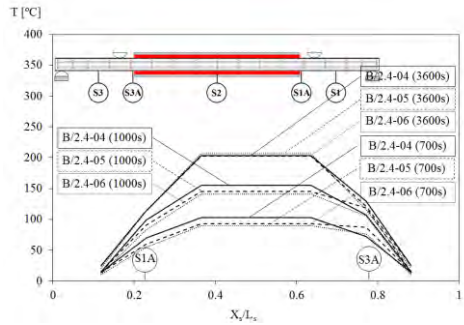


Figure 10. Temp. distribution and evolution for series 2.



Figure 11. Deformed shape mode for B/2.4-01.

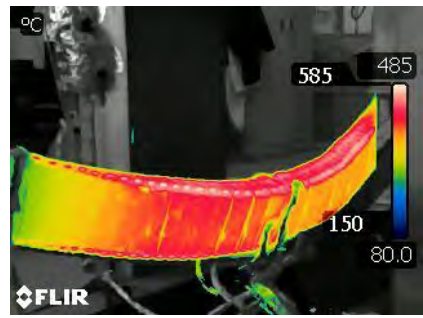


Figure 12. Temperature at the end of test for B/2.4-01.

Displacement results were determined for PEB with stirrups NW. Series 3 presented almost the same behaviour as series 1. Table 6 presents the main force events during each test for medium series. The results agree very well with exception for the ultimate load (F_u). Differences may be explained by the friction effect near the supports / load and by the deformation mode shape developed at high load level.

Table 6. Force results for medium series.

Series	Specimen	F(Mpl) [N]	F(L/30) [N]	Fu [N]
1	B/2.4-01	18890	24932	38864
	B/2.4-02	21760	26583	31533
	B/2.4-03	19920	24878	33568
2	B/2.4-04	31430	34060	36875
	B/2.4-05	30350	32953	39042
	B/2.4-06	31380	33930	34712
3	B/2.4-07	20610	24898	29000
	B/2.4-08	19270	25135	40861
	B/2.4-09	20850	25722	33246

4.2 Bending resistance of PEB (large series)

The large series includes results of PEB with $L_s=3.9$ m. Figures 13-18 present the results for transversal and lateral displacements. Results agree very well with each other, with exception to the end of the tests. Temperature evolution and distribution is also plotted in graphs. Temperature is not uniform along the beam because the insulation is not perfect and heat flows by conduction, mainly along the steel part of PEB. The deformed shape mode for series 4 was lateral torsional buckling. Plastic hinge formation was the dominant deformed shape mode verified for series 5. Some lateral displacement did also occur.

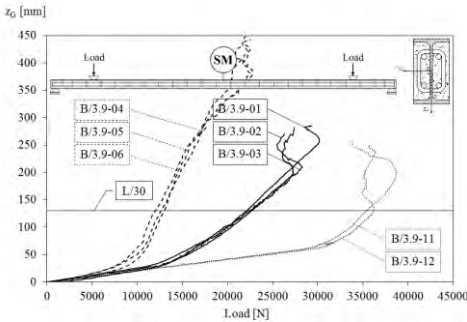


Figure 13. Deflection behaviour at SM for series 4/5/7.

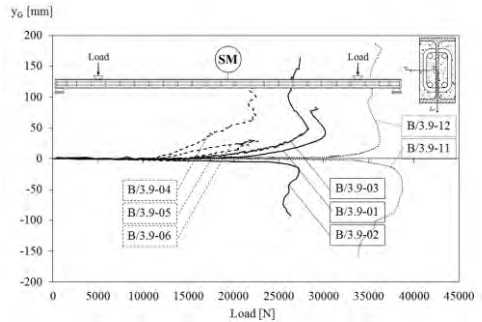


Figure 14. Lateral displacement at SM for series 4/5/7.

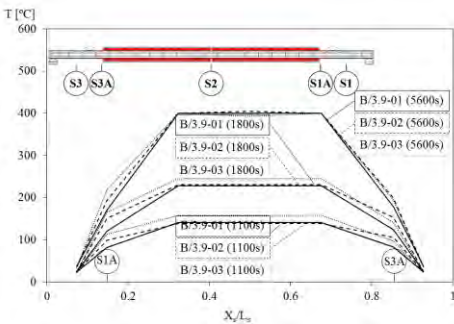


Figure 15. Temp. distribution and evolution for series 4.

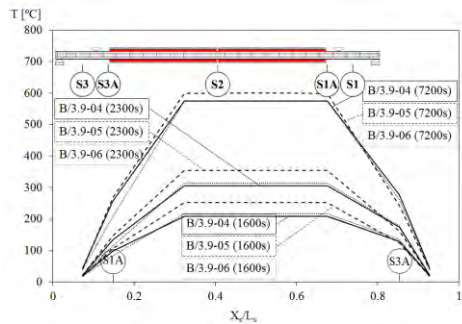


Figure 16. Temp. distribution and evolution for series 5.



Figure 17. Deformed shape mode for B/3.9-05.

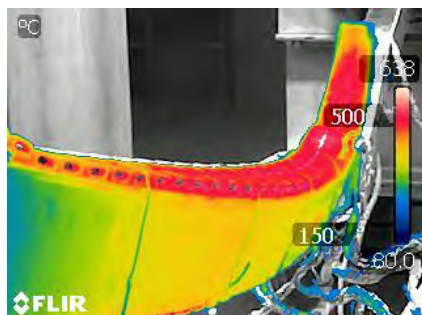


Figure 18. Temperature at the end of test for B/3.9-07.

Displacement results were determined for PEB with stirrups NW. Series 6 presented results in agreement with series 4. Table 7 presents the main force events during each test. The results agree very well with exception for the ultimate load (F_u). Differences may be explained as discussed previously.

Table 7. Force results for large series.

Series	Specimen	F(Mpl) [N]	F(L/30) [N]	F_u [N]
4	B/3.9-01	16370	22126	30204
	B/3.9-02	16360	22715	27290
	B/3.9-03	14850	22573	28337
5	B/3.9-04	9620	12641	22456
	B/3.9-05	9759	12996	21662
	B/3.9-06	9110	12025	22770
6	B/3.9-07	15000	22665	23591
	B/3.9-08	15600	24234	32642
	B/3.9-09	15100	23207	24816
7	B/3.9-11	31600	35428	38718
	B/3.9-12	32100	36161	36380
8	B/3.9-11A	-	-	19436
	B/3.9-12A	-	-	21272

5 CONCLUSIONS

Four-point bending tests were performed to evaluate bending resistance of PEB at high and room temperature. Force and displacement results are presented to compare bending resistance. The bending strength of the PEB at room temperature is almost two times the bending resistance of bare steel beam. The reduction on bending resistance of PEB is not directly proportional to the increase of temperature. An increase of temperature from 200°C to 400 °C leads to a reduction of 24 % on $F(L/30)$ for medium series, while an increase from room to 400°C, 600°C leads to a reduction of 37 % and 64% on $F(L/30)$, respectively.

The deformed shape mode was LTB for all tested PEB and bare steel beams, with exception to those tested at 600 °C.

ACKNOWLEDGMENT

Authors acknowledge material support to the following companies: Arcelor – Mittal (Spain), J. Soares Correia (Portugal), Fepronor (Portugal) and Hierros Furquet (Spain).

REFERENCES

- [1] R. Kindmann, R. Bergmann, L-G. Cajot, J. B. Scleich; "Effect of reinforced concrete between the flanges of the steel profile of partially encased composite beam"; *Journal of Constructional Steel Research*, 27, pp 107-122, 1993.
- [2] Joachim Lindner, Nikos Budassis; "Lateral torsional buckling of partially encased composite beams without concrete slab"; *Composite construction in steel and concrete IV, conference proceedings*, May 28th to June 2nd, Banff, Alberta, Canada, 2000.
- [3] R. Maquoi, C. Heck, V. Ville de Goyet, et al, (European commission), "Lateral torsional buckling in steel and composite beams"; ISBN 92-894-6414-3; Book 1,2 and 3; *Technical steel research final report EUR 20888 EN*; August 2002.
- [4] S. Nakamura, N. Narita, "Bending and shear strengths of partially encased composite I-girders", *Journal of Constructional Steel Research*, 59, pp.1435-1453, 2003.
- [5] Hunaiti, Y.; Fattah, B. A.; "Design considerations of partially encased composite columns", *Proceedings Institution of Civil Engineers Structures & Buildings*, v.106, pp.75-82, Feb. 1994.
- [6] Stefan Winter and Jörg Lange, "Behavior of Partially Encased Composite Columns Using High-Strength Steel – Service and Fire Condition", *Proceedings of the Conference, "Composite Construction IV"*, Banff, Canada, 2000.
- [7] Brent Prickett, Robert Driver, "Behaviour of partially encased composite columns made with high performance concrete", *Structural Engineering report n° 262*, University of Alberta, Department of Civil & Environmental Engineering, 2006.
- [8] António J.P. Moura Correia, João Paulo C. Rodrigues, "Fire resistance of partially encased steel columns with restrained thermal elongation", *Journal of Constructional Steel Research*, Volume 67, Issue 4, pp. 93-601, April 2011.
- [9] Paulo A. G. Piloto, Ana B. R. Gavilán, Luís M. R. Mesquita; "Temperature analysis on fire resistance experiments of partially encased beams"; *Safety and Security Engineering IV*, pp. 313-324, WIT Press, ISBN 978-1-84564-522-9, ISSN: 1746-4498 (print), ISSN:1743-3509 (on-line), University of Antwerp, Belgium, 4-6 July 2011.
- [10] CEN - EN 1994-1-1; "*Eurocode 4: Design of composite steel and concrete structures - Part 1-1: General rules and rules for buildings*"; Brussels, December 2004.
- [11] CEN - EN 1994-1-2; "*Eurocode 4: Design of composite steel and concrete structures - Part 1-2: General rules - Structural fire design*"; Brussels, August 2005.
- [12] ISO TC 164, ISO 6892-1; "*Metallic materials – tensile testing – part 1: Method of test at room temperature*"; Switzerland, international standard, 2009.
- [13] IPQ (Instituto Português da Qualidade), NP EN 933-1, "*Tests for geometrical properties of aggregates – part 1; Determination of particle size distribution, sieving method*", 2000.
- [14] Keru Wu, Bing Chen, Wu Yao, Study of the influence of aggregate size distribution on mechanical properties of concrete by acoustic emission technique, *Cement and Concrete Research*, Volume 31, Issue 6, pp. 919-923, May 2001.

EXPERIMENTAL AND NUMERICAL INVESTIGATION ON THE BEHAVIOUR OF A COMPOSITE FLOOR MADE OF CELLULAR BEAMS IN A FIRE SITUATION

Gisèle Bihina*, Bin Zhao* and Abdelhamid Bouchair**

* CTICM, Espace technologique L'Orme des Merisiers, Immeuble Apollo, F-91193 Saint-Aubin, France
e-mails: gbihina@cticm.com, bzhao@cticm.com

** Clermont Université, Université Blaise Pascal, LaMI, BP 206, F-63000 Clermont-Ferrand, France
e-mail: bouchair@cust.univ-bpclermont.fr

Keywords: Steel and concrete composite floor, Cellular beam, Fire test, Partial protection, Finite element model.

Abstract. *The mains results from an experimental and numerical investigation on a composite floor made of cellular beams at elevated temperatures are presented. A full-scale natural fire test is conducted on a purpose-built composite floor. A mechanical load is applied via evenly spaced sand bags on top of the slab to represent a realistic uniformly distributed load, while wooden cribs set on the ground are ignited to heat up the compartment. The test lasted for 150 min, including a cooling phase. The measured material properties and temperatures are used to calibrate a 3D finite element model. The behaviour of the composite floor is simulated under ANSYS code. A good correlation between the test and the numerical simulation is observed, in terms of temperatures, deformed shape and deflections.*

1 INTRODUCTION

The behaviour of composite floors at elevated temperatures has been subjected to a growing interest from building designers over last decade. In a fire situation, real scale fire tests [1] have shown that a composite floor slab can undergo significant displacements without any failure. A change of the behaviour of a thin slab, spanning in two directions with at least vertical support on its four corners, from simple bending to membrane action enables to increase its load-bearing capacity.

Taking into account membrane action in the design of a composite slab can lead to significant savings in terms of concrete thickness and fire protection. Initially developed by Bailey [2], an analytical method based on this upper-bound mechanism has been proposed to assess the load-bearing capacity of a composite floor slab in a given floor design zone [1]. Named FRACOF (*Fire Resistance Assessment of partially protected COMposite Floors*), this method considers that only perimeter beams and columns in the design zone should be protected to provide vertical support to the slab. The secondary beams which are not connected to the columns are left unprotected to allow large displacements of the slab. Designed as composite, their moment resistance is taken account of in the load-bearing capacity of the whole floor.

The method has been validated against full scale tests under standard fire or natural fire conditions [1]. It applies to flat composite slabs – including a steel deck – connected to hot-rolled steel beams spanning up to 15 m. However, large span floor panels require cross-sections with a great second moment of area, in order to meet serviceability limit state requirements. This can be achieved by using cellular beams, with savings in terms of constructional steel. Nevertheless, little research has been conducted on the behaviour of cellular beams in a fire situation, especially as parts of a structure. Some fire tests were carried out on isolated cellular composite beams [3]-[5], leading to numerical and analytical models [6]-

[8], but no data are available about composite floors made of such beams, either at normal or elevated temperature.

In the scope of a European research project FICEB (*Fire resistance of long span Cellular Beams made of hot-rolled profiles*), this paper aims at proposing a numerical model validated on the experimental results of a large scale fire test. The test was conducted on a purpose-built structure, including a composite floor slab connected to cellular beams. The results from the test are then used to calibrate the numerical model based on finite element analysis regarding the evolution of temperature, the deflection and the failure shape of the whole structural system. A simplified approach is used to represent the unprotected cellular beams in the numerical model.

2 FULL SCALE NATURAL FIRE TEST

2.1 Geometric and mechanical properties

The 15×9×3 m composite structure comprised a composite slab attached to a steel frame. In addition to the UC 203×203×86 steel columns at the four corners of the building, two UC 152×152×23 steel columns framed a glass window on the facade, reducing the beam span on that particular side. Thus, the slab was connected to two 9-m cellular primary beams (beams 1 and 2), three UB 305×165×40 5-m secondary solid beams on the façade (beams 6 to 8), and one 15-m cellular secondary beam on its 4th edge (Beam 3). The structure also included two 15-m cellular internal beams (beams 4 and 5) (see Figure 1). The geometrical data of the cellular beams are given in Table 1.

The 120-mm deep composite slab was made of a 40-mm Kingspan Multideck 50 ® dovetail steel deck vertical to the secondary beams, and A393 reinforcement mesh set 40 mm above the deck. The slab was fully connected to each beam by one row of evenly spaced Nelson shear studs.

C25/30 class normal weight concrete was used, while reinforcement and constructional steel had a nominal yield strength of 500 N/mm² and 355 N/mm² respectively.

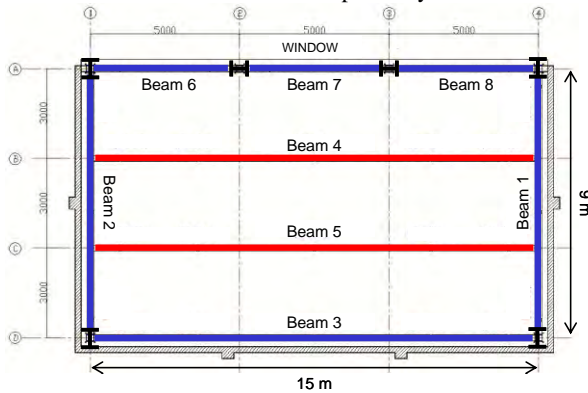


Figure 1. Frame of the purpose-built structure

Table 1. Geometrical properties of the cellular beams.

		Primary beams	Secondary beams	
		Beams 1 and 2	Beam 3	Beams 4 and 5
	Span (m)	$\ell = 9$		$L = 15$
Upper member	Section	UB 533×210×109	UB 406×178×60	
	Depth h_{top} (mm)	300	276,3	
Lower member	Section	UB 533×210×109	UB 457×191×98	
	Depth h_{bot} (mm)	300	306,7	
	Number n	15	22	21
Cells	Pitch e (mm)	600	650	
	Diameter a_0 (mm)	400	400	
	Height h_{sc} (mm)		95	
Shear studs	Diameter d (mm)		19	
	Spacing s (mm)	200		150

2.2 Loading conditions

In order to represent the behaviour of a typical office fire in accordance with [9] and [10], 44 sand bags, each weighing 1 ton, were evenly set on the top side of the slab, corresponding to a 3.26 kN/m^2 uniformly distributed load. The pre-design of the floor follows the principles of FRACOF method: only the columns and perimeter beams were applied a 2-h standard fire protection. In order to keep their aesthetical aspect, cellular beams are usually protected with intumescent coating. However, this type of fire protection was not suitable for such a wet environment as during the test. Thus 50-mm thick ceramic fibre blanket was applied.

45 wooden cribs set on the floor were ignited with paraffin to provide a thermal load of 700 MJ/m^2 , and to obtain a natural fire curve, including a cooling phase. The maximum temperature at the centre of the fire compartment is given in Figure 2. The temperatures in the fire compartment and on the structure, as well as the displacements of the beams, were recorded all through the test with thermocouples and LVDT sensors.

2.3 Experimental results

The protected perimeter beams remained rather “cold”, with average temperatures below $160 \text{ }^\circ\text{C}$ for the whole test duration. Thus, as they kept their full yield strength and more than 90 % of their Young’s modulus values at $20 \text{ }^\circ\text{C}$ [11], the perimeter beams deflected very little from the beginning to the end of the fire test, providing sufficient vertical support to the slab.

The maximum fire compartment temperature reached $1036 \text{ }^\circ\text{C}$ after 72 min from the beginning of the test. However, the maximum deflection of these two beams was recorded after 100 min, when the average temperature of the compartment had decreased to $522 \text{ }^\circ\text{C}$ (see Figure 2). This maximum deflection is close to 750 mm representing $1/20^{\text{th}}$ of the greater span of the slab. This limit is lower than the maximum allowable deflection of FRACOF method (greater span + smaller span)/30 equal to 800 mm. Since no vertical displacement was measured on the slab, the comparison is made between the deflection of the unprotected beams and this FRACOF criterion. The latter takes into account the slab thermal bowing, the reduction of the mechanical strength of the steel reinforcement, and the deflection of the beams.

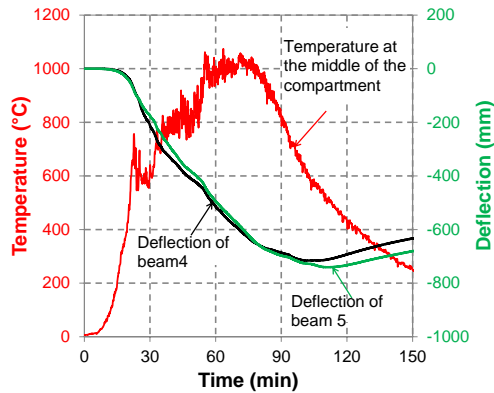


Figure 2. Gas maximum temperature and deflections of the unprotected beams.

It must be noted that both unprotected cellular beams failed owing to significant inwards lateral torsional buckling and end web-post buckling. On the one hand, maximum vertical shear forces combined with restraints at both ends of the unprotected caused web-post buckling around end openings. On the other hand, in their central part, the unprotected beams tended to twist outwards following the slab rotation. Since this twisting movement was prevented by the stiff connection to the primary beams, the upper flanges moved outwards whereas the lower flanges moved inwards.

These two opposite movements of the upper and lower parts resulted in inwards lateral torsional buckling of the internal beams, without causing any overall collapse of the structure (see Figure 3). Actually, an improper reinforcement mesh lap led to full-depth cracking in the shorter direction of the slab, generating failure in terms of integrity and mechanical resistance (see Figure 4). Before this full-depth cracking, the slab had already undergone very large displacements without failing, which implies that tensile membrane action did occur.

It was also observed that the steel deck, which reached a maximum temperature close to 900 °C, debonded from the slab. This implies a very little contribution from the steel deck in the mechanical resistance of the floor, which justifies ignoring this contribution in FRACOF method.

The results from this fire test are then used to calibrate a 3D numerical model described hereafter.



Figure 3. Deformed state of the internal beams after test.



Figure 4. Full depth cracking of the slab after test.

3 NUMERICAL MODEL

The numerical model is based on finite element analysis under ANSYS code [12]. It was initially developed for composite floors made of solid beams for the European research project FRACOF, and has been “updated” for cellular beams.

All the floor components are modelled, with an average mesh size of 300 mm (see Figure 5).

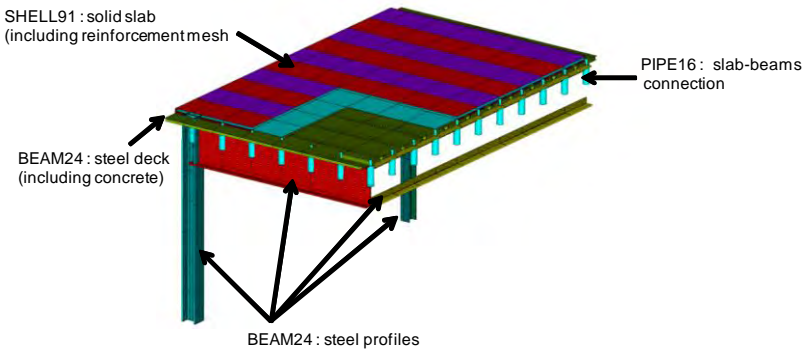


Figure 5. Modelling of a composite floor.

During the fire test described above, very small deflections were observed on perimeter cellular beams which were protected. This allows “simplifying” the modelling of protected cellular beams, considering their gross cross-section (between adjacent openings), and using double-T BEAM24 elements to account for possibly asymmetrical sections. Regarding unprotected cellular beams, a first modelling option consists in representing their actual geometry with 8-node shell elements (SHELL281; average size: 30 mm). In case of long span beams, this leads to a very great number of finite elements. Hence, a second modelling option consists in using double-T BEAM24 elements and taking account of lateral torsional buckling observed in the fire test.

Prior to simulating the real scale fire test (15×3 m slab), a smaller composite floor is modelled (9×9 m slab), using the above described mesh. The composite slab is connected to cellular beams on its four edges and to two internal cellular beams. The cellular beams have the same cell diameter and pitch as in the test.

3.1 First model of small composite floor

The 9×9 m slab comprises a 58-mm deep, trapezoidal Cofraplus 60 @ steel deck, one of the most commonly used on the French construction market. The slab is designed according to FRACOF method and [11], in order to meet *R* (load-bearing capacity), *I* (insulation) and *E* (integrity) criteria. The beams are designed according to the analytical method given in [6] considering a uniformly distributed load.

As this simulation aims at representing the behaviour of a realistic office fire in France, a fire factored load of 3.75 kN/m² (dead load = 1.25 kN/m², variable load = 5 kN/m²) - without any dead weight - is considered, a slightly greater value than in the test.

Moreover, since attention is focused on the behaviour of cellular beams at elevated temperatures, a 90 min ISO fire is considered, without any cooling phase. Considering C25/30 normal weight concrete and S500 reinforcement mesh, this leads to a 140 mm composite slab depth and ST25C reinforcement mesh, positioned 45 mm above the deck, in accordance with [13]. European S355 IPE steel profiles and symmetrical sections are selected:

- primary beams: IPE 450, overall cross-section depth = 609 mm;
- secondary beams: IPE 360, overall cross-section depth = 500 mm.

As the temperatures of the protected columns were not measured during the test, the columns remain cold in the simulation, considering a temperature of 20 °C.

An elasto-plastic behaviour is considered for all the elements, except for the shear studs which heat up a little due to the surrounding concrete, and which maintain an elastic behaviour thanks to their little mechanical load. ANSYS Drucker-Prager model is applied to the concrete, while the stress-strain curve of both structural and reinforcement steel are taken as in [11].

In a cost-effective purpose, the floor is assumed to be symmetrical, allowing modelling only its half, with *ad hoc* boundary conditions. However, in accordance with the test configuration, the slab must have no horizontal restraint, leading to the boundary conditions given in Figure 6.

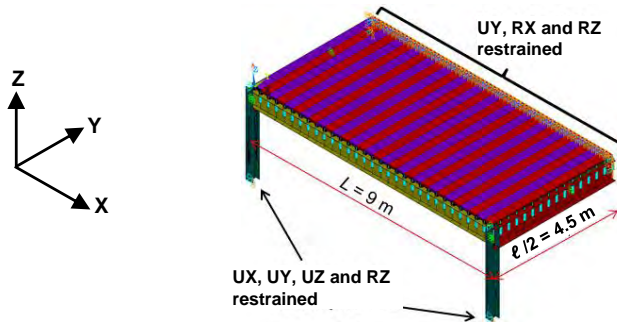


Figure 6. Boundary conditions in model 1.

Like in the test, a fin-plate beam-to-beam connection is modelled at both ends of the internal beam. Assuming a uniform gas temperature distribution, a 2D heat transfer calculation is run, in accordance with [11], considering the gross cross-section of the perimeter beams and the net cross-section of the internal beam. Two mechanical calculations are carried out. The first calculation takes account of the connection between the unprotected secondary beam and the protected primary beams. This approach generates a longitudinal thermal gradient at the two ends of the unprotected beam (model 1a). The second calculation considers a uniform temperature distribution along the unprotected beam (model 1b) (see Figure 7).

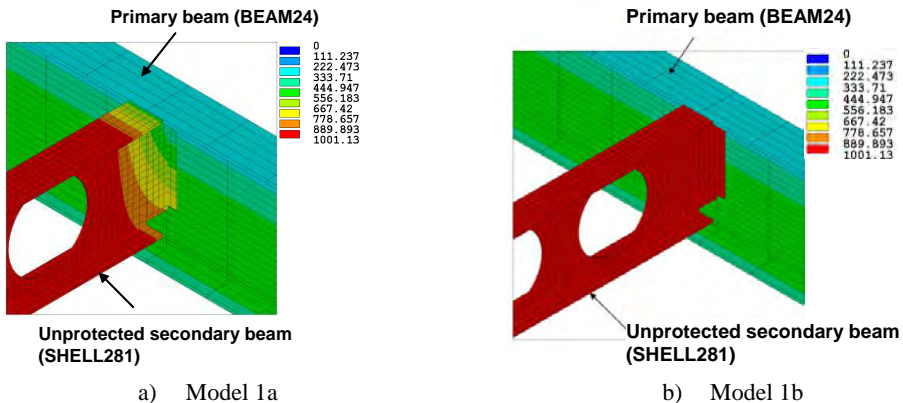


Figure 7. Temperatures at the beam-to-beam connection at $t = 90$ min.

In both calculations (models 1a and 1b), no sign of global collapse is observed after 90 min. Inwards lateral torsional buckling and end web-post buckling are observed on the unprotected beam (see Figure 8), in which the maximum temperature reaches 1001 °C, like in the natural fire test. A comparison

between the results of the two calculations does not put into evidence any noticeable deviation. The beam and slab time-deflection curves are very similar, underlining that the longitudinal thermal gradient on the unprotected beam can be neglected in the calculation [5]. When removing the initial displacements of the structure (at $t = 0$ min), this particular beam deflects to less than 450 mm (span/20), while the slab deflects to less than 600 mm, which is the maximum allowable deflection according to FRACOF method.

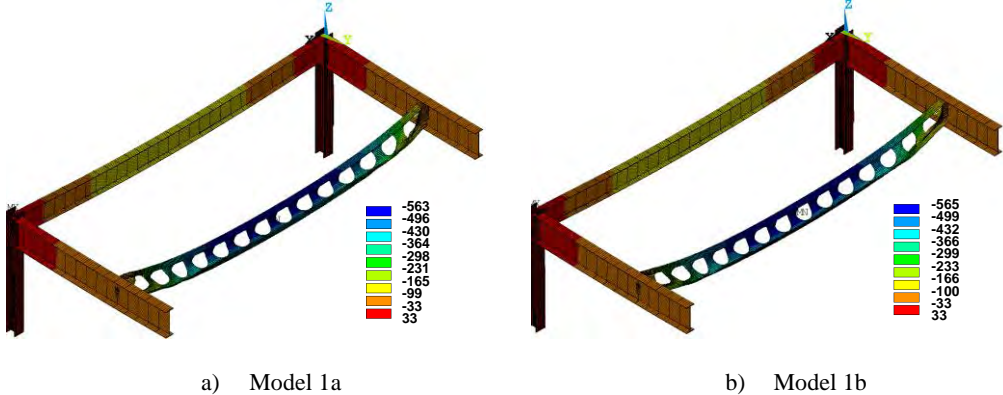


Figure 8. Vertical deflections of the steel frame at $t = 90$ min calculated with model 1 (9×9m).

This model is able to simulate the thermo-mechanical behaviour of a composite floor made of unprotected cellular beams. It allows the development of a numerical parametric study used to extend the existing FRACOF method to cellular beams [5]. The existing method accounts for the moment resistance of the unprotected beams as a contribution to the overall load-bearing capacity of the floor. Thus, using cellular beams implies to simplify their real geometry but also to provide conservative results. The following options are considered (see Figure 9):

- using the net cross-section of an unprotected beam to determine its moment resistance (model 2a);
- same as option a), but, owing to lateral torsional buckling, neglecting the mechanical properties of the lower T from 600 °C, when both steel yield strength and Young's modulus are reduced to less than 50 % of their ambient temperature value - without recovering them when cooling down;
- same as option b) but reducing the cross-section depth (thus its second moment of area) instead of neglecting the lower T.

These three options are checked in the second numerical model described hereafter.

3.2 Second model of small composite floor

The 9×9 m composite floor described above is modelled using 2-T BEAM24 elements, and a uniform longitudinal temperature distribution on all beams (protected or not). The results of these simulations are compared against those of the first model (see Figure 10).

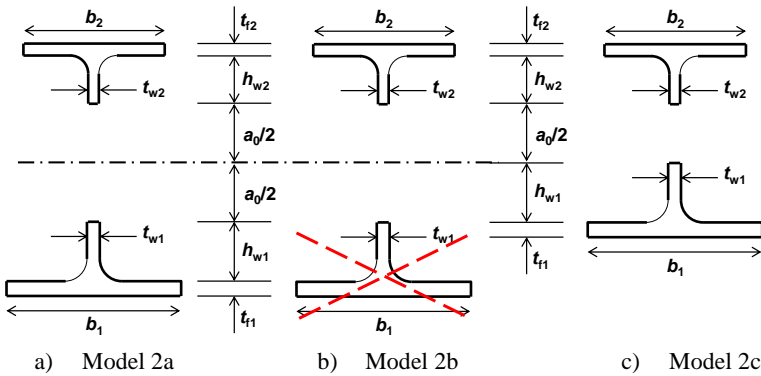


Figure 9. Cross-sections of the unprotected cellular beams in model 2.

All the parameters are kept constant except the shape of the unprotected cellular beam. At the beginning of the fire, greatest deflections are observed on model 2c. The floor deflects least with model 1 whether the ends of the beam are less hot than the rest of it (b) or not (a). Then, once the temperature of the upper T reaches 600 °C and until the end of the fire-exposure, the greatest deflections are observed with model 2b. Also, once lateral torsional buckling is initialised (model 1), the slope of the time – deflection curves starts increasing, leading to greater deflections than with models 2a and 2c.

In the end, considering a reduced cross-section depth provides more realistic results than neglecting the lower T. In order to confirm this conclusion, the fire test is simulated with double-T beam elements for unprotected cellular beams, modelling the whole floor and using the measured average temperatures.

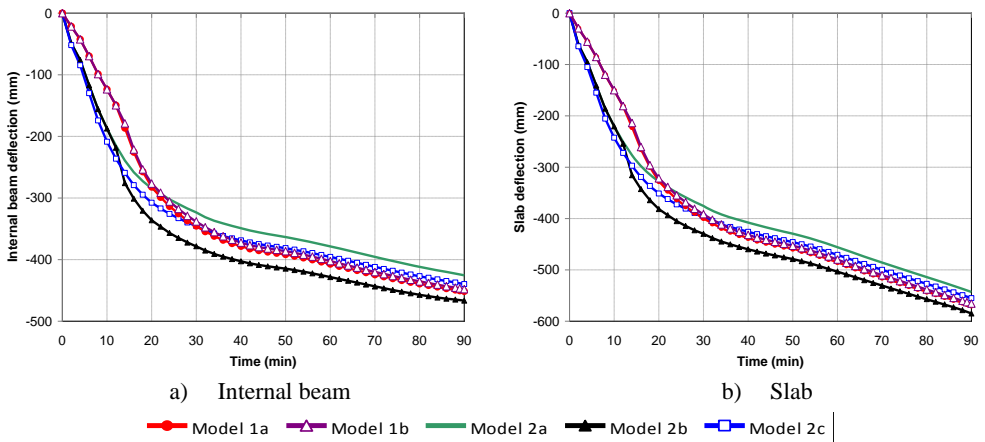


Figure 10. Deflection vs. time graph.

3.3 Simulation of the real composite floor

The real scale fire test is simulated using model 2 described above, *i.e.* representing the unprotected beams with a 2-T cross-section. The simulation takes account of the test configuration to allow free horizontal movement of the slab. Boundary conditions are applied on top and bottom of all six columns. No displacement is allowed at the bottom of the steel frame, as well as rotation about the vertical axis to prevent column torsion. In addition, for numerical stability, partial displacement restraints are applied at the top of three corner columns, leaving the three other ones free to move, as shown in Figure 11, where U refers to the displacements and R refers to the rotations.

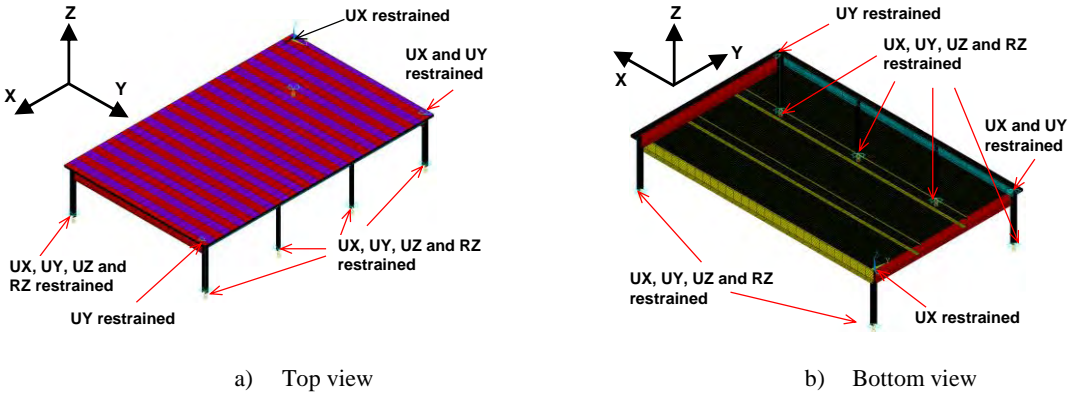


Figure 11. Boundary conditions of the model representing the real fire test.

Average temperatures measured on the beams are directly input in the model. Each protected beam is assumed to have a uniform longitudinal temperature distribution, while the unprotected beams are divided in five zones, corresponding to the five zones of thermocouples locations.

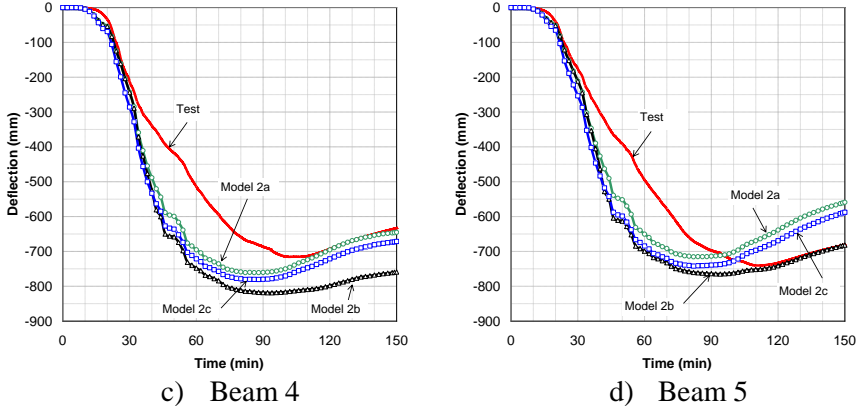


Figure 12. Deflection vs. time graph of the fire-tested unprotected cellular beams.

Model 2c allows representing unprotected cellular beams from their net cross-section with a cell diameter reduced to 50 %. It can then be used in a parametric study to compare finite element simulation and FRACOF method extended to cellular beams [5].

4 CONCLUSION

In this paper, the behaviour of composite floors made of cellular beams at elevated temperatures was investigated experimentally and numerically.

A real scale fire test was conducted under natural fire conditions to give a better understanding of such a floor in a realistic situation. The cellular internal beams were left unprotected following the principles of FRACOF method to allow large displacements of the slab, and hence membrane action.

With the temperature increase, significant deflections were observed on the unprotected parts of the floors. The internal beams failed owing to web-post buckling combined with lateral torsional buckling, without inducing any overall collapse of the floor. Global failure was rather caused by full-depth cracking of the slab, due to an improper reinforcement mesh lap in the central part of the slab.

These test results were then used to calibrate a 3D finite element model, which was capable of simulating the thermo-mechanical behaviour of the purpose-built floor. The numerical model was then simplified, using double-T beam finite elements to represent the unprotected beams and reducing their cell diameter. A comparison between the experimental results and this simplified numerical model has highlighted its accuracy.

Nevertheless, the validation of this numerical model is based on cellular beams with large web-posts. A question arises about its accuracy and conservativeness when the cells are closer to each other, which may lead to a different behaviour than that observed during the test. As a consequence, further analyses should be conducted to enlarge the field of application of the proposed model, and to propose an extension of FRACOF method to cellular beams.

REFERENCES

- [1] SCI, CTICM, "Fire Resistance Assessment of partially protected COmposite Floors (FRACOF): engineering background", Technical Report, 2009.
- [2] Bailey, C.G., "Membrane action of slab/beam composite floor systems in fire", *Engineering Structures*, October 2004, Vol. 26, Issue 12, pp. 1691-1703.
- [3] Bailey, C.G., "Indicative fire test to investigate the behaviour of cellular beams protected with intumescent coatings", *Fire Safety Journal*, November 2004, Vol. 39, Issue 8, pp. 689-709.
- [4] Nadjai, A., Vassart, O., Ali, F., Talamona, D., Allam, A., Hawes, M., "Performance of cellular composite floor beams at elevated temperatures", *Fire Safety Journal*, September-October 2007, Vol. 42, Issues 6-7, pp. 489-497.
- [5] Bihina, G., "Analysis of the fire behaviour of steel-concrete composite floors made of cellular beams", Phd Thesis, Université Blaise Pascal, Clermont-Ferrand II, France, July 2011.
- [6] Vassart, O., "Analytical model for cellular beams made of hot rolled sections in case of fire", Phd Thesis, Université Blaise Pascal, Clermont-Ferrand II, France, September 2009.
- [7] Wong, V.B., Burgess, I., Plank, R., "Behaviour of composite cellular steel – concrete beams at elevated temperatures", *International Journal of Steel Structures*, March 2009, Vol. 9, Issue 1, pp. 29-37.
- [8] Vassart, O., Bailey, C., Bihina, G., Nadjai, A., Hawes, M., Peigneux, C., Simms, I., Franssen, J.-M., "Parametrical study on the behaviour of steel and composite cellular beams under fire conditions", *In: Structures in fire: Proceedings of the 6th International Conference (Sif'10)*, 2nd-4th June 2010 Michigan State University, p. 9.
- [9] EN 1991-1-1, "Eurocode 1: Actions on structures – Part 1-2: General actions - Densities, self-weight, imposed loads for buildings", European committee for standardization (CEN) – March 2003.
- [10] EN 1991-1-2, "Eurocode 1: Actions on structures – Part 1-2: General actions - Actions on structures exposed to fire", European committee for standardization (CEN) – July 2003.
- [11] EN 1994-1-2, "Eurocode 4: Design of composite steel and concrete structures – Part 1-2: General rules – Structural fire design", European committee for standardization (CEN) February 2006.
- [12] ANSYS, ANSYS user's manual for revision 8.0 – Volume 4 - Theory, Swanson Analysis System, Inc., Houston, USA, 1992.
- [13] Newman, G.M., Robinson, J.T., Bailey, C.G., "Fire safe design: a new approach to multi-storey steel-framed buildings", Second edition, SCI (The Steel Construction Institute) Publication P288, United Kingdom, 2006.

EXPERIMENTAL AND NUMERICAL EVALUATION OF COMPOSITE FLOOR SLABS UNDER FIRE LOADING

Kristi L. Selden*, Amit H. Varma* and Erica C. Fischer*

* Bowen Laboratory, School of Civil Engineering, Purdue University
1040 S. River Road, West Lafayette, IN 47906
e-mails: kselden@purdue.edu, ahvarma@purdue.edu, fischere@purdue.edu

Keywords: Concrete, composite slab, fire, floor system, experimental, finite element modeling

Abstract. *Experimental tests were conducted at Purdue University to study the thermal and structural response of concrete slabs subjected to high temperatures. The objective was to develop an understanding of the behavior of the concrete portion of composite floor systems in the event of a fire. A series of small, unrestrained concrete slabs were subjected to high temperatures using radiant heating panels. No additional vertical loading was applied. The experimental data was used to verify finite element models and to conduct a brief concrete coefficient of thermal expansion sensitivity analysis. The results from these investigations will be used for future testing and modeling of large-scale composite beam tests that are going to be conducted at Purdue in the near future.*

1 INTRODUCTION

This paper focuses on experimental tests that were conducted to investigate the thermal and structural behavior of the concrete portions of composite floor systems subjected to fire loading. The results are used to improve 3D finite element modeling approaches to more accurately predict the thermal and structural behavior of composite floor systems. The objective was study the response and behavior of concrete slabs, focusing on the response to thermal loading without any applied gravity loads.

A number of tests have been previously conducted to study the behavior of concrete slabs at both ambient and elevated temperature, and numerous analytical investigations were conducted following the Cardington tests [1]. Many of these studies were conducted to study the behavior of the concrete slab without the steel deck. It is assumed that at elevated temperatures, the strength and stiffness of the steel deck is reduced to a point that it no longer has significant contribution to the system. The tests included thermal and structural loading, and many of them focused on the development of tensile membrane action in the concrete slab [2-5].

The goal of the tests presented in this paper was to investigate what happens to the slab when there is only thermal loading. No additional gravity loading was applied. The effects of varying the reinforcement and the slab thickness were evaluated. These tests allowed for observations regarding the temperature and the displacement responses to be obtained, and the results were used to validate finite element models. A sequentially coupled thermal-structural finite element modeling approach was used to predict the behavior, and results from both the thermal and structural models were verified using the experimental data. A brief sensitivity analysis was conducted to determine what material parameters have the most significant effect on predicting the behavior.

The findings and experimental methods in these tests will be used to conduct future studies on large-scale composite beam tests at Purdue University. The setup has already been designed and is currently being constructed; the next set of experimental tests will be conducted in the near future.

2 TEST METHODOLOGY

2.1 Specimen Design and Test Matrix

The test matrix included four concrete slabs that were 0.813m x 1.98m in plan dimensions and were subjected to thermal loading only. Using high-temperature ceramic radiant heating panels at Purdue University, the bottom surfaces of the slabs were subjected to temperatures as high as 700°C. In order to study the thermal profile through the cross-section of the slab, the time-temperature response was monitored using Type-K thermocouples that were embedded at various depths in the concrete. The deformation behavior was measured using close-range photogrammetry and digital imaging techniques, as well as conventional voltage-based linear displacement sensors.

Parameters of interest included reinforcing scheme and slab depth. The slabs that were reinforced had Grade 60 reinforcement, which was provided by either a welded wire mesh or standard reinforcing steel. The provided reinforcement ratio was 0.18%, which is the minimum temperature and shrinkage reinforcement for concrete slabs per ACI 318-11 [6]. The objectives included investigating (i) the thermal gradient that develops through the thickness of the slab as a result of heating one side and (ii) the structural response of the slab when subjected to only thermal loading.

The slabs were constructed using normal weight concrete with a compressive strength of approximately 35MPa. The size of the slab was determined by the desired heater layout, and the goal was to use four heaters positioned side by side. The heaters are 0.91m x 0.41m in plan dimensions. Roller supports were placed 0.076m from each end of the slab.

Table 1: Testing Matrix

Specimen			Size			Reinforcement		
#	Parameter	f'_c (MPa)	Width (m)	Length (m)	Depth (m)	Wire Mesh	Rebar	Reinf. Ratio
1	Concrete only	35.1	0.813	1.98	0.089	No	No	0%
2	Wire Mesh	34.3	0.813	1.98	0.089	Yes	No	0.18%
3	Rebar	34.8	0.813	1.98	0.089	No	Yes	0.18%
4	Slab Depth	34.0	0.813	1.98	0.127	Yes	No	0.18%

2.2 Testing Setup

All slabs were set up on rollers and subjected to thermal loading on the bottom surface using the four ceramic radiant heating panels. The heaters are capable of reaching a maximum surface temperature of 1275°C. The ceramic heaters were placed in custom-built metal frames that were suspended from the slab in such a way that the same distance between the heater and the concrete surface could be maintained as the slab deflected during the experiment. The starting position of the heater could be adjusted using the threaded rods and the goal was to position the heaters as close to the slab surface as possible without clamping the heater to the concrete. The ceramic heaters and the support frames were lightweight, with a total weight of less than 10% of the slab self-weight.

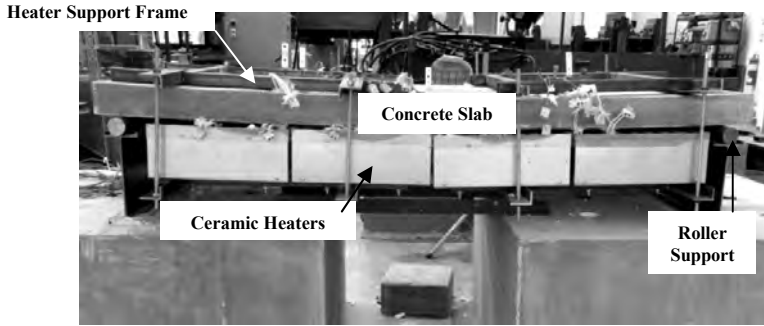


Figure 1: Test setup for concrete slab subjected to thermal loading

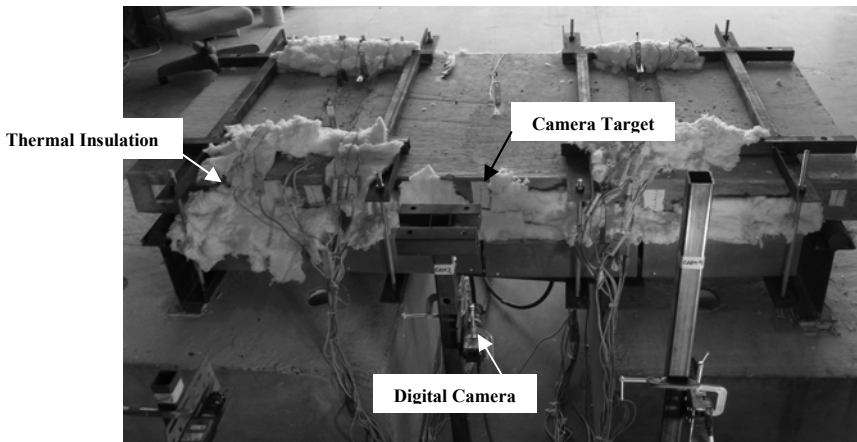


Figure 2: Top view of test setup

PID controllers were used to operate each heater individually using a feedback control loop that referenced a thermocouple on the heated surface of the concrete. The slabs were heated to a maximum temperature of 700°C at a rate of approximately 20°C/min. Cooling was initiated once the maximum temperature was obtained. In some tests, it was possible to control the cooling at 12°C/min. However, in Test 3, some of the heated surface thermocouples malfunctioned near the maximum test temperature and it was not possible to have control of the cooling phase.

Table 2: Summary of heating and cooling protocols for each test

Test	Maximum Heated Surface Temperature	Average Heating Rate	Cooling Rate
1	500°C	20 °C / min	12 °C / min
2	700°C	20 °C / min	12 °C / min
3	700°C	20 °C / min	Uncontrolled
4	700°C	20 °C / min	12 °C / min

2.4 Instrumentation

In order to study the thermal profile through the cross-section of the slab, the time-temperature response was monitored using Type-K thermocouples that were embedded at various depths in the concrete. The thermocouple “trees” were placed at four locations. Each tree consisted of a small diameter steel rod with multiple thermocouples that were welded to the rod at different locations along the length. The junction of the thermocouple extended just beyond the rod in order to measure the temperature in the concrete. Thermocouples were also attached on the top and bottom surface at the same location as the trees to get the complete thermal gradient.

Vertical displacement measurements were monitored using linear displacement transducers that were positioned at four locations (Figure 3). The deflection at midspan was measured in addition to the deflection at the quarter points. The displacement transducers were attached to a frame that was independent from the test setup in order to keep the sensors at a safe distance away from heat. The sensors and the wires were also insulated to protect them from the effects of heat and steam.

Digital cameras and close-range photogrammetry techniques were used to measure the vertical and horizontal displacements of the edge of the slab. This measurement technique is very useful in elevated temperature testing because it is a non-contact form of measurement. Digital cameras are positioned at a distance from the specimen where they are safe from the elevated temperatures. Using a network of cameras, it is possible to track the movement of target points positioned at specified locations on the test specimen. The images are time-stamped and post-processed using close-range photogrammetry and pattern-matching techniques to determine the two-dimensional displacement of the target point.

Five camera targets were placed on the side of the slab and the movement of each target was captured by a digital camera. The cameras have a fixed focal length so two different sized lenses were used in order to provide two different sized viewing areas. A larger viewing area was required for the mid-span deflection; a smaller viewing area was adequate for the camera targets at the supports where relatively small displacements were observed. Pattern matching techniques using LabView Vision Assistant were used for the post-processing of the camera data. Previous evaluation of the camera’s resolution indicated that the cameras can capture displacements with a precision of 0.001in [7].

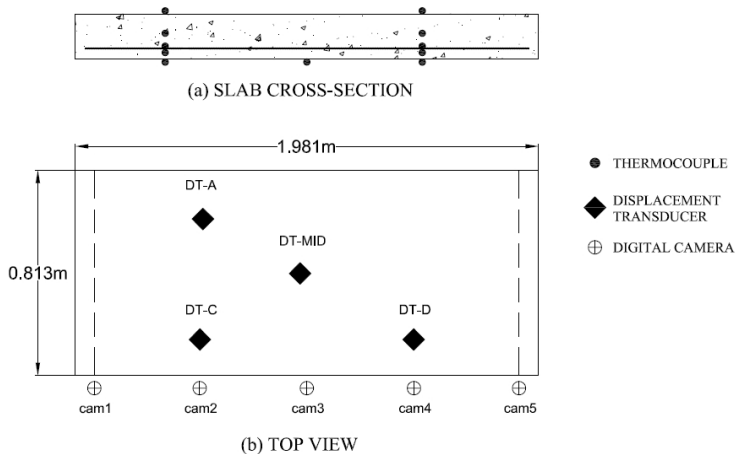


Figure 3: Instrumentation layout

3 EXPERIMENTAL RESULTS

The results from the four slab tests are presented in the following sections. The thermal and structural results are discussed separately.

3.1 Thermal Results

The figures below present the thermal profile through the thickness of the slab. The temperature measurements at each thermocouple tree were averaged to obtain the time-temperature histories. The thermal gradient is similar for each of the four test specimens. It should be noted that in Test #1, there was an accidental cooling phase that occurred near 30 minutes. Control of the heaters was regained and testing continued until the heated surface temperature reached 500°C. In the remaining three tests, heat was applied to a maximum heated surface temperature of 700°C, at which a cooling phase of 12°C/min was initiated.

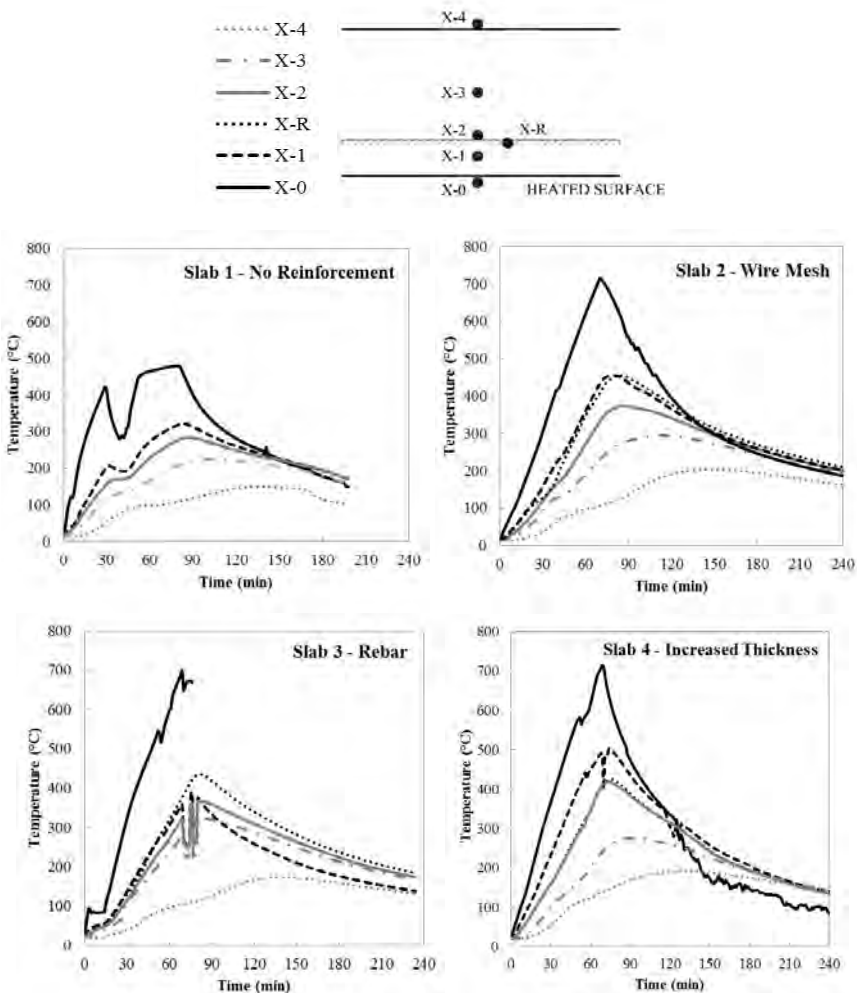


Figure 4: Time-temperature histories from slab tests

3.2 Vertical Displacement Results

The following plots display the vertical displacement measurements obtained from the displacement transducers. The average heated surface temperature is also included in the plots for better comparison of the four tests. Similar behavior was observed for the slabs reinforced with the wire mesh and the reinforcing steel. The slab with the increased thickness had smaller displacements than the other three test specimens, even though the time-temperature history and the thermal gradient was very similar to the other three slabs.

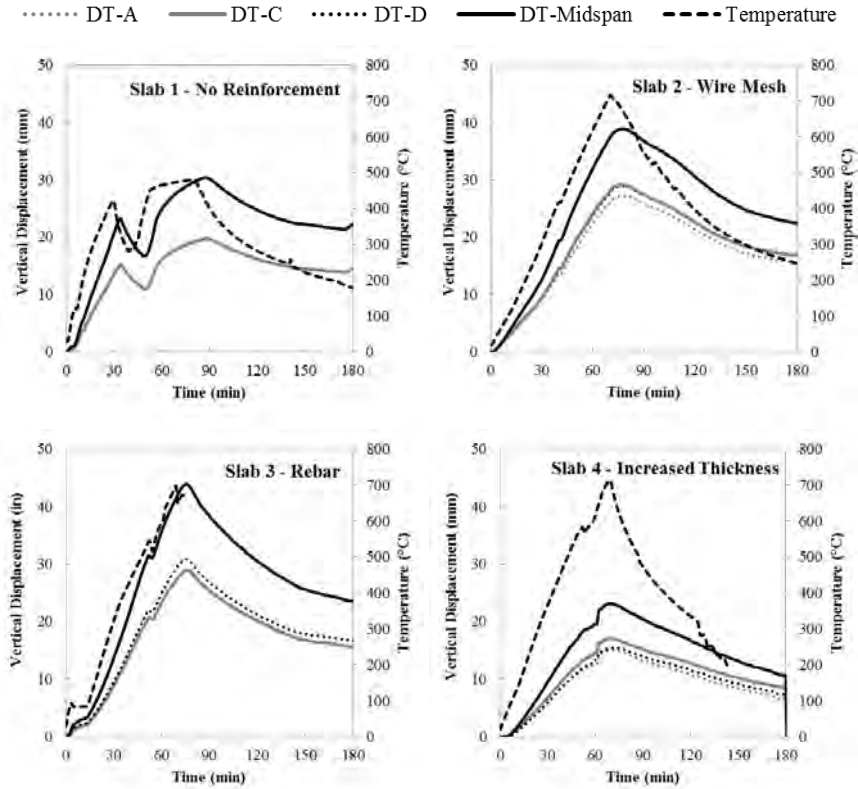


Figure 5: Displacement-time histories for the slab tests

4 FINITE ELEMENT MODELING

4.1 Modeling Approach and Methodology

The 3D finite element models were developed and analyzed using the commercially available finite element analysis program, ABAQUS [8]. This program was used because it is capable of including (i) temperature dependent material constitutive models, (ii) nonlinear heat transfer analysis, and (iii) sequentially and fully coupled thermal and structural analysis. The analysis was conducted using the sequentially coupled thermal-structural analysis approach, which is commonly used for building structural analysis under fire loads. As part of this approach, two identical finite element meshes were

developed: (i) with thermal finite elements for heat transfer analysis and (ii) with stress based finite elements for structural analysis.

The thermal model was used first to conduct the nonlinear heat transfer analysis to obtain the thermal response and the nodal temperature histories (T-t responses). These nodal temperature histories were used to define the thermal loading while conducting the structural analysis. The 3D models used solid 8-node elements with reduced integration for the concrete slab (DC3D8R for thermal and C3D8R for structural). These types of elements are suitable for large displacements and inelastic analyses. The wire mesh reinforcement was modelled using embedded truss elements.

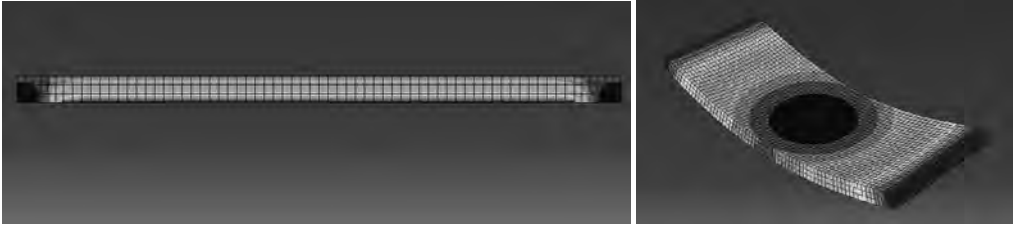


Figure 6: (a) Thermal and structural mesh (side view) and (b) vertical displaced shape

4.2 Material Models

Temperature dependent material properties from Eurocode were used with these models [9]. These properties include both thermal properties, such as specific heat, conductivity, density, and thermal expansion, as well as nonlinear mechanical properties for the steel and concrete. In the stress analysis, the Concrete Damaged Plasticity (CDP) model developed by Lee and Fenves [10] and implemented in ABAQUS was used to model the temperature dependent compressive inelasticity, smeared tension cracking, and shear retention behavior of concrete. The CDP model accounts for multiaxial behaviour, and in order to completely define the yield surface, the parameters in the following table were used. Standard uniaxial compression tests were conducted to help develop the concrete stress-strain relationship.

Table 3: Assumed CDP material model parameters

Concrete Damaged Plasticity (CDP) Parameter	Assumed Value
f_{bc}'/f_c' (Ratio of biaxial compressive strength to uniaxial strength)	1.16 [11]
K (ratio of the tensile-to-compressive meridian of the yield surface in deviatoric stress space)	0.67 [12]
Uniaxial compression stress-plastic strain relationship	σ - ϵ provided by Eurocode, with reduction factors [9]
Uniaxial tension stress-strain curve	$f_t = 0.09f_c'$

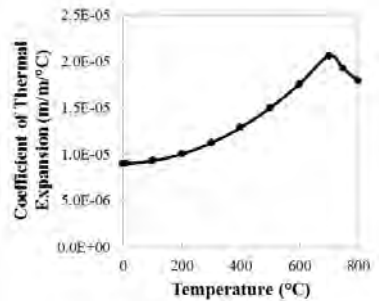


Figure 7: Coefficient of Thermal Expansion (Eurocode)

The reinforcing steel elastic properties were defined using a multi-axial isotropic elastic model that includes temperature dependency. The inelastic steel properties were defined using a multi-axial plasticity model with associated flow rule, kinematic hardening, Von Mises yield criterion, and temperature dependence. The uniaxial compressive and tensile stress-strain relationships were determined using the mathematical models provided by Eurocode [9].

4.3 Comparison of Model Results to Experimental Data

The average heated surface temperatures for each test were used in the respective finite element models. The time-temperature history was applied to the appropriate area on the bottom of the modelled slab. A heat transfer analysis was conducted using these applied temperature boundary conditions and the results were then used and applied in the structural model to obtain the displacement response.

The midspan deflection of the slab obtained from the finite element models are compared to the experimental results in Figure 7. Overall, there is good agreement and the models provide acceptable predictions of the displacement during the heating phase. The finite element models tend to over-predict the displacement at the higher temperatures.

The most noticeable discrepancy between the experimental results and the models is during the cooling phases. Work is still being conducted to refine these models and to obtain an understanding of why there is such a difference in the cooling phase.

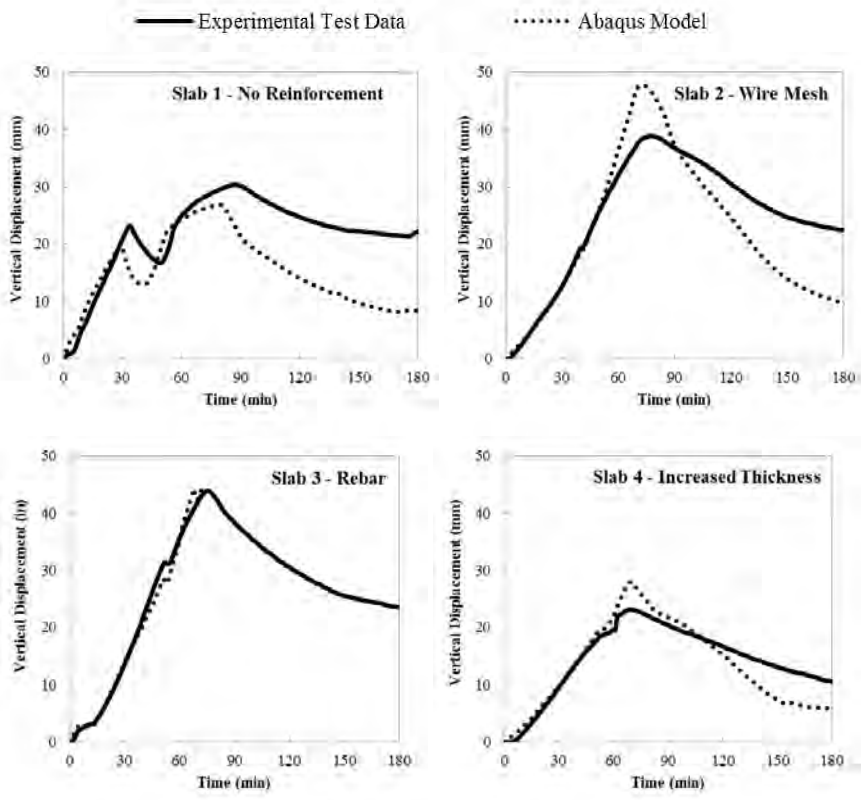


Figure 8: Comparison of midspan deflection obtained from experimental data and finite element model

5 SENSITIVITY ANALYSIS

In order to investigate if the numerical modeling approach is sensitive to changes in the coefficient of thermal expansion, a brief sensitivity analysis was conducted. Using the finite element models for the four slab tests, the coefficient of thermal expansion was varied as a percentage of the

temperature dependent values presented by Eurocode. Four cases were considered: (i) 50% reduction, (ii) 25% reduction, (iii) 25% increase, and (iv) 50% increase. The results for two of the slabs are shown graphically in the plots below. Varying the temperature-dependent coefficient of thermal expansion does have a noticeable effect on the displacement response. If it is necessary to refine the modeling approach, then it would be beneficial to conduct thermal expansion material testing to obtain a material model that is more accurate. However, using the values provided by Eurocode is sufficient for predicting the behavior.

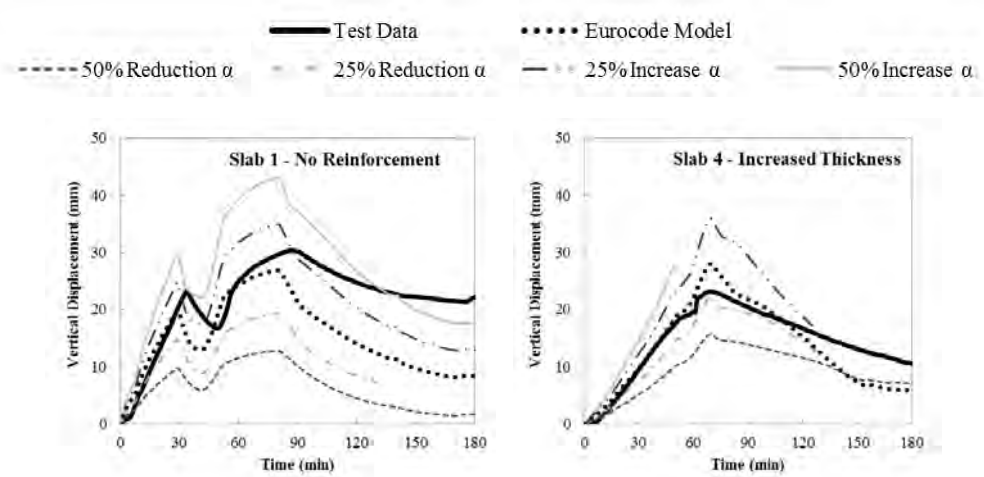


Figure 9: Concrete coefficient of thermal expansion sensitivity analysis results

An additional study was conducted to determine if the results are sensitive to changes in the uniaxial tensile strength of the concrete. Two sets of models were considered: (i) with $f_t = 0.09f_c'$ and (ii) with $f_t = 0.05f_c'$. The results from two of the studies are presented in Figure 10, and the only noticeable difference between the results from the two models is at the beginning of the cooling phase.

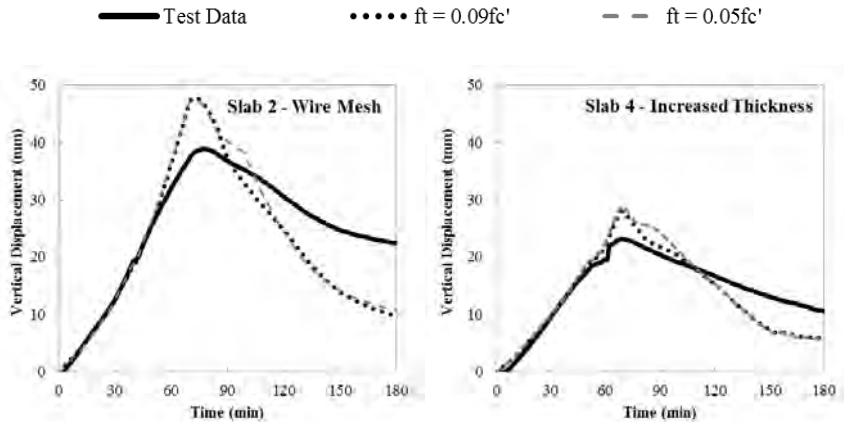


Figure 10: Concrete uniaxial tensile strength sensitivity analysis results

6 CONCLUSIONS

This paper presented the results from experimental tests that were conducted on small concrete slabs to investigate the thermal and structural response to thermal loading without additional gravity loads. Ceramic radiant heating panels were used to apply heat to the bottom of the slabs. Varying the type of reinforcement (wire mesh vs. rebar) while maintaining the reinforcement ratio does not appear to change the response of the slab. The concrete slab with increased thickness had similar thermal gradients but smaller vertical displacements. The temperature and vertical displacement data was used to verify 3D finite element models and there was good agreement for the heating phase. A brief sensitivity analysis was conducted, and it was determined that the concrete coefficient of thermal expansion provided by Eurocode and the uniaxial concrete tensile strength of $f_t = 0.09f_c'$ is adequate for making predictions. Both the experimental and numerical results from these studies will be used in future large-scale composite floor system testing that will be conducted at Purdue University in the near future.

7 ACKNOWLEDGEMENTS

The experimental work presented in the paper was performed in the Bowen Laboratory at Purdue University. The research presented was funded by the National Science Foundation Grant CMMI 0758461. Any opinions, findings, and conclusions or recommendations expressed in this paper are those of the authors and do not necessarily reflect the views of the sponsors.

REFERENCES

- [1] Sanad, A.M., Lamont S., Usmani, A.S., and Rotter, J.M., "Structural behaviour in fire compartment under different heating regimes - Part 1 (slab thermal gradients)," *Fire Safety Journal*, vol. 35, pp. 99-116, Sep 2000.
- [2] Cashell, K.A., Elghazouli, A.Y., and Izzuddin, B.A., "Experimental and analytical assessment of ductility in lightly reinforced concrete members," *Engineering Structures*, vol. 32, pp. 2729-2743, 2010.
- [3] Bailey, C.G., and Toh, W.S., "Small-scale concrete slab tests at ambient and elevated temperatures," *Engineering Structures*, vol. 29, pp. 2775-2791, 2007.
- [4] Bailey, C.G. and Toh, W.S., "Behaviour of concrete floor slabs at ambient and elevated temperatures," *Fire Safety Journal*, vol. 42, pp. 425-436, 2007.
- [5] Bailey, C.G., White, D.S., and Moore, D.B., "Tensile membrane action of unrestrained composite slabs simulated under fire conditions," *Engineering Structures*, vol. 22, pp. 1583-1595, 2000.
- [6] ACI, "Building Code Requirements for Structural Concrete (ACI 318-11) and Commentary," American Concrete Institute, 2011.
- [7] Selden, K.L., "Evaluation of a CMOS Digital Camera for Structural Engineering Measurements," Purdue University, 2010.
- [8] ABAQUS, "ABAQUS/Standard Version 6.11," Providence, RI: Dassault Systemes Simulia Corp., 2011.
- [9] CEN (2005), "Eurocode 4: Design of Composite Steel and Concrete Structures, Part 1.2: General rules - Structural fire design," European Committee for Standardization, Brussels, Belgium.
- [10] Lee, J.H. and Fenves, G.L., "Plastic-damage model for cyclic loading of concrete structures," *ASCE Journal of Engineering Mechanics*, vol. 124, pp. 892-900, Aug 1998.
- [11] Kupfer, H.B. and Gerstle, K.H., "Behavior of Concrete under Biaxial Stresses," *ASCE Journal of Engineering Mechanics*, vol. 99, pp. 853-866, 1973.
- [12] Chen, W.F. and Han, D.J., *Plasticity for Structural Engineers*. New York: Springer-Verlag, 2007.

**TIMBER STRUCTURES
AND
FIRE PROTECTION MATERIALS**

DESIGN OF POST-TENSIONED TIMBER BEAMS FOR FIRE RESISTANCE

**Phillip M. Spellman, Anthony K. Abu, David M. Carradine, Peter J. Moss, and
Andrew H. Buchanan**

Department of Civil and Natural Resources Engineering, University of Canterbury, Private Bag
4800, Christchurch 8140, New Zealand

e-mails: pms128@uclive.ac.nz, tony.abu@canterbury.ac.nz, david.carradine@canterbury.ac.nz,
peter.moss@canterbury.ac.nz, andy.buchanan@canterbury.ac.nz

Keywords: Post-Tensioned Timber, Fire Performance, Furnace Test, Design

Abstract. *This paper describes a series of three full-scale furnace tests on post-tensioned LVL box beams loaded with vertical loads, and presents a proposed fire design method for post-tensioned timber members. The design method is adapted from the calculation methods given in Eurocode 5 and NZS:3603 which includes the effects of changing geometry and several failure mechanisms specific to post-tensioned timber. The design procedures include an estimation of the heating of the tendons within the timber cavities, and relaxation of post-tensioning forces. Additionally, comparisons of the designs and assumptions used in the proposed fire design method and the results of the full-scale furnace tests are made. The experimental investigation and development of a design method have shown several areas which need to be addressed. It is important to calculate shear stresses in the timber section, as shear is much more likely to govern compared to solid timber. The investigation has shown that whilst tensile failures are less likely to govern the fire design of post-tensioned timber members, due to the axial compression of the post-tensioning, tensile stresses must still be calculated due to the changing centroid of the members as the fire progresses. Research has also highlighted the importance of monitoring additional deflections and moments caused by the high level of axial loads.*

1 INTRODUCTION

Timber is the material of choice for residential construction in New Zealand, Australia and many parts of the world, however commercial and industrial construction are dominated by steel and concrete. Post-tensioned timber is a building technique designed to offer a timber solution for multi-storey industrial and commercial buildings with long spans and open floor plans serving as an alternative to steel and concrete. There are many benefits in using post-tensioned timber over steel and concrete in that buildings can be constructed very quickly with substantially smaller lifting equipment, timber is an easy material to work with, and timber is also a green and sustainable building material which is becoming increasingly important when making decisions about building materials for larger buildings [1-3].

Post-tensioned (PT) timber construction is an adaptation of the mature technology of post-tensioned pre-stressed concrete. PT timber is made with large timber cross sections, constructed from engineered timber products such as glue laminated timber (Glulam) or laminated veneer lumber (LVL). Timber box-beams are post-tensioned with un-bonded high strength steel bars or wire tendons which run through cavities within members, fixed to steel anchorages at either end of the beams or frames [4]. The post-tensioning can be run through multiple bays of a frame to form the primary moment resisting beam-column connections as demonstrated in Figure 1.

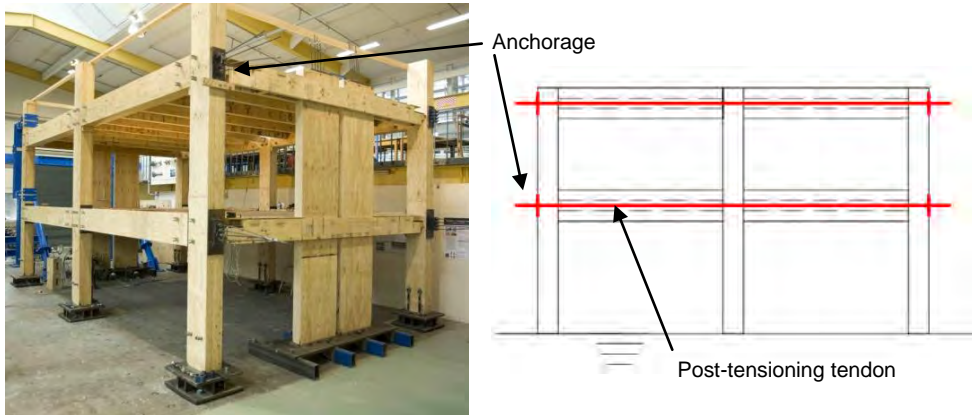


Figure 1: Left - 2/3rd scale post-tensioned timber frame used for seismic testing. Right - Multiple beam-column connections made with post-tensioning. (Thicker lines represent the steel tendons and anchorages).

Post-tensioning can be used to reduce deflections of heavy timber beams. The tendons can be draped to provide uplift at mid-span. In seismic designs the post-tensioning serves to re-centre the building following an earthquake, eliminating residual displacement. Energy dissipation can be achieved with easily replaceable mild steel energy dissipaters.[5-8]

As with any timber construction there is a commonly perceived increased risk in fire. While the fire performance of heavy timber structures is well established, PT timber has a number of factors which could lead to unique and unfavourable failure mechanisms in fire. Complications include cavities within timber members and the use of high strength steel tendons. As a result, corner rounding due to charring may have a greater influence on a PT timber member compared to a timber member with no cavity. A small rise in tendon temperature may result in substantial relaxation of the post-tensioning force, potentially causing premature loss of connections or the failure of a member.

In order to demonstrate the fire performance of post-tensioned timber members a series of 3 full-scale furnace tests on post-tensioned timber members were completed. These tests also provide data for the validation of the fire design method developed for post-tensioned timber members. The design method provides advice on the analysis of post-tensioned timber members under fire conditions, and the failure mechanisms which are important to consider.

2 FULL-SCALE FURNACE TESTS

The experimental testing took place utilising a 4m by 3m furnace at the Wellington based Building Research Association of New Zealand (BRANZ) testing facility. The beams were designated A, B and C, and were LVL box beams, each post-tensioned with two 7-wire strand (12.7mm diameter) tendons. Beam A was 426mm by 300mm, Beam B was 236mm by 190mm, and Beam C was 300mm by 190mm. Each beam was constructed from 63mm thick LVL having a published bending stiffness of 13 GPa. Beams A and B had approximately 210kN of post tensioning applied and Beam C had 230 kN post tensioning applied. Beam B failure prematurely with an unexpected failure mechanism which lead to revisions in the design calculations and eventually the construction and testing of Beam C. Because of this, no all the data for Beam B is not presented here. Further details of this series of tests is available in [9].

2.1 Failure times

The failure times for the three tests are given in Table 1, together with the failure mechanisms and the char depth.

Table 1: Char depths and failure times and mechanisms from the full-scale test series.

Beam	Char depth	Failure time	Failure mechanism
A	48mm	64 min	Shear in lower corner
B	18mm	22 min	Premature disconnection of top flange
C	40mm	56 min	Bending and compression at end of beam and beneath loading point.

2.2 Displacements

During the Beam A test the deflections remained in the order of 0.5mm-1mm for the first 45 minutes then started to increase steadily until approximately 64 minutes when the beam became unable to carry the applied load. The deflection profile during the Beam C test was similar to the Beam A test, however, due to the beam being more flexible due to its geometry, deflections were greater. The deflections measured during each test are presented in Figure 2 (left).

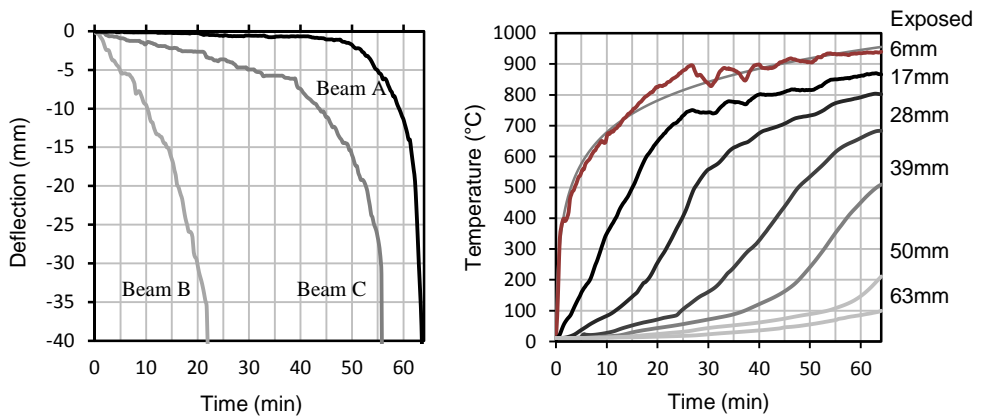


Figure 2: (left) Vertical deflections of the test beams during standard fire exposure; (right) Thermal profile through the bottom flange of Beam A.

2.3 Thermal results

The temperature profiles of each beam did not vary significantly, therefore only the behaviour of a single beam is presented. During exposure to the ISO834 fire, the temperature profiles close to the surface followed the random variations in the furnace temperature. Further into the section these features became less evident and the curves became comparatively smoother. Deeper than 17mm into the section, the temperatures approached 100 °C slowly and once 100°C was reached, heated more quickly. The bottom flanges heated slightly more quickly than the webs since the flanges shields the web from some of the furnace heat and therefore receive more radiation. Another possibility is that the width of the beam is small enough that the 2-dimensional heat transfer serves to increase the temperature more quickly. The temperature distribution for Beam A is presented in Figure 2 (right).

The temperature of the inside face of the LVL did not appreciably rise beyond 100°C whilst the beams were still intact. The tendon temperature lagged behind the internal timber surface temperature as expected. After 45 minutes the internal timber surface was approximately 25-30 °C hotter than the tendons within Beam A. The temperature of the internal surface and the tendon are presented in Figure 3 (left). The position of the tendon within the cavity in Beam A showed little effect on tendon temperature. The temperature profiles for the tendon at various positions are presented in Figure 3 (right).

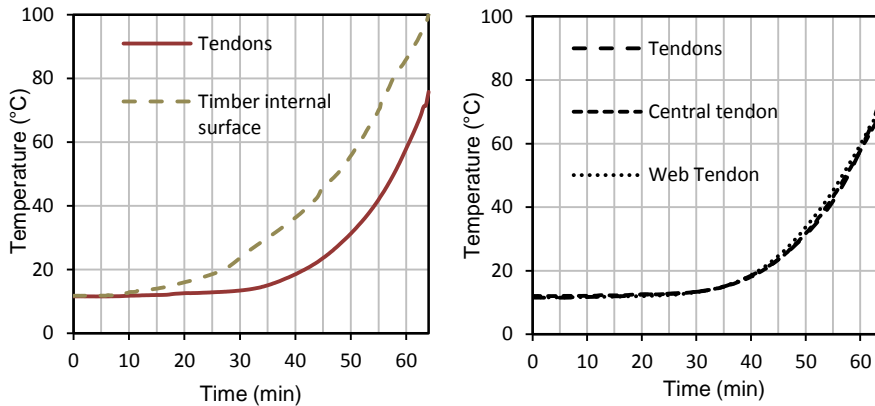


Figure 3: (Left) Average temperature of the post-tensioning tendon and the internal surface of the timber cavity of beam A; (right) Temperature profiles tendons at different positions in cavity.

2.4 Tendon post-tension force and relaxation

Over the course of each test the post-tensioning forces decreased with time. The causes of these decreases were due to the heating of the tendons and their subsequent thermal expansion and loss of stiffness, but also the loss of timber cross section, and rotation of end anchorages. During the Beam A test, at 60 minutes the tendons had lost approximately 25% of the initial applied stress. At this time the tendon temperatures were approximately 58°C.

3 FIRE DESIGN METHOD

3.1 Failure mechanisms

Under fire conditions it is important to check: combined bending and compression at mid span and at the end of beams, as well as shear in the lower corners and webs. The shear in lower corners needs to be considered due to the geometry of the beams; charring rounds the exposed corners leading to the thinnest region of the beam occurring there. These failure modes can be considered using standard methods such as a combined stress index for bending and compression and ensuring adequate strength in shear.

3.2 Section Shape during fire exposure

LVL has a char rate of 0.72mm/min, as published by the manufacturer. The corners of a timber section exposed to fire round as they char. This can be modelled by assuming the corner radius is equal to the char depth [10]. These assumptions can be used to estimate the section geometry over the fire duration. Shown in Figure 4 is a visual comparison between the geometry constructed from the above assumptions and a similar timber section which has been exposed to fire. The section geometry can be made up from a series of simple geometric shapes, which can then be used to calculate the second moment of area (I), cross-sectional area ($A_{Timber,Fire}$), centroid location, and therefore tendon eccentricity (e_{fire}).

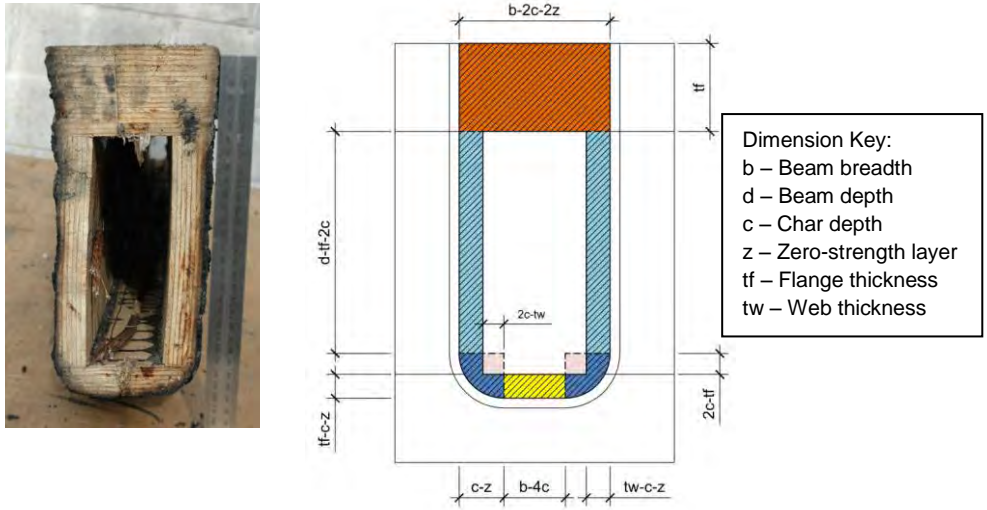


Figure 4: Comparison between an actual fire exposed timber section and the model geometry. (Note: pink coloured areas are removed for sectional analyses.)

3.3 Deflection and post tensioning relaxation analysis

When heated, the post-tensioning loses tensile load due to thermal expansion of the steel and a reduction of Young's Modulus with increased temperature. There are additional changes to the force within the tendons due to anchorage rotations, beam deflections, and the increase in compressive stresses due to the loss of area resulting in shortening of the beam. These geometry effects can be included in the analysis as effective strains. The strains in the tendon can be represented as shown in Equation (1) **Error! Reference source not found.**, where: $\varepsilon_{0,mech}$ is the total mechanical strain of the tendon at ambient conditions, $\varepsilon_{mechanical}$ is the axial strain due to the applied axial force, $\varepsilon_{thermal}$ is the thermal strain, $\varepsilon_{rotation}$ is the effective strain due to the rotation of the anchorages and subsequent elongation of the tendons final length, and $\varepsilon_{compression}$ is the effective strain due to the increased axial deflections of the timber beam.

$$\varepsilon_{0,mech} + \varepsilon_{rotation} + \varepsilon_{compression} = \varepsilon_{mechanical} + \varepsilon_{thermal} \quad (1)$$

As the calculation of deflections and post-tensioning force are non-linear and depend on one another, the calculation lends itself to being solved iteratively.

In-order to calculate the components of strain within the tendon it is important to calculate the initial length of the tendon so that each strain component is calculated with the same reference length. The initial length of the tendon can be calculated as shown in Equation (2), where, E_{Tendon} is the Modulus of Elasticity of the tendon, A_{Tendon} is the cross sectional area of the tendons, L is the length of the beam, and F_{PT} is the ambient initial post tensioning force applied to the tendons.

$$L_o = \frac{E_{Tendon} A_{Tendon} L}{F_{PT} + E_{Tendon} A_{Tendon}} \quad (2)$$

3.3.1 Post-tensioning force

The goal of this calculation is to determine the reduced post-tensioning force in the tendons after a specified fire duration. However, due to the iterative nature of this calculation it is required that an initial

value is assumed. It is easiest to assume the ambient temperature post-tensioning force as this initial value as it will allow the calculation to converge quickly.

3.3.2 Post-tensioning moment

The applied post-tensioning moment is determined from the post-tensioning force and the calculated eccentricity. It is important to include the effect of the changing eccentricity due to the changing cross section geometry.

3.3.3 Transverse loading

The external loads are determined as dictated by the fire limit state loading and will not change between iterations. The Australia and New Zealand Structural design actions standard AS/NZS:1170 [11] states that the fire limit state load case to be the dead load plus 40% of the live load.

3.3.4 Tendon temperature

The temperature of the tendon can be assumed to be the same temperature as the internal surface of the cavity within the timber member. This is a conservative assumption as the tendons will take additional time to heat. The internal timber temperature and therefore the tendon temperature can be estimated using an assumed temperature distribution for the timber underneath the char layer. Structural design for fire safety [12] presents the parabolic distribution presented in Equation (3) where: $T(x)$ is the temperature of the timber at a distance x beneath the char layer, T_i is the initial or ambient temperature of the timber (20°C), T_p is the charring or pyrolysis temperature of the timber (300°C), a is the thickness of the heat-affected layer (40mm).

$$T(x) = T_i + (T_p - T_i) \left(1 - \frac{x}{a}\right)^2 \quad (3)$$

3.3.5 Thermal strain

The thermal strain in the tendon can then be estimated using the relationship presented in Section 3.4 of Eurocode 2 which provides the thermal strain for a pre-stressing steel [13]. This calculation is intended for use with pre-stressed concrete and since the tendons being used for post-tensioned timber are the same as those used for pre-stressed concrete, it is appropriate to use this calculation. Equation (4) presents the thermal strain relationship adapted from Eurocode 2 where $\varepsilon_{thermal}$ the strain is induced in the tendon due to its temperature, and θ is the temperature of the tendon in °C.

$$\varepsilon_{thermal} = -2.016E^{-4} + 10^{-5}\theta + 0.4 \times 10^{-8} \theta^2 \quad (4)$$

3.3.6 Beam deflections

Under fire conditions it is important to consider the deflections of a post-tensioned timber beam so that the bowing moment induced by the axial loads can be included in the calculation. The deflection components which need to be monitored during design are flexural deflection due to external loads (D_{Load}), shear deflection (D_{Shear}) due to external loads, flexural deflections due to the post-tensioning moment (D_{PT}), and bowing deflection caused by the axial post-tensioning force acting on an initially deflected member (D_{Bowing}). The moment and deflections due to axial loads are dependent on the total deflection, which includes a component of its own deflection making this a non-linear problem. Equation (5) presents components of deflection and Equation (6) presents the calculation of the bowing deflection.

$$D_{Total} = D_{Load} + D_{PT} + D_{Shear} + D_{Bowing} \quad (5)$$

$$D_{Bowing} = \frac{F_{PT} D_{Total} L^2}{\pi^2 E_{Timber} I} \quad (6)$$

3.3.7 Beam end rotations

Rotation at end anchorages affects the forces developed in tendons. This occurs under both ambient and fire conditions. The beam end rotation components (φ_{end} , Equation (7)) to consider include the end rotation due to transverse loading (φ_{Load}), post-tensioning (φ_{PT}), and axial bowing ($\varphi_{Bowling}$ Equation (8)). Tendon elongation due to rotation at the anchorages can be converted to strain using Equation (9) which depends on the initial tendon length (L_o) as a reference and the tendon eccentricity (e_{Fire}).

$$\varphi_{end} = \varphi_{Load} + \varphi_{PT} + \varphi_{Bowling} \quad (7)$$

$$\varphi_{Bowling} = \frac{F_{PT,Fire} D_{total} L}{\pi E_{Timber} I} \left(-\cos\left(\frac{\pi L}{4}\right) + 1 \right) \quad (8)$$

$$\varepsilon_{rotation} = \frac{2\varphi_{end} e_{Fire}}{L_o} \quad (9)$$

3.3.8 Additional timber compression

As the timber is post-tensioned there are large axial loads which compress the timber resulting in deflections parallel to the longitudinal axis of the beams. This is implicitly taken into account during stressing, however, during fire exposure the timber area resisting the axial load is reduced which increases the stress developed in the cross section and therefore increases compression deflections. It is only the change in compressive strain which is of interest during this calculation which can be calculated using Equation (10).

$$\varepsilon_{compression} = \frac{F_{PT,fire} L}{L_o E_{timber} A_{Timber,fire}} - \frac{F_{PT} L}{L_o E_{timber} A_{Timber}} \quad (10)$$

3.3.9 Tendon strain

The mechanical strain, which is used to calculate the force within the tendon, can then be calculated using Equation (11).

$$\varepsilon_{mechanical} = \varepsilon_{0,mech} + \varepsilon_{rotation} + \varepsilon_{compression} - \varepsilon_{thermal} \quad (11)$$

3.3.10 Stiffness reduction

As a tendon is heated, Young's modulus decreases. Eurocode 2 section 3.2.4 [13] provides a relationship between the reduction of Young's modulus and tendon temperature.

3.3.11 Post-tensioning tendon force

The reduced tendon force for each iteration can then be calculated with Equation (12). Where E_{fire} is the temperature reduced young's modulus of the post tensioning tendon.

$$F_{PT,Fire}^{i+1} = \varepsilon_{mechanical} E_{fire} A_{tendon} \quad (12)$$

3.4 Design Actions

The mid-span bending action can be calculated with Equation (13): where $M_{Bowling}^*$ is the moment due to axial loads as calculated in Equation (14), M_{PT}^* is the moment due to post-tensioning and $M_{Load,Fire}^*$ is the moment due to loading. The end moment due solely to post-tensioning, as all other components are zero at the ends of beams. The axial action on beams should be the reduced post-tensioning force. The shear flow action should be calculated for the web at the centroid and at the bottom corners of beams. Stresses can then be combined in an appropriate manner and checked against strength capacities in order to design adequately performing members.

$$M_{Total,Fire}^* = M_{Bowling}^* + M_{PT}^* + M_{Load,Fire}^* \quad (13)$$

$$M_{Bowling}^* = F_{PT,Fire} D_{Total} \quad (14)$$

4 DISCUSSION

The char rate recommendation of this research is 0.72mm/min with an additional 7mm layer. Using this recommended char rate provides the best correlation between the fullscale test failure times and those predicted by the proposed design method. The predicted char depths and failure times for the three beams tested are shown in Table 2

Table 2: Predicted failure times using a 0.72mm/min char rate and 7mm zero strength layer.

Beam	Predicted Char depth	Predicted Failure time	Measured Char depth	Measured Failure time
A	47.5 mm	61 min	48mm	64 min
B	33.5 mm	37 min	18mm	22 min
C	45 mm	53 min	40mm	56 min

The hand calculation method of estimating the temperature of the inner surface of the timber has been shown to provide reasonable results, and is able to be used to estimate tendon temperatures conservatively. The hand calculation method gives results slightly cooler than those observed on the timber surface but approximately 10°C higher than the tendon temperatures recorded anywhere in the cavity. The recorded temperatures of the timber cavity surface and the tendons within beam C and those predicted with the hand calculation method are compared in Figure 5.

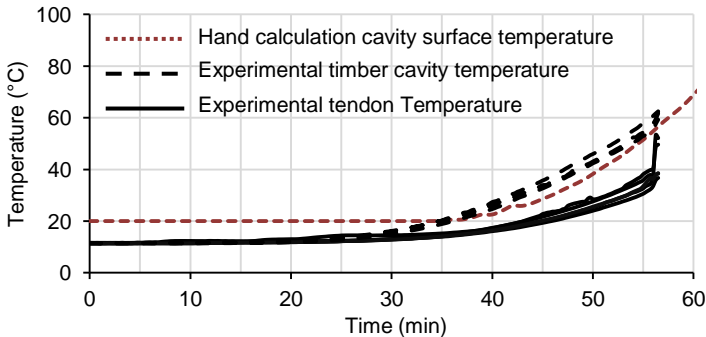


Figure 5: Tendon temperatures estimated by hand calculations and as recorded during full scale testing of Beam C.

4.1 Tendon relaxation

The simplified calculation method provides a reasonable estimate of the relaxation of the post tensioning tendons. Figure 6 shows the calculated tendon strength for Beams A and B compared to the full-scale experimental results. It was found that the tendon force is significantly better modelled by including the effects of tendon elongation or shortening due to end rotations and increased timber compression as well as the loss of stiffness and increased thermal strain. Rotation of the anchorages increases strain in the tendons. Compression stresses and strains in the timber due to axial post-tensioning increase during a fire due to the reduction in timber cross-section. Before including these effects, the relaxation calculation depended only on the thermal strain and reduction of Young's modulus and greatly over predicted the remaining force in the post-tensioning

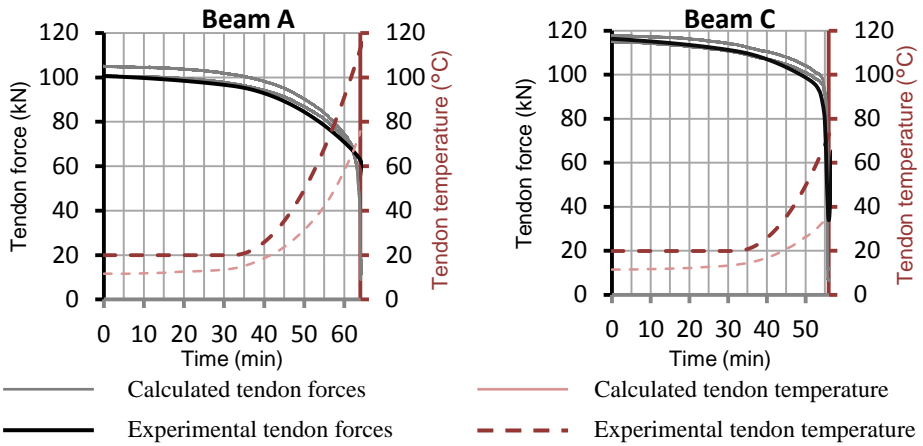


Figure 6: Simplified calculation method tendon relaxation for Beam A (left) and Beam C (right) compared with experimental results

4.2 Deflections

Deflections calculated by the hand calculation method substantially under-predict the beams deflections. Figure 7 shows the calculated deflections for both beams compared to the experimental deflections recorded. Experimental deflections were measured at the loading points and mid-span deflections were therefore slightly larger than shown. The calculated deflections for Beam A were positive due to the post-tensioning moment overcoming the loading and causing the beam to deflect upwards. The calculated deflections for Beam C follow the shape of the recorded deflections better than Beam A, but still substantially under predict deflections. Due to the non-linear nature of the deflection calculation, it can become numerically unstable and fail to reach a solution. This however should not occur before the calculation method predicts failure. The inability of the calculation method to predict deflections, casts doubt on the rest of the calculation which depends on the deflections, particularly the post-tensioning relaxation, and the design actions. A possible source of error in this calculation is the assumption for the elasticity of the timber. Timber plasticity or thermally accelerated creep may account for the increased downwards deflections observed during testing

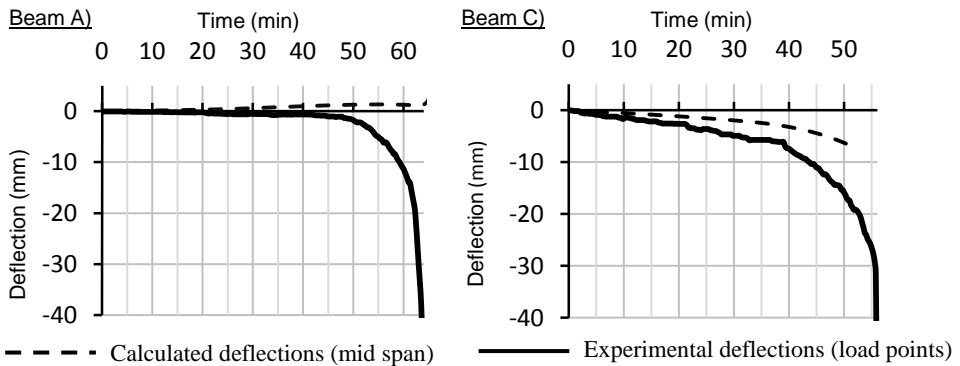


Figure 7: Calculated and experimental beam deflections

5 CONCLUSIONS

A series of full-scale fire tests were conducted on loaded post-tensioned timber beams and a design method has been proposed. The design method includes the following failure mechanisms which need to be considered during the fire design of post-tensioned timber beams:

- Shear failure in the webs at the centroid,
- Shear failure in bottom corners,
- Bending and compression failure at mid-span,
- Bending and compression failure at the ends of the beam

The proposed design method is able to predict the fire resistance of a post-tensioned timber beam and the tendon relaxation reasonably accurately. The design method recommends a char rate of 0.72mm/min and an additional 7mm zero strength layer. The design method does not yet capture the beam deflections at failure, possibly due to the lack of a model for plasticity of wood at elevated temperatures, which needs further investigation.

REFERENCES

- [1] John, S.: Environmental Impacts of Multi-Storey Buildings Using Different Construction Materials. 2008, MAF
- [2] John, S., N. Perez, and A.H. Buchanan: The Carbon Footprint of Multi-storey Timber Buildings Compared with Conventional Materials WCTE 2010, in *11th World Conference on Timber Engineering*. 2010: Riva del Garda, Trentino, Italy.
- [3] Smith, T.J.: Feasibility of Multi Storey Post-Tensioned Timber Buildings: Detailing, Cost and Construction., in *Department of Civil and Natural Resources Engineering*. 2008, University of Canterbury: Christchurch, New Zealand. p. 155.
- [4] Buchanan, A., A. Palermo, and D. Carradine: Post-Tensioned Timber Frame Buildings. *The Structural Engineer*, 2011. 89: p. 17.
- [5] Beerschoten, W.V., A. Palermo, D. Carradine, F. Sarti, et al.: Experimental Investigation on the Stiffness of Beam- Column Connections in Post Tensioned Timber Frames, in *Structural Engineers World Congress 2011*. 2011: Italy.
- [6] Iqbal, A., S. Pampanin, A. Palermo, and A.H. Buchanan: Seismic performance of full-scale post-tensioned timber beam-column joints in *The 11th World Conference of Timber Engineering*. 2010: Riva del Garda, Trentino Italy.
- [7] Newcombe, M.: Design Procedures and Numerical Analysis for Multistorey Post-Tensioned Timber Buildings (Not Yet Published). 2010, University of Canterbury, New Zealand.
- [8] Newcombe, M.: Seismic Design of Multistorey Post-Tensioned Timber Buildings. 2007, University of Pavia: Pavia.
- [9] Spellman, P., D. Carradine, A. Abu, P. Moss, et al.: Full-scale fire tests of post-tensioned timber beams, in *To be published in the 12th World Conference on Timber Engineering proceedings*. 2012: Auckland, New Zealand.
- [10] Buchanan, A.: Timber Design Guide. Third Edition ed. 2007, Wellington: New Zealand Timber Industry Federation Inc.
- [11] Standards New Zealand: AS/NZS 1170:2002 Structural design actions. 2002.
- [12] Buchanan, A.: Structural design for fire safety. 2001: Wiley Chichester, UK.
- [13] British Standard Institute: Eurocode 2: Design of concrete structures - part 1-2: General rules - Structural fire design. 2004: U.K.

INFLUENCE OF SERVICE INSTALLATIONS FOR THE SEPARATION AND STRUCTURAL PERFORMANCE OF TIMBER ASSEMBLIES EXPOSED TO FIRE

Norman Werther*, Michael Merk*, René Stein*, Stefan Winter*

* Fakultät für Bauingenieur- und Vermessungswesen,
Technische Universität München, Arcisstrasse 21, 80333 München, Germany
e-mails: n.werther@tum.de, m.merk@tum.de

Keywords: Fire safety, Service installation, Timber building, Penetrations.

Abstract. *In recent years residential buildings have been increasingly equipped by technological devices and service supplies to gain an appropriate standard of comfort. Despite these service installations and associated penetrations the fire resistance of fire separating elements must not be negatively influenced. There are currently no approved systems or recommendations for fire safe penetration sealing products in separating timber elements available. However, new measures and recommendations for fire safe service installations in timber structures can be derived from numerical simulations and fire tests conducted in a European research project and further work of the authors.*

1 INTRODUCTION

The separating function for wall and floor elements represents one of the most essential capacities in the case of fire, besides the structural stability. The building occupants and fire service must have confidence in the correct function of these elements. The evaluation of the fire resistance for such building elements occurs normally on basis of standardised fire tests, such as listed in EN 13501-2 [1], as well as approved calculation methods, such as those presented in EC 5-1-2 [2]. These methods don't normally take into account any junctions to neighbouring elements, mounting parts such as wall sockets and switches or penetrations of service installations for the likes of electrical wirings, heating systems, water and sewage pipes. However, these service installations are necessary and essential for the use of a building. Simultaneously the guarantee of fire prevention requires that for all building materials and construction methods certified sealing compounds and penetration sealing systems are used, which have the same fire resistance time as the separating building elements, to avoid the spread of fire as well as early ignition of wooden panels or combustible materials inside the elements.

However inspections and surveys of new and existing buildings repeatedly report that for all building materials and construction methods the risk for an early fire spread from one fire cell to the next is mainly caused by blocked doors and especially by inappropriately designed and sealed service installations in walls and floors. At the same time a survey found that 50% of the service installations were not installed properly and would not be able to perform well in the case of fire, resulting in significant limitations of usability for egress ways and the structural elements.

Several fire tests and technical approvals show that every type of service installation passing through fire separating elements has its own specific characteristic, level of performance and therefore range of application. Hence there is no single solution or product that will be used for all services and protect all elements in the same manner to avoid early fire spread.

For the selection and arrangement of an adequate penetration sealing system the services must be classified under consideration of number, size, material of the supply lines and transported substances.

2 ARRANGEMENT CONCEPTS AND STANDARDS

2.1 Arrangement of service installations

Penetrations of building services through separating assemblies are unavoidable, and must be planned and allowed for from the beginning of a project. This helps to avoid unnecessary penetrations and complex and expensive solutions in the latter stages of the construction. Therefore it should be aimed to include all service installations to previously defined fire compartments. This can be done by the application of following design concepts (depicted in Figure 1):

- central distribution in fire rated service shafts and ducts with appropriate sealing of the penetrated areas
- penetration sealing in each separating element (wall, floor) with approved sealing compounds and systems
- continuous encasing of each service line throughout its entire length

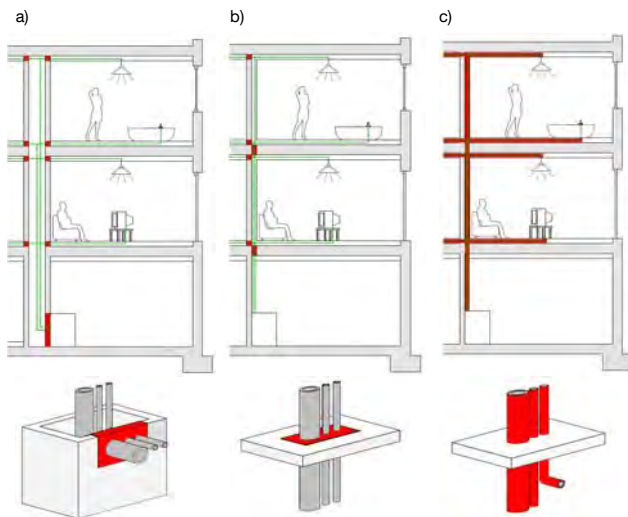


Figure 1. Arrangement concepts of service installations

All of these solutions must not only satisfy the requirements for fire safety but also the requirements for acoustic, moisture and thermal performance. Furthermore, the accessibility for revision, maintenance and additional installations should be allowed for. Based on these considerations and taking into account further aspects, such as practical execution on site and durability the solution of a service shaft in combination with timber structures shows some disadvantages. Most notably the problems of airborne sound transmission between compartments through service shafts, cracks caused by different settlement and moisture movement, and the necessity to seal each penetration through the shaft or duct and finally the high costs can be mentioned. Therefore designs of sealing the penetration of service installations in each separating element may be recommended for timber structures.

2.2 State of the art

Until now, fire tests of penetration sealing systems and sealing compounds for penetrations in timber frame and solid timber constructions are missing and acceptable solutions are rare. Approved sealing systems are typically only available for concrete or drywall construction at the moment. Further

recommendations and acceptable solutions for these structures are made in the literature all over the world [4], [5], [6]. For penetrations of service installations in timber assemblies the following weak points can be identified:

- Service installations made from combustible materials and materials that melt at fairly low temperatures, such as wirings or plastic pipes, may lead in combination with wood based panels to a quick formation of gaps or holes in the penetration area during a fire.
- Metal pipe work can increase the heat flow through the assembly, thus an early flame spread to the unexposed side or inside the assembly may be possible.
- The application of penetration sealing systems, such as coated mineral wool boards, usually reduces the cross section of the timber structures (see Figure 13). Gaps and the unprotected reveal area may lead to an early fire spread to the inside cavity of the timber assembly and a sideways passing of the penetration sealing system.

To check the applicability of existing penetration sealing systems and sealing compounds for timber frame and solid timber structures, as well as develop further design rules, numerous fire tests for penetrations of electrical wiring, pipes as well as for the fire safe installation of switches and sockets have been carried out.

3 EXPERIMENTAL INVESTIGATION

The series of experiments in these investigations have been split in to three parts. In the first part, different types of penetration sealing compounds for electrical wiring, in combination with wood based panels and solid timber elements were assessed. As timber framed and lined assemblies and non-combustible drywall constructions have similar failure mechanisms when exposed to fire (attrition and the collapse of the lining) the main focus in this study was laid on the modification of existing and already approved penetration sealing systems for drywall constructions, to achieve fire safety in combination with timber structures too. Special attention was paid to the development of measures to line and frame, the reveal area (see Figure 13) to get similar boundary and installation conditions for all sealing systems. The third step in this investigation considered the fire safe design of wall sockets / switches in separating timber elements.

3.1 Test setup for sealing of electrical cables

For the assessment of a fire safe sealing of electrical wirings in combination with wood based panels five small scale fire tests were conducted. The assemblies were made of OSB with dimensions of $W \times H = 540 \text{ mm} \times 540 \text{ mm}$ and thickness of 15 mm and 25 mm respectively. One 15 mm thick panel was additionally lined with 9.5 mm thick gypsum plasterboard. The bulk density of the panels was $\sim 580 \text{ kg/m}^3$ and moisture content $\sim 7 \%$. All panels were screwed to a wooden frame to ensure more stability in the fire tests and the mounting at the furnace. The single electrical cables or cable bundles applied in these tests are specific for electrical wiring in building structures. These consist of 3 respectively 5 PVC insulated copper conductors with a further outer PVC sheathing and can be classified according to DIN VDE 0250. All electrical cables were supported on the unexposed side, to ensure practical conditions. In these investigations gypsum putty, mineral fibre insulation plugs, fire retardant foams and mastics as well as intumescent wraps and sealing compounds were used to seal the penetration area. The tests were carried out under variation of panel thickness, type of sealing, size of annular gap (0 - 10 mm) and number of electrical wiring per penetration. In each test four different sealing setups were assessed (depicted in Figure 2). The temperature formation on unexposed side was measured at each cable and 25 mm beside the penetration area as well as in the centre of the OSB panel, to compare the failure times at penetrations and the plane undisturbed panels to each other.

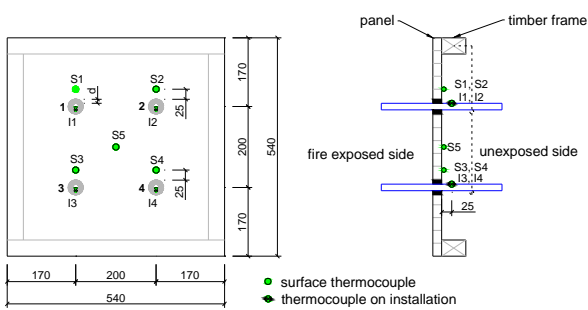


Figure 2. Setup of fire tests for sealing compounds



Figure 3. Failure at penetration sealing with non fire retardant PU foam

3.2 Test setup with penetration sealing systems

To assess the applicability of in drywall constructions approved sealing systems four small scale tests for timber frame and solid timber assemblies were conducted by TU Munich and two full scale tests for timber frame assemblies by the German Society for Wood Research (DGfH e.V.). The tests included sealing systems for plastic pipes, copper and steel pipes, various cables and cable bundles as well as measures for multiple penetrations of cables and pipes. In the small scale tests assembly dimensions of $W \times H = 1180\text{mm} \times 1180\text{mm}$ were used. The first timber frame wall was designed for a fire resistance of 30 minutes, the second and the solid timber assemblies for a fire resistance of 90 minutes each. The design and cross section of the timber frame assemblies can be taken from Figure 4. For the fire tests of solid timber elements, 120 mm thick cross laminated timber panels (CLT) were used, consisting of 5 single layers each and bonded together with melamine resin. These panels had no additional lining. In contrast to the timber frame elements an additional multi penetration sealing system was investigated in the two CLT panels. The used system was made up of an 80 mm thick mineral wool board and coated with an intumescent painting. The board was fitted tightly in the previous with fire rated gypsum plasterboards lined opening in each test. Gaps between the mineral wool board and plasterboard lining were filled by an intumescent painting according to the technical approval of the system. To ensure appropriate fire safety in the reveal area the required thickness of the attached lining has been determined approximately by numerical simulation in advance. Lining thicknesses from $2 \times 10\text{mm}$ to $2 \times 18\text{mm}$ in combination with a 100 mm wide framed lining around the exposed surface were investigated with respect to heat flow and protection capacity for the timber members located behind. Under consideration of a critical temperature of 300°C (in accordance with EC 5-1-2) the protection capacity of the cladding was determined for point "A" - directly in the corner and "I" - 35 mm above the corne (see Figure 8).

The additional influence of joints in the gypsum plasterboards were not investigated in this manner. In the FE simulations, the lined corners of the reveal areas were exposed to the ISO 834 [7] fire curve over 30, 60 and 90 minutes respectively. The applied thermal force considered a conductive and a radiative fraction at the exposed surface. Therefore emissivity ϵ and convection coefficient h were assumed equal to 0.8 and $25\text{W/m}^2\text{K}$, respectively, as suggested by Eurocode 1-1-2 [3]. For the unexposed side a convective coefficient of $9\text{W/m}^2\text{K}$ (considering of radiation losses too) and ambient temperature of 20°C were used. The thermal dependent material properties for conductivity (k), specific heat (c) and density (ρ) of timber and gypsum plasterboard were taken from Eurocode 5-1-2 [2] and from a research report [8] respectively. In addition, the influence of fasteners normally used to fix the gypsum plasterboards to each other and to the supporting timber structure such as screws and staples were investigated with respect to thermal degradation of the supporting timber members in the reveal area.

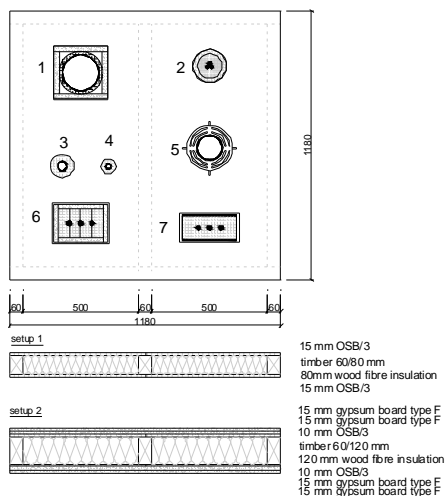


Figure 4. Setup of timber frame assemblies with installed penetration sealing systems



Figure 5. Small scale fire tests assembly (setup 2 - EI90)

Furthermore, two full scale fire tests with a timber frame wall and floor assembly in combination with a mineral wool board multi penetration sealing system and installed services were conducted [9], [10]. Before lining the reveal areas a support infill frame was attached in the opening of the timber frame wall and floor, to stabilise and support the gypsum plasterboard cladding. For these fire tests two layers of 18 mm gypsum plasterboards were used to line the reveal area. The wall and floor assembly were also lined in the entire exposed surface with the same plasterboards.

Each penetration sealing in the small and full scale fire tests was equipped with several type K thermocouples to measure the temperature formation and compare these results to the standard benchmarks. The tests were carried out in accordance with EN 1366-3 and under ISO 834 fire curve exposure. The failure criteria in all tests were measured in terms of:

- integrity (E) considering ignition of cotton pad and flame ejection on unexposed surface and
 - insulation (I) with temperature increase less than 180°C above the initial ambient temperature.
- Stability or structural adequacy was not recorded for these tests and so no additional load was applied.

4 EXPERIMENTAL RESULTS

4.1 Sealing for electrical wirings

Due to the large number of examined setups [12] only general results will be presented in this paragraph. Several of the examined approved sealing compounds showed excellent results in combination with cable penetrations in OSB panels and solid timber elements, in respect of equal failure times in the penetrated and un-penetrated areas. All conducted tests showed larger heat transfer through the cables itself in comparison to the plane panels and sealing compounds. As expected, an increase in the number and conductor diameter led to an increase of heat transfer throughout the cables and faster temperature formation in the penetration area. For one cable bundle and for inappropriate sealings an early ignition at unexposed side of the OSB lining occurred (see Figure 3).

All test results showed an influence of the annular gap size and the used sealing compounds for the temperature formation at OSB lining in the penetration areas. The tight executed cable penetration,

without annular gap, showed a self sealing effect in the penetration, due to the thermal expansion of the outer PVC sheathing. However this execution caused slightly higher temperatures in the penetration area compared to penetrations with a regular sealed annular gap. For the examined penetration sealings of electrical wirings with an annular gap sizes between 5 and 10 mm a formation of joints was obvious between the lining and the sealing material in all fire tests. Those gaps increased by time of exposure and were more distinctive for “passive” sealing compounds, such as uncompressed mineral wool plugs. Therefore a pre compression of flexible mineral wool plugs is needed for durable fire safe sealings. However better results were reached by the use of flexible sealing compounds or by the use of gypsum putty.

4.2 Penetration sealing systems

4.2.1 Single systems

As for the sealing compounds excellent results have also been reached for approved penetration sealing systems in timber structures [11], [13]. Therefore equal failure times for the plane timber elements and penetration areas have been reached (see Figure 6). As the most critical area for an early failure, the junction of penetration sealing system and timber element was found in all tests. This has been caused by problems to fill the joints properly in the entire depth of the lining (see Figure 7). This problem was more significant for multilayer and thick linings in combination with gypsum putty or viscous mastics when compared with intumescent sealing compounds. Here gaps and small voids in the sealed joints were subsequently closed by thermal expansion of the intumescent material.



Figure 6. Failure of small scale timber frame assembly



Figure 7. Failure in sealed penetration junction

4.2.2 Lining of reveal area for multi penetration systems

For designing the setup of fire tests numerical simulations were conducted to determine approximately the required thickness of gypsum plasterboard cladding in the reveal area for various fire resistance. The temperature formation between the reveal lining and the timber element can be taken from Figure 9. In the numerical simulations the 2D heat transfer influence became apparent for the corner, as expected, and resulting in a faster temperature rise as for measurement point “P”. For this point, with less thermal exposure no exceed of critical temperatures were detected in those setups with linings of at least:

- 2 x 10 mm for 30 minutes,
- 12.5 mm x 15 mm for 60 minutes and
- 2 x 18 mm for 90 minutes.

The thermal degradation of the timber members was accepted in the area of exposed corner. In this manner designed and conducted reveal areas showed excellent performance under fire exposure in combination with the 100 mm wide framed lining [13], [9], [10].

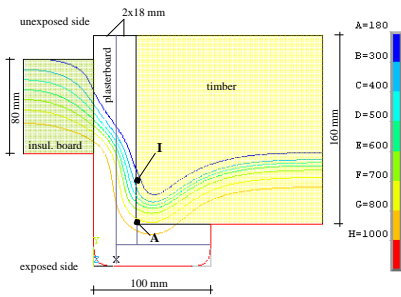


Figure 8. Assembly setup for num. simulation with isotherms for 2 x 18 mm gypsum plasterboard lining after 90 min.

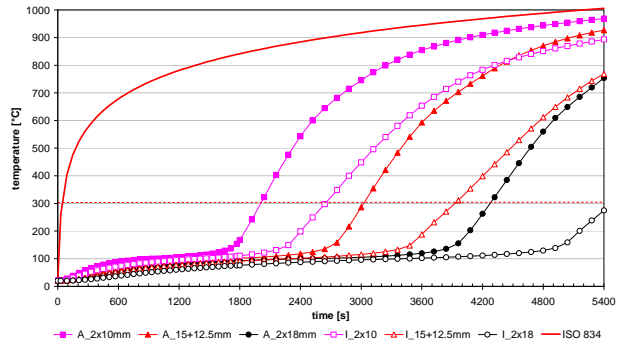


Figure 9. Temperature formation for different of reveal linings

In the pre-examinations as well as in the fire tests the influence of fasteners for the gypsum board lining was examined also. Fasteners penetrating the plasterboard lining caused higher temperatures in the timber compared to the undisturbed area of plasterboards. Screws with a larger penetration length in timber led to lower temperatures compared to shorter ones and slowed down the degradation process alongside the fasteners (see Figure 10). Furthermore skinny fastener caused less colouring and degradation in timber compared to larger fastener diameters. However no negative influences such as excessive local degradation of timber and no early ignition caused by fasteners were recorded in the tests [14].

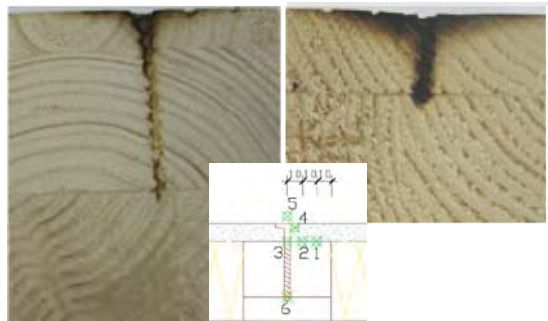


Figure 10. Charring alongside a screw (left 4.3x55mm; right 4.3x35mm) penetrating a 12.5 mm plasterboard

5 RECOMMENDATIONS

5.1 Penetration sealing for electrical wirings in timber structures

The results obtained in this study show the necessity of a proper sealing for electrical wirings in the penetration area to reach fire safety in combination with timber frame- and solid timber structures. As timber frame and drywall structures have similar failure mechanisms and material behaviour of the lining when exposed to fire, many approved sealing measures for drywall structures are appropriate for timber constructions too and should be used as presented in Table 1. Special attention must be paid to the gapless and void free sealing of the 5 – 10 mm wide annular gap in complete thickness in the penetrated lining on both sides of the elements. For solid timber elements a sealing depth of at least 40 mm on both sides is recommended to reach a fire resistance time up to 90 minutes. In the case of an annular gap less than 0.5 mm no additional sealing is needed for skinny cables. For thicker cables and cable bundles the conducted heat through the penetration increases and only highly efficient and durable measures or special penetration sealing systems shall be used.

In addition the following conditions must be observed:

- distance d between adjacent cable penetrations \geq largest penetration diameter (see Figure 11)
- density of penetrated wooden panel $\geq 400 \text{ kg/m}^3$ reaction to fire class at least D s2 d0 (EN 13501-1)
- for smoke proof connections use of permanent flexible sealing compounds or mastics

Table 1. Recommended sealing measures

Sealing measure	Annular gap size	Type of electrical cable		
		Single cable	Cable bundle **	
		NYM* $\leq 5 \times 16 \text{ mm}^2$	≤ 3 cables $1 \times \text{NYM} \leq (5 \times 16 \text{ mm}^2)$ $+ 2 \times \text{NYM} \leq (3 \times 2,5 \text{ mm}^2)$	≤ 5 cables $5 \times \text{NYM} \leq (3 \times 2,5 \text{ mm}^2)$
no further sealing	$\leq 0,5 \text{ mm}$	■		
gypsum putty	5 to 10 mm	■	■	■
intumescent wrappings sealing compounds fire retard. polyurethane foam (with technical approval)		■	■	■
flexible stone wool plugs, density $\geq 70 \text{ kg/m}^3$)		■	■	

*) cable NYM Y x Z mm²: Y PVC insulated copper conductors with a further outer PVC sheathing, cross section of conductors Z mm² each (in accordance with DIN VDE 0250)

***) for combustible cavity insulation use of non-combustible stone wool pipe linings around the cables

5.2 Application of penetration sealing systems in timber structures

5.2.1 Single systems

The assessed systems contained combustible and non-combustible service pipes in addition to penetrations of cable bundles. It is found that systems with intumescent materials (“active systems”), which expand when exposed to high temperatures, efficiently seal the gap between the sealing system and lining of the timber frame or solid timber elements. For systems with “passive” sealing materials, such as gypsum putty, the fully gapless filling throughout the complete depth of the lining is needed too. For thick linings of separating timber frame elements the application of a consistent sealing becomes difficult. To optimize these joints for fire conditions an additional 100 mm wide and minimum 12.5 mm thick non-combustible framed lining with gypsum plasterboards is strongly recommended (see Figure 12).

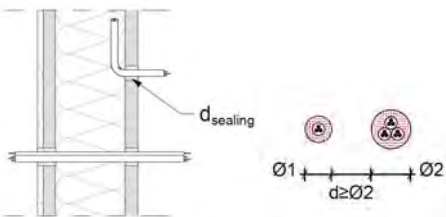


Figure 11. Penetration sealing for electrical wirings

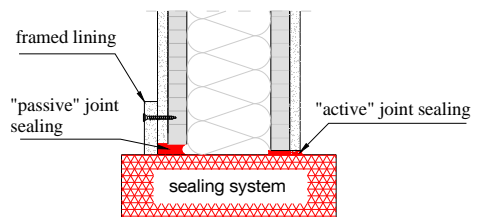


Figure 12. Joint sealing for penetration sealing systems

5.2.1 Multi systems

For the installation of multi penetration sealing systems in compartment timber structures comparable conditions to those used in concrete or drywall constructions must exist. Through this the fire spread inside the timber structure and sidewise passing of the sealing system can be excluded. The main concept is to line the reveal area of the penetrations / openings with a non-combustible encasing cladding, such as gypsum plaster - or gypsum fibre boards over the entire thickness of the separating element, including the attachment of an additional framed lining of at least 100 mm wide around both sides of the surface. This is to create joint steps and avoid continuous joints for convective heat flow through the structure and between reveal lining and structural timber element. For the setup of reveal linings two layers are preferable. In addition for timber frame constructions a support infill frame with at least 40 mm in the opening area is necessary to stabilise and support the reveal lining and the framed lining (see Figure 13).

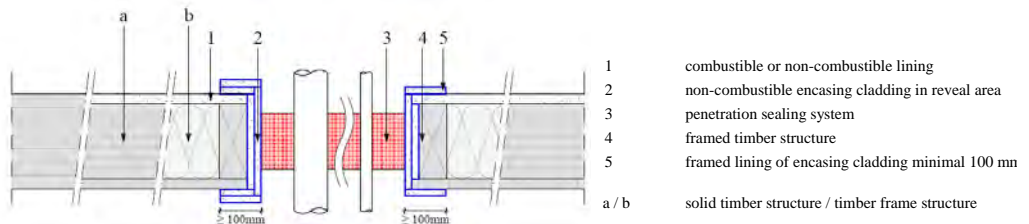


Figure 13. Fire safe lining of reveal area

6 CONCLUSION

The investigations show that the selected approved penetration sealings and systems for separating timber elements are applicable in accordance with the specified design restrictions and no early failure of the penetration will occur in the case of fire. The lining of the reveal area represents an efficient fire safety concept that provides for multiplicity of existing penetration sealing systems similar and fire safe installation conditions. National and international knowledge as well the executed fire tests show that existing penetration sealing systems can be used in combination with timber structures to assure fire safety.

7 ACKNOWLEDGEMENT

The authors wish to acknowledge all partners and colleagues in WoodWisdom-Net project "FireIn Timber" [15]. The German part of the WoodWisdom-Net program was coordinated by Projektträger Jülich and financed with funds of Federal Ministry of Education and Research (BMBF).

REFERENCES

- [1] European Committee for Standardisation (CEN), *EN 13501-2. Fire classification of construction products and building elements - Part 2: Classification using data from fire resistance tests, excluding ventilation services*; EN 13501-2:2007+A1:2009.
- [2] European Committee for Standardisation (CEN), *Eurocode 5. Design of timber structures. Part 1-2: General – Structural fire design*; EN 1995-1-2, Brussels, Belgium, 2004.
- [3] European Committee for Standardisation (CEN), *Eurocode 1. Actions on structures. Part 1-2: General actions – Actions on structures exposed to fire*; EN 1991-1-2, Brussels, Belgium, 2003.
- [4] England J.P., Young S.A., Hui M.C. and Kurban N., *Guide for the Design of Fire Resistant Barriers and Structures*, Building Control Commission Melbourne Australia, 2000.

- [5] Fachkommission Bauaufsicht der Bauminister-konferenz, *Muster-Richtlinie über brandschutztechnische Anforderungen an Leitungsanlagen (Muster-Leitungsanlagen-Richtlinie MLAR)*, 2005
- [6] Studhalter, J., Weber, H., Wiederkehr, R., Kammer, P., "Haustechnik – Installationen und Abschottungen", *Lignum-Dokumentation Brandschutz 6.1*, 2010
- [7] International Organization for Standardization (ISO), *ISO 834-1 Fire-resistance tests - Elements of building construction - Part 1: General requirements*, 1999-09
- [8] Schleifer, V., "Zum Verhalten von raumabschließenden mehrschichtigen Holzbauteilen im Brandfall", *PhD thesis*; ETH Zürich 2009.
- [9] MPA Braunschweig, "Prüfung einer etwa 285 mm dicken, raumabschließenden, wärmedämmenden Deckenkonstruktion mit einer unterseitigen „K₂60 Brandschutzbekleidung“ aus 2 x 18 mm dicken Gipskartonfeuerschutzplatten (GKF) zum baupraktischen Nachweis des „Kapselkriteriums“ in Verbindung mit Durchführungen von Kabeln und Rohren bei Brandbeanspruchung von der Deckenunterseite"; *Prüfbericht (3049/9435)-13-TP*, 25.08.2006
- [10] MPA Braunschweig, "Prüfung einer etwa 162 mm dicken, raumabschließenden Holzständerwand mit beidseitiger „K₂60 Brandschutzbekleidung“ aus 2 x 18 mm dicken Gipskartonfeuerschutzplatten (GKF) zum baupraktischen Nachweis des „Kapselkriteriums“ in Verbindung mit Durchführungen von Kabeln und Rohren bei Brandbeanspruchung von der Deckenunterseite"; *Prüfbericht (3049/9435)-7-TP*, 17.03.2006
- [11] Werther, N., "small scale fire tests for classified penetration sealing systems in combination with timber frame constructions"; *test results Nr. 09-001*, Technische Universität München - chair of timber structures and Building construction, 2009
- [12] Werther, N., "small scale fire tests for sealing systems for cables in combination with timber frame constructions"; *test results Nr. 09-002*, Technische Universität München - chair of timber structures and building construction, 2009
- [13] Werther, N., "small scale fire tests for lined cross laminated timber (CLT) wall and floor elements in combination with classified penetration sealing systems (test 1 wall penetrations) (test 2 floor penetrations)"; *test results Nr. 10-001, Nr. 10-002*, Technische Universität München - chair of timber structures and building construction, 2012
- [14] Mögele, T., "Theoretische und experimentelle Untersuchungen zum Einfluss des Befestigungssystems auf die thermische Schutzwirkung von Brandschutzbekleidungen an Holzkonstruktionen"; *Diplomarbeit*, Technische Universität München - chair of timber structures and building construction, 2010
- [15] Östman B., Mikkola E., Stein R., "Fire safety in timber buildings", *Technical guideline*, SP-Report 2010:19

FIRE PROTECTION BY MINERAL WOOL FOR TIMBER FRAME ASSEMBLIES

Alar Just* and Joachim Schmid**

* SP Wood technology, Box 5609, SE 114 86 Stockholm, Sweden and Tallinn University of Technology, Ehitajate tee 5, EE 19086 Tallinn, Estonia

** SP Wood technology, Box 5609, SE-114 86 Stockholm, Sweden
e-mails: Alar.Just@sp.se, Joachim.Schmid@sp.se

Keywords: Mineral wool, fire protection, timber.

Abstract. *This paper deals with protection provided by mineral wool to timber frame assemblies. New classification of mineral wools regarding fire resistance is needed. Protection by heat-resistant and non-heat-resistant mineral wool is analysed and compared to existing design method in EN 1995-1-2. Work is based on model-scale and full-scale fire testing.*

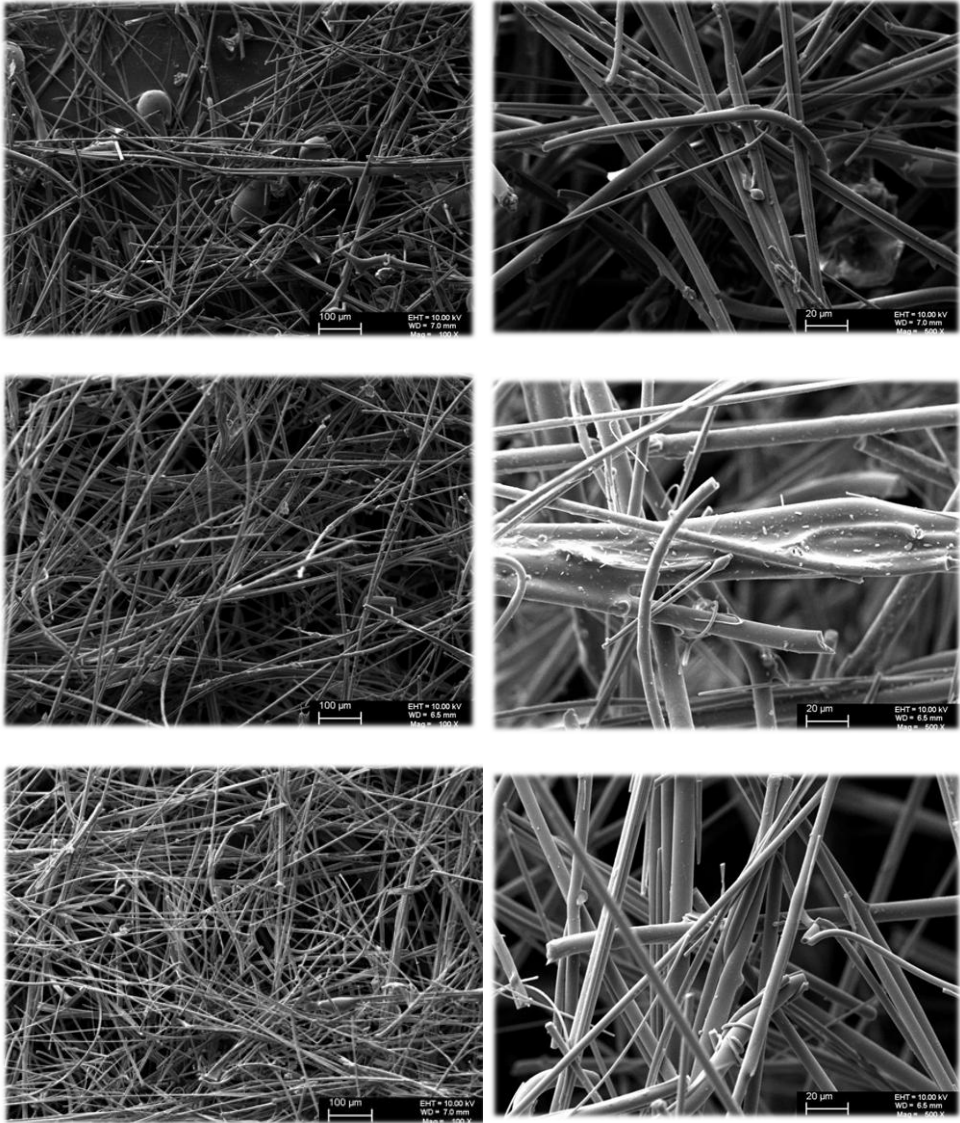
1 INTRODUCTION

Mineral wool is used for cavity insulation in many types of structures. It has to satisfy different needs, among others heat and acoustic insulation during the life time, but it may also contribute to the fire resistance of the structure. In EN 1995-1-2 terms “insulation made of glass fibre” (glass wool) and “insulation made of rock fibre” (stone wool) were introduced without any further definition. A later European standard for thermal insulation products specifies mineral wool but doesn’t distinguish between glass and stone wool. Insulation products are classified regarding their “reaction to fire” but no classification of mineral wool is available for the structural fire design and the ability of the insulation to contribute to the protection of load bearing members. The existing distinction between “insulation made of glass fibre” and “insulation made of rock fibre” is based on fire resistance tests from which it is widely known that stone wool performs better than glass wool when directly exposed to fire. At the moment, no standardized test method exists to quantify the difference in terms of product properties nor their contribution to the protection of timber members. In a revision of EN 1995-1-2 these facts have to be considered not least because the availability of a novel product on the market which is a basically glass wool, but performs in fire as a “traditional stone wool”. Furthermore other topics as the ability of the insulation to stay in place after the failure of the lining are not addressed in EN 1995-1-2.

Present research was performed with typical Scandinavian cross-sections of timber frame members with width of 45 mm.

2 MINERAL WOOL

In timber assemblies (timber frame floors and walls) timber construction members are enclosed by e.g. gypsum plasterboards or wood based panels or combinations. This cladding on the fire exposed sides provides protection of the timber member. Besides the protection of the narrow sides of timber studs or joists in timber frame assemblies additionally partly protection of the wide sides may be provided by cavity insulation. Mineral wool is often used to fill the cavities.



- a) Structure of stone wool at 100µm (left) and 20 µm scale (right).
- b) Structure of glass wool at 100µm (left) and 20 µm scale (right).
- c) Structure of the heat-resistant glass wool at 100µm (left) and 20 µm scale (right).

Figure 1. Microstructure of mineral wools [9].

Stone wool is a mineral wool manufactured predominantly from molten naturally occurring igneous rocks. Steam of air is blown through the molten rock of about 1600°C. After formation, the fibres are sprayed with binding agents, water repellents and mineral oil, and are passed through an oven and are formed into the appropriate products. The final product is a mass of fine, intertwined fibres with a typical diameter of 6 to 10 micrometers. Densities of stone wool insulations, used in structures, are usually 26 to 50 kg/m³. Traditional stone wool is not sensitive to high temperatures in a standard fire.

Glass wool is a mineral wool manufactured predominantly from sand and molten recycled glass. It consists of intertwined and flexible glass fibres, which cause it to trap air, resulting in a low density that can be varied through compression and binder content. After fusion of a mixture of natural sand and recycled glass at 1450°C, the glass that is produced is converted into fibres. The cohesion and mechanical strength of the product is provided by the presence of a binder that “cements” the fibres together. Ideally, a drop of bonder is placed at each fibre intersection. This fibre mat is then heated to around 200 °C to polymerize the resin, and is calendared to give it strength and stability. Densities of glass wool insulations, used in structures, are usually 14 to 20 kg/m³. Traditional glass wool is sensitive for high temperatures in fires. When the temperature exceeds 500°C, there can be a fast recession of traditional glass wool insulation. This will occur usually after the cladding failure.

In the market situation today there are products that do not suite into this classification. For example heat resistant glass wool (high temperature extruded wool) is also a glass wool. Fire protection provided by this wool is comparable to stone wool [6]. This type of wool can resist up to 1000°C or more. Therefore the classification to heat-resistant and non-heat-resistant mineral wool is more appropriate to use for design rules.

The product standard for mineral wool EN 13162 [2] does not classify mineral wools according to provided fire protection to timber member in timber frame assemblies. From experiences of fire resistance tests it is known that different mineral wool products may provide different fire protection, mainly based on the source material. The product standard requires the declaration among others the heat conductivity reached by the specific product but does not require the declaration of density. Hence the latter is used by [1] and the new component additive method [8] to describe the protection ability of mineral wool. This results subsequently in a problem for designers.

EN 1995-1-2 gives design rules for timber assemblies insulated with mineral wools made of two different sources - glass and stone. By doing so [1] classifies mineral wool different from [2]. But the design standard EN 1995-1-2 is not a classification standard, it may not be reasonable to keep this definition in the future. Hence different approach for different insulation materials in EN 1995-1-2 is purely caused by different protective properties in fire and has to be taken into account by the design models provided.

3 DESIGN METHODS OF EN 1995-1-2

The European design standard EN 1995-1-2 [1] provides rules for the design of timber structures in fire. Structural design is based on the charring model by König et al [3], who performed extensive experimental and simulation studies of timber-frame assemblies.

Charring is a central parameter for determining the degree of fire resistance of a timber member: the original cross-section is reduced by the charring depth.

For protected members, charring is divided into different phases, see Figure 2. No charring occurs during Phase 1 until a temperature of 300°C is reached behind a protective layer. Phase 2 is referred to as the protection phase, and protection is assumed to remain in place until the end of this phase – which is failure time t_f . The charring is relatively slow during this phase. Phase 3 is the post-protection phase, and starts at failure time of cladding. The charring is fast due to the lack of the char coal layer as thermal barrier. Mineral wool may provide protection on the wide sides of timber members during the protected phase and even during the post-protection phase when it is heat-resistant that means is not reduced in

depth. Charring of timber member may be faster when the cross-section is smaller, due to two-dimensional heat flux within the member, this is considered by means of the cross-section factor k_s .

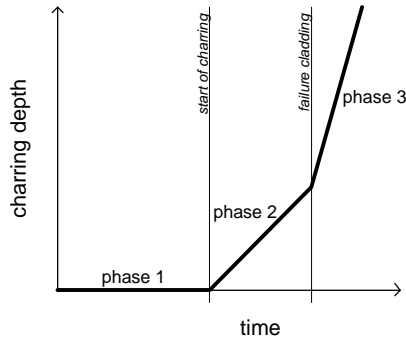


Figure 2. Charring phases of protected timber member.

According to the main part of [EN 1995-1-2] as well as the Annex C for light weight timber floors and walls cavities can be filled with any mineral wool as long as any cladding is in place, protecting the members and the cavity insulation. As soon as the cladding fails (t_f), verification can be done only if stone wool is used, since glass wool will undergo rapid decomposition. According to present design model in EN 1995-1-2 the failure of timber member is regarded to occur at time of failure of the cladding t_f when glass wool is used as insulation. For stone wool insulated assemblies and assemblies with void cavities, design rules are given for the post-protection phase in [1].

In timber frame assemblies the charring rate of initially protected timber members is given as

$$\beta_n = k_p k_s k_n \beta_0 \quad (1)$$

where β_0 is a basic one-dimensional charring rate taken as 0,65 mm/min for softwood.

The protection factor k_p takes into account the protection phase. When the cladding is still in place, factor k_2 is to be applied, when the cladding has fallen off, factor k_3 applies for the post-protection phase. Here the sub-index indicates the phase of charring. The cross-section factor k_s takes into account the width of cross-section and factor k_n is to convert actual cross-section into notional rectangular cross-section. Charring depth is taken as

$$d_{char,n} = \beta_n t \quad (2)$$

where t express time from the beginning of fire. The resulting cross-section is a notional rectangular cross-section, see Figure 3.

4 PROTECTION BY HEAT-RESISTANT MINERAL WOOL

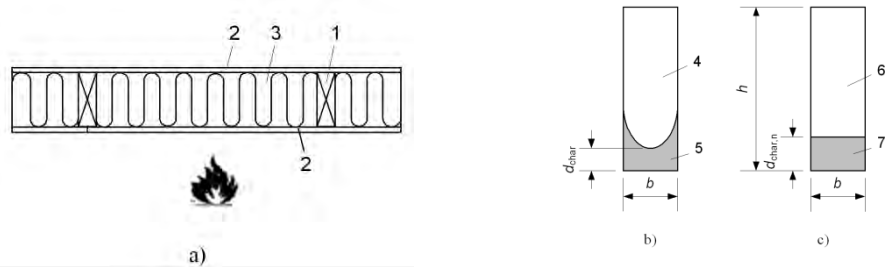
Timber frame members protected by stone wool can be calculated using method at EN 1995-1-2. Only charring from one side should be considered for the protected and unprotected phase according to

Equations (1) and (2), the effect of heat on the wide sides and corner roundings respectively is considered by using a corresponding rectangular cross-section, see Figure 3

Stone wool of different producers using different production processes is available on the market. In Annex E of [1], it is assumed that the quality of protection by stone wool is related to the density but recent research showed that the density might not be the crucial factor. The models presented in [1] base on a 30 kg/m^3 dense product available in Scandinavia. In recent research, different products, both stone wool and heat resistant glass wool were compared in a full scale wall test with direct fire exposure [4]. It shows that the models of [1] are based on one of the best products, while other products satisfying the description stone wool and representing equal densities do the same protection against heat.

Stone wool products should be additionally researched and classified by the mineral wool standard, alternatively a standard for the protection ability of insulation products for timber members may be needed.

During the last years, a novel product combining advantages of glass wool (high flexibility, lower density) and fire resistance ability of stone wool was introduced on the market. Due to the limitations of EN 1995-1-2 described above it can't be used to design timber frame structures after the failure of the cladding, although its protection ability was proven in both non load bearing and load bearing model scale and full scale tests.



Key:

- 1 Solid timber member (stud or joist)
- 2 Cladding
- 3 Insulation
- 4 Residual cross-section (real shape)
- 5 Char layer (real shape)
- 6 Equivalent residual cross-section
- 7 Char layer with notional charring depth

Figure 3. Charring of timber frame member (stud or joist): a. Section through assembly. b. Real residual cross-section and char layer. c. Notional charring depth and equivalent residual cross-section [3]

Figure 4 and Figure 5 show the comparison of charring depths of assemblies insulated with stone wool and heat-resistant glass wool. The protection provided by those two types of mineral wool is similar and the design model presented in [1] can be used for both. In Figure 4 the charring depth versus time is shown based on analysis of test results [6]. The charring of studs with cross-sections $45 \times 145 \text{ mm}$ is remarkably faster than determined by EN 1995-1-2. To take increased charring into account increased cross-section factor k_s is recommended according to [5].

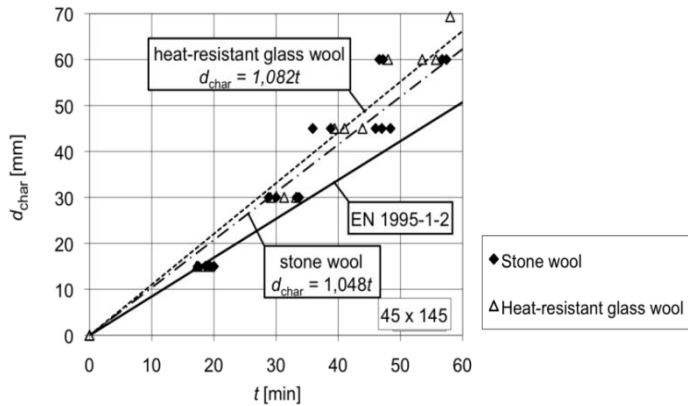


Figure 4. Linear equations for the charring rates of studs insulated by high temperature extruded glass wool and stone wool.

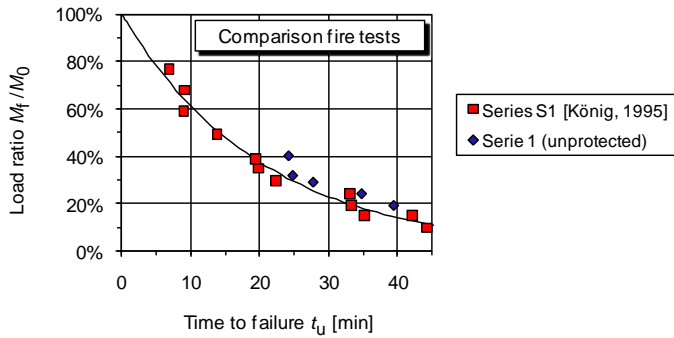


Figure 5. Comparison of failure times in fire tests of existing results using stone wool (red) and tests using high temperature extruded glass wool (blue).

There is a wide range of different stone wool products in the market. When EN 1995-1-2 was drafted there was little information available on the influence on the load bearing capacity of timber frameworks of different insulation products. It was assumed that differences are little. Based on research [6] it was shown that the design model in EN 1995-1-2 is based on one of the best products in the market. Based on full-scale test series with different stone wool products [4] the conclusion can be drawn that protection provided by stone wool may be overestimated for many stone wool products in the market.

Further research work is needed to investigate properties of different stone wool products used for fire protection.

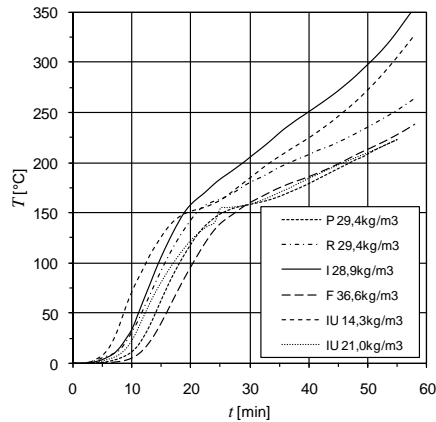


Figure 6. Temperature rise behind mineral wool of 145 mm thickness exposed to standard fire. [4]

5 PROTECTION BY NON-HEAT-RESISTANT MINERAL WOOL

Non-heat-resistant mineral wool products will undergo decomposition when exposed directly to fire. A proposal for a post-protection stage is worked out which takes a recession speed of the insulation into account; for most of the traditional glass wool products in Europe a value of $v = 30$ mm/min is proposed [7]. The design model for assemblies with cavities filled with glass wool insulation may be applied to other insulation materials that undergo thermal degradation above a critical temperature. In this case, the surface recession rate must be determined, e.g. by performing fire tests with the insulation in dense contact with the timber member.

The principle to determine the residual cross-section is shown on Figure 7. During the protected phase, the charring scenario is similar to the case with heat-resistant mineral wool. Charring at protected phase is regarded according to Equations (1) and (2) as for heat resistant mineral wool. There will be charring from three sides during the post-protection phase with respect to the delay of charring following the recession of mineral wool.

Further simplifications for this trapezoidal model are proposed in [7] where the use of equivalent rectangular cross-sections is proposed where different cross-sections can be determined for different applications (beams and studs).

The practical range of interest in Figure 8 is $W_{\text{fi}}/W = 0,2$ to $0,4$. W_{fi} is the section modulus of the residual cross-section needed to provide load carrying capacity in fire situation. If the stud has dimensions for example 95×195 mm there is a significant additional protection time provided by glass wool. Compared to limitations given in [1] the verification of timber construction can be continued at post protection phase. In the presented example additional 10-15 minutes can be achieved compared to existing rules in [1].

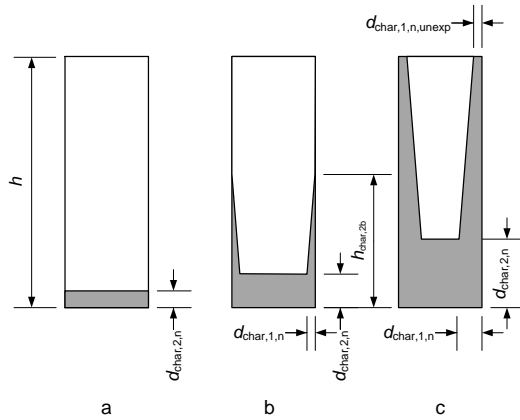


Figure 7. Charring of timber member when insulated by traditional glass wool [7]

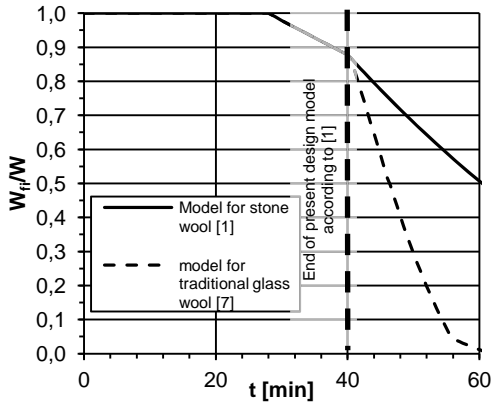


Figure 8. Example of new design model for structure with gypsum plasterboard type F (hp=15 mm) and timber studs 95 mm x 195 mm.

The model for traditional glass wool presented here may be implemented for other non-heat-resistant insulations after determining specific recession speeds.

6 DISCUSSION

According to data given in [3] the principle for design equations to determine the charring depth are based on the assumption that failure will occur before the charring depth has reached 30 mm. For larger charring depths the method may give overestimated results since a two dimensional heat effect increases the charring rate during a later stage depending on the cross-section width. This is contrary to unprotected timber members where an increased charring on the narrow side of timber cross-sections can be neglected [11]. It is proposed to take into account an increased charring rate for timber frame assemblies with insulated cavities having in mind the charring depth of 40 mm which may be realistic in many cases.

Figure 9 shows the reference fire test results with stone wool for the method reported in [3], new tests with the existing linear charring curve according to [1] and a proposed new linear curve with different slope.

Simplifications of charred cross-sections protected by heat-resistant mineral wool on the wide sides are based on the equal section modulus of the real charred cross-section and the simplified rectangular cross-section. This principle of simplifications give good results for bending elements (beams) but is conservative for studs, loaded by compression only. Different simplifications for studs and for joists are provided already for the method for non-heat-resistant mineral wool.

An important issue concerning mineral wool that must be considered by designing frame assemblies is the fixing of the mineral wool between studs and joists. Mechanical fixing can be done by fasteners or by gluing, for example. The efficiency of fixing must be proved. In some extent also overdimensions may be a solution to keep the insulation batts on place. Test results [4] show that 145 mm thick heat resistant mineral wool is staying at place in a wall assembly during 60 minutes fire without cladding at fire exposed side from the beginning of fire. Thinner mineral wool batts may fall off during fire. Mechanical fixing of the cavity insulation is even more important for floor structures. If the insulation batts are not fixed, they can fall off during the fire and the protective effect can not be taken into account.

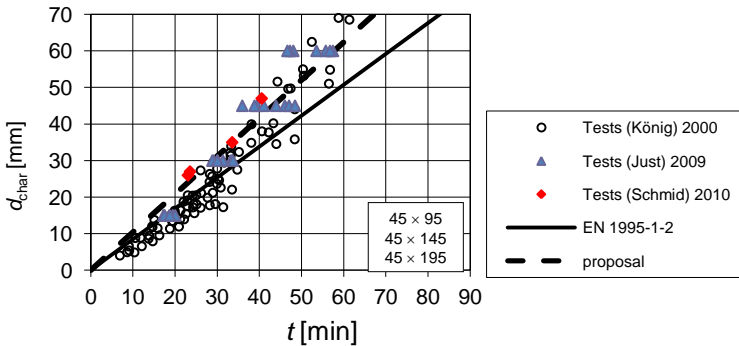


Figure 9. New and reference test results [3],[4], [10] with 45 mm wide cross-sections. Charring depth line of EN 1995-1-2 and proposal by authors of this paper is presented.



Figure 10. Hot air stream may cause local decompositions of the material (left side). Photo taken after fire test SP Wood Technology

Air tightness of assemblies is an important issue. With air flow through the structure at high temperatures local decompositions of mineral wool may occur. See Figure 10.

7 CONCLUSIONS

Existing design methods in EN 1995-1-2 should be slightly revised and improved for next revision of EN 1995-1-2. Classification of mineral wool should not be a subject of EN 1995-1-2. Grouping into heat-resistant mineral wool and non-heat-resistant mineral wool is proposed by authors of this paper. Simplified design rules should be revised taking into account different approaches for beams or studs. Research work for different stone wool products is needed.

8 ACKNOWLEDGEMENTS

Authors would like to thank European Societal Fund.

REFERENCES

- [1] EN 1995-1-2:2004, Eurocode 5: Design of timber structures – Part 1-2: General – Structural fire design. European Standard. European Committee for Standardization, Brussels, 2004.
- [2] EN 13162:2008, Thermal insulation products for buildings - Factory made mineral wool (MW) products – Specification. European Committee for Standardization, Brussels, 2008.
- [3] König, J, Walleij, L. Timber frame assemblies exposed to standard and parametric fires. Part 2: A design model for standard fire exposure. Trätec, Swedish Institute for Wood Technology Research, Report No. 0001001, Stockholm, 2000.
- [4] Just, Alar. Full scale wall tests of timber frame assemblies. Test report. Tallinn : Tallinn University of Technology, 2009.
- [5] Fire Safety in Timber Buildings. Technical guideline for Europe. SP 2010:19. Stockholm
- [6] Just, A., Schmid, J., König, J. The effect of insulation on charring of timber frame members. SP Report 2010:30, Stockholm, 2010.
- [7] Just, A. Post protection behaviour of wooden wall and floor construction completely filled with glass wool. I, SP-report 2010:28, Stockholm, 2010.
- [8] Schleifer, V. Zum Verhalten von raumabschliessenden mehrschichtigen Holzbauteilen im Brandfall. PhD Thesis No. 18156, ETH Zürich, 2009
- [9] Just, A. Structural fire design of timber frame assemblies insulated by glass wool and covered by gypsum plasterboards. PhD thesis, Tallinn University of Technology. Tallinn, 2010
- [10] Schmid, J, König, J, Just, A., Model scale fire tests of Isover Ultimate – Step 1.2: Load bearing capacity, SP report 2010:26, Stockholm. 2010.
- [11] Frangi, A, König, J. Effect of increased charring on the narrow side of rectangular timber cross-sections exposed to fire on three or four sides. Fire and Materials 35:593-605

FIRE BEHAVIOUR OF FINGER-JOINTED TIMBER BOARDS

Michael Klippel, Andrea Frangi and Mario Fontana

ETH Zürich, Institute of Structural Engineering, 8093 Zurich, Switzerland
e-mails: klippel@ibk.baug.ethz.ch, frangi@ibk.baug.ethz.ch, fontana@ibk.baug.ethz.ch

Keywords: Fire tests, Adhesive, Glued laminated timber, Charring, Fire design model.

Abstract. *For timber members with fire resistance requirements, design models usually consider the loss in cross-section due to charring and the temperature-dependent reduction in strength and stiffness of timber. For bonded timber elements such as glued laminated timber beams, it has been assumed that the adhesive does not influence the fire resistance of structural timber beams significantly; however, some concern was raised recently [1]. Thus, a comprehensive research project is in progress to investigate the influence of adhesive in bonded timber elements and to develop a simplified design model for the fire resistance of bonded structural timber elements considering the behaviour of the adhesive at elevated temperature. This paper presents the results of an extensive test series on finger-jointed timber members loaded in tension and exposed to ISO-fire. Taking into account the different failure modes, no significant influence of the adhesive on the load-carrying capacity of finger-jointed timber boards was observed.*

1 INTRODUCTION

Traditionally, for bonded connections in timber structures, such as finger joints, phenolic resorcinol formaldehyde adhesives (PRF) have been used. To prevent some of the disadvantages of PRF, novel adhesives have been developed and put on the market. These latter adhesives are cheaper, permit shorter hardening times (in the case of melamine-urea formaldehyde adhesives, MUF) and, in the case of polyurethane adhesives (PUR), are also free from formaldehyde. However, fire tests carried out by König et al. [1] on glued laminated timber beams with PUR and MUF adhesives in the finger joints exhibited bending resistances of only 70 to 80% of the bending resistance of the beams with PRF-bonded finger joints. Further, on the basis of a series of tensile tests with finger joints at elevated temperatures by Frangi et al. [2], it can be expected that the behaviour of the adhesive at elevated temperature may influence the fire performance.

A comprehensive research project on the fire resistance of bonded timber elements (e.g. glued laminated timber beams, cross-laminated timber panels) is currently in progress at the ETH Zurich. The objective of the research project is the development of simplified design models for the fire resistance of bonded structural timber elements taking into account the behaviour of the adhesive at elevated temperature. As a basis for the structural fire resistance models, an extensive series of fire tests on finger-jointed specimens was performed. This paper presents the results of the fire tests. In addition, a zero-strength layer d_0 with the help of the reduced cross-section method given in EN 1995-1-2 [3] is calculated for all tests as well as a comparison of the test results with the fire design model given in EN 1995-1-2 is discussed.

2 MATERIALS AND METHODS

2.1 Test set-up and specimen

The fire tests were performed on the small horizontal furnace with dimensions of 1.0×0.8 m using fire exposure according to ISO 834 [4] at the Swiss Federal Laboratories for Materials Science and Technology (Empa) in Dübendorf. A special testing frame was developed to apply a defined tensile load on the finger-jointed board during fire exposure. A cover closed the furnace at its top during the tests (see Figure 1, left).

The specimens designed for the fire tests should describe the real behaviour of finger joints in a fire situation relevant for glued laminated timber beams. At normal temperature, failure of such engineered wood products is usually initiated due to the failure of a finger joint, failure of a knot or other defects of the naturally grown timber. To decrease variability of the test results, the highest visually graded timber boards of strength class C30, according to EN 338 [5], were selected and taken from the production line of glued laminated timber beams (made of spruce wood) in a timber industry company in Switzerland. Lamellas with visually a low number of knot defects were chosen. The lamellas were preconditioned in a climate chamber (20/65) to $12 \pm 1\%$ moisture content. The average density of the test specimens was 447 ± 36 kg/m³.

The material properties of the test specimens of both timber and adhesives were in accordance to the tests previously performed by Frangi et al. [2]. Also the same geometry of the finger joint was used. The specimens consisted of a testing board, which was finger-jointed in the middle, and lamellas glued together with this testing board on its top and bottom. These lamellas were added in order to protect the testing board against the fire exposure from its top and bottom during the test. Hereby, a one-dimensional fire exposure from the side was achieved, which makes the evaluation of the results more reliable. The testing board was not directly exposed to fire on its bottom because due to the design at normal temperature and the reduced load level in fire designs, glulam beams normally fail when the bottom fire exposed lamella is already completely charred. The assembly of a typical test specimen is shown in Figure 1, right. To ensure that in the finger-jointed region of the testing board no load is carried by the protective lamellas, a special assembly was designed. Therefore, the protective lamellas were cut and the adhesive between the protective lamellas and the testing board was only applied as can be seen in Figure 1, right. All finger-jointed specimens were prepared under the strict supervision of the manufacturers of the adhesives.

In order to achieve failure in the finger-jointed region, the effective testing length was reduced in most of the tests to about 200 mm situated in the centre of the furnace. This was done with 50 mm thick insulation material placed on both sides of the specimen (see Figure 5). The insulation material did not influence the fire exposure in the finger-jointed region, as confirmed by measuring the development of the timber surface temperature with and without insulation.

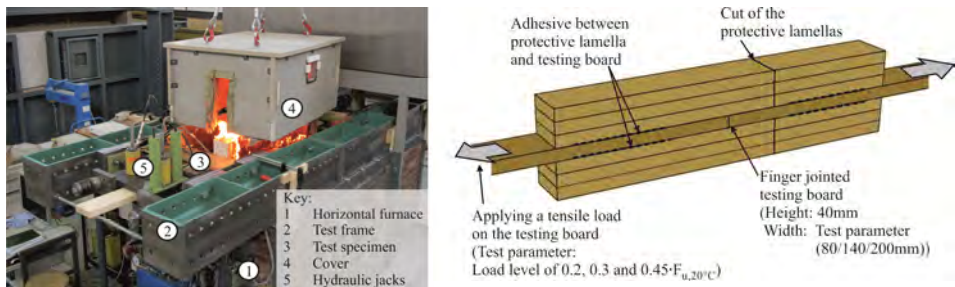
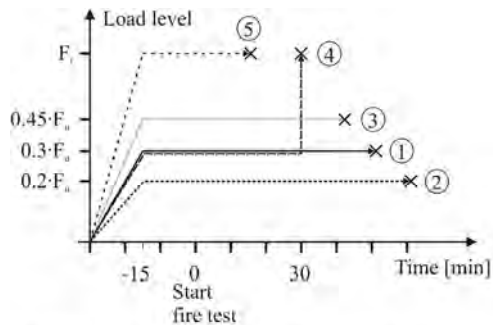


Figure 1. Test set-up while removing the cover after failure (left) and description of the test specimen (right).

To analyse the temperature development in the cross-section during the fire tests, two tests were conducted with specimens containing thermocouples placed at certain points along the cross-section width.

2.2 Test program and test parameters

The influence of different parameters on the load-bearing capacity of a finger-jointed timber board was studied. These parameters are the influence of adhesive used in the finger joint, the width of the cross-section, the load level and the type of fire exposure (one and two-dimensional) on the testing board. Thereby, two different one-component polyurethane adhesives (1K-PUR) and one melamine-urea formaldehyde adhesive (MUF) were studied in the finger joint. These adhesives were also used in the investigations carried out by Frangi et al. [2] at elevated temperatures, so that it should be possible to establish a link between these two different investigations. All adhesives fulfil current approval criteria in Europe for use in load-bearing timber components according to EN 301 [6] and EN 15425 [7].



F_u : Mean value of tensile strength at normal temperature

Figure 2. Load level during five different fire tests performed.

Table 1 gives an overview of the test program. In most fire tests a constant tensile loading in the direction parallel to grain was applied with about 10 N/mm^2 (based on the initial cross-section). This corresponds to about 30% of the mean load-carrying capacity F_u obtained in the tensile tests performed at normal temperature in [2]. The applied load level throughout the whole test can be taken from Figure 2, curve no. 1. Further, tests were performed with 20% and 45% of the average determined load-carrying capacity to study the influence of the load level applied (curve no. 2 and 3, respectively). In addition, the residual load-carrying capacity after 30 min fire exposure first loaded with $0.3 \cdot F_u$ was determined in one test (curve no. 4). The failure load determined in this test was then applied as constant load to a specimen in another fire test (curve no. 5).

3. RESULTS AND DISCUSSION

3.1 Evaluation of the fire tests

In Table 1, the mean one-dimensional charring rate measured by hand on the finger-jointed testing board after the test and the time of fire resistance is given. The fire resistance is defined as the time from start of the fire test until failure, i.e. until the applied load could not be held constant. In the following sections, the results are presented and the influence of the different parameters studied is discussed in detail.

The specimens in the tests P2.T1 and P2.T2 (according to Table 1) were equipped with thermocouples along the width of the cross-section in the finger-jointed region. The temperature was measured on both sides of the board in the depths of 30 mm and 50 mm, as well as in the depth of

70 mm, which corresponds to the middle of the cross-sections' width. Figure 3 shows the temperature development measured by the thermocouples in the finger-jointed region. It is remarkable that the temperature in 50 mm distance from the edge reached only 100°C after approximately 50 min of fire exposure. The low temperatures measured in the cross-section are due to protective function of the char-layer which is formed on the fire-exposed surfaces. The char-layer protects the remaining unburned residual cross-section against heat. This leads to a steep temperature gradient in the cross-section with low temperatures in the inner cross-section.

Table 1. Overview of test program including charring rate and fire resistance obtained in the fire tests.

Test name	Adhesive	Width [mm]	Applied load ^b [-]	Failure load [-]	Remarks (parameters tested)	One-dim. charring rate [mm/min.]	Fire resistance [min.]
P2.T1	P2	140	-		Temperature measured	0.66	-
P2.T2	P2	140	-			0.63	-
P2.1	P2	140	0.3·F _u		Load level (1) ^a , Adhesive P2	0.71	47
P2.2	P2	140	0.3·F _u			0.71	53
P2.8	P2	140	0.3·F _u			0.78	52.5
P2.10	P2	140	0.3·F _u			0.68	52
P4.1	P4	140	0.3·F _u		Adhesive P4	0.80	48
P4.2	P4	140	0.3·F _u			0.68	48
P4.3	P4	140	0.3·F _u			0.70	41
M1.1	M1	140	0.3·F _u		Adhesive M1	0.79	45
M1.2	M1	140	0.3·F _u			0.67	58
P2.80	P2	80	0.3·F _u		Width	0.78	24.5
P2.200	P2	200	0.3·F _u			0.66	66.5
P2.4	P2	140	0.2·F _u		Load level (2) ^a	0.72	59.5
P2.6	P2	140	0.45·F _u		Load level (3) ^a	0.68	35.5
P2.7	P2	140	0.3·F _u	0.60·F _u	Determination of residual strength after 30 min fire exposure (4) ^a	0.78	31.5
P2.3	P2	140	0.58·F _u		P2.7-failure load applied (5) ^a	0.62	16.5
P2.S1	P2	140	0.3·F _u		two-dimensional heat exposure	-	36
P2.S2	P2	140	0.3·F _u			-	42
V1	-	140	0.3·F _u		Solid wood	n/a	55
V2	-	140	0.3·F _u	0.63·F _u	Solid wood, determination of residual strength after 40 min fire exposure	0.83	42

^a Load level according to Figure 2

^b Given is the load level at start of the fire test (see Figure 2)

The temperature development measured in the cross-section during the fire tests was compared to results on the basis of thermal numerical analysis using two-dimensional finite element models implemented in ABAQUS [8]. The heat transfer to the member's surface was modelled using temperature-independent constant values according to EN 1991-1-2 [9] for the resultant emissivity by radiation $\varepsilon_{res} = 0.8$ and the coefficient of heat transfer by convection $\alpha_c = 25 \text{ W}/(\text{m}^2 \cdot \text{K})$. The temperature-dependent relationships for density, specific heat and thermal conductivity of wood and charcoal were

implemented according to EN 1995-1-2. The material properties of wood and charcoal used for the FE-thermal analysis were verified with a series of fire tests [10],[11]. In Figure 3, it can be seen that experimental and numerical results were in good agreement.

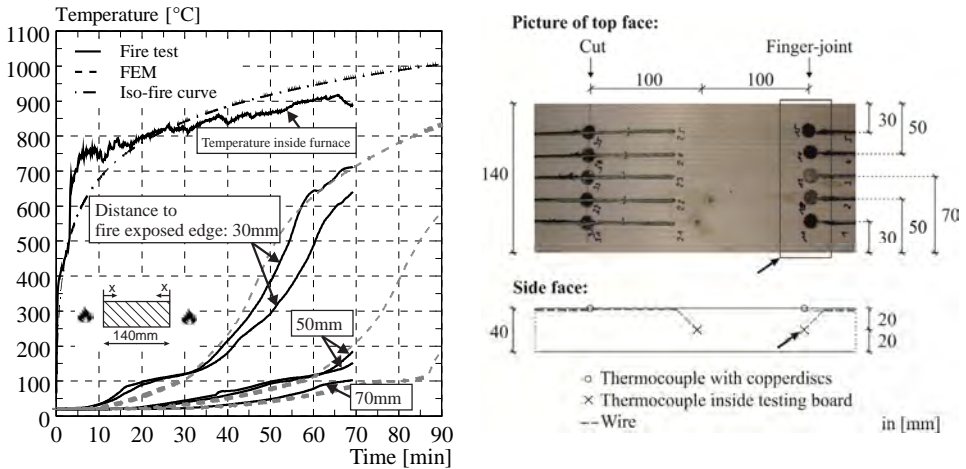


Figure 3. Temperature versus time of fire exposure measured in the test P2.T1 (left) and assembly of the thermocouples in the cross-section; the arrows indicates the location of the shown temperature development (right).

In Table 1, the one-dimensional charring rate for all tests with two sides of fire exposure is summarized. The charring rate measured by hand varied between 0.62 mm/min and 0.83 mm/min. The mean charring rate was 0.72 mm/min. This value is higher than the one-dimensional charring rate β_0 of 0.65 mm/min given in EN 1995-1-2.

Figure 4 shows the fire resistance as a function of the cross-section width depending on the failure types. Three different adhesives were tested in the fire tests (two polyurethane based adhesives (P2 and P4) and one melamine based adhesive (M1)). The adhesives are labelled according to [2]. The fire resistance varied between 40 min and 60 min for the specimens with a width of 140 mm. All specimens were loaded with a constant tensile load parallel to grain direction of $0.3 \cdot F_u$. It could be seen in some tests that weak joint sections in the solid wood region such as knots led to premature failure of the board before the finger joint reaches its maximum load-carrying capacity. Taking into account the different failure modes, no significant difference on the fire resistance was observed between the adhesives studied. This is in contradiction to tests at elevated temperatures performed with the same types of adhesives by Frangi et al. [2], who reported an influence of the adhesive on the load-carrying capacity at elevated temperatures.

Most of the fire tests were performed with 140 mm wide specimens. To study the influence of the width of the cross-section on the load-carrying capacity, one test was performed with a 80 mm wide specimen and a 200 mm wide specimen both loaded with $0.3 \cdot F_u$. A reduction of the cross-sections' width from 140 mm to 80 mm decreased the fire resistance significantly. However, an increased cross-section of 200 mm led to a rather low increase in the fire resistance. A greater fire resistance was expected in this test. It is interesting to note that additional reference tests at normal temperature on 200 mm wide specimens from the same production line showed indeed the same tensile strength as 140 mm wide specimens, however, a noticeable great amount of failure along the fingers was observed. Due to the fact that only one fire test with increased width of the cross-section was performed a reliable explanation is not possible.

To study the influence of the load level on fire resistance, one test was conducted with a reduced load of 6 N/mm^2 ($0.2 \cdot F_u$) and one test with an increased load of 14 N/mm^2 ($0.45 \cdot F_u$), respectively. All tests were performed on 140 mm wide specimens with adhesive P2 in the finger joint. For the test with

reduced load level of $0.2 \cdot F_u$ the fire resistance increased to approximately 59 min which is 8 min (16%) more than in the average fire resistance with a standard load level of about $0.3 \cdot F_u$. In the test with increased load level ($0.45 \cdot F_u$), failure occurred after 35 min of fire exposure which is a decrease of 16 min (31%) in comparison to the mean fire resistance obtained in tests with a load level of $0.3 \cdot F_u$.

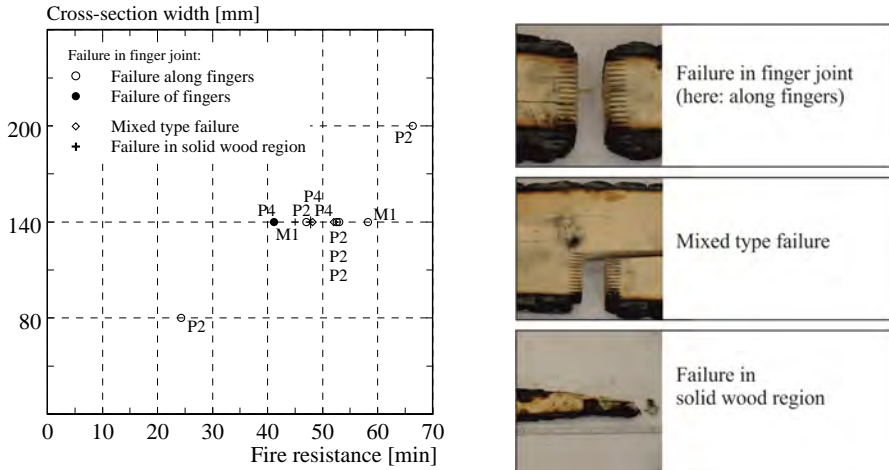


Figure 4. Fire resistance as a function of the cross-section width depending of the failure type and adhesive (P2, P4, M1). The specimens were loaded with a constant tensile load parallel to grain direction of $0.3 \cdot F_u$ (left) and corresponding crack patterns observed (right).

To investigate the difference of fire resistance for timber lamellas with different location in a glued laminated timber beam, two tests were performed with only one protective lamella glued on the bottom of the testing board, see Figure 5, left. This assembly leads to an influence of fire exposure on the testing boards from three sides. The fire resistance for two tests performed with this assembly was 10 to 15 minutes lower than the mean fire resistance (51 min.) obtained for finger-jointed lamellas protected until failure on its top and bottom and only exposed to fire on two sides. With the comparison of these tests, it is possible to draw conclusions about the influence of the lamellas' location in a glulam beam on the fire resistance.

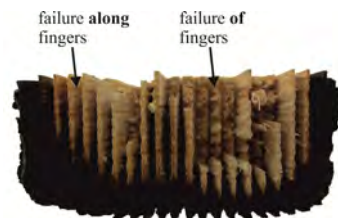
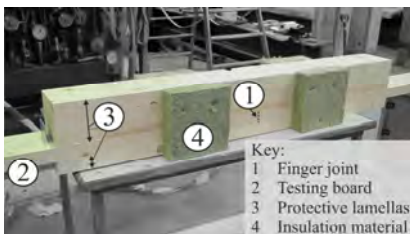


Figure 5. Test specimen (P2.S2) before the fire test equipped with insulation material on its side (left) and finger joint of test P2.S2 after the fire test, which was influenced by heat/fire from three sides (right).

Figure 5, right shows failure pattern of a finger joint exposed to heat/fire on three sides, whereas the bottom side was initially protected by a 40 mm thick timber lamella. It can be seen from the failure pattern that in the inner region of the lamella with comparatively low temperature failure of timber fibers occurred (indicated by failure of fingers). Closer to the fire exposed sides and with increasing temperature, more failure along the fingers occurred. This is in accordance to tests at elevated temperature in [2], which showed very often failure along the fingers with increasing temperatures.

3.2 Determination of zero-strength layer thickness d_0

Fire reduces the cross-section and the stiffness and strength of the heated timber close to the burning surface. The pyrolysis zone can be located between 200°C and 300°C; the front of the charred layer is found at a temperature of about 300°C [12],[13]. The temperature-dependent reduction in strength and stiffness near the charred layer can be considered by introducing an effective cross-section using the “Reduced cross-section method” according to EN 1995-1-2. Thus, an additional layer d_0 is added to the notional charring depth $d_{char,n}$. This additional layer d_0 is called “zero-strength layer” and for columns and beams has a constant depth of 7 mm. This approach was originally derived for glued-laminated timber beams. Here, the depth of the zero-strength layer was 0.3 inches (corresponding to 7.6 mm) [14]. It is assumed that the zero-strength layer is built up linearly with time during the first 20 minutes of fire exposure [12], see Figure 6. By using the reduced cross-section method, the designer requires only strength and stiffness properties of timber at normal temperature. The remaining cross-section is not affected by the temperature, hence, the modification factor is taken as $k_{mod,fi} = 1.0$ for the effective cross-section. The one-dimensional charring depth $d_{char,0}$ is determined from the relevant time of fire exposure and the one-dimensional charring rate β_0 . Thus, the effective charring depth d_{ef} is calculated as follows:

$$d_{ef} = d_{char,0} + k_0 \cdot d_0 = \beta_0 \cdot t + k_0 \cdot d_0 \quad (1)$$

d_{ef} effective charring depth

$d_{char,0}$ one-dimensional charring depth

β_0 one-dimensional charring rate perpendicular to the grain

t time of fire exposure

k_0 $k_0 = 1.0$ for $t \geq 20$ minutes; $k_0 = t/20$ for $t < 20$ minutes

d_0 zero-strength layer: $d_0 = 7$ mm

For the performed fire tests, the finger-jointed specimens were exposed to fire on two sides since the testing board was protected on its top and bottom by the protective lamellas (see Figure 1, right). For the fire tests, the zero-strength layer d_0 was calculated back using the mean tensile strength at normal temperature $f_{t,m}$ obtained in [2]. According to the reduced cross-section method, the failure load $F_{t,fi}$ measured in the tests (see Table 1) can be calculated by multiplying the mean tensile strength $f_{t,m}$ with the effective cross-section A_{ef} as follows:

$$F_{t,fi} = A_{ef} \cdot f_{t,m} = [h \cdot (b - 2 \cdot (\beta_0 \cdot t + d_0))] \cdot f_{t,m} \quad (2)$$

with h being the height ($h = 40$ mm) and b the width of the initial cross-section of the testing board.

The zero-strength layer d_0 was calculated by using equation (2) and the one-dimensional charring rate β_0 measured by hand (see Table 1) in each fire test. Figure 6 shows the zero-strength layer d_0 depending on the fire resistance obtained in the tests. The mean zero-strength layer $d_{0,mean}$ for all fire tests was calculated as 14.1 mm. However, some values differ significantly from this mean value and are indicated in Figure 6 by a surrounding circle. Very high d_0 -values were obtained for tests in which a comparatively high amount of failure of the fingers occurred. This failure is caused by exceeding the wood fibres' tensile strength (test P4.2 and P4.3). For specimen P2.200, a rather high d_0 -value was calculated since the fire resistance reached in this test was lower than expected. The high d_0 -value of specimen P2.3 can be explained by the high load level of $0.58 \cdot F_u$ and the subsequent failure in the solid wood region. Very low d_0 -values were calculated for tests P2.7 and V2, in which the residual strength was investigated after 30 and 40 minutes, respectively (see Figure 2 no. 4). One possible reason for this is that in both tests the load level was increased rapidly within one and two minutes. Excluding these d_0 -values, the mean d_0 -value was calculated as 13.2 mm. This value is higher than the d_0 -value currently used in EN 1995-1-2, however, this fact is not attributed to the adhesive used in the finger joint. It is worth to mention that one test was performed to obtain the fire resistance on a solid wood specimen (unjointed). This test is marked with V1 in the diagram and a d_0 -value of 8.7 mm was calculated.

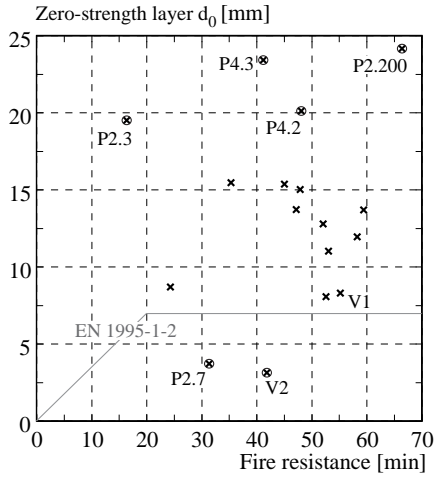


Figure 6. Zero-strength layer calculated back from the fire tests depending on the fire resistance.

3.3 Comparison to Eurocode 5

The results of the fire tests performed were compared to calculations according to the “Reduced cross-section method” given in EN 1995-1-2. For the calculation, the timber strength as well as all other factors were chosen based on European standards. The characteristic tensile strength $f_{t,k}$ of the visual graded timber (C30) was taken from EN 338 to be 18 N/mm^2 . For the calculation of the designed fire resistance $R_{d,fi}$ the design tensile strength value in fire $f_{t,d,fi}$ of timber is determined according to EN 1995-1-2 as follows:

$$f_{t,d,fi} = k_{mod,fi} \cdot \frac{f_{t,20}}{\gamma_{M,fi}} = k_{mod,fi} \cdot \frac{k_{fi} \cdot f_{t,k}}{\gamma_{M,fi}} \quad (3)$$

- $f_{t,d,fi}$ design tensile strength of timber in fire
- $f_{t,k}$ 5% fractile characteristic strength properties of timber (bending strength, tensile strength, shear strength, etc) at normal temperature
- k_{fi} modification factor for fire, taking into account the 20% fractiles of strength properties of timber ($f_{t,20} = k_{fi} \cdot f_{t,k}$), $k_{fi} = 1.25$ for solid timber
- $k_{mod,fi}$ modification factor for fire taking into account the effects of temperature on the strength properties of timber
- $\gamma_{M,fi}$ partial safety factor for timber in fire ($\gamma_{M,fi} = 1.0$)

Figure 7 compares the fire tests with a design according to the reduced cross-section method (RCSM) in EN 1995-1-2 using 20% fractile of the tensile strength and a zero-strength layer $d_0 = 7 \text{ mm}$. In this evaluation the one-dimensional charring rate $\beta_0 = 0.72 \text{ mm/min}$, measured in the fire tests of 140 mm wide specimens, is used. The comparison shows that one of the fire tests performed with a 140 mm wide cross-section did not fully reach the fire resistance predicted by the standard. However, in this test failure in the finger joint with a large amount of failure of the fingers occurred (the timber tensile strength was exceeded). Further, the only test performed with a specimen of a cross-section width of 200 mm did not reach the fire resistance according to this evaluation based on the reduced cross-section method in EN 1995-1-2. As described in the above sections, a reliable explanation for this fact based only on one test is not possible.

Figure 7 also shows an assessment according to the reduced cross-section method (RCSM), however, using the mean tensile strength $f_{t,m}$. The assessment is shown for a zero-strength layer of both $d_0 = 7$ mm and $d_0 = 10$ mm. A zero-strength layer $d_0 = 10$ mm was used based on the assessment in [15] in which an increased value for members subjected to tension was proposed. The calculation of the fire resistance with an increased d_0 -value leads obviously to a more conservative approach resulting in a lower design fire resistance. It is worth to note that the evaluation using an increased d_0 -value of 10 mm is closer to the mean fire resistance of the specimens with a cross-section width of 140 mm than the evaluation with a d_0 -value of 7 mm. On the basis of the test results afore discussed, it can be concluded that the fire resistance was not limited by the adhesive. All adhesives tested in this investigation fulfil current approval criteria for the use in load-bearing timber components in Europe and exhibited sufficient strength in the fire tests.

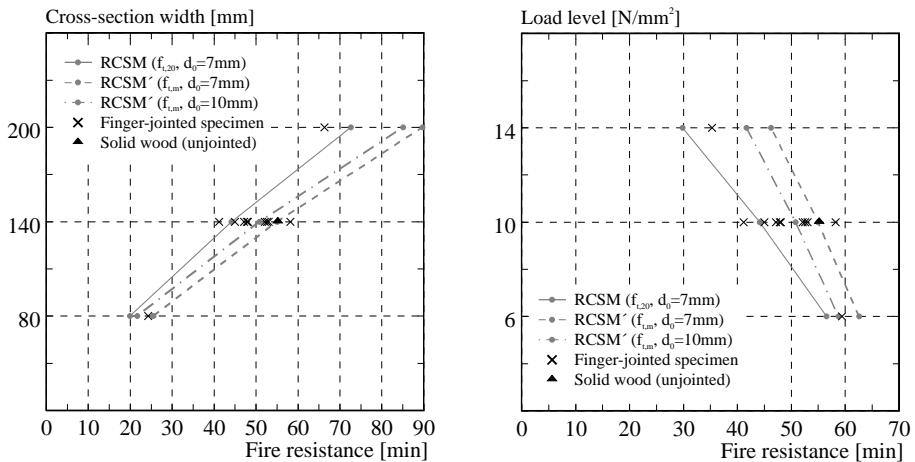


Figure 7. Comparison of the fire tests with a design according to the reduced cross-section method (RCSM) using 20% fractile of the tensile strength and a zero-strength layer $d_0 = 7$ mm according to EN 1995-1-2. The measured charring rate β_0 according to Table 1 is used. In addition, the evaluation is shown with mean tensile strength at normal temperature ($f_{t,m}$) for both a zero-strength layer of $d_0 = 7$ mm and $d_0 = 10$ mm.

4 CONCLUSIONS

The behaviour of finger-jointed timber boards was studied with an extensive testing program under ISO-fire exposure. Particular attention was given to the analysis of different influences on the load-carrying capacity such as the influence of the adhesive, influence of the width, influence of the load level and the influence of the type of fire exposure.

The set-up and the specimens' assembly were suitable for the purpose to investigate the fire behaviour of finger-jointed timber boards. Three different adhesives were tested in the fire tests. These adhesives fulfil current approval criteria according to EN 301 and EN 15425 for the use in load-bearing timber components in Europe. Taking into account the failure pattern, no significant difference was observed between these adhesives. It could be shown that the higher loss of strength for some adhesives tested at elevated temperature does not necessarily lead to the same loss of strength in fire, since defects like knots may be dominant - depending on the strength class (grading). In commercially graded glued laminated beams including boards with a large knot area ratio these defects may be the main cause of failure, whereas high quality lamellas will lead to more failures of finger joint.

The specimens tested in this experimental analysis meet the requirements of the design model according to the "Reduced Cross-Section Method" given in EN 1995 1-2. All adhesives tested showed sufficient strength in fire.

Based on the fire tests and additional analysis using finite element software, Monte-Carlo simulations will be performed to evaluate the fire resistance of glued laminated timber beams considering both the strength of timber and finger joint. The simulation will give the basis to develop a simplified design model for the fire resistance of bonded structural timber elements taking into account the behaviour of the adhesive at elevated temperature.

REFERENCES

- [1] König, J., Norén, J., and Sterley, M., "Effect of adhesives on finger joint performance in fire." *Proc., Meeting 41 of the Working Commission W18-Timber Structures, CIB, Int. Council for Research and Innovation*, Venice, Italy, Paper No. CIB-W18/41-16-11, 2008.
- [2] Frangi, A., Bertocchi, M., Clauß, S., Niemz, P., "Mechanical behaviour of finger joints at elevated temperatures." *Wood Science Technology*, DOI: 10.1007/s00226-011-0444-9, 2011.
- [3] European Committee for Standardisation (CEN). "Eurocode 5 – Design of timber structures, Part 1-2: General – Structural fire design." *EN 1995-1-2*, Brussel, Belgium, 2004.
- [4] International Organization for Standardization (ISO). "Fire-resistance tests – Elements of building construction – Part 1: General requirements." *ISO 834-1*, Geneva, Switzerland, 1999.
- [5] European Committee for Standardisation (CEN). "Structural Timber - Strength classes." *EN 338*, Brussel, Belgium, 2009.
- [6] European Committee for Standardisation (CEN). "Adhesives, phenolic and aminoplastic, for load-bearing timber structures – classification and performance requirements." *prEN 301*, Brussel, Belgium, 2011.
- [7] European Committee for Standardisation (CEN). "Adhesives - One component polyurethane for load bearing timber structures – Classification and performance requirements." *EN 15425*, Brussel, Belgium, 2008.
- [8] Dassault Systems Simulia: ABAQUS Online Documentation. Version 6.11, 2011.
- [9] European Committee for Standardisation (CEN). "Eurocode 1 – Actions on Structures - Part 1-2: General Actions - Actions on Structures Exposed to Fire." *EN 1991-1-2*, Brussel, Belgium, 2002.
- [10] König J, Walleij L. One-dimensional charring of timber exposed to standard and parametric fires in initially unprotected and postprotection situation. Swedish Institute for Wood Technology, Trätekt Report I 9908029, Stockholm, 1999.
- [11] Klippel, M., Frangi, A., Fontana, M., (2011). "Influence of the adhesive on the load-carrying capacity of glued laminated timber members in fire". *Proceedings of the 10th Symposium on Fire Safety Science*, University of Maryland, Baltimore, USA.
- [12] König J. (2005). "Structural fire design according to Eurocode 5 - Design rules and their background." *Fire Mater.*, 29, 147–163.
- [13] Schaffer, EL. (1967). "Charring Rate of Selected Woods - Transverse to Grain." *Research Paper FPL 69*, Forest Products Laboratory, Madison.
- [14] Schaffer, EL., Marx, CM., Bender, DA. and Woeste, FE. (1986). "Strength Validation and Fire Endurance of Glued-laminated Beams", *Research Paper FPL 467*. Forest Prod. Lab.: Madison.
- [15] Cachim, P.B., and Franssen JM., (2009). "Assessment of Eurocode 5 Charring Rate Calculation Methods." *Journal of Fire Technology*, 46 (1), 169-181.
- [16] European Committee for Standardisation (CEN). "Eurocode 5 - Design of timber structures, Part 1-1: General – Common rules and rules for buildings." *EN 1995-1-1*, Brussel, Belgium, 2004.

DESIGN MODEL FOR WOOD I-JOISTS IN WALL ASSEMBLIES EXPOSED TO FIRE

Joachim Schmid* and Alar Just**

* SP Wood technology, Box 5609, SE-114 86 Stockholm, Sweden
e-mail: Joachim.Schmid@sp.se

** SP Wood technology, Box 5609, SE 114 86 Stockholm, Sweden and Tallinn University of
Technology, Ehitajate tee 5, EE 19086 Tallinn, Estonia
e-mail: Alar.Just@sp.se

Keywords: Fire, I-Joist, Wall assembly, Buckling, Design model.

Abstract. *Recently a first design model for I-joists for single span floor exposed to fire from below was published in a European handbook for design of timber structures exposed to fire. However other cases as well as the design of I-joists in wall assemblies are not covered. A study was conducted to investigate the behaviour of I-joists when the exposed side is in compression. The study includes reference tests at ambient conditions, loaded model scale fire tests as well as a loaded full scale verification test. As a result for a design model in terms of known design principals is proposed. Limitations and further research needs are given.*

1 INTRODUCTION

Engineered wood makes optimum use of a renewable forest resource by combining different materials. Wood I-joists have wood flanges, the web can be metal or wood based material. In this study I-joists with wood based web are investigated. Wood I-joists provide a lot of advantages compared to sawn lumber. Wood I-joists are widely used in the Scandinavian countries as well as overseas for floor constructions where more than 50% of new produced wood frame floor constructions are wood I-joists. Due to the oil crises first technical approvals for I-joists in wall assemblies were carried out 1978 in Sweden but buckling design models for fire design are still not available. This is an enormous obstacle for companies producing wood I-joists since the load bearing fire performance has to be based on costly full scale test. For single span floors with I-joists a design model was recently published [1].

Eurocode 5 (EN 1995-1-2) [2] is the design standard in Europe for timber structures exposed to fire but no information is given regarding I-joists. This study provides first proposals for a design model of wall assemblies with I-joists in terms of the design principles of [2].

The I-joists are assumed to be integrated in floor or wall assemblies consisting of joists, linings made of gypsum plasterboard or wood-based panels, cavities completely filled with mineral insulation (glass wool or rock wool), and a decking. Test results are compared to earlier results of a numerical study, limitations of the design model and the constructions are discussed. Test results are presented in details in [3].

2 DESIGN OF TIMBER MEMBERS AT ELEVATED TEMPERATURES – THE MODEL OF EN 1995-1-2

According to the procedure of EN 1995-1-2 [2] the design of timber members shall be performed in two steps:

In a first step the residual cross-section is to be determined considering the timber member itself and the protection if attached.

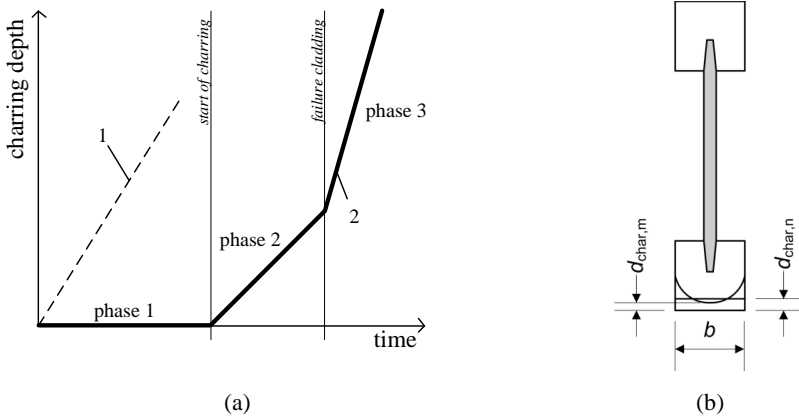


Figure 1: Charring phases (a) of initially unprotected timber members (1) and initially protected members (2). Determination of the notional charring depth for I-joists (b).

By using a converting factor k_n for a burnt cross-section the residual cross-section is converted to a rectangular geometry using a notional charring depth, see Figure 1 (b). The after protection phase (phase 3) after failure of the cladding (t_f) shows increased charring which is not reduced for small timber members.

In a second step the strength and stiffness of the residual cross-section are to be reduced since timber exposed to fire exhibits lower strength and stiffness values. To consider the reduction of mechanical properties [2] as well as other standards and handbooks provide two methods: The reduced cross-section method (RCSM) uses a zero-strength layer to compensate losses in strength and stiffness to determine an effective cross-section the reduced properties method (RPM) gives modification factors in comparison to available methods for the design of steel structures at elevated temperatures. This paper uses the RPM to describe the reduction of strength and stiffness although for the practice the RCSM is easier to use. For this purpose the modification factors proposed here can be used to derive zero-strength values for further use.

3 DETERMINATION OF MODEL PARAMETERS FOR I-JOISTS IN WALL ASSEMBLIES

This study bases on model scale tests, one full scale test and a detailed test analysis. After reference tests to investigate the material properties used for the following model scale tests eight model scale tests were performed with exposed side in compression. Two tests were performed with exposed side in tension and one full scale wall test was conducted. For claddings single gypsum plaster boards type A as well as F according EN 520 [4] and combinations were used. Tests were performed with different loads which resulted in different times to failure and charring depths respectively. For the design of I-joists at elevated temperatures modification factors were determined based on (1) and (2).

$$k_{mod,fi} = \frac{M_{fi} W}{M W_r} \tag{1}$$

$$k_{\text{mod},E,fi} = \frac{(EI)_{fi}}{(EI)_{orig}} \cdot \frac{I_{orig}}{I_{res,cold}} \quad (2)$$

where

- M is the bending moment resistance under ambient conditions;
- M_{fi} is the bending moment resistance in the fire situation
- W_r is the section modulus of the residual cross-section of the I-joist
- W is the section modulus of the original cross-section of the I-joist
- $(EI)_{orig}$ is the flexural stiffness of the original, uncharred cross-section
- $(EI)_{fi}$ is the flexural stiffness in the fire situation
- I_{orig} is the moment of inertia of the original cross-section
- $I_{res,cold}$ is the moment of inertia of the residual cross-section

The decrease of the load bearing capacity M_{fi} , the flexural stiffness $(EI)_{fi}$, the development of the charring $d_{char,m}$ as well as the geometry W_r and $I_{res,cold}$ of the I-joist after fire exposure were investigated by means of tests.

4 PERFORMED TESTS

Ambient tests were done before the fire tests, followed by model scale tests with exposed side in compression to simulate the buckling of wall studs. To verify the proposed design procedure one full-scale wall test was performed. To verify the existing model for I-joists in single span floor assemblies [1] additional model scale tests were done with exposed side in tension. All tests were performed with I-joists of the same batch. I-joists H200 with a depth of $h=200$ mm were tested with timber flanges 47mm x 47mm originally graded C30 and cleaved. Additional specific requirements regarding knots have to be fulfilled. The web is a high density wood based board (HB.HLA2 according to [5]).

4.1 Reference tests

Before the fire tests reference tests were done at ambient conditions to verify actual material properties and to derive the load bearing capacity for the following loaded model scale fire tests. Reference tests included the determination of the modulus of elasticity of a total number of 45 I-joists. In a next step 10 I-joists were selected with equal interval of measured stiffness and bended until failure. The moment capacity was determined by means of a four-point ramp load tests with span of $18h$ (1200 mm+1200 mm+1200 mm). To avoid failure caused by lateral buckling of the flange in compression the side in compression was supported approximately at every 350 mm.

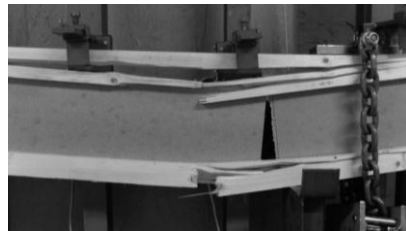
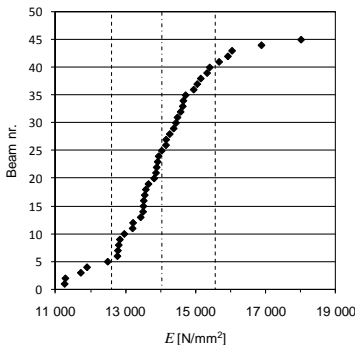


Figure 1: Results of dynamic stiffness measurements of 45 I-joists H200 (left). Reference test set-up with supported flange in compression (right).

Taking into account the failure type (tension failure and compression failure) the results of the reference bending tests I-joists were grouped to derive a function between stiffness and moment capacity at ambient temperature.

It was shown that the correlation of the failure load and the stiffness measured is greater than between density and failure load as used in other studies. Using the correlation between failure load and modulus of elasticity the ultimate load for the I-joists tested in the fire situation were determined. Results were used to define the load applied in the model scale tests. For the full scale wall tests beams with similar stiffness were used.

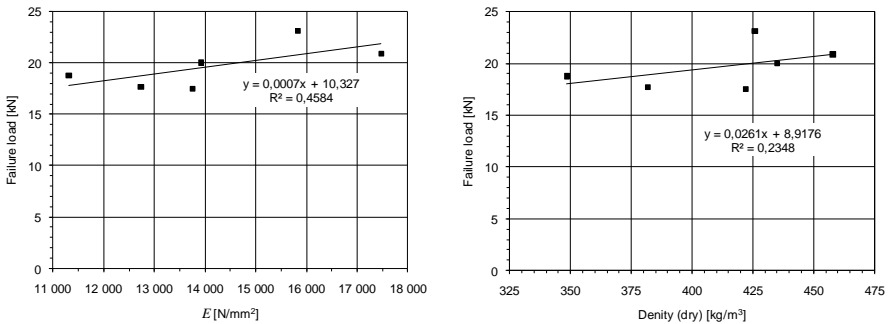


Figure 3: Correlation between failure load in compression and modulus of elasticity (left) and density (right).

4.2 Model scale tests with exposed side in compression

To consider the buckling behaviour a test series focused on the reduction of stiffness when the compression side of the I-joist is exposed to fire since wall test specimens with timber frame assemblies always deflect away from the fire. For the model scale tests a cubic gas fired furnace ($d=w=h=1000\text{ mm}$) was used, see Figure 4. The supports of the specimens were on the furnace walls outside the heated zone of one metre. The loads were applied in downward direction to have the flange in compression on the fire exposed side which corresponds the behaviour of wall assemblies.

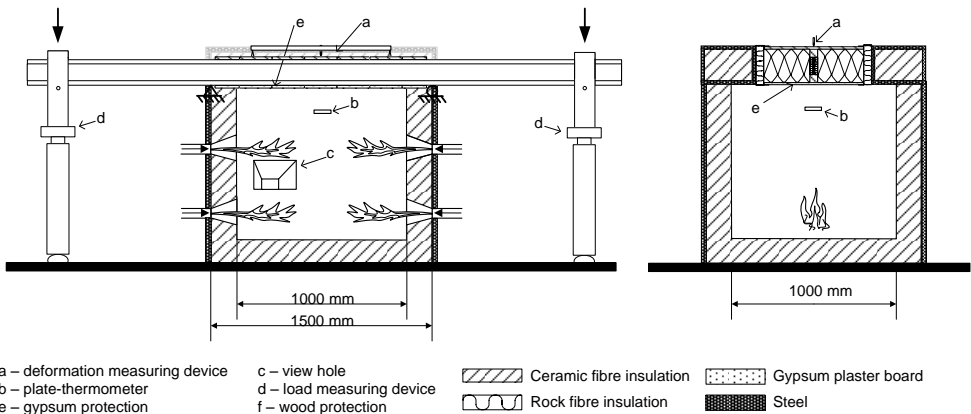


Figure 4: Test furnace, location of test specimen and loading equipment.

In the model scale tests of this series, specimens with initially protected I-joists with exposed flange in compression were tested. The loads were applied prior to the fire tests, then the furnace was started and the loads were kept constant until failure. When the load could not be held constant, the burners were

turned off, the specimen removed from the furnace and the fire in the wood extinguished with water. The time elapsed from turning off the burners to extinguishing the fire was normally from 1 to 1,5 minutes.

Since the decrease of stiffness is crucial for the load bearing capacity of columns deflection measurements were done using a length transducer. The time to failure (TTF) as well as the decrease of stiffness is highly depending on the protection of the loaded member. Thus different types of test specimens using different protections were tested; see Figure 2.

For the cladding gypsum plaster boards type F (GtF, fire rated board) and gypsum plaster boards type A (GtA, regular board) according to [4] were used. No composite action was possible between the I-joist and lining and the decking respectively. Figure 5 shows two types of tested specimens.

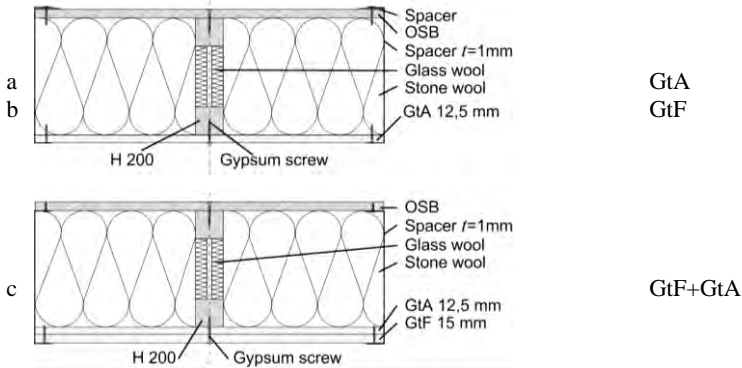


Figure 2: Cross section of the specimens of tests of series a, b and c.

For the test result and the development of the model to be proposed the data of the model scale test were evaluated. Test results for the evaluation of the residual cross section and the decrease of strength as a function of the notional charring depth $d_{char,n}$ are presented in Figure 6. The charring depth was evaluated using temperature measurements within the cross section in depths of 6, 12 and 18 mm. Additionally the charring depth of the residual cross section was determined. The decrease of load bearing capacity can be described as a function of time but as a function of the charring depth as well. The latter allows the possibility to consider different protection types and combinations.

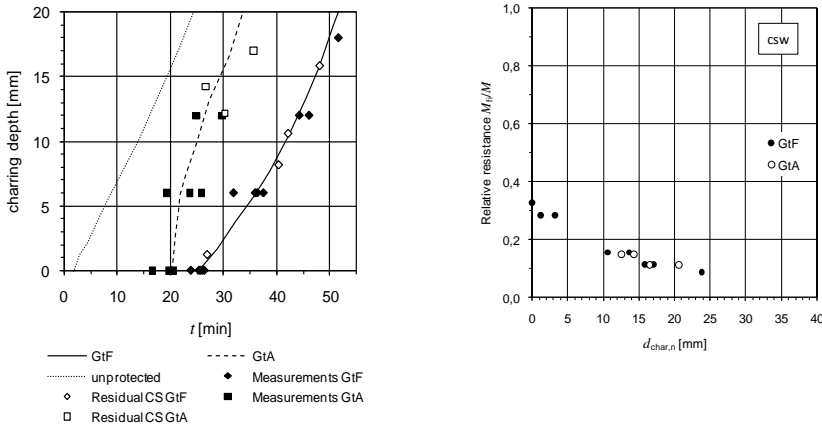


Figure 6: Simulated charring depths (curves) and measured depths $d_{char,m}$ (left); relative bending resistance vs. time (right).

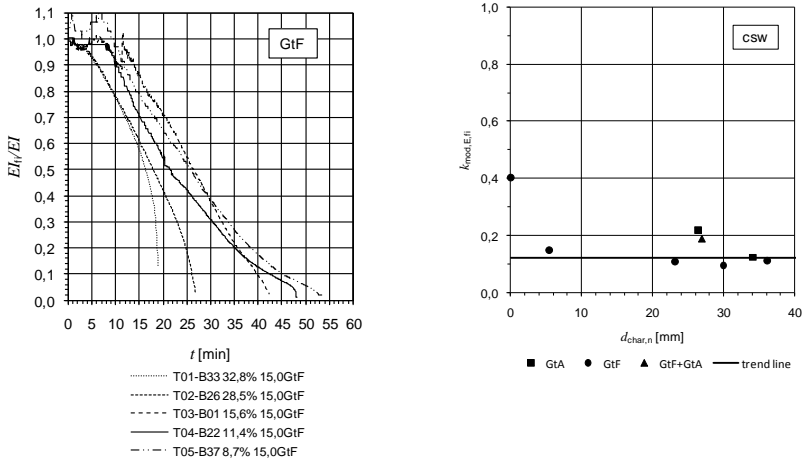


Figure 7: Bending stiffness of model scale tests of specimens protected by gypsum plaster boards type F (left). Modification factors for modulus of elasticity vs. notional charring depth for the tested I-joist H200 with exposed side in compression (right).

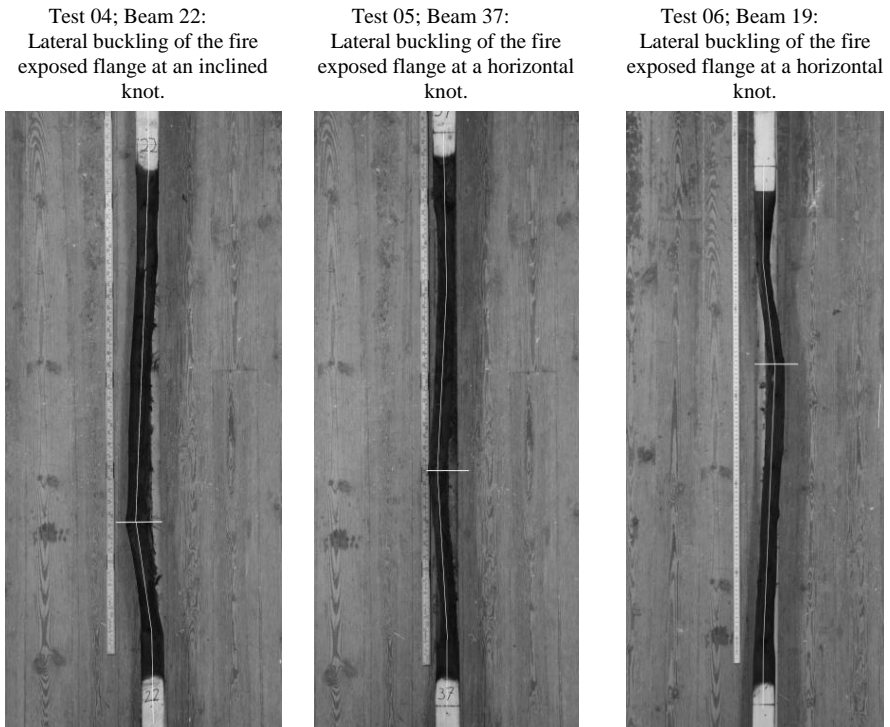


Figure 8: Examples of failure modes of I-joists. The fire exposed length was 1000mm. The centre line of the exposed flange and positions of knots are marked in the figures.

Using the results of Figure 6 as well as the geometry of the residual cross section at failure by means of equation (1) modification factors for strength were derived.

Using the geometry of the residual cross section at failure as well as deflection measurements during the tests and equation (2) modification factor for the stiffness were derived, see Figure 7: the trend line for $k_{mod,fi,E}$ depending on the notional charring rate $d_{char,n}$ is a constant line which is not expected.

By investigating the failure modes of the I-joists tested an explanation of the constant value may be found by a complex stability problem. The failure can always be lead back to a defect of the fire exposed flange. Beam 19 shows very clearly that the failure is predominantly not a failure of timber: while ca. 200 mm away from the knot a minor residual cross section can be observed the failure was caused by lateral buckling due to a knot.

Buckling of the exposed flange to the sides was observed to be crucial and linked to the appearance of centric knots; compare Figure 8 which shows the typical failure mechanism of a charring flange. Defects and centric knots appear as an important element of uncertainty for I-joists exposed to fire later in the design model. The failure mode can be described by a mechanical model using “weak-link” springs, shown in Figure 9.

For small timber members used for I-joists flanges defects such as knots may be crucial. For the grading of the lamellae’s knots in the centre are rated as minor important and affect the strength class less than knots at the edges while in case of fire and advanced charring these have strong effects on the buckling behaviour.

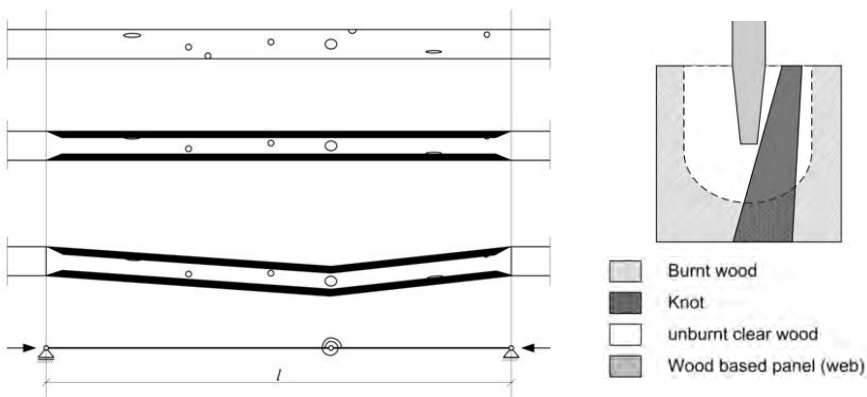


Figure 9: Failure mechanism of a I-joist flange with a centric knot in compression.

To investigate the effect of different insulation materials the charring behaviour is compared by means of simulations and tests with glass wool and stone wool insulated assemblies. Furthermore the influence of finger joints and the adhesive used respectively is demonstrated by means of loaded fire tests.

4.3 Model scale tests with exposed side in tension

Three loaded tests were conducted to compare the load bearing capacity of initially protected I-joists with and without finger joints. Model scale test were done corresponding to tests presented in 4.2. The Test were conducted with different types of claddings on the exposed side and were compared to simulation results, see Figure 10. While the test specimen GtA had no finger-joint within the exposed length specimens GtF had fire exposed finger joints.

While test GtA agrees well with the simulation result both tests specimens GtF 1 and GtF 2 failed clearly earlier than predicted due to defects. GtF 1 failed in the finger joint which was analyzed subsequently (FTIR): The result indicates that the finger joint did not show any adhesive. GtF 2 failed most likely at a screw $\varnothing 3,9$ m which led to very local charring through the flange towards the web. The distance between the web and the top of the screw was 1 mm.

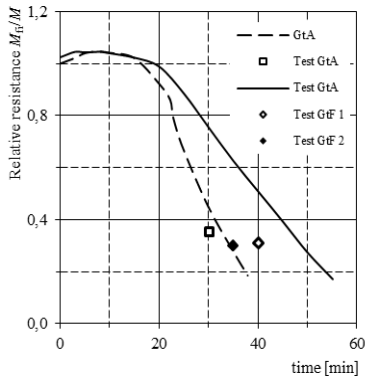


Figure 10: Simulation results for bending resistance (curves GtA and GtF) and test results (left). Cross-section of the exposed flange of the burnt but intact finger joint of test GtF 2 after the test.

4.4 Full scale wall test

The full scale test according to EN 1365-1 [7] was instrumented with additional thermocouples in the interlayer gypsum plasterboard (GtA) and I-joist. Based on the model scale test and the test results a wall was tested in full scale exposed on one side. Compared to a previous wall test certification for the same I-joist the load was increased from approximately 9 kN/stud in a 30 minutes test to 22 kN/stud; the test lasted 57 minutes.

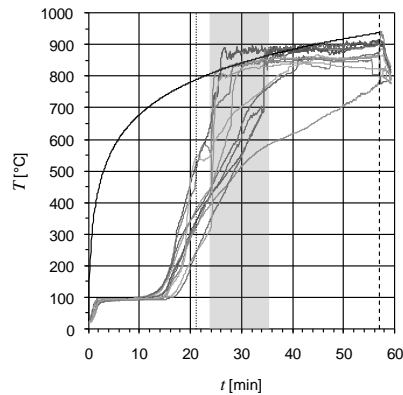


Figure 11: Full scale wall test (left). Temperature measurements in the interlayer gypsum plasterboard stud and measurements on stud 2 (right).

Figure 10 shows the failure mode of the wall, the joists at the edges were cut to not disturb the horizontal movement of the wall. The temperature measurements are shown for the interlayer behind the gypsum plasterboard, the failure of the cladding is highlighted and occurred between 24 and 35 minutes. The failure time to be assumed according to [1] is shown in dotted line, the broken line marks the failure of the wall.

Two reasons can be mentioned for the very late failure of the wall, compared to the aimed 30 minutes: The failure of the cladding (GtA) occurred late, especially on the studs but more important the support conditions reflected the reality of the construction system: contrary to [7] no hinge was attached on the

top end. Thus the load was able to move towards the non-exposed flange which was not reduced by charring.

5 MODELLING

Modelling of the residual cross section was performed using a thermal analysis (SAFIR). While the existing model developed in [6] and presented in [1] used only simulations to derive the reduction of strength in this study mainly measurements of full scale tests were used to derive modification factors for strength and stiffness.

Based on the test results the calculation model to be presented may be conservative since the modification factors for strength and stiffness which describe more or less the reduction of clear wood get mixed up with a more geometrical problem which can't be described by means of today's design process which is independent of knots. Anyhow the usage of the proposed modification factors lead to better utilization of the material than with existing certification test results. For the design of I-joists exposed on the side in compression the following relationships are proposed:

$$k_{\text{mod,fm,fi}} = 0,32 \cdot \frac{1000}{l_{\text{cr}}} \quad (3)$$

$$k_{\text{mod,E,fi}} = 0,1 \cdot \frac{1000}{l_{\text{cr}}} \quad (4)$$

where

l_{cr} is fire exposed length of the initially protected I-joist

Equations (3) and (4) are linear equations since the failure mode is related to the appearance of defects (knots) and not to a stability problem, compare Figure 7 (right) and Figure 8. By introducing a length dependency the frequency of knots may be related to the length of the tested set-up since more information is missing regarding the length dependency.

6 DISCUSSION, LIMITATIONS

For I-joists with exposed side in compression defects are crucial. It was shown that failure was always related to a knot. In today's grading standards the appearance of knots is not considered for tension members the grading does reflect questions of fire design. It is assumed that the appearance of knots (dimension and frequency) is crucial for the forming of a hinge, thus research has to be done on the critical length used in (3) and (4). For the time being the equations may be used only of the producer if the source material of the I-joists is equal to the tested ones.

The support condition is crucial for the load bearing capacity; this is already addressed by the revision of [8] where a hinge at the top end is not compulsory. The possibility of load distribution to the unexposed side has to be reflected by the connection between wall and floor, some construction methods does not allow loads to be transferred to the non-exposed side but show eccentricity towards the fire exposed side.

For I-joists with exposed side in tension it was shown that small defects may have crucial impact on the load bearing capacity. It is not clear yet if adhesives may have influence on the load bearing capacity of timber members exposed to fire. A previous study [8] showed lower moment capacity for beams with finger joints; it was concluded that some novel adhesives may have considerable influence on the load bearing capacity. Since I-joists are more sensitive to failure of a finger joint in one lamella a reduction factor was introduced in [1].

I-joists provide the possibility to test finger joints in tension easily by means of bending tests and may be used further to investigate the influence of different adhesives. Both tests with finger joints in this

research did not fail due to the adhesive but due to defects which underlines the importance of further investigation to ensure safe use of such small cross-sections for building construction. Different adhesives have to be investigated.

The influence of finger joints on the load bearing capacity of I-joists as studs is assumed to be negligible although further research is missing: if the geometry of any finger joint fits nearly no margin for movement is given for the member in compression although the adhesive may fail.

Different materials for the I-joists webs are available on the market. The heating of the end near the exposed side is limited but no investigations regarding the influence on the load bearing capacity are available. This is important since webs are cut to cross services which may weaken the structure.

7 CONCLUSION

Data presented in this paper extends the existing model for the design of I-joist assemblies given in [6] and presented in [1]. The residual cross-section is to be calculated according to [1]. Using the design equations of this paper the existing model is extended to wall assemblies. The failure of I-joists is depending on the appearance of defects and reflects a complex building material.

8 ACKNOWLEDGEMENT

The development for I-joists with exposed side in compression was funded by Masonite Beams and Vinnova. This paper was carried out at and funded by SP Wood Technology (formerly SP Trätekt), a division of SP Technical Research Institute of Sweden.

REFERENCES

- [1] Östman B.: Fire safety in timber buildings. SP Report 2010:19, SP Technical research Institute of Sweden, SP Wood technology. Stockholm, 2010.
- [2] EN 1995-1-2:2004 Eurocode 5: Design of timber structures – Part 1-2: General – Structural fire design. European Standard. European Committee for Standardization, Brussels, 2004.
- [3] Schmid, J., König, J., Just, A.: Fire exposed wooden I-joists for wall assemblies. SP Report 2011:27, SP Technical research Institute of Sweden, SP Wood technology, Stockholm, in preparation.
- [4] EN 520:2004, Gypsum plasterboards – Definitions, requirements and test methods. European Committee for Standardization, Brussels, 2004.
- [5] EN 12369-1:2001, Wood-based panels - Characteristic values for structural design - Part 1: OSB, particleboards and fibreboards. European Committee for Standardization, Brussels, 2001.
- [6] König, J, 2006, Fire exposed simply supported wooden I-joists in floor assemblies. SP Report 2006:44.
- [7] EN 1365-1:1999, Fire resistance tests for loadbearing elements - Part 1: Walls. European Committee for Standardization, Brussels, 1999.
- [8] König, J, Norén, J, Sterley, M, Effect of adhesives on finger joint performance in fire. CIB W18, Meeting 41, St. Andrews, Canada. Lehrstuhl für Ingenieurholzbau, University of Karlsruhe, Karlsruhe, Germany, 2008.

EXPERIMENTAL AND NUMERICAL ANALYSIS OF THE THERMO-MECHANICAL BEHAVIOR OF STEEL-TO-TIMBER CONNECTIONS IN TENSION PERPENDICULAR TO THE GRAIN

Maxime Audebert*, Dhionis Dhima**, Abdelhamid Bouchaïr*, Mustapha Taazount*

* Clermont Université, Université Blaise Pascal, LaMI, BP 206, F-63000 Clermont-Ferrand, France.
e-mails: (maxime.audebert; bouchaïr; mustapha.taazount)@polytech.univ-bpclermont.fr

** CSTB, 84 avenue Jean Jaurès, 77447 Marne-la-Vallée Cedex 2, France
e-mail: dhionis.dhima@cstb.fr

Keywords: Timber connections, ISO-fire tests, finite element modeling, tension perpendicular to grain, fire resistance

Abstract. *The paper presents a summary of results from a series of experimental and numerical studies on the fire behavior of steel-to-timber connections subjected to tension perpendicular to grain. Tests are conducted in cold and under ISO-fire conditions. The experimental results are presented and commented. These results are then used to validate a finite element model. This model allows simulating the heat transfer inside the connections as well as their mechanical and thermo-mechanical behaviors. The brittle character of the wood in the transversal directions has been studied for plastic yielding by Hill criterion, combined with the Tsai-Wu failure criterion. The Tsai-Wu criterion allows to take into account the asymmetry of behavior of the material between tension and compression. The numerical model allows calculating the fire resistances of the connections which are compared to the experimental failure times. It can predict with a good accuracy the thermo-mechanical behavior of the studied connections*

1 INTRODUCTION

In order to improve the fire safety of timber structures of buildings, it's necessary to have highest knowledge in the fire behavior of the connections, which are key elements. Their complex thermo-mechanical behaviour is one of the most difficult to predict. The design procedure given in Eurocode 5 (EN 1995-1-2) [1] is based on a limited number of experimental and numerical results [2, 3]. This is due to the high cost and to the complexity of the large-scale experiments of connection components in fire conditions.

Most of the available studies concerning the thermo-mechanical behavior of timber connections deal with connections subjected to tension parallel to grain. However, in real dowelled timber connections, timber is loaded in tension or compression parallel or perpendicular to grain combined with shear [4]. Thus, there is a need for testing timber connections loaded in tension perpendicular under fire exposure. In fact, due to the brittle character of the wood material in direction perpendicular to grain, the knowledge of the behavior of the connections in this direction is of main importance. In normal conditions, as well as in fire situations, the number of researches on this type of connections is limited [5, 6].

The fire behaviour of timber connections was analysed with an extensive experimental and numerical programme conducted in France from 1999 to 2010 [7-10]. The experimental part of this programme allowed to determine the fire resistance of timber connections subjected to various loadings: parallel and perpendicular-to-grain tension, tension with an angle of 45° to the grain and bending. Numerical models, validated on the basis of the experimental results, have been developed for timber connections subjected to a tension parallel to grain [11-13]. These models allowed to simulate with a good accuracy the thermo-

mechanical behaviour of the connections [12] and were used to analyse the load distribution among the fasteners of steel-to-timber connections [13].

In this study, these numerical models are adapted for steel-to-timber connections subjected to tension perpendicular to grain. In a first part, the tested connections are presented and the experimental results are commented. Then the main assumptions considered in the elaboration of the 3D finite element model are presented. The thermo-mechanical modelling is made from two different meshes; the first for the thermal modelling and the second for mechanical modelling. The heat transfer model is validated on the basis of the temperatures measured inside the connection under fire, whereas the mechanical model is validated using tests results performed in cold. Finally, the thermo-mechanical model, based on the two previous modelling, is used to simulate the thermo-mechanical behaviour of the tested connections in ISO-fire conditions. This model is validated by the comparisons of experimental and simulated fire failure time resistance of the connections, as well as the comparison of experimental and simulated (numerical) slip-time curves.

2 EXPERIMENTAL APPROACH

2.1 Characteristics of the connections

Two different types of connections, with different fasteners diameters and timber thicknesses, loaded in tension perpendicular to grain, have been tested under ISO-fire and in normal conditions (20°C). They concern a double shear steel-to-timber connection with four dowels. Six tests were realized in normal conditions in order to determine the load-displacement curves, the load-bearing capacity and mainly the stiffness of tested connections. Then, four tests were performed at CSTB under ISO-fire exposure for the same specimen types. The mechanical loads applied for connections tested in fire conditions have been defined in function of failure loads (N_u) obtained by tests carried out in cold conditions. The load ratios applied have been taken equal to: $\eta_{fi}=(10, 30 \text{ or } 45\%)*N_u$.

Two dowels diameters associated to two thicknesses of timber elements were considered. Figure 1 and Table 1 show the geometrical configurations and dimensions of the tested connections. The spacings and dimensions of these connections satisfy the requirements of EN1995-1-2. The perpendicular to grain loading is applied to the steel plate extremity (Figure 1).

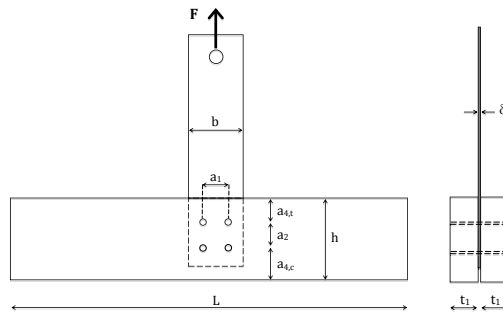


Figure 1. Geometrical configuration of the tested connections.

Table 1. Geometrical data of the tested connections (mm).

Connections	ϕ	t_1	L	h	b	δ	a_1	a_2	$a_{4,t}$	$a_{4,c}$	a_{fi}
A16	16	77.5	2000	267	115	8	65	60	65	58	42
A20	20	105	2000	320	115	10	65	60	88	88	42

2.2 Test results in normal and fire situations

In cold conditions, the relative slip between the metal plate and the timber is measured with displacement sensors. The experimental loading followed for these tests is the one of the standard NF-EN 26891. After plastic deformations due to the dowel bending, the failure occurs by wood splitting at the level of the low line of dowels, the most remote from the loaded side.

The ultimate loads obtained during the tests in cold conditions are given in Table 2. These loads are next used to define the load ratios for fire tests. The difference between the experimental ultimate loads of connections A16 and A20 is mainly due to the increase of the timber beam thickness. The experimental values are compared to the ones calculated according to Eurocode 5 (EN1995-1-1) [14]. The comparison shows that the theoretical values lower than the experimental ones. Thus, the prediction of the failure load and mode seems to be acceptable, because these results are in safety side.

Table 2. Experimental and theoretical load bearing capacities of connections.

Connections	$N_{u,test}$ (kN)				$N_{u,EC5}$ (kN)
	Test 1	Test 2	Test 3	Mean value	
A16	84.2	89.0	74.7	82.6	77.1
A20	129.1	139.1	118.1	128.8	110.6

During the fire tests, the displacement between the steel plate and the supports of the connection is measured outside the furnace using a wire displacement sensor. After a pre-loading cycle defined from NF-EN26891, the specimens are loaded to the value of the load ratio η_{fi} chosen (10, 30 or 45% $*N_{u,test}$). Then, the fire exposure, defined from the ISO 834 curve, is started and the applied mechanical load is kept constant until the failure of the connection. Several type-K thermocouples (21) are introduced at different locations inside the connection members to measure the temperatures during fire tests.

Table 3 presents the experimental values of fire resistance $t_{fi,test}$ depending on the load ratio η_{fi} . In spite of the brittle character of the timber in tension perpendicular to the grain, the obtained fire resistance durations (failure time) exceed one hour in most of tested cases. The failure mode of these connections in fire situations is the same than in normal condition. The failure occurs by wood splitting at the level of one line of dowels. The increase of the load ratio from 10 to 30 % for the connection type A16 leads to a reduction of 23 minutes of the fire resistance. For connections type A20 the increase of load ratio from 30% to 45% leads to a reduction of 7 minutes of fire resistance.

Table 3. Experimental and theoretical failure times of the connections.

Connections	η_{fi} (% $N_{u,test}$)	F_{fi} (kN)	$t_{fi,test}$ (min)
A16-1	10	8.3	71
A16-2	30	24.8	48
A20-1	30	38.7	69
A20-2	45	58.1	62

3 FINITE ELEMENT MODELING

A three-dimensional (3D) finite element model (FEM) is developed using the MSC.MARC software package in two stages to simulate the behavior of the tested steel-to-timber connections. The first stage simulates the heat transfer inside the connection components and the second stage represents the non-linear mechanical behavior of the connections in fire.

3.1 Heat transfer modeling

3.1.1 Main assumptions of the numerical modeling

The heat transfer modeling is done for the real geometry of connections. The evolutions of the thermal properties of different materials as a function of the temperature have been taken into account to simulate the heat transfer inside the connections exposed to fire.

The well-known thermo-physical characteristics of steel, as homogenous material, are assumed according to Eurocode 3 part 1.2 (EN 1993-1-2 2005) [15]. However, the thermo-physical properties of timber as orthotropic material are less known. The thermal characteristics used in the numerical simulations of the heat transfers were chosen on a basis of a sensitivity study realized from several researches results on the evolution of the thermal conductivity and specific heat versus the temperature [16]. The two models selected for the numerical model were obtained by combination of the thermal conductivity given by Janssens and the specific heat given by Fredlund/Janssens (Fig. 2) [17, 18].

The property of specific heat given by Fredlund/Janssens does not take into account the physical effects of the evaporation peak at 100°C, while the values given by other research take into account this effect. However, an important heat transfer phenomenon appears at the interface between the wood members and the steel plate. Due to the thermal gradient and pressure gradient inside timber grains a part of water migrate towards the timber-steel plate interface. The measured temperatures in fire exposure tests show the presence of a temperature plateau between 90°C and 100°C. In order to take into account the latent heat of water migrated near steel plate, a peak of specific heat of 100 kJ/(kg. K) is introduced at 100°C for 3D-FEM modeling. This value of specific heat is used only for a thin layer of timber (3 mm) in contact of steel plate in both sides. This hypothesis was validated by the simulations of heating of several tests of connections subjected to longitudinal tension [12].

<i>Temp (°C)</i>	<i>c (J/(kg.K))</i>
0	1440
20	1440
200	2140
300	720
1000	720

a) Specific heat (Fredlund / Janssens)

<i>Temp (°C)</i>	<i>λ (J/(kg.K))</i>
0	0.12
100	0.16
117	0.125
200	0.15
350	0.12
600	0.15
1000	0.22
1200	0.27

b) Thermal conductivity (Janssens)

Figure 2. Thermo-physical properties of wood used for the heat transfers modelling.

For the thermal analysis, the 3D-FEM model is developed using 20-noded hexahedral elements. By considering the symmetry, only half of the connection geometry was modeled: symmetrical plans are adiabatic surfaces. A perfect contact, with continuous meshing, is considered at all the interfaces between timber, steel plates and fasteners. The external temperature applied to the connections is given with the evolution of the normalized time-temperature curve ISO 834.

3.1.2 Results and validation of the heat transfer modeling

The validation of the thermal model concerns the comparison between tests and numerical results regarding both the average charring rate of the timber members and the values of temperatures measured.

Numerically, the charring rate can be defined as the ratio between the charring depth defined by the isotherm of 300°C and the exposure time at which this value is reached. As the charring rate is not

constant during the fire, this value of exposure time considered in the model is taken equal to the experimental fire resistance duration of the connections. From tests, the mean values of charring rates are obtained from the residual wood thicknesses measured at the end of the fire test. Table 4 summarizes the charring rate values obtained after tests and from numerical model. These results show that the heat transfer model is based on satisfactory and safe assumptions.

Table 4. Experimental and theoretical failure times of the connections.

	β_0 for lateral sides of timber members (mm/min)	β_0 for upper and lower sides of timber members (mm/min)
Tests	0.60	0.77
3D-FEM	0.70	0.77

Figures 3 to 5 show the evolutions of the calculated and the measured temperatures for different components of the connection A16.

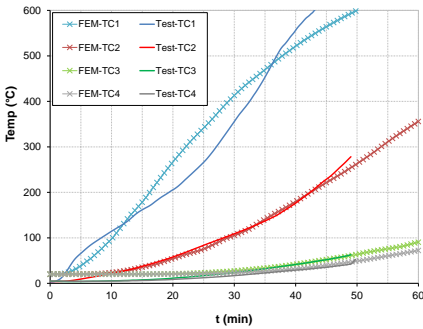


Figure 3. Numerical and experimental temperatures in timber members.

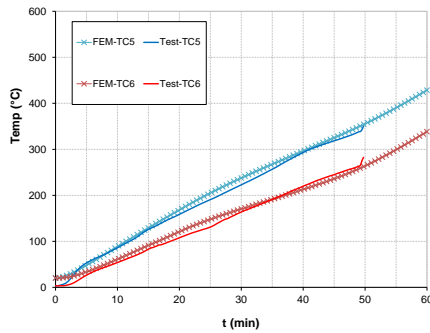


Figure 4. Numerical and experimental temperatures in fasteners.

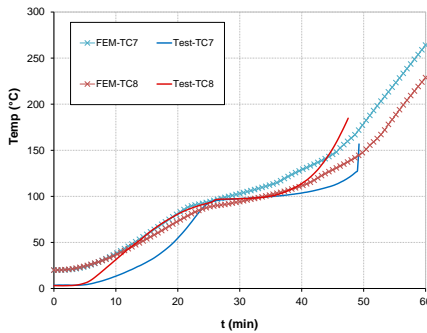


Figure 5. Numerical and experimental temperatures on steel plate.

These curves show a good agreement between measured and computed values of temperature. Similar results were obtained for all tests of the connections in tension perpendicular presented in this paper using the same thermal properties and hypothesis of the model. The validated numerical thermal model is used as a basis for the thermo-mechanical model.

3.2 Mechanical modeling

The mechanical model concerns the connections in normal conditions considering the non linear behavior of materials and the contact between the different components of the connections.

3.2.1 Main assumptions of the numerical modeling

Concerning the material modeling, steel is considered isotropic (Young modulus $E = 210\,000$ MPa and Poisson ratio $\mu = 0.3$). The mechanical characteristics of steel are taken from the stress-strain curves given by tests (yield and ultimate limits: f_y and f_u). The von Mises criterion is used to manage the plastic behavior of steel.

The timber behavior is considered with transverse isotropy assuming identical properties in the radial and the tangential directions. The laminated timber used for these tests is of class GL24h. The measured average density of the timber is 438 kg/m^3 . The mean values of the elastic modulus and the Poisson's coefficients retained are the ones relative to a laminated timber of class GL24h (Table 5).

Table 5. Mechanical properties of timber used in the model.

E_0 (MPa)	E_{90} (MPa)	G_{mean} (MPa)	$\nu_{TR} = \nu_{LT}$	ν_{RL}	ρ (kg/m ³)
11600	390	750	0.41	0.02	438

Shear and tension strength values of the timber are mean values obtained from the characteristic values of the standard NF EN 1194 by using a coefficient equal to 1,2. Longitudinal and perpendicular compressive strength ($f_{c,0}$ and $f_{c,90}$) values are determined by tests (Table 6).

Table 6. Mechanical properties of timber used in the model.

$f_{c,0}$ (MPa)	$f_{c,90}$ (MPa)	$f_{t,0}$ (MPa)	$f_{t,90}$ (MPa)	f_v (MPa)
39	3.4	19.8	0.48	3.24

The Hill yield criterion is used to manage the plastic behavior of timber components. This criterion is a generalized version of the von-Mises yield criterion to consider the anisotropy of the material (1).

$$2 \cdot \sigma^2 = a_1 \cdot (\sigma_y - \sigma_z)^2 + a_2 \cdot (\sigma_z - \sigma_x)^2 + a_3 \cdot (\sigma_x - \sigma_y)^2 + 3a_4 \cdot \tau_{zx}^2 + 3a_5 \cdot \tau_{yz}^2 + 3a_6 \cdot \tau_{xy}^2 \quad (1)$$

$$\text{with: } a_1 = \frac{2}{f_{c,90}^2} - \frac{1}{f_{c,0}^2} ; a_2 = a_3 = \frac{1}{f_{c,0}^2} ; a_4 = a_5 = a_6 = \frac{2}{3 \cdot \tau^2}$$

However, the yield Hill criterion is a symmetric criterion which does not take into account the asymmetry of the mechanical behavior of timber in compression and tension. The high difference between the values of $f_{c,90}$ and $f_{t,90}$ requires to take into account this asymmetry. Thus, the Hill criterion is combined with the Tsai-Wu failure criterion [19]. It is expressed as follow:

$$F_i \cdot \sigma_i + F_{ij} \cdot \sigma_i \sigma_j = 1 \quad \text{avec } i, j \in [1,6] \quad (2)$$

This criterion needs 27 coefficients to be identified. Its linear terms σ_i take into account the dissymmetry between tension and compression. A condition of stability on the interaction terms F_{ij} is introduced to avoid the surface represented by the criterion to have an opened shape as hyperboloïdal type. The surface represented by this criterion will have intersection points with all the axes defining the considered space of stress:

$$F_{ii} \cdot F_{jj} - F_{ij}^2 > 0 \quad (3)$$

The assumption of orthotropic symmetry reduces the number of coefficients to 12. Then, the Tsai-Wu criterion can be expressed as follow:

$$F_{11}\sigma_1^2 + F_{22}\sigma_2^2 + F_{33}\sigma_3^2 + F_{44}\sigma_{12}^2 + F_{55}\sigma_{13}^2 + F_{66}\sigma_{23}^2 + 2F_{12}\sigma_1\sigma_2 + 2F_{23}\sigma_2\sigma_3 + 2F_{13}\sigma_1\sigma_3 + F_1\sigma_1 + F_2\sigma_2 + F_3\sigma_3 = 1 \quad (4)$$

The main difficulty in using the Tsai-Wu criterion lies in the evaluation of the parameter F_{12} . Its estimation was made theoretically. Wu and Starchurski [20] proposed limit values of the interaction coefficients allowing to make sure that the failure surface of the Tsai-Wu criterion is closed:

$$F_{12}^2 < \frac{1}{f_{t,0}f_{c,0}} \cdot \frac{1}{f_{t,90}f_{c,90}}; F_{23}^2 < \frac{1}{f_{t,90}f_{c,90}} \cdot \frac{1}{f_v^2}; F_{31}^2 < \frac{1}{f_{t,0}f_{c,0}} \cdot \frac{1}{f_v^2} \quad (5)$$

In the numerical model, fictive values of the interaction coefficients are considered. These values are taken positive and equal to the limit values calculated according to the Wu and Starchuski equations.

The interaction between the different components of the connections is modeled using deformable contact elements at each interface. Thus, the meshing of the mechanical model is discontinuous and differs from that used for heat transfer. A friction coefficient of 0.3 is taken into account between fasteners and timber [12].

3.2.2 Results and validation of the mechanical modeling

The 3D-FEM mechanical model is validated on the basis of the load-slip curves of the connection in normal conditions. Figure 6 shows the comparison between the experimental and the calculated load-slip curves for the connection A16 with two mechanical models: one using only the yield Hill criterion (model-1) and the other using the Hill criterion associated to the Tsai-Wu one (model-2).

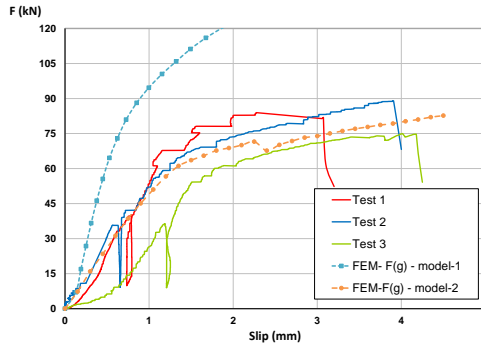


Figure 6. Comparison of experimental and numerical load-slip curves.

These comparisons show that the model-1, using the Hill criterion alone, does not allow representing the elasto-plastic behavior of the connection. The model integrating the Tsai-Wu criterion represents well both the initial stiffness of the connection and its elastic strength.

3.3 Thermo-mechanical modeling

The thermo-mechanical analysis of connections is based on the same 3D-FEM used for the mechanical modeling in cold condition, but the evolution of mechanical properties in function of the temperature has been taken into account. The evolutions of these reduction factors of mechanical properties were assumed according to EN1993-1-2 for steel and EN1995-1-2 for timber.

The meshings of the mechanical and thermal models are different. So, the calculated temperatures in the thermal model cannot be directly read in the mechanical meshing. Then a procedure has been developed to make the transposition of the temperatures calculated with thermal meshing to mechanical meshing. This procedure makes an interpolation to assign a value of temperature to each integration point in the mechanical model. This method gives the possibility to adapt the meshing density to the zones where the physical or the mechanical phenomena exhibit the higher gradient.

The results of the thermo-mechanical model are evaluated on the basis of the predicted time of fire resistance of the connections in comparison with the experimental values. They are defined using the slip-time curves. Figure 7 shows the comparison between experimental and simulated curves for connections A20-1. The high increase of displacement, representing the failure of the connection, is well predicted by the model. In order to define the calculated time of fire resistance, a tangent method is used. Table 7 shows comparisons between the calculated ($t_{fi,sim}$) and the experimental ($t_{fi,test}$) times to failure with the relative error (ε_1).

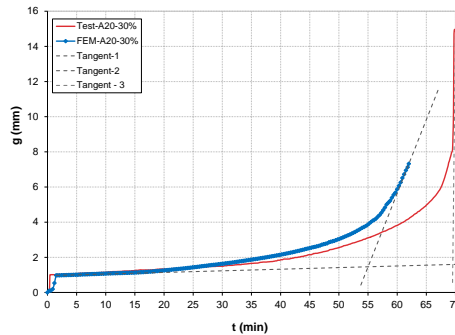


Figure 7. Time-slip comparison of connection A20-1 ($\eta_{fi} = 30\%$ of $N_{u,test}$).

Table 7. Comparison of the experimental and the numerical fire resistances of the connections.

Type	$t_{fi,sim}$ (min)	$t_{fi,test}$ (min)	Relative error ε_1 (%)
A16	58	71	18.3
	45	48	6.2
A20	55	69	20.3
	52	62	16.1

The failure times of the connections calculated using the thermo-mechanical model are always lower than the experimental values. The relative error is due partly to the non-convergence of the model from the moment to which the slip accelerates. However, the thermo-mechanical model predicts well the first stage of the failure characterized by a significant acceleration of the local displacement (slip). Experimentally, the connections show few minutes of additional resistance beyond the failure point defined numerically.

4 CONCLUSION

This study presents original results of real-scale tests on steel-to-timber connections subjected to a tension perpendicular to grain under ISO-fire exposure. The experimental results show high values of fire resistance of tested connections in spite of the brittle character of wood in this orthotropic direction.

The numerical approach developed to simulate the thermo-mechanical behavior of the tested connections gives the possibility to make different meshes for the thermal and the mechanical calculations, increasing the precision of each one. The heat transfer model is validated on the basis of the measured temperature fields inside the connections and by comparison between the experimental and numerical charring rates of timber. The mechanical model in normal conditions is validated on the basis of the load-slip curves. This model integrates the failure criterion of Tsai-Wu combined with the elasto-plastic Hill criterion to take into account the difference of strength between tension and compression in the direction perpendicular to grain. The thermo-mechanical model is validated on the basis of the fire resistances of connections. It allows obtaining more precise results of fire resistance than the current design methods proposed by Eurocode 5 part 1-2. The fire resistances defined by the numerical modeling are all the time in safety side and it can be considered that these values are correct to define simplified formula, in order to design steel-to-timber connections subjected to tension perpendicular to the grain.

The model will be used as a tool to extend the application domain of the Eurocode. The model is validated for the connections in tension parallel and perpendicular to grain. As a general tool, it will be extended to other types of connections loaded in tension at 45 ° and in bending.

REFERENCES

- [1] EN 1995-1-2: 2004, Eurocode 5. Design of timber structures. Part 1-2 : General rules - Structural fire design. CEN TC 250-SC5, 2004.
- [2] König J., Fontana M. "The performance of timber connections in fire-test results and rules of Eurocode 5", Aicher A., Reinhardt HW., editors. *Proceedings of the international RILEM symposium*, RILEM publications, 639-648, 2001.
- [3] König J. "Calculations vs. fire testing – limitations of Eurocode 5 and the need of fire testing", *International symposium on advanced timber and timber-composite elements for buildings*, 27-29, 2004.
- [4] Bouchaïr A., Racher P., Bocquet JF. "Analysis of dowelled timber to timber moment-resisting joints", *Materials and Structures*, 40,1127-1141, 2007.
- [5] Xu B.H., Bouchaïr A., Taazount M., Vega E.J., "Numerical and experimental analyses of multiple-dowel steel-to-timber joints in tension perpendicular to the grain", *Engineering Structures*, 31, 2357-2367, 2009.
- [6] Moss PJ., Buchanan AH., Nilsen TM., Fragiaco M. "Fire resistance of connections using steel plates and mechanical fasteners in timber structures", *Journal of Structural Fire Engineering*, 2(4), 243-257, 2011.
- [7] Dhima D. "Vérification expérimentale de la résistance au feu des assemblages d'éléments en bois", Saint Remy les Chevreuses: CTICM, 61p. 1999.
- [8] Ayme N., Joyeux D. "Comportement au feu d'assemblages bois. Assemblages bois-métal en double cisaillement", *Rapport SRI-03/121-NA/PB n°030156*, CTICM, 62p. 2003.
- [9] Laplanche K., "Etude du comportement au feu des assemblages de structures bois: Approche expérimentale et modélisation", PhD Thesis, Université Blaise Pascal Clermont-Ferrand et CSTB, France, 140p, 2006.
- [10] Audebert M., "Approche expérimentale et modélisation du comportement au feu d'assemblages bois sous différents types de sollicitations", PhD Thesis, Université Blaise Pascal Clermont-Ferrand et CSTB, France, 233p, 2010.
- [11] Racher P., Laplanche K., Dhima D., Bouchaïr A. "Thermo-mechanical analysis of the fire performance of dowelled timber connections", *Engineering Structures*, 32, 1148-1157, 2010.

- [12] Audebert M., Dhima D., Taazount M., Bouchaïr A., “Numerical investigations on the thermo-mechanical behaviour of steel-to-timber connections exposed to fire”, *Engineering Structures*, 33, 3257-3268, 2011.
- [13] Audebert M., Dhima D., Taazount M., Bouchaïr A. “Behavior of dowelled and bolted steel-to-timber connections exposed to fire”, *Engineering Structures*, doi: 10.1016/j.engstruct.2012.02.010, 2012.
- [14] EN 1995-1-1: 2004, Eurocode 5: Design of timber structures. Part 1-1: General rules and rules for buildings. CEN/TC 250/CS5, 2004.
- [15] EN 1993-1-2: 2005, Eurocode 3: Design of steel structures – Part 1-2: General rules – Structural fire design. CEN/TC 250/SC3, 2005.
- [16] Audebert M., Bouchaïr A., Taazount M., Dhima D. “Thermal and thermo-mechanical behaviour of timber connections in fire”, *Proceedings of the COST Action C26 Conference – Urban Habitat Constructions Under Catastrophic Events*, Naples, 189-194, 2010.
- [17] Fredlund B. “Modelling of heat and mass transfer in wood structures during fire”, *Fire Safety Journal*, 20, 39-69, 1993.
- [18] Janssens M. “Thermo-physical properties for wood pyrolysis models”, *Pacific Timber Engineering Conference Gold Coast*, Australia, 1994.
- [19] Tsai SW., Wu EM. “A general theory of strength for anisotropic materials”, *Journal of Composite Materials*, 5, 58-80, 1971.
- [20] Wu RY., Starchuski Z. “Evaluation of the normal stress interaction parameter in the tensor polynomial strength theory for anisotropic materials”, *Journal of Composite Materials*, 18, 456-463, 1984.

THE ADAPTATION OF DIANA FOR SIMULATING FIRE EXPOSED TIMBER STRUCTURES IN NATURAL FIRE CONDITIONS

Danny Hopkin EngD MEng CEng MIFireE*

* Trenton Fire, Staniford House, Wedgewood Road, Bicester, OX26 4UL, UK.
e-mail: Danny.Hopkin@TrentonFire.co.uk

Keywords: Timber, Fire, Numerical Modelling, Heat Transfer, Finite Element Analysis.

Abstract. *The simulation of fire exposed timber is complex for a number of reasons. Unlike steel and concrete it is combustible, it contains a relatively large amount of free water, it is orthotropic and also undergoes irreversible phase changes. All of these attributes have implications for both the thermo-physical and mechanical response of timber at elevated temperatures. In terms of the thermal response, EN 1995-1-2 gives 'Advanced Calculation' properties in Annex B for implementation in simulations. These are limited in scope as they were derived on the basis of standard fire exposure calibrations which consider the heating phase of a fire only. When advances are made towards the mechanical response of timber structures in fire, further barriers exist due to complexity of the constitutive behaviour of timber under different states of strain. Particularly, as strength and stiffness reduction are not only temperature dependant, but also depend upon whether an element is subject to tensile, compressive or possibly both strain states, as is the case in bending. The mechanical modelling of timber members at high temperature has to date been limited to adhoc sectional analysis tools and uni-axial load cases. This paper proposes a number of novel design considerations which advance the scope of timber simulations when subject to fire. In particular, it sets out a method for accurately deriving the temperature of timber members in non-standard fires, explicitly considering the effects of heat generation/combustion. Finally, the paper outlines mechanical sub-routines which are able to distinguish between strain states and also the impact of cooling and the irreversible changes that occur within timber upon heating.*

1 INTRODUCTION

In recent years structural fire engineering has developed to the extent that large and complex buildings can be designed to withstand the effects of a realistic credible worst case fire scenario based on a detailed knowledge of material behaviour at elevated temperature. This has been achieved as a result of extensive research and the development of advanced numerical methods for analysing structural behaviour at elevated temperature. Timber structures are increasing in popularity due to sustainability and environmental drivers. In recent years the UK has seen the construction of the world's largest residential timber structure, reaching 10 storeys in height. However, the fire design of timber buildings has not received the same degree of attention as other materials such as steel and concrete. Deemed to satisfy rules, based upon standard testing, are still used to detail the fire aspects of a building. In such cases it is difficult to quantify the margin of safety a building inherently achieves against a given design fire. To this end, performance based fire design of timber buildings is a necessary development. Numerical modelling has facilitated the performance based fire design of buildings constructed from steel and concrete. The same tools will become increasingly important for achieving robust fire designs for large timber buildings. However, at present a number of barriers exist.

The simulation of fire exposed timber is complex for a number of reasons. Unlike steel and concrete it is combustible, it contains a relatively large amount of free water, it is orthotropic and also undergoes irreversible phase changes. All of these attributes have implications for both the thermo-physical and

mechanical response of timber at elevated temperatures. In terms of the thermal response, EN 1995-1-2 [1] gives 'Advanced Calculation' properties in Annex B for implementation in simulations. It is important to note that strict limitations are placed on the use of these properties due to the methods from which they were derived. Essentially, these properties were calibrated against standard fire tests and have been shown to yield inconsistencies when applied to other fire conditions. For this reason EN 1995-1-2 explicitly states that the Annex B properties should not be adopted for any condition other than standard fire exposure. This is a barrier to innovation and rational fire design. Inspection of the thermal properties in EN 1995-1-2 identifies a number of important factors. Firstly, the properties are 'effective'. That is, the properties implicitly include the consequences of a number of complex behaviours, inclusive of combustion and mass flow. Secondly, the properties implicitly account for a moisture content of 12% and not variations above or below this value. Finally, the properties are intended for application in the heating phase of a fire (or for a fire of continuous growth, i.e. the standard fire).

The extension of the properties to include other design fires such as parametric fires requires a more robust approach, whereby important thermal characteristics are considered explicitly. In particular, the implications of combustion and heating rate on the rate of char development need to be understood. It is accepted that the formation of char in large timber sections is dependent upon a number of factors, in particular the rate at which the surface is heated. Therefore, it is appropriate to make correlations between heating rate and effective properties. König [2] was able to show that the effective thermal conductivity of the char layer depends upon the fire heating rate, however robust correlations were not made.

Extensions of this work by the author [3], which includes a proposed modified conductivity model for softwood, indicates that this correlation alone is not sufficient to describe the behaviour of heated and cooled timber due to the influence of combustion, which is particularly influential in the decay phase of a fire. In the heating phase of a fire, the energy received by a timber element from the burning surroundings is large relative to the energy generated internally due to combustion of the timber member. However, in the cooling phase this is not the case. When the fire environment begins to cool, combustion within the timber member continues through char oxidation. In such cases the heat generated within the element is large relative to the heat flux received from the cooling fire. For this reason, it is important to consider internal heat generation due to combustion explicitly.

2 PREDICTING THE THERMAL RESPONSE OF TIMBER DURING HEATING

In an earlier publication the author proposed a modified conductivity model (MCM) for softwood timber [3] based upon the principles outlined in König's [2] research and upon EN 1995-1-2 specific heat modifications proposed by Cachim and Franssen [4]. The MCM was derived using numerical calibrations of a fire load- (q_{ld}) and heating rate- (Γ) dependent modification factor and the depths of char present in parametric design fires. In the latter case the depth of char in such fires was determined using the Annex A approach of EN 1995-1-2. The full derivation of the proposed model can be found elsewhere [3]. However, the resulting relations are shown in Table 1. and Equations 1-4. As noted, these correlations alone were found to be insufficient to characterise the full temperature development behaviour of timber behaviour during a natural fire in its entirety [3].

3 PREDICTING THE THERMAL RESPONSE OF TIMBER DURING COOLING

In recognition of the limitations of the proposed MCM outlined in Section 2, the author sort to determine an appropriate method for predicting the thermal consequences of combustion and oxidation in timber members exposed to fire. It was found that analogies could be made between the hydration process within concrete and the combustion process within timber. Both processes are fundamentally exothermic reactions which result in the generation of heat. In concrete, during curing, heat is generated due to the chemical reaction of cement with water. This process is analogous to combustion, where energy is generated due to the burning of material. Many commercial finite element codes include routines for determining the 'heat of hydration' in concrete members and this paper proposes methods in which these

simple inherent routines can be adopted to simulate the combustion process within structural timber members.

Table 1. Summary of MCM including specific heat proposals by Cachim and Franssen

Temperature (°C)	Conductivity (W/m K)	Temperature (°C)	Density ratio G	Cachim and Franssen moisture modified specific heat (J/kg K)
20	0.12	20	1+ω	(1210+4190ω)/G
200	0.15	99	1+ω	(1480+4190ω)/G
350	0.07	99	1+ω	(1480+114600ω)/G
500	0.09k _{λ,mod}	120	1.00	(2120+95500 ω)/G
800	0.35k _{λ,mod}	120	1.00	2120/G
1200	1.50k _{λ,mod}	200	1.00	2000/G

$$k_{\lambda,mod} = k_{\Gamma,mod} k_{qtd,mod} \tag{1}$$

With $k_{\Gamma,mod} = 1.5\Gamma^{-0.48}$, $k_{qtd,mod} = \sqrt{\frac{q_{td}}{210}}$ & $\Gamma = \frac{(O/b)^2}{(0.04/1160)^2}$ (2-4)

Where ω is the moisture content of timber (%), O is an opening factor (m0.5) and b is compartment thermal inertia (J/m²s^{0.5}K).

3.1 Analogies with heat of hydration analyses and extensions to burning timber

Many commercial finite element programs, including DIANA [5], contain routines for determining the heat generated as a result of concrete hydration. The routines are simple and can be extended to consider the energy arising as a result of any reaction, including combustion within timber members. The heat generated by a continuum in a FEA package is often based upon the concept of the evolution of a reaction. This introduces a variable known as the degree of reaction (r) which simply describes the progress of a reaction from start (i.e. r = 0) to end (i.e. r = 1). Specific to the generation of heat, the variable r is equal to the momentary cumulative heat production divided by the total heat production per unit area [5], i.e.:

$$r = \frac{\int_0^t q_v .dt}{\int_0^\infty q_v .dt} \tag{5}$$

The magnitude of heat produced depends upon the temperature history during the evolution of the reaction. At a given time the momentary heat production rate (q_v) can be described as follows:

$$q_v = \alpha .q_r .q_T \tag{6}$$

As noted previously, the degree of reaction (r) ranges from zero to unity. The heat production also depends upon heat production rate (α), the temperature (T), the temperature dependant heat production

(q_T) and also the degree of reaction dependant rate of energy production (q_r). The heat production rate (α) describes the maximum amount of energy which can be released per unit time and volume. The temperature dependant heat production (q_T) is a scaling factor determining the proportion of energy released at a given time and temperature. The degree of reaction dependant energy release (q_r) is a scaling factor describing the relationship between the degree of reaction (r) and the potential energy release. For example when the heat generation reaction is 10% complete the potential energy release may be 20% of the heat production rate. This would correspond to $r = 0.1$ and $q_r = 0.2$. The temperature dependant aspect of the reaction can be determined using a simple Arrhenius function as follows:

$$q_T = e^{-\frac{C_A(r,T)}{T+273}} \tag{7}$$

C_A describes an Arrhenius constant which controls the amount of temperature dependant heat energy that can be generated per unit time. From the background equations it is simple to see how concrete hydration routines can be used to determine the energy arising as a result of burning. For a timber section the total amount of energy that can be released as a result of burning depends upon the heat of combustion (Δh_c) and density (ρ) of the material (8). The transient rate of energy release (α) is influenced by charring rate (β) as shown in (9).

$$\int_0^\infty q_V \cdot dt = \Delta h_c \rho \quad \text{and} \quad \alpha = \beta \Delta h_c \rho \tag{8-9}$$

Depending upon the nature of the problem, i.e. one dimensional or two dimensional, the one dimensional or notional charring rates should be considered. Finally, at the ignition temperature of timber the temperature dependant heat production rate (q_T) should approach unity. For this to be the case the Arrhenius constant adopted should be small. The above formulations combine to describe the additional heat energy generated as a result of a reaction, in this proposal combustion. This energy is added to the external flux vector in a heat transfer analysis.

3.2 Calibration and validation of the proposed thermal approach

Inspection of the heat of hydration background theory highlights a number of unknowns. Firstly, the required magnitude of the Arrhenius constant (C_A) is not clear. What is apparent is that the value of C_A should be such that the temperature dependant heat generation term (q_T) is approximately equal to unity. Secondly, the transient rate of energy release (α) depends upon the charring rate (β) which in turn varies according to density (ρ) and heating rate (Γ). For most species of softwood a mean one dimensional charring rate in natural fires approaching 0.5mm/min can be assumed. For a heat of combustion of 18 MJ/kg and a density of 450 kg/m³, this gives an energy release rate (α) approaching 68kW. However, both the charring rate and heat of combustion can be highly variable depending upon environmental conditions. Finally, the degree of reaction related energy release is entirely uncertain. To this end, a number of parametric studies have been previously conducted to derived appropriate parameters. Based upon these parametric studies reported in a supporting publication [6], appropriate constants are outlined below.

Table 2. Calibrated constants to simulate energy generated by burning timber.

C_A (K)	α (kW)	Equivalent β (mm/min)	ρ (kg/m ³)	Δh_c (MJ/kg)	q_r @ $r=0$	q_r @ $r=1$
300	50	0.37	450	18	1.0	1.0

Comparisons between simulations, adopting the thermal proposals reported, and experimental data are shown in Figure 1. Note that test data is taken from studies by Konig and Walleij [7] for experiment C4.

Comparisons of simulated depth of char within a timber member without consideration of heat generation and where it is considered explicitly is shown in Figure 2. Note that in this instance, the depth of char is benchmarked against that calculated via Annex A of EN 1995-1-2 in the absence of test data.

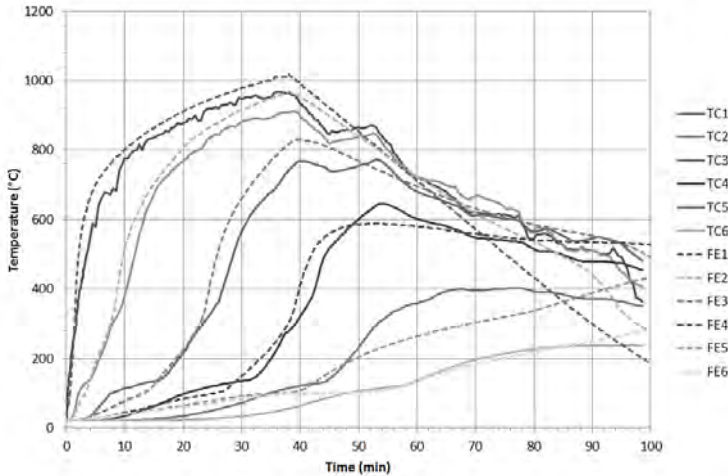


Figure 1- Comparison of measured (TC) and simulated (FE) temperatures through the depth of a timber slab subject to a parametric design fire (Test data from Konig and Walleij- Experiment C4)

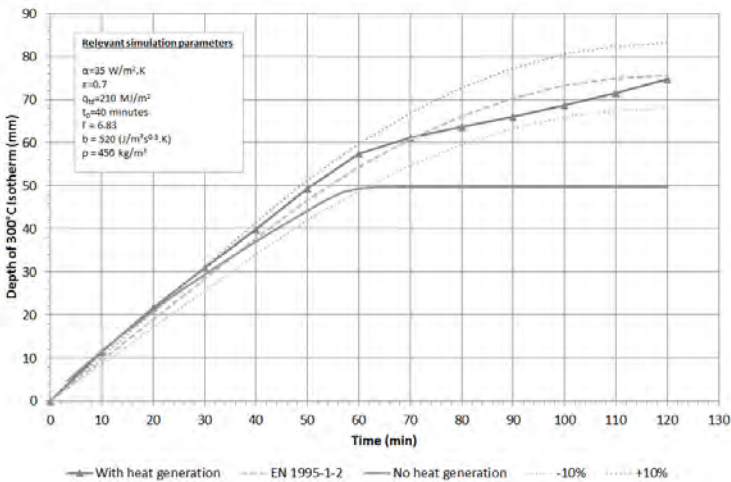


Figure 2- Comparison of depth of char within a timber member with and without the simulation of heat generation, benchmarked against EN 1995-1-2 Annex A. Relevant model parameters are included in the legend.

4 MECHANICAL RESPONSE AT HIGH TEMPERATURE

Determining the temperature of a timber member is only one aspect of performance based design. The coupling with mechanical response is critical to accurately determine the way in which a structure

responds when subject to fire. Similar to the thermal case, the mechanical response of timber with increasing temperature is not simple and often requires the adaptation of common software tools to appropriately characterise constitutive behaviour.

4.1 Background

The adoption of generic FEA codes to simulate the uni-axial behaviour of heated timber is fairly simple as only a tensile or compressive stress state exists at any one time. As such it is possible to simply define unique relationships between temperature, strength and stiffness. The use of more general finite element packages, such as DIANA and ABAQUS, for modelling more complex timber structures exposed to fire has yet to become common due to a number of complexities relating to the behaviour of timber. For example, it is brittle and fractures in tension, while being more ductile and plastic when subject to compression. In addition, with increasing temperature, the degradation of timber's constitutive behaviour in tension is different from that in compression. As a result, timber's Modulus of Elasticity (MOE) depends on its state of stress. Therefore, a single MOE-temperature relationship cannot be defined.

Finally, upon heating timber undergoes a phase change whereby wood becomes friable char. Upon cooling, char still has little or no strength or stiffness. Therefore, it is not appropriate to specify timber strength on the basis of temperature alone when cooling is to be considered. Knowledge of the full temperature history is required. Most commercial FE programs do not incorporate many of the above characteristics in a direct way. Therefore, it is necessary to adapt such codes to accommodate these behaviours. An approach for doing this is described in the remainder of this section. Implementation of the approach in the FEA software DIANA via FORTRAN user-supplied subroutines (USS) is also described.

4.1 Deriving the stiffness of timber in real fires under different strain states

DIANA offers a number of subroutine options for customising the analyses performed. One such subroutine is the USRYOU option. This allows users to return MOE based upon a number of inputs, including integration point strain and temperature. The author has developed a USRYOU USS for determining the MOE of timber exposed to both heating and cooling regimes.

Firstly, integration point and element numbers are called from the program along with temperature at the given integration point. Temperature history of elements is recorded via a common block, which determines whether the temperature of the timber (a) exceeds the charring temperature of 300°C, (b) exceeds the moisture evaporation temperature of 100°C, or (c) is below 100°C, i.e. timber neither charred nor suffered moisture evaporation. Based on this, the temperature history common block is updated incrementally, which allows state history to be recorded via a state variable (SV). The state variables being; 0- corresponding to wood that has not undergone irreversible changes (20-100°C), 1- wood that has undergone irreversible changes due to moisture migration (100-300°C) and 2- wood that is charred and extensively damaged (300+°C).

Using the recorded temperature state history the stress state may be investigated. The strains in the local element coordinates are called from DIANA. The dominant integration point strain is determined, which is then used to evaluate MOE appropriate for the temperature and the strain state. For example, if ϵ_{xx} is found to be the largest element strain and the strain is negative (compressive), the MOE is returned, based upon EN 1995-1-2 compression (-ve) reduction factors ($K_{EC,mod,\theta,i}$) and element temperature. The converse case would be adopted if ϵ_{xx} was found to be positive (+ve). In this instance reduction factors are defined as $K_{ET,mod,\theta,j}$. This process is shown diagrammatically in Figure 3.

4.2 Determining tensile and compressive strength

Two more USSs, namely USRCST and USRTST, are available in DIANA for determining the tensile and compressive strength, respectively. These routines in particular are for implementation with Total Strain Based constitutive models, i.e. strains are not discretised into elastic, plastic and crack components. The routines utilise the temperature history common block initialised in the above USRYOU routine to calculate tensile and compressive strength using EN 1995-1-2 reduction factors. The element number and

integration point number are used to reference allocated memory slots, where temperature state variables are stored. Compressive and tensile strengths (limiting stresses) are passed to DIANA for implementation in the adopted Total Strain Based Constitutive model. This process is shown in a flow diagram in Figure 4.

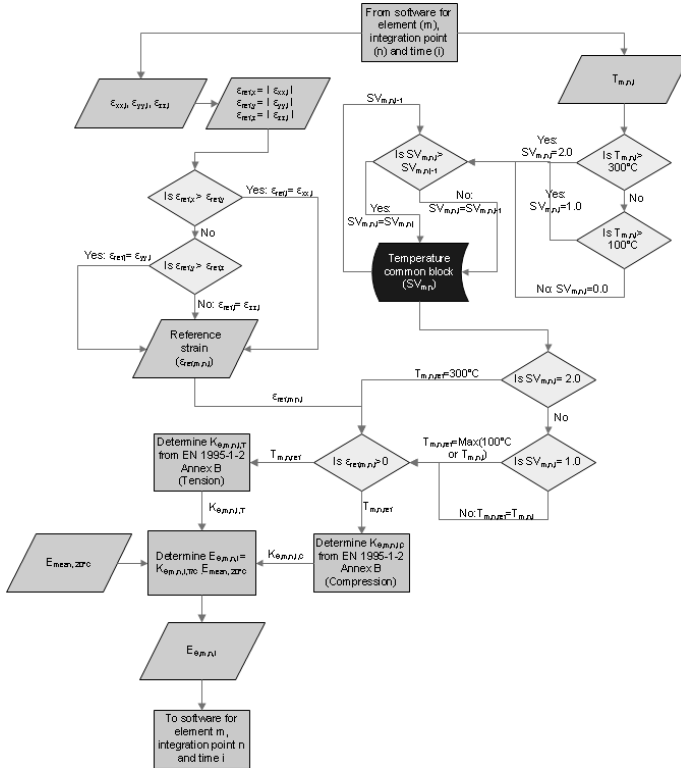


Figure 3. Flow chart for deriving the MOE of timber at high temperature, considering cooling effects

4.3 Post-cracking behaviour of timber at high temperature

EN 1995-1-2 gives guidance on the properties, both thermal and mechanical, that should be adopted in the simulation of timber structures exposed to fire. It is common to assume ideally brittle behaviour of timber under tensile strains, however it is apparent from the literature that at ambient temperature strain energy is not instantaneously dissipated at the moment a crack forms in timber under tensile loading (i.e. its behaviour is not perfectly brittle).

After cracking, tension softening is apparent whereby the fracture energy is gradually dissipated with increasing crack strain. Modelling this behaviour is not only desirable from a physical point of view but is often necessary to ensure numerical stability in simulations. However, no guidance is given in EN 1995-1-2 regarding a magnitude of fracture energy at ambient or elevated temperature. To this end, in another publication [3], the author proposed appropriate post cracking fracture regimes. For completeness these are summarised below (Figure 5) and will be adopted in a later example.

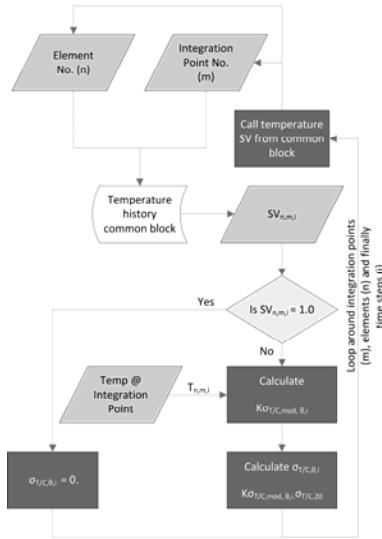


Figure 4. Flow chart for deriving the tensile and compressive strength of timber at high temperature

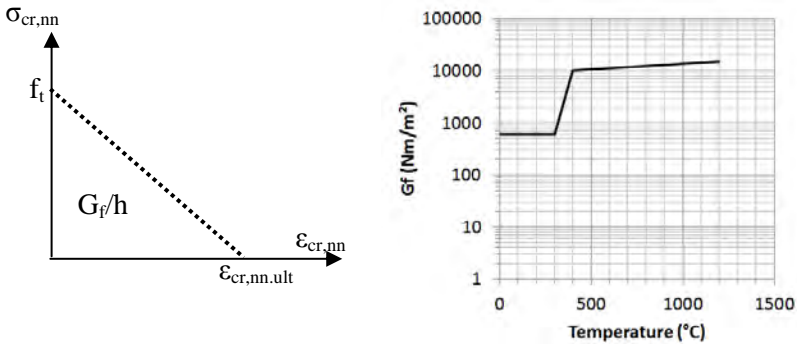


Figure 5- (a) Proposed post fracture constitutive model as a function of crack band width (h); (b) Proposed relationship between temperature and fracture energy (G_f)

5 ANALYSIS OF A SIMPLE ELEMENT SUBJECT TO A COOLING FIRE

The implementation of the proposed mechanical developments can be demonstrated by simulating the behaviour of a simply supported beam subject to a temperature gradient. Such a beam was modelled in DIANA using a number of first-order 2D beam elements. Temperatures were specified at 11 integration points through the cross section of beam elements. Integration point distribution was according to a Simpson integration scheme. The adopted temperature profiles are shown in Figure 6a. The legend indicates fire from below with 11 integration points numbered from the top down. The applied temperatures are largely fictitious and serve only to demonstrate implementation of the mechanical developments. The modelled beam is 4 m in length and has a 100 mm x 250 mm cross-section. The beam is subject to a nominal load of 5 kN/m. The development of deflection upon heating, followed by cooling

can be seen in Figure 6b. In this case, the beam temperature has developed beyond 300°C. Therefore, permanent deformation due to charring and moisture migration is apparent. In addition, a case where temperature history is not considered (i.e. the transition to char), is also shown for comparison.

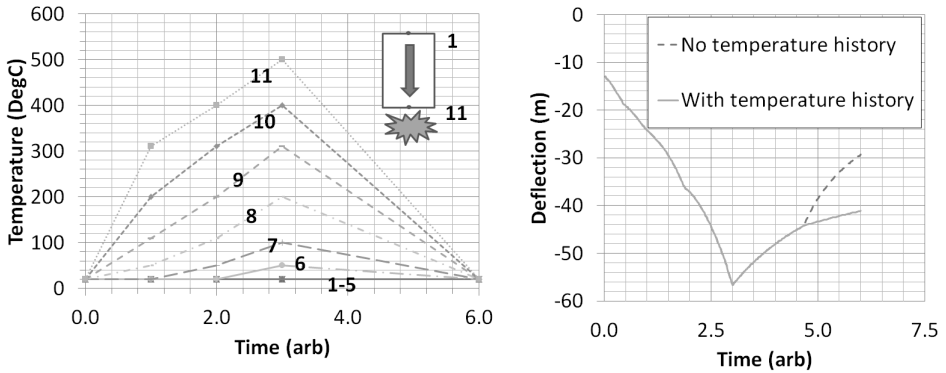


Figure 6- (a) Adopted temperature regime through depth of beam; (b) deflection versus arbitrary time for cases where temperature history is explicitly considered and disregarded.

6 DISCUSSION

The paper has presented an overview of a number of novel developments relating to the performance based design of timber structures for fire resistance. The first of these developments is concerned with the accurate characterisation of timber temperature development in non-standard fire conditions. This is a critical but complex area which has limited progress in the performance based design of timber structures for a number of years.

FEA routines have been presented which explicitly consider the impact of combustion on the heat transfer characteristics of softwood, particularly during the cooling phase of a realistic fire. These routines are inherent within DIANA and have been adapted from ‘heat of hydration’ theory, used to describe the exothermic curing reaction within cementitious materials. These routines have been shown to be an improvement on many existing proposals relating to the subject of the thermal response of timber members in fire. The routines, based upon limited benchmarking against experimental data, have been shown to adequately characterise the combustion process within timber structural members using relatively simple Arrhenius principles. The developments can be considered a step change towards the performance based design of timber members for fire resistance.

Predicting temperature is only one important part of rationalising the way timber is designed for fire. Thermal behaviour needs to be coupled with mechanical response to accurately characterise the way timber structures behave at high temperature. The constitutive behaviour of timber is complex and as a result, many commercial FEA codes are not inherently setup to analyse timber at high temperature. To this end, adaptations are required. Presented herein are a number of routines for implementation within DIANA which allow the stiffness and strength characteristics of timber with increasing temperature, to be accurately described considering temperature history and irreversible changes in state.

The proposals reported herein have been applied to the simple example of a simply supported beam. From this it is apparent that ignoring irreversible changes such as charring and moisture migration have significant implications for deformation behaviour and residual deflections. It is accepted that the proposals reported in this paper are largely theoretical at present. This is necessary as test data for timber members exposed to natural fires is not readily available. Where test data is present, it often lacks sufficient measurements of critical parameters such as temperature profiles and transient deflection

development. It is proposed that the developments made by the author are benchmarked against robust test data.

7 CONCLUSIONS

Based upon the research undertaken and presented herein, conclusions can be drawn as follows:

- Heat of hydration routines which are standard in many FEA codes, including DIANA, are sufficiently flexible to be applied to the thermal analysis of timber members exposed to fire, where combustion must be considered explicitly. This is the case where cooling is to be considered as part of any analysis and/or design.
- Many commercial FEA codes do not inherently contain mechanical material models appropriate for applications concerning heated timber, due to constitutive complexities. Where cooling is considered, it is also important to incorporate the impact of temperature history as irreversible phase changes occur within timber upon first heating. This paper has presented novel theoretical developments to adapt DIANA for such applications, where temperature history is recorded via state variables and strain state is interrogated at each integration point.
- The above developments, when incorporated into a simple example problem, have shown the importance of considering temperature history and combustion during the cooling phase. In such cases, large permanent deflections develop which would not be incorporated using Annex B of EN 1995-1-2 proposals alone.
- The paper has highlighted the importance of validating the proposed developments. At present there is not a plethora of test data available for benchmarking. It is hoped in the near future that such experiments will be undertaken which will further develop the proposals presented herein.

8 ACKNOWLEDGEMENTS

The author would like to acknowledge the contribution of his former supervisors Tom Lennon, Jamal El-Rimawi and Vadim Silberschmidt. The support received from TNO DIANA, in particular Giovanna Lilliu and colleagues at SP Trätekt is also gratefully acknowledged.

REFERENCES

- [1] BRITISH STANDARDS INSTITUTION, 2004. Eurocode 5: Design of timber structures – Part 1-2: General – Structural fire design. BS EN 1995-1-2. London: BSI.
- [2] KONIG, J., 2006. Effective thermal actions and thermal properties of timber members in natural fires. *Fire and materials*, 30(2), pp 51-63.
- [3] HOPKIN, D.J., 2011. The fire performance of engineered timber products and systems. EngD Thesis, CICE: Loughborough University Press.
- [4] CACHIM, P.B. and FRANSSEN, J.M., 2009. Comparison between the charring rate model and the conductive model of Eurocode 5. *Fire and materials*, 33(3), pp 129-143.
- [5] MANIE, J., 2010. DIANA User's Manual. 9.4 edn. Delft: TNO.
- [6] HOPKIN, D.J., 2012. Predicting the thermal response of timber structures in natural fires using computational 'heat of hydration' principles, *Fire and materials* [In Print].
- [7] KONIG, J. and WALLEIJ, L., 1999. One-dimensional charring of timber exposed to standard and parametric fires in initially unprotected and postprotection situations. I9908029. Stockholm: SP Trätekt.

FIRE INDUCED DESORPTION AND MIGRATION OF HYGROSCOPIC MOISTURE IN WOOD

Marjan Sedighi Gilani* and Erich Hugi*

* Empa, Swiss Federal Laboratories for Materials Science and Technology, Switzerland
e-mails: Marjan.Gilani@empa.ch, Erich.Hugi@empa.ch

Keywords: Thermo-hydro-mechanics, moisture migration, temperature gradient, neutron imaging, wood

Abstract. *Physical and mechanical properties of wood are moisture and temperature dependent. Behaviour of timber structures, with respect to their resistance to fire, is directly influenced by interrelated thermal-hygric-mechanical properties of wood, migration of adsorbed water induced by temperature gradient and its evaporation as a source of latent heat. This study investigates the heat induced transport of moisture in two different hardwood and softwood species. By means of thermal neutron radiography, the processes of moisture desorption and migration is visualized and quantified. First in-situ evidence for formation of a zone with accumulated moisture, in the neighbourhood of a progressing drying front is provided. The moisture distribution in the samples shows that both the drying and the moisture accumulation zones evolve non-uniformly. We found a clear dependency of moisture migration on the (micro-) structure of wood species and their seasonal growth layers.*

1 INTRODUCTION

Wood is a widely used sustainable building material with a vast application in building industry. During the last two decades, a multitude of significant and comprehensive research work on timber frame constructions under the premise of fire safety has been performed worldwide. As a consequence, many national fire regulations within Europe, North America and Asia have been revised in terms of allowing of wood members at structural level for four to six storey buildings, most often used for residential occupancies [1]. However, light timber constructions are still designed oversized, not only because of the natural variance of the wood properties itself, but also because of deficient understanding of the temperature and moisture dependent change of wood properties at elevated temperatures [2] that originates from its biological origin: the hierarchical, hygroscopic, anisotropic multi-scale porous structure. This makes the implementation of an advanced simulation for studying the interrelated thermal, hygric and mechanical properties of wood difficult. The simplified simulations on the other hand, used in accordance to the regulations for structural designs against fire, are mainly based on material properties derived from large scale experiments, which do not give an adequate insight of the occurring physical processes, especially at material-level. Thus, understanding these processes at finer material scales, e.g. *micro to meso-scale*, during exposure to elevated temperatures becomes relevant for a sustainable design.

Mechanical properties of wood are temperature and also moisture dependent. On the one hand, a rise in temperature leads to drying, initiation of shrinkage and thus micro-cracks in the structure that degrades the overall mechanical properties. Apart from degradation of the material properties due to development of checks, higher temperatures than 80°C degrades the mechanical properties of the wood components lignin, hemicellulose and cellulose [3]. The extent of thermal degradation depends on the temperature and on the duration of the exposure to it. Around 150-200 °C, the degradation rate increases due to decomposition of wood components until the material experiences critical damage and finally charring occurs at 250-300°C [4, 5, 6]. On the other hand, mechanical properties of wood are strongly moisture

dependent below the fibre saturation point (moisture content at which the wood cell walls get saturated). Up to about 12% moisture content, the tensile strength of wood slightly increases while the modulus of elasticity remains constant [3]. With a further increase in moisture content, the latter acts as a softener of the cellulose and hemicellulose polymers and decreases significantly the tensile strength, modulus of elasticity and fracture toughness [3, 7, 8]. Once the fibre saturation point is reached, i.e. 28% moisture content, liquid water appears on the surfaces of the cell lumens and does not affect the mechanical properties anymore.

Though variation of wood mechanical properties with respect to moisture or temperature changes have been studied quite extensively but the multiple effect of heat induced moisture migration on mechanical properties is still undetermined. There are studies showing that temperature has a larger influence on the mechanical properties at higher moisture contents [9, 10]. The fibre saturation point and so the hygroscopic range, within which the mechanical properties are highly correlated with the moisture content, are also temperature dependent parameters [11, 12]. There are evidences showing that in a wood member exposed to a high (fire like) temperature, a *transition zone* is built up between the progressing charring zone and a zone of still intact material not affected by elevated temperature or increased moisture content. The temperature in this zone ranges from 80 to 300 °C, leading to simultaneous initiation of pyrolysis, migration and accumulation of adsorbed water. Moisture content in accumulation zone may reach twice the initial [13] that is a source of local change in the mechanical properties.

All these interrelated phenomena are usually covered in uncertainty factors of standard building codes, while understanding them, e.g. understanding the process of moisture migration in wood at high temperatures in relation to its hierarchical porous structure, will be the way forward for optimizing the engineering design of novel timber structures against fire in future. A non-destructive visualization and quantification means is required to document the time dependent spatial process of moisture transport for such an investigation. In this study, we use neutron image analysis to investigate, at seasonal growth layers scale, the spatial and temporal distribution of water in wood, which is exposed to an elevated temperature of 250°C for 10 minutes. A device is custom developed for single-edge exposing of samples from hardwood (beech) and softwood (spruce) to a given temperature curve. Temperature rise within the probes is measured at different distances from the heating source by using thin thermocouples. We explore the process of change in the moisture content, based on neutron images, and compare it to the profile of the temperature rise. Results are used to explain the processes of heat induced migration of moisture in wood at elevated temperatures.

2 MATERIALS AND METHODS

We cut samples of beech and spruce species, side by side out of their planks, quarter-sawn in dimensions of 40 x 40 x 10 mm³. Density of each sample was obtained after it was dried and weighted with precision balance. Then, the samples were conditioned in a desiccator over saturated Potassium Bromide solution at 80% relative humidity until equilibrium.

In Figure 1, the custom made setup for the heating experiment is presented. It consists of a heating plate that is a shim underlying strip of 0.05 mm covering the base heating thermocouples. Step rise of the temperature in those base thermocouples is provided by a power supply with a maximum power of 50 A and 120 V. An algorithm for controlling steep time-temperature steps has been developed in terms of heating the base edge of the sample with high degree of reproducibility. The temperature measured with thermocouples, inserted inside drilled holes of 0.4 mm diameter and 20 mm length, at different locations along the heating was also stored by a data acquisition system. Thermocouples are of NiCr-CuNi-type having a diameter 0.1 mm. The sample is placed on the heating plate by means of a horizontal clamp on top that is fixed on the base plate by using two long vertical screws. Two small metallic spacers make a gap between the sample top and the horizontal clamp to prevent moisture condensation and accumulation at the top surface.

Temperature is measured at each 5 mm along the sample height (7 points in total). Measurement is repeated in 3 samples of each species for statistical accuracy and averaged results are put together to derive the temperature profile.

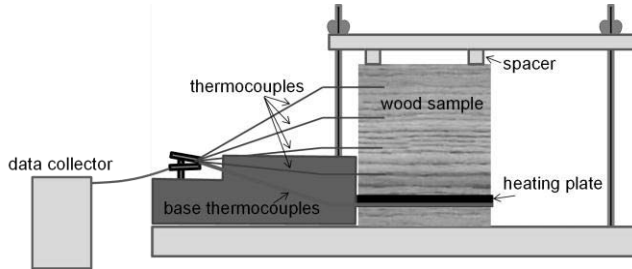


Figure 1. Custom made set-up for heating meso-scale samples based on a given steep time-temperature step.

We used the imaging facilities of the Neutron Transmission Radiography (NEUTRA) beamline at the Paul Scherrer Institute (PSI), Switzerland for imaging and quantification of time resolved migration of moisture in wood during a heating experiment. Neutron radiography at NEUTRA station relies on a neutron beam within a thermal spectrum having an energy level of about 25 meV.

Figure 2 shows the schematic overview of the neutron beamline. The x- and y-axes correspond to the detector plane axes while the z-axis shows against the neutron beam direction. The detector consisted in a scintillator-CCD camera-system with a total field of view of $87 \times 87 \text{ mm}^2$. The scintillator is from $100 \mu\text{m}$ thick zinc sulfide, doped with ^6Li as the neutron absorbing agent, to convert the neutron signals into visible light photons. The photons are then led via a mirror onto a cooled 16-bit CCD camera (1024×1024 pixels). An initial neutron image is obtained as soon as the sample is set on the heating plate. Then the heating plate starts to heat the bottom side of the sample by a step rise of temperature to 250°C , which is maintained for 10 minutes, while neutron images are acquired at regular intervals of 12 seconds with resolution of 100 microns.

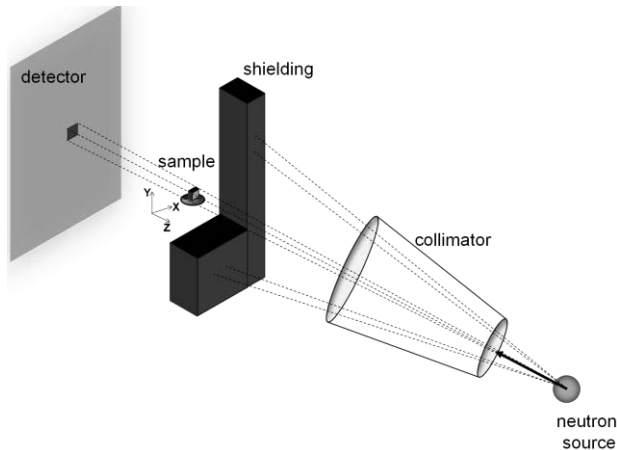


Figure 2. Schematic overview of the experimental setup for neutron radiography.

Analysis of neutron images for quantification and visualization is based on intensity measurements of the transmitted neutron beam through an object. For a monochromatic beam, the transmitted intensity, I , is described by the Beer-Lambert law:

$$I = I_0 e^{-\mu \cdot z} \quad (1)$$

where I_0 is the intensity of the incident neutrons, z is the total thickness of the object along the neutron beam direction and μ is the effective attenuation coefficient. For a compound material like wood or water, the total attenuation coefficient that describes the degree to which the material interacts with neutrons, is defined as a function of attenuation coefficients of individual elements including hydrogen, oxygen or carbon. Assuming the composition of our tested samples consist of wood and water, we use the bi-layer approximation method to quantify the change in the moisture content [14]. At a time t , the effect of migrated moisture from wood on the neutrons attenuation is considered equivalent to the effect of a water layer with thickness z_w added to the dry wood sample. Implementing this description, Eq. (1) becomes:

$$I(t) = I_0 e^{-(\mu_s \cdot z_s + \mu_w \cdot z_w)} \quad (2)$$

where the subscript s refers to the wood and w to the migrated water. At each time t during the experiment, the change in the beam intensity with respect to the initial stage is induced by the change of moisture content, i.e. the “effective” water layer in the bi-linear model. Eq. (2) can be rewritten as:

$$I(t) = I_{init} e^{-\mu_w \cdot z_w(t)} \quad (3)$$

where $I_{init} = I_0 e^{-\mu_s \cdot z_s}$ is intensity of the neutron beam transmitted through the sample in the initial state. Solving for the change in water thickness yields:

$$z_w(t) = -\frac{1}{\mu_w} \ln\left(\frac{I(t)}{I_{init}}\right) \quad (4)$$

Multiplying the effective water layer thickness by the water density ρ_w and dividing by the sample thickness z yields the change in the moisture content (kg/m^3). It allows plotting the differential distribution of the moisture content at different times.

$$w(t) = -\frac{\rho_w}{z \cdot \mu_w} \ln\left(\frac{I(t)}{I_{init}}\right) = -\frac{\rho_w}{z \cdot \mu_w} (\ln I(t) - \ln I_{init}) \quad (5)$$

We used a standard procedure, common to all radiation transmission-based imaging methods, to correct raw neutron images for artefacts. It includes correction for background noise of the CCD camera, for spatial fluctuations of the incident beam, for scattering by the experimental configuration and environment and polychromaticity of beam energy spectrum. We used a Quantitative Neutron Imaging (QNI) algorithm, developed at Paul Scherrer Institute [15], based on iterative reconstruction of the measured image by overlapping point scattered functions calculated in Monte-Carlo simulation. Quantification based on uncorrected radiographs results in underestimation of the water content, up to 50%, compared with corrected radiographs.

Desorption of adsorbed water during a heating experiment, makes the wood sample to shrink. Moisture content, based on Eq. (5) is obtained from logarithmic subtraction of the current image taken at time t from the initial image taken at time $t = 0$. Due to the change in geometry and dimensions of the shranked sample, subtraction of images causes artefacts and inaccuracy in evaluation of moisture content. We used a transformation algorithm to scale back each object and align its edges with the edges of the object in the reference image, at initial time. For this purpose, TurboReg plugin of ImageJ was used that is based on bilinear image registration algorithm [16].

3 RESULTS AND DISCUSSIONS

3.1 Differential change of moisture distribution in relation to wood structure

Figure 3 and 4 present the spatial migration of adsorbed water in beech and spruce samples for longitudinal heating. The first and last images in each figure show the neutron reference image at initial state and the final one after 10 minutes heating. Earlywood and latewood growth layers (grown in spring

and summer, respectively) are distinguishable by the lighter grey colour corresponding to the latewood. Other plots show the quantified distribution of differential change in the moisture content (based on Eq. 5), after 1, 3, 6 and 10 minutes heating at 250°C. The drying front is not a straight line, showing inclination close to the unsealed sides of the sample due to heat convection and evaporation of moisture on those sides. A significant increase of the moisture content is recognized above the progressing drying zone. Moisture migrates irregularly from the heating source, while the jagged pattern of change in the moisture content is clearly dependent on geometry of the seasonal growth layers. Local lower moisture content in the drying zones coincides with location of earlywood layers, while moisture peak occurs at the location of latewood layers in the moisture accumulation zone. At similar time steps, the drying front in beech (e.g. areas with 0-20 kg/m³ decrease of moisture content in figure 3) proceeds a shorter distance from the heating source, comparing to spruce (in figure 4). Plots of differential change in moisture content are presented in the range of ± 60 kg/m³. As the initial moisture content is about 60 kg/m³ in spruce and 80 kg/m³ in beech, differential moisture content plots show there are parts of earlywood layers within the drying zone that get totally dried close to the heating source, after 6 minutes.

Dependency of the local change in the moisture content on geometry of seasonal growth layers indicates the important part of the wood porous structure regarding its desorption process. As shown in figure 5, earlywood cells in spruce have higher porosity due to possessing larger lumens (longitudinal void in the center of cell), thinner walls and more abundant pitting on their cell walls, compared to latewood cells. Consequently, the high porosity earlywood layers are the preferential desorption pathways, and show lower moisture level within the drying zone. The same explains why moisture peaks in the accumulation zone are observed at latewood layers that have lower porosity and higher density. Vessels, presenting in hardwood, are the major structural differences between the two species. They are larger in earlywood, compared to latewood and they are surrounded by thick walled and small lumen longitudinal cells (called fibers in hardwood). This structure gives hardwood a higher density and lower overall porosity that explains the slower drying of beech, compared to spruce and occurrence of a larger zone of moisture accumulation (e.g. see the areas with 40-60 kg/m³ increase in moisture content in figure 3) with more regular shape.

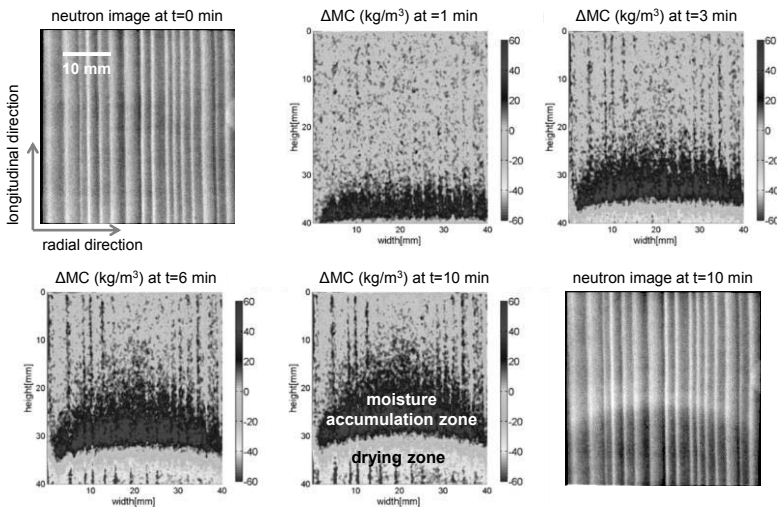


Figure 3. Differential distribution of moisture content in beech after 1, 3, 6 and 10 minutes heating at the bottom surface.

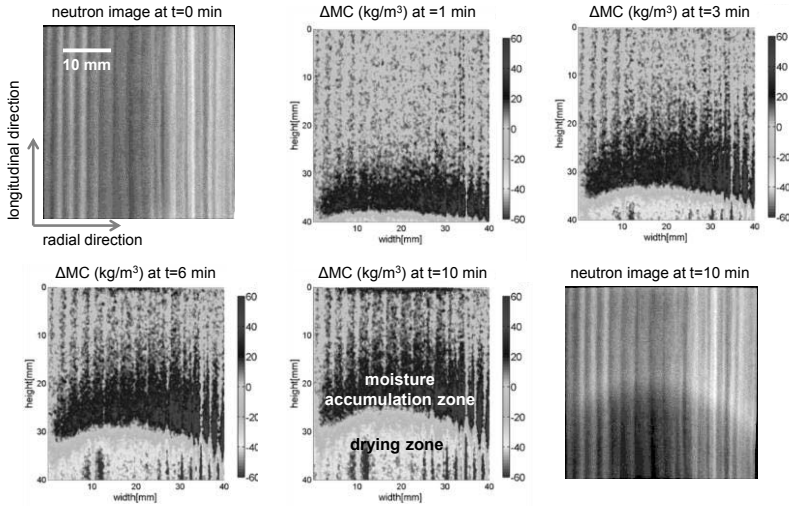


Figure 4. Differential distribution of moisture content in spruce after 1, 3, 6 and 10 minutes heating at the bottom surface.

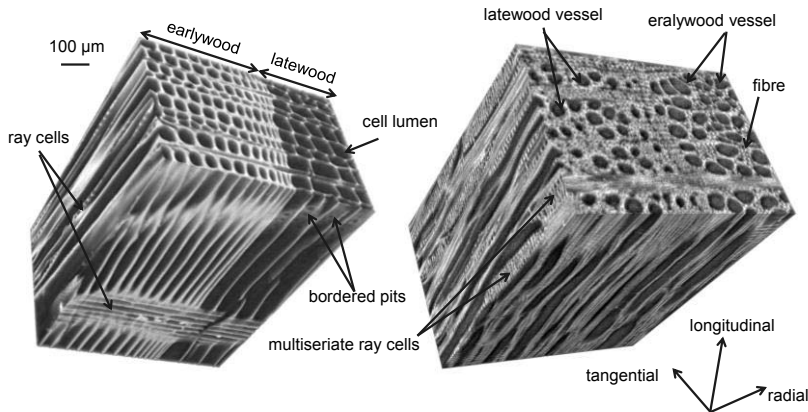


Figure 5. Microstructures of softwood (spruce) and hardwood (beech), documented with high resolution synchrotron X-ray tomography.

3.2 Moisture and temperature profiles

Temperatures measured by thermocouples were used to reproduce the temperature profiles along the sample height. These profiles, together with the profile of differential change in the moisture content, are used to discuss the detail process of temperature induced moisture migration in wood. In figure 6 (a and b), profiles of temperature and differential change in the moisture content in beech and spruce samples are presented. The vertical axis corresponds to the sample height. Moisture content has been averaged over a zone of 18 mm (180 pixels), situated in the middle of each sample. Local increase of the moisture content above the drying front is clearly visible with different ranges for different species. The decrease of the moisture content profile relative to the initial condition (negative differentials), for instance after 1 minute

heating, represents the location of the drying front at the corresponding time, which is in that case about 3 mm above the heating source. The temperature within the dried zone is higher than 100 °C. As explained previously, each temperature on the profile is the average of measured temperatures in three samples (with standard deviation of less than ± 5 °C). The drying in beech proceeds slightly slower than in spruce. After 10 minutes, the drying front extends to 10.8 mm above the heating source in beech and 12.7 mm in spruce, while the temperature at the corresponding heights is about 100°C in both samples. Moisture accumulation peak in beech is larger than in spruce (35 kg/m^3 vs 26 kg/m^3), indicating that beech retains a higher moisture quantity, and gets more humid in the neighbourhood of the drying front at elevated temperatures.

After 10 minutes heating, temperature at 10 mm from the heating source rises to 100 °C and close to the sample top, at 35 mm from the heating source, is about 45 °C. Assuming that the heat is mainly transferred by conduction from the wood cell wall substance, thermal conductivity along the longitudinal direction is expected to be higher due to orientation of cellulose molecular chains within the cell wall. However, apart from this structure-property relation that has been usually discussed in literature [17, 18], heat transfer in wood is dependent on other interrelated parameters, including initial moisture content and possible phase changes between vapour, liquid and adsorbed water.

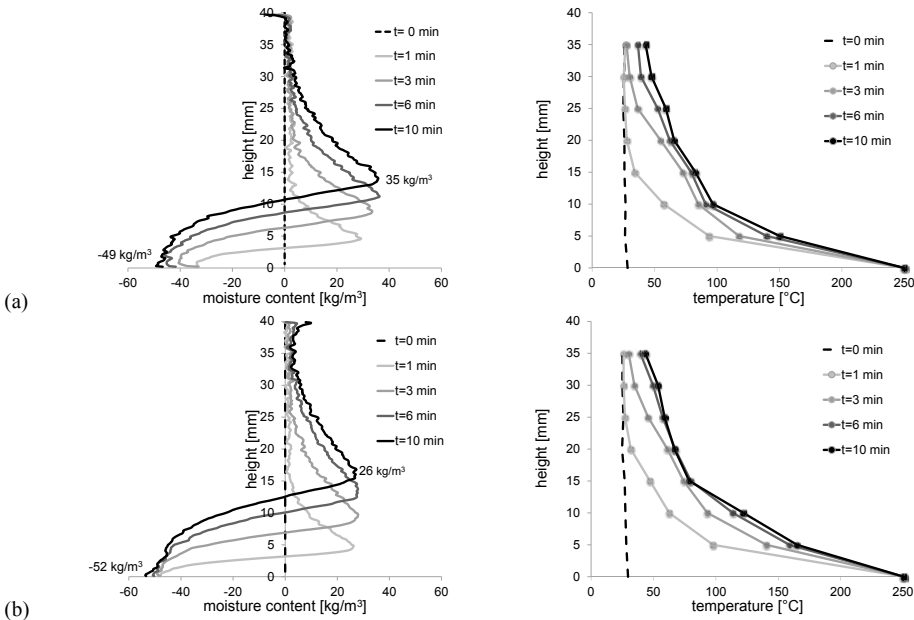


Figure 6. Differential profile of moisture content and profile of temperature at different time steps for (a) beech and (b) spruce.

Within this context the question is raised: Does the adsorbed water move away from the heating source through the cell lumens after it evaporates, or does it still move in the adsorbed phase within the cell wall? It is important to know that the condensed vapour to liquid water contributes more to the overall thermal conductivity than the adsorbed water within the cell wall [17, 19]. Possible phase change of the vapour or adsorbed water to liquid, above the drying zone, is dependent on the local temperature, pressure and also the hygroscopic properties of the wood cell walls in terms of fibre saturation point. Fibre saturation point is an inverse temperature dependent property that is estimated from sorption isotherm curves [11, 12]. It means that at higher temperatures, lower moisture contents can cause the cell

walls reaching the fibre saturation point and consequently appearance of liquid water on the lumen surfaces. While vapour condensation can be predicted from comparing the profiles of moisture migration and temperature, phase changes of the adsorbed water from liquid to gas phase need to be discussed more carefully. Back to the figure 6(b) for example, the drying front in spruce reaches after 10 minutes heating to 12.6 mm above the heating source. At the same time, the maximum of the accumulated moisture profile is 26 kg/m³, or 6.1% when wood density is 425 kg/m³. The maximum moisture is measured at 17 mm above the heating source and fades gradually toward the top of the sample. In the same area, 17 to 35 mm from the heating source, temperature ranges 45 to 75 °C. Literature review implies that the fibre saturation point decrease by 0.1% per degree rise in temperature [19, 20]. Therefore, the fibre saturation point of spruce, that is 28% at 25°C from literature, reduces down by 2 to 5% within the temperature range of 45 to 75 °C [19]. Given the initial moisture content of spruce sample in our experiment of 14%, maximum moisture content within the moisture accumulation zone reaches 20%, that is less than the fibre saturation point for the given temperature range. Consequently, if the adsorbed water in the cell wall does not change to vapour, it may be pushed away from the heating source and locally accumulate above it, all within the hygroscopic range, while it never crosses the fibre saturation point and changes to liquid water on the cell wall surfaces. However, fibre saturation point is a material property that is different in different wood species and different seasonal growth layers. While condensation of vapour to liquid is quiet possible in the moisture accumulation zone with lower temperatures, this leads us to conclude that the contribution of adsorbed water and its phase change to liquid water should be discussed more detailed.

4 CONCLUSION

Neutron image analysis with simultaneous temperature measurements along the sample height were used for in-situ investigation of the migration process of adsorbed water in wood at elevated temperatures. It was shown that single edge heating at constant temperature of 250 °C pushes the adsorbed water away from the heating, building up a progressing drying front and an area with increased moisture content due to accumulation of the evaporated moisture. Spatial plots of differential change in moisture content show drying and moisture accumulation zones proceed in a non-uniform pattern within the samples, depending on the location of growth layers which have different structures. Time resolved spreads of the drying front and moisture accumulation zone varies by species: desorption rate and advancing of the drying front were faster in spruce compared to beech. Investigating the profile of moisture content together with the temperature profile indicated that the water migrates away from the heating source in the vapour as well as in the adsorbed phases. The migrated moisture might change to liquid phase in the accumulations zone, depending on the local temperature and change in the fibre saturation point as a result of heating. Results from this study will be used to validate our coupled thermo-hygro-mechanical model in terms of understanding the material behaviour at high temperatures; i.e. fire and wood thermal modification.

REFERENCES

- [1] *Fire safety in timber buildings. Technical guideline for Europe*, Technical Research Institute of Sweden, 2010.
- [2] *Eurocode 5– Design of timber structures*, Part 1-2: General – Structural fire design, EN 1995-1-2:2004 +AC:2006 (E).
- [3] Ostman B.A.L., “Wood tensile strength at temperatures and moisture contents simulating fire conditions”, *Wood Science and Technology*, 19: 103-116, 1985.
- [4] Stamm A. J., “Thermal Degradation of Wood and Cellulose”, *Industrial Engineering Chemistry*, 48(3): 413-417, 1956.
- [5] Marc Borrega PP., “Effect of relative humidity on thermal degradation of Norway spruce”, *Journal of wood Science*, 54 (4): 323-328, 2008.

- [6] Meincken M., Smith N.H., Steinmann D., “Physical properties of burnt timber, with special focus on the drying performance”, *European Journal of Wood Products*, 68:455–461, 2010.
- [7] Reiterer A., Tschegg G., “The influence of moisture content on the mode I fracture behaviour of sprucewood”, *Journal of Material Science*, 37:4487–4491, 2002.
- [8] Vasic V., Stanzl-Tschegg S., “Experimental and numerical investigation of wood fracture mechanisms at different humidity levels”, *Holzforschung*, 61: 367 – 374, 2007.
- [9] DeXin Y., Ostman B.A.L., “Tensile strength properties of particle boards at different temperatures and moisture contents”, *Holz als Roh- und Werkstoff*, 41(7): 281–286, 1983.
- [10] Gerhards C.C., “Effects of moisture content and temperature on the mechanical properties of wood: an analysis of immediate effects”, *Wood and Fiber Science*, 4-36, 1980.
- [11] Rasmussen EF., *Dry kiln: operator’s handbook NO. 188*, Forest Products Laboratory, Forest Service, U.S. Dept. of Agriculture, 1961.
- [12] Hill C.A.S., Norton A.J., Newman G., “The water vapour sorption properties of Sitka spruce determined using a dynamic vapour sorption apparatus”, *Wood Science and Technology*, 44(3): 497–514, 2010.
- [13] Schaffer R.H., “Transient moisture gradient in fire-exposed wood slab”, *Wood Fiber*, 13: 17-38, 1981.
- [14] Sedighi-Gilani M., Griffa M., Mannes D., Lehmann E., Carmeliet J., Derome D., “Visualization and quantification of liquid water transport in softwood by means of neutron radiography”, submitted to *International Journal of Heat and Mass Transfer*, 2012.
- [15] Hassanein R., “Correction methods for the quantitative evaluation of thermal neutron tomography”, PhD thesis, ETHZ Zurich, Switzerland 2006
- [16] Thevenaz P., Ruttimann U.E., Unser M., “A Pyramid Approach to Subpixel Registration Based on Intensity”, *IEEE Transactions on image processing*, 7(1): 27-41, 1998.
- [17] MacLean J.D., “Thermal Conductivity of Wood”, *Heating, Piping and Air Conditioning*, 13: 380-391, 1941.
- [18] Suleiman B.M., Larfeldt J., Gustavsson M., “Thermal conductivity and diffusivity of wood”, *Wood Science and Technology*, 33: 465-473, 1999.
- [19] Siau J.F., *Transport processes in wood*, Springer-Verlag, New York Tokyo 1984.
- [20] Time B., *Hygroscopic moisture transport in wood*, PhD Dissertation Norwegian University of Science and Technology, 1998.

MODELLING THE FIRE PERFORMANCE OF STRUCTURAL TIMBER FLOORS

**James W. O'Neill, Anthony K. Abu, David M. Carradine, Peter J. Moss
and Andrew H. Buchanan**

Department of Civil and Natural Resources Engineering, University of Canterbury,
Private Bag 4800, Christchurch 8140, New Zealand;
E-mail: james.oneill@pg.canterbury.ac.nz, tony.abu@canterbury.ac.nz,
david.carradine@canterbury.ac.nz, peter.moss@canterbury.ac.nz, andy.buchanan@canterbury.ac.nz

Keywords: Timber Floors, Thermal Modelling, Furnace Testing, ABAQUS, Sequential.

Abstract. *This paper describes numerical modelling to predict the fire resistance of engineered timber floor systems. The floor systems under investigation are timber composite floors (various timber joist and box floor cross sections), and timber-concrete composite floors. The paper describes 3D numerical modelling of the floor systems using finite element software, carried out as a sequential thermo-mechanical analysis. Experimental testing of these floor assemblies is also being undertaken to calibrate and validate the models, with a number of full scale tests to determine the failure mechanisms for each floor type and assess fire damage to the respective system components. The final outcome of this research will be simplified design methods for calculating the fire resistance of a wide range of engineered timber floor systems.*

1 INTRODUCTION

With the advent of high performance wood materials such as glue laminated timber, laminated veneer lumber (LVL) and cross-laminated timber (CLT), timber floors are once again a viable alternative to using steel or concrete in multi-storey buildings. This raises the question of fire resistance, because timber is a combustible material. The loss of wood section due to charring, the anisotropy of the material and the detailing of connections all complicate the estimation of the fire resistance of timber floor systems. This research focuses specifically on the fire performance of different timber floor types used in multi-storey timber buildings.

1.1 Timber Composite Floors

Timber composite systems such as ribbed panel floors and hollow box floors are generally categorised as having sheathing on one or both sides which acts as part of the structural system based on the performance of the connection between sheathing and beam elements (commonly a nailed, glued or screwed connection along the beams, or some combination of glue and fasteners). Composite action achieved by the floor system must be accounted for to obtain a proper estimate of fire resistance, however composite action is not considered in the simple design methods currently available [1].

The composite joist floor currently being researched consists of LVL beams ranging from 200 mm to 600 mm deep, bound by small LVL bottom flanges and a continuous LVL slab system as the primary supporting floor panel (top flange). A schematic drawing of a typical composite floor is shown in Figure 1. Similar types of flooring systems are discussed in detail by Grant [2].

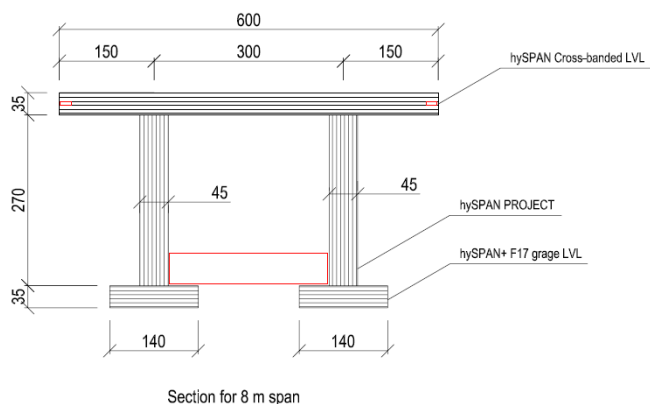


Figure 1. Timber composite joist floor system.

Typically these floors span from 5 metres to 12 metres and are designed for normal service loads in office buildings and similar multi-storey applications. When compared with a simple joist type composite floor, this configuration gives the added mechanical advantages of supporting greater loads at a higher level of stability, hence resulting in the overall reduction of the floor member sizes after geometrical optimisation. However a larger area of timber is exposed to the fire in this regard, and due to the smaller member sizes the expected unprotected fire resistance of these floors will be lower under similar loading conditions.

The composite box floor under study is identical to the joist floor in all aspects but construction geometry. The bottom flanges of the joists are made continuous between each second pair, resulting in a box type system with every second panel missing on the bottom chord, allowing for services to be installed in the gaps. The advantage of a system such as this over the previous composite floor discussed is that the surface area of timber exposed to the fire is greatly decreased, hence the expected fire performance will be greater by a simple change in geometry.

1.2 Timber Concrete Composite Floors

The concept of timber-concrete composite systems arose in Europe as a method of strengthening existing timber floor systems using a concrete slab. A summary is given by Lukaszewska *et al.* [3]. This was then applied to construction of new buildings, and is currently under investigation in many parts of the world such as the United States [4], Germany [5,6] and New Zealand [1,7]. The performance of the flooring system depends mainly on the connection between the timber beams and the concrete slab, as a very stiff connection is required to ensure that sufficient composite action is achieved, resulting in a higher ultimate strength and decreased deflections.

The fire resistance of timber-concrete composite elements is mainly influenced by the timber and the connectors [8]. Effects of the fire on the timber such as heating and reducing overall section size act to weaken both the timber section and the connection between timber and concrete. The form of connection is also important, as the integrity of the connection during the fire will be governed by its weakest element which can sometimes be difficult to predict.

Timber concrete composite floors have been researched previously at the University of Canterbury [9,10], and a full set of fire performance data is available for two full-scale tests which were undertaken as a part of that research. Due to time constraints however, an in-depth analysis of the floor system was not possible and hence a simplified design method for these floors was not developed. Part of the current research is aimed at remedying this issue, and the timber-concrete composite floors shown in Figure 2 are being investigated alongside the fully timber systems.

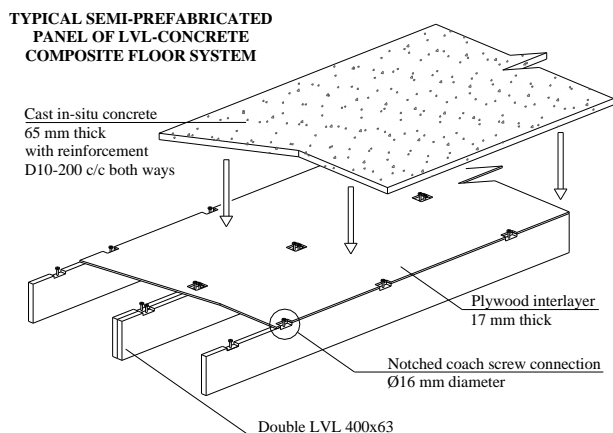


Figure 2. The timber-concrete composite floor system [9].

The type of composite floor under study is a semi-prefabricated system comprising of "M" panels that are built with LVL beams and sheathed with a thick plywood interlayer, which acts as a permanent formwork for the concrete. The plywood interlayer has holes cut into it to accommodate the notched form of connection being used between beams and the concrete slab. These panels are prefabricated off-site then transported to site and craned into position. Steel reinforcement can then be assembled and the concrete slab cast in-situ, with the floors being propped as required.

A simplified design method developed for timber-concrete composite floors [11] based on the effective cross section method from Eurocode 5 [12] gave good results when compared with large scale fire tests. Although these systems have some major differences to the one under investigation in terms of connection type, timber species and major floor element geometries, it provided an insight into methods in which the issue of fire resistance for these systems can be addressed.

2 MATERIAL PROPERTIES

2.1 Laminated Veneer Lumber

New Zealand laminated veneer lumber (LVL) consists of 3-4mm thick rotary peeled veneers of Radiata Pine glued with resorcinol adhesive. These layers have the grain orientation running in the same direction (as opposed to plywood alternating grain orientation by 90° for each layer) which gives the highest strength properties for bending and tension in one direction. Such beams can resist much greater loads and hence span longer distances compared with traditional sawn timber. The manufacturing process of LVL also allows for greater dimensional accuracy, and additives such as fire retardants can also be implanted in the veneers depending on the desired performance.

The fire behaviour of LVL has been investigated in recent years. Research by Lane [13] has looked into the ignition, charring and structural performance of LVL. In terms of the glue lines in LVL affecting the charring rates, Lane found in a number of un-instrumented char tests that there was relatively no difference between charring parallel or perpendicular to the grain. These results suggest that the presence of the glue lines do not influence the burning behaviour of the material.

Lane conducted cone calorimeter tests on LVL samples, and furnace tests on LVL members. This furnace testing consisted of subjecting LVL members to the standard ISO 834 fire [14] in a pilot furnace, and also in a full scale furnace under loaded conditions. From this research he suggested a charring rate for New Zealand manufactured Radiata Pine LVL of 0.72 mm/min under standard fire exposure. This is similar to the charring rate of 0.70mm/min for LVL in Eurocode 5 [12].

3 NUMERICAL MODELLING

Advanced numerical modelling is required when a problem becomes too complex to be solved by hand, and a greater understanding is required of the underlying principles and mechanisms involved in the analysis of the problem. This is often desirable to the alternative of experimental testing, as testing can be uneconomical, time and labour intensive, and only one particular set of circumstances can be investigated in each test. Furthermore when considering the modelling of floors, a numerical modelling approach allows for vast amounts of data to be calculated for many different types of floor geometries and loading conditions in an economical and efficient manner. Complex geometries and load transfer between floor components can be designed and accounted for, while very precise loading arrangements and material properties can be specified for a particular situation. This enables the user to obtain results directly proportional to the quality and quantity of the input into the software, and at a specified level of detail. It is important that the analytical method used is not pushed beyond its limits of applicability [15]. Higher order effects of fire impact on timber such as mass transfer (moisture movement), thermal creep, char cracking and drop-off can also be incorporated into the analysis, thus enabling many different influences on floor performance to be investigated at once and key factors affecting the overall performance of the floors to be isolated.

The software ABAQUS [16] was used for the numerical simulations. The approach taken in this research was stepwise, gradually introducing increased levels of detail into both the thermal and structural analyses. Initially only one-dimensional problems were considered, moving on to two-dimensional (2D) simulations and eventually graduating to three-dimensional (3D) analyses. The models were constantly compared with test results where applicable to ensure reasonable output was being achieved at each step of the analysis, and the previous models used to ensure the accuracy of the results.

The ultimate goal of this modelling was to conduct 3D sequentially coupled thermo-stress analyses to determine the effects of a fire on floor assemblies under load. This involved a thermal analysis to determine the temperature profile of the floor assemblies for the duration of modelling, and then a stress analysis using the temperature profile as an input into the structural model. This procedure was used as the stress profile of a timber member is influenced by the temperature profile, but the converse is not true, in other words the temperature is not affected by mechanical stresses and can be computed as a separate initial step.

3.1 Thermal Modelling

For greater confidence in the results obtained, three separate numerical software suites were run in collaboration during this research focussing on defining acceptable material parameters and expected behaviour. The numerical software used in this research was ABAQUS [16], however both ANSYS [17] and SAFIR [18] have been used for verification.

The first objective of the thermal modelling was to determine the acceptable range of parameters to use in ABAQUS to appropriately model one- and two-dimensional heat transfer through timber sections. A second objective was to define an appropriate set of effective material properties comparable with experimental results found in literature, and what was achieved through modelling in similar software packages. Detailed results of this and comparisons between the three software suites are described by Werther *et al.* [19]. As a baseline for configuring the material model of timber for heat transfer in ABAQUS, the properties found in Annex B of Eurocode 5 [12] were used; specifically these were the thermal conductivity, specific heat, latent heat and density. Using these values was recommended as a way of accounting for the physical and chemical changes that occur as timber combusts, such as moisture movement, charring and shrinkage. These effective values also encompass many second order effects and allowed for simplified modelling of heat transfer through timber, while still giving a good approximation to timber behaviour in reality.

The input of thermal properties into software was implemented in two separate procedures. The first was a user defined kpc model, where the symbols represent the thermal conductivity, density and specific heat, respectively. The specific heat is defined as the amount of energy required to change the temperature

of a material by a unit amount, in SI units this is measured in kJ/kgK. In the case of timber there is a peak in the reported values of specific heat, most commonly taken as between 99 to 120°C. This is to account for the vaporisation of water in the timber, and results in a large increase in energy required to facilitate this phase change from liquid to gas. The second procedure was the latent heat model that allows for the removal of this peak from the specific heat curve, as it accounts for the extra energy of phase change over the specified temperature range. Further validation of this work in comparison to experimental results is also discussed by Werther et al. [19].

For the 3D thermal modelling of timber floors, the temperature distribution in the cross section was computed as an uncoupled heat transfer analysis using 8 node linear solid elements, DC3D8 [16]. Depending on the floor geometry, beams are generally subjected to 3 sided exposure to the ISO834 fire as a standard temperature input into the models, and this is also applied to the underside surfaces of the floors. This was applied via surface film conditions and surface radiation to the exposed surfaces, and ambient conditions were modelled on the top of the slab. The convection coefficient and emissivity were taken from Eurocode guidance [12,21] and assumed to be 25 W/m²K and 0.8, respectively. As an initial starting point for 3D thermal modelling the cross section was discretised into a 6 mm mesh, and along the length of the floor the mesh was left very coarse (greater than 10 times the cross-section mesh size). This coarseness allowed for faster computation times, however when the mesh was translated to the structural model it proved to be poor for the stress analysis. Therefore once the final floor design was chosen a more appropriate mesh size was used along the length.

3.2 Structural Modelling

The objectives of the structural modelling were twofold. Firstly, prototype modelling of different simple loading conditions on timber such as tension, compression and bending, were compared with experimental results to give confidence in the modelling techniques. The second objective was to model the timber floor systems described in this report via sequentially coupled thermo-stress analysis.

When sequentially modelling the floors in 3D the same mesh from the thermal analysis was imported into the structural model, and the element type used was an 8 node 3D linear solid element, C3D8R [16]. To consider the reduction in mechanical properties with temperature, values for the reduction in strength and modulus of elasticity were taken from the Eurocode [12]. Timber behaves in a brittle manner in tension, and exhibits elasto-plastic behaviour in compression. Currently the material model being used to characterise these stress-strain relationships for timber is a steel yield model, which means only one stress strain curve can be adopted for both compression and tension. Future research will include development of a timber material model in which different relationships for compression and tension can be defined.

3.3 Thermo-mechanical Analysis

Sequential modelling has been conducted on timber members and systems in the past however it very commonly only considers members in either tension or compression. Modelling of bending in timber is more complex than simple compression or tension, as it is three-dimensional and buckling must be considered, as well as the method of failure being properly defined and modelled. The orthotropy of the material and appropriate failure criteria must also be included.

Numerical modelling must account for redistribution of stresses to the inner region of the beam as the extreme fibres in tension approach failure. To obtain sensible results it is important to ensure that what others in the field have done can be modelled alongside the research at each stage of development, so a final three-dimensional model can be achieved with a reasonable level of certainty.

There are a number of studies which have been conducted in the past focussing on structurally modelling timber in fires. One such study is that of Fragiaco et al. [22] which involved the experimental testing of LVL in tension in a small scale furnace, and the efforts to numerically model the tests. The tests were conducted on rectangular sections of LVL, half immersed in a furnace and loaded under a constant tension force. A sequential thermal-stress analysis was carried out in ABAQUS concentrating on modelling the experimental testing by first building a thermal profile of the timber section, then inputting this into the three-dimensional structural model considering axial forces only.

Failure was considered to occur when the elements were no longer able to properly redistribute stresses to cooler regions, hence the solution was seen as diverging and the failure time taken as the last increment in the model. The results of this modelling slightly under-predicted the temperature in the timber when compared with the experiments, but overall provided a good approximation. The work provided insight into ways in which ABAQUS can be used to model simple structural behaviour under fire conditions.

Bobacz [23] also investigated axially loaded timber members in tension and compression under fire conditions. A large portion of his research was defining an appropriate charring model based on other work. A generic thermal model was developed to predict the temperature profile throughout a cross-section of timber, and then the simulated member was structurally analysed under fire conditions in ANSYS. In terms of assessing failure, Bobacz only considered cross section analyses in which a displacement controlled strain was applied until the ultimate strength reached, and then ultimate load at this point was derived from the integration of the stresses over this cross-section. From this he proposed a stochastic method of sizing members for fire resistance based on inputs of the three major modelling sections above. At each major step the modelling was checked against the simplified methods available in literature [12], and validated against experimental testing where possible. This research was comprehensive in both defining timber properties in fires and simplified ways of thermally and structurally modelling timber, and provided an excellent point of comparison when conducting the current research.

4 EXPERIMENTAL TESTING

A portion of this research is dedicated to calibration and validation of the numerical modelling; hence full-scale testing of these floors is required.

4.1 Tests of TCC floors

Testing was conducted at the BRANZ facilities in 2009 [10] on two timber-concrete composite floors. The primary objective of the full scale testing was to investigate the failure behaviour of timber-concrete composite floors when exposed to fire, which encompassed a wide range of information that was required to be collected from different parts of the floor system. Specifically, the failure mode of the floors was an important part of this as it would identify the critical component of the floor system that governs the design for fire safety, whether it was failure in the beams, the concrete slab or the connections between the two. Other important areas of interest were the charring behaviour of the timber beams, the spalling behaviour of the concrete, the fire damage about the connections and the performance of the plywood sheathing. The test fire was the ISO 834 standard test fire [14].

Due to their combustibility, timber beams cannot be scaled down in size as their fire behaviour is dependent on the actual cross-section present. This required that the loads on the floor units be scaled up in such a way that similar stresses were induced in the load bearing members of the floor and the same bending moment at the mid-span of the floors was obtained. The design loads of the test specimens were based on a live load of 2.5 kPa and a dead load of the self-weight of the floor only, with no additional dead load. The first floor specimen tested was the 300 mm beam floor, which was tested to destruction. Failure occurred at 75 minutes under the ISO 834 design fire and applied design load. The side with notched connections (Figure 2) failed first, and the testing was terminated. The second floor was the 400 mm beam floor and is shown in Figure 3 directly after furnace testing. This test was stopped shortly after 60 minutes to assess the damage at that time and to provide insight into how the beams were charring before complete destruction.



Figure 3. Full scale testing of a timber-concrete composite floor system at BRANZ.

4.2 Charring

The initial and remaining section sizes are shown in Table 1. Measurements represented in the table were taken from intermediate regions in the beams as the char depth across the beams was very uniform along the beams based on inspection of the charred remains.

Table 1. Residual Beam Sizes After Testing.

Test Specimen	Size Before Test (WxH mm)		Size After Test (WxH mm)		Burning Time
300 mm	126	300	44	130	75
400 mm	126	400	52	255	60

The charring rate on the sides of the LVL beams in the full scale testing was found to be 0.58 mm/min on average, lower than reported values of 0.72 mm/min based on research conducted by Lane [13] on similar LVL at the BRANZ facilities. The charring rate on the underside of the beams was very high, being on average four times as large as the charring rate from either side of the beams. This was expected as the majority of this charring occurred in the latter stages of burning once the residual section had been reduced to such a size that the central area of the timber beams had increased above the initial ambient temperature, thus increasing the rate of heating and burning of the remaining section. Further work on the charring behaviour of these configurations of beams considering different fastener types and configurations is detailed by Tsai [23].

4.3 Displacement

For both floors tested the measured vertical displacement up to the point of runaway structural failure was less than 1/20 of the span (200 mm) and the rate of increase of displacement was also low (until runaway failure occurred). Some common structural requirements specify deflections of less than 1/20 of the span or a limiting rate of deflection when deflection is 1/30 of the span [24].

4.4 Tests of Timber Composite Floors

For testing of all-wood Timber Composite Floors, a beam type floor and a box type floor will be tested at the Building Research Association New Zealand (BRANZ) facilities in Wellington. Both will have pin/roller supports and a span of 4 metres parallel to the long axis of the furnace, loaded through the

centreline at two points. The first phase of this testing will be undertaken in March 2012, to be reported at the SIF 2012 conference, and the second phase in July 2012.

5 NUMERICAL RESULTS

At this stage in the research the sequential modelling of LVL beams and composite timber floors has been conducted to such a degree that viable results have been obtained for load displacement and heat transfer. Modelling the concrete slab is currently underway, however the development of an appropriate material model to accurately predict the concrete slab behaviour has not yet progressed enough for publication. The following section compares results between the beam modelling and the test results obtained during the timber-concrete composite floor tests described.

5.1 Heat Transfer

The 300 °C thermal wave at 60 minutes for the 400 mm deep beam occurred at approximately 39 mm (48 mm remaining beam width). This compared well to the experimental results presented in Table 1 of 52 mm remaining beam width, but is slightly conservative. Further comparisons of experimental results with this thermal modelling of LVL can be found in the previously mentioned study [19].

5.2 Displacement

Figure 4 shows the results obtained for the 300mm beam modelling in terms of runaway displacement failure. This is compared to the measured fire resistance time of the 300mm floor in the test, and the calculated fire resistance time of the spreadsheet method derived from this testing.

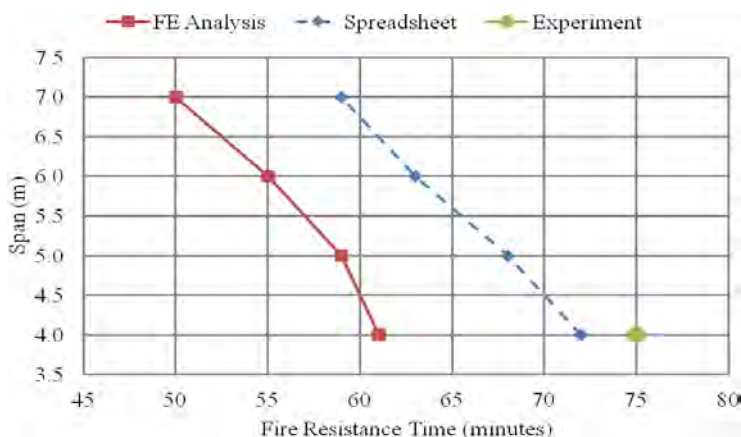


Figure 4. Modelling and experimental results for fire resistance time of 300 mm beams and floors.

The prediction of the numerical modelling for failure times of the beam shows that the model follows the same trend as the TCC floor spreadsheet calculations (based on the test data), and is on the conservative side of the data. This is expected as the TCC floors have a large degree of composite action taking place when the residual beam size becomes small, providing a longer fire resistance time.

Figure 5 shows the same results as Figure 4 but for the larger 400 mm floor. Note that the full-scale test did not go to destruction hence there is no experimental value incorporated in this plot. As before the numerical modelling prediction follows a similar trend to the calculated floor resistance times, and it is expected that once concrete slab behaviour is incorporated into the model the curves will sit closer together.

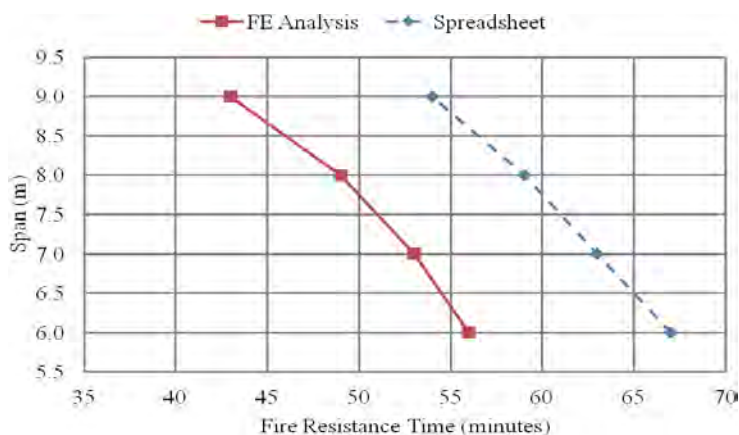


Figure 5. Modelling results for fire resistance time of 400 mm beams and floors.

6 CONCLUSIONS

This paper details the research being conducted to sequentially model timber composite floors under fire exposure. Appropriate thermal properties have been defined for the timber, verified against experimental results, allowing 3D thermal modelling to be conducted and temperature profiles of timber cross sections to be determined. Sequential thermo-stress analyses have been conducted for LVL beams and compared to experimental data from furnace tests. It was found that at this stage in the modelling the prediction of fire resistance by displacement compares well to the experimental results.

As this research is a work in progress, there remains a portion of work yet to be completed. In terms of numerical modelling, the development of more appropriate material models for timber and concrete are required to incorporate the desired mechanical properties necessary for the advanced floor analysis. Upcoming full scale furnace tests of both timber joist and box floors are also being conducted in 2012. The results of these tests will be used to validate the results obtained in the numerical modelling.

The end goal of this research is the development of simplified design methods based on the numerical modelling and experimental testing, such that the fire resistance of composite timber floor assemblies can be quickly calculated for a range of floor geometries, loading conditions and material types.

REFERENCES

- [1] Buchanan A.H., "Timber Design Guide", Third Edition. *New Zealand Timber Industry Federation Inc.*, Wellington, New Zealand, 2007.
- [2] Grant, G., "Evaluation of Timber Floor Systems for Fire Resistance and Other Performance Requirements", *Fire Engineering Research Report*, University of Canterbury, Christchurch, New Zealand, 2010.
- [3] Lukaszewska E., Johnsson H., and Fragiacommo M., "Performance of Connections for Prefabricated Timber-Concrete Composite Floors", *Materials and Structures*, RILEM, Vol. 41, Issue 9, pp. 1533-1550, 2008.
- [4] Fragiacommo M., Gutkowski R.M., Balogh J., Fast R.S., "Long-Term Behavior of Wood-Concrete Composite Floor/Deck Systems with Shear Key Connection Detail", *ASCE Journal of Struct. Engrg.*, Vol. 133, Issue 9, pp. 1307-1315, 2007.

- [5] Kuhlmann U., Michelfelder B., "Optimized Design of Grooves in Timber-Concrete Composite Slabs", *Proc. The 9th World Conference on Timber Engineering WCTE 2006*, Portland, Oregon, USA, CD, 2006.
- [6] Bathon L., Bletz O., Schmidt J., "Hurricane Proof Buildings-An Innovative Solution using Prefabricated Modular Wood-Concrete-Composite Elements", *Proc. 9th World Conference on Timber Engineering*, Portland, Oregon, USA, 2006.
- [7] Buchanan A., Deam B., Fragiacommo M., Pampanin S., and Palermo A., "Multi-storey prestressed timber buildings in New Zealand", *Structural Engineering International*, IABSE, Special Edition on Tall Timber Buildings, 2007.
- [8] Frangi A., Fontana M., "Fire Behaviour of Timber-Concrete Composite Slabs", *Proc. The 6th International Symposium on Fire Safety Science*, Poitiers, France, July 5-9, 1999.
- [9] Yeoh D., "Behaviour and Design of Timber-Concrete Composite Floors under Short and Long-Term Loading", *Doctorate Thesis in Civil Engineering*, University of Canterbury, Christchurch, New Zealand, 2009.
- [10] O'Neill J.W., "The Fire Performance of Timber-Concrete Composite Floors", *Master's Thesis in Fire Engineering*, University of Canterbury, Christchurch, New Zealand, 2009.
- [11] Frangi A., Fontana M., "A Design Model for the Fire Resistance of Timber-Concrete Composite Slabs", *Proc. Innovative Wooden Structures and Bridges*, Lahti, Finland, August 29-31, 2001.
- [12] EC5 "Eurocode 5: Design of Timber Structures, Part 1-2: General - Structural Fire Design", EN 1995-1-2: 2004, European Committee for Standardisation, Brussels, Belgium, 2004.
- [13] Lane W.P., "Ignition, Charring and Structural Performance of Laminated Veneer Lumber", *Fire Engineering Research Report*, School of Engineering, University of Canterbury, 2005.
- [14] ISO "Fire Resistance Tests - Elements of Building Construction", *ISO 834: 1975*, International Organisation for Standardisation, 1975.
- [15] Cook R.D., "Finite Element Modelling for Stress Analysis", First Edition. *John Wiley and Sons, Inc.*, USA.
- [16] ABAQUS version 6.10 Dassault Systèmes Simulia Corporation, Providence, RI, USA, 2010.
- [17] ANSYS version 12.0 ANSYS Inc., Canonsburg, PA, USA, 2009.
- [18] SAFIR University of Liège, Liège, Belgium, 2011.
- [19] Werther N., O'Neill J.W., Spellman P.M., Abu A.K., Moss P.J., Buchanan A.H., Winter S., "Parametric Study of Modelling Structural Timber in Fire with Different Software Packages", *Proc. The 7th International Conference on Structures in Fire*, Zurich, Switzerland, June 6-8, 2012.
- [20] EC1 "Eurocode 1: Actions on Structures. Part 1-2: General – Actions on Structures Exposed to Fire", EN 1991-1-2:2003, European Committee for Standardisation, Brussels, Belgium, 2003.
- [21] Fragiacommo M., Menis A., Moss P.J., Clemente I., Buchanan A.H., "Numerical and Experimental Thermal-structural Behaviour of Laminated Veneer Lumber (LVL) Exposed to Fire", *Proc. World Conference on Timber Engineering*, Riva del Garda, Italy, June 20-24, 2010.
- [22] Bobacz D., "Behavior of Wood in Case of Fire - Proposal for a Stochastic Dimensioning of Structural Elements", *Doctoral Thesis in Civil Engineering*, University of Natural Resources and Applied Life Sciences, Vienna, Austria, 2006.
- [23] Tsai K., Carradine D., Moss P. And Buchanan A., "Charring rates for double beams made from laminated veneer lumber (LVL) ", *Fire and Materials*, Published online in Wiley Online Library (wileyonlinelibrary.com). DOI:10.1002/fam.2112, 2012.
- [24] Buchanan A.H., *Structural Design for Fire Safety*, John Wiley & Sons Ltd, Chichester, 2001.

EXPERIMENTAL AND NUMERICAL ANALYSIS OF THE THERMO-MECHANICAL BEHAVIOR OF STEEL-TO-TIMBER CONNECTIONS IN BENDING

Dhionis Dhima*, Maxime Audebert**, Abdelhamid Bouchaïr**, Mustapha Taazount**

* CSTB, 84 avenue Jean Jaurès, 77447 Marne-la-Vallée Cedex 2, France
e-mail: dhionis.dhima@cstb.fr

**Université Blaise Pascal, Institut Pascal, BP 206, F-63000 Clermont-Ferrand, France.
e-mails: (maxime.audebert; bouchaïr; mustapha.taazount)@polytech.univ-bpclermont.fr

Keywords: Fire tests, steel-to-timber connections, ISO-fire, bending, 3D finite element model.

Abstract. *Two different configurations of steel-to-timber connections are tested in bending in normal conditions and under ISO-fire exposure. To observe the influence of clearances in the connection area on the fire resistance of the connections, two specimens were previously tested under cyclic loadings. These tests consist in the application of an increasing-decreasing strength of connections by imposed displacements. The experimental results of connections tested in cold and under ISO-fire conditions are analyzed and commented. These results are then used to validate a finite element model. This model allows simulating the evolution of the temperatures inside the connections as well as their mechanical and thermo-mechanical behaviors. The modelling of the mechanical behaviour of timber is made by using the Hill yield criterion in combination with the Tsai-Wu failure criterion. The thermo-mechanical modeling allows obtaining fire resistances of the tested connections in good agreement with the experimental ones.*

1 INTRODUCTION

In timber structure, the connections exhibit more sensitive and complex thermo-mechanical behaviour. The design procedure given in Eurocode 5 (EN 1995-1-2) [1] is based on a limited number of experimental and numerical results [2,3]. This is due to the high cost and to the complexity of the large-scale experiments of connection components in fire conditions. To improve the level of knowledge concerning the thermo-mechanical behaviour of timber connections, real-scale tests and numerical investigations were realised in France from 1999 to 2010 [4-7]. This research concerned tests of various timber connections with bolts and dowels realised at normal temperature and under ISO-fire, and subjected to different loadings: tension parallel to grain, tension perpendicular or with an angle to the grain, and bending. The experimental results show the real fire resistance of the tested connections and are used to validate numerical simulated results. A 3D finite element model has been developed the last years to simulate the mechanical and thermo-mechanical behaviour of timber connections subjected to a longitudinal tension [8-10].

Nevertheless, in real conditions the timber connections are seldom loaded in pure longitudinal traction. In most of the cases, they worked in traction or compression parallel or perpendicular to grain combined with shear [11]. For example, frame connections or truss connections are exposed, at the same time, to loads in tension or compression and shearing. Thus, it appears necessary to extend the experimental and numerical analysis to timber connections subjected to combined stresses. This paper concerns the experimental and numerical analysis of timber connections loaded in bending.

In the first part, the experimental results of steel-to-timber connections in bending tested in cold conditions and under ISO-standard fire exposure are presented and commented. To observe the influence of clearances in the connection area on the fire resistance of the connections (e.g. due to a seismic event), two specimens were tested under cyclic loadings before the fire tests. Then, the numerical analysis is realised by using two different 3D models: one for the heat transfer and the second one for the mechanical and thermo-mechanical behaviour. The main assumptions considered for the modelling are presented and justified. Each step of the modelling of the thermo-mechanical behaviour of the tested connections is validated on the basis of the experimental results. The heat transfer model is validated on the basis of the measured and calculated charring rates as well as the measured temperatures inside the various components of the connections. The mechanical model is validated by the use of experimental load-slip curves obtained after tests in normal conditions. Finally, the thermo-mechanical model is validated by comparison of the fire resistance durations obtained by the experimental and numerical time-slip curves.

2 EXPERIMENTAL STUDY

2.1 Tests setups

The connections are made with timber of glulam resistance class GL24h assembled with a steel plate and 6 dowels of diameter 16 mm. The thickness of the timber members is 77.5 mm. The connections have been designed in accordance with the minimum requirements of the EN1995-1-1 [12] for spacing and size. Two dispositions of fasteners are tested: connections of Type A are composed with two rows of three dowels while connections of Type B are composed with three rows of two dowels. The two experimental configurations are illustrated on the figures 1 and 2. On the Table 1, are summarized the geometrical data of the connections.

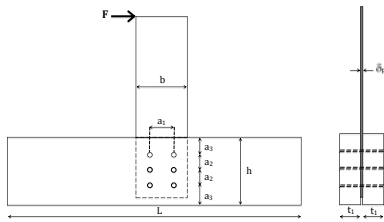


Figure 1. Geometrical configuration of the tested connections (Type 1).

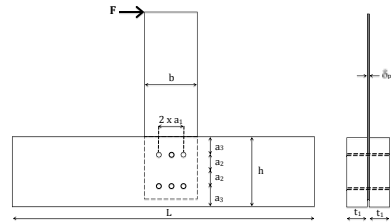


Figure 2. Geometrical configuration of the tested connections (Type 2).

Table 1. Geometrical data of the tested connections (mm).

Connections	ϕ	t_1	L	h	b	δ	a_1	a_2	a_3
Type A	16	77.5	2000	445	260	8	200	108	115
Type B	20	77.5	2000	445	260	8	100	216	115

For each configuration, two tests were realized in normal conditions of temperature and three tests were realized under ISO-fire exposure. Tests in normal conditions allow determining the load-displacement curves of the connections and mainly their stiffness and load-carrying capacity. The loading was applied on the steel plate in accordance with the protocol of the standard NF-EN 26891. The relative displacement between the steel plate and the timber members were measured using LVDT sensors.

Afterwards, equivalent specimens were tested in fire conditions under a nominal standard fire. In addition, the failure loads $N_{u,tests}$ obtained by the tests in normal conditions were used to define the load to be applied on the connections during fire tests, using the chosen load ratio η_{fi} . Three load ratios have

been applied for fire tests: $\eta_{fi} = (12, 38 \text{ or } 45\%) * N_{u,tests}$. Several thermocouples (24) were introduced at different locations inside the connection members to measure the temperatures during the fire tests. Two displacement sensors were used to measure the horizontal and the vertical displacement of the steel plate. The loading protocol for mechanical fire tests was defined by the standard NF-EN 26891. After preloading up to 40% and unloading to 10% of $N_{u,tests}$, the specimen was reloaded to the chosen load ratio η_{fi} . Then, the fire exposure according to the curve ISO 834 was started. The load ratio was kept constant throughout the exposure to fire until the failure of the connections.

To observe the influence of clearances in the connection area on the fire resistance of the connections (e.g. due to a seismic event), two specimens (one of each configuration type) were previously tested under cyclic loadings, according to EN 12512 [13]. Thus, a cyclic loading was applied to the steel plate with increasing amplitude determined according to the displacement. Indeed, the controlled displacement applied to the plate had to increase gradually until 75% of the value of u_y , which was the limit relative slip of the connections measured at the failure during tests in normal conditions. Figure 3 shows the loading protocol used for these tests and figure 4 shows the load-slip curve obtained for the connection of Type B. At the end of these tests, the steel plates were “rickety”, which illustrates that there was creation of clearances inside the connections.

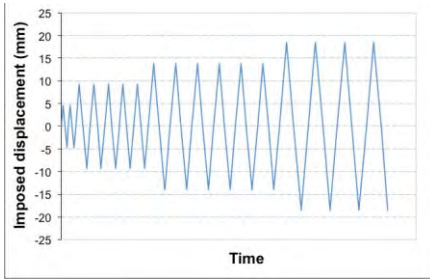


Figure 3. Loading protocol for tests under cyclic loadings (connection Type A).

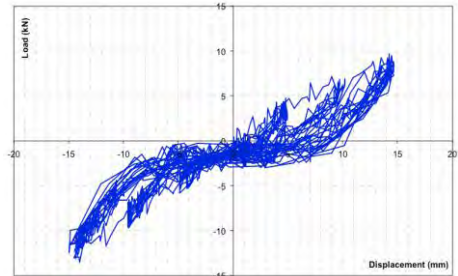


Figure 4. Load-slip curves for cyclic test (connection Type B).

2.2 Test results in normal conditions

For each configuration type, two tests were realized in normal conditions of temperature ($\sim 20^\circ\text{C}$). Connections of Type A showed the most ductile behaviour, with high plastic deformations due to the dowel bending. For connections of Type B, a splitting failure appeared in the connection area on one of the timber member. Nevertheless, the ductile behaviour of the connection stays predominant (Figure 5).

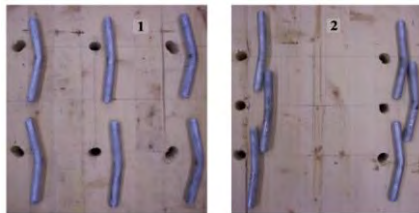


Figure 5. Deformations of timber and dowels in the connection area.

Table 2 gives the values of yield and ultimate strengths F_y and F_u of the tested connections, as well as the value of the limit relative slip at the end of the test. The connections of Type A have a load-

carrying capacity slightly lower than u_y those of Type B. The strength values of the connections calculated according to EN1995-1-1 [12] are compared to the experimental strength values (Table 3). The comparison shows that the theoretical values are lower than the experimental ones. Thus, the prediction of the failure load and mode is acceptable, because these results are in safety side.

Table 2. Experimental results in normal conditions.

Connections	Test	u_y (mm)	F_y (kN)	F_u (kN)	F_u / F_y
Type A	1	22.4	32.4	33.9	1.05
	2	22.5	31.1	33.3	1.07
Type B	1	22.8	34.9	38.9	1.12
	2	19.1	34.2	38.6	1.13

Table 3. Experimental and theoretical strength values of the connections.

Connections	EN1995-1-1		Tests	
	F_y (kN)	F_u (kN)	F_y (kN)	F_u (kN)
Type A	23.5	25.6	31.8	33.6
Type B	26.5	31.1	34.5	38.8

2.3 Fire test results

Table 4 presents the experimental values of fire resistance $t_{fi,exp}$ depending on the load ratio η_{fi} . High values of fire resistances were obtained. The presence of clearances within the connections seems to have a little influence on the fire resistance with a reduction of 4 minutes for both types of connections. The increase of the load ratio from 12 to 38 % for Type A connections leads to a reduction of 18 minutes of the fire resistance. For Type B connections the increase of load ratio from 38% to 45% leads to a reduction of 6 minutes of fire resistance. In spite of the higher load-carrying capacity in normal condition of Type 2 connections, the two configurations allow to obtain similar fire resistance values.

The failure of these connections occurs by large deformations due to the embedding of wood (Fig. 6). No brittle failure, by splitting, was obtained. The failure is experimentally defined for a quick acceleration of the displacements. Thus, to define fire resistance durations of the connections, a tangent method was used on the experimental global load-slip curves. No deformation of the dowels or the steel plates was observed.

Table 4. Experimental fire resistances of the connections.

Connections	Test	η_{fi} (% $N_{u,tests}$)	$t_{fi,test}$ (min)	Cyclic tests
Type A	1	12	66	-
	2	38	48	-
	3	38	44	Yes
Type B	1	38	46	-
	2	38	42	Yes
	3	45	40	-



Figure 6. View of specimen B1 after fire test.

3 FINITE ELEMENT MODELLING

A three-dimensional (3D) finite element model (FEM) is developed to predict the thermo-mechanical behaviour of the connections exposed to fire. Two different meshes are used for the thermal and the thermo-mechanical calculations. The model is validated at each stage on the basis of the experimental results.

3.1 Numerical modelling of heat transfer

For the thermal analysis, the 3D-FEM model is developed by using the MSC.MARC software package with 20-noded hexahedral elements. Taking into consideration the symmetry, only half of the connection was modelled: adiabatic surface in symmetrical plan. A perfect contact, with continuous meshing, is considered at all the interfaces between timber, steel plates and fasteners. The external temperature applied to the connections is given with the evolution of the normalized time-temperature curve ISO 834.

The numerical simulations of heat transfer within the connection are performed considering the evolutions of the thermo-physical properties of the materials such as the thermal conductivity and the specific heat. The thermo-physical properties of steel are given by EN1993-1-2 [14]. The evolutions of the thermo-physical properties of timber which depend on temperature were taken from a sensitivity analysis performed using several values of thermal conductivity and specific heat proposed by different authors [15]. The goal was to find the most appropriate thermo-physical characteristics to be used in the modelled connections. This sensitivity analysis showed that for wood components the best combination of thermal conductivity and specific heat, giving the best numerical results, is obtained using the thermal conductivity values proposed by Janssens and the specific heat values proposed by Fredlund and Janssens (Figure 7). Due to the thermal gradient and pressure gradient inside timber grains a part of water migrates towards the timber-steel plate's interface. The measured temperatures in fire exposure tests show the presence of a temperature plateau between 90°C and 100°C. In order to take into account the latent heat of water migrated near steel plate, a peak of specific heat of 100 kJ/(kg K) is introduced at 100°C for 3D-FEM modelling. This value of specific heat is used only for a thin layer of timber (3 mm) in contact of steel plate in both sides. This hypothesis was validated by the simulations of heating of several tests of connections subjected to a parallel to grain tension [9].

The heat transfer model gives the distribution of the temperature field on the nodes of the elements constituting the connection components for each step of time. The first comparison between tests and numerical results concerns the average charring rate of the wood members. For the simulation, the charring rate is defined by the isotherm of 300°C and the exposure time at which this value is reached. The experimental mean values of charring rate are obtained from the measurements on residual wood thicknesses of the specimens after fire tests. Table 5 summarizes the charring rate values obtained by tests and from the numerical model. These results show that the heat transfer model is based on satisfactory and safe assumptions.

Temperature (°C)	c (J/(kg.K))
0	1440
20	1440
200	2140
300	720
1000	720

a) Specific heat (Fredlund / Janssens)

Temperature (°C)	λ (J/(kg.K))
0	0.12
100	0.16
117	0.125
200	0.15
350	0.12
600	0.15
1000	0.22
1200	0.27

b) Thermal conductivity (Janssens)

Figure 7. Thermo-physical properties of wood used for the heat transfers modeling.

The heat transfer model gives the distribution of the temperature field on the nodes of the elements constituting the connection components for each step of time. The first comparison between tests and numerical results concerns the average charring rate of the wood members. For the simulation, the charring rate is defined by the isotherm of 300°C and the exposure time at which this value is reached. The experimental mean values of charring rate are obtained from the measurements on residual wood thicknesses of the specimens after fire tests. Table 5 summarizes the charring rate values obtained by tests and from the numerical model. These results show that the heat transfer model is based on satisfactory and safe assumptions.

Table 5. Experimental and theoretical failure times of the connections.

	β_0 for lateral sides of timber members (mm/min)	β_0 for upper and lower sides of timber members (mm/min)
Tests	0,64	0,76
3D-FEM	0,68	0,72

Figures 8 to 10 show the evolutions of the calculated and the measured temperatures for different components of the connection A16. These curves show a good agreement between measured and computed values of temperature. Similar results were obtained for all tests of the connections using the same thermal properties and hypothesis of the model. On the basis of these results, the heat transfer model is validated.

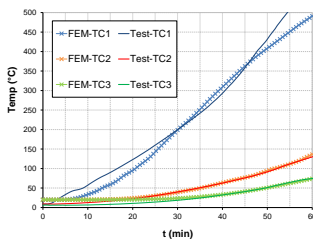


Figure 8. Numerical and experimental temperatures in timber members.

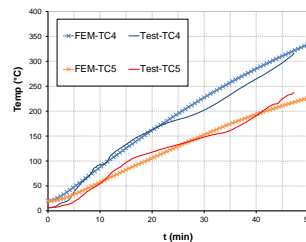


Figure 9. Numerical and experimental temperatures in fasteners.

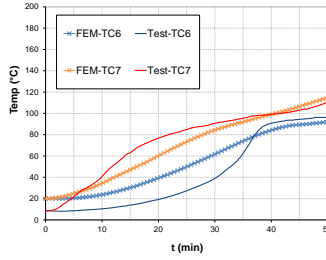


Figure 10. Numerical and experimental temperatures on steel plate.

3.2 Numerical mechanical model in normal conditions

The numerical model representing the behaviour of connections in normal conditions takes into account the material and the geometrical nonlinearities. To describe accurately the evolution of the contact in the interfaces between the connection components, the meshing is refined in an extended zone around the fasteners. Boundary conditions representing the real experimental conditions are applied. The load application is performed by an imposed gradual displacement on the extremity of the steel plate. The interaction between the different components of the connections is modelled using deformable contact elements at each interface. The meshing of the mechanical model is so discontinuous and differs from that used for heat transfer. A friction coefficient of 0.3 is taken into account between fasteners and timber [9].

The steel material is considered as nonlinear isotropic (Young modulus $E = 210\,000$ MPa and Poisson ratio $\mu = 0.3$). The evolution of plasticity in the fasteners until reaching the plastic hinges is considered using the von Mises yield criterion. The mechanical behaviour of wood is considered with transverse isotropy assuming the same properties of the material for both radial and tangential directions. The laminated timber used for these tests is of class GL24h. The measured average density of the timber is 438 kg/m^3 . The mean values of the elastic modulus and the Poisson's coefficients retained are the ones relative to a laminated timber of class GL24h (Table 6). Shear and tension strength values of the timber are mean values obtained from the characteristic values of the standard NF EN 1194 by using a coefficient equal to 1,2. Longitudinal and perpendicular compressive strength ($f_{c,0}$ and $f_{c,90}$) values are determined by tests (Table 7).

Table 6. Mechanical properties of timber used in the model.

E_0 (MPa)	E_{90} (MPa)	G_{mean} (MPa)	$\nu_{\text{TR}} = \nu_{\text{LT}}$	ν_{RL}	ρ (kg/m ³)
11600	390	750	0.41	0.02	438

Table 7. Mechanical properties of timber used in the model.

$f_{c,90}$ (MPa)	$f_{c,0}$ (MPa)	$f_{t,90}$ (MPa)	$f_{t,0}$ (MPa)	f_v (MPa)
39	3.4	19.8	0.48	3.24

The Hill yield criterion is used to manage the plastic behaviour of timber components. This criterion is a generalized version of the von-Mises yield criterion to consider the anisotropy of the material (1).

$$2 \cdot \sigma^2 = a_1 \cdot (\sigma_y - \sigma_z)^2 + a_2 \cdot (\sigma_z - \sigma_x)^2 + a_3 \cdot (\sigma_x - \sigma_y)^2 + 3a_4 \cdot \tau_{xz}^2 + 3a_5 \cdot \tau_{yz}^2 + 3a_6 \cdot \tau_{xy}^2 \quad (1)$$

$$\text{with: } a_1 = \frac{2}{f_{c,90}^2} - \frac{1}{f_{c,0}^2}; \quad a_2 = a_3 = \frac{1}{f_{c,0}^2}; \quad a_4 = a_5 = a_6 = \frac{2}{3\tau^2}$$

However, the yield Hill criterion is a symmetric criterion which does not take into account the asymmetry of the mechanical behaviour of timber in compression and tension. The high difference between the values of $f_{c,90}$ and $f_{t,90}$ requires to take into account this asymmetry. Thus, the Hill criterion is combined with the Tsai-Wu failure criterion [16]. It is expressed as follow:

$$F_i \sigma_i + F_{ij} \sigma_i \sigma_j = 1 \quad \text{with: } i, j \in \{1, 2, 3, 4, 5, 6\} \quad (2)$$

This criterion needs 27 coefficients to be identified. Its linear terms σ_i take into account the dissymmetry between tension and compression. A condition of stability on the interaction terms F_{ij} is introduced to avoid the surface represented by the criterion to have an opened shape as hyperboloidal type. The surface represented by the criterion will have intersection points with all the axes defining the considered space of stress:

$$F_{ii} F_{jj} F_{ij}^2 > 0 \quad (3)$$

The hypotheses of orthotropic symmetry reduces the number of coefficients to 12. Then, the Tsai-Wu criterion can be expressed as follow:

$$F_{11}\sigma_1^2 + F_{22}\sigma_2^2 + F_{33}\sigma_3^2 + F_{44}\sigma_{12}^2 + F_{55}\sigma_{13}^2 + F_{66}\sigma_{23}^2 + 2F_{12}\sigma_1\sigma_2 + 2F_{23}\sigma_2\sigma_3 + 2F_{13}\sigma_1\sigma_3 + F_{11}\sigma_1 + F_{22}\sigma_2 + F_{33}\sigma_3 = 1 \quad (4)$$

The main difficulty while using the Tsai-Wu criterion lies in the evaluation of the parameter F_{12} which characterizes the interaction between the direction of orthotropy X and Y. The evaluation of this term requires a specific and complex test using a bi-axial loading protocol. Its estimation was made theoretically. Wu and Starchurski [17] proposed limit values of the interaction coefficients allowing to ensure that the failure surface of the Tsai-Wu criterion is closed (5). In the numerical model, fictive values of the interaction coefficients are considered. These values are taken positive and equal to the limit values calculated according to the Wu and Starchuski equations.

$$F_{12}^2 < \frac{1}{f_{t,0}f_{c,0}} \frac{1}{f_{t,90}f_{c,90}}; F_{23}^2 < \frac{1}{f_{t,90}f_{c,90}} \frac{1}{f_v^2}; F_{31}^2 < \frac{1}{f_{t,0}f_{c,0}} \frac{1}{f_v^2} \quad (5)$$

The 3D-FEM mechanical model is validated on the basis of the load-slip curves of the connection in normal conditions. Figure 11 shows the comparison between the experimental and the calculated load-slip curves for the connection Type A-2 with two mechanical models: one using only the yield Hill criterion (model-1) and the other using the Hill criterion associated to the Tsai-Wu one (model-2).

These comparisons show that the model-1, using the Hill criterion alone, does not allow to represent the elasto-plastic behaviour of the connection. The model integrating the Tsai-Wu criterion represents well the stiffness of the connection measured experimentally when the phase of reloading is considered. Large displacements, higher than 50 mm, are generated by these connections, with large plastic deformations by embedding of wood. The numerical calculations develop a non-convergent process, arising with significant displacements. Nevertheless, the model allows representing well the elastic and ultimate strength of the connections.

3.3 Numerical model for thermo-mechanical analysis

The thermo-mechanical analysis of the connections is based on the same 3D-FEM used for the mechanical modelling considering the temperature-dependent mechanical properties of the materials. The evolutions of these characteristics are taken into account by using the reduction factors, depending on the temperature, of the mechanical properties, taken from EN1993-1-2 for steel and from EN1995-1-2 for timber. The meshes of the thermal and the mechanical models are different. In order to insure the thermal continuity between the various members of connection, the heat transfer model mesh is continuous, whereas the mechanical model mesh is discontinuous in order to take into account the contact between these members. To perform the thermo-mechanical analysis of the connection, the field of temperature

inside the connection calculated using the thermal model is stored for each increment of temperature. A procedure was developed to make the transition between the stored field of temperature and the thermo-mechanical model considering the correspondence between the nodes of the meshes and the adequate boundary conditions of each model.

The results of the thermo-mechanical model are validated on the basis of the numerical time-slip curves which are graphically compared to the experimental curves. The predicted time of fire resistance of the connections is defined by using a tangent method on the time-slip curves. Figure 12 shows the comparison between experimental and simulated curves for A-1 type connection.

The high increase of displacement, representing the failure of the connection, is well predicted by the model. Table 8 shows the comparison between the calculated ($t_{fi,sim}$) and the experimental ($t_{fi,test}$) times to failure, both determined by a tangent method, with the relative error (ϵ_1). The failure times of the connections calculated with the thermo-mechanical model are always lower than the experimental values. The relative error is due partly to the non-convergence of the model which does not succeed to represent the large plastic deformations of the connections. However, the thermo-mechanical model predicts well the first stage of the failure characterized by a significant acceleration of the local displacement. Experimentally, the connections show additional minutes of resistance.

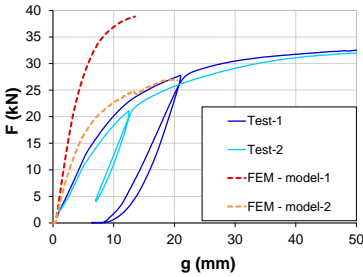


Figure 11. Load-slip comparison of connection Type A ($\eta_{fi} = 38\% * N_{u,test}$).

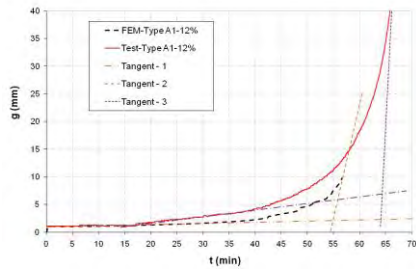


Figure 12. Time-slip comparison of connection Type A ($\eta_{fi} = 12\%$ of $N_{u,test}$).

Table 8. Comparison of the experimental and the numerical fire resistances of the connections.

Type	η_{fi} (% $N_{u,tests}$)	$t_{fi,sim}$ (min)	$t_{fi,test}$ (min)	Relative error ϵ_1 (%)
A	12	55	64.5	16.7
	38	31	48.0	35.4
B	38	30	46.0	34.7
	45	25	40.0	37.5

4 CONCLUSION

Real-scale tests were conducted on steel-to-timber connections subjected to a bending loading under ISO-fire exposure. The experimental results show that the connections have a good fire resistance and exhibit a ductile thermo-mechanical behaviour with large plastic deformations due to the embedding of wood. Original tests with cyclic loadings were realized before two fire tests to observe the influence of clearances within the connections' components. This influence seems to be negligible but the results would require to be confirmed by more tests.

A numerical model is developed in two stages, to simulate both the heat transfer and the thermo-mechanical behaviour of the tested connections. The model allows obtaining good agreements between the calculated and the measured temperatures fields inside the connection components. The fire resistance defined by the numerical modelling are lower than the experimental ones and thus in safety side. The numerical model is not adapted to simulate the large plastic deformations occurring after the beginning of

the failure process but is accurate to represent the transition between the elastic and the plastic behaviour of the connections.

This numerical model will be used as a tool to analyze the complex thermo-mechanical behaviour of timber connections in fire situations. In its extension, it will be used to extend the application domain of the Eurocode and to calibrate some simplified analytical formulae which could be used by engineers to design easily the timber connections in fire.

REFERENCES

- [1] EN 1995-1-2: 2004, Eurocode 5. Design of timber structures. Part 1-2 : General rules - Structural fire design. CEN TC 250-SC5, 2004.
- [2] König J., Fontana M. "The performance of timber connections in fire-test results and rules of Eurocode 5", Aicher A., Reinhardt HW., editors. *Proceedings of the international RILEM symposium*, RILEM publications, 639-648, 2001.
- [3] König J. "Calculations vs. fire testing – limitations of Eurocode 5 and the need of fire testing", *International symposium on advanced timber and timber-composite elements for buildings*, 27-29, 2004.
- [4] Dhima D. "Vérification expérimentale de la résistance au feu des assemblages d'éléments en bois", Saint Remy les Chevreuses: CTICM, 61p. 1999.
- [5] Ayme N., Joyeux D. "Comportement au feu d'assemblages bois. Assemblages bois-métal en double cisaillement", *Rapport SRI-03/121-NA/PB n°030156*, CTICM, 62p. 2003.
- [6] Laplanche K., "Etude du comportement au feu des assemblages de structures bois: Approche expérimentale et modélisation", PhD Thesis, Université Blaise Pascal Clermont-Ferrand et CSTB, France, 140p, 2006.
- [7] Audebert M., "Approche expérimentale et modélisation du comportement au feu d'assemblages bois sous différents types de sollicitations", PhD Thesis, Université Blaise Pascal Clermont-Ferrand et CSTB, France, 233p, 2010.
- [8] Racher P., Laplanche K., Dhima D., Bouchaïr A. "Thermo-mechanical analysis of the fire performance of dowelled timber connections", *Engineering Structures*, 32, 1148-1157. 2010.
- [9] Audebert M., Dhima D., Taazount M., Bouchaïr A., "Numerical investigations on the thermo-mechanical behaviour of steel-to-timber connections exposed to fire", *Engineering Structures*, 33, 3257-3268, 2011.
- [10] Audebert M., Dhima D., Taazount M., Bouchaïr A. "Behaviour of dowelled and bolted steel-to-timber connections exposed to fire", *Engineering Structures*, doi: 10.1016/j.engstruct. 2012.02.010, 2012.
- [11] Bouchaïr A., Racher P., Bocquet JF. "Analysis of dowelled timber to timber moment-resisting joints", *Materials and Structures*, 40, 1127-1141, 2007.
- [12] EN 1995-1-1: 2004, Eurocode 5: Design of timber structures. Part 1-1: General rules and rules for buildings. CEN/TC 250/CS5, 2004.
- [13] EN 12512-2001, Timber Structures – Tests Methods – Cycling testing of joints made with mechanical fasteners. CEN, 2002.
- [14] EN 1993-1-2: 2005, Eurocode 3: Design of steel structures – Part 1-2: General rules – Structural fire design. CEN/TC 250/SC3, 2005.
- [15] Audebert M., Bouchaïr A., Taazount M., Dhima D. "Thermal and thermo-mechanical behaviour of timber connections in fire", *Proceedings of the COST Action C26 Conference – Urban Habitat Constructions Under Catastrophic Events*, Naples, 189-194, 2010.
- [16] Tsai SW., Wu EM. "A general theory of strength for anisotropic materials", *Journal of Composite Materials*, 5, 58-80, 1971.
- [17] Wu RY., Starchuski Z. "Evaluation of the normal stress interaction parameter in the tensor polynomial strength theory for anisotropic materials", *Journal of Composite Materials*, 18, 456-463, 1984.

COMPARISON OF FIRE RESISTANCE OF TRADITIONAL SOLID JOIST LUMBER AND ENGINEERED I-JOISTS

Venkatesh Kodur*, James Stein*, Rustin Fike*, and Mahmood Tabdador**

* Department of Civil and Environmental Engineering, Michigan State University, USA
e-mails: kodur@egr.msu.edu, steinjal@msu.edu, fikerust@msu.edu

** UL LLC, Northbrook, Illinois, USA
e-mail: Mahmood.Tabdador@ul.com

Keywords: Fire resistance, Wood joists, Engineered I-joists, Hybrid joists, Wood joist floors.

Abstract. *This paper presents an evaluation of fire resistance of engineered wood joists used in the construction of floor systems in residential housing. For developing this information, fire resistance tests were carried out on four types of wood joists used in traditional and more modern residential construction. The test variables included type of wood joist, support conditions, and fire protection (insulation). The fire resistance tests were carried out by exposing the loaded wood joists to ASTM E-119 fire exposure. Data generated from fire resistance tests, including temperatures, displacements, and strains, is utilized to evaluate thermal and structural response of different types of wood joists. Results from these tests indicate that engineered joists have much lower fire resistance than traditional solid joist lumber.*

1 INTRODUCTION

Engineered wooden I-joists are very efficient in resisting floor loads over short spans, and therefore these joists are widely used in the construction of floor systems in residential housing. The engineered joists capitalize on the strength of wood and the efficiency of the I-shaped section to enhance flexural load bearing capacity, while at the same time reducing the mass and cost of the structural member. Thus the use of I-shaped sections for joists leads to a sustainable and economical option for typical residential construction. However, in recent years there have been numerous instances where fire fighters entering these houses, during fire fighting, fell through engineered joist floor systems, without any warning, leading to injuries and death, and thus fire resistance of these members has come into question [1,2,3]. To explore the reasoning for this problem, there have been limited fire tests on engineered wooden joist floor systems, primarily undertaken by Underwriters Laboratories (UL) [4], National Institute of Standards and Technology (NIST) [5], National Fire Protection Research Foundation [6], and National Research Council Canada [7]. In these limited test programs, the focus was on evaluating fire resistance of entire floor system (comprising of engineered joist, insulation, and protective layers). Results from these tests point to lowered fire performance of floors with engineered wood joists as compared to floors made with traditional joists. Based on these limited studies, various researchers recommended fire tests be carried out on individual joists to quantify the fire performance of engineered joists at the elemental level.

To develop a fundamental understanding of the fire resistance of engineered lumber, Michigan State University (MSU), in a combined effort with UL and with funding from NIST, carried out a series of fire tests on individual joists using traditional solid joist lumber and a variety of modern engineered lumber. Test variables included joist type, end restraint conditions, and joist insulation. Data generated from tests on seven joists is utilized to evaluate thermal and structural performance of different types of wood joists under fire conditions. With this test data, the fire resistance of existing engineered lumber was assessed

and the effectiveness of different fire protection techniques was also evaluated. This paper presents details on the fabrication of the test specimens, test setup, test procedure, and the thermal and structural response parameters generated in the fire resistance tests.

2 PREPARATION OF TEST SPECIMENS

The test program consisted of fire resistance tests on seven floor joists. All specimens were tested under ASTM E-119 [8] fire exposure and loaded conditions. Four types of wood joists, namely traditional lumber, engineered I-joist, castellated I-joist, and steel/wood hybrid joist, were selected for the experimental studies. Two of the joists tested were (2 x 10 inch nominal dimensions) traditional solid joist lumber designated as T3 and T4; three were engineered I-joists with a constant cross-section designated as E1, E2, and E3; one was a castellated I-joists designated as C1; and the remaining one was a steel/wood hybrid joist designated as H1. Table 1 provides details of the specimens together with test parameters. Pictures of the four different types of joists tested as part of this study are shown in Figure 1. The moisture content, measured following ASTM D-4442 procedure [9], was found to be 10.5% in traditional joists and 9.2% in the different types of engineered joists.

Table 1. Summary of test parameters and results from fire resistance tests on wood joists.

Joist #	Joist Type	Joist Depth mm (in)	Axially Restrained	Protection	Failure Time (min:sec)	Failure Mode
T3	Traditional joist	235 (9.25)	No	-	16:40	Cross-section reduction
T4	Traditional joist	235 (9.25)	Yes	-	20:40	Cross-section reduction
E1	Engineered I-joist	302 (11.875)	No	-	6:15	Web burn through
E2	Engineered I-joist	302 (11.875)	Yes	-	6:25	Web burn through
E3	Engineered I-joist	302 (11.875)	Yes	Intumescent coating	24:05	Web burn through
C1	Castellated I-joist	406 (16)	No	-	7:10	Web burn through
H1	Hybrid joist	355 (14)	No	-	6:00	Connection failure

The castellated joists comprised of an engineered I-joist with portions of the web removed. The hybrid joists comprised of an engineered I-joist with a web only at the ends. Light gauge steel fixed to both top and bottom chords replaced the web for the open mid-section [10].

In order to enhance fire resistance, an intumescent coating commonly used for structural steel members was applied to engineered I-joist E3 over the fire exposed region.

Typical sheathing used in residential construction was attached to the top of the test specimens. To avoid fire exposure to all four sides of the joist, plywood sheathing on top of the joists was provided with ceramic blankets to simulate, as closely as possible, the fire exposure conditions encountered in residential housing construction [10].



Figure 1. Typical traditional and engineered wood joists considered in fire resistance tests.

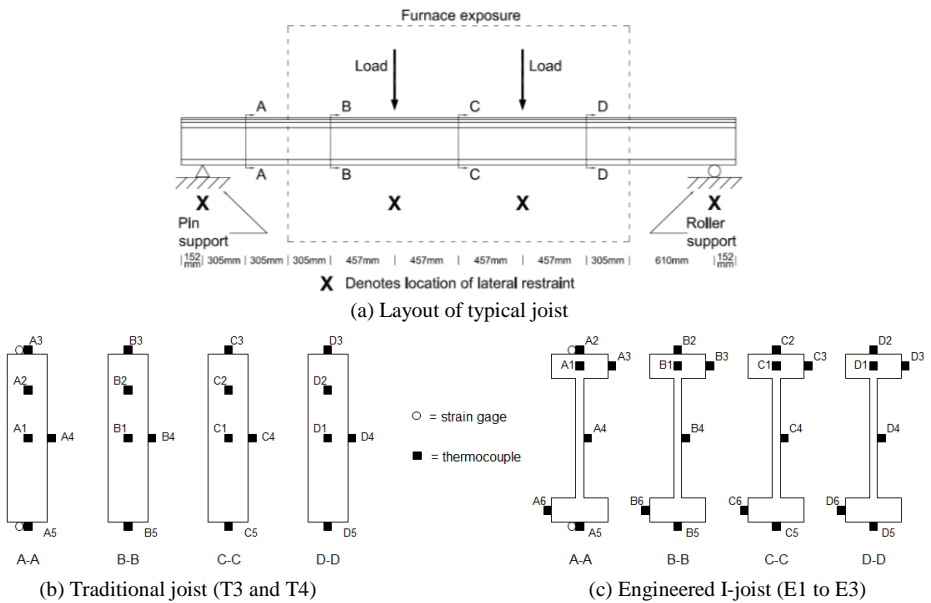


Figure 2. Typical joist layout and thermocouple and strain gage network in different wood joists.

The test specimens (joists) were instrumented with thermocouples, strain gauges, and deflection gauges. To measure cross-sectional temperatures, twenty four welded Type K thermocouples (0.91 mm) were mounted on each engineered joist, while twenty thermocouples were mounted on each of the traditional joists (see Figure 2 for thermocouple locations on traditional and engineered I-joists). Internal thermocouples were inserted into holes drilled from the top surface of the joist. Strain gauges (120 Ω , 30 mm long, from Texas Instruments) were only placed at locations outside the fire exposed zone as depicted in Figure 2. Strain gauges were affixed to the top and bottom surfaces of axially restrained joists only.

Deflections in the joists were measured by linearly varying displacement transducers attached to each test specimen at the center of the joist and also at one loading point. On unrestrained joists, axial deformations were also measured at the location of the joist's centroid [10].

The furnace and joist cross-sectional temperatures, strains, and deflections were recorded at 5 second intervals using DAQ 32 data acquisition software. Photographs and video recordings were also taken at frequent intervals or whenever major events occurred during each test.

3 FIRE RESISTANCE TESTS

The fire resistance tests were conducted at MSU's structural fire test facility. The test furnace (Figure 3) is capable of generating a maximum heat output of 2.5 MW (8.53×10^6 Btu/hour) [10,11]. The joists were placed in the furnace such that no additional support was offered to the joists as they deflected down. To help produce three sided fire exposure, the top of the joists were placed against the furnace lid such that no additional load was applied to them. Voids between the joists and the furnace wall were sealed with ceramic fiber insulation.



Figure 3. MSU's structural fire test facility

The furnace temperature was measured by six Type K chromel alumel thermocouples specifically designed for quick response. The thermocouples were spatially distributed within the combustion chamber, and the average of the six thermocouple temperatures was used to control the furnace temperature.

As displayed in Figure 2a, two point loads were applied to each joist during fire exposure. These loads were incrementally applied 30 minutes prior to fire exposure and remained unchanged throughout fire exposure duration until structural failure occurred in the joists. The applied load represented 50% of the design load, ranging from 0.8 to 2.1 kN (180 to 480 pounds) per point load [10].

The joists were laterally braced at the loading points and at the end restraints during fire exposure as shown in Figure 2a. The end supports for all tested joists were spaced 3.66 m (12 feet) apart. At one end, round bar stock was used as a roller support, while square bar stock was used at the support at the second end to simulate a pin support. The support locations and configuration are illustrated in Figure 2a [10].

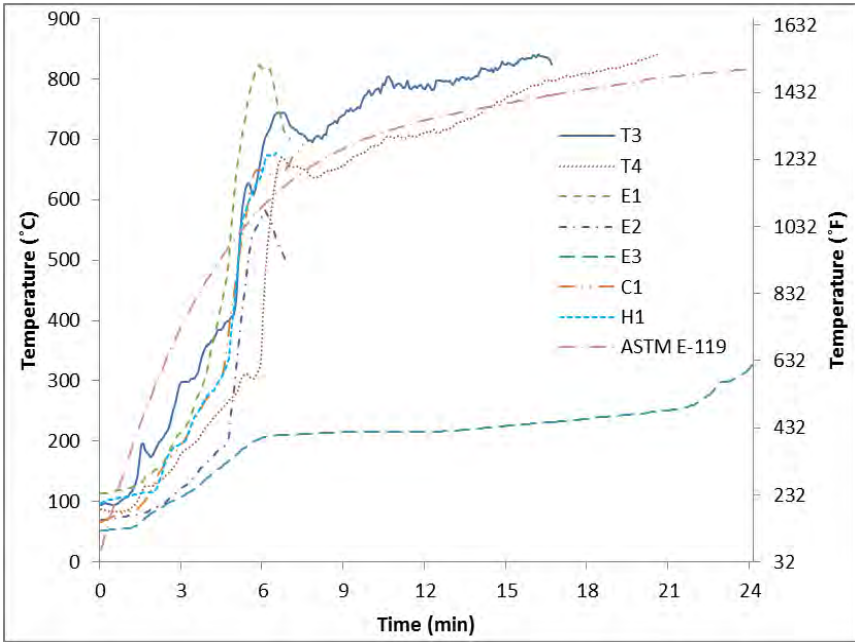


Figure 4. Comparison of average temperatures at bottom surface (center) in different joints.

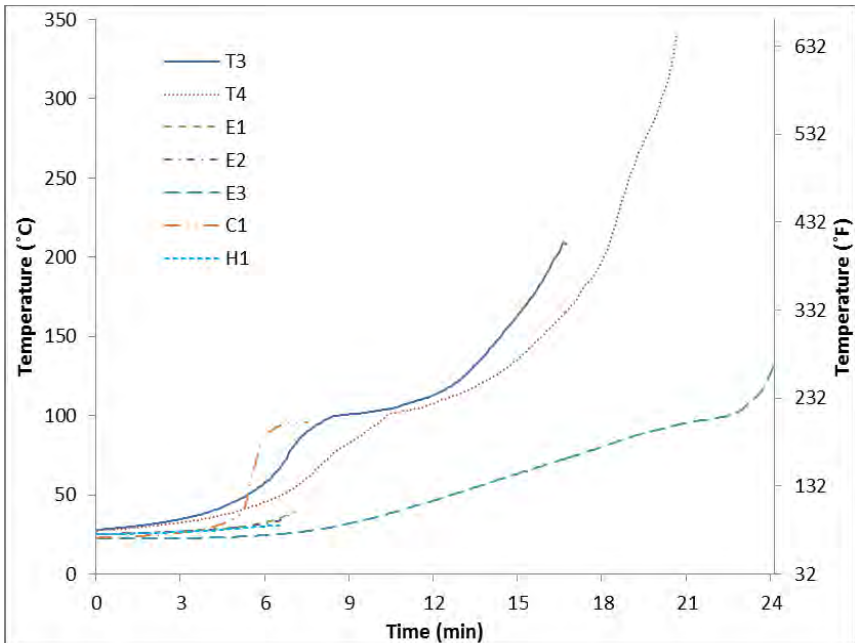


Figure 5. Comparison of average interior temperatures in different joints.

All tests were carried out by exposing the joists to ASTM E-119 fire, as shown in Figure 4 [8]. Control of the furnace temperature was achieved through a manual control valve which the operator adjusts based on the real time average of six thermocouples spatially distributed in the combustion chamber [10].

During fire exposure, failure of the joist was assessed based on the strength and stability criterion. The joists were allowed to reach runaway deflection prior to the termination of the test. After the failure was observed, the gas to the furnace was shut off, but the joists continued to burn due to the inability to extinguish the fire within the furnace. As such, there was no opportunity to undertake post-fire assessment of the joists immediately after the test (fire exposure) was terminated, as the entire joist was consumed by fire.

4 FIRE PERFORMANCE OF ENGINEERED JOISTS

Data generated in the fire tests, which include surface and cross-sectional temperatures, deflections and strains in the joists, and visual observations, is used to compare the fire performance of different types of wood joists. A summary of fire resistance tests on seven wood joists is provided in Table 1 in which the failure time and mode of failure are given for each joist. A comparison of measured temperatures at key locations in the different types of joists is plotted in Figures 4 and 5. Progression of mid-span deflections with fire exposure time is plotted in Figures 6.

4.1 Thermal response

The fire performance of traditional wood joists can be gauged by examining the progression of cross-sectional temperature profiles shown in Figures 4 and 5. Figure 5 shows the comparison of interior temperatures within different types of joists as a function of fire exposure time. The average temperatures displayed for traditional joists (T3 and T4) were recorded at mid-depth of the joists (thermocouple location 1 in Figure 2b), and those displayed for engineered joists (E1, E2, E3, C1, and H1) were recorded at the center of the top chord (thermocouple location 1 in Figure 2c). The data plotted in Figure 5 shows that the temperatures within traditional joists (T3 and T4) reached 208 and 342°C (407 and 647°F) respectively around the time of failure (16 and 20 minutes). Due to shorter test duration, the unprotected engineered joists (E1, E2, C1, and H1) remained much cooler, reaching only 31 to 96°C (88 to 204°F) around the time of failure (6 to 7 minutes). This suggests that high temperatures (and consequential strength loss of wood) attained within traditional joists contributed to their failure, while temperatures developed within the top chord of engineered lumber did not play a significant role in failure.

Unprotected joists T3, T4, E1, E2, C1, and H1 all had a similar progression of surface temperatures as shown in Figure 4. In these joists, the temperatures followed the same general trend, illustrated by grouping of the temperature profiles for the joists. These trends were experienced for the first 6 to 7 minutes until the engineered joists (E1, E2, C1, and H1) failed.

The temperature data plotted in Figures 4 and 5 can be used to gauge the protective capabilities of the intumescent coating applied to joist E3. In these figures, joist E3 experienced lower temperatures than the unprotected joists. For example, Figure 4 shows that the bottom surface temperatures on joists T3 and T4 were 824 and 771°C (1515 and 1421°F) respectively at 15 minutes, while the surface temperature of joist E3 was only 225°C (438°F). Clearly the intumescent coating applied to joist E3 helped in slowing down heat transfer to the joist resulting in lower joist temperatures and higher fire resistance.

4.2 Structural response

The measured vertical displacements of joists (at mid-span) during fire resistance tests are plotted in Figure 6. Traditional joists (T3 and T4) experienced negligible displacement until 6 minutes into testing, at which point the deflections increased gradually and reached 38.1 mm (1.5 inches) in 16 and 20 minutes respectively. At this time, the traditional joists experienced run-away conditions (failure). In the engineered joists (E1, E2, C1, and H1), the displacements increased gradually from 0 at 4 minutes to 38.1

mm (1.5 inches) at 6 minutes. At this point, the joists failed, achieving run-away conditions. In joist E3, which had an intumescent coating, deflections began to increase gradually at around 4 minutes. By 24 minutes, the deflections reached about 50.8 mm (2 inches), and the joist failed, reaching run-away conditions.

Data from the tests can be used to gauge the effect of axially restraint conditions on fire resistance. Joists T3 and T4 were tested under similar conditions except that joist T3 had simple supports, while joist T4 had axially restrained end conditions. Joist T3 failed at 16 minutes into fire exposure, while joist T4, which was axially restrained, failed at 20 minutes into fire exposure. Similarly, joists E1 and E2 were tested under two different end restraint conditions. Joist E1 had simple supports, while joist E2 had axially restrained end conditions. In this case, both joists E1 and E2 failed at similar durations. Therefore, this data suggests that while axially restraint conditions enhance fire resistance in traditional solid wood joists, its effect is minimal in engineered joists.

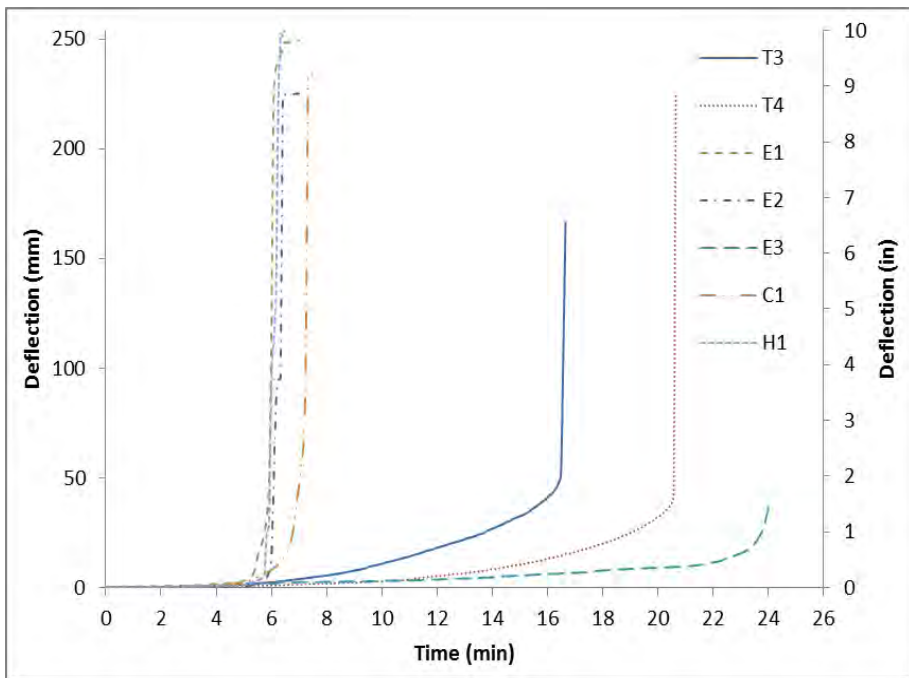


Figure 6. Measured mid-span deflections as a function of fire exposure time in different joists.

4.3 Failure modes

Test observations indicated that the unprotected joists generally ignited at about 4 minutes after the start of the fire. However, the ignition in joist E3, which had the intumescent coating, occurred much later. Also, traditional lumber (joists T3 and T4) developed a char layer that helped to protect the interior of the joists and increase fire resistance. This was mainly due to thicker cross section of these traditional joists. It was observed that engineered joists failed before significant charring could develop.

From visual observations made during the fire resistance tests and the recorded test data, the failure modes of different joist types can be assessed. The failure times for joists T3 and T4 was 16 and 20 minutes respectively. Because of high internal temperatures recorded within these joists, it was determined that the failure mode for the traditional joists (T3 and T4) was through the loss of cross-section (charring and burning) resulting from combustion. The failure of traditional joist, T4, is depicted

in Figure 7a. Engineered joists, E1 and E2, each failed at around 6 minutes. During the fire resistance test, it was observed that the web of these joists (E1 and E2) burned through before the top and bottom chords and thus the failure was through the burn-out of the web. Figure 7b depicts this failure in Joist E1. The failure time for joist E3 (with intumescent coating) was 24 minutes. The intumescent coating applied to joist E3 made observations difficult, but it was determined that its failure mode was also through web burn-out. Castellated joist C1 failed at around 7 minutes, and the failure was through web burn-out. Hybrid joist H1 failed at around 6 minutes, resulting from failure of the steel to wood connection.

The effect of joist type on fire resistance can be gauged by comparing the failure times in different joists. Traditional joists T3 and T4 failed at 16 and 20 minutes, providing the highest fire resistance. Engineered joists E1, E2, and H1 all failed at around 6 minutes, while castellated I-joist C1 failed at around 7 minutes. In general, engineered joists had only 30 to 50% of the fire resistance of traditional joists. This test data on individual joists supports the trends seen in fire resistance tests on full floor assemblies [4]. Therefore, future test programs can start with individual joist testing for simplicity and cost savings.



(a) Traditional joist (T4)



(b) Engineered I-joist (E1)

Figure 7. Typical failure modes of (a) traditional and (b) engineered joists.

5 PRACTICAL IMPLICATIONS

Although engineered wood joists offer numerous advantages during ‘normal’ conditions, they have much lower fire resistance than traditional wood joists. Data generated from these tests provides insight on the fire performance of engineered lumber and can provide a quick methodology to comparing different wood technologies or protection techniques, thus increasing the safety of building occupants and fire fighters in the event of a fire. Improvements to engineered lumber, such as the application of an intumescent coating on engineered I-joists, can enhance fire resistance. This improvement can increase fire resistance from a paltry 6 minutes to about 24 minutes. This clearly indicates that passive fire protection that delays burning of the web can improve the fire resistance of engineered lumber possibly on par with traditional lumber (joists).

Another potential way of increasing the fire resistance of engineered lumber is to use gypsum board as demonstrated in fire tests on floor assemblies carried out by UL [4]. From the tests conducted by UL, it was found that floor assemblies constructed with engineered I-joists and a 12.7 mm (½ inch) thick fire rated gypsum board ceiling could possibly provide fire resistance equivalent to that of unprotected traditional lumber [4].

6 CONCLUSIONS

Based on the fire resistance test results on wood joists presented in this report, the following conclusions can be drawn:

- Traditional solid lumber joists have much higher fire resistance (about 16 minutes) than engineered wood joists (about 6 minutes).
- The webs of engineered I-joists and castellated I-joists are highly susceptible to fire, and failure generally occurs through the burn-out of the web.
- The application of an intumescent coating on an engineered I-joist significantly enhances its fire resistance and yields a similar level of fire resistance as that of a traditional lumber joist.
- The steel to wood connections in the hybrid (engineered) joists are the weakest link during exposure to fire.
- The fire resistance test data on individual joists support the trends seen in fire resistance tests on full scale floor assemblies comprising of joists, gypsum board protective layers, and other attachments. As such, future tests on fire resistance could start with individual joists for simplicity and economy.

REFERENCES

- [1] NIOSH. “Preventing injuries and deaths of fire fighters due to truss system failures.” Publication No. 2005-132, U.S. Department of Health and Human Services, Centers for Disease Control and Prevention, National Institute for Occupational Safety and Health, Morgantown, WV: U.S., 2005.
- [2] NIOSH. “Career engineer dies after falling through floor while conducting a primary search at a residential structure fire – Wisconsin.” Report F2006-26, U.S. Department of Health and Human Services, Centers for Disease Control and Prevention, National Institute for Occupational Safety and Health, Fatality Assessment and Control Evaluation (FACE), Morgantown, WV: U.S., 2006.
- [3] NIOSH. “Volunteer fire fighter dies after falling through floor supported by engineered wooden-I beams at residential structure fire – Tennessee.” Report F2007-07, U.S. Department of Health and Human Services, Centers for Disease Control and Prevention, National Institute for Occupational Safety and Health, Fatality Assessment and Control Evaluation (FACE), Morgantown, WV: U.S., 2007.

- [4] Backstrom, B., Tabdador, M., and Gandhi, P., D. "Fire performance of engineered versus traditional lumber." Structures in Fire: Proceedings of the Sixth International Conference, Michigan State University, East Lansing, MI, 2010.
- [5] Harman, K. A. and Lawson, J. R. "A Study of Metal Truss Plate Connectors When Exposed to Fire," NISTIR 7393, Fire Research Division, Building and Fire Research Laboratory, National Institute of Standards and Technology, Gaithersburg, MD, 2007.
- [6] Grundahl, K. "National Engineered Light Weight Construction Fire Research Project Technical Report." National Fire Protection Research Foundation, Quincy, MA, 1992.
- [7] Sultan, M. A., Séguin, Y.P., and Leroux, P. "Results of fire resistance tests on full-scale floor assemblies." IRC-IR-764, Institute for Research in Construction, National Research Council Canada, Ottawa, Canada, 1998.
- [8] ASTM D4442-07. "Standard test methods for direct moisture content measurement of wood and wood-base materials." ASTM International, West Conshohocken, PA, 2007.
- [9] Kodur, V., Stein, J., and Fike, R. "Fire resistance tests on engineered wood joists." Research report (submitted to Underwriters Laboratories), Michigan State University, East Lansing, MI, 2011.
- [10] Kodur, V. K. R., and Fike, R. "Guidelines for improving the standard fire resistance test specifications." *Journal of ASTM International (JAI)*, 6(7), 16, 2009.
- [11] ASTM E119-08b. "Standard test methods for fire tests of building construction and materials." ASTM International, West Conshohocken, PA, 2008.

ACKNOWLEDGEMENTS

The research presented in this paper is sponsored by Underwriters Laboratories (UL) as part of a larger research project funded by National Institute of Standards and Technology (NIST) under the American Recovery and Reinvestment Act (ARRA). All opinions, findings, and conclusions expressed in this paper are of the authors only and do not necessarily reflect the policies and views of Michigan State University, UL, or NIST.

PARAMETRIC STUDY OF MODELLING STRUCTURAL TIMBER IN FIRE WITH DIFFERENT SOFTWARE PACKAGES

Norman Werther*, James W. O'Neill**, Phillip M. Spellman**, Anthony K. Abu**,
Peter J. Moss**, Andrew H. Buchanan** and Stefan Winter*

* Fakultät für Bauingenieur- und Vermessungswesen, Technische Universität München,
Arcisstrasse 21, 80333 München, Germany
e-mails: n.werther@tum.de, winter@tum.de

** Department of Civil and Natural Resources Engineering, University of Canterbury,
Private Bag 4800, Christchurch 8140, New Zealand;
e-mail: james.oneill@pg.canterbury.ac.nz, phillip.spellman@pg.canterbury.ac.nz,
tony.abu@canterbury.ac.nz, peter.moss@canterbury.ac.nz, andy.buchanan@canterbury.ac.nz

Keywords: Timber, numerical modelling, ANSYS, SAFIR, ABAQUS, thermal properties

***Abstract.** In a bid to accurately model structural behaviour of timber buildings in fire, a number of obstacles have been identified which must be fully understood before advanced computer modelling can accurately be used to represent physical behaviour. This paper discusses the obstacles, with suggestions on how to mitigate them, incorporating the challenges of using general purpose finite element software. The paper examines modelling with ANSYS, SAFIR and ABAQUS and the individual and collective challenges related to thermal analyses of timber structures in fire conditions. It considers the effects various model parameters (thermal and structural) may have on physical interpretation of experimental data in comparison with the accuracy of numerical solutions. In detail, the study looks at the effects of 1D and 2D heat transfer analyses, finite element mesh sizes, time steps and different thermal property approaches on thermal models of timber members in fires. It further recommends how best to model these structures using the different finite element software packages.*

1 INTRODUCTION

The increasing demand for timber as a building material is noticeable all over the world. This is especially true for residential, office and administration buildings as well as special purpose buildings. There are many benefits to using timber structures, such as visual and tactile attractiveness, high energy efficiency, quick erection time and a low carbon footprint. The greatest concerns by authorities over the use of timber as a building material in modern buildings are normally related to fire safety and these concerns are not adequately addressed by design codes.

The fire resistance of timber structures can be assessed by standardised fire tests, such as EN13501-2 [1] or ISO 834 [2], and can be calculated by methods such as those suggested in EN1995-1-2 [3] or NZS3603 [4]. Design standards such as Eurocode 5 part 1.2 [3] allow the use of “advanced calculation methods”, which eliminate the cost of expensive fire testing by using validated numerical finite element (FE) computer models to determine the thermal and structural performance of timber members exposed to fire. However, the use of such software tools requires sufficient knowledge of the material and structural response under fire exposure, sufficient experience of the user to assess the results of the simulation, an understanding of the boundary conditions for heat transfer and structural calculations and, especially, well validated thermal and physical properties of timber materials. Different prior knowledge of users, boundary conditions, and material property selection influence the models that are produced and

effectively affect the perceived performance of timber structures in fire. The authors of this paper had difficulties in independently modelling the behaviour of various types of timber structures in fire conditions, and needed to ascertain the effectiveness of their individual software packages for thermal and structural modelling in fire conditions, especially as literature [5] suggests that FE packages do not adequately predict heat transfer in timber structures. The structures the authors tried to model included:

- post-tensioned timber box beams and walls,
- timber and timber concrete composite floor systems and
- metal fasteners and joist hanger connections in timber structures.

As a result, a collaborative research project has been established at the University of Canterbury to compare different finite element software packages used by the authors (ANSYS, ABAQUS and SAFIR) under identical boundary conditions to model timber structures in fire conditions. It is well known that all these software tools solve the same fundamental equations, so it is often assumed they should give the same results with the same input data, but this has never been verified for timber elements. The project is principally of two parts – thermal and structural modelling. This paper reports on the thermal assessment. In particular, it investigates the influence of mesh size, time-step size and two approaches to modelling the influence of moisture on model accuracy. Furthermore this study explores the limitations of the individual software packages and recommends the best ways to accurately achieve comparable results for the different programs.

2 SOFTWARE TOOLS USED FOR NUMERICAL SIMULATIONS

For the numerical analyses presented in this paper full versions of the programs SAFIR 2011, ANSYS 12 and ABAQUS 6.10 were used. An overview of each package, its capabilities and limits as well as advantages and disadvantages are discussed.

2.1 SAFIR

SAFIR 2011 is a special purpose finite element program developed at the University of Liege, Belgium, for analysing the behaviour of structures under ambient or elevated temperatures. It consists of an integrated thermal and structural analysis program for carrying out 2D and 3D analyses of steel, concrete, timber and composite structures in fire conditions. SAFIR possesses a variety of finite elements such as beam, truss, solid and shell elements for modelling a variety of civil engineering problems. The thermal and mechanical properties of steel, concrete and timber, following the Eurocodes, are incorporated into the program, but one can also use user-defined materials for the thermal or structural analysis [6].

2.2 ANSYS

The finite element software ANSYS 12 solves structural, fluid dynamic, acoustic, thermodynamic and electro-magnetic problems and combinations of these. The program allows the user to input all information with a purpose-built design language (APDL) or through a graphic user interface (Workbench), which can read CAD files. For a thermal and structural analysis the user inputs all material properties and heat transfer conditions, both temperature-dependent and directional. The user then specifies user-dependent structural and thermal loads, the kinds of geometry, mesh sizes, element properties, and solution algorithms. Sequential or coupled thermo-structural analyses are possible. The ability to specify each property, boundary condition and load input requires a deep understanding and background knowledge of the software and the system being modelled. The program can be obtained from ANSYS Inc., Canonsburg USA [7]

2.3 ABAQUS

The finite element software ABAQUS 6.10 has been developed to solve an array of general purpose finite element tasks, similar to ANSYS, by solving a set of equations implicitly at specified time increments. It also has the ability to solve dynamic problems explicitly using a direct integration

procedure, pursuing a desired solution through time without solving a coupled system of equations at each time increment. The program has both the traditional user input file method of building and running simulations and a graphical user interface (CAE) which automates many of these processes and aids in the visualisation of a problem. In terms of heat transfer, ABAQUS 6.10 can perform uncoupled heat transfer analyses, sequentially coupled thermal-stress analyses, fully coupled thermal-stress analyses and adiabatic analyses. The user can specify structural and thermal loading conditions and user-specified regimes, all physical geometry including mesh sizes, element and material properties, boundary conditions and the numerical solution method. The material properties input is both versatile and vast with a huge array of material types available and in CAE there are ready-made functions to account for latent heat and many other thermal parameters. The range of inputs and outputs is vast; care must be taken in understanding how the inputs influence the simulation. The program can be obtained from Dassault Systèmes Simulia Corporation, Providence, RI, USA [8].

3 MATERIAL PROPERTIES

Many different proposals can be found in literature for the temperature dependent thermal properties of timber [9-14]. However, to be consistent in the comparisons described here, and in line with current good practice the Eurocode 5 part 1.2 relationships are adopted for conductivity (k), specific heat (c) and density (ρ) (see Table 1). Such relationships account implicitly for the complex physical and chemical phenomena, so that a simple conductive heat transfer analysis can be carried out without requiring many of the physical complexities of timber combustion and charring to be specifically modelled. Thus effects like moisture migration, formation of char, shrinking and cracking of charcoal are represented by adjusted “effective values” rather than using real measured material properties.

Table 1: Material properties used in this study according Eurocode 5 part 1.2

Temperature [°C]	Conductivity [W/(mK)]	Specific heat [J/(kgK)]	Density ratio ¹⁾ [-]
20	0.12	1530	1+w
99	-	1770	1+w
99	-	13600	1+w
120	-	13500	1
120	-	2120	1
200	0.15	2000	1
250	-	1620	0.93
300	-	710	0.76
350	0.07	850	0.52
400	-	1000	0.38
500	0.09	-	-
600	-	1400	0.28
800	0.35	1650	0.26
1200	1.5	1650	0

1) density ratio – ratio of density at specific temperature to dry density

To use more realistic values requires the consideration of more complicated algorithms within the simulation, such as thermal transport by mass flow (moisture movement), the constantly changing geometry, and the formation of cracks in the charcoal introduced by thermal stresses. The complexity of these problems leads to a huge input effort, coupled simulations and long calculation time which the user would normally want to avoid. The basis of the thermal analysis conducted in this work is a heat balance equation obtained from the principles of energy conservation to calculate nodal temperatures and other

thermal quantities. This relationship can physically be described for solid anisotropic materials by the Fourier law, stated in equation (1).

$$c_p(\vartheta)\rho(\vartheta)\frac{\partial\vartheta}{\partial t} = \frac{\partial}{\partial x}\left(k_x(\vartheta)\frac{\partial\vartheta}{\partial x}\right) + \frac{\partial}{\partial y}\left(k_y(\vartheta)\frac{\partial\vartheta}{\partial y}\right) + \frac{\partial}{\partial z}\left(k_z(\vartheta)\frac{\partial\vartheta}{\partial z}\right) + \frac{\varepsilon_p}{\rho(\vartheta)c_p(\vartheta)} \quad (1)$$

- with: $k(\vartheta)$ thermal conductivity [W/mK]
- $c_p(\vartheta)$ specific heat [J/(kgK)]
- $\rho(\vartheta)$ density [kg/m³]
- ε inner heat generation rate [W/m²]

4 PARAMETRIC STUDIES

4.1 Setup of 1D and 2D heat transfer examination

The comparative investigations begin with one-dimensional (1D) heat transfer in a solid timber member. To ensure that the different software packages could approximate physical behaviour, a 1D heating test, performed by König and Walleij [9] was selected as the basis for the comparisons. The tests, and subsequent numerical modelling, led to the timber properties mentioned in Eurocode 5 part 1.2, which are listed in Table 1. A 45 mm x 95 mm strip of solid timber was exposed to the standard ISO 834 fire curve for 90 minutes. Temperature measurements were taken at various depths into the wood and compared to numerical simulations (Figure 1). In the 1D heat transfer model described here, a 24 mm x 96 mm strip is modelled to be representative of the central strip tested by König and Walleij. The moisture content of the timber was taken as 12%, with a bulk density of 480 kg/m³. In the simulations, one narrow side of the specimen was exposed to the ISO 834 fire curve. The applied thermal exposure consisted of a convective and radiative fraction, to effectively mimic realistic heat transfer and heat loss at the boundary surface. The emissivity ε and convection coefficient h were assumed equal to 0.8 and 25 W/m²K, respectively, as suggested by EN1991-1-2 [15]. For the opposite (unheated) side a convective coefficient of 9 W/m²K (which accounts for both radiative and convective losses) and an initial ambient temperature of 20°C were applied to the surface. The two longer sides were treated as adiabatic surfaces. The temperatures inside the cross-section were measured along the centreline of the specimen at depths of 0, 6, 18, 30, 42, 54 mm away from the fire-exposed surface (see Figure 2). This allowed easier comparison to the König and Walleij's [9] fire experiment.

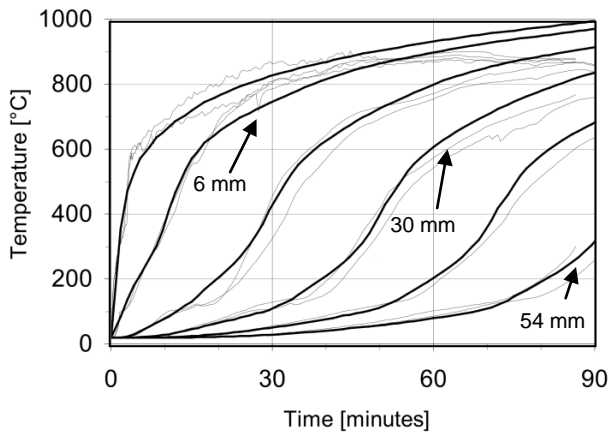


Figure 1. Experimental and numerical results of 1D heat transfer in timber (adapted from [9])

The second step analysed the two-dimensional (2D) heat transfer in a square timber column exposed to the ISO 834 fire on all four sides for 90 minutes. The dimension of the timber column, with an initial moisture content of 12% and a bulk density of 480 kg/m³, was 156 mm x 156 mm. To optimise the setup and runtime, symmetry conditions were used and only a quarter of the section was modelled. Thus the two outer sides were treated as fire exposed and the inner surfaces as adiabatic. For material properties, heat transfer conditions and the locations of temperature measurement inside the cross section, the same values as used in the 1D heat transfer analyses were applied. The column test results and comparisons can be found in [16]. The setup of both assemblies with measurement points and exposure is depicted in Figure 2. The geometries of both assemblies were implemented in the simulation tools and discretised in square meshes with sizes of 1, 3 and 6 mm respectively, using plane elements. The elements had four nodes each with a temperature degree of freedom at each node.

4.2 Data input

The influence of temperature on the thermal properties is implemented in the FE software tools used in this study by defining the material through its thermo-physical parameters which govern the heat conduction process. The finite element code allows the user to implement a variation of such quantities with temperature as a piecewise-linear curve. The input of thermal properties into all three finite element software programs was implemented in two separate procedures that considered the inclusion of the initial moisture content differently. The results were then compared to each other.

The more common approach is to use the given material properties in a “*k-ρ-c* model”, with an implicit consideration of a moisture content of 12% in the density function and as heat of vaporisation in the specific heat function. The specific heat capacity is defined as amount of heat which is required to change a unit mass of a substance by one degree of temperature. In SI units this is measured in kJ/kgK. In the case of timber there is a peak in the reported values of specific heat, most commonly taken as between 99°C to 120°C. This is to account for the latent heat of vaporisation of water in the timber, and results in a large increase in energy required to facilitate this phase change.

Alternatively the moisture content can be considered explicitly as a latent heat or enthalpy for a user-specified moisture content. The latent heat model allows for the removal of this peak from the specific heat curve mentioned above, as it specifically accounts for the extra energy of this phase change over the specified temperature range. In ANSYS and ABAQUS these were input into the material models manually, whereas in SAFIR this feature is automatically implemented.

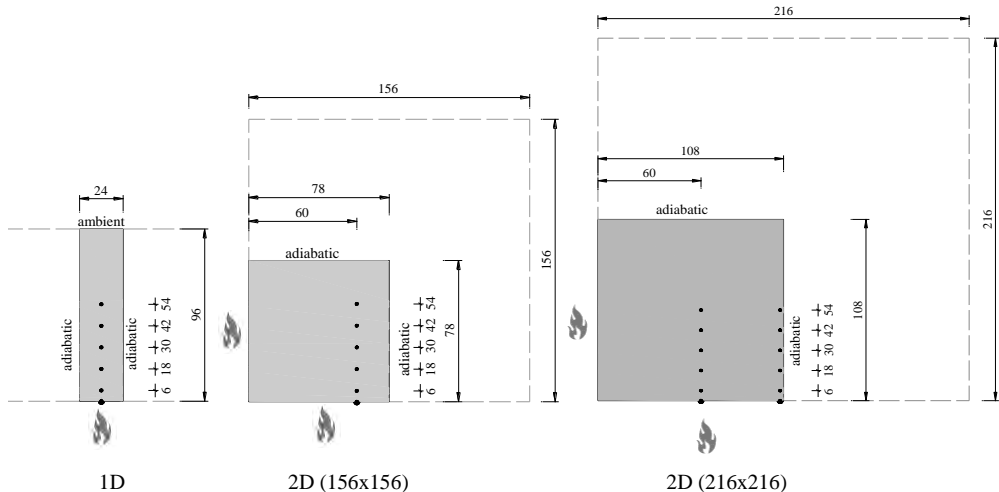


Figure 2. Setup of 1D and 2D examples (dimensions in mm)

The values for the temperature dependent material properties for conductivity (k), specific heat (c) and density (ρ) were taken from EN1995-1-2 [3], and are presented in Table 1.

4.3 Parametric study / Variations

In addition to the two approaches for modelling the effect of moisture content described above, the study also investigated the influence of mesh size and time-step size on thermal analyses of timber structures. Table 2 presents a detailed account of the parameters that were modified in the study. Comparisons of temperatures were performed between the software packages and test results, under each scenario.

Table 2: Overview of variation in the numerical simulations

	k - ρ - c model	latent heat / enthalpy model
FE mesh size		1, 3 and 6 mm
	(automatic time stepping - minimum 1×10^{-3} sec, maximum 60 sec)	
Time step size		1, 30, 60 and 120 seconds
		(with mesh size 1 mm)

5 RESULTS AND DISCUSSION

For clarity the results mostly show temperatures at 6 mm, 30 mm and 50 mm depths into the heated timber element.

5.1 1D heat transfer analysis with “ k - ρ - c model”

Figures 3 and 4 show the influence of the mesh size, varying between 1 mm and 6 mm, on the 1D heat transfer problem described in section 4, for the three programs. The results are for the default k - ρ - c approach. They show that an increase of the mesh size leads to a deviation in the results obtained between the programs. However, there was practically no distinction between the results for the 1 mm and 3 mm mesh sizes, hence the results for the 3 mm mesh are not shown. For the 6 mm mesh size, differences up to 150°C were observed between the different programs. This deviation was most prominent in the temperature range of ~100 to ~500°C and more so at shallow depths, compared with areas deeper in the cross section. It was observed that the results converged after the analyses exceeded this temperature range. Particularly noticeable was that an increase in the FE mesh size (1 mm to 6 mm) produced higher temperatures for ANSYS and lower temperatures for ABAQUS in the ~100 - 150°C temperature range. This shows that the different solver techniques present in each program has an effect on the simulation results. However, all temperatures are an acceptable approximation to the real fire test results.

The analysis of the influence of time-step size showed numerical problems for some programs, because the default numerical convergence criteria could not be met with the k - ρ - c model. Particularly early in the simulations, with rapid increase in temperature, very small time-steps were necessary to ensure convergence. This resulted in very long calculation times for some scenarios. The analyses showed that if these automatic convergence criteria (of very small time-steps in scenarios with rapidly increasing temperature) are ignored, temperature differences of up to 100°C, for instance, occurred at a depth of 30 mm into the cross-section, with between 1 and 120 s time-step increments.

5.2 1D heat transfer analysis with latent heat/enthalpy model

The FE analysis and results showing the influence of the different mesh sizes for the k - ρ - c model were repeated using the evaporation energy as latent heat. The results were almost identical to those shown in Figures 3 and 4. Further analyses to investigate the effect of time-step size are shown in Figures 5 and 6. It is clear from these figures that choosing time-steps up to 120 seconds has only a minor influence on the results and this can reduce the total calculation time significantly, without compromising

the accuracy of the solutions. In comparison to the $k\rho c$ approach, no numerical instabilities were encountered in any of the programs. Further investigation revealed that time-steps of up to 480 s could be used without any significant loss in accuracy. The negligible differences were most prevalent in the early phase of the fire exposure, where the temperature increase was rapid.

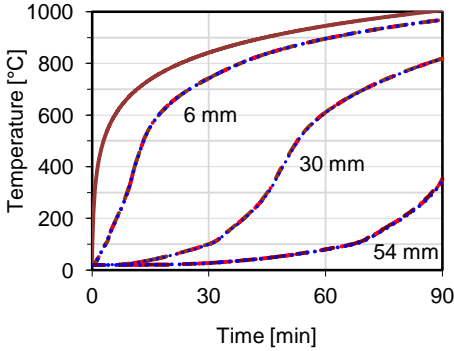


Figure 3. Influence of mesh size and software tool on results for the $k\rho c$ model with 1 mm mesh size

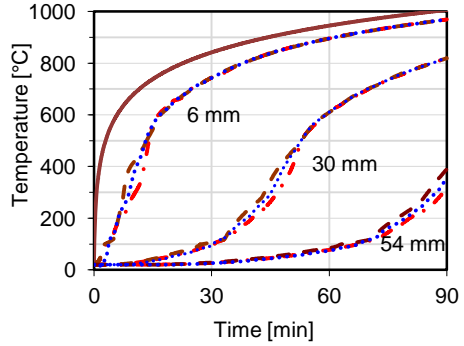


Figure 4. Influence of mesh size and software tool on results for the $k\rho c$ model with 6 mm mesh size

— ISO 834 - - - - - ABAQUS
 - - - - - ANSYS ····· SAFIR

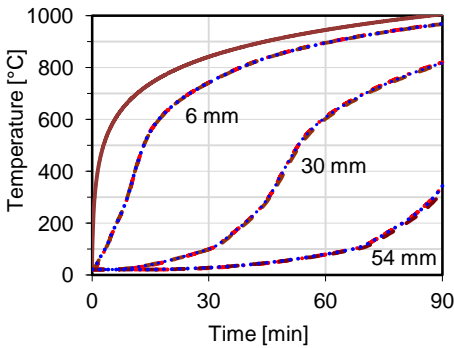


Figure 5. Influence of software tools on results for latent heat model, 1 second time-steps

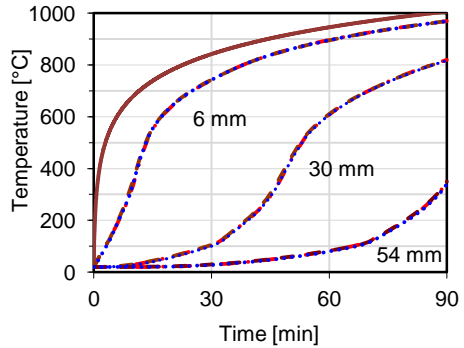


Figure 6. Influence of software tools on results for latent heat model, 120 second time-steps

5.3 2D heat transfer analysis

The FE modelling for the 2D heat transfer showed similar behaviour to the 1D heat transfer simulations. Based on the fact that each finite element received considerable heat flow from two surfaces their temperature increase was much faster, and so the deviation in the observed results between increasing mesh sizes (1 mm to 6 mm) became less significant. Thus the smallest differences were found close to the heated corner, where the influence of the 2D heat flow was most significant (see Figure 7), as expected. As described in the 1D heat transfer studies it is observed that the time-step size has a negligible influence when a latent heat model is used instead of the $k\rho c$ approach for the 2D heat transfer as well. Results of the 2D latent heat/enthalpy thermal analyses in comparison with the test

results of the 156 mm x 156 mm column are shown in Figure 7. The numerical results are taken at 6, 12, 18, 30, 42 and 54 mm (as illustrated in Figure 2) while the test temperatures are taken at 6, 10, 20, 30, 42 and 54 mm into the cross-section.

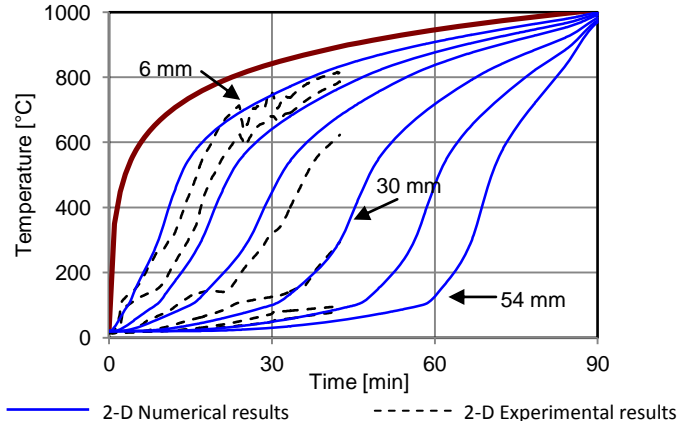


Figure 7. 2D heat flow numerical simulation, compared to experimental results [16]

5.4 Deductions

There are occasions where a one-dimensional heating profile is assumed to adequately approximate the heating profile of parts of a timber cross-section, sufficiently remote from a two-dimensional heat source. Examples include the side charring of a timber beam exposed to fire on three sides or wide columns that are rectangular in shape. A brief investigation has pointed to the fact that it may not always be on the safe side to assume a 1D heat transfer. Figure 8 shows temperatures at 6, 30 and 54 mm depths into a column section (216 mm x 216 mm) exposed to fire on all sides, as depicted in Figure 2. It further shows temperatures at the same depths, but at distances of 60 and 108 mm from the heated corner, and results of a one-dimensional heat transfer analysis superimposed on the 2D results. It is observed that the 1D approximation gets worse the further the position of interest is from the heat source and the surface of the cross-section. Hence, for accurate structural simulation of cases of this nature, a 2D thermal analysis should be employed.

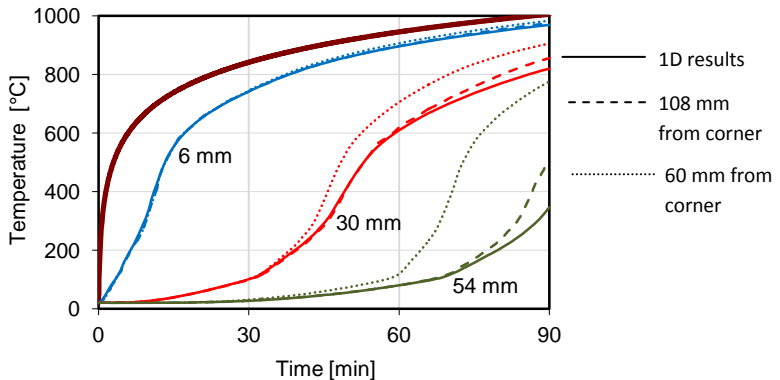


Figure 8. 2D heat flow numerical results compared to 1D results

For structural analysis of timber under fire conditions temperatures over 300°C are normally neglected, because of the minor load bearing capacity of charcoal. Thus temperature readings above 300°C can be neglected for the comparison in this study as well. On that basis, it is observed that the choice of software can influence the calculation of charring rate, depending on the desired fire resistance time. Figure 9 (which is based on a 1D heat flow numerical simulation with 6 mm mesh size and k - ρ - c approach) shows that ANSYS reports a char depth of 21 mm at 30 minutes of fire exposure while ABAQUS quotes 24 mm. At 60 minutes the char depths differ by about 1 mm. This discrepancy disappears with small mesh sizes and increase of heat flow – a further incentive to use smaller mesh sizes for accuracy.

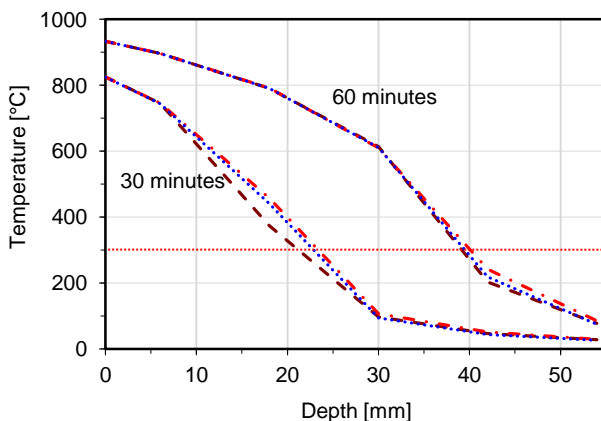


Figure 9. Temperature-depth profile for 6mm mesh, compared to a 300°C isotherm

7 CONCLUSION

The results show that the approach used to account for the moisture content of timber in numerical simulations has a large influence on the temperature development. To avoid numerical problems and long calculation times, a latent heat or enthalpy model is recommended. To optimise calculation time, at the beginning of the simulation when there is a rapid temperature increase in the ISO 834 fire curve, smaller time-steps up to 120 seconds should be used. Further on, larger time-steps and the use of an automatic time-step is recommended.

Due to the negligible differences between 1 and 3 mm mesh sizes, as compared to 6 mm, it is recommended that an initial mesh size of 3 mm is used for simple heat transfer analyses in timber, to ensure accuracy while saving on computational time.

Further recommendations:

- checking of the mesh size suitability into the analysis (as the study shows that for elements with a higher rate of heat increase the mesh size can be increased with negligible effect on the results).
- Particular attention should be paid to areas of impinging 2D heat flows, to ensure the mesh size used is appropriate for the desired application.

The research shows that by being cautious of the advantages and limitations of each of the three software packages and approaches, accurate approximations of the thermal behaviour of timber structures can be made. It also concludes that the programs give comparable results to each other and real fire tests.

The project further seeks to investigate the influence of different temperature-time curves and explore the development of appropriate models for monitoring structural performance of timber buildings in fire conditions.

REFERENCES

- [1] European Committee for Standardisation (CEN). EN13501-2. *Fire classification of construction products and building elements - Part 2: Classification using data from fire resistance tests, excluding ventilation services*; EN13501-2:2007+A1:2009.
- [2] International Organization for Standardization (ISO). ISO 834-1. *Fire-resistance tests - Elements of building construction - Part 1: General requirements*; 1999-09.
- [3] European Committee for Standardisation (CEN). *Eurocode 5. Design of timber structures. Part 1-2: General – Structural fire design*; EN1995-1-2. Brussels, Belgium, 2004.
- [4] Standards New Zealand (SNZ). *NZS3603. Timber Structures Standard*, 1993.
- [5] Badders B.L., Mehaffey J.R. and Richardson L.R., “Using commercial FEA software packages to model the fire performance of exposed glulam beams”, *Structures in Fire – Proceedings of the 4th International Workshop*, P.V. Real, J.-M. Franssen and N. Lopes (eds.), University of Aveiro Press, Aveiro, Portugal, 931-938, 2006.
- [6] *SAFIR 2011*, University of Liège, Liège, Belgium, 2011.
- [7] ANSYS version 12.0 ANSYS Inc., Canonsburg, PA, USA, 2009.
- [8] ABAQUS version 6.10 Dassault Systèmes Simulia Corporation, Providence, RI, USA, 2010.
- [9] König J., Walleij L., *One-dimensional charring of timber exposed to standard and parametric fires in initially unprotected and post-protected situations. Report I 9908029*, Swedish Institute for Wood Technology Research, Stockholm, Sweden, 1999.
- [10] Buchanan A.H., *Structural Design for Fire Safety*, John Wiley & Sons Ltd, Chichester, 2001.
- [11] Frangi A., *Brandverhalten von Holz-Beton-Verbunddecken*. PhD Thesis, Institute of Structural Engineering, ETH, Zurich, Switzerland, 2001.
- [12] König J., “Effective thermal actions and thermal properties of timber members in natural fires”, *Fire and Materials* 30(1), 51-63, 2006.
- [13] Cachim P.B., Franssen J.-M., “Comparison between the charring rate model and the conductive model of Eurocode 5”. *Fire and Materials* 33(3), 129-143, 2009.
- [14] Hopkin D.J., El-Rimawi J., Silberschmidt V., Lennon T., “An effective thermal property framework for softwood in parametric design fire - comparison of the Eurocode 5 parametric charring approach and advanced calculation models”, *Construction and Building Materials* 25(5), 2584-2595, 2011.
- [15] European Committee for Standardisation (CEN). *Eurocode 1. Actions on structures. Part 1-2: General actions – Actions on structures exposed to fire*; EN 1991-1-2. Brussels, Belgium, 2003.
- [16] MFPA Leipzig. *Results of fire tests on loaded and unloaded timber members*. 2005 (unpublished)

NUMERICAL MODELLING

A CONTINUUM-MECHANICAL MODEL FOR FE-SIMULATIONS OF STEEL CONSTRUCTIONS IN FIRE

Sebastian Hauswaldt*, Manfred Korzen* and Stefan Hartmann**

* BAM Federal Institute for Materials Research and Testing, Unter den Eichen 87, 12205 Berlin, Germany. e-mails: sebastian.hauswaldt@bam.de, manfred.korzen@bam.de

** Institute of Applied Mechanics, Clausthal University of Technology, Adolph-Roemer-Str. 2a, 38678 Clausthal-Zellerfeld, Germany. e-mail: stefan.hartmann@tu-clausthal.de

Keywords: Constitutive Equation, Viscoplasticity, Endochronic Plasticity, UMAT, Finite Element Method, Fire Resistance

Abstract. *This paper presents a thermoviscoplastic constitutive model within the framework of continuum mechanics for the description of the behavior of structural steel subjected to fire loading. The model is represented through a set of ordinary differential equations and belongs to the class of so-called unified theories which do not separate plastic and creep strains. The material parameters are identified for the structural steel S 235 on the basis of tension and compression tests at constant temperature with varying strain rates and verified against transient creep test with varying temperature. For effective numerical simulations with the finite element program ABAQUS the model is prepared with a stress algorithm and consistent tangent operator. The simulations are compared with experimental data of fire resistance tests on columns.*

1 INTRODUCTION

For the design of steel structures in fire the common material model of EC3-1-2 [1] is formulated as an one-dimensional rate-independent relationship between stress and mechanical strain. It can be shown that the material behavior of carbon steel is well described for monotonically increasing temperatures and constant loading.

But in case of fire, structures are also exposed to varying thermal and mechanical boundary conditions requiring additional considerations. For the simulation of these processes a model should be chosen that exhibits inelastic properties and is capable to describe creep and relaxation at any heating or cooling condition.

Therefore, a thermoviscoplastic material model for the simulation of structural steel members under fire conditions has been developed.

2 A THERMOVISCOPLASTIC MATERIAL-MODEL

Within the framework of small deformations the deviatoric part \mathbf{T}^D of the stress tensor \mathbf{T} is assumed to be additively decomposed into two parts, i.e.

$$\mathbf{T}^D = \mathbf{T}_{eq}^D + \mathbf{T}_{ov}^D \quad (1)$$

with an equilibrium stress \mathbf{T}_{eq} and an overstress \mathbf{T}_{ov} , with the deviatoric decomposition $\mathbf{T}^D = \mathbf{T} - 1/3tr(\mathbf{T})\mathbf{I}$ with the trace $tr(\mathbf{T}) = T_{ii}$.

The spherical part of the stress tensor is assumed to be defined using the trace operator $tr(\cdot)$ via the classical thermoelastic relationship

$$tr(\mathbf{T}) = 3Ktr(\mathbf{E}_m) \quad (2)$$

with the mechanical strain tensor

$$\mathbf{E}_m = \mathbf{E} - \alpha[\theta - \theta_0]\mathbf{1} \quad (3)$$

the absolute temperature θ and reference temperature θ_0 , the strain tensor \mathbf{E} and the material parameters of the bulk modulus K and thermal expansion coefficient α .

In view of assigning specific material properties to the stress components in eq. (1), see [3], \mathbf{T}_{eq} will be assumed to be a rate-independent functional whereas \mathbf{T}_{ov} has to be a rate-dependent functional of the process history.

Based on the theory of endochronic plasticity [4] the equilibrium stress is assumed to be described by

$$\dot{\mathbf{T}}_{eq}^D = 2G_s \dot{\mathbf{E}}^D - \frac{\dot{z}}{\beta} [\mathbf{T}_{eq}^D - 2G_t \mathbf{E}^D] \quad \text{with} \quad \mathbf{T}_{eq}^D(0) = 0 \quad (4)$$

where $\dot{(\)}$ denotes the material time derivative, with the strain deviator \mathbf{E}^D , the initial shear modulus G_s , the limit shear modulus G_t and the hardening parameter β . The variable z is defined through the differential equation

$$\dot{z} = \left| \dot{\mathbf{E}}^D - \frac{\kappa}{2G_s} \dot{\mathbf{T}}_{eq}^D \right| \quad (5)$$

with the additional material parameter κ constrained to $0 \leq \kappa < 1$ (see Fig. 1). Eqs. (4) and (5) define a rate-independent functional for the equilibrium stress. It is characterized by the fact that the strain is not decomposed into elastic and plastic parts and that no yield surface and corresponding loading conditions have to be defined as it is the case in classical elasto-plastic constitutive models with a yield function.

The overstress is assumed to be defined by the differential equation

$$\dot{\mathbf{T}}_{ov}^D = -\frac{1}{\lambda} \mathbf{T}_{ov}^D + 2G_0 \dot{\mathbf{E}}^D - \dot{\mathbf{T}}_{eq}^D \quad \text{with} \quad \mathbf{T}_{ov}^D(0) = 0 \quad (6)$$

with the instantaneous shear modulus G_0 and relaxation time λ , which is given as a function of the overstress

$$\lambda(\mathbf{T}_{ov}^D) = a_0 + a_1 \left[1 - \tanh \left(\frac{a_2 + \|\mathbf{T}_{ov}^D\|}{a_3} \right) \right] \quad (7)$$

Taking into account that $\dot{\mathbf{T}}_{eq}^D$ is defined by (4), eq.(6) can be interpreted as a modified Maxwell model of viscoelasticity with respect to the equilibrium stress, i.e. \mathbf{T}_{ov}^D vanishes asymptotically for slow motions or for a relaxation process at constant strain as time is going to infinity.

All material parameters, i.e. K , α , G_s , G_t , β , κ , G_0 , a_0 , a_1 , a_2 and a_3 may depend on the temperature θ .

3 UNIAXIAL STRESS CASE

For analyzing the proposed constitutive model in more detail, we apply it to the situation of simple extension with a uniaxial stress state.

Taking into account the relationships

$$\frac{1}{E_s} = \frac{1}{3G_s} + \frac{1}{9K} \quad \text{and} \quad \frac{1}{E_t} = \frac{1}{3G_t} + \frac{1}{9K} \quad (8)$$

we arrive at

$$\dot{\sigma}_{eq} = \frac{E_s \beta - \text{sgn}(\dot{\epsilon}) [\sigma_{eq} - E_t \epsilon_m]}{\beta - \text{sgn}(\dot{\epsilon}_m) \left[\frac{1}{9K} + \frac{\kappa}{3G_s} \right]} \dot{\epsilon}_m \quad \text{with } \sigma_{eq}(0) = 0 \quad (9)$$

$$\dot{\sigma}_{ov} = -\frac{1}{\lambda} \sigma_{ov} + E_0 \dot{\epsilon}_m - \dot{\sigma}_{eq} \quad \text{with } \sigma_{ov}(0) = 0 \quad (10)$$

with the mechanical strain $\epsilon_m = \epsilon - \alpha[\theta - \theta_0]$ and the total strain ϵ in σ -direction (cf. [5]). The material response of the equilibrium stress σ_{eq} , i.e. eq.(9), for monotonic loading is depicted in Fig. 1 together with the associated material parameters E_s , E_t , κ and β to identify their physical significance.

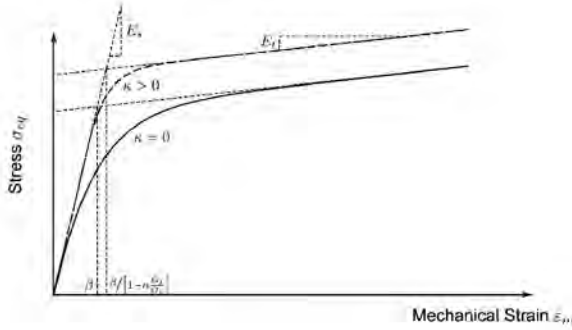


Figure 1. Stress-strain curves of the equilibrium stress (see eq. (9)) for monotonic loading at constant temperature.

A spring-dashpot representation of the whole one-dimensional model (Eqs. (9)-(10)) is presented in Fig. 2a.

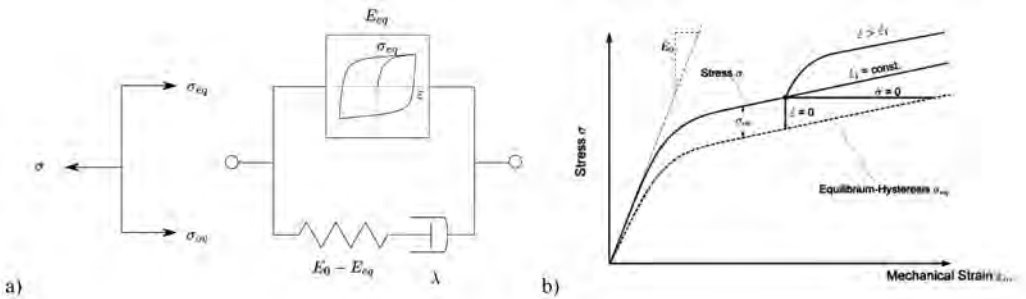


Figure 2. a) Spring-dashpot representation b) Material response for different inputs.

Please note that for fast loadings the model responds always with the instantaneous modulus of elasticity E_0 . The material response of the total stress σ at constant temperature is depicted in Fig. 2b for different input functions characterized by the fact that they change after a period of constant strain rate $\dot{\epsilon}_1$ discontinuously the magnitude or type of input rate. Particular focus has to be drawn to relaxation $\dot{\sigma} = 0$, creep for $\dot{\sigma} = 0$ and an increase of strain-rate from $\dot{\epsilon}$ to $\dot{\epsilon}_1$.

4 EXPERIMENTS AND IDENTIFICATION OF THE MATERIAL PARAMETERS

The material parameters as functions of the temperature were identified on the basis of tensile tests at 20, 300, 400, 500 and 600 °C with varying strain rates and hold times of 9000 seconds. The tests of the S 235 specimens were performed at BAM on a servo-hydraulic testing machine. In Table 1 the Chemical Composition analysed with a spark emission spectrometer is noted.

Table 4. Chemical Composition S 235 in %.

C	Si	Mn	P	S	Cr	Mo	Ni	Al	Cu	N
0.15	0.2	0.49	0.019	0.016	0.05	0.01	0.07	<0.01	0.05	0.003

In Fig. 3 you can see the stress-strain diagram with the strain rates for a 600 °C tensile test and the identified equilibrium stress based on eq. (9) for the tested temperature. It was assumed that the stress values at the end of hold times tend toward equilibrium states which are interpreted as points of the equilibrium stress.

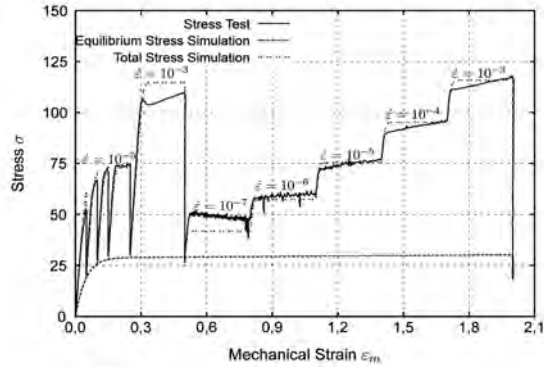


Figure 3. Stress-strain-diagram of strain-controlled tensile test with hold times at 600 °C.

The instantaneous Young's modulus E_0 as a function of temperature is determined from the aforementioned tests (see Tab. 2). Bulk and shear modulus are calculated from these values with the assumption of the temperature dependence of Poisson's ratio according to [7], i.e.

$$\nu = 0.292 + 0.000054 \theta \quad (11)$$

Table 2. Measured instantaneous Young's modulus and calculated bulk and shear modulus.

Temperature	E_0	K	G_0
20	213000	171502	82332
300	204500	177680	78151
400	194500	173688	73939
500	177000	163012	67108
600	152500	144678	57548

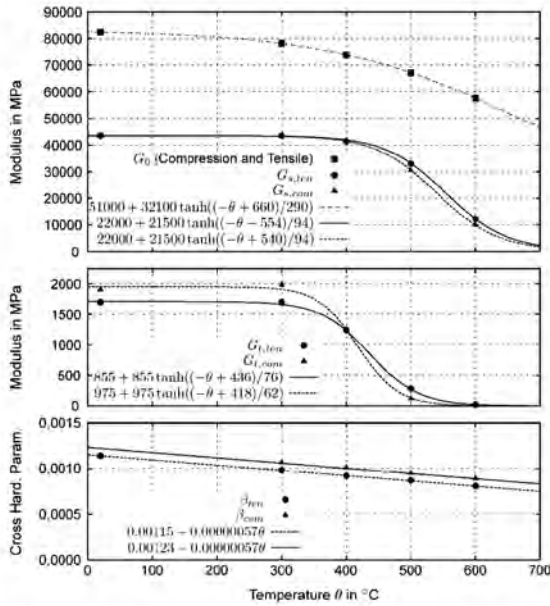


Figure 4. Material parameters of the equilibrium stress as a function of temperature.

The material parameters of the equilibrium stress are identified using eq. (9). The parameters with the corresponding parameter functions of temperature are depicted in Fig. 4. The parameter $\kappa = 0.7$ is assumed to be constant and temperature independent.

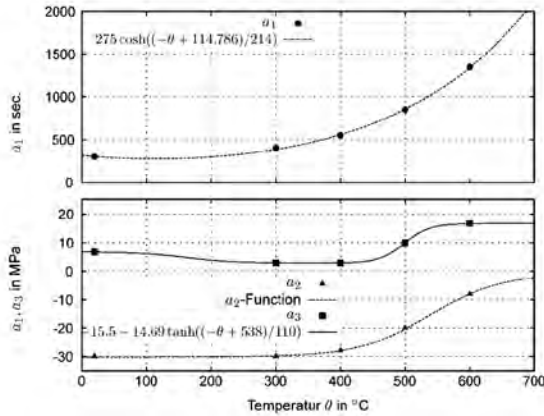


Figure 5. Material parameters of the overstress as a function of temperature.

The overstress has to be identified on the basis of the difference between equilibrium stress and measured total stress according to eq. (10). The material-parameters a_1 , a_2 and a_3 are depicted in Fig. 5. The parameter $a_0 = 0.01 s$ is constant and temperature-independent.

5 IMPLEMENTATION OF THE CONSTITUTIVE MODEL INTO FE-SOFTWARE

The stress state at time t_{n+1} develops from

$$\mathbf{T}_{n+1} = \mathbf{T}_n + \Delta t \dot{\mathbf{T}} \quad (12)$$

with the time increment Δt and the stress rate $\dot{\mathbf{T}} = \Delta \mathbf{T} / \Delta t$

The spherical part of the stress tensor is

$$tr(\mathbf{T}_{n+1}) = 3Ktr(\mathbf{E}_{m,n+1}) \quad (13)$$

According to eq. (4) $\Delta \mathbf{T}_{eq}^D = \mathbf{T}_{eq,n+1}^D - \mathbf{T}_{eq,n}^D$ can be determined using a Backward Euler method leading to

$$2G_s \Delta \mathbf{E}^D - \frac{1}{\beta} \Delta z \left[\mathbf{T}_{eq,n}^D + \Delta \mathbf{T}_{eq}^D - 2G_t \mathbf{E}_{n+1}^D \right] - \Delta \mathbf{T}_{eq}^D = 0 =: \hat{\mathbf{L}} \quad (14)$$

Here $\Delta \mathbf{E}^D = \mathbf{E}_{n+1}^D - \mathbf{E}_n^D$ is prescribed. From eq. (5) follows the incremental formulation of the arc-length

$$\Delta z = \sqrt{\frac{2}{3} \left[\Delta \mathbf{E}^D \cdot \Delta \mathbf{E}^D - \frac{\kappa}{G_s} \Delta \mathbf{E}^D \cdot \Delta \mathbf{T}_{eq}^D + \frac{\kappa^2}{4G_s^2} \Delta \mathbf{T}_{eq}^D \cdot \Delta \mathbf{T}_{eq}^D \right]}. \quad (15)$$

According to eq.(6), the overstress $\mathbf{T}_{ov,n+1}^D$ can be calculated with

$$\mathbf{T}_{ov,n+1}^D = \frac{\lambda}{\lambda + \Delta t} \left[\mathbf{T}_n^D + G_0 \Delta \mathbf{E}^D - \mathbf{T}_{eq,n+1}^D \right]. \quad (16)$$

For effective numerical simulations with the finite element method in addition to the stress formulation we need the consistent tangent operator. The tangent operator is needed to develop the structure stiffness matrix in a finite element analysis.

Since the stress computation is based on an iterative procedure, the implicit function theorem has to be applied requiring the application of the chain-rule applied to eq. (14), see [6] and the literature cited therein.

$$\frac{\partial \hat{\mathbf{L}}}{\partial \mathbf{E}} + \frac{\partial \hat{\mathbf{L}}}{\partial \mathbf{T}_{eq}^D} \frac{d \mathbf{T}_{eq}^D}{d \mathbf{E}} = \mathbf{0}. \quad (17)$$

$\partial \hat{\mathbf{L}} / \partial \mathbf{E}$ can be found using Gâteaux-derivatives. With the derivative of the arc-length with respect to the strain tensor

$$D_{\Delta z}(\mathbf{E}_{n+1})[\mathbf{H}] = \frac{1}{2\Delta z} \frac{2}{3} \left[2\Delta \mathbf{E}^D - \frac{\kappa}{G_s} \Delta \mathbf{T}_{eq}^D \right] [\mathbf{H}] \quad (18)$$

we obtain

$$\begin{aligned} D\hat{\mathbf{L}}(\mathbf{E}_{n+1})[\mathbf{H}] &= \left[2G_s + 2G_t \frac{\Delta z}{\beta} \right] \left[\mathcal{I} - \frac{1}{3} \mathbf{I} \otimes \mathbf{I} \right] [\mathbf{H}] \\ &\quad - \frac{1}{\beta} \frac{1}{3\Delta z} \left[\mathbf{T}_{eq,n}^D + \Delta \mathbf{T}_{eq}^D - 2G_t \mathbf{E}_{n+1}^D \right] \otimes \left[2\Delta \mathbf{E}^D - \frac{\kappa}{G_s} \Delta \mathbf{T}_{eq}^D \right] [\mathbf{H}] \end{aligned} \quad (19)$$

Furthermore the derivative of the arc-length with respect to the equilibrium stress increment

$$D_{\Delta z}(\Delta \mathbf{T}_{eq}^D)[\mathbf{H}] = \frac{1}{3\Delta z} \left[-\frac{\kappa}{G_s} \Delta \mathbf{E}^D + \frac{\kappa^2}{2G_s^2} \Delta \mathbf{T}_{eq}^D \right] [\mathbf{H}] \quad (20)$$

is required and the expression $\partial \hat{\mathbf{L}} / \partial \Delta \mathbf{T}_{eq}^D$ follows

$$D \hat{\mathbf{L}}(\Delta \mathbf{T}_{eq}^D)[\mathbf{H}] = \left[\frac{1}{\beta} \frac{1}{3\Delta z} \frac{\kappa}{G_s} \left[\mathbf{T}_{eq,n}^D + \Delta \mathbf{T}_{eq}^D - 2G_r \mathbf{E}_{n+1}^D \right] \otimes \left[\frac{\kappa}{2G_s} \Delta \mathbf{T}_{eq}^D - \Delta \mathbf{E}^D \right] - \left[\frac{\Delta z}{\beta} + 1 \right] \mathcal{I} \right] [\mathbf{H}]. \quad (21)$$

After rearranging eq. (17)

$$\frac{\partial \hat{\mathbf{L}}}{\partial \mathbf{T}_{eq}^D} \frac{d \mathbf{T}_{eq}^D}{d \mathbf{E}} = - \frac{\partial \hat{\mathbf{L}}}{\partial \mathbf{E}} \quad (22)$$

the tangent operator of the equilibrium stress $\mathbf{C}_{eq}^D = d \mathbf{T}_{eq}^D / d \mathbf{E}$ can be determined by the use of a numerical solver with LU decomposition since eq. (22) represents a system of equations with several right-hand sides.

The tangent operator of the overstress

$$\mathbf{C}_{ov}^D = D \mathbf{T}_{ov,n+1}^D(\mathbf{E}_{n+1})[\mathbf{H}] = \frac{\lambda}{\lambda + \Delta t} \left[G_0 \left[\mathcal{I} - \frac{1}{3} \mathbf{I} \otimes \mathbf{I} \right] - \mathbf{C}_{eq}^D \right] [\mathbf{H}] \quad (24)$$

is derived from eq. (16).

The model is adapted to the finite element program ABAQUS [2] using the UMAT interface. FORTRAN subroutines which includes the implementation of the stress algorithm and the associated tangent operator have been and are used for FE-Simulations.

6 TRANSIENT CREEP

In Fig. 6a simulations of transient creep tests at constant heating rates are presented. The simulated strain-temperatures curves correspond to the observations of transient creep tests of S 460 [8] depicted in Fig. 6b.

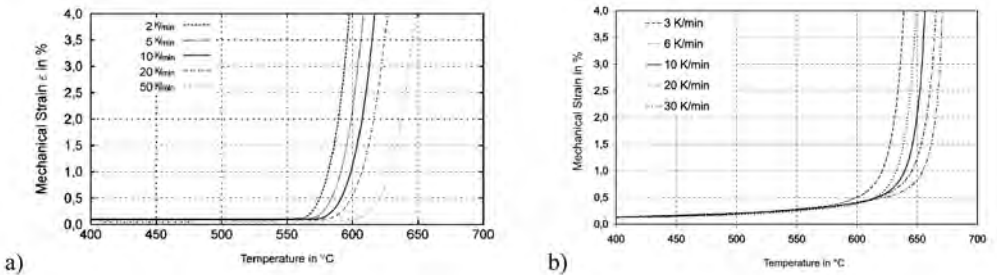


Figure 6. a) Simulation of transient creep tests of S 235 at -100 MPa with different heating rates b) Results of transient creep tests on S 460 at 170 MPa [8].

Within the framework of compression and tensile tests on S 235 transient creep tests at constant stress of -100 MPa have been carried out. The temperature rate was 7.2 K/min till the maximum temperature of

600 °C was reached after 5000 seconds. The following cooling phase with a temperature rate of -7.2 K/min. ended at 120 °C when natural cooling was not fast enough.

Temperature, uniaxial stress and strain were recorded and compared to results of a simulation of the test as depicted in Fig. 7. In the heating phase the calculated strain increases to higher values then in the transient creep test. At higher temperatures when cooling down the simulated strains are in good agreement with the experiment.

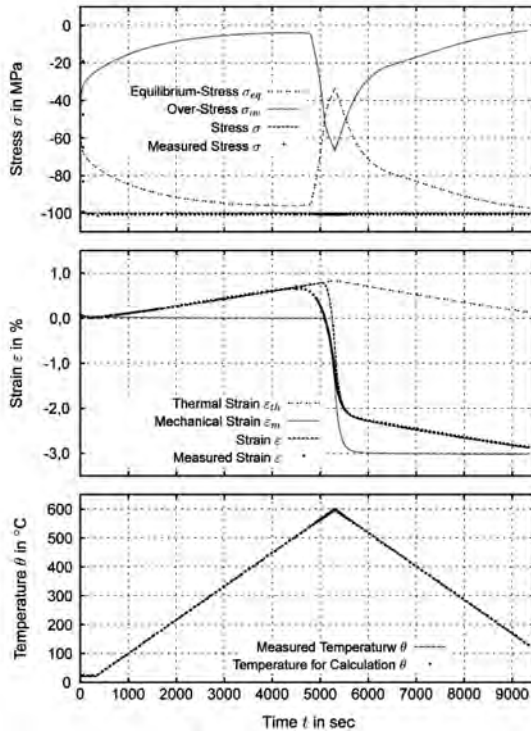


Figure 7. Transient creep test and simulation of S 235.

7 COLUMN TESTS

Furthermore, component simulations are compared with the results of two column fire tests. The steel columns with a height of 3.56 m were fixed at the top while the bottom end was free to move vertically. The mechanical load applied at the center of the bottom of the column was constant. By the use of a servohydraulic testing machine an elastic foundation was applied additionally [10]. Axial loading and stiffness of the foundation are presented in Tab. 3.

Table 3. Test Program Columns

Specimen	Load	Stiffness
HEA 140	492 kN	47 kN/mm
HEB 180	1052 kN	69.5 kN/mm

The furnace was heated up according to the so called uniform-temperature-time-curve according to EN 1363-1 standard [9]. The measured surface temperatures were recorded with 30 thermocouples at 11 measuring stations (see Fig. 8a).

The temperature field of the columns has been calculated via the finite element method (ABAQUS) using the measured surface temperatures at Dirichlet boundary conditions and the material properties of thermal conductivity, density and heat capacity according to [1].

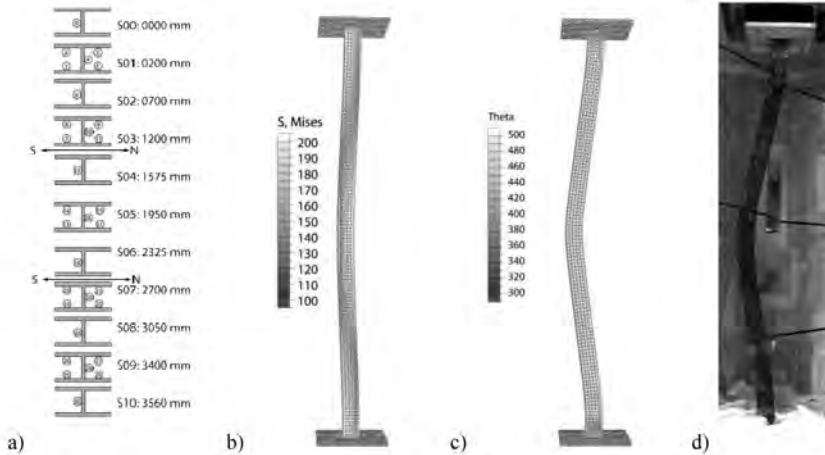


Figure 8. HEA 140: a) Temperature measuring stations b) V. Mises stresses of deformed column at 255 sec. of the simulation c) Temperature field at deformed column at 1600 sec. of the simulation d) Deformed column after test.

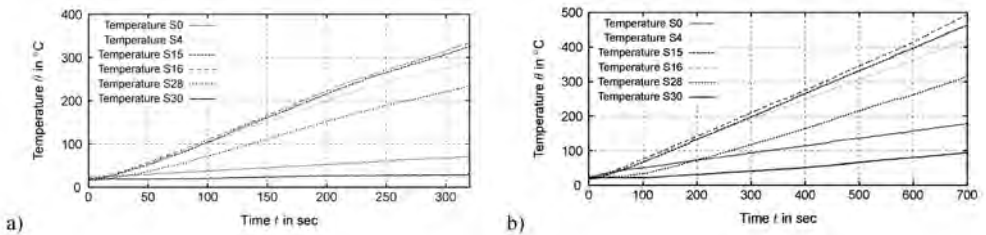


Figure 9. Steel Temperatures a) HEA 140 b) HEB 180.

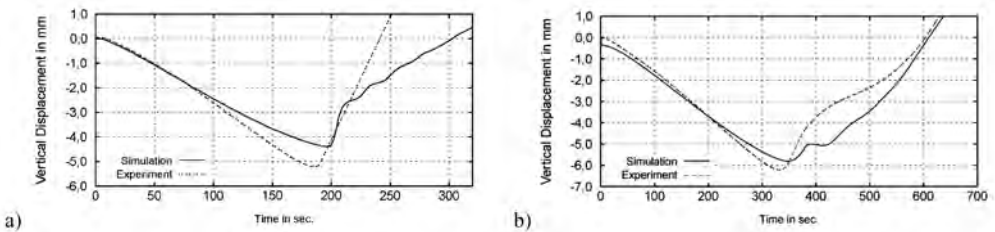


Figure 10. Vertical displacement a) HEA 140 b) HEB 180.

With the use of the calculate temperature field the column tests were simulated with the presented thermoviscoplastic material model. For the evaluation of the results the vertical displacements of the load application point at the bottom of simulation and experiment are compared in Fig. 10. It can be seen that time and temperature of maximum displacement and zero passage are in good agreement.

8 SUMMARY AND CONCLUSIONS

A so-called unified thermoviscoplastic constitutive model for the simulation of the behavior of structural steel is presented. Due to the modular concept with an additive decomposition of the stress into an equilibrium stress and an overstress specific material properties of rate-independent classical plasticity and rate dependent viscoelasticity can be associated to experimental observations.

Based on this concept the identification of the temperature-dependent material parameters for structural steel S235 are realized within a series of strain-controlled tensile and compression tests with varying strain-rates at constant temperature between 20 °C and 600 °C.

The modular concept of the constitutive model influences also the numerical solution strategy. Whereas the numerical integration of the overstress might be realized by an explicit algorithm the corresponding procedure for the equilibrium stress are treated via an implicit Backward-Euler algorithm. This stabilizes essentially the computational procedure. The necessary consistent tangent operator splits into two parts as well. Whereas the tangent operator for the overstress is written analytically via Gâteaux derivative, the corresponding operator of the equilibrium stress is solved numerically. The numerical implementation has been programmed as a user subroutine UMAT for the FE-program ABAQUS.

Comparing simulation results with experimental data it is shown that stress-controlled transient creep tests are described with sufficient accuracy. The comparison of experimental data of fire resistance tests on columns with numerical simulations show that the presented constitutive model is applicable without problems and is capable to describe the column behavior quite reasonably. In contrast to rate-independent models as in [1] the presented model is able to describe properly the material behavior as a function of the heating-rate.

REFERENCES

- [1] EN 1993, Eurocode 3: Design of steel structures - Part 1-2: General rules – Structural fire design, CEN, Brussels, Belgium, December 2010.
- [2] ABAQUS 6.11-1: *Abaqus Analysis User's Manula Version 6.11-1*, Dassault Systèmes Simulia Corp., Providence, RI, USA, 2011.
- [3] Haupt, P.: "On the Mathematical Modelling of Material Behaviour in Continuum Mechanics, Acta Mechanica", 100, 129 -154, 1993.
- [4] Valanis, K.C.: "Fundamental Consequences of a New Intrinsic Time Measure Plasticity as a Limit of the Endochronic Theory", Archives of Mechanics 32, 171-191, 1980.
- [5] Korzen, M.: "Constitutive Equations for Structural Steel Subjected to Fire", *Applications of Structural Fire Engineering – Proceedings of International Conference*, F. Wald, K. Horová, J. Jirku (eds.), Prague, 2011.
- [6] Hartmann, S.: "A remark on the application of the Newton-Raphson method in non-linear finite element analysis", Computational Mechanics, 36 (2), 100-116, 2005.
- [7] Richter, F.: *Physikalische Eigenschaften von Stählen und ihre Temperaturabhängigkeit*, Stahleisen Sonderberichte Heft 10, Verlag Stahleisen, Düsseldorf, Germany, 1983
- [8] Schneider, R.: „Untersuchungen zum zeitabhängigen mechanischen Materialverhalten von S460 im Brandfall“, Diss. , Darmstadt, Germany, 2011
- [9] EN 1363: Fire Resistance Tests - Part 1: General Requirements
- [10] Korzen, M.; Magonette G. and Buchet P.: "Mechanical Loading of Columns in Fire Tests by Means of the Substructuring Method," Zeitschrift für Angewandte Mathematik und Mechanik, 79, 617–618, 1999.

NUMERICAL MODELLING OF CREEP IN STRUCTURAL STEEL EXPOSED TO FIRE

James Lee*, Martin Gillie*

* University of Edinburgh, BRE Centre for Fire Safety Engineering, Edinburgh, United Kingdom
e-mails: james.lee@ed.ac.uk, m.gillie@ed.ac.uk

Keywords: Creep, Fire, Steel, Numerical Modelling, Material behaviour.

Abstract. *The ability to model the behaviour of structures in fire conditions numerically has advanced rapidly in recent years with many complex phenomena now routinely represented. However, creep strains at elevated temperatures have been largely ignored to date. This is unfortunate because creep behaviour may significantly affect the time to failure of a heated structure and this time is crucial when egress is being considered. This paper seeks to examine the material behaviour governing creep as well as constitutive relations used for modelling creep to demonstrate how a sound understanding of both can lead to accurate numerical modelling of creep. This approach is used to model the effects of creep numerically in the stress relaxation of post tensioned steel tendons at elevated temperatures displaying a high degree of accuracy.*

1 INTRODUCTION

It is generally considered that creep in steel is relatively insignificant up to 400-500°C [5]. Correspondingly, in Eurocode 3 [4] the effects of creep are not explicitly accounted for in temperature dependent plastic stress-strain curves for structural steel. Neither are the effects of creep explicitly accounted for in Eurocode 2 [3] temperature dependent plastic stress-strain curves for prestressing steel. This is generally not a problem up to around 400°C where the Eurocode curves adequately account for the creep component of the overall plastic strain implicitly. There is evidence however that creep strain can and does become significant in steel above 400°C pushing total plastic strain far beyond the plastic strains suggested in Eurocode design stress strain curves. Finite element stress relaxation models performed in ABAQUS of prestressed steel tendons at elevated temperatures using Eurocode 2 stress strain curves for prestressing steel show a significant gap to experimental stress relaxation curves [11] in the 400-650°C range (Fig 1). This implies creep in this case and any other case where temperatures in structural steel could exceed 400°C should be explicitly considered. Failure to adequately account for creep in such temperature ranges could significantly affect time to failure which could be critical when egress is being considered.

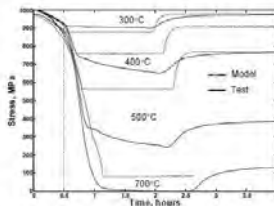


Figure 1. Modelled stress relaxation curves for post tensioned steel tendons using Eurocode 2 design plastic stress strain curves compared to experimental stress strain curves [11].

In particular it is desirable to model creep in these situations numerically in commercial Finite Element Method (FEM) software packages. This can only be done accurately with an understanding of the microscopic material mechanisms governing creep and a knowledge of the constitutive relations of elasto-viscoplasticity.

Without an understanding of the material behaviour behind creep the modelling process is somewhat blind; loosely based around attempts to empirically fit the standard primary, secondary and tertiary creep phases into any given analysis. Such an approach is often highly flawed when extreme stresses or temperatures are considered as well as in transient stress and temperature cases. Indeed with a basic understanding of the material behaviour in such situations it is often possible to simplify the modelling process significantly as well as attain greater accuracy and confidence in results.

FEM software packages typically compute the multiaxial creep strain rate using the Von Mises flow rule based around constitutive models for elasto-viscoplasticity. Typically this requires the user to provide an algorithm via a user defined subroutine for the magnitude of the creep strain rate usually in terms of the Von Mises stress. Other parameters such as temperature may also be included in this algorithm. It is therefore desirable as well as providing a far more concise and theoretically justifiable approach if such an algorithm is compatible with the constitutive relations of elasto-viscoplasticity.

It is the aim then of this paper to provide an understanding of microscopic material behaviour governing high-temperature creep as relevant to steel in buildings allowing justifiable modelling decisions and assumptions to be made. The underlying constitutive theories of elasto-viscoplasticity are covered as a framework for numerical modelling of creep. This material understanding with constitutive elasto-viscoplastic theory is then used to demonstrate that it is possible to accurately and concisely model creep numerically. This will be achieved through modelling the effects of creep in the stress relaxation problem above (Fig 1).

2 CREEP DEFORMATION MECHANISMS

The type of creep or viscoplastic deformation at stresses and temperatures of interest in structural fire safety engineering is known as *power law* or *power law breakdown* creep. These names owe to a frequently observed power law relationship between shear stress, σ_s , and creep strain rate, $\dot{\epsilon}_{cr}$ (Eqn 1). As stresses increase the exponent, n , in Eqn 1 also increases until the power law representation begins to breakdown. From this point the observed creep is referred to as power law breakdown creep where the creep strain rate appears to have an exponential dependence on shear stress (Eqn 2). The transition stress between power law and power law breakdown creep is generally taken as one thousandth of the temperature dependent shear modulus, μ [8].

$$\dot{\epsilon}_{cr} \propto \left(\frac{\sigma_s}{\mu} \right)^n, \quad \sigma_s < 0.001\mu \quad (1)$$

$$\dot{\epsilon}_{cr} \propto \exp\left(\frac{\sigma_s}{\mu} \right), \quad \sigma_s \geq 0.001\mu \quad (2)$$

At low temperatures when the stress applied to a metal exceeds the yield stress, the metal deforms and the new stress state becomes the yield stress state. The resulting plastic deformation is permanent, finite and is assumed to happen instantaneously. The physical plastic deformation results from the motion of dislocations (Fig 2) along a slip plane. The finite nature of this deformation results from obstructions to the dislocations motion along the slip such as precipitates, impurities or other dislocations. As a result the metal is said to have hardened and can now behave elastically to a greater stress than before.

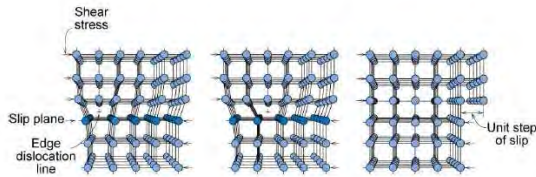


Figure 2. Dislocations, Slip Planes, Dislocation Cores or Lines and Recovery [6]

Power law creep is generally believed to begin when elevated temperatures facilitate a microscopic mechanism known as *dislocation climb* [2,8]. Dislocation climb allows dislocations to overcome the obstacles mentioned earlier as they progress along the slip plane; this continuous motion along the slip plane is known as *dislocation glide* [8]. This however is not the end of the creep deformation process; in fact it is often only the very beginning of a process known as *recovery* [2,6,8]. Around all dislocations, obstructed dislocations, locked subgrain and grain boundaries there exists localised strain fields. The recovery process involves the release of this stored strain energy as these obstructed dislocations, locked subgrains and grains are freed and aligned resulting in the growth of subgrains and grains towards a lower energy state material. Remaining grains are generally offset at larger angles approaching the perpendicular that require too much energy to align (higher energy grain boundaries). In this case under continued stress the grains will begin to shear creating voids and cracks, thus the metal goes from displaying ductile behaviour towards brittle behaviour ultimately leading to rupture.

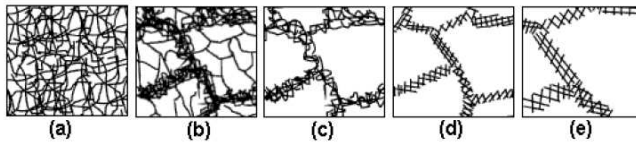


Figure 3. The Recovery Process; (a) Pile Up, (b) Cell Formation, (c) Annihilation, (d) Subgrain Formation, (e) Grain Growth [2]

Fig 3 outlines the recovery process. It is these mechanisms involved in the recovery process that give rise to the so called primary, secondary and tertiary creep phases (Fig 4). Both power law and power law breakdown creep appear to start with the rapid movement of newly mobile dislocations which then begin to pile up as they back up against existing subgrain and grain boundaries [6] (Fig 3a). This pile up which is essentially strain hardening results in the deceleration in creep strain rate observed within the primary phase (Fig 4). As these dislocations back up and pile up within the existing subgrains they begin to concentrate in lines as illustrated in Fig 3b forming cells. Over time these cells become more defined as more dislocations concentrate at their boundaries. As dislocations of opposite polarity begin to annihilate ever more defined cell boundaries are formed and thus cells begin to turn into subgrains [2] (Figs 3c, 3b and 3d). The process ends with the alignment of lower energy subgrain and grain boundaries under continued applied stress leading to grain growth and a lower internal energy state material [2,6].

At which point secondary creep begins it appears is largely down to stress. It has been observed in metallurgical tests mainly on metals such as aluminium, copper and tin around the boundary between power law and power law breakdown creep that nearly all of the steady state deformation comes from subgrain and grain boundary sliding as well as grain growth [12] (Fig 3(d) and 3(e)). The density of mobile dislocations in polycrystalline materials in general (once viscoplastic behaviour has been initiated) is seen to be proportional to the square of the stress [8]. At high stresses this creates considerable back up and pile up against existing subgrain and grain boundaries and in turn a greater density of cells are formed. Indeed it has been observed that the size of subgrains formed within aluminium through the recovery process is inversely proportional to a power of the stress that appears close to 2 [16]. This

implies the range of motion for mobile dislocations within existing grains is extremely limited at high stresses around the power law breakdown range. It is likely the bulk of the steady state secondary creep deformation in many polycrystalline materials including steel then could indeed be the result of the sliding, alignment and growth of newly formed subgrains and grains.

At lower stresses well within the power law range what mechanism forms the bulk of the deformation is still open to debate. It has long been assumed the bulk of the steady state secondary phase deformation happens within subgrains and grains [12]. The dislocation density is not as high resulting in lower density cell formation and the formation of larger subgrains. In these cases the mobile dislocations have considerably greater range of motion prior to cell formation. The steady state nature then would result from a balance between dislocation glide, pile up, cell formation and annihilation all happening simultaneously aided by dislocation climb (Figs 3(b) & 3(c)) [12]. As the secondary phase progresses fewer mobile dislocations exist and the softening affects of dislocation glide are reduced. At this point subgrain and grain boundary softening affects come in to maintain the steady state strain rate as cell formation becomes largely complete.

The tertiary phase across all stress ranges appears to begin when only higher energy grain boundaries remain. At this point brittle behaviour begins; the accelerating deformation is the result of voids and cracks appearing and can rapidly lead to rupture.

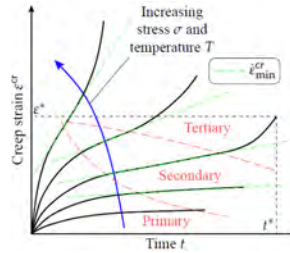


Figure 4. Creep strain against time at constant stress and temperature [9]

A final note referring to the apparent differences in the recovery process (or rather the difference in which parts of the recovery process dominate the deformation) between power law and power law creep refers to temperature effects. Power law creep is observed to begin at temperatures exceeding around 0.6 times the absolute melting temperature of the material. As creep is a kinetic process its rate also depends on an activation energy. This activation energy appears to be the same as that of a process known as *self diffusion* or *lattice diffusion* [8, 15]. This represents the diffusion of *vacancies* (Fig 5) through the material crystal lattice where the number of vacancies and the rate of diffusion is related to temperature through an Arrhenius relationship (Eqns 3 and 4).

$$N_v = N \exp\left(\frac{-Q_v}{kT}\right) \quad (3)$$

$$D = D_0 \exp\left(\frac{-Q_d}{RT}\right) \quad (4)$$

Where in Eqn 3 N_v represents the number of vacancies in a given quantity of material [6], N represents the number of atomic sites, Q_v is the energy required to form a vacancy, T is the temperature in Kelvins and k is the Boltzmann constant. In Eqn 4, D is the rate of diffusion in m^2/s , D_0 is a stress dependent temperature independent constant in m^2/s , Q_d is the activation energy of self diffusion in Joules per Mole and R is the gas constant (8.314 J/molK).

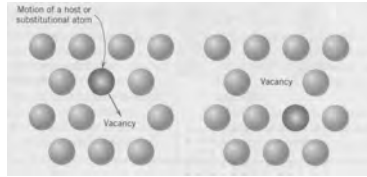


Figure 5. Vacancies as gaps in a lattice from freed atoms diffusing under localised strain fields through the opposite movement of a substitutional atom [6]

The magnitude of the diffusion rate is dictated by the strength of localised stress-strain fields around obstructed dislocations which is further influenced by the strength of the global stress field from the applied loads. It is this self diffusion that facilitates dislocation climb, the vacancy effectively providing the dislocation an extra degree of freedom in which to move allowing the dislocation to climb the obstacle [2]. At lower temperatures down to 0.4 times the absolute material melting point power law creep can also be observed in some metals where the activation energy is slightly lower appearing to match that of *core diffusion*. In this case the diffusion of vacancies appears to be through dislocation lines or cores (Fig 3) requiring less energy.

Power law breakdown creep however can be observed at much lower temperatures than those above. Creep in prestressing steel tendons creep has been observed at temperatures down to below 300°C [1]. This is approximately 0.3 times the absolute melting point of carbon steel. In this case the activation energy for creep is seen to be higher than that of self diffusion. This further appears to highlight the influence of high stress in the power law breakdown regime. It has been established that the mobile dislocation density once viscoplastic behaviour has commenced is proportional to the square of the shear stress [8]. Further to this excess vacancies may be created through increased plastic deformation [14] facilitating dislocation climb. Clearly vacancy diffusion must also have an effect though substantially reduced through the lower temperatures, possibly highlighting the limited distances dislocations can glide given the density before forming cells and subgrain boundaries.

The key points to take from this discussion are the differences between primary and secondary creep as a function of stress and temperature. It is extremely important to note that the difference in strain rate between these phases at high temperatures and high stresses is often quite small to the point of being negligible in some cases (Fig 4). In power law creep at temperatures greater than 0.6 times the absolute melting point this has been noted by Jonas et al [10] stating softening effects appear to overcome the hardening effects. This is likely due to the high density of vacancies at high temperatures and thus high rates of self diffusion effectively allowing initially mobile dislocations to maintain their mobility as creep strain and deformation increases. At high stresses the mobile dislocation density is so high once creep is activated that cells begin to form and steady state creep begins almost immediately (with respect to overall deformation time scales). This process can only be accentuated by increasing temperatures as would be expected in fire situations with an ever increasing number of vacancies according to Eqn 3 assisting the formation of cells and subgrains.

3 CONSTITUTIVE MODELLING

Multiaxial creep modelling in metals typically operates within a Von Mises flow rule. In the case of classical elasto-plasticity any increase in applied stress beyond the elastic yield stress is immediately associated with an increase in the radius of the yield surface, representing a new internal yield state. Therefore a stress state cannot exist outside the yield surface. In the case of elasto-viscoplasticity any increase in applied stress beyond elastic yield is associated with a delayed *viscous* response from the yield surface as it expands to represent a new internal yield state. In this case the applied stress is permitted to represent a stress state outside the yield surface. This stress state is typically represented as an *over stress*, f , where f represents the perpendicular distance from the yield surface to the applied stress state in

principle stress space. On the yield surface f is then equal to zero as in classical plasticity with the condition that for viscoplastic behaviour to occur f must be greater than zero.

It is the time dependent response of the yield surface that dictates the rate of viscoplastic (creep) deformation. This rate of deformation depends on the magnitude of the over stress and the viscosity of an effective media through which the yield surface has to expand. This viscosity is defined by the effects of temperature, accumulated plastic strain (strain hardening) and other internal state variables.

A viscoplastic potential function, Ω , is thus defined as a function of the over stress and viscosity parameters such as temperature and various internal state variables dictating the time dependant response of the yield surface. The associated flow rule is then represented as in Eqn 5 [7] representing the multiaxial creep strain rate via the viscoplastic strain rate tensor $\dot{\epsilon}_{ij}^{cr}$.

$$\dot{\epsilon}_{ij}^{cr} = \frac{\partial \Omega(f)}{\partial \sigma_{ij}} = \frac{\partial \Omega}{\partial f} \frac{\partial f}{\partial \sigma_{ij}} = \dot{p} \frac{\partial f}{\partial \sigma_{ij}} = \dot{p} n_{ij} \quad (5)$$

The rate at which the yield surface approaches the applied stress state (along the perpendicular path) and the material deforms is the gradient of the viscoplastic potential, Ω , with respect to the over stress, f . This quantity, \dot{p} , is referred to as the *viscoplastic multiplier* and is the norm of the viscoplastic strain rate in plastic strain space and thus represents the magnitude of the creep strain rate. The tensor, n_{ij} , is known as the *flow direction tensor* and represents the direction of the viscoplastic flow.

Most Finite Element Method (FEM) software packages compute the flow direction tensor, n_{ij} , from the existing plastic stress state at each increment. Therefore generally the user need only define the viscoplastic multiplier as a function of the Von Mises stress resulting from the applied stress state. The viscoplastic multiplier can be defined in the form of Perzyna [13] (Eqn 6) with a viscosity parameter, η , out with the over stress function.

$$\dot{p} = \frac{\partial \Omega}{\partial f} = \frac{\langle \Psi(f) \rangle}{\eta} \quad (6)$$

The Macaulay brackets in Eqns 6 indicate that when f falls below zero the stress state has fallen back within the elasticity domain. Therefore the chosen form of the viscoplastic multiplier function takes on a value of zero and there is no more plastic straining. A common choice of a viscoplastic multiplier function following from Section 2 (Eqn 1) would be a power law function as in Eqn 7.

$$\dot{p} = \frac{1}{\eta} \left\langle \frac{f}{D} \right\rangle^n = \left\langle \frac{f}{D'(p, T, S_i)} \right\rangle^n \quad (7)$$

$$D' = D \eta^{1/n} \quad (8)$$

In Eqn 7, D , represents is a normalising stress normalising f such that when $f = D$ the creep strain rate reduces to the inverse of the viscosity parameter, η . The viscosity parameter defines the apparent viscosity opposing yield surface expansion; this naturally can depend on temperature, accumulated plastic strain (strain hardening) or other internal state variables. D' in Eqns 7 and 8 has been modified to act as a *drag stress* [7] in which the viscosity parameter has been taken inside the function of the over stress. It also is then defined as a function of accumulated plastic strain, p , temperature, T , and other internal state variables, S_i . The viscosity parameter and the normalising stress D , can both be normalised such that a known creep strain rate is represented at $f = D_0$ (Eqn 9).

$$\dot{p} = \frac{1}{\eta_0} \left\langle \frac{f}{D_0} \right\rangle^n = \dot{\epsilon}_0 \left\langle \frac{f}{D_0} \right\rangle^n \quad (9)$$

With this it is often possible to reduce the sensitivity within the power law to changes in temperature and other internal state variables which may be of use in FEM modelling with regards to convergence.

The use of a power law breakdown model within the above framework carries problems given that a zero value for the plastic multiplier cannot be achieved in a finite stress range. In order to produce a plastic multiplier less than unity the model must be normalised in a similar means as in Eqn 9 (Eqn 10).

$$\dot{p} = \frac{1}{\eta_0} \exp\left\langle \frac{f}{D_0} \right\rangle = \exp\left\langle \left\langle \frac{f}{D_0} \right\rangle - \eta' \right\rangle \quad (10)$$

$$\eta' = \ln(\eta_0) \quad (11)$$

In the above Eqns 10 and 11 the viscous stress is brought into the exponential to act as a drag stress, η' , as shown, the denominator, D_0 , within the exponential retains only a normalising roll.

4 MODELLING THE EFFECTS OF CREEP ON STRESS RELAXATION OF POST TENSIONED STEEL TENDONS AT ELEVATED TEMPERATURE

The previous sections have outlined the constitutive theories used as a framework for the numerical modelling of creep as well as the material behaviour that governs the macroscopic deformations. This theoretical knowledge will now be put to use in modelling creep in the relaxation of post tensioned steel tendons at elevated temperature.

In order to explicitly model creep in the stress relaxation of post tensioned steel tendons in fire firstly an appropriate algorithm is developed to predict the magnitude of the creep strain rate at the appropriate stresses and temperatures. This algorithm is then used in a full FEM post tensioned tendon stress relaxation model (using ABAQUS). The full relaxation model will then be verified against the experimental stress relaxation curves from MacLean [11] displayed in Fig 1.

4.1 Developing an algorithm for the magnitude of the creep strain rate (viscoplastic multiplier) in post tensioned steel tendons

In Section 3 the viscoplastic constitutive relations that form the framework for multiaxial numerical creep modelling have been identified. This constitutive theory will now be used as the basis to develop a creep model for use in the prediction of stress relaxation in post tensioned steel tendons at elevated temperatures (Fig 1). As the creep model is to be used in the commercial FEM software package ABAQUS, an algorithm for the magnitude of the creep strain rate (plastic multiplier) is required (Eqn 6). ABAQUS will compute the flow direction tensor, n_{ij} , at each increment.

Using the information detailed in Section 2 an appropriate stress relationship for the magnitude of the creep strain rate can be selected based on the relationship of the tensioning stress in the tendons to their shear modulus. The shear modulus as a function of temperature can be represented as in Eqn 9 [8]. In this case it has been normalised to room temperature where μ_0 is the shear modulus at room temperature with temperature in Kelvin. The melting temperature of steel, T_m , is taken as approximately 1800 Kelvin.

$$\mu = \mu_0 \left[1 - 1.09 \left(\frac{T - 300}{T_m} \right) \right] \quad \mu_0 = 8.1 * 10^4 \text{ GPa} \quad (12)$$

From Fig 1 and Eqn 12 ratios of the tensioning stress to the shear modulus can be determined. This shows over a wide stress and temperature range the macroscopic creep behaviour can be best represented by a power law breakdown model of the type in Eqn 2.

From Eqns 10 & 11 a yet to be normalised version of the power law breakdown model is used as a base model represented in Eqn 13.

$$\dot{p} = \exp\left(\frac{f}{\sigma_0} - \eta'\right) = \exp\left(\frac{\sigma_{vm} - \sigma_y(p, T, S_i)}{\sigma_0} - \eta'\right) \quad (13)$$

In Eqn 13 the overstress, f , has been expanded into its constituents, those being the Von Mises stress resulting from the applied stress, σ_{vm} , and the yield surface stress, σ_y . Eqn 13 uses a normalising stress on f as the transition stress between power law and power law breakdown creep, σ_0 , where $\sigma_0=0.001\mu$ [8]. The yield surface stress is also a function of the viscous parameters, accumulated strain, temperature and other internal state variables. Therefore in normalised form (divided by σ_0) the yield stress can be associated to the drag stress, η' , to create a combined viscosity parameter as a sum of both parts [7]. This combined parameter can then be extracted from the exponential in Eqn (13) such that a normalised form for the creep strain rate (viscoplastic multiplier) around the Von Mises stress can be achieved as in Eqn 14.

$$\dot{p} = \exp\left(-\left[\frac{\sigma_y}{\sigma_0} + \eta'\right]\right) \exp\left(\frac{\sigma_{vm}}{\sigma_0}\right) = \dot{\epsilon}_0 \exp\left(\frac{\sigma_{vm}}{\sigma_0}\right) \quad (14)$$

At this point an assumption has been made based on the justifications highlighted at the end of Section 2 and observable in Fig 2. That being any strain hardening that may occur happens so rapidly or is so insignificant in this stress range that primary and secondary phases are indistinguishable. To this end any hardening effects as a function of accumulated plastic strain, p , have been eliminated from Eqn 14. Further to this all other viscous effects arising from anything other than temperature have been neglected in the assumption that temperature effects in the absence of strain hardening will dominate the viscosity. To this end the creep strain rate at $\sigma_{vm}=\sigma_0$, is normalised in terms of the viscosity parameter and yield stress as an Arrhenius function of temperature (Eqn 15). In this manner the fact that creep is a kinetic process with associated activation energy, Q_c , is addressed. Further, the creep strain rate retains a temperature dependence at $\sigma_{vm}=\sigma_0$, whilst σ_0 also retains a temperature dependence through its relation to the temperature dependent shear modulus (Eqn 12).

$$\dot{\epsilon}_0 = \exp\left(-\left[\frac{\sigma_y}{\sigma_0} + \eta'\right]\right) = \alpha \exp\left(\frac{-Q_c}{RT}\right) \quad (15)$$

In Eqn 15 the parameter, α , is used to normalise $\dot{\epsilon}_0$ such that the Arrhenius relation to temperature represents the viscosity opposing the creep deformation. In full form then the chosen algorithm to represent the creep strain rate (viscoplastic multiplier) in the above stress relaxation problem is represented in Eqn 16.

$$\dot{p} = \alpha \exp\left(\frac{-Q_c}{RT}\right) \exp\left(\frac{\sigma_{vm}}{\sigma_0}\right) \quad (16)$$

4.2 Verification of the creep model in the stress relaxation of post tensioned steel tendons at elevated temperature

Eqn 16 leaves two constants to be determined; the activation energy, Q_c and the normalising constant, α . For the activation energy the activation energy of self diffusion for 1% Cr-Mo-V steel has been used with a value of 251 KJ/mole [8]. It has been stated in Section 2 that the activation energy of creep in the power law breakdown region is generally observed to be higher than that of self diffusion. Through fitting Eqn 16 to the data in Fig 1 it should be possible to find an appropriate value of the normalising constant, α , to account for this slight inaccuracy. Doing so a value of $\alpha=10^{13} \text{ hr}^{-1}$ is found. Using this value pre exponential normalising strain rates (Eqn 15) of the order $2*10^{-7} \text{ hr}^{-1}$ at 400°C and $7*10^{-3} \text{ hr}^{-1}$ at 600°C are achieved thus representing the creep strain rate magnitude at the transition stress.

The algorithm for creep strain rate in Eqn 16 has been incorporated into the FEM software package ABAQUS via a user defined subroutine. Using this subroutine post tensioned steel tendons were modelled according to the tests carried out by MacLean [11]. In these tests isolated 5400mm length, 13mm diameter prestressing steel tendons were tensioned to approximately 1000MPa with approximately 11% of their length heated in a tube furnace about their centre. In each test the centre of the tendon was heated at 10°C per minute to pre determined soak temperatures of 300°C, 400°C, 500°C or 700°C. This heating rate is based on the anticipated heating rate at 20 mm concrete cover within a unbonded post tensioned slab [3,11]. The soak phase lasted for 90 minutes from which point the tendons were allowed to cool naturally. These models are displayed in Fig 6 below against the experimental results from MacLean [11].

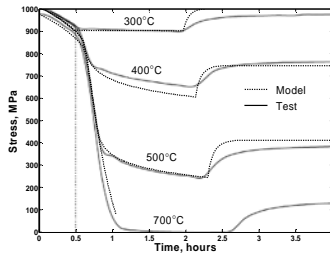


Figure 6. Modelled stress relaxation curves against experimental relaxation curves [11] explicitly accounting for the contribution of creep through a power law breakdown creep model

The model in Eqn 16 appears to work very well and thus implies that material based assumptions regarding the potential lack of strain hardening in this case are valid. Slight inaccuracies in the cooling curves are observable, most likely due to the convective and radiative cooling parameters used within ABAQUS. The model soaking at 700°C crashed at around a stress approaching the transition stress between power law and power law breakdown; the model could not achieve convergence when using implicit numerical integration schemes to ultimately find a stress solution at that increment.

5 CONCLUSION

This paper has evolved as a result of the lack of explicit consideration for creep behaviour in structural steel in design codes in temperature ranges where its effects may contribute significantly to the overall plastic strain.

Material behaviour in response to stress and temperature has been presented in order to better understand the effects of stress and temperature on the macroscopic effects of creep. This understanding is particularly important in accurately modelling creep. This understanding has been successfully unified with constitutive elasto-viscoplastic relations and theory to demonstrate the possibility for accurate modelling when an attempt is made to understand such behaviour and theories. The accuracy of the example stress relaxation model explicitly including the affects of creep justifies the assumptions made regarding the negligible affects of strain hardening applicable in this particular case. This directly highlights the importance of material understanding, especially if it is desired to justify such an approach.

The structural implications relating to the consequences of the inconsideration of creep explicitly in certain structural situations have not been considered in this paper. The example used relates to fire in Unbonded Post Tensioned (UPT) concrete slab structures. It has been shown via Figs 1 and 6 that if the affects of creep are not considered significant underestimates in the relaxation of stress in the post tensioned tendons could be made especially at temperatures beyond 400°C. Under a localised fire at midspan a tendon at 25 mm concrete cover could potentially reach this sort of temperature in around 60 minutes [3]. In an unbonded case a local fire in a single bay could then produce significant relaxation in

compressive stress across an entire strip of floor. Of far more concern is the propensity for spalling in modern high strength concretes as used in UPT concrete slabs. In such a case concrete cover to a tendon could be significantly reduced or even lead to direct exposure to fire. Such cases could have significant consequences regarding anticipated time to failure. Therefore there should be more awareness of cases where creep could be significant in terms of failure and time to failure and from this greater attention paid to accurately predicting its affects.

REFERENCES

- [1] Anderberg Y., *The Impact of Various Material Models on Structural Fire Behaviour Prediction*. Fifth International Conference on Structures in Fire, Singapore, pp13, 2008.
- [2] Babu B., *Physically Based Model for Plasticity and Creep of Ti-6Al-4V*, Licentiate Thesis 2008:40, Department of Applied Physics and Mechanical Engineering, Lulea University of Technology, Sweden, 2008.
- [3] British Standard, *Eurocode 2: Design of concrete structures, Part 1-2: General rules – Structural fire design, BS EN 1992-1-2:2004*
- [4] British Standard, *Eurocode 3: Design of steel structures, Part 1-2: General rules – Structural fire design, BS EN 1993-1-2:2005*
- [5] Buchanan A.H., *Structural Design for Fire Safety*, John Wiley & Sons Ltd, Chichester, 2001.
- [6] Callister W.D., *Materials Science and Engineering an Introduction, Seventh Edition*, John Wiley & Sons Ltd, New York, 2006.
- [7] Chaboche J.L., *A Review of some Plasticity and Viscoplasticity Constitutive Theories*, International Journal of Plasticity, Vol 24, 1642-1693, 2008.
- [8] Frost H. J., Ashby M. F., *Deformation mechanism maps*. Oxford: Pergamon press, 1982.
- [9] Gorash Y., *Development of a Creep-Damage Model for Non-Isothermal Longterm Strength Analysis of High-Temperature Components Operating in a Wide Stress Range*. Ph.D. Thesis, National Technical University, Kharkiv, Ukraine, 2008.
- [10] Jonas J.J., Sellars C.M., Tegart W.J.M., *Strength and Structure under Hot-Working Conditions*, Metallurgical Reviews, Vol 14, pp 1-24, 1969.
- [11] MacLean K., *Post-Fire Assessment of Unbonded Post-Tensioned Concrete Slabs: Strand Deterioration and Prestress Loss*. M.Sc thesis, Department of Civil Engineering, Queen's University, Kingston, ON, Canada, 2007
- [12] Nabarro F.R.N., *Do we have an Acceptable Model of Power Law Creep?*, Materials Science and Engineering, A 387-389, 2004.
- [13] Perzyna P., *Fundamental Problems in Viscoplasticity*, Advances in Applied Mechanics, Vol 9, pp 243-377, 1966.
- [14] Robinson S.L., Sherby O.D., *Mechanical Behaviour of Polycrystalline Tungsten at Elevated Temperature*, Acta Metallurgica, Vol 17, pp 109, 1969.
- [15] Sherby O.D., Weertman J., *Diffusion-Controlled Dislocation Creep: A Defense*, Acta Metallurgica, Vol 27, pp 387-400, 1979.
- [16] Young C.M., Robinson S.L., Sherby O.D., *Effect of Subgrain Size on the High Temperature Strength of Polycrystalline Aluminium as Determined by Constant Strain Rate Tests*, Acta Metallurgica, Volume 23, pp 633-639, 1975.

DEVELOPMENT OF AN INTERFACE BETWEEN CFD AND FE SOFTWARE

Nicola Tondini*, Olivier Vassart** and Jean-Marc Franssen***

* University of Trento, Italy
e-mail: nicola.tondini@ing.unitn.it

** ArcelorMittal, Luxembourg
e-mail: vassart.olivier@arcelormittal.com

*** University of Liege, Belgium
email: jm.franssen@ulg.ac.be

Keywords: CFD-FE interface, Weak coupling, Compartment fires.

Abstract. *The paper presents the assumptions and the issues that arise when developing an integrated modelling methodology between a Computational Fluid Dynamics (CFD) software applied to compartment fires and a Finite Element (FE) software applied to structural systems subjected to fire. In particular, a weak coupling approach used to simulate a fire exposed structure by modelling the fire development in the compartment, the heat penetration in the structure and the mechanical response is described. The advantages and the disadvantages of such a technique are highlighted compared to a full coupling that conversely takes into account all mutual interactions. The favourable aspect of computing the thermal response of the structure in the FE model in order to avoid modelling the structure in the CFD model is underlined, namely a sensitive reduction of computational demand. Finally, a practical application is presented.*

1 INTRODUCTION

Integrated modelling methodologies applied to compartment fires in order to obtain the thermo-mechanical response of structures exposed to fire would represent a powerful tool to widen the application field of structural fire safety engineering by overcoming limitations associated to simplified procedures. The exploitation of such strategies based on the coupling between CFD and FE programs are already used in medicine, e.g. for modelling the blood flow in arteries [1]. However, in the fire engineering field, very few applications are available and the ones that have been developed are often limited to specific software pairs [2]. The Research Fund of Coal and Steel (RFCS) project called FIRESTRUCT [3] dealt with this issue by studying different coupling approaches and employing different software. In this paper is described the weak coupling approach developed here between the CFD software Fire Dynamics Simulator (FDS) and the FE software SAFIR, but it has to be underlined that the methodology could be used with any CFD and any FE software. The study is illustrated by an application of this methodology about an experimental campaign dealing with the problem of columns engulfed in a fire source.

2 OVERVIEW ON INTEGRATED CFD-FE METHODOLOGY

2.1 Compartment fires: problem definition

Three problems have to be solved when modelling the behaviour of a structure subjected to a compartment fire, each of them being governed by different physical phenomenon and, hence, by different equations: 1) temperature development in the compartment; 2) thermal response of the structure and 3) mechanical response of the structure. The fire development analysis yields the temperatures of gasses and the radiative and mass flows in the compartment. By means of the thermal analysis, the temperatures in the structural elements are obtained. The mechanical response provides the behaviour of the structural system, i.e. stresses, deflections etc. Several differences distinguish these three processes. First, the spatial scale of the thermal analysis in the structure is an order of magnitude smaller than the spatial scale used for the compartment temperature development and the mechanical response. Second, the time scale may be different to solve the problem within CFD and FE. Third, for the temperature development in the compartment and the mechanical response a 3D analysis is generally required, whereas for the thermal analysis a 2D analysis is usually sufficient. Thus, some issues arise when an integrated methodology CFD-FE is to be used to tackle the whole problem. It is natural to assign the task of performing the compartment temperature development analysis to the CFD model and the mechanical response to the FE model, but it is not so straightforward to decide where to carry out the thermal analysis. Both software may be exploited to fulfil the task. The advantages to perform the thermal analysis in the CFD model are first to get direct information from the compartment temperature development analysis and, second, to allow consideration of the energy absorbed by the structure to be considered in the analysis of the compartment. On the other hand, if the thermal analysis in the structure is carried out in the FE model, all data necessary are directly available by the FE code to determine the mechanical response. Whatever the choice, the difficulties arise when data have to be exchanged between the two software, because of different scales in space and time. Moreover, if the thermal analysis is performed in CFD software, the compartment model must include the structure as well. The latter aspect is not desirable as described later on.

2.2 Levels of coupling

From the description of the problem it is clear that coupling CFD to FE model is far from straightforward and that the selected level of coupling influences the complexity of the model. In reality all three problems are mutually coupled (full coupling or two-way coupling) as shown in Fig. 1 and reported in Table 1, where the main phenomena involved in a compartment fire are listed along with their mutual interaction.

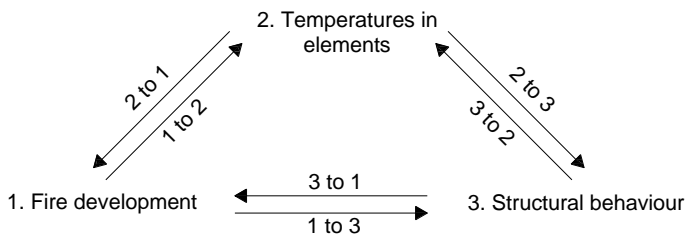


Figure 1. Full coupling strategy between the main phenomena involved in a compartment fire

Table 1. Mutual interactions of main phenomena involved in a compartment fire

	COUPLING					
	1 to 2	2 to 3	3 to 1	1 to 3	3 to 2	2 to 1
FIRE						
Convection and radiation to structural elements	x					
VELOCITY OF GASES						
Convection factors	x					
Dynamic pressure on walls, windows				x		
PRESSURE						
Static pressure on walls, windows				x		
TEMPERATURE IN MATERIALS						
Thermal elongation of elements		x				
Degradation of mechanical properties		x				
Absorption of energy from the compartment						x
PLASTICITY AND CRACKING IN ELEMENTS						
Generation of heat or heat leakage			x		x	
Modification of material thermal properties					x	
DISPLACEMENTS IN ELEMENTS						
Modification of the gas flow			x			
Modification of the element thermal exposure					x	

The implementation of a full coupling allows taking into account all phenomena and it guarantees a general field of application as well as a solution that tends to be exact. An example of full coupling is the interface developed between VESTA, a CFD software, and DIANA, an FE software developed by TNO in the Netherlands [3]. However, an integrated methodology that relies on full coupling is very complex to achieve. The first reason lies in various uncertainties that question the so-called exactness of the method. For instance, heat leakage through cracks in concrete or gypsum plaster boards enclosures are still very difficult to quantify because they do not follow deterministic rules. Moreover, from a programming point of view, the code of the selected CFD software and the code of the FE program have to be modified so that they can communicate for the exchange of data, but it means that in most cases the integrated methodology will not work if another CFD or another FE software is used. This is a clear drawback in terms of versatility and flexibility. Furthermore, for each simulation, a CFD specialist as well as an FE specialist are required since the two models cannot be run independently. Other typical issues that may occur in the design practice are related to possible modifications that the structure undergoes during the construction project as well as modifications of the structure that have to be applied because of an unsatisfactory behaviour in terms of fire safety requirements. Since the structural elements must be included in the CFD model, any changes in the structural system imply that the whole analysis must be re-run, entailing large time consuming analyses.

From these considerations, a simplified approach, the so-called weak coupling, is proposed to overcome the major aforementioned issues with the aim to be applicable to a wide number of likely-to-occur scenarios in compartment fires.

3 PROPOSED WEAK COUPLING METHODOLOGY

3.1 Assumptions and general remarks

In the proposed weak coupling (or one-way) approach the mutual interactions are discarded, as illustrated in Fig. 2. The CFD software models the fire development, while the FE program performs the thermal and the mechanical analyses. The fire development is calculated independently of the thermal response in the linear elements of the structure such as, for example, steel columns, beams or truss girder. If part of the structure is made of planar elements that also constitute boundaries of the compartment such as, for example, concrete walls or slabs, they must be modelled, perhaps with some degrees of approximation [4], in the fire development analysis. The detailed temperature field in these structural elements will nevertheless be computed subsequently by the FE software. As a consequence, if p variations of the structure must be evaluated under q fire scenarios, only q CFD analyses have to be performed, compared to $p \cdot q$ coupled analyses in a full coupling approach.

In this strategy, the thermal response of the structure represents the input of the mechanical analysis. Hence, it can be performed first, over the whole time domain, and then the resulting data are transferred at the beginning of the mechanical analysis which is performed subsequently.

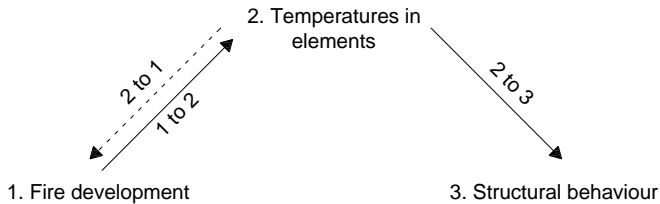


Figure 2. Weak coupling strategy between the main phenomena involved in a compartment fire

Nonetheless, these simplifications imply some limitations:

i) the dimensions of the structural elements and their displacements perpendicular to their longitudinal axis must be small compared to the dimensions of the compartment in order not to significantly influence the temperatures and the air flow around the elements. According to this assumption a series of 2D thermal analyses rather than a unique 3D thermal analysis is made on the structural elements because the transverse dimension of the section of the elements is small with respect to the longitudinal dimensions. For instance, a $1 \times 1 \text{ m}^2$ concrete columns in a 100 m^2 compartment must clearly be considered in the CFD model. This would also be the case for 1-meter deep concrete beams in a car park with a distance from the floor to the beams that is on the order of magnitude of 2 meters. Very flexible structures that are sensitive to air pressure variation are also not suitable for such integrated methodology because the effects of air pressure variation on the displacements of the structure cannot be neglected. Floor systems designed according to the tensile membrane action also exhibit very large displacements during the fire and may also not comply with this requirement if the floor to ceiling distance is small compared to the displacement.

ii) It is possible, for each 2D thermal analysis, to consider the boundary conditions at the surface of the section at the same point, namely the point of the section located on the node line of the beam element, for example at the centre of gravity of the section. The influence of the distance from the node line of the section to the border of the section is neglected. This is consistent with the fact that the structure is not present in the CFD analysis because the size of the section perpendicular to the longitudinal axis is negligible with respect to the size of the compartment; the distance from the centre of the section to the border (approximately $\frac{1}{2}$ of the size of the section) is then also negligible.

iii) Generally, in the CFD model the dimensions of a parallelepipedic compartment correspond to the clear distances between opposite walls. However, in the FE model a slab is generally modelled in correspondence to its centreline as illustrated in Fig. 3. Thus, the slab would fall outside the CFD domain and assumptions have to be made in order to determine thermal information at the slab centreline.

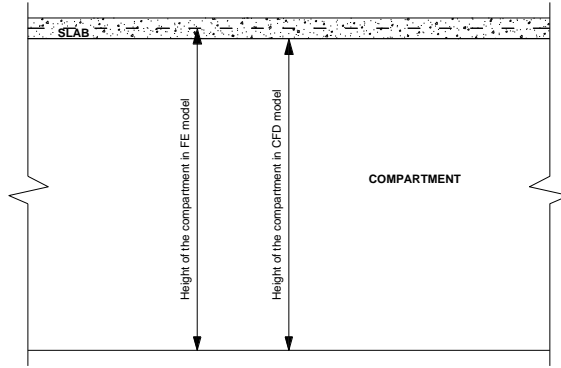


Figure 3. Different compartment dimensions for the CFD and the FE model.

iv) Since the structure is not included in the CFD model, the effect of shielding from any structural elements on others cannot be detected. For example, if a series of closely-spaced columns one behind the other is impinged by a radiant flux with direction parallel to the column series, the magnitude of the flux received by each column will only depend on the distance of each single column from the fire source and no effects of shielding will be taken into account on the columns behind the first one.

v) Irrigated structures in which water is circulating in order to keep the temperature of the structure within acceptable limits cannot be neglected because they may contribute in evacuating important amount of energy from the compartment.

This procedure is thus particularly well adapted for metallic structures made of relatively thin members (frame, truss girders) and located in very large compartments (railway or airport entrance halls, exhibition halls) where a localised fire is developing and simplified thermal models, such as those proposed in EN1991-1-2 [5], cannot be employed because the geometry of the compartment is too complex or the position of the structure in the compartment or with respect to the position of the fire is not within the field of application of simplified model.

3.2 How it works

In this section, the practical issues that have to be solved when implementing such an approach are presented. The programs used in this paper to illustrate the proposed integrated methodology are FDS [6] and SAFIR [7]. The main steps needed to couple CFD and FE are:

1) at the end of the CFD analysis, a transfer file containing all information regarding the state in the compartment, i.e. temperature of gas, convection factors and radiant intensities from various directions, is produced. These quantities can be provided at each grid point of the CFD model (the grid that was required to allow a precise determination of the solution) or instead at grid points of a coarser mesh reckoned by the CFD user as sufficient to get a sufficiently accurate representation of the solution that has been obtained. The mesh of considered points can also be refined around the structure that will be analysed and coarser away from the structure.

The format of the transfer file should be as standardised as possible so that in a future perspective it could be used for any choice of CFD and FE software. Hence, type of file (e.g. ASCII), syntax, type of reference system, type and format of numbers, presence of blank lines etc. have to be clearly stated. Such a format has been proposed within the FIRESTRUCT project and can be obtained from the authors. Radiant intensities from different directions are preferred to impinging radiant fluxes on predefined

surfaces because the structural elements are not included in the CFD model and thus no information is available at that stage about the shape of the cross-sections. The fluxes at the surface of the structural elements will be computed within the FE software by integrating the radiant intensities which allows taking into account possible shadow effects in concave sections.

2) A 3D Cartesian spatial interpolation is needed because the points of the structure where the information is needed (called here “the structural points”) generally do not coincide with the points of the CFD grid where the information is provided. If any structural points fall outside the CFD domain for the reason described above, they are moved to the closest boundary of the CFD domain where the Cartesian interpolation can be made, namely the boundary corresponding to the centre of the outermost cells because FDS provides the information at the centre of cells (see Fig. 4). A trilinear interpolation algorithm was successfully implemented in SAFIR to fulfil the 3D Cartesian interpolation.

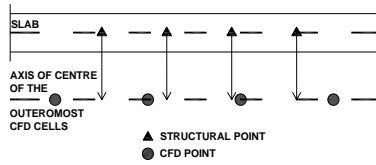


Figure 4. Case of structural points outside the CFD domain.

3) An interpolation in the time domain is also necessary because the time steps of the CFD analysis and the time steps of the thermal analysis may not be the same. In this case a simple linear interpolation may be used.

4) In order to get the impinging fluxes q on the surface of the structural elements a spherical numerical integration of radiant intensities I has to be performed. A numerical integration can be performed according to Eq 1.

$$q = \sum_i^n I_i \cos \theta_i \omega_i \tag{1}$$

where n is the number of intensities considered for the integration, ω_i is the solid angle associated to the direction i and θ_i is the angle between the direction of the radiant intensity i and the normal to the surface.

The directions of the intensities which are required to perform the spherical integration are generally not the directions in which the intensities are given by the CFD analysis. This is particularly the case if the structural elements are not parallel to the axes of the system of coordinates used in the CFD analysis (e.g. for diagonals in a truss girder). A spherical interpolation is thus performed in order to obtain the radiant intensities in the directions required by the numerical integration. Rotations of local axes are required to find the surface system of coordinates taking into account the direction of the longitudinal axis and the shape of the cross-section.

It is essential that the type of mesh and type of system of coordinates used in the CFD analysis (step 1) be clearly defined and taken into account in steps 2 and 4. The format of the transfer file established within the FIRESTRUCT project is based on the hypotheses of a structured parallelepipedic mesh in a dextrorsum Cartesian system of coordinates. The position of the origin of the system of coordinates and the directions of the “X”, “Y” and “Z” axes as well as the direction of gravity must be common in the CFD and in the FE analyses.

4 AN EXAMPLE OF PRACTICAL APPLICATION

The authors are currently involved in a research project that deals with the problem of columns engulfed in a fire source and the assessment of the real effect of the emissivity of flames. For this purpose,

two experimental tests with two types of combustible liquid are envisaged: i) a preliminary small scale test serving as a feasibility study; a 60.3 mm diameter, 1500 mm high circular tube is engulfed in a 300 mm diameter pool fire and ii) a 203 mm diameter, 3000 mm high circular tube engulfed in a 1000 mm diameter pool fire. In order to measure temperatures at different heights, an instrumentation set-up was designed. Fig. 5 shows the system designed for the larger pool fire while Fig. 6 shows the system used in the preliminary small-scale tests. Since the steel rack system used to support the bars where the thermocouples are installed is slender and thermal information (temperatures, fluxes, etc) around the pool fire was not known, the described methodology was exploited to check whether the rack could undergo deformations that could affect the set-up configuration during the tests. Therefore, the pool fire of diameter 1 m was firstly simulated in FDS to get all information at the rack location. Then, the thermal analysis and the mechanical response of the rack modelled in SAFIR were carried out on the basis of the results provided by the CFD analysis. In detail, a kerosene pool fire, having a constant Rate of Heat Release (RHR) of 1634 kW/m^2 , was simulated without including the rack into the CFD model. At the end of the simulation the transfer file including all thermal information due to the pool fire was created.

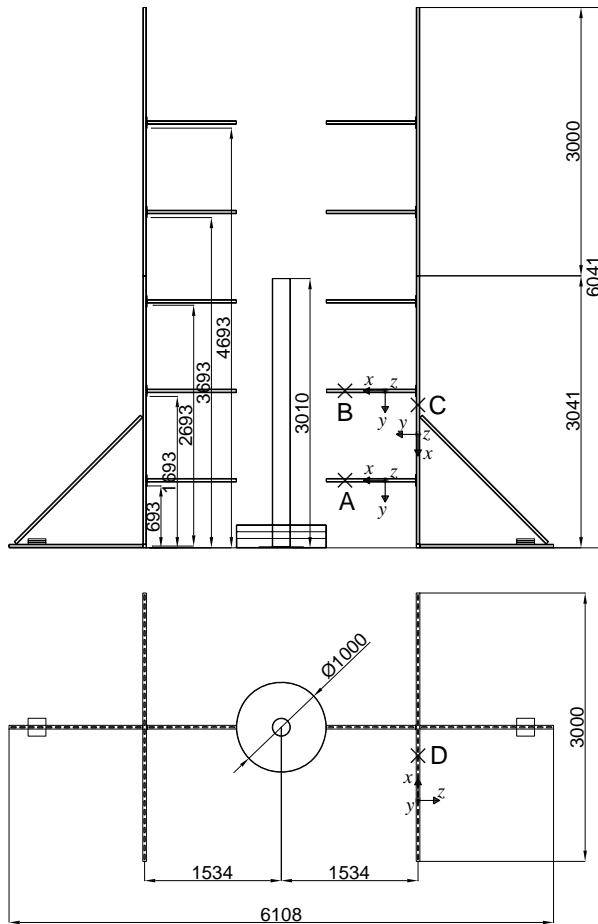


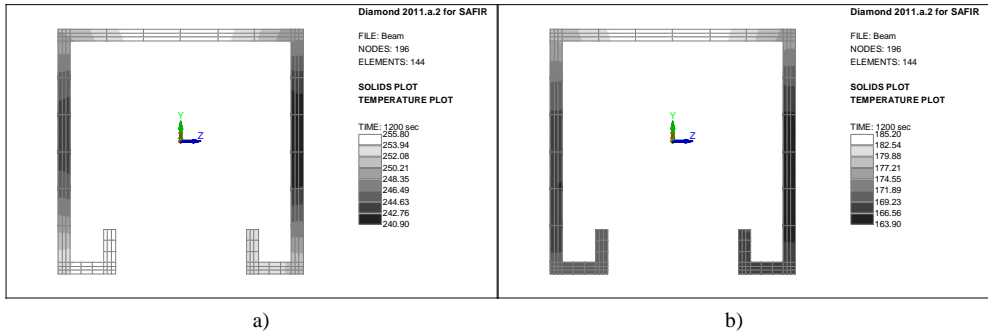
Figure 5. Instrumentation set-up for a pool fire of diameter 1 m in which a column 3 m high and of diameter of 203 mm is placed (dimensions in mm).



Figure 6. Instrumentation set-up used to measure temperatures at different heights of a pool fire of diameter of 300 mm which engulfs a steel circular column 1500 mm high and of diameter 60.3 mm.

The rack was modelled in SAFIR by means of Bernoulli-type 3D beam elements. A 2D thermal analysis was thus performed at each of the longitudinal point of integration in the beam elements. In Fig. 7 the temperature distribution in the sections located as indicated by a cross in Fig. 5 is reported. The local axes of each beam element are also depicted in Fig. 5 to show the orientation. From Fig. 7 the effect of the non-uniform radiation affecting the sides of the sections is clearly visible and a coherent temperature distribution in the section on the basis of the orientation of the element with respect to the fire location is highlighted. Then, the results of the thermal analysis were used to calculate the mechanical response of the rack; the calculated displacements are shown in Fig. 8, amplified by a factor of 20. Moreover, the structure was moved inside the compartment in order to find the best location in terms of space optimisation in the lab but no additional CFD analyses were required.

This simple case highlights the usefulness and the versatility as well as the capability of this integrated methodology to overcome problems that cannot be analysed by simplified models.



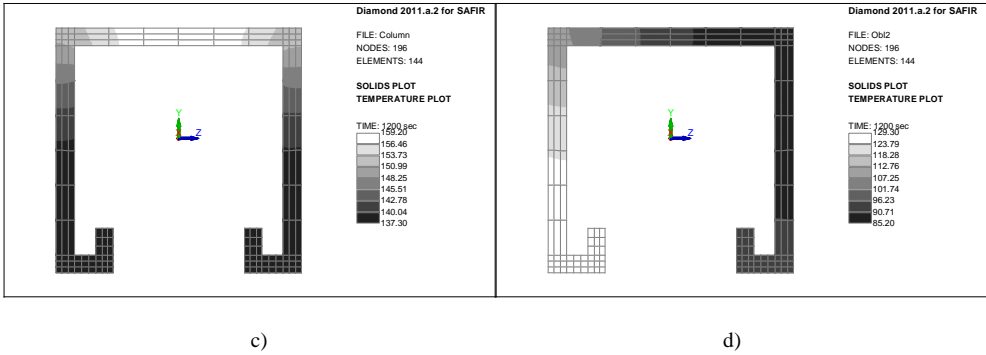


Figure 7. Temperature distribution at 1200 s in: a) beam section A; b) beam section B; c) column section C; d) bracing section D.

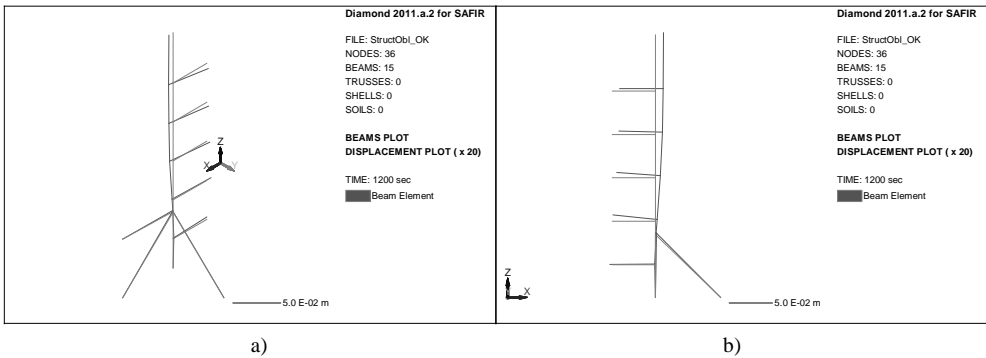


Figure 8. Displacements of the rack at 1200 s scaled by a factor of 20: a) isometric view; b) side view.

5 CONCLUSION

This paper describes assumptions and issues of an integrated modelling methodology for the behaviour of a structure located in a fire compartment by implementing a weak coupling approach. It is suitable for localised fires in very large compartments built with relatively thin structures where the transverse dimensions of the structural elements can be neglected. In this respect, a practical application of the methodology demonstrated its usefulness and its capability to overcome problems that cannot be analysed by simplified models. The choice to perform the fire development analysis independently from the thermal analysis of the structure and from the mechanical response analysis by neglecting the structural elements in the CFD model allows reducing the computational demand and enhances the versatility of the methodology.

REFERENCES

- [1] Zhao S. Z., Xu X. Y. and Collins M. W., The numerical analysis of fluid–solid interactions for blood flow in arterial structures Part 2: development of coupled fluid–solid algorithms, Proceedings of the Institution of Mechanical Engineers, Part H: *Journal of Engineering in Medicine*, 212: 241, 1998.

- [2] Fellingner J. H. H, Kenyon Y. M., Breunese A. J. and Lemaire A. D., A coupled CFD-FEA study of a tunnel structure exposed to a fire, *INTERFLAM*, 10: 1349–1360, 2004
- [3] Kumar S., Miles S. Welch S., Vassart O., Zhao B., Lemaire A.D., Noordijk L. M., Fellingner J. H. H. and Franssen, J.-M., FIRESTRUC – *Integrating advanced three-dimensional modelling methodologies for predicting thermo-mechanical behaviour of steel and composite structures subjected to natural fires*, RFCS project RFS-PR-02110, European Commission report, 2008.
- [4] Cooper L., Franssen J.-M., A Basis for Using Fire Modeling with 1-D Thermal Analyses of Partitions to Simulate 2-D and 3-D Structural Performance in Real Fires, *Fire Safety Journal*, Vol. 33, 115-128, <http://hdl.handle.net/2268/38130>, 1999.
- [5] CEN, *Eurocode 1 : Actions on structures – Part 1-2 : General actions – Actions on structures exposed to fire*, Bruxelles, 2004.
- [6] McGrattan K. et al., *Fire Dynamics Simulator (Version 5) - Technical Reference Guide*, NIST Special Publication 1018-15, National Institute of Standards and Technology, Gaithersburg, MD, 2007.
- [7] Franssen J.-M., SAFIR. A Thermal/Structural Program Modelling Structures under Fire, *Engineering Journal*, A.I.S.C., Vol 42, No. 3 , 143-158, 2005.

FINITE ELEMENT RELIABILITY ANALYSIS FOR STRUCTURAL SAFETY EVALUATION IN FIRE

Qianru Guo* and Ann E. Jeffers*

* Department of Civil and Environmental Engineering, University of Michigan, Ann Arbor, MI USA
Email: qianru@umich.edu, jffrs@umich.edu

Keywords: Structural Reliability, Stochastic Finite Element Method, First-Order Reliability Method, Direct Differentiation Method.

Abstract. *The finite element reliability methods are extended here to evaluate the structural reliability in fire. A reliability framework, which contains the fire scenario, the thermal conduction model, and the structural model, was formulated for simulating structural response under the natural fire. In particular, the first order reliability method (FORM) following the improved Hasofer-Lind-Rackwitz-Fiessler (iHL-RF) algorithm was extended to evaluate the reliability of a beam exposed to fire. Both the direct differentiation method (DDM) and the finite difference method (FDM) were used for calculating the parameter sensitivities that are required for locating the failure surface within the first-order reliability analysis. The accuracy and efficiency of the finite element reliability analysis was evaluated based on comparisons to Monte Carlo simulations. Results demonstrate that the FORM combined with the DDM offers much promise for efficiently assessing the reliability of structures in fire.*

1 INTRODUCTION

The quantification of risk and reliability are vital to ensuring a safe and economic infrastructure. Current fire resistant design codes provide a minimum level of safety but fail to offer a quantitative measure of structural reliability. Despite considerable advances in the area of engineered structural fire resistance, structural reliability is typically inconsistent with the design for other types of hazards [1] and indeterminate based on current procedures of analysis [2, 3]. The quantification of structural reliability is essential to risk-based engineering because tradeoffs in cost and utility can be explored to identify the best engineered solution given a target level of performance [4]. Thus, reliability analysis is a key component of performance-based design.

Structural response in fire has been shown to be highly sensitive to a number of parameters, and there are limited methodologies for quantifying the reliability of structures given the multi-physical nature and the high order of dimensionality of the problem. Previous research has sought to use Monte Carlo simulation to quantify the uncertainty in the fire scenario [5-7] and structural systems threatened by fire [8-12]. Despite its versatility, Monte Carlo simulation is extremely computationally expensive because it requires an unreasonably large sample size to accurately predict the reliability, particularly in regions with low failure probabilities [13]. On the other hand, finite element reliability methods, which have been well-developed for ambient temperature analysis of structures [14], may offer promising advantages toward addressing the uncertainties when simulating structural response under fire due to their improved efficiency. No known research to date has sought to extend the stochastic finite element method to the analysis of structures in fire, and it is therefore unknown whether the method can reasonably be used to capture uncertainties that are present in the fire, thermal, and structural domains.

This research therefore seeks to extend the perturbation-based stochastic finite element method to simulate structural response under natural fire. The present study uses the First Order Reliability Method (FORM) to calculate the structural reliability by considering a first order Taylor expansion about the limit

state function. The FORM is one of the most commonly used reliability methods for predicting the safety of structures at ambient temperature because it can efficiently quantify the reliability of the system given a large number of uncertain parameters. In the FORM, only the response and response gradients with respect to each uncertain parameter are needed to evaluate the reliability of the system. Therefore, the FORM can provide a more accurate result at a fraction of the computational expense that is needed for Monte Carlo simulation, especially in the analysis of structures with extremely low probabilities of failure. In the stochastic finite element method, the response gradients are determined by using either the finite difference method (FDM) or the direct differentiation method (DDM). Two case studies are introduced in this paper to demonstrate the extension of the stochastic finite element method to the analysis of structures in fire.

2 ANALYTICAL SYSTEM

The analysis of structures in fire involves three sequentially coupled processes as illustrated in Fig. 1: the fire behavior, the thermal response of the structure, and the mechanical response of the structure. The fire temperature and/or surface flux can be evaluated by a parametric fire curve, zone model, or computational fluid dynamics simulation. Based on the thermal boundary conditions, the temperatures in the structure are evaluated by a finite element or finite difference simulation. Knowing the transient temperature distribution in the structure, the mechanical response can subsequently be evaluated by a finite element analysis in a commercial program such as ABAQUS or ANSYS. Within each domain shown in Fig. 1, there are parameters that exhibit some degree of uncertainty as indicated in the left column. For example, the amount, type, and distribution of fuel at a given point in time have significant uncertainty. The uncertainty in the fuel will produce fire temperatures and surface fluxes (shown on the right in Fig. 1) that also exhibit some degree of uncertainty. This variability feeds into the conduction heat transfer model in the calculation of temperatures in the structure and ultimately affects the force-deformation response of the system.

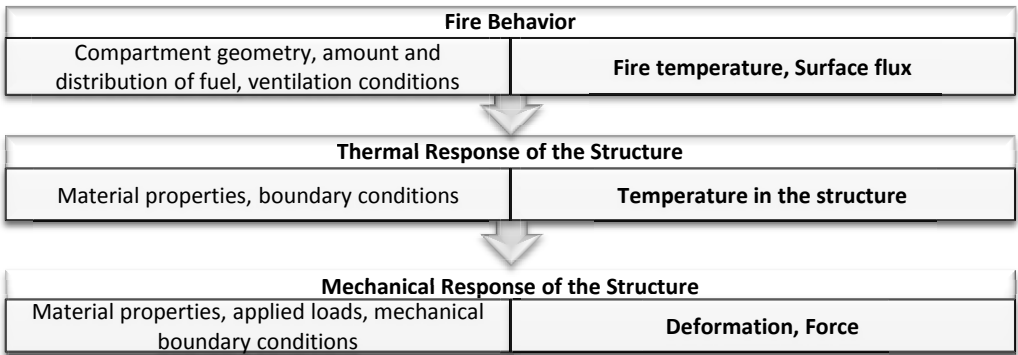


Figure.1 Propagation of uncertainty in the structural fire simulation

As the probabilistic simulation of the structural fire response involves a number of uncertain parameters in multiple physical domains, a reliability-based framework must be employed that involves: (1) the identification and characterization of the sources of uncertainty in the model, (2) the definition of appropriate performance function(s) by which failure can be evaluated, (3) the development of a stochastic model for the system that captures the propagation of uncertainty illustrated in Fig. 1, and (4) the quantification of the system reliability, which is generally expressed in terms of a failure probability P_f or reliability index β . In this paper, the thermo-structural analysis is carried out in a special-purpose code based on the fiber element model proposed by Jeffers and Sotelino [15]. The model is extended here to incorporate the reliability analysis described in Section 3.

3 METHODOLOGY

This paper focuses on extending the First Order Reliability Method (FORM) to the analysis of structures in fire. The FORM uses a first-order Taylor series expansion about the limit state function such that the response $g(\mathbf{X})$ and response gradients $\partial g(\mathbf{X})/\partial X_i$ with respect to each uncertain parameter X_i are the only values that are needed to evaluate the reliability of the system. The FORM uses an optimization algorithm to determine the reliability index β by identifying the design point on the failure surface. The approach involves (1) transforming the statistically correlated random variables \mathbf{X} into a set of uncorrelated variables \mathbf{Y} that are expressed in standard space (i.e., each variable in standard space has zero mean and unit standard deviation), (2) approximating the failure surface $g(\mathbf{X}) = 0$ as a linear function, and (3) evaluating the reliability index β as the distance to the failure surface [16]. Because the performance function $g(\mathbf{X})$ is not explicitly stated in terms of parameters \mathbf{X} , an iterative solution algorithm is employed to find the design point on the limit state surface. Prior research has shown that the improved Hasofer-Lind-Rackwitz-Fiessler (iHL-RF) exhibits rapid convergence and numerical stability for problems comprising normal and non-normal variables [17-19]. The present study therefore uses the iHL-RF algorithm to identify the design point and estimate the failure probability.

Response gradients $\partial g(\mathbf{X})/\partial X_i$ can be determined by a finite difference approximation or by direct differentiation of the governing finite element equations. The finite difference method (FDM) uses a finite difference approximation for the gradient such that

$$\frac{\partial g(\mathbf{X})}{\partial X_i} \approx \frac{\Delta g(\mathbf{X})}{\Delta X_i} \quad (1)$$

Thus, the response $g(\mathbf{X})$ is evaluated twice: at X_i and at $X_i + \Delta X_i$, where ΔX_i represents a small perturbation in the parameter X_i . The difference $\Delta g(\mathbf{X})$ is then calculated and inserted in Eq. 1. As ΔX_i goes to zero, Eq. 1 converges to the true response gradient. Although the FDM is versatile and widely applied in probabilistic analysis software such as NESSUS, it is computationally inefficient because it requires additional simulations to evaluate the response for each perturbation. Furthermore, the accuracy of the FDM is limited by the size of the perturbation, and there is no way to determine *a priori* the size of the perturbation that is needed to achieve the converged solution.

The direct differentiation method (DDM) is an alternate approach to evaluating the response gradients that are needed for the reliability analysis. The DDM involves deriving analytical expressions for the response gradients based on directly differentiating the governing finite element equations. The DDM provides an exact estimate of the response sensitivity with minimal computational expense. A significant amount of research has sought to apply the DDM to the analysis of structures at ambient temperature. The present study extends the formulation to account for the propagation of uncertainty from the thermal to the structural domain.

3.1 Response sensitivity analysis in the structural domain

The governing equation for nonlinear structural analysis is

$$\mathbf{P}_n^{\text{int}} = \mathbf{P}_n^{\text{ext}} \quad (2)$$

where $\mathbf{P}_n^{\text{int}}$ = the vector of internal forces, and $\mathbf{P}_n^{\text{ext}}$ = the vector of the external forces. This equation should be satisfied at every time step n . Differentiating Eq. (2) by parameter X_i gives [20]

$$\mathbf{K}_n \frac{\partial \mathbf{u}_n}{\partial X_i} = \frac{\partial \mathbf{P}_n^{\text{ext}}}{\partial X_i} - \frac{\partial \mathbf{P}_n^{\text{int}}}{\partial X_i} \quad (3)$$

where \mathbf{K}_n = the algorithmically consistent stiffness matrix given by [21] and \mathbf{u}_n = the vector of nodal displacements. $\partial \mathbf{u}_n / \partial X_i$ is the displacement sensitivity vector, which is needed in the evaluation of the response gradient $\partial g(\mathbf{X})/\partial X_i$. $\partial \mathbf{P}_n^{\text{ext}} / \partial X_i$ can readily be evaluated in most cases because the external

force acting on a structure is typically known. The challenge therefore is in deriving expressions for the sensitivity $\partial \mathbf{P}_n^{\text{int}} / \partial X_i$ of the internal force vector.

The vector of internal forces $\mathbf{P}_n^{\text{int}}$ is calculated directly from the internal stress $\boldsymbol{\sigma}_n$ and obtained by assembling the contributions from all elements in the structure [22], i.e.,

$$\mathbf{P}_n^{\text{int}} = \sum_{i=1}^{N_{\text{els}}} (\mathbf{p}_n^{\text{int}})_i = \sum_{i=1}^{N_{\text{els}}} \left(\int \mathbf{B}^T \boldsymbol{\sigma}_n dV \right)_i \quad (4)$$

where $\mathbf{p}_n^{\text{int}}$ = vector of internal force calculated in each element, \mathbf{B} = strain-displacement matrix, $\boldsymbol{\sigma}_n$ = stress vector, and V = element's volume. By differentiating Eq. (4) by parameter X_i , the sensitivity of the internal force vector is found to be

$$\left. \frac{\partial \mathbf{P}_n^{\text{int}}}{\partial X_i} \right|_{u\text{-fixed}} = \sum_{i=1}^{N_{\text{els}}} \left(\int \left(\left. \frac{\partial \mathbf{B}^T}{\partial X_i} \right|_{u\text{-fixed}} \boldsymbol{\sigma}_n + \mathbf{B}^T \mathbf{E} \left. \frac{\partial \boldsymbol{\varepsilon}_n}{\partial X_i} \right|_{u\text{-fixed}} + \mathbf{B}^T \left. \frac{\partial \boldsymbol{\sigma}_n}{\partial X_i} \right|_{\varepsilon\text{-fixed}} \right) dV \right)_i \quad (5)$$

where $\mathbf{E} = \partial \boldsymbol{\sigma}_n / \partial \boldsymbol{\varepsilon}_n$ is the tangent modulus of the material.

As both $\boldsymbol{\varepsilon}_n$ and $\boldsymbol{\sigma}_n$ are evaluated under the element temperatures, parameters X_i that are included in the thermal model can be calculated by using the chain rule, i.e.,

$$\left. \frac{\partial \mathbf{P}_n^{\text{int}}}{\partial X_i} \right|_{u\text{-fixed}} = \sum_{i=1}^{N_{\text{els}}} \left(\int \left(\left. \frac{\partial \mathbf{B}^T}{\partial X_i} \right|_{u\text{-fixed}} \boldsymbol{\sigma}_n + \mathbf{B}^T \mathbf{K}_t \left. \frac{\partial \boldsymbol{\varepsilon}_n}{\partial X_i} \right|_{u,T,\text{fixed}} + \mathbf{B}^T \mathbf{K}_t \left. \frac{\partial \boldsymbol{\varepsilon}_n}{\partial \mathbf{T}} \frac{\partial \mathbf{T}}{\partial X_i} \right|_{u\text{-fixed}} \right. \right. \\ \left. \left. + \mathbf{B}^T \left. \frac{\partial \boldsymbol{\sigma}_n}{\partial X_i} \right|_{\varepsilon,T,\text{fixed}} + \mathbf{B}^T \left. \frac{\partial \boldsymbol{\sigma}_n}{\partial \mathbf{T}} \frac{\partial \mathbf{T}}{\partial X_i} \right|_{\varepsilon\text{-fixed}} \right) dV \right)_i \quad (6)$$

where \mathbf{T} = the vector of temperatures, which are passed from the thermal model.

By using Eq. (6), the partial derivative of internal force for all parameters related to the structural analysis and thermal field can be evaluated. Eq. (6) is substituted into Eq. (3) to obtain the displacement sensitivity, which is used directly in the evaluation of the response gradient $\partial g(\mathbf{X}) / \partial X_i$.

3.2 Response sensitivity analysis in the thermal domain

The governing equation for transient thermal analysis is given by [22]:

$$\mathbf{C}\dot{\mathbf{T}} + \mathbf{K}\mathbf{T} = \mathbf{R} \quad (7)$$

where \mathbf{C} = heat capacity matrix, $\dot{\mathbf{T}}$ = an array containing the first derivatives of the nodal temperatures with respect to time, \mathbf{K} = conductivity matrix, \mathbf{T} = array of nodal temperatures, and \mathbf{R} = an array of thermal loads.

By considering temperature states \mathbf{T}_n and \mathbf{T}_{n+1} over time step Δt and applying the backward difference technique, the temperature at time step $n + 1$ is given by

$$\mathbf{T}_{n+1} = \mathbf{T}_n + \Delta t \dot{\mathbf{T}}_{n+1} \quad (8)$$

Combining Eq. (7) and Eq. (8) gives

$$\left(\frac{1}{\Delta t} \mathbf{C} + \mathbf{K} \right) \mathbf{T}_{n+1} = \frac{1}{\Delta t} \mathbf{C} \mathbf{T}_n + \mathbf{R}_{n+1} \quad (9)$$

Eq. (9) is subsequently differentiated by parameter X_i using the chain rule. All partial derivatives related to the temperature \mathbf{T}_n from the previous time step n are retained. Thus, the response sensitivity for the thermal analysis is given by

$$\left(\frac{1}{\Delta t}\mathbf{C} + \mathbf{K}\right)\frac{\partial \mathbf{T}_{n+1}}{\partial X_i} = -\frac{1}{\Delta t}\frac{\partial \mathbf{C}}{\partial X_i}\mathbf{T}_{n+1} - \frac{\partial \mathbf{K}}{\partial X_i}\mathbf{T}_{n+1} + \frac{1}{\Delta t}\frac{\partial \mathbf{C}}{\partial X_i}\mathbf{T}_n + \frac{1}{\Delta t}\mathbf{C}\frac{\partial \mathbf{T}_n}{\partial X_i} + \frac{\partial \mathbf{R}_{n+1}}{\partial X_i} \quad (10)$$

where

$$\frac{\partial \mathbf{C}}{\partial X_i} = \frac{\partial \mathbf{C}}{\partial X_i}\bigg|_{\mathbf{T}_n, \mathbf{T}_{f,n}, \text{fixed}} + \frac{\partial \mathbf{C}}{\partial \mathbf{T}_n}\bigg|_{\mathbf{T}_{f,n}, X_i, \text{fixed}}\frac{\partial \mathbf{T}_n}{\partial X_i} + \frac{\partial \mathbf{C}}{\partial \mathbf{T}_{f,n}}\bigg|_{\mathbf{T}_n, X_i, \text{fixed}}\frac{\partial \mathbf{T}_{f,n}}{\partial X_i} \quad (11)$$

$$\frac{\partial \mathbf{K}}{\partial X_i} = \frac{\partial \mathbf{K}}{\partial X_i}\bigg|_{\mathbf{T}_n, \mathbf{T}_{f,n}, \text{fixed}} + \frac{\partial \mathbf{K}}{\partial \mathbf{T}_n}\bigg|_{\mathbf{T}_{f,n}, X_i, \text{fixed}}\frac{\partial \mathbf{T}_n}{\partial X_i} + \frac{\partial \mathbf{K}}{\partial \mathbf{T}_{f,n}}\bigg|_{\mathbf{T}_n, X_i, \text{fixed}}\frac{\partial \mathbf{T}_{f,n}}{\partial X_i} \quad (12)$$

$$\frac{\partial \mathbf{R}_{n+1}}{\partial X_i} = \frac{\partial \mathbf{R}_{n+1}}{\partial X_i}\bigg|_{\mathbf{T}_n, \mathbf{T}_{f,n}, \text{fixed}} + \frac{\partial \mathbf{R}_{n+1}}{\partial \mathbf{T}_n}\bigg|_{\mathbf{T}_{f,n}, X_i, \text{fixed}}\frac{\partial \mathbf{T}_n}{\partial X_i} + \frac{\partial \mathbf{R}_{n+1}}{\partial \mathbf{T}_{f,n}}\bigg|_{\mathbf{T}_n, X_i, \text{fixed}}\frac{\partial \mathbf{T}_{f,n}}{\partial X_i} \quad (13)$$

Here, $\mathbf{T}_{f,n}$ = the fire temperature at step n . As the heat capacity matrix \mathbf{C} , conductivity matrix \mathbf{K} , the thermal load vector \mathbf{R} , and temperature \mathbf{T}_n from the previous time step n are known, the temperature sensitivity $\partial \mathbf{T}_{n+1} / \partial X_i$ can readily be obtained.

3.3 Solution algorithm

The performance function $g(\mathbf{X})$ is an expression that relates the loads acting on the structure to the resistance provided by the structure. Because structural resistance in fire is heavily dependent on the temperature in the structure, failure can be more appropriately defined in terms of a limiting deformation, as is often done in fire resistance tests. The present study focuses on assessing the reliability of a single beam exposed to fire, in which failure can be described in terms of a limiting deflection (e.g., $L/30$) in the beam. Therefore, the performance function becomes

$$g(\mathbf{X}) = u(\mathbf{X}) - L/30 \quad (14)$$

where u is the maximum displacement in the beam. Thus, the performance function and its gradient are directly related to the deformation in the beam.

A schematic of the algorithm used to evaluate the reliability of the beam is shown in Fig. 2. Traditional finite element analysis is used to evaluate the limit state function g , while the response gradients are computed based on the FDM or DDM. Iterations are carried out based on the iHL-RF algorithm to identify the design point. Once the iHL-RF algorithm converges, the reliability index is calculated as the distance to the failure surface at the combination of parameters \mathbf{X}^* that have the highest probability of failure. \mathbf{X}^* is referred to as the design point or the most probable point (MPP).

4 APPLICATIONS

Two examples were studied to evaluate the proposed stochastic finite element approach in its ability to predict the reliability of structures in fire. The first demonstrates the adequacy of the structural model, while the second accounts for the propagation of uncertainty across the fire, thermal, and structural domains. Comparisons are drawn between the FORM and Monte Carlo simulation. Comparisons are also drawn between the FDM and DDM for calculating response sensitivities in the thermal and structural domains.

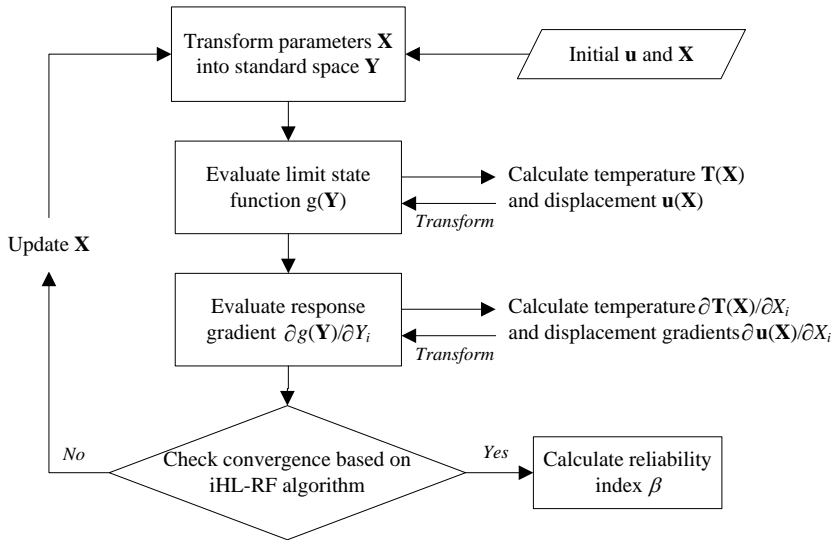


Figure 2. Reliability algorithm

4.1 Uniformly heated steel beam

To evaluate the reliability algorithm applied to the structural model alone, an analysis was carried out on an IPE80 steel beam with a total length of 114 cm subjected to uniform heating. As shown in Fig. 3, this simply supported beam is based on the fire resistance tests conducted by Rubert and Schaumann [23]. In the present study, the applied load P and the yield stress F_y of the steel at ambient temperature were treated as random variables, with mean values equal to the experimental values and normally distributed with coefficients of variation of 0.05.

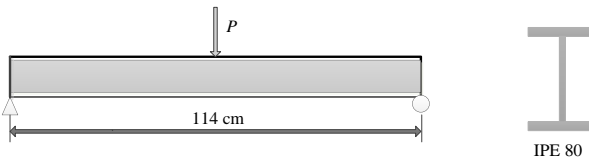


Figure 3. The uniformly heated steel beam

A special-purpose finite element code was written in Matlab to conduct the reliability analysis. The program used a displacement-based fiber beam element to model the structural response under fire conditions. The Eurocode model for steel was utilized to account for the nonlinear, temperature-dependent material response. Results from a deterministic analysis are shown in Fig. 4a to illustrate the level of accuracy achieved by the Matlab code in comparison to simulations in Abaqus and to the experimental results for two load cases (i.e., $P = 0.7P_u$ and $P = 0.85P_u$).

A first-order reliability analysis was conducted for the beam with the applied load of $0.7P_u$ based on the method described in Section 3. The sensitivity of the mid-span deflection with respect to load P and temperature T was calculated by FDM and DDM, and excellent agreement was achieved as illustrated in Fig. 4b. In assessing the probability of failure, comparisons were made between the FORM and Monte Carlo simulations (MCS) with a sample size of 1,000. The evolution of the failure probability with

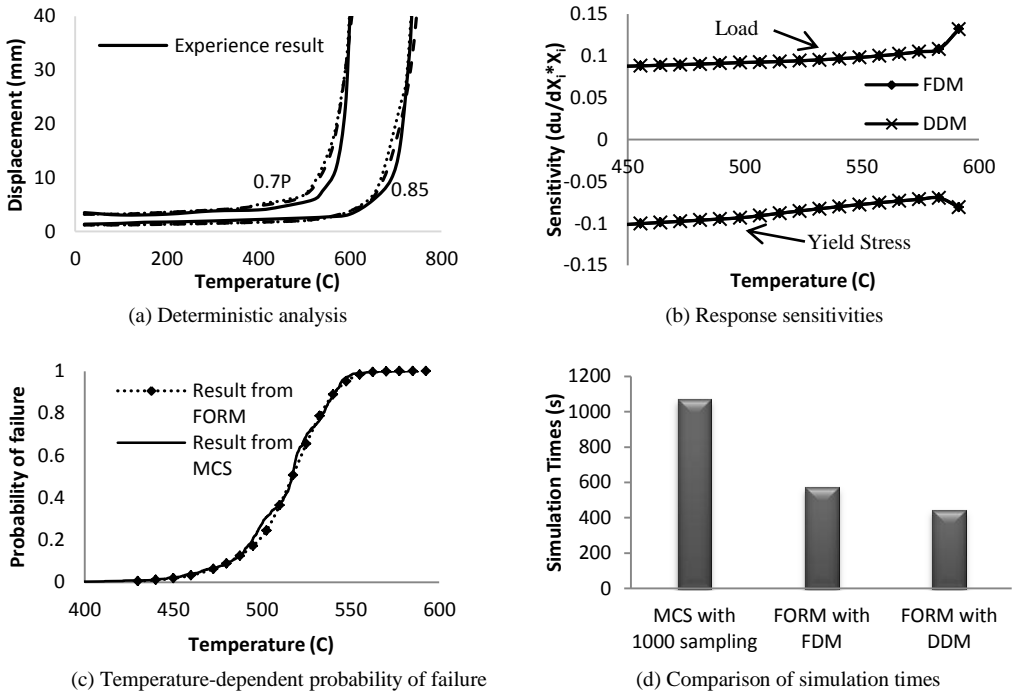


Figure 4. Results from the uniformly heated beam

increasing temperature is shown in Fig. 4c. As can be seen in Fig. 4c, the probability of failure rises significantly over temperatures ranging from 450-550 C due to the degradation of steel in this temperature range. Good agreement was achieved between the FORM and MCS, despite the relatively crude sampling in the MCS. A comparison of simulation times is shown in Fig. 4d. It is apparent that the FORM offers significant cost savings in comparison to MCS. These cost savings would be amplified for larger MCS sample sizes, which would be necessary in regions with low failure probabilities. The results also indicate modest savings by the DDM in comparison to the FDM. While the difference between the DDM and FDM is relatively small in this case, it is important to note that the savings that can be realized by DDM would increase significantly in a more complex problem with a larger number of random variables.

4.2 Protected steel beam exposed to compartment fire

To illustrate the general stochastic finite element formulation presented in Section 3, which accounts for propagation of uncertainty from the thermal to the structural domain, a stochastic analysis was conducted for a protected steel beam exposed to a natural fire. The system, which is shown in Fig. 5, is a simply supported beam subjected to a uniformly distributed load. The beam was assigned a W8×28 cross-section based on the AISC steel design specification and the ANSI/UL 263 requirements for prescriptive fire resistant design in the U.S. A cementitious spray-applied fire resistant material shown in Fig. 5b was selected to provide a one-hour fire resistance rating. This beam supported a concrete slab, which was assumed to be non-compositely with the beam. It was assumed that the concrete slab affected the heat transfer to the beam and did not contribute to the structural response. The fire exposure was modeled according to the Eurocode parametric fire curve as modified by [24].

Shi et al. [12] analyzed this system previously using Monte Carlo simulation (MCS). Input values in the present analysis were based on values published in [12]. Due to the large number of input parameters,

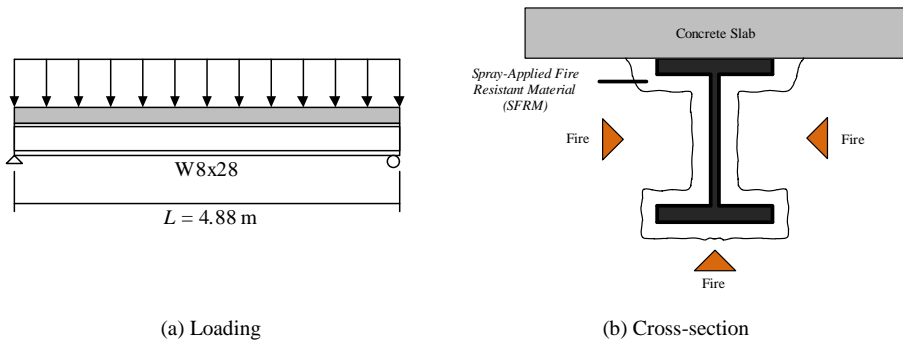


Figure 5. Protected steel beam exposed to fire

a response sensitivity analysis was conducted to determine the model parameters that have the largest influence on the response. Consequently, the present study considers the following parameters as random variables: the ventilation factor F_v , the thermal inertia of the surroundings b , the fuel load e_f , the thickness t_{SFRM} of the fire resistant material, the conductivity k_{SFRM} of the fire resistant material, and the distributed dead and live loads.

A special-purpose code was written in Matlab to perform the first-order reliability analysis. The model was based on the fiber element approach described in [15], except that the heat transfer model was reduced to a 2D heat transfer analysis over the section and the structural model utilized a displacement-based formulation for simplicity. Displacement sensitivities were calculated by FDM and DDM and are shown in Fig. 6 as functions of time. Note that excellent agreement was obtained between the FDM and DDM.

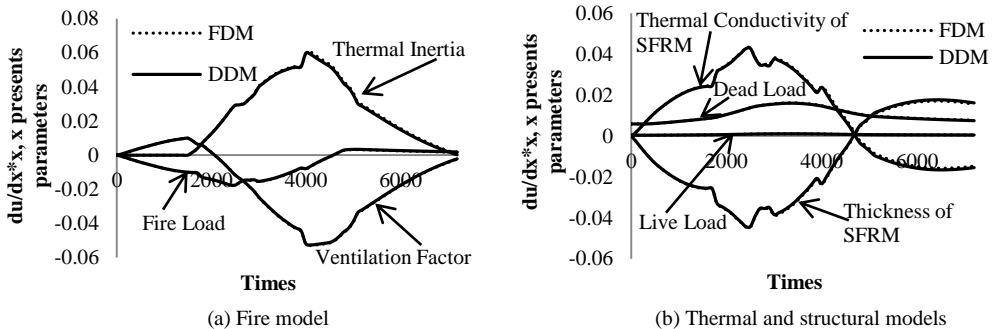


Figure 6. Response sensitivity to various model parameters in the fire, thermal, and structural models

The probability for failure was evaluated using the FORM and compared to Monte Carlo simulations carried out on the same system with a sample space of 10,000. It was found that the failure probability was predicted to be 7.2 percent using MCS and 8.4 percent using the FORM. There is some discrepancy between the two analyses that might be attributed to one of two phenomena. Firstly, the MCS sample size may be insufficient for predicting the relatively small failure probability. Secondly, the first-order approximation used in the FORM may be inadequate for the problem considered here. Improved accuracy may be achieved using a higher-order analysis (i.e., using the second-order reliability method). While a higher-order analysis typically provides greater accuracy, it is not as computationally efficient as the first-order analysis. The simulation time was 29.2 hours for MCS. However, the FORM required only 0.8 hours using FDM and 0.4 hours using DDM. Thus, it is apparent that the FORM was able to provide a

conservative prediction of the failure probability at only a fraction of the time needed for the MCS. Furthermore, the DDM is shown to offer additional costs savings over the FDM.

5 CONCLUSION

The perturbation-based stochastic finite element method was extended to the analysis of structures in fire to specifically account for the propagation of uncertainty across multiple physical domains. In particular, the first-order reliability method (FORM) was applied to the analysis of structures in fire with response gradients calculated by the finite difference method (FDM) and the direct differentiation method (DDM). Comparisons between the FORM and Monte Carlo simulations (MCS) demonstrate that the methodology exhibits good accuracy and offers significant savings in computational cost. Furthermore, the proposed approach is adequate for predicting the reliability of structures with low failure probabilities, which is a severe limitation to MCS. Comparisons between the FDM and DDM demonstrate that both methods offer excellent agreement. However, significant advantages can be realized by utilizing the DDM, as response gradients are evaluated exactly based on the governing finite element equations and fewer calculations are required.

This novel application of the stochastic finite element method enables accurate and efficient computation of the time-variant probability of failure, allowing the analyst to evaluate a system design based on an acceptable level of risk. The quantification of structural reliability in fire is essential to the realization of a holistic performance-based framework in which structural fire resistance is appropriately accounted for. The preliminary studies presented here demonstrate that the stochastic finite element method offers a more efficient means for assessing the reliability of structures in fire, and therefore offers much promise for the performance-based design of the structural systems.

ACKNOWLEDGEMENTS

This work was supported by the U.S. National Science Foundation under Grant No. CMMI-1032493. Any opinions, findings, conclusions or recommendations are those of the authors and do not necessarily reflect the views of the sponsoring agency.

REFERENCES

- [1] Ellingwood B.R., "Load combination requirements for fire-resistant structural design," *Journal of Fire Protection Engineering*, 15, 43-61, 2005.
- [2] Lange D., Usmani A., and Torero J., "The reliability of structures in fire," *Proceedings of the 5th International Conference on Structures in Fire*, K.H. Tan, V.K.R. Kodur, T.H. Tan (eds.), Research Publishing Services, Singapore, 760-770, 2008.
- [3] Fellingner J.H.H. and Both C.K., "Fire resistance: Reliability vs. time analyses," *Proceedings of Composite Construction in Steel and Concrete IV*, J.F. Hajjar (ed.), ASCE, USA, 816-827, 2000.
- [4] Singh V.P., Jain S.K., and Tyagi A., *Risk and reliability analysis: A handbook for civil and environmental engineers*, ASCE, USA, 2007.
- [5] Phillips, W.G.B., "Simulation-Models for Fire Risk Assessment," *Fire Safety Journal*, 23(2), 159-169, 1994.
- [6] Magnusson S.E., Frantzich H., and Harada K., "Fire safety design based on calculations: Uncertainty analysis and safety verification," *Fire Safety Journal*, 27(4), 305-334, 1996.
- [7] Frantzich, H., "Risk analysis and fire safety engineering," *Fire Safety Journal*, 31(4), 313-329, 1998.
- [8] Hietaniemi J., "Probabilistic simulation of fire endurance of a wooden beam," *Structural Safety*, 29, 322-336, 2007.

- [9] Sakji S., Soize C., and Heck J.V., "Probabilistic uncertainty modeling for thermomechanical analysis of plasterboard submitted to fire load," *Journal of Structural Engineering*, 134, 1611-1618, 2008.
- [10] Jensen E., Van Horn J., and Eamon C.D., "Variability of fire and concrete temperatures and the associated uncertainty in structural behavior," *Proceedings of the 6th International Conference on Structures in Fire*, V. Kodur and J.M. Franssen (eds.), DESTech Publications, USA, 959-966, 2010.
- [11] Van Coile R., Annerel E., Caspeele R., and Taerwe L., "Probabilistic analysis of concrete beams during fire," *Proceedings of the International Conference on Applications in Structural Fire Engineering*, F. Wald, K. Horova, J. Jirku (eds.), Praska Technika, Prague, 127-132, 2011
- [12] Shi K., Guo Q., and Jeffers A.E., "Stochastic Analysis of Structures in Fire by Monte Carlo Simulation," *Proceedings of the 2nd International Conference on Applications in Structural Fire Engineering*, F. Wald, K. Horova, J. Jirku (eds.), Praska Technika, Prague, 355-360, 2011.
- [13] Au S.K., Wang Z.H., and Lo S.M., "Compartment fire risk analysis by advanced Monte Carlo simulation," *Engineering Structures*, 29(9), 2381-2390, 2007.
- [14] Der Kiureghian A., and Ke J.-B., "The stochastic finite element method in structural reliability," *Probabilistic Engineering Mechanics*, 3(2), 83-91, 1988.
- [15] Jeffers A.E. and Sotelino E.D., "An efficient fiber element approach for the thermo-structural simulation of non-uniformly heated frames," *Fire Safety Journal*, in press, doi:10.1016/j.firesaf.2012.02.002, 2012.
- [16] Kleiber M., Antunez H., Hien T.D., and Kowalczyk P., *Parameter sensitivity in nonlinear mechanics*, John Wiley and Sons, England, 1997.
- [17] Lind N.C., "Formulation of Probabilistic Design," *Journal of the Engineering Mechanics*, 103(2), 273-284, 1977.
- [18] Rackwitz R. and Fiessler B., "Structural reliability under combined random load sequences," *Computers and Structures*, 9(5), 489-494, 1978.
- [19] Haldar A. and Mahadevan S., *Reliability assessment using stochastic finite element analysis*, John Wiley & Sons, New York, 2000.
- [20] Haukaas, T., "Efficient computation of response sensitivities for inelastic structures," *Journal of Structural Engineering*, 132(2), 260-266, 2006.
- [21] Simo J.C. and Hughes T.J.R., *Computational inelasticity*, Interdisciplinary applied mathematics, v. 7, Springer, New York, 1998.
- [22] Cook R.D., Malkus, D.S., Plesha, M.E., and Witt, R.J. *Concepts and applications of finite element analysis*, 4th ed., Wiley, New York, NY, 2001.
- [23] Rubert A. and Schaumann P., "Structural-steel and plane frame assemblies under fire action," *Fire Safety Journal*, 10(3), 173-184, 1986.
- [24] Buchanan A.H., *Structural design for fire safety*, John Wiley and Sons Ltd, Chichester, England, 2001.

MODELLING OF AN EARTHQUAKE DAMAGED RC FRAME SUBJECTED TO FIRE

Mariyana A. Ab-Kadir*, Jian Zhang*, Jian Jiang*, Asif S. Usmani*, Martin Gillie*,
Umesh K. Sharma** and Pradeep Bhargava**

*School of Engineering, University of Edinburgh, Edinburgh, UK EH9 3JF e-mails: m.ab-kadir@ed.ac.uk, j.zhang@ed.ac.uk, asif.usmani@ed.ac.uk, M.Gillie@ed.ac.uk

** Department of Civil Engineer, Indian Institute of Technology, Roorkee, Roorkee, India 247667 e-mails: umuksfce@iitr.ernet.in, bhdpf@iitr.ernet.in

Keywords: Fire following an earthquake, finite element modelling, reinforced concrete frame

Abstract. Fires are a relatively likely event consequent to earthquakes in urban locations and in general are an integral part of the emergency response strategies focussed on life safety in most developed economies. Similarly building regulations in most countries require engineers to consider the effect of seismic and fire loading on the structures to provide an adequate level of resistance to these hazards, however only on a separate basis. To the authors knowledge there are no current regulations that require buildings to consider these hazards in a sequential manner to quantify the compound loading and design for the required resistance. This paper offers a preliminary report of a modelling exercise undertaken to simulate a novel test on a full-scale RC frame subjected to simulated earthquake and fire loads. The results from the first test indicate that the test frame could withstand a pre-damage corresponding to a seismic performance level and subsequent one-hour fire exposure without collapse. The modelling has been carried out using the ABAQUS and OpenSees finite element software and the results from the models are compared against observed data from the experiment.

INTRODUCTION

Earthquakes are natural hazards in seismic region and can cause devastating damage to urban infrastructure and lifelines. Buildings constructed in seismic regions are vulnerable not only to earthquakes but also to subsequent secondary hazards such as fires and flooding etc. This study is concerned with the effect of fires on structures damaged in an earthquake. Botting reported that a significant conflagration occurred following 15 out of 40 of major earthquakes [1]. For example, a significant proportion of the damage to infrastructure and facilities in the 1994 Northridge and the 1995 Kobe earthquakes could be attributed to fires following the earthquake [2]. The damaged buildings due to earthquakes are more vulnerable to fire effects than undamaged buildings [2,3]. In design, these two events are considered to occur separately and no current regulations explicitly require consideration of this load combination for civil infrastructure. This situation may change with increasing acceptance of performance based options in building standards, however considerable new research is required in this area before these options can be fully exploited in the profession [4].

This paper presents results from 2D and 3D modelling of a full-scale reinforced concrete test frame subjected to a severe fire following cyclic lateral loading applied to simulate realistic seismic damage. The test was carried out as part of the collaborative UK-India research programme and preliminary results and modelling have been reported in [5], this paper builds on that work. The modelling was carried out

using the commercial software package ABAQUS and the open source software framework OpenSees [6]. The results from the modelling have then been compared against selected measured data from the test.

BUILDING CONFIGURATION

A four-storey reinforced concrete building was designed using the Indian Building Code [7]. For the purpose of this study, a single storey frame from this building was constructed for the test which considers the loading from the storeys above. The total height of the constructed frame was 6.0m with the distance between the plinth and top beams being 3.0m. The cross section of the columns was 300mm x 300mm and that of the beams was 230mm x 230mm topped up further by 120mm thick slab. Eight steel bars of 20 mm diameter were used as main reinforcement for columns and six steel bars of 16mm diameter were used for beams (3 each on the top and bottom). The slab was reinforced with 8mm reinforcing steel in the tension zones in both directions on top and bottom. Each column was loaded with an 80kN load coming from upper storey and the slab was loaded with a uniformly distributed load of 2.3kN/m².

STRUCTURAL MODELLING

ABAQUS models

Finite element software ABAQUS [8] was used to analyse both the thermal and mechanical response of the frame. For the 2D model, beams, columns and slab are modelled using beam elements as shown in Figure 1(a). The slab was modelled as part of the overall beam cross section in the 2D beam element model. Linear Timoshenko beam element (B21) that allows transverse shear strain is used in this model. In the 3D model the whole frame is constructed using shell elements as shown in Figure 1(b). Shell elements (S4R) are used. Only a half of the frame is modelled assuming symmetry to reduce computation time. Both the 2D and 3D analyses were fully nonlinear. The reinforcing steel in the 2D model is modelled as truss elements (T2D2) that only allow axial forces. In the 3D model, reinforcing steel is modelled as discrete rebars. The rebars are defined by specifying the size and distribution of the reinforcing steel in the cross section.

The mechanical properties of the reinforcing steel and the concrete at elevated temperatures is assumed to comply with Eurocode 2 [9]. The ambient compressive strength of concrete is 34MPa and tensile ambient strength is 3.4MPa. Mechanical properties of reinforcing steel are shown in Table 1. The applied loading on the frame was constant throughout the analysis. Continuum plasticity based damage model known as “concrete damaged plasticity” in ABAQUS is used to simulate the material nonlinearity of concrete. This model takes into consideration of degradation of strength of the concrete under both compression and tension. It assumes that the two main failure mechanisms are tensile cracking and compressive crushing of the concrete material and that the uniaxial tensile and compressive response of concrete is characterized by damaged plasticity [10]. The analysis is implemented using implicit integration (ABAQUS/Standard) which more computationally efficient and reliable for highly nonlinear problems than explicit dynamics (ABAQUS/Explicit), however it is also more difficult to obtain convergent results using this approach.

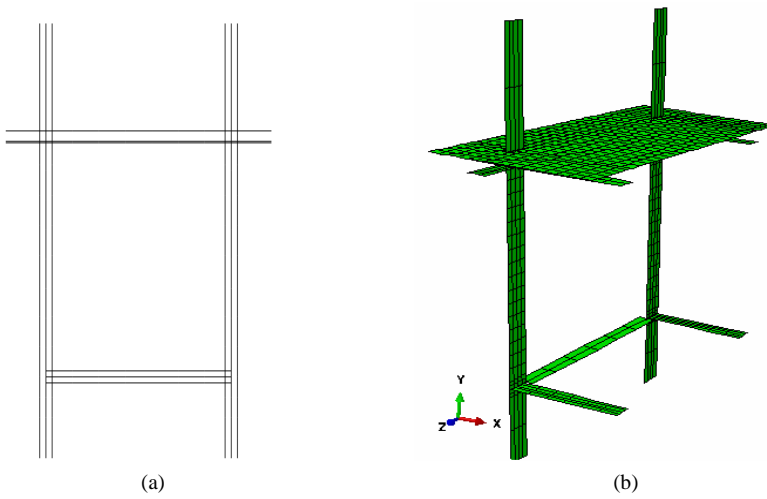


Figure 1: 2D (a) and 3D (b) finite element models using ABAQUS

Table 1. Mechanical properties of reinforcing steel

Diameter of reinforcing steel (mm)	Yield stress (MPa)	Ultimate Stress (MPa)	Yield Strain (mm/mm)	Ultimate Strain (mm/mm)	Elongation (%)	Young's Modulus ($\times 10^5$ MPa)
8	551	643	0.0047	0.207	20.7	2.14
10	447	538	0.0042	0.196	19.6	2.13
16	420	541	0.0023	0.1389	16.9	2.03
20	449	568	0.0021	0.1458	14.6	2.1

OpenSees models

OpenSees is an open source object oriented software framework developed at UC Berkeley and currently supported by PEER and Nees. It has been further developed by a team at the University of Edinburgh to perform thermo-mechanical analyses. More details can be found in the reference [11].

The numerical model of the original frames is shown in Figure 2. Due to the simplification to the 2D frame, the slab and roof beams are considered as one structural member (see Section 1-1 in Figure 2). Similarly, two lower beams are regarded as one beam (see Section 2-2 in Figure 2), and the cross section of “the double column” is Section 3-3. Non-linear beam-column elements are used in the modelling. To get sufficient precision in the calculation and to obtain values of displacement, deflection, stress and at different sections, each frame member in the model is divided into many elements. This would also help in comparing the deformed shapes of the model to the frame shape in the tests at various loading stages.

FIRE LOADING

The result of mock fire tests done in IIT, Roorkee, India is shown in Figure 3. The height was measured from the plinth beam. Based on the temperature curve in Figure 3 (obtained from mock fire test carried out in a compartment without the concrete frame), a heat transfer analysis was done using ABAQUS in order to capture the distribution of the temperature in the element cross-section. The

temperature distributions obtained were used in the thermo-mechanical analysis for the 2D and 3D models using ABAQUS and OpenSees.

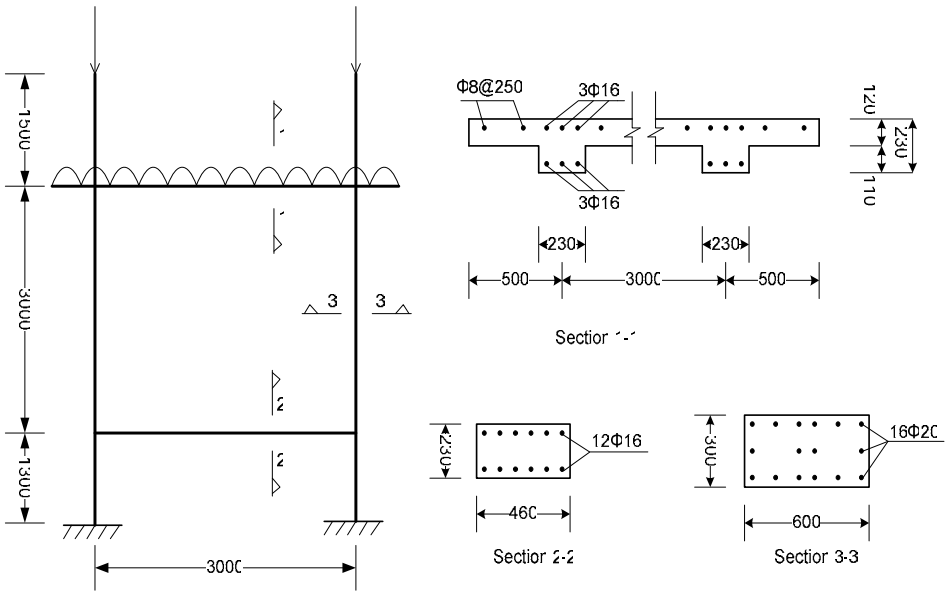


Figure 2. 2D frame model and member sections

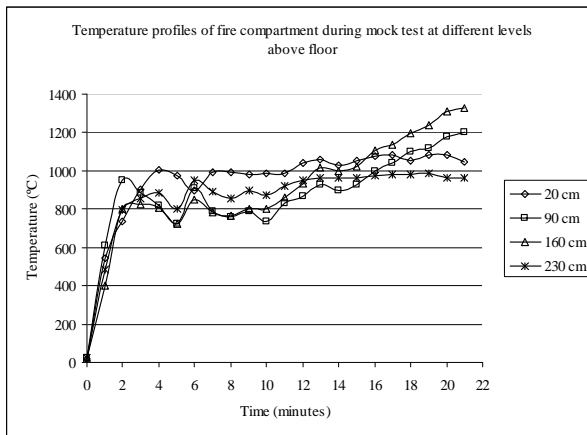


Figure 3. Temperatures curves from the mock test

RESULTS AND COMPARISON WITH TESTED DATA

Base Shear versus roof displacement curve (capacity curve)

The capacity curve is plotted to represent the first mode response of the building based on the structural response to a seismic input predominantly in its fundamental mode of vibration. Incremental

lateral loading in displacement control mode is applied until nonlinear static capacity curve is reached. Target displacement at which seismic performance evaluation of the structure is to be performed can be obtained from the capacity curve. The peak loads against corresponding displacement from hysteretic curve of the test and 2D numerical modelling using ABAQUS and OpenSees are plotted in Figure 4. Target displacement of 90mm corresponding to 2% drift ratio is chosen for further analysis.

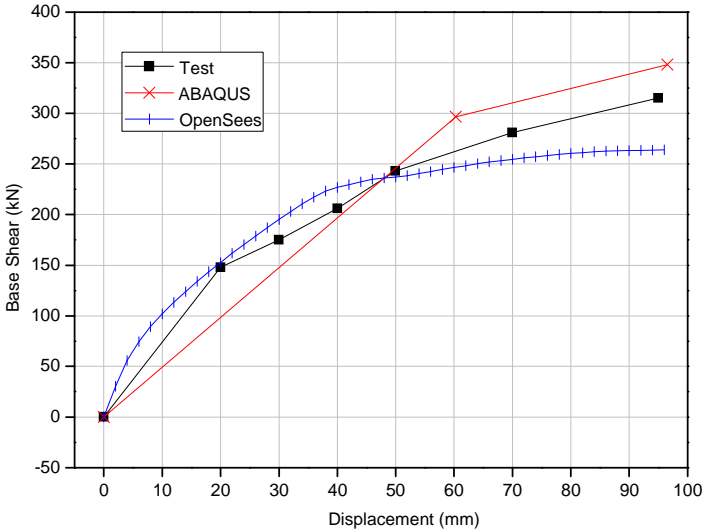


Figure 4. Base shear-roof plotted against roof displacement

Cyclic Analysis

Cyclic lateral loading was applied in the test to simulate the earthquake damage to the frame. Based on the target displacement obtained from the capacity curve, the frame is loaded with horizontal cyclic displacements at the slab level in negative and positive directions. The displacement history applied is shown in Figure 5.

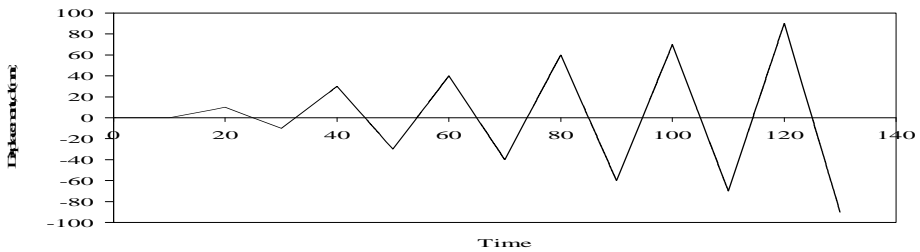


Figure 5. Displacements history for cyclic loading analysis

Figure 7 shows the hysteresis curve obtained from tested frame after seven cycles of loading. The cyclic loading in the test were applied in a quasi-static manner in load controlled mode. The peak load was about 316 kN and 267kN corresponding to a 95mm displacement in one and 85mm displacement in the other direction respectively. The residual displacement of the frame at end of the cyclic loading phase was approximately 19mm (towards the left). Figure 7 shows hysteresis curves from the 2D and 3D OpenSees models. The peak load from 2D model is 250kN corresponding to a displacement of 90mm and

the peak load from the 3D model is 350kN corresponding to a displacement of 90mm. Permanent residual displacements of approximately 15mm are predicted by both OpenSees models.

Figure 8 (a) shows the hysteresis curve obtained from ABAQUS for 2D model. The peak load is approximately 350kN and the permanent residual displacement is 44mm. The hysteresis curve of 3D shell element model is shown in Figure 8 (b). The peak load from the analysis is 230kN is lower than obtained in 2D beam element model and the permanent residual displacement is 38mm. Pinching behaviour due to bonding effects is not considered in both 2D and 3D ABAQUS model.

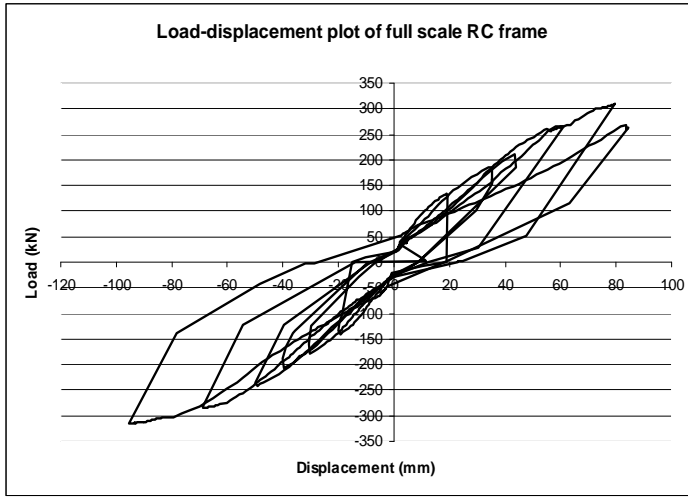
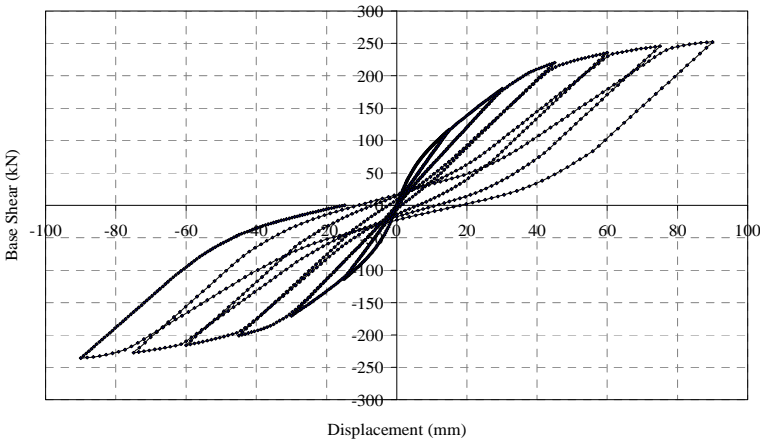


Figure 6. Hysteresis curve tested frame



(a)

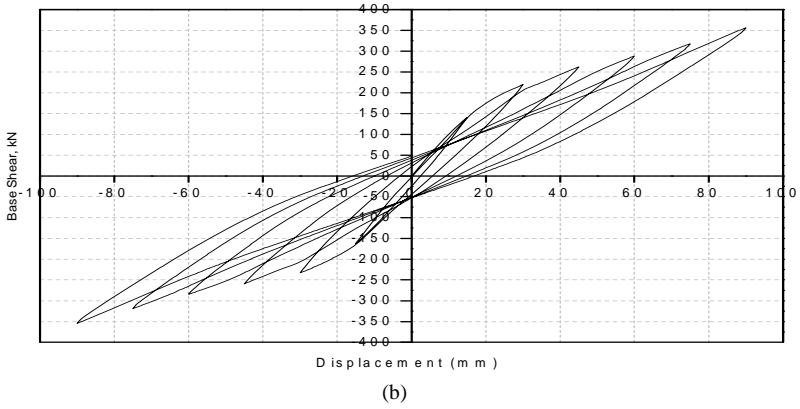


Figure 7. Hysteresis curve from OpenSees Model (a) 2D model (b) 3D model

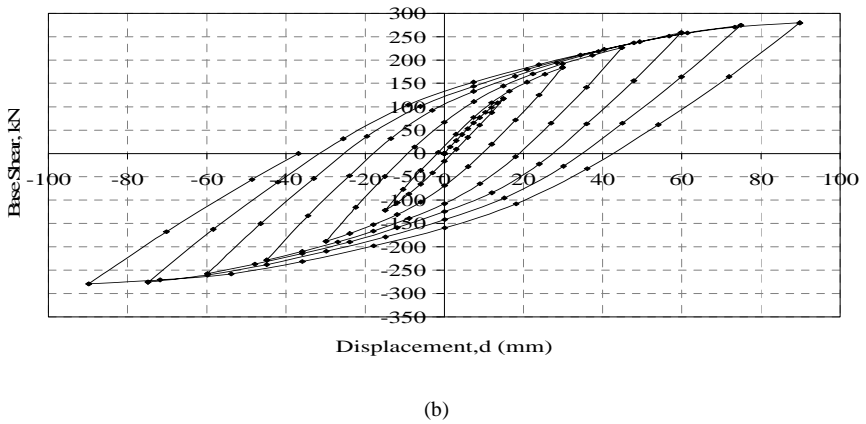
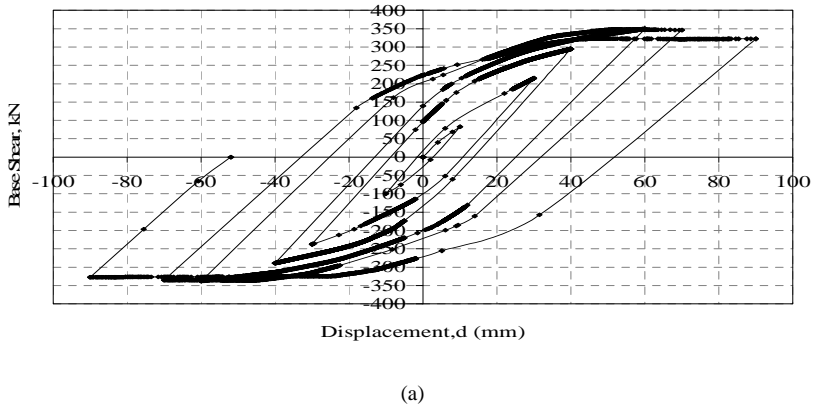


Figure 8. Hysteresis curve of ABAQUS analysis(a) 2D beam element model (b) 3D shell element model

Result of thermo-mechanical analysis

After simulating damage from cyclic loading the frame was subjected to a 1 hour compartment fire with a fixed ventilation opening [5]. A maximum displacement of 46mm at the middle of slab was recorded. The 3D OpenSees model showed maximum slab vertical displacement of 23mm as shows in Figure 9. The horizontal displacement of the columns as a result of the fire (starting from the point of permanent residual displacement) predicted by the 2D and 3D OpenSees models are shown in Figure 10. There is a mismatch in these results as the 2D model suggests a small recovery in the residual displacement but this is absent in the 3D model, which corresponds better with the test where no such recovery was recorded.

Figures 11 and 12 show the horizontal displacement of the column along the height of the columns from 2D and 3D models using ABAQUS. The height is measured from the plinth beam. The both columns appear to stiffen under the heating and the residual displacement seems to recover slightly.

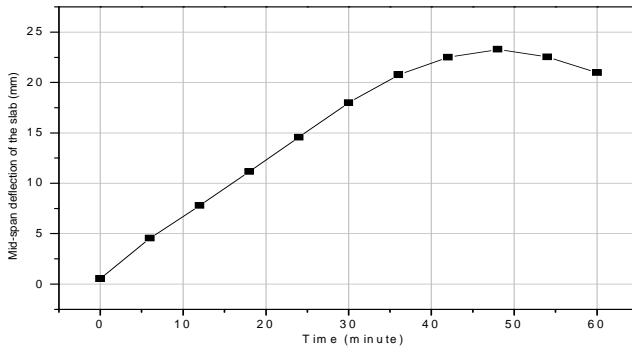
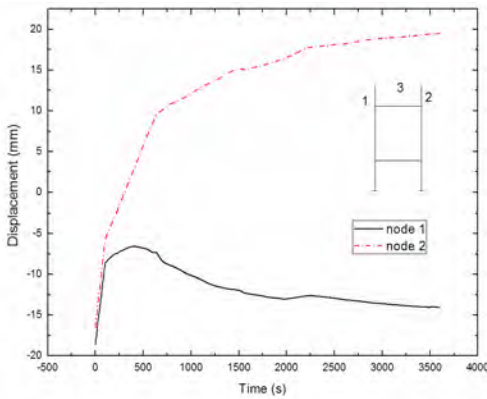
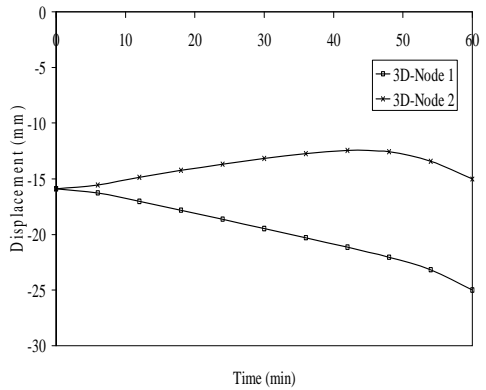


Figure 9. Vertical displacement of the slab from 3D OpenSees model



(a) 2D model



(b) 3D model

Figure 10. Horizontal displacement of columns of model by OpenSees

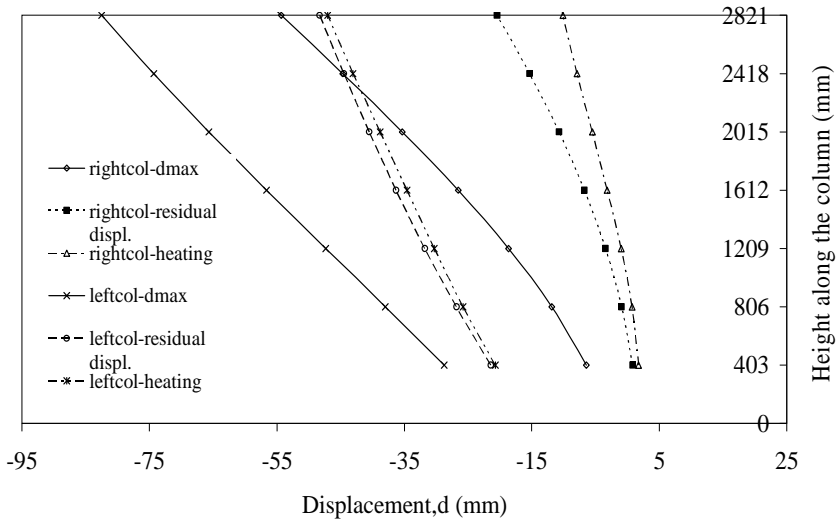


Figure 11. Horizontal displacement of the column along the height (ABAQUS 2D model)

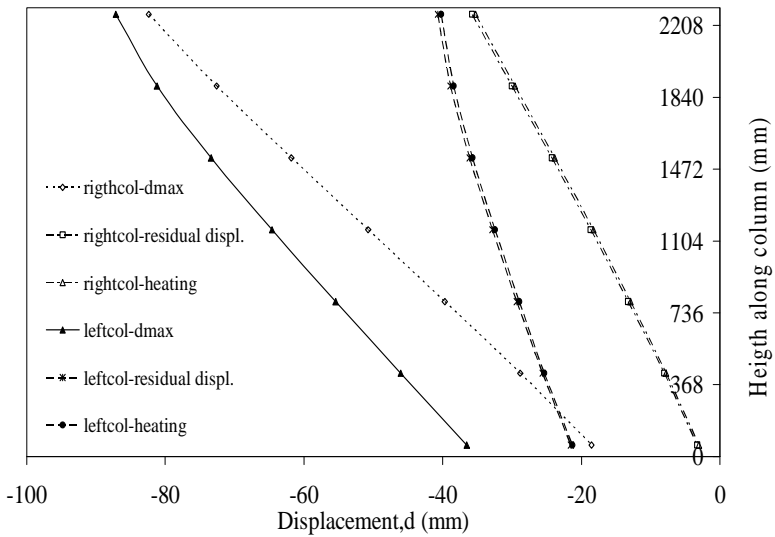


Figure 12. Horizontal displacement of the column along the height (ABAQUS 3D model)

DISCUSSION AND CONCLUSION

2D and 3D analyses of a damaged reinforced frame subjected to fire carried out using ABAQUS and OpenSees has been presented and compared with selected test results. Temperature distributions obtained from a heat transfer analysis (based on a mock compartment fire) are used as an input (applied at integration points of the elements).

The tested frame was reported to withstand the mechanical damage and subsequent fire without collapse. The observed capacity curve using ABAQUS and OpenSees predicted the test reasonably in terms of peak load and the target displacement, however there were some large differences between models. A permanent residual displacement in the tested frame of approximately 20mm after the cyclic loading phase seems to agree well with the OpenSees predictions, suggesting that the simulated damage was modelled reasonably well. The residual displacements from ABAQUS models showed much larger values than the test results. The phenomenon of ‘pinching’ during cyclic loading was clearly observed in the test results. The OpenSees model using a “pinching material” and could capture this effect in the analysis, it was not possible to capture it in the ABAQUS model. Considerable differences were observed between individual models and the test and work is going on to understand the reasons for these differences which should help understand the behaviour of earthquake damaged RC frames subjected to a subsequent fire.

ACKNOWLEDGEMENTS

This studies were carried out as part of a research project involving the University of Edinburgh and Indian Institute of Technology (IIT) Roorkee, India with the financial support of the UK-India Education and Research Initiative (UKIERI).

REFERENCES

- [1] Botting, R. The Impact of Post-Earthquake Fire on the Built Urban Environment. Fire Engineering Report 98/1. University of Canterbury, Christchurch, New Zealand, (1998).
- [2] Scawthorn, C., Eidinger J.M. and Schiff, A.J., editors, Fire Following Earthquake, ASCE Publications (2005)
- [3] Botting, R. and Buchanan, A. H. Building Design for Fire After Earthquake. Proc 12th World Conference on Earthquake Engineering (Auckland) Jan 13 to Feb 4. paper 1569, (2000).
- [4] Usmani, A.S., Research priorities for maintaining structural fire resistance after seismic damage, The 14th World Conference on Earthquake Engineering, Beijing, China, October 12–17, (2008).
- [5] Sharma, U.K. *et. al.*, Full scale testing of a damaged RC frame in fire, Structures and Buildings, Proceedings of the ICE, in press, 2012.
- [6] Mazzoni, S., F. McKenna, and G.L. Fenves, OpenSees command language manual. Pacific Earthquake Engineering Research (PEER) Center, 2007.
- [7] Bhargava, P., *et. al.*, Fire Testing of an Earthquake Damaged RC Frame, Sixth International Conference on Structures in Fire, Michigan, June 2010
- [8] ABAQUS, ABAQUS 6.8. 2008, Dassault Systemes Simulia Corp: Providence
- [9] European Committee for Standardisation, Eurocode 2: Design of Concrete Structures- Part 1-2: General Rules - Structural Fire Design. 2004, BS EN 1992-1-2:2004.
- [10] Lee, J., and G. L. Fenves, Plastic-Damage Model for Cyclic Loading of Concrete Structures, Journal of Engineering Mechanics, vol. 124, no.8, pp. 892-900, (1998).
- [11] Usmani, A., Zhang, J., Jiang, J. Jiang, J. and Ian May, I., Using Opensees for Structures in Fire, J. of Structural Fire Engineering, vol. 3, no. 1, pp. 57-70, (2012).

ANALYSIS OF UNPROTECTED CONCRETE FILLED STEEL TUBE COLUMNS IN FIRE

In-Rak Choi*, Kyung-Soo Chung* and Do-Hwan Kim*

* Research Institute of Industrial Science & Technology
e-mails: irchoi@rist.re.kr, kschung@rist.re.kr, dohwan.kim@rist.re.kr

Keywords: Finite element analysis, Fire, Composite columns, Structural behavior.

Abstract. *This paper presents analytical approach for predicting the structural behavior of concrete filled steel tube (CFT) columns in fire. Material properties at elevated temperatures were evaluated and numerical models were developed for heat transfer and stress analysis. The proposed analysis model was verified against experimental data. The influence of the material properties on the structural behavior of CFT columns in fire were studied and discussed.*

1 INTRODUCTION

Concrete-filled steel tube (CFT) columns consisted of a steel tube and concrete infill combine the benefits of the two materials. That is the steel tube works as formwork and provides confining pressure to the concrete infill, and the concrete infill delays local buckling of the steel tube. Also in fire condition, due to the presence of concrete infill, CFT columns show more efficient fire resistance compared to the steel columns even though without external fire protection. However, the structural behaviour of CFT columns in fire condition is more complex than at ambient temperature. Material properties such as stiffness, strength and expansion of the steel and concrete are changed depending on the temperature with different rate.

Many tests were performed to investigate the structural behavior of CFT columns exposed to fire [e.g. 1-3]. However, because of the fire test was conducted in furnace, it had difficulties in monitoring and measuring of the specimen during the test. Therefore, in order to represent or further analyze the test results, numerical models that can simulate the material properties and stress distribution between the steel and concrete are more importantly needed in fire test.

In this study, material models established in design codes [4, 5] and manual [6] were compared to the test results conducted in Korea [7-9]. Based on the Eurocode model, three-dimensional finite-element model for CFT column was developed and heat transfer and nonlinear thermal stress analysis were performed using ABAQUS [10]. The proposed analysis model was verified against experimental data performed in Korea. The influence of the material properties on the structural behavior of CFT columns were studied and discussed.

2 MATERIAL MODEL

Thermal, mechanical and deformation properties of steel and concrete vary with temperature and these properties also influenced by the phase changes occurred in high temperatures. In addition, concrete is a composite material produced by aggregate, cement, and water. Also, the type of aggregate that occupies 60-80% of its volume can have an important role on the thermal properties of concrete. Therefore, in order to accurately predict fire behavior of CFT columns, the material thermal properties should be evaluated in advance.

In Korea, extensive research project has been performed to establish material model database at elevated temperatures [7-9]. These test data was compiled and compared with the material thermal property models provided by the design codes such as Eurocode [4], AISC [5] and ASCE manual [6].

2.1 Structural steel

The thermal properties that required to calculate the temperature of steel tube are thermal conductivity and specific heat. Figure 1 shows test data (Lee et al. [7]) on thermal conductivity and specific heat of steel as a function of temperature, respectively. Relationships between design codes (Eurocode 2 [4] and ASCE manual [6]) and test data also compared in Figure 1. In thermal conductivity, measured data of SM520 (Korean standard, nominal yield strength $F_y = 365\text{MPa}$) and SM570 ($F_y = 460\text{MPa}$) were less than design models below 600°C . However, in thermal conductivity, there is little variation between measure data and design models. The increase in specific heat around 735°C is due to the phase change that occurs in steel in which the atoms transition from a face centered cubic to a body centered cubic structure.

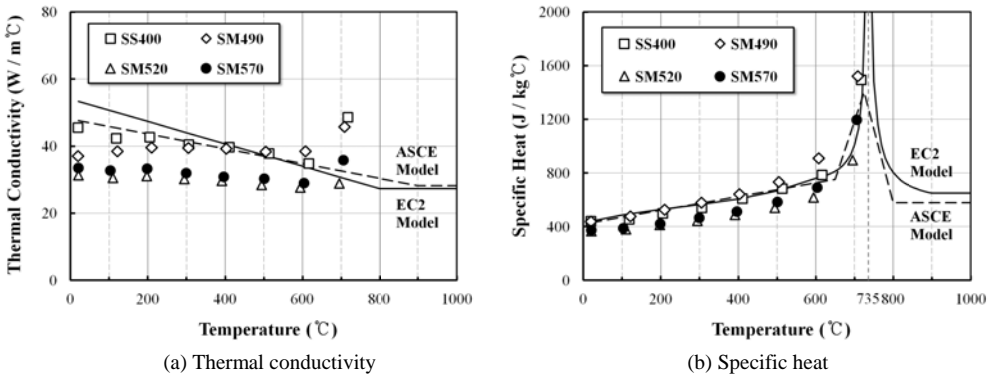


Figure 1. Comparison of test data and design models: thermal properties of steel

In order to obtain strength properties of steel at elevated temperatures, test is generally conducted in two ways: steady-state and transient-state tests. In steady-state tests, the test specimen is heated to a specific temperature and then a tensile test is carried out. Stress-strain values are recorded under constant temperature. On the contrary, in transient-state tests, the test specimen is subjected to a constant load and then exposed to uniformly increasing temperature. Generally, the transient-state tests are more close to the fire condition, however, the steady-state tests are easier to obtain stress-strain values at elevated temperatures and therefore many tests are conducted using this method including the test conducted by Lee et al. [7].

Figures 2(a-c) show the yield strength and stiffness reduction factors for steel as a function of temperature, respectively. In Eurocode and AISC models, the yield strength is defined as a strength at 2% strain and the curve is transited from the elastic to the plastic range after the proportion limit. However, in ASCE model, yield point is defined as the strength at 0.2% offset strain. As shown in Figures 2(a and b), the yield strength is decreased as temperature increase and the variation of the test data does not significant. Regardless of the definition of the yield strength, test data is well agreed with code provided models. Also, the same result is obtained in the elastic modulus of steel at elevated temperatures.

Figure 2(d) shows the thermal strain of steel at elevated temperatures. According to the test data and design model, the thermal strain is increased with temperature up to nearly 750°C and then it becomes nearly constant up to 860°C , after this point it starts to increase again. This is because, as mentioned before, a phase change takes place around 735°C .

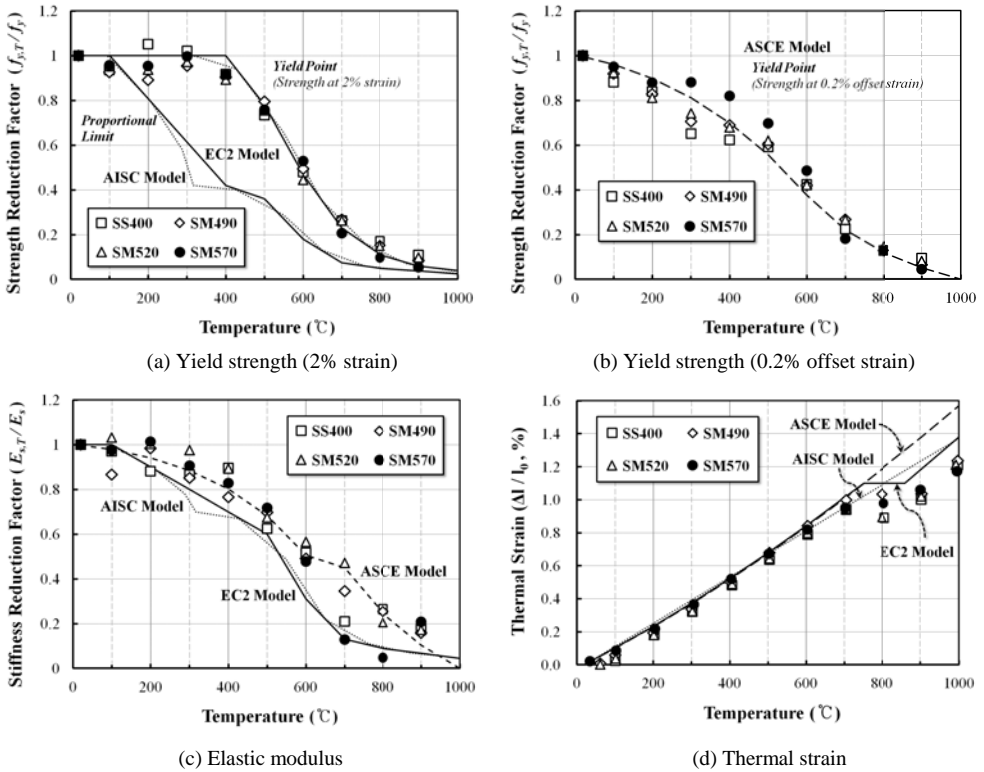
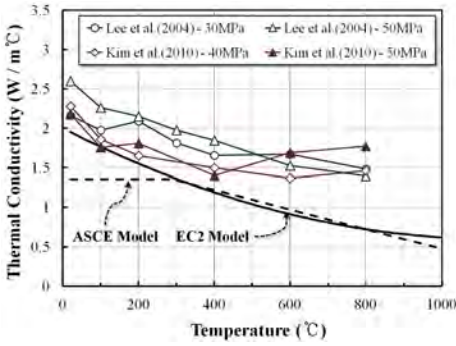


Figure 2. Comparison of test data and design models: mechanical properties of steel

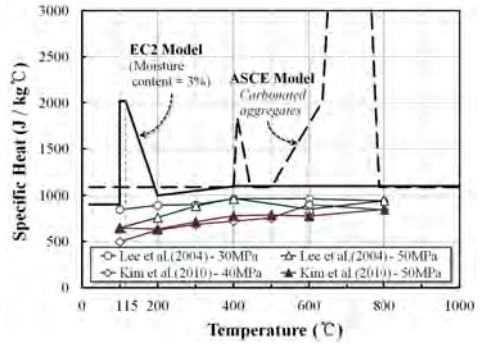
2.2 Normal strength concrete

The thermal properties and strength of concrete at elevated temperatures were also presented and compared with existing design models. These test data included thermal conductivity, specific heat, compressive strength, and thermal strain of plain concrete made of siliceous aggregate produced in Korea (Lee et al. [7], Kim et al. [8] and Kim et al. [9]). In this study, the normal-strength concrete, characteristic compressive cylinder strength (f_{ck}) lower than 50MPa, was compiled and compared with appropriate design model.

Figure 3(a) shows the thermal conductivity of concrete as a function of temperature. Measured thermal conductivity of siliceous aggregate concrete decreased with an increase in temperature. However, test data is higher than design models. The specific heat of siliceous aggregate concrete at elevated temperatures is shown in Figure 3(b). Because of the temperature interval is more than 100°C, a peak of specific heat does not presented in this figure and test data is less than design models. In the Eurocode model, the increase of specific heat from 100°C to 200°C is to consider the evaporation of free water from the cement paste. In the ASCE model, the increase of specific heat above 500°C is likely caused by the dissociation of the dolomite in the carbonate concrete (Kodur and Sultan [11]).



(a) Thermal conductivity



(b) Specific heat

Figure 3. Comparison of test data and design models: thermal properties of concrete

Figures 4(a-c) show compressive strength of silicate aggregate concrete at elevated temperatures. Generally, three different test methods: (1) stressed, (2) unstressed, and (3) unstressed residual test method were used to evaluate mechanical properties of concrete at high temperatures. (1) In the stressed test, specimen was preloaded with 20 to 40 percent of its room-temperature compressive strength ($f'_{c,20^\circ C}$) and loaded to failure when the steady-state temperature is reached at the target temperature. (2) In the unstressed test, the specimen was heated up to the target temperature without preload and loaded to failure. (3) In the unstressed residual test, specimen was loaded to failure at room temperature after exposed to target temperature. Table 1 presents summary of test programs compiled in this paper.

Table 1. Summary of test method and test specimens

Researcher	Test method (preload, %)	Specimen (mm)	Compressive strength (MPa)		Water-cement ratio (%)	Heating rate (°C/min)
			f_{ck}	$f'_{c,20^\circ C}$		
Lee et al. (2004)	Stressed(30)	Φ100 X 200	30	32	52	ISO curve
	Unstressed		50	50	32	
	Unstressed residual					
Kim et al. (2010)	Unstressed	Φ100 X 200	40	45	35	ISO curve
	Unstressed residual		50	51	30	
Kim et al. (2011)	Stressed(20, 40)	Φ100 X 200	27	30	55	1
	Unstressed		40	48	42	

Figures 4(a-c) show compressive strength reduction factors of the compiled tests data in Table 1 and comparison with the design models. In general, the compressive strength of concrete was decreased as the temperature increased. At 100°C, compressive strength was decreased 27% in stressed test and 30% in unstressed test. However, in unstressed residual test, compressive strength loss was 6% at 100°C. That is, strength loss at 100°C can be recovered after cooling. Also, as the temperature increased to 200°C and 300°C, compressive strength was recovered and some data exceeded its room-temperature strength due to hydration of the calcium silicate hydrate (CSH) caused by evaporation of free water and low heating rate. Above 300°C, compressive strength was decreased again and it was not recovered.

Figure 4(d) shows measured thermal strain data compared with design models. As shown in this figure, variation of the thermal strain at elevated temperatures was similar to that specified in Eurocode 2. However, the thermal strain was about 30% less than that of Eurocode 2 model for siliceous aggregate.

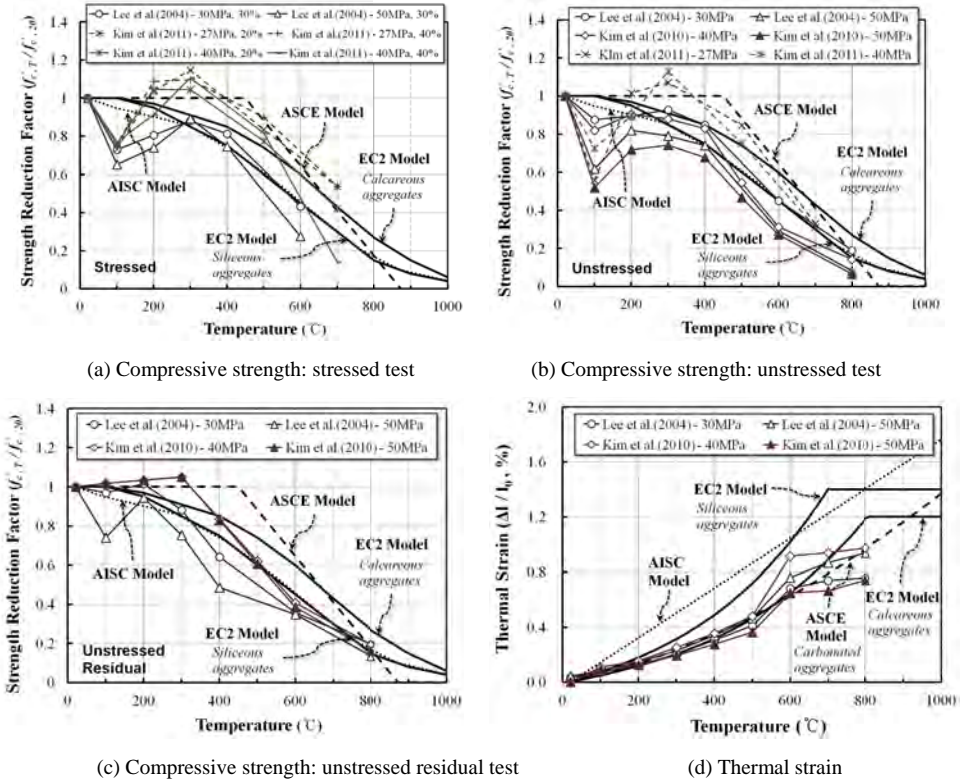


Figure 4. Comparison of test data and design models: Mechanical properties of concrete

3 FINITE ELEMENT ANALYSIS

In order to investigate the effect of thermal and mechanical properties on the fire resistance of CFT column, nonlinear finite-element analysis was performed using ABAQUS [10]. Three-dimensional finite-element model for CFT column was developed and heat transfer analysis and nonlinear thermal stress analysis were conducted. The analysis models were verified against experiment on CFT columns at elevated temperatures (Chung et al. [12]).

3.1 Heat transfer analysis

For heat transfer analysis, four-node shell heat transfer (DS4) elements were used for steel tube and eight-node continuum heat transfer (DC3D8) elements were used for concrete infill [See Figure 5]. The thermal boundary conditions were defined according to the recommendations in Eurocode 1 [13]. That is, the coefficient of heat transfer by convection of $25 \text{ W/m}^2\text{C}$ were used and for the radiant boundary condition, the resultant emissivity was taken as 0.8. The column is assumed to be exposed to fire all surfaces and when it is exposed to fire, an air gap may develop at the interface between the steel tube and

the concrete infill. Therefore, the thermal conductivity between the steel tube and concrete infill was taken as $100 \text{ W/m}^2\text{°C}$ (Ding and Wang [14]).

The thermal material properties required to heat transfer analysis are thermal conductivity, specific heat, and density. These thermal material properties of steel tube and concrete infill are adopted basically from the Eurocode 4. The moisture content of the CFT column is assumed to be 10% according to Eurocode 4.

3.2 Stress analysis

By assuming that the stress analysis was uncoupled from the heat transfer analysis, nonlinear stress analysis was performed sequentially using ABAQUS. The temperatures calculated in the heat transfer analysis were read as an input of stress analysis. In order to read the temperature data of each node, the mesh on the cross-section of the column in the stress analysis model was kept the same as the mesh in the heat transfer analysis model.

Three-dimensional models were used to predict the structural behavior of CFT column at elevated temperatures. The steel tube and concrete infill were modelled using four-node shell (S4R) elements and eight-node continuum (C3D8R) elements, respectively. The concrete damaged plasticity model implemented in ABAQUS was used to define a yield function of concrete infill. To simulate the interface action between the steel tube and concrete infill, general contact model in ABAQUS was used. In the general contact model, the contact pressure, acting on the respective surfaces, was calculated by the hard contact model in ABAQUS. Also, the frictional stress occurred in the direction tangential to the contact surface was expressed by the Column friction model and the friction coefficient taken as 0.2 (Ding and Wang [14]).

The temperature dependent mechanical properties recommended in Eurocode 4 were used in the stress analysis. In the Eurocode 4 model, creep behavior of steel and concrete are implicitly considered in their stress-strain relationships at elevated temperatures (Kodur et al. [15] and Gernay and Franssen [16]).

The initial imperfection was included to predict overall buckling of the column. The first buckling mode shape was obtained by conducting eigenvalue analysis of the finite-element model subjected to axial loading. According to Hong and Varma [17], the initial imperfection value of $L/6500$ was used (L = length of column).

3.3 Verification of analysis models

The effect of different thermal and mechanical material models on fire resistance predictions was investigated through fire resistance analysis on CFT columns tested by Chung et al. [12]. The elevation and dimensions of the test specimens are shown in Table 2 and Figure 5. The length of the column was 3 m including 50 mm thick end plate located at the top and bottom of the column. For specimen C-N, the diameter of the steel tube was 406.4 mm and the thickness was 9 mm. The measured yield strength (f_y) of steel tube was 311 MPa, and the tensile strength (f_u) was 490 MPa on average. For specimen S-N, the dimension of the steel tube was \square -360 \times 360 mm and the thickness was 9 mm. The measured yield strength (f_y) of steel tube was 363 MPa, and the tensile strength (f_u) was 490 MPa on average. The measured value of 28-day cylinder compressive strength of concrete infill was 36 MPa on average. The concrete mix properties used in this test was presented in Table 3.

Table 2. CFT column specimen detail (Chung et al. 2011)

Specimen	Dimension (mm)	Length (mm)	Steel tube			Concrete	Axial load (kN)
			t (mm)	f_y (MPa)	f_u (Mpa)	f_c (MPa)	
C-N	Φ -406.4	3000	9	311	490	36.1	1689
S-N	\square -360 \times 360	3000	9	363	490	36.1	1670

Table 3. Mix properties of concrete

Water-Cement ratio (W/C, %)	Sand-aggregate ratio (S/a, %)	Water (kg/m ³)	Cement (kg/m ³)	Sand (kg/m ³)	Aggregate (kg/m ³)
27	44	147	545	720	900

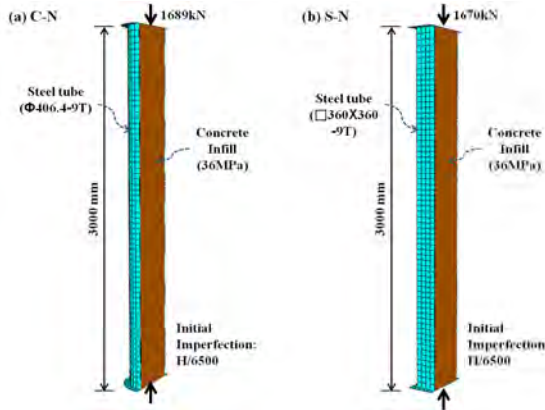


Figure 5. Analysis model of CFT columns

The test was conducted by exposing the CFT columns to fire in a furnace located in Korea. Both columns had pin-ended boundary condition. Constant axial load was applied before the fire test started and maintained until it was stabilized. Applied axial load was 1689 and 1670 kN for specimen C-N and S-N, respectively. The temperature of the furnace was controlled according to ISO-834 [18] standard temperature-time curve defined by

$$T = 345 \log_{10} (8t + 1) + 20 \tag{1}$$

where, T = furnace temperature (°C) and t = fire time (min).

Figure 6 shows heat transfer analysis results and measured temperatures at the steel tube and concrete infills at different points. The analysis model predicted the temperatures of the specimens with a reasonable precision. The predicted temperatures of concrete infill were slight less than measured temperatures. This is partly due to the differences of material thermal properties and moisture contents of the concrete infill. However, the analysis results show that the material thermal properties specified in Eurocode 4 can be used to simulate heat transfer behavior of CFT columns.

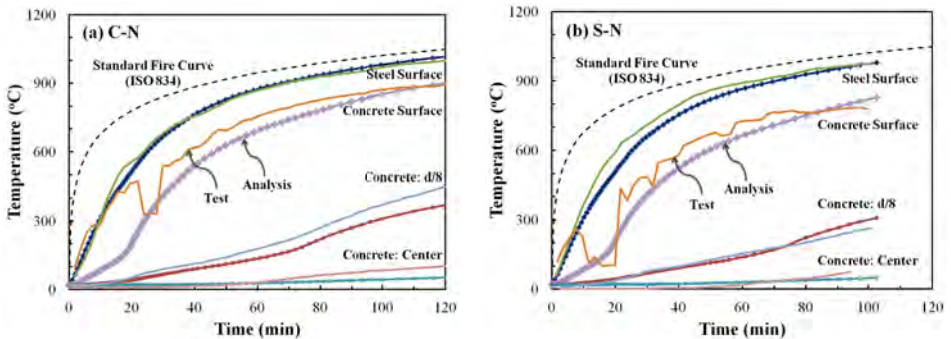


Figure 6. Heat transfer analysis results

Figure 7 compares the numerically predicted axial displacement-time relationship with those measured experimentally. These comparisons indicate that the analysis models predict the high-temperature behavior for the column specimens reasonably but with some discrepancies in failure time. Analysis results show that, as the specimen was directly exposed to fire, the temperature on the steel tube was more rapidly increased (See Figure 6) and started to expand longitudinally. Therefore, a greater portion of axial load was resisted by the steel tube but the yield strength of the steel tube was gradually decreased with the temperature increased. Finally, the steel tube was yielded or buckled, and then the load was transferred to the concrete. After that, the deformation is dominated by the softening behavior of concrete. As the temperature increased in the concrete, the strength of concrete was also decreased and no longer support the axial load applied to the column.

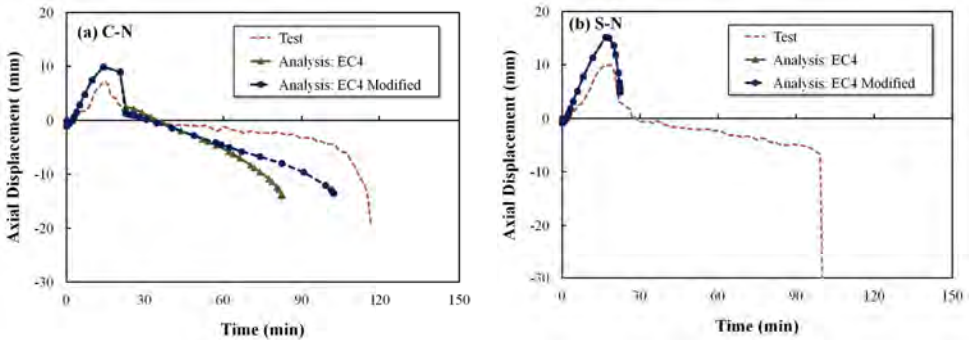


Figure 7. Stress analysis results

The measured thermal expansion and compressive strength of concrete at elevated temperatures were lower than the values specified in Eurocode (See Figure 4). Therefore, modified analysis model was applied during the analysis. That is, the thermal expansion coefficient was decreased by 30% and the compressive strength reduction factor was decreased according to the stressed test result [Figure 4(a)]. The modified thermal expansion coefficient and strength reduction factor are presented in Table 4.

The modified analysis model shows more favourable result compared to the Eurocode 4 model. The more rapid decrease of axial displacement in Eurocode 4 model was related to the differenced in thermal expansion of concrete with variation of temperature. The large thermal expansion in the surface of concrete cause stress concentration where the stiffness was decreased due to the high temperature. In the specimen S-C, analysis model did not converged after steel tube was buckled.

Table 4. Mechanical properties used in modified model

Temperature (°C)	Thermal expansion coefficient ($\times 10^{-6} \text{ } ^\circ\text{C}^{-1}$)	Strength reduction factor
20	6.50	1.00
100	6.50	0.75
200	7.02	0.95
300	7.85	1.00
400	9.01	0.90
500	1.05	0.75
600	1.23	0.55
700	1.44	0.40
800	1.26	0.20
900	1.11	0.10

4 CONCLUSIONS

In order to investigate the structural behavior of CFT columns exposed to fire, material properties at elevated temperatures were evaluated. The thermal properties required to calculate the temperature of CFT column were thermal conductivity and specific heat. Also, the yield strength, stiffness, and thermal expansion of the steel and concrete were requested to simulate strength degradation at the elevated temperature.

Using the compiled test data performed in Korea, these material thermal properties were compared with design code [4, 5] and manual [6]. The thermal and mechanical properties of steel were well agreed with design models except the thermal conductivity. Measured thermal conductivity was slightly less than that of design model below 600 °C. Thermal and mechanical properties of concrete were highly influenced by the type of aggregate. According to the test results using siliceous aggregate used in Korea, thermal conductivity was slightly higher than that of design models and specific heat was slightly less than that of design models. The compressive strength of concrete was suddenly decreased at 100 °C and recovered as the temperature increased to 200 °C and 300 °C. The thermal expansion of concrete was about 30% less than the value specified in Eurocode.

Based on the Eurocode thermal material model, three-dimensional finite element model for CFT column was developed using ABAQUS. Heat transfer and nonlinear thermal stress analysis were conducted and verified against CFT column fire test results. Comparison between the analysis and test results showed that the analysis model predict the temperature of steel tube and concrete with reasonable precision. Also, the analysis model simulate high-temperature behavior for the column specimens reasonably. When the thermal expansion coefficient and strength reduction factor were modified, more favourable results could be obtained.

ACKNOWLEDGEMENTS

This research is supported by a grant from High-Tech Urban Development Program funded by the Ministry of land, transport and maritime affairs through Super-Tall Building R&D Project(VC-10); the authors are grateful to the authorities for their support.

REFERENCES

- [1] Lie, T. T. and Irwin, R. J., "Fire resistance of rectangular steel columns filled with bar-reinforced concrete", *Journal of Structural Engineering*, 121(5), 797-805, 1995.
- [2] Han, L. H., Yang, Y. F and Xu, L., "An experimental study and calculation of the fire resistance of concrete filled SHS and RHS columns", *Journal of Constructional Steel Research*, 59, 427-452, 2002.
- [3] Sakumoto, Y. Okada, T., Yosida, M. and Taska, S., "Fire resistance of concrete filled fire steel tube columns", *Journal of Materials in Civil Engineering*, 6(2), 169-184, 1994.
- [4] European Committee for Standardization., "General rules – Structural fire design, EN-1994-1-2", Eurocode 4, Brussels. 2005.
- [5] American Institution of Steel Construction (AISC)., "Specification for structural steel buildings", ANSI/AISC 360-10, Chicago. 2010.
- [6] American Society of Civil Engineers (ASCE)., "Structural fire protection", ASCE committee on fire protection, Manual No. 78, ASCE, Reston, Va. 1992.
- [7] Lee, S. H. et al., "Development of fire resistance design method in building", Construction & Transportation R&D Final Report, 2004. (in Korean)

- [8] Kim, H. Y., Kim, H. J., Jeon, H. K., and Youm, K. S., “Study on fire performance and heat transfer of HPC column with fiber-coctail in ISO fire under loading condition”, *Journal of the Korea Concrete Institute*, 22(1), 29-39, 2010. (in Korean)
- [9] Kim, K. Y., Lee, T. G., Min, C. S., Lee, K. H., Nam, J. S., and Kim, Y. S., “ Evaluation on mechanical properties of concrete subjected to high temperature and loading condition”, *Journal of Architectural Institute of Korea (Structure & Construction)*, 27(3), 91-98, 2011. (in Korean)
- [10] ABAQUS, *Version 6.10 user’s manual*, Dassault systems simulia corp., Providence, RI, USA, Dassault Systems, 2010.
- [11] Kodur, V. K. R. and Sultan, M. A., “Effect of temperature on thermal properties of high-strength concrete”, *Journal of Materials in Civil Engineering*, 15(2), 101-107, 2003.
- [12] Chung, S. K., Kim, S. H., Lee, S. H., and Choi, S. M., “Fire resistance of concrete filled double skin tubular columns under axial load”, *Journal of Korean Society of Steel Construction*, 23(1), 51-59, 2011. (in Korean)
- [13] European Committee for Standardization., “Actions on structures, EN-1991-1-2”, Eurocode 1, Brussels. 2002.
- [14] Ding, J. and Wang, Y. C., “Realistic modelling of thermal and structural behaviour of unprotected concrete filled tubular columns in fire”, *Journal of Constructional Steel Research*, 64, 1086-1102, 2008.
- [15] Kodur, V., Dwaikat, M., and Fike, R., “High-temperature properties of steel for fire resistance modelling of structures”, *Journal of materials in civil engineering*, 22(5), 423-434, 2010.
- [16] Gernay, T. and Franssen, J. M., “Consideration of transient creep in the Eurocode constitutive model for concrete in the fire situation”, *Structures in Fire - Proceeding of the Sixth International Conference*, Michigan, 2010.
- [17] Hong, S. D. and Varma, A. H., “Analytical modelling of standard fire behavior of loaded CFT columns”, *Journal of Constructional Steel Research*, 65, 54-69, 2009.
- [18] ISO (International Standards Organization), *ISO834: Fire resistance tests, elements of building construction*, Switzerland, 1980.

MODELLING OF PROGRESSIVE FAILURE OF CONNECTIONS AND DUCTILITY DEMAND OF CONNECTIONS IN FIRE

Ruirui Sun*, Ian W. Burgess*, Zhaohui Huang** and Gang Dong*

* University of Sheffield, Department of Civil and Structural Engineering, UK
e-mails: cip07rs@sheffield.ac.uk, ian.burgess@sheffield.ac.uk

** Brunel University, School of Engineering & Design, UK
e-mail: zhaohui.huang@brunel.ac.uk

Keywords: Progressive collapse, Connections, Ductility, Fire.

Abstract. *An effective numerical procedure for progressive collapse has been developed. Combined with the parallel development of a component-based connection finite element model, it has been shown to be an effective tool to track the structural behaviour in fire from the static stable phase, through progressive failure of components in connections and complete detachment of members, to total collapse of the frame. This type of procedure, which is capable of simulating progressive collapse, is necessary for performance-based structural design which includes structural robustness assessment. A study, based on a simplified connection model, on the influence of connection ductility on the structural resistance to progressive collapse, has been carried out. This has provided initial information on how the designed-in ductility of connections, in tension, compression and rotation, affects the robustness of structures in fire.*

1 INTRODUCTION

It is traditionally assumed that beam-to-column connections have sufficient fire resistance, because of their cooler temperatures and slower rate of heating than the members to which they are attached. However, the full-scale fire tests at Cardington in the 1990s showed that the connections are more vulnerable than has conventionally been assumed in fire, because the forces and deformations to which they are subjected during a fire are significantly different from those assumed in design. The internal forces in connections change from moment and shear at ambient temperature to moment, shear and compression due to thermal restraint in the initial stages of a fire, and finally, to shear and tension in the later catenary action stage. These conditions demand that connections possess high ductility to retain their robustness. The variation of internal forces is so extreme in the course of a fire that numerical models are needed to investigate the detailed behaviour of connections, and the component-based method gives a practical way of doing this. A component-based connection model is one in which the connection is represented by an assembly of individual components with known mechanical properties. This methodology has been developed by many researchers [1-3], and has been validated as an acceptable representation of the key behaviour of some connection types in fire [4-8]. Because of the nature of conventional quasi-static analysis, it can only trace the behaviour of a connection up to the point where its first component fails. A connection may either be able to regain its capacity after the initial fracture of a component, or the first failure may trigger a cascade of failures of other components, leading to complete detachment of the members. This possibility should be considered in performance-based design when a structure is being tested for robustness. If members are to avoid the possibility of becoming detached at connections, this numerical modelling must be capable of predicting the sequence of failures of components, rather than simply their first loss of stability. A numerical procedure, in which the whole behaviour, from first instability to total collapse, can be modelled effectively, has been developed in *Vulcan*.

After a member has completely detached at its connections, the load-paths within the remaining frame will be totally changed. The effective lengths of vertical support members may be changed by the loss of restraint from the detached beams. These effects are important for structural robustness assessment. In order to model them in a single analytical run a numerical procedure, illustrated in Fig. 1, in which the whole behaviour from first instability to total collapse can be modelled effectively, has been developed in *Vulcan*. Combined with the parallel development of general component-based connection finite elements, this procedure can effectively trace the behaviour of connections, from the initial fracture of a component, via the failure of successive bolt-rows, to final detachment from the column. Furthermore, the analysis can then continue to trace the movements of detached beams and the load-sharing mechanisms in other members which still maintain their integrity with surrounding structure, until the total collapse happens.

In this paper, this procedure is described in detail, and its capability is illustrated by a robustness analysis of a steel frame. The influence of the ductility of connections on the behaviour of steel beams is studied by using this developed procedure with simplified connection models.

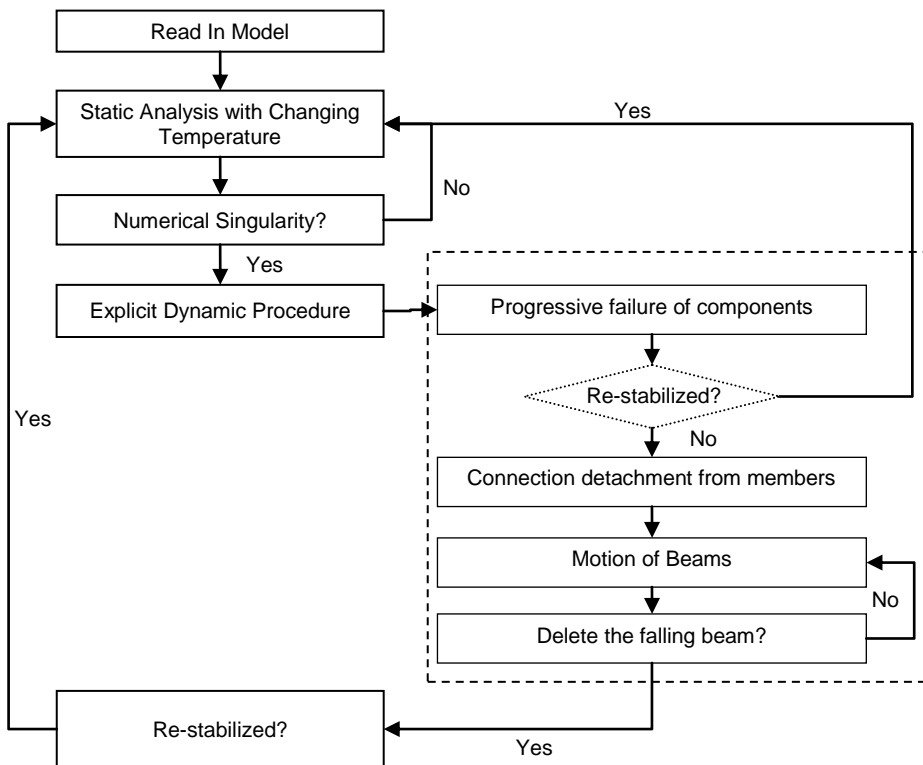


Figure 1. Flowchart of developed procedure modelling failure of connections

2 DEVELOPMENT OF NUMERICAL PROCEDURE

The model combines alternate static and dynamic analyses, attempting to use both to best advantage. Static analysis is used to trace the behaviour of the structure at changing temperature until an instability happens; beyond this point an explicit dynamic procedure is activated to track the motion of the system until stability is regained. This tool has been comprehensively validated against practical cases, and has been used to carry out several scenario-based robustness analyses in fire [9-10].

It is believed that this procedure, combined with the parallel development of general component-based connection elements, is able to trace the connection behaviour, from the initial fracture of a component, via the failure of successive bolt-rows, to final detachment from the column. Based on this expectation, a numerical package has been developed aiming to simulate the structural behaviour from static equilibrium, through progressive failures, to the total collapse of the frame. The developed package is based on the framework of the recently developed static-dynamic version of *Vulcan*. Some new features, shown in the dotted box in Fig.1, have been added to model the progressive failure of connections and the motion of beams after their complete detachment from columns.

2.1 Component-based connection model

The component-based connection model, which has been developed by one of the authors [11], is used to simulate the connections between beams and columns in this study. A joint is divided into a collection of key components, whose behaviour is characterised as that of nonlinear springs. Its essential properties, including temperature variation, physical connection details and unloading characteristics, are taken into account in assigning properties to its components. Therefore, individual components are capable of dealing with loading-unloading-reloading cycles, and changing temperature. Fig.2 shows a typical layout of an endplate connection component assembly. The connection element has two nodes which connect to the beam and column respectively, and internally consists of several tension bolt rows and two compression spring rows. A tension bolt row is characterised by an effective spring composed of a group of springs in series, representing the endplate in bending, a bolt in tension and the column flange in bending. The maximum resistance of a bolt row is defined by the weakest spring in its series. The detail of the component-based connection model can be found in [11].

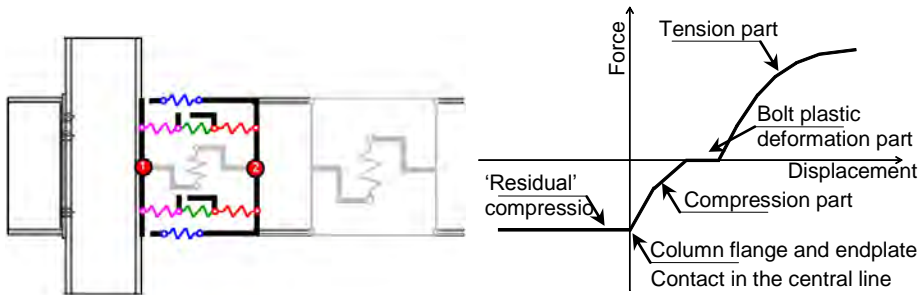


Figure 2. Layout of component-based model and typical bolt-row force-displacement curve

2.2 Dynamic modelling of failure process in connection

The static analysis will terminate due to the numerical singularity induced by the failure of a component in the connection. At this point, the dynamic analysis is initiated. The general equation of motion is as follows:

$$M\ddot{u} + C\dot{u} + F(u) = Q(t) \quad (1)$$

in which M is the mass matrix, C is damping matrix, $F(u)$ is the internal force vector and $Q(t)$ is the external force vector; t , u , \dot{u} and \ddot{u} are time, displacement, velocity and acceleration vectors, respectively.

The progressive failure of a connection is a discontinuous process. In the component-based model adopted, the components vanish after failure, which means that the strength and stiffness of failed components drops to zero instantaneously. This will induce numerical singularity into a static analysis. In this case, the dynamic procedure is initiated to continue the analysis. If the force shed by failed

components can be redistributed among other components in a connection without inducing the failure of the whole connection, the static analysis will be re-activated as the temperature rises.

3 ILLUSTRATION OF DEVELOPED PACKAGE

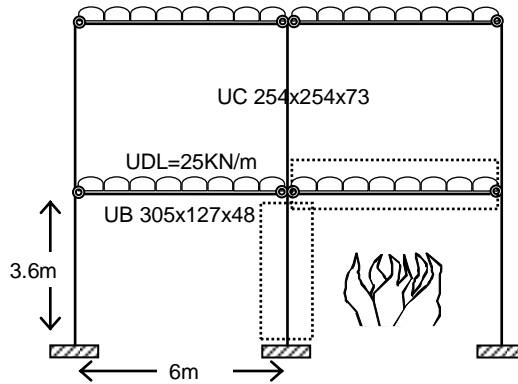


Fig. 3 the studied frame with end-plate connections

In order to demonstrate the capacity of the procedure, a progressive collapse analysis of a plane frame with two storeys and two spans is carried out. The dimensions of the studied frame are shown in Fig. 3. The cross sections of columns and beams in the frame are UC 254x254x73 and UB 305x127x48 respectively. The uniformly distributed load on the beams is 25kN/m. It is assumed that the fire occurs in the right-hand side bay of the lower storey and the members in the dotted box are heated by a standard fire. The component-based connection element described above is used for the beam-column connections in this model. These each consist of five tension bolt rows, each of which has three components including those for the end-plate, bolt and column flange, and two compression bolt rows.

In fact the analysis depicted in Fig. 4 carries on beyond connection fracture, until final structural collapse occurs due to column buckling at a higher temperature. It is clearly illustrated that the developed procedure is efficient not only in tracing the progressive failure of the connections; it also simulates the structural behaviour beyond connection fracture until final structural collapse.

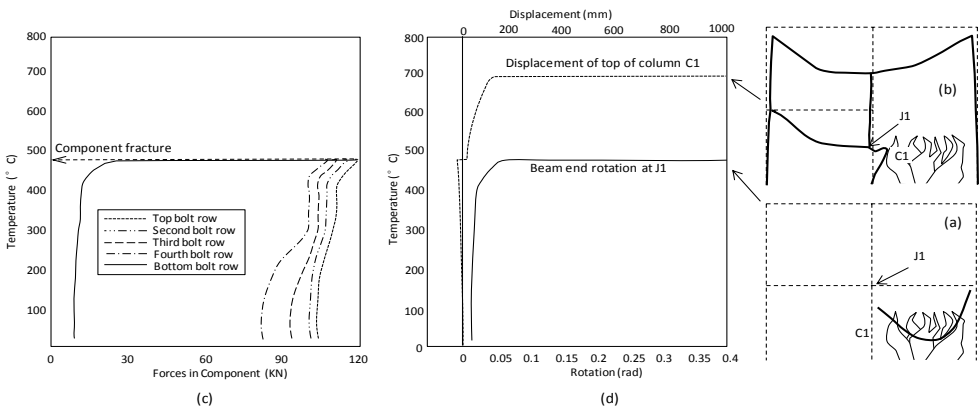


Figure 4: Progressive failure of connection with elevated temperature.

4 DUCTILITY DEMAND OF CONNECTION

It is difficult to evaluate the ductility of a complex connection in accurate way, since it is determined and limited by so many components. In this study a simplified connection model, which consists of four rows of springs is adopted to simulate the beam-column connections; it has top tension and compression springs, and bottom tension and compression springs. Using the developed procedure, a study of the ductility demand of the connections in fire is carried out, based on this simplified connection model. The main aim is to understand in general terms the ways in which designing connections specifically for ductility could influence a structure's resistance to progressive collapse. The simplified model is relatively straightforward as a way of defining the rotational and axial ductility properties of a connection, and it is possible to reflect these ductilities in generic terms rather than by modelling a real connection in detail. The ductilities of each bolt row are defined in two parts; compressive ductility and tensile ductility. In this study, it is assumed that a bolt row fails after its tensile displacement exceeds the tension ductility limit, but the stiffness of a bolt row becomes infinite after its compressive displacement exceeds the compressive ductility limit.

A beam with connections at both ends, heated by fire, as shown as Fig. 5, is chosen as the basic model. Different factors, including the depth/span ratio of the beam and the tensile and compressive ductilities of the connections, have been investigated. Their effects on the structural robustness of the beam are studied.

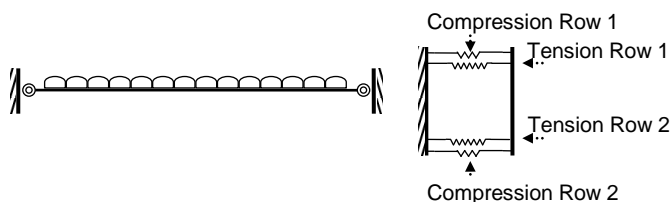


Fig. 5 Tested beam and characteristics of the connection

4.1 Stiffness, Strength and Ductility

Table 1. Summary of results with different stiffness, strength and ductility

Ductility Index= Ultimate Deformation/Depth of Connection					
Case	Stiffness (N/mm)	Strength (N)	Tensile Ductility Index	Compressive Ductility Index	Failure Temperature (°C)
1	50000	100000	0.02	0.02	623
2	50000	100000	0.1	0.1	649
3	50000	200000	0.02	0.02	643
4	50000	200000	0.1	0.1	679
5	100000	100000	0.02	0.02	623
6	100000	100000	0.1	0.1	651

Three key properties (initial stiffness, strength and ductility) are considered in the design of connections at ambient temperature. In robustness assessment, the failure of a connection is more important than its initial moment-rotation behaviour. In these terms, the ductilities of connections prevent them from completely detaching the connected members, by providing enough deformation capacity before components fracture. In order to test which are the key parameters to increase the robustness of connections, several analyses are carried out, all based on the basic model above with different

connections. Table 1 shows the properties defined for the different connections, and the failure temperatures at which the members completely detached at their connections. It is indicated that connections with different stiffnesses, but same strengths and ductilities, generate very similar failure temperatures. The initial stiffness of a connection does not play an important role in enhancing its robustness, which is mostly related to the fracture of its components and breakage of the connection. On the other hand, the strengths and ductilities of components in a connection have much more influence on its failure temperature. Higher strength and higher ductility can retain the robustness of a connection for a longer period in a fire, increasing its failure temperature. This is because the strength and ductility of a component directly reflect the point at which the component steps into plasticity and its deformation capacity. These are the key factors for connections to retain their integrity in fire. Since this study is concerned with the influence of ductility on resistance to progressive collapse in fire, all following case studies focus solely on how the change of ductility in connections, rather than strength, affects the behaviour of the supported beams.

4.2 Depth:Span Ratio

All beams are selected as 514×356×17UB and the connections' depth is selected as 500mm. The depth of connections: span of beams (D:S) ratio is varied by adjusting the beam length. All beams are assumed to be straight and prismatic. Neither local nor lateral-torsional buckling is considered in the FEM formulations.

With temperature rising, the general behaviour of beams can be categorised into three stages. In the first stage thermal expansion dominates, and therefore the compression force increases in restrained beams. In the second stage the degradation of material dominates, so that the displacement at mid-span increases. In the third stage, the displacement becomes large enough for catenary action to be activated. The axial resultant forces in beams become catenary tension.

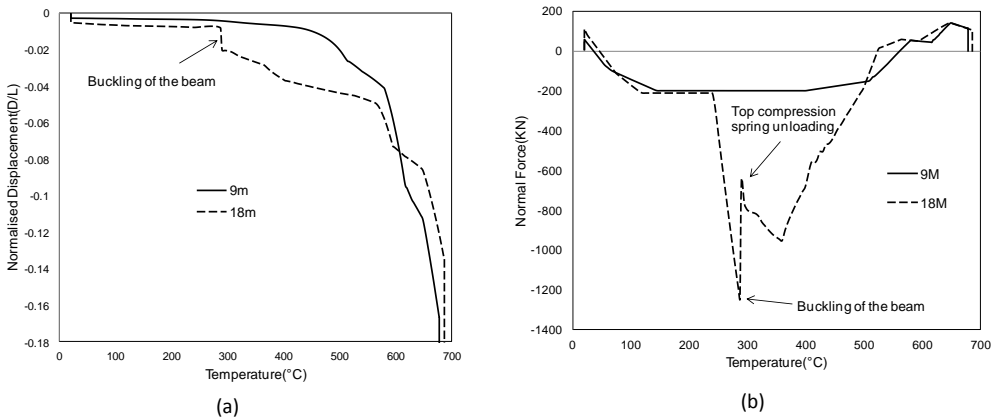


Fig. 6 Mid-span displacement and axial force in connection against temperature: (a) Mid-span displacement of beam; (b) Normal force in connection

Fig. 6 shows the mid-span displacements of beams and the normal forces in connections, plotted against temperature. In the first stage, the compressive forces in connections to longer beams are obviously larger than those in connections to shorter beams. That is because longer beams experience larger thermal expansion, which can push the connection against the column flange. This brings two negative effects: firstly, the larger compression force can push columns, especially those on the edge of the building, outwards and therefore reduce their buckling capacities somewhat; secondly, the larger compression force can induce buckling of the beam, which can be observed in Fig. 6. The model used is two-dimensional, so the beam buckles here with respect to its major axis; in reality, either minor-axis or

lateral-torsional buckling would be induced beforehand. Slender beams require higher compressive ductility in connections to retain their stability.

The high-temperature catenary tension shows that the lengths of beams have little influence on the tensile normal forces in the connections. That is because in the catenary action stage the tensile force dominates is dependent on the transverse load carried and the deflection magnitude.

4.3 Compressive Ductility

Part.4.2 indicates that longer beams require more compressive ductility to retain their stability. Beams with different D:S ratios are now tested with connections of different compressive ductility. The ductilities for different cases are listed in Table. 2. Table 2 also shows the rotation capacities of the connections and the failure temperature of each case.

Table 2. Results for cases with different compressive ductilities

Ductility Index= Ultimate Deformation/Depth of Connection				
Beam Section	Depth:span	Compressive ductility (C_p)	Rotation Capacity (rad)	Failure Temperature ($^{\circ}\text{C}$)
UB 533x210x122	1:18	0.04	.6068	679
		0.06	.6099	679
		0.10	.6099	679
		0.16	.6099	679
UB 533x210x122	1:36	0.04	.4497	687
		0.06	.4584	687
		0.10	.4659	689
		0.16	.4647	689

Fig. 7 shows the displacement at the beam mid-span and the normal force in its connections, against temperature. It is indicated that longer beams require more compressive ductility to prevent their connections pushing against the column face, and thus to prevent them buckling. This phenomenon has been described in Part 4.2; it is shown in Fig. 7 that the maximum compression forces in connections decrease as their compressive ductilities increase. After some point, the compression force is no longer affected by the change of compressive ductility. This is because, with enough compressive ductility, the connections allow the beam ends move towards the column flange without contacting it. It is also indicated that the failure temperature of a beams is not very sensitive to the compressive ductility of its connections, since the final failure of connections is actually tensile.

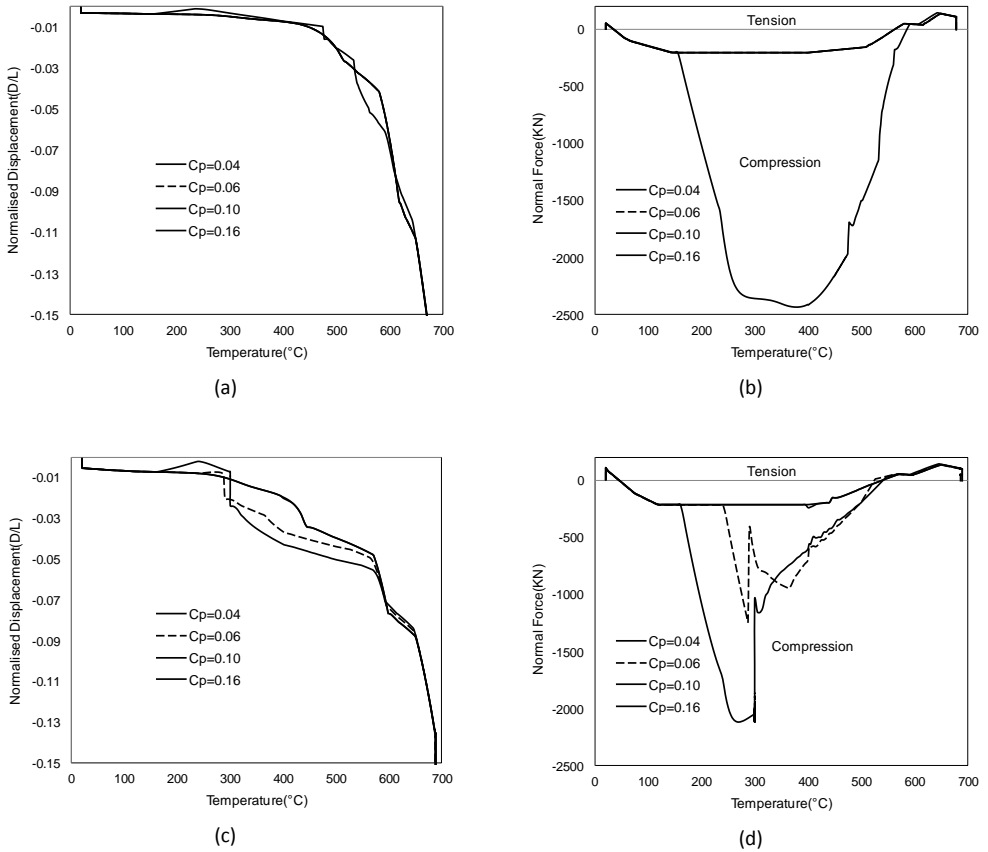


Fig.7 The mid-span displacement of beams and the normal forces in connections: (a),(b) for beams with D:S ratio 18; (c),(d) for beams with D:S ratio 36.

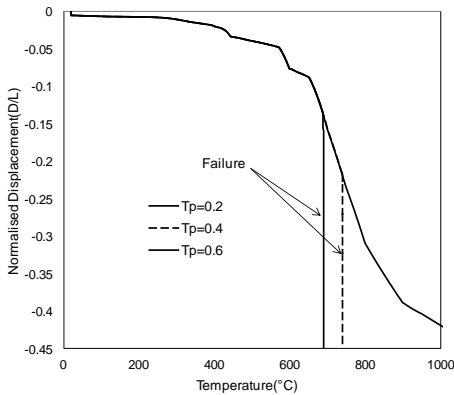
4.3 Tensile Ductility

Tensile ductilities of connections affect the behaviour of beams under fire conditions. Catenary force reduces with the movement at the ends of the beams, some of which can be allowed by the connections. Beams with connections which have different tensile ductilities are now tested. Table 3 shows the failure temperatures and final rotation capacities of connections in different cases. It can be seen that tensile ductility dominates the failure of connections at the beam ends. High tensile ductility can even prevent the connection detaching from the column at high temperature, and also allows the connections to have large rotations.

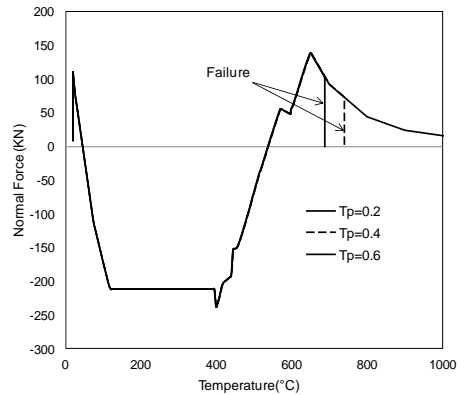
Fig. 8 shows the beam displacement at mid-span and the normal connection force against temperature for the longer beams, from which it can be seen that the catenary force decreases as the deflection and temperature increase. If the tensile ductility of the connections is sufficient, the collapse of beams can be avoided.

Table 3. Results for cases with different tensile ductility

Ductility Index= Ultimate Deformation/Depth of Connection				
Beam Section	Depth:span	Tensile ductility(T_p)	Rotation Capacity (rad)	Failure Temperature ($^{\circ}\text{C}$)
UB 533x210x122	1:18	0.2	.6099	679
		0.4	.9530	735
		0.6	----	----
UB 533x210x122	1:36	0.2	.4659	689
		0.4	.7089	739
		0.6	----	----



(a)



(b)

Fig. 8 Mid-span beam displacement and axial force in connection against temperature: (a) Mid-span displacement of beam; (b) Normal force in connection

5 CONCLUSION

A procedure to simulate the progressive failure of connections and frames has been developed. It has been shown that the behaviour of a structural frame can be modelled throughout the duration of a fire with the combined static/dynamic solution process, so that transient failures of parts of connections do not terminate the analysis, and re-stabilization can be identified if it occurs. This kind of analysis will be necessary in future for true performance-based analytical design of framed buildings against fire.

The ductile design of connections is important for enhancement of structural robustness, since it relates to the deformation capacity of connections. In order to test the influence of ductilities of connections on the structural behaviour of beams under fire conditions, parametric studies using a simplified connection model have indicated that the compressive ductility of connections is helpful by reducing the push-out of perimeter columns, and by reducing the possibility of buckling of beams, especially for those with long spans. Tensile ductility contributes more to avoiding total connection failure and enhancing their rotation capacity, by reducing the catenary force necessary for beams to carry their loads at high temperatures.

REFERENCES

- [1] Zotemeijer, P., A design method for the tension side of statically loaded, bolted beam-to-column connections. *Heron 20, No.1*, Delft University, Delft, Holland, 1974.
- [2] Tschemmernegg, F. & Humer, C. The design of structural steel frames under consideration of the non-linear behaviour of joints. *Journal of Constructional Steel Research*, 11, 73-103, 1988.
- [3] Jaspart J.-P., Braham, M. & Cerfontaine, F. Strength of joints subjected to combined action of bending moments and axial forces. *European Conference on Steel Structures – Eurosteel*, 465-468, 1999.
- [4] Leston-Jones LC. The influence of semi-rigid connections on the performance of steel framed structures in fire. *PhD Thesis*. University of Sheffield; 1997.
- [5] Al-Jabri KS. The behaviour of steel and composite beam-to-column connections in fire. *PhD Thesis*. University of Sheffield; 1999.
- [6] Spyrou S. Development of a component based model of steel beam-to-column joints at elevated temperatures. *PhD Thesis*. University of Sheffield; 2002.
- [7] L. Simões da Silva, A. Santiago, P. Vila Real, A component model for the behaviour of steel joints at elevated temperatures. *Journal of Constructional Steel Research*, 57, 1169 - 1195, 2001.
- [8] Ramli Sulong NH, Elghazouli AY, Izzuddin BA, Analytical modelling of steel connections at elevated temperature. In: Proceedings. *Eurosteel 2005—fourth European conference on steel and composite structures*, Maastricht, The Netherlands, 2005;C:5.1 - 25.
- [9] Sun, R.R., Huang, Z. and Burgess, I.W., Progressive collapse analysis of steel structures under fire conditions, *Engineering Structures*, 34, 400-413, 2012.
- [10] Sun, R.R., Huang, Z. and Burgess, I.W., The Collapse Behaviour of Braced Steel Frames Exposed to Fire, *Journal of Construct Steel Research*, 72, 130–142, 2012.
- [11] Dong, G., Burgess, I.W. and Davison, J.B., Component-Based Element for Endplate Connections in Fire, *Proceeding ASFE 2011*, Prague, 195-200, April 2011.

CHEMOPLASTIC MODELLING FOR CONCRETE AT HIGH TEMPERATURE

Rabah Hammoud*, Rachid Boukhili* and Ammar Yahia**

* École Polytechnique de Montréal, Montréal (Québec), Canada
e-mails: rabah.hammoud@polymtl.ca, rachid.boukhili@polymtl.ca

** Université de Sherbrooke, Sherbrooke (Québec), Canada
e-mail: ammar.yahia@usherbrooke.ca

Keywords: Chemoplastic, Concrete, Constitutive law, Elastoplastic material, High temperature

Abstract. *The paper describes the development of numerical model to simulate the impact of high temperature on conventional concrete under chemoplastic framework. The model is based on new formulation of a constitutive law with new chemoplastic potential. By overlaying the chemoplastic potential on the modified Etse and Willam yielding surface, both defined on the Haigh-Westergaard coordinates, it was found that the two curves do not undergo similar stress state at the same strength parameter. For an adequate evaluation of normal vectors, each surface is forced to go through the current stress state. Keeping the loading surface unchanged, the plastic potential calculation need to be modified. The proposed constitutive model is validated through comparison between predicted and experimental data. The model is accurate to predict different stress state of concrete under different temperatures levels.*

1 INTRODUCTION

Exposure of concrete to elevated temperature affects its physical and mechanical properties and, under certain conditions, the concrete surfaces could spall due to the increase of local steam pressure [1]. It has been established that the mechanical properties of concrete can be adversely affected by elevated temperature exposure [2]. One of the most important reasons of the damage of concrete under elevated temperatures is the thermally induced dimensional changes due to release of moisture and gases. When concrete is exposed to temperatures exceeding 1000°C, heat and mass transfer take indeed place in the material leading to development of high gas pressures in the pores and thermal expansions. Under elevated-temperature exposure, the paste experiences physical and chemical changes that contribute to development of shrinkage, transient creep, and changes in mechanical properties and degradation of concrete. Such degradation may necessitate repair and strengthening to restore the structural integrity and improve safety of damaged structures.

An understanding of the behavior of concrete under elevated-temperatures is essential for reliable formulation of concrete and design evaluations. It is also necessary to assess such degradation in order to develop predictive tools and validate existing design codes. The degradation of concrete can be assessed by non-destructive methods or numerical simulations. The framework of elastoplastic modeling is indeed well adapted to many structural problems, and is mostly used to simulate behavior of concrete under various load types.

The manner how to include the dependence of temperature on the mechanical behavior of materials is to use conventional models of elastoplasticity and to vary certain parameters [3-5]. Until now, the temperature dependence in the existing models has the main effect of changing the strength of materials. However, the magnitude of permanent deformation generated after exposure remains always unchanged.

Generally, for any material that undergoes a decrease in its mechanical resistance, the deformation should increase under circumstances that caused the decrease in strength. The permanent deformation should then vary as a function of temperature.

The analysis of the fire in the Chunnel tunnel, Ulm et al. [6] proposed new formulation by taking into account the impact of temperature. The authors assumed the behavior of plain concrete subjected to high temperatures as a dehydration process (i.e. reverse of the hydration phenomena) by considering a coupled thermo-chemo-mechanical problem [7-8]. On the other hand, the resistance and stiffness development with the degree of hydration is treated as a chemo-plastic hardening. Therefore, dehydration process becomes a chemo-plastic softening. This model was then developed within the framework of the thermodynamic of closed reactive porous media [9]. The formulation included the reversible thermal expansion, irreversible shrinkage, and irreversible changes in the stiffness and strength development processes. The failure criterion of Drucker-Prager function of the degree of dehydration with an isotropic hardening is adopted.

Cervera et al. [10] overused the theory of porous media developed by [8] to propose a coupling thermo-chemo-mechanical model considering the effect of aging on the evolution of various mechanical properties of concrete. Hellmich et al. [11] treated the coupling thermo-chemo-mechanical aspect of shotcrete. The model is extended to a chemo-plastic model and uses two failure surfaces corresponding to the surface of Drucker-Prager and tensional failure. The plastic volumetric expansion serves as hardening variable.

Based on the experimental results [2], dehydration is shown to be directly proportional to the decrease in compressive strength, which is a function of temperature (thermal damage). As pointed by [7-8], it is necessary to link the degree of evolution of the binding phase (cement paste) with an observable characteristic, such as, the uniaxial compressive strength or Young modulus. Subsequently, the mechanical properties and the model coefficients to be identified will depend on the degree of dehydration. The objective of this investigation is to develop a new chemoplastic constitutive model for concrete exposed to high temperature.

2 DEGREE OF DEHYDRATION AS CHEMOELASTIC DEGRADATION INDEX

Using the linear chemo-mechanical coupling theory [6, 8], the degree of dehydration is defined as follow:

$$\xi = \frac{f_c(T)}{f_c} \tag{1}$$

Where- $f_c(T)$ is the uniaxial compressive strength at temperature T , while f_c is the uniaxial compressive strength at ambient temperature. The degree of dehydration is given by thermoactivated kinetics, which is typically a non linear ordinary differential equation (ODE) with time. This degree is significantly decreased after exposure to high temperatures.

3 FORMULATION OF THE CONSTITUTIVE MODEL

3.1 Loading surface

The triaxial constitutive formulation of concrete at high temperature is based on the extended Leon model (ELM). This model is based on a non-associated flow theory of plasticity with isotropic hardening and isotropic softening in the pre- and post-peak regime, respectively. The encompassing loading surface proposed by [12] can be used to describe the triaxial behavior of the material in a wide range of loading histories as follow:

$$F(\sigma_m, \rho, r(\theta)) = \frac{3}{2} \left[\frac{\rho r(\theta)}{f_c} \right]^2 + \frac{m_f}{f_c} \left[\sigma_m + \frac{\rho r(\theta)}{\sqrt{6}} \right] - 1 = 0 \tag{2}$$

where σ_m , ρ and θ denote the coordinates of the Haigh-Westergaard stress space, f_c the uniaxial compressive strength and the function $r = r(\theta)$ describes the variation of the deviatoric strength $\rho = \rho(\theta)$ as a function of the Lode angle in analogy to the elliptic approximation of the five parameter model of [13]. While the parameter m_f is defined as follow: $m_f = f_c / f_u$, f_u is assumed equal to the uniaxial tensile test as supposed by Rankine criterion. The failure surface showing the meridional sections, $\theta = 0$ for tensile meridian and $\theta = 60^\circ$ for compressive meridian, is plotted in Fig.1 (a). As can be observed, the depicted surfaces are smoothes and a C^1 -continuous curvilinear trace. From the triaxial envelope, two-dimensional failure curve can be determined [Fig.1 (b)].

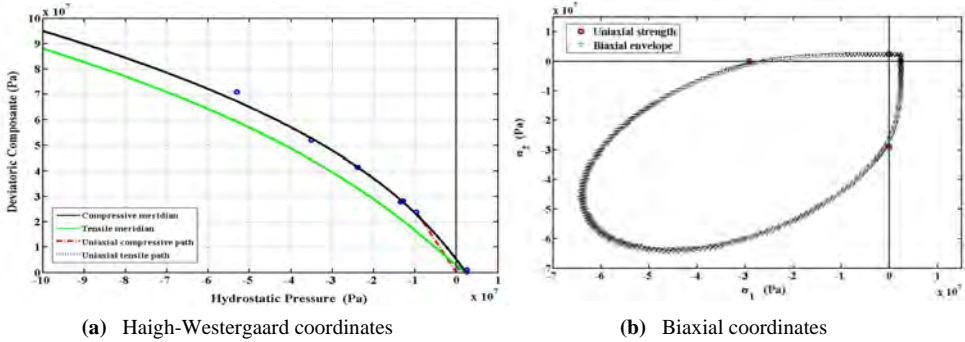


Figure1. Failure envelope at $\xi = 0.64$ (300°C) (Data from [2])

As the concrete strength varies with temperature and chemical degradation occurs, appropriate failure envelope can reproduce these changes by expressing the parameters of the model as a function of degree of dehydration ξ . The failure criterion becomes then:

$$F(\sigma_m, \rho, r(\theta), \xi) = a_f(\xi) \left[\frac{\rho r(\theta)}{f_c(\xi)} \right]^{\alpha_f(\xi)} + \frac{m_f(\xi)}{f_c(\xi)} \left[\sigma_m + \frac{\rho r(\theta)}{b_f(\xi)} \right] - 1 = 0 \quad (3)$$

3.2 Isotropic loading surfaces in pre- and post-peak

Two assumptions were made: (1) The concrete is isotropic and remains isotropic during the entire deformation history; and (2) the elastic-plastic coupling is neglected, which imply that the stiffness properties do not degrade during plastic flow. During the hardening stage, the failure surfaces are generated individually considering specific values of normalized strength parameter, where $0 \leq k \leq 1$. At the same time, the cohesion parameter c related to the softening regime remains constant. At the beginning of loading, the elastic regime is limited by a surface loading with initial value of $k = k_0$. The function of the failure envelope as defined in Eq.3 is then modified as follow:

$$F(\sigma_m, \rho, r, k, c, \xi) = \left\{ (1-k) \left[\frac{\sigma_m}{f_c(\xi)} + \frac{\rho r(\theta)}{b_f(\xi) f_c(\xi)} \right]^2 + a(\xi) \frac{1}{\alpha_f(\xi)} \frac{\rho r(\theta)}{f_c(\xi)} \right\}^{\alpha_f(\xi)} + \frac{k^{\beta_f(\xi)} m_f(\xi)}{f_c(\xi)} \left[\sigma_m + \frac{\rho r(\theta)}{b_f(\xi)} \right] - k^{\beta_f(\xi)} c = 0 \quad (4)$$

The Eq. 4 defines the surface loading and is highly important in the chemoplastic model. Its original form was initially formulated by [12] considering k^2 instead of β_f parameter. The latter parameter was introduced by [14] for carbonaceous materials. The originality of the proposed triaxial failure function consist in its ability to reproduce the hardening of the material in tension and compression through the use of β_f parameter which was added to reproduce experimental $\sigma - \varepsilon$ curves while other models [15-

16] do not consider. This is essential to the hardening process in tension because this failure mode can be observed. The β_f parameter is then introduced in the proposed model. The shape of the surface of loading is shown in Fig.2. The surface is closed to define a certain elastic region. It is assumed that the material begins to hardening at 20% of its ultimate strength. Through the uniaxial compression path, the hardening is linear because the distance between two successive surfaces is substantially the same. In uniaxial tension, the hardening is not linear because the surface at $k=0.8$ is superimposed on that obtained for $k=1$.

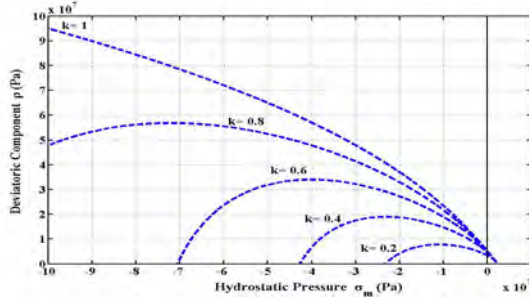


Figure 2. Triaxial failure envelope at $\xi = 0.64$ (300°C) in hardening mode

4 CHEMOPLASTIC POTENTIAL FUNCTION

The evolution of plastic strain rate is determined by the flow rule as follow:

$$\dot{\epsilon}_p = \dot{\lambda} \frac{\partial Q}{\partial \sigma} = \dot{\lambda} \mathbf{m} \quad (5)$$

where Q denotes the chemoplastic potential, and λ is the plastic multiplier. To reduce excessive dilatation in the low confinement region, a non-associated flow rule is introduced. A new chemoplastic potential is defined by re-using the loading function and replacing the adequate set parameters. The plastic potential function is given by the following formula:

$$Q(\sigma_m, \rho, r(\theta), \xi) = a_q(\xi) \left[\frac{\rho r(\theta)}{f_c(\xi)} \right]^{\alpha_q(\xi)} + \frac{m_f(\xi)}{f_c(\xi)} \left[\sigma_m + \frac{\rho r(\theta)}{b_q(\xi)} \right] - 1 = 0 \quad (6)$$

To identify the parameters of the chemoplastic potential, it is necessary to know the normal to the potential at rupture for some cases of loading. The relationship between volumetric and deviatoric components of the normal potential must be the same as that obtained in compression tests. For the chemoplastic potential, the circular deviatoric forms were used. The computing time needed to integrate the constitutive law is then less and simpler. The equation of the chemoplastic potential in the hardening/softening regimes takes the same form as that of the failure surface:

$$Q(\sigma_m, \rho, r, k, c, \xi) = \left\{ (1-k) \left[\frac{\sigma_m}{f_c(\xi)} + \frac{\rho r(\theta)}{b_q(\xi) f_c(\xi)} \right]^2 + a(\xi)^{\frac{1}{\alpha_q(\xi)}} \frac{\rho r(\theta)}{f_c(\xi)} \right\}^{\alpha_q(\xi)} + \frac{k^{\beta_q(\xi)} m_f(\xi)}{f_c(\xi)} \left[\sigma_m + \frac{\rho r(\theta)}{b_q(\xi)} \right] - k^{\beta_q(\xi)} c = 0 \quad (7)$$

5 STRESS RETURN ALGORITHM

5.1 Evaluation of the proper stress for plastic potential

By overlaying the chemoplastic potential on the Etse and Willam yielding surface, both defined on the Haigh-Westergaard coordinates, it is possible to establish that, at the same strength parameter k , the two curves do not undergo the same stress states. For an adequate evaluation of normal vectors, it is necessary that each surface goes through the current stress state. Keeping the loading surface unchanged, the calculation related to the plastic potential need to be modified. This consists in identifying a new value of deviatoric component ρ prior to the evaluation of the gradient of plastic potential. Such modification is necessary by moving vertically the stress state of the plastic potential for $Q=0$. This method is valid for both hardening and softening regimes. However, it is essential to use circular deviatoric sections by using analytical derivatives, because it is impossible to isolate ρ , then modify the calculation of numerical derivatives. To minimize the potential, the new value of ρ is obtained by using the following iterative relationship:

$$\rho_{i+1} = \rho_i - \frac{Q(\sigma_m, \rho_i, r, k)}{\frac{\partial Q(\sigma_m, \rho_i, r, k)}{\partial \rho}} \quad (8)$$

Special attention is focused on the calculations of the derivatives. The terms $\frac{\partial Q}{\partial \sigma_m}$ and $\frac{\partial Q}{\partial \rho}$ are evaluated with ρ_Q while $\frac{\partial \rho}{\partial \sigma}$ and $\frac{\partial \sigma_m}{\partial \sigma}$ are evaluated with the real vector of stress.

5.2 Resolution scheme

A backward-Euler (Euler implicit) algorithm as defined by [17] is applied for constitutive integration. The algorithm for each integration point for a given state can be summarized by means of the following steps:

- Calculating the first elastic prediction.
 1. From the stress at point B (Fig.3), calculate the value of F and the gradient
$$\mathbf{n} = \frac{\partial F(\sigma_m, \rho, r, k)}{\partial \sigma}.$$
 2. In the presence of non-associated flow, identify a particular value of ρ for $Q=0$ and calculate the gradient
$$\mathbf{m} = \frac{\partial Q(\sigma_m, \rho, r, k)}{\partial \sigma}.$$
 3. Compute $\Delta\lambda = \frac{F_B}{\mathbf{n}_B^T \mathbf{H} \mathbf{m}_B + H_{gB}}$ and the stress at point C with equation: $\sigma_C = \sigma_B - \Delta\lambda \mathbf{H} \mathbf{m}_B$ where σ_B is the elastic test point, \mathbf{H} is elasticity tensor, and H_g is effective plastic modulus (g is generic variable, g = p for hardening and g = c for softening).
 4. Update the equivalent plastic strain $\varepsilon_p(\varepsilon_f)$ in hardening and the strength parameter $k(c)$ during the hardening (softening).
- Beginning the implicit backward-Euler method:
 5. Compute F and \mathbf{n} at the current point C.
 6. Minimize the potential for $Q=0$ and calculate the gradient \mathbf{m} .
 7. Compute the residual
$$\mathbf{r}_C = \sigma_C - \left\{ \sigma_B - \Delta\lambda \mathbf{H} \mathbf{m}_C \right\}.$$

8. Compute the change of the plastic multiplier $\delta\lambda = \frac{F_{C0} - \mathbf{n}_C^T \left[\mathbf{I} + \Delta\lambda H \frac{\partial \mathbf{m}}{\partial \boldsymbol{\sigma}} \Big|_C \right]^{-1} \mathbf{r}_0}{\mathbf{n}_C^T \left[\mathbf{I} + \Delta\lambda H \frac{\partial \mathbf{m}}{\partial \boldsymbol{\sigma}} \Big|_C \right]^{-1} H \mathbf{m}_C + H_{gC}}$ and then change the stress: $\delta\boldsymbol{\sigma} = - \left[\mathbf{I} + \Delta\lambda H \frac{\partial \mathbf{m}}{\partial \boldsymbol{\sigma}} \Big|_C \right]^{-1} \{ \mathbf{r}_0 + \delta\lambda H \mathbf{m}_C \}$.
9. Update the stress at the point C: $\boldsymbol{\sigma}_{C_n} = \boldsymbol{\sigma}_0 + \delta\boldsymbol{\sigma}$, then the changes in the plastic multiplier from B: $\Delta\lambda_n = \Delta\lambda_0 + \delta\lambda$.
10. Update the equivalent plastic strain $\varepsilon_p(\varepsilon_f)$ and the strength parameter $k(c)$ during the hardening (softening).
11. Repeat the procedure from step 5 until \mathbf{r} and F are below a certain tolerance.

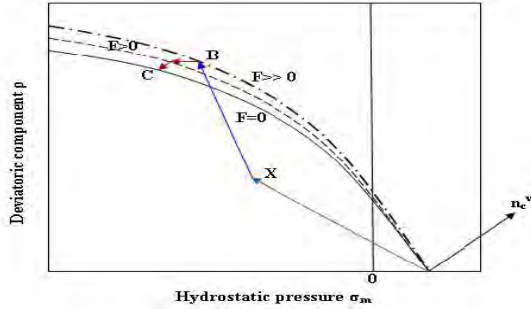


Figure 3. Return mapping process in yield surface

6 CALIBRATION

The first required parameter to identify the failure envelope F is the parameter α_f used to express the relation $\rho(\sigma_m)$ as a power function. This parameter is set to 2.5. The second parameter is β_f that appears in the hardening term. As a first approximation, the parameter β_f is constant and can be similar to the parameter α_f . The parameters a_f and b_f are identified manually by trials and errors to allow that the criterion goes through the most experimental points. The selected combination should offer the lowest absolute error (Root Mean Square (*RMS*)) between the measured shear stress values and those defined by criterion at the same pressures. The same analysis for parameters identification is repeated for the chemoplastic potential. Three parameters (a_q , b_q , and α_q) are identified. The chemoplastic potential used for the concrete must have the following characteristics [15]:

1. It should promote a positive change in volume plastic in the region of positive pressure related to the mode of crack opening.
2. It should promote a change in plastic form in the region of negative pressure related to the mode of cracking or splitting in shear.

By setting values of α_q , it is possible to obtain a pronounced curvature of the relation $\rho(\sigma_m)$. The parameters a_q and b_q are identified as follow: manually set the values for a_q and b_q , and simulate a failure to observe the permanent components of volumetric and deviatoric plastic strains. The model was programmed in the Matlab software and the loading is controlled by stress and by imposing increments in the axial direction. The resulting permanent deformations are then used to calculate the plastic volumetric

and deviatoric strains components. These values are then compared to those measured in the laboratory. Fig.4 shows the results for a simple compression test. According to the obtained simulated results, the ratio of the deviatoric component and the volumetric component is almost preserved until the failure. However, during the hardening, the plastic volumetric strain component has greater amplitude. Fig.5 shows numerical and experimental correlations obtained through a uniaxial compression test. If the correlation is satisfied, the values used for a_q , b_q and α_q are considered acceptable. Fig.1 shows the constitutive model with this set of parameters. The calibration operation was taken regardless of the temperature level.

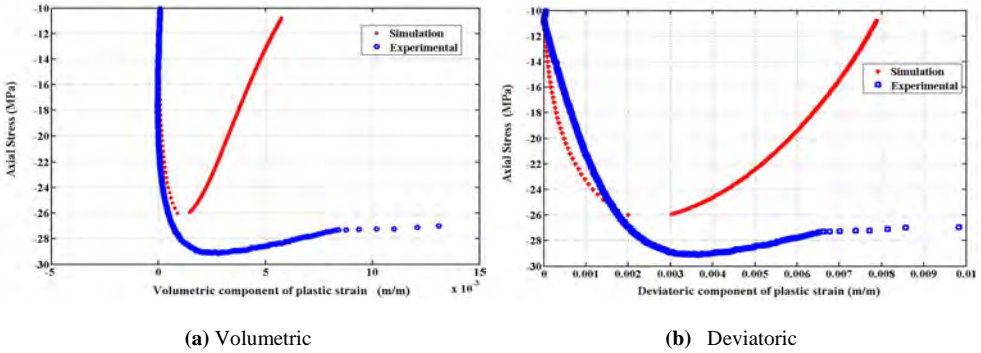


Figure 4. Volumetric and deviatoric plastic components correlations at $\xi = 0.64$ (300°C) for simulated and experimental data

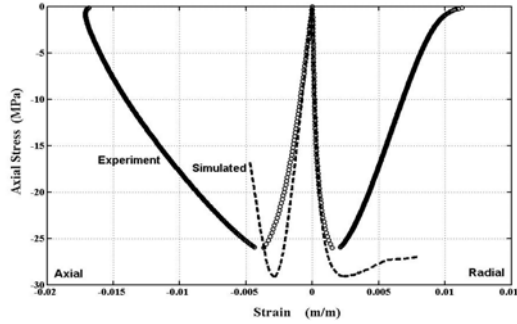


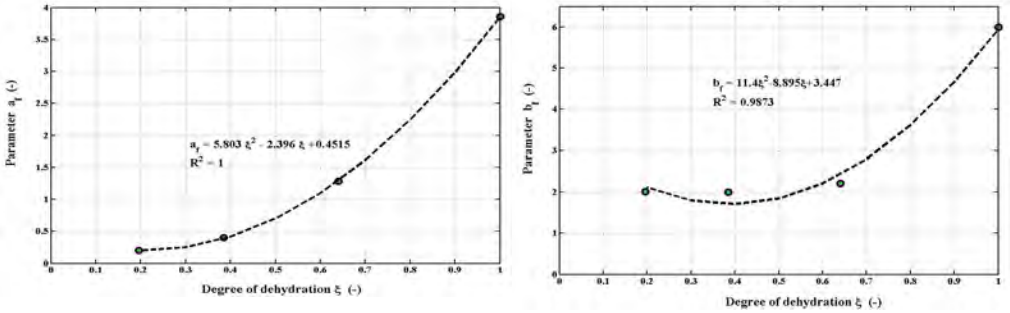
Figure 5. Numerical and experimental stress-strains in axial compression at $\xi = 0.64$

7 PARAMETERS EVOLUTION OF LOADING SURFACE AND CHEMOPLASTIC POTENTIAL

7.1 Fitting parameters of the loading surface

Referring to Eq.3 for the failure envelope, the five parameters are expressed as functions of the degree of dehydration to include the strength degradation with degree of dehydration. The first parameter is the absolute value of the uniaxial compressive strength f_c according to the degree of dehydration ξ . As the degree of dehydration is directly obtained from the mechanical strength, a linear relationship is obtained between the two variables (Eq.1). The second parameter is the relationship between the absolute value of the uniaxial compressive strength and the uniaxial tensile strength depending on the degree of dehydration ξ . The last parameters a_f and b_f of the loading surface according to the degree of dehydration ξ are shown in Fig.6.

These parameters defining the failure envelope are known as function of degree of dehydration and allow the presentation of the compressive meridian as function of hydrostatic pressure and the degree of dehydration (Fig. 7). The resulting smoothing operation offers convex surface for any stress state. Since this condition is met, this surface makes it possible to determine any stress leading to the rupture of concrete given the degree of dehydration.



(a) Parameter a_f (b) Parameter b_f
 Figure 6. Evolution of failure envelope parameters a_f and b_f as function of the degree of dehydration

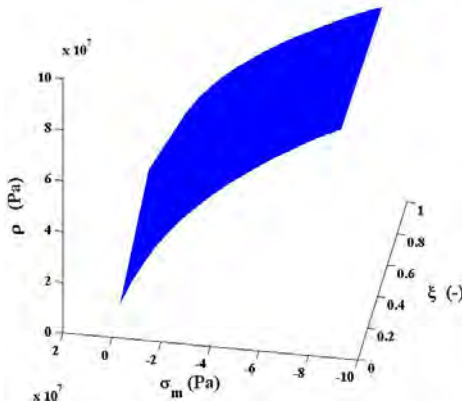


Figure 7. Evolution of the shear strength of the compressive meridian of the failure envelope according to the hydrostatic pressure and the degree of dehydration

7.2 Fitting parameters of the chemoplastic potential

The first parameters of the chemoplastic potential Q are a_q and b_q . These parameters are different from those of the loading surface. Fig.8 illustrates the relationship defined as function of the degree of dehydration. Referring to Eq.7, the parameter β_q appears in hardening. It is also different for the failure envelope F . The plastic potential Q is used to define the dependence of the resistance as a power function.

8 SOME NUMERICAL EXPERIMENTS FOR VARIOUS LOADING SCENARIOS

The capability and performance of the proposed model is improved by comparing predicted results to experimental tests taken from [2]. Comparisons between numerical and experimental results for concrete under uniaxial compression in both axial and radial directions are summarized in Fig. 5. It can be observed, the correlation is reasonable. The simulated hardening regime is shown to be very similar so

the experimental one. At the end of the softening, the model slightly overestimates the axial stress. Fig.9 shows comparison between numerical and experimental results for concrete under triaxial compression and various confinement levels. The correlation is acceptable for both axial and radial directions. The respective experimental data are relatively close to the numerical results.

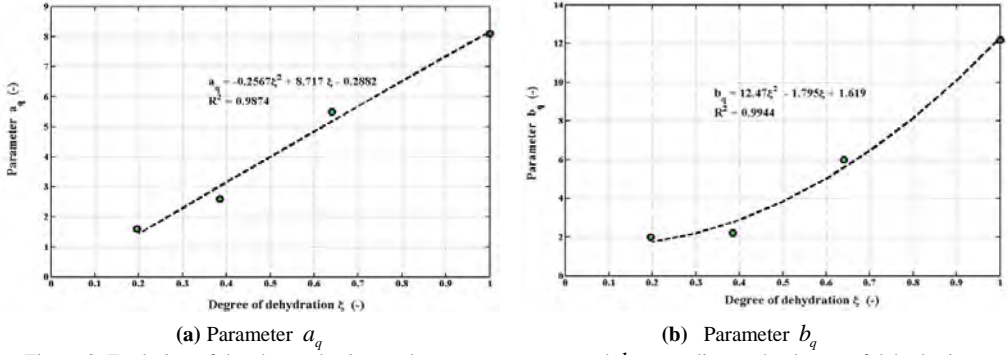


Figure 8. Evolution of the chemoplastic envelope parameters a_q and b_q according to the degree of dehydration

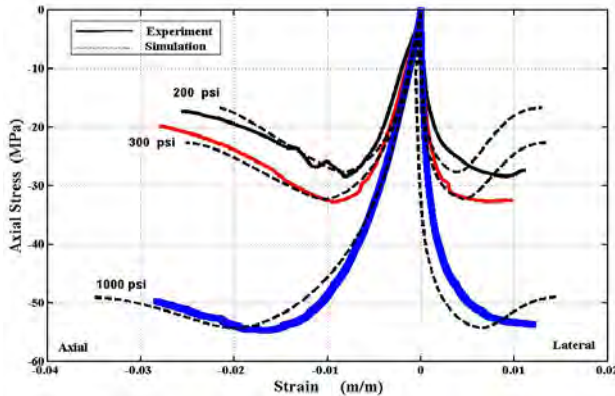


Figure 9. Numerical and experimental triaxial compression tests at $\xi = 0.39$ (500°C)

9 CONCLUSIONS

A novel tri-dimensional constitutive model has been developed and validated. The simulations were performed to identify key parameters required for modelling the behaviour of concrete at high temperatures.

A three dimensional constitutive law, based on the extended Leon model (ELM) model has been formulated. Comparisons between simulated and measured stress-strains relationships have been carried out. Test results showed that the use of proposed model was adequate to simulate experimental stress-strain curves of concrete at wide range of the temperature levels.

REFERENCES

[1] Phan, L., Lawson, J. and Davis F., “Effects of elevated temperature exposure on heating characteristics, spalling, and residual properties of high performance concrete”, *Materials and Structures*, 34, 83-91, 2001.

-
- [2] Hammoud, R., Yahia, A. and Boukhili R., "Triaxial residual stress-strain behaviour of concrete after being subjected to high temperature", *Materials and Structures* (submitted).
- [3] Khennane, A. and Baker G., "Plasticity models for the biaxial behaviour of concrete at elevated temperatures, Part I: Failure criterion", *Computer Methods in Applied Mechanics and Engineering*, 100, 207-223, 1992.
- [4] Luccioni, B.M., Figueora, M.I. and Danesi R.F., "Thermo-mechanic model for concrete exposed to elevated temperatures", *Engineering and Structures*, 25, 729-742, 2003.
- [5] Nechnech, W., Meftah F. and Reynouard J.M., "An elasto-plastic damage model for plain concrete subjected to high temperatures", *Engineering Structures*, 24, 597-611, 2002.
- [6] Ulm, F.-J., Coussy, O. and Bazant Z.P., "The chunnel fire. I: Chemoplastic softening in rapidly heated concrete", *Journal of Engineering Mechanics*, 125, 272-282, 1999.
- [7] Ulm, F.-J. and Coussy, O., "Modeling of thermomechanical couplings of concrete at early ages", *Journal of Engineering Mechanics*, 121, 785-794, 1995.
- [8] Ulm, F.-J. and Coussy O., "Strength growth as chemo-plastic hardening in early age concrete", *Journal of Engineering Mechanics*, 122, 1123-1132, 1996.
- [9] Coussy O., *Mechanics of porous continua*, Wiley, Chichester, New York, USA, 1995.
- [10] Cervera, M., Oliver, J. and Prato T., "Thermo-chemo-mechanical model for concrete. I: Hydration and aging", *Journal of Engineering Mechanics*, 125, 1018-1027, 1999.
- [11] Hellmich, C., Ulm, J.-F. and Mang H.A., "Multisurface chemoplasticity. I: Material model for shotcrete", *Journal of Engineering Mechanics*, 125, 692-701, 1999.
- [12] Etse, G. and Willam, K., "Fracture energy formulation for inelastic behaviour of plain concrete", *Journal of Engineering Mechanics*, 120, 1983-2011, 1994.
- [13] Willam, K.J. and Warnke, E.P., "Constitutive Model for the Triaxial Behavior of Concrete", *Proc. Intl. Assoc. Bridge Structl. Engrs*, Report 19, Section III, Zurich, 1994.
- [14] D'amours, G., Développement de lois constitutives thermomécaniques pour les matériaux à base de carbone lors du préchauffage d'une cuve d'électrolyse. Ph.D. Thesis, Laval University, Québec (Québec), Canada, 2004.
- [15] Kang, H.D., Triaxial constitutive model for plain and reinforced concrete behavior, Ph.D. Thesis, University of Colorado, Colorado, USA, 1997
- [16] Crouch, R.S. and Tahar, B., "Application of a stress return algorithm for elastoplastic hardening-softening models with yield surface curvature", E. Onate, Editor et al., *Proceedings of European Congress on Computational Methods in Applied Sciences and Engineering* (CD-Rom), CIMNE Pubs, Barcelona, 2000.
- [17] Crisfield M.A., *Non-linear finite element analysis of solids and structures*, Vol.1, Wiley, 1991.

**CONCRETE STRUCTURES
AND
OTHER TOPICS**

BEHAVIOURS OF SEISMIC DAMAGED RC COLUMNS IN POST-EARTHQUAKE FIRE

Bo Wu*, Wei Xiong*

* State Key Laboratory of Subtropical Building Science, Department of Civil Engineering,
South China University of Technology, Guangzhou 510640, P. R. of China
e-mails: bowu@scut.edu.cn, xiongweiscut@sina.com

Keywords: Post-earthquake fire, RC columns, Seismic damage, Fire resistance

Abstract: *The post-earthquake fire (PEF) is a major threat to the RC structures due to the heat tending to be transferred into the inner of the seismic damaged members with cracks and crushing of concrete cover more rapidly. However, design code considering these extreme but common events is not available now. To investigate the fire performance of seismic damaged columns, a simple but rational method is proposed in this paper.*

This study develops an empirical model to determine the crushed length of concrete cover under a design earthquake first and then numerically models the seismic damaged columns in ABAQUS by removal of the crushing concrete. A comparison work between the fire behaviours of undamaged and damaged columns is conducted to examine the influence of PEF.

1 INTRODUCTION

Post-earthquake fire (PEF) is prone to be triggered by damaged gas/electric/fuel services in seismic regions. Some past earthquakes, e.g. the 1906 San Francisco, 1923 Tokyo, 1971 San Fernando, 1994 Northridge and 1995 Kobe earthquakes were followed by fires which brought about greater loss than the original earthquake [1]. Due to a high thermal inertia of concrete, the intact reinforced concrete (RC) structural members always perform well in an ordinary fire disaster, however, for the earthquake-damaged RC structural members with crushing of concrete cover and/or significant concrete cracks subjected to PEF, the heat tend to be transferred into the inner of the structural members more rapidly and even the reinforcements may be heated directly, and thus the mechanical properties of the seismic damaged structural members in PEF decreases faster than those of the non-seismic damaged structural members in fire. Although PEF is a severe threat to the seismic damaged structures, researchers focused on the fire performances of the non-seismic damaged ones during past decades, and only a little knowledge about fire behaviours of the seismic damaged RC structures is available until recently. [1, 2]

To evaluate the fire performance of the seismic damaged RC columns in PEF, a preliminary study is conducted in this paper. Above all, an empirical model based on the test results collected in Pacific Earthquake Engineer Research Centre, PEER's database [3] is proposed to assess the geometrical damaged properties of flexure-critical rectangular RC columns caused by earthquake. As a preliminary research only the crushing of concrete cover is taken into account here and the influence of cracks is not considered. According to the crushed model, the thermal configuration of damaged columns can be determined. After numerically modelling the damaged columns in the commercial software ABAQUS by removal of the crushed concrete, a series of thermo-mechanical analysis are carried out to investigate the

correlation between the seismic damage state and the corresponding fire performance in terms of fire resistance (FR) by comparing with the undamaged columns.

2 CRUSHED MODEL OF CONCRETE COVER

Based on the database of RC columns under seismic loadings collected by the PEER, some useful information is provided in the experimental images. For example, the length of crushed concrete cover can be obtained from the pictures of seismic damaged columns related to different column's axial load ratio, mechanical lateral confinement ratio, shear-span ratio, and lateral displacement. Due to lacking of images related to intermediate damaged states, an empirical model to determine the length of crushed cover related to the ultimate limit state, l_u , is proposed first and then an interpolation is carried out to assess the crushed length corresponding to any intermediate damage state according to the lateral displacement.

2.1 Data collection

This paper focuses on the flexure-critical rectangular normal strength columns, so the abundant data in the PEER's database should be filtered. In addition, the test results without photos or with blurred photos are not included because the photos of seismic damaged specimens are essential for this study. Finally, 17 columns were selected and listed in Table 1. The detail information (i.e., the axial load, shear-span ratio, lateral confinement, etc.) about these specimens is available in the database and readers can refer to the website (<http://www.ce.washington.edu/~peer1/>).

Take the No.1 specimen carried out by Soesianawati et al [4] listed in Table 1 as an example to show the method to obtain the crushed length of concrete cover. Fig.1 shows the overall view of the double-ended specimen after two cycles of lateral loading with a ductility ratio of 6.0. The virtual lengths of crushed concrete cover related to four locations (i.e., $l_{v,1}$, $l_{v,2}$, $l_{v,3}$, and $l_{v,4}$) are, respectively, measured from this photo. The virtual sectional depth of this column, h_v , can also be measured directly from this photo, and the real depth of the column cross section, h , is 400mm. In this way, the real length of crushed concrete cover can be approximately determined by a converting calculation as $l_i = h \times l_{v,i} / h_v$ ($i=1, 2, 3, 4$), and an equivalent length is obtained as the average value of $l = (l_1 + l_2 + l_3 + l_4) / 4$ for this column. All the columns' crushed length corresponding to different drift ratio is compiled in Table 1.

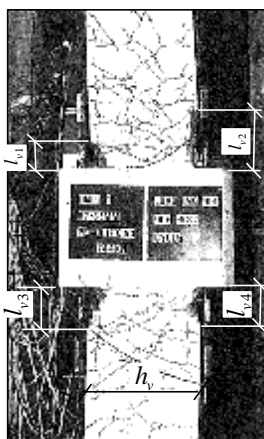


Figure 1. Overall view of No.1 column at ductility ratio of 6

Table 1: Selected columns for analysis of the length of crushed concrete cover

No.	Specimens	Drift ratio	Crushed length(mm)	No.	Specimens	Drift ratio	Crushed length(mm)
1	Soesianawati [4], Unit 1	1/228	0	2	Soesianawati [4], Unit 2	1/254	0
		1/82	0			1/94	0
		1/41	90			1/47	180
		1/27	160			1/32	310 ^U (76%)
		1/20	250			1/23	310
		1/16	260 ^U (72%)			1/19	340
3	Soesianawati [4], Unit 3	1/296	0	4	Soesianawati [4], Unit 4	1/229	0
		1/105	0			1/181	0
		1/53	170			1/89	40
		1/33	230 ^U (76%)			1/59	160
						1/45	200
				1/36	230 ^U (73%)		
5	Li [5] T/M=0	1/44	130	11	Watson,[8] Unit 5	1/41	410 ^U (77%)
		1/13	620 ^U (78 %)	12	Watson,[8] Unit 6	1/63	260 ^U (78%)
6	Tanaka [6] Unit 6	1/15	300 ^U (84%)	13	Watson,[8] Unit 8	1/86	370 ^U (77%)
7	Tanaka [6] Unit 7	1/20	540 ^U (83%)	14	Watson,[8] Unit 9	1/36	450 ^U (74%)
8	Tanaka [6] Unit 8	1/19	500 ^U (83%)	15	Saatcioglu [9], BG-2	1/19	300 ^U (76%)
9	Zahn [7] Unit 7	1/16	410 ^U (72%)	16	Saatcioglu [9] BG-2	1/15	370 ^U (74 %)
10	Zahn [7] Unit 8	1/27	430 ^U (75%)	17	Aziznamini [10] NC-2	1/20	400 ^U (79%)

Note: a) The superscript “U” denotes the length of crushed concrete cover related to the column’s ultimate limit state;

b) The bracketed datum denotes a ratio of the residual lateral load related to the ultimate limit state to the maximum lateral load.

2.2 Crushed model

It’s critical to determine the lateral displacement at the onset of concrete cover crushing, Δ_c and that related to the ultimate limit state, Δ_u to develop the displacement-based model. The ultimate limit state is identified as the point on the descending branch of the column’s lateral load-lateral displacement skeleton curve, at which the lateral load is 80% of the maximum lateral load. However, it’s impossible to get a seismic damaged column’s picture that is exactly related to this point, so the photo corresponding to a lateral load that is 70%~85% of the maximum lateral load is approximately regarded as the picture of the column’s ultimate limit state in this study and labelled with a superscript “U” in Table 1. The ratio of the residual lateral load to the maximum lateral load is also given in Table 1.

A semi-empirical method also based on the PEER’s database proposed by Jiang et al. [11] to estimate the lateral displacements of flexure-critical rectangular RC columns at different damage states is adopted herein to determine the Δ_c and Δ_u . The crushed length is assumed to be zero before the onset of concrete crushing, and reaches the maximum value l_u at the ultimate limit state. According to the data listed in Table 1 with superscript “U” and taking the axial load ratio, mechanical lateral confinement ratio, shear-span ratio into account, an empirical model for the length of crushed concrete cover related to the ultimate limit state, l_u , is developed as:

$$\frac{l_u}{h} = 1.05 + 0.422n - 4.04\left(\frac{\rho_{yh}f_{yh}\lambda^2}{f_c'}\right)^{-0.5} \tag{1}$$

where the n is the axial load ratio, and the λ is the shear-span ratio. The ρ_{yh} , f_{yh} , f_c' denote the volumetric stirrup ratio, yield stress of stirrups, compression strength of concrete, respectively.

Fig. 2 (a) shows a comparison between the calculated lengths using Eq. (1) and the measured ones given in Table 1. For the ratio of the calculated length to the measured length, the mean value and coefficient of variation (COV) are 1.03 and 0.17, respectively. It can be seen from Fig.2 that the measured length of crushed concrete cover related to the ultimate limit state ranges from 0.5h to 1.2h for the flexure-critical rectangular RC columns under seismic loadings.

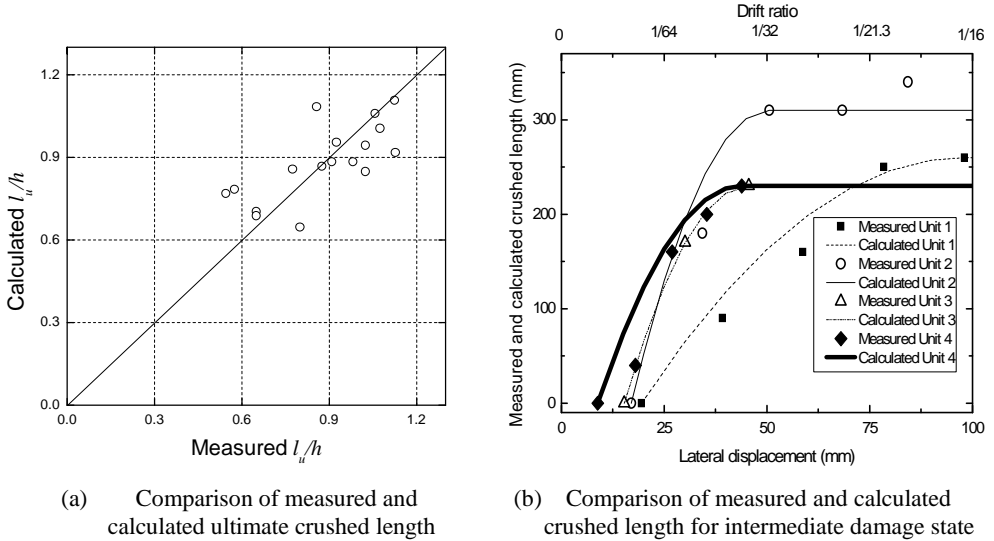


Figure 2. Comparison of measured and predicted crushed length

Then an interpolation should be conducted to assess the crushed length at the intermediate damaged state. The trend that the increasing of the crushed concrete length tend to be slower with an increase of the column’s lateral displacement can be found by carefully investigating into the test results reported by Soesianawati et al. [4]. Therefore a parabolic interpolation is applicable to predict the intermediate crushed length, and the model can be expressed as:

$$l = \begin{cases} 0 & (\Delta \leq \Delta_c) \\ \frac{(\Delta - \Delta_c)(2\Delta_u - \Delta_c - \Delta)}{(\Delta_u - \Delta_c)^2} l_u & (\Delta_c < \Delta \leq \Delta_u) \\ l_u & (\Delta > \Delta_u) \end{cases} \tag{2}$$

where the Δ denotes the lateral displacement of the columns under a design earthquake, which can be obtained from a common structure seismic simulation.

Fig. 2 (b) shows a comparison between the calculated lengths using Eq.(2) and the measured ones listed in Table 1 for different damage states of columns tested by Soesianawati et al [4]. It can be seen from this figure that Eq. (4) is capable of predicting the crushed concrete length related to any intermediate damage state with a good accuracy on the whole.

3 THERMO-MECHANICAL SIMULATION

3.1 Numerical models

Three RC columns (named as Column A, Column B and Column C) with length of 3000 mm and fixed-fixed end conditions are considered here. The sectional dimensions, reinforcement details, material properties, and applied axial loads of Columns A and B are, respectively, identical with those of the No.1 and No.2 specimens tested in fire by Lie and Irwin [12]. The Column C is resembled to the Column A except the longitudinal reinforcement. There are 4 longitudinal steel bars arranged in Column A, while 8 steel bars with area as half as the bars in Column A are arranged in Column C, so the total area of reinforcement are identical in the two columns.

For the seismic damaged Columns A, B and C, the crushed lengths of concrete cover on two opposite sides in the plastic hinge region related to different lateral displacements can be determined using Eqs.(1)~(2). In addition, the thickness of crushed concrete is assumed to be the clear concrete cover to the transverse reinforcements, and the core concrete is supposed to be intact due to the confining effect produced by the steel stirrups. Table 1 shows the relative crushed length (a ratio of the crushed length to the column's sectional depth, RCL) related to different lateral displacements.

Table 2: Selected columns for analysis of the length of crushed concrete cover

Specimen	Lateral displacement (mm)	RCL	FR(min)	Damaged FR/undamaged FR
No. 1	$\Delta_c=27.5$	0	179	1
	32.8	0.37	96	0.54
	38.1	0.63	80	0.45
	43.4	0.79	70	0.39
	$\Delta_u=48.7$	0.84	54	0.30
No. 2	$\Delta_c=30.9$	0	248	1
	37.6	0.34	142	0.57
	44.2	0.59	118	0.48
	50.9	0.73	98	0.40
	$\Delta_u=57.5$	0.78	87	0.35
No.3	$\Delta_c=24.1$	0	194	1
	29.1	0.37	116	0.60
	34.1	0.63	92	0.47
	39.0	0.79	81	0.42
	$\Delta_u=44.0$	0.84	66	0.34

The finite element analysis software ABAQUS is employed to simulate the fire behaviours of the undamaged and seismic damaged columns exposed to ISO834 standard fire. The thermal properties of concrete (i.e., density, thermal conductivity, and specific heat capacity) are determined according to Eurocode 2 [13]. The constant convective coefficient for the exposed surface and the concrete thermal emissivity are assumed to be 25W/m²K and 0.7, respectively. The stress-strain relationship of concrete under high temperature proposed by Lie and Irwin [12] is adopted in this paper, and a simplified method

to account for the transient thermal strain of concrete in ABAQUS suggested by Wang and Xue [14] is utilized here. The yield strength, ultimate strength, and modulus of elasticity of steel reinforcement under high temperature are determined according to the formulas given by Guo and Shi [15]. The thermal expansion coefficients of concrete and steel recommended in Eurocode 2 [13] are used in this study. Both the 3-D solid element (C3D8R) and 3-D truss element (T3D2) available in ABAQUS are utilized to model the concrete and reinforcement, respectively. The reinforcement is embedded in the concrete. Heat transfer analysis is conducted firstly to obtain the time-dependent thermal fields of the column during fire, and then mechanical behaviors of the column in fire are calculated.

3.3 Results and discussion

3.3.1 Thermal analysis

The temperature fields when heating to 180min of the Column A without crushed concrete cover (non-seismic damaged column) and that of the column with crushed concrete cover (seismic damaged column, RCL=0.84) are, respectively, shown in Fig.3(a). For the damaged column, the crushed concrete has been removed in the numerical model.

It can be seen that the two columns' temperature distributions are quite different near the crushed region. Considering the undamaged section 1-1 and seismic damaged section 2-2 of Column A as shown in Fig. 3(a), the temperature-time curves of the centre of the two sections and that related to the longitudinal reinforcement are plotted in Fig. 3(b) for both sections. The temperature at the centre of Section 2-2 is 160°C higher than that of the Section 1-1, and the temperature of the longitudinal reinforcement at Section 2-2 is 484°C higher than that of Section 1-1.

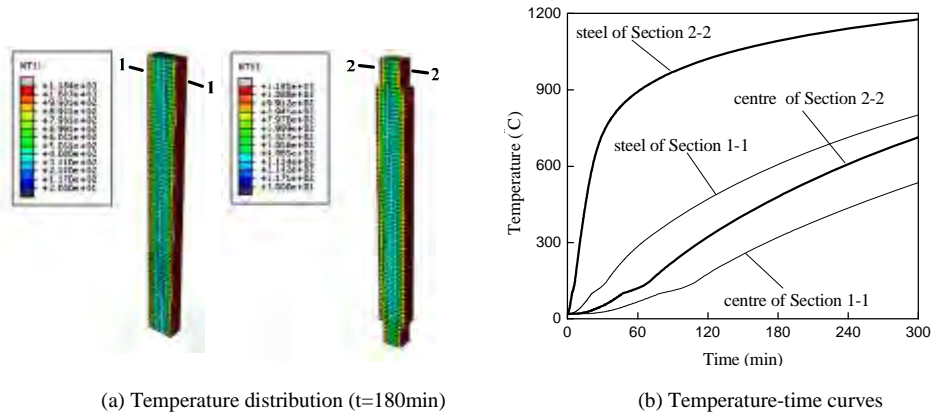


Figure 3. Comparison of temperature distribution of columns without/with crushed concrete cover

3.3.2 Mechanical analysis

The mechanical analysis following the thermal analysis is conducted to examine the fire performance of seismic damaged columns.

The axial deformation-time curves and fire resistance of the seismic damaged Columns A, B and C with different RCL are illustrated in Fig.4, and compared with those of the undamaged ones with RCL=0. It can be seen that the FR drops dramatically after crushing of concrete cover, and with an increasing of the RCL, the fire endurance decreases gradually. This is attributed to the fact that the FR of the axially loaded RC columns with a compressive failure pattern in fires mainly depends on their strength capacity.

Regardless of the length of crushed concrete, the cross section in damaged region becomes the weakest section with great loss of strength capacity, which is responsible for the whole column's failure.

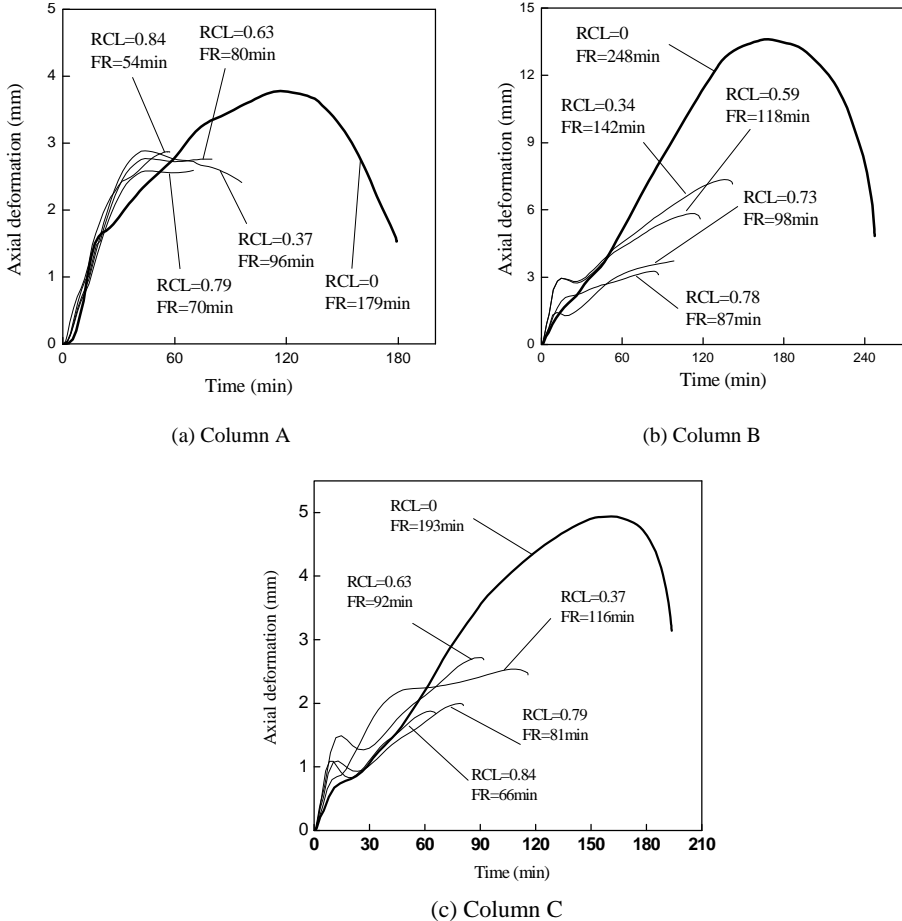


Figure 4. Axial deformation-time curves of columns without/with crushed concrete cover in PEF

Fig.4 also reveals the fact that with an increasing of the RCL, the maximum axial elongation reduces greatly first and then decreases smoothly on the whole. However, the elongation for the damaged columns is a little larger than the undamaged columns in the early stage of heating process. It can be attributed to the higher average temperature in the damaged section resulting in larger thermal expansion.

Table 2 also provides the ratios of the fire resistance of the seismic damaged column to that of the undamaged column. The ratio of Column A is a little less than that of Column C related to the same damaged state. It can be attributed to the fact that there are 8 bars are arranged in column C but only 4 in Column A (as shown in Fig.5). It can be seen from this figure that all 4 steel bars in Column A are very close to fire, while 2 steel bars in Column C are fully protected by concrete cover, and thus the decreasing of the sectional load bearing capacity of Column C is slower than that of Column A.

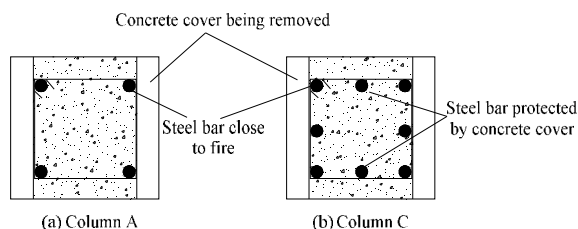


Figure 5. Schematic diagram of cross-sections in damaged specimens No.1 and No.2

4 CONCLUSION

This paper develops a simple but rational method to examine the behaviours of RC columns subjected to PEF. An empirical model based on the test results is proposed in this paper first to evaluate the crushed length of damaged columns. This model is proved to evaluate the crushed length with a satisfied result. By removal of the crushed concrete, the numerically model of damaged columns can be easily built in the ABAQUS, and then a series of thermo-mechanical analysis are carried out to investigate the fire behaviours of the seismic damaged columns.

The thermal field in the crushed region of a seismic damaged column is quite different from that of the reference undamaged column. The temperature of the corner longitudinal reinforcement in the crushed region is much higher than that located in the undamaged column. The damaged column's FR drops sharply after crushing of concrete cover, and with an increasing of the RCL, the fire endurance decreases gradually. With an increasing of the crushed concrete length, the maximum axial elongation of the seismic damaged column in post-earthquake fire reduces greatly first and then decreases smoothly on the whole. However, the thermal elongation of the seismic damaged column is a little larger than that of the reference undamaged column in the early stage of the heating process. For a given reinforcement ratio, increasing the number of steel bars can slightly improve the fire endurance of the seismic damaged axially loaded column in post-earthquake fire. Further investigation into the influence brought by the cracks is carried out in progress to achieve a more complete picture.

Acknowledgements

The research reported was financially supported by the National Natural Science Foundation for Distinguished Young Scholars (51025829), the National Basic Research Program of China (973 Program: 2011CB01 3800), the Funds of State Key Laboratory of Subtropical Building Science of China (2011ZB07), and the Fundamental Research Funds for the Central Universities (2012ZP0011). The financial supports are highly appreciated.

REFERENCES

- [1] Bhargava P., Sharma U.K., and Singh Y. et al., "Fire Testing of an Earthquake Damaged RC Frame". *Structures in Fire – Proceedings of the Sixth International Conference*, V. Kodur, J. M. Franssen (eds.), DEStech Publications, Lancaster, 231-238, 2010.
- [2] Ervine A., Gillie M., and Pankaj, "Behaviour of Earthquake Damaged Reinforced Concrete Structures in Fire." *Structures in Fire – Proceedings of the Sixth International Conference*, V. Kodur, J. M. Franssen (eds.), DEStech Publications, Lancaster, 224-230, 2010.
- [3] Berry M., Parrish M., and Eberhard M., "*PEER structural performance database user's manual*". Pacific Earthquake Engineering Research Centre, University of California Berkeley, California, 38pp, 2004

- [4] Soesianawati M. T., Park R., and Priestley M. J. N., "Limited ductility design of reinforced concrete columns". *Report 86-10*, Department. of Civil Engineering, University of Canterbury, Christchurch, New Zealand, 208pp,1986
- [5] Li Q., Belarbi A., and Prakash S. S., "Seismic performance of square RC bridge columns under combined loading including torsion with low shear". *Proceedings of International Conference on Engineering, Science, Construction, and Operation in Challenging Environment-Earth and Space*, ASCE, Honolulu, 3011-3018, 2010
- [6] Tanaka H., Park R., "Effect of lateral confining reinforcement on the ductile behavior of reinforced concrete columns". *Report 90-2*, Department of Civil Engineering, University of Canterbury, Christchurch, New Zealand, 458pp, 1990
- [7] Zahn F. A., Park R., Priestley M. J. N., "Design of reinforced bridge columns for strength and ductility". *Report 86-7*, Department of Civil Engineering, University of Canterbury, Christchurch, New Zealand, 330pp, 1986
- [8] Watson M. T., Park R., "Design of reinforced concrete frames of limited ductility". *Report 89-4*, Department of Civil Engineering, University of Canterbury, Christchurch, New Zealand, 232pp, 1989
- [9] Saatcioglu M., Grira M., "Confinement of reinforced concrete columns with welded reinforcement grids". *ACI Structural Journal*, 96(1), 29-39, 1999.
- [10] Azizinamini A., Corley W. G., Johal L. S. P., "Effects of transverse reinforcement on seismic performance of columns". *ACI Structure Journal*, 89(4), 442-450, 1992.
- [11] Jiang H. J., Lv X. L., Kubo T., "Damage displacement estimation of flexure-dominant RC columns" . *Advances in Structural Engineering*, 13(2), 357- 368, 2010.
- [12] Lie T.T., Irwin R.J., "Evaluation of the fire resistance of reinforced concrete columns with rectangular cross-section", *Internal Report No.601*, Institute for Research in Construction, Canada, 79pp, 1990
- [13] Eurocode 2. "*Design of concrete structure, General rules, Structural fire design*", British Standards Institution, BSEN 1992-1-2, London,1992
- [14] Wang G.Y., Xue S.D., "Transient thermal strain of concrete and its calculation", *Journal of Beijing University of Technology*, 34(4),387-390,2008. (in Chinese)
- [15] Guo Z.H., Shi X.D., "*Behaviour of Reinforced Concrete at Elevated Temperature and its Calculation*", Tsinghua University Press, Beijing, 2003 (in Chinese)

A MULTIAXIAL CONCRETE MODEL FOR APPLICATIONS IN STRUCTURAL FIRE ENGINEERING

Thomas Gernay* and Alain Millard**

* The National Fund for Scientific Research, Belgium
Structural Engineering Division, University of Liege
e-mail: Thomas.Gernay@ulg.ac.be

** CEA/DEN/DANS/DM2S/SEMT/LM2S, CEN Saclay, France
e-mail: Alain.Millard@cea.fr

Keywords: Concrete model, Plasticity, Damage mechanics, Structures in Fire.

Abstract. *Temperature-dependent material models are required in numerical softwares dedicated to the nonlinear analysis of structures in fire. Although structural concrete is widely used in civil engineering, proper modelling of its thermo-mechanical behaviour remains a challenging issue for engineers mainly because of the complexity of the phenomena that result from the microcracking process in this composite material and because of the lack of numerical robustness of the models. This paper presents a new multiaxial concrete model developed for the analysis of concrete structures in fire. The multiaxial model is based on a plastic-damage formulation and incorporates an explicit term for transient creep strain. After implementation in a finite element software for structural fire engineering calculations, numerical simulations have been performed to highlight the ability of the model to capture some of the main phenomena that develop in concrete (permanent strains, degradation of the elastic properties, unilateral effect) as well as the ability to be used for the fire analysis of large-scale structural elements.*

1 INTRODUCTION

In performance-based analysis, the response of structures subjected to thermo-mechanical loading is assessed by temperature-dependent calculations. These calculations require a general stress-strain relationship for modelling the behaviour of concrete at elevated temperatures. The concrete model should fulfil the criteria of reliability, accuracy and numerical robustness. Accuracy and reliability ensure that the model captures properly the behaviour of the concrete material in all the situations of stress and temperature in the applicability domain. Numerical robustness ensures that the model is applicable to complex and large-scale engineering problems. In addition, the model should contain a limited number of parameters that can be identified from elementary tests. The present research aims at developing a multiaxial model able to reproduce the phenomenological behaviour of concrete at elevated temperature and satisfying to the requirements of structural fire engineers.

The behaviour of concrete at the macroscopic level results from the initiation and growth of microcracks in the cementitious matrix. The microcracking process causes softening behaviour, stiffness degradation and unilateral effect. These observed phenomena can be captured by models within the framework of continuum damage mechanics. On the other hand, concrete exhibits inelastic volumetric expansion in compression, referred to as dilatancy in the literature. Proper modelling of dilatancy is very important for simulating concrete structures under multiaxial loading [1]. Dilatancy can be modelled by the development of plastic strains in concrete. Therefore, combination of the elastoplasticity theory with the damage theory results in an efficient strategy for modelling the mechanical behaviour of concrete.

Constitutive models for concrete at ambient temperature based on plastic-damage formulation have been proposed by several authors. Although concrete experiences different microcracking in different directions, models developed for structural applications usually combine plasticity with isotropic damage [1, 2, 3], in order to avoid the inherent complexities of numerical algorithms required by most of the anisotropic damage models [4, 5]. The isotropic damage process can be characterized by one scalar, several scalars or a tensor. The use of different scalars to capture the damage process in concrete [1] is consistent with the experimentally observed different damage mechanisms developing in tension and in compression; a minimum of two scalar variables are necessary to describe these different damage mechanisms. Some authors have proposed a fourth-order damage tensor to characterize the state of isotropic damage in concrete [5, 6], because a fourth-order tensor is required to capture the unilateral effect. As a result, even for isotropic damage, proper description of the damage state in concrete requires a fourth-order tensor based on two scalar variables. Stress-based plasticity may be formulated either in the effective stress space [1, 2, 5] or in the nominal (damaged) stress space [3, 7]. Effective stress is meant as the average micro-level stress applied to the undamaged volume of the material whereas nominal stress is meant as the macro-level stress and is defined as force divided by the total area. Formulation of the plastic response in the effective stress space relies on the assumption that plastic flow occurs in the undamaged material micro-bounds by means of effective quantities [8]. This formulation allows for decoupling the plastic part from the damage part in the computation process; computation of the plastic response then constitutes a standard elastoplastic problem in the effective stress space. As a result, the combination of stress-based plasticity formulated in the effective stress space and isotropic damage constitutes an interesting approach for modelling the behaviour of concrete.

At elevated temperatures, the situation is even more complex due to additional phenomena that develop in heated concrete. Elevated temperatures are the cause of degradations at the micro-level that result in loss of stiffness and strength of the material. Moreover, a particular phenomenon appears in concrete subjected to elevated temperatures: the transient creep strain. Physically, the transient creep strain is the difference in strain between concrete that is heated under load and concrete that is loaded at elevated temperature; this strain develops during first-time heating and is irrecoverable [9]. Transient creep strain has to be incorporated in any constitutive model dedicated to fire-exposed structural concrete. Due to the high complexity of the many phenomena involved, few multiaxial models coupling plasticity and damage have been proposed for the mechanical behaviour of concrete at elevated temperature; an example of such model combining stress-based plasticity in the effective stress space and isotropic damage, extended at elevated temperature, has been proposed by Nechnech *et al.* [10]. Yet, research efforts are still required to give further insight into concrete modelling at elevated temperature and to extend the latest developments of ambient temperature models to elevated temperature; this is the purpose of the present study.

2 PRESENTATION OF THE MODEL

2.1 Assumptions

The mechanical behaviour of concrete at elevated temperatures is captured by constitutive relationships between the total strain tensor and the stress tensor. The total strain $\underline{\underline{\epsilon}}_{tot}$ is decomposed into free thermal strain $\underline{\underline{\epsilon}}_{th}$, transient creep strain $\underline{\underline{\epsilon}}_{tr}$, elastic strain $\underline{\underline{\epsilon}}_{el}$ and plastic strain $\underline{\underline{\epsilon}}_p$ according to Eq. (1).

$$\underline{\underline{\epsilon}}_{tot} = \underline{\underline{\epsilon}}_{th} + \underline{\underline{\epsilon}}_{tr} + \underline{\underline{\epsilon}}_{el} + \underline{\underline{\epsilon}}_p \quad (1)$$

The sum of the elastic strain and the plastic strain is referred to as instantaneous stress-related strain $\underline{\underline{\epsilon}}_{sp}$. Basic creep strain is not taken into account here but this term could easily be added to the strain decomposition.

The characterization of plastic response is formulated in the effective stress space. The elastic strain tensor is related to the effective stress tensor $\underline{\underline{\sigma}}$ by means of the fourth-order isotropic linear-elastic stiffness tensor $\underline{\underline{C}}_0$, see Eq. (2).

$$\underline{\underline{\sigma}} = \underline{\underline{C}}_0 : \underline{\underline{\varepsilon}}_{el} = \underline{\underline{C}}_0 : (\underline{\underline{\varepsilon}}_{\sigma} - \underline{\underline{\varepsilon}}_p) \quad (2)$$

The plastic response accounts for the development of irreversible strains in the material. Yet, the degradation of the elastic properties resulting from the development of microcracks is not addressed at this stage; the unloading stiffness in the effective stress space remains equal to the isotropic linear-elastic stiffness.

Concrete exhibits different damage mechanisms in tension and in compression. In this model, a tensile damage scalar and a compressive damage scalar are adopted to capture the phenomenological effects induced by microcracking in concrete under tension and compression, respectively. Based on the work by Wu *et al.* [5], these two damage scalars lead to a fourth-order damage tensor employed to characterize the state of isotropic damage in concrete. The use of a fourth-order damage tensor allows for appropriate description of the unilateral effect inherent to concrete behaviour. Mapping of the effective stress $\underline{\underline{\sigma}}$ into the nominal stress $\underline{\underline{\sigma}}$ is performed by this fourth-order isotropic damage tensor $\underline{\underline{D}}$ according to Eq. (3), where $\underline{\underline{I}}$ is the fourth-order identity tensor.

$$\underline{\underline{\sigma}} = \left(\underline{\underline{I}} - \underline{\underline{D}} \right) : \underline{\underline{\sigma}} \quad (3)$$

It is assumed that the plasticity and damage phenomena are coupled and evolve simultaneously in the material; therefore, the two phenomena are driven by the same internal variables in the model.

Finally, the new concrete model is a fully-3D constitutive model that can be used with solid finite elements or with shell finite elements; in the latter case, the plane stress version of the model is used.

2.2 Plasticity

A composite yield surface is used for capturing the concrete non-symmetrical behaviour in tension and in compression; a Rankine yield criterion is used to limit the tensile stresses and a Drucker-Prager yield contour is used for compression. The equations of the composite yield surface are written in terms of effective stresses, see Eq. (4).

$$f_t(\underline{\underline{\sigma}}, \kappa_t) \leq 0 \quad ; \quad f_c(\underline{\underline{\sigma}}, \kappa_c) \leq 0 \quad (4)$$

In Eq. (4), κ_t and κ_c are the tensile and compressive hardening parameters, respectively.

Plastic flow rules have to be postulated to govern the evolution of plastic flow when the effective stress state reaches the yield surfaces. As concrete is a frictional material, in which dilatancy occurs when loaded in compression, a non-associated flow rule is adopted in compression. The plastic flow rules, in combination with the Kuhn-Tucker and consistency conditions, allow for calculation of the accumulated plastic strains in tension and compression; these accumulated plastic strains are chosen as internal variables in the model. The hardening parameters depend on the accumulated plastic strains and therefore are induced by plastic flow; these hardening parameters govern the evolution of the yield surface through the definition of the hardening laws.

2.3 Damage

The isotropic state of damage of concrete is addressed by a fourth-order damage tensor which is calculated from the tensile damage scalar d_t and the compressive damage scalar d_c as given by Eq. (5). In this equation, the fourth-order projection tensors based on the eigenvalues and eigenvectors of the effective stress tensor are noted $\underline{\underline{P}}^+$ and $\underline{\underline{P}}^-$.

$$\underline{\underline{D}} = d_t \underline{\underline{P}}^+ + d_c \underline{\underline{P}}^- \quad (5)$$

The projection tensors allow for a decomposition of the effective stress tensor into positive and negative components. As a result, the tensile damage scalar only affects the positive part of the effective stress tensor whereas the compressive damage scalar only affects the negative part of the effective stress tensor. Hence, the unilateral effect is captured without the need for an additional parameter.

By assumption, damage mechanism is coupled to plasticity in the model. Consequently, there is no specific threshold for damage and the evolution laws for tensile and compressive damage are driven by the accumulated plastic strains (in tension and compression, respectively). Once convergence has been obtained in the plastic return mapping algorithm, update of the damage variables is thus an explicit calculation.

2.4 Transient creep strain

In the numerical calculation process, computation of the increment in transient creep strain is performed at the beginning of the time step (s), separately from the computation of elastic and plastic strains. The Explicit Transient Creep (ETC) Eurocode model, developed at University of Liege for uniaxial relationships [11, 12], is extended to the multiaxial case by adopting the methodology proposed by de Borst and Peeters [13], see Eq. (6). In Eq. (6), f_{ck} is the compressive strength at 20°C; the function $\Phi(T)$ is the transient creep function given in Table 1 and the fourth order tensor $\underline{\underline{H}}$ is given by Eq. (7).

The material parameter γ that appears in Eq. (7) can be taken equal to Poisson's ratio [10], in accordance with Thelandersson's multiaxial data [14].

$$\Delta \underline{\underline{\varepsilon}}_{tr} = \left[\phi \left(T^{(s)} \right) - \phi \left(T^{(s-1)} \right) \right] \left[\underline{\underline{H}} \otimes \left(\underline{\underline{\sigma}}^- \right)^{(s-1)} / f_{ck} \right] \quad (6)$$

$$H_{ijkl} = -\gamma \delta_{ij} \delta_{kl} + 0.5(1 + \gamma) \left(\delta_{ik} \delta_{jl} + \delta_{il} \delta_{jk} \right) \quad (7)$$

Table 1. Transient creep function $\Phi(T)$.

T [°C]	20	100	200	400	600	800
Φ [-]	0.0000	0.0010	0.0018	0.0049	0.0274	0.0733

Accordingly, it is assumed that the process of transient creep does not induce any anisotropy. The negative part of the effective stress tensor is considered in Eq. (6) because, on the one hand, transient creep strain is assumed to occur only in compression and, on the other hand, this mechanism occurs in the undamaged part of the material.

Computation of the transient creep strain increment takes into account the stress-temperature history. Between step (s) and ($s-1$), there is an increment in transient creep strain, which value is computed by Eq. (6), if and only if the three following conditions are fulfilled: the temperature has increased between step (s) and ($s-1$), the negative part of the (converged) effective stress at time ($s-1$) is non-null, and the material is in the ascending branch of the constitutive relationship. It is thus assumed that the positive part of the effective stress tensor does not induce transient creep strain. Besides, the transient creep strain is irreversible at both load and temperature decrease.

2.5 Model parameters

The model contains ten material parameters that can be obtained by three basic tests: uniaxial compression test until failure comprising one unloading-reloading at peak stress, biaxial compression test until peak stress, and uniaxial tension test until failure.

Concrete subjected to elevated temperatures exhibits thermo-mechanical degradation of its properties of strength and stiffness; this effect is taken into account through proper temperature dependency of the

material parameters. The evolution laws of the parameters with temperature are taken from design codes such as the Eurocode, when available, or from experimental data published in the literature.

3 VALIDATION OF THE MODEL

The concrete model has been validated against experimental data. The ability to capture the concrete behaviour for simple loading cases, e.g. uniaxial tension and compression, at both ambient and elevated temperature, is not demonstrated in this paper, due to the need to be concise. However two experimental tests are simulated here to demonstrate the ability of the new concrete model to capture the main phenomena observed in concrete material and the ability to be used for the simulation of structural members in fire. The numerical simulations have been conducted with the software SAFIR [15].

3.1 At ambient temperature

A test of uniaxial tension followed by uniaxial compression on a concrete sample has been simulated using the new concrete model and the results are compared against experimental data [16], see Figure 1. The numerical results obtained with an elastoplastic concrete model are also plotted on Figure 1. The new concrete model succeeds at capturing the development of permanent strains, the degradation of the elastic properties and the stiffness recovery due to crack closure (unilateral effect), whereas elastoplastic models can only capture the development of permanent strains.

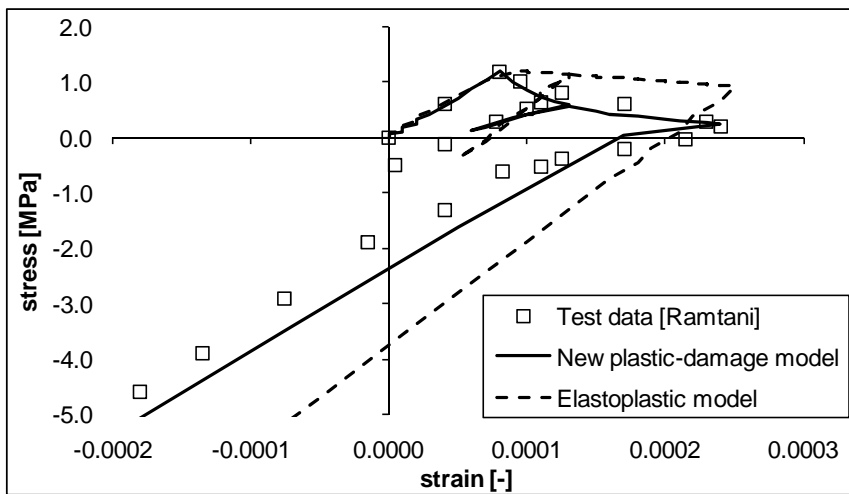


Figure 1. Numerical simulation of a uniaxial tension-compression test.

3.2 At high temperatures

The concrete model is validated at the structural level against experimental results on a reinforced concrete flat slab in fire. The experimental test has been carried out at BRANZ and is described in a paper by Lim et al. [17]. The tested slab is 3.30 m wide by 4.30 m long with a clear span between the supports in the long and the short directions of 4.15 m and 3.15 m, respectively. The slab is simply supported at all four edges with the edges horizontally unrestrained. The flat slab is 100 mm thickness and is reinforced by 200 mm²/m steel reinforcement in each direction. The yield strength of the steel used in the slab is 565 MPa whereas the concrete compressive strength on cylinder is 37 MPa. The concrete cover is 25 mm. The slab was subjected to ISO fire exposure for 3 hours while carrying a constant uniformly distributed live load equal to 3.0 kPa. The slab, which deformed into double curvature, survived the 3 h ISO fire exposure without collapse.

Numerical simulation of this experiment has been performed with the software SAFIR. First, the thermal analysis is conducted to determine the temperature distribution in the concrete slab during fire. The thermal properties for concrete are taken from Eurocode 1992-1-2. Siliceous concrete was chosen, with a density of 2400 kg/m³ and a water content of 72 kg/m³. The emissivity was taken as 0.7 and the coefficient of convection was 25 W/m²K. Temperatures in the slab were recorded during the test at the heated surface, at the unheated surface and at 55 mm depth within the slab. Figure 2 gives the comparison between the temperatures predicted by SAFIR and the measured temperatures at these locations; predicted and measured temperatures agree well.

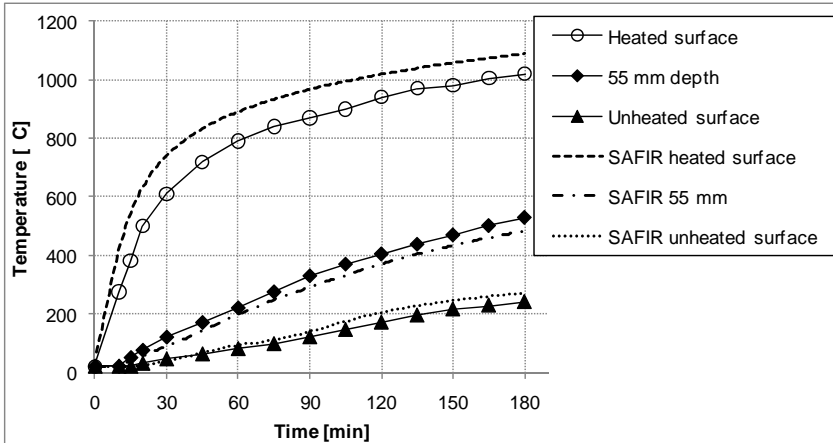


Figure 2. Computed and measured temperatures in the concrete slab.

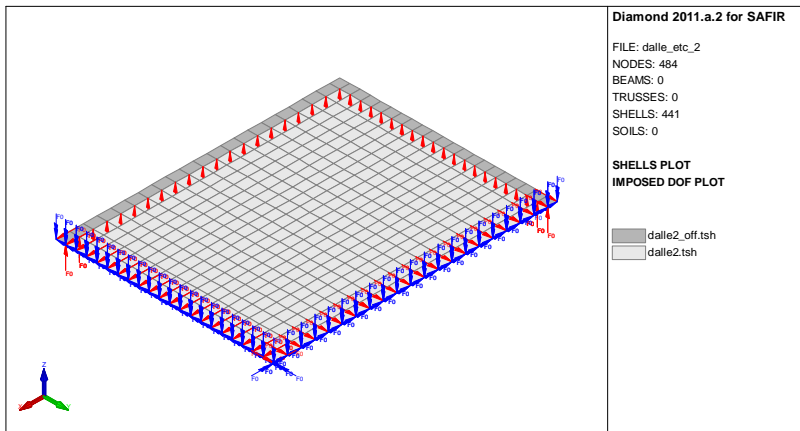


Figure 3. Finite elements model of the flat slab.

Then, the structural analysis is carried out to determine the structural behaviour of the reinforced concrete slab in fire. Shell finite elements are used for modelling the slab. Only a quarter of the full slab was modelled to take advantage of the symmetrical load and support conditions, see Figure 3. The slab is subjected to a uniformly distributed load of 5.4 kPa which represents the sum of the self-weight, 2.4 kPa, and the live load, 3.0 kPa. This applied load of 5.4 kPa corresponds to a load ratio of approximately 0.40 for this slab. The temperature evolution in the slab is given by the SAFIR thermal analysis. The concrete

model presented in this paper is used for the thermo-mechanical behaviour of concrete whereas the material model for the steel reinforcement is taken from Eurocode 1992-1-2. The concrete compressive and tensile strength are 37.0 MPa and 1.0 MPa. The other material parameters of the concrete model are calibrated on elementary tests and no additional calibration is required on the concrete slab.

The predicted and measured vertical deflection at mid-span of the slab in fire is shown in Figure 4. The results of the numerical simulation using the new concrete model agree with the experimental results. The numerical simulation has also been performed using the elastoplastic concrete model currently implemented in SAFIR; however this numerical simulation suddenly stopped before the end of the calculation due to numerical problems in the integration of the concrete law. Numerical robustness is a major issue in concrete modelling and an important requirement in structural fire engineering, as typical applications include large structural elements subjected to complex stress-temperature histories. The present example illustrates the efforts that have been made to ensure the numerical robustness of the new concrete model.

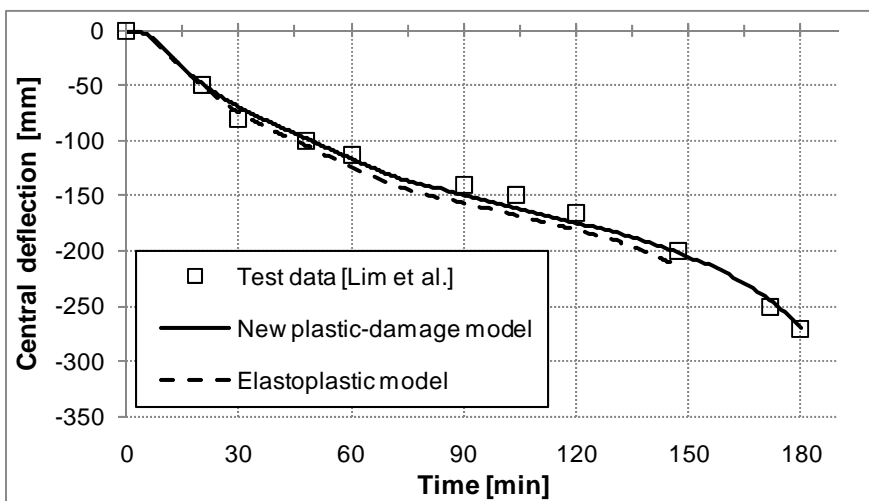


Figure 4. Computed (SAFIR) and measured values of the mid-span vertical deflection.

4 FIRE ANALYSIS – REHABILITATION OF A CONCRETE SHELL ROOF

In the framework of a concrete building rehabilitation, the fire resistance of a shell roof structure was studied for *ICB-Ingénieurs Conseils en Bâtiments*. This practical example is used here to illustrate the ability of the concrete model to be used for structural fire engineering applications.

The SAFIR finite elements model of the structure is shown on Figure 5. Only half of the roof has been modelled with proper symmetry conditions imposed at the edge of the model. As the shell structure has variable thickness, 10 different sections have been used in the model with a thickness varying from 160 mm to 100 mm. The steel tie beams have been modelled using beam finite elements. The concrete shell roof is reinforced in both directions by means of steel reinforcement mesh. The concrete compressive strength is 20 MPa, the reinforcement steel yield strength is 400 MPa and the tie beams yield strength is 235 MPa. The fire analysis of the structure is performed under self-weight loads.

At room temperature, collapse of the structure arises by yielding of the steel tie beams when the applied loads exceed the load bearing capacity of the structure. Yielding of the steel beams leads to decrease in their stiffness; therefore, the horizontal force transmitted by the concrete shell roof is not equilibrated any more by the steel tie beams and the structure collapses. Figure 6 shows the membrane forces in the structure loaded at room temperature. The applied loads are transmitted by the concrete shell

through compressive forces toward the supports and the steel tie beams. The concentration of the forces at the location of the steel tie beams is clearly visible in Figure 6.

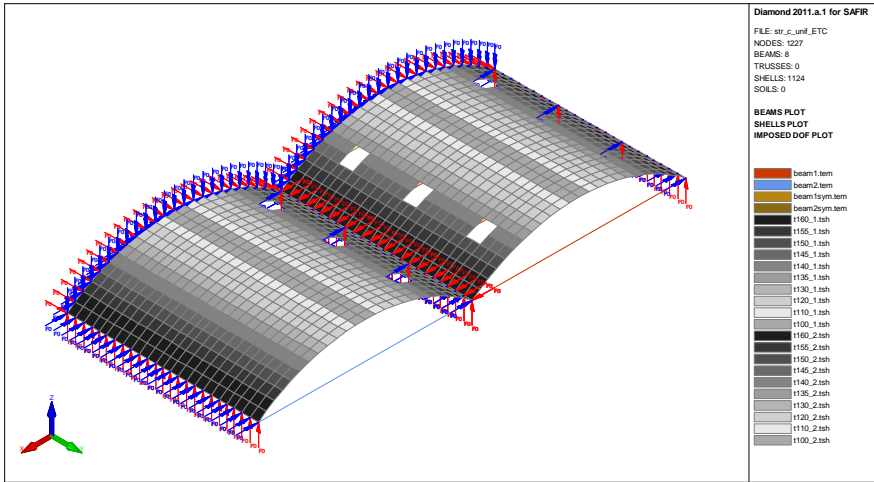


Figure 5. SAFIR structural model of the shell roof subjected to fire.

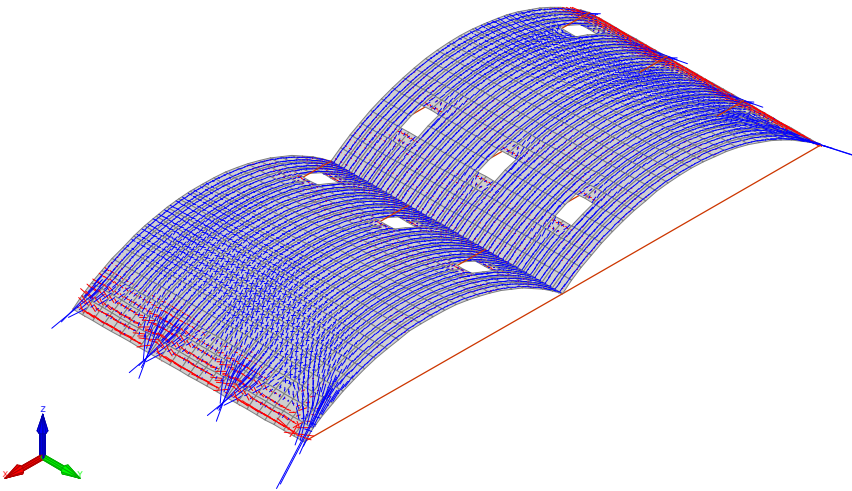


Figure 6. Membrane forces in the structure loaded at room temperature (SAFIR model).

At elevated temperature, the temperature increase in the steel tie beams leads to thermal expansion and decrease in stiffness and strength of these beams. As a consequence, the concrete shells lose their horizontal supports and the structure stiffness decrease. Finally, collapse arises as shown in Figure 7. If the steel tie beams are left unprotected, the fire resistance of the structure is lower than 15 minutes. It is found that collapse arises at a time when the temperature in the steel tie beams reaches approximately 550°C; therefore an efficient way to improve the fire resistance of the structure is to limit the temperature increase in the steel tie beams.

The robustness of the multiaxial concrete model is highlighted by this example as it was possible to simulate the structural behaviour of a large structure in fire until collapse. The consistency of the concrete

model for capturing the behaviour of a complex structure is highlighted by the analysis of the membrane forces distribution on Figure 6.

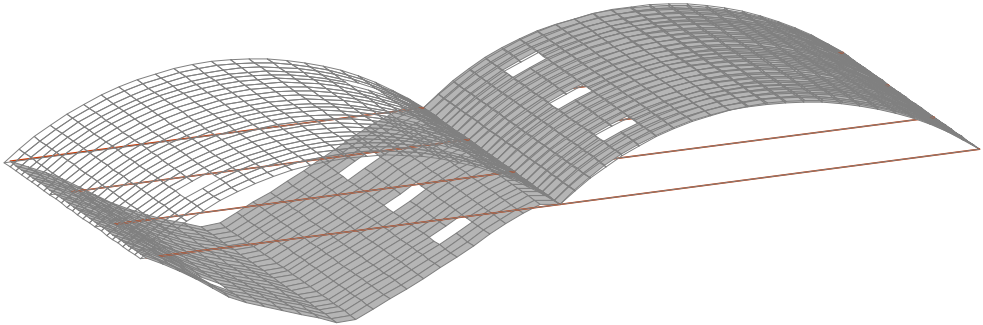


Figure 7. Deformed shape at collapse of a concrete shell roof subjected to fire (SAFIR model).

5 CONCLUSION

A plastic-damage concrete model has been developed and implemented in the software SAFIR for the analysis of structures in fire. The model is able to capture the phenomenological behaviour of concrete at ambient and elevated temperature and is sufficiently robust to be used in large-scale fire analysis. The model parameters can be identified by three elementary tests: uniaxial compression, uniaxial tension and biaxial compression. Transient creep strain is explicitly computed and takes into account the stress-temperature history in the material.

Validation of the new model has been performed against experimental data given in the literature at ambient and elevated temperature. It has been shown that the plastic-damage model accurately captures the unilateral effect due to the closing of the tensile cracks during unloading from tension to compression, whereas elastoplastic models are unable to capture this effect. At the structural level, the model has been validated by comparison against a test carried out at BRANZ on a reinforced concrete flat slab, 3.30 m wide by 4.30 m long, subjected to ISO fire exposure during 3 hours. Finally, the ability of the model to be used in large-scale structural simulations has been illustrated by presenting the fire analysis of a concrete shell roof, in the framework of the rehabilitation of a concrete building.

REFERENCES

- [1] Lee J. and Fenves G., “Plastic-damage model for cyclic loading of concrete structures”, *J. Eng. Mech. ASCE*, 892-900, 1998.
- [2] Grassl P. and Jirasek M., “Damage-plastic model for concrete failure”, *Int. J. Solids Struct.*, 43 (22-23), 7166-7196, 2006.
- [3] Krätzig W. and Polling R., “An elasto-plastic damage model for reinforced concrete with minimum number of material parameters”, *Computers and Structures*, 82, 1201–1215, 2004.
- [4] Carol I., Rizzi E. and Willam K.J., (2001), “On the formulation of anisotropic elastic degradation. II. Generalized pseudo-Rankine model for tensile damage”, *Int. J. Solids Struct.* 38, 519–546, 2001.
- [5] Wu J.Y., Li J. and Faria R., “An energy release rate-based plastic-damage model for concrete”, *Int. J. Solids Struct.*, 43 (3-4), 583-612, 2006.
- [6] Ju J., “Isotropic and anisotropic damage variables in continuum damage mechanics”, *J. Eng. Mech. ASCE*, 116 (12), 2764–2770, 1990.

- [7] Lubliner J., Oliver J., Oller S. and Onate E., “A plastic-damage model for concrete”, *Int. J. Solids Struct.*, 25 (3), pp. 299-326, 1989.
- [8] Ju J., “On energy-based coupled elasto-plastic damage theories: constitutive modeling and computational aspects”, *Int. J. Solids Struct.*, 25, 803-833, 1989.
- [9] Anderberg Y. and Thelandersson S., *Stress and deformation characteristics of concrete at high temperatures: 2 experimental investigation and material behavior model*, Bulletin 54, Lund Institute of Technology, Sweden, 1976.
- [10] Nechnech W., Meftah F. and Reynouard J.M., “An elasto-plastic damage model for plain concrete subjected to high temperatures”, *Engineering structures*, 24 (5), 597-611, 2002.
- [11] Gernay T. and Franssen J.-M., “Consideration of transient creep in the Eurocode constitutive model for concrete in the fire situation”, *Structures in Fire – Proceedings of the Sixth International Conference*, V. Kodur, J.-M. Franssen (eds.), DEStech Publications, Lancaster, 784-791, 2010.
- [12] Gernay T., “Effect of transient creep strain model on the behaviour of concrete columns subjected to heating and cooling”, *Fire Technology*, 48 (2), 313-329, 2012.
- [13] de Borst R. and Peeters P., “Analysis of concrete structures under thermal loading”, *Computer methods in applied mechanics and engineering*, 77, 293-310, 1989.
- [14] Thelandersson S., “Modelling of combined thermal and mechanical action in concrete”, *ASCE J. Engrg. Mech.*, 113, 893-906, 1987.
- [15] Franssen J.-M., “SAFIR, A thermal/Structural Program for Modeling Structures under Fire”, *Eng J A.I.S.C.*, 42, 143-158, 2005.
- [16] Ramtani S., “Contribution à la modélisation du comportement multiaxial du béton endommagé avec description du caractère unilatéral”, thesis: Univ. Paris VI E.N.S. Cachan, Paris, 1990.
- [17] Lim L., Buchanan A., Moss P. and Franssen J.-M., “Numerical modelling of two-way reinforced concrete slabs in fire”, *Engineering Structures*, 26, 1081-1091, 2004.

RELIABILITY ANALYSIS OF STEEL PERIMETER COLUMNS UNDER FIRE

Negar Elhami Khorasani*, Maria E. Garlock* and Paolo Gardoni**

* Graduate Student – Princeton University, Associate Professor – Princeton University
e-mails: nelhami@princeton.edu, mgarlock@princeton.edu

** Associate Professor - University of Illinois at Urbana-Champaign
e-mail: gardoni@illinois.edu

Keywords: Reliability, Perimeter column, Fire, Probabilistic demand, Probabilistic capacity.

Abstract. *This paper provides a probabilistic study of a typical perimeter column under fire. Random variables in demand and capacity models are identified and their corresponding probabilistic models are developed. In particular, probabilistic models are developed for the mechanical and thermal properties of steel and properties of insulating materials. Using probability distributions for selected variables and Monte Carlo Simulation, an estimate of the probability of failure of the perimeter column is determined. The methodology can be easily used in other structural evaluations.*

1 INTRODUCTION

For years, the available design procedures for fire have been largely based on perspective codes or performance-based guidelines with deterministic input variables; however, performance-based design provides the designer with more flexibility and opportunity for higher level of safety at lower costs. Therefore, the fire engineering community has started to move towards performance-based design procedures in which the probabilities of achieving specified performance levels are specified. In order to satisfy the performance targets, a probabilistic analysis should be carried out and uncertainties at various levels of design and analysis of the structure should be considered. Although in recent years, regulatory authorities have started to put together the available methodologies, there is still no document that describes the step-by-step procedure for the probabilistic analysis of a structural member under fire.

This paper proposes a probabilistic framework to evaluate the performance of a perimeter column under fire. As part of the probabilistic analysis, it is required to consider uncertainties in the input variables of the formulation. Therefore, probabilistic models for the fire load density, thermal and mechanical properties of steel and properties of insulating materials are developed and presented. The new probabilistic model presented in this paper is specific to perimeter column members of office buildings; however, given the developed probabilistic models for input variables, the procedure can be easily extended to other structural members.

The procedure has two main steps: (1) Demand model: in which randomness in the fire load density is modeled and the fire temperature-time evolution is obtained; (2a) Capacity Model-Thermal Analysis: in which randomness in thermal properties of steel and insulating materials is modelled and the steel temperature-time evolution is obtained and (2b) Capacity Model-Structural Analysis: in which randomness in mechanical properties of steel is modelled and a structural analysis that considers the thermal loads is performed. In this paper, Monte Carlo Simulations are employed to perform the probabilistic evaluation of the structural member.

The paper first explains the developed framework. The procedure is then applied to a prototype perimeter column in an office building. The analysis is performed on both protected and unprotected columns. Probability of failure and time to failure of the column for each case is calculated.

2 DEMAND MODEL

During a fire event, compartment temperatures depend mainly on three factors: (1) geometric characteristics of the compartment, (2) properties of the boundary of enclosure and (3) fire load density. All three groups of variables have uncertainties related to them; however, Hurley [1] indicates that thermal properties of the enclosure linings are not likely to change and the results are not highly sensitive to those variables. On the other hand, value of the fire load is one of the most important factors that influences temperatures reached during a fire event and a great deal of uncertainty exists in estimating the design value of fire load.

The basis for developing temperature-time curves for this paper is the parametric curves of Eurocode1 (EC1) [2], which provide a closed-form deterministic solution. The Eurocode provides suggestive deterministic values for the characteristic fire load density q_{fk} , which is one of the random variables in the EC temperature-time curve solution. The fuel loads have large uncertainties associated with them, therefore surveyed data for fire loads are used to develop a probabilistic model for q_{fk} . For this purpose, the available fire load survey results were studied [3, 4, 5, 6] and compared with the values suggested in the Eurocode. Details of this study can be found in [7]. Based on the survey results, a new probabilistic fire load is calculated in this paper considering the room usage and room floor area. First, two categories of rooms are considered: (1) light-weight which include general, clerical, lobby and conference rooms; and (2) heavy-weight which include filing, storage and libraries in an office. Using the survey data, the deterministic Eurocode model is then modified by application of a methodology proposed by Gardoni et al. [8].

Gardoni et al. [8] developed a Bayesian-based procedure that takes available deterministic models and systematically creates a probabilistic model that accounts for uncertainties such as model errors (in case of inaccurate model in which variables are missing), measurement errors or statistical uncertainty. In this procedure correction terms, which include variables that are thought to be missing, are added to the deterministic model. Unknown parameters in the correction terms are calculated based on the actual measured data and a Bayesian probability formulation. The final probabilistic model includes the deterministic model, the correction terms and a term that defines the model error.

Eqs. 1 and 2 present the corrected models for fire load density, where q_{fk} is the design value taken from EC1 (MJ/m^2) and A_f is the compartment floor area (m^2). The last term in both equations represent the model error in which values of 0.5712 (in Eq. 1) and 0.5708 (in Eq. 2) represent the standard deviation of the model error and ϵ is the random variable with standard normal distribution (i.e., normal distribution with zero mean and unit variance). These models include the influence of room usage and size. Details of the model derivation are explained in [7].

$$\text{Light-weight compartments: } q_{fk,corrected} = \exp\left[\ln(q_{fk}) + 0.3178 - 0.0047(A_f \times 10.76) + 0.5712\epsilon\right] \quad (1)$$

$$\text{Heavy-weight compartments: } q_{fk,corrected} = \exp\left[\ln(q_{fk}) + 1.6188 - 0.0081(A_f \times 10.76) + 0.5708\epsilon\right] \quad (2)$$

Figs. 1 and 2 show a comparison of fire loads from survey results $q_{fk,data}$ with predicted fire loads by the Eurocode ($q_{fk,Eurocode}$) using the “uncorrected” values (existing Eurocode methodology q_{fk}) and the “corrected” values $q_{fk,corrected}$, Eqs. 1 and 2. The 1:1 lines drawn on the plots represent a perfect match between the data and Eurocode. The corrected models for both light and heavy weight categories demonstrate an improvement for fire load values when compared to the data from the survey results. Fig. 1 shows that the correction improves the accuracy of the prediction in particular for $q_{fk} < 1500 \text{ MJ/m}^2$, the correction does not work as well for higher values of q_{fk} ; however, q_{fk} greater than 1500 MJ/m^2 is highly improbable for a light-weight category. Similarly, Fig. 2 shows that for extremely large loads in the range of 4000 MJ/m^2 , the model is not well fitted, but again such large loads are highly improbable for a room in an office building.

To perform probabilistic analysis, it is assumed that q_{fk} has a lognormal distribution with mean of 420 MJ/m² and standard deviation of 126 MJ/m² calculated based on the statistics provided in the EC1 [2]. A randomly generated value for q_{fk} is then corrected based on Eqs. 1 and 2. Finally, EC1 closed-form solution [2] is applied to calculate the temperature-time curve.

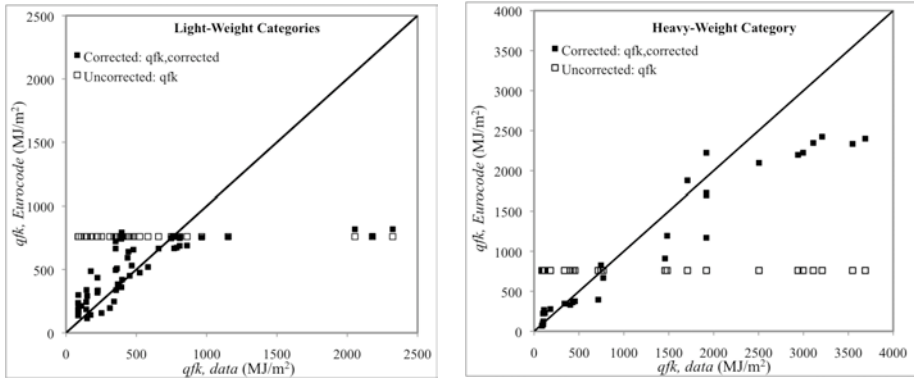


Figure 1. Corrected fire load density compared to Eurocode predictions

3 CAPACITY MODELS

The lumped mass procedure described in [9] is a simple closed-form procedure that can be used to determine the temperature in a steel section assuming uniform temperature through the depth. When a temperature gradient is expected (e.g., for columns on the perimeter of a building), a closed-form methodology developed by Quiel and Garlock [10] will be used to calculate the gradient.

Beam-columns are members that are designed to carry both axial load (P) and bending moment (M). In general, the structural capacity of a beam-column member is controlled by one of the three limit states: full section yielding, global buckling and local buckling. Focus of this paper will be on the first limit state for wide-flange (WF) sections with thermal gradient under combined P and M . Closed-form solutions for predicting the structural response of a perimeter column, developed by Quiel and Garlock [10], are based on the model shown in Fig. 2 and Eq. 3.

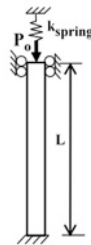


Figure 2: Column model for Quiel and Garlock’s model [10]

$$P = P_o + (\epsilon_{total} - \epsilon_o) k_{spring} \quad L \geq P_o \quad (3)$$

where ϵ_o represents the initial strain experienced by the column, L is length of the column, ϵ_{total} is comprised of the mechanical strain (ϵ_σ) plus the thermal strain (ϵ_T), which equals the coefficient of

thermal expansion times the change in the fiber's temperature. The total strain is adjusted by ε_o so that only upward displacements can induce an increase in P . Finally, P_o represents the initial applied axial load experienced by the column and the vertical spring k_{spring} in Fig. 2 represents the resistance to vertical thermal expansion. A detailed description of this methodology for every time-step in the analysis is given by [10].

As part of the probabilistic analysis, random variables of the capacity model by Quiel and Garlock [10] are identified and uncertainties in the variables are included in the analysis. The random variables in the capacity model can be grouped into three categories: (1) Mechanical properties of steel (F_y and E_y), (2) Thermal properties of steel (thermal conductivity k_s , specific heat c_s and thermal strain α) and (3) Properties of insulating materials (thermal conductivity k_i , specific heat c_i and density ρ_i).

Properties of steel and insulating materials change with temperature. Predicting such changes at high temperatures is not an easy task. A similar approach, which was used to obtain the probabilistic fire load density q_{fR} is again employed to include the uncertainties in mechanical and thermal properties of steel and fire protection materials. It should be noted that the three groups of random variables are typical to any method of thermal analysis and the probabilistic material properties developed in this paper can be used in other types of thermal analysis of structural members.

3.1 Properties of Steel at High Temperatures

A recently published report by the National Institute of Standards and Technology (NIST) [11] provides a comprehensive study on the yield strength of steel (F_y) at various temperatures and for various types of steel. The report includes the available data in the literature as well as results of another study by NIST on structural steel properties as part of the World Trade Center (WTC) collapse investigation. The NIST report proposes the following closed form solution for the yield strength of steel at various temperatures ($F_{y,T}$), which is a continuous exponential function:

$$k_{y,T} = \frac{F_{y,T}}{F_y} = \exp \left[\frac{-1 \left(\frac{T^*}{590} \right)^{5.708}}{2} - \frac{1 \left(\frac{T^*}{919} \right)^{1.0}}{2} \right] \quad \text{where } T^* = T - 20 \quad (4)$$

The deterministic NIST Model is modified based on the collected data following Gardoni's methodology (Table 1). Fig. 3 shows the available data and F_y variation at different temperatures. The measured data used for the analysis were collected and reported in the NIST study [11]. In the figure, the proposed envelope is \pm one standard deviation of the proposed mean value, which reflects a smaller dispersion of data at higher temperatures. At every temperature, a value within the envelope can be randomly selected for the value of F_y in which standard deviation of the model error is included.

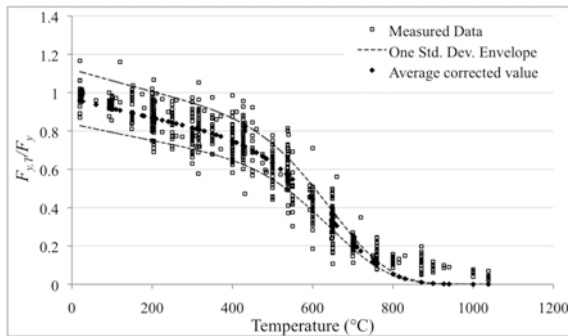


Figure 3: Proposed probabilistic model for $F_{y,T}$ based on the deterministic model by NIST

A similar procedure is also applied to obtain a probabilistic model for the Modulus of Elasticity E_y . The corrected solution (in Table 1) is based on the measured data collected by Kodur et al. [12] and the

deterministic model in Eq. 5 provided by ASCE in Structural Fire Protection Manual [13]. Fig. 4 shows the corrected model and one standard deviation envelope. Random values within the envelope can be selected at all temperatures. The plot shows that values of E_y at any temperature are limited to the value of E_y at the ambient temperature. Dispersion of measured data for E_y is relatively large, especially at larger temperatures. The proposed envelope considers the scatter of data and is optimized over all data points.

$$k_{E,T} = \frac{E_{y,T}}{E_y} = \left\{ \begin{array}{l} 1 + \frac{T}{2000 \ln\left(\frac{T}{1100}\right)} \quad T \leq 600^\circ \text{C} \\ \frac{690 - 0.64 \times T}{T - 53.5} \quad T > 600^\circ \text{C} \end{array} \right\} \quad (5)$$

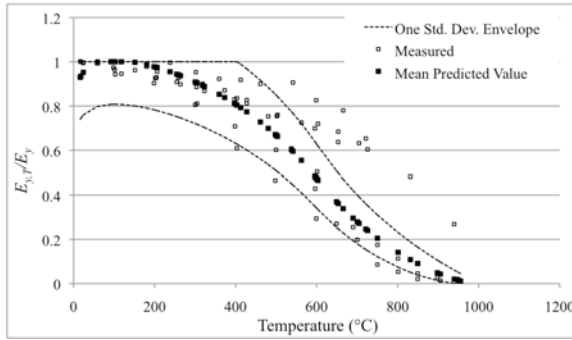


Figure 4: Proposed probabilistic model for $E_{y,T}$ based on the deterministic model by ASCE

Finally, deterministic Eurocode3 (EC3) [14] solutions for thermal conductivity k_s , specific heat c_s and thermal strain $\alpha=\Delta/l$ (Eqs. 6,7 and 8) are corrected based on the measured data from [12] and following Gardoni's methodology. In the case of thermal conductivity (Eq. 6), for temperature values less than 800°C , as the temperature increases, thermal conductivity decreases with a linear relationship. For temperature values above 800°C , the number of measured data is limited and the predicted thermal conductivity in the corrected model varies slightly between 30 and 35 W/m K. The specific heat of steel increases with temperature until a large spike forms at around 750°C (Eq. 7). This is due to a phase change that occurs in steel at which point steel absorbs considerable energy. Finally, the thermal strain increases linearly with temperatures up to 750°C , at which point the phase change occurs (Eq. 8). The thermal strain stays almost constant at temperatures between 750°C and 800°C and starts to increase again at above 800°C .

$$\begin{aligned} \text{For } T < 800^\circ \text{C} \quad k_s &= 54 - 3.33 \times 10^{-2} T \\ \text{For } T \geq 800^\circ \text{C} \quad k_s &= 27.3 \end{aligned} \quad (6)$$

$$\begin{aligned} \text{For } T < 600^\circ \text{C} \quad c_s &= 425 + 7.73 \times 10^{-1} T - 1.69 \times 10^{-3} T^2 + 2.22 \times 10^{-6} T^3 \\ \text{For } 600 \leq T < 735^\circ \text{C} \quad c_s &= 666 + \frac{13002}{738 - T} \\ \text{For } 735 \leq T < 900^\circ \text{C} \quad c_s &= 545 + \frac{17820}{T - 731} \\ \text{For } 900 \leq T \leq 1200^\circ \text{C} \quad c_s &= 650 \end{aligned} \quad (7)$$

$$\begin{aligned} \text{For } T < 750^\circ\text{C} \quad \frac{\Delta l}{l} &= 1.2 \times 10^{-5} T + 0.4 \times 10^{-8} T^2 - 2.416 \times 10^{-4} \\ \text{For } 750 \leq T \leq 860^\circ\text{C} \quad \frac{\Delta l}{l} &= 1.1 \times 10^{-2} \\ \text{For } 860 < T \leq 1200^\circ\text{C} \quad \frac{\Delta l}{l} &= 2 \times 10^{-5} T - 6.2 \times 10^{-3} \end{aligned} \tag{8}$$

Table 1 provides the probabilistic closed form solutions for thermal and mechanical properties of steel at various temperatures. In each equation, ε is a random variable with the standard normal distribution. The table shows that the corrected equations involve either an exponential function or a square root function. These two functions are used to stabilize the variance in the measured data.

Table 1: Probabilistic formulations for thermal and mechanical properties of steel at high temperatures

Property	Basis	Proposed Model*
Yield Strength	NIST [11]	$k_{y,T,corrected} = \exp[\log(k_{y,T}) - 0.0421 + \varepsilon \times 0.1464]$
Elastic Modulus	ASCE[13]	$k_{E,T,corrected} = [(\text{sqrt}(k_{E,T})) + 7.0597 - 0.0002 \times T - 7.1932 \times T^{0.0051} + \varepsilon \times 0.1042]^2$
Thermal Conductivity	EC3 [14]	$k_{s,corrected} = \exp[\ln(k_s) - 0.0831 + 0.0003 \times T + \varepsilon \times 0.0626]$
Specific Heat	EC3 [14]	$c_{s,corrected} = \exp[\log(c_s) - 0.0272 + 0.0001 \times T + 0.4555 / (0.9989 - T) + \varepsilon \times 0.061]$
Thermal Strain	EC3 [14]	$\alpha_{corrected} = \alpha - 0.0039 + \varepsilon \times 0.0495$

* where T is the Temperature and ε is the standard normal variable.

3.2 Properties of Protecting Materials at High Temperatures

The report by NIST [15] provides results of a study on passive fire protection for buildings, in particular the WTC buildings, and presents test results for properties of insulating materials at high temperatures (k_i , c_i , ρ). Three sprayed fire-resistive materials (SFRMs) were tested. Properties of these insulating materials varied from type to type; therefore an average of measured data was used as the deterministic predicting values and it was left to Gardoni’s methodology to generate the probabilistic closed-form solutions relating temperature to the material property under study, as summarized in Table 2.

It was observed that density of insulating materials decreases linearly with increasing temperature up to 600°C. This is expected since with an increase in temperature, volume increases and consequently density decreases. Very limited data points were available for temperatures above 600°C but this data showed an increase in material density. The sudden change in behavior of material with a few available data points was hard to explain. However, this might have been due to measurement errors at high temperatures. The data points above 600°C were not included in the analysis and the corrected model decreases linearly at high temperature values. Also, the specific heat and thermal conductivity of insulating material increase linearly as temperature increases.

Table 2: Probabilistic formulations for thermal properties of insulating materials at high temperatures

Property	Proposed Model
Density	$\rho_i = \exp[\ln(258.9) + 0.0716 - 0.0003 \times T + 0.0656 \times \varepsilon]$
Thermal Conductivity	$k_i = 0.17705 - 0.1438 + 0.0003 \times T + 0.0493 \times \varepsilon$
Specific Heat	$c_i = 1.384 - 0.3178 + 0.0008 \times T + 0.892 \times \varepsilon$

4 PROBABILISTIC PERFORMANCE

The column under study is based on an actual perimeter column from One Meridian Plaza (1MP) steel structural frame, which suffered a multi-story fire in 1991 [16]. The column section is W14x314 and is positioned such that it takes moment on the strong axis.

4.1 1MP Demand Model

The Eurocode compartment fire model, modified by the procedure explained in Section 2, is used to approximate the probabilistic fire time-temperature curve. Floor plans of 1MP show that a typical floor has closed offices on the perimeter with open offices arranged in the interior area [16]. The offices are not aligned with the position of the columns; therefore, the compartment size in Eqs. 1 and 2 is selected as the tributary area of the column. Gypsum plaster was assumed as the compartment lining material. The compartment fire load density was corrected with the light-weight category equation (Eq. 1). Heavy-weight categories (Eq. 2) are derived for smaller room areas (such as storage and etc.), therefore when the equation is used to correct larger compartments, it results in smaller fire load densities. Also, it is assumed that the compartment has automatic water extinguishing system, automatic fire detection and smoke detector, safe access routes, regular fire fighting devices and smoke exhaust system.

Based on the above assumptions, Fig. 5 shows the Probability Distribution Function (PDF) for the maximum fire temperature in the compartment and the temperature-time curve for the highest, lowest, and mean maximum temperature obtained considering 18000 random realization of EC1 formulation [2]. The average maximum temperature is 788 °C and the highest maximum temperature obtained is 1161 °C with standard deviation of 92.8. When compared to a deterministic study by [16], the estimated maximum temperature for the same column was calculated to be 1000 °C. According to [16] this was consistent with the estimated maximum temperature reached in the WTC towers. It should be noted that [16] assumed a decay rate of 5°C per minute to be consistent with the observations during the actual 1MP fire. The temperature-time plot in Fig. 5 assumes a decay rate of 5°C per minute.

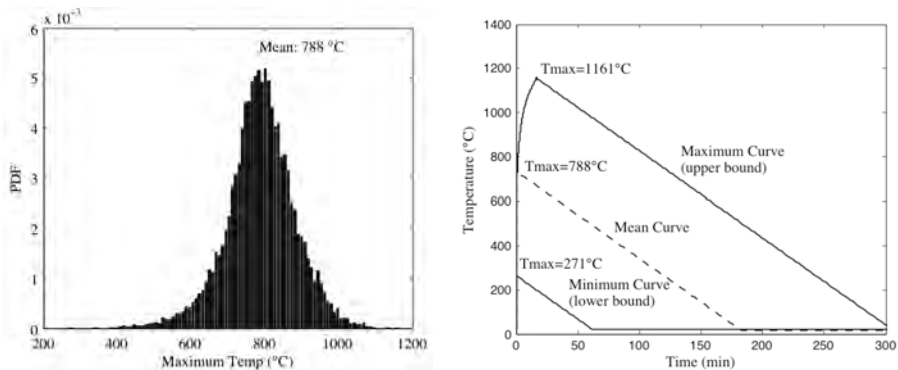


Figure 5: (Left): Probability Distribution Function of the maximum fire temperature, (Right): The temperature-time curve for the highest maximum fire temperature

4.2 1MP Capacity Model

The methodology is applied to the W14x314 column with and without fire protection materials. Regulations require all columns to be protected, but the fire protection materials may be dislodged due to events such as blast or impact or even by the loss of cohesion over time. Therefore the unprotected cases are not unrealistic and represent the conservative envelope of possible behavior. On the other hand, the protected cases, which assume that the fire protection material is flawless and remains intact for the duration of the fire, represent the upper limit of all possible behaviors [16].

After defining the demand model, the procedure explained in Section 3 is applied to perform structural and thermal analysis of the W14x314 column. Properties of the insulating materials for the protected column are also defined based on the probabilistic models explained in Section 3.

Given the developed probabilistic demand and capacity models, Monte Carlo Simulations (MCS) are used to calculate the probability of failure for a prototype perimeter column with and without fire protecting materials. Fig. 6 shows the column thermal analysis for the highest obtained temperature. Results show that in the case of the unprotected column, the steel temperature passes 1000 °C, at which point, the value of yield strength and modulus of elasticity of steel is reduced by more than 90%. On the other hand, the steel temperature in the protected column is always less than 250 °C. This indicates that in the case of protected column, the steel yield strength is not reduced and the modulus of elasticity is reduced no more than 10%.

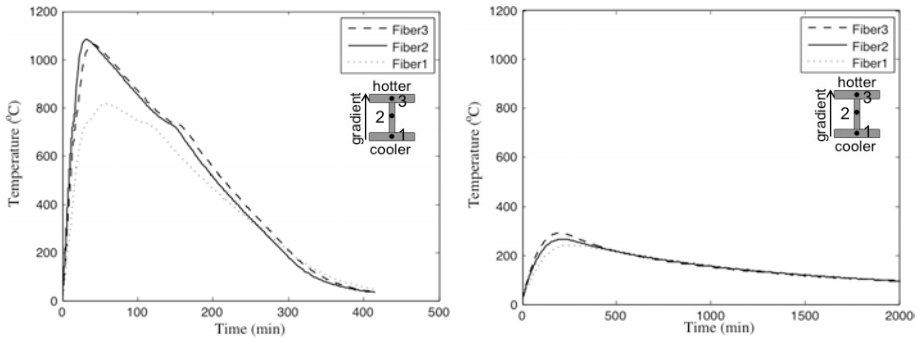


Figure 6: Steel temperature-time curve for the unprotected case (left) and the protected case (right)

The MCS results show that probability of failure for the unprotected column is 0.108 (considering 18000 realizations) and the protected column will not fail. Fig. 7 shows the Cumulative Distribution Function (CDF) for the failure time of the unprotected column. The plot shows that if the unprotected column fails, the average failure time for the column is 43.5 min while 50% of the time the column fails at about 38 min. This figure also shows that, for example, if the column fails, about 80% of the time it will fail in less than 60 min and only 20% of the time it fails in less than 30 min. Tables 3 and 4 compare results of the probabilistic analysis with those of a deterministic study by [16]. Comparing the mean failure time from the probabilistic analysis with the deterministic results shows that deterministic results are relatively conservative.

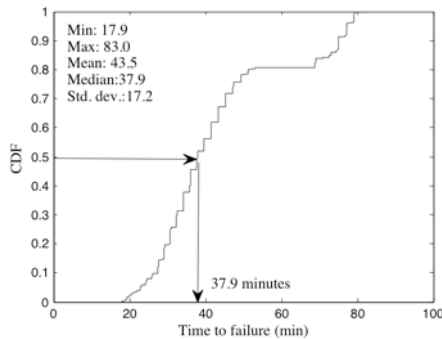


Figure 7: The cumulative distribution function for the failure time of the unprotected case

Table 3: Statistics of the failure time for unprotected column

Probabilistic Analysis (Matlab)	Time to Failure (minutes)				
	Minimum	Maximum	Mean	Median	Std. Dev.
	17.9	83.0	43.5	37.9	17.2

Table 4: Calculated failure time for the unprotected column based on Quiel [16]

	Finite Element	Deterministic Analysis (Matlab)
Time to Failure (minutes)	34	32

Fig. 8 shows the path of P/P_y and M/M_y of the unprotected column over time and the plastic P-M capacity envelope at the failure time. The plot corresponds to a case with failure time close to the mean failure time (43.5 minutes). The plot indicates that for the unprotected case, the combined P and M reaches the plastic capacity envelope at about 41.5 minutes. As time passes and temperature increases, P_y decreases implying that P/P_y increases, explaining why the path of P/P_y and M/M_y is moving up.

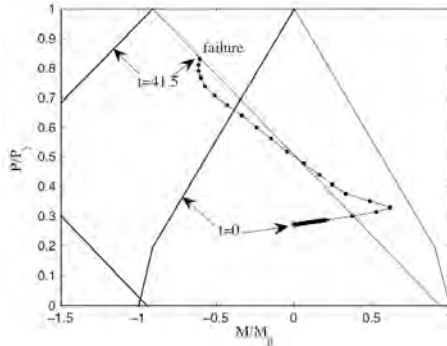


Figure 8: Normalized P-M performance for the unprotected case

5 CONCLUSION

The paper provided a probabilistic framework to evaluate performance of steel perimeter columns in high-rise buildings under fire. As part of the framework, a Bayesian approach was used to develop probabilistic models for fire load density, thermal and mechanical properties of steel and properties of insulating materials. The proposed probabilistic models can be used to evaluate the thermal performance of any structural member. Results of the Monte Carlo Simulations showed that the maximum temperature achieved in the compartment under study was slightly higher than 1100 °C, at which point, the value of yield strength and modulus of elasticity of steel is reduced by more than 90%. Given the probability distribution of fire temperatures, the mean failure time for the unprotected perimeter column in an office building was about 43 minutes and 80% of the time the column failed in less than an hour. On the other hand, the protected column did not fail.

REFERENCES

- [1] Hurley, M., "Design Fire Scenarios", *Proceedings of NIST-SFPE Workshop for Development of a National R&D Roadmap for Fire Safety Design and Retrofit of Structures*, NISTIR 7133:107-117, 2004.

- [2] European Committee for Standardization (CEN), *Actions on structures – Part 1-2: General actions – actions on structures exposed to fire*, Eurocode 1, Brussels, Belgium, 2002.
- [3] Culver, C., *Survey results for fire loads and live loads in office buildings*, National Bureau of Standards, Washington, D.C., 1976.
- [4] Kumar S. and Kameswara Rao C.V.S., “Fire loads in office buildings”, *Journal of Structural Engineering*, 123(3), 1997.
- [5] National Fire Protection Association (NFPA), “Validation of Methodologies to Determine Fire Load for Use in Structural Fire Protection – Final Report”, *The fire protection research foundation – research in support of the NFPA mission*, Carleton University, May 2011.
- [6] VKF and AEAI, “Note Explicative De Protection Incendie – Evaluation en vue de la determination de la grandeur des compartiments coupe-feu”, *Vereinigung Kantonalder Feuerversicherungen (VKF) and Association des établissements cantonaux d’assurance incendie (AEAI)*, 2007.
- [7] Elhami-Khorasani, N., Garlock M. and Gardoni, P., “A Probabilistic Assessment of Fire Load Model and Parametric Time-Temperature Curves”, *Manuscript in preparation*.
- [8] Gardoni, P., Der Kiureghian, A., and Mosalam, K.M., “Probabilistic Capacity Models and Fragility Estimates for Reinforced Concrete Columns based on Experimental Observations”, *Journal of Engineering Mechanics*, 128(10), 2002.
- [9] Buchanan A.H., *Structural Design for Fire Safety*, John Wiley & Sons Ltd, Chichester, 2001.
- [10] Quiel, S., and Garlock, M., “Closed-Form Prediction of the Thermal and Structural Response of a Perimeter Column in a Fire”, *The Open Construction and Building Technology Journal*, 4, 64-78, 2010.
- [11] Luecke, W.E., Banovic, S. and McColskey, J.D., “High-Temperature Tensile Constitutive Data and Models for Structural Steels in Fire”, *NIST Technical Note 1714*, U.S. Department of Commerce, National Institute of Standards and Technology, November 2011.
- [12] Kodur, V., Dwaikat, M. and Fike, R., “High-Temperature Properties of Steel for Fire Resistive Modeling of Structures”, *ASCE Journal of Materials in Civil Engineering*, 22(5), 2010.
- [13] Lie, T.T., “Structural Fire Protection: Manual of Practice”, *ASCE Manuals and Reports of Engineering Practice*, No. 78. American Society of Civil Engineers, 1992.
- [14] European Committee for Standardization (CEN), *General Rules – Structural Fire Design – EN1993-1-2*, Eurocode 3, Brussels, Belgium, 2005.
- [15] Carino, N.J., Stranes M.A. Gross, J.L., Yang, J.C. and et al., *Federal Building and Fire Safety Investigation of the World Trade Center Disaster – Passive Fire Protection*, NIST NCSTAR 1-6A, September 2005.
- [16] Quiel, S., *Behavior and Analysis of Fire-Exposed Steel Beam-Columns that Develop Thermal Gradients*, Dissertation for the Degree of Doctor of Philosophy, Princeton University, 2009.

RESIDUAL FRACTURE ENERGY OF CONCRETE SUBJECT TO HIGH TEMPERATURES

YU Jiangtao, YU Kequan, LU Zhoudao

Research Institute of Engineering & Disaster Reduction, Tongji University, Shanghai, China
e-mail: yujiangtao@tongji.edu.cn, zjzykq@163.com

Research Institute of Engineering & Disaster Reduction, Tongji University, Shanghai, China
luzhoudao@163.com

Keywords: high temperatures; fracture energy; brittleness; weight loss

Abstract. *The investigations on the residual Mode-I fracture behaviors of concrete subject to high temperatures were carried out in present paper. The test specimens were exposed to temperatures varying from 65°C to 600°C with their weight losses monitored. The wedge splitting method was employed to obtain the Load-CMOD (crack mouth opening displacement) curves of post-fire specimens from which the fracture energy G_F was calculated. It was demonstrated that G_F sustained a hold-increase-decrease tendency with T_m . Furthermore, the characteristic length l_{ch} as a brittleness parameter was calculated and shared a similar tendency with G_F , which meant these two parameters had the same function to be the index of brittleness for post-fire concrete. Finally the fracture and brittleness parameters could be closely related to the ultimate weight loss.*

1 INTRODUCTION

To date, much attention has been paid to the fracture properties at room temperature, whereas limited tests focuses on the fracture behaviours subject to high temperatures. As well as mechanics properties (including strength and stiffness), the fracture energy is a very useful fracture toughness parameter for designing concrete structures, manufacturing high-performance concrete materials and analyzing structure behaviours subject to various high-temperatures environments.

Based on the three-point bending and eccentric compression tests on both dry and saturated concrete specimens heated up to 200°C, Bazant and Pratt[1] reported G_F tests. Three different (out geometrically similar) notched specimen sizes were applied and the maximum loads to infinite size were extrapolated by means of the Bazant size-effect-law. Hot tests are performed at 4 temperatures, 20°C, 65°C, 120°C and 200°C on the ordinary concrete with limestone aggregate (w/c=0.6). The fracture energy derived by means of size-effect-law decreases monotonically with temperature to about 50% at 200°C compared with its value at room temperature. For saturated specimens tested in hot water the decreasing effect is even stronger.

Baker[2], B.Zhang[3] conducted the three-point bending tests on the notched preheated beams, and found that the fracture energy bore an increase-decrease tendency with increasing temperatures. Their experimental result at lower temperature is contradictory to that of Bazant and Pratt. Nielsen and Bicanic [4] also measured the residual fracture energy of normal-strength gravel concrete and high-performance basalt concrete subject to high temperatures and obtained a similar increase-decrease tendency. B.Zhang [5] investigated the effects of heating temperatures up to 450°C and testing conditions (hot and cold) on the fracture energy of high-performance concrete, and found that the fracture energy generally sustained a decrease-increase tendency with the heating temperatures for hot concrete but a hold-increase-decrease tendency for the cold concrete. However, Felicetti et al. [6] did not get a conclusive result when measured fracture energy of concrete specimens preheated to 500°C.

In mainland, China, Gai-Fei Peng [7] investigated the residual fracture energy of fiber-toughened concrete exposed to high temperatures ranging from 200°C to 800°C. The experiment showed that fiber concrete had much higher fracture energy than plain concrete and the residual fracture energy increased significantly until a transition point was reached at 400°C, thereafter it decreased continuously up to 800°C.

This article presents experimental results on temperature dependency of the fracture energy G_F by conducting wedge splitting tests on the notched preheated specimens. The complete load-crack mouth opening displacement curve (P - $CMOD$) was obtained. The residual fracture energy G_F of specimens after being exposed to elevated temperatures T_m was calculated and its relationship with T_m was identified. Furthermore, the ultimate weight loss w of test specimens after cooling was monitored and could be used to further study the fracture behaviour of concrete, thus the relationships between G_F and w were established. Finally, the characteristic length l_{ch} as a brittleness parameter was also calculated.

2 THE EXPERIMENTAL DETAILS

Overall 50 concrete specimens with the same dimensions 230×200×200mm were prepared in the test. All the specimens had a precast notch of 80mm height and 3mm thickness by placing a piece of steel plate into the molds prior to casting. The concrete mix ratios were listed in table 1, with common Portland cement mixed medium sand and 16mm graded coarse aggregate. The slump of the concrete was controlled between 90mm and 150mm. Meanwhile, 24 standard concrete prisms with dimensions 150×150×300mm were also casted to determine the residual compressive strength and residual Young's modulus of post-fire specimens. Each wedge splitting specimens and prisms were embedded a thermal couple for temperature control. After 60 days of natural curing, compressive test were carried out at ambient temperature, given the compressive strength of 35.5 MPa, Young's modulus of 32.8 GPa.

Table 1 Concrete mix design

Contents	Cement	Sand	Coarse aggregate	water
Quantities:kg/m ³	230	791	1010	185
Ratio	1.00	3.44	4.39	0.80

Nine heating temperatures range from 65°C to 600°C ($T_m=65^\circ\text{C}$, 120°C, 200°C, 300°C, 350°C, 400°C, 450°C, 500°C, 600°C) were adopted with ambient temperature for reference. Since it was recognized that the fracture behaviour measurements were generally associated with significant scatter, for each temperature 5 repetitions were performed. An electric furnace with net dimensions 150×150×300mm was employed for heating. The initial furnace temperature was set 100°C higher than the specified temperature T_m considering the undesirable thermal conductivity of concrete. When the temperatures in the concrete approached target value (approximately 80% of the final temperature), the furnace temperature was turned down to T_m . Finally, when the designated T_m was reached, the furnace was shut down and the specimens were naturally cooled for 7 days prior to test.

A closed-loop servo controlled hydraulic jack with the maximum capacity of 1000kN was employed to conduct the wedge splitting test. Two Clip-on Extensometers were suited at the mouth and the tip of crack respectively to measure the crack mouth opening displacement (CMOD) and crack tip opening displacement (CTOD). To obtain the complete load-deflection curve (P-CMOD), the test rate was at a fixed rate of 0.4mm/min, hence it approximately took 20 mins to complete a single test of specimens subject to less than 300°C, and 30 mins for beyond 300°C. In the compressive test, the post-fire prisms were first prepressed to 0.5MPa and then unload to zero; thereafter it was compressed to failure at a fixed rate of 1mm/min.

2.1 The experimental phenomena

In the cases of loading test on specimens exposed to relatively lower temperatures (20°C~200°C), the splitting load generally reached its peak with no visible crack observed. However, once the first crack initiated, the splitting load dropped dramatically. The crack propagated vertically and rapidly to the

bottom of specimen along with the precast notch. The fracture surfaces obtained at these temperatures were granular in character. The cohesion of the grains with the cement paste was high at those temperatures, which caused grain cracks in numerous sites. At temperatures above 200°C, it was obvious that more than one cracks branching from the tip of notch and competing to form the final fracture. The fracture surfaces tended to be more tortuous and less cracks across the grains were observed, pulling from the grains out of the cement paste occurred. It could be attributed to degradation of cohesion between the coarse aggregates and mortar paste. Above 400°C complete destruction took place in the cement paste, resulting in the propagation of a fracture through the cement paste. The test phenomenon of post-fire specimens was shown in figure 2.

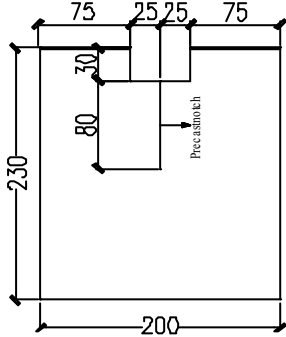


Fig. 1 The geometry of specimens



Fig. 2 The testing phenomenon of post-fire

2.2 The residual compressive strength f_{pr}

Figure 3 shows that the residual compressive strengths generally sustained a three-stage decrease-recovery-decrease tendency with T_m . It first sharply decreased at 100°C, and then slightly recovered up to 300°C, thereafter it continuously decreased again. f_{pr} decreased from 31.41 MPa at the room temperature to 22.91 MPa at 100°C, with a sudden drop of 8.5 MPa or 27% and gradually recovered to 26.34 MPa at 300°C. Thereafter it continuously decreased to 16.74 MPa at 600°C with a net drop of 14.67 MPa or 48%. The f_{pr} - T_m curve was expressed by using the following combined quadratic and linear relationship as:

$$f_{pr} = 0.0003 T_m^2 - 0.1218 T_m + 33.153 \quad r = 0.951 \quad 20^\circ\text{C} < T_m < 300^\circ\text{C} \quad (1)$$

$$f_{pr} = -0.0377 T_m + 38.112 \quad r = 0.908 \quad 300^\circ\text{C} < T_m < 600^\circ\text{C} \quad (2)$$

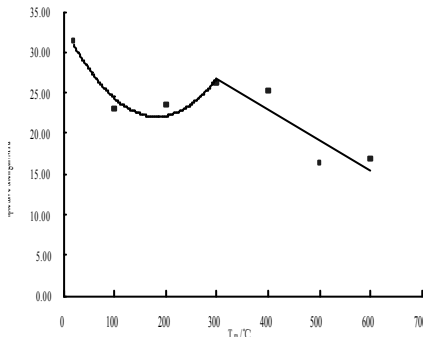


Figure 3 the residual compressive strength f_{pr} with T_m

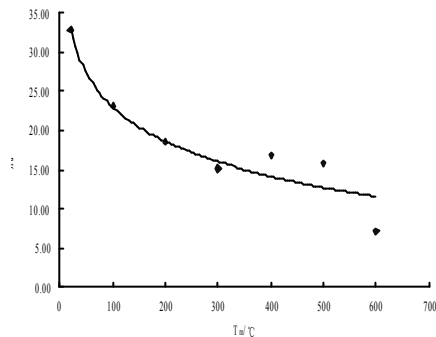


Figure 4 The residual Young's modulus E with T_m

2.3 The Residual Young's modulus E

Figure 4 shows that the residual Young's modulus of the concrete, E , decreased monotonously with the increasing heating temperatures. It could be explained by the fact that higher heating temperatures always caused higher moisture evaporation from the concrete reduced the stiffness of cement paste and aggregates. Young's modulus E continuously decreased from 32.80 GPa at room temperature to 15.1GPa at 300°C, and finally 7.18 GPa at 600°C with a significant loss of 25.62 GPa or 78%. The E - T_m curve could be expressed using a logarithmic equation as follows with the correlation coefficients $r=0.951$.

$$E = -6.3311\ln(T_m) + 52.093 \quad 20^\circ\text{C} < T_m < 600^\circ\text{C} \quad (3)$$

2.4 The Weight Loss w_u for different heating temperatures T_m

Figure 3 shows that w_u increased tri-linearly with T_m . At first, w_u increased rapidly with T_m up to 200°C, thereafter it kept increasing at a small, steady rate with T_m ranging from 200°C to 450°C, and above 450°C, w_u increased quickly again. In the first stage, w_u was due to the evaporation of the macroscopic capillary water in the concrete which could be regarded as a predominantly physical process. When T_m was varied between 200°C and 450°C, w_u was mainly due to the evaporation of gel water. The smaller evaporation rate was attributed to the difficulty for gel water to escape from the gel pores with small sizes. This stage can be described as a physico-chemical process due to the evaporation of mesoscopic gel water. In the third stage, w_u was mainly attributed to the dehydration and decomposition of hardened cement paste and aggregates, representing a predominantly chemical process due to evaporation of microscopic, chemically combined water. Typically, w_u was 7.01% for 200°C, 7.18% for 450°C and 8.52% for 600°C.

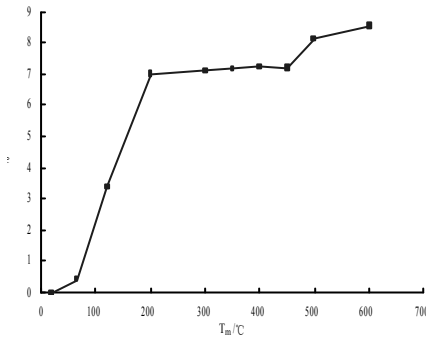


Fig. 5 The weight loss of specimens with T_m

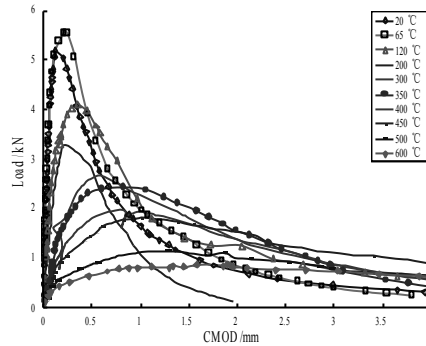


Fig. 6 Load vs. CMOD curves of specimens with T_m

2.5 The Complete Load-Deflection (P-CMOD) curve

To determine the fracture energy of concrete for varied heating scenarios, the complete load-displacement curves (P-CMOD curves) are crucial. A complete load-displacement curve can represent a number of findings: the initial stiffness, the ultimate load capacity, the displacements at cracking and failure, hardening and softening properties, etc. Even its geometric shape can reflect the toughness and brittleness in some way: When the P-CMOD curve is tall and spiky, the concrete can be described as brittle. When it is short and extended, the concrete is less brittle and softer.

Figure 6 presents typical complete load-displacement curves for different heating temperatures up to 600°C from the wedge splitting tests on the concrete specimens. A curve obtained for unheated specimens at the room temperature is also plotted in the figure as a reference. It shows that the ultimate load P_u generally decreased significantly with increasing temperatures T_m while the crack mouth opening displacement (CMOD) increased monotonously with T_m . The initial slope of ascending branches decreased with heating temperatures and the curve became gradually shorter and more extended. Figure 7 shows P_u slightly increased from 5.198 kN at room temperature to 5.563 kN at 65°C. It then continuously

decreased to 4.09 kN at 120°C, with a sudden drop of 1.47 kN, 3.287 kN at 200°C, 1.957 kN at 400°C, and 0.884 kN at 600°C, with a final drop of 83%. Meanwhile, the critical CMOD corresponding to the ultimate load P_u was increased from 0.120 mm at 20°C to 0.212 mm at 65°C, and 0.357 mm at 120°C, 0.213 mm at 200°C, 1.032 mm at 400°C, and 1.908 mm at 600°C with a final increase of 15 times. From figure 6 and 7, it was concluded that the concrete became less brittle with the increasing heating temperature. The P_u^T/P_u^0 and $CMOD_c^0/CMOD_c^T$ curve could be expressed by the following exponential equations:

$$P_u^T/P_u^0 = 1.2865e^{-0.0033 T_m} \quad r=0.965 \quad 200^\circ C \leq T_m \leq 600^\circ C \quad (4)$$

$$CMOD_c^0/CMOD_c^T = 1.0498e^{-0.0045 T_m} \quad r=0.9965 \quad 200^\circ C \leq T_m \leq 600^\circ C \quad (5)$$

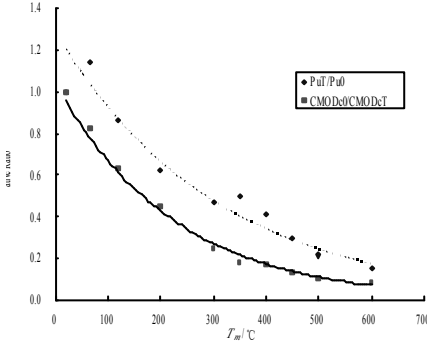


Fig. 7 P_{max} and $CMOD_c$ of specimens varied with T_m

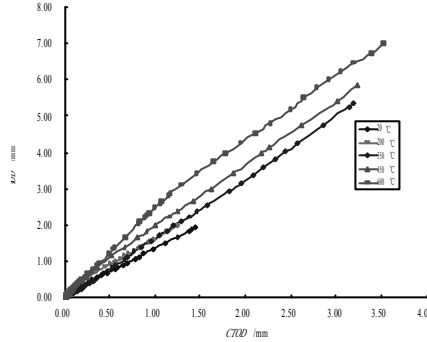


Fig. 8 the relationship of $CMOD_c$ and $CTOD_c$ with T_m

2.6 The relationship between CMOD and CTOD

Figure 8 presents that the crack mouth opening displacement (CMOD) and the crack tip opening displacement (CTOD) was in a linear relationship for all heating scenarios. The lines slope increased with T_m , that meant the CMOD increased with heating temperatures corresponding to the same CTOD, the heating effect made the concrete softer and ductile.

3 FRACTURE ENERGY G_F

The fracture energy, G_F , defined as the total energy dissipated over a unit area of the cracked ligament, was obtained on the basis of the work done by the force (the area under a load-displacement curve in wedge splitting test on a centrally notched specimens). The fracture energy G_F was calculated based on the following equation

$$G_F = \frac{\int_0^{\Delta_0} P(\Delta)d\Delta}{B(H - a_0)} \quad (6)$$

Here, Δ_0 is the ultimate displacement when the specimen is broken, $P(\Delta)$ presents corresponding load to Δ , B, H are the thickness and height of the specimen, a_0 is the initial notch depth of the test specimen.

3.1 Fracture energy for different heating temperatures T_m

Figure 9 presents the residual fracture energy G_F from wedge splitting test on the concrete specimens. The magnitude of G_F at each heating scenarios was significantly discrete, whereas the average value sustained a hold-increase-decrease tendency. G_F first kept constant up to 105°C at approximately 400N/m, and then it suddenly decreased to 317N/m at 200°C with a net drop of 80N/m or 20%. Thereafter it

increased with T_m to 438N/m at 300°C, and 488N/m at 450°C. Generally, for temperatures under 200°C appeared not to induce much thermal damage to concrete, the cracking resistance was kept constant. Heating temperatures between 200°C and 450°C helped to further hydration of the cement paste and strengthen the interface with the aggregates, and the fracture surface tended to be more tortuous than those observed at lower temperatures, so more energy were dissipated in these specimens. However, higher heating temperatures would cause more microcracks, dehydration and decomposition and degrade the resistance. After 450°C, G_F continuously decreased with T_m and eventually drop down to 233N/m at 600°C, which was much smaller than the reference value at room temperature. The G_F - T_m curve could be expressed by using the following cubic equation as:

$$G_F = -0.000007T_m^3 + 0.0053T_m^2 - 0.8258T_m + 409.89 \quad 200^\circ\text{C} \leq T_m \leq 600^\circ\text{C} \quad (7)$$

with correlation coefficient $r=0.82$.

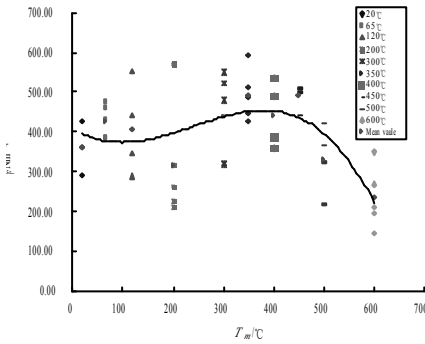


Fig.9 The fracture energy of specimens with T_m

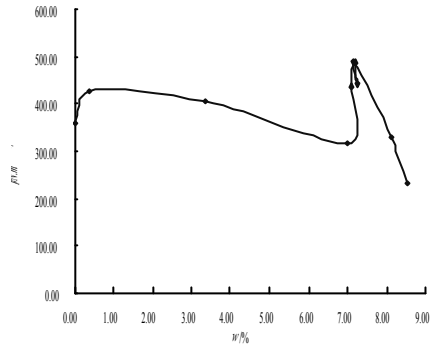


Fig.10 The fracture energy of specimens with w_u

3.2 Fracture energy against w_u

Figure 10 depicted the relationship of G_F with the ultimate weight loss w_u . The reference fracture energy at room temperature, corresponding to the zero weight loss, was also included. Generally, the G_F - w_u shared the same three-stage hold-increase-decrease tendency as G_F - T_m . That is, at the first stage, G_F changed very little up to 200°C when the transition point w_{u1} reached. The damage to the concrete caused by the vapour pressure during heating eliminated the toughening effect associated with the weight loss. At the second stage, G_F rapidly increased until another transition weight loss w_{u2} was reached. In this study, w_{u2} was 7.18% corresponding to 450°C. This stage was accompanied by the evaporation of gel water which promoted the further hydration of the cement paste and strengthened the interface with the aggregates, and the fracture surface tended to be more tortuous. In the final stage, G_F decreased monotonously with w_{u3} , mainly due to the dehydration and decomposition of hardened cement paste and aggregates.

4 CONCRETE BRITTLENESS

Brittleness is commonly understood to be the tendency for a material or a structure to fracture abruptly before significant irreversible deformation occurs. Different brittleness of toughness parameters are used to assess concrete brittleness, including energy-based and complex parameters. Hillerborg et al. [9] proposed the characteristic length l_{ch} as a brittleness parameter:

$$l_{ch} = \frac{G_F E_C}{f_t^2} \quad (8)$$

Where f_t is the tensile strength of the concrete, which could be replaced by f'_t . The value of f'_t would take from literature [8] also done by authors. Because l_{ch} includes a combination of energy, stiffness and strength parameters, it is regarded as a synthetic brittleness parameter. The larger the value of l_{ch} , the less brittle of tougher the concrete is.

4.1 l_{ch} against T_m

Figure 11 presents that l_{ch} sustained a hold-increase-decrease tendency with T_m . l_{ch} generally kept a constant value until a transition point was reached at 200°C, then it increased rapidly with heating temperatures up to 450°C, the ultimate l_{ch} value reached 3.79 m, which held 5.05 times larger than that at room temperature. Thereafter, l_{ch} decreased continuously with heating temperatures to 600°C, with final l_{ch} value of 2 m or a net increase of 288% to the room temperature. The l_{ch} - T_m curve was expressed by using the following combined quadratic and linear relationship as:

$$l_{ch} = 0.00005 T_m^2 - 0.0096 T_m + 1.1041 \quad r = 0.992 \quad 20^\circ\text{C} \leq T_m \leq 450^\circ\text{C} \quad (9)$$

$$l_{ch} = -0.0113 T_m + 8.957 \quad r = 0.988 \quad 450^\circ\text{C} \leq T_m \leq 600^\circ\text{C} \quad (10)$$

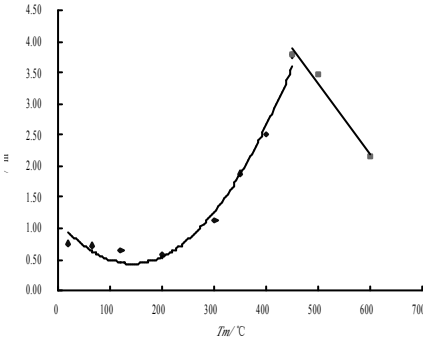


Fig. 11 The characteristic length of specimens with T_m

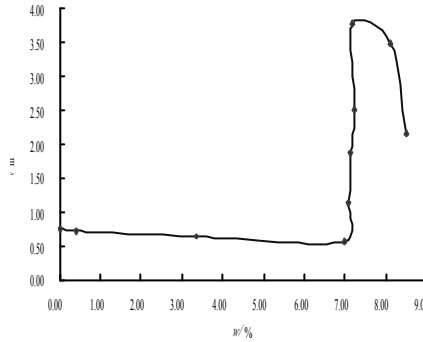


Fig. 12 The characteristic length of specimens with w_u

4.2 l_{ch} against w

Figure 10 shows the relationship between l_{ch} and w_u which shared the same tendency as l_{ch} - T_m . Generally, the weight loss due to heating helped to toughen the concrete so as to reduce the brittleness. The value of l_{ch} first kept constant even slightly decreased with w until a transition w_{t1} was reached at 200°C, and thereafter increased sharply with T_m until another threshold value w_{t2} reached. Finally, from 450°C to 600°C, l_{ch} decreased continuously with the final value at 600°C was 4 times than that at room temperature.

The brittleness of concrete was greatly dependent on the composition and structure of the concrete. When $w < w_{t1}$, the evaporation of capillary water only slightly changed l_{ch} or brittleness, because it did not cause many structural changes during this physical process. When $w_{t1} < w < w_{t2}$, l_{ch} increased very dramatically with w_u , mainly owing to the evaporation of gel water and chemical bound water and even decomposition. These chemical reactions induced a lot of microcracks so as to increase the toughness significantly. However when $w > w_{t2}$, due to the dehydration and decomposition of hardened cement paste and aggregates, the concrete suffered significant damages that the capacity of resisting fracture is consequently decreased. This result was a little different from the conclusions of literatures [3] and [4]. Furthermore, the l_{ch} - T_m curve shared the same tendency with G_f - T_m curve, which meant these three parameters have the same function to be the index of brittleness for post-fire concrete.

5 CONCLUSIONS

The effects of heating temperatures on the residual fracture properties of concrete, including the strength parameter (compressive strength f_{pr}), the stiffness parameter (Young's modulus E), the fracture energy parameter (G_F) and finally the brittleness parameter (the characteristic length l_{ch}) have been investigated by conducting wedge splitting tests on the pre-notched heated specimens. The following conclusions could be drawn:

(a) The residual compressive strengths f_{pr} generally sustained a three-stage decrease-recovery-decrease tendency with T_m , it finally decreased by 16.74 MPa or 48% at 600°C.

(b) The residual Young's modulus of the concrete, E , decreased monotonously with the increasing heating temperatures T_m . Higher heating temperatures always caused higher moisture evaporation from the concrete reduced the stiffness of cement paste and aggregates and it finally decreased to 7.18 GPa at 600°C with a net drop of 78%.

(c) The weight loss, as a continuous non-reversible process, steadily increased in a three-stage tendency, including the predominantly physical process, physico-chemical process, chemical process,

(d) The complete load-displacement (P-CMOD) curves were obtained from the wedge splitting test on specimens. The heating temperatures significantly influenced the shapes of curves. High temperatures generally lower the peak and extended the curves, so that decreased the brittleness of the concrete.

(e) The magnitude of fracture energy G_F at each heating scenarios had a significant discreteness, whereas the average value sustained a hold-increase-decrease tendency with increasing heating temperatures. The G_F changed with weight loss w_w in a similar way. At first, the evaporation of capillary water at low heating temperatures only slightly affected G_F , and then the evaporation of gel water significantly increased the fracture energy. Thereafter the dehydration and decomposition of hardened cement paste and aggregates reduced the fracture energy greatly.

(f) The characteristic length l_{ch} sustained a hold-increase-decrease tendency with T_m , and a combined quadratic and linear relationship showed a good coincidence with variation tendency. Meanwhile, the relationship between l_{ch} and w_w changed in a similar way as l_{ch}/T_m . This result was a little different from the existed literatures. Furthermore, the $l_{ch}-T_m$ curve shared the same tendency with G_F-T_m curve, which meant these two parameters have the same function to be the index of brittleness for post-fire concrete.

REFERENCES

- [1] Bazant Z.P. and Prat P.C: Effect of temperatures and humidity on the fracture energy of concrete. *ACI Materials Journals*, 1988, 85, No.4, p. 262.
- [2] Baker G: The effect of exposure to elevated temperatures on the fracture energy of plain concrete. *RILEM Materials and Structures*, 1996, 29, No.190, p.383.
- [3] Zhang B., Bicanic N., Pearce C.J. and Balabanic G.: Residual fracture properties of normal and high-strength concrete subject to elevated temperatures. *Magazine of Concrete Research*, 2000, 52, No.2, p.123.
- [4] Nielsen C.V. and Bicanic N.: Residual fracture energy of high-performance and normal concrete subject to high temperatures. *RILEM Materials and Structures*, 2003, 36, No.262, p.515.
- [5] B. Zhang and N. Bicanic: Fracture energy of high-performance concrete at high temperatures up to 450°C: the effects of heating temperatures and testing conditions (hot and cold). *Magazine of Concrete Research*, 2006, 58, No.5, p.277.
- [6] FELICETTI R., GAMBAROVA P.G., ROSATI G.P., CORSI F. and GIANNUZZI G. Residual mechanical properties of high-strength concretes subject to high-temperature cycles. *4th International Symposium on Utilizations of High Strength/High Performance Concrete*, Paris, 1996, 579-588.

- [7] Gai-Fei Peng, Wen-Wu Yang, Jie Zhao, Ye-Feng Liu, Song-Hua Bian, Li-Hong Zhao. Explosive spalling and residual mechanical properties of fiber-toughened high-performance concrete subject to high temperatures. *Cement and Concrete Research* (36) 2006, 723-727.
- [8] Yu Jiangtao. Experimental and Theoretical Research on Damage Assessment of Reinforced Concrete Member after Fire. Shanghai: Tongji University, 2007.
- [9] HILLERBORG A., MODEER M. and PETERSON P.E. Analysis of crack formation and crack growth in concrete by means of fracture mechanics and finite elements. *Cement and Concrete Research*, 1976, 6, No. 6, 773-782.

RESIDUAL AND POST-COOLING STRESS-STRAIN CURVES FOR TRADITIONAL AND SELF-COMPACTING CONCRETE

Emmanuel Annerel* and Luc Taerwe*

* Magnel Laboratory for Concrete Research, Department of Structural Engineering, Faculty of Engineering & Architecture, Ghent University
e-mails: emmanuel.annerel@ugent.be, luc.taerwe@ugent.be

Keywords: fire, concrete, load ratio, post-cooling storage, stress-strain model, Sargin

Abstract. *This paper presents a model for the stress-strain relationship of both traditional and self-compacting concrete after exposure to fire. The model is based on the Sargin model which is used in EN1992-1-1 and takes further into account the load ratio maintained during heating, the temperature level and the storage period after cooling. Therefore, a test program is conducted with variation of the load ratio up to 30% of the initial strength, temperatures up to about 500°C and storage periods of 0 days (immediately tested after cooling) or about 50 days in moist air.*

1 INTRODUCTION

After a fire, concrete structures behave in most cases very well. Although damage to the structure will occur, it is of economic interest to assess the structures after fire and calculate the remaining load bearing capacity. For this purpose, an adequate understanding of the post-cooling behaviour is necessary, as well as mechanical models which take into account the changes due to heating and storage.

When concrete is heated, its strength decreases gradually with temperature, which is influenced by the applied load (beneficial effect) and the heating rate (possible thermal shock for fast heating). Also the cooling rate has an influence. Fast cooling such as quenching into water introduces a thermal shock with possible additional strength losses of up to 30-35% as found for the concretes studied in this paper [1]. Furthermore, during post-cooling storage in moist air, further strength losses appear due to the formation of new portlandite which is accompanied by a 44% internal expansion. For the concretes studied in this paper, strength losses of up to 20-30% are observed around 7 days of storage [1]. Finally, the strength may slowly recover due to hydration of unhydrated cement particles, resulting in a possible strength recovery of up to 10% as found for the studied concretes [1].

The proposed residual and post-cooling stress-strain models in this paper, take these effects into account by testing the remaining strength immediately after cooling (residual strength) and after a storage period in moist air for about 50 days. A full description of the test results is given in [2].

2 TEST PROGRAMME

A traditional vibrated concrete (TC) and a self-compacting concrete (SCC) are considered in this paper. Both concretes are made with OPC and siliceous aggregates. The specimens are cast with a diameter of 106 mm and a height of 320 mm. These specimens are cured for 28 days at 20±1°C and >90% R.H., followed by storage at 60% R.H. and 20±1°C for about 29 months. The concrete composition and the initial mechanical properties are given in Table 1.

Table 1. Concrete mix and initial mechanical properties.

	SCC	TC
sand [kg/m ³]	782	640
gravel 2-8 mm [kg/m ³]	300	525
gravel 8-16 mm [kg/m ³]	340	700
Portland cement I 52.5 [kg/m ³]	400	350
water [kg/m ³]	192	165
limestone powder [kg/m ³]	300	-
superplasticizer [l/m ³]	2.90	-
W/C [-]	0.48	0.47
density at 28 days [kg/m ³]	2344	2374
f _{ccub150,28d} [N/mm ²]	65.0	55.9
f _{ccil106x320,900d} [N/mm ²]	63.3	46.0
E _{ccil106x320,900d} [N/mm ²]	38500	37500

The concrete specimens are heated to different target temperatures (about 175°C, 300°C and 500°C respectively) under external load ratios of 0, 20 and 30% of the initial strength. The target temperatures are chosen as follow: at 175°C a total loss of the free moisture content is assumed, 300°C corresponds to the onset of strength loss and 520°C is related to the decomposition of portlandite. Each target temperature and load condition is tested for each concrete twice, except for the load ratio 0% for TC which is only tested once. The heating rate equals 5°C/min, which is slow heating compared to ISO 834 standard fire, but corresponds to accidental heating according to [3]. To reach uniform temperature inside the concrete, the maximum temperature is held constant for 750 minutes. After heating, the specimens are allowed to cool slowly in a closed oven at a heating rate of about 0.5°C/min. When the specimens are cooled down to ambient temperature, the load is removed and the specimens are stored at moist air (60% R.H. and 20±1°C) for 7 weeks (TC) and 8 weeks (SCC). The specimens are tested for Young's modulus after this post-cooling storage period, whereas a second series of cylinders heated without load is also tested for Young's modulus immediately after cooling. Notice that these conditions are beneficial for the compressive strength (slow heating and slow cooling: no thermal shock), except for the post-cooling storage that may result in an additional strength loss of up to 20-30%.

Preliminary tests show a high spalling risk for both TC and SCC samples. This spalling results in the total loss of the specimen, which makes it impossible to test the remaining mechanical properties. Also to avoid damage to the test setup, the specimens are dried to reduce the spalling risk. The TC specimens are pre-dried for 1 day, while the SCC samples are pre-dried for 1 week (till constant mass).

3 TEST SETUP

Figure 1 illustrates the test setup, consisting of an electric split oven, a loading system, a specially designed displacement device and a PC unit (Vishay S5000 data acquisition system). The oven is positioned on top of welded HE 200 M profiles and a concrete block. A hydraulic jack placed in a loading frame transfers the load via a series of X105 Cr Mo 17 steel cylinders towards a concrete specimen inside the oven. The hydraulic jack is connected to a pump and an accumulator. Once the required pressure is reached in the hydraulic jack, the pump is disconnected. From then on, the pressure is maintained by means of the accumulator, which is filled with oil to about half of its volume and the other half with nitrogen gas.

To protect the oven from damage as a consequence of possible spalling, the concrete cylinders are placed in a surrounding steel tube. The gap at the top opening of the oven is filled during the heating test with high temperature glass fibres insulation.



Figure 1. Test setup: (1) loading frame, (2) hydraulic jack, (3) series of X105 Cr Mo 17 steel cylinders, (4) tube around concrete specimen, (5) HE 200 M profiles, (6) concrete block, (7) accumulator, (8) oven.

4 RESIDUAL AND POST-COOLING STRESS-STRAIN MODEL

After the heating test and the applied subsequent post-cooling storage, the concrete cylinders are tested for Young's modulus (displacement controlled test according to NBN B 15-203: 0.002 mm/s). As a basis for a residual and post-cooling stress-strain model, the analytical formulation as proposed by Sargin and Handa [4] and given in EN 1992-1-1 is used. The model is modified by defining the different parameters as temperature dependent, given in Eq. 1 by the subscripts T.

$$0 < |\varepsilon| < |\varepsilon_{cu1,T}| : \frac{\sigma_T}{f_{cm,T}} = \frac{k \cdot \eta - \eta^2}{1 + (k-2) \cdot \eta} \quad \text{and} \quad \eta = \varepsilon / \varepsilon_{c1,T} \quad (1)$$

where ε , occurring strain; $\varepsilon_{c1,T}$, strain corresponding to the compressive strength of heated concrete; $\varepsilon_{cu1,T}$, nominal ultimate strain of heated concrete; σ , occurring stress (N/mm²); $f_{cm,T}$, compressive strength of heated concrete (N/mm²).

Initially the k-parameter is the ratio of the tangent modulus at the origin to the secant modulus taken at the compressive strength, while in the new model it is a function of temperature found from non linear regression. Besides this k-parameter, Table 2 also presents the ratios of the temperature altered strain and compressive strength to their initial properties as function of temperature. This process is repeated for each concrete, load ratio and post-cooling storage period.

Figure 2 shows the recorded stress-strain curves of TC in comparison with the values found from the modified Sargin model, respectively for load ratios of 0% and 0 days of storage (a), 0% and 49 days of storage (b), 20% and 49 days of storage (c), 30% and 49 days of storage (d). Adequate agreement is found between both, especially in the lower temperature region (<300°C). At 520°C, a larger difference is observed between the model and the measured curve for some cases. Similar relationships are found for the SCC specimens.

Table 2. Formulas for the parameters of the modified Sargin model

Storage [days]	α [%]	k [-]	$\varepsilon_{c1,T} / \varepsilon_{c1,20^\circ\text{C}}$ [-]	$f_{cm,T} / f_{cm,20^\circ\text{C}}$ [-]
<i>Traditional concrete TC</i>				
0	0	$k = -1.468\text{E-}03.T + 1.718$ $\varepsilon_{c1,T} / \varepsilon_{c1,20^\circ\text{C}} = 9.658\text{E-}06.T^2 - 2.607\text{E-}03.T + 1.034$ $f_{cm,T} / f_{cm,20^\circ\text{C}} = -8.873\text{E-}07.T^2 - 6.320\text{E-}04.T + 9.886\text{E-}01$		
49	0	$k = -6.576\text{E-}04.T + 1.342$ $\varepsilon_{c1,T} / \varepsilon_{c1,20^\circ\text{C}} = 1.190\text{E-}08.T^3 - 6.000\text{E-}04.T + 1.012$ $f_{cm,T} / f_{cm,20^\circ\text{C}} = 4.355\text{E-}07.T^2 - 1.675\text{E-}03.T + 1.035$		
49	20	$k = -8.216\text{E-}04.T + 1.448$ $\varepsilon_{c1,T} / \varepsilon_{c1,20^\circ\text{C}} = 7.450\text{E-}09.T^3 - 7.000\text{E-}04.T + 1.014$ $f_{cm,T} / f_{cm,20^\circ\text{C}} = -5.113\text{E-}07.T^2 - 1.090\text{E-}03.T + 1.018$		
49	30	$k = -7.682\text{E-}04.T + 1.403$ $\varepsilon_{c1,T} / \varepsilon_{c1,20^\circ\text{C}} = 1.220\text{E-}08.T^3 - 1.150\text{E-}03.T + 1.024$ $f_{cm,T} / f_{cm,20^\circ\text{C}} = -8.272\text{E-}07.T^2 - 1.013\text{E-}03.T + 1.025$		
<i>Self-compacting concrete SCC</i>				
0	0	$k = -2.489\text{E-}04.T + 1.161$ $\varepsilon_{c1,T} / \varepsilon_{c1,20^\circ\text{C}} = -2.990\text{E-}06.T^2 + 2.635\text{E-}03.T + 9.308\text{E-}01$ $f_{cm,T} / f_{cm,20^\circ\text{C}} = -5.877\text{E-}06.T^2 + 2.426\text{E-}03.T + 9.545\text{E-}01$		
56	0	$k = -2.306\text{E-}04.T + 1.147$ $\varepsilon_{c1,T} / \varepsilon_{c1,20^\circ\text{C}} = 1.29\text{E-}08.T^3 - 8.000\text{E-}04.T + 1.020$ $f_{cm,T} / f_{cm,20^\circ\text{C}} = -2.416\text{E-}06.T^2 + 4.813\text{E-}05.T + 1.001$		
56	20	$k = -2.682\text{E-}04.T + 1.162$ $\varepsilon_{c1,T} / \varepsilon_{c1,20^\circ\text{C}} = 1.020\text{E-}08.T^3 - 7.000\text{E-}04.T + 1.017$ $f_{cm,T} / f_{cm,20^\circ\text{C}} = -2.832\text{E-}06.T^2 + 3.736\text{E-}04.T + 9.921\text{E-}01$		
56	30	$k = -3.071\text{E-}04.T + 1.188$ $\varepsilon_{c1,T} / \varepsilon_{c1,20^\circ\text{C}} = 9.190\text{E-}09.T^3 - 6.000\text{E-}04.T + 1.016$ $f_{cm,T} / f_{cm,20^\circ\text{C}} = -3.810\text{E-}06.T^2 + 7.663\text{E-}04.T + 9.841\text{E-}01$		
$\varepsilon_{c1,20^\circ\text{C}}$	strain corresponding to the initial compressive strength [-]			
$f_{cm,20^\circ\text{C}}$	initial compressive strength [N/mm ²]			

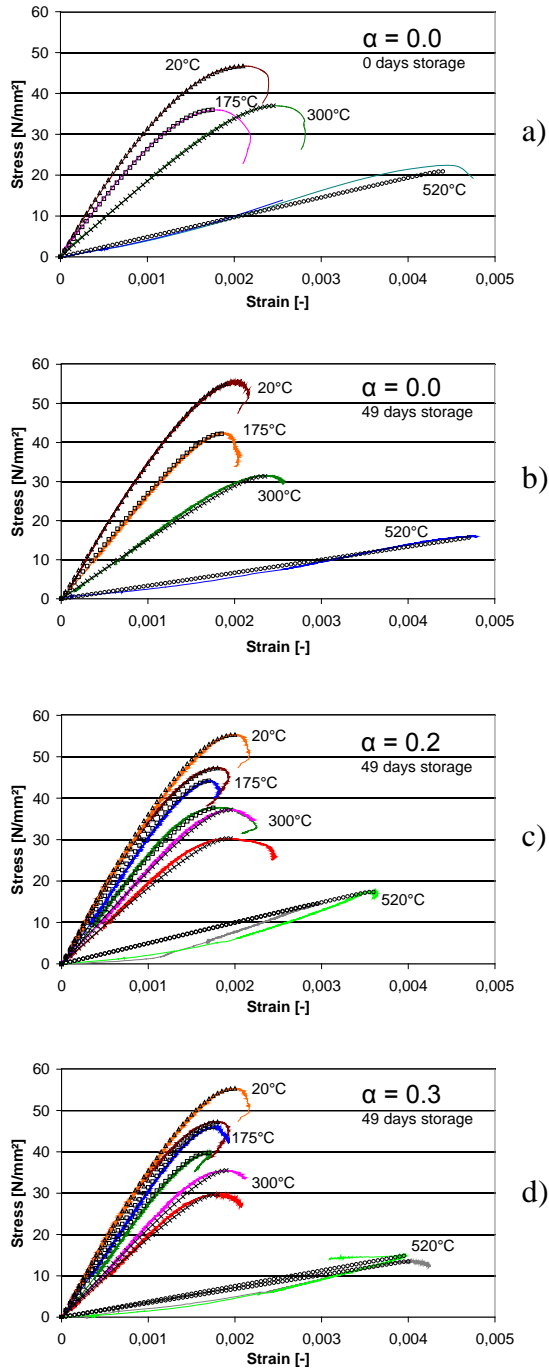


Figure 2. Residual (0d) and Post-cooling (49d) stress-strain curves of TC for different load ratios

Figures 3 and 4 illustrate for TC, respectively SCC the stress-strain curves found from the models belonging to a heating cycle without external load ($\alpha = 0.0$). For this load ratio, the specimens are tested for Young's modulus immediately after cooling (0 days) and after a post-cooling storage in moist air (60% R.H. and $20 \pm 1^\circ\text{C}$) for 7 weeks (TC) and 8 weeks (SCC). The curves are depicted relatively to the initial compressive strength and its corresponding strain. It is found that the post-cooling storage yields a loss of the compressive strength of up to 20% for TC and up to 30% for SCC. Similar values were found in [1, 5] for 150 mm cubes. Furthermore, the Young's modulus drops significantly due to the exposure after fire to the moisture from the environment. The strain corresponding to the compressive strength seems to increase with storage time due to the loss of mechanical properties. However, for SCC, this is only observed for the samples heated to 530°C .

For 205°C and also 315°C , Figure 4 shows for the curves belonging to SCC without post-cooling storage an increase of the compressive strength of up to 20% compared to the initial strength. This phenomenon is also observed for 150 mm cubes and is due to the drying procedure at 105°C till constant mass [5]. Drying at 105°C for a short period results in a loss of the compressive strength of about 20%, whereas drying till constant mass results in a recovery of the strength to the initial strength for TC and even a strength increase for SCC [5]. Similar observations can also be found in [6]. The loss of 20% corresponding to a short drying period of 1 day can be found in Figure 3 for the TC curve belonging to 0 days of post-cooling storage.

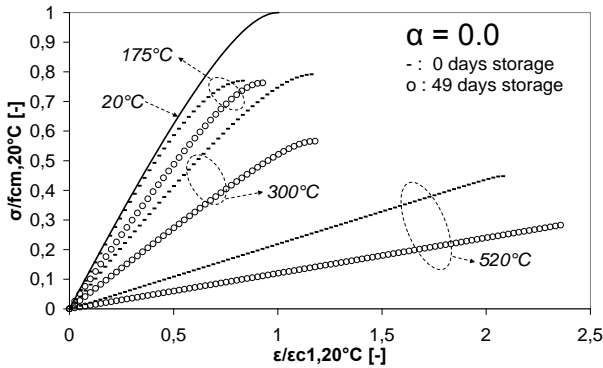


Figure 3. Stress-strain models of TC ($\alpha = 0.0$) with variation of temperature and post-cooling storage

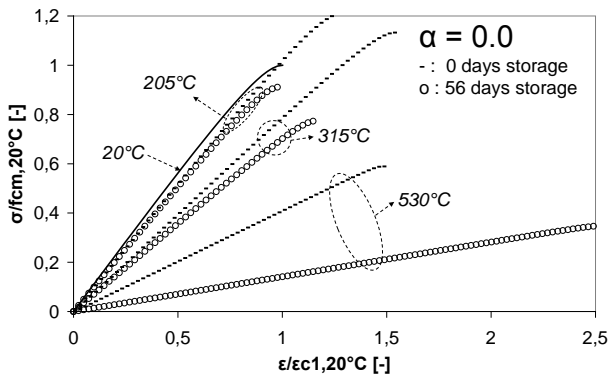


Figure 4. Stress-strain models of SCC ($\alpha = 0.0$) with variation of temperature and post-cooling storage

Figures 5 and 6 show for TC and SCC the stress-strain models corresponding to different temperatures and load levels for the specimens submitted to a post-cooling storage. Several conclusions can be derived from these figures:

- Generally, the effect of load during heating shows for the same temperature level an increase of compressive strength and Young's modulus. The concrete seems to suffer less from the degradation due to heating. However, the improvement of the compressive strength is only about 3 to 9%. At about 500°C, the strength even drops for the samples heated with a load ratio of 0.3 compared to 0.2. Notice that the drying process at 105°C may have altered the compressive strength and its ratio to the non dried reference at 20°C.
- At about 175°C and 300°C, the Young's moduli of the specimens heated under load are close to each other. When compared with Figures 3 and 4, the Young's moduli of the samples heated under load are comparable to the ones without load, but tested immediately after cooling.
- At about 500°C, the strains reach 2 to 2.5 times the value at 20°C. For lower temperatures, the increase of the strains is rather small.

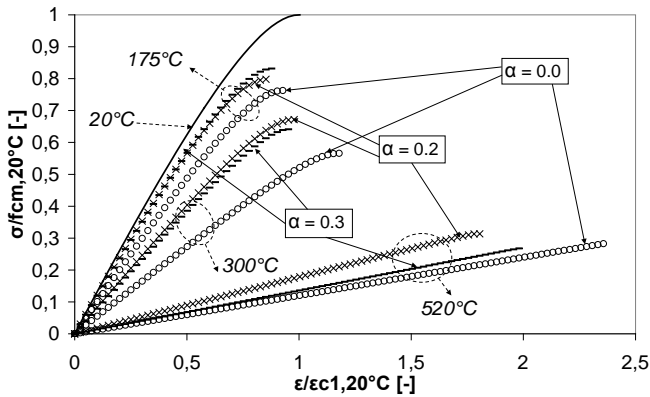


Figure 5. Stress-strain models of TC with variation of temperature and load level (7 weeks post-cooling storage)

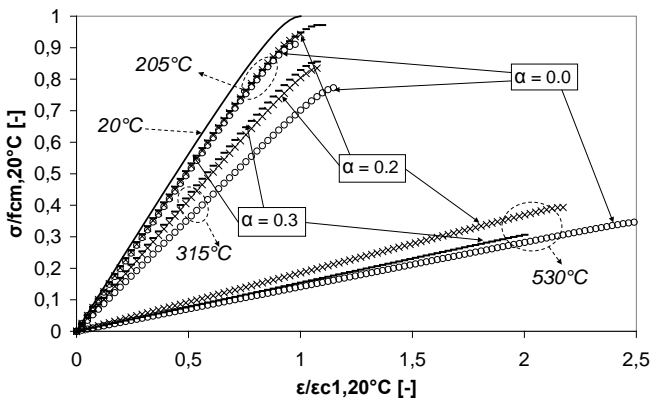


Figure 6. Stress-strain models of SCC with variation of temperature and load level (8 weeks post-cooling storage)

Figures 7 and 8 illustrate the compressive strength reduction of TC, respectively SCC. The following observations can be derived:

- Compared to TC, SCC is characterized by a less steep reduction in compressive strength as function of temperature (see also Figures 5 & 6).
- Significant differences are found between the curve belonging to the specimens tested immediately after cooling (0 days storage) and the curves belonging to several weeks of storage. As mentioned in the introduction, further strength loss will occur upon storage due to the expansive reaction of newly formed portlandite. Additional strength losses of up to 20% for TC and 30% for SCC are found and are not influenced by the load ratio.
- In the temperature range 175-300°C, a different behaviour is stated for TC and SCC for the curve belonging to 0 days storage. A strength drop is found for TC, whereas a strength increase is observed for SCC.

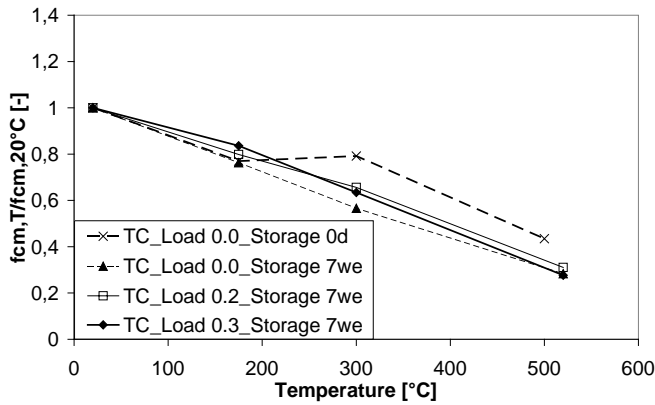


Figure 7. Compressive strength reduction of TC

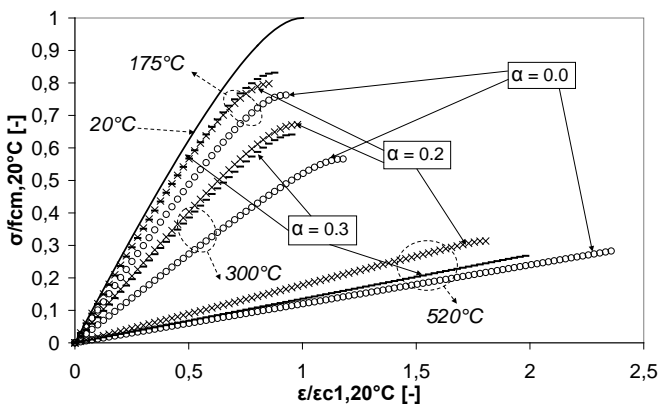


Figure 8. Stress-strain models of TC with variation of temperature and load level (7 weeks post-cooling storage)

5 CONCLUSIONS

- For both TC and SCC, a residual and post-cooling stress-strain model is derived. As a basis the Sargin model defined in EN 1992-1-1 is used. The different parameters are modified as temperature dependent, for which a relationship with the initial property is found by means of non linear regression analysis. The models result in adequate agreement with the experimental data. However, in some cases, the agreement is less for high temperatures of about 500°C.
- Due to slow heating and slow cooling, no thermal shock is introduced that can result in additional strength losses. However, the model takes into account the effect of strength losses during the post-cooling storage period. Compressive strength losses of up to 20% for TC and 30% for SCC are found, whereas the Young's modulus also decreases. In most cases, the strain corresponding to the compressive strength also increases with storage time.
- The effect of load during heating and cooling results in an increase of the compressive strain of about 3 to 9%, while the Young's modulus also increases and reaches for temperatures till about 300°C the values found immediately after cooling.
- The compressive strength as function of temperature decreases faster for TC than for SCC.

6 ACKNOWLEDGEMENT

The authors would like to thank the Fund for Scientific Research in Flanders (FWO) for the financial support through the research grant "Damage assessment and estimation of the residual strength of concrete members after exposure to fire".

REFERENCES

- [1] Annerel E., Taerwe L., "Approaches for the assessment of the residual strength of concrete exposed to fire", *Proceedings of the international workshop: fire design of concrete structures, from materials modelling to structural performance*, J.P.C. Rodrigues, G.A. Khoury, N.P. Høj (eds.), University of Coimbra, Coimbra, 489-500, 2007.
- [2] Annerel E., Taerwe L., "Evolution of the strains of traditional and self-compacting concrete during and after fire", *Materials and Structures*, 8 (44), 1369-1380, 2011.
- [3] Schneider U., Felicetti R., Debicki G., Diederichs U., Franssen J.-M., Jumppanen U.-M., Khoury G.A., Leonovich S., Millard A., Morris W.A., Phan L.T., Pimienta P., Rodrigues J.P.C., Schlangen E., Schwesinger P., Zaytsev Y., "Recommendation of RILEM TC 200-HTC: mechanical concrete properties at high temperature – modelling and applications. Part 7: Transient creep for service and accident conditions", *Materials and Structures*, 31 (209), 290-295, 1998.
- [4] Sargin M., Handa V., *A general formulation for the stress-strain properties of concrete*, Report No.3, Solid Mechanics Division, University of Waterloo, Ontario, 1969.
- [5] Annerel E., *Assessment of the Residual Strength of Concrete Structures after Fire Exposure*, Ghent University, Ghent, 2010.
- [6] Sarshar R., Khoury G.A., "Material and environmental factors influencing the compressive strength of unsealed cement paste and concrete at high temperatures", *Magazine of Concrete Research*, 45 162, 51-61, 1993.

COMPRESSIVE STRENGTH AND THERMAL EXPANSION PROPERTIES OF GEOPOLYMER CONCRETE AT ELEVATED TEMPERATURE

Shaikh F. U. Ahmed * and Vanissorn Vimonsatit *

* Department of Civil Engineering, Curtin University, Perth, Australia.
e-mails: s.ahmed@curtin.edu.au, v.vimonsatit@curtin.edu.au

Keywords: Geopolymer concrete elevated temperature, compressive strength and thermal expansion.

Abstract. *This paper presents the results of an experimental study on the effect of elevated temperature up to 800°C on the compressive strength and thermal expansion of geopolymer concrete. The effects of molarity of alkali activator and curing conditions on the compressive strength of geopolymer concrete at elevated temperature up to 800°C are also studied. The results show that, the geopolymer concrete gained between 10% and 50% of its ambient strength after exposure to 800°C temperature, compared to 80% loss of OPC concrete. Geopolymer concrete exhibited about 10% less strain to that of OPC concrete mix containing same aggregates. Geopolymer concrete with low molarity (10 Molars) benefited with significant strength gain whereas geopolymer concrete with high molarity (16 Molars) only attained minor increase in strength at elevated temperatures above 400°C. The same is true when geopolymer concrete was cured for a longer duration.*

1 INTRODUCTION

Ordinary Portland cement (OPC) concrete is one of the most widely used construction materials in the world. It generally offers adequate fire resistance for most normal applications. It is a non homogenous composite material whose fire performance is controlled by that of aggregates and cement paste. Concrete has a low thermal conductivity (50 times lower than steel) and therefore heats up very slowly in fire. It is the low thermal conductivity that provides good inherent fire resistance of concrete structures. It is non-combustible and does not produce any smoke, toxic gases or emissions in a fire situation. Although concrete provide excellent performance in fire, but it is blamed to be the main source of greenhouse gas emission into atmosphere. It is estimated that, to produce one tonne of cement about one tonne of CO₂ is released in the atmosphere [1]. Moreover, around 5-8% of global CO₂ emission is from cement manufacture and makes it the third most polluting activity of mankind [2]. Therefore, it is necessary to look into alternative ways of reducing the use of cement in concrete. The introduction of “geopolymers” as a novel binder promises to be a good prospect as an alternative to Portland cement [3]. The term “geopolymer” is first proposed by a French materials scientist named Joseph Davidovits in 1978 after he activated the materials of geological origin with alkaline liquids to obtain the cementing properties [3].

Geopolymer comes from a family of inorganic polymers with an amorphous microstructure instead of crystalline. It is a series of chains or networks of mineral molecules that are linked with a covalent bond. Geopolymer concrete is a ‘new’ material that does not use Portland cement as a binder. Instead, source materials such as fly ash, slag, metakaoline, etc., that are rich in Silicon (Si) and Aluminium (Al), are used to react with alkaline liquids to produce the binder [4].

Considerable researches have been conducted on geopolymer concrete [5]. However, very little is reported on the behaviour of geopolymer concrete in fire and at high temperature [6-7]. Most published research focused on the residual strength of geopolymer concrete tested at ambient temperature after exposure to elevated temperatures. Currently, no data exists on the in-situ compressive strength of geopolymer concrete at elevated temperature. Also not much is known about the thermal expansion behaviour of geopolymer concrete when heated up to 800°C during fire. This paper presents the results of an experimental study on the effect of elevated temperatures on the thermal expansion and compressive strength of geopolymer concrete. The effects of molarity of alkali activator and curing conditions on the residual compressive strength of geopolymer concrete at elevated temperature up to 800°C are also evaluated in this study.

2 EXPERIMENTAL PROGRAM

In total, six series of mixes were considered. Three series were for geopolymer concrete and the rest were OPC concrete. In each series, several concrete cylinders of 100mm in diameter and 200mm in height were cast and tested. The first and second series were designed for a target 28-day compressive strength of 50 MPa for geopolymer and OPC concrete, respectively. These two series were designed to compare the thermal expansion of geopolymer concrete with that of OPC concrete of same strength. In the third series, the total aggregate content was kept similar to that of the first series and by comparing these two series (series 1 and 3) the effect of geopolymer binder on the thermal expansion of geopolymer concrete can be evaluated. Series 4 was a geopolymer mix, which was similar to series 1, but subjected to 40 hours of steam curing at 60°C. The comparison of series 4 with series 1 would reveal the effect of long steam curing on the compressive strength of geopolymer concrete at elevated temperatures. In series 5 the molarity of sodium hydroxide was increased to 16 and by comparing the results with that of series 1, where 10 molar of sodium hydroxide was used, the effect of high molar alkaline liquids on the compressive strength of geopolymer concrete at elevated temperatures was evaluated. Series 6 was designed to evaluate the effect of elevated temperatures on OPC concrete and compared with that of geopolymer concrete. In each series, three cylinders were cast and tested for each elevated temperature regime. The results shown in section 5 are average of three cylinders.

3 MATERIALS, MIX PROPORTIONS AND CURING

The cement used in the study is general purpose (GP) Portland cement which corresponds to ASTM type I. The fly ash used is originated from Collie power station in Western Australia and satisfies ASTM class F classification. The fly ash consists of an amorphous part about 60% by wt. and a crystalline part about 40% by wt. The chemical composition of fly ash is shown in Table 1. The crystalline part of the fly ash has low reactivity and acts as fine aggregate in the binder system. The activating solutions used are sodium silicate with a chemical composition of (wt.%): $\text{Na}_2\text{O} = 14.7$, $\text{SiO}_2 = 29.4$ and water = 55.9. The other characteristics of the sodium silicate solution are: specific gravity = 1.53 g/cc, and viscosity at 20°C = 400 cp. The sodium hydroxide solution is prepared from analytical grade sodium hydroxide pellets. The mass of the NaOH solids in the solution varied depending on the concentration of the solution expressed in terms of molar, M. In this study, the NaOH solution with a concentration of 10M is considered in all geopolymer concrete, except series 5, and consisted of $10 \times 40 = 400$ gms of NaOH solids per litre of the solution, where 40 is the molecular weight of NaOH. The NaOH (Sodium Hydroxide) is first mixed with de-ionized water with the ratio of 0.4:1 and produce sodium hydroxide solution. During the mixing of sodium hydroxide solution, the white sodium hydroxide pellets were slowly dissolved by the addition of de-ionized water. A rise of temperature occurred as the sodium hydroxide pellet slowly dissolved into solutions. And then the sodium hydroxide solution is mixed with Na_2SiO_3 (Sodium Silicate) with the ratio of 0.4:1 and produced the alkali activator. The alkali activator solution is then used for the mixing of

Table 1. Chemical compositions of fly ash

SiO ₂	Al ₂ O ₃	Fe ₂ O ₃	CaO	MgO	SO ₃	Na ₂ O	K ₂ O	LOI
51.5%	23.63%	15.3%	1.74%	1.2%	0.28%	0.38%	0.84%	1.78%

geopolymer based cementitious composites. The mixing is carried out in a pan mixer. First, the aggregates and cement or fly ash (in case of geopolymer matrix) are dry mixed for approximately 2-3 minutes and then the water or alkaline activator solution (in case of geopolymer matrix) and superplasticizer are slowly added into the mix and continues to mix for another 3-4 minutes. The geopolymer specimens are then subjected to steam curing at 60°C immediately after casting, for 24 hours and 40 hours, for series 6 samples only. The steam curing is carried out in the steam curing room in the laboratory. The specimens are then demolded after 24 hours and stored in the laboratory in open air until the date of testing. The OPC concrete cylinders are demolded after 24 hours and stored in the curing tanks where they are subjected to standard wet curing conditions. Detail mix proportions of all series in this study are shown in Table 2.

Table 2 Mix proportions of geopolymer and OPC concrete

Series	Mix proportions in kg/m ³										
	Cement	Fly ash	Sand	Coarse agg. Size (mm)			Alkali activator			Added water	Super-plasticizer
				7	10	20	NaOH		Na ₂ SiO ₃		
							10M	16M			
1	-	408	647	647	554	-	41	-	103	14.3	6.1
2	500	-	770	-	330	770	-	-	-	225	-
3	497	-	647	647	554	-	-	-	-	250	-
4	-	408	647	647	554	-	41	-	103	14.3	6.1
5	-	408	647	647	554	-	-	41	103	14.3	6.1

4 THERMAL EXPANSION AND COMPRESSIVE STRENGTH MEASUREMENT

In order to heat the concrete specimens to temperatures upto 800°C, a 36 litre locally manufactured kiln was used. An Orton Express controller was used to control the temperature elevation rate and the maximum temperature in the kiln. In this study, the set temperature elevation rate was 800°C per hour, and the maximum temperature was set at 900°C. These two variables were kept constant during the whole experiment. Two 150 mm diameter holes were drilled through top and bottom of the furnace of the kiln to facilitate easy access of thermocouples to concrete cylinder, ceramic rods for expansion measurements and stainless steel cylinders to facilitate the compression testing and expansion measurements inside the furnace. Heat resistant materials were used to block any heat escaped through the holes at top and bottom. The experimental setup can be seen in Figure 1.

Before heating any concrete sample in the furnace, the top few millimetres of concrete specimens were sawed off by a diamond cutter to produce an even surface for the ceramic rod and stainless steel cylinder to rest upon. The samples were then put in an electric oven at 105°C for 24 hours to dry any excess moisture in accordance with AS 1774.30 [8].

In the case of thermal expansion measurements, the concrete cylinder was placed inside the furnace and was supported on a stainless steel cylinder, which was inserted through the bottom hole of the furnace. The remaining portion of the stainless steel cylinder at the bottom of the furnace was wrapped by thermal insulation cloth to minimise heat loss. The detail experimental setup for thermal expansion measurement is as shown in Figure 2(a). Figure 2(b) shows the inside image of the furnace. In this



Figure 1. Experimental setup for compression and thermal expansion tests of concrete cylinders at elevated temperatures.

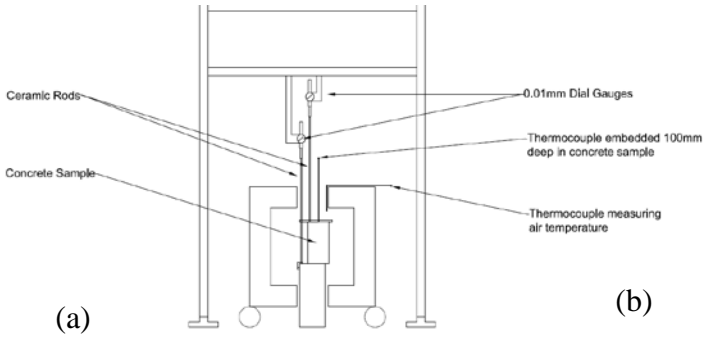


Figure 2. (a) Experimental setup for the measurement of thermal expansion of geopolymer and OPC concrete samples. (b) Inside view of kiln with concrete cylinder and ceramic rod.

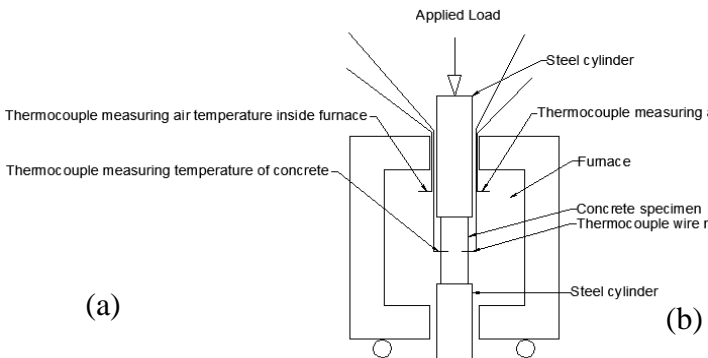


Figure 3. (a) Experimental setup for the measurement of in-situ compressive strength of geopolymer and OPC concrete samples. (b) Inside view of kiln with stainless steel cylinders on top and bottom of concrete cylinder.

study, ceramic rods were used to measure the thermal expansion of concrete cylinder. The purposely drilled hole on top of the furnace allowed the ceramic rods to extrude out of the kiln and dial gauges were placed on top of the rods, which were able to read the expansion of the rods. The thermal expansion of the stainless steel was not a great concern since two ceramic rods were used to measure the relative expansion of the concrete sample, using the stainless steel surface as a reference. Once the concrete sample was placed in the furnace, the specimen was then initially heated to 50°C and then readings were taken from there on. Dial readings were manually taken at every 50°C increments of concrete core temperature. Concrete temperature was measured through the thermocouples attached to the concrete specimen. Also at every 50°C increase in concrete temperature, the air temperature was also taken so that the expansion of the ceramic rods were taken into account and corrected for.

As for the in-situ compressive strength testing of concrete cylinders at elevated temperatures, when the concrete temperature reached the desired temperature, the kiln was turned off and load was applied through the top stainless steel. The detail test setup for compressive strength measurements is as shown in Figure 3. In this study, the compressive strength was tested under a steady state condition of the temperature at 175, 400 and 800°C.

5 RESULTS AND DISCUSSION

5.1 Compressive strength of geopolymer concrete at ambient temperatures

The development of compressive strength of various geopolymer concrete (series 1, 4 and 5) at 7, 14 and 28 days are shown in Figure 4. It can be seen that by applying longer steam curing (40 hours in series 4 in this study) to geopolymer concrete, the compressive strength can be increased and at 28 days it exhibited about 22% increment. Similar improvement was observed at 7 and 14 days by increasing the molarity of alkali liquids from 10M to 16M. However, no such improvement was noticed at 28 days.

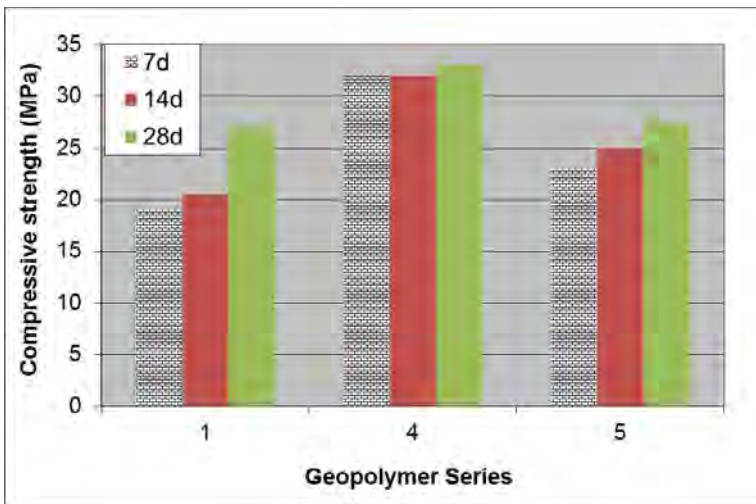


Figure 4 Development of compressive strength of geopolymer concrete at ambient temperature

5.2 Compressive strength of geopolymer concrete at elevated temperatures

The effect of elevated temperatures (175, 400 and 800⁰C used in this study) on the compressive strength of geopolymer concrete are shown in Figure 5. The results presented in the figure represent the in-situ compressive strength of heated concrete cylinders inside the kiln, which was done through a special experimental setup shown in Figure 3. It can be seen that all geopolymer concrete exhibited reduction in compressive strength when they were heated upto 175⁰C (see Figure 5(a)). Similar behaviour was also observed in OPC concrete (see Figure 5 (b)). When the temperature was increased to 400⁰C a slight gain in compressive strength was observed in geopolymer concrete. However, no such improvement is observed in OPC concrete. When the concrete cylinders were heated upto 800⁰C, the geopolymer concrete exhibited slight increase in compressive strength compared to their ambient strengths, except series 5. The OPC concrete on the other hand exhibited significant reduction of its ambient compressive strength when it is heated upto 800⁰C.

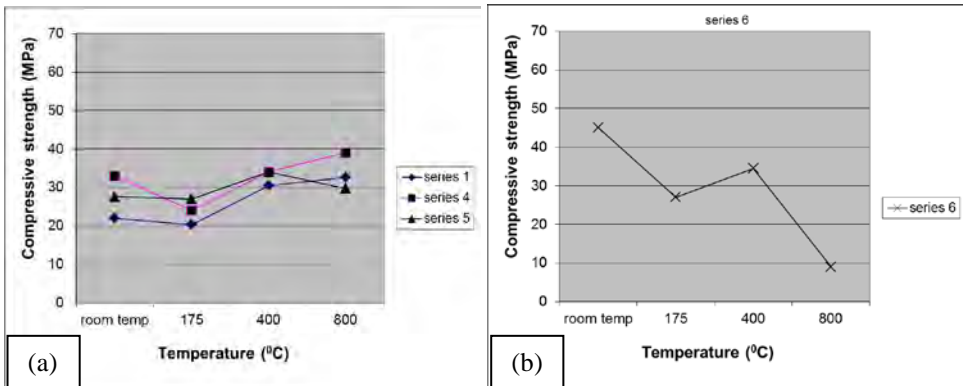


Figure 5. Compressive strength of geopolymer and OPC concrete at elevated temperatures

5.3 Effects of curing and molarity of alkaline activator on the compressive strength of geopolymer concrete at elevated temperatures

The effect of long steam curing on the compressive strength of geopolymer concrete at elevated temperatures can be seen in Figure 6(a). It can be seen that by increasing the steam curing period from 24 hours to 40 hours, the compressive strength of geopolymer concrete at elevated temperatures was increased by about 15 to 20%. The geopolymer concrete, which obtained longer steam curing (40 hours), exhibited about 20% compressive strength capacity at 800⁰C compared to 48% compressive strength capacity at the same temperature when it obtained 24 hours steam curing (see Figure 7).

By increasing the molarity of alkaline activators in geopolymer concrete better performance in compressive strengths at high temperatures was observed except at 800⁰C (see Figure 6(b)). The increase of molarity from 10M to 16M exhibited about 23% and 7% residual compressive strength capacity at 400⁰C and 800⁰C, respectively, while maintaining similar compressive strength at 175⁰C (see Figure 7).

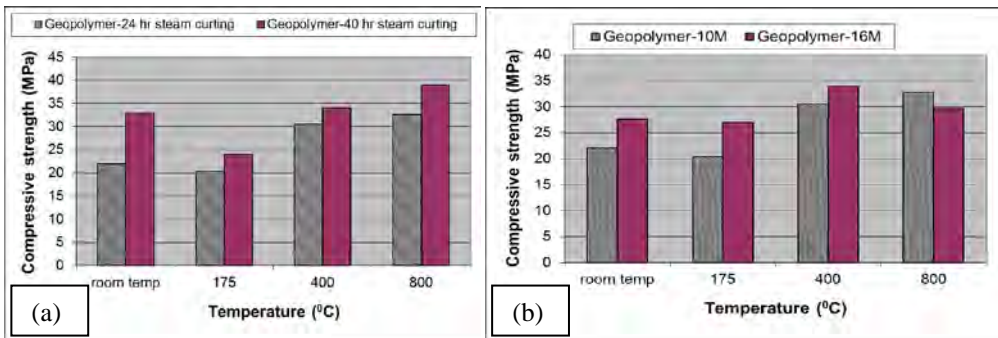


Figure 6. Effect of curing and molarity of NaOH on the compressive strength of geopolymer concrete at elevated temperatures

5.4 Thermal expansion of geopolymer concrete at elevated temperatures

The development of thermal expansion of geopolymer and OPC concrete at elevated temperatures upto 800⁰C is shown in Figure 8. The figure shows that, the geopolymer concrete (series 1) achieved the lower thermal expansion compared to the OPC concrete (series 2 and 3). Series 1 and 2 were designed for same 28 day compressive strength. By comparing series 1 with 2, the positive effect of geopolymerization on the thermal expansion of concrete at elevated temperatures can be revealed. The geopolymer concrete exhibited about 19% lower thermal expansion compared to OPC concrete. However, it should be noted that, the OPC concrete (series 2) contained bigger size coarse aggregates than that used in the geopolymer concrete. This discrepancy can be eliminated by using the same size of coarse and fine aggregates of same contents as used in series 3. And by comparing series 1 with 3, it can be seen that the geopolymer concrete also exhibited lower thermal expansion (about 10%) than that of OPC concrete containing aggregates of equal amount and size. This clearly indicates that the geopolymer paste greatly contributed to the thermal expansion behaviour of concrete. Paste research indicates that the shrinkage of geopolymer paste is slightly less than that of cement paste at 800⁰C [9-10]. However, the result in this study indicates that the shrinkage of cement paste is slightly less than that of geopolymer paste (comparing series 1 with 3), given that fact that both concrete contained same amount of aggregates of same size.

6 CONCLUSIONS

This paper presents results on the compressive strength and thermal expansion behaviour of geopolymer concrete exposed at elevated temperatures. The experimental studies led to the following conclusions:

1. Geopolymer concrete exhibited higher or at least similar compressive strength at and above 400⁰C temperature compared to their ambient compressive strengths.
2. The application of longer steam curing in geopolymer concrete is found to improve the compressive strength both at ambient and elevated temperatures.
3. The increase of molarity of alkaline activator in geopolymer concrete is found to improve the compressive strength both at ambient and elevated temperatures except at 800⁰C.
4. The thermal expansion of geopolymer concrete is found to be about 10 to 19% less than that of OPC concrete.

Further research is on-going to investigate the effect of the geopolymerization process on the fire-resistant properties of geopolymer concrete. A successful establishment on the inherent fire resistance in geopolymer concrete could lead to another regime of fire-protective materials.

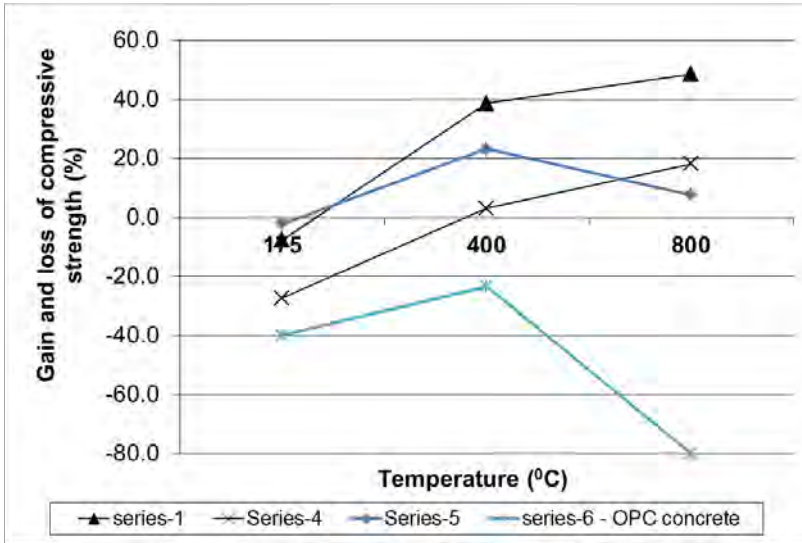


Figure 7. Gain and loss of compressive strength of geopolymer and OPC concrete relative to ambient temperature after heating at 175, 400 and 800°C. (Positive and negative signs indicate gain and loss of strength, respectively due to heating.)

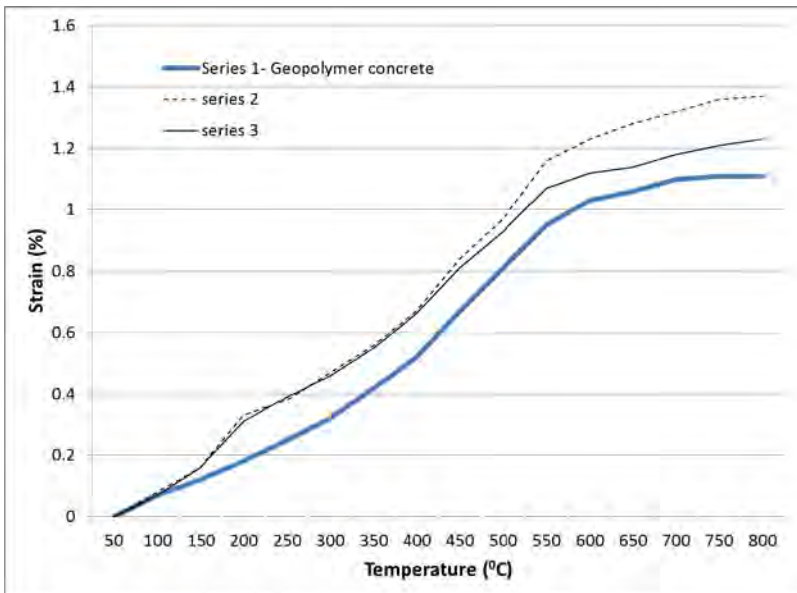


Figure 8. Thermal expansion of geopolymer and OPC concrete at elevated temperatures up to 800°C

ACKNOWLEDGEMENT:

Authors wish to acknowledge to final year project students Mr Kenneth Woo, Mr Ang Hendra Suputra and Mr Willy Utoyo for their assistance in casting and testing of specimens in this study.

REFERENCES:

- [1] Malhotra, V.M., "Supplementary cementing materials for concrete", *CANMET*, Canada, 1987.
- [2] Zeobond. (2009). "Zeobond Engineering Summary." <http://www.zeobond.com/env.htm>
- [3] Davidovits, J., "Global Warming Impact on the Cement and Aggregates Industries." *World Resource Review*, 6(2): 263-278, 1994.
- [4] Hardjito, H. and Rangan, B.V., "Development and properties of low-calcium fly ash based geopolymer concrete", Research report GCI. Faculty of engineering, Curtin University, Perth, Australia, 2005.
- [5] Rangan, B.V., "Low calcium fly ash based geopolymer concrete". In: Nawy EG editor. Concrete construction engineering handbook. New York, CRC press, 2007.
- [6] Davidovits, J., "Geopolymers: Inorganic Polymeric New Materials." *Journal of Thermal Analysis*, 37: 1633-1656, 1991.
- [7] Kong, D.L.Y. and Sanjayan, J.G., "Damage behaviour of geopolymer composites exposed to elevated temperatures", *Cement and concrete composites*, 30, 986-991, 2008.
- [8] AS 1774.30, Refractories and refractory materials – physical test methods- drying and firing schedules, *Standards Australia*, 2005.
- [9] Kong, D. L. Y., and Sanjayan. J. G., "Effect of elevated temperatures on geopolymer paste, mortar and concrete", *Cement and Concrete Research*, 40 (2): 334-339, 2010.
- [10] Cruz, C.R. and Gillen, M., "Thermal expansion of Portland cement paste, mortar and concrete at high temperatures", *Fire and materials*, 4(2), 66-70, 1980.

DETERMINATION OF FIRE SPALLING OF CONCRETE – RELEVANCE OF DIFFERENT TEST METHODS

Robert Jansson and Lars Boström

SP Technical Research Institute of Sweden
e-mails: robert.jansson@sp.se, lars.bostrom@sp.se

Keywords: Spalling, specimen size, loading conditions, heating regime

Abstract. *Results from small scale fire spalling tests are published in many large peer review journals dealing with fire and concrete. In the simplest approach an electrical furnace is used to slowly heat cubes or cylinders. From the results general conclusions are drawn regarding the phenomenon of fire spalling of concrete, i.e. the fire spalling phenomenon of concrete is threaded as equivalent to a material property. There are several reasons for having large doubts about this approach.*

1 INTRODUCTION

Severe spalling of a concrete structure exposed to fire can be dangerous from a safety perspective and can lead to high expenses for the society as in the case of the large tunnel fires where the traffic flow can be strangled for a long time during refurbishing. The main focus in this research area is then naturally focused on trying to find suitable active measures to prevent the occurrence of spalling in sensitive concrete mixes. The question is then how to validate a concrete mix or spalling preventing system. For some systems such as insulating products the validation is generally no problem since standardised test procedures are available, although great care must be taken to ensure that the test setup is properly designed as the anchoring system for the protection is a critical parameter [1], but when a concrete in itself shall be validated it is more difficult. It is generally not possible to perform full scale tests on concrete structures; not only from an economical perspective but also that it would be very difficult to make such tests. The question is thus how the spalling sensitivity of a concrete mix experimentally can be determined. As a researcher it is natural to try to simplify the question at issue as far as possible to be able to draw valid general conclusions, but great care must be taken when trying to simplify the spalling phenomenon as the influence from the shape of the geometry and boundary conditions cannot be quantified in detail. The implication of this is that, the further away you are from testing a real construction, the less valid conclusions you can draw about the involved phenomenon. In the case of testing unloaded small concrete specimens exposed to slow heating this factor is very seldom properly addressed.

2 INFLUENCES ON FIRE SPALLING FROM GEOMETRY AND LOAD

During the late sixties and early seventies an extended test campaign was carried out by Meyer-Ottens [2] and a good presentation and analysis of his results were done by Sertmehmetoglu [3]. The experimental series included investigations of the influence on fire spalling from aggregate type, concrete quality, compressive stresses, reinforcement, shape of the member and moisture content. Major findings in context of the scope of the present article are:

- During heating from two sides thin specimens with closely placed reinforcement are more sensible to spalling than thick specimens without reinforcement.
- During heating from two sides higher compressive stresses and thin cross sections led to increase in the occurrence of spalling. A diagram from the work of Meyer-Ottens was included in a previous version of the Eurocode 1992-1-2:1995. This nomogram, shown in figure 1, is omitted from the most recent version of this document, probably due to the fact that these two factors, thickness and load, are not the only important parameters influencing spalling.
- During one side heating when testing similar specimens with reinforcement close to the fire exposed surface or close to the cold surface the specimens with reinforcement placed close to the surface caused spalling whereas the specimens with reinforcement close to the cold side did not spall.

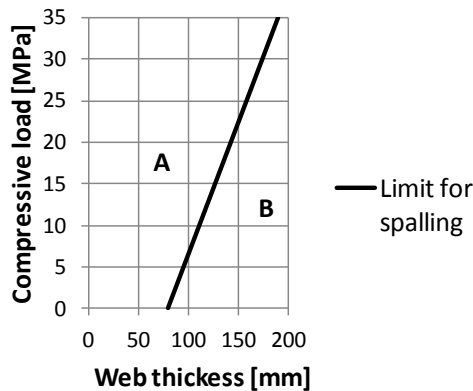


Figure 1 Area A: high risk of explosive spalling, Area B: low risk of explosive spalling. Figure redrawn from ENV 1992-1-2:1995.

Hertz [4] performed tests on unloaded slabs with size $600 \times 600 \times 200 \text{ mm}^3$ that was only heated from one side in the centre $200 \times 200 \text{ mm}^2$. During these tests the cold concrete around the heated area worked as a restraint for thermal expansion. During the tests the concrete spalled heavily for 20 minutes until the frame of cold concrete cracked leading to release of the restraint and immediately the spalling stopped.

According to Dougill [5-6] cracking is often beneficial as it limits the development of thermal stresses. In experiments with round mortar slabs moulded in a metal ring made of brass with a diameter of 30 cm he found that a local heating with a oxy-acetylen flame in the centre led to melting of the hot area surrounded by extensive cracking but no spalling. When the same experiment was performed with a more general heating of the surface it spalled violently. In the first case the heated area was probably too small for building up enough potential energy to be released in a violent spall and in the second case the restraint from the brass ring combined with the built up of energy from thermal expansion lead to the instantaneous brittle failure we call spalling.

When heating the edge of $600 \times 500 \times 200 \text{ mm}^3$ specimens no spalling was recorded during ten minutes of intense heating, see figure 2. The reason that no spalling occurred was probably that cracking released stresses and moisture was released. When then letting the specimen cool down for approximately half an hour and heating the specimen in the centre violent spalling started, illustrated in figure 3. This shows clearly that the restraint is an important factor in the spalling phenomenon. A small specimen not

loaded or restrained will crack as in the case of the first heating which limits spalling. This phenomenon can also often be observed when testing large slabs heated from one side when a boundary zone without spalling occurs close to the edges.



Figure 2. First heating no spalling. In the slab on the left side PP fibres were included.



Figure 3. Second heating severe spalling caused by restraint of cold concrete. Note the cracking and moisture flow out from the edge of the spalled concrete.

The spalling behaviour during fire exposure of small unloaded specimens is not equal to the behaviour of large loaded slabs. During a test including 8 loaded slabs, $1800 \times 1200 \times 200 \text{ mm}^3$, and 9 corresponding cubes made of the same concretes this size effect was clearly shown. Three of the large slabs spalled but none of the cubes spalled, see figure 4.



Figure 4 Before and after a fire test in a horizontal furnace. Non of the fire tested cubes spalled but spalled material from the corresponding large slabs used as a roof during the fire test can be seen around the cubes after the fire test.

In a study for development of a suitable test methodology for an upcoming test program on fire spalling of concrete different shapes of specimens including cubes, slabs and cylinders were compared with large slabs, $1800 \times 1200 \times 400 \text{ mm}^3$ [7]. During the fire test in a horizontal furnace the large slabs were loaded with 2.1 MPa in compression with an internal post stressing system and all small specimens were unloaded, see figure 2. During the tests on concretes for tunnels a specially designed fire curve for the Malmö City tunnel were used where the temperature after 26 minutes was 1000°C and after 180 minutes 1280°C . None of the small specimens shown in figure 5 spalled before melting which should be compared to the large loaded slab shown in figure 6 that had an maximal spalling depth of 272 mm. Small slabs made of the same mixes were also tested on a small furnace and some cylinders were sent to DTU for tests according to the small scale method developed by Hertz [8]. In the Hertz method the flat surface of restrained standard cylinders are fire exposed. Results from tests with the Hertz method showed no spalling for the same concrete that is shown in figure 3 whereas the tests on small slabs showed spalling but not the same amount as during the large test. Based on the results of the initial study, which includes more different shapes then described in this article [7][9], it was decided to use loaded slabs $600 \times 500 \times 200 \text{ mm}^3$ as main test shape but also to complement the small slabs with $1800 \times 1200 \times 200 \text{ mm}^3$ slabs as a reference and verification. The exact spalling depth of small loaded slabs of thickness 200 mm does not correspond to the results from the large loaded slabs with the same thickness but similar trends in behaviour could be seen. A conclusion from this is that small loaded slabs might be used as a rough estimation of the spalling sensibility and can be a tool for comparing different factors but no conclusion could be drawn regarding the actual spalling depth of larger specimens. The specimen shape effect on fire spalling cannot be explained in detail with the present knowledge about the phenomenon. The main reason for this is probably the complex interaction between crack development, moisture transport and change of material properties due to the presence of moisture [10][11].



Figure 5 Small unloaded test specimens made of tunnel concrete in fire testing furnace before fire test.

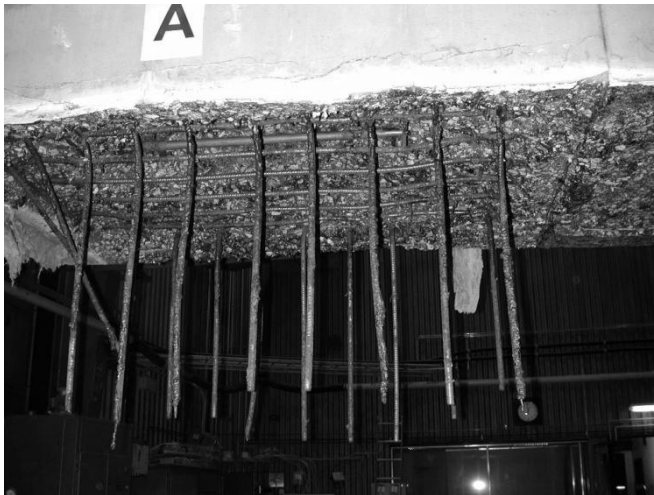


Figure 6 Large slab made of tunnel concrete after fire test. Severe spalling, up to 272 mm, followed by melting of the surface.

3 INFLUENCE OF HEATING SCENARIO

There is a large difference in material response if a specimen is heated slowly as during material testing were a typical heating ramp is 0.5-2 degrees per minute compared with rapid heating as during real fire exposure. During rapid heating much more surface cracks evolves by the thermal gradient which often leads to lower maximum pore pressure close to the surface [12]. Many of the early warnings of the spalling sensibility of high strength concrete came as a spin-off from material testing i.e. when material

testing at high temperature was going to be performed the specimens suddenly exploded during heating [13][14].

When analysing explosions from material testing the phenomenon driving the spalling is different compared with fire exposure of real elements. Therefore great care must be taken if conclusions about influence from different material parameters on fire spalling of concrete shall be deduced from small slowly heated unloaded test specimens as fire spalling of concrete is not a material property. More focus must be put on the structural influence.

4 DISCUSSION AND CONCLUSIONS

Fire spalling is not a material property. The shape of the specimen and to what extent the specimen is loaded or restrained during heating is crucial for the amount of spalling during fire. Very big differences have been recorded when testing small unloaded specimens at the same time as larger loaded specimens. The main reasons for this difference are:

- The lack of load or restrain. It is well known from material tests that the mechanical properties are highly influenced by the presence of load during heating [15-17]. This effect is probably even higher in the surface layers in a rapidly heated concrete specimen. If the mechanical degradation during heating is changed by the shape and restrain of the test specimen the spalling sensibility is consequently also changed. When heating concrete the aggregate and cement paste behaves differently. Initially during heating both the cement paste and the aggregate expand but as the temperature rises the cement paste shrinks leading to tensile stresses in the cement paste. When an external load is present this tensile stresses arising from this difference is reduced. This limits the development of cracks during heating under load [17] leading to accumulation of energy that in some cases are released at higher temperatures in the spalling process.
- The flow path for moisture during heating. The size and geometry as well as the loading conditions affect the cracking developed during heating. Since the crack system affects the moisture transport (the permeability) and the moisture condition is closely related to the spalling behaviour it has a major effect on spalling. Small specimen's results in short flow paths and as unloaded specimens cracks more than specimens loaded during heating the permeability grows rapidly which amplifies the moisture transfer. When moisture is not drained from the critical spalling zone the reduction in strength by the presence of moisture [10][11] along with a contribution from the stresses from thermal expansion and pore pressure triggers the phenomenon of spalling and a flake of the surface is violently detached.

When doing assessment of the spalling sensibility of a concrete construction the test specimen must be manufactured to be as close to the real construction as possible if reliable results should be obtained. In real constructions during a developing fire there is no concrete that is not loaded or restrained by its own cold areas except maybe to some extent small sculptures, so very limited conclusion could be drawn about fire spalling of real constructions by testing unloaded cubes or cylinders.

REFERENCES

- [1] Boström L.& Larsen C.L. "Concrete for Tunnel Linings Exposed to Severe Fire Exposure" Fire Technology, 42, 351–362, 2006
- [2] Meyer-Ottens C. (1972), "Zur Frage der Abplatzungen an Betonbauteilen aus Normalbeton bei Brandbeanspruchung", PhD-thesis, Braunschweig, 1972
- [3] Ingason H. (2000) "Time temperature curves for X2000 and Öresund trains" (in Swedish), SP Technical Research Institute of Sweden , Report P003814

- [4] Hertz K. D. "Limits of Spalling of Fire-Exposed Concrete" *Fire Safety Journal* 38 (2003)
- [5] Dougill J. W. "Some Observations on Failure of Quasi Brittle Materials Under Thermal Stress" *Cement and Concrete Research*. Vol, 3, pp. 469-474, 1973.
- [6] Dougill J. W." The Effects of High Temperature on the Strength of Concrete with Reference to Thermal Spalling" PhD thesis University of London, King's College, 1971
- [7] Boström L., Innovative self-compacting concrete - Development of test methodology for determination of fire spalling, SP Report 2004:06, Sweden, 2004, 224 pp.
- [8] Hertz K. D. & Sørensen L.S. "Test method for spalling of fire exposed concrete" *Fire Safety Journal* 40 (2005) 466–476
- [9] Boström L. & Jansson R. "Test Methods for Determine Spalling" 5th International Symposium on Tunnel Safety and Security, ISTSS, New York, USA, March 14-16, 2012
- [10] Jansson R. , Boström L. "Fire spalling – the moisture effect" 1st International Workshop on Concrete Spalling due to Fire Exposure - From Real Life Experiences and Practical Applications to Lab-scale Investigations and Numerical Modelling, MFPA Institute Leipzig, Germany 3 - 5 September 2009
- [11] Jansson R., Boström B, "The influence of pressure in the pore system on fire spalling concrete" *Fire Technology*, Vol 46, No 1, 2010.
- [12] Mindeguia J-C. 2009. "Contribution Experimentale a la Comprehension des Risques D'instabilite Thermique de Betons" PhD thesis, Université de Pau et des pays de l'Adour, France
- [13] Hertz K., "Explosion and residual strength of heated silica concrete" (in Danish), Report 162, Technical University of Denmark, Lyngby, 1982
- [14] Jumppanen, U-M "Effect of strength on fire behaviour of concrete" *Nordic Concrete Research*, Publication No. 8, 1989
- [15] Malhotra, H.L. " The effect of temperature on the compressive strength of Concrete" *Magazine of Concrete Research*, No 23, 1957
- [16] RILEM TC 44-PHT "Properties of Materials at High Temperatures- Concrete" edited by Ulrich Schneider, 1985
- [17] Hertz K. D. "Concrete strength for fire safety design" *Magazine of Concrete Research*, 2005, 57, No. 8, October, 445–453

THE INFLUENCE OF PORE PRESSURE ON THE APPARENT TENSILE STRENGTH OF CONCRETE

Roberto Felicetti*, Francesco Lo Monte* and Pierre Pimienta**

* Department of Structural Engineering, Politecnico di Milano, Milan, Italy
e-mails: roberto.felicetti@polimi.it, lomonte@stru.polimi.it

** Université Paris Est, CSTB, Centre Scientifique et Technique du Bâtiment, Marne la Vallée, France
e-mail: pierre.pimienta@cstb.fr

Keywords: Concrete, spalling, tensile strength, vapour pressure.

Abstract. *The rise of pore pressure is generally recognised as one of the governing factors of explosive spalling in concrete structures exposed to fire. However, to what extent spalling is related to concrete fracture properties is still an open issue. In order to clarify this point a special setup has been designed, aimed at performing simple indirect-tension tests (split-cube tests) under different levels of sustained pore pressure. These levels are achieved by preliminarily heating two opposite faces of cubic specimens, whereas the lateral sides are sealed and thermally insulated, so as to create a mono-dimensional thermo-hygral transient field. Fracture is induced in the symmetry plane, where both temperature and pressure are monitored by means of a customised probe. The results show that pore pressure and the concurrent reduction of the apparent tensile strength have comparable values. Simple considerations based on linear-elastic fracture mechanics corroborate this evidence. The conclusion is that pore pressure may be, in itself, a sufficient driving force to trigger explosive spalling in concrete members exposed to fire.*

1 INTRODUCTION

The more or less sudden separation (spalling) of concrete layers or pieces from the surface of R/C members subjected to fire is a still hot issue in structural design, since this phenomenon may lead to a sizeable reduction of the cross-sectional area and to the direct exposure of rebars to the flames. A number of studies have been conducted on this topic, stressing the role of both internal material factors (moisture content, porosity, tensile strength, fibre content) and external structural factors (heating rate, applied loads and constraints). These aspects control the relative roles of the two main mechanisms to which this phenomenon can be ascribed [1, 2]. On the one hand the restrained thermal dilation of the exposed concrete leads to compressive stresses parallel to the surface and to radial tensile stress in curved members and corners. On the other hand, vapour pressure build-up in the pores substantially contributes to the explosive nature of spalling with thin splinters breaking off in HPC (High-Performance Concrete) [3]. The latter evidence justifies the rather recent and fast increasing attention to the thermo-hygral behaviour of concrete exposed to fire.

From the experimental point of view, several authors [4-5] have directly measured the local pressure in concrete specimens subjected to thermal transients. In most cases this was performed by embedding thin stainless steel pipes provided with external electronic sensors. Possible alternatives [5] come from the adoption of a porous sensing head (to measure the mean pressure of rather high volumes) and filling the pipe with thermally stable silicon oil (to prevent any moisture leakage). It has to be noted that the pressure measured in this way results from the equilibrium reached by the probe inside cement matrix because of the gas pressure (vapour + air) in the pores. Nonetheless, consistent results are generally obtained in different test conditions (concrete grade, moisture content, heating rate) and values as high as 5 MPa have been reported in case of HPC; lower values are reported for NSC (Normal-Strength Concrete). A second

research trend is based on numerical models simulating the heat and mass transfer taking place in concrete exposed to high temperature. This involves the solution of a complex set of coupled differential equations and several approaches, based on different simplifying assumptions, have been proposed in the last thirty years [6]. Their consistency is often tested against the ability to fit the temperature and pressure values obtained in experimental tests. In these models, one critical problem in assessing the risk of concrete spalling is the mutual interaction between pore pressure and the mechanical response of the material. As commonly done in multi-phase porous media, the total stress \mathbf{t}^{tot} is split into the effective stress \mathbf{t}^{eff} , borne by the solid skeleton and the solid phase pressure p^s exerted by the pore fluids [7]:

$$\mathbf{t}^{\text{tot}} = \mathbf{t}^{\text{eff}} - p^s \cdot \mathbf{I} \# \quad (1)$$

where \mathbf{I} is the unit tensor (tensile stress and compressive pressure are assumed to be positive).

The solid pressure can be expressed as a combination of the gas and capillary pressures and different expressions have been proposed in the literature. In some models only the gas phase is considered, with different weight coefficients. One option, according to Biot's theory for compressible fluids inside a stiff skeleton, is to introduce the bare gradients of the gas pressure into the equilibrium equations [8]. Another – and opposite – option is to assume that gas pressure is exerted inside the pores and should be multiplied by the material porosity [2]. Intermediate values [9] are obtained by considering the elastic solution for the stress intensification around a spherical cavity. More sophisticated models take the capillary pressure into account as well [6], this pressure being multiplied by the fraction of skeleton area in contact with liquid water. Nonetheless, the role of capillary pressure is not critical neither in fast thermal and moisture transients [10], nor in increasing significantly the mechanical damage [11], to the point that the combined action of the restrained thermal strain is often considered as the most likely factor in triggering explosive spalling in concrete structures exposed to fire. Also the thermal dilation of liquid water inside the fully saturated pores may initiate the micro-cracking of cement paste [12].

One general remark about the cited models is that they consider the material as a porous solid in fluid analysis of the fluid phases, whereas the material is assumed to be a homogeneous continuum in the mechanical analysis of the solid skeleton. However, exceeding the “tensile strength” is in itself the macroscopic result of an unstable flaw propagation through the same porous network where fluid pressure is exerted. Considering the influence of pressure in this internal instability would be a more consistent way to work out a spalling criterion. In order to substantiate this viewpoint the problem of performing a fracture test under different levels of sustained pore pressure has been tackled in this study. Contrary to most experimental techniques for material characterization at high temperature, requiring a uniform steady-state thermo-hygral condition, here the test is carried out during a controlled transient. The objective is to clarify whether the tensile strength of hot concrete may be exceeded by pore pressure, without any significant contribution by thermal stress.

2 TEST PRINCIPLE AND SETUP

Concrete members exposed to fire undergo high thermal gradients, due to concrete low thermal diffusivity, and pressure build-ups, because of the gradual evaporation of water in the pores. The latter is the main driving force for mass transfer, leading to both progressive drying close to the surface and vapour migration toward the cold core of the structure. As a result, a quasi-saturated layer is formed where pressure peak develops, because of reduced gas permeability [1]. This phenomenon is even more severe along symmetry planes, where moisture transport is impossible. Examples are concrete cylinders and spheres, whose higher sensitivity to spalling comes also from the curved shape of the isostatics [13]. Another example is the thin web in precast I-beam (Fig. 1), which may exhibit delaminations and even through holes after a fire, in spite of the limited time required to dry. This latter example is the starting point of the approach adopted in the following: the mono-dimensional thermo-hygral transient occurring in a thin web (Fig. 1b) can be re-created by properly heating concrete cubes (Fig. 1c), to check concrete fracture response along the symmetry plane. This scheme involves the problem of heating two opposite faces and to prevent any thermal and mass flow through the lateral faces, as will be discussed.

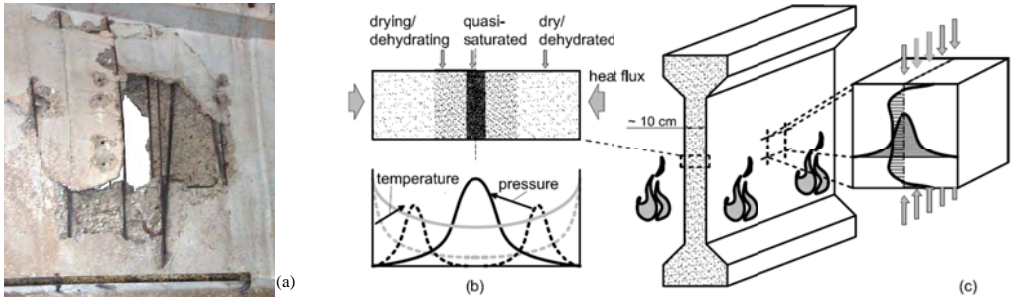


Figure 1. Thin web in a fire-exposed I-beam: (a) through hole, (b) temperature, pressure and moisture plots in the web during the heating process and (c) specimen philosophy.

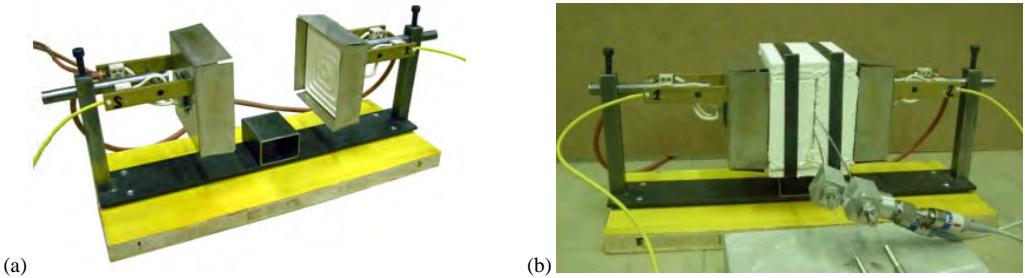


Figure 2. (a) Heating system and (b) insulated specimen during heating.

On the contrary, the significant thermal stress which develops in the actual structure is substantially smoothed down in the proposed test, to limit the investigation to the role that pore pressure has in reducing the apparent tensile strength of heated concrete. Testing in tension is performed by splitting [14], which requires a rather simple test setup and can be easily implemented in the case of hot specimens; contrary to bending tests, this technique brings in far less structural effects, with an almost constant ratio between the indirect tensile strength and the “true” tensile strength [15].

2.1 Heating system

The heating system consists of two radiant panels (Fig. 2a) placed on two opposite faces of the concrete cubes (Fig. 2b), in order to guarantee the symmetry heating with respect to the mid-plane of the specimen. Radiant panels allowed to obtain a variety of heating rates (up to 120°C/min) thanks to the built-in thermocouples connected to separate controllers. Though the significance of the internal heater temperature is debatable, this allows repeatable testing conditions.

2.2 Sealing

Sealing is fundamental in creating a mono-dimensional hygral flux, by preventing the specimen from drying through the lateral faces. Different combinations of materials were tested: (a) high-temperature resistant silicon (OTTOSEAL S17 by Otto chemical) with carbon fibres and, (b) epoxy resin (DP 760 by 3M) with aluminum foils. In the first combination a carbon-fibre fabric was placed on the silicon layer, previously smeared on concrete surfaces. The purpose of the carbon-fibre fabric is to allow the in-air hardening of silicon and to avoid the formation of air bubbles, that may be caused by vapour pressure acting on specimen surfaces. The second combination consists of epoxy and aluminum foils (same procedure as before). Two sets of drying tests were performed: in the first, 4 plain-concrete cubes were tested (2 unsealed and 2 sealed – one for each insulation technique), while in the second, 3 plain-concrete and 3 fibre-reinforced cubes were tested (4 unsealed and 2 sealed by means of epoxy resin and aluminum foils). The cubes were sealed and tested two months after casting.

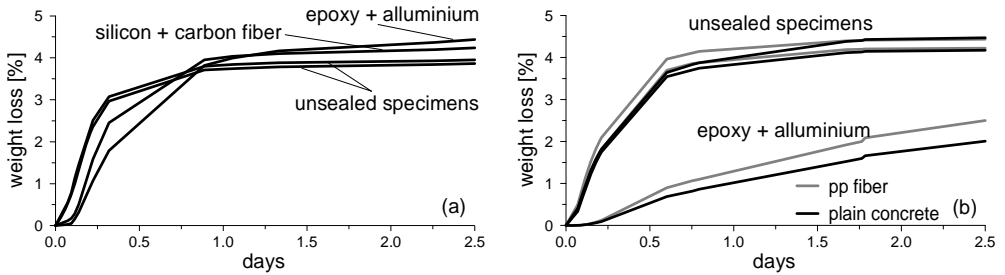


Figure 3. Comparison among different sealing systems: (a) first drying tests and (b) second drying tests.

The temperature was set at 120 °C. In the first set of tests the objective was to identify the best material combination, which turned out to be that based on epoxy layers and aluminum foils (best bond to concrete and best sealing ability, Fig. 3a). However, as sealing was not fully successful, a second set of drying tests was performed on specimens in which epoxy resin was smeared both on concrete and on aluminum foils. The sealing system showed to be much more effective (Fig. 3b). Finally, the aluminum foils on opposite faces were cut in the splitting plane, to prevent any contribution to the tensile strength of the cube; then the thin cuts were sealed with silicon (Fig. 5a).

2.3 Pore pressure measurements

The measurement of the pore pressure was performed by using capillary steel pipes fitted with sintered metal heads. Great attention was paid to the shape of both the head and the pipe, in order to affect in the least possible way concrete mechanical response. Hence, aggregate-shaped heads (Fig 4a, right) and curved steel pipes (Fig. 4b) were used, in order to prevent the probed from lying in the mid-plane of the cube (that is the fracture plane in the splitting test). The pipes were filled with silicon oil and had a thermocouple inside. Hence, both pressure and temperature inside the head of the probe were measured.

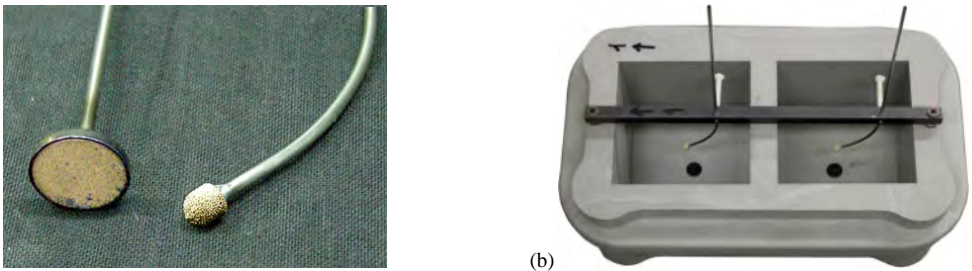


Figure 4. Probe: (a) head used by Kalifa [1] and Mindeguia [4] (left) and head used in the present study (right) and, (b) curved probes fastened to the mould.

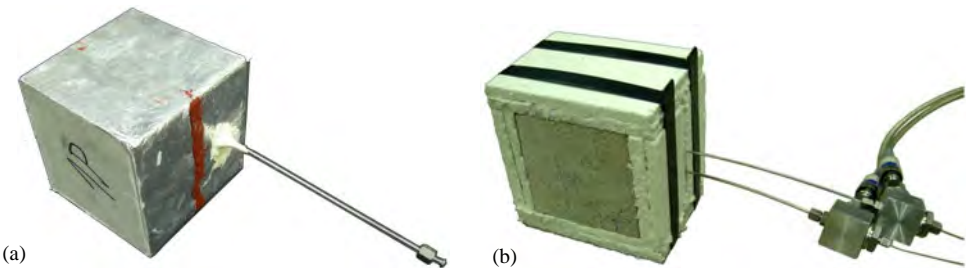


Figure 5.(a) Sealed probe-fitted specimen and, (b) sealed and insulated specimen ready for heating.

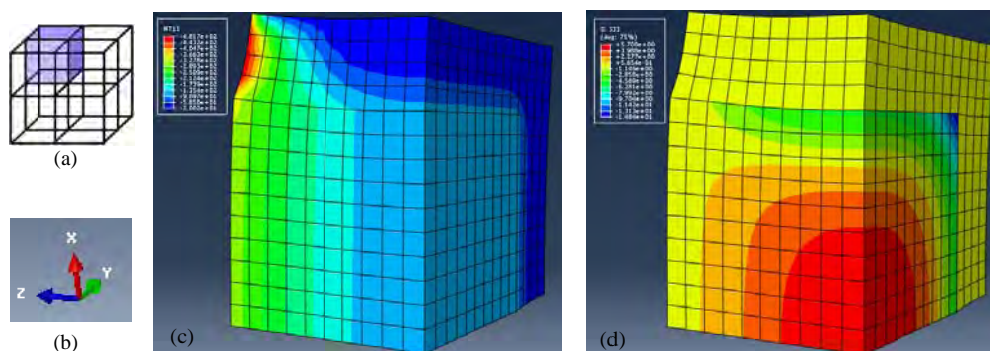


Figure 6. Numerical analyses results: (a) modelled eighth of the specimen, (b) reference system – z, longitudinal direction-, distribution of the temperature (c) and of the stresses (d) after 30 min for 120°C/min heating rate.

2.4 Insulation

Thermal insulation is necessary to create a mono-dimensional heat flux; hence, the four cold faces were covered with 20 mm-thick insulating layer of ceramic fibre material (Fig. 5b). Numerical analyses were performed to check the effectiveness of the insulation (Fig. 6).

2.5 Heating rate

The choice of the heating rate is quite critical: very high heating rates cause severe damage in the concrete (and low values of pore pressure, the vapour being free to escape through the micro-cracks); very low heating rates cause drying (leading, again, to very low values of pore pressure).

In order to understand the effect that the heating rate has on concrete with regard to pore pressure and thermal stresses, some preliminary experiments (to understand the order of magnitude of pore pressure) and numerical analyses (to evaluate the thermal stresses) were performed.

The thermo-mechanical numerical analyses were performed by means of ABAQUS FE code, by modelling an eighth of the insulated cube (Fig. 6a). Four heating rates were investigated: 1°C/min, 2°C/min, 10°C/min and 120°C/min. As expected, fast heating induces much higher thermal stresses than slow heating. (The maximum tensile stress occurs in the centroid of the specimen in the direction of the heat flux, i.e. longitudinal direction; the values are comprised between 5.7 MPa after 30 minutes and 1.3 MPa after 280 minutes, heating rates = 120°C/min and 1°C/min, respectively).

3 EXPERIMENTAL PROGRAM

3.1 Mix design

The concrete type B40, thoroughly investigated by Mindeguia [4], was used; the mix design is reported in Table 1. This concrete type has a mechanical behaviour in between HPC and NSC, meaning that spalling is unlikely to occur.

In some specimens, poly-propylene fibres were introduced (2 kg/m³).

Table 1. Mix design.

Constituent	Quantity [kg/m ³]
Cement	347
8/12.5 Calcareous	327
12.5/20 Calcareous	714
0/2 Sand	838
Water	186
Additive	Up to 1% of the cement

Table 2. Reference tensile strength in virgin and dried specimens.

	Virgin specimens			Dried specimens		
	All	PP fibre	Plain	All	PP fibre	Plain
Mean [MPa]	2.76	2.73	2.79	3.60	3.56	3.66
St. dev. [MPa]	0.31	0.43	0.25	0.27	0.31	0.23

3.2 Casting and curing

Concrete was cast in 10 cm-side plastic cubic moulds (Fig. 4b) and specimens were de-moulded after one day. Afterwards they were hermetically sealed in bags for one week. Then, the bags were opened and the cubes were kept in laboratory environment for three weeks. Finally, the bags were closed in order to prevent drying due to air exposure, until experiments were conducted (about 90 days after casting).

3.3 Cold tests

In order to define the reference tensile strength in virgin condition, splitting tests were performed on unheated specimens (6 fibre-reinforced and 4 plain-concrete); moreover further six specimens (3 fibre-reinforced and 3 plain-concrete), previously dried in oven at 120°C for 16 days (weight loss ~ 4 - 4.5%), were tested. Observing the results (Table 2) it is worth noting that, in terms of strength, there is no difference between plain and fibre-reinforced concrete in both virgin and dried conditions; on the contrary, drying process leads to a significant decrease in the splitting tensile strength (about 23% less).

3.4 Hot tests

A total of 22 specimens (16 plain and 6 fibre-reinforced concrete) were tested, by applying 4 different heating rates: (a) 1°C/min (2 plain-concrete), (b) 2°C/min (4 plain and 2 fibre-reinforced concrete), (c) 10°C/min (4 plain and 4 fibre-reinforced concrete) and, (d) 120°C/min (6 plain-concrete).

During heating, both pressure and temperature were monitored in the centroid of the cubic specimen; when the maximum pore pressure was reached, the specimen was brought (in about two minutes) under the press for the splitting test, while continuously measuring pressure and temperature. Unfortunately, in some specimens (named 12 P, 35 Fi and 21 P), the probes were clogged by cement paste for about 1 cm from the centre of the cube and thermocouples couldn't penetrate fully; this means that pressure was measured quite correctly, while temperature was measured a little bit far from the mid-section (so nearer to the heated face) obtaining slightly higher values.

4 RESULTS

4.1 Pore pressure trends at increasing temperature

In Fig. 7a-d, the results of 22 tests are reported in terms of pressure-temperature curves for the 4 heating rates adopted, together with the saturation vapour pressure curve, P_{SV} . The results confirm the pore pressure values obtained by Mindeguia [4]. Observing the results, four aspects can be underlined:

- the qualitative development of pore pressure is similar for all the tests: the dramatic pressure rise occurs almost at the beginning of a plateau in the time-temperature curve (that corresponds to the water vaporization) and the peak is achieved at the end of this plateau;
- fast heating rates (10°C/min and 120°C/min) cause pore pressure plots to lie close to the saturation vapour pressure curve, whereas significant gaps were observed for slow heating rates (1°C/min and 2°C/min), probably due to a more pronounced drying;
- fibre-reinforced concrete leads to lower pressures than plain-concrete (even more than 75% less);
- in the initial stage, there is a not-negligible overpressure caused by the partial pressure of the dry air in the pores media (this overpressure induced pore pressure to be higher than P_{SV} [4]).

The dispersion of the pressure peaks at the same nominal testing conditions can be ascribed to some variability among specimens in the effectiveness of the sealing system. Nonetheless, this is functional for performing the fracture test under the same thermo-mechanical conditions but different pressures.

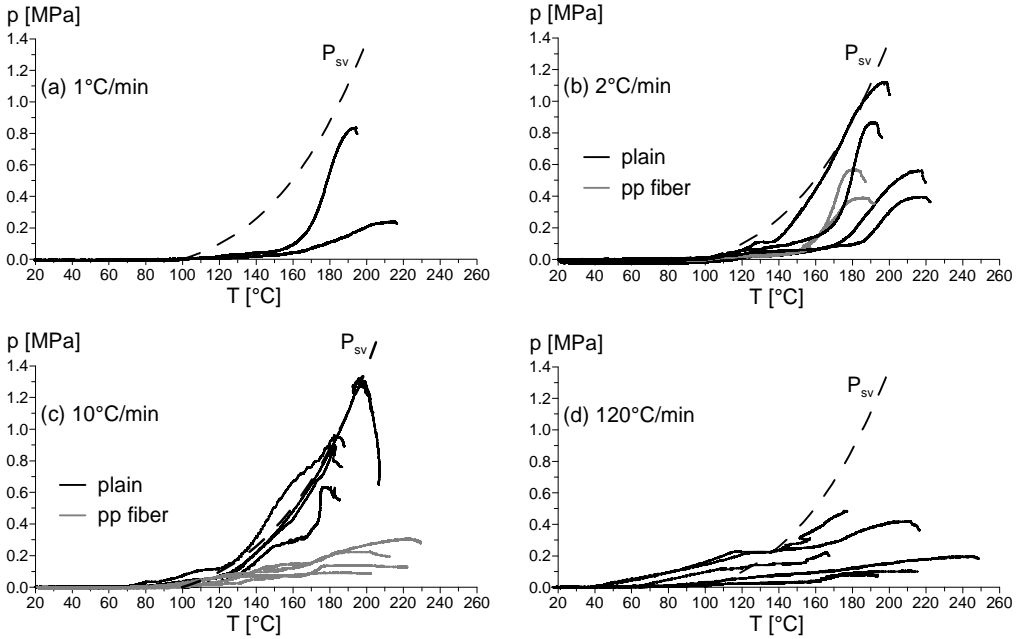


Figure 7. Saturation vapour pressure curve (P_{sv}) and pore pressure-temperature curves for the different heating rates: (a) 1°C/min, (b) 2°C/min, (c) 10°C/min and, (d) 120°C/min.

4.2 Influence of pore pressure on the splitting tensile strength

As said before, splitting test was performed when maximum pore pressure was reached; this means that experiments had not been performed at a specific temperature. However, peak pressures were achieved in a narrow range of temperature (175°C to 225°C), as shown in Fig. 8a. Then, the possible chemo-physical decay of concrete at the time of testing may be assumed uniform in the whole set of specimens.

The results obtained from the splitting tests are reported in Fig. 8b as a function of the pressure measured during the test. Considering only the data belonging to 2°C/min and 10°C/min a linear regression has been performed, obtaining a negative slope equal to -1.24. The choice of considering only the two mentioned heating rates for the linear regression was suggested by the large range of pressures covered by them with respect to the other heating rates.

Then, for each heating rate, the barycentre of the data distribution (p^{AV} , f_{ct}^{AV})_{HR} was evaluated and four straight lines with a slope equal to -1.24 and passing through these average points are plotted in Fig. 8b.

The comparison between the values of tensile strength obtained experimentally, f_{ct}^{ex} , and theoretically by applying the linear model (four lines), f_{ct}^{th} , is shown in Table 3. Obviously the mean value of the distribution $f_{ct}^{ex} - f_{ct}^{th}$ is null; the standard deviation is 0.27 considering all the data (while is 0.03, 0.15, 0.35 and 0.34 considering separately 1°C/min, 2°C/min, 10°C/min and 120 °C/min, respectively). These values are of the same order of magnitude of the standard deviation of the tensile strength measured in virgin condition (Table 2) and this aspect underlines the reliability of the proposed linear model. Hence, it can be inferred that the detrimental effect of pore pressure on the indirect tensile strength is almost independent on the heating rate and it revealed to be linear and proportional to a value close to 1.24.

On the other hand, the intercept of the lines strongly depends on the heating rate. This is the combined effect of the possible internal deterioration due to heating and the influence of thermal stresses induced by temperature gradients. At the slowest heating rate (1°C/min) the intercept is 3.5 MPa, namely 98% of the tensile strength in virgin cubes; this indicates that the material decay at about 200°C is negligible.

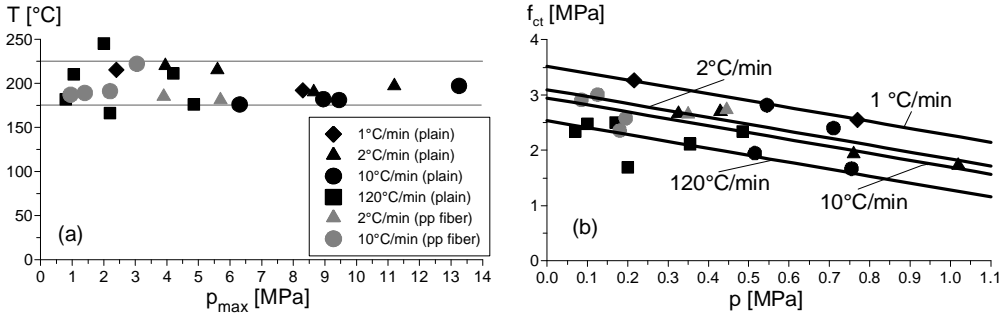


Figure 8. (a) Temperature at the peak pore pressure and, (b) tensile strength – pore pressure plot.

Table 3. Experimental and theoretical tensile strength (f_{ct}^{ex} and f_{ct}^{th} , respectively) at the pressure p measured during the splitting test, for the different heating rates; in particular: (a) 1°C/min, (b) 2°C/min, (c) 10°C/min and, (d) 120°C/min.

Spec./HR	p [MPa]	f_{ct}^{ex} [MPa]	f_{ct}^{th} [MPa]	Spec./HR	p [MPa]	f_{ct}^{ex} [MPa]	f_{ct}^{ex} [MPa]
23 P/(a)	0.22	3.27	3.25	9 P/(c)	0.52	1.95	2.30
20 P/(a)	0.77	2.55	2.56	35 Fi/(c)	0.18	2.36	2.72
15 P/(b)	0.76	1.93	2.15	31 Fi/(c)	0.13	3.01	2.79
26 P/(b)	1.02	1.73	1.83	38 Fi/(c)	0.20	2.58	2.70
10 P/(b)	0.43	2.70	2.56	37 Fi/(c)	0.09	2.91	2.84
19 P/(b)	0.33	2.66	2.69	22 P/(d)	0.20	1.69	2.28
41 Fi/(b)	0.45	2.74	2.54	17 P/(d)	0.07	2.34	2.44
40 Fi/(b)	0.35	2.66	2.66	16 P/(d)	0.49	2.34	1.93
7 P/(c)	0.55	2.82	2.27	18 P/(d)	0.36	2.12	2.09
8 P/(c)	0.71	2.40	2.06	21 P/(d)	0.17	2.50	2.32
6 P/(c)	0.76	1.67	2.01	25 P/(d)	0.10	2.48	2.41

Increasing the heating rate, up to 120°C/min, a sizeable reduction of the tensile strength at zero pressure become evident, leading to a decay of about 30%. These results are consistent with the thermal stress peaks induced, as shown by numerical analyses (see section 2.5).

It is worth noting that concrete strength has been evaluated through an indirect tensile test that, as is well known, gives higher values with respect to direct tensile tests. It has been shown [15] that for no thermal damage, the direct tensile strength over indirect tensile strength ratio is 1.12 – 1.25 and can reach value close to 1.70 for severe thermal damage. Hence, it is reasonable to infer that the linear relation between pore pressure and direct tensile strength is proportional to a value close to -1, as will be substantiated in the following, on the basis of fracture mechanics.

5 INTERPRETATION OF THE EXPERIMENTAL RESULTS

As discussed, the apparent tensile strength f_{ct}^{app} measured in the experimental tests resulted to be a function of: (a) the real material strength $f_{ct}(T)$ (including only the effect of thermo-physical transformation occurring at temperature T), (b) the pore pressure p_{gas} developed in the pores and, (c) the detrimental effect $\Delta f_{ct}(T, HR)$ of thermal stress due to the inhomogeneous heating:

$$f_{ct}^{app}(p, T, HR) = f_{ct}(T) - p_{gas}(HR) - \Delta f_{ct}(T, HR) \quad (2)$$

where the latter term proved to be negligible in case of slow heating rate HR (up to 1°C/min in our tests).

This finding seems to confirm the approach based on the effective stress (Equation 1) in case the Biot's coefficient is assumed equal to 1 [8] and the role of the capillary pressure [6, 7] is neglected.

One alternative approach to explain this role of gas pressure is based on fracture mechanics and on the stability of the inherent material defects.

5.1 Fracture mechanics model

The tensile behaviour of concrete may be interpreted as the global effect of many micro defects, which reach an unstable propagation when a critical level of stress is reached, according to fracture mechanics approach. The local stress concentration around a defect is governed by the stress intensity factor, K_I , which is a function of both load level and boundary conditions. The defects propagate when K_I reaches a critical value K_{Ic} , which is a property of the material - $K_{Ic} = f(E_c, G_f)$, where E_c and G_f are the elastic modulus and the fracture energy, respectively.

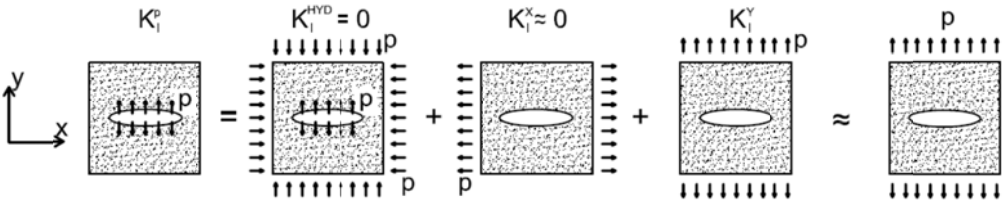


Figure 9. Square part of concrete with one defect.

Let us consider a concrete element including a defect which governs the material tensile response on y-direction (Fig. 9). A pressure p , exerted inside the defect, can be equivalently considered as the summation of three loading cases: hydrostatic pressure all around the boundaries, external tensile stress in both x and y directions. Hydrostatic pressure has no effect in fracture propagation ($K_I^{HYD} = 0$); moreover, for sharp-shaped defects, the stress intensification due to parallel loading ($K_I^x \sim 0$) is negligible compared to the effect of transverse loading (K_I^y). This means that pressure inside defects (pores) is equivalent, from the fracture mechanics point of view, to an intensification of the tensile stress by the same value. This conclusion complies with the experimental results.

6 CONCLUSIONS

In this paper the influence of transient thermo-hygral conditions in the fracture response of concrete was investigated. The main conclusions that can be drawn on the basis of a comprehensive experimental programme are summarized in the following:

- the temperature at the peak pressure is almost independent from both fibre content and heating rate, with values comprised in a narrow range (175-225°C). In this range the mechanical decay due to chemo-physical transformations proved to be negligible;
- fast heating rates ($\geq 10^\circ\text{C}/\text{min}$) allow to measure higher pore pressures but at the same time cause severe thermal stresses which sizeably affect the experimental results;
- pore pressure significantly affects the apparent tensile strength of concrete almost independently from both fibre content and heating rate, with a linear decrease that is proportional to -1.24 for the splitting tensile strength and, reasonably, proportional to -1 for the actual tensile strength.

Based on the last conclusion, it seems that higher pore pressures than those measured in this study (values up to 4-5 MPa were observed by several authors in HPC) may be, in themselves, a sufficient driving force to trigger explosive spalling in R/C members exposed to fire. As a partial confirmation, in a splitting test under just 1 MPa pore pressure the fracture process becomes dramatically faster than in ordinary tests and the two halves of the splitted cube are violently projected apart.

7 AKNOWLEDGMENTS

The authors wish to thank Mehmet Baran Ulak and Murat Hacıoglu from Turkey, who actively contributed to this study in partial fulfilment of their MS degree requirements at Politecnico di Milano.

REFERENCES

- [1] Kalifa P., Menneteau F.-D., Quenard D., "Spalling and pore pressure in HPC at high temperatures", *Cement and Concrete Research* 30, 1915-1927, 2000.
- [2] Dwaikat M.D. and Kodur V.K.R., "Hydrothermal Model for Predicting Fire-induced Spalling in Concrete Structural Systems", *Fire Safety Journal* 44: 425-34, www.elsevier.com/locate/fire saf, 2009.
- [3] Zeiml M., Lackner R. and Mang A., "Experimental insight into spalling behaviour of concrete tunnel linings under fire loading", *Acta Geotechnica* 3:295–308, 2008.
- [4] Mindeguia J. C., "Contribution Expérimental a la Compréhension des Risques d'Instabilité Thermiques des Béton", Ph.D. Thesis (French), Université de Pau et des Pays de l'Adour, 2009.
- [5] Bangi M.R. and Horiguchi T., "Pore pressure development in hybrid fibre-reinforced high strength concrete at elevated temperatures", *Cement and Concrete Research* 41, 1150–1156, 2011.
- [6] Gawin D., Pesavento P and Schrefler B.A., "What physical phenomena can be neglected when modelling concrete at high temperature? A comparative study. Part 1 and 2", *International Journal of Solids and Structures* 48, 1927–1961, 2011.
- [7] G. Gray W.G. and Schrefler B.A., "Analysis of the solid phase stress tensor in multiphase porous media", *International Journal for Numerical and Analytical Methods in Geomechanics*, 31:541–581, 2007.
- [8] Tenchev R., Purnell P., "An application of a damage constitutive model to concrete at high temperature and prediction of spalling", *International Journal of Solids and Structures* 42, 6550–6565, 2005.
- [9] Ichikawa, Y., England, G.L., "Prediction of moisture migration and pore pressure build-up in concrete at high temperatures", *Nuclear Engineering and Design* 228, 245–259, 2004
- [10] Davie, C.T., Pearce, C.J., Bicanic, N., "Coupled heat and moisture transport in concrete at elevated temperatures – effects of capillary pressure and adsorbed water", *Numerical Heat Transfer* 49 (8), 733–763, 2006.
- [11] Gawin, D., Pesavento, F., Schrefler, B.A., "Towards prediction of the thermal spalling risk through a multi-phase porous media model of concrete", *Computer Methods in Applied Mechanics and Engineering* 195 (41-43), 5707–5729, 2006a.
- [12] Dal Pont S., Dupas A., Ehrlicher A., and Colina H., "An Experimental Relationship between Complete Liquid Saturation and Violent Damage in Concrete Submitted to High Temperature", *Magazine of Concrete Research* 57.8: 455-61, web, 2005.
- [13] Debicki G., Hanihe R. and Delhomme F., "An experimental method to investigate concrete spalling in temperature", *Proc. 2nd International Workshop Concrete Spalling due to Fire Exposure*, E.A.B. Koenders and F. Dehn (Eds), RILEM, Delft, (5-7/10), 189-195, 2011.
- [14] CEN European Committee For Standardization, EN 12390-6 *Testing hardened concrete, Part 6: Tensile splitting strength of test specimens*, European Standard, 2000.
- [15] Bamonte P. and Felicetti R., "On the Tensile Behaviour of Thermally-Damaged Concrete", *Proc. of the 6th International Conference on Fracture Mechanics of Concrete Structures (FraMCoS 6)*, Catania, Italy, pp. 1715-1722, 2007.

RESTRAINT FORCES INDUCED IN REINFORCED CONCRETE COLUMNS SUBJECTED TO ECCENTRIC LOADS AT ELEVATED TEMPERATURES

Hai K. Tan^{*}, Thang T. Nguyen^{*}

^{*} School of Civil and Environmental Engineering, Nanyang Technological University, Singapore
e-mails: ckhtan@ntu.edu.sg, ntthang@ntu.edu.sg

Keywords: Reinforced concrete, Columns, Restraint forces, Eccentric loads, Elevated temperatures.

Abstract. *This paper introduces an analytical model based on a simplified approach to determine the restraint forces induced in reinforced concrete (RC) columns subjected to eccentric loads at elevated temperatures. The proposed model, which is based on the concepts of equivalent distributed temperature as well as a load eccentricity- and fire exposure-dependent reduction factor of the column axial stiffness, takes into account the effects of load eccentricity, load level, axial restraint, material thermal properties, concrete spalling, and transient strain under fire conditions. Computer program SAFIR and fire tests on six axially-restrained RC columns under uniaxial bending conducted recently at Nanyang Technological University, are respectively used for numerical study and experimental validation of the analytical model. Good agreement obtained with test results shows that this model is capable of predicting thermal-induced forces of columns in realistic restraint, loading, and fire conditions.*

1 INTRODUCTION

Due to their different thermal responses, structural members in framed buildings are constrained from free elongation when a fire occurs. It has been indicated from a numerical approach proposed by Dwaikat et al. [1] and validated by a number of experimental studies [2,3], that fire resistance of reinforced concrete (RC) beams increases when they are restrained. However, for RC columns the issue may be different since additional thermal-induced compression forces, together with deteriorations of material strength and stiffness at elevated temperatures, may cause premature failure in either squashing or instability mode. Thus, a proper prediction of restraint force is critical in the fire resistance analysis of restrained columns. On the other hand, although it is common for columns to simultaneously support axial force and bending moments in reality, previous research works on restrained RC columns in fire mostly focused on the effect of pure compression [4-8]. Besides, no provision in current structural fire-resistant design codes [9,10] is available for restrained RC columns subject to eccentric loads. Furthermore, new fire tests conducted at Nanyang Technological University (NTU) by the authors [11] showed that restrained RC columns when subjected to eccentric loads, failed prematurely compared to predictions by numerical models that neglect concrete spalling and implicitly account for concrete transient strain. Hence, to the authors' knowledge, there is an essential need to study the simultaneous effects of axial restraint and eccentric load on the development of restraint forces within heated columns.

In this paper, an analytical model for the determination of restraint forces is proposed based on the concepts of equivalent distributed temperature, as well as a reduction ratio of axial stiffness that depends on load eccentricity and fire exposure. Effects of concrete spalling and transient strain are also incorporated into the model through a factor considering the fire exposure, concrete grade, and fire time at which concrete spalling first occurs. The model is applied to predict the restraint forces induced in six axially-restrained RC columns under uniaxial bending tested by the authors in the above-mentioned experimental study [11]. Finite element-based computer program SAFIR [12] is also used for the numerical study on the specimens. Comparisons between the analytical, experimental and numerical

results show that the proposed analytical model is capable of demonstrating a similar trend on the effects of uniaxial load eccentricity and load level observed from tests and numerical predictions. From the three different approaches, clearly, restraint force increases with an increase of uniaxial load eccentricity but decreases with an increase of load level. Besides, the effect of axial restraint ratio on restraint force can also be derived from the proposed formula. On the other hand, it is shown that the analytical and numerical analyses neglecting concrete spalling and using material models which implicitly consider concrete transient strain, over-predict the restraint forces induced in axially-restrained RC columns when subjected to eccentric loads at elevated temperatures. Relatively good agreement is obtained from analytical predictions and test results, which shows that the proposed analytical model can be efficiently used in performance-based approaches for the fire resistance analysis of RC columns under realistic fire, loading, and restraint conditions.

2 ANALYTICAL MODEL

A pin-roller-and-pinned column under axial restraint is used for the derivation of the proposed analytical model (figure 1(a)). The column, which is assumed to be an idealised elastic material, has an initial length denoted as L_c and an ambient axial stiffness $K_c^{20} = E^{20}A^{20}/L_c$, where E^{20} and A^{20} are the elastic modulus and gross cross-section at room temperature, respectively. The axial restraint is simulated by an idealised elastic spring with a temperature-independent stiffness K_r .

When subjected to an axial load N_0 with a first-order eccentricity e at room temperature, at its roller end the column contracts axially by an amount of u_0 which is also the expansion of the spring (figure 1(b)). As a result, a self-reaction force of $N_a^{20} = -K_r u_0$ is generated. On the other hand, the mechanical relationship within the column can be expressed as $(N_0 + N_a^{20}) = (k_e^{20} K_c^{20}) u_0$ where the reduction factor k_e^{20} is to account for the adverse effect of load eccentricity on axial deformation at ambient condition. This factor equals to unity in the case of pure compression and instantly decreases when the load eccentricity increases. Based on the above equations, the term N_a^{20} can be derived as:

$$N_a^{20} = -\frac{K_r}{k_e^{20} K_c^{20} + K_r} N_0 \quad (1)$$

When exposed to a fire at an elevated temperature T , if there is no axial restraint, the element would elongate freely from A to A₁ with an axial deformation $u_{th} = \varepsilon_{th} L_c$, where ε_{th} is thermal strain. However, due to the spring, the column will be compressed from A₁ back to A₂ with a mechanical axial deformation u_σ resulting from a combination of axial forces $(N_0 + N_a^T)$, with the mechanical relationship $u_\sigma = (N_0 + N_a^T)/(k_e^T K_c^T)$, where $N_a^T = -K_r u_{tot}$ is the additional axial force generated when the column and the spring axially deform by a total amount of u_{tot} ; k_e^T is also an additional factor accounting for the adverse effects of load eccentricity as well as fire exposure; and K_c^T is the temperature-dependent axial stiffness of the column. The physical compatibility condition at A₂ can be expressed as: $u_{tot} = u_{th} + u_\sigma$ (figure 1(c)). Hence, the term N_a^T can be derived as shown in equation (2):

$$N_a^T = \frac{K_r}{k_e^T K_c^T + K_r} \left(-k_e^T K_c^T u_{th} - N_0 \right) \quad (2)$$

It is noteworthy that at ambient condition, since $(k_e^T K_c^T) = (k_e^{20} K_c^{20})$ and $u_{th}=0$, the term N_a^T given in equation (2) also equals to the term N_a^{20} shown in equation (1).

Compared to ambient condition, the actual increment of axial force occurs within the element at temperature T , $\Delta N_a^T = (N_0 + N_a^T) - (N_0 + N_a^{20})$, which is the thermal-induced restraint force, can be obtained from equations (1) and (2):

$$\Delta N_a^T = \frac{K_r}{k_e^T K_c^T + K_r} \left(k_e^T K_c^T (-u_{th}) - \frac{k_e^{20} K_c^{20} - k_e^T K_c^T}{k_e^{20} K_c^{20} + K_r} N_0 \right) \quad (3)$$

It can be observed from equation (3) that: (i) without any axial restraint ($K_r=0$), there is no thermal-induced restraint force, and (ii) at ambient condition $T=20\text{ }^\circ\text{C}$, since $u_{th}=0$ and $(k_e^T K_c^T) = (k_e^{20} K_c^{20})$, then $\Delta N_a^T = 0$.

The restraint force obtained is normalised to applied load N_0 as shown in equation (4).

$$\frac{\Delta N_a^T}{N_0} = \frac{K_r}{k_e^T K_c^T + K_r} \left(\frac{k_e^T K_c^T (-u_{th})}{N_0} - \frac{k_e^{20} K_c^{20} - k_e^T K_c^T}{k_e^{20} K_c^{20} + K_r} \right) \quad (4)$$

It can also be noted that all derivations presented here are based on positive sign convention for compressive forces and axial deformations as shown in figure 1(d).

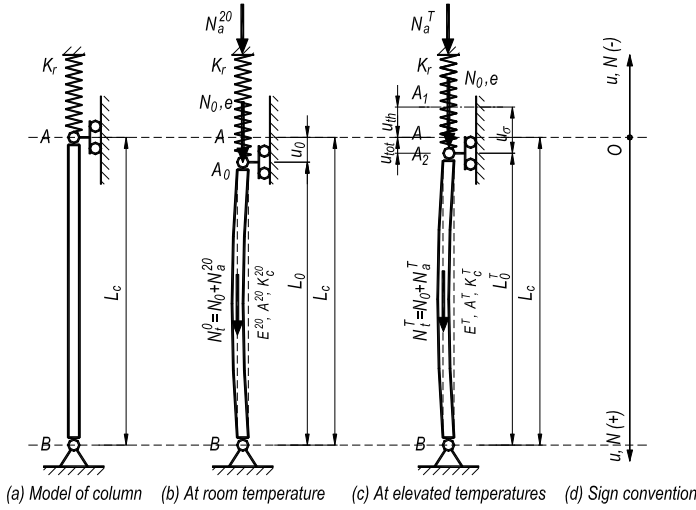


Figure 1. Pin-ended column for simplified analytical derivation.

In order to apply equation (4) for RC columns, which are neither idealised materials nor subjected to uniform temperature distribution, an analytical model is proposed for column cross-section. As shown in figure 2, the model includes a two-dimensional array of $(m \times n)$ unique rectangular concrete sub-elements with an area $A_{c-ij} = d_{iy} \times d_{iz}$ ($ij=1$ to $m \times n$) and a number of round-shaped elements representing reinforcing steel bars, namely, S_j to S_p , with the corresponding areas A_{s-k} ($k=1$ to p). It is assumed that temperature distribution and mechanical properties are uniform within each sub-element.

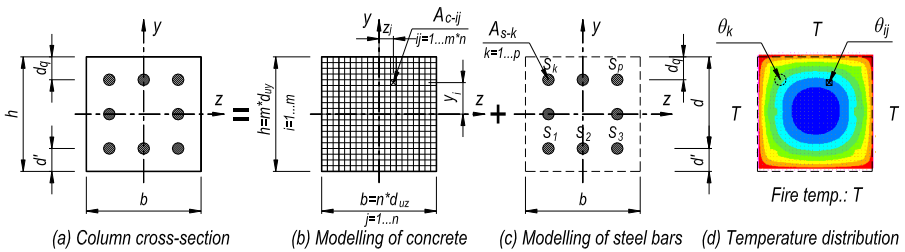


Figure 2. Analytical model for column cross-section.

At any temperature T of fire exposure, the unknown terms in equation (4) can be determined from equations (5-7).

$$K_c^T = \frac{1}{L_0} \left(\sum_{ij=1}^{m \times n} E_{c-ij}^{\theta ij} A_{c-ij} + \sum_{k=1}^p E_{s-k}^{\theta k} A_{s-k} \right) \quad (5)$$

$$K_c^{20} = \frac{1}{L_0} \left(E_c^{20} \sum_{ij=1}^{m \times n} A_{c-ij} + E_s^{20} \sum_{k=1}^p A_{s-k} \right) \quad (6)$$

$$K_c^T (-u_{th}^\theta) = \sum_{ij=1}^{m \times n} E_{c-ij}^{\theta ij} A_{c-ij} (-\varepsilon_{th-ij}^{\theta ij}) + \sum_{k=1}^p E_{s-k}^{\theta k} A_{s-k} (-\varepsilon_{th-k}^{\theta k}) \quad (7)$$

where $E_{c-ij}^{\theta ij}$ and $E_{s-k}^{\theta k}$ are the respective elastic moduli of the particular concrete and rebar sub-elements at which the corresponding distributed temperatures θ_{ij} and θ_k are obtained from heat transfer analysis; L_0^T is the column length at fire temperature T ; $\varepsilon_{th-ij}^{\theta ij}$ and $\varepsilon_{th-k}^{\theta k}$ are the temperature-dependent thermal strains at concrete and reinforcing steel sub-elements, respectively. These thermal strains attain negative values according to the sign convention shown in figure 1(d). The terms E_c^{20} and E_s^{20} denote the elastic moduli of concrete and reinforcing steel at room temperature, respectively. It is also assumed that fire exposure is uniform along the column length.

Based on equations (5-6), a reduction factor depending on both load eccentricity and temperature distribution within the column cross-section, namely, α_e^θ , is proposed as shown in equation (8).

$$\alpha_e^\theta = \frac{k_e^T K_c^T}{K_c^{20}} = k_e^T \frac{\sum_{ij=1}^{m \times n} E_{c-ij}^{\theta ij} A_{c-ij} + \sum_{k=1}^p E_{s-k}^{\theta k} A_{s-k}}{\sum_{ij=1}^{m \times n} E_c^{20} A_{c-ij} + \sum_{k=1}^p E_s^{20} A_{s-k}} \frac{L_0}{L_0^T} \quad (8)$$

where the term θ stands for an equivalent distributed temperature and satisfies the following:

$$E_c^\theta \sum_{ij=1}^{m \times n} A_{c-ij} + E_s^\theta \sum_{k=1}^p A_{s-k} = \sum_{ij=1}^{m \times n} E_{c-ij}^{\theta ij} A_{c-ij} + \sum_{k=1}^p E_{s-k}^{\theta k} A_{s-k} \quad (9)$$

It can be observed from equation (8) that at room temperature $\alpha_e^{20} = k_e^{20} K_c^{20} / K_c^{20} = k_e^{20}$ and for columns subjected to pure compression $\alpha_e^{20} = k_e^{20} = 1$.

Based on the axial stiffness ratio $\alpha_r = K_r / K_c^{20}$, the relationship $k_e^T K_c^T = \alpha_e^\theta K_c^{20}$ taken from equation (8), and by eliminating the term K_c^{20} , equation (4) can be derived in a simpler form as:

$$\frac{\Delta N_a^T}{N_0} = \frac{\alpha_r}{\alpha_e^\theta + \alpha_r} \left(\frac{\alpha_e^\theta K_c^{20} (-u_{th}^\theta)}{N_0} - \frac{\alpha_e^{20} - \alpha_e^\theta}{\alpha_e^{20} + \alpha_r} \right) \quad (10)$$

In this study, the equivalent thermal axial deformation u_{th}^θ is also dependent on the temperature distribution (equation (7)), the axial stiffness ratio α_r can be obtained from experiments, and the axial stiffness reduction factor α_e^θ can be determined from numerical analyses.

3 EXPERIMENTAL PROGRAMME

Fire tests on six axially-restrained RC columns subjected to uniaxial bending conducted at NTU are presented in detail in Nguyen et al. [11]. Only a brief introduction of test specimens, test set-up, and

restraint forces measured in these tests will be presented. Table 1 lists the column specimens subjected to uniaxial load eccentricities varying from 0 to 80 mm. All test specimens had 300 mm square cross-section and 3.3 m long. Load eccentricities were produced by two 500×500×300 (mm) end blocks designed and cast with centre lines deviated from the centroid of the column. All the columns were reinforced with six 20 mm-diameter main bars (6T20) and had 55.3 MPa concrete compressive cylinder strength and main bars of 550.2 MPa yield strength. They were subjected to load levels of 0.45 and 0.55 and an axial stiffness ratio of 0.0365.

Table 1. Test specimens

Series	Specimens	Load eccentricity (mm)		f_c (MPa)	f_y (MPa)	Detailing (mm)	Load level μ_{fi}	Restraint ratio α_r
		e_y	e_z					
S1	C1-1-00	00	00	55.3	550.2	300×300	0.45	0.0365
	C1-2-00	00	00					
	C1-3-25	00	25					
	C1-4-40	00	40					
	C1-5-60	00	60					
	C1-6-80	00	80					

The test set-up is schematically shown in figure 3. Working load N_0 from an actuator was applied to the mid-span of a transverse steel beam simply supported onto two A-frames. The pin-ended column was connected to the transverse beam and to the test frame through knuckle bearing blocks. A pre-designed fire condition was generated by an electric furnace. At room temperature the specimen was loaded to 100% of N_0 and was held constant when the specimen was exposed to fire. The heated specimen tended to elongate but was constrained by the restraint steel beam. It was subjected to an axial restraint arising from the flexural stiffness of the transverse beam. The restraint forces developed within the column during the test could be obtained from the reaction forces at the restraint beam ends through load cells LC_1 and LC_2 . The fire tests were conducted until the combination of the constantly-held working load and the developing restraint force could not be sustained by the specimen, indicating the occurrence of failure.

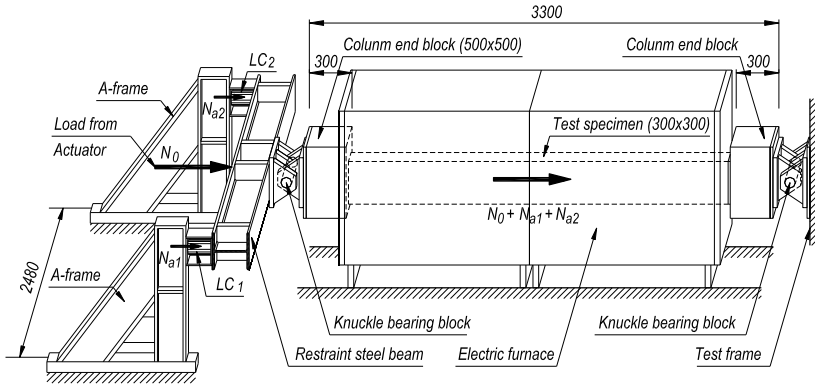


Figure 3. Schematic image of test set-up.

4 NUMERICAL STUDY

Numerical study on the above-mentioned test specimens is conducted by SAFIR, a computer program for the combined analyses of heat transfer and structural response of three-dimensional structures under

fire condition [12]. The software has been well validated by a large number of fire tests conducted at different laboratories [13]. Nonlinear thermal properties and temperature-dependent stress-strain relationships of concrete and reinforcing steel, as well as geometrical imperfection specified in EC2 Pt.1.2 [9], are incorporated in the study.

At every time step, based on the development of the equivalent distributed temperature θ (equation (9)) using the temperature profile that had been interpreted from SAFIR thermal analysis into the analytical model introduced in Section 2, the reduction factor of axial stiffness, α_e^θ , can be determined numerically for unrestrained columns to eliminate the effect of transient strain. Nine levels of uniaxial load eccentricity, in terms of the ratio to the depth of column cross-section, e/h , viz. 0, 0.083, 0.133, 0.200, 0.267, 0.333, 0.400, 0.467, and 0.500, are investigated. Particular equivalent distributed temperatures of 20, 100, 150, 200, 250, 300, 350, 400 and 450 °C are chosen. Higher temperatures are not investigated since all test specimens failed before the equivalent distributed temperature reached 450 °C. At every time interval, with the corresponding fire temperature T and equivalent distributed temperature θ , the following numerical steps are conducted: (1) Total axial deformation, u_{tot}^θ , is extracted from SAFIR analysis; (2) Equivalent thermal deformation, u_{σ}^θ , is determined based on equation (7); (3) Equivalent mechanical deformation, u_{σ}^θ , is computed as $u_{\sigma}^\theta = u_{tot}^\theta - u_{\sigma}^\theta$; (4) Equivalent axial stiffness is determined based on the conventional mechanical relationship $k_e^T K_c^T = N_0 / u_{\sigma}^\theta$; and (5) Reduction factor of axial stiffness is calculated: $\alpha_e^\theta = k_e^T K_c^T / K_c^{20}$.

The two- and three-dimensional graphs of the reduction factor of axial stiffness for columns under uniaxial bending are shown in figure 4, in which the factor α_e^θ equals to unity in the case of pure compression at ambient condition and gradually decreases when either load eccentricity or equivalent distributed temperature increases.

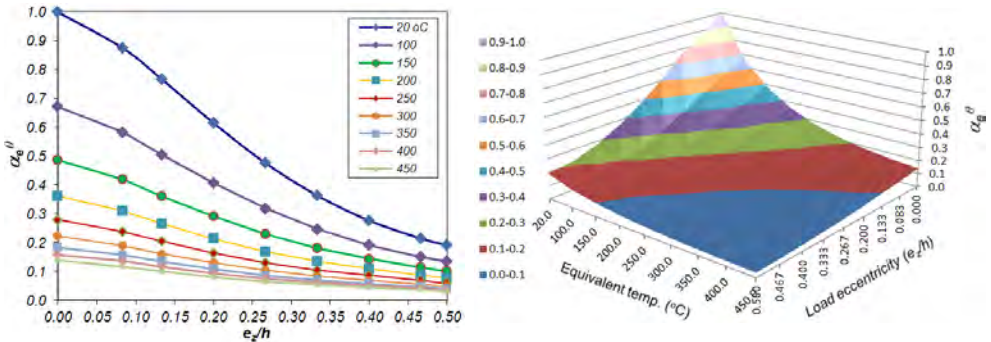


Figure 4. Reduction factor of axial stiffness for uniaxial bending.

It is shown in figure 4 that factor α_e^θ can be expressed as a function of eccentricity ratio (e_z/h) as well as equivalent distributed temperature θ . This relationship is also numerically determined from least-squares adjustment and is shown in equation (11).

$$\alpha_e^\theta = (a_{11}e^{a_{12}\theta})\left(\frac{e_z}{h}\right) + (a_{21}e^{a_{22}\theta}) \quad \text{when } \frac{e_z}{h} \leq 0.1 \quad (11-a)$$

$$\alpha_e^\theta = (a_{31}e^{a_{32}\theta})\left(\frac{e_z}{h}\right)^2 + (a_{41}e^{a_{42}\theta})\left(\frac{e_z}{h}\right) + (a_{51}e^{a_{52}\theta}) \quad \text{when } \frac{e_z}{h} > 0.1 \quad (11-b)$$

With fire exposure-dependent parameters a_{i1} , a_{i2} ($i=1\div 5$) determined by least-squares as listed in table 2, equations (11(a-b)) reflect the fact that α_e^θ decreases when either temperature or load eccentricity increases.

Table 2. Parameters for determination of α_c^θ of uniaxial bending and fire exposure used in the tests

a_{11}	a_{12}	a_{21}	a_{22}	a_{31}	a_{32}	a_{41}	a_{42}	a_{51}	a_{52}
-1.5438	-0.004	1.0043	-0.005	2.3588	-0.005	-3.0432	-0.005	1.1199	-0.005

5 RESULTS OF VALIDATION

The restraint forces, in terms of the normalised ratio ($\Delta N_a^T / N_0$) developed within the six test specimens introduced in Section 3, are analytically determined from equation (10) employing the reduction factor α_c^θ proposed in equations (11(a-b)). Computer program SAFIR is also used for structural analysis of the restrained test specimens to obtain numerical restraint forces. Figure 5 depicts the restraint forces obtained from numerical, experimental and analytical approaches which are plotted in hidden, continuous, and double lines, respectively.

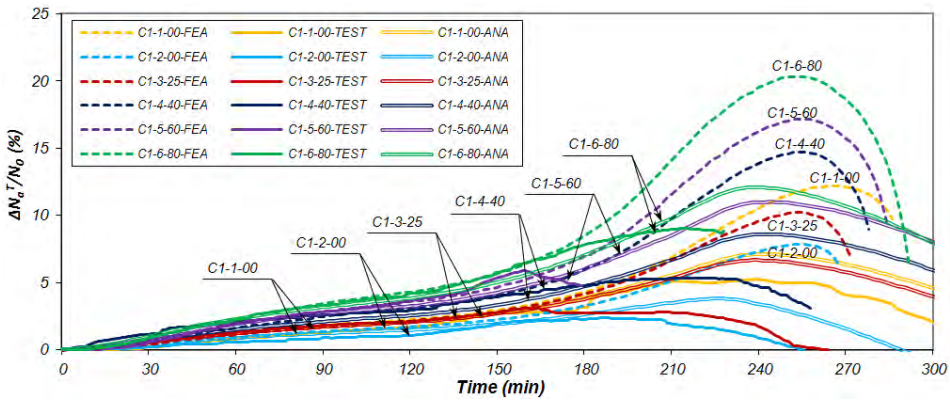


Figure 5. Validation of analytical approach.

It can be observed from figure 5 that the analytical predictions are in good agreement with experimental results. They also reflect similar trends as well as deviations between the numerical and experimental results in terms of the effects of load eccentricity, load level, axial restraint ratio, concrete spalling, and transient strain, which will be discussed in the next section.

6 DISCUSSIONS

6.1 Effects of load eccentricity and load level

A similar trend can be observed from analytical, experimental, and numerical results shown in figure 5. These columns which are subjected to higher load eccentricities, experience higher restraint forces. This trend is also shown in figure 6 which is constructed based on the proposed analytical approach (equation (10)).

It can be explained that under uniaxial bending, the ambient resistance of the column in term of axial force decreases with an increase of load eccentricity, leading to a lower level of initial applied load N_0 (in case the same load ratio μ_{fi} is employed). Since the term N_0 is located at the denominator of the component in brackets of equation (10), a reduction of N_0 results in an increase of ($\Delta N_a^T / N_0$).

It is also illustrated in equation (10) that under the same load eccentricity, a lower load level μ_{fi} leads to a lower initial applied load N_0 resulting in an increase in the restraint force. As shown in figure 5, this

trend can be observed from test results of specimen C1-1-00 ($\mu_{\bar{r}}=0.45$), which attained higher restraint forces than those of specimen C1-2-00 ($\mu_{\bar{r}}=0.55$).

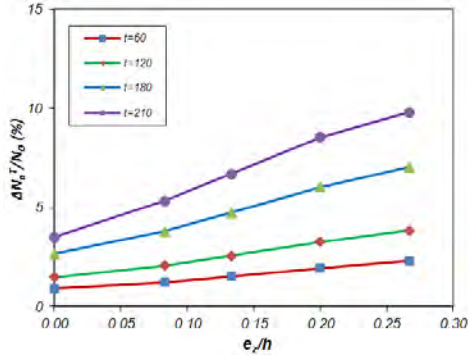


Figure 6. Effect of load eccentricity on restraint force.

6.2 Effect of restraint ratio

Equation (10) is also able to predict an obvious trend that columns subjected to a higher ratio of axial restraint, α_r , suffer higher restraint forces. Figure 7 illustrates the proportional relationship between restraint ratio α_r and restraint forces ($\Delta N_a^T / N_0$) when the other parameters are constant.

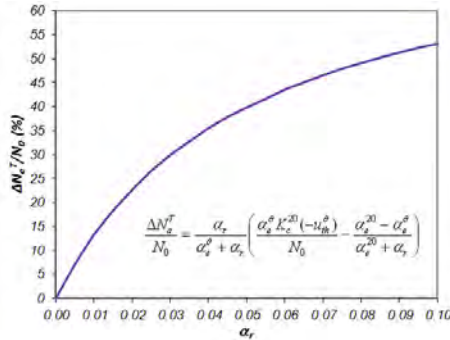


Figure 7. Effect of restraint ratio on restraint force.

6.3 Effects of concrete spalling and transient strain

It can be observed from figure 5 that although having good agreement at the initial stage, there are deviations between the experimental and numerical results of restraint forces from certain times at which concrete spalling started to occur. Beyond these times, the restraint forces predicted numerically are all greater than those measured in the fire tests.

It is noteworthy that concrete spalling is not considered in the numerical analyses conducted in this study. Since the surface concrete layers spall off, some interior parts of concrete and reinforcing steel are directly exposed to fire attack and the applied load is only sustained by smaller-in-area but hotter and weaker parts of the cross-section, resulting in a more rapid reduction of α_e^0 . As demonstrated in figure 8 that is constructed from equation (10), a reduction of α_e^0 also results in a reduction of restraint forces ($\Delta N_a^T / N_0$). Hence, it can be deduced from the proposed analytical model that models neglecting the effect of concrete spalling may over-predict restraint forces.

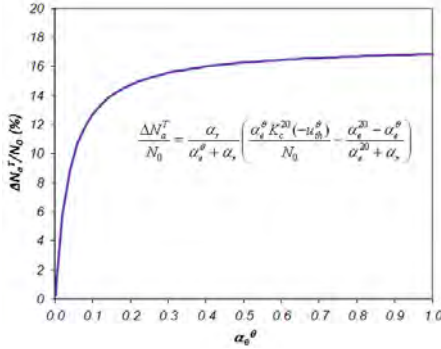


Figure 8. Effect of reduction factor α_e^θ on restraint force.

It should also be mentioned that the numerical study conducted in this paper adopts EC2 elevated-temperature mechanical properties of concrete [9], in which transient strain is implicitly considered. By definition, transient strain only changes when temperature increases at a constant level of stress whereas it remains constant with increasing stress at unchanged temperature. Different from unrestrained one, axially-restrained RC columns experience the simultaneous increases in both temperature and stress under fire conditions. This leads to the deviation between restraint forces predicted numerically and those measured in the tests.

In order to account for the effects of concrete spalling and transient strain on the more-rapid reduction of α_e^θ , an additional reduction factor, namely, χ_{cfb} , is proposed as shown in equations (12-13).

$$\frac{\Delta N_a^T}{N_0} = \frac{\alpha_r}{\chi_{cfb} \alpha_e^\theta + \alpha_r} \left(\frac{\chi_{cfb} \alpha_e^\theta K_c^{20} (-u_{th}^\theta)}{N_0} - \frac{\alpha_e^{20} - \chi_{cfb} \alpha_e^\theta}{\alpha_e^{20} + \alpha_r} \right) \tag{12}$$

$$\chi_{cfb} = 1 - k_{cfb} (t - t_{sp}) \leq 1 \tag{13}$$

where t is fire exposure time; t_{sp} is the time concrete spalling first occurs, which was recorded in the tests to be 160 min; and k_{cfb} is a parameter that depends on concrete grade, fire exposure, as well as the uniaxial/biaxial bending moment acting on the column, which was determined numerically to be 0.0015.

Reasonable good agreement between the test results and the improvement made on the analytical model can be observed in figure (9).

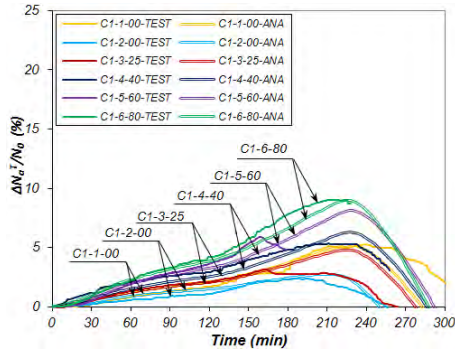


Figure 9. Improved analytical equation vs. Test results.

7 CONCLUSION

The analytical model proposed in this paper can be used to determine restraint forces induced in RC columns subjected to eccentric loads at elevated temperatures, taking into account the effects of load eccentricity, load level, restraint ratio, concrete spalling, and transient strain, so that it can be employed in performance-based fire resistance analysis of RC columns under realistic fire, loading, and restraint conditions. The model is well validated by fire tests conducted recently at NTU and is capable of explaining a similar trend as well as deviations observed from experimental data and numerical predictions. Future work is to conduct further investigations on restraint forces induced in columns subjected to biaxial bending under fire conditions.

ACKNOWLEDGEMENT

The authors wish to acknowledge the Singapore Agency of Science, Technology and Research (A*STAR) for their financial support.

REFERENCES

- [1] Dwaikat M.B., Kodur V.K.R., "A Numerical Approach for Modelling the Fire Induced Restraint Effects in Reinforced Concrete Beams", *Fire Safety Journal*, 43, 291-307, 2008.
- [2] Lin T.D., Gustaferro A.H. and Abrams M.S., "Fire Endurance of Continuous Reinforced Concrete Beams", *PCA R&D Bulletin RD072.01B*, 1981.
- [3] Dotreppe J.C., Franssen J.M., "The Use of Numerical Models for the Fire Analysis of Reinforced Concrete and Composite Structures", *Eng Anal CML Publ*, (2), 67-74, 1985.
- [4] Lie T.T, Lin T.D., "Influence of Restraint of Fire Performance of Reinforced Concrete Columns", *First international symposium, International Association for Fire Safety Science*, 1985.
- [5] Wang Y.C, Moore D.B., "Effect of Thermal Restraint on Column Behaviour in a Frame", *The fourth International Symposium of Fire safety science, Ottawa*, 1055-66, 1994.
- [6] Ali F., Nadjai A., Silcock G. and Abu-Tair A., 'Outcomes of a Major Research on Fire Resistance of Concrete Columns', *Fire Safety Journal*, 39, 433-445, 2004.
- [7] Wu B., Li Y-H., "Experimental Study on Fire Performance of Axially-Restrained NSC and HSC Columns". *Structural Engineering and Mechanics*, 32(5), 635-48; 2009.
- [8] Martins A.M.B., Rodrigues J.P.C., "Behaviour of Concrete Columns Subjected to Fire". *Proceedings of the Sixth International Conference SiF, USA*, 181-188, 2010.
- [9] EN 1992-1-2, Eurocode 2, "Design of Concrete Structures – Part 1-2: General Rules, Structural Fire Design", *CEN*, 2004.
- [10] ACI/TMS Committee 216, "Code Requirements for Determining Fire Resistance of Concrete and Masonry Construction Assemblies (ACI 2.16.1-07/TMS-216-07)", *American Concrete Institute*, 2007.
- [11] Nguyen T.T., Tan K.H., "An Experimental Study on Reinforced Concrete Columns Subjected to Eccentric Loads and Axial Restraint at Elevated Temperatures". *Proceedings of the Seventh International Conference SiF, Zurich*, 2012.
- [12] Franssen J.M., "SAFIR. A Thermal/Structural Program Modelling Structures under Fire", *Engineering Journal A.I.S.C.*, 42(3), 143-158, 2005.
- [13] Franssen J.M., Sheleich J.B., Cajot L.G. and Azpiazu W., "A Simple Model for Fire Resistance of Axially Loaded Members - Comparison with Experimental Results". *Construction Steel*, 37, 175-204, 1996.

AN APPROACH TO ACCOUNT FOR TIE CONFIGURATION IN EVALUATING FIRE PERFORMANCE OF REINFORCED CONCRETE COLUMNS

Wasim Khaliq* and Venkatesh Kodur*

*Civil and Env. Eng., Michigan State University, East Lansing, MI 48824-1126
e-mails: khaliqwa@egr.msu.edu, Kodur@egr.msu.edu

Keywords: Reinforced concrete columns, Fire resistance, Tie configuration, Spalling, Numerical model.

Abstract. *High strength concrete (HSC) columns exhibit lower fire resistance, as compared to conventional normal strength concrete columns, due to occurrence of fire induced spalling and faster degradation of strength and stiffness properties of concrete with temperature. Fire resistance tests on HSC columns have shown that fire performance of HSC columns can be enhanced through bending the ends of ties at 135° into the concrete core, instead of placing the ties at 90°. This paper presents an analytical approach to model the effect of tie configuration on fire resistance of reinforced concrete (RC) columns. The proposed approach is based on seismic design principles and involves calculation of force acting on ties by evaluating effective stresses resulting from pore pressure, mechanical strains and thermal expansion. The force on ties are compared against temperature (time) dependant bond strength (tie-concrete interface) to evaluate the failure of ties. The proposed tie sub model is built in to an existing macroscopic finite element based fire resistance analysis computer program that is capable of tracing the fire response of RC columns in the entire range of behavior. The applicability of the model is demonstrated through case studies on reinforced concrete columns with different tie configurations.*

1 INTRODUCTION

Fire represents one of the most severe environmental conditions to which reinforced concrete (RC) structures may be subjected; therefore, provision of appropriate fire safety measures to structural members is an important aspect in building design. Generally, structural members made of conventional concrete exhibit good performance under fire situations. However, in the last three decades a number of new types concrete have come in to market place as a result of significant research and development. These new concretes, often referred to as high strength concrete (HSC) or high performance concrete (HPC), have excellent strength and durability properties, but exhibit poor fire performance due to fire induced spalling and faster degradation of strength and stiffness properties of concrete with temperature.

To mitigate fire induced spalling in HSC structural members, researchers have recommended the addition of polypropylene and/or steel fibers to concrete mix [1-3]. Under fire conditions, the polypropylene fibers that are dispersed in concrete mix melt at relatively low temperature (about 160-170°C) and create randomly oriented micro and macro channels inside concrete, which facilitate dissipation of fire induced vapor pressure [4, 5]. In the case of steel fibers, tensile strength of concrete (both at ambient and elevated temperatures) gets enhanced as steel fibers help to arrest the initiation and progression of microcracks. This improved tensile strength of concrete is sufficient to resist the vapor pressure generated from steam for a longer duration and thus the extent of spalling gets minimized and fire resistance gets enhanced [4].

In lieu of adding fibers, some researchers recommend modifying tie configuration to limit the spalling and enhance fire resistance [6, 7]. Based on limited fire tests on HSC columns, these researchers have shown that fire performance of HSC columns can be enhanced by bending the ends of ties at 135°

into the concrete core, instead of bending the ties at 90° [8, 7]. Figure 1 illustrates the two types of tie configuration that can be used in HSC columns and comparative state of the HSC columns after exposure to ASTM E119 standard fire [7]. Researchers hypothesized that 135° bent ties delay the opening up of ties during a fire event and thus enhance fire resistance of concrete columns. Kodur and McGrath [7], based on fire tests have reported significant increase in fire resistance of an HSC columns through altering the tie configuration from 90° to 135° bents and also by reducing spacing of the ties.

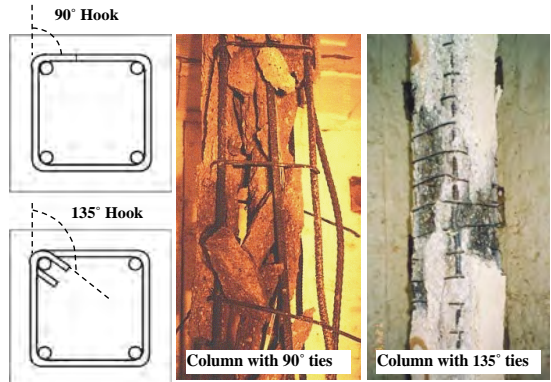
This improvement in fire resistance, resulting from 135° bent ties, is critical in realizing high fire resistance in HSC columns. However, at present, there is no analytical approach to quantify the effect of tie configuration on fire resistance of RC columns. To develop such an approach, a numerical 'tie sub model' was developed to model the effect of tie configuration on fire response of RC columns. The approach is based on seismic design principles and involves calculation of effective stress acting on ties which is the sum of stresses generated from pore pressure, thermal and mechanical strains. The force resulting from effective stress is compared against the degrading bond strength of the tie. This tie sub model is built in to a macroscopic finite element based fire resistance computer program that is capable of evaluating the fire response of RC columns.

2 APPROACH TO MODEL TIE CONFIGURATION

The beneficial effect of lateral confinement in concrete columns, both tie configuration (135°) and closer spacing of ties, has been well recognized in seismic design of columns [9-11]. This design philosophy is based on the principle that the compressive strength of the confined core of a column after stress induced spalling should be equal to the strength of the gross section of the column before the occurrence of spalling [11]. The ties in columns when bent at 135° achieve sufficient lateral confinement and enhance ductility of columns under earthquake loading [9, 12, 10]. Similar approach, as that developed for seismic loading, can be applied to model the effect of tie configuration on fire resistance of reinforced concrete columns. However, in the case of fire conditions, stresses due to temperature induced vapor pressure and thermal strains are to be considered in addition to stresses due to loading on the column. Also, bond strength that develops at the tie-concrete interface, deteriorates with temperature and also due to occurrence of fire induced spalling. The force acting on the ties from effective stress should be checked against this bond strength so as to ensure that the ties have sufficient resistance and do not open-up through yielding.

When RC columns are exposed to fire, temperatures in concrete, steel reinforcement and ties gradually increase. The increasing temperatures in concrete lead to build-up of pore pressure which cannot be dissipated due to low permeability of concrete (characteristic of HSC). When this pore pressure exceeds tensile strength of concrete, spalling occurs. The fire induced spalling in concrete usually occurs in high strength concrete (HSC) structural members because of low permeability associated with HSC. Such spalling not only leads to loss of cross-section in the column, but also alters the bond resistance of the ties.

When exposed to fire, significant level of internal stresses are generated on ties and these result from load induced mechanical strains, temperature induced thermal expansion, and fire induced vapor pressure as a result of water becoming vapor. These three stresses (thermal, mechanical, and vapor pressure) are



(a) Tie configuration (b) HSC columns after fire tests

Figure 1. Comparison of fire performance of RC columns with conventional 90° ties and modified 135° ties

added to evaluate the effective stress that acts as hoop stress on ties. The ties resist the effective stress through bond strength developed in the ties which also degrades with increasing temperatures. When the force resulting from effective stress exceeds the bond strength of ties, the ties will open up (fail) by yielding.

The necessary equations for confinement damage model under fire conditions can be derived based on approach adopted in seismic analysis of concrete columns. The pressure exerted by the expanding concrete core in the form of hoop stress on ties and the effect of confinement of ties on longitudinal rebars can be used to model the tie behavior.

Free body diagram of various components of an RC column and forces acting on rebar and ties is illustrated in Figure 2. The longitudinal rebar between the two ties is subjected to a force which varies as sinusoidal wave function [9]. At the level of ties a lateral restraint is provided by tie corners, and the resulting force on longitudinal rebar is higher (Figure 2(a)). At the mid-level between the two ties, the force is the lowest as the concrete core can expand relatively easily and thus exert force on longitudinal rebars. This force varies along the longitudinal rebar and its variation can be taken as:

$$F_{(x)} = F_0 + F_v \times \cos\left(\frac{2\pi x}{s}\right) \geq 0 \tag{1}$$

where $F_{(x)}$ is force function along longitudinal rebar, F_0 = average force acting on longitudinal rebar; F_v = magnitude of variable part of force; x = coordinate along the length of rebar and s = tie spacing as shown in Figure 2(b) and (c). The unknowns in Eq (1), F_0 and F_v , can be determined by applying force equilibrium and geometric boundary conditions. These two unknowns can be related to tie spacing (s) and critical tie spacing (s_{cr}). Critical tie spacing, taken from the approach used in seismic design, is at the mid-height between two ties where effective confined concrete area is assumed to be zero [9].

This implies that if $s = s_{cr}$ at $x = s_{cr}/2$, the force exerted by ties on longitudinal rebars ($F_{(x)}$) becomes zero, leading to variable part of the force F_v as:

$$F_v = F_0 \left(\frac{s}{s_{cr}}\right)^2 \tag{2}$$

By substituting the value of F_v back to Eq (1), the force acting on longitudinal rebars can be calculated as:

$$F_{(x)} = F_0 \left[1 + \left(\frac{s}{s_{cr}}\right)^2 \times \cos\left(\frac{2\pi x}{s}\right) \right] \tag{3}$$

The force developed in the ties can be obtained by integrating the force on longitudinal rebar and applying boundary conditions:

$$F_{tie} = 2 \int_0^{s/2} F_{(x)} dx \tag{4}$$

Solving Eq (4) gives the total tie force acting on the corner of the longitudinal rebar which translates to:

$$F_{tie} = 2A_{tie} \sin\left(\frac{\pi}{4}\right) \sigma_{core} \tag{5}$$

where A_{tie} = cross sectional area of tie, σ_{core} = stress resultant which is the sum of load induced stress, thermal stress and pore pressure coming from concrete core.

Knowing the applied load on the column, load induced (mechanical) stress can be evaluated at any given time step. It should be noted that this stress significantly increases with increasing temperature due to degradation of strength properties of concrete and steel. Further, if there is any fire induced spalling, the cross-section of column reduces and this leads to higher mechanical stresses in column. The second component of the stress on the ties is the fire induced thermal stress which can be evaluated knowing the temperatures in the column. The thermal stress is evaluated by utilizing the high temperature material properties and thermal expansion of concrete which varies as a function of temperature.

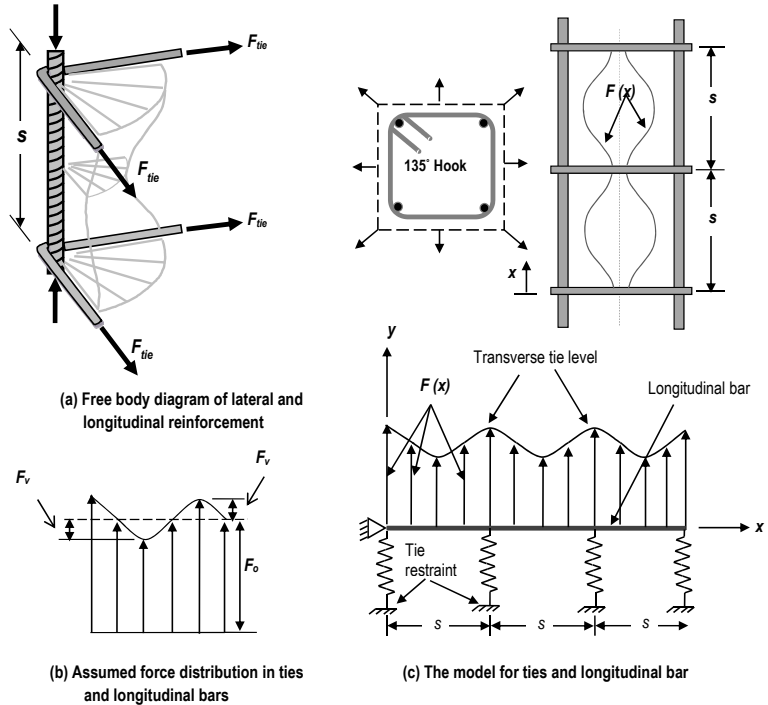


Figure 2. Longitudinal rebars and transverse tie model with assumed forces

The third component of the stress that is acting on the ties is the pore pressure in concrete which can be evaluated through an hydrothermal model [13]. This model uses the principles of mechanics and thermodynamics including the conservation of mass of liquid water and water vapor to predict the pore pressure in the concrete exposed to fire [14]. In the hydrothermal model, the mass transfer equation for water vapor inside heated concrete can be written as:

$$A \left(\frac{dP_V}{dt} \right) = \nabla B \nabla P_V + C \tag{6}$$

where: P_V = pore pressure, t = time, A , B and C = parameters that depend on pore pressure, temperature, rate of increase in temperature, permeability of concrete, initial moisture content, and the isotherms used in the analysis. Isotherms are used to predict the liquid water inside concrete as a function of pore pressure for a constant temperature.

Finite element analysis is used to solve Eq (6) and compute the pore pressure (P_V) distribution within the elements of each segment along the length of the structural member. With this stress from pore pressure (σ_{P_V}) inside concrete is calculated, it is combined with other two stresses to get the effective stress exerted by concrete core on ties. The equation governing this condition is given by:

$$\sigma_{core} = \sigma_{P_V} + \sigma_{thermal} + \sigma_{mechanical} \tag{7}$$

where σ_{pv} is stress due to pore pressure, σ_{thermal} is stress coming from thermal expansion of concrete core and $\sigma_{\text{mechanical}}$ is stress resulting from axial load on column. With the effective stress (σ_{core}) in tie known, the force acting on ties (F_{tie}) is computed using Eq (5).

The resisting bond strength of the ties decreases with temperature and is given by the relation:

$$F_{\text{bond}} = (2\pi r l_d) f_{s,T} \quad (8)$$

where $f_{s,T}$ is the stress in of steel at temperature T.

Knowing the force acting on ties and bond strength that develops in ties, the state of tie can be checked and failure (opening up of ties) is said to occur when.

$$F_{\text{tie}} > F_{\text{bond}} \quad (9)$$

3 INCORPORATION OF TIE SUBMODEL INTO THE FIRE RESISTANCE MODEL

The above described ‘tie sub model’ is incorporated into a macroscopic finite element (MFE) based computer program for evaluating fire resistance of RC columns. This MFE model utilizes the M– κ relationships to trace the fire response of RC columns. The analysis is carried out by incrementing time in steps. At each time step the analysis is carried out in three stages namely, (1) establishing temperatures due to fire, (2) carrying out heat transfer analysis to determine temperature distribution in the cross-section and evaluation of pore pressure, and (3) at each time step performing strength and stiffness analysis of the column. In step 3, fire induced axial restraint force in columns is calculated and then M– κ relationship is generated for various segments in the column. The output parameters generated from the above program, at each time step, include temperatures at various locations (including rebars and ties), stress due to mechanical loading, thermal stress and pore pressure.

The ‘tie sub model’ is built into the above computer program in stage 3 of the analysis. Using the parameters, the effective stress at a given time step is evaluated as the sum of three stresses namely pore pressure, thermal and mechanical stresses. The effective stress is utilized to compute the force acting on the ties. Also the bond strength can be evaluated knowing the temperatures at the ties. Then the force acting on the tie is checked against bond strength to evaluate if the ties have opened-up (yielded).

4 VALIDATION OF THE NUMERICAL MODEL

The validity of the above macroscopic finite element model is established by comparing the predictions from the analysis with fire test data on RC columns reported in literature. For this purpose, four HSC columns (HSC2, HSC3, HSC5, and HSC6) and one NSC column (NSC) were selected from fire resistance tests carries out at National Research Council of Canada [7, 15]. The geometric and material properties of the selected columns are tabulated in Table 1. The columns were analyzed by exposing the columns to ASTM E119 standard time-temperature curve as in the case of fire tests [16]. For concrete and reinforcement, high temperature property relationships specified in ASCE manual [17] are used in the analysis. The fire resistance of columns was calculated based on strength failure criterion and the time at which ties opened up (through yielding) was also evaluated. Predictions from the analysis are compared to the measured values from fire tests in Figures 3, 4 and Table 1.

The predicted temperatures at three different cross-sectional locations, namely rebar, at 176 mm depth in concrete and at mid depth (in concrete) of HSC2 column, are compared against the measured temperatures as shown in Figures 3. It can be seen that the predicted temperatures are generally in good agreement with the measured values with lower temperatures at farther locations from the fire exposure surface throughout the analysis range. Figure 4 shows comparison of axial deformations as a function of fire exposure time for columns HSC2 and HSC6. Again the model predictions are in agreement with the measured deformations. The deformations in the column result from the effects of thermal expansion, loading and high temperature creep. Both columns undergo expansion in early stages of fire exposure due

to rise in temperature in concrete and steel rebars. However, column HSC2 experienced mostly expansion, while column HSC6 experienced contraction. This is because load induced deformations dominated in column HSC6 as a result of higher applied load on the column, while the effect of thermal expansion dominated in column HSC2 (due to lower load). The fire resistance predicted by model is compared to the measured fire resistance values for HSC2, HSC3, HSC5 and HSC6 columns in Table 1 and the predicted values are close to measured values in tests.

Table 1. Parameters and results for RC columns used in the validation study

Column designation	Size (mm)	Tie configuration/spacing	Concrete strength (MPa)	Column strength (kN)	Load ratio (%)	Applied load (kN)	Relative humidity (%)	Fire resistance measured	Fire resistance predicted	Ties opened
NSC	305	90°@h	37	-	-	1333	15	240	360	No
HSC2	406	90°@h	86	5900	0.4	2406	86	224	213	Yes
HSC3	406	90°@h	96	7400	0.6	4919	57	104	120	No
HSC5	305	135°@h/4	120	3145	0.4	2363	68	290	282	No
HSC6	305	135°@h/4	120	3145	0.6	2954	64	266	254	No

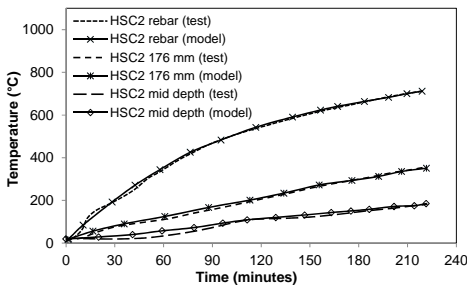


Figure 3. Comparison of measured and predicted temperatures in HSC2 column

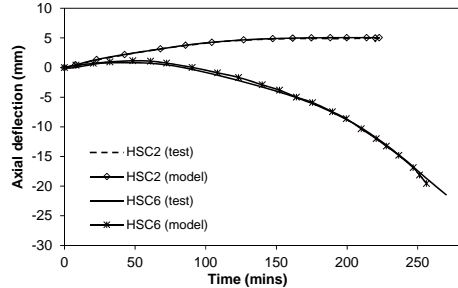


Figure 4. Comparison of measured and predicted axial deformations in HSC2 and HSC6 columns

Results from fire resistance analysis indicate that in the case of NSC and HSC2 columns, with 90° ties, the ties did not open up. However, in column HSC3 with 90° ties, failure of the column occurred just after the opening-up of ties and this occurred at much lower duration in to fire exposure. Column HSC3 failed in 120 minutes, as compared to column HSC2 that lasted for 213 minutes. The failure of ties in column HSC3 is due to higher force acting on ties as a result of higher applied load on the column.

Columns HSC5 and HSC6, with 135° bent ties, did not experience failure in ties. While HSC3 column failed at 120 minutes, no failure of ties occurred in column HSC6. The benefit of modified tie configuration (135° bent ties) is quite evident by comparing the performance of columns HSC3 (with 90° bent ties) and HSC6 (with 135° bent ties).

5 CASE STUDY

To illustrate the applicability of ‘tie sub model’ in evaluating the fire response, a case study was carried out on RC columns with different tie configurations and concrete strengths by exposing the columns to ASTM E119 standard fire [16]. For the case study one NSC column (NSC) and two HSC columns (HSC1, HSC2) with 90° bent ties and two similar HSC columns (HSC3 and HSC4) with 135° bent ties were selected. The compressive strength and permeability of concrete in NSC column is assumed to be 40 MPa and $2 \times 10^{-16} \text{ m}^2$ while that in HSC columns it is 100 MPa and $2 \times 10^{-18} \text{ m}^2$ respectively. Columns NSC, HSC1 and HSC3 were axially loaded to 40% of their capacity, while columns HSC2 and HSC4 were loaded to 60% of their room capacity to study the effect of load level. All five columns were of square cross section of 305x305 mm, 3810 mm length, and steel reinforcement consisted of 4 #8 (25

mm) rebars as main reinforcement, and #3 (10 mm) rebars as ties placed at 305 mm spacing. Specified yield strength of steel rebars and ties was assumed to be 420 MPa. Figure 5 illustrates the cross-sectional dimensions for columns used in the case study.

Fire resistance analysis is carried out on the above five columns by idealizing in to a number of segments along length and discretization of each segment (cross-section) in to elements. At each time step, analysis is carried out by first establishing the fire temperatures (ASTM E119 fire scenario). Then thermal analysis is carried out by calculating cross-sectional temperatures and pore pressure. When the pore pressure in an element exceeds temperature dependant tensile strength of concrete, that element is removed from the cross-section for further analysis. Results from the analysis show that spalling of concrete cover in HSC columns accrued 60 minutes. No spalling was assumed to have occurred in NSC column. Next, the strength and stiffness analysis is carried out by using high temperature concrete and steel material properties. The output parameters namely temperatures at various locations (ties), mechanical stress, thermal stress and pore pressure are generated from the model. Using these parameters effective stress is evaluated and the force acting on the tie is computed. Also with increasing temperatures in ties and loss of concrete cover bond strength degrades with time. The force acting on the tie is then checked against bond strength to evaluate failure of the ties. This procedure is repeated for each time step till the failure of column occurs through reaching one of the failure limit states [14].

Figure 6 illustrates the predicted pore pressure in five columns as a function of fire exposure time, where in the pore pressure increases with time, reaches a peak value and then drops with time. The increase in pore pressure can be attributed to build-up of moisture clog resulting from moisture movement inside concrete matrix. As the temperature in concrete layers increase beyond 100°C, water present in concrete evaporates, leading to build-up of pore pressure that increases with depth. This pore pressure build-up drives part of water vapor to move away from heated surface deep into the inner layers of concrete member. This migrated water vapor condensates and results in saturation of concrete microstructure. This phenomenon is referred to as moisture clog and depending on concrete microstructure (strength) this can result in to significant variation in pore pressure during fire exposure [14].

Figure 6 shows that the pore pressure is highly dependent on permeability of concrete. Results from the analysis show that a peak pore pressure of 4.5 MPa gets developed in HSC concrete columns, whereas in NSC column it is closer to 1 MPa. The lower pore pressure in NSC column can be attributed to the fact that NSC has high permeability, which facilitates dissipation of water vapor and thus there is no build-up of pore pressure. On the other hand in HSC columns, the lower permeability [18, 19] does not facilitate the escape of water vapor and resultantly, higher pore pressure gets developed in these columns.

In addition to pore pressure development, another phenomenon that occurs with increase in cross-sectional temperatures is the degradation of bond between reinforcement (ties) and concrete. The degradation of bond strength for different tie configurations (10 mm ties) is illustrated in Figure 7. The bond strength is dictated by the temperature level in ties and any loss of cross section due to fire induced spalling.

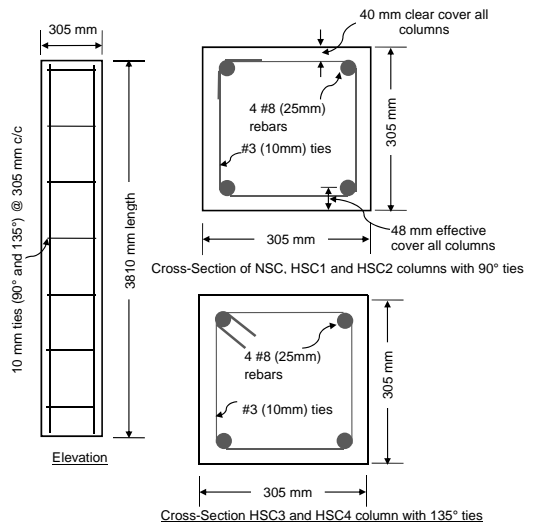


Figure 5. Elevation and cross-sections of RC columns used in case study

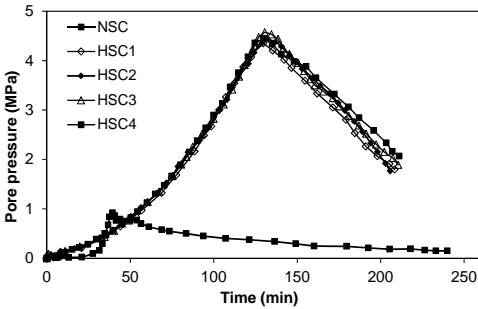


Figure 6. Predicted pore pressure at cover depth for different RC columns

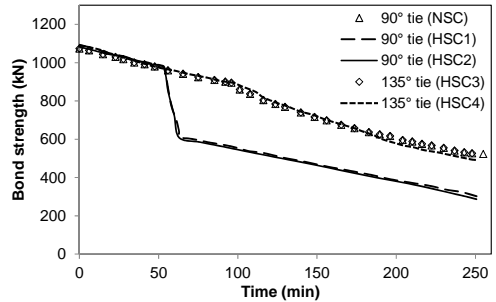


Figure 7. Predicted bond strength offered by various ties in selected columns

The significant drop in bond strength in 90° bent ties, at about 60 minutes, results from high temperatures developing in ties due to direct heating from fire. This occurs as a result of loss of cover concrete from fire induced spalling. The bond strength reduces to half of its original value. Such loss in bond strength is not encountered in 135° bent ties as the legs of the ties are bent inward and embedded in to the concrete core. Since no spalling occurs in the NSC column, the bond strength does not degrade significantly in spite of this column havign 90° bent ties. The lower bond strength in HSC1 and HSC2 columns at 60 minutes into the fire exposure occurs due to loss of concrete cover from fire induced spalling.

The effective force that is acting on ties results from the combination of stresses generated from pore pressure, mechanical strain (loading) and thermal strain in fire exposed columns. Figure 8 illustrates the effective tie force plotted against the bond strength for columns NSC, HSC1 and HSC2, with 90° bent ties. For NSC column the predicted effective tie force is much lower than the resisting bond strength. This can be attributed to the lower pore pressure that develops in NSC column that leads to lower total effective stress under fire conditions. This indicates that for conventional NSC columns, changing the tie configuration will not add to fire resistance.

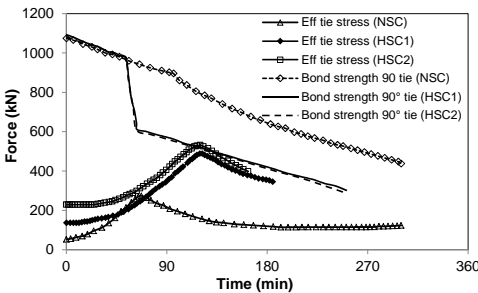


Figure 8. Predicted effective tie force compared to bond strength in 90° tie in NSC, HSC1 and HSC2 columns

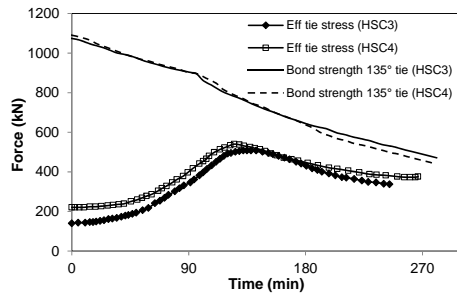


Figure 9. Predicted effective tie force compared to bond strength in 135° tie in HSC3 and HSC4 columns

Due to fire induced spalling in columns HSC1 and HSC2 (90° bent ties), at about 60 minutes into the fire test bond strength significantly decreases in these columns. The predicted effective tie force in column HSC2 is higher than that in column HSC1 and this is due to higher loading ratio (0.6). The effective force acting on tie in column HSC2 increase with time and then reduces at a faster rate than that in column HSC1 which can also be attributed to higher steel stress in tie in column HSC2. The analysis shows that the ties (bent at 90°) failed due to opening-up (yielding) in column HSC2 at 120 minutes into the fire exposure and this led to failure of this column. On the other hand, ties did not fail in column HSC1, which can be attributed to lower mechanical stress induced from loading in column HSC1.

Figure 9 illustrates the effective force on ties and resisting bond strength in 135° bent ties for columns HSC3 and HSC4. Both of these columns had 135° bent ties and therefore exhibited similar bond strength degradation in ties. However, as column HSC4 was subjected to higher load ratio (0.6), the predicted effective tie force induced in column HSC4 was higher than that in column HSC3 which can be attributed to higher load ratio.

Although fire induced spalling was assumed in HSC3 and HSC4 columns at 60 minutes into the fire exposure, the predicted bond strength in ties was not lost as that in 90° bent ties, this shows clear advantage of bending ties at 135° into concrete core over conventional 90° bent ties. As a result of higher bond strength in 135° bent ties, the fire resistance of columns HSC3 and HSC4 was significantly increased.

6 PRACTICAL IMPLICATIONS

The use of HSC in columns offers numerous advantages over that of conventional NSC. However, HSC is much more susceptible to fire induced spalling and thus has lower fire resistance. This aspect can be overcome either through the addition of fibers or by reconfiguring the ties through bending the ends of ties at 135° into the concrete core. Since mixing and placing the fibre reinforced concrete in a job site can be labor intensive, bending the ties at 135° can offer a practical and economical solution in many situations.

An approach to account for the effect of tie configuration in fire resistance evaluation of RC columns is proposed. This approach clearly illustrates the enhancement of fire resistance that can be achieved through 135° bent ties in HSC columns. The proposed approach can be applied to quantify the influence of various factors, such as tie spacing, bent angle, concrete strength, load ratio, and fiber reinforcement, on the fire resistance of concrete columns.

7 CONCLUSIONS

- A numerical procedure for accounting the effect of tie configuration on fire resistance of reinforced concrete columns is presented. The proposed approach is based on principles used in seismic design and accounts for fire induced pore pressure, thermal and mechanical strains, as well as temperature induced bond degradation in ties.
- The pore pressure generated in typical high strength concrete columns can reach about 4.5 MPa, while the corresponding pore pressure in conventional normal strength concrete columns is only about 1 MPa.
- The degradation of bond strength in ties is dependent on the extent of loss of cross-section from fire induced spalling in columns. If cover concrete is lost due to fire induced spalling in columns then the bond strength in 90° bent ties degrade at a much faster rate than the case with 135° bent ties.
- Provision of 135° bent ties is much more beneficial in HSC columns, since the bent ties develop higher bond strength to resist higher level of effective stress.

ACKNOWLEDGMENTS

The research presented in this paper is supported by Michigan State University through Strategic Partnership Grant (No. 71-4434). Any opinions, findings, and conclusions or recommendations expressed in this paper are those of the authors and do not necessarily reflect the views of the sponsors.

REFERENCES

- [1] Ali, F., et al., Outcomes of a major research on fire resistance of concrete columns. *Fire Safety Journal*, 39(6): p. 433-445, 2004.

- [2] Bilodeau, A., V.R. Kodur, and G.C. Hoff, Optimization of the type and amount of polypropylene fibers for preventing the spalling of lightweight concrete subjected to hydrocarbon fire. *Cement and Concrete Composites*, 26(2): p. 163-174, 2004.
- [3] Hertz, K.D., Limits of spalling of fire-exposed concrete. *Fire Safety Journal*, 38(2): p. 103-116, 2003.
- [4] Ali, F. and A. Nadjai, Fire resistance of concrete columns containing polypropylene & steel fibers. *ACI Special Publication, SP-255-9*, American Concrete Institute, Farmington Hills, MI, 255(9): p. 199-216, 2008.
- [5] Kodur, V.K.R. and L. Phan, Critical factors governing the fire performance of high strength concrete systems. *Fire Safety Journal*, 42(6-7): p. 482-488, 2007.
- [6] Kodur, V.R. and R. McGrath, Effect of silica fume and lateral confinement on fire endurance of high strength concrete columns. *Can. J. Civ. Eng.*, 33: p. 93-102, 2006.
- [7] Kodur, V.R. and R. McGrath, Fire endurance of high strength concrete columns. *Fire Technology*, 39(1): p. 73-87, 2003.
- [8] Kodur, V.R. and R. McGrath, Fire endurance of high strength concrete columns, in NRCC-45141, National Research Council Canada, Ottawa, Canada. p. 1-13, 2003.
- [9] Bayrak, O. and S.A. Sheikh, Plastic hinge analysis. *Journal of Structural Engineering, ASCE*, 127(9): p. 1092-1100, 2001.
- [10] Pantazopoulou, S.J., Detailing for reinforcement stability in RC members. *Journal of Structural Engineering, ASCE*, 124(6): p. 623-632, 1998.
- [11] Richart, F.E., A. Brandtzaeg, and R.L. Brown, A study of the failure of concrete under combined compressive stresses, Engineering Experimental Station, Univ. of Illinois: Urbana IL, 1929.
- [12] Berry, M.P. and M.O. Eberhard, Practical performance model for bar buckling. *Journal of Structural Engineering, ASCE*, 161(7): p. 1060-1070, 2005.
- [13] Kodur, V.R., M. Dwaikat, and N. Raut, Macroscopic FE model for tracing the fire response of reinforced concrete. *Engineering Structures*, 31(6): p. 2368-2379, 2009.
- [14] Dwaikat, M.B. and V.K.R. Kodur, Hydrothermal model for predicting fire induced spalling in concrete structural systems. *Fire Safety Journal*, 44(3): p. 425-434, 2009.
- [15] Lie, T.T. and J.L. Woolerton, Fire resistance of reinforced concrete columns - test results, National Research Council Canada, Ottawa, Canada, 1988.
- [16] ASTM E119-08b, Standard test methods for fire tests of building construction and materials, ASTM International: West Conshohocken, PA, 2008.
- [17] ASCE, Structural fire protection, ASCE Committee on Fire Protection, Structural Division, American Society of Civil Engineers, New York, 1992.
- [18] Mindess, S., J.F. Young, and D. Darwin, *Concrete*. 2nd ed, New Jersey, USA: Pearson Education, Inc., 2003.
- [19] Noumowé, A., R. Siddique, and G. Debicki, Permeability of high-performance concrete subjected to elevated temperature (600°C). *Construction and Building Materials*, 23 (5): p. 1855-1861, 2009.

PERFORMANCE IN FIRE OF FIBRE REINFORCED POLYMER STRENGTHENED CONCRETE BEAMS AND COLUMNS: RECENT RESEARCH AND IMPLICATIONS FOR DESIGN

Mark F. Green*, Kevin Hollingshead* and Noureddine Bénichou **

* Dept. of Civil Engineering, Queen's University, Canada
e-mails: greenm@civil.queensu.ca, kevin.hollingshead@ce.queensu.ca

** National Research Council, Canada
e-mail: Noureddine.Benichou@nrc-cnrc.gc.ca

Keywords: Fire, Fibre Reinforced Polymers, Concrete, Strengthening, Repair, Rehabilitation.

Abstract. *This paper considers the fire performance of concrete beams and columns that have been strengthened with fibre reinforced polymers (FRPs). Results from four recent full-scale tests are presented. A newly developed type of insulation was employed and the thickness of the insulation (15 to 20 mm) was approximately half that provided in earlier tests. All of the members survived four hours of the fire exposure. A conceptual model for design is also presented. Further research needed to fully develop the conceptual model to a more practical design tool is outlined.*

1 INTRODUCTION

Fibre reinforced polymer (FRP) materials are increasingly being applied in many areas of construction, particularly for strengthening of concrete beams and columns. However, concerns associated with fire remain an obstacle to applying FRP materials in buildings and parking garages due to their susceptibility to degradation at elevated temperatures [1,2].

The first research in the area of fire and FRP strengthening was conducted in Switzerland. Deuring [3] tested beams strengthened with CFRP sheets in fire conditions, and found that insulated beams obtained satisfactory fire endurance. Additional work was conducted in Belgium on CFRP plated beams using multiple insulation schemes [4]. More recent work has considered the performance in a real compartment fire [5], and these authors found that the FRP strengthening schemes performed poorly even with insulation systems. On the other hand, Palmieri et al. [6] found that concrete beams strengthened with surface mounted FRPs could achieve a 2 hour fire endurance when appropriate insulation was provided.

Over the past ten years, Queen's and the National Research Council have collaborated to investigate the performance of FRP strengthened concrete structures in fire [2,7,8,9]. Four recent full-scale tests have been conducted to expand knowledge from earlier work, and the results from these tests are presented in this paper. These new results extend previous knowledge because the loads on the members were higher than the design capacity of the unstrengthened member, and the thickness of the insulation was approximately half that provided in earlier tests.

In addition to the paucity of test data on FRP strengthened concrete members in fire, design guidance for fire endurance is extremely limited [1,10,11]. To address this deficiency, a conceptual model for the design of FRP strengthened concrete structures for fire conditions is presented. The model is based on the experience gained from conducting 17 full-scale tests over the past ten years and from numerical models developed to predict the performance of FRP strengthened concrete structures in fire.

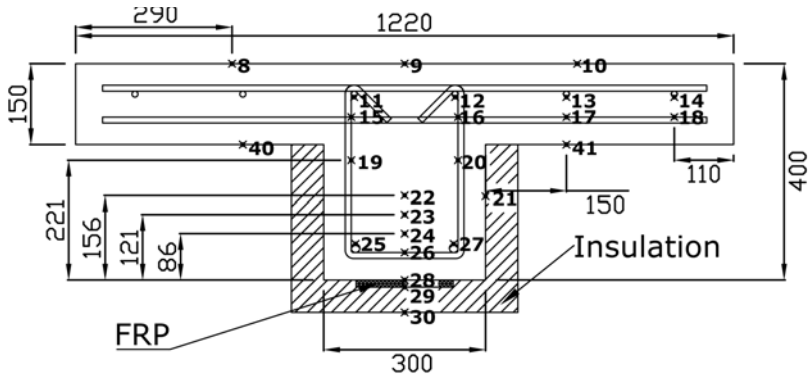


Figure 1. T-beam dimensions and thermocouple locations (shown by x).

2 RECENT TESTS AND RESULTS

Four recent full-scale tests have been conducted to expand knowledge from earlier work. Two full-scale T-beams (3.9 m span), one circular column, and one square column were all strengthened with external FRP. Fire protection for the FRP was provided by sprayed insulation.

2.1 T-beams

The T-beams (figure 1) were chosen to be 400 mm deep, with a web breadth of 300 mm and a 1220 mm \times 150 mm flange. Two 15 mm diameter steel reinforcing bars were provided as tensile reinforcement in the web at an effective depth of 340 mm. The clear cover to the reinforcement was 40 mm. The reinforcement had a tested yield strength of 406 MPa while the concrete was carbonate aggregate with a tested 28 day strength of 36 MPa. Each beam was fitted with a 100 mm wide, single-layered strip of carbon FRP for flexural strengthening (Tyfo SCH-41), which ran longitudinally along the bottom of the web as shown in figure 2. U-shaped glass FRP sheets were wrapped around the ends of the beams to provide anchorage for the longitudinal FRP. The carbon FRP had a design strength of 834 MPa, a design modulus of 82 GPa, a design failure strain of 0.85%, and a thickness of 1.0 mm. This FRP strengthening scheme provided a 23% strength increase according to ACI 440 [10]. The beams were extensively instrumented with thermocouples as shown in figure 1.

Figure 2 shows the insulation being applied to the beams. One beam was insulated with a 13 mm thick layer of insulation, which covered the entire web and extended 100 mm along the bottom of the flange on either side of the web. The other beam was insulated with a 19 mm thick layer, but it was to be placed more sparingly. Near the U-wraps, the insulation covered the entire web, but in the central part of the beam, the insulation only covered a portion of the side of the web. The insulation in this location only extended approximately 150 mm up the side of the web from the bottom of the beam. The thickness of the insulation for these beam tests was approximately half the thickness provided in earlier work [2,7,8,9].

For the fire tests, a superimposed load was applied such that the total load on the beam during the fire exposure was 10% greater than the design load of the beam without considering the strength of the FRP. This resulted in a test load ratio of 0.72 calculated as the total load during the test divided by the strengthened design capacity according to ACI 440 [10]. Furthermore, the beams were tested in a simply supported condition without any lateral or moment restraint. The beams were allowed sufficient space to expand at the ends without touching the sides of the supporting frame. Thus, the testing conditions were more severe than those considered in previous work [8] where the beams were restrained laterally and

subjected to lower loads. The beams were then exposed to a standard ASTM E119 [12] fire scenario from below.



Beam D - Average Temperatures

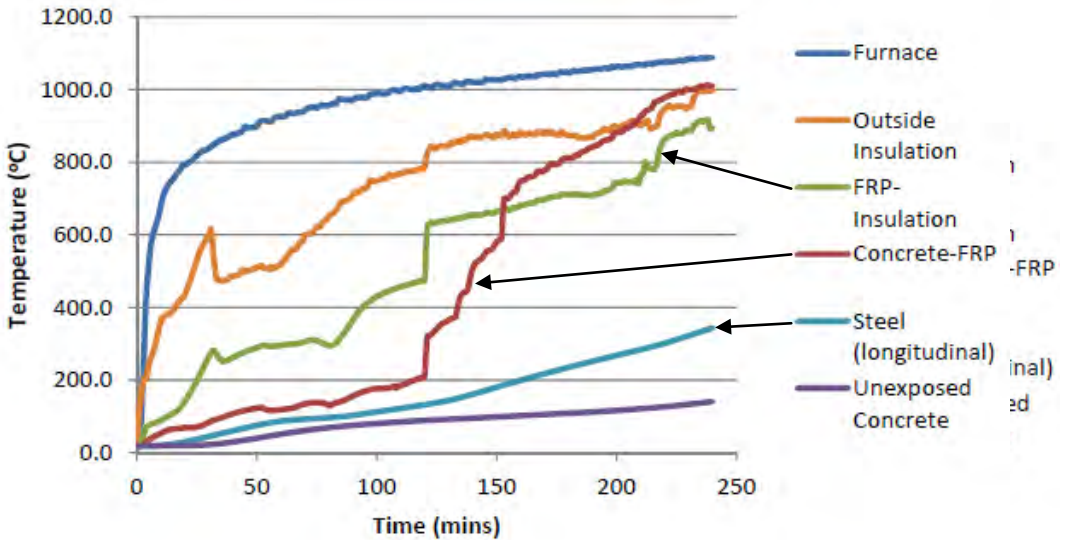


Figure 3. Temperatures measured in the T-beam with 19 mm of insulation.

During the test, the most significant area of interest was the slow deterioration of the insulating materials. Over the course of the four hours, insulation protecting certain key areas began cracking, delaminating from the concrete, and eventually falling off completely. After approximately 15 minutes of the test, cracking of the insulation and flames coming from the cracks were noticed. As the test progressed, pieces of insulation, bordered by the aforementioned cracks, began delaminating and eventually falling from the beams. This occurred more quickly with the beam with 19 mm of insulation because only part of the web was protected and the insulation could start to delaminate on the side of the web. At 120 minutes into the test, a large portion of insulating materials fell from one side of this beam. In figure 3, the temperatures in the FRP increased considerably after this point. At the end of the test, it was clear that both beams had completely lost their CFRP strengthening because most of the strips had burned away.

The temperatures at various locations on the beam with 19 mm of insulation are shown in figure 3. This beam experienced much more significant debonding of the insulation than the other beam. The temperatures in the FRP increased fairly steadily over the first 120 minutes. At this point, the temperature at the interface between the concrete and the FRP reached approximately 200 °C. Based on previous material testing [13], the FRP is expected to start to lose its bond to the concrete at approximately 50 °C while it can retain approximately half of its strength up to 200 °C. After 120 minutes, the temperatures in the FRP increase rapidly because of delamination of insulation. The FRP is undoubtedly ineffective after this point. Nevertheless, the insulation is still effective in reducing temperatures in the concrete and reinforcing steel because the temperature in the reinforcing steel does not exceed 400 °C at any point in the four hour test.

At the end of the four hour fire exposure, the load on the beams was increased but the beams did not fail. As a result, the beams will be tested at a later date for residual strength.

2.2 Columns

Figure 4 shows the dimensions and details of the two column specimens. One column was circular with spiral reinforcement while the other was square with tied lateral reinforcement. The height of the columns was 3810 mm. Two 38 mm thick square steel plates were attached above and below the columns. These plates were attached to the loading machine to provide fixed-fixed loading conditions.

The circular column was constructed with 35 MPa concrete while the square column had a concrete strength of 28 MPa. Carbonate aggregate was used in both concrete mixes. Clear cover to the reinforcement was 40 mm. Eight 20 mm diameter steel bars with a tested strength of 456 MPa were provided as longitudinal reinforcement for the circular column while four 25 mm bars with a tested strength of 477 MPa were provided for the square column. The circular column was strengthened with two layers of the same carbon FRP used for the T-beams while three layers were applied to the square column. The calculated strength increase according to ACI [10] was 27% for the circular column and 20% for the square column. The square column was protected with a 19 mm thick layer of insulation while the circular column had an insulation thickness of 15 mm.

The fire test scenario for these columns was the ASTM E119 standard fire. The load applied during the fire test was 5% greater than the unstrengthened design strength for the circular column (test load ratio of 0.85) and 10% greater than the unstrengthened design strength for the square column (test load ratio of 0.97). All of these calculations were based on ACI 440 [10].

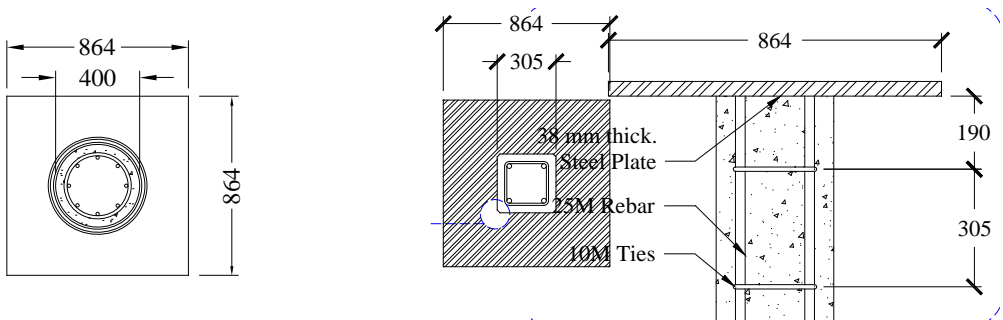


Figure 4. Dimensions of columns (a) Circular (35 MPa concrete, 8-20M longitudinal bars, 10M spiral with 50 mm pitch, 40 mm clear cover to spiral) (b) Square (28 MPa concrete, 4-25M longitudinal bars, 40 mm clear cover to ties).

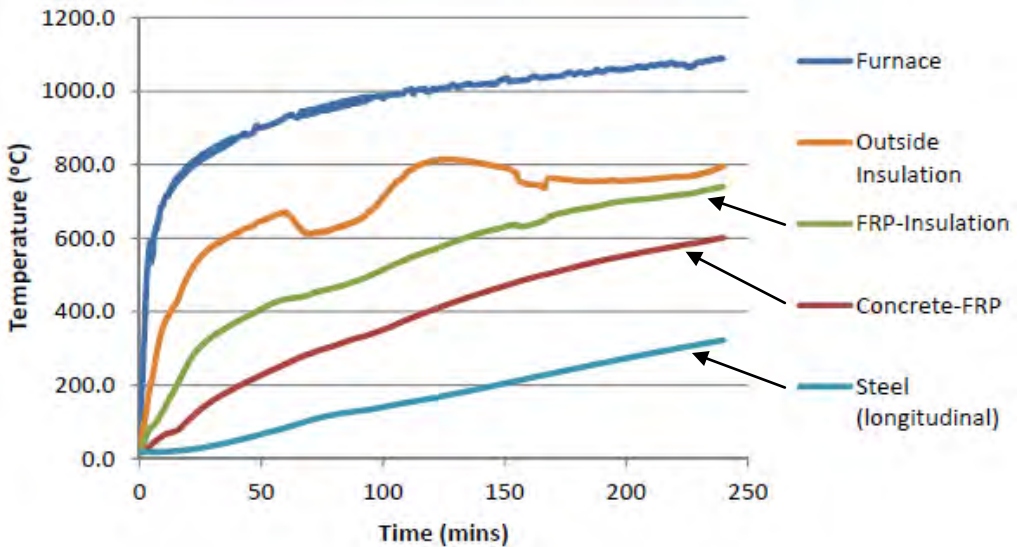


Figure 5. Temperatures measured in the circular column with 15 mm of insulation.

Figure 5 shows the temperatures at various locations in the circular column. With only 15 mm of insulation, the temperature in the FRP increases rapidly but steadily to 150 °C after 30 minutes and to almost 400 °C after 120 minutes. During the testing of this column, a single small vertical crack was first noticed at 57 minutes at the mid-height of the front-right side of the column (with respect to the furnace doors). Flames were also observed coming out from the crack, which initially rose in intensity, but eventually ceased after 140 minutes. As the test progressed, this sole crack elongated and widened. After 184 minutes, the crack was over one metre long, and 3-4 mm wide. After the full 240 minutes, upon opening the furnace doors, this crack opened even more as the insulating materials cooled. Despite all of this, no insulation fell from the column, unlike in the beam tests.

Figure 6(a) shows a photo of the column at the end of the fire test. The insulation on this column was later knocked off with a long stick in order to inspect the state of the underlying FRP as shown in figure 6(b). The FRP appeared intact; however the epoxy had presumably burned off by this point, effectively negating its strengthening benefits. The free-ends of the confining wraps were also completely debonded from the layer below, which supported the theory that the epoxy had been consumed in the fire.

Despite the lack of contribution from the FRP at the end of the fire test, the columns both were able to carry the applied load for the full four hours of fire testing. Although the insulation did not protect the FRP completely, it reduced temperatures in the reinforcing steel and concrete. For example, the temperature in the reinforcing steel was approximately 350 °C after four hours of the fire exposure. At this temperature, neither the steel nor the concrete would have lost much of their original room temperature strength. As a result, the strength of the column after four hours of fire exposure is expected to be close to the room temperature strength of the unstrengthened column.



Figure 6. Circular column after fire testing.

3 DESIGN IMPLICATIONS

Based on the research conducted over the past ten years, a reasonable understanding of the performance in fire of FRP strengthened concrete structures has been obtained through full-scale testing [2,7,8,9]. To extend this knowledge from the constraints of the specific fire tests, numerical models have been developed for slabs, beams, and columns [14,15,16,17]. These models can predict both the thermal and structural performance of the members, and have been validated against the full-scale tests conducted as part of the research program [14,15,16,17]. The details of these numerical models are presented in other publications [14,15,16,17] and thus are not reproduced in this paper.

The models, however, have demonstrated that the fire behaviour of FRP strengthened concrete members can be predicted with reasonable accuracy with standard structural fire endurance procedures as long as the thermal properties and material performance at high temperature are known. For concrete and steel, both the thermal properties and material properties are characterized with sufficient accuracy [18], and thermal properties of insulation can generally be obtained from manufacturers or from testing [14,15,16,17]. A major impediment to the accuracy of models for strength prediction is the characterization of the strength and bond degradation of FRP at high temperatures.

FRP materials are susceptible to high temperatures mainly because of their polymer resins. The glass or carbon fibres that provide the strength and stiffness of the composite material are relatively unaffected by high temperature up to 500 °C [2]. However, the polymer resin that helps transfer load between individual fibres and bonds the FRP to the concrete starts to lose strength and stiffness when the resin reaches its glass transition temperature. For FRP materials applied in concrete strengthening, the glass transition temperature is generally between 60 to 80 °C [2]. Material testing as part of this overall research program has shown that FRP materials lose approximately half their tensile strength near the glass transition temperature of the resin [13]. If bond is not an issue, FRP materials do not lose any

additional strength up to temperatures of 200 °C [13]. For bond-critical applications, almost all of the bond strength may be lost at temperatures near the glass transition temperature.

With the knowledge gained from the full-scale tests, material tests, and numerical modelling, the general understanding of FRP strengthened concrete structures is starting to reach the point at which rational fire design procedures can be proposed. An approach suggested by ACI 440 [10] is to estimate the loss in strength in fire of an FRP strengthened concrete member by using procedures similar to those recommended by ACI 216 [18] for reinforced concrete members.

In this paper, a conceptual model for fire design is proposed that follows the philosophy advocated by ACI 440 [10]. Figure 7 provides an illustration of this conceptual model with the vertical axis representing the amount of strengthening and the horizontal axis the required fire resistance. The essential idea behind the conceptual model is that a trade off exists between the amount of FRP strengthening that is provided and the required fire resistance. When little or no fire resistance is required then only flame spread resistance is required, regardless of the amount of FRP strengthening. For example, one column tested as part of the overall research program obtained a fire endurance rating of over three hours without any insulation [19]. At this low level of strengthening and fire endurance requirements, most of the information is available in existing design procedures [10,18] to conduct these calculations for design purposes. The only unknown is that burning of the FRP on the surface of the concrete will increase internal temperatures in the concrete and reinforcing steel. This effect is likely to be minor as long as the surface burning does not cause spalling of the concrete. For high performance concrete structures where spalling may be a concern regardless of the presence of FRP, insulation should likely be provided.

As the required fire resistance increases, even structures with a minor amount of strengthening may require some insulation to protect the structural performance of the original reinforced concrete. This is the intermediate range of fire performance, and many strengthening applications in buildings will fall into this range. For designs in this range, the FRP would not be considered structurally active during the fire, but the effect of the insulation would need to be taken into account to estimate the structural performance of the concrete and steel. Numerical simulation models would need to be used to include the effect of the insulation. Alternatively, such numerical models could be employed to develop design charts to predict internal temperatures in reinforced concrete members with different amounts of insulation. A significant amount of research and development is still required to develop such design charts.

The final range of fire performance occurs when high levels of fire endurance are needed for structures that also require a significant amount of strengthening. In this case, the strength of the FRP will need to be protected during the fire event and thus the insulation requirements are even higher than in the intermediate range. The numerical simulation programs developed as part of this overall research program could be used to estimate fire performance in this range [14,15,16,17]. Nevertheless, many unknowns still exist regarding the material behaviour of FRP and how the strength of the FRP strengthened concrete member will deteriorate in fire conditions. More research is needed in this area.

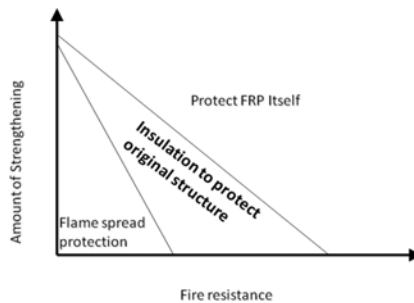


Figure 7. Conceptual fire design model.

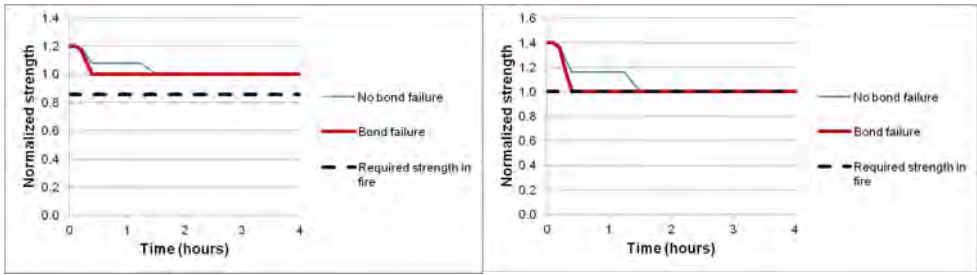


Figure 8. Fire endurance estimates for FRP strengthened slabs with 40 mm clear cover to internal reinforcement **with insulation** (a) 20% strengthening (b) 40% strengthening.

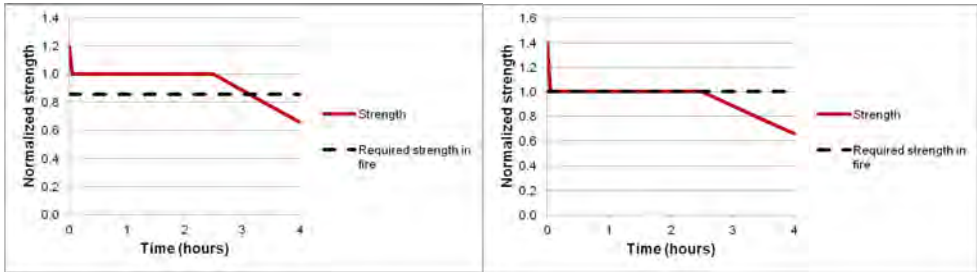


Figure 9. Fire endurance estimates for FRP strengthened slabs with 40 mm clear cover to internal reinforcement **without insulation** (a) 20% strengthening (b) 40% strengthening.

To provide more guidance for how the conceptual model could be developed, some estimates for fire performance for a 150 mm thick reinforced concrete slab with 40 mm clear cover to the reinforcement and carbonate aggregate are provided in figures 8 and 9. Such a slab would be expected to have a four hour fire rating before strengthening. For estimating fire endurance, reinforcing steel temperatures were either estimated from ACI 216 [18] or from fire tests on FRP strengthened slabs. Figure 8 shows that providing 20 mm of insulation to the slabs can allow the slabs to have a fire endurance of over four hours. However, once strengthening is increased beyond 40%, the fire endurance will be reduced because the expected loads during the fire will increase to beyond the capacity of the original reinforced concrete slab. Figure 9 demonstrates the fire endurance of the same FRP strengthened slab when insulation is not provided. In this case, three hours of fire endurance is expected for 20% strengthening and only two hours for 40% strengthening. To provide fire endurance for strengthening above 40%, more insulation would be required to enable the FRP to maintain strength for a longer period in the fire.

Based on this example slab, some numbers can be applied to the conceptual model of figure 7 as shown in figure 10. In this case, for strengthening percentages of up to 40%, insulation is not required unless the required fire endurance is greater than two hours. To achieve fire endurance greater than two hours, insulation is required to protect the original member (i.e., these slabs fall into the intermediate range of required fire performance). Additionally, if the required fire endurance is very minimal (less than 30 minutes), insulation to protect the original member is sufficient for any practical level of strengthening. For strengthening above 40%, the FRP itself would need to be protected in the case of the fire because the FRP would need to carry a portion of the load for most of the fire exposure.

For design calculations, the results in figure 10 should not be applied at the present time because they are only meant to be illustrative of the type of approach that could be taken with the proposed conceptual model. Many assumptions have been made about FRP material properties and temperature profiles for insulated reinforced concrete beams. More research and development is required to produce more refined charts that could be applied in design practice.

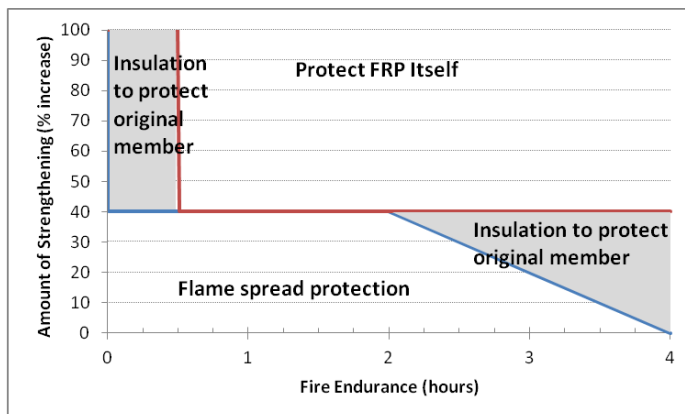


Figure 10. Conceptual design model for FRP strengthened slabs with 40 mm clear cover to internal reinforcement.

4 CONCLUSIONS

The results of four full-scale fire tests on reinforced concrete beams and columns strengthened with FRP were presented. All the specimens were insulated with between 15 to 20 mm of insulation. The loads applied on the members in the fire test were greater than the unstrengthened design capacity of the member. The research demonstrated that insulated FRP strengthened reinforced concrete beams can obtain fire endurance ratings of four hours with approximately half the amount of insulation as previously tested. A conceptual design approach was presented along with numerical computations to demonstrate how it could be applied in fire design. The conceptual design approach was shown to have promise for future design practice. More research is required to develop the approach further. In particular, better information on high temperature material properties, a more complete understanding of the strength deterioration of FRP strengthened members in fires, and design curves for estimating internal temperatures in insulated concrete members are all required to refine the conceptual approach into a practical design tool.

ACKNOWLEDGEMENTS

The research presented herein was conducted in collaboration with the National Research Council of Canada (NRC), Intelligent Sensing for Innovative Structures (ISIS Canada), Queen's University and industrial partners FibrWrap and Sika Canada. The authors would like to acknowledge these organisations and their technical staff for their support and participation in this research. The authors would also like to thank graduate students Masoud Adelzadeh and Greg Shier.

REFERENCES

- [1] ACI Committee 440. *ACI 440R-07: Report on Fiber-Reinforced Polymer (FRP) Reinforcement for Concrete Structures*, American Concrete Institute, Farmington Hills, Michigan, 2007.
- [2] Bisby, L.A., Green, M.F., and Kodur, V.K.R., 2005. "Response to fire of concrete structures that incorporate FRP", *Progress in Structural Engineering and Materials*, 7(3), 136-149, 2005.

- [3] Deuring, M., “Brandversuche an Nachtraglich Verstärkten Tragern aus Beton”, *Research Report EMPA No. 148,795*, Swiss Federal Laboratories for Materials Testing and Research, Dübendorf, Switzerland, 1994.
- [4] Blontrock, H., Taerwe, L., and Vandeveld, P., “Fire Tests on Concrete Beams Strengthened with Fibre Composite Laminates”, *Third PhD Symposium*, Vienna, Austria, 2000.
- [5] Stratford T.J., Gillie M., Chen J.F. and Usmani A.S., “Bonded fibre reinforced polymer strengthening in a real fire”, *Advances in Structural Engineering*, 12 (6), 867–878, 2009.
- [6] Palmieri, A., Matthys S. and Taerwe, L., “Fire testing of RC beams strengthened with NSM reinforcement”, *SP-275-51, Fiber-Reinforced Polymer Reinforcement for Concrete Structures 10th International Symposium*, 2011.
- [7] Bisby, L.A., Green, M.F., and Kodur, V.K.R., “Fire Endurance of Fiber Reinforced Polymer Confined Concrete”, *ACI Structural Journal*, 102(6), 883-891, 2005.
- [8] Williams, B.K., Kodur, V.K.R., Green, M.F., and Bisby, L.A., “Fire Endurance of FRP Strengthened Concrete T-Beams”, *ACI Structural Journal* 105(1), 60-67, 2008.
- [9] Green, M.F., Adelzadeh, M., Khalifa, T., Eedson, R., Bisby, L., Bénichou, N., Bao, X., and Li, W., “Performance in Fire of Fibre Reinforced Polymer Strengthened Concrete Beams Including Embedded Fibre Optic Sensors”, *Structures in Fire (SiF 2010)*, East Lansing, MI, 2-4 June. CD-Rom 8p., 2010.
- [10] ACI Committee 440. *ACI 440.2R-08: Guide for the Design and Construction of Externally Bonded FRP Systems for Strengthening Concrete Structures*, American Concrete Institute, Farmington Hills, Michigan, 2008.
- [11] Green, M.F., Bénichou, N., Kodur, V.K.R., and Bisby, L.A., “Design Guidelines for Fire Resistance of FRP-Strengthened Concrete Structures,” *Eighth International Conference on FRP in Reinforced Concrete Structures (FRPRCS-8)*, Patras, Greece, July 16-18, CD-Rom 10p., 2007.
- [12] ASTM. *Standard Test Methods for Fire Tests of Building Construction and Materials, Test Method E119a-08*, American Society for Testing and Materials, West Conshohocken, PA, 2008.
- [13] Chowdhury, E.U., Eedson, R., Bisby, L.A., Green, M.F., and Benichou, N., “Mechanical Characterization of FRP Materials at High Temperature”, *Fire Technology*. Online 8 Nov 2009.
- [14] Bisby, L.A., Green, M.F., and Kodur, V.K.R., “Modeling the Behavior of Fiber Reinforced Polymer Confined Concrete Columns Exposed to Fire”, *ASCE Journal of Composites for Construction*, 9(1), 15-24, 2005.
- [15] Williams, B.K., *Fire Performance of FRP-Strengthened Reinforced Concrete Flexural Members*, Ph.D. Thesis, Queen's University, 2004.
- [16] Chowdhury, E.U., Bisby, M.F., Green, M.F., Bénichou, N., and Kodur, V.K.R. “Heat transfer and structural response modelling of FRP confined rectangular concrete columns in fire”, *Construction and Building Materials*, 25(12), 1-28. Online 1 Jul 2011.
- [17] Adelzadeh, M., Green, M.F., and Bénichou, N., “Behaviour in fire of FRP strengthened T-beams and slabs”, *Structures and Buildings, Proceedings of the ICE*, In press, 2012.
- [18] ACI Committee 216, *ACI 216R-89: Guide for Determining the Fire Endurance of Concrete Elements*, American Concrete Institute, Farmington Hills, Michigan, 1989.
- [19] Chowdhury, E.U., Bisby, L.A., Green, M.F. and Kodur, V.K.R., “Investigation of insulated FRP-wrapped reinforced concrete columns in fire”, *Fire Safety Journal*, 42(6-7), 452-460, 2007.

FIRE PERFORMANCE OF PRESTRESSED I-SHAPED BEAM WITH MULTIPLE OPENINGS

Shigeaki Baba*, Shintaro Michikoshi**, Shigehiro Sakamoto** and Takeo Hirashima***

* Technology Center, Taisei Corporation, Japan
e-mail: shigeaki.baba@sakura.taisei.co.jp

** Technology Center, Taisei Corporation, Japan, Dr. Eng.
e-mails: shintaro.michikoshi@sakura.taisei.co.jp, shigehiro.sakamoto@sakura.taisei.co.jp

*** Dept. of Architecture and Urban Science, Chiba University, Japan, Dr. Eng.
e-mail: hirashima@faculty.chiba-u.jp

Keywords: Prestressed concrete, Beam, Bending strength, Shear strength, Multiple openings, Fire

Abstract. *In order to investigate shear and bending behavior in fire of I-shaped prestressed precast concrete (PCaPC) beams with high-strength rebars and multiple large openings, three specimens for PCaPC beams were tested. Main parameters of this test are the level of vertical loading and distance between openings. The fire resistance time, temperature of cross section and deformation of PCaPC beams was confirmed from the test results. The evaluation method for bending and shear strength of PCaPC beams at high temperature, as well as the results of the fire experiment will be presented. In this analytical method of bending and shear strength, the authors proposed two modes of resistance mechanism of PCaPC beam, one mode is RC beam, the other mode is gate structure consisting of upper and lower beams. This proposed method taking into account of the temperatures of longitudinal and shear rebars, concrete and bond strength can almost calculated the fire resistance time.*

1 INTRODUCTION

Precast prestressed (PCaPC) concrete beam, using high strength concrete and rebars, and with multiple large openings, have a tremendous potential for use in architectural projects, because not only they enlarge building space and decreasing building weights but also they enable equipment system changed and can be supplied in high quality. So this can realize the short depth of the beam section and large diameter of the opening. These beams use longitudinal deformed bars as prestressing bars. In this viewpoint, the authors have developed and researched the fire performance of PCaPC beam on rectangular cross section [1]. Furthermore, the developed PCaPC beam with I-shaped cross section has feature that can achieve the longer span because of its light weight.

In Japan, under the current Building Standard Law of Japan aside from conventional prescription-based fire safety regulations, it is now possible for designers to test and confirm the fire resistance performances of new materials and new members for applying them on projects. Their performances can be evaluated based on fuel loads and fire scenarios calculated room by room. In this regard, the fire test for new prestressed precast beams was conducted by the authors for extracting their performances.

This paper is intended to provide a summary of the findings obtained from the fire experiment, that is, the fire resistance time, temperature of cross section and deformation of PCaPC beam. Additionally, evaluation method for bending and shear strength of PCaPC beams at high temperature, as well as the results of the fire experiment, will be presented. The shear resistant mechanism of PCaPC beams that is used for evaluating their strength is based on the lower boundary theorem with truss and arch model at

high temperature. It will be clarified from the results that analytical model presented in this paper can predict precisely the beam strength at high temperature.

2 FIRE RESISTANCE TEST

2.1 Test program

The first objective of the test program is to obtain experimental evidence that the PCaPC beam is designed to meet the fire resistance requirements. Concretely, the beam should not collapse during the equivalent endurance time. In this regard, three I-shaped PCaPC specimens with multiple actual openings were tested.

The test specifications are listed in Table 1. Elevation and the cross-sectional details are given in Figure 1 and Figure 2, respectively. Three full-scale section pre-stressed beam specimens with I-shaped cross section and slab were fabricated and tested in this program. The test parameters include the distance between openings (1200 mm or 800 mm) the level of vertical loading (23% or 35% of ultimate bending moment at room temperature). The specimens consist of PCaPC beam and slab, the PCaPC beams are 865mm high and 300 mm in width. The slabs are 135 mm high and 600 mm width. The beams have five or seven openings, whose diameters are about 400 mm, with the distance of 1,200 mm or 800 mm. All specimens were pre-stressed with the pre-tensioning system. The prestress force is 3120kN or 3500kN. The PCaPC specimens with slab are 8000mm in length, and their spans are 6800mm. The beams were steam treated after setting, for enhancing strength in early age because it is preferable to introduce prestressed force in early age. Moreover, for improving the fire resistance, organic fibers were added in the PCaPC beam concrete.

The compressive strength at the age of the fire test ranges from 134 to 141MPa. Compressive strength were determined on cylinder specimens of $\phi 100 \times 200$ mm cured under similar conditions of temperature history expected in the beams during setting. All specimens were dried in the laboratory for ten months prior to the fire test. The moisture content as of testing was about 4 %.

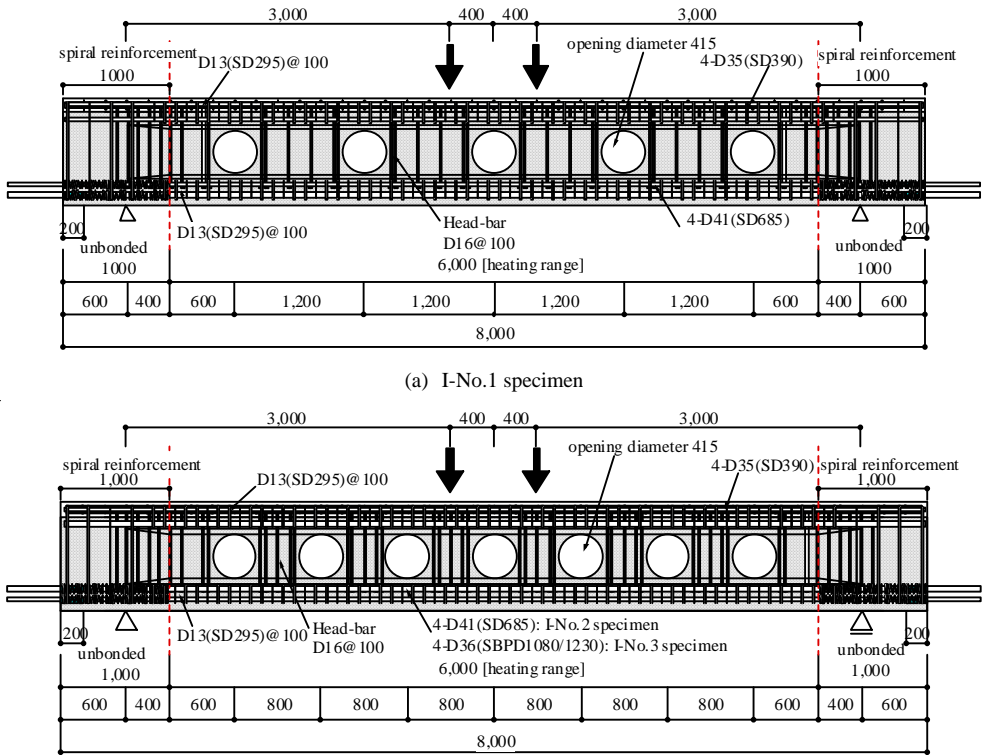
Table 1 Test specifications

Specimen	Prestressing bar	Prestress Force (kN)	Distance of openings (mm)	Acting moment at middle of span M (kNm)	Bending strength M_I (in calculation) (kNm)	M/M_I
I-No.1	SD685 (4-D41)	3120	1200	660	2924	0.23
I-No.2	SD685 (4-D41)	3120	800	660	2924	0.23
I-No.3	SBPD1080/1230 (4-D36)	3500	800	1248	3604	0.35

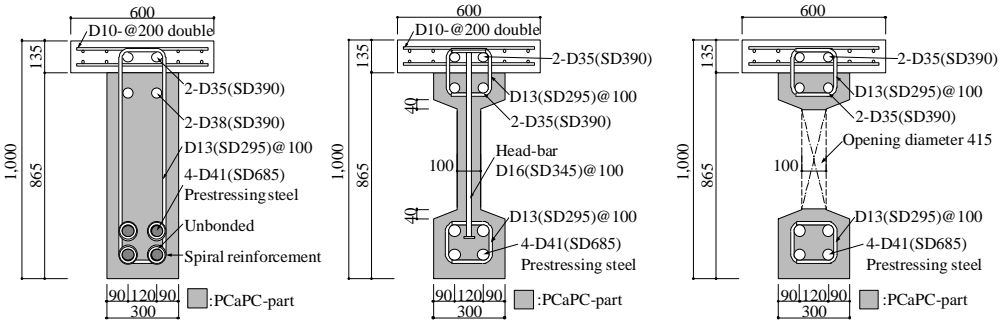
2.2 Test setup

Figure 3 shows the setup of the test for the PCaPC beams subjected to fire. All specimens are simply supported with a support length of 6800mm. Two hydraulic jacks, located 3000mm distance of the supporting points, act the downward force on the beam.

The measurements include vertical displacements at the middle of the span and at the supporting points etc., furnace temperatures, temperatures of the concrete throughout the specimen thickness and temperatures of longitudinal and shear reinforcement steel. All measurements were conducted every 30 seconds during the test. The specimens were subjected to the fire temperature history as specified in ISO 834 [2].



(a) I-No.1 specimen
(b) I-No.2 and I-No.3 specimens
Figure 1 Elevation of specimens.



(a) Section at the end of specimen (b) Section at non-opening (c) Section at opening

Figure 2 Cross section of specimens. (I-No.1 and I-No.2 specimens)

The deflection at the middle of span were evaluated as follows: (1) measure displacements at the middle of span and at the supporting points, (2) average the displacements of both supporting points, (3) subtract the displacement at the middle of span from the averaged displacement at supporting point.

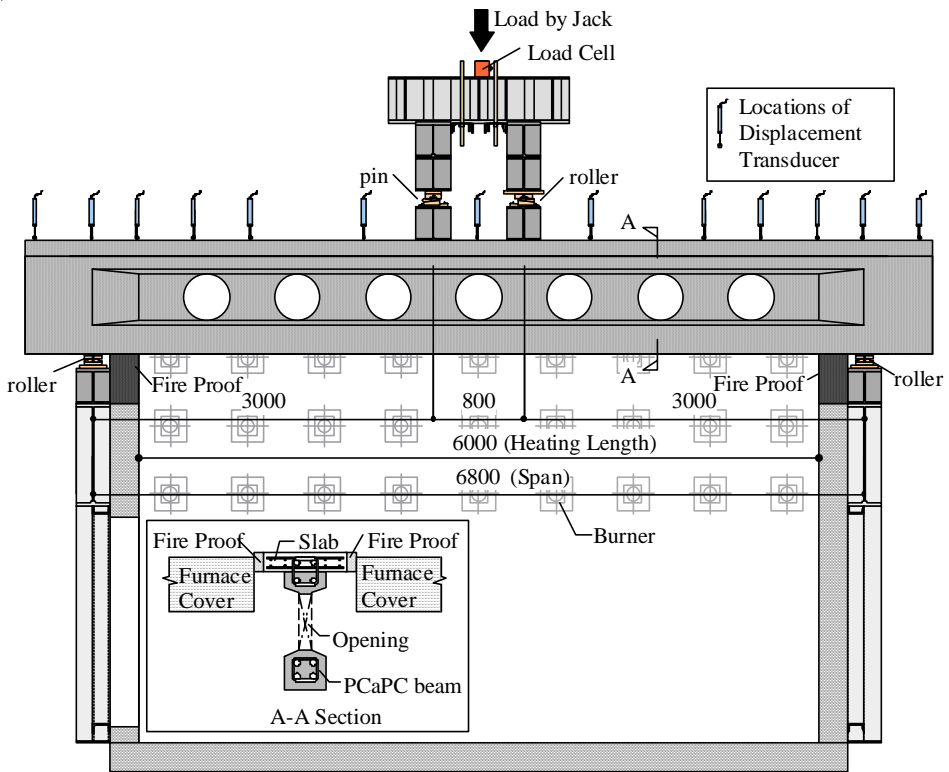


Figure 3 Test setup. (I-No.2 specimen)

2.3 Test Result

Crack patterns of specimens after heating are illustrated in Figure 4. No significant material loss by explosive spalling was observed during fire test. The fire resistance times of specimens were 260 minutes (I-No.1 specimen), 248 minutes (I-No.2 specimen) and 100 minutes (I-No.3 specimen). The fire resistance indicated in minutes is the time from the beginning of heating up to the failure of the specimen.

In I-No.1 and I-No.2 specimens, shear cracks occurred between openings, and bending cracks occurred along upper and lower beam. In I-No.3 specimen, the larger shear crack than I-Nos. 1 & 2 occurred between openings.

The temperature of longitudinal and pre-stressing steel is shown in Figure 5 for I-No.1 specimen. The temperature was about 60 degrees Celsius at 30 minutes, about 480 degrees Celsius at 240 minutes of heating. The temperature of shear reinforcement is shown Figure 6 for I-No.1 specimen. The temperature of head-bar was about 300 degrees Celsius at 60 minutes, about 900 degrees Celsius at 240 minutes of heating. Temperatures for the I-No.2 and I-No.3 specimens are almost similar as I-No.1 specimen.

The deflection at the middle of span is shown in Figure 7 for all specimens. Comparing I-No.1 specimen with I-No.2 specimen in the same acting load, the influence of distance between openings is less for fire resistance time. The deformation distribution is shown in Figure 8. It turns out that the deformation near support is upwards from the early stages of heating. This reason is the effect of negative moment by prestress and the effect by the gate structure on mode II (after-mentioned). In large deformation, this tendency was remarkably observed.

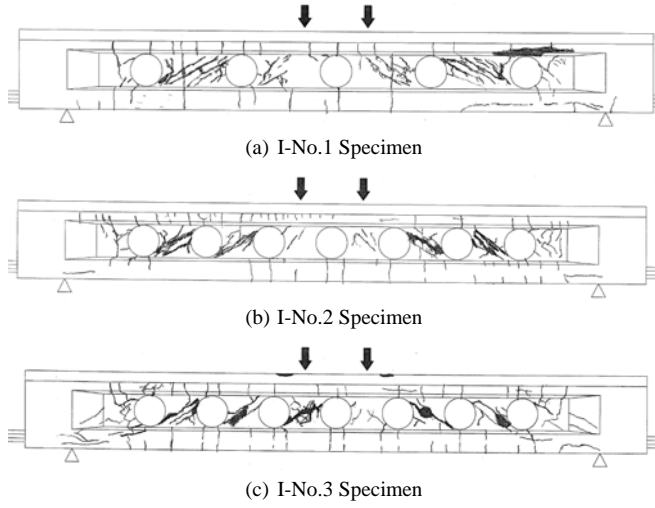


Figure 4 Crack patterns of specimens after heating.

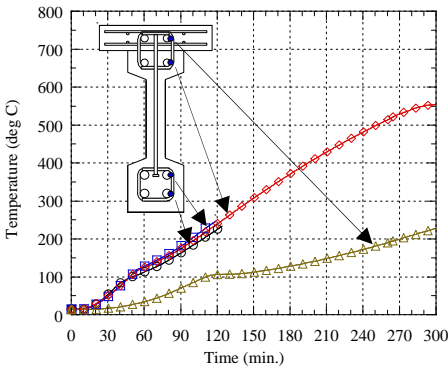


Figure 5 Temperature of longitudinal steel. (I-No.1 specimen)

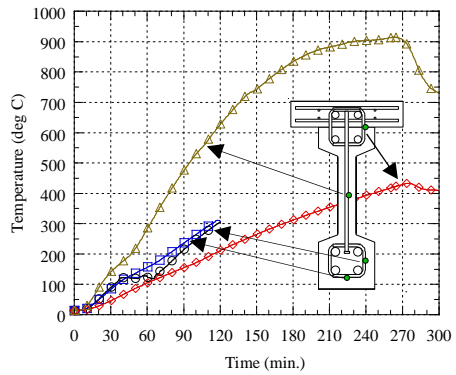


Figure 6 Temperature of shear reinforcement. (I-No.1 specimen)

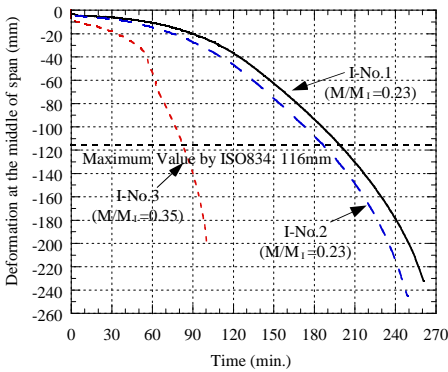


Figure 7 Deformation at the middle of span.

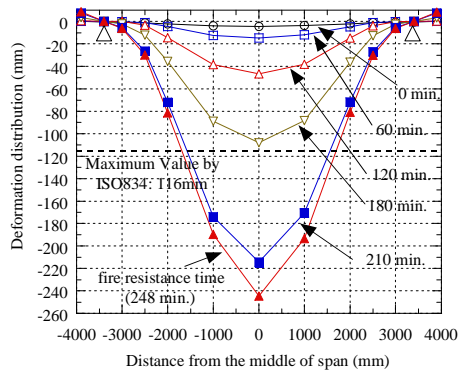


Figure 8 Deformation distribution. (I-No.2 Specimen)

3 ESTIMATION OF FIRE RESISTANCE

3.1 Methodologies

An estimated ultimate strength in fire on PCaPC beam which has multiple openings is examined. In the shear strength evaluation method [3], the shear strength consists of 3 parts; shear strength by the truss action of upper and lower beam, shear strength by truss action formed of strut over an openings and shear strength by the arch action of upper and lower beam. Bending strength of beam was evaluated as RC beam. This resistance mechanism is written as "mode I".

However, shear failure occurred between openings with I-shaped beam. Therefore truss mechanism with strut over the openings cannot be formed. Then, the mode which pays resistance mechanism to the gate structure was considered, gate structure consists of upper and lower beams. This resistance mechanism is written as "mode II". Hereafter, an ultimate strength is described to two kinds of failure modes in fire.

3.1.1 Resistance mechanism on mode I

(a) bending strength

The following assumption yields a simple equation (Equation 1) to estimate the time up for bending failure: If reinforcing / pre-stressing steel reaches yielding before the concrete reaches critical compressive strain, the ultimate bending moment of the member is governed only by the temperature of reinforcing / pre-stressing steel regardless of pre-stressing force. Shear force at bending strength is shown in equation 2.

$$M_I = \sum_{i=1}^N 0.9 \times i a_i \times i \sigma_y \times i d \quad (1)$$

$$Q_{M1} = M_I / L_I \quad (2)$$

where, M_I : ultimate bending strength, Q_{M1} : shear force at bending strength, N : the number of reinforcing / pre-stressing steel, L_I : shear span, $i a_i$: cross-section area of reinforcing / pre-stressing steel i , $i \sigma_y$: yield strength of reinforcing / pre-stressing steel i , $i d$: depth to reinforcing / pre-stressing steel i

(b) shear strength

In generally, the truss action is formed by tensile force of shear reinforcement, the diagonal compressive force of concrete, and the bond of a longitudinal rebar and concrete. Therefore, shear strength which can be transmitted by a truss action, as shown in equation 3, is minimum value under yield of shear reinforcement, compressive failure and bond failure.

$$Q_t = \min(\overset{rebar}{Q_t}, \overset{conc}{Q_t}, \overset{bond}{Q_t}) \quad (3)$$

$$\overset{rebar}{Q_t} = b \times j_t \times p_w \times \sigma_{wy} \times \cot \phi, \overset{conc}{Q_t} = b \times j_t \times \nu \cdot \sigma_B \times \sin \phi \cdot \cos \phi, \overset{bond}{Q_t} = j_t \times A_l \times \tau_{bu} \quad (3a)$$

where, Q_t : shear strength by truss action, $\overset{rebar}{Q_t}$: shear strength by truss action at yield of shear reinforcement, $\overset{conc}{Q_t}$: shear strength by truss action at compressive failure, $\overset{bond}{Q_t}$: shear strength by truss action at bond failure, σ_{wy} : yield strength of shear reinforcement, ν : a factor less than 1.0, τ_{bu} : bond strength of reinforcement, ϕ : truss angle, j_t : distance between the centroids of the axial reinforcement, b : width of beam, p_w : shear reinforcement ratio, A_l : circular length of longitudinal rebar, σ_B : compressive strength

It is described at forescript "up" for upper beam, "low" for lower beam, "p" for between openings and "o" at opening. Shear strength at an opening is shown in equation 4. When shear strength between openings is larger than shear strength at opening, then strut over between openings is proposed. Shear strength in this truss action is shown in equation 5 (refer to Figure 9). As mentioned above, shear strength on mode I by truss action taken into account two truss action is shown in equation 6.

$${}_o Q_t = {}_{up} Q_t + {}_{low} Q_t \tag{4}$$

$${}_n Q_t = ({}_p Q_t - {}_o Q_t) / {}_p Q_t \times {}_{out} A_w \times {}_{out} \sigma_{wy} \tag{5}$$

$$Q_{1,t} = \begin{cases} {}_o Q_t + 2 \times {}_n Q_t & ({}_p Q_t \geq {}_o Q_t) \\ {}_p Q_t & ({}_p Q_t \leq {}_o Q_t) \end{cases} \tag{6}$$

where, ${}_n Q_t$: shear strength of truss with strut over openings, ${}_{out} A_w$: cross-section area of truss using shear reinforcement, ${}_{out} \sigma_{wy}$: shear strength of truss using shear reinforcement, $Q_{1,t}$: shear strength of truss action on mode I

The arch action is formed with the tensile force of longitudinal rebar and diagonal compressive force. Therefore, shear strength of arch action is shown in equation 7.

$$Q_a = \min({}^{rebar} Q_a, {}^{conc} Q_a) \tag{7}$$

$${}^{rebar} Q_a = a^l \times \sigma_y^l \times \tan \theta, \quad {}^{conc} Q_a = b \times j_t \times \sigma_a \times \sin \theta \cdot \cos \theta \tag{7a}$$

where, Q_a : shear strength of arch action, ${}^{rebar} Q_a$: shear strength of arch action at yield of longitudinal rebars, ${}^{conc} Q_a$: shear strength of arch action at diagonal compressive failure, a^l : cross section area of longitudinal rebar, σ_y^l : yield strength of longitudinal rebars, θ : arch angle, σ_a : compressive strength for arch action

As mentioned above, taking into account upper and lower beam under arch action shown in Figure 10, shear strength on mode I Q_1 can be expressed in equation 8.

$$Q_1 = Q_{1,t} + {}_{low} Q_a + {}_{up} Q_a \tag{8}$$

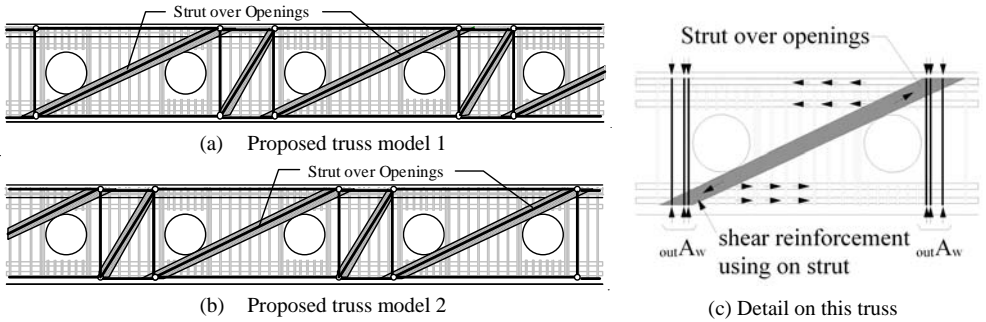


Figure 9 Proposed strut on truss model.

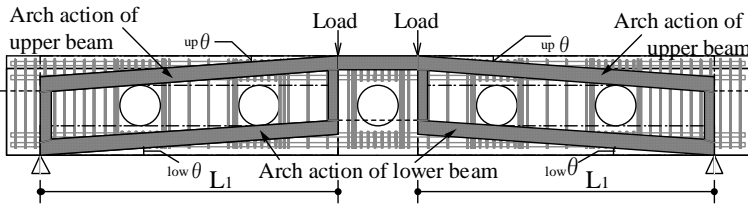


Figure 10 Proposed arch model.

3.1.2 Resistance mechanism on mode II

(a) Bending strength

Since the PCaPC beam end is reinforced, resistance mechanism mode II as shown in Figure 11 was considered the gate structure where upper and lower beam were assumed. The bending strength on mode

II was calculated from the moment distribution assumed in Figure 11. At this time, shear force at bending strength can be expressed in equation 9.

$$Q_{MII} = {}_{up}Q_{MII} + {}_{low}Q_{MII} \quad (9)$$

$${}_{up}Q_{MII} = ({}_{up}M^R + {}_{up}M^L) / L_2 \quad (10)$$

$${}_{up}M^R = {}_{up}^l a \times {}_{up}^l \sigma_y^R \times {}_{up}j^R, \quad {}_{up}M^L = {}_{up}^u a \times {}_{up}^u \sigma_y^L \times {}_{up}j^L \quad (10a)$$

$${}_{low}Q_{MII} = ({}_{up}M^R + {}_{up}M^L) / L_2 \quad (11)$$

$${}_{low}M^R = {}_{low}^l a \times {}_{low}^l \sigma_y^R \times {}_{low}j^R, \quad {}_{low}M^L = {}_{low}^u a \times {}_{low}^u \sigma_y^L \times {}_{low}j^L \quad (11a)$$

where, Q_{MII} : shear force at bending strength, ${}_{up}Q_{MII}$: shear force at bending strength for upper beam, ${}_{low}Q_{MII}$: shear force at bending strength for lower beam, ${}_{up}M^R$: bending strength for upper beam at acting point, ${}_{up}M^L$: bending strength for upper beam at the end of fire heating, ${}_{low}M^R$: bending strength for upper beam at acting point, ${}_{low}M^L$: bending strength for upper beam at the end of fire heating, ${}_{up}j^R = {}_{up}j_t$, ${}_{up}j^L = 0.9 \cdot {}_{up}d_{II}$, ${}_{low}j^R = {}_{low}j_t$, ${}_{low}j^L = 0.9 \cdot {}_{low}d_{II}$

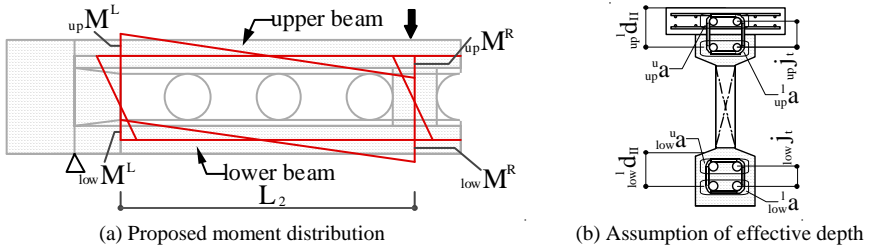


Figure 11 Resistance mechanism on mode II.

(b) Shear strength

Resistance mechanism mode II does not contribute to shear force between openings, then shear strength becomes summation of shear strength of upper and lower beam. Therefore, shear strength on mode II Q_{II} is shown in equation 12.

$$Q_{II} = {}_{low}Q_t + {}_{up}Q_t + {}_{low}Q_a + {}_{up}Q_a \quad (12)$$

3.1.3 Ultimate strength in fire

In fire, it is thought that a resistance mechanism is shown to mode I. But when a truss mechanism as shown in Fig. 9 disappears, a resistance mechanism transferred mode II as the gate type structure by upper and lower beam. Therefore, ultimate strength is estimated by the resistance mechanism of the larger one of the mode I and the mode II in fire. Ultimate strengths on mode I Q_{uI} and mode II Q_{uII} were shown in equation 13 and equation 14, respectively, so ultimate strength of PCaPC beam Q_u can be shown in equation 15.

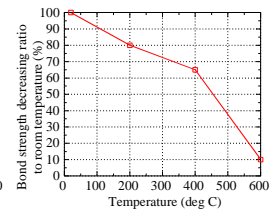
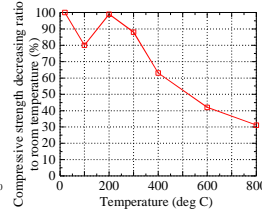
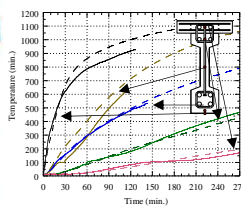
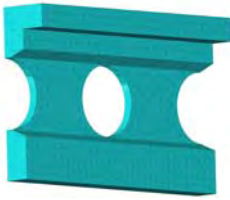
$$Q_{uI} = \min(Q_{M I}, Q_I) \quad (13)$$

$$Q_{uII} = \min(Q_{M II}, Q_{II}) \quad (14)$$

$$Q_u = \max(Q_{uI}, Q_{uII}) \quad (15)$$

3.2 Estimation Results

By calculating of ultimate strength in fire, the heat transfer analysis result was used for concrete temperature, and the experimental result was used about steel materials. A heat transfer analysis result is shown in Figure 12. In analysis, a comparatively good result was brought to the experiment.

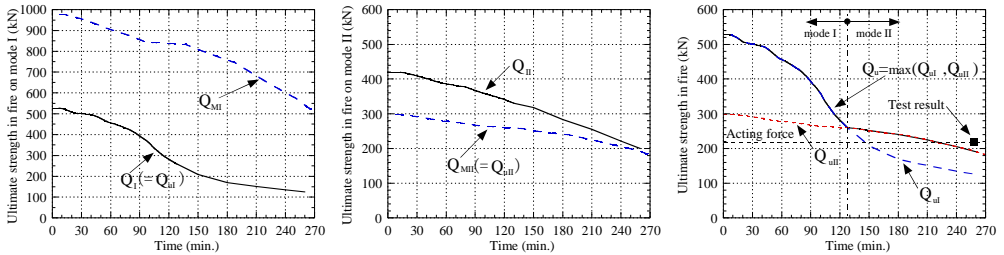


(a) Analytical model (b) comparison of result Figure 12 Analytical result of temperature. Figure 13 Assumption of compressive strength. Figure 14 Assumption of bond strength.

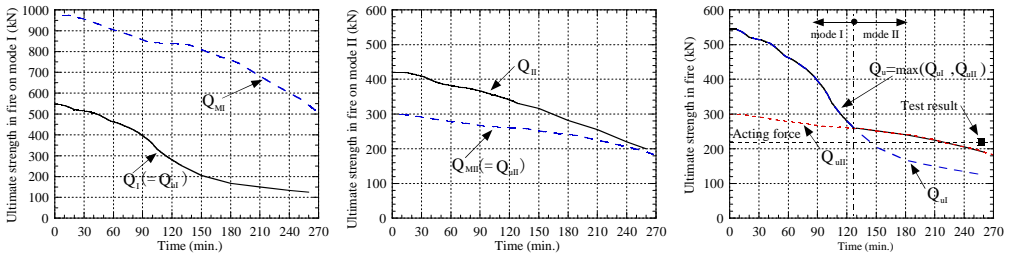
Assumed compressive and bond strength [4] at high temperature are shown in Figure 13 and Figure 14, respectively. Yield strengths of steel are also considered at high temperature in reference 4.

The estimation results in fire were shown in from Figure 15 to Figure 16. Figure 15 shows the examination result in I-shaped section of PCaPC beam, Figure 16 shows examination of the experimental result in the rectangle section shown in the literature 1. The rectangle section specimens shown in the literature 1 write R before the specimen number. In each figure, it shows the ultimate strength on mode I, mode II and ultimate strength of PCaPC beam. The fire resistance time based on calculation is the point that ultimate strength acts cross acting shear force in experiment.

Resistance mechanism of I-No.1 and I-No.2 specimens was resisted as an RC beam in the early stages in fire, resistance mechanism transferred to mode II, finally I-No.1 and I-No.2 specimens occurred bending failure on mode II at fire resistance time. In I-No.3 specimen, the resistance mechanism of RC beam by mode I is presented from the early stages to fire resistance time, and it is thought that I-No.3 specimen occurred shear failure on mode I. In the case of a rectangle section, in all specimens (R-No.1, R-No.2 and R-No.3 specimens), resistance mechanism showed mode I in fire, all specimens occurred shear failure on mode I.



(a) I-No.1 specimen

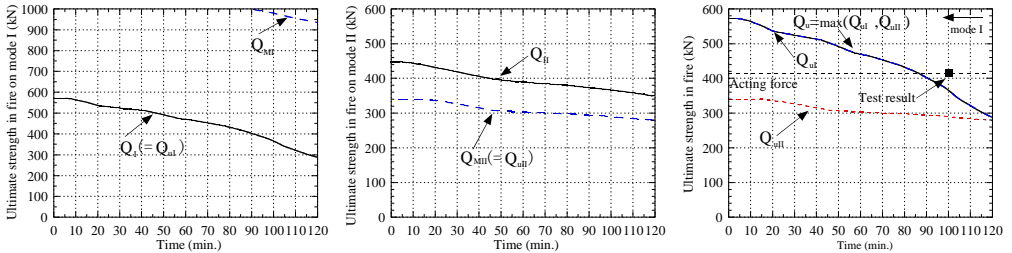


(b) I-No.2 specimen

continued on the next page

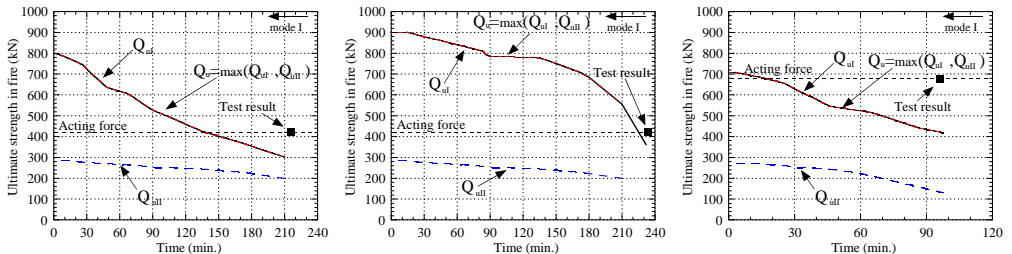
Figure 15 Estimation results of I-shaped specimens.

continued from the preceding page



(c) I-No.3 specimen

Figure 15 Estimation results of I-shaped specimens.



(a) R-No.1 specimen

(b) R-No.2 specimen

(c) R-No.3 specimen

Figure 16 Estimation results of rectangular specimens.

4 CONCLUSION

Fire resistance test of PCaPC beams were carried out and their fire resistance performances were clarified. The tests were conducted with specimen of the actual size. In the test results, the influence with the difference in opening interval is less than an experimental result in comparatively small load. Furthermore, the ultimate bending moment and the shear strength by using truss and arch model was estimated. It is proposed that two modes of resistance mechanism was considered, and it was shown that ultimate strength of PCaPC beam is determined by the failure mode of the larger one. In I-shaped specimens, in the range with comparatively small load, it turned out that I-shaped specimen occurred bending strength on mode II so distance of openings does not influence at fire resistance time. In the rectangular section specimens, shear failure occurred in all specimens on mode I.

REFERENCES

- [1] BABA S., MICHIKOSHI S., SAKAMOTO S. and HIRASHIMA T., "Fire Performance of Precast Prestressed Concrete Beam with Openings", *Structures on Fire – Proceedings of the Sixth International Conference*, V. Kodur, J.-M. Franssen (eds.), DESTech Publications, Lancaster, 157-164, 2010.
- [2] ISO/FDIS 834-1, 1999. "Fire-resistance tests –Elements of building construction-, Part 1 General requirements".
- [3] BABA S., MICHIKOSHI S., SAKAMOTO S. and HIRASHIMA T., "Study on ultimate strength of Precast Prestressed Beam with Multiple Large Openings Exposed to Fire Heating" (in Japanese), *Journal of Structural and Construction Engineering*, Architectural Institute of Japan, Vol. 76, No. 661, 703-711, 2011.3.
- [4] Architectural Institute of Japan, "Guide Book for Fire-Resistive Performance of Structural Materials" (in Japanese), 2003. 11

DEFORMATION CHARACTERISTICS OF TWO HIGHER STRENGTH CONCRETES EXPOSED TO ELEVATED TEMPERATURES AND MECHANICAL LOADS

Elin A. Jensen*, Brittany L. Schuel* and Meenakshi Joshi*

* Lawrence Technological University
21000 West 10 Mile Road, Southfield MI, 48076, USA
e-mails: ejensen@ltu.edu, bschuel@ltu.edu, mjoshi@ltu.edu

Keywords: Concrete, Elevated Temperatures, Axial Deformation, Cooling, Fire

Abstract. *The focus of this paper is the deformation characteristics of two higher strength plain concretes exposed to mechanical and fire loads. This includes a comparison of their relative performance and their deformation characteristics with existing deformation models. Experimental investigations were conducted to determine the total deformations during axial loading, heating and subsequent cooling (decay phase). Concrete prisms with dimensions of 10.2 cm by 10.2 cm and 91.4 cm long were studied. The study variables are 1) cold compressive strength of the concrete; 2) stress ratio, α , defined by the ratio of applied axial stress and the cold compressive strength of the concrete; and 3) maximum core temperature when cooling is induced. The compressive strength of the two concrete are 50 and 78 MPa, respectively; the stress ratios are 0, 17, 33 and 50 %; and the maximum core temperatures are 200, 400, 600 and 800° C.*

1 INTRODUCTION

Performance based design for structural fire safety allows engineers to quantify the behavior of a structural system throughout the entire fire. Such predictions are warranted for large framing or critical structures where members are highly stressed during the fire. While such methods provide detailed information about the structural performance, it also requires adequate and accurate material models, analysis tools and detailed information about the model input parameters. Constitutive relationships for concrete exposed to loads and extreme temperatures are available and they are derived from tests performed in electrical furnaces combined with a hydraulic load test system. Furthermore, these relationships are largely based on results from concrete made with high water to cement ratios; and on cylinders with diameters ranging from 60 to 75 mm and lengths ranging from 150 to 300 mm^{1, 2, and 3}. The aim of this study is to determine if the thermal deformation characteristics determined in these earlier studies are also representative of the characteristics observed when larger concrete specimens, made from a contemporary and high strength structural concrete mixes, are tested in a gas fuelled fire chamber.

The total deformation or strain of concrete is considered the sum of four components; which are, thermal strain, stress related strain, creep strain and transient strain. The thermal strain, ϵ_{th} , causes thermal expansion and is a function of the temperature (T). The stress related strain (ϵ_{σ}) is a function of stress (σ) and the temperature (T). Transient strain (ϵ_{tr}) is a function of both stress (σ) and temperature (T) and is only observed in the first heating cycle. The creep strain, (ϵ_{cr}) is a function of the time (t), stress (σ) and temperature (T). Creep strain is typically insignificant in concrete below 600 °C and due to computational difficulties it is often ignored in the constitutive models⁴. The total strain is:

$$\epsilon = \epsilon_{th}(T) + \epsilon_{\sigma}(\sigma, T) + \epsilon_{cr}(\sigma, T, t) + \epsilon_{tr}(\sigma, T) \quad (1)$$

Work reported by researchers such as Schneider^{2, 3 and 4}, Anderberg and Thelandersson¹, and Khoury⁵ provide a fundamental understanding of the deformation characteristics of concrete at high temperatures. An earlier paper published by the authors⁶ demonstrated that the deformations predicted by the model proposed by Khoury as well as Terro^{5, 7 and 8} are in good agreement with the observed deformation characteristics of the 50 MPa concrete also referenced in this study. However, the model is only valid for stress ratios up to 30%. Furthermore, this study showed that only two of seven tested specimens loaded with a stress ratio of 33% did not fail before they reached 600 °C. This indicates that significant irreversible strain or damage is developed. This is confirmed by the permanent deformation observed during the cooling stage.

The objective of this study is to determine (1) if the 78 MPa higher strength concrete exhibits similar deformation behavior as the 50 MPa concrete under combined heating, mechanical loading, and subsequent cooling, and (2) which of the traditionally applied models can adequately describe the development of the thermal strains, transient strains and the total strains due to the combined heating and mechanical loading. The strain vs. temperature curves for the models used in comparison to experimental data were obtained by applying the equations proposed by the researchers.

2 METHODOLOGY AND EXPERIMENTAL SET-UP

The project specific experimental test-setup was designed and constructed. Extensive resources were allocated for the development of the test method including determination of the adequate combination of chamber heating rate, net concrete heating rate, and concrete moisture conditions. A profile view of the test set-up is shown in Figure 1. The specimen on the right is instrumented with thermocouples measuring the thermal gradient of the specimen. It is only subjected to thermal loading and therefore the free thermal expansion of the concrete is obtained from this specimen. The specimen on the left is subjected to compressive axial load and thermal load simultaneously. The development of the deformation is obtained from measuring the displacement of the ram and base. The actuator is located above the furnace roof (not pictured) and controls the load throughout the test. The axial load was applied before heating was initiated, and was held constant throughout the test.

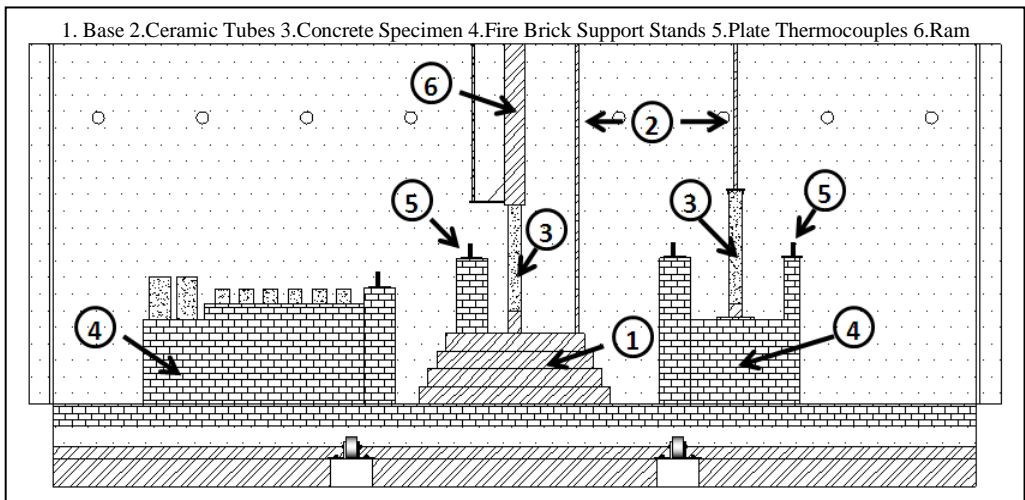


Figure 1. Front view of fire chamber setup for axial elongation test

To measure the displacement of each component, hollow mullite tubes, with a known coefficient of thermal expansion ($5.4 \times 10^{-6}/^{\circ}\text{C}$)⁹ extend from each reference surface. The mullite tubes were then

connected to displacement sensor test brackets installed on the exterior roof beams of the furnace. The effect of the thermal expansion of the mullite tubes on the total expansion was considered in the analysis.

The following axial deformation characteristics were obtained: thermal strains (free expansion) and total strain (thermal induced strain + strain due to sustained load). Tests were performed with different axial load levels of 0, 90, 180 and 270 kN for the 50 MPa concrete and 0, 135, 270, and 400 kN for the 78 MPa concrete. These load levels correspond to about 0, 17, 33 and 50 % of the concrete cold compressive strength. The specimens were heated to a maximum core temperature before cooling began. The maximum core temperatures were 200, 400, 600, and 800°C. The ambient heating rate was about 1.5°C/min for the first three test series, and it was about 2.0°C/min for the 800°C test series. The initial target temperature during furnace start-up was 120°C after which point the environmental (ambient) temperature was increased at the average rate mentioned earlier. The environmental (ambient) temperatures were measured using plate thermocouples¹⁰ arranged as shown in Figure 1. The specimen shape was a prism with dimensions 10.2 cm by 10.2 cm and 91.4 cm long which yields similar aspect ratio as used by Nielsen¹¹.

The internal relative humidity for the 50 MPa normal strength concrete was 84% or below before testing to avoid extreme spalling. These specimens were air dried at room temperature conditions after 28 days of wet curing. The normal strength concrete mix contained limestone (calcareous) coarse aggregates, cement content of 312 kg/m³ and had a water to cement ratio of 0.41.

The 78 MPa higher strength concrete was poured in May 2011 and was immediately wet cured for 28 days. In September the internal relative humidity had reached 90 - 93%. Due to the risk of explosive spalling, the internal relative humidity had to be reduced to about 80 - 84 %, based on the experience of the authors. The concrete prisms were dried in a controlled environment of 40 °C and 75 % RH for an additional 3 months. Specimens were then placed in laboratory conditions in December 2011 at which time the internal relative humidity had reached the target level. The high strength concrete mix contained limestone (calcareous) coarse aggregates, cement content (with 25% slag cement) of 402 kg/m³ and had a water to cement ratio of 0.35. Note that this concrete mix had an expected strength in excess of 90 MPa based on preliminary results provided by the concrete producer. However, only 78 MPa was achieved.

Table 1. Test Matrix for 50 MPa Concrete

Temp (°C)	Axial Load (kN)			
	Strength Ratio α			
	0	90	180	270
	0	0.17	0.33	0.5
200 °C	X	X	X	X
400 °C	X	X	X	X
600 °C	X	X	X	
800 °C	X	X		

(*X denotes completed testing)

Table 2. Test Matrix for 78 MPa Concrete

Temp (°C)	Axial Load (kN)						
	Strength Ratio α						
	0	110	135	220	270	320	400
	0	0.14	0.17	0.28	0.33	0.4	0.5
200 °C							
400 °C	X		X	X	X	X	X
600 °C	X	X	X	X	X		
800 °C	X		X				

(*X denotes completed testing)

The test matrixes, shown in Table 1 and Table 2, outline the successful experiments for both the 50 MPa and 78 MPa concretes to date. Each of the loaded specimens was tested with an accompanying unloaded specimen to capture the free expansion and the concrete temperatures.

3 RESULTS AND DISCUSSION

The concrete specimen undergoes a length change as core temperature increases which results in a deformation of each component of the system. Deformation of various components such as free expansion, base, ram, and actuator are recorded and plotted with time and temperature as raw data. Representative examples of the measured deformations and associated temperatures are presented below.

At the end of this section, the development of total axial strains with temperature for different load levels are presented and compared with existing data and models.

3.1 Temperature vs. Time

Figure 2 is a representation of the development of environmental, surface and core temperature for the duration of a test. Displacements recorded from the loaded specimen, the free expansion specimen, and the base with time are shown in Figure 3. Elongation of each specimen as the core temperature increases is presented in Figure 4. All three graphs represent a specimen that was heated to 600°C at the concrete core with an environmental heating rate of 1.5°C/min and subjected to a load of 110kN. The temperature gradient through each specimen is typically between 0.5 and 1.0°C/min.

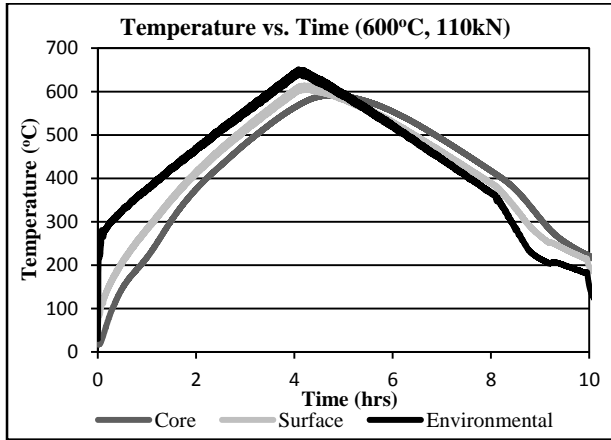


Figure 2. Temperature vs. Time

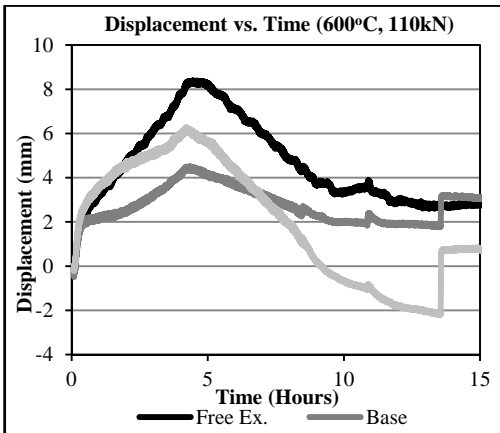


Figure 3. Displacement vs. Time

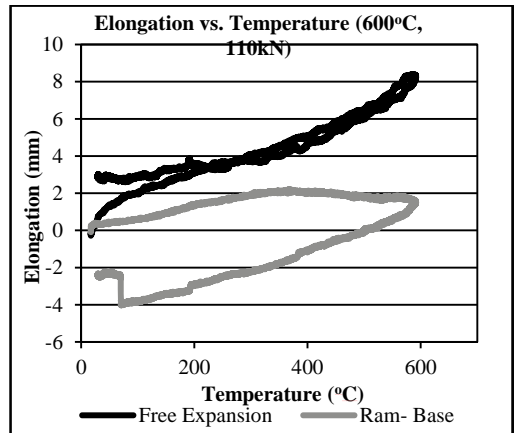


Figure 4. Elongation vs. Temperature

3.2 Strain Development as Function of Temperature

The development of the total strain with increasing temperatures is shown for different stress ratios in Figure 5 and 6. In general the deformation characteristics are similar for the two concretes for stress ratios up to 33%. For increasing stress ratios the HSC has a tendency for increased deformations. At this time the HSC subjected to a stress ratio of 50% did not successfully complete the heating through 400 °C.

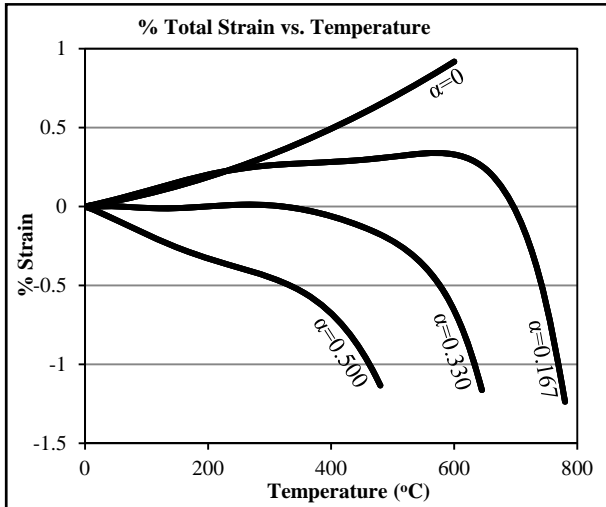


Figure 5. Total Strain vs. Temperature for NSC

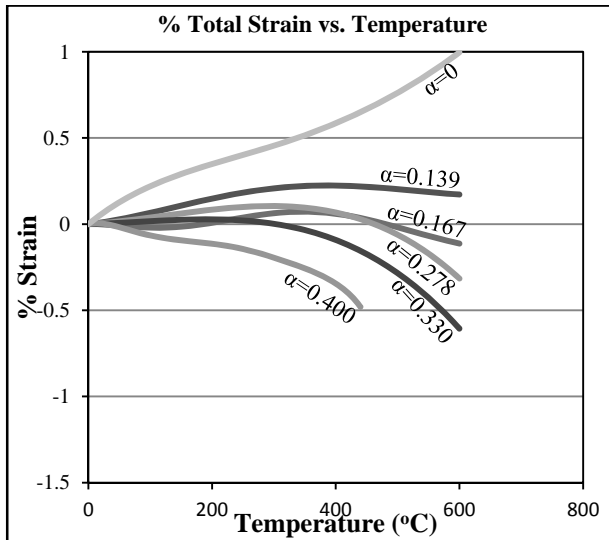


Figure 6. Total Strain vs. Temperature for HSC

The total strain through heating and cooling are shown in Figures 7 through 10 for the NSC and the HSC elevated to a core temperature of 400 and 600 °C, respectively. It is observed that the permanent deformation increases with increasing applied stress ratio during heating and cooling as well as with increasing temperatures. For the case of a maximum core temperature of 600 °C, the HSC exhibits slightly higher levels of permanent deformation upon cooling. Furthermore, it is noted that the NSC specimen loaded with a stress ratio of 50% and the HSC specimens loaded with a stress ratio of 40% fails at or near 400 °C. Evaluation of the failed specimens showed crushing failure.

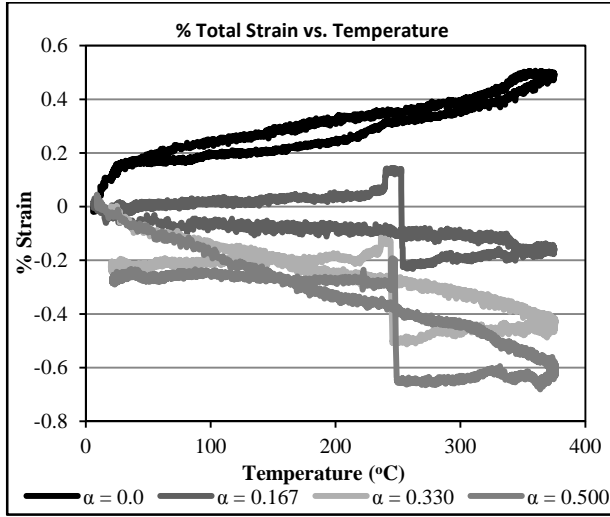


Figure 7. %Total Strain vs. Temperature for NSC at 400°C Core Temperature

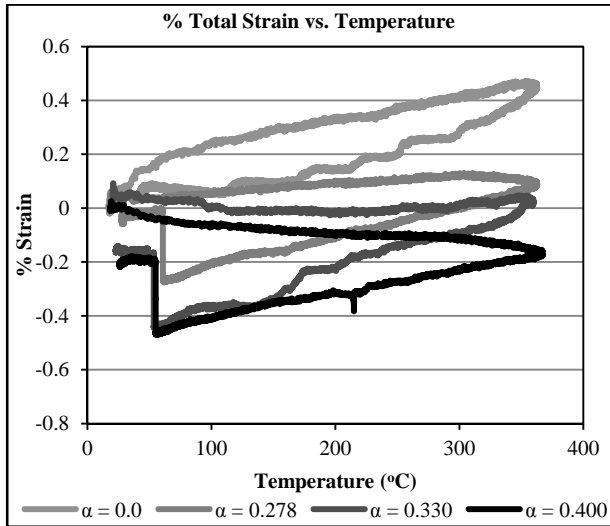


Figure 8. % Total Strain vs. Temperature for HSC at 400°C Core Temperature

The development of the transient strain during the first heating cycle is shown for different stress ratios in Figure 11 and 12. In general, for all temperatures and stress levels the HSC shows higher transient strains than that of the NSC.

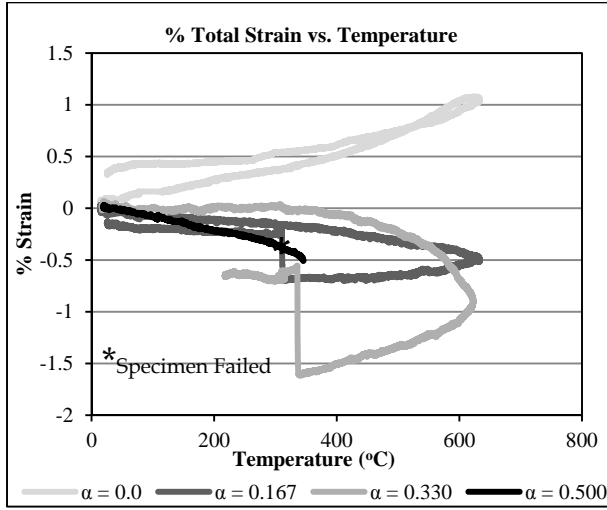


Figure 9. %Total Strain vs. Temperature for NSC at 600°C Core Temperature

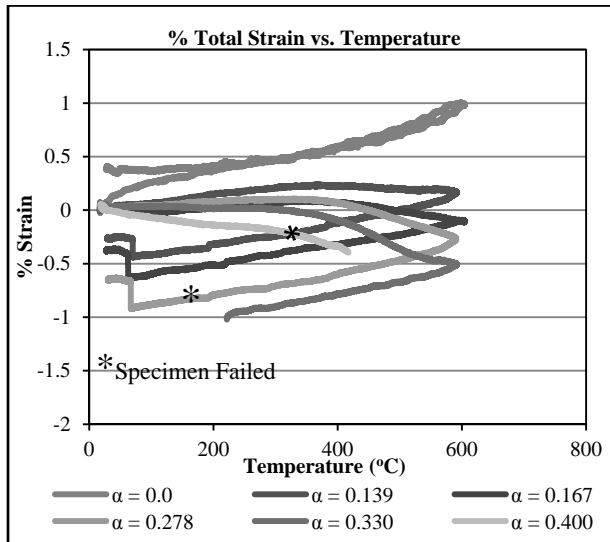


Figure 10. %Total Strain vs. Temperature for NSC at 600°C Core Temperature

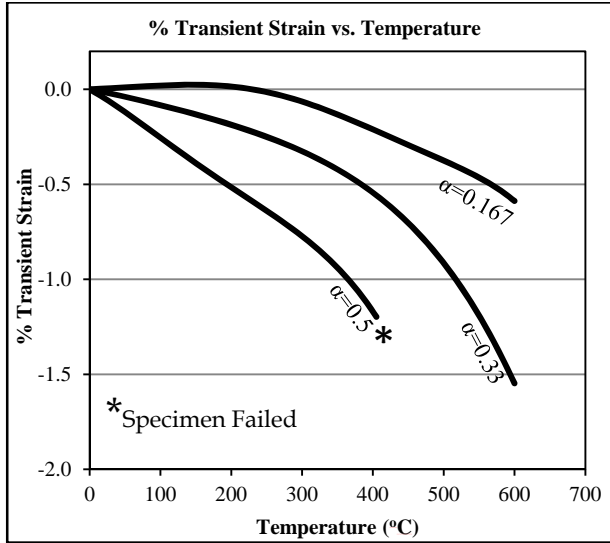


Figure 11. %Transient Strain vs. Temperature for NSC

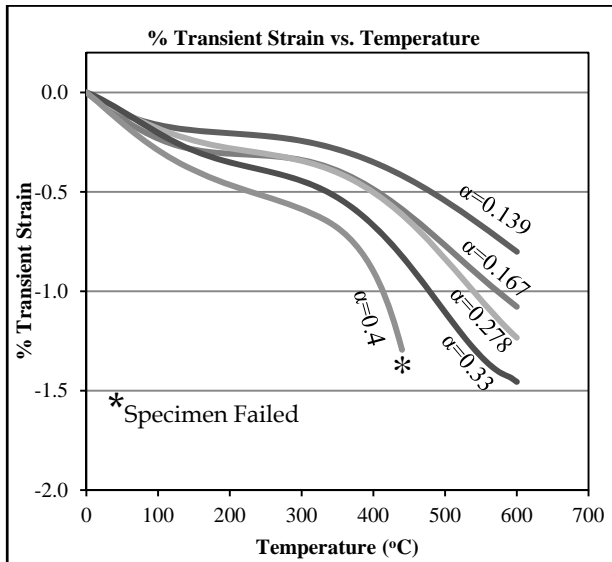


Figure 12. %Transient Strain vs. Temperature for HSC

3.3 Stress Development in Axial Restrained Specimens

Restrained tests on normal strength concrete with low initial stress levels are performed for the specimens with same specifications (grade of concrete, size of specimen, relative humidity etc.) as for those used in force controlled tests. To obtain restrained condition the actuator was held at a constant displacement throughout the heating cycle. The initial load of 18 kN is applied on the specimen and the displacement of the actuator corresponding to this load is held constant for the whole test duration. The net heating rate is the same as in above experiments and equal to 1.5 – 2.0 °/min.

The resulting stress development was observed to be on the order of about 11 kN (1.1 MPa) per 100 °C. Small deformations were observed in the test specimens since it was the actuator position rather than the length of specimen that was held constant during testing. Compressive strains developed in loaded specimen of about 0.2 % for temperatures up to 400 °C. With increasing temperatures the behaviour switched to tensile strains (contraction) of about 0.2 % for 600 °C (see Figure 13 and 14). To determine the percent restraint achieved during the test, the displacement data collected for the loaded (restrained) specimen are interpolated between zero percent restraint i.e. ‘free expansion strain’ and 100% or fully restraint i.e. ‘no expansion or zero strain.’ The results showed the percent restraint achieved is about 98% for low temperatures and decreases to 95% with increasing temperatures (up to 800 °C).

As expected relaxation is developing as a result of sustained deformation during heating. However, the relaxation observed in this study is higher than that reported in the literature for normal strength concrete (Nielsen, 2002). One reason may be that this study preloaded the specimen before heating to 1.75 MPa, whereas the specimens in Nielsen’s (2002) study were fully unloaded.

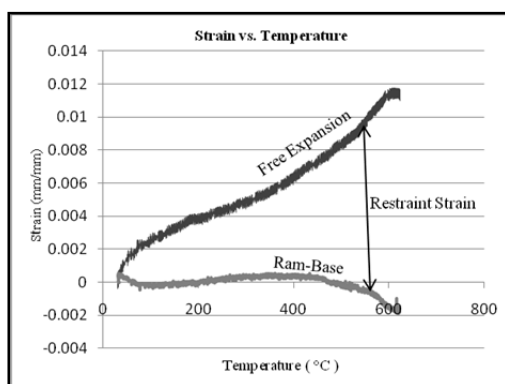


Figure 13. Strain vs. Temperature for 600°C

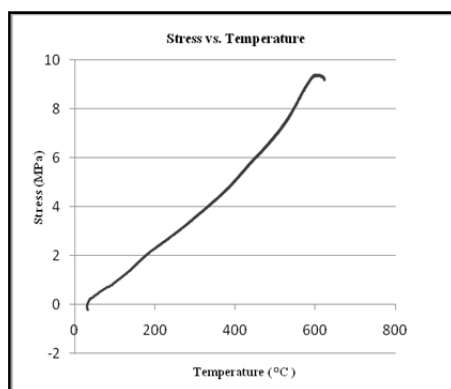


Figure 14. Stress vs. Temperature for 600 °C

4 CONCLUSION

The data presented in this paper supports the following conclusions:

- The NSC and the HSC have similar deformation characteristics for loaded specimens up to temperatures of 400 °C and for unloaded specimens (free expansion) for measured temperatures up to 600 °C
- Above 400 °C the HSC shows tendencies of higher contractions under load compared to the NSC.
- The combined effect of peak temperature before cooling and the magnitude of load significantly affects the deformation of axially loaded concrete. The NSC and the HSC exhibit similar levels of permanent deformation upon cooling at 400 °C. The preliminary data for the HSC indicate an increased level of permanent deformation upon cooling from 600 °C.
- The preliminary data on the stress development during restraint ends indicate a higher relaxation of the NSC used in this study compare to that reported in the literature.

REFERENCES

- [1] Anderberg, Y. and Thelandersson, S. (1976) “Stress and Deformation Characteristics of Concrete”, 2 – Experimental Investigation and Material Behavior Model, Bulletin 54, University of Lund, Sweden. (Referenced by Purkiss J.A., 2007).
- [2] Schneider, U. (1986a) “Properties of Materials at High Temperatures – Concrete” (Second Edition), RILEM Report, Gesamthochschule Kassel, Germany. (Referenced by Purkiss J.A.).
- [3] Schneider, U. (1988) “Concrete at High Temperatures – A General Review”, Fire Safety Journal, 13, pp. 55-68.
- [4] Schneider, U. “Modeling of Concrete Behavior at High Temperatures” In: Anchor R.D., Malhotra H.L., Purkiss J.A. Proceeding of International Conference of Design of Structures against Fire. 1986. pp. 53-69.
- [5] Khoury, G.A., “Strain Components of Nuclear-Reactor-Type Concretes during First Heat Cycle” Nuclear Engineering Design 1995; 156(1/2) pp. 313-332. (Referenced by Li and Purkiss, 2005)
- [6] Jensen, E., Van Horn, J. and Joshi, M (2010). Axial Deformation of Concrete Exposed to Fire and Loading. Proceedings for Interflam 2010, Nottingham Conference Centre, UK
- [7] Li, L.Y. and Purkiss, J.A. (2005) “Stress-strain constitutive equations of concrete material at elevated temperatures” Fire Safety Journal, 40, pp. 669-686.
- [8] Terro MJ. “Numerical modeling of thermal and structural responses of reinforced concrete structures in fire”. PhD thesis, Department of Civil Engineering, Imperial College, 1991. (Referenced by Li and Purkiss, 2005).
- [9] Engineering Properties of Concrete, viewed on 10 May 2010, <http://accuratus.com/mullite.html>
- [10] Wickstrom, Ulf. Adiabatic Surface Temperature and the Plate Thermometer for calculating Heat Transfer and Controlling Fire Resistance Furnaces. Conference proceedings from 9th IAFSS Symposium, Karlsruhe, Germany, 2008
- [11] Nielsen, Claus. *Mekaniske egenskaber under brand*. Centre for Green Concrete. Gronbeton.dk, 2002 (report in Danish)

ACKNOWLEDGEMENTS

This work was made possible with funding from NSF Award #0747775, and support from the Center for Innovative Materials Research (CIMR) at Lawrence Tech. The authors wish to thank the undergraduate student research team including Daniel Ziemba and Carl Durden.

COMPARISON BETWEEN RESULTS OF NUMERICAL SIMULATIONS AND EXPERIMENTAL TESTS ON FRP RC SLABS IN FIRE SITUATION

Emidio Nigro*, Giuseppe Cefarelli*, Antonio Bilotta*,

Gaetano Manfredi*, Edoardo Cosenza*

* Department of Structural Engineering – University of Naples Federico II
e-mails: emidio.nigro@unina.it, giuseppe.cefarelli@unina.it, antonio.bilotta@unina.it,
gamanfre@unina.it, cosenza@unina.it

Keywords: Fire, Concrete slab, FRP, Numerical simulation, Tests.

Abstract. *A key-aspect of the behaviour of concrete slabs reinforced with FRP bars is given by the effects of the exposure to fire at slab's top and bottom. In those cases, the mechanical properties' deterioration of the fibre-reinforced composite materials and of the bond at high temperatures determines a reduction of the resistance and stiffness of the elements working in flexure. In this paper experimental results of tests performed by authors to evaluate the performances of eleven concrete slabs reinforced with Fibre Reinforced Polymer (FRP) bars will be briefly summarized. Strains and displacements recorded during the tests by means of strain gauges and displacement transducers applied on concrete and FRP bars are showed and compared with the results of numerical simulations. The good agreement between experimental and numerical results increases the trust in the use of FRP as internal reinforcement of concrete members also for constructions subject to fire risk.*

1 INTRODUCTION

In the past, the authors performed experimental flexural tests ([1],[2],[3]) in order to evaluate the performances in fire situation of nine concrete slabs reinforced with Fibre Reinforced Polymer (FRP) bars (continuous end to end) by varying external loads in the range of the service loads, concrete cover in the range of usual values (30-50mm), bar end shape (straight or bent) and its length at the end of the concrete members (namely in the zone not directly exposed to fire). Moreover, two slabs were tested in normal condition [4].

In the following sections the experimental results of fire tests are briefly summarized. Moreover, a 3D nonlinear finite element model of the tested slabs is developed; the strains and displacements recorded during the tests by means of several strain gauges and displacement transducers applied on the concrete surface and FRP bars are compared with the results of numerical simulations.

2 EXPERIMENTAL RESULTS

Table 1 shows the main geometrical properties of nine of eleven slabs, those tested in fire situation, divided into three sets (namely Set I: S1,S2,S3, Set II: S4,S5,S6 and Set III: S7,S8,S9). The slabs S7, S8, S9 were identical to slabs S1, S2, S3, respectively, except for the shape of the longitudinal bottom bars

bent at the end (see Figure 1). To avoid forming bar splice anchorages in the span of the slab, a single GFRP bar whose length was that of the slab minus 20mm (i.e. twice the 10mm of concrete cover at each end of the slab) was employed for every slab.

The experimental investigation consisted of standard fire tests on the simply-supported slabs. Since the span between supports was 3200mm, the slabs 3500mm long (Set I and Set III) were external to furnace at each end for a length of 150mm, whereas the slabs 4000mm long (S4,S5,S6) for a length of 400mm. A strip of about 100mm of rock wool was used to protect the steel supports from fire exposure. Therefore, the ends of each slab were not directly exposed to fire action for a length, namely anchoring length, of about 250mm for Sets I,III and 500mm for Set II (see Table 1). The slabs S1, S4, S7 have not loaded during the fire exposure. Slabs S2, S5, S8 and S3, S6, S9 have been loaded with a predefined service load corresponding to about the 40% and 60%, respectively, of the ultimate bearing capacity of the slab in normal temperature design.

Experimental outcomes highlighted that the failure of the concrete slabs can be attained due to the rupture of the fibres in the middle of the member if a continuous reinforcement from side to side of the concrete element is used and zones not directly exposed to fire are guaranteed. These zones, near the supports, are necessary to ensure adequate anchorage of bars at the ends once in the fire exposed zone of slab the glass transition temperature is achieved and the resin softening reduces the adhesion at the FRP-concrete interface. Moreover it was shown that the length of this anchoring zone, which was not directly exposed to fire, can be reduced if the bars are bent at the end. However the bars cannot be overlapped in the area directly exposed to fire because the temperature attains so high values that the loss of adhesion at the concrete-FRP interface may occur and then the failure of structure could take place in a few time.

Furthermore, if the bar anchorage allows the pull out of bars to be avoided the failure of slabs is attained due to very high temperatures, namely much higher than glass transition temperature T_g . Bars temperature during fire exposure largely depends on the concrete cover value and fire endurance depends on the fibres strength at high temperatures and consequently it may depend on the fibres types.

Table 1. Fire test main parameters for FRP reinforced concrete slabs.

Set	Slab	Length [mm]	Width [mm]	Thickness [mm]	Cover [mm]	Bottom bars (diameter/spacing) [mm]		Anchoring length [mm]	Bar shape
						longitudinal	transversal		
I	S1	3500	1250	180	32	$\Phi 12/150$	$\Phi 12/200$	250	Straight
	S2					$\Phi 12/225$			
	S3								
II	S4	4000	1250	180	51	$\Phi 12/125$	$\Phi 12/200$	500	Straight
	S5					$\Phi 12/200$			
	S6								
III	S7	3500	1250	180	32	$\Phi 12/150$	$\Phi 12/200$	250	Bent
	S8					$\Phi 12/225$			
	S9								

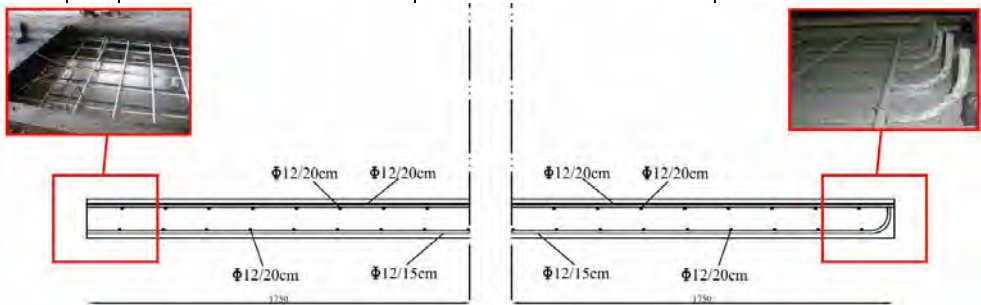


Figure 1. Geometrical details of bars' end

3 FEM MODEL

The thermo-mechanical modeling of the slabs tested under fire conditions is performed through the finite element software ABAQUS/Standard [5], which allows to model accurately some aspects of the mechanical behavior, including the lack of bond between bars and concrete in the zone directly exposed to fire. As usual, decoupling of thermal problem and mechanical problem is assumed. Therefore, the mechanical analysis is developed by associating to the FEM model the temperature field obtained through a previous thermal analysis, in which the effects of stress-strain on the thermal behavior are neglected. The boundary conditions and load application were identical to that used during the Phase 1 of the test (see [1]), characterized by a constant load during the fire exposure. The dead load representing the weight of the slab was applied as a static uniformly distributed load on the top surface of the slab. The jack load was applied as a static distributed load over the area of the spreader steel members.

3.1 Geometry

In order to reduce computational time of numerical model of each slab, a representative longitudinal strip is modelled for each slab, with a width cross section equal to the overall slab width (1250mm) divided by the number of bars. Moreover, for symmetry with respect to the midspan of the slab and to the vertical plane passing through the centroidal axis of the bar, only a quarter of the strip is analyzed (see Figure 2). In Table 2, the main geometrical details of the model are summarized for each slab. Note that slabs are reinforced with bars of nominal diameter 12mm having an area of 113mm².

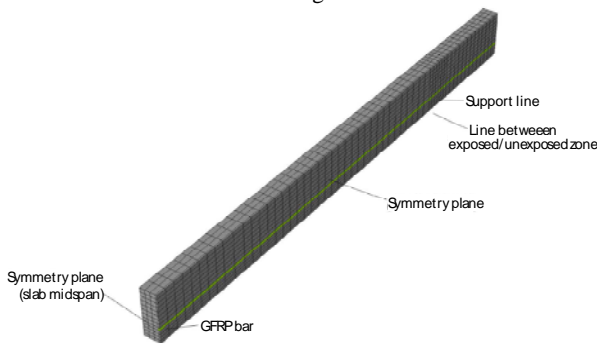


Figure 2. FEM Model (slab S4)

Table 2. Geometrical details of the numerical model

Set	Soletta	Copriferro [mm]	Longitudinale [mm]	Dimensione		Area di armatura [mm ²]
				Trasversale [mm]		
I	S1	32 ^(*)	3500/2=1750	(1250/9)/2=69.444		113/2=56.5
	S2			(1250/6)/2=104.167		
	S3					
II	S4	51 ^(*)	4000/2=2000	(1250/10)/2=62.500		113/2=56.5
	S5			(1250/7)/2=89.286		
	S6					
III	S7	32 ^(*)	3500/2=1750	(1250/9)/2=69.444		113/2=56.5
	S8			(1250/6)/2=104.167		
	S9					

(*) Spessore del copriferro di calcestruzzo misurato tra l'intradosso della soletta ed il baricentro della barra.

The experimental tests showed that in the area directly exposed to fire, for temperatures above the glass transition temperature, the adhesion bar-concrete is severely damaged (after about 15 minutes for slabs of Set I and Set III, and 20 minutes for slabs of Set II). Therefore, to simplify the modeling, we assumed that, in the zone directly exposed to fire, the GFRP bar and the concrete does not exchange bond stresses since the application of external loads. For this purpose "Contact pair" interface element

available in ABAQUS was used: the master surface corresponds to the surface of the concrete around the bar, while the slave surface corresponds to the surface of the bar. The two surfaces cannot penetrate, and when they are in contact, they can move each other only normal stresses and shear stresses. By contrast, in the area not directly exposed to fire perfect bonding between bar and concrete is assumed (“Constraint” interface element). Note that the perfect adherence bars-concrete is quite correct only for slabs of Set II and Set III, whereas it is certainly not valid for slabs of Set I. Therefore, the numerical analyses will be performed only for slabs of Set II and Set III.

3.2 Thermal properties

The thermal analyses were carried out by using the “HEAT TRANSFER” option available within ABAQUS. Each slab is divided into finite elements “Brick” type “Hex” (parallelepiped elements), with maximum dimensions of 70mm x 28mm x 20mm, 8 linear node (ABAQUS C3D8 element). Both the exposed and not exposed to fire surface was defined in accordance with the conditions of thermal exposure of the slabs during the tests. According to EN1991-1-2 [6]:

- constant convective coefficients $\alpha_c = 25 \text{ W/m}^2\text{K}$ and $\alpha_c = 9 \text{ W/m}^2\text{K}$ were assumed for the exposed and unexposed surfaces, respectively;
- the radiative heat flux was calculated by using a concrete emissivity $\epsilon = 0.7$. This flux has been considered only for the exposed surface.

Concrete specific heat and thermal conductivity relationships provided by Lie [7] were assumed. As concerns the concrete thermal expansion, three different relationships were assumed: two are provided by EN1991-1-2 for calcareous and siliceous concrete, respectively; the third one was obtained by averaging the first two.

FRP specific heat and thermal conductivity relationships provided by Bai et al. [8] for GFRP bars, characterized by a similar ratio fiber / matrix equal to 61%, not far from the 70% that characterizes the GFRP bars used for the specimens, were assumed. As concerns the FRP thermal expansion Bai et al. [8] relationships was modified as showed in Figure 3.

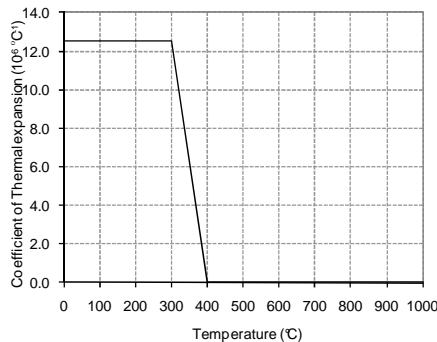


Figure 3. FRP thermal expansion (Bai et al. [8] modified).

3.3 Mechanical properties

Concrete mechanical behaviour, represented by the stress-strain relationship provided by EN1992-1-2 [1] for calcareous aggregate, on the basis of examples available in the literature (see [9]), is modeled through the “damaged plasticity model” implemented in ABAQUS, which models the behavior in both compression and tension of reinforced concrete.

Under axial compression, at the generic temperature T , the concrete behavior is assumed linear up to the limit of proportionality, $f_{cp,T}$, at a strain equal to the 50% of the strain related to the compressive cylindrical strength $f_{c,k,T}$, at temperature T . The latter, in agreement with EN1992-1-2, is equal to $k_{c,T} f_{cm}$, where f_{cm} is the average compressive strength at a temperature of 20°C (see [1]). In Figure 4 concrete stress-strain relationships are showed for different temperatures.

Under axial tension, at the generic temperature T , the stress-strain response is modeled by a modified Belarbi & Hsu model [11] in which the softening branch is characterized by exponent equal to 0.3 instead of 0.5. At the generic temperature T , the tensile strength is $f_{ct,T} = k_{c,T} \cdot f_{ct}$ where $f_{ct} = 0.3 \cdot (f_{ck})^{2/3}$ is the tensile strength at a temperature of 20° C, according to EN1992-1-1. The characteristic cylinder compressive strength, $f_{ck} = f_{cm} - 8$ [N/mm²] is assumed.

The mechanical behavior of GFRP bar was assumed linear elastic at the generic temperature T , with elastic modulus $E_f(T) = \rho_E(T) \cdot E_f$, where E_f is the elastic modulus in ambient conditions (50 GPa) and $\rho_E(T)$ the reductive coefficient of the elastic modulus at temperature T . Particular attention should be paid to the modeling of the bar stiffness, because it influences the slab deformability. In the absence of detailed data on the thermo-mechanical GFRP bars properties, based on the Wang et al. [12] tests, ρ_E is assumed according to Figure 5.

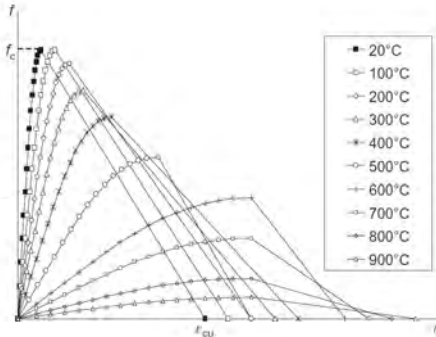


Figure 4. Stress-strain relationship for concrete in compression at high temperature [9]

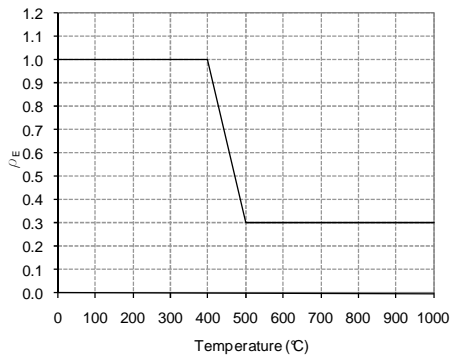


Figure 5. FRP Young's modulus reduction versus temperature

4 NUMERICAL RESULTS

In Figure 6 the thermal distribution of slab S4, obtained by numerical analysis at fire exposure time equal to 60 minutes, is showed. Thanks to the 3D modeling heat diffusion in the neighborhood of the separation line between the surface directly exposed and not directly exposed, near the supports, can be observed. This heat diffusion clearly show that temperatures and hence deterioration of bar-concrete bond in the area not directly exposed to fire are low.

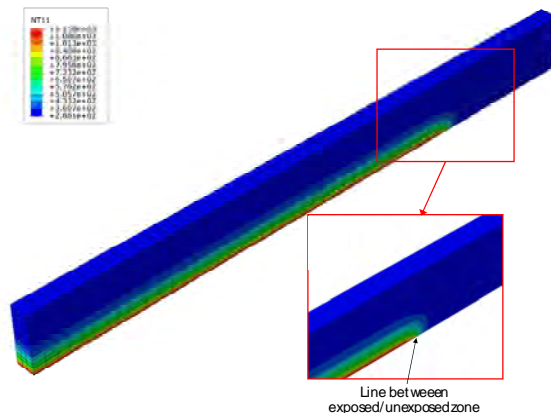
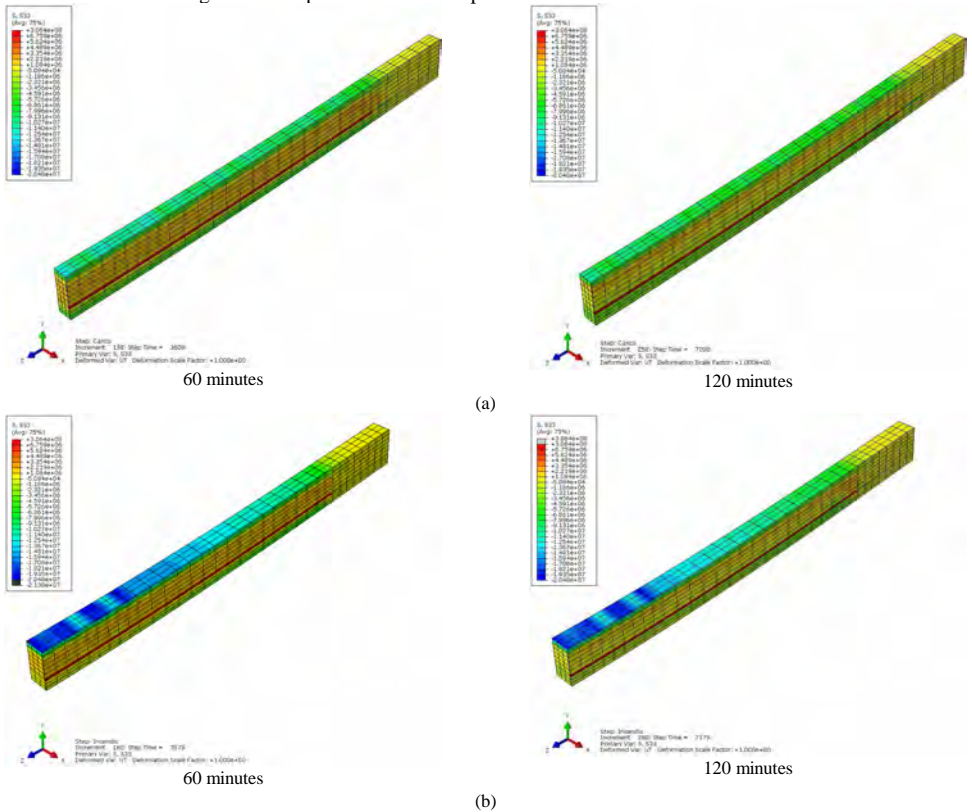
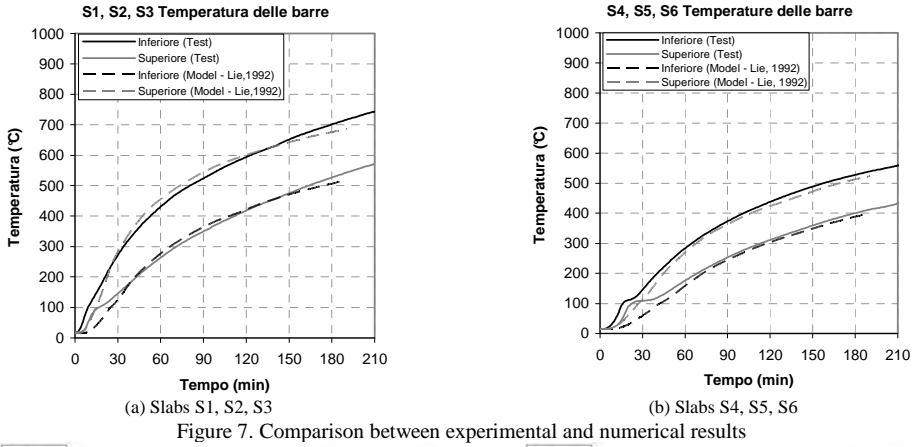


Figure 6. Slab S4: Temperatures distribution at 60 minutes of fire exposure time (temperature in Kelvin)

Figure 7a,b, for slabs S1, S2, S3 (with 32mm concrete cover) and S4, S5, S6, (with 51mm concrete cover) respectively, shows that time-temperature curves, above and below the bar, obtained with the FEM model in ABAQUS, are in good agreement with the experimental results. In particular, the results obtained with ABAQUS are very similar to those obtained with SAFIR2007 (see [2]).



The stress distribution showed via stress-maps in Figure 8 for slabs S4 and S6 at 60 and 120 minutes show that stresses along the FRP bar are constant and reduce only at the end of the slab, not directly exposed to fire. For simplicity the degradation of the adhesion bar-concrete above mentioned was not modeled, as stated in the FEM model description. In Figure 9, the experimental deflections of slab S4 and S6 are compared with the numerical obtained for different concrete thermal expansion properties, by using two relationships provided by EN1991-1-2 for calcareous and siliceous concrete and an average curve of these two. The Figure 9 shows that this thermal properties can particularly affect the simulation results. The average thermal expansion curve allow to simulate the behavior of slab S4 (not loaded during the fire exposure) better than slab S6. Concrete and FRP strains at the top fiber of concrete slab and the top fiber of bottom FRP bars were simulated for slab S4 and S6 by assuming this average curve (see Figure 10a,b and Figure 11a,b).

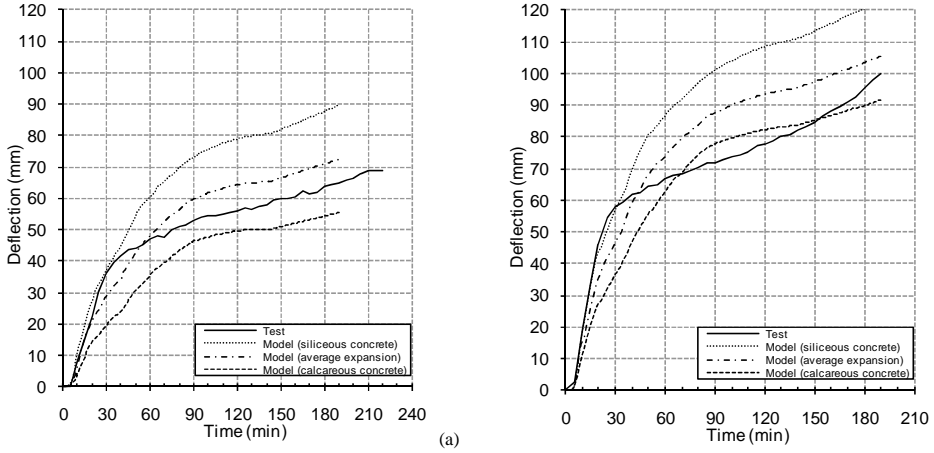


Figure 9. Comparison of Displacement vs time: (a) Slab S4, (b) Slab S6

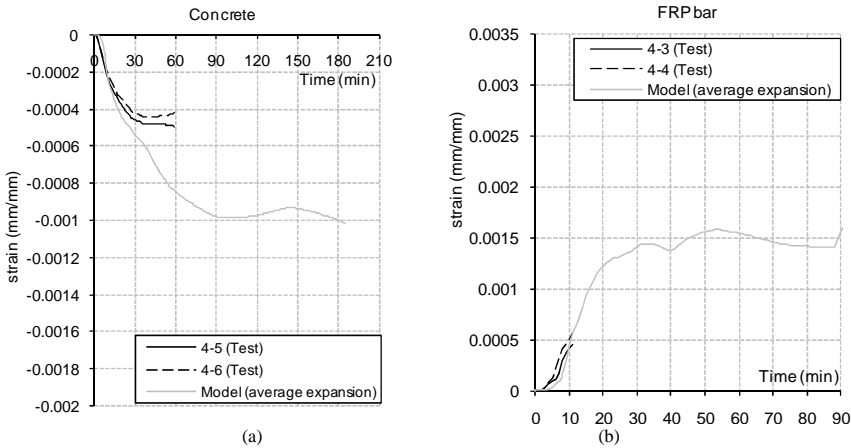


Figure 10. Slab S4: Experimental and numerical strains vs time: (a) concrete, (b) FRP.

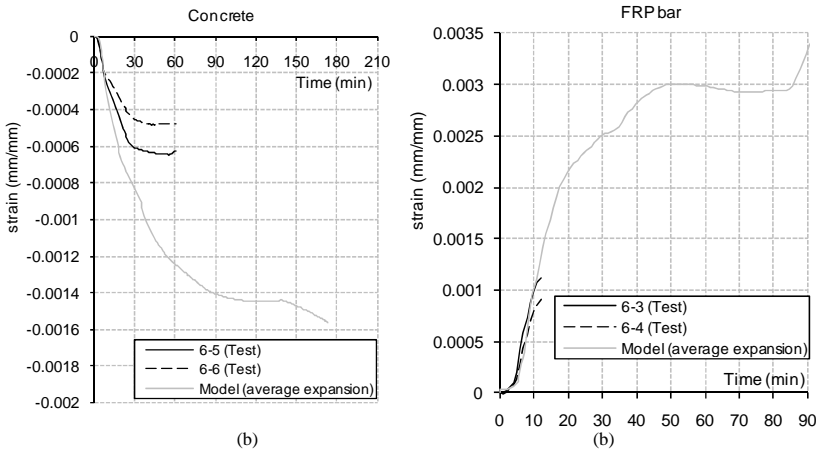


Figure 11. Slab S6: Experimental and numerical strains vs time: (a) concrete, (b) FRP.

The strains on the concrete were recorded up to about 60min of fire exposure; unfortunately, the comparison for the FRP bars can be showed only for few minutes due to bond damage that strain gauges underwent after glass transition temperature of bars was achieved. The figures show a good agreement between experimental and numerical strains on FRP bars. Moreover they confirm that simulations provide better provisions for slab S4 than for slab S6.

The agreement between experimental and numerical strains seems to validate enough the numerical model to be used in order to evaluate the stresses in the slab during the fire exposure.

The stresses obtained by the numerical simulation, at significant points of the concrete in the middle section of the slab are shown, in Figure 12a,b for Slab S4 and S6, respectively. In particular the stresses are related to three significant fibers: the bottom fiber (slab intrados), the mid fiber (at an height corresponding to centroid of the bar) and the top fiber (slab extrados). For slab S4 the stress in the bottom fiber, initially in tension, becomes compression after less than 5 minutes of fire exposure, due to the contrast exerted by the colder internal fibers to its thermal expansion. Conversely, the mid fiber, colder than the bottom fiber, initially undergoes an increase in tensile stress up to the reaching of the concrete tensile strength at an exposure time of about 5 minutes. When this strength value is attained, the tension in the fiber cannot longer increase. Therefore the softening branch of concrete constitutive law in tension is activated with a decrease in tensile stress.

For slab S6, load during fire exposure, the termo-mechanical behaviour is similar to that of the unloaded slab S4, however the compressive stress in top fiber is higher. Moreover, after fire exposure time equal to about 100 minutes the bottom fiber return in tension.

Finally, in Figure 13a,b, for slab S4 and S6, respectively, the GFRP bar stress are reported during the fire exposure time. For the concrete tensile strength, initially, the bar stress is low (about 0.5N/mm^2). At a time of fire exposure equal to about 30 min the stresses increase up to about 80 and 125 MPa for slab S4 and S6 respectively (different values are due to different loads). Stresses remain quite constant up to 90min. Then they increase up to about 140min of fire exposure. At this time the bars temperature achieves a value higher than 400°C . For this reason the reduction of the elastic modulus (see Figure 5) leads to a decrease in tensile stress.

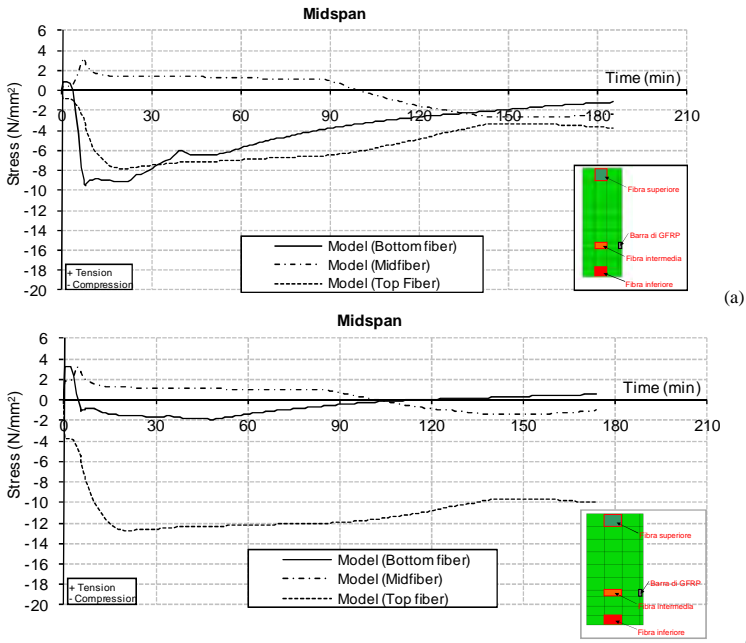


Figure 12. Numerical simulation: stress vs time: (a) Slab S4, (b) Slab S6

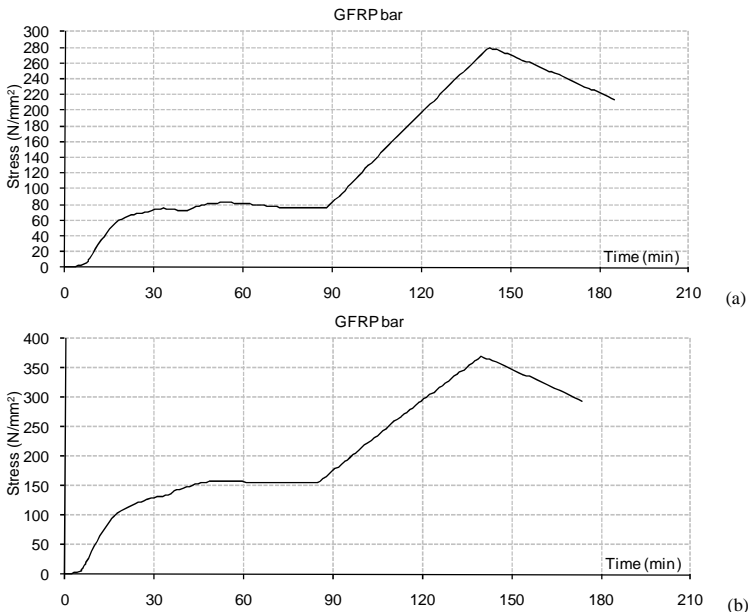


Figure 13. Numerical simulation: GFRP bar stress vs time: (a) Slab S4, (b) Slab S6

4 CONCLUSIONS

Experimental results of tests performed by the authors on nine concrete slabs reinforced with GFRP bars exposed to fire action according to the ISO 834 standard time–temperature curve allowed to refine a numerical 3D FEM model, useful to evaluate[1] their thermal and mechanical behavior. Thermal fields in the concrete slabs and stresses in concrete and FRP bars were simulated. The dependence of both temperatures and mechanical properties on the specific thermal properties of concrete and FRP was taken into account by using the relationships provided by both theoretical models and the European technical code. Preliminary comparisons between numerical and experimental outcomes showed a very good agreement in terms of temperature field, and comfortable results for the mechanical simulations. The FEM model will be refined with the aim of addressing future research concerning specific thermal properties of concrete and FRP.

REFERENCES

- [1] Nigro E., Cefarelli G., Bilotta A., Manfredi G., Cosenza E., “Fire resistance of concrete slabs reinforced with FRP bars. Part I: experimental investigations on the mechanical behaviour”, *Composites: Part B*, Engineering - Elsevier, vol. 42, p. 1739–1750, ISSN: 1359-8368, doi:10.1016/j.compositesb.2011.02.025, 2011.
- [2] Nigro E., Cefarelli G., Bilotta A., Manfredi G., Cosenza E., “Fire resistance of concrete slabs reinforced with FRP bars. Part II: experimental results and numerical simulations on the thermal field”, *Composites: Part B*, Engineering - Elsevier, vol. 42, p. 1751–1763. ISSN: 1359-8368, doi:10.1016/j.compositesb.2011.02.026, 2011.
- [3] Nigro E., Cefarelli G., Bilotta A., Manfredi G., Cosenza E., “Tests at high temperatures on concrete slabs reinforced with bent FRP bars”, *ACI Special Publication SP-275*, ID-50, 20 pp, American Concrete Institute, ISBN: 087031412220, 2011.
- [4] Nigro E., Bilotta A., Cefarelli G., Manfredi G., Cosenza E., “Flexural tests on GFRP RC slabs: experimental results and numerical simulations”, *6th International Conference on Bridge Maintenance, Safety and Management*, CRC Press/Balkema, Taylor & Francis group, Stresa, Lake Maggiore, Italy, July 8-12, 2012.
- [5] Abaqus Standard/Explicit User’s Manual. *Hibbitt, Karlsson and Sorensen*, Inc. Vol. 1, 2 and 3, Version 6.5, USA, 2006.
- [6] European committee for standardization, *EN 1991-1-2. Eurocode 1. Actions on Structures – Part 1-2: General Actions – Actions on structures exposed to fire*, November, 2002.
- [7] Lie. T.T, *Structural Fire Protection*. American Society of Civil Engineers Manuals and Reports on Engineering Practice No. 78. ASCE, NewYork, 1992.
- [8] Bai Y, Vallée T, Keller T., “Modeling of thermo-physical properties for FRP composites under elevated and high temperature”, *Composites Science and Technology*, Vol. 67, pp. 3098–3109, 2007.
- [9] Ellobody E, Bailey CG., “Modelling of bonded post-tensioned concrete slabs in fire”. *Struct Build*, ICE Proc, Thomas Telford J 2008;61(6):311-323, 2008.
- [10] European committee for standardization, *EN 1992-1-2. Eurocode 2. Design of concrete structures – Part 1-2: General Rules – Structural Fire Design*, March, 2004.
- [11] Belarbi H. & Hsu T.C.C., “Constitutive laws of concrete in tension and reinforcing bars stiffened by concrete”, *ACI Structural Journal*. 91(4): 465-474, 1994.
- [12] Wang Y., Wong P.M.H., Kodur V., “An experimental study of the mechanical properties of fibre reinforced polymer (FRP) and steel reinforcing bars at elevated temperatures”, *Composite Structures* 80(2007), pp 131-40, 2007.

HIGH TEMPERATURE CREEP DEFORMATION AND FAILURE BEHAVIOUR OF PRESTRESSING STEEL

John Gales*, Luke Bisby* and Tim Stratford*

*BRE Centre for Fire Safety Engineering, University of Edinburgh
e-mails: j.gales@ed.ac.uk, luke.bisby@ed.ac.uk, tim.stratford@ed.ac.uk

Keywords: Creep, Prestressing steel, High temperature strain, Digital image correlation, Necking

Abstract. Concrete slabs in modern buildings increasingly contain prestressing steel running continuously across the floor plate. When this steel is unbonded and post-tensioned (UPT), localized damage can affect the integrity of the entire building. During localised fires, locally-heated UPT steel is prone to rupture due to stress/strength/time interactions that are influenced by high temperature creep. Creep should thus be considered during the fire safe design of UPT buildings. Existing creep modelling parameters for prestressing steel are dated and overestimate deformation. Using a bespoke optical strain measurement technique, high temperature tensile tests were performed to analyze creep in two 'equivalent' prestressing steels. The response of stressed UPT strands exposed to localised heating is modelled for validation, and compared against tests. The new creep parameters are shown to improve the ability to model all phases of high temperature creep, including tertiary creep and eventual failure.

1 INTRODUCTION AND OBJECTIVES

Prestressing steel is a favoured form of reinforcement for modern, highly optimized concrete flat slabs used in multi-storey construction; this is owing to various sustainability, economic, and constructability benefits. In this construction method, prestressing steel is typically cast into the concrete as continuous, placed inside draped ducts, often left unbonded to the concrete and post-tensioned being anchored only at the ends of the prestressing strand (a construction technique called unbonded post-tensioned (UPT) concrete). However, the continuity of UPT steel across multiple bays of a structure can have potential drawbacks – particularly during fire. Localized heating of UPT tendons, as would probably occur during real building fires due to any of: spalling, compartmentation, or ceiling jets etc., could result in tendon rupture and would affect slab integrity in areas of the structure distant from the fire [1]. Indeed, recent experiments on stressed UPT tendons of realistic length which were locally heated have demonstrated that UPT tendon rupture can occur at temperatures well below those at which uniformly heated tendons would fail [2].

The propensity for rupture of UPT tendons at elevated temperature in a concrete structure depends on a complex interaction between thermally induced loss of strength and tendon stress variations which are due to a time, stress, and temperature dependent irrecoverable deformation (i.e. creep). In the absence of full scale multi-bay fire testing of UPT concrete slabs, an accurate, robust, explicit method for predicting creep effects for any possible transient heating regime is necessary to computationally assess the performance of UPT buildings both during and after a fire. A computational model (see Gales et al [2]) for predicting high temperature stress variation of locally-heated UPT prestressing strands has previously been developed and shown to predict appropriate behavioural trends. However, previous modelling was forced to make use of dated input parameters from the 1970s. When applied to predict the response of modern prestressing steels exposed to localized heating, the model greatly overestimated creep deformation. Overestimation creep deformation may be unconservative for predicting UPT tendon

rupture during fire [2]. An accurate understanding of the creep behaviour of modern prestressing steels at high temperature is therefore needed to ensure conservative fire design of UPT buildings.

To address the above knowledge gap, the high temperature creep response of two ‘equivalent’ modern prestressing steels were analyzed through uniaxial steady-state and transient thermal regime tensile tests. A validated non-contact strain and deformation measurement technique using high resolution Digital Image Correlation (DIC) has been applied to accurately characterize the high temperature creep behaviour of these modern prestressing steels. Conventional contact strain instrumentation does not easily allow for accurate derivation of high temperature material properties for a variety of reasons, hence the new bespoke optical technique has been developed.

Creep model parameters for use in the previously developed computational model [2] are produced herein for “equivalent” grades (BS 5896 (2011) and ASTM 416 (2008)) of prestressing steels used in the United Kingdom and North America, respectively. The creep behaviour of these modern prestressing steels is then compared against that of antiquated prestressing steel from the 1970s (ASTM 421 (1970)). Furthermore, the results of the new tests using DIC challenge classical creep theory and provide initial insights into the true nature of Tertiary creep and in modelling runaway creep failure. Finally, validation of the creep parameters and predicted behaviour is provided by comparison against tests on locally heated unbonded and stressed prestressing steel tendons.

2 CLASSICAL HIGH TEMPERATURE CREEP THEORY

Creep strain (ϵ_{cr}) is permanent deformation which depends on metallurgy, stress, temperature, and time. For either transient (load-then-heat) and steady state (heat-then-load) uniaxial heating test conditions, plotting the measured ϵ_{cr} (after careful removal of elastic thermal expansion and mechanical strains) for a constant sustained uniaxial tensile stress level gives a sigmoidal (S-shaped) curve with respect to a lumped time-temperature coefficient, commonly called ‘Temperature Compensated Time’, θ [3]. Invoking an assumed empirical coefficient $\Delta H/R$ (the so-called ‘activation energy’ for creep, which is measured in Kelvin), the Temperature Compensated Time can be described using an Arrhenius equation:

$$\theta = \int_0^t e^{-\Delta H / RT} dt \quad (1)$$

where t is measured in hours. A typical example of an ϵ_{cr} versus θ curve for prestressing steel is given in Figure 1a. The ϵ_{cr} curve (at constant uniaxial tensile stress) has three classical phases; the Primary phase is characterised by a decreasing deformation rate, which slows to a ‘steady’ minimum strain rate during the Secondary phase. The straining rate then accelerates in ‘run away’ during the final Tertiary phase.

In fire engineering design [3][4][5], Equation 2 is often used to describe ϵ_{cr} for various steel alloys;

$$\epsilon_{cr} = \frac{\epsilon_{cr,0}}{\ln 2} \cosh \left(2 \frac{Z\theta}{\epsilon_{cr,0}} \right) \quad (2)$$

This equation assumes two basic, empirically determined input parameters; $\epsilon_{cr,0}$, which is used to describe primary creep, and Z (the so-called Zener-Holloman Parameter which is measured in hrs^{-1}), which is intended to describe the slope of the secondary phase; i.e. the minimum creep rate. The extraction of these parameters from a sustained stress uniaxial creep test is illustrated in Figure 1a. A typical set of Z parameters available in the literature, for ASTM 421 (1970) prestressing steel, originally derived in reference [5], are given in Figure 1b.

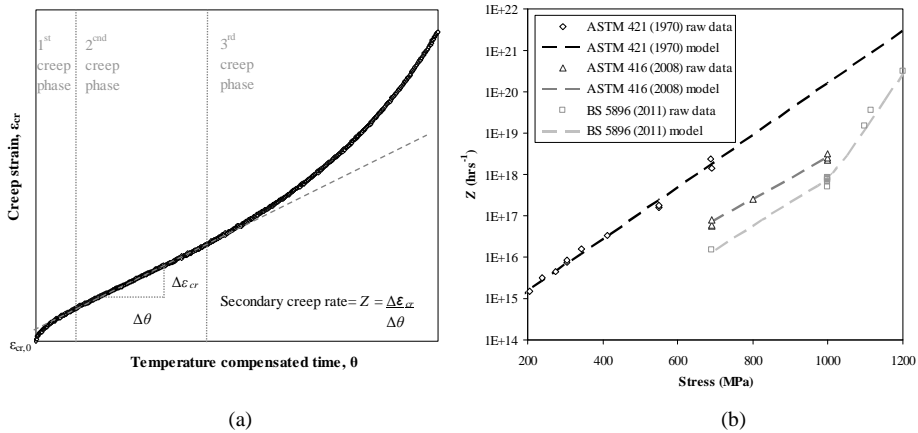


Figure 1. (a) Traditional creep theory applied to prestressing steel with the Harmathy [5] equation and (b) variation of the measured Zener Holloman parameter, Z , with tensile stress level for different prestressing steels.

Equation 2 has historically only been assumed valid until the transition between the Secondary and Tertiary creep phases; it does not account for cross sectional area reduction which occurs during Tertiary creep and was intended for use where ‘true’ stresses change relatively slowly with time. It is also noteworthy that Z may not readily be extractable from creep data sets for all metal alloys, since ϵ_{cr} may not exhibit linearity with respect to θ in all cases and therefore Equation 2 is not considered universal. For prestressing steels, however, Equation 2 has been shown to satisfactory to represent creep behaviour [2, 6], and it is therefore applied herein to derive new parameters for use in high temperature creep modelling (i.e., Z , $\epsilon_{cr,\theta}$) based on a new series of novel tensile creep tests.

3 EXPERIMENTAL PROCEDURES

Both transient and steady state uniaxial tensile tests were conducted to define new creep parameters for Grade 1860 ASTM 416 [7] and BS 5896 [8] prestressing steel core wire (4.4 and 4 mm in diameter, respectively, and cut to 660mm in total length).

Rather than utilize only traditional bonded foil strain gauges (which are generally limited to about 2% strain at ambient temperature and thus unable to capture the full plastic response) or a high temperature contact extensometer (which would be damaged by failure of the specimen), a non contact DIC technique using the GeoPIV8 algorithm [9] for post-test digital image processing was used to obtain strain and deformation measurements. A digital single lens reflex (SLR) Canon EOS 5D Mark II (21 mega pixel image resolution) camera was used to acquire images of the test specimens at a predefined rate of 0.2Hz. An Instron 600LX servo-hydraulic materials testing frame equipped with a custom environmental chamber – capable of heating samples up to 625°C – was used in all testing. Figure 2 shows the testing apparatus. Temperatures were recorded using K type thermocouples evenly distributed along the prestressing steel specimens within the environmental chamber. Since the accuracy of the DIC algorithm is dependent on image contrast, the specimens were painted with high temperature matt black paint and speckled with matt white paint. Table 1 provides an overview of the full test series conducted for the current paper.

A variety of slightly different testing regimes were utilised in this paper to study various aspects of the creep response of prestressing steel at elevated temperature. Steady state tensile tests were performed wherein the sample was heated to a predefined constant temperature, and images were then acquired while load was increased up to a sustained target stress or until failure. Transient tensile tests were also

performed in which the specimens were loaded initially to a target stress at ambient temperature, and images were then acquired while the specimens were heated at a uniform heating rate until failure. Post test analysis using the image correlation processing algorithm allowed the total strain to be determined; mechanical and thermal expansions were then isolated and removed to obtain a measured creep strain, ϵ_{cr} .



Figure 2. Test setup and digital SLR camera used for DIC analysis.

Table 1. Summary of ASTM 416 and BS 5896 creep test series.

ASTM 416						BS 5896					
Test series	Test type	Target stress (MPa)	Target temp. (°C)	Loading (mm/min or °C/min)	# tests	Test series	Test type	Target stress (MPa)	Target temp. (°C)	Loading (mm/min or °C/min)	# tests
1a	SC ^a	690	427	-	1	1b	SC ^a	1115, 1200	365	-	2
2a	TC ^b	690	-	2	1	2b	TC ^b	690	-	2	1
3a	TC ^b	800	-	2	1	3b	TC ^b	1000	-	2	4
4a	TC ^b	1000	-	2	2	4b	TC ^b	1000	-	1	1
5a	TC ^b	1000	-	10	1	5b	TC ^b	1000	-	10	1
6a	CL ^c	1000	-	-	1	6b	TC ^b	1100	-	2	1
7a	TE ^d	0	500	10	2	7b	TE ^d	0	500	10	2
8a	S ^e	-	22-500	2	2	8b	S ^e	-	22-500	2	12

Notes: ^a Steady state creep, ^b Transient state creep, ^c Constant load, ^d Thermal expansion, ^e Strength

A validation and configuration study was performed for the DIC method as this was the first time that such as technique had been used for this type of measurement. A sensitivity analysis suggested an optimum axial gauge length of 25mm. A steady state test to failure at ambient temperature (on ASTM 416 prestressing steel) demonstrated a resolution of better than 0.0002 strain for a gauge length of 25mm and a maximum measurement difference of only 0.0008 as compared with bonded electrical resistance foil gauges (up until the foil gauges debonded at less than 2% strain). Strain measurement by DIC was however able to capture the full plastic response of the specimens. Furthermore, high temperature unrestrained thermal expansion tests (a uniaxial transient heating test with no applied load) showed a

maximum difference of <0.0003 strain when the test data were compared against Eurocode 2 [10] predictions and also against readings from a high temperature ceramic arm contact extensometer.

4 EXPERIMENTAL RESULTS

4.1 Strength failure

The strength behaviour of modern prestressing steel is discussed in this section by comparison against the Eurocode 2 (EC2) [10] temperature based strength reduction factors for both Class A and Class B prestressing steel. The strength reduction results obtained during testing for BS 5896 steel are shown in Figure 3a (these data are based on steady state testing at a crosshead displacement rate of 2 mm/min). An average ultimate strength at ambient temperature of 2200 ± 11 MPa (standard deviation) was obtained for the BS 5896 strand's core wire, with subsequent strength reductions determined at 100°C intervals up to 500°C . These strength reductions are based on an *engineering* definition of stress, wherein the cross-sectional area of the specimen is assumed constant up to failure and the Poisson and necking effects are ignored. Also shown in Figure 3a is a curve showing the reductions in strength with temperature if a *true* stress definition is adopted. This is based on an optically measured reduction of cross-sectional area (i.e. necking) which has also been carefully measured using DIC at elevated temperature. The true versus engineering stress versus strain responses for tests up to 500°C with different loading rates are shown in Figure 3b, where it can be seen that the true stress actually increases drastically approaching failure.

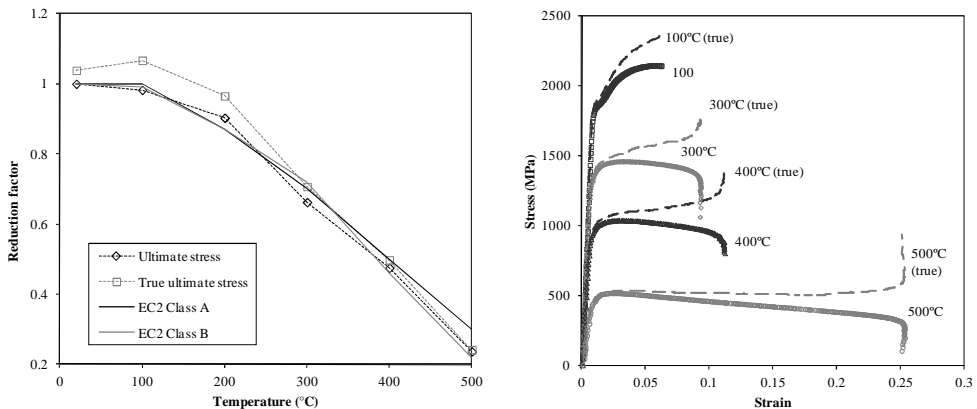


Figure 3. (a) Strength reduction of BS 5896 prestressing steel with temperature at a crosshead stroke rate of 2mm/min during steady-state testing as compared against Eurocode 2 [10] and (b) stress versus strain curves at a steady-state temperature for BS 5896 prestressing steel.

Figure 3a shows that the strength reduction of the BS 5896 steel follows the expected behaviour based on EC2 predictions [10]; this provides further credence to the use of the new DIC strain measurement technique for materials characterization at elevated temperatures. Figure 3a also shows that the true strength retention of prestressing steel at elevated temperature is actually better than assumed on the basis of an engineering stress definition, at least up to about 300°C where the engineering stress-strain response experiences post-peak softening (Figure 3b) and the distinction between true and engineering stress disappears (interestingly this post-peak softening is not captured by the EC2 models for stress-strain response at elevated temperature but may be important for modelling the response of structures to fire).

4.2 Creep parameters

This section considers the creep behaviour of all prestressing steels including a historical and regional comparison. Table 2 gives the chemical composition of the prestressing steels considered in the current paper; ASTM 421 (1970), ASTM 416 (2008), and BS 5896 (2011). Since creep is dependent on metallurgy and crystal structure, and given the considerable variability between each sample's material compositions, the creep response is expected to be somewhat different; how much difference to expect, given these variations, is open but worthy of consideration.

Table 2. Chemical composition of the three different prestressing steels studied herein.

	BS 5896 (2011)	ASTM 416 (2008)	ASTM 421 (1970)
C	0.90	0.80	0.79
Cr	0.011	0.04	-
Mn	0.66	0.87	0.78
P	0.0070	0.023	0.012
Si	0.25	0.45	0.19
S	0.014	0.12	0.031
Ni	0.021	-	-
Cu	0.011	-	-

Note: Trace elements are not considered in this table

An empirically derived $\Delta H/R$ of 30550K [5] was assumed for all prestressing steels (note that subsequent testing confirmed that the ASTM 416 and BS 5896 steels still exhibited $\Delta H/R$ parameters in the range of this assumed value). Creep parameters were extracted from the ϵ_{cr} versus θ curves produced for each tensile test (refer to Figure 1a). Figure 1b overlays Z parameters determined experimentally for all three steels at different stress levels. The plotted Z parameters for the ASTM 421 steel were extracted from reference [5] and were all determined from steady state tensile testing; the plotted creep parameters for the ASTM 416 and BS 5896 steels are from a combination of steady state and transient tensile testing performed during the current study.

The Z parameters determined based on steady state and transient tensile tests were similar to each other at the same stress levels (e.g. 690 MPa for the ASTM 416 steel, and 1100 MPa for the BS 5896 steel, respectively) indicating that either steady state tests or transient tests can be used to give empirical creep parameters for prestressing steel. Both test methods exhibited the classical three phase creep response when ϵ_{cr} was plotted against θ , and both test methods confirmed that the slope of the secondary creep phase (Z) increases with increasing stress.

A major criticism of steady state creep tests is that these can take days to complete and creep parameter values can be erroneously quantified by miscalculating the degree of mechanical strain during initial loading; since in steady state tests the specimen is heated during initial loading some creep will occur during loading to the target stress level. A transient test, however, can be performed rapidly, allows control over improper quantification of mechanical strain as mechanical loading occurs before heating and is therefore relatively unaffected by elevated temperature creep, and since thermal expansion is an easily predictable strain it can be removed in post test analysis giving an accurate determination of creep strain. One issue of interest in performing transient tests to determine creep parameters is the repeatability of such tests. In theory, the transient test should be repeatable; although it should be noted that creep can be disproportionately influenced by microscopic imperfections on (or in) the specimens. To examine repeatability of testing, four transient creep tests performed at a sustained stress of 1000MPa and equivalent heating at 2°C/min are given in Figure 4. Although the individual tests exhibit some variability ($Z = 7.64 \pm 0.62 \times 10^{17} \text{ hrs}^{-1}$) from one to another, and the computed Z parameters were different to a small degree, all curves lie within an envelope (shown in Figure 4) which is defined by the accuracy of the Type K thermocouples used for specimen temperature measurements ($\pm 2^\circ\text{C}$).

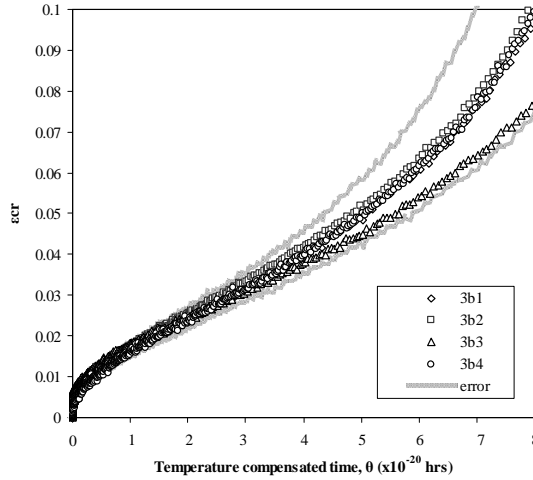


Figure 4. Repeatability of transient creep tests at 1000MPa (BS 5896 prestressing steel) with potential errors due to temperature measurement accuracy included.

Additional experiments were conducted using a different heating rate for the transient tensile test (with heating rates varying from 1 to 10°C/min) for both of the ‘modern’ prestressing steels. Again the Z parameters extracted had similar magnitudes ($Z = 10^{17} \text{ hrs}^{-1}$) as given in Figure 1b; in fact the tests exhibited less variability than the steady state repeatability tests presented in reference [5]. The small variability in the transient tests shown however may suggest that modelling errors may occur with different heating rates, as could be seen in a real fire, which indicates that additional investigation is required on the role of transient heating in the temperature compensated time relationships used.

Combining all of the tests performed for the current paper, and based on Figure 1b, the following equations (with SI input coefficients) for both $\epsilon_{cr,o}$ and Z for each prestressing steel are defined in equations 3 to 5 (with an assumed constant activation energy of 30550K, as noted previously):

$$\text{ASTM 421 (1970); } Z = ae^{B\sigma} = 8.21 \times 10^{13} e^{0.0145\sigma} \quad \text{for } 172 \text{ MPa} < \sigma < 690 \text{ MPa} \quad (3a)$$

$$\epsilon_{cr,0} = c\sigma^D = 9.26 \times 10^{-5} \sigma^{0.67} \quad \text{for } 172 \text{ MPa} < \sigma < 690 \text{ MPa} \quad (3b)$$

$$\text{ASTM 416 (2008); } Z = ae^{B\sigma} = 2.70 \times 10^{13} e^{0.012\sigma} \quad \text{for } 690 \text{ MPa} < \sigma < 1000 \text{ MPa} \quad (4a)$$

$$\epsilon_{cr,0} = c\sigma^D = 1.13 \times 10^{-7} \sigma^{1.63} \quad \text{for } 690 \text{ MPa} < \sigma < 1000 \text{ MPa} \quad (4b)$$

$$\text{BS 5896 (2011); } Z = ae^{B\sigma} = 1.60 \times 10^{12} e^{0.013\sigma} \quad \text{for } 690 \text{ MPa} < \sigma < 1000 \text{ MPa} \quad (5a)$$

$$\epsilon_{cr,0} = c\sigma^D = 1.51 \times 10^{-14} \sigma^{3.90} \quad \text{for } 690 \text{ MPa} < \sigma < 1100 \text{ MPa} \quad (5b)$$

$$Z = ae^{B\sigma} = 3.42 \times 10^4 e^{0.030\sigma} \quad \text{for } 1000 \text{ MPa} < \sigma < 1200 \text{ MPa} \quad (5c)$$

The Z coefficients and equations 3 and 4 plotted in Figure 1b are functions of stress. It is clear that the BS 5896 steel exhibits the lowest potential for creep (and therefore stress relaxation) at equivalent stress levels at elevated temperature. The antiquated ASTM 421 steel exhibits the greatest potential for creep amongst the steels tested herein. This was to some extent expected given that using the dated parameters determined from tests on this steel results in over estimation of creep and subsequent stress relaxation for modern locally heated prestressing steels [2]. It should be noted that the stress range for which creep parameters have been derived for the modern prestressing steels is incomplete; however, these are considered satisfactory for performing preliminary model validation studies.

4.3 Creep failure

A limitation described in Section 2 is that Equation 2 can only be applied up to the point where tertiary creep begins – i.e. when plastic instabilities begin to dominate. Figure 5 shows the ϵ_{cr} versus θ behaviour for a steady state creep test of ASTM 416 steel at 690MPa. Also shown is the cross sectional area reduction (measured using DIC) versus θ response. Figure 5 shows that at the point where the creep curve stops behaving linearly and initiates run away behaviour (i.e. Tertiary creep), area reductions at different locations also begin to deviate from one another, indicating the well known formation of a localised necking region. The cross sectional area reduction is small during the primary and secondary phases of creep, and is given by Poisson's ratio, therefore the test could be considered approximately constant stress during these phases. After the second phase this no longer holds and cross sectional area becomes important and the creep curve exhibits 'run away' creep failure. Figure 5 also shows an 'extrapolation' of the Equation 2 into the tertiary phase using the corresponding creep parameters for true stress (on the basis of *measured* area reduction). Figure 5 shows good correlation, with error of less than 10%, indicating that the Tertiary creep phase is simply a manifestation of necking and that Secondary creep parameters can be used to model creep into the Tertiary phase (providing cross sectional area is known). Similar trends were observed during transient tests.

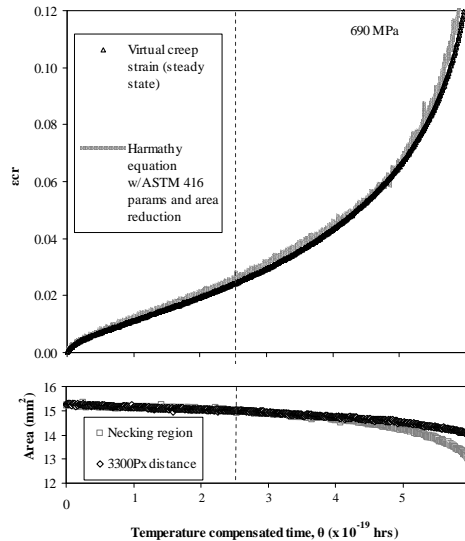


Figure 5. Measured and predicted creep curves using the Harmathy equation [3] but accounting for area reduction due to necking during the Tertiary creep phase.

5 MODELLING ACCURACY

The motivation behind the current work stems from the observed over prediction of a computational model [2] to predict stress relaxation (from creep deformation) during tests of locally-heated UPT prestressing tendons [6]. As already noted, this overestimation is believed to be due to the use of dated creep parameters formulated in reference [5]. High temperature creep parameters for modern steels are indeed different, as shown in previous sections; therefore a verification exercise was performed using the new parameters (Z , $\epsilon_{cr,0}$) to predict stress relaxation (from creep deformation) that occurred during the previously performed tests using the aforementioned computational stress relaxation model.

Details of these tests are given in reference [6]. Locally-heated UPT tendons of realistic lengths (18.3 m from anchor to anchor) were stressed to a realistic service stress of 1000 MPa against a ‘strong back’ testing frame. A custom tube furnace was installed at midspan to heat approximately 3% of the tendon length. The tendons were 12.7mm diameter 7 wire Grade 1860 prestressing steel taken from the same coil as the ASTM 416 core wires used in the creep tests for the current paper. Stress relaxation was monitored during the tests using load cells at the anchorages and strain gauges bonded along the tendon, and thermocouples were used to record temperatures of the tendons inside and outside the furnace.

Three locally-heated tests from the previous experimental series are of interest here. The stress behaviour for these tests falls within the stress range of the parameters given in Equation 4. These tests involved transient heating at rates of 2, 10 and 30°C/min up to a steady-state temperature of 400°C which was held for approximately 90 minutes. The tendons were then allowed to cool to ambient temperature. Figure 6 shows the stress versus time response recorded during one of these ‘strong back’ tests conducted with a transient heating ramp rate of 2°C/min.

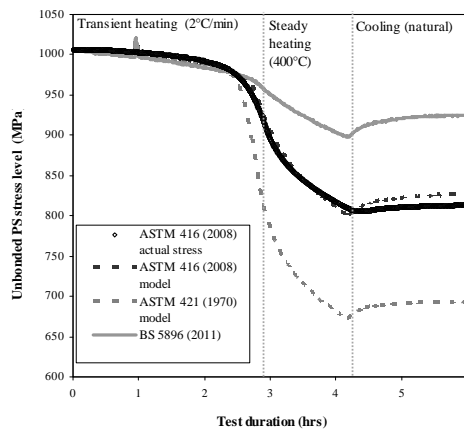


Figure 6. Experimental data and modelling de-stressing behaviour of a locally heated unbonded PS strand

Also shown in Figure 6 are the stress relaxation curves predicted using the computational model described in reference [2] which uses the temperatures and initial stresses recorded during the tests. Model predictions made using the antiquated ASTM 421 (Equation 3) creep parameters overestimate stress relaxation by up to 18%. The new ASTM 416 creep parameters developed in the current paper (Equation 4) model stress relaxation much more accurately, with only 2% maximum error. For other tests the modelling accuracy decreased as the heating rate increased and was least accurate for the test with a transient ramp rate of 30°C/min, however with a maximum error of only 7% even in this case. Creep parameters should only be used for the steel in which they were developed. BS 5896 creep parameters underestimate stress relaxation for ASTM 416 PS steel. This is intuitive since creep parameters proposed for BS 5896 indicated less deformation when compared to ASTM 416 prestressing steel parameters.

The improvement in the model predictions of the computational model for stress relaxation provides an additional independent check upon the new creep model input parameters given in Section 4. These new creep parameters give more precise predictions of tendon stress, and hence can be used to help predict modern UPT tendon deformation in real buildings during real fires.

It must be noted that in a real, full-scale UPT concrete building subjected to real fires, the tendon stress will be dependent on complex interactions between tendon creep and relaxation, load shedding to the bonded steel reinforcement (if present), redistribution of load through the structure, and the potential offset of tendon de-stressing due to thermal expansion of the concrete floor plate.

6 CONCLUSIONS

Creep parameters for modern prestressing steels have been derived using a novel optical DIC technique for accurate strain and deformation measurement at elevated temperature. Results indicate that modern prestressing steel is more creep resistant than its older counterparts, while comparably graded modern prestressing steels from both Europe and North America also demonstrate clear creep deformation behaviour differences. Using DIC for cross sectional area reduction analysis during elevated temperature tensile testing has allowed initial assessment of high temperature creep behaviour in the Tertiary phase, indicating that this appears as merely a manifestation of localised necking in prestressing steel - it has also been shown that Primary and Secondary creep parameters can be useful for predicting the behaviour of steel within the runaway Tertiary creep phase. Finally, a high degree of modelling improvement for unbonded and stressed prestressing steel exposed to variable, localized, transient heating scenarios has been demonstrated, thus verifying an independent check of the new high temperature creep modelling input parameters obtained in the current study. These new creep parameters are suggested for future use in modelling of the full structure response of UPT concrete structures for structural fire safety design.

ACKNOWLEDGEMENTS

The authors would like to thank and acknowledge the intellectual contributions of Dr Andy Take, Queen's University, Canada. The authors gratefully acknowledge the support of the Ove Arup Foundation, the UK Royal Academy of Engineering, the University of Edinburgh, Bridon UK, and NSERC Canada. The Scottish Funding Council is thanked for its support of the Joint Research Institute for Civil and Environmental Engineering, part of the Edinburgh Research Partnership in Engineering and Mathematics (ERPem). Thanks are given to Kevin MacLean for earlier contributions to this work.

REFERENCES

- [1] Gales, J. Bisby, L. and Gillie, M., "Unbonded Post Tensioned Concrete in Fire: A Review of Data from Furnace Tests and Real Fires", *Fire Safety Journal*, 46, 151-163, 2011.
- [2] Gales, J. Bisby, L. and Gillie, M., "Unbonded Post-Tensioned Concrete slabs in Fire- Part II- Modelling Tendon Response and Consequences of Localized Heating", *Journal of Structural Fire Engineering*, 2(3), 154-171, 2011.
- [3] Harmathy, T., "Comprehensive creep model", *Transactions of the ASME Journal of Basic Engineering*, 89(3), 496-502, 1967.
- [4] Purkiss, JA., *Fire Safety Engineering: Design of Structures*. 2008. BH, London, UK.
- [5] Harmathy, T. and Stanzak, W., "Elevated- temperature tensile and creep properties of some structural and prestressing steels", *Fire Test Performance ASTM STP 464*, 186-208, 1970.
- [6] Gales, J. Bisby, L. Gillie, M., "Unbonded post-tensioned concrete slabs in fire – Part I – Experimental response of unbonded tendons under transient localized heating" *Journal of Structural Fire Engineering*, 2011, 2(3),139-153.
- [7] BS 5896. Specification for high tensile steel wire and strand for the prestressing of concrete. BSI. 2000.
- [8] ASTM A416. Standard specification for steel strand, uncoated seven-wire for prestressed concrete. American society for testing and materials. 2010.
- [9] White, DJ. Take, WA. and Bolton, MD., "Soil deformation measurement using particle image velocimetry (PIV) and photogrammetry", *Geotechnique*, 53(7), 619-631, 2003.
- [10] ENV-1992-1-2. Eurocode 2: Design of concrete structures, Parts 1–2: General rules-structural fire design. European Committee for standardization, Brussels, 2004.

DIRECTIONAL DEPENDENCE OF DEFLECTIONS AND DAMAGES DURING FIRE TESTS OF POST-TENSIONED CONCRETE SLABS

Johan Sjöström, David Lange, Robert Jansson and Lars Boström

SP Technical Research Institute of Sweden

E-mails: johan.sjostrom@sp.se, robert.jansson@sp.se, david.lange@sp.se, lars.bostrom@sp.se

Keywords: Concrete slab, Fire, Deflection, Post-tension, Standard fire curve, Hydrocarbon fire curve, Ultrasonic pulse velocity, Crack formation.

Abstract. *Two furnace tests, using two different fire curves, on unbonded post-tensioned concrete slabs are reported. As a signature of the curvature, the relative deflections on the cold surfaces are measured in directions both parallel (longitudinal) and orthogonal (transverse) to the prestressing tendons. The curvature is more pronounced in the transverse direction relative the longitudinal as the central parts of the slabs are being pulled towards the fire. This leads to crack formed predominantly in the longitudinal direction. While the transverse curvature direction relaxes back the original state after the cooling phase the curvature in the longitudinal direction relaxes to positive values with the central part deflecting upwards. These differences in curvature have direct consequences for directional differences in the residual properties of the concrete as probed by the ultrasonic pulse velocities. Finally the phenomena are quantitatively captured in a finite element model which complies with the Eurocode requirements.*

1 INTRODUCTION

The behaviour of concrete slabs exposed to fires has drawn a lot of attention recent years. The research has generally been focused on large displacement [1], cracking [2] and spalling [3]. The literature often analyse the response close to different failure mechanisms for different types of building systems involving concrete slabs.

One such system is unbonded post-tensioned concrete slabs which are commonly used in construction due to their capacity over long spans and adjustability in stress levels. The technique enables a more efficient use of the building elements and a rapid construction time. However, concerns have been raised regarding the fire performance of post-tension slabs in general, and those using unbonded tendons in particular [4]. The fact that tendons run continuously across multiple-bay slabs increases the risk of failure during a fire [5]. The advantage of post-tensioned slabs, the possibility of long span and thin depth, also makes the system more vulnerable to explosive spalling, especially when high-strength concrete is used [6].

Gales *et al* [5] give a thorough review of unbonded post-tensioned concrete exposed to both furnace tests [7, 8] and real fires. It is concluded that furnace tests provide little insight to the performance of unbonded post-tensioned concrete slabs in construction since they often do not cover the problems described above. Tests on both unbonded and bonded post-tensioned slabs have been conducted by Bailey and Ellobody [4, 8]. They experienced crack along the tendon direction on the cold side of the slabs and transverse (orthogonal to tendons) cracks on the hot surface. One of their slabs collapsed, apparently as a result of tendon rupture. The rupture was said to be caused by transverse cracking allowing for local heating of the tendon. Further work was done by them to model the results of their tests using finite element software [9, 10]. They also studied the response of their previously validated model to multiple travelling fires [11]. As well as highlighting the impact of localized and travelling fires on prestressed

construction, their conclusions appear to support the suggestion that the heated length ratio has a considerable impact on the response of unbonded post tensioned floors in fire.

Apart from measuring absolute deflections very little experimental studies are available concerning the curvature in different directions for unbonded post-tensioned slabs and the implications of these to residual material characteristics. In this paper we present results of fire tests on such specimens. The relative deflections of the slabs are measured both longitudinally and transverse to the tendon direction. These results are thereafter compared to the investigation of concrete damage through the ultrasonic pulse velocity. The experiments are also modelled using finite element techniques which show that material properties that comply with Eurocode requirements catch the qualitative features well. The model also satisfies the quantitative results of the experiments.

2 EXPERIMENTAL

2.1 Materials

Two types of slabs were cast. Slab 1 (S1) had dimensions of 1700 x 1200 x 200 mm and slab 2 (S2) 1700 x 1200 x 250 mm. Both slabs had a water cement ratio of 0.4. Some measured properties of the mixes are summarized in table 1. Two layers of reinforcing steel with diameter of 6 mm and grid size of 150 mm were positioned 30 mm from the lower and upper surfaces in both slabs. Running mid-way between the surfaces in the long direction (hereafter referred to as the longitudinal direction) were six ducts (PVC pipes of 50 mm diameter), see figure 1. Polypropylene fibres were added to prevent spalling at the amount of 0.8 kg/m³ for S1 and 1.2 kg/m³ for S2. After moulding the slabs were stored under water for two months with an additional month in a dry atmosphere before fire tests. The compressive strength, tested on cubes, was determined at the day of the test for both slabs.

Table 1. Summary slab specimens.

	Dimensions (mm)	Compressive strength (MPa)		Density (kg/m ³)	Moisture content (%)	VCT	PP-fibres (kg/m ³)
		28 days	Test day				
S1	1700 x 1200 x 200	49	63	2340		0.4	0.8
S2	1700 x 1200 x 250		54	2330	5.7	0.4	1.2

2.2 Fire tests

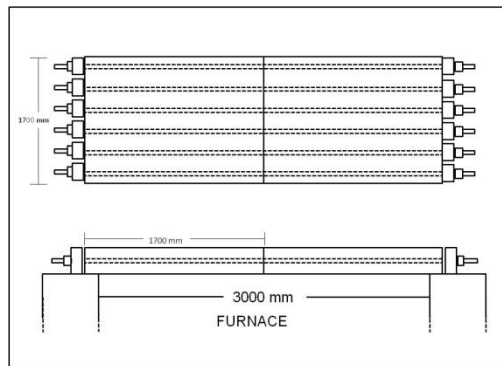


Figure 1. Sketch of concrete slabs, sharing tendon two-by-two, situated on the furnace seen from above (top) and sideways (bottom).

Two furnace tests were performed, in each furnace test one of the two slabs in the pair shown in figure 1 was analysed. The two tests used different fire curves during one hour. Concrete S1 was exposed to the standard fire curve according to EN 1363-1 and S2 was exposed to the hydrocarbon (HC) curve EN 1363-2. The outer 200 mm of each slabs short side was used to support its weight on the furnace frame according to figure 1. Both slabs were post tensioned longitudinally two-by-two together with identical slabs using tendons of 32 mm in diameter running freely through the ducts. At the start of the tests the load was 7 and 4.5 MPa for S1 and S2, respectively. The load forces were continuously measured during the tests and the following cooling phases. In total 8 individual panels, comprising 4 post tensioned units were tested in each test. The units were placed side by side with mineral wool packing between the slabs and solid concrete blocks at the edges.

Temperatures were measured in two positions, along the long central line, 500 mm from each other. Thermocouples were placed in each position at a depth of 10, 20 40, 80 and 120 mm from the fire exposed side for both slabs.

On the non-exposed side relative deflections were measured in the longitudinal direction as well as orthogonal to the post-tensioning tendons (hereafter referred to as the transverse direction). The deflections were measured using devices consisting of a 90 cm long steel section with three supports. On both sides, mid-way along the section, linear displacement transducers with a sub- μm resolution were positioned, see figure 3. In addition an extra transducer was placed along the section to confirm that non-local phenomena influenced the measurements. Two such devices were cross-laid on the concrete surface to probe the displacement in both longitudinal and transverse direction.



Figure 2. Photo showing an example of ultrasonic pulse velocity measurements on concrete cores [12].

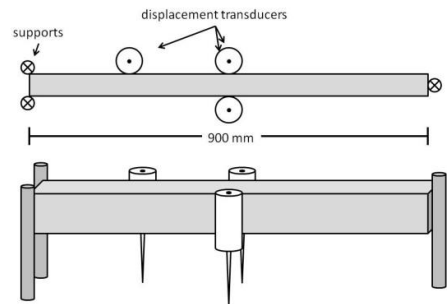


Figure 3. Sketch of the devices to measure relative deflections.

2.3 Ultrasonic pulse velocity measurements

After the cooling phase, cores free from reinforcement bars, 100 mm in diameter were drilled out of the slabs. The positions of the cores, four from S1 and five from S2, were evenly distributed over the surfaces. The ultrasound velocity was measured along the diameter of the cores in both longitudinal and transverse direction. Measurements were performed at different depths, every 10th mm from 20 to 80 mm as well as 100, 120, 140 and 180 mm from the fire exposed side, see figure 2. In addition, for the thicker slab (S2) depths of 200 and 240 mm from the fire exposed surface were measured. Good contact between heads and concrete was attained using contact gel. Each value of the velocity was an average of three measurements.

The method is well established for assessment of damaged concrete [12, 13] and relies on the following relationship, $v = (KE/\rho)^{1/2}$, where v is the ultrasonic pulse velocity, E is the bulk modulus of elasticity, ρ is the density, $K=(1-\mu)/((1+\mu)(1-2\mu))$ and μ is the Poisson ratio [13]. A lower bulk modulus is a signature of crack formation in concrete. The method is not suited for a quantitative assessment of the material properties as there are too many unknowns in the formulation during analysis but the measured values gives a good indication of the relative damage at different sections of the sample.

3 EXPERIMENTAL RESULTS

3.1 Temperatures and load force.

The difference between the temperatures at same depth of the two different positions is generally less than 20 %. In the following we therefore present only the average values for each depth. Figure 4 shows the temperature evolution of the slabs in both heating and cooling phase as well as the average temperature of the furnace. In the test using the standard fire curve the furnace temperatures satisfyingly matched the standard fire. However, when using the HC fire curve the furnace temperature exhibited some deviations, both positive and negative. No sign of spalling was identified for any of the slabs.

During the test of the S2 slab it is possible that a more intense cracking was present close to the surface after approximately 40 minutes of fire exposure. The irregular temperature development is an indication of this. This causes the somewhat higher heating rate for S2 to decrease. Simultaneously, the heating rate further into the concrete is increased. Similar behaviour is found for S1 but to a lesser extent. Despite the differences in heating rates and fire temperatures the final temperatures throughout the cross sections were very similar. At depths below 40 mm from the fire exposed side the maximum temperatures were reached at the end of the heating phase, or shortly after. At 80 mm depth however, thermal conduction influences the temperature to reach a maximum well over one hour after the heating phase. At 10 mm depth the temperature reached 650 °C at the end of the heating phases whereas the temperature in the middle of the slabs reached just over 100 °C. Given the temperature distribution through the slabs the tendon temperature should stay under 150 °C during these tests, bearing in mind that no major cracks formed during test and therefore we assume limited opportunity for local heating.

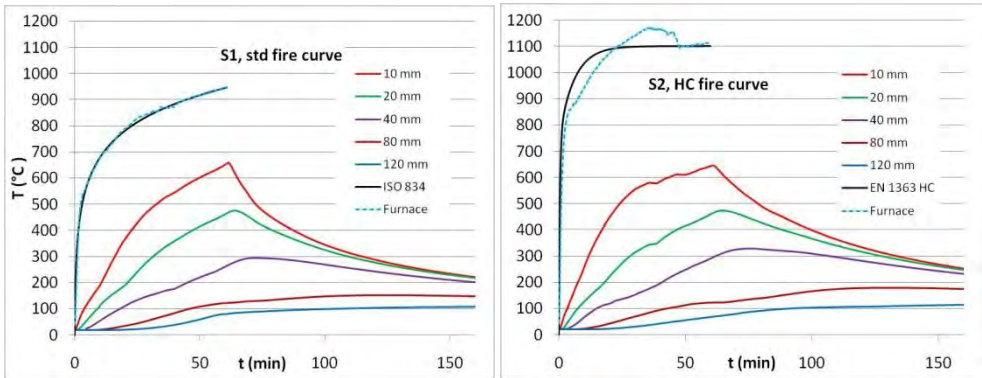


Figure 4. Temperature evolution in S1 (left) and S2 (right) at different depths from the fire exposed surface.

The load forces, distributed on the six tendons are shown in figure 5. During initial heating the thermal expansion increases the load in the tendons as they act as partial restraint to the expansion of the slabs. This effect is clearly observable in the first 30 minutes of the figure. With increased heating bowing begins to take effect and the downwards displacement at the centre of the slab relieves some of the additional load which has developed in the tendons. However at the edges of the slab where the deflection

is lower, there is no relief of the stress in the tendons. This is evidenced in the lower stresses which are shown over the course of the study in the figure – particularly in the 2nd 30 minutes. It should be noted that the tendons were not tightly fit within the ducts and had 10 mm radially for deflection before they would come into contact with the slab – if this happened then it may be expected that the stress in the tendons at the middle of the slab would increase as they are forced to follow the deflection of the concrete. If the tendons were a tighter fit within the ducts then the opposite effect may be expected – i.e. the load in the tendons at the middle of the slab where higher deflections are experienced may be expected to be higher than those tendons at the edges where low deflection is observed. The effect of tendons coming into contact with the ducts may be seen in the last 10 minutes of heating in the inset where the reduction in load in the central tendons is arrested and appear to increase again following the heating phase in the main figure. Finally, with heating of the concrete and slower heating of the tendons the prestress may be expected to decrease as expansion of the tendon relieves some of the prestressing load. Since concrete temperature at the mid depth of the slab continues to increase after the end of the fire, this effect is likely to continue for some time after the test.

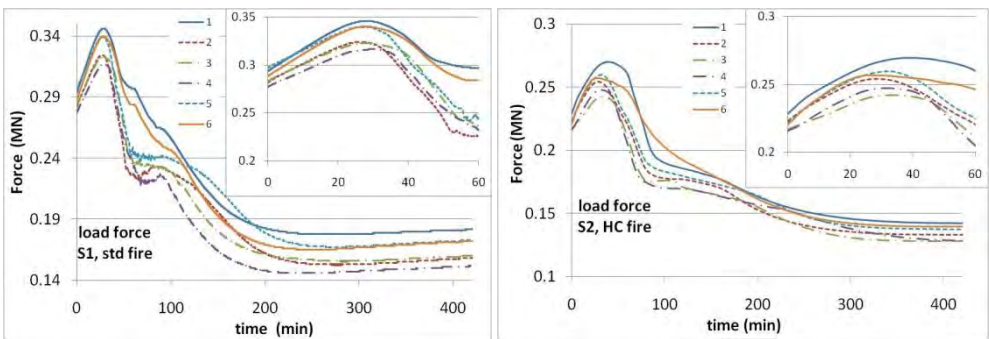


Figure 5. Load force on the tendons during the heating and cooling phases. The tendons are numerated 1-6 in their consecutive order. The insets show the load force only during heating phases.

3.2 Relative deflections

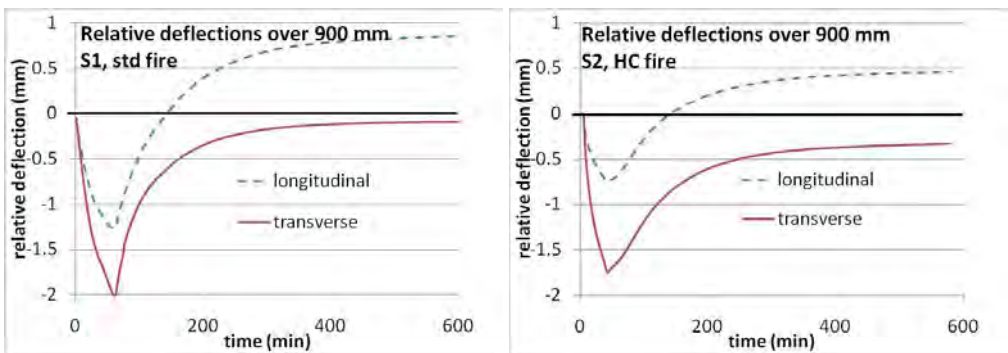


Figure 6. Relative deflections over 900 mm for S1 (left) and S2 (right).

Figure 6 and 7 show the results of the relative deflection measurements for S1 and S2, respectively. The absolute values in the figures are the relative deflection over 900 mm. As the lower parts of the slabs becomes increasingly warmer during heating phase the thermal expansion induces a curvature in the slab

resulting in a midspan deflection towards the fire. The deflection increases all through the heating phase and reaches the maximum after one hour. The deflections during heating are larger in the transverse direction compared to the longitudinal. As the concrete cools the gradient of thermal expansion decreases throughout the depth of the slabs and the deflections decrease. In the transverse direction the deflection almost reaches back to the situation at the start of the tests. However, in the direction parallel to the tendons the deflections relax back even more, to positive values, indicating a positive curvature (the centre of the surface is pulled upwards).

The deflections are generally larger for S1 compared to S2, a natural consequence of the thicker depth of the S2 slab (250 mm compared to 200 mm). Nevertheless, the same qualitative behaviour is found. The absolute values indicated in the figures correspond to larger deflections over the entire slabs. As an example, in the case of S1, assuming constant curvature over the slabs the mid-point between the slabs with common tendons would exhibit a deflection of 18 mm after one hour.

3.3 Ultrasonic pulse velocities

The measured ultrasonic pulse velocities are presented in figure 7. Far from the fire exposed surface the velocities vary around 4 km/s for all the cores and in both longitudinal and transverse direction. At 100 mm depth from the fire the damages to the concrete can be detected by the pulse measurements. The velocity decreases monotonically with the distance towards the surface. The scattering of the data is due to the sensitivity of the velocity to the amount of gravel in the cross section. At 20 mm depth the velocity has decreased to between 2 and 3 km/s. In general we see a slower velocity from the S2 cores but only at the fire damaged depths. This is also a signature of the more intense cracking that was also indicated from the temperature evolutions of figure 4. Since this slab generally had milder cracking due to its thicker depth the difference is probably mainly due to the more severe fire load.

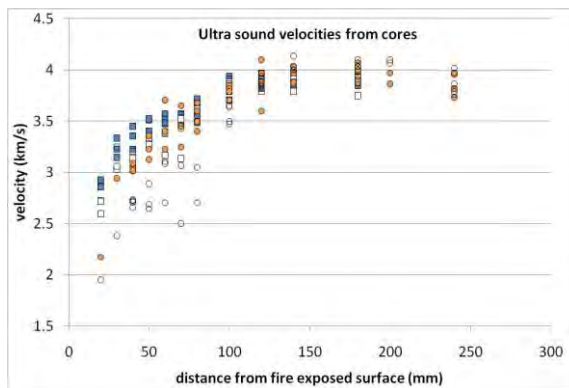


Figure 7. Ultrasonic pulse velocities from the cores drilled from S1 (squares) and S2 (circles). The solid symbols correspond to the measurements in the longitudinal direction and the open symbols to the transverse direction.

It is evident that the pulse velocity is even lower in the transverse direction compared to the longitudinal. However, this difference can only be resolved at depths where the damages are clear (≤ 100 mm). This is even more evident from figure 8 where the fraction of transverse and longitudinal velocity is shown. Although a lot of scatter is present it is evident the fraction of the properties in the two directions vary around one at depths above 100 mm but closer to the fire exposed surface the anisotropy grows. S2 exhibits a greater anisotropy, as much as 30 %, compared to S1 at about 10 %. This is again an indication that the cracks that were formed were predominantly in the longitudinal direction. Note that no stress is applied to the concrete at the time of the ultrasonic pulse measurements.

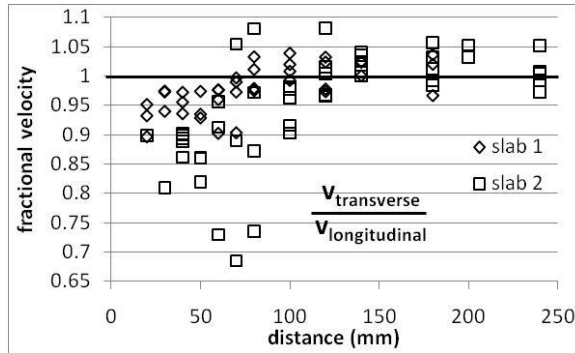


Figure 8. Fraction of pulse velocities in transverse and longitudinal directions. A value of 1 indicates isotropic planes.

4 MODELLING

Modelling was carried out with the ABAQUS finite element software package [14] and applied to the S1 slab only. Throughout the study, a conscious decision was taken to follow Eurocode requirements as far as was reasonable possible, with respect to heat transfer boundary conditions and the material properties. The analysis was conducted in two stages, a heat transfer analysis conducted using the standard solver and a mechanical analysis conducted using the dynamic explicit solver.

For the heat transfer analysis, concrete density was taken to be 2300 kg/m^3 , and conductivity was 1.5 W/mK , specific heat of concrete was 1.470 kJ/kgK . Boundary conditions were as follows: a film condition with a convective heat transfer coefficient of $25 \text{ W/m}^2\text{K}$ on the exposed face of the slab and $4 \text{ W/m}^2\text{K}$ on the unexposed faces; emissivity of the concrete was assumed to be 0.7; and the gas and radiation temperatures were both assumed to follow the standard temperature time curve for a period of 1 hour. The results of the heat transfer analysis were applied to the mechanical model as a field variable.

The mechanical analysis was run using ABAQUS explicit. Material properties were concrete damaged plasticity – the ultimate compressive stress at ambient was 63 MPa , as measured; and the modulus of elasticity was estimated based on the initial slope of the stress strain curve. Ultimate tensile strength was assumed to be 0.8 of the ultimate compressive strength, and the tensile properties were defined using an ultimate strain. Steel was linear elastic, with a modulus of elasticity of $210,000 \text{ MPa}$. The Poisson ratio was held constant over temperature. The concrete slab was modelled as a solid using 7200 3 dimensional 8 noded continuum elements. The tendon was modelled using truss elements, which transmit only axial loads and no moments. Nodes of the tendons were tied to the nodes of a tube of massless surface elements with zero stiffness to allow contact between the tendon and the duct. The duct was also modelled explicitly using surface elements which were embedded within the solid slab, figure 9. There was a clear gap between the internal surface of the duct and the outer surface of the tendon of 10 mm at the beginning of the analysis.

Contact between the duct and the surface of the tendon was frictionless. The anchorage plates were explicitly modelled using shell elements and these were tied to the end of the tendon and to the edge of the slab. Boundary conditions comprised a simple support at the midpoint of the slab at the free edge, allowing for uplift of the corners and translation along the plane of the slab, and symmetry at the mid-line. The finite element model is shown in figure 10.

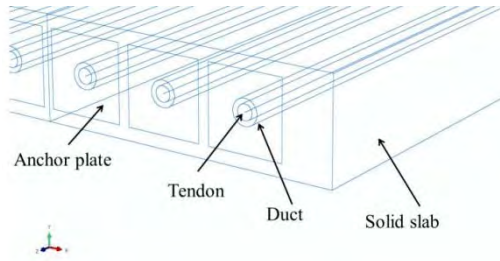


Figure 9. Detail of the tendon, duct and anchorage

Pre-stressing was applied to the slab and the tendons as an initial condition and then was afforded a single equilibrating step before mechanical loading, comprising the self-weight applied as a body force, and then thermal loading were applied in two additional steps.

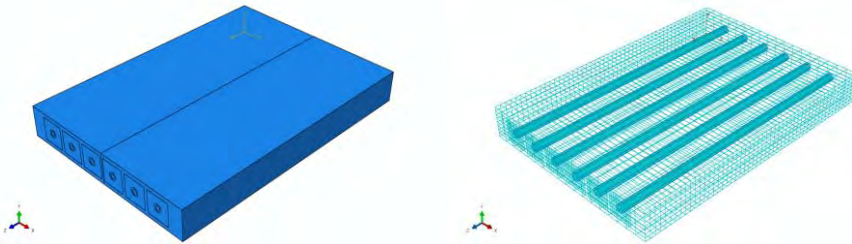


Figure 10. The finite element model Geometry and Mesh

3.3 Modelling results

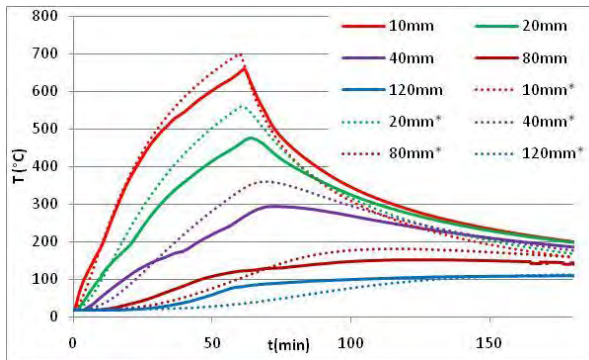


Figure 11. Heat transfer results and comparison with measured values for S1. Calculated values are indicated with a *.

The results of the heat transfer analysis are shown in Figure 11 along with the measured values of the temperatures in the concrete. At the exposed surface of the slab, the predicted values are quite close at the start of the analysis, however at the peak of the heating phase they are around 50 °C higher. This trend is prevalent closer to the heated surface however the values further from the heated region show a lag behind the measured values. This suggests that the actual diffusivity of the concrete was higher than the

values used in the calculation, however the good prediction of temperatures at the heated surface suggests that the boundary conditions are a good approximation of the conditions in the furnace.

The tendon temperature was not measured in the tests or calculated in the model, however for inclusion in the mechanical calculation it was assumed to be 80 % of the temperature at 8 mm from the heated surface with a linear lag over the duration of heating.

The results of the heat transfer analysis were applied to the mechanical model as a field variable. In this paper and discussion only the response calculated during the heating phase will be discussed.

At this stage in the analysis, the difference between a prestressed and an unstressed slab was evaluated numerically. The relative deflections conforming with the relative deflection plot in Figure 6 are compared in Figure 12. As expected the slab modelled without the prestressing force over predicts the deflections however this is only by as much as 25%, whereas the prestressed model underpredicts the relative deflections by around half as much. Some of this may be attributable to the heat transfer calculation; some to the lack assumptions which are made with regards the lateral restraint of the long side. At this stage the opportunity was also taken to model the slab with and without the reinforcement. It was found that this made little to no difference to the deflections which were calculated.

The forces in the tendons also show a reasonable agreement with experimental data. In particular it catches the larger force in the outermost tendons.

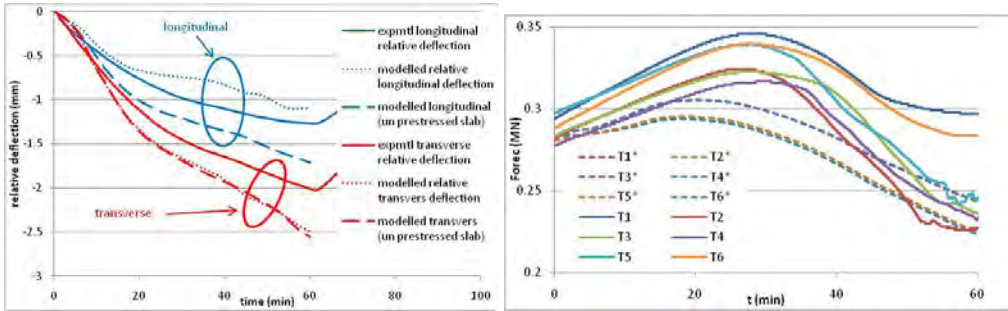


Figure 12. Left: Comparison of deflections. Solid lines are experimental values (same as figure 6) and dotted are modelled. The dashed lines represent the model without any prestressing. Right: Comparison of forces in tendons. The solid lines are experimental data (figure 5). The outermost modelled forces T1* and T6* are almost completely overlapping in the figure and are hard to separate. The same applies for T2* and T5* as well as for T3* and T4*.

4 SUMMARY AND OUTLOOK

We have presented experimental data on the relative deflections in longitudinal and transverse directions for unbonded post-tensioned concrete slabs as an indirect measure of the curvature. The prestressing reduces the curvature in the longitudinal direction. The relaxation phase as the concrete cools shows significantly different behaviour in the two directions. The transverse direction relaxes back to pre-fire conditions whereas the longitudinal direction deflects upwards with a midspan deflection away from the fire due to the loss in stiffness in the more severely exposed regions. This is an important finding which needs to be analyzed in more detail since absolute deflections (downwards) of slabs are commonly used as a first assessment of the fire-damaged concrete slabs.

The characteristics of curvature due to the post-tensioning can be directly observed in the cracking phenomena represented by the ultrasonic pulse velocities in the two different directions as the transverse direction, with larger deflections, experience a lower pulse velocity, a signature of cracks running longitudinally in the slab. These longitudinal cracks might be a source for failure at larger loads.

The FEM model presented here follows the Eurocode requirements and naturally suffers from incomplete description (like a temperature independent Poisson ratio). Nevertheless, it catches the phenomena of the experiments and has a reasonable degree of accuracy in quantitative output. Future work on this topic includes application of the measured temperature field to the model. Having verified the model in heating, a user subroutine will be added to the analysis to prevent the material properties from returning to their ambient state in a procedure similar to that described by Law [15]. With a fully compliant model extensions to multiple-bay spans can be performed.

REFERENCES

- [1] Huang, Z.H., Burgess, I.W. and Plank, R.J., "Modeling membrane action of concrete slabs in composite buildings in fire. I: Theoretical development", *Journal of Structural Engineering – ASCE*, 129(8), 1093-1102, 2003.
- [2] Georgali, B. and Tsakiridis, P.E., "structure of fire-damaged concrete. A case study", *Cement & Concrete Composites*, 27(2), 255-259, 2005.
- [3] Hertz, K.D., "Limits of spalling of fire-exposed concrete", *Fire Safety Journal*, 38(2), 103-116, 2003.
- [4] Bailey, C.G., Ellobody, E., "Comparison of unbonded and bonded post-tensioned concrete slabs under fire conditions", *The Structural Engineer*, 87(19), 23-31, 2009.
- [5] Gales, J., Bisby, L.A. and Gillie, M., "Unbonded port tensioned concrete in fire: A review of data from furnace tests and real fires", *Fire Safety Journal* 46, 151-163, 2011.
- [6] Kalifa, P., Chene, G. and Galle, C. "High-temperature behaviour of HPC with polypropylene fibres - From spalling to microstructure", *Cement and Concrete Research*, 31(10), 1487-1499, 2001.
- [7] Zheng, W. and Hou, X., "Experiment and analysis on the mechanical behaviour of PC simply supported slabs subjected to fire", *Advances in Structural Engineering*, 11(1), 71-89, 2008.
- [8] Bailey, C.G. and Ellobody, E., "Fire tests on unbonded post-tensioned one-way concrete slabs", *Magazine of Concrete Research*, 61(1), 67-76, 2009.
- [9] Ellobody, E. and Bailey, C. G., "Testing and modelling of bonded and unbonded post-tensioned concrete slabs in fire," *Proceedings of the 5th International Conference on Structures in Fire (SiF '08)*, 392-405, 2008.
- [10] Ellobody, E. and Bailey, C. G., "Modelling of unbonded post-tensioned concrete slabs under fire conditions," *Fire Safety Journal*, 44(2), 159-167, 2009.
- [11] Ellobody, E. and Bailey, C. G., "Structural performance of a post-tensioned concrete floor during horizontally travelling fires," *Engineering Structures*, 33(6), 1908-1917, 2011.
- [12] Albrektsson, J., Flansbjer, M., Lindqvist, J.-E. and Jansson, R., *Assessment of concrete structures after fire*, SP Report 2011:19, 2009.
- [13] Naik, T.R., Malhorta, V.M. and Popovics, J.S., "The Ultrasonic Pulse Velocity Method", in *Handbook on nondestructive testing of concrete*, Malhorta, V.M. and Carino, N.J. (eds), 2nd Ed., CRC Press, London, 2004.
- [14] Dassault Systèmes Simulia Corp, "ABAQUS 6.11." 2011.
- [15] Law, A., *The assessment and response of concrete structures subject to fire*, PhD Thesis, The University of Edinburgh, 2010.

VERIFICATION OF CODE FIRE RATINGS OF PRECAST PRESTRESSED CONCRETE SLABS

**Jeong-Ki Min, Anthony K. Abu, Peter J. Moss, Rajesh P. Dhakal and
Andrew H. Buchanan**

Department of Civil & Natural Resources Engineering, University of Canterbury, Private Bag 4800,
Christchurch 8140, New Zealand.

e-mails: jgki.min@gmail.com, tony.abu@canterbury.ac.nz, peter.moss@canterbury.ac.nz,
rajesh.dhakal@canterbury.ac.nz, andy.buchanan@canterbury.ac.nz

Keywords: Precast concrete, Simple Calculation Methods, Advanced Calculation Methods.

Abstract. *In fire design for floors, the three criteria of stability, integrity and insulation are required for the specified fire resistance duration. Among these, stability is not easy to confirm. For solid prestressed concrete slabs of uniform thickness, Eurocode 2 provides tabulated data and specifies an axis distance to the centroid of strands to achieve particular fire resistance ratings, but it is not clear if this data can be used for a wide range of different prestressed slab profiles. In order to verify the current code-fire ratings for precast prestressed slabs, both simple and advanced calculation methods are investigated. This paper examines use of calculation methods, accounting for the real behaviour of unprotected simply supported prestressed concrete slabs exposed to the standard ISO 834 fire. The calculated fire resistance of each prestressed concrete slab is compared with tabulated data in Eurocode part 1.2, with detailed discussion.*

1 INTRODUCTION

Precast prestressed concrete slabs in multi-storey buildings have been widely used over the last decades in New Zealand and overseas. The floors have the advantage of off-site manufacture, long spans and high load capacity. Among the prestressed floors, the popular types are hollowcore slabs, tee slabs and prestressed flat slabs.

In their fire design, the three criteria of stability, integrity and insulation need to be satisfied for the specified fire resistance period. Integrity and insulation are usually dictated by the thickness of the slab and construction detailing to reduce gaps. Stability on the other hand is difficult to predict. As a result, standard fire testing is used to determine the stability of structures. However, this test is expensive and time-consuming, it is not ideal to test every floor configuration. As such, tabulated data of minimum thickness and axis distance exist in Eurocode 2 [1] and manufacturer data to achieve particular fire resistance ratings. However, this data is not always confirmed by fire tests [2] and has not been verified for a wide range of different prestressed slab profiles.

In order to overcome the limitations of current code-fire ratings for precast prestressed slabs, Eurocode 2 allows fire resistance to be assessed by a recognised calculation method. However, the simplified calculation methods included in Eurocode 2 are only appropriate for reinforced concrete structures. A special purpose, non-linear finite element program, SAFIR, developed at the University of Liege (Belgium), capable of conducting both thermal and structural analysis of structures, can be used to verify the implementation of the advanced calculation approach. The program can capture fundamental physical behaviour in thermal and mechanical behaviour in structural analysis of fire-exposed prestressed slabs.

This paper compares existing approaches of assessing fire resistance of prestressed concrete slabs in New Zealand, United States and Europe. The precast prestressed slabs considered are hollowcore slabs, tee slabs and prestressed flat slabs. They are all simply-supported but with different axis distances, and exposed to the standard ISO 834 fire. The thermal and mechanical properties of concrete and steel at elevated temperatures, used in the analyses, follow Eurocode 2 part 1.2. To simplify the comparisons, it has been assumed that spalling does not occur. In addition, advanced methods using finite element analysis are validated against the results of published fire tests [3] on prestressed concrete slabs. The time–temperature relationships, time–vertical displacement relationships and fire resistances of the prestressed slabs are evaluated by the finite element model. For each slab type, a relevant finite element model has been applied to evaluate fire resistance. The fire resistance of the prestressed concrete slabs obtained from the finite element analyses is compared with the design values obtained from Eurocode 2 at elevated temperatures.

The objective of this study is to examine the efficiency of using the various calculation methods (tabulated data, simple calculations and advanced calculations) to account for the real behaviour of unprotected simply-supported prestressed concrete slabs exposed to the standard ISO 834 fire. Key considerations that influence the fire resistance and behaviour of the prestressed concrete slabs are discussed for the different design approaches.

2 FIRE DESIGN OF PRECAST PRESTRESSED CONCRETE SLABS

Most countries throughout the world require structures to meet minimum fire safety requirements. Typically, design provisions offer a hierarchy of design methods, such as tabulated data, simplified calculations and advanced methods. The hierarchy varies in complexity of application, with tabulated data being the easiest and the advanced methods being the most complex. Therefore, most design provisions are typically established through either tabulated data or simplified calculations. However, in recent years performance-based methods have been introduced to give more flexibility to designers through the adoption of a rational approach. In this section, an overview of United States, European and New Zealand design provisions is presented.

2.1 United States

The American Concrete Institute (ACI) standards [4] references ACI 216.1 [5] for fire provisions of structural concrete members. The ACI provisions for prestressed concrete slabs are similar to the Precast/Prestressed Concrete Institute Design Handbook [6] and International Building Code [7]. These codes use tabulated data and simplified procedures to establish the fire performance of a prestressed concrete beam, as required by the ASTM E119 [8] standard fire test. Ratings are based on minimum concrete cover and depend on restraint and aggregate type. The tabulated prescriptive method gives fire ratings for 1, 1.5, 2, 3 and 4 hours for prestressed slabs. In addition, the PCI design standard, however, provides a simple calculation method for prestressed concrete slabs.

2.2 Eurocode 2

All reinforced and prestressed concrete structures are governed by EN 1992-1-1 [9], with their corresponding fire provisions given in EN 1992-1-2 [1]. The tabulated data, simplified calculations and advanced methods may be used. The quickest method to crudely determine the fire resistance of a prestressed slab is through the tabulated data. The tabulated prescriptive approach gives fire ratings for 0.5, 1, 1.5, 2, 3 and 4 hours. Ratings are based on minimum slab thickness and average axis distance of tendons to the exposed surface. The tables are also based on support conditions.

2.3 New Zealand

The New Zealand Concrete Standard NZS 3101 [10] uses tabulated data to establish the fire performance of prestressed concrete slabs. The ratings are based on minimum concrete cover. Through this parameter, the prescriptive method gives ratings for 0.5, 1, 1.5, 2, 3, or 4 hours.

3 FIRE DESIGN METHODS OF PRECAST PRESTRESSED CONCRETE SLABS

3.1 Tabulated data

Tabulated data is the easiest way to evaluate fire resistance of precast prestressed concrete slabs. A rating is given for each minimum axis distance. In order to meet the insulation criterion, the tabulated data also provides a minimum thickness, but an evaluation of the insulation criterion is not included in this paper.

3.2 Simplified calculation method

There is a general lack of simplified calculation methods for assessing the fire resistance of precast prestressed concrete slabs. For the current paper two calculation methods are considered: the step-by-step method and the PCI method. In both methods, failure occurs when the computed capacity is less than the applied moment.

3.2.1 Step-by-step method [11]

In the step-by-step method the surface temperatures, concrete temperatures and steel temperatures are determined for given fire temperatures using Wickström's formula [11]. In this method the flexural capacity of simply supported prestressed slabs under fire conditions is calculated by

$$M_f = A_s f_{y,T} (d - a_f/2) \quad (1)$$

where A_s is the area of the prestressing steel, $f_{y,T}$ is the yield stress of the prestressing steel at elevated temperature, d is the effective depth of the cross section and a_f is the depth of the rectangular stress block, reduced by fire. Thus, the fire resistance can be determined based on the tensile stress capacity of the prestressing strands as they lose their strength with increasing temperature.

3.2.2 PCI method [12]

The PCI method provides graphs showing the relationships between moment intensity and axis distance for various fire endurance in order to calculate the fire resistance. In principle, the theoretical moment capacity of prestressed concrete slabs can be calculated from the relationship

$$M_n = A_{ps} f_{ps} (d - 0.5a) \quad (2)$$

where A_{ps} is the area of the prestressing steel, f_{ps} is the stress in prestressing steel in flexural member at ultimate load, d is the effective depth of the prestressing steel and a is the depth of the rectangular stress block. Instead of an analysis based on strain compatibility, the value of f_{ps} can be taken to be

$$f_{ps} = f_{pu} \left(1 - 0.5 \frac{A_{ps} f_{pu}}{b d f'_c} \right) \quad (3)$$

where f_{pu} is the ultimate strength of prestressing steel, b is the width of the slab, and f'_c is the compressive strength of the concrete. From the calculations above, the moment intensity (M/M_n) and $\omega_p (= A_{ps} f_{pu} / b d f'_c)$ are determined. The fire resistance can then be obtained from charts, based on the aggregate type (e.g. see Figure 1 for siliceous aggregates). In the application of the PCI method, there are some limitations. As observed in Figure 1, the range of the moment intensity is limited to between 0.15 and 0.7.

3.3 Advanced calculation method

In order to critically evaluate the performance of advanced calculation methods, in comparison to simple calculations and tabulated data, the non-linear finite element analysis program, SAFIR [13, 14], was validated by comparing predictions from the model with measured data from fire tests on six prestressed flat slabs.

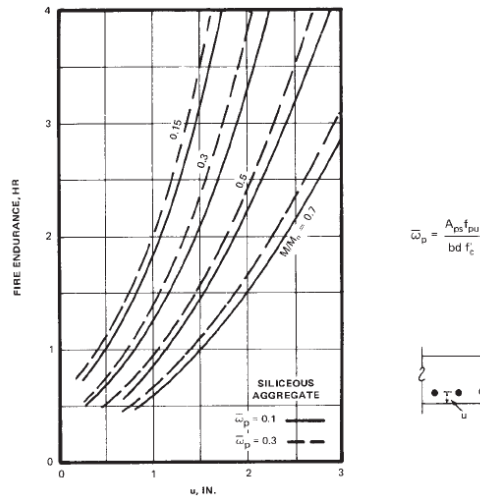


Figure 1. Fire endurance of prestressed concrete slabs as affected by moment intensity and axis distance [12]

3.3.1 Fire tests

Fire tests on simply supported prestressed concrete slabs were performed by Gustafarro [3] in the United States. A total of eleven prestressed concrete slabs, were tested in accordance with ASTM E119 [15]. Six of the specimens were made of normal weight concrete, and the rest were made of lightweight concrete. As the aim of the paper is to compare results for normal weight concrete, the validation only considers the results for those tests with normal weight concrete. Figures 2(a) and 3(a) show the loading arrangements of the tested specimens. Of the six tests, three had specimens with five-11.1 mm diameter strands in a slab spanning 6096 mm, as shown in Figure 2(a). The other three specimens had fifteen-6.35 mm diameter strands in slabs spanning 3661.6 mm (see Figure 3(a)). All slabs were 696.6 mm wide and 165 mm thick in cross-section, as shown in Figures 2(b) and 3(b). Depending on the test, the strands had different cover thickness; 25.4 mm, 50.8 mm and 76.2 mm.

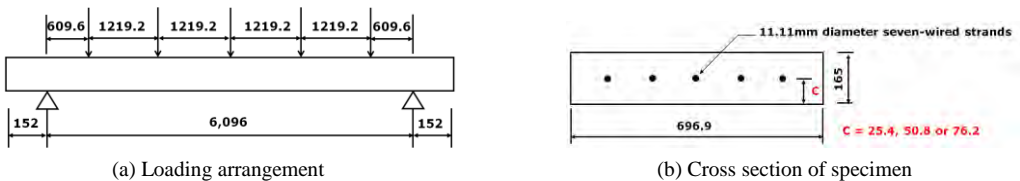


Figure 2. Specimen details for slabs with five-11.1 mm diameter tendons [3]

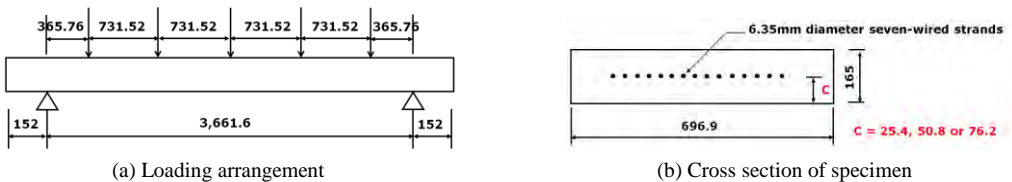


Figure 3. Specimen details for slabs with fifteen-6.35 mm diameter tendons [3]

Table 1 summarises the details of concrete strength and loading for each test. The measured ultimate tensile strength for the 11.1 mm diameter strand was 1806 MPa and 1896 MPa for 6.35 mm diameter strand. Partial loss of prestress was assumed to be 18%. The load intensity during the tests ranged between 40-60% of the calculated ultimate capacities.

Table 1. Specimen strength and loading details [3]

Slab Type	Concrete cover, mm	Concrete strength, MPa	Number and size of strands	Applied load, P (kN)
NWSLAB1	25.4	37.5	5-11.1 mm	5.77
NWSLAB2	50.8	34.7	5-11.1 mm	4.35
NWSLAB3	76.2	43.7	5-11.1 mm	2.86
NWSLAB7	25.4	35.7	15-6.35 mm	11.43
NWSLAB8	50.8	53.3	15-6.35 mm	9.05
NWSLAB9	76.2	37.4	15-6.35 mm	6.7

3.3.2 Finite element modelling of the prestressed concrete slabs

The finite element modelling of the prestressed concrete slabs begins with their thermal analysis. The cross-section of each prestressed concrete slab was modelled and analysed. It was assumed that the specimens were only exposed to fire on the bottom surface. For the structural analysis, the whole length of the specimens was modelled with 10 beam elements using the results of the thermal analysis.

3.3.3 Temperature distribution

Figure 4 shows the numerical results of the thermal analysis, highlighting the exposed and unexposed surfaces. It also shows the ASTM E119 and ISO 834 fires for comparison. A comparison of the thermal analysis and measured test temperatures is not presented, as temperature test data was not available. The exposed surface temperature increased to 1100°C during a 4-hour fire exposure. On the other hand, the temperature of the unexposed side in the numerical analysis was less than 300°C at the end of analysis. As a result, there is a large temperature gradient between the exposed and unexposed surfaces.

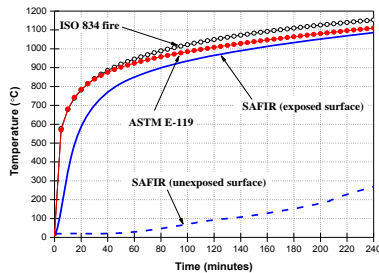


Figure 4. Comparison of temperature development between tests and numerical results

3.3.4 Comparison of numerical and test results

Figures 5, 6 and 7 illustrate the comparisons of central vertical deflections of the test and numerical results for specimens with five-11.11 mm strands. The comparisons with respect to specimens with fifteen-6.35 mm strands are shown in Figures 8, 9 and 10. All tests continued until the structural failure was imminent [3].

The SAFIR central deflection of the slab with five-11.11 mm strands and 25.4 mm cover thickness shows slightly lower deflections than their corresponding test results. On the other hand, the comparison

of central vertical deflections of the equivalent slabs of five-11.11 mm strands with 50.8 mm and 76.2 mm cover thicknesses show better agreement between numerical and test data. In the earlier part of the fire exposure, the numerical result is observed to be stiffer than the test result. This is possibly due to shear deformation, which is not modelled in the numerical analysis. The commonly specified failure criterion (a deflection of span/20) is compared with the test and numerical results. It can be seen that for both cases (five-11.11 mm stands with 50.8 mm and 76.2 mm cover thickness) the numerical simulations accurately predict their behaviour for the duration of the fire. Both test and numerical results meet the failure criterion.

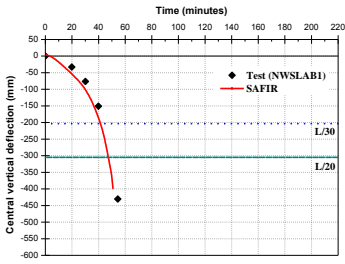


Figure 5. NWSLAB1

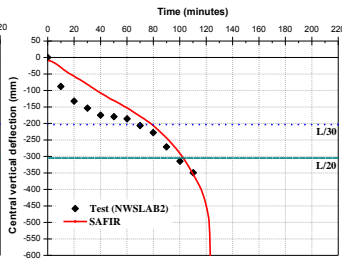


Figure 6. NWSLAB2

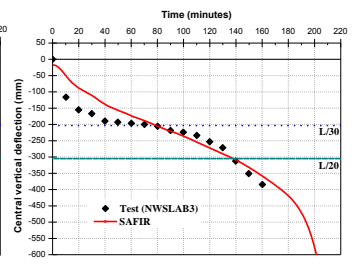


Figure 7. NWSLAB3

The comparison of central vertical deflections of test results and numerical simulations of slabs with fifteen-6.35 mm strands and 25.4 mm cover thickness shows that the numerical results are relatively stiffer than the corresponding test results, while those test results with 50.8 and 76.2 mm cover show a much better agreement throughout the fire exposure.

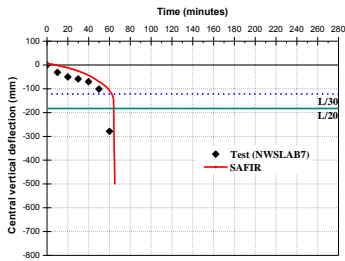


Figure 8. NWSLAB7

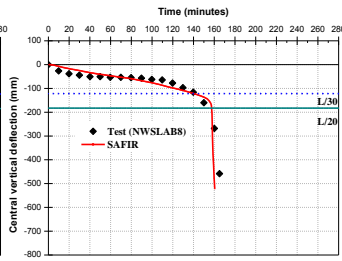


Figure 9. NWSLAB8

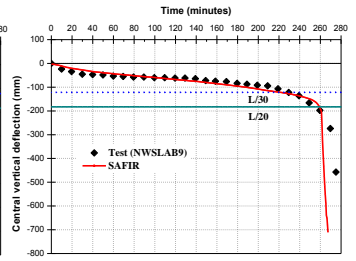


Figure 10. NWSLAB9

4 HOLLOWCORE SLABS

4.1 General

A 10 m long simply-supported 200 mm deep and hollowcore slab with 65 mm topping concrete was chosen to investigate the efficiency of each fire resistance design approach. The slab was 1200 mm wide. The strength of the precast concrete slab and topping concrete were 45 MPa and 30 MPa respectively. Seven 12.9 mm diameter, stress relieved seven-wire strands were used. The yield strength of the prestressing steel was 1.87 GPa. With a self weight (G) of 3.88 kPa and a live load (Q) of 3.3 kPa, the total load on the hollowcore slab in fire conditions was 5.53 kPa.

4.2 Results

Figure 11 shows time-vertical deflection relationship of the simply-supported hollowcore slab with axis distance varying from 25 – 55 mm. The cases with 70 and 80 mm axis distance could not be modelled because they could not be realistically manufactured.

Comparison among the tabulated data, the simplified calculation results and the advanced calculation results in terms of failure time is shown in Table 3. In the simplified calculation methods, the voids of a hollowcore slab are not considered as the fire resistance is only determined by the reduced moment capacity caused by the reduced tensile stress of the prestressing strands. It can be seen that the simplified calculation approach gives longer predictions of fire resistance, compared to the tabulated data. On the other hand, the advanced calculation method provides conservative prediction for low axis distance while the method is unconservative for axis distance of 55 mm or more.

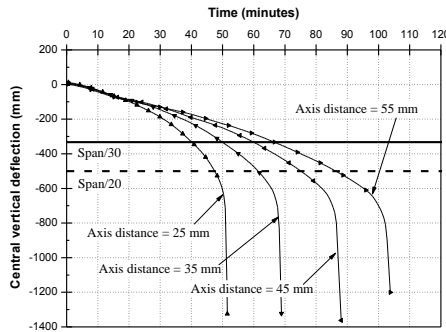


Figure 11. Comparison of central vertical deflection for 10 m span at each axis distance

Table 3. Comparisons of fire resistance for a single 200 mm deep hollowcore slab

Eurocode 2	Tabulated data (minutes)	Simple calculation methods (minutes)		Advanced calculation methods (minutes)		
		Step-by-step method	PCI method	Span/30	Span/20	End of analysis
Axis distance (mm)	Solid slab					
25	30	68	65	40	47	51
35	60	102	85	50	61	68
45	90	142	135	60	75	88
55	120	182	150	66	86	103
70	180	245	200	Not available (geometric problem)		
80	240	286	230	Not available (geometric problem)		

5 TEE SLABS

5.1 General

A simply-supported 500 mm deep, 150 mm wide, 14 m long, single-tee slab with 75 mm topping concrete was chosen to investigate the three design approaches. The slab was 1200 mm wide. The strength of precast concrete and topping concrete were 45 MPa and 20 MPa respectively. Five multiple

strands were used along the height. The yield strength of prestressing steel was 1.86 GPa. The total load applied at the fire limit state was 6.25 kPa.

5.2 Results

Figure 12 shows a plot of vertical deflection with time for the simply-supported single tee slab with increasing axis distance. For tee slabs, multiple strands are used within their cross-section. As such the cases with 30, 60 and 90 mm axis distance were not modelled, due to the geometric limitations of prestressing strand arrangements. With regard to tapered single or double-tee slabs, to-date no simplified calculation method is available. Even though the PCI method provides the temperature at the centroid of the prestressing tendons at each fire exposure time, i.e. 0.5, 1, 1.5, 2, 3 and 4 hours, these can only be used to assess the fire resistance at those specific times. Comparison between the tabulated data and the advanced calculation method, in terms of failure time is shown in Table 4. It can be seen that the advanced calculation method gives a conservative prediction of the fire resistance, compared to the tabulated data, as the bottom prestressing has less concrete cover and is quickly exposed to fire.

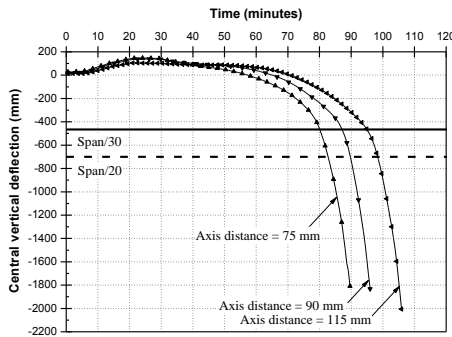


Figure 12. Comparison of central vertical deflection for 14 m span at increasing axis distance

Table 4. Comparisons of fire resistance for a 500 mm deep single tee slab

Eurocode 2	Tabulated data (minutes)	Advanced calculation methods (minutes)		
		Span/30	Span/20	End of analysis
Axis distance (mm)	Ribbed slab			
30	30	Not available (geometric problem)		
50	60	Not available (geometric problem)		
60	90	Not available (geometric problem)		
75	120	80	82	89
90	180	87	90	95
105	240	95	98	105

6 PRESTRESSED FLAT SLABS

6.1 General

A simply supported 75 mm deep and 6 m long prestressed flat slab with 130 mm topping concrete was chosen to investigate the fire resistance design, based on each calculation method. The slab was 1200 mm wide. The strength of precast concrete and topping concrete were 40 MPa and 20 MPa respectively. Eight 12.9 mm diameter, stress relieved seven-wire strands were used. The yield strength of prestressing steel was 1.84 GPa. A load of 9.65 kPa was applied at the fire limit state.

6.2 Results

Figure 13 shows the time-vertical deflection relationship of the simply-supported prestressed flat slab with increasing axis distance. Simplified calculations, using the PCI method were only carried out in the case with 25 mm and 30 mm axis distance as the other axis distances generated moments outside of the applicable range. Comparisons among the different approaches are shown in Table 5. It can be seen that in general, the tabulated data was the most conservative whilst the advanced calculation method produced longer times of fire resistance..

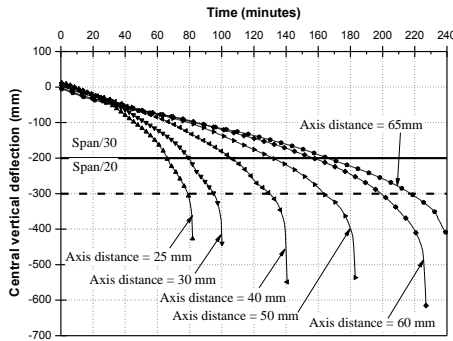


Figure 13. Comparison of central vertical deflection for 6 m span at each axis distance

Table 5. Comparisons of fire resistance for prestressed flat slabs

Eurocode 2 Axis distance (mm)	Tabulated data (minutes) Flat slab	Simple calculation method (minutes)		Advanced calculation method (minutes)		
		Step-by-step method	PCI method	Span/30	Span/20	End of analysis
25	30	56	45	65	78	81
30	60	70	50	79	95	100
40	90	96	Out of range ($M/M_n=0.74$)	106	129	140
50	120	118	Out of range ($M/M_n=0.81$)	132	163	182
60	180	140	Out of range ($M/M_n=0.91$)	157	199	226
65	240	148	Out of range ($M/M_n=0.96$)	165	217	Designated end time

7 CONCLUSIONS

The tabulated data for fire resistance of prestressed concrete slabs was compared with the results of, simplified calculation methods and advanced calculation methods. In all cases, the tabulated data is in general agreement with the trends from the calculation methods. For the advanced calculation methods, it is important to define the failure criterion, because large deflections can occur well before final failure. The use of a specified deflection, such as span/20, is recommended.

The results of the comparison are summarised below:

- For prestressed flat slabs, both the simple and advanced calculation methods give results larger than the EC2 tabulated data, generally with good agreement. The tabulated data appears to be on the safe side.
- For T-slabs, the advanced calculation method gives results much lower than the tabulated data, but only for a limited range of geometries.
- For hollowcore slabs, the simple calculation method gives higher fire resistance than the tabulated data. Whereas the advanced calculation method gives lower results because voids are included in the calculations, but not in the tabulated data. More research is needed for hollowcore slabs.

The numerical modelling approach used in the advanced calculation methods has been validated with some test results available in the literature, but the models do not accurately predict all possible failure modes. Due to the limitations of all calculation methods and lack of appropriate test results, more experimental and numerical research is needed to accurately predict the fire resistance of prestressed concrete floors in fire conditions.

REFERENCES

- [1] EC2, *Eurocode 2: Design of concrete structure. EN 1992-1-2: General rules – Structural fire design*, European Committee for Standardization, Brussels, 2004.
- [2] Chang, J., Buchanan, A.H., Rajesh, R.P. and Moss, P.J., “Fire Performance of Hollowcore Floor Systems in New Zealand”. *SESOC Journal*, Vol. 21, No. 1, pp. 5-17, 2008.
- [3] Gustaferro, A.H. “Fire Endurance of Simply Supported Prestressed Concrete Slabs”. *PCI Journal*, Vol. 12, No. 1, pp. 37-52, 1967.
- [4] ACI 318, *Building code requirements for structural concrete and Commentary*. American Concrete Institute. Detroit, MI, USA, 2005.
- [5] ACI 216.1 *Code Requirements for Determining Fire Resistance of Concrete and Masonry Construction Assemblies*. American Concrete Institute. Farmington Hills, MI, USA, 2007.
- [6] Precast/Prestressed Concrete Institute, *PCI Design Handbook 6th edition: precast and prestressed concrete*. Chicago, IL, USA, 2004.
- [7] International Code Council (ICC), *International Building Code*. Falls Church, VA, USA, 2006.
- [8] ASTM E119-98, *Standard test methods for fire tests of building construction and materials*. American Society for Testing and Materials International, 1998.
- [9] EC2, *Eurocode 2: Design of Concrete Structures. prEN 1992-1-1: General Rules and Rules for Buildings*, European Committee for Standardization, Brussels, 2003.
- [10] NZS 3101, *Concrete Structures Standard, NZS3101, Parts 1 & 2*, Standards New Zealand, Wellington, New Zealand, 2006.
- [11] Buchanan A.H., *Structural Design for Fire Safety*, John Wiley & Sons Ltd, Chichester, 2001.
- [12] Gustaferro, A. H., and Martin, L. D., *Design for Fire Resistance of Precast Prestressed Concrete*, 2nd Ed., Prestressed Concrete Institute, Illinois, USA, 1989.
- [13] Franssen, J. M., “A Thermal/Structural Program Modelling Structures under Fire,” *Engineering Journal, A.I.S.C.*, Vol. 42, No. 3, pp. 143-158, 2005.
- [14] Franssen, J. M., *User’s Manual for SAFIR 2007: A Computer Program for Analysis of Structures Subjected to Fire*, Liège: University of Liège, Belgium, 2007.
- [15] ASTM E119-98, *Standard test methods for fire tests of building construction and materials*. American Society for Testing and Materials International, 1998.

PUNCHING SHEAR STRENGTH OF R/C SLABS SUBJECTED TO FIRE

Patrick Bamonte*, Miguel Fernández Ruiz** and Aurelio Muttoni**

* Politecnico di Milano, Milan, Italy
e-mail: patrick.bamonte@polimi.it

** École Polytechnique Fédérale de Lausanne, Lausanne, Switzerland
e-mails: miguel.fernandezruiz@epfl.ch, aurelio.muttoni@epfl.ch

Keywords: punching shear, flat slabs, Critical Shear Crack Theory.

Abstract. *This paper illustrates a study on the punching shear strength of reinforced concrete slabs in fire conditions. To this end, a set of experimental data on the punching strength of heated slab specimens was interpreted by adapting the well-known Critical Shear Crack Theory to include the effects of high temperature and fire. The comparison between experimental and numerical results is rather good, considering the several uncertainties affecting the problem under consideration. It turns out that the proposed approach is a reliable tool to evaluate the punching strength of thermally-damaged slabs, and this is a good premise for a more in-depth study of the behaviour of punching-sensitive flat slabs in fire conditions.*

1 INTRODUCTION

Fire has traditionally represented a real threat to the safety of buildings and civil structures. As it is well known, the effects of high temperature on structures are two-fold: (a) the mechanical properties of the building materials, such as strength and stiffness to name the most important, are adversely affected by temperature; and (b) the thermal dilation and the ensuing deformations and displacements bring in supplementary “indirect actions”, that can, generally speaking, significantly increase the internal forces with respect to the values in ordinary conditions. The synergy of these two effects can be particularly detrimental, whenever a significant decay of the strength, and therefore of the bearing capacity of structural members, is accompanied by an increase of the state of stress.

A typical way of tackling this problem, from the point of view of structural safety, is to compare the bearing capacity at a given section of a structural member, with the internal force at the location, both functions of the fire duration. The calculation of the bearing capacity as a function of the fire duration is usually carried out by making reference to the classic assumptions of structural mechanics (for example, in the case of beams and columns). The effects of high temperature are then taken into account by reducing the strength and stiffness of the materials at each point of the given section, on the basis of the temperature ensuing from the fire exposure. Several works in the related literature illustrate this kind of approach for common structural members [1,2], and simplified and designer-friendly methods are available in the codes [3]. The evolution of the internal forces with the fire duration, on the contrary, is a highly non-linear problem, that requires the use of sophisticated numerical techniques, and is therefore rather demanding from the computational point of view [4,5]. A possible alternative to overcome these problems is to resort to classic limit analysis, that makes it possible to avoid structural analysis, and therefore greatly simplifies the safety verifications in the time domain. Such an approach is particularly advantageous in highly-redundant and complex structures, where performing a fully non-linear structural analysis is rather demanding, and, from the designer’s point of view, almost prohibitive.

The possibility of using a plastic approach in fire is limited, as in ordinary conditions, by premature brittle failures, like, for instance, shear in beams and columns, and punching shear in slabs. The former is

certainly a big problem in columns of frame structures, where the thermal dilation of beams induces an additional shear force in the columns. It is fair to say, however, that shear failures in fire are rather uncommon [3]. In the case where they are of concern, the main driving parameter is, as it is usually the case in compact under-reinforced sections, the transverse reinforcement [6], and not the concrete, unless, for example, in the case of precast members with rather thin sections [7].

As for punching shear in slabs, the problem is of much more significance, because more or less significant increases of the internal forces (and, therefore, of the punching forces) are to be expected in the case of fire [8] (Fig. 1).

Moreover, a significant role in the punching resistance is played by concrete tensile strength and aggregate interlock; these two effects are both taken into account in some way in the current design equations of the most popular standards [9]. It is fair to say, however, that the aforementioned code equations were obtained on a semi-empirical basis, by operating a regression of the available experimental data: an immediate extension of these expressions to the case of fire is, therefore, highly questionable, to say the least. To tackle the problem of the punching shear resistance in fire in a rational way is only then possible, if reference is made to a physical-based model, such as the “critical shear crack” theory, that was developed during the last years at the EPFL in Lausanne, in the framework of a vast experimental campaign, with some 100 slab specimens tested in punching [10,11].

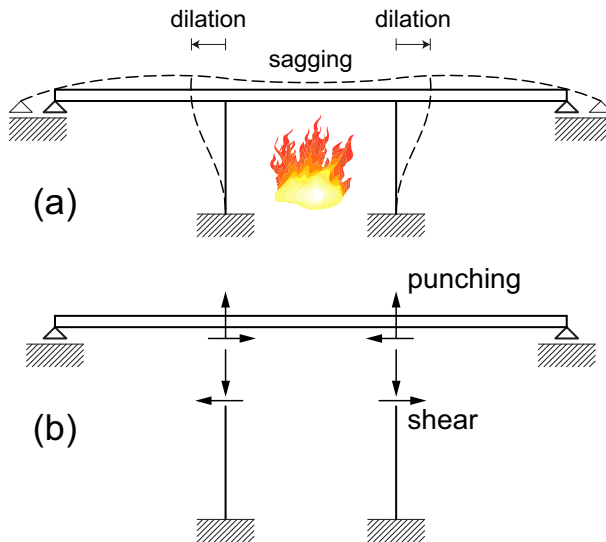


Figure 1. Flat slabs in fire: (a) temperature-induced displacements; and (b) indirect actions.

Despite the wide-spread use of reinforced concrete slabs, no adequate attention has been devoted so far to punching shear in fire. Nevertheless, the topic is of interest, because of the large use of slabs in fire-sensitive structures (like, for example, underground garages), and also in buildings.

In this paper, an extension of the critical shear crack theory to the case of fire is presented. The main assumptions of the model are adapted to incorporate the effects of high temperature, i.e. the two backbone curves of the model (namely, the failure criterion and the load-deformation curve) are modified in order to account for the thermal-induced strength decay and deformability increase. The extension of the model is validated against the few available experimental data, and some design-oriented conclusions are drawn.

2 EXPERIMENTAL DATA

Punching shear of slabs in ambient conditions has been extensively investigated in the past (both experimentally and theoretically). In the case of slabs in fire, however, no adequate attention has been devoted so far to punching shear, and only two references can be cited: the first about the residual behaviour of small circular slabs [12], where a few design equations commonly used at ambient temperature are extended to cover the case of high temperature exposure, and the second on real-scale fire tests on two-way slabs [13]. In the following, reference will be made to the latter; to this end, in this section the main features of the tests are briefly recalled.

Ten specimens were cast and tested; the choice of the specimens' dimensions, as well as of the test set-up, were calibrated on the basis of (a) the prescriptions of the Eurocode 2 (1992 version); and (b) previous tests in fire conditions carried out at the Technical University of Braunschweig (Germany).

The test set-up is shown in Figs. 2a and b. The specimens consist of square slabs (dimensions = $250 \times 250 \times 20 \text{ cm}^3$) with a short column "stub" (dimensions = $25 \times 25 \times 40 \text{ cm}^3$) in the middle.

At the top of the loading frame, the specimens are loaded through a hollow-core hydraulic jack. On the bottom the load is applied through a tendon ($\varnothing = 36 \text{ mm}$, St 1080/1230), provided with thermal insulation, that passes through a hole in the specimen, and is anchored to the bottom face of the column stub at one end, and to the hydraulic jack at the other. The proper distribution of the load from the tendon to the column is achieved through a 50 mm-thick steel plate. The column stub is insulated during the whole fire duration, by means of vermiculite plates (thickness = 100 mm). On the top of the slabs, the load is transferred from the tendon to two HEM 260 beams, that are supported by the loading frame, namely a 400 mm-thick plate with an octagonal hole in the centre portion. The load is then transferred from the frame to the specimen by means of 16 loading points, that are uniformly distributed over a circle (diameter $\varnothing = 220 \text{ cm}$). The applied load is measured through a load cell, that is placed at the top end of the tendon. The overall dimensions of the furnace chamber are $230 \times 230 \times 100 \text{ cm}^3$. The whole test set-up (specimen + loading frame + loading devices) is supported by reaction bearings, that are positioned on the perimeter of the furnace area (side = 230 cm), at a distance of approximately 75 cm from each other.

It is worth noting that the punching load applied to the specimen results from a self-equilibrated system; in other words, the punching action is a sort of prestressing load applied via the tendon at the bottom, and through the 16 loading points on top: therefore, the state of stress and deformation resulting from the punching load is approximately axisymmetric. As for the heating, a standard temperature-time curve (ISO-834) was adopted in all cases.

Following are the main characteristics of the tested specimens:

- thickness = 200 mm, axis distance to the reinforcement (= gross cover) $\approx 35 \text{ mm}$;
- effective depth = 167 mm;
- geometric reinforcement ratio over the column stub: two values (0.50 and 1.50%) were adopted;
- three specimens were provided with "hat-type" shear reinforcement.

Figs. 3a,b shows the layout of the reinforcement in one quarter of specimen, for the two groups of specimens (with light and heavy reinforcement, respectively). The properties of the materials used in the specimens are as follows:

- concrete compressive strength: $f_c^{20} = 35\text{-}52 \text{ MPa}$
- yield strength of bending reinforcement: $f_y^{20} = 504\text{-}590 \text{ MPa}$
- yield strength of transverse reinforcement: $f_y^{20} = 533 \text{ MPa}$

Finally, it is worth mentioning that 5 out of 10 tested slabs underwent spalling on the heated face. The spalling depth was in most cases approximately equal to the gross cover ($\approx 40 \text{ mm}$); in one case (Slab 9) spalling was limited to 20 mm.

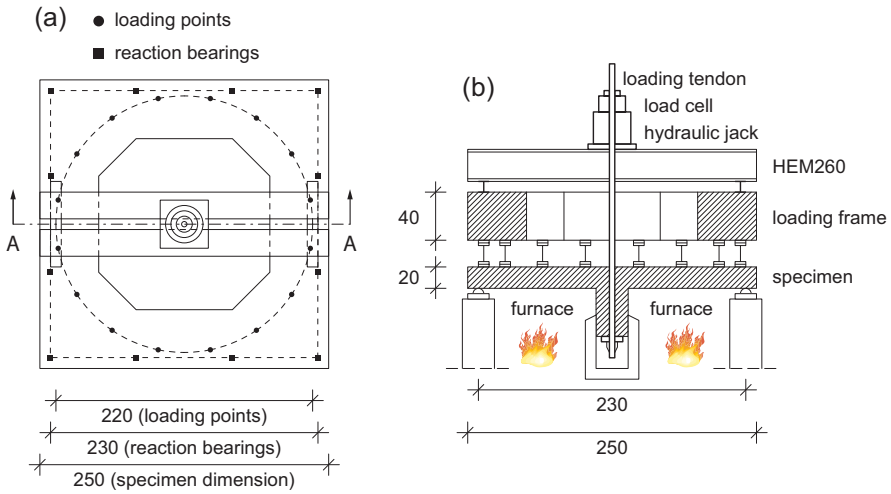


Figure 2. Test set-up (adapted from [13]): (a) top view; and (b) section cut along A-A.

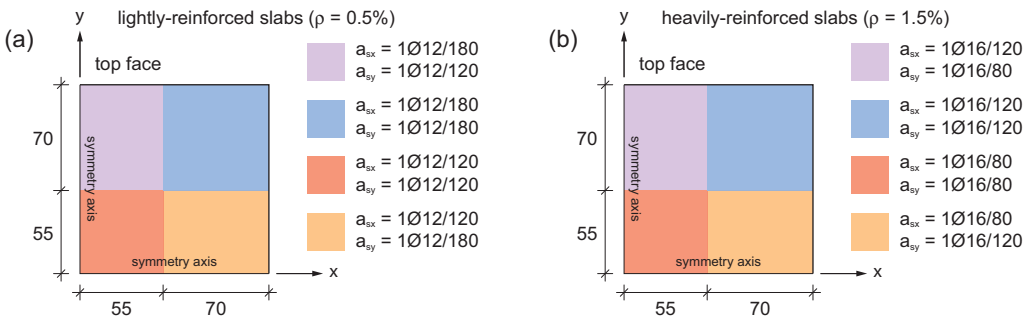


Figure 3. Layout of the negative reinforcement: (a) lightly-reinforced slabs ($\rho = 0.5\%$); and (b) heavily-reinforced slabs ($\rho = 1.5\%$).

The load at the beginning of each test was calibrated on the basis of the design load in fire conditions as per Eurocode = $0.7 \times$ punching resistance at room temperature. In most cases (8 slabs out of 10), the load was increased during the first 30 minutes by variable amounts (0%-70%), to simulate the load redistribution that could potentially take place in an actual flat slab exposed to fire. Beyond 30 minutes, the load was kept constant throughout the whole duration of the test. In the cases, where the specimens stood the constant load phase without collapsing, they were loaded to failure at the end of the heating process. The failure loads and times to failure of the 10 specimens are summarized in Table 1.

Table 1. Summary of the failure loads and times to failure of the specimens tested by Kordina [10].

specimen	1	2	3	4	5	6	7	8	9	10
test duration [min]	120	120	27	17	90	90	29	70	90	22
failure load [kN]	492	475	550	810	386	380	500	568	410	460

3 THEORETICAL MODEL

The model developed to interpret the behaviour of the slabs described in the previous section is an extension of the Critical Shear Crack Theory (CSCT) [10,11] to the case of high temperature and/or fire. This theory, that has been demonstrated to provide a reliable tool for estimating the punching resistance of flat slabs in ordinary conditions, is first briefly recalled; following, the modifications introduced to take the effects of high temperature into account are outlined.

3.1 CSCT – Original formulation

The Critical Shear Crack Theory is a semi-empirical approach, aimed at the evaluation of the punching resistance of flat slabs. It was originally developed for axisymmetric slabs without shear reinforcement, and later on adapted to take into account the role played by the various types of shear reinforcement. The main assumption is that in a slab-column assembly subjected to the highly-concentrated load of a column, a diagonal shear crack will form, where the deformations will localize. As a consequence, in an axisymmetric layout, the deflected shape outside the crack will be conical, i.e. the downward displacement will be linear, and the rotation Ψ constant. This assumption greatly simplifies the description of the structural behaviour, that can be expressed as a closed-form load-rotation relationship of the slab-column assembly.

The increase of the rotation Ψ upon increasing external applied loads is limited by the ability of the critical diagonal shear crack to transfer the shear stresses: the explanation is that the crack opening increases with increasing rotation Ψ , and thus the aggregate interlock, that is responsible for carrying most of the shear stresses, is reduced. On the basis of several experimental data from different authors, a semi-empirical failure criterion was worked out, to relate the rotation of the slab portion surrounding the column, and the shear force that can be transmitted across the diagonal crack (Fig. 4a):

$$\frac{V_u}{b_0 \cdot d \cdot \sqrt{f_c}} = \frac{3/4}{1 + 15 \cdot \frac{\Psi d}{d_{g0} + d_g}} \quad (1)$$

where b_0 is the critical perimeter, d is the effective depth of the reinforcing bars close to the extrados, f_c is the compressive strength of concrete, d_g is the maximum aggregate size, and d_{g0} is a reference aggregate size. Note that whereas the second member of Eq. (1) takes into account the detrimental effect of increasing crack width on aggregate interlock, the denominator of the first member accounts for the strength of the highly-stressed concrete in compression close to the face of the column.

The punching failure occurs when the load-induced rotation is such, that the shear force can no longer be transferred through the crack. From the analytical point of view, the punching failure is determined by the intersection between the load-rotation curve (that represents the structural response of the slab-column assembly), and the failure criterion (Fig. 4b), expressed by Eq. (1).

3.2 Extension of CSCT to high temperature

Being largely based on a clear framework of reasonable mechanical assumptions, the CSCT can be efficiently adapted to cover the case of flat slabs subjected to high temperature.

The main assumption of the theory, namely that a diagonal shear crack forms at early loading stages and influences the behaviour of the whole slab-column assembly, is retained as such.

As for the displacement profile along the slab, a preliminary distinction should be introduced:

$$w_{\text{tot}} = w_{\text{load}} + w_{\text{th}} \quad (2)$$

where w_{tot} is the total displacement, w_{load} is the load-induced (or mechanical) displacement, and w_{th} is the thermal displacement.

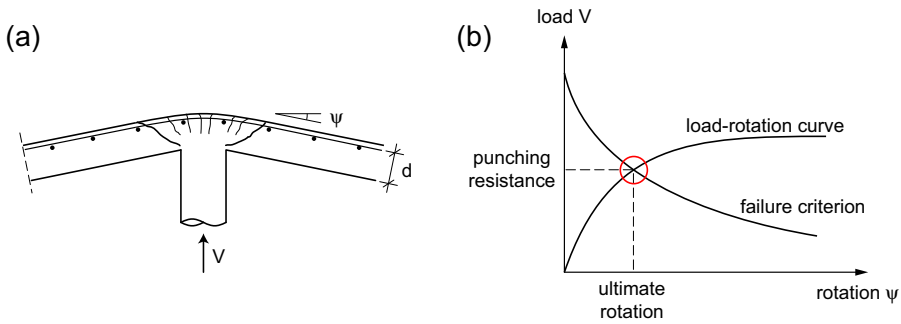


Figure 4. Critical Shear Crack Theory: (a) typical slab-column assembly considered; and (b) determination of the punching resistance in the load-rotation domain.

The load-induced displacement w_{load} is the displacement that ensues from the applied load: it is affected by high temperature, because of the temperature-induced materials' decay, that brings in a stiffness decay (in regions subjected to negative bending mainly because of the reduction of the effective depth), and, upon prolonged fire durations, also the decay of the ultimate strength.

The thermal displacement w_{th} is the deflection caused by thermal sagging, that in turn originates from the thermal dilation of the hot layers of material, and the ensuing thermal curvature on the slab's thickness. The following assumptions are introduced:

- a) outside the diagonal crack, the load-induced rotation Ψ is constant: therefore, the load-induced displacement w_{load} is a linear function of the radial coordinate, outside the diagonal crack (Fig. 5a);
- b) the thermal displacement w_{th} is a 2nd-order parabola of the radial coordinate (Fig. 5b).

The first assumption implies that, upon loading, the kinematic behaviour of the slab sector is similar to that in ordinary conditions, the only difference being the aforementioned stiffness reduction ensuing from the thermal damage.

The second assumption originates from the consideration that in an axisymmetric slab sector subjected to uniform heating, the radial and tangential thermal curvatures are also uniform: therefore, the deflected shape ensuing from the thermal curvatures is spherical, or, with the usual first-order approximation on the radius of curvature, a 2nd-order parabola. It is worth noting that if the edge of the slab is simply supported, a spherical deflected shape implies neither radial nor tangential bending moments, i.e. a uniform distribution of thermal curvatures is not restrained by the boundaries.

A key point in the previous assumptions is the concept of "thermal curvatures": as a matter of fact, in a slab subjected to high temperature and high heating rates, the thermal gradient along the thickness is non-linear. Moreover, when concrete is heated well above ambient temperature, the dilation coefficient is highly temperature-dependent, at least below 700°C. As a consequence, the free thermal strains along the thickness are not linear, and therefore a free thermal curvature as such (i.e. the slope of a linear distribution of free thermal strains) cannot be defined. Fig. 6 shows the typical moment-curvature diagrams in pure bending of a slab section subjected to heating from below. It is worth noting that the decay of stiffness and ultimate capacity is more pronounced in positive bending, as should be expected, since the bottom reinforcement undergoes a significant temperature increase. Most notably, however, there is a translation of the diagrams towards the positive curvatures, that increases with increasing fire duration: in other words, the section will undergo a thermal curvature, even if no load is applied on the section ($M = 0$). In the following, on the basis of the previously-introduced decomposition of the displacements, the thermal curvature is defined as the intersection between the diagrams and the horizontal axis, i.e. the curvature corresponding to no bending moment applied. The diagrams deprived of the contribution of the thermal curvature are "moment vs. load-induced curvature" diagrams, and can be used to work out the load-induced displacement w_{load} (Fig. 5a).

Note that, if the thermal curvature and the relationship between moment and load-induced curvature are defined by means of the aforementioned approach, the superposition principle can be applied, because the different non-linear phenomena taking place on the section (i.e. the self-stresses ensuing from the non-linear thermal strains) are implicitly taken into account in the calculation of the moment curvature diagram.

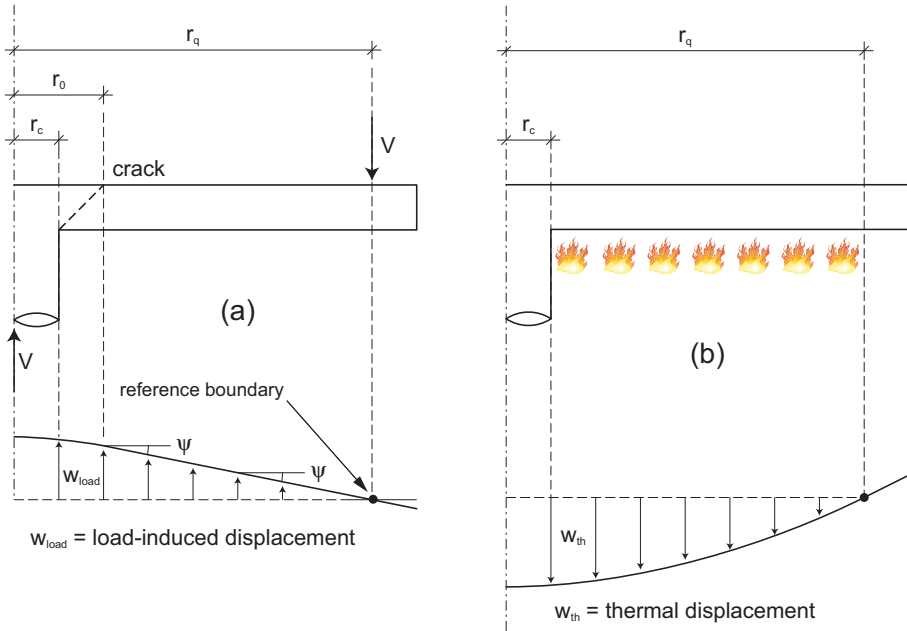


Figure 5. Displacement decomposition at high temperature: (a) load-induced displacement; and (b) thermal displacement.

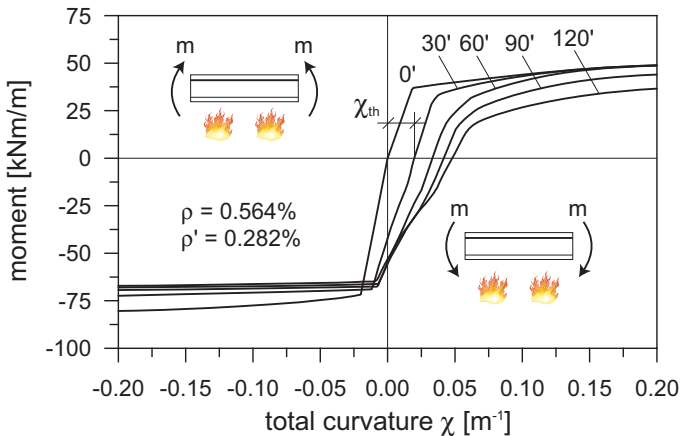


Figure 6. Typical moment-curvature diagrams of the lightly-reinforced slabs tested in [10].

As for the failure criterion, the effects of fire have to be taken into account separately. Considering Eq. (1), the square root of the compressive strength is related to the post-peak softening branch in

compression, or to the toughness in tension. An in-depth investigation of these aspects, however, is beyond the scope of this paper; moreover, it would require a significant number of experimental data on shear failures of plain concrete members at high temperature. Therefore, the decay of this term is evaluated by simply considering an average reduction of the compressive strength along the thickness, or, equivalently, by reducing the effective depth on the basis of the decay of the compressive strength. As the critical perimeter is proportional to the effective depth, also b_0 undergoes a similar reduction.

The denominator of the second member of Eq. (1), that takes into account the decrease of aggregate interlock with increasing crack opening, should be reduced in a similar way, since the reduction of the effective depth will increase the crack opening. This fact, however, is implicitly taken into account by the fact that the rotation used in the failure criterion is the load-induced rotation, and therefore it increases with the reduction of the bending stiffness (as evaluated in the moment-curvature diagrams). It could be argued, however, that the rotation to be considered in the failure criterion is the total rotation, which is smaller because of the contribution of the thermal rotation. There are two main reasons to make reference to the sole load-induced rotation (i.e. to neglect the thermal rotation): (a) in the vicinity of the column, the rotations ensuing from the thermal displacements are small; (b) compared to the load-induced rotation, the thermal rotation is favourable, because its effects are opposite to those ensuing from the load applied.

4 COMPARISON BETWEEN EXPERIMENTAL AND NUMERICAL RESULTS

The proposed extension of the CSCT was validated by simulating the experimental results. The comparisons were carried out both in terms of load-total displacement curves, as well as with reference to the ultimate load.

The first task is accomplished by working out, for any given fire duration, the relation between the load and the mechanical rotation. By considering, for the same fire duration, the applied load (as per load protocol used in the tests) the mechanical rotation can be worked out by means of the moment-curvature diagrams, and the displacement at the face of the column is then calculated by applying the previous kinematic assumption concerning the load-induced displacement. As for the thermal displacement, it can be worked out directly, by integrating the thermal curvature for any given fire duration. The failure load is evaluated by means of the procedure illustrated in Fig. 4b, i.e. as the intersection between the load-rotation curve and the failure criterion for the maximum fire duration reached during the test.

The decay of the mechanical properties and the thermal dilation, in lack of more accurate information, were evaluated according to the provisions of Eurocode 2 [3], assuming the properties of a calcareous concrete. As for the thermal properties, the value of the thermal conductivity was back-fitted, in order to have thermal profiles in good agreement with those provided in [13].

Fig. 7 shows the comparison between the experimental and numerical results, expressed in terms of net deflection (= total deflection devoid of the deflection at the onset of heating) at the centre of the slab, as a function of the fire duration. It is worth noting that the net deflection is always positive (= downward), even though the load at the centre of the slab is directed upward: this indicates that in the tests under consideration the role of the thermal curvature prevails over the load. Most notably is also that in Fig. 7a, Slab 2 exhibits a smaller net displacement than Slab 1 as should be expected, since the load applied to the former (and maintained constant throughout the whole test) was higher than the load applied to the latter.

Fig. 8 illustrates the application of the proposed approach for the evaluation of the failure load; in both cases, the load-rotation curve and the failure criterion were evaluated taking into account the thermal damage corresponding to the time of failure. On the whole, the agreement between the numerical and the experimental failure load (represented by the horizontal dashed line) is satisfying. Moreover, it is interesting to observe that the failure in lightly-reinforced slabs (Fig. 8a) occurs when the load-rotation curve is very close (or even at) the yield plateau, i.e. in lightly-reinforced slabs, even in the case of exposure to fire, the ultimate punching load corresponds to a ductile failure. On the contrary, the heavily-

reinforced slab considered (Fig. 8b) reaches its ultimate load in the ascending phase of the load-rotation curve, i.e. the punching failure occurs prior to yielding of the reinforcement.

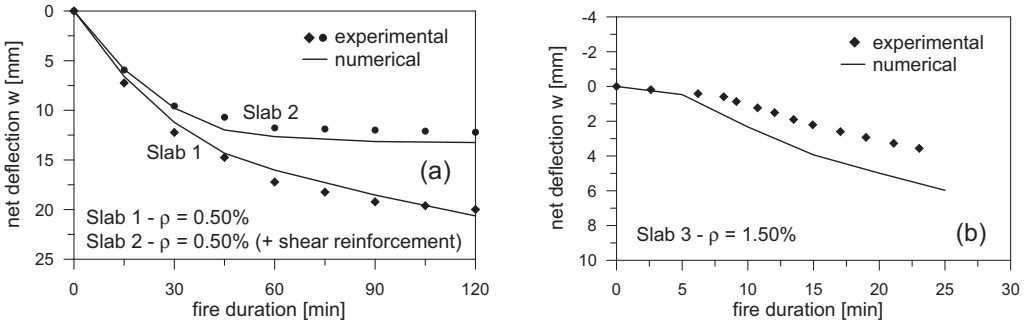


Figure 7. Comparison between experimental and numerical displacement at the centre of the slabs as a function of the fire duration: (a) lightly-reinforced slabs ($\rho = 0.50\%$); and (b) heavily-reinforced slab ($\rho = 1.50\%$).

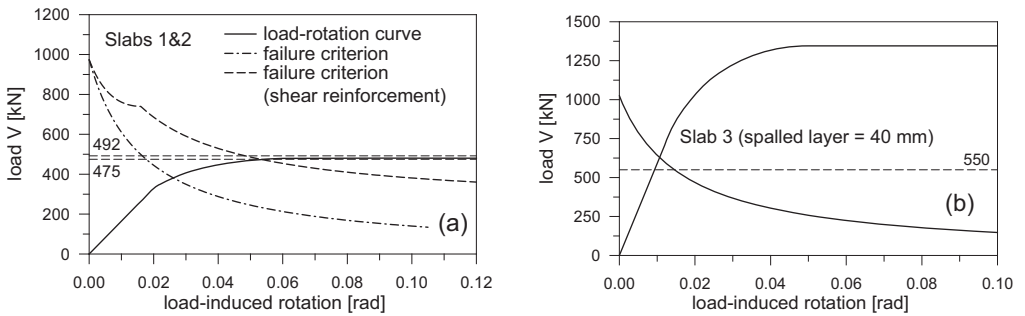


Figure 8. Evaluation of the failure load: (a) lightly-reinforced slabs ($\rho = 0.50\%$); and (b) heavily-reinforced slab ($\rho = 1.50\%$).

5 CONCLUDING REMARKS

On the basis of the preliminary results presented in this paper, the following conclusions can be drawn:

- the Critical Shear Crack Theory, that is used in ordinary conditions to work out the punching resistance of flat slabs, provides a rational tool to study the punching shear strength of flat slabs in fire conditions;
- the numerical fitting of the experimental results taken into consideration is rather good, with respect to both the structural behaviour (displacement vs. fire duration) and to the failure load.

Further research is needed in order to clarify several aspects, such as (a) the role of membrane stresses, that are rather important whenever the structural layout is such that the thermal elongations are restrained (something that did not occur in the tests considered herein); and (b) the possibility of evaluating the bearing capacity in punching by simply adapting the code equations available for ordinary conditions.

REFERENCES

- [1] Meda, A., Gambarova, P.G., and Bonomi, M., “High-Performance Concrete in Fire-Exposed Reinforced Concrete Sections,” *ACI Structural Journal*, V. 99, No. 3, pp. 277-287, May-June 2002.
- [2] Caldas, R.B., Sousa, J.B.M., Hallal Fakury, R., “Interaction diagrams for reinforced concrete sections subjected to fire”, *Engineering Structures*, V. 32, No. 9, pp. 2832-2838, 2010.
- [3] CEN, European Committee for Standardization. EN 1992–1–2, Eurocode 2: Design of concrete structures – Part 1–2: General rules – Structural fire design, Brussels, Belgium, 2004.
- [4] Riva, P., and Franssen, J.-M., “Structural Behaviour of Continuous Beams and Frames,” Chapter 4 in *fib Bulletin 46: “Fire Design of Concrete Structures—Structural Behaviour and Assessment,”*, 210 pp, 2008.
- [5] Biondini, F., and Nero, A., “Cellular Finite Beam Element for Nonlinear Analysis of Concrete Structures under Fire”, *ASCE Journal of Structural Engineering*, V. 137, No. 5, pp. 543-558, 2011.
- [6] Faria, R., Xavier, H.F., and Vila Real, P. “Simplified Procedure for Shear Failure Assessment of RC Framed Structures Exposed to Fire”, *Structures in Fire – Proceedings of the Sixth International Conference*, V. Kodur, J.-M. Franssen (eds.), DEStech Publications, Lancaster, pp. 197-205, 2010.
- [7] Bamonte, P., Felicetti, R., Gambarova, P.G., and Giuriani, E., “Thin-Walled Open-Section P/C Beams in Fire: A Case Study”, *fib Bulletin 57 “Shear and punching shear in RC and FRC elements”*, pp. 173-193, 2011.
- [8] Bamonte, P., Felicetti, R., and Gambarova, P.G., “Punching Shear in Fire-Damaged Reinforced Concrete Slabs”, *ACI Special Publication 265 “Thomas T.C. Hsu Symposium on Shear and Torsion in Concrete Structures”*, pp. 345-366, 2009.
- [9] CEN, European Committee for Standardization. EN 1992–1–1, Eurocode 2: Design of concrete structures – Part 1–1: General rules and rules for buildings, Brussels, Belgium, 2004.
- [10] Muttoni, A., “Punching Shear Strength of Reinforced Concrete Slabs without Transverse Reinforcement,” *ACI Structural Journal*, V. 105, No. 4, pp. 440-450, July-August 2008.
- [11] Fernández Ruiz, M., and Muttoni, A., “Applications of Critical Shear Crack Theory to Punching of Reinforced Concrete Slabs with Transverse Reinforcement”, *ACI Structural Journal*, V. 106, No. 4, pp. 485-494, July-August 2009.
- [12] Felicetti, R., and Gambarova, P. G., “On the Residual Behavior of HPC Slabs Subjected to High Temperature,” *PCI/FHWA/FIB International Symposium on High-Performance Concrete*, Orlando, FL (USA), pp. 598-607, September 2000.
- [13] Kordina, K., “Über das Brandverhalten punktgestützter Stahlbetonplatten” (On the Fire Behavior of Reinforced Concrete Flat Slabs), *Deutscher Ausschuss für Stahlbeton (DAfStb)*, Berlin (Germany), Heft 479, 106 pp, 1997.

FIRE RESISTANCE OF HOLOW CORE SLABS. INFLUENCE OF REINFORCEMENT ARRANGEMENT

Jose V. Aguado*, **Ana Espinos***, **Antonio Hospitaler***, **Javier Ortega**** and **Manuel L. Romero***

* Instituto de Ciencia y Tecnología del Hormigón, Universitat Politècnica de València, Valencia, Spain
e-mails: joaglo1@etsii.upv.es, aespinos@mes.upv.es, mromero@mes.upv.es, ahospitaler@cst.upv.es

** Centro Técnico del Fuego, AIDICO, Valencia, Spain
e-mail: javier.ortega@aidico.es

Keywords: hollow core slabs, fire, precast construction, reinforcement.

Abstract. *This paper describes four full scale fire tests conducted on precast prestressed hollow core slabs under flexure. The influence of the reinforcement arrangement was investigated in tests using two test parameters: the average axis distance (from 30.1 to 46.7 mm), and the type of reinforcement (5 mm diameter wires and 3/8" diameter strands). An ISO 834 standard fire was applied maintaining the load level constant in a four-point test arrangement. The method for measuring temperatures inside the slab is explained in detail, discussing the results and suggesting some improvements for future investigations. From the test observations, it is well established that behavior of hollow core slabs under fire conditions can be divided in three different stages. The structural causes that explain behavior during each stage are identified and analyzed. Finally, it was shown that wires displayed optimal behavior as opposed to strands, because they suffered no splitting cracking and no sliding.*

1 INTRODUCTION

Precast prestressed hollow core (HC) slabs are widely used in concrete or composite floor structures in buildings. Because of their excellent structural performance at room temperature, advanced manufacturing methods, and low-cost installation, HC slabs have an important market presence in many countries. Prestressed reinforcement improves the serviceability performance of HC slabs compared to plain slabs (those without voids), increasing the cracking moment as well as the load-bearing capacity. Span lengths of up to 16 meters and high load levels can be achieved with HC slab floor systems. HC slabs must be installed in different ways depending on the support conditions and desired behavior of the floor structure [1]. Considerable efforts were made in order to evaluate the behavior of HC slabs at room temperature, and in most cases, an acceptable agreement between design provisions and test results was found [2,8]. However, some authors have pointed out the complexity of the thermo-mechanical behavior of HC slabs [9] which causes problems when fire resistance has to be assessed. When the slab heats up, phenomena such as thermal stresses and degradation of material properties should be taken into account as well as their interaction with the four known failure modes of HC slabs (bending, shear tension, shear compression, and anchorage) [2]. Moreover, temperature field is significantly affected by the moisture content of concrete and the presence of cavities (i.e. hollow cores) [9]. The simultaneous consideration of all the phenomena occurring in fire situations leads to a highly non-linear problem which usually requires the use of numerical methods for its resolution. In contrast, design standards such as Eurocode 2 (EC2) [10] provide simplified methods in order to easily meet fire resistance requirements, but they give rise to uncertainties and unexpected failures. In the course of the last few years some authors have conducted fire tests to further knowledge of HC slab behavior at elevated temperatures although a significantly

smaller amount of test data is available in comparison to that of room temperature. For instance, Cooke [11] carried out 14 tests but only two specimens were HC slabs while the other 12 were precast concrete floor slabs without voids or prestressed reinforcement. However, detailed information on temperatures and deflections was provided, enabling important observations to be made and applied to HC slabs. Borgogno and Fontana [12] studied the behavior of slim floors in fire situations and developed a method for calculating thermal stresses. Fellingner et al. [13] investigated shear and anchorage behavior of HC slabs exposed to fire. A total of 25 reduced scale tests were carried out and a numerical model was developed which took into account bond models for reinforcement steel-concrete interface. Double-rib specimens cut from entire slabs were used in most of those tests. It was concluded that shear and anchorage could lead to premature and unexpected failure. Finally, van Overbeek et al. [14] studied the premature partial collapse of HC slab floor structures following a real fire in a car park in Rotterdam. It was found that premature failure occurred in 45% of the tests consulted, something which shows the need for further research. Design codes such as EC2 [10] evaluate fire resistance using different methods such as the 500°C Isotherm Method or the Tabulated Data Method, which are intended for calculating bending and fire resistance. The main parameter of these methods is average axis distance and its value determines fire resistance. This approach is usually assumed to be appropriate and able to predict fire resistance accurately. In consequence, research efforts have mainly concentrated on the assessment of shear capacity of HC slab units or HC slab floors at elevated temperatures. The interaction between shear tension and anchorage failures has also been outlined by many authors [12,13]. However, flexural failure at elevated temperatures has been relatively neglected and few tests are available. Although the influence of the reinforcement arrangement at room temperature is clear when studying bending behavior, other aspects such as the effects of using wires or strands have not been analyzed at high temperatures.

Hence the objective of this research is to develop an experimental program to expand the knowledge of bending behavior at elevated temperatures and to evaluate the influence of different reinforcement arrangements in the fire resistance rating (FRR).

2 EXPERIMENTAL PROGRAM

2.1 Tested specimens

A total of four full scale tests were performed within this experimental program. These slabs tend to be manufactured in very small batches and given the expense of producing a limited number of slabs expressly for the program the HC slabs chosen for testing were commercially available.

Table 1. Geometry of tested specimens

Geometric parameters							
Cross-section height	250 mm		No. Voids / Void width		9 / 79 mm		
Cross-section width	1.20 m		Void height		194 mm		
Slab length	5.70 m		Top flange min. thickness		28 mm		
No. Webs / Web thickness	10 / 42 mm		Bottom flange min thick.		28 mm		
Reinforcement parameters							
	Row 1	Row 2	Row 3	Row 4	Row 5	A_p (mm ²)	a_m (mm)
Axis Dist ¹	22.5	39.5	56.5	73.5	210.5		
HC25-A1	12xØ5	4xØ5	2xØ5	--	4xØ5	431.9	30.1
HC25-A2	4xØ3/8"	4xØ5	2xØ5	2xØ5	4xØ5	443.6	35.1
HC25-A3	4xØ5	4xØ3/8"	2xØ5	2xØ5	4xØ5	443.6	41.3
HC25-A4	--	4xØ3/8"	8xØ5	--	4xØ5	443.6	46.7

¹Axis Distance measured from below

In addition, manufacturers usually design the reinforcement arrangement with a view to satisfying a required bending moment at room temperature. Thus the four HC slabs selected had very similar flexural capacity at room temperature but different reinforcement arrangements and different expected fire resistance times. Specimens tested were identified as follows: HCxx-Ay, where ‘xx’ is the cross-section height and ‘y’ identifies the reinforcement arrangement. Slab identification is ordered from lowest to highest average axis distance (defined below in equation (1)), i.e. the average axis distance of HC25-A1 is less than that of HC25-A2. Table 1 and Figure 1 characterize their geometry. All HC slabs were 250 mm high, 1200 mm wide, 5700 mm long, and only the reinforcement arrangement was varied. Two types of tendons were used: 5 mm diameter wires and 3/8” diameter strands. Reinforcement was distributed along the cross-section in five rows and most of the tendons were placed on the central web axis. Only 4 wires in row number 1 of specimen HC25-A1 were eccentrically placed 18 mm away from the central web axis, Figure 1a.

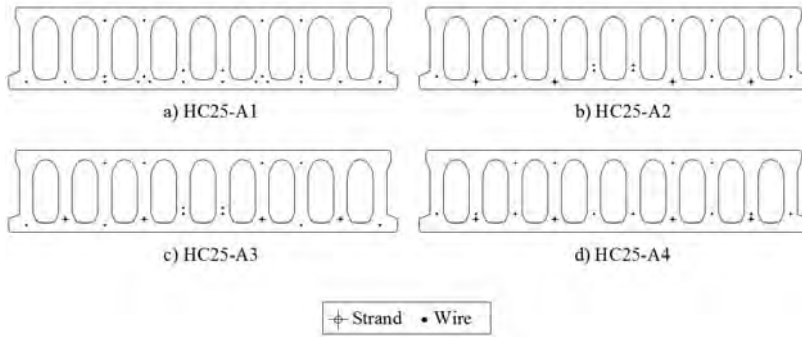


Figure 1. Cross-section and reinforcement arrangement of the HC slabs tested.

As the influence of reinforcement arrangement in bending failure is investigated in this work, the most important parameter to be studied is the average axis distance. This will be calculated as follows in compliance with EC2:

$$a_m = \frac{\sum_i A_{pi} \cdot f_{pi} \cdot a_i}{\sum_i A_{pi} \cdot f_{pi}} \tag{1}$$

Where:

A_{pi} is the cross-sectional area of the tendon ‘i’.

f_{pi} is the real tensile strength of the tendon ‘i’, which was obtained as explained in section 2.3.

a_i is the axis distance of the tendon ‘i’ from the nearest exposed surface.

Therefore, real strength of steel is used and only reinforcement under tension (rows 1 to 4) is considered in the calculation. Average axis distance of each HC slab is shown in Table 1.

2.2 Concrete

Normal-strength concrete (45 MPa) and calcareous aggregates were used in the experimental program. The real compressive strength of concrete was determined by testing two cylinders, 300 long and 150 mm diameter, on the same day the HC slab was tested. The cylinder compressive strength of concrete f_c was calculated as the average of the two test results. Since flexural failure is expected, the real

tensile strength of concrete f_{ct} is also needed. A Brazilian test procedure [15] was performed using one cylindrical sample. All data are summarized in Table 2. The humidity of concrete was also measured using cubic samples cut from each slab on the same day they were tested. The weight of each specimen was measured before and after drying them in a small oven at 150°C. This made it possible to obtain the moisture level directly.

Table 2. Test properties and results

Id	Id.	a_m (mm)	μ_{exp} (%)	f_c (MPa)	f_{ct} (MPa)	Moist. (%)	Max.D/ Max.DR	Limits reached	FRR min
1	HC25-A1	30.1	36	52.1	3.50	3.90	374.9/52.2	D/DR	84
2	HC25-A2	35.1	35	54.6	4.00	3.80	247.0 ¹ /13.8	DR	96
3	HC25-A3	41.3	36	57.1	3.45	2.90	235.5/20.0	DR	105
4	HC25-A4	46.7	37	52.4	4.05	3.30	322.4/30.0	D/DR	92

D: Deflection ; DR: Deflection Rate

¹ The hydraulic jack reached its maximum displacement, so the test had to be halted. The problem was solved for the other tests (HC25-A2 was tested first). However, the slab had already failed, as the DR limit had been reached.

2.3 Prestressing steel

Cold-worked prestressing steel wires and strands were used. Strands were made up of six wires rolled together in a helical form around a central wire. The characteristic tensile strength of steel f_{pk} was 1860 MPa in all cases. However, real strength was established by experimental coupon tests. A tensile strength of 1931 MPa was obtained for strands, while the tensile strength measured for wires was 1883 MPa. These values apply to all HC slabs tested as the steel used in all cases belonged to the same batch. The 0.1% proof-stress of prestressing steel $f_{p,0.1}$ was also obtained, given that it was of interest for the calculation of the real ultimate bending moment at room temperature. It was established that $f_{p,0.1}$ was equal to 90% of real tensile strength of steel f_p for both wire and strands. This result matched the recommendations of EC2, which suggest considering the same percentage (90%) in absence of experimental data.



Figure 2. a) General view of the experimental setup. b) Inside the furnace. c) Voids infilling.

2.4 Test setup and procedure

All tests were performed in the testing facilities of AIDICO (Instituto Tecnológico de la Construcción) in Valencia, Spain. Both the experimental setup and test procedure were in compliance with standard EN 1363 [16] for fire resistance tests. A 5x3 m furnace equipped with a hydraulic jack of 1000 kN maximum capacity was used. There were 16 gas burners inside the furnace chamber, arranged in two horizontal rows of 8 burners each, located at mid-height on opposite walls. Slabs were placed covering the furnace, and only supported at the ends. Figure 2a shows a general view of the experimental setup, while the interior of the furnace can be seen in Figure 2b. As bending behavior was of interest, a four-point test arrangement was used to apply the load. Figure 3 shows a setup scheme indicating the principal lengths. There was no interaction between shear and bending in the two load points, that is to say, pure bending occurs. Mid-span deflection was measured using a displacement transducer.

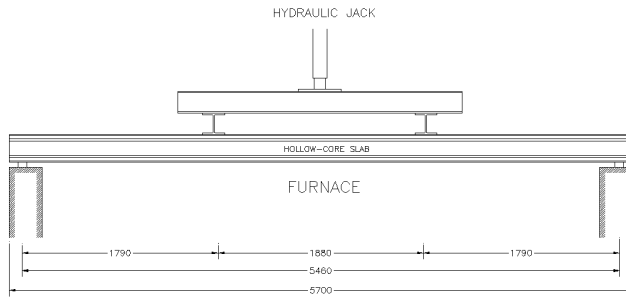


Figure 3. Representation of the experimental setup.

Furnace temperature was automatically controlled by five thermocouples following standard fire curve ISO-834 [17]. Pressure sensors were also located inside the furnace chamber in order to prevent excessive values. Temperatures inside each HC slab were measured with sixteen thermocouples distributed in two cross-sections (section A and section B) equidistant from the mid-span (Figure 4).

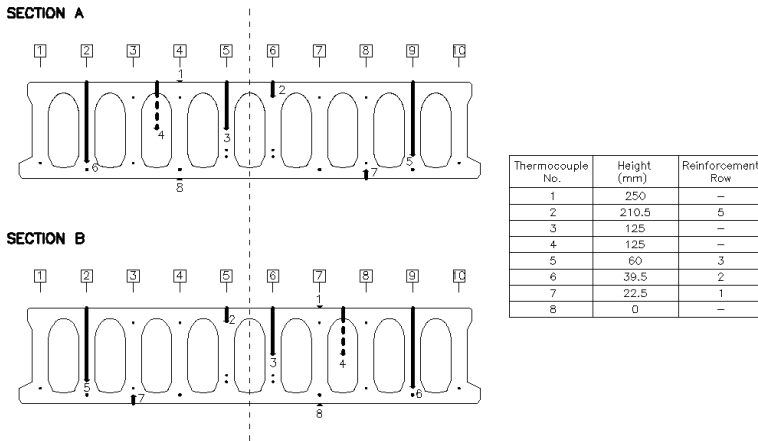


Figure 4. Thermocouple arrangement of slab HC25-A2

Thermocouples were arranged in both sections according to the following criteria:

- Thermocouple No. 1 on the unexposed (top) surface.
- Thermocouple No. 3 at mid-height.
- Thermocouple No. 8 on the exposed (bottom) surface.
- Thermocouple No. 4 inside one void.
- The other four thermocouples (numbers 2, 5, 6, and 7) were placed at the same height as a reinforcement row, which provided an indirect reading of the reinforcement temperature. In the case of specimen HC25-A4 only three out of four thermocouples were installed because of the reinforcement arrangement.

In order to place the thermocouples inside the concrete it was necessary to drill holes to an appropriate length. Once the thermocouples were placed, the holes were filled with thermal insulation. Figure 4 shows an example of the thermocouple arrangement system used in Section A and Section B of slab HC25-A2 respectively, with thicker lines representing the drilled holes. Both arrangements can be seen to be symmetrical. For example, thermocouple number 6 in Section A is placed inside the second web while thermocouple number 6 of Section B is placed inside the ninth web. The second and ninth webs are symmetrical to the center of the section. This disposition makes it possible to perceive any difference in temperature and ensures uniform heating. Moreover, because of the border effects any thermocouple placed inside the outer webs (1 and 10) could distort the temperature measurement process. Finally, Figure 2c shows how the void ends of the HC slabs were filled with insulating material. The purpose of this was to prevent air renovation inside the void and reproduce building conditions in the test. The load applied was identical for all slabs tested and was calculated aiming to obtain an average nominal load level of 45%. The individual load level of each slab was calculated as follows:

$$\mu_{nom} = \frac{M_{Test}}{M_{Rd,nom}} \quad (2)$$

where M_{Test} is the bending moment produced by the applied load and $M_{Rd,nom}$ is the ultimate bending moment at room temperature using the nominal properties for materials and the corresponding partial factors. Nominal properties were used as these calculations were made before the experimental data of materials were available. The average nominal load level was considered to be equal to 45% as this value leads to an average FRR of 90 minutes from the 500°C Isotherm Method, using nominal properties of materials and partial factors $\gamma_{M,fi}$ in a fire situation equal to one [10]. Moreover, temperatures were taken from the product standard for HC slabs EN 1168 [18], which provides a temperature profile throughout the section for each time of fire exposure. It should be noted that these temperature profiles are identical to those given in EC2, despite the fact that these are intended for solid slabs. The bending moment in all tests M_{Test} could be calculated (52.6 m•kN) from an average nominal load level of 45%. The test load P_{Test} could also be calculated immediately considering the loading system shown in Figure 3. Consequently, a test load of 58.80 kN was obtained and applied in all tests.

In contrast, the experimental (i.e. real) load level of the slabs tested is another important parameter. When real material properties are known, the experimental load level can be calculated as follows:

$$\mu_{exp} = \frac{M_{Test}}{M_{Rd,exp}} \quad (3)$$

where $M_{Rd,exp}$ is the ultimate bending moment at room temperature, calculated by means of the experimentally measured properties of materials. Therefore, partial factors for materials were not needed in this case. Table 2 summarizes μ_{exp} values of each slab. As was stated in section 2.1, the ultimate bending moments at room temperature were almost equal for all slabs, and therefore, the experimental load levels are very similar.

3 TEST RESULTS

3.1 Mid-span deflection and failure mechanism

When HC slabs showed a flexural failure at elevated temperatures, three different stages were identified in the deflection versus time curve. These stages are noted in Figure 5.

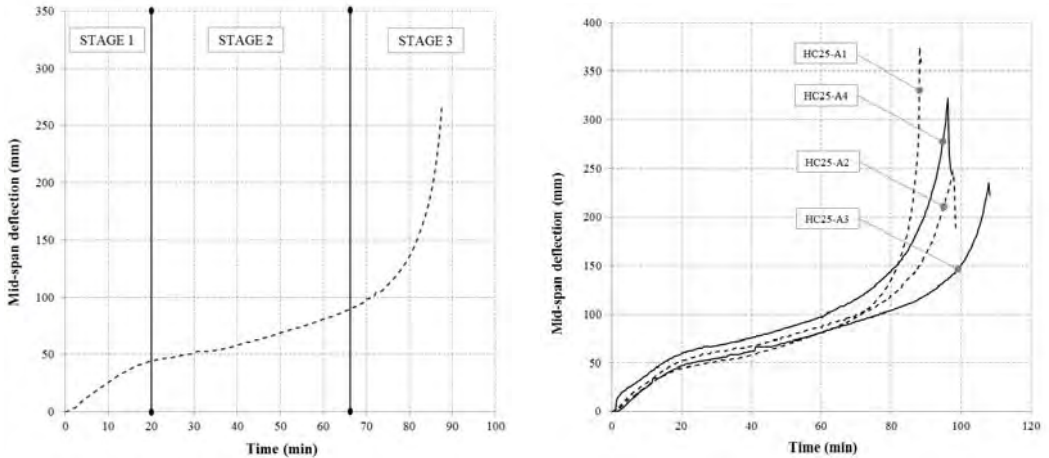


Figure 5. Left: Identification of each stage. Right: Mid-span deflection of each slab tested

In the first stage, which comprised the first 20 minutes of the fire testing approximately, heating from below gave rise to a non-linear temperature profile through the cross-section which led to the development of tensile thermal stresses in the web, while the top and bottom flanges were in compression [12]. The tensile thermal stresses led to the web cracking and therefore the deflection increased rapidly at this stage. In contrast, the steel reinforcement was barely affected by the temperature for the first 20 minutes, so this pronounced loss of stiffness cannot be attributed to its loss of strength. After 20 minutes, the second stage began. There was an almost linear increase in mid-span deflection. The webs were completely cracked and the temperature profiles through the section became smoother, so the loss of stiffness slowed down. The moisture vaporization at 100°C also contributed to delaying the rise in temperature. During this stage, the deflection mainly took place because of the degradation of material properties. Therefore, as the rise in temperature slowed down, the materials slowly lost their mechanical properties and the deflection rate was moderated. The second stage concluded when the steel reinforcement lost its strength and the deflection rate increased quickly, so that the timespan of this stage was variable and depended on the reinforcement arrangement of each slab. During the third stage, the HC slab fully lost its load-bearing capacity. A high deflection rate was observed up until the test was finished (see Figure 9). Before the test began, the reinforcement steel operated in the elastic range since the real load level was low (about 36%). As the slab heated up, the elastic modulus of the steel decreased, and therefore the deflection rose. The applied load was maintained during the test so the stress level did not change in order to maintain overall equilibrium. At a given temperature yielding stress and current stress became equal, which meant that the steel showed plastic strain. As the steel yielded and the temperature kept rising, the steel continued to lose strength and therefore some tensile force was transferred to the rows of reinforcement above (when possible). Depending on the area of reinforcement of the rows above and their lever arm, the increment of stress produced by the tensile force released was of greater or lesser significance. When the steel area of the bottom row was much greater than the area of the other rows, the tensile force released produced a great increment of steel stress in the rows above. This increment could

immediately lead to the steel in the row yielding. This process continues until all steel rows have yielded or the concrete in compression has been crushed.

Figure 5 shows the mid-span deflection measured during the test for each slab. Although all four curves are similar, some differences can be noticed in the third stage of each HC slab. While the deflection rate of HC25-A1 increases very rapidly in the final stage, that of HC25-A3 is considerably lower. This behavior is explained by the failure mechanism described earlier. Finally, the three stages distinguished in the time-deflection curve of the HC slabs and which show flexural failure can be observed in the plain slabs (i.e. without voids) when experiencing the same type of failure. Results from Cooke [11] support this observation.

3.2 Fire resistance rating

According to EN 1363 [16], failure is considered to occur when the deflection limit or the deflection rate limit, are reached. These are calculated as follows:

$$D = \frac{L^2}{400 \cdot d} \quad (\text{mm}) \quad ; \quad \frac{dD}{dt} = \frac{L^2}{9000 \cdot d} \quad (\text{mm}/\text{min}) \quad (4)$$

where L is the distance between supports and d is the distance between the extreme zone in compression and the extreme zone in tension in bending at room temperature, both expressed in millimeters. Accordingly, Table 2 shows the fire resistance rating (FRR) of each slab tested within this experimental program. Table 2 also shows the maximum deflection reached for each slab and the maximum deflection rate, indicating the exceeded limits. Slab HC25-A4 appeared to be very damaged so the decision was made to halt the test, thus preventing the slab from falling inside the furnace. In the case of slab HC25-A2, which was tested first, the hydraulic jack reached its maximum displacement, so that the test had to be stopped. This problem was solved and all subsequent tests were carried out without further incidents. Even so, both HC25-A2 and HC25-A4 had also reached at least one of the limits when their respective tests concluded (see Table 2).

FRR time measurements ranged from 84 to 105 minutes. This means that all four slabs failed within a time-span of 21 minutes despite the different reinforcement arrangements. Results from Table 2 also show that greater average axis distances led to greater FRRs, except in the case of unit HC25-A4 which displayed the second shortest FRR despite having the greatest average axis distance.

3.3 Temperatures

The temperatures measured were expected to be similar for all the slabs as the concrete section was the same and the influence of the reinforcement could be neglected [10]. Only the moisture content was expected to produce differences in the temperatures measured, because the standard fire curve ISO 834 was almost perfectly followed thanks to the furnace temperature control system. Figure 6 compares the time-temperature curves recorded by thermocouple number 3, located at mid-height, for each slab tested with the purpose of evaluating the influence of moisture. For this reason the moisture content has been indicated beside each curve. As expected, greater moisture content leads to an extended plateau at 100°C. In addition, the timespan of these plateaus corresponds to the experimentally measured moisture, that is to say similar moisture contents lead to similar plateau timespans. As stated before, curves for all slabs are almost identical and differences are due to the moisture content for each slab. However, the analysis of test results shows that a measuring error might have been induced when thermocouples were drilled from below. Figure 11 shows also thermocouple number 6 (at 39.5 mm from the exposed face) in Section A of each slab, where two groups of curves can be identified. The first group corresponds to slabs drilled from above (DfA), while those drilled from below (DfB) show a time-temperature curve almost parallel but about 100°C higher. Furthermore, moisture vaporization is apparent when drilling from above, but not when drilling from below.

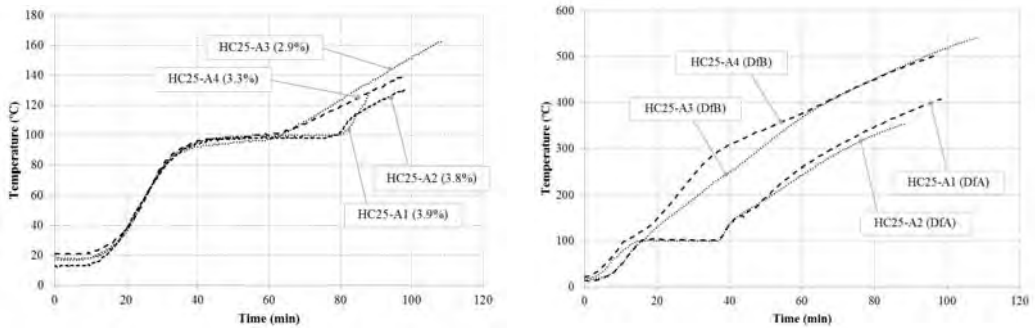


Figure 6. Left: Influence of moisture content. Comparison of thermocouple number 3. Right: Temperatures at 39.5 mm from the exposed surface of each slab (Thermocouple number 6). DfA stands for Drilled from Above while DfB stands for Drilled from Below.

These different measurements have been observed in spite of the fact that the holes drilled for placing thermocouples were filled with thermal insulation. Thus, it appears that thermocouples placed by drilling the bottom surface provide overrated measurement readings, which means that a different positioning system for thermocouples should be designed for future research. Placing all thermocouples from above might solve this problem but it would be necessary to get round the reinforcement in order to reach the lower rows.

4 CONCLUSIONS

From the test observations and the discussion of results presented above, the following conclusions can be drawn:

- When fire bending tests were carried out four types of cracking occurred in HC slabs: thermal cracking, flexural cracking, splitting cracks, and longitudinal cracking.
- Three stages are identified in the time versus mid-span deflection curve when flexural failure occurs. In the first stage deflection is driven by thermal cracking, while in the third stage the slab suffers failure due to the loss of strength of the steel.
- Wire reinforcement showed optimal behavior, because wires did not suffer splitting nor sliding. However, a more extensive experimental program is needed to support this observation.
- The reinforcement arrangement determines the shape of the time-deflection curve in the third stage.

REFERENCES

- [1] Capuano G., Della Bella B., Ghittoni P., Morandi P. and Pereswiet-Soltan S., *Il solaio alveolare Progettazione e Impieghi*, second ed., Associazione Produttori di Solai Alveolari Precompressi (ASSAP), Verona (Italia), 1999. (In Italian)
- [2] Walraven, J.C. and Mercx, W.P.M., “The bearing capacity of prestressed hollowcore slabs”, *Heron*, 28, 1-46, 1983.
- [3] Becker, R.J. and Buettner, D.R., “Shear tests of extruded hollow core slabs”, *PCI Journal*, 30, 40-54, 1985.
- [4] Pajari, M. and Koukari, H., “Shear resistance of PHC slabs supported on beams. I: Tests”, *Journal of Structural Engineering*, 9, 1050-1061, 1998.

- [5] Hegger, J., Roggendorf, T. and Kerkeni, N., "Shear capacity of prestressed hollow core slabs in slim floor constructions", *Engineering Structures*, 31, 551-559, 2009.
- [6] Pisanty, A., "The shear strength of extruded hollow-core slabs", *Materials and Structures*, 25, 224-230, 1992.
- [7] Lam, D., Elliott, K.S. and Nethercot, D.A., "Parametric study on composite steel beams with precast concrete hollow core floor slabs", *Journal of Constructional Steel Research*, 54, 283-304, 2000.
- [8] Song, J.Y., Elliott, K.S., Lee, H. and Kwak, H.G., "Load distribution factors for hollow core slabs with in-situ reinforced concrete joints", *International Journal of Concrete Structures and Materials*, 1, 63-69, 2009.
- [9] Dotrepe, J.C. and Franssen, J.M., "Precast hollow core slabs in fire: numerical simulations and experimental tests", *Structures in Fire - Proceedings of the Third International Workshop*, 219-232, 2004.
- [10] *EN 1992-1-2 Eurocode 2: Design of concrete structures. Part 1-2: General rules – Structural fire design*, Comité Européen de Normalisation, Brussels (Belgium), 2004.
- [11] Cooke, G.M.E., "Behaviour of precast concrete floor slabs exposed to standardized fires", *Fire Safety Journal*, 36, 459-475, 2001.
- [12] Borgogno, W. and Fontana, M., "Structural behaviour of slim floor slabs with prestressed hollow core elements at room temperature and in fire", *Composite Construction in Steel and Concrete - Proceedings of the IV Conference*, 4, 768-779, 2000.
- [13] Fellingner, J., Stark, J. and Walraven, J., "Shear and anchorage behaviour of fire exposed hollow core slabs", *Heron*, 50, 279-301, 2005.
- [14] Overbeek, T., Breunese, A., Gijsbers, J., Both, K., Maljaars, J. and Noordijk, L., "New regulations for hollow core slabs after premature partial collapse", *Structures in Fire – Proceedings of the Sixth International Conference*, 141-148, 2010.
- [15] *EN 12390-6, Testing hardened concrete. Part 6: Tensile splitting strength of test specimens*, Comité Européen de Normalisation, Brussels (Belgium), 2009.
- [16] *EN 1363-1, Fire resistance tests. Part 1: General requirements*, Comité Européen de Normalisation, Brussels (Belgium), 1999.
- [17] *ISO 834, Fire resistance tests, elements of building construction*, International Standards Organization, Switzerland, 1980.
- [18] *EN 1168 Precast concrete products. Hollow core slabs*, Comité Européen de Normalisation, Brussels (Belgium), 2006.

FIRE RESISTANCE OF HOLLOW CORE FLOORS REGARDING SHEAR AND ANCHORAGE CAPACITY

Wim Jansze*, Arnold Van Acker*, Bruno Della Bella*, Ronald Klein-Holte*, Gösta Lindström*, Andreas Nitsch*, Jean-Paul Py*, Fabienne Robert*, Matthieu Scalliet*

*BIBM, the European Federation for Precast Concrete,
Boulevard du Souverain 68 B-1170 Brussels, Belgium
e-mails: wim.jansze@consolis.com, arnold.van.acker@skynet.be, info@bibm.be

Keywords: hollow core slab, EN1168:A3 Annex G, fire, shear resistance, validation, meta-analysis.

***Abstract.** In 2011, a new formula for the shear and anchorage capacity of hollow core slabs under fire was introduced in Annex G of product standard EN1168:A3 [2]. A thorough meta-analysis performed by the authors to evaluate the new formula against 42 independent fire tests on hollow cores proofed that the formula is safe. The evaluated 42 independent small-scale ISO-fire tests exhibited a distinct shear and anchorage failure and were conducted between 1966 and 2010 on double-web hollow core elements, single hollow core slab units and full hollow core floors systems. The paper concludes that this newly introduced formula is 7% on the safe side when all 42 small-scale fire tests are considered. When only 14 fire tests on hollow core floor systems are considered it gives even a 24.0% higher safety.*

1 INTRODUCTION

The fire resistance of a concrete structure exposed to fire is a very complex phenomenon. There is the intensity and the extension of the fire, the location of the fire within the structure, and the size of the building. Also the structural lay-out and components of the building are influencing the response to a fire. And finally there are the dimensions of the concrete elements, the concrete composition, axis distance to the reinforcement, moisture content of the hardened concrete, etc. Fortunately, concrete structures possess not only a high fire resistance, but also a large resilience to fire because of its robustness and its redistribution capacity to the acting loading. This is also valid for precast concrete hollow core floors.

In precast concrete floor construction the hollow core slab has been a very successful product for residential and non-residential building structures, both in concrete and steel frames. This success is largely due to the highly efficient design and production methods, flexibility in use, surface finishing and structural efficiency. Yearly about 20 to 25 million square metres hollow core floors are erected in Europe. The estimated total stock of installed hollowcore floors nowadays in Europe amounts to 1000 million square meters. Figure 1 shows an example of quick erection of a precast hollow core slab floor.

But due to its success and easy erection, the precast hollow core slab is also the most often studied concrete element exposed to fire in small-scale laboratory tests. In this study 162 fire tests have been identified that were executed between 1966 and 2010 in European laboratories. The main conclusion from these fire tests is that a hollow core slab is capable to achieve the required fire resistance provided that sufficient cover to the prestressing strands is respected, and provided that a good small-scale fire test design is made corresponding to the real application of the hollow slabs cores in a floor structure.

Unfortunately, not always a correct small-scale fire test design was made with hollow core slabs. A few cases of premature shear failure in standard fire tests were reported [5,7,8]. As a consequence, it led to reluctant clients, although in practical applications shear hardly governs floor design [6]. The question was raised if this constitutes a real structural problem for this type of floor, or whether the reason lies in a lack of understanding of the behaviour of hollowcore floors during fire, resulting in poor design,

particularly for small-scale laboratory test set-ups. The discussions affected the good image of the hollow core slab among clients in some European countries.

Accordingly, in order to systematically study shear failure under fire, laboratory tests were conducted between 1998 and 2005 in Belgium [4,11], The Netherlands [6] and Denmark [9]. These fire have been reported on, however, publications lacked a good guideline to design for shear and anchorage. Only recently, in 2011, the European Standardisation Institute CEN published rules in EN1168:A3 Annex G [2], the product standard for hollow core slabs. Amendment A3 provides a formula to design for shear and anchorage for single span hollow core slabs without shear reinforcement exposed to fire.



Figure 1. Erection of precast hollowcore slabs in a floor structure of a building.

2 FIRE RESISTANCE ACCORDING TO EN1168:A3 ANNEX G

The informative Annex G of product standard EN1168:A3 [2] gives rules for the resistance to fire of hollow core slabs. The fire resistance (R) may be calculated according to EN 1992-1-2:2004 4.2 or 4.3 with additional rules for prestressed hollow core slabs regarding bending failure and shear and anchorage. According to Annex G of EN1168, the fire resistance regarding shear and anchorage failure may be determined by using simplified calculation methods (see EN 1992-1-2 clause 4.2 and Annex B and Annex D), but taking into account the following rules:

- First, it is assumed that below the level on which the total web width is equal to the core width (level $a_{50\%}$), the temperature is equal to the temperature of a solid slab (see Figure 2).
- Secondly, above that level a linear interpolation is taken between the temperature at that level and the temperature at the top of the floor. The maximum allowed temperature for the insulation criterion is 160°C ($140^{\circ}\text{C} + 20^{\circ}\text{C}$ ambient temperature);
- Thirdly, to determine the shear and anchorage resistance under fire, formula (1) is used, with parameters $C_{\theta,1}$ (formula 2), α_k (formula 3), and $C_{\theta,2}$ (formula 4) (see also Figure 3).
- For a fire resistance class $\leq R60$ this verification is not needed.

As hollow core slabs exposed to fire are subjected to thermal vertical web cracking over the full span including support region [4,6], the shear flexure formula 6.2.a. of Eurocode EN 1992-1-1 [1] was chosen

as basic model rather than the shear tension formula, which is only applicable for non-cracked sections. For fire this formula 6.2.a was adapted, and validated in [3] with 9 fire tests.

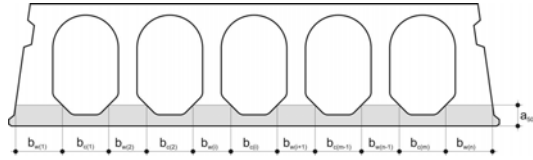


Figure 2. Area where solid slab temperatures may be assumed (grey area).

$$V_{Rd,c,fi} = [C_{\theta,1} + \alpha_k \cdot C_{\theta,2}] \cdot b_w \cdot d \tag{1}$$

$$C_{\theta,1} = 0.15 \cdot \min(k_p(\theta_p) \sigma_{cp,20^\circ C}; \frac{F_{R,a,fi,p}}{A_c}) \tag{2}$$

$$\alpha_k = 1 + \sqrt{\frac{200}{d}} \leq 2,0 \tag{3}$$

$$C_{\theta,2} = \sqrt[3]{0.58 \cdot \frac{F_{R,a,fi}}{f_{yk} \cdot b_w \cdot d} \cdot f_{c,fi,m}} \tag{4}$$

- $C_{\theta,1}$ Coefficient accounting for concrete stress under fire conditions
- $k_p(\theta_p)$ Strength reduction factor for the prestressing steel (EN 1992-1-2 clause 4.2.4.3.)
- $\sigma_{cp,20^\circ C}$ Average concrete stress due to prestressing at normal temperature
- A_c Concrete section area
- $F_{R,a,fi,p}$ Force capacity of prestressing steel anchored in considered cross section
- $C_{\theta,2}$ Coefficient accounting for anchored longitudinal reinforcement:
- $F_{R,a,fi}$ Force capacity of prestress and reinforcement anchored in considered cross section
- f_{yk} Characteristic yield strength of the reinforcement
- $f_{c,fi,m}$ Average strength of concrete at elevated temperature, $f_{c,fi,m}$
- b_w Total web thickness of the hollow core slab
- d Effective depth at ambient temperature

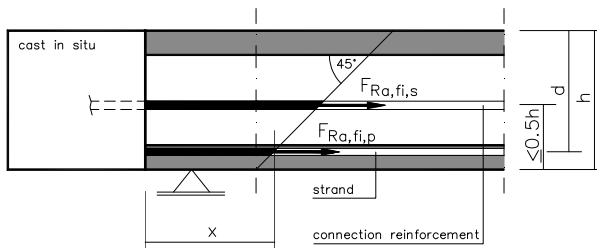


Figure 3. Model for calculating shear and anchorage resistance (example without protruding strands)

3 FIRE TESTS EXHIBITING SHEAR AND ANCHORAGE FAILURE

3.1 Fire tests description

From literature, 42 small-scale ISO fire tests conducted between 1966 and 2010 have been identified that exhibited a shear and anchorage failure, see Table I. The independent fire tests have been conducted over a period of 45 years in several European countries, namely Belgium (RUG), Finland (VTT), Switzerland (EMPA), Denmark (DIFT), Netherlands (TNO), Poland (ITB), and Sweden (SPTRI). Table I contains 30 fire tests on 255-275 mm height hollow core slabs, 8 fire tests on 185-220 mm height, and 4 tests on 400 mm height hollow core slabs. The tested geometries varied from 0,4-0,6 m wide double-web hollow core elements (16 tests), to 1.2 m wide single hollowcore slab units (12 tests), to full floor systems (14 tests) with hollow cores assembled together to floor widths of mostly 2,4 m (Figure 4). Only in some fire tests connection reinforcement was used.

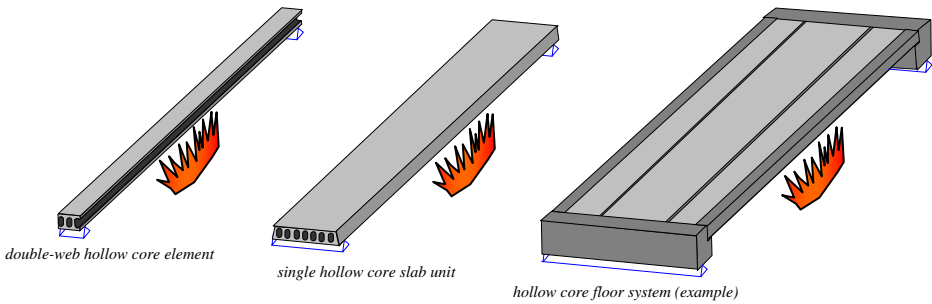


Figure 4. Geometries of hollow core elements used in fire tests – double-web element, slab unit, and floor system

Figure 5 overviews the fire tests on shear as tabulated in Table 1 by depicting the fire resistance time versus shear load applied in the fire test. It emerges that 15 fire tests (mostly single units) failed in shear before 40 minutes, and 10 fire test failed only after 90 minutes.

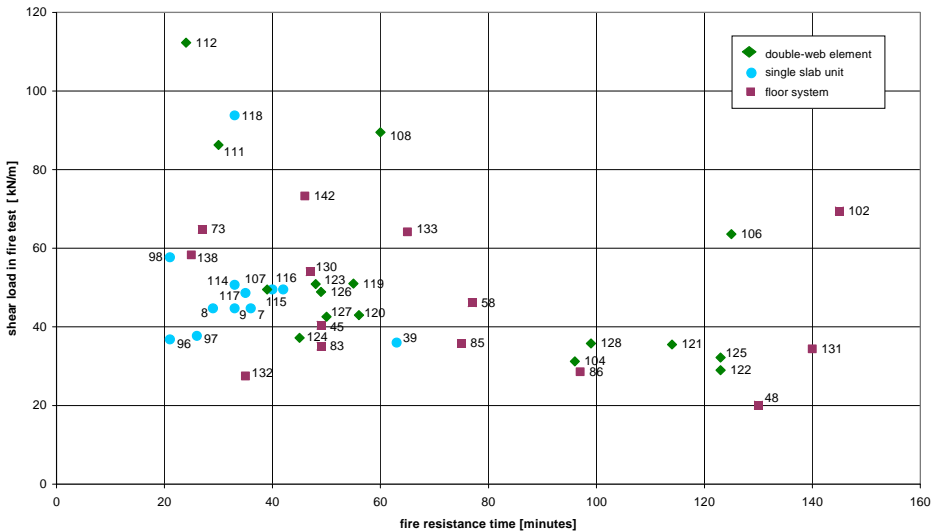


Figure 5. All 42 fire test maximum shear loads depicted as a function of the fire resistance times

In all these 42 fire tests shear and anchorage failure played a dominant role. Of the 42 tests, in 20 fire tests (RUG, VTT, EMPA, DIFT, ITB) the slab(s) failed unexpectedly and prematurely [5,7,8]. 21 fire tests (TNO, SPTRI) were designed to fail during the fire test [6,9,11] in order to study systematically shear under laboratory conditions; but two fire tests did not fail. In these 2 fire tests [6], and another fire test [(RUG 9158) 4], the slabs were loaded up to shear failure after fire exposure. To summarise, a total of 39 fire tests had a shear and anchorage failure during the fire test, while in 3 fire tests (H102, H106, H125) during the fire failure did not occur, so that the slabs were loaded afterwards to shear failure.

3.2 Observations on independent fire tests with more or less identical hollow core cross section

In 16 tests of the reported 42 tests a more or less identical cross section was used. The cross section as depicted in Figure 6 is a hollow core slab with depth between 260-275 mm and contains 5 cores. The total web width varied between 233 mm and 370 mm, and the amount of prestress from 312 mm² to 930 mm². The graph gives an outcome of analysis of fire resistance time versus shear load as a function of the amount of prestress and web width in the slab cross section. Particularly 11 tests are carried out using 558 mm² (6 strands 12.5). These fire tests are from the researches RUG (H7, H8, H9, H102), VTT (H39, H45, H48, H58), TNO (H114, H115, H116, H117), ITB (H130, H131), and SPTRI (H142).

There are clearly some (interacting) tendencies when these independent researches are compared. At first, it can be observed from the graph that when a lower shear load is applied in the fire test, a longer fire time is achieved as comparable data points go down with increasing time. Secondly, when a larger web width is used or/and connection reinforcement is included in the test floor, the shear capacity is higher. At the same, it can be seen from the data points in the graph that when floor systems are used, and especially connection reinforcement with the support, the shear capacity is higher compared to individual slabs. Finally, it emerges that applying more prestress improves the shear capacity.

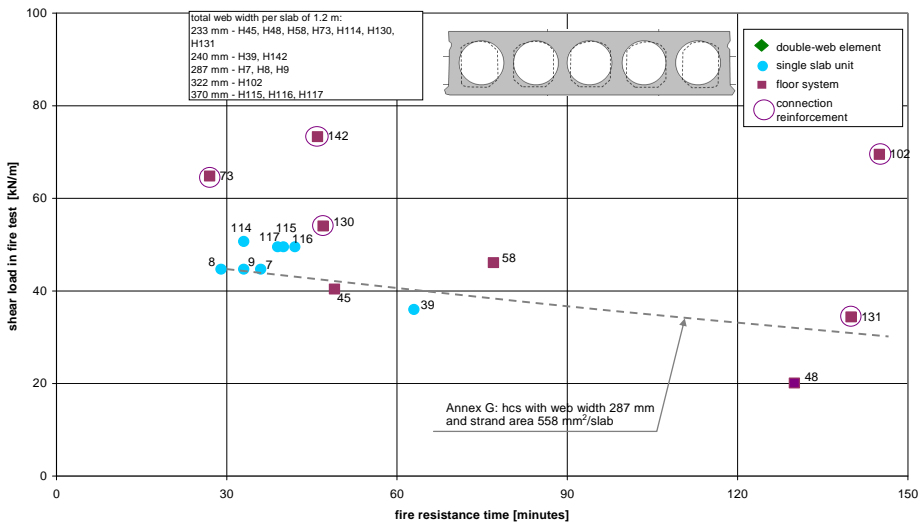


Figure 6. Shear load in fire tests with depth 260-275 with 5 cores in relation to fire resistance time

Table 1 Fire tests from database that exhibited shear and anchorage failure (all ISO fires)

H#	Test ID	Slab Depth [mm]	Slab Width [mm]	Top-ping [mm]	Strands per slab width [-]	Webs Unit System	Objective to fail in test/ Premature failure
H7	RUG 943 element I [1971]	265	1200	0	6ø12.5	Unit	No / Yes
H8	RUG 943 element II [1971]	265	1200	0	6ø12.5	Unit	No / Yes
H9	RUG 943 element III [1971]	265	1200	0	6ø12.5	Unit	No / Yes
H39	VTT PAL 2480 [1982]	275	1200	0	6ø12.5	Unit	No / Yes
H45	VTT PAL 4248 [1984]	265	2400	0	8ø12.5	System	No / Yes
H48	VTT PAL 4450 [1984]	265	1200	0	6ø9.3	System	No / Yes
H58	VTT PAL 566d [1985]	265	1200	0	6ø12.5	System	No / Yes
H73	VTT PAL 90228 [1990]	265	1200	0	6ø12.5/4ø9.3	System	No / Yes
H83	EMPA B2-2 [1995]	200	1200	0	12ø9.3	System	No / Yes
H85	EMPA B2-4 PL [1995]	200	1200	0	12ø9.3	System	No / Yes
H86	EMPA B3-1 [1995]	200	1200	0	12ø9.3	System	No / Yes
H96	DIFT X52650d [1998]	185	1200	0	8ø9.3	Unit	No / Yes
H97	DIFT X52650e [1998]	220	1200	0	8ø9.3	Unit	No / Yes
H98	DIFT X52650f [1998]	270	1200	0	4ø15.2/4ø12.5	Unit	No / Yes
H102	RUG 9158 [1999]	265	1200	30	10ø9.3	System	No / No
H104	TNO R-A200 [1999]	200	314	0	2ø9.3	2-webs	Yes / Yes
H106	TNO R-XB200 [1999]	200	316	0	2ø9.3	2-webs	Yes / No
H107	TNO R-VX265 [1999]	275	444	0	2ø12.5	2-webs	Yes / Yes
H108	TNO R-K400 [1999]	400	561	0	4ø12.5 - 4ø9.3	2-webs	Yes / Yes
H111	TNO R-K400-R [1999]	400	582	0	4ø12.5 - 4ø9.3	2-webs	Yes / Yes
H112	TNO R-K400-F [1999]	400	570	0	4ø12.5 - 4ø9.3	2-webs	Yes / Yes
H114	TNO U-VX265 [1999]	265	1200	0	6ø12.5	Unit	Yes / Yes
H115	TNO U-HVP260A-1 [2000]	260	1200	0	6ø12.5	Unit	Yes / Yes
H116	TNO U-HVP260A-2 [2000]	260	1200	0	6ø12.5	Unit	Yes / Yes
H117	TNO U-HVP260A-3 [2000]	260	1200	0	6ø12.5	Unit	Yes / Yes
H118	TNO U-K400 [2000]	400	1200	0	8ø12.5/8ø9.3	Unit	Yes / Yes
H119	TNO R-HVP260A23 [1999]	255	445	0	2ø12.5	2-webs	Yes / Yes
H120	TNO R-HVP260A20 [2001]	260	440	0	2ø12.5	2-webs	Yes / Yes
H121	TNO R-HVP260A17 [2001]	260	448	0	2ø12.5	2-webs	Yes / Yes
H122	TNO R-HVP260A14 [2001]	260	446	0	2ø12.5	2-webs	Yes / Yes
H123	TNO R-HVP260S23 [2001]	260	444	0	2ø12.5	2-webs	Yes / Yes
H124	TNO R-HVP260S17 [2001]	260	444	0	2ø12.5	2-webs	Yes / Yes
H125	TNO R-HVP260S11 [2001]	260	444	0	2ø12.5	2-webs	Yes / No
H126	TNO R-HVP260A23F [2001]	260	444	0	2ø12.5	2-webs	Yes / Yes
H127	TNO R-HVP260A20F [2001]	260	444	0	2ø12.5	2-webs	Yes / Yes
H128	TNO R-HVP260A17F [2001]	260	444	0	2ø12.5	2-webs	Yes / Yes
H130	ITB LP 534.2 [2001]	265	1200	50	10ø12.5	System	No / Yes
H131	ITB LP 534.3 [2002]	265	1200	50	6ø12.5	System	No / Yes
H132	ITB test 1 (F.18.1)	200	1200	0	6ø9.7	System	No / Yes
H133	ITB test 4 (F.19.1)	270	1200	50	7ø12.5	System	No / Yes
H138	DIFT DCPA [2004] (F.22)	265	1200	0	10ø12.5	System	No / Yes
H142	SPTRI P502076 SP3 [2005]	265	1200	0	10ø12.5	System	Yes / Yes
		255-275 = 30x			2-webs = 16x		
		185-220 = 8x			Unit = 12x		
		400 = 4x			System = 14x		

Table 2 Validation of fire test with EN1168 Annex G with concrete strength at 28 days

TEST ID		Fire test result		EN1168:A3	Fire test /
		Shear load [kN/m]	Time to failure [min]	Annex G Shear capacity [kN/m]	EN1168-G [%]
H7	RUG 943 element I [1971]	44.7	36	45,2	98,9%
H8	RUG 943 element II [1971]	44.7	29	45,3	98,7%
H9	RUG 943 element III [1971]	44.7	33	40,7	109,8%
H39	VTT PAL 2480 [1982]	36.0	63	34,0	105,9%
H45	VTT PAL 4248 [1984]	40.4	49	25,4	159,1%
H48	VTT PAL 4450 [1984]	20.1	130	23,0	87,4%
H58	VTT PAL 566d [1985]	46.1	77	26,4	174,6%
H73	VTT PAL 90228 [1990]	64.8	27	47,1	137,6%
H83	EMPA B2-2 [1995]	35.1	49	32,9	106,7%
H85	EMPA B2-4 PL [1995]	35.8	75	29,5	121,4%
H86	EMPA B3-1 [1995]	28.6	97	15,1	189,4%
H96	DIFT X52650d [1998]	36.8	21	38,3	96,1%
H97	DIFT X52650e [1998]	37.7	26	42,2	89,3%
H98	DIFT X52650f [1998]	57.7	21	56,2	102,7%
H102	RUG 9158 [1999]	(27.2) 69.5	(120) 145	56,9	122,1%
H104	TNO R-A200 [1999]	31.2	96	29,4	106,1%
H106	TNO R-XB200 [1999]	(32.9) 63.6	(120) 125	34,2	186,0%
H107	TNO R-VX265 [1999]	48.6	35	37,2	130,6%
H108	TNO R-K400 [1999]	89.5	60	90,9	98,5%
H111	TNO R-K400-R [1999]	86.3	30	91,0	94,8%
H112	TNO R-K400-F [1999]	112.3	24	91,3	123,0%
H114	TNO U-VX265 [1999]	50.7	33	42,8	118,5%
H115	TNO U-HVP260A-1 [2000]	49.5	40	56,3	87,9%
H116	TNO U-HVP260A-2 [2000]	49.5	42	55,5	89,2%
H117	TNO U-HVP260A-3 [2000]	49.5	39	55,9	88,6%
H118	TNO U-K400 [2000]	93.8	33	93,2	100,6%
H119	TNO R-HVP260A23 [1999]	51.0	55	54,4	93,8%
H120	TNO R-HVP260A20 [2001]	43.0	56	51,4	83,7%
H121	TNO R-HVP260A17 [2001]	35.5	114	44,5	79,8%
H122	TNO R-HVP260A14 [2001]	29.0	123	42,9	67,6%
H123	TNO R-HVP260S23 [2001]	50.9	48	50,7	100,4%
H124	TNO R-HVP260S17 [2001]	37.2	45	51,4	72,4%
H125	TNO R-HVP260S11 [2001]	(24.5) 32.2	(120) 123	35,9	89,7%
H126	TNO R-HVP260A23F [2001]	48.9	49	54,2	90,2%
H127	TNO R-HVP260A20F [2001]	42.6	50	54,1	78,7%
H128	TNO R-HVP260A17F [2001]	35.8	99	46,7	76,7%
H130	ITB LP 534.2 [2001]	54.0	47	58,0	93,1%
H131	ITB LP 534.3 [2002]	34.4	140	35,9	95,8%
H132	ITB test 1 (F.18.1)	27.5	35	26,7	103,0%
H133	ITB test 4 (F.19.1)	64.2	65	61,9	103,7%
H138	DIFT DCPA [2004] (F.22)	58.3	25	58,1	100,3%
H142	SPTRI P502076 SP3 [2005]	73.3	46	51,7	141,8%
				Avg =	107.0%
				CoV =	26.5%

4 VALIDATION ON EN1168:A3 ANNEX G WITH 42 FIRE TESTS

Despite the fact that it is well known that in fire tests redistribution between slabs and even between webs within the slabs is important to increase the fire resistance, the fire tests on double-web hollowcore elements are not neglected in this meta-analysis. Main reason is that this study is by definition a meta-analysis taking into account all different independent research studies. Accordingly, the double-web results make this meta-analysis richer and the outcome more reliable. It is however stated by the authors that there is no practical use for individual double-web hollow core elements in construction practices.

4.1 Recalculation of fire resistance regarding shear and anchorage capacity all 42 fire tests

Table 2 presents the results of fire tests that have been recalculated using the concrete strength at 28 days. When in the meta-analysis the shear and anchorage capacity was evaluated, it was done such that at the time the fire test collapsed the shear capacity was calculated. So, when in fire test H39 (VTT 2480 [1982]) the fire test ended at 63 minutes, the shear capacity at 63 minutes of fire loading was calculated (34.0 kN/m) and evaluated against the shear load present at support (36.0 kN/m) leading to a quotient of 105.9%.

It is concluded from the meta-analysis that the EN1168:A3 Annex G calculated capacities are on average 7.0% higher (107.0%) than the average capacities directly obtained from fire tests. The coefficient of variance (CoV) is 26.5%. Hence, it can be concluded that the EN1168:A3 Annex G formula is safe.

4.2 Recalculation of fire tests – distinction in element geometry used in fire test

In the practical application of a hollow core slab, the hollow core slab is always applied in a floor system; where the joints are cast to ascertain cooperation and redistribution between the slabs. From fire tests it is evident that a system performs better than a single unit or double web element. Therefore, the fire tests shown in Table 1 and Table 2 were evaluated against the type of element used in the test and presented in Figure 7 by using different markers. This Figure shows on the horizontal axis the shear load in kN/m at the support in the small-scale fire test that led to shear failure. On the vertical axis the calculated capacity of EN1168 Annex G is shown. The grey line at 45 degrees indicates where V_{firetest} equals V_{AnnexG} . The area above this grey line represents unsafe results as the experimentally obtained capacity is lower than the calculated capacity. On the contrary, the area under this line contains safe results. In addition to the grey line, two dashed lines are drawn that indicate a coefficient of variance (CoV) of 15%. This 15% is about twice the variance one would find in a normal shear tests under ambient conditions.

The following can be concluded from the graphs with respect to element geometry and height, when in accidental design the 28-day strength is used:

- 16 out of 42 fire tests were conducted on simply supported double-web elements. On average, the fire test results are 98.2% of the calculated shear capacity. The formula is 1.8% on the unsafe side for double-ribbed elements. The CoV is higher, namely 29.5% and results are more on the unsafe side than the safe side. The scatter can be explained by the fact that no redistribution takes place outside the two webs, and in these double-web elements variation of geometry and heat transfer in furnace have a bigger influence than on full slabs.
- 12 out of 42 fire tests were conducted on simply supported full slab unit. On average, the fire test results are 98.8% of the calculated shear capacity. The formula is 1.2% on the unsafe side for single slabs. The CoV is only 9.6%, which is actually in the same order of magnitude of shear tests loaded under ambient conditions under Annex J.
- 14 out of 42 fire tests conducted on floor system with slab units tied together. On average, the fire test results are 124.0% of the calculated shear capacity. The formula is 24.0% on the safe side for hollow core elements applied in floor systems. The CoV is 25.9%, and there are no

datapoints outside the 15% CoV in the unsafe zone. The high variance comes from the fact that some tests are far more on the safe side, which is actually good. It is clear that the formula does not account for all positive effects of a floor system; this can be seen as additional safety.

- The 4 tests on 400 mm hollow core slab height and 8 tests on 185-220 mm hollow core slab height show the same dispersion around the theoretical line as the 30 255-275 mm height fire tests. Hence, the EN1168:A3 Annex G is valid for heights up to 400 mm as covered by EN1168.

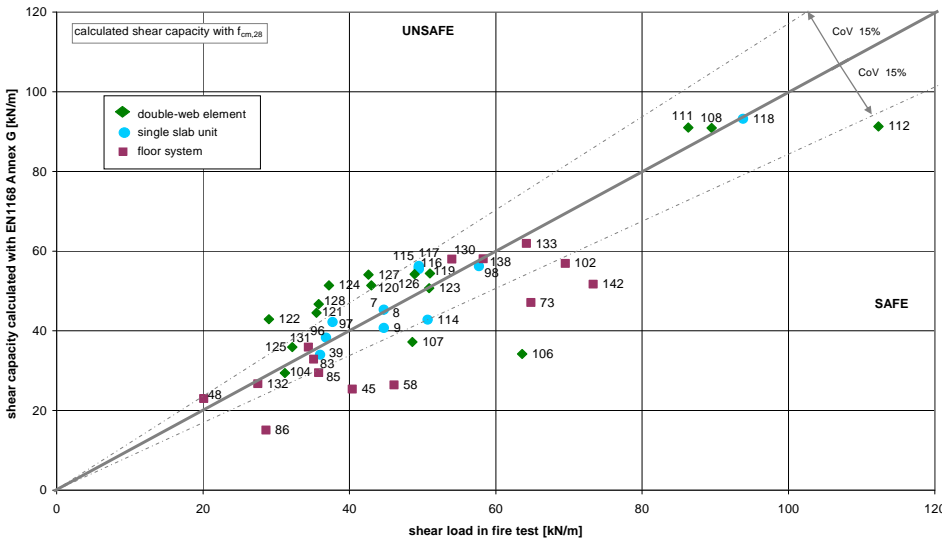


Figure 7. Relation shear capacity from fire test versus shear capacity calculated with EN1168 Annex G

5 CONCLUSIONS

- The shear capacity obtained from all 42 small-scale ISO fire tests on double-web hollow core elements, single hollow core slab units and hollow core floor systems, and using the 28-day strength of concrete, is on average 7.0% (107.0%) higher than the calculated shear and anchorage capacity calculated with Annex G of EN1168:A3.
- The validated fire tests confirm that the shear capacity increases when a larger web width is used or/and connection reinforcement is included in the test floor. Also, when the amount of prestressing strands in a hollow core is increased, the shear capacity improves. When a lower shear load is applied in the fire test, a longer fire time is achieved.
- In practical applications, the hollow core slab is always applied in a floor system. In a system the joints are cast to ascertain cooperation and redistribution between the slabs. The shear capacity obtained from 14 ISO fire tests on hollow core floor systems is on average 24.0% (124.0%) higher than the calculated shear-anchorage capacity with formula of EN1168:A3 Annex G.
- EN1168:A3 Annex G does not account for all the positive effects of the shear capacity of a floor system. These additional positive effects do give significant additional safety on the shear capacity and confirms that in practical applications shear hardly governs floor design [6].
- EN1168:A3 Annex G is valid for all hollow core slab heights covered by EN1168.

Overall, it is concluded that for accidental design situations - on the basis of a meta-analysis on 42 small-scale ISO fire tests conducted between 1966 and 2010 on double-web hollow core elements, full hollow core slab units, and hollow core floor systems - the shear and anchorage resistance of precast hollow core floors under fire calculated according to EN1168:A3 Annex G is significant safe. Hence, the formula given in the hollow core product standard can be used for daily construction design practices.

REFERENCES

- [1] CEN, EN1992-1-1 EC2: "Design of concrete structures. Part 1-1: General rules and rules for buildings", 2004.
- [2] CEN, EN1168:A3 "Precast concrete products – Hollow core slabs" - *Annex G: Resistance to fire*, 2011.
- [3] CEN/TC229/WG1/TG1, "Background report on Annex G of EN11682, February 2010.
- [4] Van Acker, A., "Shear resistance of prestressed hollow core floors exposed to fire". *Structural Concrete*, Volume 4, Issue 2, pp. 65 –74, 2003.
- [5] Hietanen, T. "Fire tests for Finnish hollow core slabs". Published by the Association of the Concrete Industry of Finland, p. 17, May 1992.
- [6] Fellinger, J. "Shear and anchorage behaviour of fire exposed hollow core slabs", *PhD thesis Delft University of Technology*, ISBN 90-407-2482-2, p. 261, 2004.
- [7] Andersen, N.E., Lauridsen, D.H. "Hollow Core Concrete Slabs, Basismiddel project X52650", *Technical Report X 52650*, part 2, p. 29, 1999.
- [8] Bogogno, W., Fontana, M. "Versuche zum Tragverhalten von Betonhohlplatten mit flexibler Auflagerung bei Raumtemperatur und Normbrandbedingungen". *Institut für Baustatik und Konstruktion*, ETH Zurich, p. 246, 1996.
- [9] Jensen, J.F. "Huldæk og Brand - dokumentation vedrørende forskydningskapacitet". *Udarbejdet for Betonelement-Foreningen, Birch & Krogboe A/S*, p. 24, 2005.
- [10] C.G. Bailey, Lennon "Full-scale fire tests on hollowcore floors". *The Structural Engineer*, 18, pp. 33-39, March 2008.
- [11] Van Acker, A. "Fire safety of prestressed hollowcore floors, shear capacity of hollow core floors". *CPI Concrete Plant International*, 1, pp. 182-196, 2010.

ACKNOWLEDGEMENTS

The support of BIBM for this research project is gratefully acknowledged. The authors are grateful to Manhal Said for the programming of EN1168:A3 Annex G and the many shear and anchorage calculations provided for this paper.

TESTING OF FULL-SCALE RC FRAME UNDER SIMULATED FIRE FOLLOWING EARTHQUAKE

Umesh Kumar Sharma*, **Virendra Kumar***, **Bhupinder Singh***, **Pradeep Bhargava***,
Yogendra Singh*, **Praveen Kamath***, **Asif Usmani****, **Jose Torero****, **Martin Gillie****,
Pankaj Pankaj**

* Indian Institute of Technology Roorkee, Roorkee – 247667
e-mails: umuksh@rediffmail.com, kumarvirendra57@gmail.com, bhupifce@iitr.ernet.in,
bhpdpfce@iitr.ernet.in, yogenfeq@iitr.ernet.in, praveen.kamath@hotmail.com

** The University of Edinburgh, School of Engineering, The King's Buildings, Mayfield Road.
Edinburgh, EH9 3JL
e-mails: asif.usmani@ed.ac.uk

Keywords: Fire following earthquake, multi-hazard events, RC structures.

Abstract. *In present study, a full-scale testing of reinforced concrete (RC) frame sub-assembly has been investigated under fire subsequent to simulated seismic loading. The RC frame sub-assembly was designed for 60 minutes fire resistance per relevant Indian code. First part of the sequential loading consisted of a quasi-static cyclic lateral loading on the test frame so as to provide a reasonable simulation of the damage expected to occur under real seismic loading. The quasi-static lateral loading history of the frame sub-assembly corresponds to life safety level of structural performance. In the second part of the test, a compartment fire was ignited to the pre-damaged test frame for one hour duration simulating fire following earthquake (FFE) scenario. The test frame was instrumented exhaustively with sufficient numbers of different types of sensors. The first cracking was observed at the end joints of the roof beams after the frame experienced a 30 mm cyclic lateral displacement. After the mechanical load test, the RC frame was exposed to one hour compartment fire. One hour heating and eleven hour cooling was tracked and temperatures were recorded. A knocking sound was heard from the fire compartment after the fire ignition which could be attributed to the spalling of concrete from the roof slab. Severe thermal micro-cracks, massive spalling with exposed reinforcement in roof slab and excessive degradation of the concrete at a number of locations of the frame sub-assembly were observed during visual inspection after the fire test. The test results developed understanding of the behaviour of RC frame sub-assembly in FFE.*

1 INTRODUCTION

A fire by itself poses a high risk scenario on buildings and structures, but it may be further exacerbated by another hazardous event(s) such as an earthquake or explosions. These are learnt from the past fire following earthquakes(FFE) accidents, like 1906 San Francisco, 1923 Tokyo, 1989 Loma Prieta, 1994 Northridge, 1995 Kobe earthquakes or tragic event like collapse of World Trade Centre on September 11, 2001. The impact of many more fire following earthquakes on the buildings and urban environments were analyzed in detail [1, 2]. The consequences of losses in terms of financial losses as well as human fatalities imposed by fires that follow an earthquake are much greater than that caused by the earthquake itself [3]. Generally, the conventional design practices adopted by structural engineers are sensitive to the effect of earthquake and fire loads acting on a structure separately. Relatively little or no consideration is given to the possibility of both of these loads acting sequentially and their serious

consequences thereof. Hence, a comprehensive research effort is required to explore adequately the challenges posed by FFE events, some of which are discussed in literature [4, 5]. Very few investigations on the performance of buildings under a combination of these events are available for general practices in design of structures. Also, the current design guidelines never practice to consider two extreme events occurring consecutively on a structure. The development of simplified design tools that predict the fire performance of structures is of utmost importance to practicing structural engineers. Thus, it is important to explore such feasibility in the design of a building constructed in especially in seismic areas. The stability of buildings under FFE events is extremely necessary to avert a major catastrophe. Here, besides satisfying the structural design requirements for gravity loads including seismic and fire loads, buildings should be designed to withstand the FFE events for certain minimum duration of time, which is critical for the safe evacuation of the buildings. In present testing, a roof displacement corresponding to the life safety level of structural performance was initially aimed through simulated cyclic quasi-static lateral loading to the test frame. The mechanical loading to the RC frame was followed by a compartment fire of one hour duration to simulate the fire following earthquake. The test results have concluded with several important findings that may be very useful for further research and design of the structures.

2 EXPERIMENTAL PROGRAMME

2.1 RC Frame Construction

A two phase full-scale test of RC frame sub-assembly was conducted to get some beneficial outcomes over the standard small-scale fire tests. The behaviour of the entire frame may help to resolve several issues concerned with the fire following earthquake conditions. The present test frame sub-assembly of full-scale was constructed at I. I. T. Roorkee. Basically, it has plan and elevation of symmetrical 4-storeyed RC framed building from which, a sub-assembly of a single frame was considered for simplicity as shown in Figure 1. The test frame sub-assembly had four columns (300 mm x 300 mm), four roof beams (230 mm x 230 mm), four plinth beams (230 mm x 230 mm) and a roof slab (120 mm thick) with an all around projection 500 mm of beams and roof slab to get proper joint behaviour. All the elements of the frame sub-assembly were cast monolithically with the column fixity at the base into a raft slab [6]. At the time of the lateral load tests, the average cube compressive strength of concrete in the test frame was 33.6 MPa. The ductile design detailing of the frame sub-assembly was made per the recommendations of IS 13920:1993 [7]. As the test frame is a part of RC building of G + 3 floors, an equivalent gravity load of the upper floors were computed first. Now, these gravity loads were distributed on the top of the four columns of the sub-assembly with the help of an additional orthogonal arrangement of rolled steel I-sections, which served as a loading platform. It was kept in mind that as per recommendations of the Indian seismic design code, IS 1893 (Part-1): 2002, only 25 % of the assumed imposed uniformly distributed floor load of 2 kN/m² is to be considered for seismic weight calculations [8].

2.2 Instrumentation

A comprehensive instrumentation was planned for the test frame to record the data for the two-phased test: Simulated equivalent lateral cyclic loading followed by a fire test. The strain gauges and thermocouples were installed at the pre-decided critical locations of the frame sub-assembly before pouring the concrete. High temperature strain gauges as well as ambient temperature strain gauges were mounted on the steel reinforcement with appropriate high performance adhesive at 154 different locations on longitudinal rebars of the beams, columns and roof slab of the frame sub-assembly. Moreover, 301 K-type thermocouples were embedded inside the concrete at different sections of the beams, columns and roof slab of the test frame to record the temperature profile in the concrete during the fire test. Three sections in each member i.e. near end support sections and at midspan / mid-height section were chosen for embedding the thermocouples.

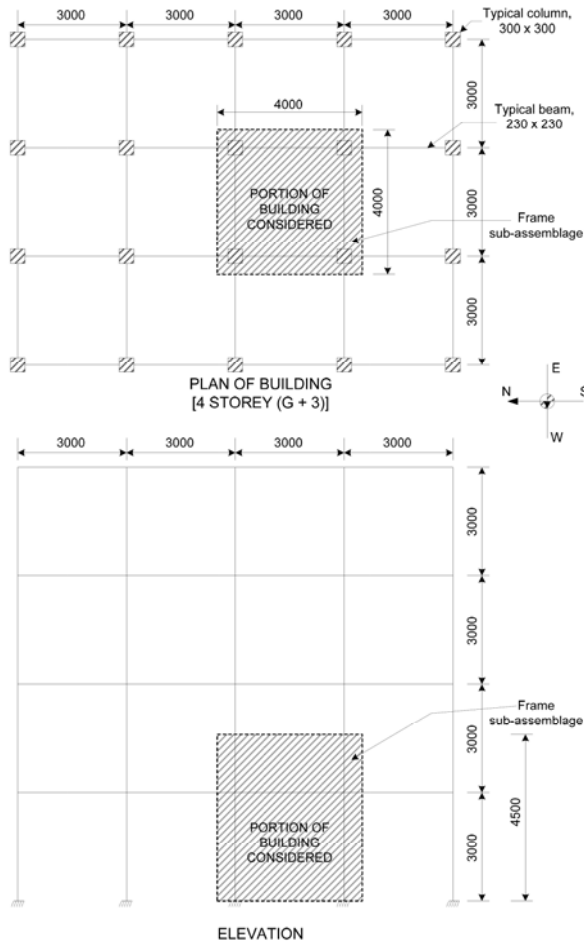


Figure 1. Building configuration and the frame sub-assembly.

Each section consisted of nine thermocouples. Five thermocouples were embedded along the depth in the roof slab at five different locations. Additionally, sufficient numbers of mineral insulated (MI) steel type thermocouples were also placed inside the fire compartment for capturing the gas temperature profile during fire test.

On the other hand, a secondary steel frame in the periphery of the test frame was erected to support the Linear Variable Displacement Transducers (LVDT). This independent steel frame helps to take the orthogonal horizontal displacement of the test frame as well as the vertical displacement of the roof beams and roof slab at the designated locations so that it would be free of any localized frame deflections. The imposed cyclic lateral loads on the test frame were measured using pressure sensors mounted on the hydraulic rams and the corresponding displacements at the roof level were recorded using LVDTs. All the instruments and sensors were ascertained for satisfactory functioning before the frame test.

2.3 Mechanical loading

A simulated cyclic lateral load was applied on the test frame in a quasi-static manner using load-controlled mode facilitated by a pair of double-acting hydraulic rams acting in tandem with each other against a reaction wall. The desired nominal loading history of the frame sub-assembly corresponding to life safety structural performance level of FEMA 356:2000 is presented in Figure 2 [9]. The maximum targeted roof level lateral displacement of the test frame was 76 mm which corresponds to a roof drift ratio of 2 %. To ensure a quasi-static loading, it was envisaged that a typical loading cycle of Figure 2 would be completed over a time interval of about 300 seconds.

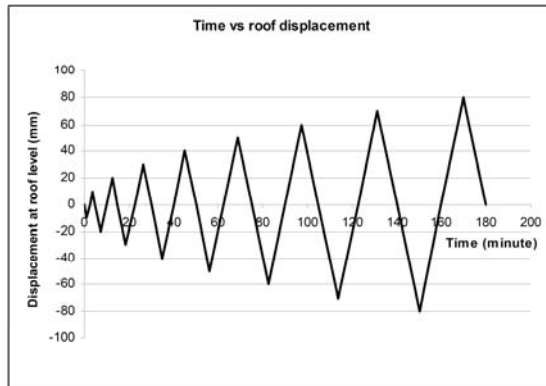


Figure 2. Proposed loading history of the test frame.

2.4 Fire test

Before exposing the pre-damaged frame to fire, mock fire tests were conducted in a brick masonry fire compartment of size 3 m x 3 m x 3 m with a window of 1 metre height by 3 m length. A tray burner with a kerosene oil-pool of size 1 m x 1 m and a depth of 0.05 m was placed at the center of the fire compartment. The maximum temperatures in the range of about 1327 °C were recorded after 21st minutes. The peak burning rate for the chosen opening configuration was approximately 0.117 kg/m²/s for maintaining a post flashover temperature of above 1000°C within 5 minutes after fire. In the fire test of the pre-damaged frame sub-assembly, on similar pattern, a burner of 1m x 1m plan dimensions with a depth of 0.05 m was placed centrally inside the fire compartment. Four fire proof panels were fabricated separately and assembled together around the RC test frame sub-assembly as shown in Figure 3(a). The secondary frame of four detachable panels made of iron angle section and mild steel sheet was erected. These detachable panels were initially covered with a sheet of ceramic wool (0.0254 m thick) and then blocks of ceramic wool of size 0.3 m x 0.3 m x 0.20 m (thick) were attached to the panels. After the cyclic loading, the pre-damaged test frame was exposed to compartment fire as schematically shown in Figure 3(b). The desired time-temperature behaviour as achieved in mock fire tests was obtained precisely and a full blown fire with flashover was attained within 5-7 minutes of ignition.



Figure 3 a). Pre-loaded frame before fire b).Fire test.

3 TEST RESULTS AND DISCUSSIONS

The application of mechanical loading history was achieved as close as possible to the desired history shown in Figure 2. The targeted lateral displacement in the first cycle of loading was 10 mm and this displacement was incremented by 10 mm in successive loading cycles. The loading cycles of the test frame were subjected to a displacement of 76 mm in order to induce mechanical pre-damage corresponding to Life safety level of structural performance per FEMA 356 [9]. As expected, the first crack was observed at the end sections (near joints) of the roof beams oriented along N-S direction at a lateral displacement of 35 mm (roof drift ratio of 0.92 %) corresponding to a base shear of 185 kN. Cracks were more pronounced at different location in roof beams, columns and plinth beams in successive lateral loading cycles. Some spalling in roof beams were also visualized at a roof drift ratio 2 % with widening of the cracks in the columns. The test was terminated at a roof displacement of 80 mm (roof drift ratio of 2.11 %) corresponding to a base shear of 267 kN. Figure 4 shows the hysteretic curve of the test frame which depicts a maximum displacement of 95 mm in the “push” cycle and 85 mm in the “pull” cycle, recorded corresponding to base shears of 316 and 267 kN, respectively. Stiffness degradation and pinching of the hysteresis loops between successive cycles of loading is seen in Figure 4 though the hysteresis loops continued to remain stable without any significant degradation of strength. The test frame did not suffer any significant structural damage.

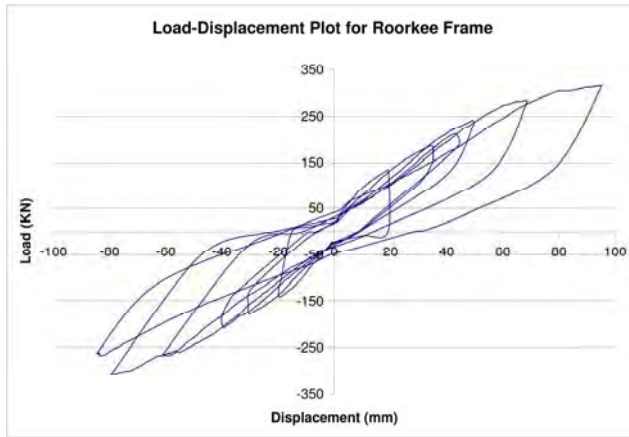


Figure 4. Hysteretic curve of the test frame.

Figure 5(a) shows a typical gas temperature history recorded inside the fire compartment. However, a gas temperature of above 1000 °C was attained within 5 minutes after ignition of fire indicating the attainment to flashover. Figure 5(b) depicts the nomenclature used for identifying the locations in the RC frame. The sound of concrete spalling off from the roof slab was heard after 5 minutes of ignition, which continued for another 15 minutes. The spalling sound corresponded to a compartment temperature between 300 to 400 °C. The structure showed no signs of collapse during and after the fire test. Unfortunately, the data acquisition of vertical displacements of slab became unsuccessful due to instrument malfunctioning when exposed to a high temperature environment. A maximum vertical residual displacement of 46 mm was recorded in the roof slab.

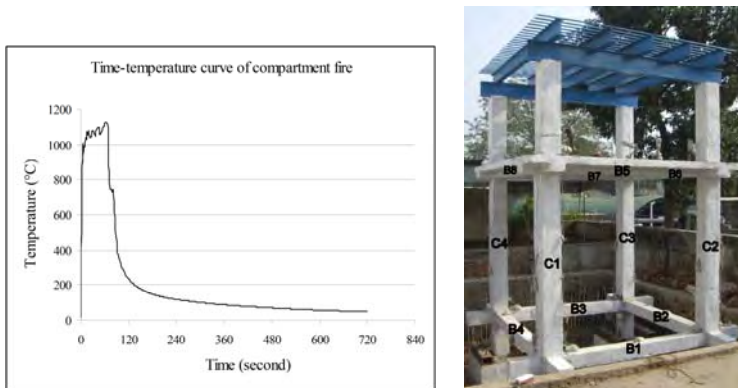


Figure 5 (a). Time-temperature plots for the compartment fire. (b). Sub-assembly nomenclature.

Significant amount of cracking and spalling in columns and beams can be visualized from the picture shown in Figure 6(a). Many more thermal micro-cracks were formed on the exposed surface of the columns in addition to the longitudinal cracks. The soffit of the beam spalled with partial exposure of the longitudinal and transverse reinforcements. Figure 6 (a) shows the beams and columns after the fire test and depicts the signature of the structural stability exhibited by the RC frame sub-assembly after the

fire test. Extensive damage was registered in the roof slab in terms of spalling of concrete and resultant exposure of reinforcement. This was mainly due to the movement of fire plume towards the ceiling causing a rapid flow of hot gases in the radial direction termed as a ceiling jet. The extent of spalling, which exposed the bottom reinforcement in some portions of the roof slab is explained in Figure 6 (a). The pictures shown in Figure 6 (b) also add on to show the extent of the spalling. Despite this, the test frame withstood one hour fire exposure without losing its structural integrity in terms of complete collapse.



Figure 6 (a). Frame sub-assembly after the fire test (b). Extent of spalling (debris) on compartment floor.

3.1 Temperature histories

The typical temperature profile and gradients of the sub-assembly of the test were recorded for heating and cooling regime and then redrawn to study the thermal behaviour on the structural members. The following were the depths of temperature recording gauge points from the exposed surface of the sub-assembly where thermocouples were embedded into the concrete.

Roof beams: 5 mm, 25 mm, 115 mm, 205 mm and 225 mm.

Columns: 5 mm, 40 mm, 150 mm, 260 mm and 295 mm.

Roof slab: 5 mm, 30 mm, 60 mm, 90 mm and 115 mm.

Figure 7(a) shows typical temperature distribution for column C3 at the mid-height section. The maximum temperatures recorded at the mid-height of column C3 along N-S direction were 924 °C, 587 °C, 221 °C, 25 °C and 103 °C after 52, 56, 128, 718 and 286 minutes of fire initiation respectively. Overall, a maximum temperature of 924 °C was recorded on the surface of column at the mid-height section. The surfaces of the columns were exposed to temperatures above 500°C for about 58 minutes during the fire. Similar types of observations were made for other columns. It has been observed that the temperature gradients at the mid-height were critical after 30 minutes of fire ignition as indicated in Figure 7(b). The maximum recorded temperature was about 924 °C at the surface whereas the temperature at the mid-span section never exceeded 221 °C. Therefore, the variations in temperature across the depth at mid-height sections were quite high. Degradation of concrete was prominently observed at locations that experienced either high gradients or high temperature levels (above 600°C). However, despite a few localized failures caused by an accelerated heat transfer due to pre-damage, the

structural stability of the columns remained unaffected after the fire test. It was observed that the maximum temperature gradients were greater than $3.5\text{ }^{\circ}\text{C}/\text{mm}$ for the portion above mid-height section of the column. Degradation of concrete in the columns also corroborated the results of the recorded temperature gradients at the different locations.

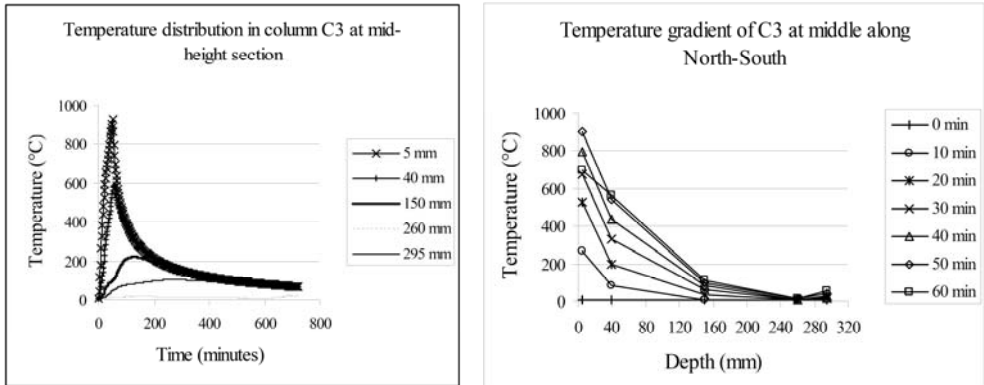


Figure 7(a). Time-temperature curves for column C3. (b). Temperature gradients at mid-height section for column C3

Typical temperature distributions in roof beam B5 are shown in Figure 8(a). The peak temperatures were $784\text{ }^{\circ}\text{C}$, $527\text{ }^{\circ}\text{C}$, $123\text{ }^{\circ}\text{C}$, $84\text{ }^{\circ}\text{C}$ and $76\text{ }^{\circ}\text{C}$ at the midspan section after 52, 54, 154, 284 and 282 minutes of fire ignition respectively. Overall, a temperature of $784\text{ }^{\circ}\text{C}$ was observed as the maximum on the surface at the midspan section of the roof beam. The temperature gradients at midspan section of roof beam B5 attained significant values gradually as fire progressed as evident from Figure 8(b). The maximum temperature recorded was about $784\text{ }^{\circ}\text{C}$ at the surface whereas the temperatures at the mid-height section were not more than $123\text{ }^{\circ}\text{C}$. Hence, the temperature variations across the depth of the beam section at right end section were quite appreciable at a time lapse of 20 minutes after the fire ignition. However, despite that all the roof beams remained intact and structurally stable. Every point of the roof beam had a maximum temperature gradient of above $6.45\text{ }^{\circ}\text{C}/\text{mm}$ which caused severe deterioration of the concrete in these beams. Apparently, the roof beam suffered a maximum degradation of the concrete which was clearly evident during the visual inspection. Concrete degradation was also observed at several points where the temperature crossed $600\text{ }^{\circ}\text{C}$.

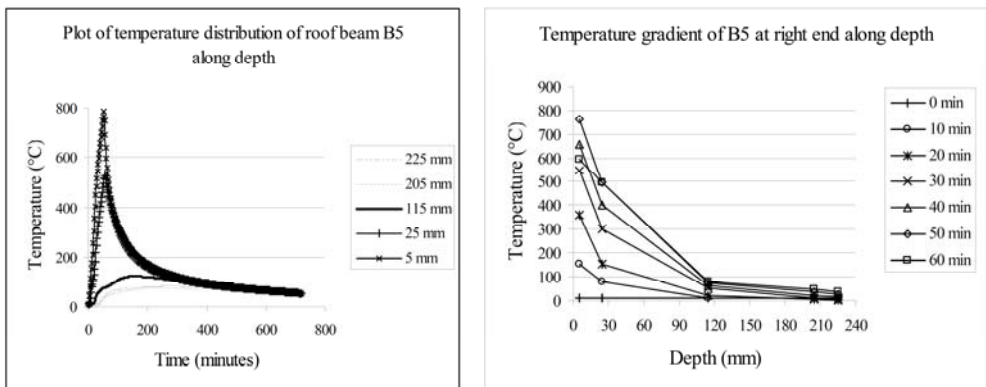


Figure 8(a). Time-temperature curves for roof beam B5. (b). Temperature gradients at mid-section of roof beam B5.

Figure 9(a) shows typical temperature profiles of roof slab at the points located along North-side. The peak temperatures obtained at North side away from the window opening were 1062 °C, 777 °C, 1305 °C, 1220 °C and 1275 °C at 56, 60, 50, 56 and 56 minutes of fires, respectively. An absolute maximum temperature of 1038 °C was recorded on the soffit of the roof slab at the centre. Considerable thermal gradients were observed at many locations in the roof slab. A maximum value of 13.55 °C/mm was noted, which explains the reason for severe spalling of the cover concrete in roof slab. It was noticed that the temperature gradients along North side and near the central location were most critical for the roof slab as shown in Figures 9(b). A massive concrete spalling all along the soffit of the roof slab was observed, which is attributed to a high temperature gradient coupled with high pore pressure. The maximum temperatures recorded at few locations in the slab were as high as 1305°C after 50 minutes of fire. Despite the considerable spalling, roof slab remained structurally intact and continued to carry superimposed loads.

It is a well known fact that the strength of the steel rebars decreases with increase in temperature and yielding of the rebar occurs even at lower temperature rise under sustained load. Most of the strain gauges in the sub-assembly of the RC frame close to exposed surface of the fire compartment de-bonded at high temperatures. Analysis and interpretation of strain data was a complex task. As expected, many strain gauges malfunctioned at high temperatures and questioned the accuracy of obtained values. However, the results of measured strain at few locations were very encouraging and traced the behaviour of the frame sub-assembly in fire.

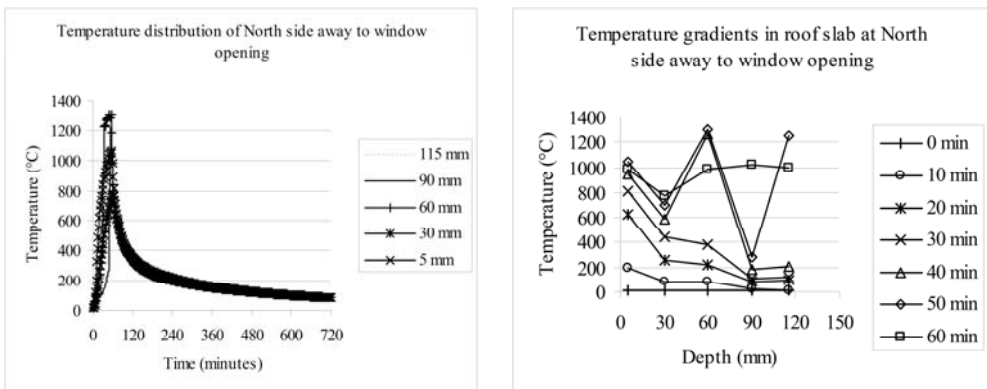


Figure 9(a). Time-temperature curves for roof slab. (b). Temperature gradients roof slab.

4 SUMMARY AND CONCLUSIONS

The testing of full-scale RC frame sub-assembly under quasi-static lateral loading applied as simulated earthquake loading followed by compartment fire has been presented. As expected, the test frame was able to withstand a pre-damage corresponding to life safety structural performance level without collapse and with appearance of some cracks in roof beams and columns. The designed flashover temperature of above 1000 °C was obtained within 5 minutes of fire ignition through the mock tests and the same was implemented to the pre-damaged test frame successfully. Maximum gas temperature above 1100 °C was attained inside the fire compartment which is attributed to a good insulation provided by thick ceramic wool. It was seen that the highest temperature attained in the concrete sub-assemblies of the test frame was 1038 °C in the roof slab. In columns, a maximum temperature of 1021 °C was observed on the surface at the mid-height section. The sound of concrete spalling off from the roof slab was heard after 5 minutes of ignition, which corresponded to temperatures between 300 to 400 °C. A non-uniform temperature gradient leading to a zone of severe temperature is considered to be the main cause of massive concrete spalling as observed in the roof slab. This was quantified to be detrimental for the

structure causing a significant damage to the bottom reinforcement of the roof slab, eventually degrading its strength and stiffness further questioning the feasibility of retrofit or re-occupancy. An abrupt change was observed in the measured strain values which were proportional to increase in temperature. The maximum temperature gradients calculated were greater than 3.5 °C/mm and corroborated the results causing major degradation of the concrete sub-assembly. A maximum temperature gradient value of 13.55 °C/mm was observed on the roof slab, which justifies severe spalling of the cover concrete. Thus, the full-scale testing of the RC sub-assembly justified the structural stability of the frame without collapse despite it being subjected to the fire followed by a quasi-static lateral cyclic mechanical loading.

Acknowledgements

The present research work has been funded under the U.K.-India Education and Research Initiative (UKIERI) project. Thanks to the Department of Civil Engineering, Indian Institute of Technology Roorkee for the laboratory facilities to carry out the testing.

REFERENCES

- [1] Scawthorn C., Eidinger J.M. and Schiff, A.J., “*Fire Following Earthquake*”, ASCE Publications, 2005.
- [2] Botting R., University of Canterbury, *The Impact of Post-Earthquake Fire of the Built-Urban Environment*, Fire Engineering Research Report 98/1, 1998.
- [3] Mousavi S., Bagchi A. and Kodur V.K.R., “Review of Post-Earthquake Fire Hazard to Building Structures”, *Canadian Journal of Civil Engineering*, 35: 689-698, 2008.
- [4] Robertson J. and Mehaffey J., “Accounting for Fire Following Earthquakes in the Development of Performance Based Building Codes”, *12th World conference on Earthquake Engineering*, Auckland, 2000.
- [5] Usmani A.S., “Research priorities for maintaining structural fire resistance after seismic damage”, *The 14th World Conference on Earthquake Engineering*, Beijing, China, October 12-17, 2008.
- [6] Indian Standard, *Code of Practice for Plain and Reinforced Concrete*, IS 456:2000 (fourth revision), 2000.
- [7] Indian Standard, *Ductile Detailing of Reinforced Concrete Structures Subjected to Seismic Forces*, IS 13920: 1993, 1993.
- [8] Indian Standard. *Criteria for Earthquake Resistant Design of Structures - General Provisions and Buildings*, IS 1893: (Part 1):2002, 2002.
- [9] FEMA. *Prestandard and commentary for the Seismic rehabilitation of buildings / FEMA 356*, Chapter 1: Rehabilitation Requirements, Table C1-3, pp. 14, 2000.

MECHANICAL PROPERTIES OF UNDAMAGED AND DAMAGED STEEL REBARS AT ELEVATED TEMPERATURES

Praveen Kamath*, Umesh K. Sharma*, Pradeep Bhargava*, N.M. Bhandari* and Asif Usmani**

* Indian Institute of Technology Roorkee, Roorkee - 247667

e-mails: praveen.kamath@hotmail.com, umuksh@rediffmail.com, bhdpdfce@iitr.ernet.in,
nmbcfce@iitr.ernet.in

** The University of Edinburgh, School of Engineering, The King's Buildings, Mayfield Road.

Edinburgh, EH9 3JL

e-mail: asif.usmani@ed.ac.uk

Keywords: Steel Rebars, Damage, Earthquake, Fire, Elevated Temperatures, Mechanical Properties.

Abstract. *Evaluation of mechanical properties of undamaged and damaged steel rebars at elevated temperature finds its applications in development of steel material models likely to be used in designing reinforced concrete structural members subjected to earthquake triggered fire. In the present experimental investigation, 84 rebar specimens (cylindrical) of length 700mm and diameters 8mm, 10mm, 16mm and 20mm were tested. Test specimens were prepared from the materials used in construction of 1:1 scaled reinforced concrete frame subjected to earthquake and fire. The specimens were initially stressed to a certain known limit (yield stress + 50% of yield stress) to simulate damage caused by an earthquake. After inducing the damage, they were exposed to a desired temperature level (Ambient, 250°C, 500°C and 750°C) in a circular furnace arrangement coupled with a 400 kN universal testing machine. The temperature was sustained inside the furnace for about 30 minutes to ensure a steady state heat transfer inside the specimen. The bars were then tested under uniaxial tensile loading conditions. The elongation was recorded by using two LVDTs fixed between gauge lengths of 265mm at the mid-height. Results obtained in the tests were then utilized to carry out regression analysis and propose various relationships: Tensile Strength, Peak-Strain, Elongation and Elastic Modulus vs. Temperature, Stress vs. Strain at elevated temperatures.*

1 INTRODUCTION

Fire and earthquake are often considered extraneous. Both are considered as distinct loading conditions when considered for design requirements. Fire following earthquake is a complex scenario, involving many sequential and situational components. The biggest threats to people's safety immediately after a significant earthquake are fire and explosions. [1] When considered precisely, fire becomes a major source for damages caused due to earthquake. Reckoning the properties of building materials used in earthquake prone zones are utmost important while designing the structures. Fairly good literature [2-5] is available on testing and mechanical properties of undamaged steel rebars at elevated temperatures whereas the information available on damaged steel rebars is scanty. A quantitative comparison of results reported by various authors is not feasible due to the differences in materials used and testing conditions. Analysis of reinforced concrete structures in context of fire following earthquake requires properties of damaged steel rebars at elevated temperatures. The damage induced by the earthquake is simulated in lab conditions by applying a preload in tension on rebars before subjecting to elevated temperatures. Behaviour of concrete and steel rebars at high temperature is important for predicting the response of reinforced concrete structures at elevated temperatures [3]. The deterioration of the mechanical properties

of yield strength and modulus of elasticity is considered as the primary element affecting the performance of steel structures under fire [4].

In the present experimental investigation, a number of steel rebar specimens were tested to reckon its tensile stress and strain. 8mm, 10mm, 16mm and 20mm diameter rebar specimens were considered for investigation, which were analogous to the diameter of rebar specimens used in construction of a full-scale RC test frame constructed and tested for fire following earthquake. Data from testing of each specimen were collected automatically using data acquisition systems. Effect of temperature on mechanical behaviour of FE 500 TMT steel rebars. It is seen that the yield strength and ultimate strength degrades when steel is exposed to elevated temperatures. However, an increase in yield strength is registered in steel upto a temperature of 300 degrees before it degrades.

2 EXPERIMENTAL PROGRAMME

An experimental investigation was conducted on 8, 10, 16 and 20mm diameter rebars as mentioned before. A specimen of length 700mm was chosen in order to ensure proper grip of jaws outside the furnace. A total gauge length of 265mm was considered for the measurement of expansion. The rebar specimens were exposed to three different temperature ranges: 20, 250, 500 and 750 °C. A heating rate of 5 °C / minute was employed to reach the target temperature. The target temperature was maintained constant for duration of 30 minutes in order to achieve a steady state in rebars. The specimen was loaded uniaxially in tension with a very low and constant loading rate (< 10 ton/min).

Three samples of each dia were tested at a particular temperature. Table 1 shows the experimental plan.

Table 1. Testing plan for undamaged and damaged rebars at elevated temperatures

Dia (mm)	Temperature				Total
	20°C	250°C	500°C	750°C	
8	3+3	3+3	3+3	3+3	24
10	3+3	3+3	3+3	3+3	24
16	3+3	3+3	3+3	3+3	24
20	3+3	3+3	3+3	3+3	24

2.1 Test Setup

A unique testing arrangement facilitated application of mechanical and thermal loads simultaneously. Figure 1 shows a schematic of the testing arrangement for steel rebars at elevated temperatures. A round electrical furnace with a 50mm diameter and 260mm long heating zone encapsulated the test specimen. An aluminium clamp arrangement was devised to capture the expansion between gauge lengths just outside the furnace. Measures were taken to insulate the arrangement from getting affected by heat. Figure 2 shows the tensile testing of steel at elevated temperature test in progress.

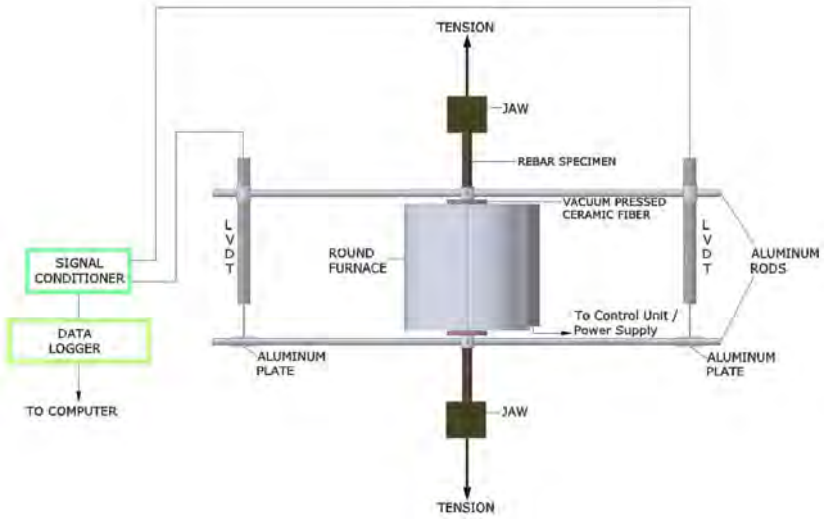


Figure 1. Steel Rebar Specimen Testing Arrangement at Elevated Temperature



Figure 2. Rebar test at elevated temperature in progress

2.2 Instrumentation

Two K-type thermocouples were positioned on top and bottom inside the furnace to monitor the temperature throughout the test. Loads were continuously logged at a frequency of 1 second using pressure sensors connected to the hydraulic supply unit of universal testing machine. Expansion was measured using two LVDTs positioned on either side across the gauge length of rebars. These LVDTs were capable of measuring an expansion of upto 100mm. Temperature, load and expansion data were collected at a frequency of 1 second using automated data acquisition system connected to a laptop computer.

3 RESULTS AND DISCUSSION

Results obtained from the tests exhibit a reduction in tensile strength, elastic modulus and strain at peak stress at elevated temperatures as it is more pronounced from available literature. The test is ultimately aimed at generating stress-strain profiles, effect of diameter, development of mechanical strains and other relationships for undamaged and damaged steel rebars at elevated temperatures. A detailed multiple linear regression analysis will be carried out on the obtained stress-strain data to propose empirical and normalized stress-strain models for undamaged and damaged reinforced concrete at elevated temperatures. Figure 3 shows typical time-temperature curves, to which the rebar specimens were exposed.

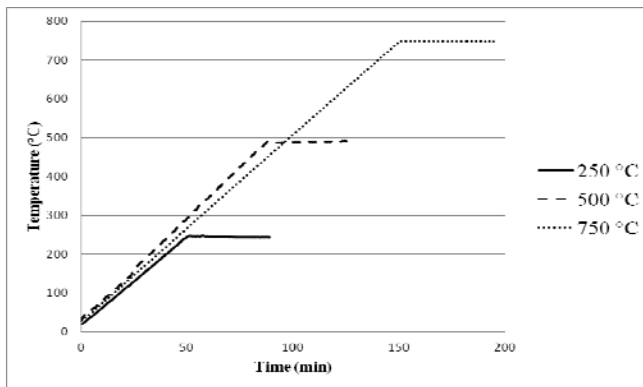


Figure 3. Typical temperature-time curves

3.1 Stress-Strain Relationships

Figure 4 (a), (b), (c) and (d) show the stress-strain diagrams for 8, 10, 16 and 20mm dia undamaged rebars subjected to 20, 250, 500 and 750 °C respectively. From the above plots, it can be clearly seen that the peak stress in 8mm dia and 10mm dia rebars did not show much degradation upto a temperature of 250 degrees. However, in case of 16mm and 20mm dia rebars, the peak stress showed a significant increase in peak stress at 250 °C as compared to 20 °C. Further, the peak stress in rebars of all dia exhibited an enormous degradation in peak stress at elevated temperatures. The ultimate strain in rebars of all dia increased with increase in temperature. This is attributed to the softening of rebars at high temperatures.

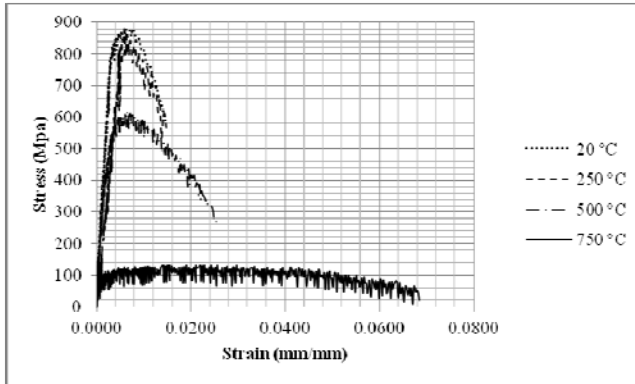


Figure 4 (a). Stress-strain curve for 8mm dia steel rebars

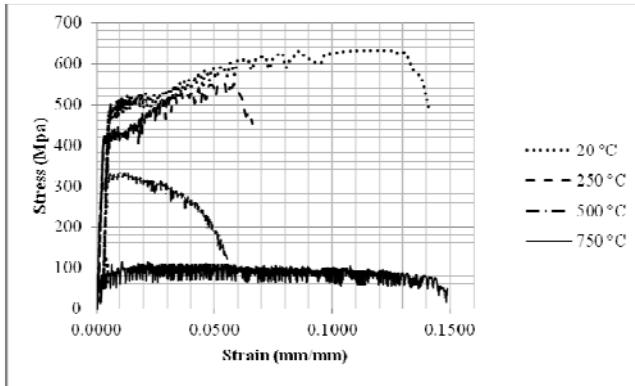


Figure 4 (b). Stress-strain curve for 10mm dia steel rebars

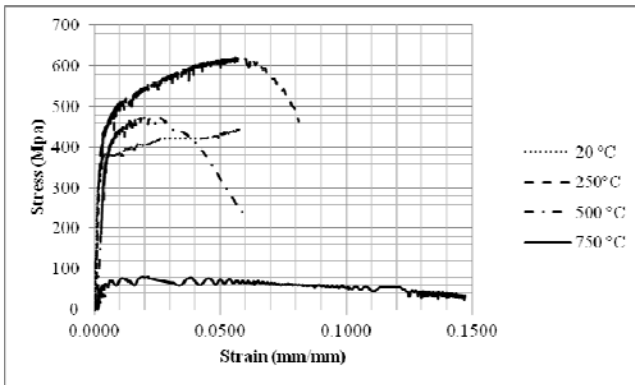


Figure 4 (c). Stress-strain curve for 16mm dia steel rebars

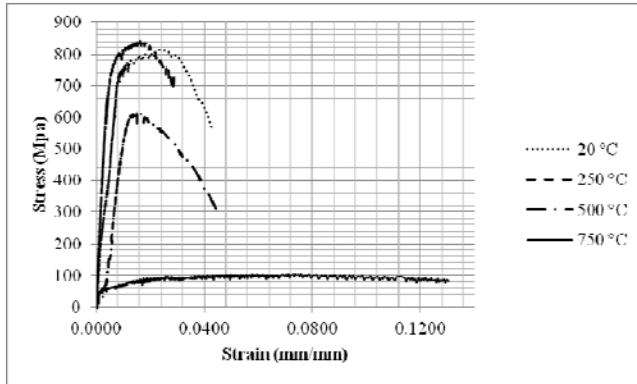


Figure 4 (d). Stress-strain curve for 20mm dia steel rebars

Table 3 summarizes the results from the test. Peak stress, ultimate strain and strain at peak stress for each dia rebar at a particular temperature has been given in Table 3. No change in material behaviour is observed at about 250 °C. A slight increase in strength is registered at temperature range from 200 – 300 °C. This phenomenon is attributed to the fact that no degradation in strength occurs until re-crystallization temperature of 450 °C is reached. About 40-70% of the peak stress is retained at 500 °C. It can be clearly seen that only about 9-15% peak stress is retained at 750 °C due to maximum reduction in dislocation density by re-crystallization process coupled with grain growth [6].

Table 3. Test Results

Temp.	Peak Stress	Ultimate Strain	Strain at Peak Stress
8mm Dia			
20 °C	879.78	0.0146	0.0076
250 °C	879.14	0.0147	0.0058
500 °C	619.90	0.0255	0.0065
750 °C	133.41	0.0685	0.0220
10mm Dia			
20 °C	631.03	0.1416	0.1254
250 °C	599.68	0.0539	0.0507
500 °C	336.79	0.0554	0.0124
750 °C	112.56	0.1489	0.0219
16mm Dia			
20 °C	813.44	0.0430	0.0246
250 °C	839.81	0.0287	0.0167
500 °C	613.51	0.0443	0.0157
750 °C	103.85	0.1967	0.0582
20mm Dia			
20 °C	447.28	0.0575	0.0575
250 °C	620.32	0.0813	0.0561
500 °C	471.93	0.0606	0.0222
750 °C	80.53	0.1469	0.0211

3.2 Failure Modes

Failure in steel rebars typically occurs in a cup and cone failure mode. At 20 °C, the rebar specimens usually registered a failure just outside the furnace either near the top jaw or the bottom jaw. At 250 °C, failure occurred usually at the junction of furnace opening, normally just outside the furnace. This fact can be attributed to strengthening of the thermo-mechanically treated rebars at temperatures around 250 °C. Due to this, a stress concentration is developed at the portion of rebar just outside the furnace. At 500 °C, rebar becomes more ductile and a plastic softening is observed. Cross-sectional dimensions of the rebar inside the furnace show a decrement and failure normally occurs at the middle third of the specimen inside the furnace. However, the cup and cone mode of failure is still observed. Failure at 750 °C follows a different trend. The rebar becomes very soft and continues elongating until it fails. Basically the bar loses almost 80-90% of its strength and fails with a pointed tip at the centre inside the furnace. Figure 5 shows typical failure modes of rebars at 20, 250, 500 and 750 °C.

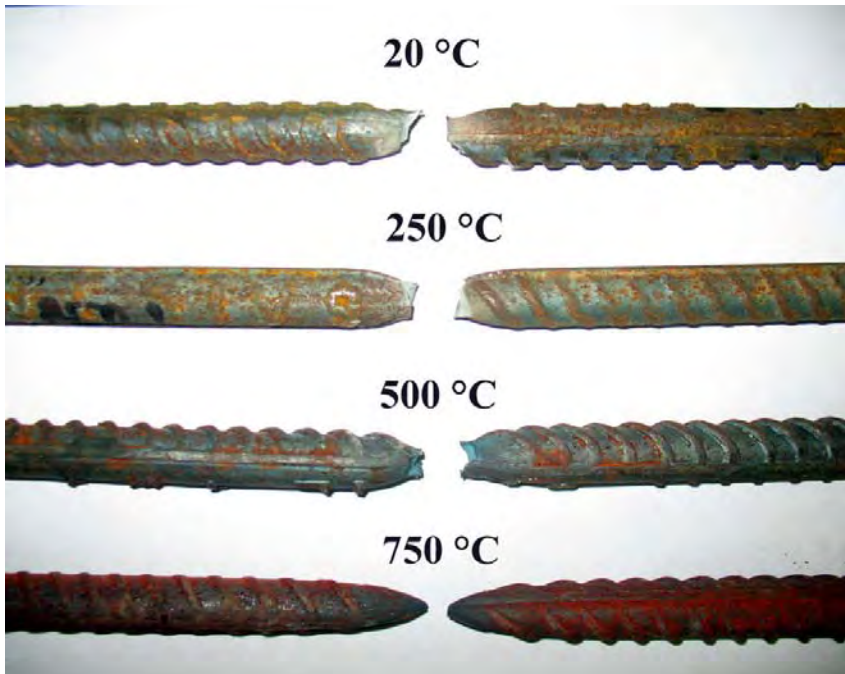


Figure 4 (d). Failure modes of steel rebars at elevated temperatures.

4 SCOPE FOR FURTHER RESEARCH

A series of tests on rebars at elevated temperatures aims at capturing the changes in mechanical properties of steel rebars at elevated temperatures. Rebars of different dia in the first phase of the series were tested without inducing any damage. Subsequently, a damage corresponding to design yield strength per Indian Standards [7] (0.85 times the yield stress f_y factored by 1.5) will be introduced in the rebars of the same dia. The loading will be kept constant and the furnace will be heated until the target temperature is reached. The loading will be then increased at a constant rate until the failure of the specimen. A thorough comparison of the mechanical properties will be made using the results obtained from tests on undamaged and damaged rebars. The data obtained will then be used to carry out regression analysis and build material models of undamaged and damaged steel rebars at elevated temperatures. Also, an attempt

will be made to study the effect of cooling on undamaged and damaged rebars subjected to elevated temperatures.

5 SUMMARY AND CONCLUSIONS

As it has been predicted by previous studies in the literature [2-5], degradation in strength of TMT steel rebars is conspicuously seen from the obtained results. In the current study, mechanical properties of undamaged steel rebars at elevated temperatures have been studied. TMT rebars exhibited a brittle mode of failure under elevated temperature upto 250 °C. At 500 °C, the mode of failure was in transition from ductile to brittle. However, at 750 °C, the mode of failure was purely ductile. Loss of strength was in the order of 0-30%, 30-40% and 80-90% for rebars exposed to 250 °C, 500 °C and 750°C respectively. Stress-strain relationships were plotted for each dia at a particular temperature. A comprehensive testing plan was worked out for reckoning the behavior of damaged steel rebars at elevated temperatures based on the results obtained for undamaged steel rebars.

REFERENCES

- [1] Suresh N. and Kamath P., "Fire Hazards Due to Earthquake", *Proceedings of the International Conference on Earthquake Engineering*, J. Venkataramana, K.-S R Mohan, S Ravindar (eds.), SASTRA, Tanjavur, TN, India, 554-564, 2006.
- [2] Elghazouli, A.Y., M., Cashell, K.A. and Izzuddin, B.A., "Experimental evaluation of the mechanical properties of steel reinforcement at elevated temperature", *Fire Safety Journal*, 44(6), 909-919, 2009.
- [3] Takeuchi M., Hiramoto M., Kumagai N., Yamazaki N. and Kodaira A., "Material properties of concrete and steel bars at elevated temperatures", *Nuclear Engineering and Design*, 12(1), 133-138, 1993.
- [4] Topçu, İB. and Karakurt C., "Properties of Reinforced Concrete Steel Rebars Exposed to High Temperatures", *Research Letters in Materials Science*, 2001(1), 1-4, 2008.
- [5] Nishiyama N., "Mechanical Properties of Concrete and Reinforcement — State-of-the-art Report on HSC and HSS in Japan", *Journal of Advanced Concrete Technology*, 7(2), 157-182, 2009.
- [6] Rollason EC., *Metallurgy for Engineers*, Edward Arnold, London, 1983
- [7] IS 1786: 2008 "*High Strength Deformed Steel Bars and Wires for Concrete Reinforcement Specification*" (fourth revision), Bureau of Indian Standards, 2008

STEEL RING-BASED RESTRAINT OF HSC EXPLOSIVE SPALLING IN HIGH-TEMPERATURE ENVIRONMENTS

Toru Tanibe*, Mitsuo Ozawa**, Ryota Kamada* and Keitetsu Rokugo**

* Research & Development Laboratory, Taiheiyo Materials Corporation, Japan
E-mail: Toru-Tanibe@taiheiyo-m.co.jp, Ryota-Kamata@taiheiyo-m.co.jp

** Department of Civil Engineering, Gifu University, Japan
E-mail: mitsu@gifu-u.ac.jp, rk@gifu-u.ac.jp

Keywords: explosive spalling, HSC, steel ring, thermal stress, vapor pressure

Abstract *This paper reports on an experimental study regarding the behavior of restrained high-strength concrete in response to the type of extreme heating associated with fire. The study was intended to support estimation of thermal stress from the strain in a restraining steel ring and vapor pressure in restrained concrete under the conditions of a RABT 30 rapid heating curve. The size of the specimens was $\phi 300 \times 100$ mm, and the results showed that explosive spalling occurred between 4 and 10 minutes in terms of heating time. It was also observed that the thermal stress was greater than the vapor pressure value of 0.1 MPa at a point 10 mm from the heated surface at 5 minutes. The maximum spalling depth was about 61 mm, and the depth at the center part was greater than that at the outer part. The specimens were severely damaged. It was inferred that spalling behavior caused by thermal stress may become predominant under restrained conditions. The residual strength of the concrete after the heating tests was also assessed.*

1 INTRODUCTION

Fire represents one of the most severe risks to buildings and concrete structures because it often results in explosive concrete spalling related to two phenomena. One is the occurrence of restrained thermal dilation resulting in the formation of biaxial compressive stress states parallel to the heated surface, which creates tensile stress in the perpendicular direction [1]. The other is the build-up of concrete pore pressure due to vaporization of physically/chemically bound water, resulting in tensile loading on the microstructure of the heated concrete [2]. Polypropylene fibers are often added to high-strength concrete (HSC) as an effective measure to prevent explosive spalling, and a number of studies have also analytically demonstrated that the role played by thermal stress in such spalling is more significant than that played by vapor pressure [3 – 6]. However, few papers to date have outlined actual experimental studies on the exact influence of thermal stress [7, 8].

This paper reports on an experimental study regarding the behavior of restrained concrete in response to the type of extreme heating associated with fire. The study was intended to support the estimation of thermal stress from the strain in a restraining steel ring and vapor pressure in restrained concrete under the conditions of a RABT 30 rapid heating curve. The residual strength of the concrete after the heating tests was also assessed.

2 ESTIMATION OF THERMAL STRESS

Figure 1 shows the method used to estimate thermal stress. First, the specimens were prepared using concrete with restrained steel rings. Heating tests were performed on the restrained specimens with the target measurements of internal concrete temperature, steel ring temperature, steel ring strain, vapor pressure inside the concrete, spalling time and spalling depth. When the internal concrete deformed due to thermal expansion and vapor pressure caused by heating, it was restrained by the steel ring, and compressive stress was induced. Although such test setups have previously enabled qualitative evaluation, no simple procedure to routinely quantify the characteristics of materials under restrained expansion has been established. In this study, an instrumented ring setup was used to quantify the behavior of concrete under restrained expansion during heating. Thermal stress calculation was based on thin-walled cylinder model theory [9] as shown in Eqs. (1) and (2). Vapor pressure was measured at 10 and 20 mm from the heated surface.

$$\sigma_r = \varepsilon_s \times t \times E_s / R \quad (1)$$

$$\sigma_r = \sigma_{th} + \sigma_{vap} \quad (2)$$

Where,

σ_r : restrained stress (MPa)

σ_{th} : thermal stress of concrete (MPa)

t : steel ring thickness (mm)

E_s : steel ring elastic modulus (MPa)

R : steel ring inside radius (mm)

σ_{vap} : vapor pressure (MPa)

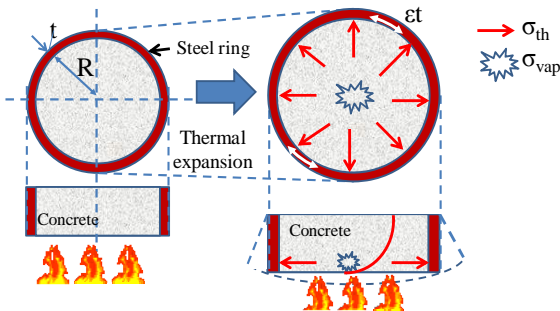


Figure 1. Estimation of thermal stress.

3 OUTLINE OF THE HEATING TEST

3.1 Concrete

Table 1 shows the mix proportions of high-strength concrete (HSC). A water-cement ratio of 0.3 and high-early-strength Portland cement (density: 3.13 g/cm³) were used in this study, and crushed stone with a maximum grain size of 25 mm was used as coarse aggregate. The main component of the superplasticizer (SP) was polymeric acid. After being cast, the concrete specimens were left in the formwork for one day, and were then wet cured at 20 ± 2°C for 28 days. Heating tests for all specimens were

performed after this time. Table 2 shows the values obtained for compressive strength, tensile strength, elastic modulus and water content ratio.

Table 1. Mixture proportion.

W/C	Water	Cement	Fine agg.	Coarse agg.1 less than 15mm	Coarse agg.2 less than 25 mm	Super plasticizer
0.3	132	440	814	524	524	8.8

Table 2. Strength and Water content ratio.

Compressive strength (MPa)	Elastic modulus (GPa)	Tensile strength (MPa)	Water content ratio (%)
90	42	5.5	3.1

3.2 Specimen dimensions and heating tests

The configuration and dimensions of the specimens are shown in Figure 2. Two pairs of steel rings were used (diameter: 300 mm; thickness: 8 mm; length: 50 mm; E_c (elastic modulus): 210 GPa; F_y (yield strength): 295 MPa), two strain gauges and two thermocouples and two LVDTs (sensitivity: 1/1,000 mm) were attached at 25 and 75 mm from the heated surface and outer surface of the steel rings, and three LVDTs were attached at the center and side of the top surface. Stainless steel pipes (inner diameter: 2 mm; length: 200 mm) were placed in the concrete at distances of 10 and 20 mm from the heated surface and parallel to it. Six type-K thermocouples were placed in the central zone of the specimens at 5, 10, 20, 30, 40 and 50 mm from the heated surface. Before testing was performed, a stainless steel pipe extending from the specimen was connected to a miniature pressure transducer (pressure range: 0 – 10 MPa) located outside the furnace. The entire pore pressure assembly (i.e., the stainless steel pipe and the transducer) was filled with hydraulic jack oil, and the pressure transducer and thermocouples were connected to a data acquisition system to enable recording of pressure and temperature values. The heating tests were based on a RABT 30 heating curve (Figure 3). Strain gauges and thermocouples were attached at 25 mm and 75 mm from the heated surface and the outer surface of the steel ring.

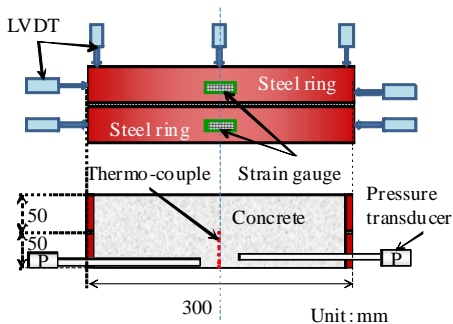


Figure 2. Dimension of the specimens.

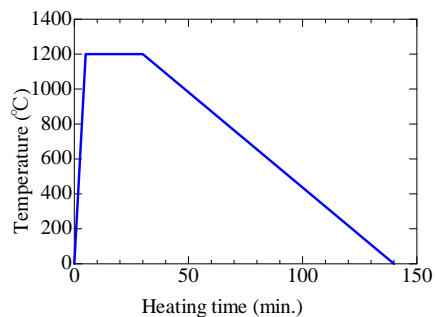


Figure 3. Heating curve(Rabt 30).

4 HEAT CONDUCTION ANALYSIS

Figure 4 shows a model of the heat conduction analysis, which was executed to allow comparison of restrained stress as calculated from the temperature measurement results with that calculated from the heat conduction analysis results. Table 3 shows the concrete and steel thermal characteristics applied in the heat conduction analysis, which were those of Eurocode 4 [10].

Table 3. Thermal characteristics of Steel and Concrete.

Thermal characteristics of steel		
Thermal conductivity W/m·K	$20 \leq T \leq 800^\circ\text{C}$	$\lambda = 54 - 3.33 \cdot 10^{-2} \cdot T$
	$800 < T \leq 1200^\circ\text{C}$	$\lambda = 27.3$
Specific heat J/g·K	$20 \leq T \leq 600^\circ\text{C}$	$c = 425 + 0.773 \cdot T - 1.69 \cdot 10^{-3} \cdot T^2 + 2.22 \cdot 10^{-6} \cdot T^3$
	$600 < T \leq 735^\circ\text{C}$	$c = 666 - (13,002 / (T - 738))$
	$735 < T \leq 900^\circ\text{C}$	$c = 545 - (17,820 / (T - 731))$
	$900 < T \leq 1200^\circ\text{C}$	$c = 650$
Thermal characteristics of concrete		
Water content %	3.1	
Thermal conductivity W/m·K	$\lambda = 2 - 0.24(T/120) + 0.012(T/120)^2$	
Specific heat J/g·K	$c = 900 + 80(T/120) - 4(T/120)^2$	

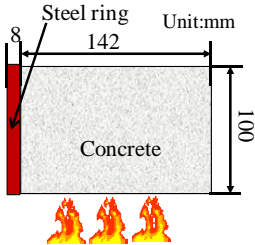


Figure 4. Model of the heat conduction analysis.



a) UPV test b) Compressive strength test
Figure 5. Estimation of residual strength.

5 ESTIMATION OF RESIDUAL STRENGTH AFTER THE HEATING TESTS

To allow estimation of residual strength after the heating tests, ultrasonic pulse velocity (UPV) testing and compressive strength testing were carried out using a specimen with a diameter of 25 mm and a length of 40 mm. Figure 5 shows the setups for the two tests. Six core specimens were taken from a non-heated surface area in the ring specimen after heating. Control specimens (diameter: 50 mm; length: 100 mm) that non-heated were also used.

6 RESULTS AND DISCUSSION

6.1 Heating tests

Figures 6 and 7 show the temperatures inside the specimen and the furnace, respectively. Explosive spalling was seen between 4 and 10 minutes in terms of heating time. The internal temperatures measured at points 5 and 10 mm from the heated surface were 350°C and 150°C, respectively, at 5 minutes, and explosive spalling occurred up to 10 mm from the heated surface at this time. Figure 8 shows the steel ring temperature, which reached 22°C at a point 25 mm (the gauge point) from the heated surface at 5 minutes. Figure 9 shows a time history of vapor pressure at points 10 and 20 mm from the heated surface at 10 minutes. The vapor pressure started to increase at 100°C and reached 0.1 MPa at a point 10 mm from the heated surface at 5 minutes, then reached 0.3 MPa at a point 20 mm from the heated surface at 7 minutes. When explosive spalling occurred, the vapor pressure had built up to 0.1 MPa and 0.3 MPa at points 10 and 20 mm from the heated surface, respectively. Recent papers have reported that vapor pressure observed during heating built up to 2 – 4 MPa [11, 12]. Although the vapor pressure values measured in this study were small, it was found that vapor pressure build-up underwent a drastic change before spalling occurred. We compared the development of vapor pressure with that of the saturated vapor pressure (SV) during the course of the heating experiment. As shown in Figure 10, the measured values followed the SV curve during the ascending branch, which seems to confirm that the vapor pressure measured using our experimental setup is indeed the pore pressure. However, for some results, the measured pressure values are smaller than those for SVP above 80°C and 120°C at 10 mm and 20 mm from the heating surface, respectively. As this is theoretically impossible, it can be inferred that vapor pressure is not responsible for this low pressure. Rather, it is likely to be caused by the partial pressure of dry air enclosed in the mortar. The partial pressure of air in a pore is strongly dependent on its liquid water saturation.

Figures 11 and 12 show horizontal and perpendicular displacement during heating. Horizontal displacement and the temperature in the steel ring 5 minutes after heating were 0.06 mm and 10°C, respectively, and the expansion-related displacement of the ring due to heating was about 0.035 mm. It was determined that expansion of the concrete due to heating was restrained by the steel ring. The perpendicular displacement results indicated that the specimen deformed due to bending during heating.

Figure 13 shows a time history of restrained stress at points 25 and 75 mm from the heated surface at 10 minutes. It can be seen that the value reached 6 MPa at 10 minutes at a point 25 mm from the heated surface.

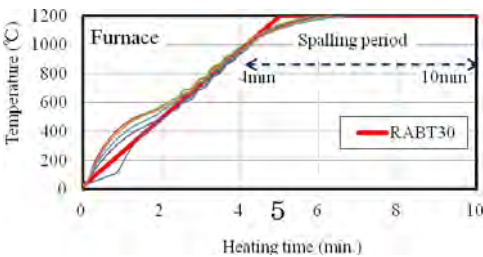


Figure 6. Temperatures of furnace.

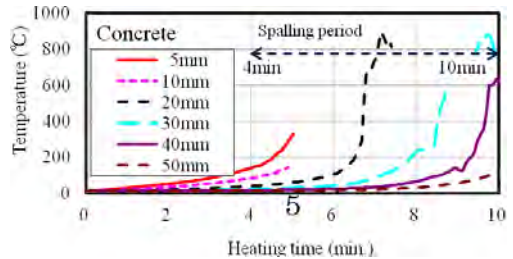


Figure 7. Temperatures of inside concrete.

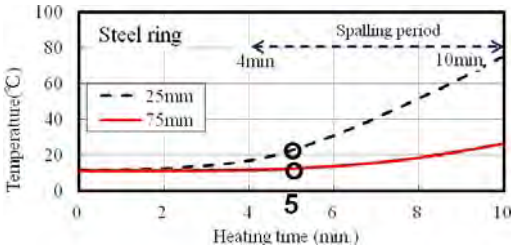


Figure 8. Temperature of steel ring.

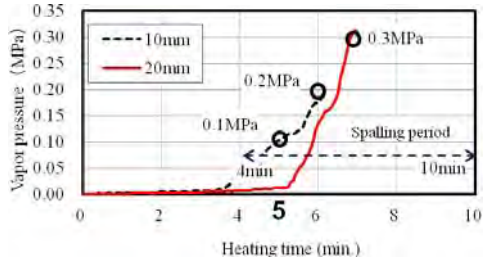


Figure 9. Vapour pressure.

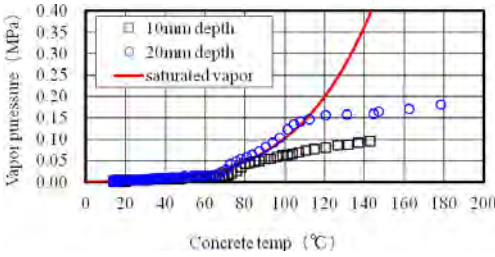


Figure 10. Vapour pressure and SV.

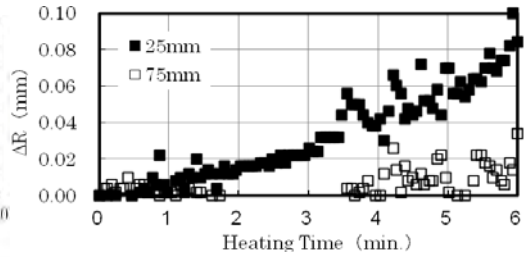


Figure 11. Horizontal displacement.

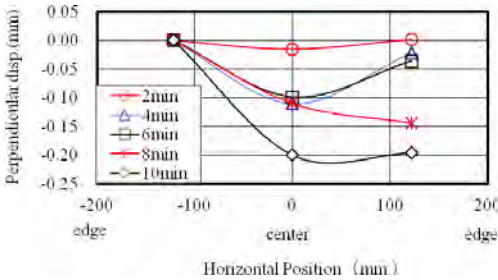


Figure 12. Perpendicular displacement.

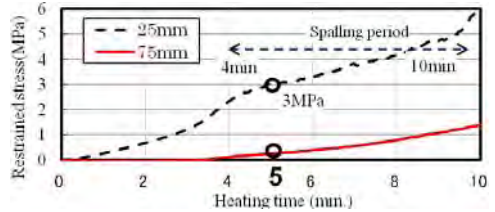


Figure 13. Restrained stress.

6.2 Estimation of thermal stress

Figure 13 shows the results of restrained stress calculation using the strain of the ring 25 mm from the heated surface. After 5 minutes of heating, the value reached 3 MPa at this point. The thermal stress was greater than the vapor pressure value of 0.1 MPa at a point 10 mm from the heated surface at 5 minutes.

Figure 14 shows the distribution of temperature from heat conductive analysis and the measurement results at 5 minutes after the start of heating. A close correlation is seen in the temperature results. The temperature of the heated surface was about 500°C.

Figure 15 shows the distribution of restrained stress at 5 minutes after the start of heating. The restrained stress at a point 10 mm from the heated surface was calculated as 11 MPa at this time, and the vapor pressure was about 0.1 MPa at a point 10 mm from the heated surface. It was thus confirmed that restrained stress mainly consisted of thermal stress at 5 minutes. The restrained stress at the heated

surface of the concrete was about 42 MPa, and the residual strength there was about 54 MPa at 5 minutes as calculated using Eurocode 4.

The restrained stress at the surface therefore reached the compressive strength (residual strength), and compressive failure occurred. This result indicates that spalling caused by thermal stress may become predominant under restrained conditions.

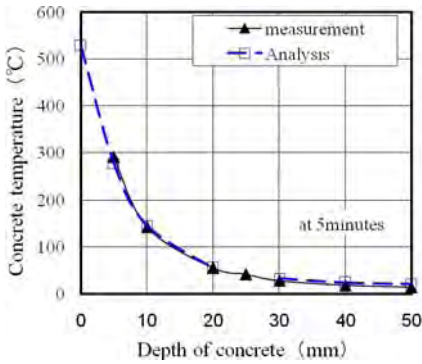


Figure 14. Distribution of temperature at 5min.

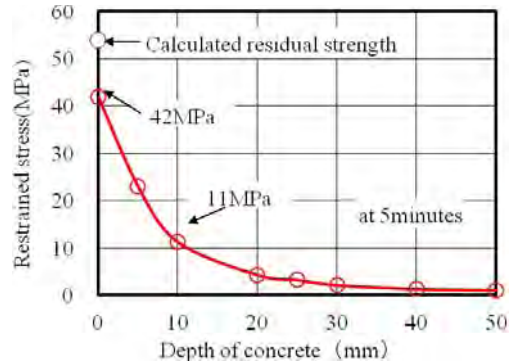


Figure 15. Distribution of restrained stress at 5min.

6.3 Residual strength and UPV test results

Figure 16 shows results for the depth of spalling after the heating test. The maximum value was about 61 mm, and the depth at the center part was greater than that at the outer part. The specimens were severely damaged.

Figure 17 shows UPV results and compressive strength results from the periods before and after heating. The residual compressive strength and the residual strength ratio were 72 MPa and 80%, respectively. Reduced compressive strength after the heating tests was observed. The residual UPV value was 4,000 m/s, and the residual UPV ratio was 86%. Although the calculated residual stress is shown as 54 MPa at 5 minutes in Figure 15, the results from the compressive strength test performed after heating showed about 72 MPa. This highlights the difficulty of estimating residual strength after heating.

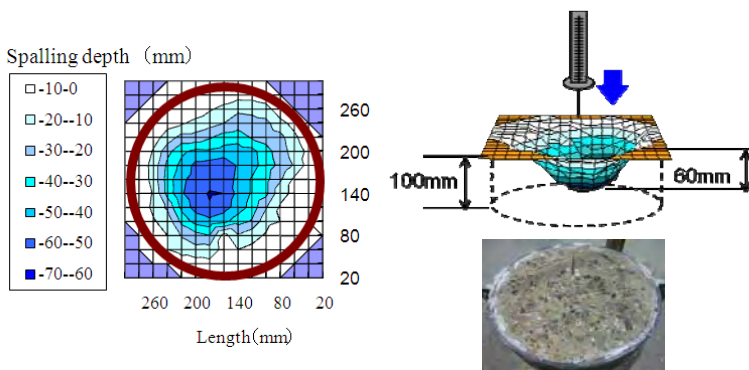


Figure 16. Spalling depth.

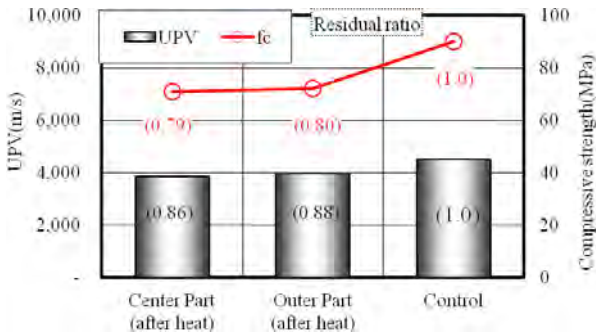


Figure 17. UPV results and compressive strength results periods before and after heating.

7 CONCLUSION

The results obtained from the study can be summarized as follows:

- 1) The proposed method involving the restraint of concrete with steel rings in heat testing can be used to clarify characteristics of thermal stress and explosive spalling behavior.
- 2) The thermal stress measurements obtained in the study were greater than those for vapor pressure.
- 3) The measured vapor pressure followed the SVP curve during the ascending branch.
- 4) The restrained stress at the heated surface of the concrete was about 42 MPa, and the residual strength there was about 54 MPa at 5 minutes as calculated using Eurocode 4.
- 5) The restrained stress at the surface therefore reached the compressive strength (residual strength), and compressive failure occurred. This result indicates that spalling caused by thermal stress may become predominant under restrained conditions.
- 6) It was observed that both ultrasonic pulse velocity and compressive strength decreased after the heating tests.
- 7) The maximum spalling depth was about 61 mm, and the depth at the center part was greater than that at the outer part. The specimens were severely damaged.

ACKNOWLEDGEMENTS

This study was supported by the Grant-in-Aid for Scientific Research C (General) of the Japan Society for the Promotion of Science 2010, No. 22560461 (Head: Dr. M. Ozawa) and Japan's Maeda Engineering Foundation 2011. The authors would like to express their gratitude to the organization for its financial support.

REFERENCES

- [1] Ulm, F.J., Coussy, O., Bazant, Z. P., "The "Chunnel" Fire. II Analysis of concrete damage", *Journal of Engineering Mechanics*. 125, 283-289, 1999.
- [2] Anderberg Y., "Spalling phenomena in HPC and OC", *Proceedings of the International Workshop on Fire Performance of High-Strength Concrete*, L.T.Phan, N.J.Carino, D.Duthinh, E.Garbozci (eds.), Gaithersburg, MD: NIST; 69-73, 1997.

- [3] Kalifa, P., Menneteau, F.D., Quenard, D., “Spalling and pore pressure in HPC at high temperatures”, *Cement and Concrete Research*, 30, 1915-1927,2000.
- [4] Phan, L.T., “Pore pressure and explosive spalling in concrete”, *Materials and Structures*, 41,1623- 1632,2008.
- [5] Khoury, G.A., Willoughby, B., “Polypropylene fibres in heated concrete Part 1: Molecular structure and materials behavior”, *Magazine of Concrete Research*, 60, 125-136,2008.
- [6] Khoury, G. A., “Polypropylene fibres in heated concrete Part 2: Pressure relief mechanisms and modelling criteria”, *Magazine of Concrete Research*, 60, 189-204,2008.
- [7] Connolly, R. J., “The Spalling of Concrete in Fires”, PhD thesis submitted to Aston University, 1995.
- [8] Tanibe, T. et al., “Explosive spalling behavior of restrained concrete in the event of fire”, *Proceedings of the 2nd International Rilem Workshop on Concrete Spalling due to Fire Exposure*, E.A.Koender, F.Dehn,(eds.)Netherlands, Delft, 319-326, 2011.
- [9] Kogouchi, Y., “Engineering of Ductwork, Mechanical Design”, Kougaku-tosho (in Japanese),1964.
- [10] Eurocode 4, “Design of Composite Steel and Concrete Structures”, Draft for Part 1.2: Structural Fire Design, CEN/TC250/SC4N56 prENV, 1994.
- [11] Kalifa, P.,”Spalling and pore pressure in HPC at high temperatures”, *Cement and Concrete Research*, 30, 1915-1927,2000.
- [12] Mugume, R. B., Horiguchi, T., “Pore pressure development in hybrid fibre-reinforced high strength concrete at elevated temperatures”, *Cement and Concrete Research*, 41, 1150- 1156,2011.

PREVENTIVE EFFECTS OF DIFFERENT TYPES OF FIBERS ON UFC SPALLING AT HIGH TEMPERATURES

Mitsuo Ozawa*, Zhou Bo*, Yuichi Uchida** and Hiroaki Morimoto*

* Department of Civil Engineering, Gifu University, Japan
E-mail: mitsu@gifu-u.ac.jp, p3121013@edu.gifu-u.ac.jp, morimt@gifu-u.ac.jp

** Information and Multimedia Center, Gifu University, Japan
E-mail: uchida@gifu-u.ac.jp

Keywords: Ultra-high-strength fiber-reinforced concrete (UFC), spalling, high temperature, synthetic fibers, natural fibers

Abstract *The authors examined the relationship between spalling behavior and weight loss for ultra-high-strength fiber-reinforced concrete (UFC) containing different kinds of short fibers (jute, PP, WSPVA) in high-temperature environments at 400, 600 and 800°C. The explosive spalling that occurred under these conditions caused severe damage to the control specimen without fiber reinforcement but only slight damage to the jute specimen. It was therefore inferred that adding 0.19% by volume of natural jute fibers (length: 12 mm) to UFC is effective in the prevention of spalling-related damage.*

1 INTRODUCTION

In response to increasing demand for a higher level and a wider range of concrete performance, active research has been conducted in recent years to meet these needs. One example of a product stemming from such developments is ultra-high-strength fiber-reinforced concrete (UFC), which offers ultra-high strength exceeding 180 N/mm² in compression and flowability with a low water binder ratio. It has been introduced into practical use, with recommendations for its design and construction (draft) being published by the Japan Society of Civil Engineers [1].

High-strength steel fibers are used for the UFC detailed in these recommendations to achieve superior mechanical performance. To eliminate the possibility of steel fiber corrosion related to concrete cracking, the recommendations stipulate that there should be no cracking in UFC during its period of service. Due to the difficulty of achieving this, the use of synthetic fibers with high corrosion resistance instead of steel fibers has been investigated. However, it has been reported that some mechanical performance aspects (such as flexural strength) of UFC using synthetic fibers are substantially inferior to those of UFC made with steel fibers [2]. Against this background, the authors focused on the use of aramid fibers (which have higher strength and a higher elastic modulus than other synthetic fibers) as a substitute for steel fibers and investigated the mechanical properties of UFC with aramid fibers [3].

UFC is known to be particularly susceptible to spalling in fire. Generally, synthetic fibers are often added to high-strength concrete (HSC) as an effective measure to prevent explosive spalling [4, 5], but few studies have investigated the effectiveness of adding natural fibers and other types of synthetic fibers to UFC to prevent spalling in high-temperature conditions. The authors previously reported on the effectiveness of adding natural jute fibers and water-soluble poly-vinyl alcohol (WSPVA) fibers to HSC in order to prevent spalling in high-temperature environments [6].

In this study, we examined the relationship between the spalling behavior of UFC with added natural jute fibers, WSPVA fibers and polypropylene (PP) fibers when specimens were subjected to heating. The volume mixing ratios used were 1.75% for aramid fibers and 0.19% for jute, WSPVA and PP fibers.

2 OUTLINE OF THE EXPERIMENT

2.1 Mixture proportions

Table 1 gives the mix proportions of the mortar matrix used in this study, which were established in reference to a past report [7]. Strictly speaking, the mix was mortar rather than concrete because no coarse aggregate was used. Silica fume cement with a density of 3.08 g/cm^3 was used as the binder with a water-binder ratio (W/ C) of 0.19 (the total chemical admixture dosage was included in the calculation as part of the water content). Silica powder with a density of 2.6 g/cm^3 and a specific surface area of $8,180 \text{ cm}^2/\text{g}$ was used as filler for the microstructure, and Class-6 silica sand with a density of 2.6 g/cm^3 was used as fine aggregate. The chemical admixture was apolycarboxylate ether-based super plasticizer for ultra-high-strength concrete. It should be noted that all these materials are commercially available; they were not specially developed for this study.

Table 1. Mixture Proportion

W/B	Unit weight kg/m^3					
	Silica fume cement	Water	Silica sand	Silica powder	Aramid fiber	Super plasticizer
0.19	1258	208	682	248	26.2	31.5

Table 2. Fibers.

Type of fiber	Length	Diameter	Melting point	Density	note
	mm	μm	$^{\circ}\text{C}$	g/cm^3	
Jute	3,12	10~30	-	1.3-1.45	Carbonization
WSPVA	4	12	220-240	1.3	Water solving
PP	12	42	170	0.91	Melting

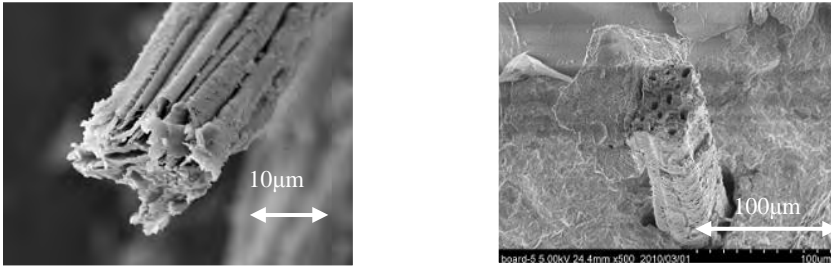
2.2 Fibers

The aramid fibers (copolyparaphenylene 3,4'-oxydiphenylene terephthalamide) used in this study had a density of 1.39 g/cm^3 , a tensile strength of $3,430 \text{ N/mm}^2$ and a tensile elastic modulus of 72.5 kN/mm^2 , and were bundled using vinyl ester resin into sticks with an external diameter of $200 \mu\text{m}$ and a length of 15 mm. Table 2 shows the properties of the natural jute [6] fibers and the synthetic WSPVA [6] and PP fibers used (jute fiber addition ratio: 0.19 vol%; length: 3 and 12 mm; WSPVA fiber addition ratio: 0.19 vol%; length: 4 mm; PP fiber addition ratio: 0.19 vol%; length: 12 mm). Photos 1 (obtained with a scanning electron microscope (SEM)) show the straw-like structure of the jute fibers.

WSPVA fibers have a lower dissolving point (50°C to 90°C) than other synthetic types, and also have a lower melting point. These properties have been used for more than 30 years in Japan to improve the permeability of concrete and thereby reduce the likelihood of explosion in refractory castables.

Figure 1 shows the results of thermal analysis of jute fiber using differential scanning calorimetry (DSC) and thermogravimetric analysis (TGA). The exothermic peak (which represents the amount of heat released from the sample) of the DSC curve for such fibers was observed at a maximum temperature

of 360°C. The TGA curve initially exhibits a slight decrease in weight at temperatures below 100°C due to moisture loss, but both curves begin to show decomposeure at 265°C and 340°C. The decomposition temperature for the jute fiber sample at 80% weight loss was 390°C. Figure 2 shows the DSC and TGA results for PP fibers, whose melting, vaporization and burning points were 173°C, 341°C and 447°C, respectively. Higher temperatures reduce their viscosity via the two mechanisms of increased molecular energy and reduced molecular size caused by thermal degradation. Figure 3 shows the DSC and TGA results for WSPVA fibers, whose melting, vaporization and burning points were 227°C, 246°C and 470°C, respectively.



a) Shape

b) Jute fiber in concrete

Photo. 1. Jute fiber (SEM observations)

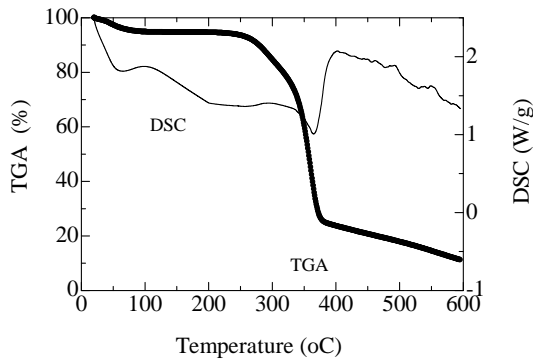


Figure 1. DSC and TGA results (Jute fiber).

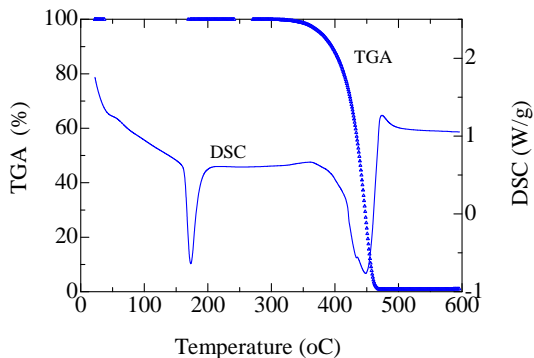


Figure 2. DSC and TGA results (PP fiber).

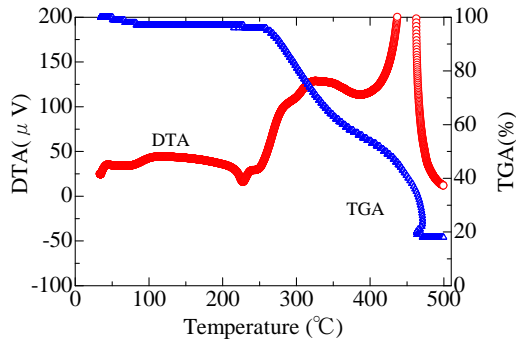


Figure 3. DTA and TGA results (WSPVA fiber).

2.3 Mixing and flow test

The mortar components were placed into a 10-liter Hobart mixer and agitated. Mixing process is belows:

- 1) Add Silica fume cement, silica powder, class-6 silica sand, mix for 1 minutes.
- 2) Add water and super plasticizer, mix for 2minutes, scrape bowl and mix for 5minutes.
- 3) Add aramid fiber and other fibers mix for 4minutes.

The flowability of the mortar was evaluated in a flow test using a cone mold with dimensions of 70 mm (top diameter) × 100 mm (bottom diameter) × 60 mm (height). Drops were not included in the mortar flow measurement.

2.4 Specimen fabrication and curing

Heating test specimens with 50 mm in diameter and 100 mm in height were used for this study. The concrete was placed in molds and consolidated using a table vibrator. The surfaces of the specimens were plastic-wrapped immediately after placement and left to stand for two days in a thermostatic room at 20°C. After demolding, hot water curing was carried out for two days at a temperature of 90°C.

2.5 Heating tests

Five specimens were heated in a muffle furnace with an operating temperature range of 100°C to 1,150°C. The unit used was a 2.5 kW iron-chrome wire heater with a 220V power source. Figure 4 shows the test's heating times and temperature ranges, which were 400°C and 30 minutes, 600°C and 20 minutes, and 800°C and 15 minutes. After being heated, the specimens were allowed to cool naturally.

Weight loss after heating were calculated as shown in Eq. (1)

$$\alpha_{loss} = (W_{ini} - W_{after}) / W_{ini} \times 100 \quad (1)$$

Where

α_{loss} : Weight loss (%)

W_{ini} : Weight before heating (g)

W_{after} : Weight after heating (g)

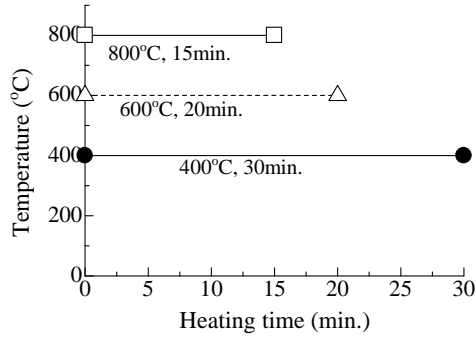


Figure 4. Heating temperature and time.

3 RESULTS AND DISCUSSION

3.1 Fresh properties and mechanical properties

Figure 5 gives the flow test results. The flow values obtained were: control specimen: 250 mm; jute 3: 197 mm; jute 12: 210 mm; PP: 208 mm; and WSPVA: 221 mm. Figures 6 and 7 show the compressive strength and bending strength test results, and indicate values ranging from 140 MPa to 150 MPa for the specimens. The average bending strength in the control specimen was 30 MPa.

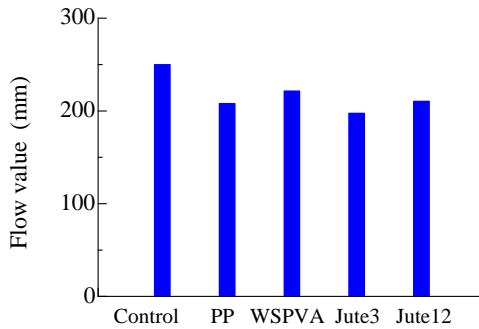


Figure 5. Flow test.

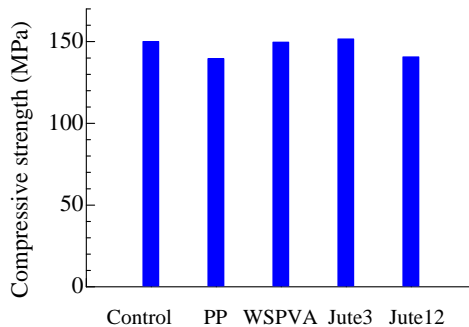


Figure 6. Compressive strength.

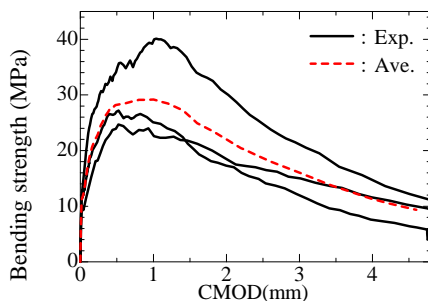


Figure 7. Bending strength of notched beam specimen.

3.2 Heating test results

Figure 8 shows the extent of spalling in all specimens after the fire tests. The control specimens became more severely damaged as the temperature increased from 400°C to 800°C. For the specimens with added fibers, it was clear that the spalling tendency decreased. With a heating temperature of 400°C and a heating time of 30 minutes, explosive spalling was observed in the control, PP, WSPVA and jute 3 specimens, but not in the jute 12 specimen. The extent of spalling in the WSPVA and jute 3 specimens was small. With a heating temperature of 600°C and a heating time of 20 minutes, explosive spalling was observed in all specimens. The control and PP specimens were severely damaged, while the extent of spalling in the jute 12 specimens was small. With a heating temperature of 800°C and a heating time of 15 minutes, explosive spalling was observed in all specimens. The control, PP and jute 3 specimens were severely damaged, while the extent of spalling in the jute 12 specimens was small.

3.3 Weight loss due to fire exposure

Figure 9 shows the relationship between weight loss and heating temperature in all specimens. As expected, the results are proportional to the extent of spalling observed in the photographs (Fig. 8). Results of weight loss were including of moisture loss during the fire tests. The most extreme result was seen with the control concrete, which underwent 72% weight loss at 800°C.

The effectiveness of jute 12 is clear in comparison to that of other fiber types at 800°C: jute 3 showed a 32% weight loss, PP 28% and WSPVA 22%. The results were dramatically improved by adding different types of fibers. In particular, weight loss of just 17% was seen with jute 12 at a fiber content ratio of 0.19%. Generally, PP fibers are often added to high-strength concrete (HSC) as an effective measure to prevent explosive spalling. However, this type of spalling was observed in the PP specimens. It is considered that explosive spalling occurred in the PP specimens before PP fibers in the surface area melted. It can be inferred that the addition of jute fibers at a ratio of 0.19% by volume and a fiber length of approximately 12 mm to UFC is effective in preventing spalling, as the straw structure of jute prevents the development of significant vapor pressure in the concrete. Additionally, jute fibers become carbonized during the heating process, which may create pressure-induced tangential spaces (PITS; Fig. 10 a) at the fiber-concrete interface (as suggested by Khory [8]), which help to dissipate vapor from concrete to the outside. It can therefore be assumed that the degree of adhesion between the fibers and concrete is generally poor. If this is the case, then the role of the fiber-concrete interface as a channel for moisture transfer in high-pressure conditions cannot be ignored.

It can also be inferred that the addition of WSPVA fibers at a ratio of 0.19% by volume and a fiber length of approximately 4 mm to UFC is effective in preventing spalling, as vapor pressure peaks were reduced using this approach. We assume that the presence of WSPVA fibers supported the development of PITS (Fig. 10 b) at the fiber-concrete interface when the WSPVA became more flexible in the dissolving temperature range of 50 – 90°C in water.

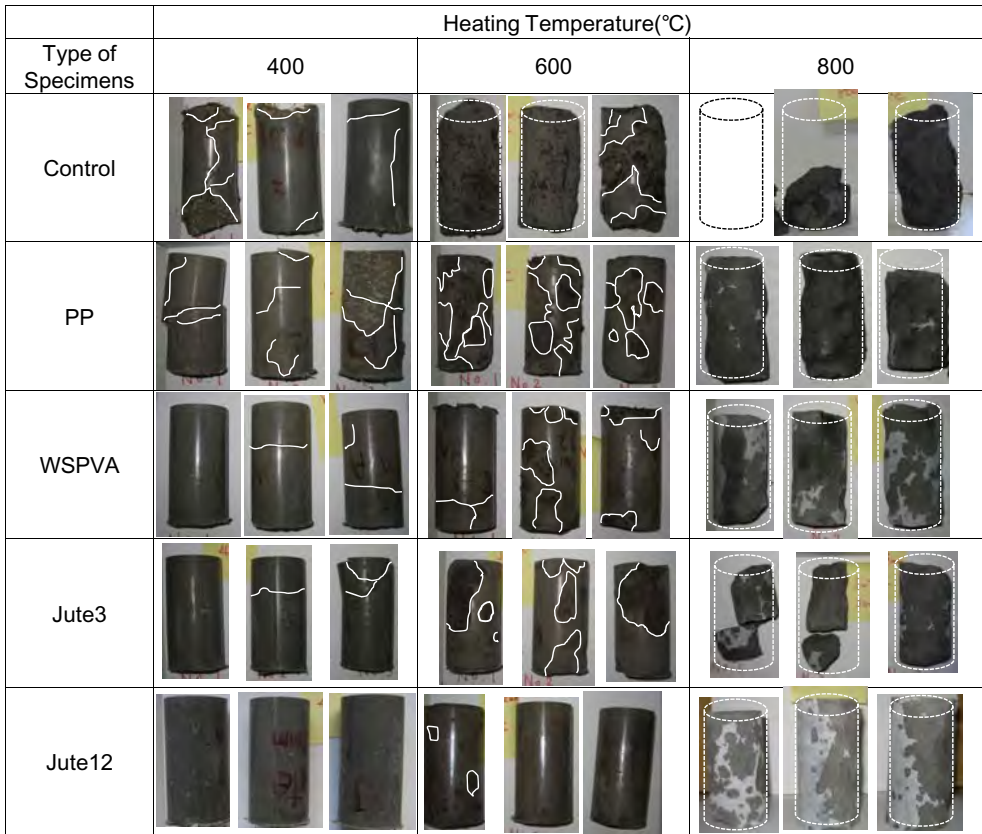


Figure 8. Extent of spalling.

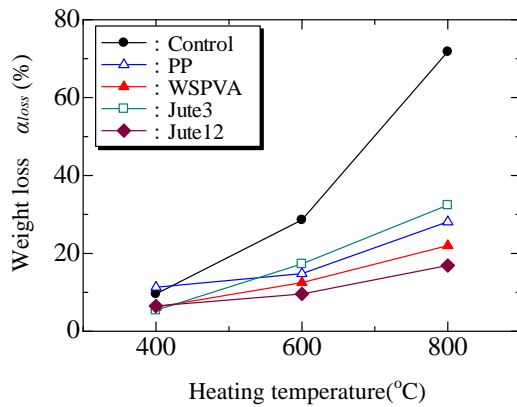
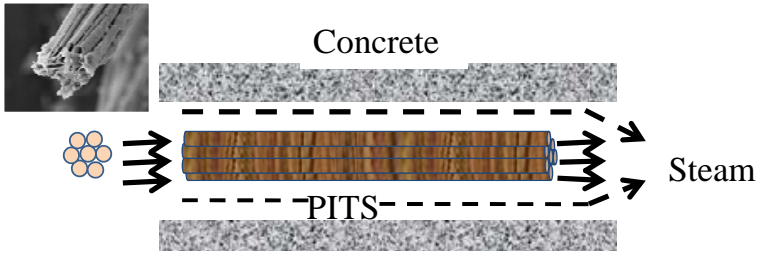
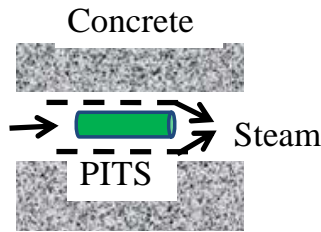


Figure 9. Weight loss.



a) Jute fiber(straw structures)



b) WSPVA(Dissolving 50-90°C in liquid water)

Figure 10. Pressure-induced tangential spaces (PITS).

4 CONCLUSION

The results obtained from the study can be summarized as follows:

The control specimens developed severe damage as the temperature increased from 400°C to 800°C, while it was clear that the spalling tendency decreased in all specimens with fibers added. The most extreme result was seen with the control concrete, which underwent 72% weight loss at 800°C. Explosive spalling occurred in the PP specimens. The weight loss results were dramatically improved by adding different types of fibers. In particular, weight loss of just 17% was seen with jute 12 at a fiber content ratio of 0.19%.

ACKNOWLEDGEMENTS

This study was supported by the Grant-in-Aid for Scientific Research C (General) of the Japan Society for the Promotion of Science 2010, No. 22560461 (Head: Dr. M. Ozawa). The authors would like to express their gratitude to the organization for its financial support, and also wish to thank Tesac Co., Ltd., Kuraray Co., Ltd. and Teijin Co., Ltd. for their assistance in this study.

REFERENCES

- [1] JSCE, "Recommendations for Design and Construction of Ultra High Strength Fiber Reinforced Concrete Structures," 2006.
- [2] Kawaguchi T. et al., "Mechanical Properties of Flexural Members Using Ultra High Strength Fiber Reinforced Concrete," *Proceedings of the 8th International Symposium on Utilization of High-Strength and High-Performance Concrete*, (2): JCI, JPCEA and fib. 1069-1074, 2008.
- [3] Uchida Y., Takeyama T. and Dei T., "Ultra high strength fiber reinforced concrete using aramid fiber," *Proceedings of Fracture Mechanics of Concrete and Concrete Structures – High Performance, Fiber Reinforced Concrete, Special Loadings and Structural Applications*, 1492-1494, 2010.
- [4] Baba S. et al., "Fire Resistance of Pre-Stressed Slabs in Ultra High Performance Concrete for Use in an Office Building Retrofit Project," *Proceedings of the 8th International Symposium on Utilization of High-Strength and High-performance Concrete*, CD-ROM, 2008.
- [5] Ozawa M., Morimoto H., "High-Strength Concrete Reinforced Jute Fiber and Water-Soluble PVA Fiber under High Temperature," *Proceedings of the Sixth International Conference on Structures in Fire*, 864-871, 2010.
- [6] Heo, Y. S., Sanjayan, J. G., Han, C. G., Han, M. C., "Synergistic effect of combined fibers for spalling protection of concrete in fire," *Cement and Concrete Research* 40,1547-1554,2010.
- [7] Richard, P., Cheyrezy M., "Composition of Reactive Powder Concrete," *Cement and Concrete Research* 25 (7), 1501-1511, 1995.
- [8] Khoury, G. A., "Polypropylene fibers in heated concrete Part 2: Pressure relief mechanisms and modeling criteria," *Magazine of Concrete Research*, 60 (3), 189-204, 2008.

AN EXPERIMENTAL STUDY ON REINFORCED CONCRETE COLUMNS SUBJECTED TO ECCENTRIC LOADS AND AXIAL RESTRAINT AT ELEVATED TEMPERATURES

Thang T. Nguyen^{*}, Hai K. Tan^{*}

^{*} School of Civil and Environmental Engineering, Nanyang Technological University, Singapore
e-mails: ntthang@ntu.edu.sg, ckhtan@ntu.edu.sg

Keywords: Concrete, Columns, Axial restraint, Eccentric loads, Elevated temperatures.

Abstract. *Fire tests on six axially-restrained reinforced concrete columns subjected to eccentric loads are introduced in this paper. Experimental evidences of the effects of load level, axial restraint and uniaxial load eccentricity on the column behaviour in fire in terms of deflections and restraint forces, as well as failure mode and failure time, are presented. Finite element-based computer program, SAFIR, is used for comparison. It is shown that at similar load levels and axial restraint ratios, both column deflections and restraint forces are affected by load eccentricity. It is also observed that numerical models neglecting concrete spalling tend to over-predict the restraint forces induced in concrete columns under realistic loading, restraint, and fire conditions. Besides, a modified criterion of EN 1363 can be used to predict stability failure times of specimens subject to non-standard fire conditions.*

1 INTRODUCTION

When fire incidents occur in reinforced concrete (RC) framed buildings, columns are simultaneously subjected to eccentric loads and axial restraints due to non-uniform fire attack, concrete spalling, as well as non-uniform thermal responses of adjacent structural elements. However, to the authors' best knowledge, there have been very limited literature and design provisions for RC columns under such a heating condition. Previous fire tests on restrained RC columns were mostly conducted under pure compression with very small load eccentricities [1-5]. The state-of-the-art review and research-need assessment of the fire performance of RC columns presented by Kodur et al. [6] also indicated that there has been little published information on the behaviour of RC columns under realistic loading, restraint, and fire conditions. A number of robust finite element procedures for modelling of RC structures in fire accounting for the impact of concrete spalling and concrete transient strain have been proposed by Raut et al. [7], Huang et al. [8], etc. Nevertheless, limited test results on restrained columns under eccentric loads had been used for the validation of these numerical models. More importantly, current codes of practice for structural fire design [9,10] only provide tabulated data and simplified design methods for RC columns in braced structures, without any consideration of the combined effects of bending moments and restraint forces. Hence, there is a pressing need to conduct such experiments to enhance understanding of structural responses of RC columns under simultaneous effects of eccentric loads and axial restraint in fire conditions.

The lack of published test results and understanding in this area provide the motivation for the experimental programme in this paper. Six full-size pin-ended concrete column specimens were tested under axial restraint and uniaxial bending at elevated temperatures. The test results including axial deformation, mid-height lateral deflection, thermal-induced restraint force, failure mode and failure time, are presented. They were then compared to those obtained from numerical studies using a finite element-based computer program (SAFIR [11]) for the analyses of heat transfer and behaviour of three-dimensional structures under fire conditions. Both experimental and numerical results showed that under

similar load levels and restraint ratios, column deflections and restraint forces are both affected by uniaxial load eccentricity. On the other hand, it was demonstrated that although premature failures occurred in the tests, numerical models neglecting concrete spalling over-predicted thermal-induced restraint forces of the test specimens. Hence, in order to obtain better predictions of column failure times, the authors propose a modified criterion for rate of change of deflection based on EN 1363-1:1999 [12].

2 EXPERIMENTAL PROGRAMME

2.1 Test specimens

The column specimens tested in this programme are shown in table 1 and figure 1. All the six columns had identical length of 3.3 m and a 300 mm square cross-section. They were all reinforced by six 20 mm-in-diameter longitudinal rebars (6T20) and 8 mm stirrups at a spacing of 250 mm (R8/250). Compressive strength of concrete cylinders and yield strength of reinforcing steel were 55.3 and 550 MPa, respectively. Two specimens, namely, C1-1-00 and C1-2-00, were tested under pure compression whereas the remaining four specimens, namely, C1-3-25, C1-4-40, C1-5-60 and C1-6-80, were subjected to increasing uniaxial load eccentricities of 25, 40, 60, and 80 mm, respectively. In the tests, most of the columns were loaded up to a level of 55% of their individual ambient ultimate strengths with load eccentricity determined based on EC2 Pt.1-1 specifications [13], excluding column C1-1-00, which was subjected to 45%. The columns were all exposed to a non-standard fire condition with an axial restraint ratio of 3.65% until failure occurred.

Table 1. Test specimens

Specimens	Load eccentricity (mm)		Restraint ratio α_r	Test load (kN)	Load level μ_{fi}
	e_y	e_z			
C1-1-00	00	00	0.0365	1720	0.45
C1-2-00	00	00	0.0365	2100	0.55
C1-3-25	00	25	0.0365	1700	0.55
C1-4-40	00	40	0.0365	1400	0.55
C1-5-60	00	60	0.0365	1100	0.55
C1-6-80	00	80	0.0365	900	0.55

Load eccentricity was employed by two blocks with dimensions of $500 \times 500 \times 300$ (mm³) that were designed and cast at both ends of the specimens. Load was applied at the cross-section centre of the end blocks. Hence, eccentricity can be applied by shifting the load application point at the end block relative to the column centroid, as shown in figure 1. It is also shown in the figure that thermocouples were placed at different positions of three column cross-sections, namely, section A-A, B-B, and C-C. For each specimen, a total of fourteen thermocouples were embedded during casting to measure temperature distribution inside the column in the tests.

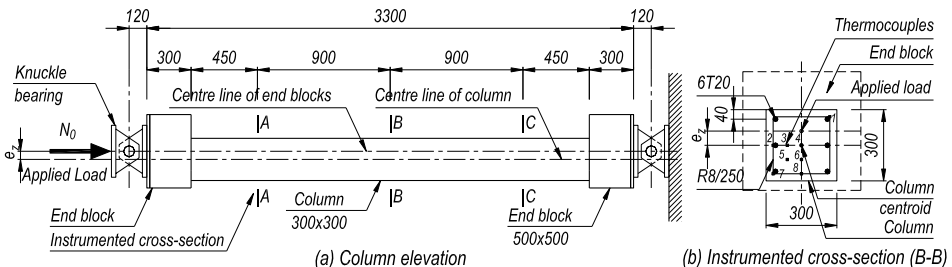


Figure 1. Test specimen.

2.2 Test set-up and apparatus

As illustrated in figure 2, fire tests were conducted on column specimens horizontally placed inside an electric furnace chamber which could be monitored to produce pre-designed fire conditions. The specimen was connected to a steel bulk-head at the right hand side of a self-reaction steel test frame by a knuckle bearing block and was subjected to a horizontal load from a 5000 kN-capacity servo actuator located at the left hand side. The actuator was also fixed to another steel bulk-head of the test frame. Axial restraint was produced in the tests by a transverse steel beam, which was supported by an A-frame at each end. Another knuckle bearing block was located in between the restraint steel beam and the column to provide pin-ended conditions for the test specimen.

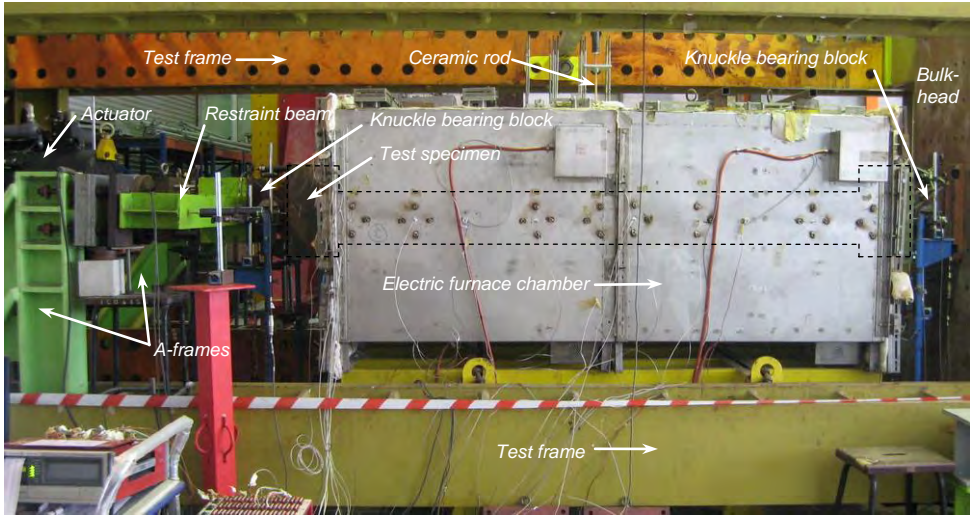


Figure 2. Test set-up and apparatus.

The furnace chamber consisted of four L-shaped electrical panels. Each panel, which was of a power capacity of 22kW/400V/2 phases, could be controlled individually to achieve the maximum allowable operating temperature of 1050 °C with the maximum heating rate of 12 °C/min. Temperatures within the furnace chamber were measured by a number of K-type thermocouples including eight units embedded into the four panels and another eight units installed at different internal positions having the same distance of 70 mm from the heating elements. Temperatures at the four surfaces of the column at its mid-height cross-section were also measured by another four thermocouples.

A number of linear variable differential transformers (LVDTs) were used to measure the displacements of the specimen. For measurement of column axial deformation, four LVDTs were directly attached to the steel plates of the end blocks which were outside of the furnace. Another four LVDTs were used to trace the out-of-plane displacement of the specimen. It was impossible to use LVDTs to obtain direct measurements of lateral deflections at the column mid-height, since this point was inside the furnace and LVDTs do not work properly at high temperatures. Hence, an intermediate measuring system employing ceramic rods was used to transmit the column lateral deflection outward from within the furnace. The deflection could be captured by an LVDT located outside of the furnace. Ceramic rods with a low coefficient of thermal expansion of $7.8 \times 10^{-6}/^{\circ}\text{C}$ were used for the specially-fabricated system. Actual thermal expansion of ceramic rods was calculated and subtracted from the recorded lateral deflection of the column.

2.3 Test procedure

In order to prevent physical damage to the furnace heating elements due to debris from spalling or crushing of concrete, all test specimens were covered by steel meshes. Once the specimen was installed into the test frame, the furnace chamber was closed, all the gaps were sealed with insulation wool and cloth, and LVDTs were positioned. In order to eliminate undesirable slacks within the test system, a preload equalled to 15% test load was repeatedly applied and then released. After that, the specimen was loaded at a constant rate to 100% of the corresponding test load listed in table 1 and was kept unchanged when the supports of the restraint beam onto the reaction A-frames were connected. The elevated-temperature condition according to the non-standard heating curve shown in figure 4 was generated until the combination of the constant applied load and the increasing thermal-induced restraint force could not be sustained by the specimen, indicating the failure occurrence.

3 NUMERICAL SIMULATION

Well verified finite element-based computer program SAFIR [11] was used to predict thermal and structural responses of all test specimens. Temperature-dependent material models for concrete and reinforcing steel specified in EC2 Pt.1-2 [9] were adopted. Mesh sensitivity studies were conducted to determine proper discretizations of 900 two-dimensional (2-D) rectangular solid elements and fifteen 3-D beam elements for modelling cross-section and the column height, respectively (figure 3). An idealised elastic 3-D beam element was used to simulate axial restraint. The column was modelled as a half-sine curve with a crookedness of 8.85 mm at mid-height to account for initial imperfection. This value was adopted based on EC2 Pt.1-1 specification [13], which is 1/400 of the effective column height.

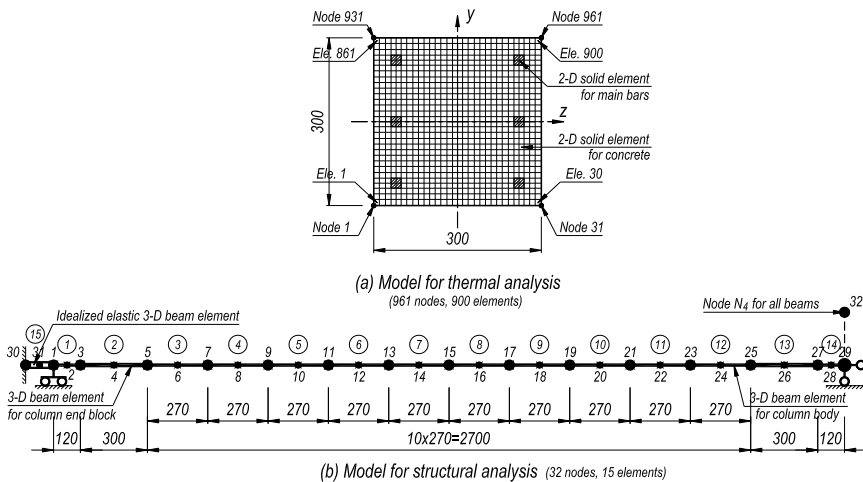


Figure 3. Numerical models for thermal and structural analyses.

4 RESULTS AND DISCUSSIONS

4.1 Heat transfer

Figure 4 depicts the non-standard heating curve set to the furnace, surface temperature modifications of a test specimen, as well as predicted temperature profiles and measurements at points 1, 4, and 8 of the column mid-height cross-section, which were at the corner main bar, centroid, and stirrups, respectively (figure 1(b)). Good agreement between the experimental and numerical results can be observed during the

first 160 min of the test. Beyond this time, the measured temperatures were higher than those predicted by numerical analysis. This is because concrete spalling, which caused some inner parts of the cross-section to be directly exposed to fire and thus resulted in a faster heat transfer, was not considered in the numerical model. Hence, the heating curve at the surface had to be modified in order to fit the numerical data to the measured temperature (figure 4). This curve was then used as the boundary thermal condition to obtain the temperature profile used for numerical analysis of structural response.

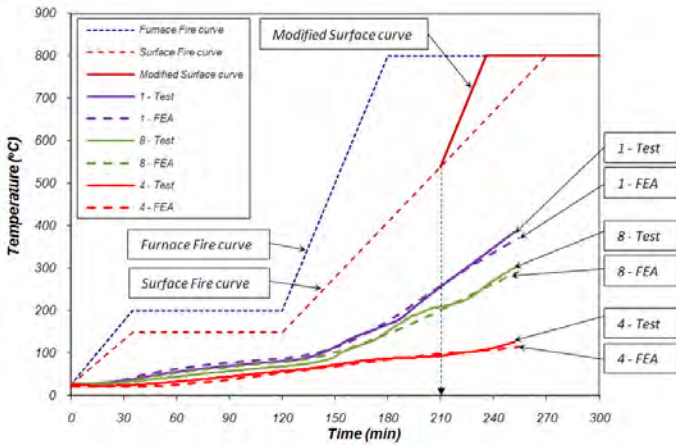
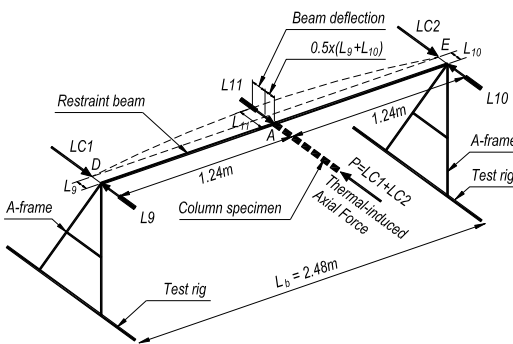


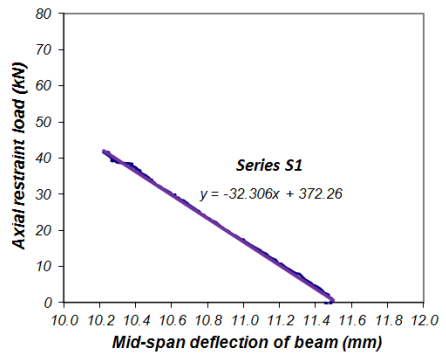
Figure 4. Temperature profiles - Experimental and numerical results.

4.2 Axial restraint

To simulate the axial restraint from surrounding cooler structural elements in framed building systems, a S275 universal steel beam of W10×10×5.25 with a second moment of area $I=4917 \text{ cm}^4$ was used. The restraint beam was supported at its ends by two A-frames at a distance of 2.48 m. The actual axial restraint stiffness, k_A , was experimentally determined to be 32.3 kN/mm, based on the gradient of the graph representing the relationship between the beam mid-span deflection and axial restraint force measured by the two load cells located at the A-frames (figure 5). The spring stiffness k_B of the right steel bulk-head in figure 1 was also experimentally determined to be 1218.4 kN/mm. From the conventional formula $1/k_e=1/k_A+1/k_B$ [14], the equivalent stiffness was calculated as $k_e=31.43 \text{ kN/mm}$, forming a restraint ratio of 0.0365 compared to the column axial stiffness of 861.6 kN/mm.



(a) 3-D view of test set-up



(b) Test result

Figure 5. Axial restraint

4.3 Deflections

Deflections of all test specimens including the axial deformation (u -curve) and mid-height lateral deflection (v -curve) measured in the tests are shown in figures 6 and 7, in a comparison with the corresponding curves obtained from finite element analysis (FEA). The test and FEA curves are plotted in continuous and hidden lines, respectively.

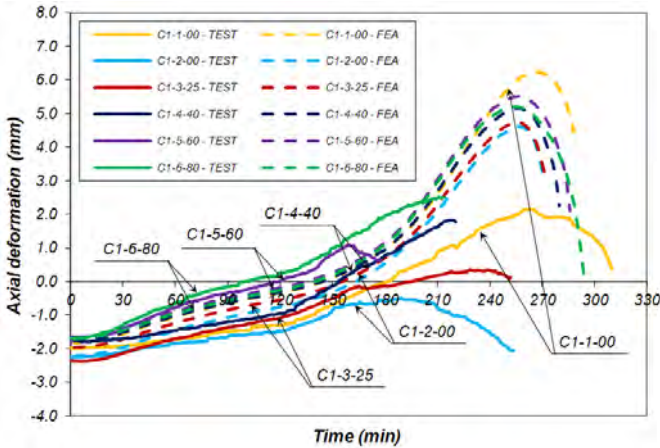


Figure 6. Axial deformation - Experimental and numerical results.

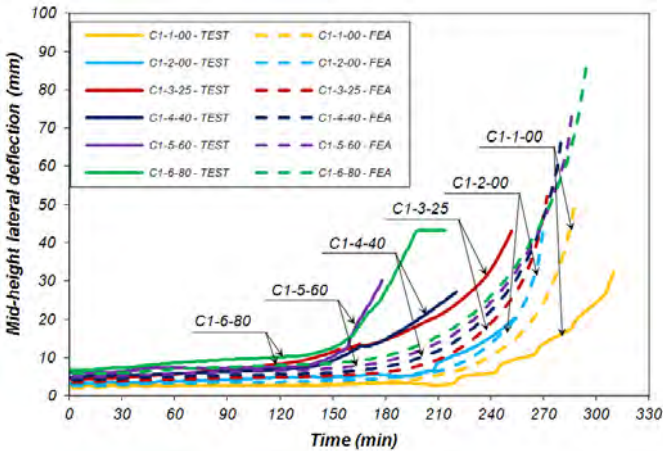


Figure 7. Mid-height lateral deflection - Experimental and numerical results.

A number of observations can be made from figures 6 and 7. Firstly, the test results agreed reasonably well with the numerical predictions during the first 160-min of fire exposure. Beyond this time, specimen C1-3-25 had similar measured and predicted v -curves while the two test and FEA u -curves of specimen C1-4-40 were quite close to one another. However, specimen C1-5-60 had deviations in both axial deformations and mid-height lateral deflections. It was recorded in the test of C1-5-60 that concrete spalling occurred at 159 min. Hence, spikes can be seen on both test u - and v -curves of this specimen. Secondly, it is illustrated by both experimental and numerical results that under the same load level, columns subjected to higher load eccentricities had greater deflections, since all test and FEA u - and v -

curves of specimens C1-2-00, C1-3-25, C1-4-40, C1-5-60, and C1-6-80 arranged in an increasing manner with the extent of load eccentricity. Thirdly, structural responses of columns were affected by load level, since all test and FEA u - and v -curves of specimen C1-2-00, which was at a load level of 55% were higher than those of C1-1-00 subjected to a load level of 45%.

4.4 Restraint forces

Figure 8 depicts the development of thermal-induced compression forces when restrained specimens were heated up, experiencing so-called restraint forces ΔN_a^T . The forces can be expressed in a normalised form which is the ratio of ΔN_a^T to the applied working load N_0 . The experimental and numerical results are also plotted in continuous and hidden lines, respectively.

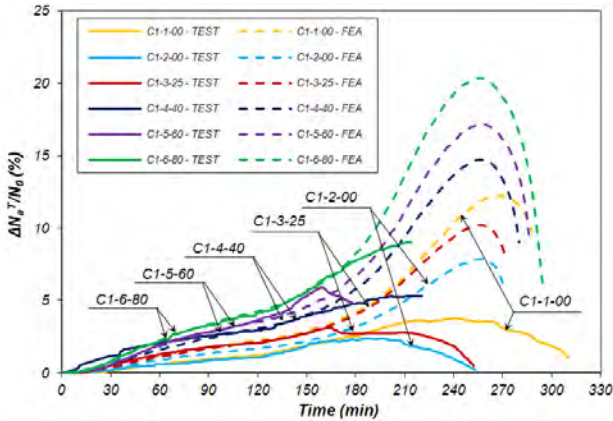


Figure 8. Restraint force - Experimental and numerical results.

Similar trends can be observed from both test and FEA curves shown in figure 8. Firstly, specimen C1-1-00 and C1-2-00 demonstrated that under the same load eccentricity, a higher load level resulted in a lower restraint force represented by the ratio of $(\Delta N_a^T / N_0)$, since specimen C1-2-00 was under a load level of 55% whereas C1-1-00 was at 45%. Secondly, under the same load level, columns subjected to higher load eccentricities suffered greater restraint forces, since both test and FEA curves representing restraint forces of specimens C1-2-00, C1-3-25, C1-4-40, C1-5-60, and C1-6-80 also arranged in an increasing manner with the extent of load eccentricity. Thirdly, it can be seen that numerical predictions were greater than experimental results.

4.5 Failure

Figure 9 is a typical image of specimens dismantled after testing.



Figure 9. Typical failure of test specimens.

It is shown that the failed specimen attained significant mid-height lateral deflection due to global flexural bending, indicating stability failure. Besides, material failure was also obvious since concrete in

compression zone crushed and spalled severely. Being exposed to fire and subjected to high compression forces, the main bars in compression zone buckled between the stirrups. Hence, the specimen can be considered to have failed in a combined manner of global stability and local material failure modes. The times at which concrete spalling occurred were also recorded during the tests when there were either gentle sounds or explosive noises.

Based on the structural behaviour, stability failure (t_s) could be defined when the axial forces shown in figure 8 reached the maximum value. It can be seen in figure 7 that the time to achieve the maximum axial force also roughly corresponded to run-away mid-height lateral deflection. Material failure (t_M) was recognised when the axial deformation reduced indicating that the specimen could not sustain the combined constantly applied and increasing restraint forces. If the material failure occurred after the stability failure, it could be considered as a combined failure (t_c). The failure modes and failure times recorded in the experiments and predicted by numerical analysis are listed in table 2.

Table 2. Test and FEA failure times

Specimens	TEST results (min)			FEA prediction (min)			Comparison		
	t_S^{Test}	t_C^{Test}	Failure mode	t_S^{FEA}	t_C^{FEA}	Failure mode	$\frac{t_S^{FEA}}{t_S^{Test}}$	$\frac{t_C^{FEA}}{t_C^{Test}}$	
C1-1-00	244	310	C	268	288	C	1.098	0.929	
C1-2-00	195	251	C	256	270	C	1.313	1.055	
C1-3-25	215	252	C	256	274	C	1.191	1.034	
C1-4-40	209	221	C	256	280	C	1.225	1.267	
C1-5-60	159	180	PC	256	286	C	1.610	1.589	
C1-6-80	214	-	S	254	294	C	1.187	-	
<i>Notes: S: Stability - C: Combined - PC: Premature Combined failure mode</i>							Mean	1.271	1.125
							COV	0.164	0.323

The table shows that stability failure time (t_s) and combined failure time (t_c) for specimen C1-1-00 agreed well with the FEA predictions with mean ratios of 1.098 and 0.929, respectively. Meanwhile, specimen C1-5-60 attained a large deviation with respective ratios of 1.610 and 1.589. This is because the premature combined failure, which is denoted as PC in the table, was resulted from an explosive spalling recorded at 159 min of the test. With the respective mean ratios of 1.271 and 1.125, the stability and combined failure times of all test specimens were generally over-predicted by FEA, in which concrete spalling was not considered.

A modification of the analysis of numerical results based on Eurocode specification for fire resistance tests given in EN 1363-1:1999 [12] was proposed to obtain better predictions of stability failure time. It is proposed that the performance criteria of load-bearing capacity should be based on the magnitude and the rate of flexural deflection for columns tested in a standard fire condition. Since a non-standard fire was used in this study, the EN 1363 criterion was modified to be $v' = k_{fire} L^2 / 9000d$ where L is the clear span of specimen at 3540 mm, d is the distance from the extreme fibres of the cold design zones of compression tension of the cross-section at 230 mm, k_{fire} is a modified factor that accounts for fire exposure and concrete spalling. Two values of 1.0 and 1.5 for k_{fire} corresponding to the respective deflection rates of 0.10 and 0.15 mm/s were investigated. The modified stability failure times, namely, t_S^{FEA*} , are listed in table 3. It is shown that with a mean ratio of 1.009, the deflection rate of $v'=0.15$ mm/s provided a much better agreement between the modified FEA and test results. Thus the proposed equation for lateral deflection can be chosen as the numerical criterion of stability failure time in this study.

The stability failure times obtained from tests and predicted by modified FEA results are summarised in figure 10, from which the following observations can be made: (i) the column subjected to a lower load level attained a longer stability failure time. For specimen C1-1-00, which was under a load level of 45%, t_S^{Test} is 244 min whereas that of specimen C1-2-00 tested with a load level of 55% is 195 min; and (ii) for uniaxially-loaded columns under similar levels of working load and axial restraint (specimens C1-2-00,

C1-3-25, C-1-4-40, C1-5-60, and C1-6-80), the higher the load eccentricity, the shorter is the stability failure time attained.

Table 3. Test and modified FEA stability failure times

Specimens	TEST results t_S^{Test} (min)	Modified FEA t_S^{FEA*} (min)		Comparison t_S^{FEA*} / t_S^{Test}	
		$k_{fire}=1.0$	$k_{fire}=1.5$	$k_{fire}=1.0$	$k_{fire}=1.5$
C1-1-00	244	210	226	0.861	0.926
C1-2-00	195	209	217	1.072	1.113
C1-3-25	215	195	209	0.907	0.958
C1-4-40	209	186	199	0.890	0.952
C1-5-60	159	180	193	1.132	1.214
C1-6-80	214	178	191	0.832	0.893
			Mean	0.949	1.009
			COV	0.112	0.115

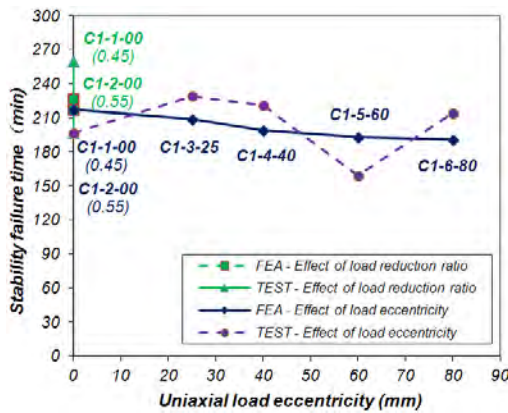


Figure 10. Stability failure time – Test results and modified FEA predictions.

5 CONCLUSION

This paper presents the fire tests conducted on six concrete columns simultaneously subjected to eccentric loads and axial restraint. The experimental evidences obtained were compared to the numerical predictions using SAFIR program. The column structural responses under such critical loading and restraint conditions at elevated temperatures can be observed to be: (i) under the same load level and restraint ratio, columns subjected to higher load eccentricities experienced higher axial deformations, mid-height lateral deflections, as well as greater development of restraint forces; (ii) under the same restraint ratio and load eccentricity, columns subjected to a higher load level had a lower development of restraint forces; (iii) premature failures could occur due to concrete spalling; and (iv) the numerical analysis that ignores concrete spalling over-estimated restraint forces.

A modified criterion for deflection change rate based on the Eurocode specification for standard fire tests has been proposed to obtain better numerical predictions of stability failure times. Results of the modified approach showed that stability failure time of axially-restrained columns subjected to eccentric loads was both affected by load eccentricity and load level.

In order to supplement understanding of structural behaviour of columns under realistic fire, loading, and restraint conditions, an experimental programme on axially-restrained concrete columns subjected to

biaxial bending has also been conducted by the authors and will be presented as soon as the analyses are completed.

ACKNOWLEDGEMENT

The authors gratefully acknowledge the research project MINDEF-NTU/JPP/FY05/14 and Singapore Agency of Science, Technology and Research (A*STAR) who financially support for this study. Mr Yao Yao, who contributed in the early stage of the experimental programme, is also acknowledged.

REFERENCES

- [1] Lie T.T., Lin T.D., “Influence of Restraint on Fire Performance of Reinforced Concrete Columns”, *Proceedings of the First International Symposium of Fire Safety Science*, Gaithersburg, 1985.
- [2] Wang Y.C., Moore D.B., “Effect of Thermal Restraint on Column Behaviour in a Frame”, *The fourth International Symposium of Fire safety science*, Ottawa, p1055-66, 1994.
- [3] Ali F., Nadjai A., Silcock G. and Abu-Tair A., ‘Outcomes of a Major Research on Fire Resistance of Concrete Columns’, *Fire Safety Journal*, 39, 433-445, 2004.
- [4] Wu B., Li Y-H., “Experimental Study on Fire Performance of Axially-Restrained NSC and HSC Columns”. *Structural Engineering and Mechanics*, 32(5), 635-48; 2009.
- [5] Martins A.M.B., Rodrigues J.P.C., “Behavior of Concrete Columns Subjected to Fire”. *Proceedings of the Sixth International Conference SiF, USA*, 181-188, 2010.
- [6] Kodur V.K.R., Raut N., “Fire Resistance of Reinforced Concrete Columns – State-of-the-art and Research Needs”, *ACI Special Publication*, 255, 97-124, 2008.
- [7] Raut N., Kodur V.K.R., “Response of Reinforced Concrete Columns under Fire-induced Biaxial Bending”, *ACI Structural Journal*, 108(5), 610-619, 2011.
- [8] Huang Z., Burgess I.W, and Plank R.J, “Three-dimensional Analysis of Reinforced Concrete Beam-column Structures in Fire”, *Journal of Structural Engineering*, 135(10) 1201-1212, 2009.
- [9] EN 1992-1-2, Eurocode 2, “Design of Concrete Structures – Part 1-2: General Rules, Structural Fire Design”, *CEN*, 2004.
- [10] ACI/TMS Committee 216, “Code Requirements for Determining Fire Resistance of Concrete and Masonry Construction Assemblies (ACI 2.16.1-07/TMS-216-07)”, *American Concrete Institute*, 2007.
- [11] Franssen J.M., “SAFIR. A Thermal/Structural Program Modelling Structures under Fire”, *Engineering Journal A.I.S.C.*, 42(3), 143-158, 2005.
- [12] EN 1363-1:1999, “Fire resistance tests. Part 1: General requirements”, *European Committee for Standardization (CEN)*, 1999.
- [13] EN 1992-1-1, Eurocode 2, “Design of Concrete Structures – Part 1-1: General Rules and Rules for Buildings”, *CEN*, 2004.
- [14] Huang Z.F., Tan K.H., “Structural Response of Restrained Steel Columns at Elevated Temperatures. Part 2: FE Simulation with Focus on Experimental Secondary Effects”, *Engineering Structures*. 29, 2036-2047, 2007.

FIRE PERFORMANCE OF RESTRAINED RC COLUMNS WITH TIME-DEPENDENT SIDESWAY

Bo Wu*, Xiaomei Chen*

*State Key Laboratory of Subtropical Building Science, Department of Civil Engineering,
South China Univ. of Technology, Guangzhou 510640, P. R. of China
e-mails: bowu@scut.edu.cn, X.M.Chen_scut@hotmail.com

Keywords: Time-dependent sidesway, Restrained RC columns, Fire performance

Abstract: *Abundant research has been conducted on the fire performance of reinforced concrete (RC) columns, as they are the most important load-bearing components in the RC frame structures. In the past decades most of the researches focused on the independent RC columns and restrained RC columns without sidesway to investigate the columns' thermal and mechanical behaviours in fire and the interactions between the columns and their adjacent structural components. However, lateral displacements do exist at the column ends, due to the thermal expansion of the adjacent beams in fire, and this may affect the fire behaviours of the columns to some extent.*

Therefore, an evaluation model is proposed firstly in this paper for the time-dependent lateral displacements at the column ends. Then, the fire behaviours of the restrained columns with time-dependent sidesway are studied and compared with those without sidesway.

1 INTRODUCTION

The performance of a building structure in fire depends greatly on the fire behaviours of the columns. In the past decades, there were many researches on the fire behaviours of individual RC columns^[1, 2]. For consideration of the interaction between RC columns and their adjacent structural components, restraints were applied to the columns^[3, 4], leading the fire behaviours of the columns more reasonable. However, when a frame structure is in fire, the lateral displacements at the column ends, due to the thermal expansion of the beams, do exist and may affect the fire behaviours of the columns or even the whole structure to some extent^[5].

Till now there are few studies on the lateral displacements of RC columns due to thermal expansion of the beams^[6]. So in this paper, through analyses of RC frame structures in fire, an evaluation model is proposed firstly for the time-dependent lateral displacements at the column ends, and the variation of the column's sidesway with time is further determined. Then, the fire behaviours of restrained RC columns with time-dependent sidesway are investigated and compared with those without sidesway.

For all the analyses in this study, the computer program SAFIR developed at the University of Liege is used, and the ISO834 standard fire is considered.

2 TIME-DEPENDENT SIDESWAY OF COLUMNS

2.1 Validation of analytical method

In this paper, the computer program SAFIR is used for all the analysis. In this section, some RC columns and frame structures tested by former researchers are analyzed firstly, and the simulation results are compared with the measured results to ensure the effectiveness of the analytical method.

Twelve RC columns with square or special-shaped cross section were tested in fire in literature [7]. A comparison between the measured axial deformation-time curve of Specimen Z12 and the corresponding simulated curve is shown in Fig. 1, and the measured and simulated fire endurance of this specimen are, respectively, 165 min and 175 min with an error of only 6%. It can be seen that the analytical result is in good agreement with the test result on the whole.

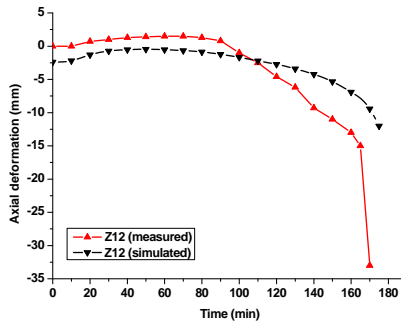


Figure 1. Comparison of measured and simulated axial deformation-time curves of Specimen Z12.

In 1996, four RC plane frames were tested in fire by Yao and Zhu [8]. The measured and simulated lateral displacement-time curves at Point 2 in Specimens FFR-3 and FFR-4 are compared in Fig. 2. It also can be seen that the analytical results are in good agreement with the test results on the whole.

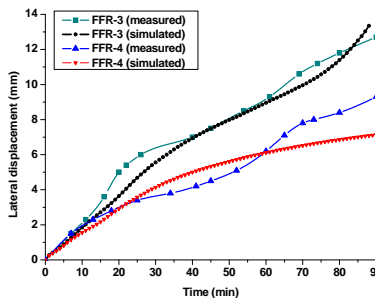


Figure 2. Comparison of measured and simulated lateral displacement-time curves at Point 2 in Specimens FFR-3 and FFR-4.

2.2 Evaluation model of time-dependent sidesway

In order to investigate the column's time-dependent sidesway, an example RC frame structure with 5 storeys and 5 bays is considered in this study (see Fig. 3). For the example structure, the fundamental parameters (i.e., dimensions of the columns and beams, loading situation, and strengths of concrete and steel bar) are listed in Table 1. Four fire scenarios (i.e., only the 3rd storey in fire - Fire Condition 1, both the 2nd and 3rd storeys in fire - Fire Condition 2, both the 3rd and 4th storeys in fire - Fire Condition 3, and the 2nd, 3rd and 4th storeys in fire - Fire Condition 4) are taken into account.

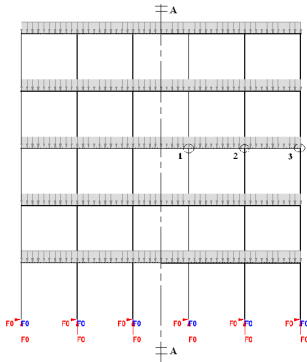


Figure 3. Example structure.

Table 1. Parameters of example structure.

Sectional dimensions of column	300 mm × 600 mm
Column length	3000 mm
Sectional dimensions of beams	250 mm × 400 mm
Beam span	3000 mm
Uniform distributed load of beam	15 kN/m
Prismatic compressive strength of concrete	22.8 MPa
Yield strength of steel bar	375 MPa

The lateral displacement-time curves at beam-column joints 1, 2, and 3 (see Fig. 3) are, respectively, shown in Fig. 4 for different fire conditions mentioned above. It can be seen that: (a) the lateral displacements at the beam-column joints increase significantly with the increasing of the heating time, due to the thermal expansion of the heated beams; (b) the lateral displacements at the beam-column joints increase with the number of storeys in fire, while those related to Fire Conditions 3 are larger than those corresponding to Fire Condition 2; and (c) the lateral displacement at the beam-column joint increases greatly with an increasing of the distance between the joint and the symmetric axis A-A of the example structure.

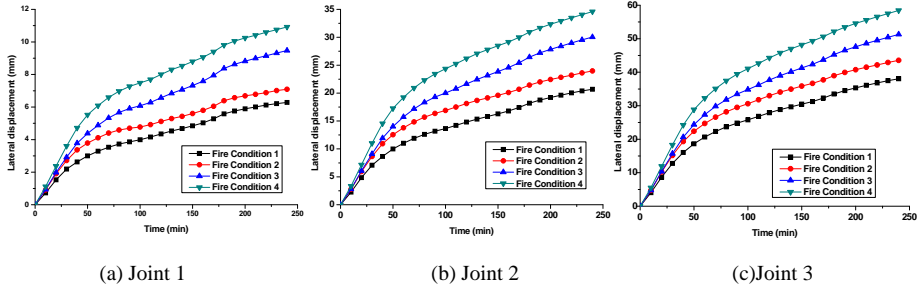


Figure 4. Lateral displacement-time curves at beam-column joints 1, 2, and 3.

For the example structure with different values of beam’s span and sectional dimensions and different column’s length and sectional dimensions, extensive simulations are conducted and conclusions similar to those from Fig. 4 can be obtained. Based on the simulation results, the time-dependent lateral displacement at any beam-column joint of the 3rd storey, $S(t)$, is expressed as follow:

$$S(t) = \eta \cdot \beta \cdot f(t) \tag{1}$$

in which t is the heating time; η is an adjusting factor to consider different fire conditions; β is related to the location of the beam-column joint; and $f(t)$ is the time-dependent lateral displacement at the outermost beam-column joint of the 3rd storey (i.e., Joint 3) under Fire Condition 1.

2.3 Determination of η , β , and $f(t)$

2.3.1 Discussion on η

Based on the extensive simulation results mentioned above, η is defined as a ratio of the time-dependent lateral displacement of a given beam-column joint at the 3rd storey under Fire Condition i ($i=1, 2, 3, 4$) to that under Fire Condition 1. Fig. 5 illustrates the variation of η with the heating time related to Joint 3. It can be seen that for a given fire condition, η is almost changeless with an increasing of the heating time except that in the early heating stage. Referring to Fig. 6, the following empirical formula is presented to determine the value of η at Joint j as:

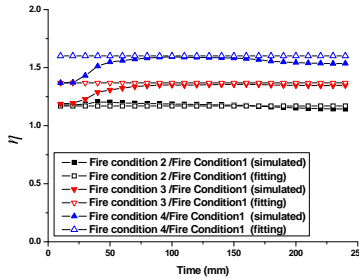


Figure 5. Variation of η with heating time.

$$\eta = b^n; \quad b(L_j, K_j) = 1.4 \times 10^{-5} L_j + 0.22 \lg K_j; \quad K_j = \sum_{k=j}^m K_{ck} \quad (2)$$

in which n is a fire condition factor with a value of 0, 1, 2, 3 for Fire Conditions 1, 2, 3, 4, respectively; K_j , K_{ck} and L_j are all related to the situation that only one storey in fire (i.e., Fire Condition 1 in this paper); K_{ck} is the lateral stiffness of the column k just above the fired storey, N/mm²; and L_j is the distance between the symmetric axis A-A and Joint j , mm. For Joint 3 in Fig. 3, the calculated η using Eq.(2) is also listed in Fig. 5. It is found that Eq.(2) can be utilized to determine the value of η effectively.

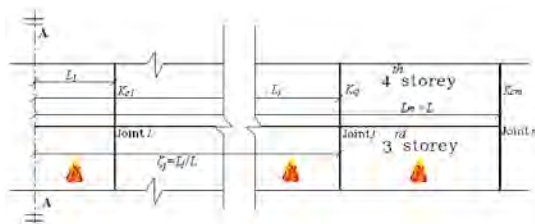


Figure 6. Example structure in Fire Condition 1.

2.3.2 Discussion on β

Based on the extensive simulation results mentioned above, β is defined as a ratio of the time-dependent lateral displacement of a given beam-column joint at the 3rd storey to that of Joint 3 under Fire Condition 1. Fig.7 shows the variation of β with the heating time. It can be seen that for a given beam-column joint at the 3rd storey, β can be regarded as a constant approximately. Referring to Fig.6, the following expression is proposed to determine the value of β at Joint j as:

$$\begin{cases} \beta = 0.95\zeta_j & \zeta_j < 1 \\ \beta = 1.0 & \zeta_j = 1 \end{cases} \quad (3)$$

in which $\zeta_j = L_j / L$, and L is the distance between the symmetric axis A-A and the outmost Joint m (see Fig.6). The calculated β using Eq.(3) is also shown in Fig.7. It is found that Eq.(3) can be used to determine the value of β approximately.

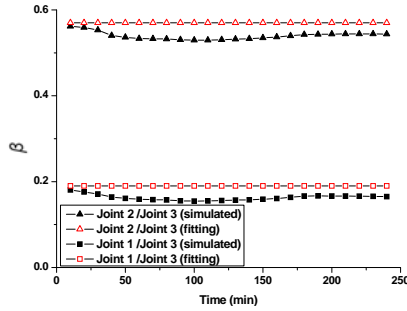


Figure 7. Variation of β with heating time.

2.3.3 Discussion on $f(t)$

To analyze the time-dependent lateral displacement at the outermost beam-column joint of the 3rd storey (i.e., Joint 3) under Fire Condition 1, a simplified model shown in Fig.8 is considered. The fundamental parameters of the simplified model are the same as those listed in Table 1. Fig. 9 shows a comparison of the lateral displacements of Joint 1, 2 and 3 in the example structure under Fire Condition 1 with those in the simplified model.

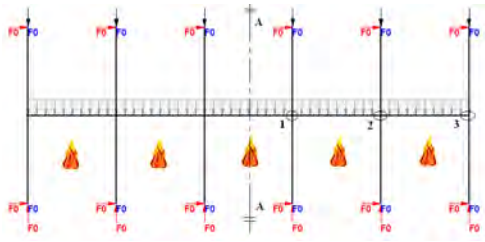


Figure 8. Simplified model.

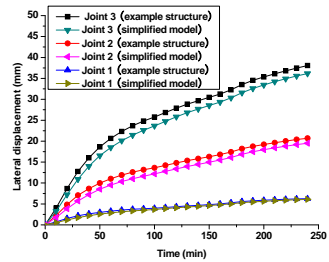
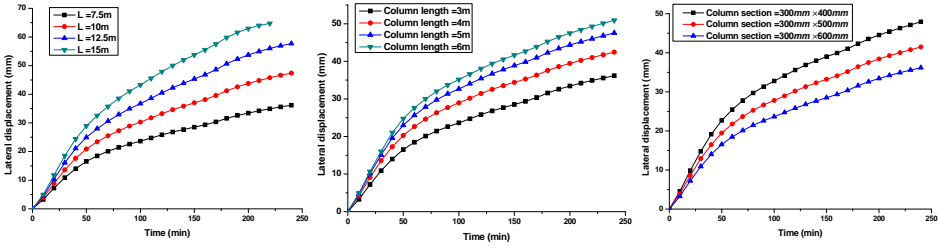


Figure 9. Comparison of the lateral displacements

in the example structure with those in the simplified model.

It can be seen from Fig.9 that the simulation results from the simplified model are in good agreement with those from the example structure, and the errors between them are less than 10%. In this way, the simplified model is adopted hereafter to analyze $f(t)$.

It is found through parametric study that some parameters (including the distance between the symmetric axis A-A and the outmost joint, L , sectional dimensions of column, and column length) affect $f(t)$ greatly. This is attributed to the fact that the lateral displacement at the outmost joint depends mainly on the total length of the heated beams while is restricted by the columns. Fig.10 shows the influences of these parameters on the lateral displacement at the outmost joint (i.e., Joint 3 in Fig.8).



(a) Influence of L (b) Influence of column length (c) Influence of column's sectional dimension

Figure 10. Influences of main parameters on the lateral displacement at the outmost joint.

Based on the extensive numerical simulations, the following expression is suggested to evaluate $f(t)$ as:

$$f(t) = (0.04t^3 - 2t^2 + 400t) \times 10^{-6} \times L \times K_{total}^{-1/6} \quad (0 \leq t \leq 240 \text{ min}) \quad (4)$$

in which t is the heating time; and $K_{total} = \sum_{k=1}^m K_{ck}$, K_{ck} is given in Eq.(2).

3 FIRE PERFORMANCE OF RC COMLUMNS WITH SIDESWAY

Fire performance of a RC column with a cross section of 300 mm×600 mm shown in Fig.11 subjected to ISO834 standard fire is investigated in this paper by using SAFIR, taking the axial and rotational restraints into account. Meanwhile, the time-dependent lateral displacement is applied to the column's upper end. In Fig.11, N is the axial load applied to the column, and K_l and K_r are, respectively, the axial and rotational restraint stiffness at the column ends. Axial restraint ratio β_l and rotational restraint ratio β_r are defined as:

$$\beta_l = \frac{K_l}{E_0 A_c / H}; \quad \beta_r = \frac{K_r}{4E_0 I_c / H} \quad (5)$$

in which E_0 is the elastic modulus of concrete at room temperature; A_c is the sectional area of the column; H is the column length; and I_c is the moment of inertia of the column section.

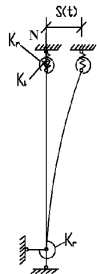


Figure 11. Restrained RC column with sidesway

For convenience, the time-dependent lateral displacements at Joint 3 of the example structure with parameters listed in Table 1 under Fire Conditions 1, 2, 3 and 4 are, respectively, nominated as $S(t)_1$, $S(t)_2$, $S(t)_3$, and $S(t)_4$. In the case that the axial and rotational restraint ratios are 0.1 and 2.0, respectively, and the column's axial load ratio is 0.2, the axial force and axial deformation related to the column with lateral displacement at the upper end are compared with those without sidesway and shown in Fig.12. It can be seen that the axial force in the column with sidesway is less than that without sidesway, but the axial deformation of the column with sidesway is larger than that without sidesway.

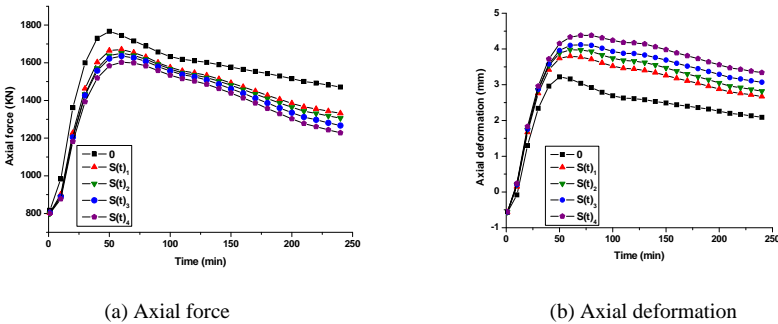


Figure 12. Comparison of fire behaviours of columns with and without sidesway (axial load ratio=0.2).

In the case that the axial and rotational restraint ratios are 0.1 and 2.0, respectively, and the column's axial load ratio is 0.6, the axial force and axial deformation related to the column with lateral displacement at the upper end are compared with those without sidesway and shown in Fig.13. It can be seen that the fire endurance of the column with sidesway $S(t)_2/S(t)_3/S(t)_4$ is much less than that without sidesway. This is due to that larger axial load ratio combined with larger sidesway leads to severer second order moment in the column, resulting in significant reducing in the fire performance of the restrained column.

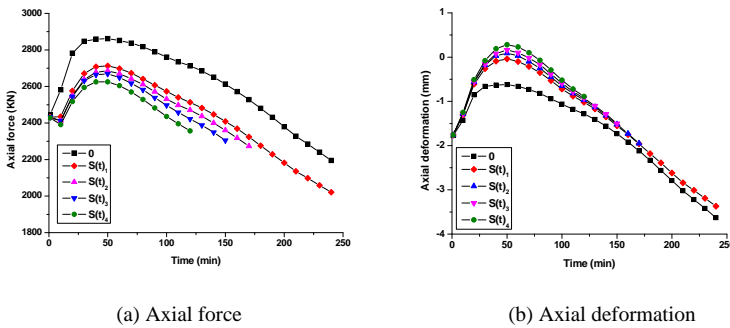


Figure13. Comparison of fire behaviours of columns with and without sidesway (axial load ratio=0.6).

4 CONCLUSIONS

(1) An evaluation model is proposed in this paper to determine the time-dependent lateral displacement at the frame column end in fire. It is found that the lateral displacement increases significantly with an increasing of the heating time and relies on the frame structure's fire scenario greatly.

(2) The axial force in the restrained column with sidesway is less than that without sidesway, but the axial deformation of the restrained column with sidesway is larger than that without sidesway.

(3) In the case that the column's axial load ratio is large, the fire endurance of the restrained column with sidesway may be much less than that without sidesway. Therefore it is necessary to take the time-dependent sidesway into account when the fire performance of the restrained column is studied.

ACKNOWLEDGEMENT

The research reported was financially supported by the National Natural Science Foundation for Distinguished Young Scholars (51025829), the National Basic Research Program of China (973 Program: 2011CB013800), the Funds of State Key Laboratory of Subtropical Building Science of China (2011ZB07), and the Fundamental Research Funds for the Central Universities (2012ZZP0011). The financial supports are highly appreciated.

REFERENCES

- [1] Lie T. T., Celikkol B., "Method to calculate the fire resistance of circular reinforced concrete columns", *ACI Materials Journal*, 88(1), 84-91, 1991.
- [2] Tan K. H., Yao Y., "Fire resistance of four-face heated reinforced concrete columns", *J. of Structural Engineering*, 129 (9), 1220-1229, 2003.
- [3] Benmarce A., Guenfound M., "Behaviour of axially restrained high strength concrete columns under fire", *Construction & Building Materials*, 58 (9), 1211-1230, 2002.
- [4] Wu B., Xu Y. Y., "Behavior of axially and rotationally restrained concrete columns with '+'-shaped cross section and subjected to fire", *Fire Safety Journal*, 44 (2), 212-218, 2009.
- [5] Mostafaei H., Sultan M. A., Benichou N., "Performance of structural systems in fire", *Applications of Structural Fire Engineering - Proceedings of International Conference*, Pražská technika Publications, Prague, Czech, 604-609, 2009.
- [6] Xavier H. F., Faria R., Real P. V., "Influence of thermal elongation of beams on the fire resistance of RC frames", *Structures on Fire – Proceedings of the Sixth International Conference*, V. Kodur, J.-M. Franssen (eds.), DESTech Publications, Lancaster, 262-269, 2010.
- [7] Xu Y. Y., "Fire resistance of reinforced concrete columns with special-shaped cross section", *Ph.D. dissertation*, Dept. of Civil Engineering, South China Univ. of Tech., Guangzhou, China, 2006 (in Chinese).
- [8] Yao Y. X., Zhu B. L., "Experimental studies on fire-resistance of reinforced concrete frames", *J. of Tongji University*, 24(6), 619-624, 1996 (in Chinese).

GLOBAL RESISTANCE FACTOR FOR CONCRETE SLABS EXPOSED TO FIRE

Ruben Van Coile*, Robby Caspee* and Luc Taerwe*

* Magnel Laboratory for Concrete Research, Ghent University
e-mails: ruben.vancoile@ugent.be, roby.caspee@ugent.be, luc.taerwe@ugent.be

Keywords: structural fire safety, global resistance factor, concrete slab, fire.

Abstract. *In this paper a safety format is proposed to be applied when using Finite Element Models (FEM) to calculate the structural response of concrete slabs during fire. It is suggested to divide the structural resistance obtained with a FEM analysis by a global partial factor. While maintaining a high level of simplicity, the proposed method takes into account the consequence class of the structure and the fire incidence rate, and allows for the incorporation of other fire protection measures.*

1 INTRODUCTION

Non-linear FEM analyses have become increasingly important for the assessment of new and existing concrete structures. Since this type of analysis takes into account the structural interaction between different sections and possible stress redistributions, a more economic design can be obtained. However, there are no clear prescriptions in the current codes on which safety format should be used for a design based on non-linear FEM analysis. Especially for concrete structures exposed to fire a non-linear FEM analysis can be of great value and an adequate safety format should be proposed.

2 A SAFETY FORMAT FOR NON-LINEAR FINITE ELEMENT ANALYSIS

Different possible safety formats for non-linear analysis are listed by Cervenka [1]. It is concluded that the standard partial safety factor method (PSFM) cannot be applied to non-linear FEM calculations since the use of the extremely low design values for material properties may alter the structural response calculated by the non-linear FEM analysis. Furthermore, the variability of the concrete cover has an important influence on the obtained safety level of concrete elements exposed to fire due to its effect on the reinforcement temperature [2]. These effects cannot be accounted for directly with the PSFM.

Different alternatives to the partial factor method have been developed [1], [3-6]. From a theoretical point of view a full probabilistic finite element analysis (PFEA) is preferable. The use of PFEA however requires significant computational efforts due to the repeated random sampling and subsequent non-linear FEM analysis [6]. Specifically for elements exposed to fire, the calculation time further increases due to the time-dependent response to fire exposure. This can be considered prohibitive for practical applications. Furthermore, PFEA requires basic knowledge on the distributions and corresponding parameters of all probabilistic variables.

It is concluded that the global resistance factor (GRF) is the most promising safety format to be used for non-linear fire design of concrete structures. In this approach a single non-linear analysis is performed using mean values for the material characteristics and geometrical properties. Subsequently the calculated resistance μ_R is divided by a global resistance factor γ_R to derive the design value for the structural resistance R_d (1), [4].

$$R_d = \frac{\mu_R}{\gamma_R} \quad (1)$$

This paper derives a global resistance factor γ_R to be used when calculating the bending moment capacity of concrete slabs exposed to fire.

3 THE GLOBAL RESISTANCE FACTOR

In accordance with EN 1990 [7], the design value for the structural resistance is defined by (2), with Φ the standardized cumulative normal distribution, α_R the sensitivity factor of the resistance and β the reliability index.

$$P[R \leq R_d] = \Phi(-\alpha_R \beta) \quad (2)$$

Assuming a lognormal distribution for the structural resistance R , (3) is derived from (2), with V_R the coefficient of variation of the resistance.

$$R_d \cong \mu_R \exp(-\alpha_R V_R \beta) \quad (3)$$

If the resistance follows a normal distribution, R_d is defined by (4).

$$R_d = \mu_R (1 - \alpha_R V_R \beta) \quad (4)$$

Combining equations (1) and (3) yields (5). This equation was used by Holický to demonstrate the large variability of γ_R for concrete elements at normal temperatures [5].

$$\gamma_R = \exp(\alpha_R V_R \beta) \quad (5)$$

If the resistance R follows a normal distribution, equation (6) should be used.

$$\gamma_R = \frac{1}{1 - \alpha_R V_R \beta} \quad (6)$$

It is clear from these equations that γ_R depends on the target value of the reliability index β and the coefficient of variation V_R of the resistance effect.

4 THE TARGET RELIABILITY INDEX β IN CASE OF FIRE

For the reliability index β in equations (5) and (6), the target reliability index $\beta_{t,fi}$ for structural elements exposed to fire (considering a reference period of 1 year) is defined by (7) with $P_{f,fi}$ the maximum allowable probability of structural failure during fire (i.e. at elevated temperatures), $P_{f,EN1990}$ the annual probability of structural failure during normal design conditions (i.e. at 20°C), p_{fi} the annual probability that the structure is exposed to a fully developed fire that threatens structural integrity and $\beta_{t,EN1990}$ the target reliability index for structures in normal conditions for a one year reference period [9].

$$P_{f,fi} = \frac{P_{f,EN1990}}{p_{fi}} = \frac{\Phi(-\beta_{t,EN1990})}{P_{fi}} = \Phi(-\beta_{t,fi}) \quad (7)$$

This safety concept was developed by Weilert and Albrecht [9] and is now incorporated in the German code [10]. An English summary of the concepts and calculations is provided in [11].

Although it is demonstrated by Holický and Retief that the tabulated values for $\beta_{t,EN1990}$ are often a crude simplification and the actual target reliability index for a construction should be calculated based

on the design working life, an appropriate discount rate and the consequences of a structural failure [8], the values prescribed by EN 1990 will be accepted in this paper in order to maintain full compatibility with the Eurocodes.

The annual probability p_{fi} that the structure is exposed to a fire that threatens structural integrity is calculated by equation (8), taking into account the annual probability of fire initiation p_1 , the probability that the fire is not extinguished by the users of the structure p_2 , nor by the fire brigade p_3 , and the probability of failure of the sprinkler system p_4 . A table with values for p_1 is suggested in [12]. Other fire mitigation measures can easily be included in the calculation.

$$p_{fi} = p_1 p_2 p_3 p_4 \tag{8}$$

The calculation procedure is illustrated by Table 1 for different types of buildings and for different consequence classes RC [7]. For a warehouse the value of p_{fi} is largely dependent on the compartmentation. In Table 1, a warehouse compartment of 1000 m² is assumed. The calculations are performed for buildings where no sprinkler system is available (i.e. $p_4 = 1$).

Table 1. Calculation of $\beta_{t,fi}$ for different building with different use and consequence class

Example building	Consequence Class	$\beta_{t,EN1990}$ [-]	p_{fi} [-]	$\beta_{t,fi}$ [-]
Hospital	RC3	5,2	$1,12 \cdot 10^{-4}$	3,12
Office building	RC2	4,7	$4,2 \cdot 10^{-5}$	1,87
Residential building	RC2	4,7	$9,4 \cdot 10^{-5}$	2,20
Production hall	RC2	4,7	$1,28 \cdot 10^{-4}$	2,32
Warehouse	RC1	4,2	$1,4 \cdot 10^{-3}$	2,34

For practical use $\beta_{t,fi}$ is illustrated in Figure 1 as a function of the consequence class and the probability of a fully developed fire p_{fi} .

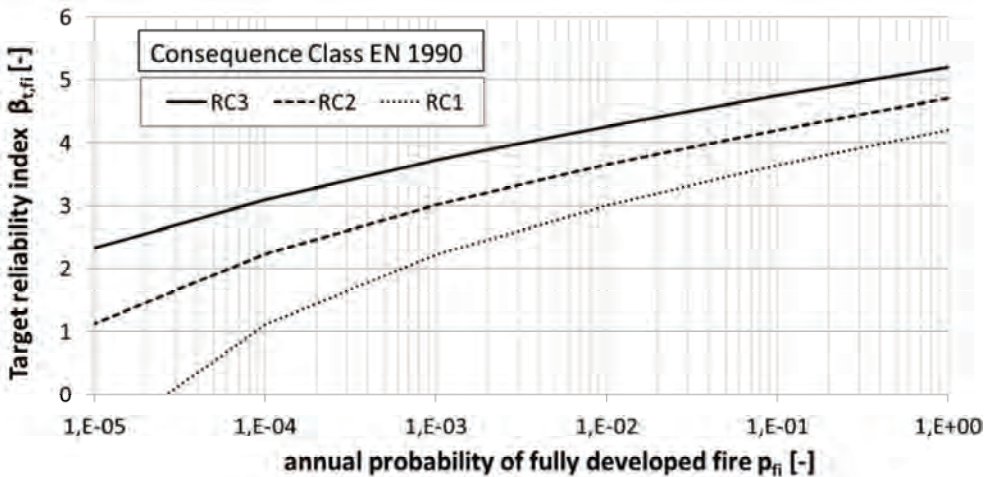


Figure 1. Target reliability index $\beta_{t,fi}$ for structural elements exposed to fire, for different consequence classes RC, as a function of the annual probability p_{fi} of a fully developed fire.

5 CALCULATION OF THE GLOBAL RESISTANCE FACTOR IN CASE OF CONCRETE SLABS

The sensitivity factor α_R for the resistance effect can generally be approximated by 0,8 [13]. The evaluation of the global resistance factor γ_R through equations (5) and (6) requires an assessment of the coefficient of variation V_R of the bending moment capacity of concrete slabs during fire. The computational effort of calculating the mean and standard deviation of R through a probabilistic finite element analysis (PFEA) makes PFEA inefficient for many practical design situations. One can however assess the mean μ_R and standard deviation V_R of the slab configuration through Monte Carlo simulations using a simplified full-probabilistic model, adapted from [14].

The mechanical strain $\epsilon_{\sigma,\theta}$ at temperature θ is calculated by (9), adapted from [15], with $\epsilon_{th,\theta}$ the free thermal elongation and $\epsilon_{tot,\theta}$ the total cross section deformation. For slabs the influence of transient strains can be neglected [16].

$$\epsilon_{\sigma,\theta} = \epsilon_{tot,\theta} - \epsilon_{th,\theta} \quad (9)$$

Mechanical material properties of concrete and reinforcement are applied in accordance with EN 1992-1-2 [17], but taking into account an additional uncertainty with respect to the reduction of the mechanical properties at elevated temperatures as explained in [14]. The actual calculation of the bending moment capacity is based on the same assumptions as made by Kodur and Dwaikat [18]:

1. Plane sections remain plane (Euler-Bernouilli hypothesis)
2. Bond slip between concrete and reinforcement is neglected
3. Spalling is neglected

No model uncertainty was taken into account, as it isn't yet clear which model uncertainty would be appropriate for non-linear FEM analysis for concrete elements exposed to fire and how these would need to be incorporated.

For a concrete slab with nominal properties according to Table 2, the calculated evolution and scatter of the bending moment capacity during fire are visualized in Figure 2.

Table 2. Nominal properties of the analysed concrete slab.

Symbol	Name	Dimension	Nominal value
h	thickness	mm	200
$f_{ck}(20^\circ\text{C})$	20°C characteristic concrete compressive strength	MPa	20
$f_{yk}(20^\circ\text{C})$	20°C characteristic steel yield strength	MPa	500
$E_c(20^\circ\text{C})$	20°C concrete modulus of elasticity	GPa	28.8
$E_s(20^\circ\text{C})$	20°C steel modulus of elasticity	GPa	200
c_{nominal}	concrete cover	mm	35
\emptyset	reinforcement diameter	mm	10
s	bar spacing bottom reinforcement	mm	100

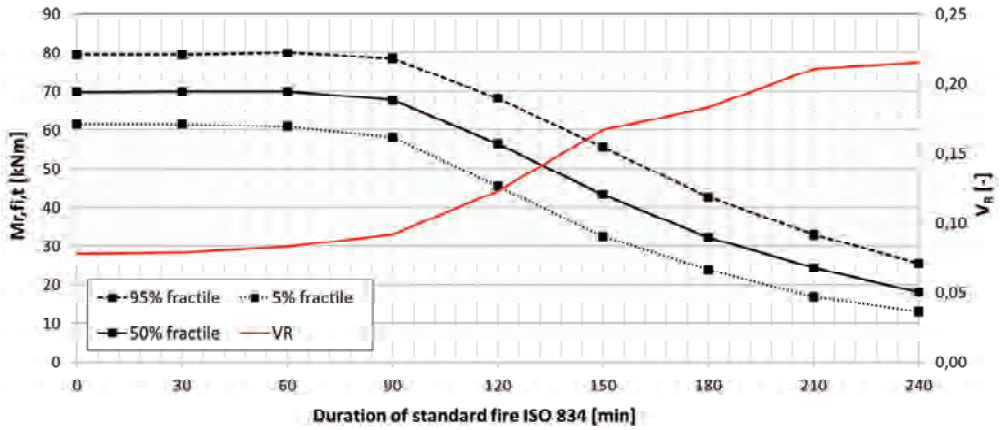


Figure 2. Calculated bending moment capacity $M_{R,fi,t}$ and coefficient of variation V_R as a function of the time of fire exposure.

It is clear that after 90 minutes of exposure to the standard fire, both the mean value μ_R and the standard deviation of the bending moment capacity decrease, while the coefficient of variation V_R increases.

The Monte Carlo simulations allow the visualization of the evolution of the distribution of the bending moment capacity during fire. Figure 3 shows a comparison between the observed histogram 'A' based on the simulations and the lognormal approximation 'LN' at different durations of exposure to the ISO 834 standard fire curve.

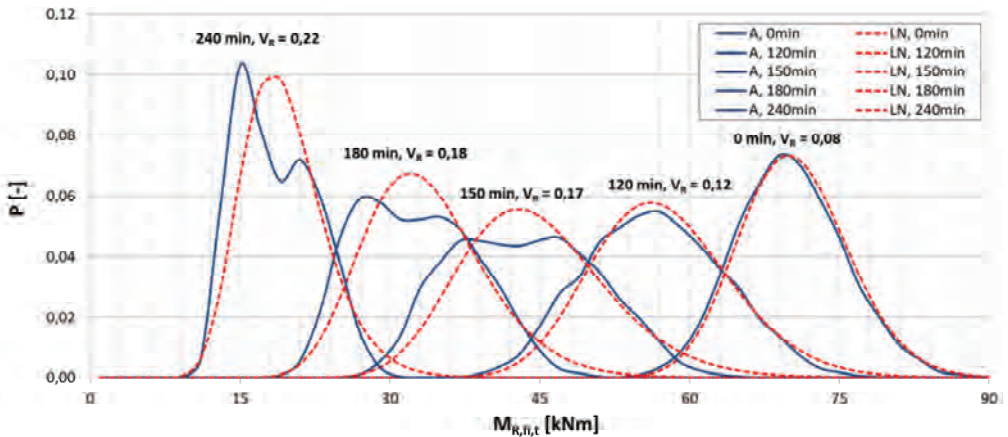


Figure 3. Distribution of the bending moment capacity $M_{R,fi,t}$ for different times of fire exposure.

The lognormal approximation is found to result in slightly higher values compared to the simulations. However, after a long fire exposure time, a normal approximation would result in overly conservative values for the global resistance factor. Therefore, equation (5) – based on a lognormal assumption – is used for the evaluation of γ_R . Results for the buildings according to Table 1 are given in Table 3.

Table 3. Global resistance factor γ_R for different types of buildings, as a function of the duration of the ISO 834 standard fire.

Building type	0 min	30 min	60 min	90 min	120 min	150 min	180 min	210 min	240 min
Hospital building	1,21	1,22	1,23	1,26	1,36	1,52	1,58	1,69	1,71
Office building	1,12	1,12	1,13	1,15	1,20	1,28	1,31	1,37	1,38
Residential building	1,15	1,15	1,16	1,17	1,24	1,34	1,38	1,45	1,46
Production hall	1,16	1,16	1,17	1,19	1,26	1,36	1,40	1,48	1,49
Warehouse	1,16	1,16	1,17	1,19	1,26	1,37	1,41	1,48	1,50

Table 3 indicates that as soon as the bending moment capacity starts decreasing after 90 minutes of exposure (Figure 1), the global resistance factor increases significantly. This stresses the necessity of calculating a time-dependent value of γ_R for concrete elements exposed to fire. However, the above mentioned results are related to the specific evolution of V_R for the slab configuration of Table 2. Research is ongoing to generalize the results of Table 3.

Figure 4 shows the evolution of the global resistance factor as a function of the fire exposure time for different target values for the reliability index during fire $\beta_{t,fi}$ and assuming a lognormal distribution of $M_{R,fi,t}$. For practical applications, it is possible to interpolate between the different curves.

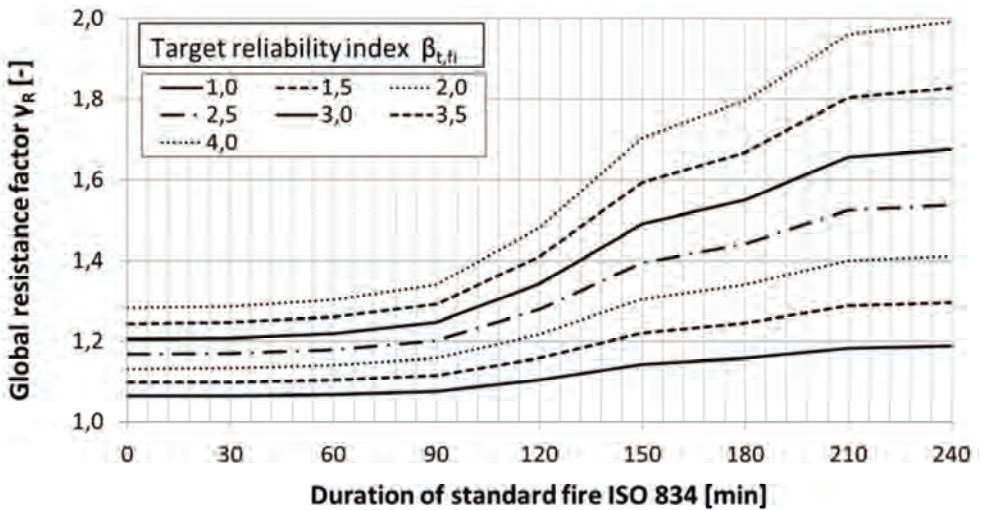


Figure 4. Global resistance factor γ_R for different target reliability indices $\beta_{t,fi}$, as a function of the time of exposure to the ISO 834 standard fire curve.

The important influence of the reinforcement temperature on the bending moment capacity of concrete slabs exposed to fire is well known. Therefore, the concrete cover and the presence of insulation significantly affect the structural fire resistance for a given slab configuration. While the global resistance factors in Figure 4 can be considered a good approximation for conditions with a standard concrete cover and no insulation, γ_R in case of a specific design situation can also be expressed as a function of the nominal reinforcement temperature (Figure 5).

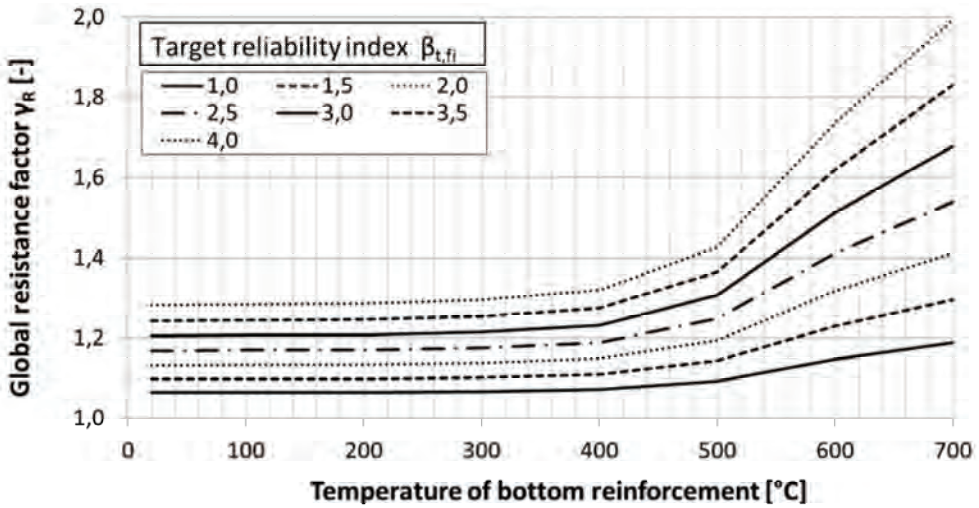


Figure 5. Global resistance factor γ_R for different target reliability indices $\beta_{t,fi}$, as a function of the bottom reinforcement temperature.

If the fire resistance should be assessed with respect to a natural fire or hydrocarbon fire, a designer can use the reinforcement temperature calculated in the single FEM analysis and the target reliability index $\beta_{t,fi}$ calculated by (7) to find the appropriate γ_R in Figure 5.

6 APPLICATION EXAMPLE

In order to validate the before mentioned global partial factor approach, a 2D FEM analysis of a slab with nominal values according to Table 2 is performed with the FEM program Atena [19]. For all design variables the mean values are used (e.g. Table 4).

Table 4. Mean material properties of analysed concrete slab.

Symbol	Name	Dimension	Nominal value
$f_c(20^\circ\text{C})$	20°C mean concrete compressive strength	MPa	25.4
$f_y(20^\circ\text{C})$	20°C mean steel yield strength	MPa	581.4

The calculation of the bending moment capacity of the slab is carried out in three steps. First the response to the self-weight of the slab is calculated. Subsequently, the slab is exposed to the ISO 834 standard fire curve for a required duration. In this example, calculations are performed for multiples of 30 minutes, up to 240 minutes of fire exposure. Finally, a load displacement analysis is performed with a point load in the middle of the slab in order to determine the ultimate load capacity and calculate the corresponding bending moment capacity of the slab after the specified time of fire exposure (e.g. 30 minutes, 60 minutes...). Figure 6 shows the evolution of the calculated μ_R and gives an overview of the different values of $M_{Rd,fi,t}$ as a function of the target reliability index $\beta_{t,fi}$, calculated based on the proposed global partial factors.

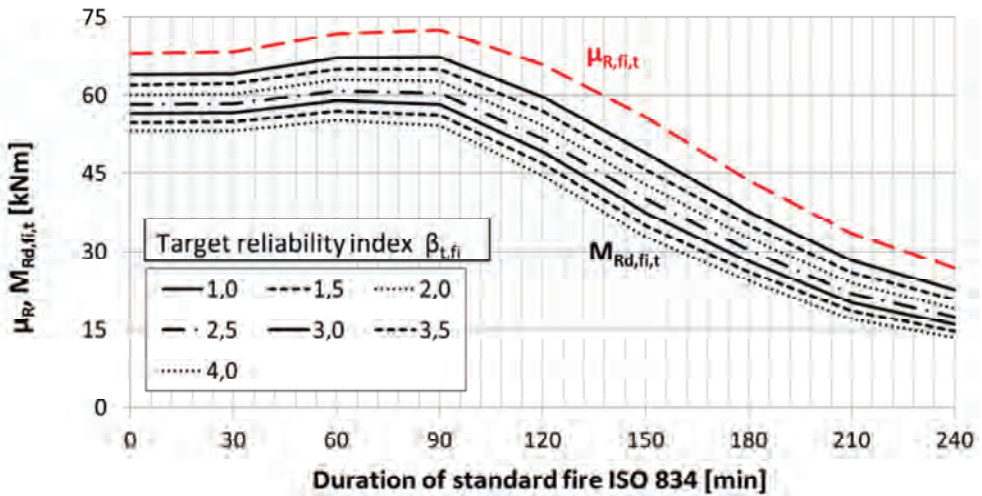


Figure 6. Design value of the bending moment capacity of the analysed slab configuration for different target reliability indices $\beta_{t,fi}$, as a function of the time of exposure to the ISO 834 standard fire curve.

Based on the single FEM simulation, $M_{Rd,fi,t}$ can be calculated once the target reliability index $\beta_{t,fi}$ and the corresponding global resistance factor γ_R are chosen. The resulting value for $M_{Rd,fi,t}$ should be compared to the design value of the bending moment induced by the design loads $M_{Ed,fi,t}$ in order to assess whether the required fire resistance time is achieved. In accordance with EN 1992-1-2 [17], $M_{Ed,fi,t}$ can be assumed constant during the fire and can be approximated by 0,7 times M_{Ed} , the design value calculated for normal conditions.

7 CONCLUSION

- A global partial factor format for non-linear FEM analysis of concrete slabs exposed to fire is proposed.
- The necessary computational efforts are minimized by requiring only a single FEM analysis to derive the appropriate design value of the bending moment resistance.
- While taking into account the consequence class of the building, the fire incidence rate and the probability of the fire growing to a fully developed fire, the proposed method remains easy to use due to the availability of some illustrating graphs.

8 CONCLUSION

Ruben Van Coile is a Research Assistant of the FWO Research Foundation of Flanders. The author wishes to thank the FWO for the financial support on the research project “Probabilistic formulation of the structural reliability of concrete structures subjected to fire in relation to risk-based decision making and risk-transfer mechanisms”.

REFERENCES

- [1] Cervenka C., “Global safety format for nonlinear calculation of reinforced concrete”, *Proc. of the 5th International Probabilistic Workshop*, L. Taerwe and D. Proske (eds.), Ghent (28-29/11), 183-194, 2007.
- [2] Van Coile R., Caspeele R., Annerel E. and Taerwe L., “Assessment of the reduction of the safety level of concrete slabs during fire”, *Proc. of the 8th International Probabilistic Workshop*, P. van Gelder, L. Gućma and D. Proske (eds), Szczecin (18-19/11), 61-72, 2010.
- [3] Allaix, D.L., Carbone, V.I. and Mancini, G., “Global resistance factor for reinforced concrete beams”, *Proc. of the 5th International Probabilistic Workshop*, L. Taerwe and D. Proske (eds.), Ghent (28-29/11), 183-194, 2007.
- [4] Allaix, D.L., Carbone, V.I. and Mancini, G., “Probabilistic approach to the safety format for non-linear analysis of concrete structures”, *Proc. of the 9th International Probabilistic Workshop*, H. Budelmann, A. Holst and D. Proske (eds), Braunschweig (17-18/11), 73-80, 2011.
- [5] Holický, M., “Probabilistic approach to the global resistance factors for reinforced concrete members”, *Proc. of the 5th International Probabilistic Workshop*, L. Taerwe and D. Proske (eds.), Ghent (28-29/11), 183-194, 2007.
- [6] Novák, D., Vorechovský, M., Lehký, D., Rusina, R., Pukl, R. and Cervenka, V. “Stochastic nonlinear fracture mechanics finite element analysis of concrete structures”, *Proceedings of the 9th Int. conf. on Structural Safety and Reliability Icosar*, Rome (20-23/06), 781-788, 2005.
- [7] CEN, EN 1990: Basis of structural design. European Standard, 2002.
- [8] Holický, M., Retief, J. “Theoretical Basis of the Target Reliability”, *Proc. of the 9th International Probabilistic Workshop*, H. Budelmann, A. Holst and D. Proske (eds), Braunschweig (17-18/11), 91-102, 2011.
- [9] Weilert, A. and Albrecht, C., Übergreifendes Sicherheitskonzept für Brandschutznachweise mit Ingenieurmethode, *Proceedings of the Braunschweiger Brandschutz-Tage '09*, Braunschweig (29-30/09), 89-110, 2009.
- [10] DIN, EN 1991-1-2/NA Nationaler Anhang – National festgelegte Parameter – Eurocode 1 – Einwirkungen auf Tragwerke – Teil 1-2/NA: Allgemeine Einwirkungen – Brandeinwirkungen auf Tragwerke, 2010.
- [11] Albrecht C., Hossier, D., “Risk-informed framework for performance-based structural fire protection according to the eurocode fire parts”, *Proc. of the 12th Interflam Conference*, Nottingham (5-7/07), 1031-1042, 2010.
- [12] Hossier, D, Weilert, A. Klinzmann, C., Schnetgöke, R. and Albrecht, C. “Erarbeitung eines Sicherheitskonzeptes für die brandschutztechnische Bemessung unter Anwendung von Ingenieurmethoden gemäß Eurocode 1 Teil 1-2”, Abschlussbericht zum DIBT-Forschungsvorhaben ZP 52-5-4.168-1239/07, Institut für Baustoffe, Massivbau und Brandschutz, Technische Universität Braunschweig, 2008.
- [13] Gulvanessian H, Calgaro J.-A., Holický, M., *Designers' guide to EN 1990: eurocode: basis for structural design*. Thomas Telford, London, 2002.
- [14] Van Coile R., Annerel E., Caspeele R. and Taerwe L., “Assessment of the safety level of concrete slabs during fire”, *Fire Safety Science – Proc. of the 10th International Symposium*, IAFSS, Maryland (19-24/06), 1115-1124, 2011.
- [15] Blontrock, H., “Analysis and modeling of the fire resistance of concrete members strengthened with externally bonded composite laminates” (in Dutch), PhD thesis, Ghent, 2003.

- [16] Lu, L., Annerel, E., Taerwe, L. and Yuan, Y., "Influence of transient strain on fire resistance of concrete elements", *Proceedings of the Application of Structural Fire Engineering Conference (ASFE)*, Prague (29/04), 109-114, 2011.
- [17] CEN, EN 1992-1-2: Design of concrete structures: Part 1-2: General rules – Structural fire design. European Standard, 2004.
- [18] Kodur, V.K.R. and Dwaikat, M., "A numerical model for predicting the fire resistance of reinforced concrete beams", *Cement and Concrete Composites*, 30(5), 431-443, 2008.
- [19] Cervenka, V and Pukl, R., *Atena Program Documentation*, Cervenka Consulting, Czech Republic, 2003.

EVALUATING FIRE RESPONSE OF CONCRETE BEAM REINFORCED WITH FRP REBARS

Baolin Yu* and Venkatesh Kodur*

* Department of Civil and Environmental Engineering, Michigan State University
e-mails: yubaolin@msu.edu, kodur@egr.msu.edu

Keywords: FRP rebars, Concrete beams, Fire resistance, Numerical model, Fire protection

Abstract. *This paper presents the development of a numerical model for evaluating the fire response of a concrete beam reinforced with FRP rebars. The model is based on macroscopic finite element approach and accounts for high temperature properties of constitutive materials, load and restraint conditions, as well as bond degradation at the FRP-concrete interface. The validity of the model is established by comparing predictions from the model with data from fire tests. Also, a case study on concrete beams with different types of reinforcement is presented. Results from numerical studies indicate that conventional concrete beam with steel reinforcement achieves higher fire resistance than beam with FRP rebars. Also, a concrete beam reinforced with CFRP rebars attains higher fire resistance than that of a beam with GFRP rebars. It is also shown that appropriate insulation scheme can significantly increase the fire resistance of concrete beams with FRP reinforcement.*

1 INTRODUCTION

Since the 1990s, the construction industry has shown significant interest in the use of fiber-reinforced polymer (FRP) reinforcing bars as an alternative to conventional steel reinforcement in concrete structures. FRP rebars possess numerous advantages over steel reinforcement, such as lightweight, high strength and stiffness, low conductivity, corrosion resistance and high durability. Therefore, FRP reinforcement in concrete members has been used in a diverse range of applications, including bridges, parking structures, coastal piers, and power plants. However, when used in buildings, provision of appropriate fire resistance to structural members is a major design requirement. It is well established that at elevated temperature, FRP reinforcement experiences faster degradation of strength and stiffness properties than that of steel reinforcement [1,2,3]. Also, when the temperature of FRP exceeds glass transition temperature (GTT), the bond between FRP rebar and concrete starts to deteriorate rapidly due to melting (or softening) of polymer matrix [2,4,5]. This will result in loss of functionality of FRP rebars as tensile reinforcement, and finally might lead to failure of the structural member. Therefore, concern exists on the fire performance of concrete members reinforced with FRP rebars.

There are very limited studies on the fire performance of concrete members with FRP reinforcement. Sakashita et al. [6] carried out fire test on 11 concrete beams reinforced with different types of FRP rebars. They concluded that beams reinforced with CFRP (carbon fiber reinforced polymer) rebars achieved the highest fire resistance, followed by the beams reinforced with GFRP (glass fiber reinforced polymer) rebars, and then the beams with AFRP (aramid fiber reinforced polymer) rebars. Also, the beams with spiral or straight fiber rebars yielded higher fire resistance than that with braided fiber rebars. Abbasi and Hogg [7] evaluated the fire response of GFRP reinforced concrete beams through experimental study. They inferred that concrete beams reinforced with GFRP rebars and provided with sufficient concrete cover, can provide minimum required fire resistance for building applications. Rafi et al. [8] carried out fire test on two concrete beams with CFRP rebars. In the test, polymer matrix of CFRP rebar almost

burned out, but the carbon fibers continued to support the concrete beam through “a tied arch” mechanism. Thus they concluded that the anchorage at two ends of rebars is vital to obtain adequate fire resistance.

The above review indicates that the previous studies mainly involved in undertaking standard fire tests on concrete beams reinforced with FRP rebars to develop relevant fire resistance ratings. There is no information on the response of such beams under realistic fire, loading and restraint conditions. Further, due to availability of different types of FRP rebars in the market, it is almost impossible to conduct numerous fire tests to characterize fire response of concrete members with different types of FRP reinforcement. An alternative to the tests is the use of a numerical model to trace the fire response of concrete members reinforced with FRP rebars. This paper presents the development of a numerical model for evaluating the fire response of concrete beams reinforced with FRP bars.

2 NUMERICAL MODEL

A numerical model, initially developed for tracing the fire behavior of conventional concrete beams reinforced with steel rebars [9], is extended to simulate the fire performance of concrete beams reinforced with FRP rebars. The model is based on a macroscopic finite element approach and utilizes time dependent moment-curvature ($M-\kappa$) relationships to trace the response of reinforced concrete beams from the initial pre-loading stage to collapse of beam. The numerical model is in the form of computer program and the analysis is carried out in two stages, namely, thermal analysis and structural analysis.

The fire resistance analysis is carried out at incrementing time steps. In the analysis, the beam is divided into a number of segments along the length, and the cross-sectional area of each segment is subdivided into a number of elements, as shown in Figure 1. The fire temperature at each time step is evaluated through known time-temperature relations of a specified fire. Then the temperature distribution in the beam cross section is established by applying heat transfer principles and relevant high temperature thermal properties of concrete and fire insulation.

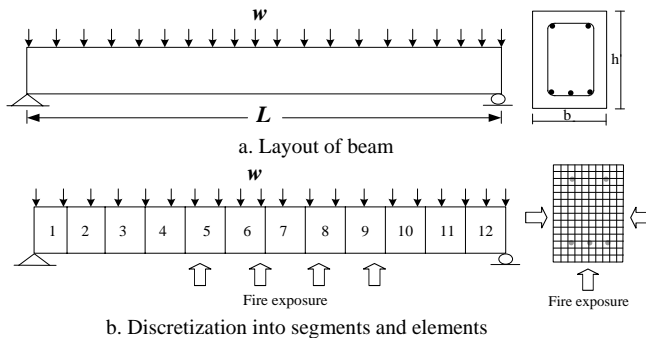


Figure 1 Typical beam layout and discretization of beam into segments and elements

In the strength analysis, segmental $M-\kappa$ relationships at each time step is generated by applying equilibrium and compatibility principles. The calculation starts with an assumed value of strain (ϵ_t) at the top fiber of concrete and curvature (κ), and the total strain (ϵ_i) in each element of concrete, steel and FRP rebar can be evaluated as:

$$\epsilon_i = \epsilon_c + \kappa y \tag{1}$$

where, ϵ_i is the total strain in any element; ϵ_c is the strain at the top most fiber in concrete; κ is the curvature; y is the distance from the top layer (concrete) to the center of corresponding element. The mechanical strain in each element of concrete, steel and FRP rebar is evaluated by subtracting the strains due to thermal, mechanical, transient and creep effect from the total strain:

$$\epsilon_{mec} = \epsilon_{tc} - \epsilon_{thc} - \epsilon_{crc} - \epsilon_{trc} (\text{concrete}) \tag{2}$$

$$\varepsilon_{mes} = \varepsilon_{ts} - \varepsilon_{ths} - \varepsilon_{crs} (steel) \quad (3)$$

$$\varepsilon_{mef} = \varepsilon_{tf} - \varepsilon_{thf} + \varepsilon_{slip} (FRP) \quad (4)$$

where: ε_{tc} , ε_{thc} , ε_{mec} , ε_{crs} , ε_{trc} represent total, thermal, mechanical, creep, and transient strain respectively in concrete element; ε_{ts} , ε_{ths} , ε_{mes} , ε_{crs} represent total, thermal, mechanical, and creep strain respectively in steel rebar; and ε_{tf} , ε_{thf} , ε_{mef} , ε_{slip} represent total, thermal, mechanical, and slip strain respectively in FRP reinforcement.

The computed mechanical strains are used to obtain stress and force in each element, utilizing temperature-dependant stress-strain relations of concrete, steel and FRP. An iterative procedure is applied to calculate the curvature and stress for a given concrete strain (ε_c), till force equilibrium is satisfied. For each time step, various points on the $M-\kappa$ curve are generated until concrete strain at the top most fiber reaches its limit or FRP rebar reaches its rupture strain.

The above generated time-dependant $M-\kappa$ relationships are utilized to carry out stiffness analysis of the beam at each time step and to evaluate deflections in the beam. For this stiffness analysis, the secant stiffness of each segment is determined based on the moment level reached in that particular segment. The global stiffness equation is established by assembling stiffness matrix, loading and displacement vector of each segment of beam. Then an iterative procedure is applied to solve force-displacement equations and to evaluate deflections of the beam [10].

The model generates various output parameters including temperatures, strains and stresses in rebar and concrete, deflections, and flexural capacity. These parameters are utilized to evaluate the failure of the beam, which is said to occur when one of these limit states is reached:

- 1) The moment due to applied service loading exceeds the strength of the beam [11].
- 2) The deflection of the beam exceeds $L/20$ (where L is the length of beam) at any fire exposure time [12].
- 3) The rate of deflection exceeds the limiting deflection rate [$L^2/9000d$ (mm/min), d is the effective depth of beam] [12].

3 HIGH TEMPERATURE MATERIAL PROPERTIES

The properties of constitutive materials, which vary with temperature, have significant influence on thermal and structural response of concrete members exposed to fire. For concrete, high-temperature thermal and mechanical property relations as per Eurocode [13] and ASCE [14] provisions are built into in the computer program, and a user can select appropriate properties according to specified concrete strength (normal strength or high strength) and aggregate type (carbonate or siliceous). For steel and FRP rebars, the thermal properties (thermal conductivity and specific heat) are not specifically considered in the model since they do not significantly affect temperature distribution within the beam cross section [15]. However, relevant temperature-dependant stress-strain relations of reinforcing steel, taken from in Eurocode [13] and ASCE [14] standards, are built into the computer program.

For FRP rebars, the temperature dependent stress-strain response can be represented through a set of linear relations [16]. At about 400°C, the strength and modulus of elasticity of CFRP rebar reduces to 40% of its room temperature strength and stiffness, while for GFRP rebar the reduction is much more severe, to about 25%. When the temperature exceeds 400°C, the strength and elastic modulus of FRP is assumed to decrease linearly from 40% (CFRP) or 25% (GFRP) to zero at 1000°C, since fibers continue to have some strength till 1000°C [17]. The degradation of strength and elastic modulus of CFRP and GFRP in 20-1000°C range is shown in Figure 2a.

To account for the slip between FRP rebar and concrete, the strain resulting from slip is incorporated as one component of the total strain. At each time step, the shear stress at FRP-concrete interface (τ) is evaluated as:

$$\tau \cdot (\pi d_{bar} \cdot L_{eff}) = \sigma_{FRP} \cdot (\pi d_{bar}^2) / 4 \quad (5)$$

where, σ_{FRP} is the tensile stress of FRP reinforcement; d_{bar} is the diameter of FRP reinforcement; L_{eff} is the effective bond length of FRP reinforcement, obtained based on experimental results reported by Hashemi and Al-Mahaidi [18]. Then the slip strain at each time step is evaluated as

$$\epsilon_{slip} = \begin{cases} \tau / E_{bond} & \tau > f_{bond} \\ 0 & \tau \leq f_{bond} \end{cases} \quad (6)$$

where, f_{bond} and E_{bond} represent bond strength and elastic modulus. The temperature-dependant bond strength and elastic modulus up to 300°C are plotted in Figure 2b based on the experimental data reported by Katz et al. [4].

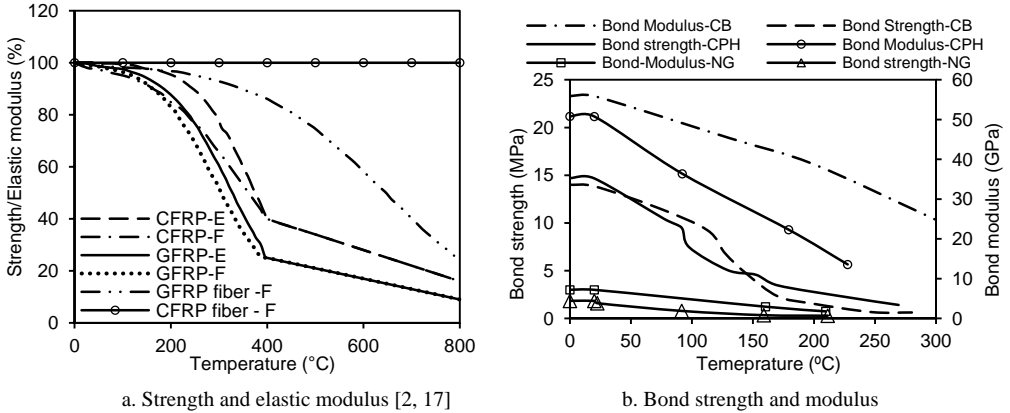


Figure 2 Variation of strength (F), elastic modulus (E), and bond strength and bond modulus of FRP with temperature

Under fire conditions, thermal strain in FRP reinforcement resulting from temperature rise can also influence the behavior of FRP reinforced concrete beams. In the numerical model, FRP rebars are assumed to be deeply embedded inside the concrete members, and thus only longitudinal thermal expansion of FRP rebar is accounted for in the model. A review of literature indicates that coefficient of thermal expansion (CTE) is small in 20 to 200°C temperature range and it fluctuates around zero [19, 20]. This is because the longitudinal thermal expansion of FRP is dominated by the expansion of fiber, which has negligible thermal expansion at high temperature. Therefore, the CTE is assumed to be zero in 20 to 200°C range. For temperatures higher than 200°C, there is lack of test data on CTE of FRP, and a value of $5 \times 10^{-6}/K$ is assumed in 200-1000°C range as recommended in previous studies [19].

4 MODEL VALIDATION

The above developed model is validated by comparing the predicted response parameters from the model with measured data from fire tests on two types of concrete beams. The first beam (Beam I), which was tested by Rafi et al. [8], is of 120x200 mm rectangular cross-section with an effective span length of 1.75 m. The main flexural reinforcement in the beam is comprised of two ϕ 9.5 mm CFRP rebars, while two ϕ 8 mm steel rebars form the compressive reinforcement. The simply supported beam is loaded at two points and is exposed to ISO 834 standard fire [21]. Details of beam configuration and material properties are shown in Figure 3 and Table 1.

The validation process involved a comparison of predicted thermal and structural response parameters from the analysis with measured data from tests. For thermal response validation, a comparison of predicted and measured FRP and concrete temperatures is shown in Figure 4a. It can be seen in the figure that the temperature in FRP rebar (N1) increased steeply from the early stages of fire exposure. This is

attributed to the fact that the CFRP rebars are located at the bottom corners and thus are heated from two sides of beam (soffit and side surface). Also, the concrete cover to FRP rebars is quite small (20 mm). After about 40 minutes, temperature in FRP rebar exceeds critical temperature of CFRP (360°C), indicating a significant degradation in strength and elastic modulus. Critical temperature is defined as the temperature at which FRP loses 50% of room-temperature strength. Compared to the corner rebar (N1), the temperature rise at the point mid-way between two rebars (N2), is relatively slower, since it is farther from the two side surfaces. Also, the temperature at the mid-depth of the beam (N3) remained quite low throughout the fire exposure duration, and reached only 300°C at the time of failure. Thus, most of the concrete in the upper layers of the beam (in compression zone) did not experience any loss of strength and stiffness. Overall, the predicted temperatures followed closely the measured values at different locations of the cross section (N1, N2 and N3).

To validate structural response, mid-span deflections predicted by the model are compared with measured values from the fire test in Figure 4b. It can be seen from the figure that the beam reinforced with CFRP rebars behaved quite stiff during most of the fire exposure duration, and the deflection at the mid-span of the beam reached only 9 mm (1/195 of span) after 50 minutes into fire exposure. This stiff behavior can be attributed to the fact that carbon fibers lose strength and stiffness at a slow pace (as shown in Figure 2a), and thus the beam can retain a high portion of strength and stiffness, even though the resin matrix gets melted (or softened). However, when the temperature in FRP exceeds 500°C (at 60 minutes), the slip strain in FRP becomes significant and thus FRP can not contribute fully to resist applied moment. At the final stage of fire exposure, Beam I experienced sudden increase in deflection due to debonding of FRP rebar with concrete in the support regions. The numerical model is not able to capture this sudden deflection drop as a result of convergence problems. The analysis predicted a fire resistance of 65 minutes for this beam, which is slightly higher than the measured value in fire test (63 minutes). Overall, the predicted mid-span deflections compare well with the measured data in the entire range of fire exposure.

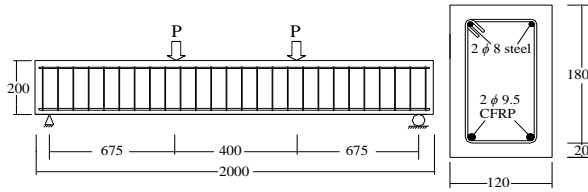
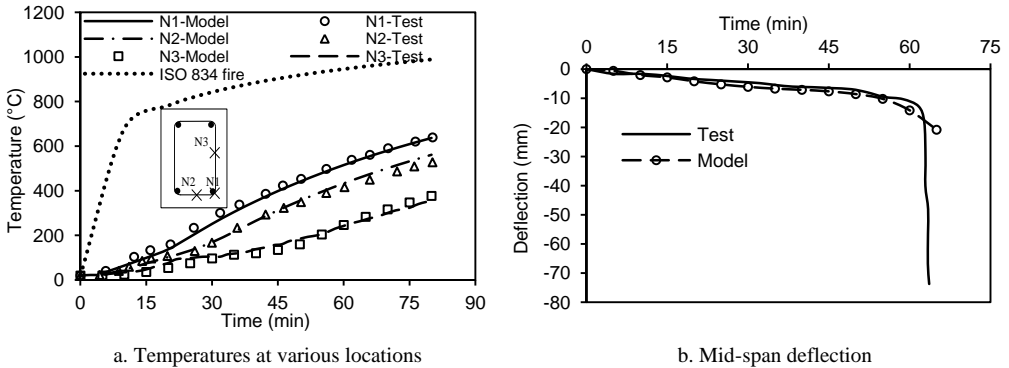


Figure 3 Layout and configuration of beam (Beam I) used in validation (units: mm)



a. Temperatures at various locations
b. Mid-span deflection
Figure 4 Comparison of predicted and measured temperatures at various locations in Beam I

As a part of validation process, a second beam (Beam II) reinforced with GFRP rebars (tested by Abassi and Hogg [7]) was also analyzed and predictions from the analysis were compared with measured

values from fire test. As in the case of Beam I, the predicted rebar temperatures (GFRP) and mid-span deflections compared well with the measured data. The plots showing the comparisons are not presented herein due to space constraints. The predicted and measured fire resistance for this beam is 125 and 120 minutes, respectively, indicating a good agreement. In all, the macroscopic finite element model and the high-temperature constitutive relations in use, are deemed appropriate for evaluating fire performance of concrete beams reinforced with FRP bars.

Table 1 Summary of beam properties and results of numerical studies

Properties	Beam I	Beam II	Beam III	Beam IV	Beam V
Cross section (mm)	120 x 200	350x400	305x533	305x533	305x533
Span (m)	1.75	4.4	6.01	6.01	6.01
Compression rebar(mm)	2 ϕ 8 steel	2 ϕ 12.7 GFRP	2 ϕ 12.7 steel	2 ϕ 12.7 steel	2 ϕ 12.7 steel
Tension rebar(mm)	2 ϕ 9.5 CFRP	7 ϕ 12.7 GFRP	8 ϕ 16 steel	8 ϕ 16 GFRP	4 ϕ 12.7 CFRP
f_c' (MPa)	42	42	34.5	34.5	34.5
f_{FRP} (MPa)	1676	690	413	634	1379
E_{FRP} (GPa)	136	40.8	200	46.4	138
Load ratio	35%	13%	50%	50%	50%
Load	30 kN	40 kN	27 kN/m	27 kN/m	27 kN/m
Concrete cover (mm)	20	50	38.1	38.1	64
Fire exposure	ISO 834	BS476	ASTM E119	ASTM E119	ASTM E119
Measured fire resistance (mins)	63	120	--	--	--
Predicted fire resistance (mins)	65	125	150	70	85

5 CASE STUDY

The validated numerical model is applied to evaluate the comparative fire response of concrete beams reinforced with different types of reinforcement.

5.1 Beam configuration and analysis details

Three beams (Beams III, IV and V), designed for typical building applications [22], were selected for the fire resistance analysis. All three beams are of 305x533 mm rectangular cross-section with a span length of 6.01 m. Beam III has eight ϕ 16 mm steel rebars (in two layers) as tensile reinforcement, while Beam IV has eight ϕ 16 mm GFRP rebars (in two layers), and Beam V has four ϕ 12.7 mm CFRP rebars (in one layer). These beams are designed to yield similar flexural capacity and based on the room-temperature analysis, the nominal flexural strength of Beams III, IV and V is 271, 264, and 264 kN-m, respectively. Detailed information on beam characteristics and material properties are shown in Figure 5 and Table 1.

Fire resistance analysis was carried out on these above three beams using the above developed computer program. The beams were exposed to ASTM E119 standard fire from three sides and subjected to a uniform distributed load, which is equivalent to 50% of room temperature flexural capacity (see Table 1).

5.2 Effect of type of reinforcement

The thermal response of three beams is shown in Figure 6a, where temperature in the corner rebars is plotted as a function of fire exposure time. Since GFRP (Beam III) and steel rebars (Beam IV) are located at identical positions in the cross section (two layers), they experienced similar temperature rise at a given fire exposure time. As expected, the lower layer rebars in Beams III and IV experienced faster temperature rise than the rebars at the upper layer, due to the effect of cover thickness. However, GFRP rebars experienced faster degradation in strength and stiffness at high temperatures as compared to steel rebars, and thus at any fire exposure time, beam with GFRP rebars (Beam III) had lower capacity than

that of beam with steel rebars (Beam III). Also, GFRP rebar attained the critical temperature limit (300°C) at earlier time. However in Beam V, which had only one layer of CFRP rebars, the temperature rise is slower than GFRP rebars due to relatively larger concrete cover. Also, since CFRP rebar has slightly better fire resistance than that of GFRP rebars (see Figure 2), CFRP rebar retains much more strength as compared to GFRP rebar in the entire range of fire exposure.

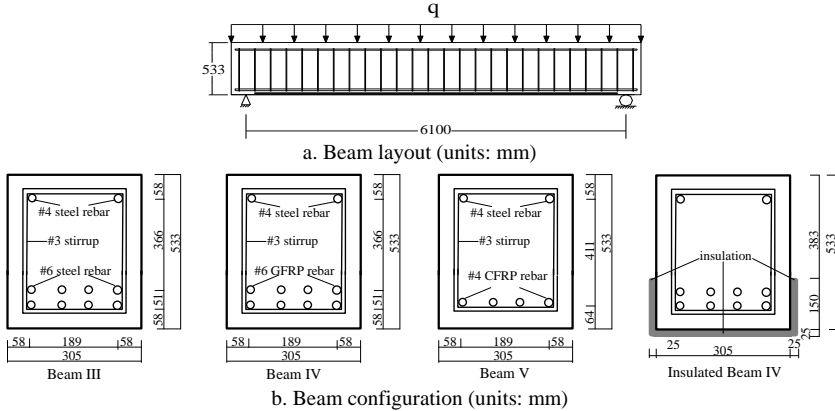


Figure 5 Layout and configuration of the beams used for case study

The variation of moment capacity in each beam, with fire exposure time, is presented in Figure 6b. It can be seen that at any fire exposure time, conventional steel reinforced concrete beam (Beam III) had higher moment capacity than beams reinforced with GFRP and CFRP rebars (Beams IV and V). This can be attributed the fact that steel rebars retain higher strength and stiffness at elevated temperature. In fact, Beam III (with steel rebars) did not have any degradation in moment capacity till 60 minutes into fire exposure, due to no significant strength loss in steel rebars till about 350°C. However, in the cases of Beams IV and V, the moment capacities started to degrade from the initial stages of fire exposure. After 30 minutes into fire exposure, Beams IV and V experienced severe degradation in (moment) capacity. This is due to the fact that the polymer matrix starts to decompose (at about 200°C) and FRP rebars lose much of their strength. Beam reinforced with GFRP rebars (Beam IV) lost moment capacity at a faster rate since GFRP rebars, at the bottom layer, reached their critical temperature and lost most of their strength. Finally, Beams IV and V failed at 70 and 85 minutes respectively, by reaching flexural strength limit. However, Beam III achieved a fire resistance of 150 minutes. Therefore, a conventional steel reinforced concrete beam (Beam III) exhibits better fire response than that of beams with FRP rebars (Beams IV and V). Of the different types of FRP reinforced concrete beams, a beam with CFRP rebars exhibits better fire response than that of a beam with GFRP rebars.

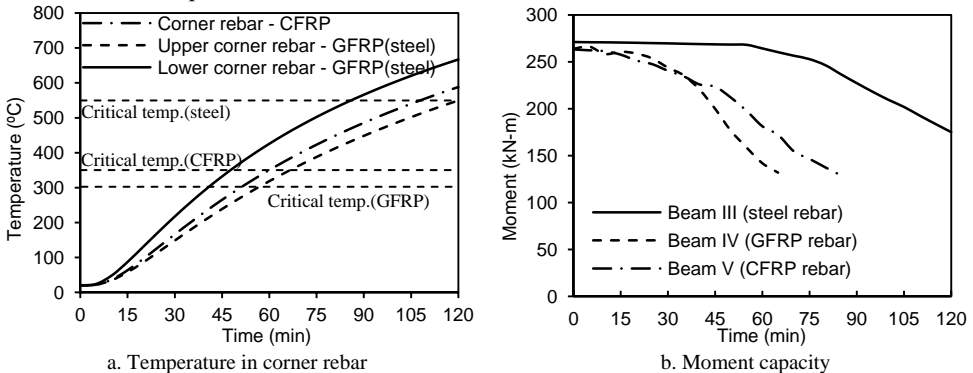


Figure 6 Effect of type of reinforcement on fire resistance of reinforced concrete beams

5.3 Effect of fire insulation

Based on the above analysis, a typical concrete beam reinforced with GFRP rebars (Beam IV) achieved a fire resistance of 70 minutes under ASTM E119 fire exposure. This does not meet the required fire resistance (ratings) needed in most (practical) building applications. To achieve adequate fire resistance, appropriate fire insulation can be applied on beams with FRP rebars. Therefore, Beam IV was analyzed by applying a U-shaped (bottom and side surfaces) fire insulation to study the effect of insulation on fire response, as shown in Figure 5b. In the analysis, the insulation thickness was varied from 15 to 35 mm, while the depth of insulation on side surface was kept constant at 150 mm. The thermal properties (thermal conductivity and specific heat) of fire insulation (VG-EI) follow the test data reported by Bisby [23].

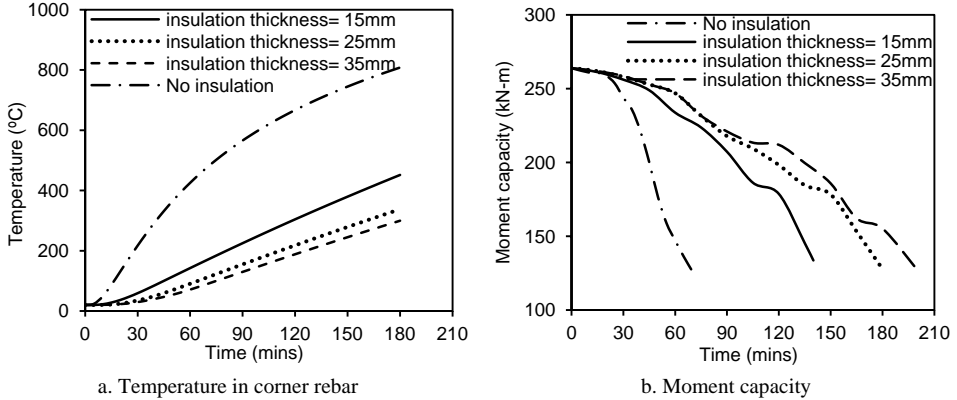


Figure 7 Effect of insulation scheme to fire response of concrete beams reinforced with GFRP rebar

Figure 7a illustrates the effect of insulation thickness on the fire response of reinforced concrete beams. The temperature rise in corner GFRP rebar is plotted against fire exposure time for four cases, one without any insulation (Case 1) and other three with varying insulation thickness at beam soffit (Cases 2, 3 and 4). It can be seen that the application of insulation significantly slows down the temperature rise in GFRP rebar, and this in turn leads to slower degradation of strength and stiffness in FRP rebar. Further, when the insulation thickness increases from 15 to 25 mm, the temperature in GFRP rebar decreases significantly at any given fire exposure time, especially in inner FRP rebar, where the temperature remained below critical temperature of GFRP even at 180 minutes. This indicates that a concrete beam with an insulation thickness of 25 mm can achieve a fire resistance of 3 hours. However, when the insulation thickness is increased from 25 to 35 mm, there is no major advantage, since the temperature in GFRP rebar is already below the critical temperature limit.

Table 2 Effect of insulation thickness on fire resistance of beams with GFRP rebars

Case	Insulation (mm)		Load level (% of room-temp. capacity)	Corner rebar temperature (°C)	Fire resistance (minutes)
	Thickness	Extension on side surfaces			
1	none	none	50%	808	70
2	15	150	50%	452	140
3	25	150	50%	337	180
4	35	150	50%	300	200

The structural response of beams with varying insulation thickness is shown in Figure 7b, by plotting variation of moment capacity with fire exposure time. It can be noticed that the beams with fire insulation retained much higher moment capacity than uninsulated beam throughout the fire exposure duration. In

all three insulated beams, there is no major loss of flexural capacity till 60 minutes into fire exposure, while in the case of uninsulated beam, the moment capacity starts to decrease at about 15 minutes into fire exposure. Of the three beams with insulation, beams with 25 mm and 35 mm thick insulation experienced moment degradation starting at 75 minutes and after that follow similar trend. However, the beam with 15 mm thick insulation experiences drop in moment capacity starting at about 60 minutes, due to relatively higher temperatures developing in corner and inner FRP rebars. The beam with 15 mm thick insulation achieved a fire resistance of 150 minutes, while the beams with 25 mm and 35 mm thick insulation failed at 180 and 200 minutes respectively, as shown in Table 2. This analysis inferred that beyond an optimum insulation thickness, increasing insulation thickness does not help to achieve higher fire resistance. Therefore, for this types of insulation and beam configuration, the optimum thickness of fire insulation is 25 mm. Also, this analysis clearly illustrates usefulness of the numerical model in developing optimum insulation scheme for concrete beams reinforce with FRP rebars.

6 CONCLUSIONS

Based on the information presented in this paper, the following conclusions can be drawn:

1. The fire response of a concrete beam reinforced with FRP rebar is different from that of conventional concrete beam reinforced with steel rebars. There is limited information in the literature on the fire performance of concrete beams reinforced with FRP rebars.
2. The numerical model presented in this paper is capable of predicting the fire response of concrete beams reinforced with FRP rebars. The model accounts for high temperature properties of concrete, FRP and fire insulation, temperature-induced slip at FRP-concrete interface and different fire and loading conditions.
3. Concrete beams reinforced with FRP rebars have lower fire resistance than that of conventional steel reinforced concrete beams. Further, concrete beams reinforced with GFRP rebars have lower fire resistance than that of beams with CFRP rebars.
4. Provision of appropriate fire insulation can significantly enhance the fire resistance of concrete beams reinforced with FRP rebars. Providing 25 mm thick fire insulation at the bottom, and extending to 150 mm depth on two sides of beam, can increase the fire resistance of a beam with GFRP rebars from 70 minutes to 180 minutes.

7 ACKNOWLEDGEMENTS

This material is based upon work supported by the National Science Foundation (NSF) under Grand No. CMMI-0855820. Any opinions, findings, and conclusions or recommendations expressed in this paper are those of the authors and do not necessarily reflect the views of the sponsors.

REFERENCES

- [1] Saafi, M., "Effect of fire on FRP reinforced concrete members", *Composite Structures*, 58(1), 11-20, 2002.
- [2] Bisby, L.A., Green, M.F. and Kodur, V.K.R., "Response to fire of concrete structures that incorporate FRP", *Progress in Structural Engineering Material*, 7(3), 136-149, 2005.
- [3] Wang, Y.C., Wong, P. and Kodur, V.K.R., "An experimental study of the mechanical properties of fibre reinforced polymer (FRP) and steel reinforcing bars at elevated temperatures", *Composite Structures*, 80(1), 131-140, 2007.
- [4] Katz, A., Berman, N. and Bank, L.C., "Effect of high temperature on bond strength of FRP rebars", *Journal of Composites for Constructions*, 3(2), 73-81, 1999.
- [5] Galati, N., Nanni, A., Dharani, L.R., Focacci, F., and Aiello, M.A., "Thermal effects on bond between FRP rebars and concrete", *Composite: Part A*, 37(8), 1223-1230, 2006.
- [6] Sakashita, M., Masuda, Y., Nakamura, K. and Tanano, H., "Deflection of Continuous Fiber Reinforced Concrete Beams Subject to Loaded Heating", *Non-Metallic (FRP) Reinforcement for*

- Concrete Structures. Proceedings of 3rd International Symposium*, Sapporo, Japan, Vol. 2, 51-58, 1997.
- [7] Abbasi, A. and Hogg, P. J., "Fire testing of concrete beams with fiber reinforced plastic rebar." *Composite: Part A*, 37(8), 1142-1150, 2006.
- [8] Rafi, M.M., Nadjai, A. and Ali, F., "Fire resistance of carbon FRP reinforced concrete beams." *Magazine of Concrete Research*, 59(4), 245-255, 2007.
- [9] Kodur, V.K.R. and Dwaikat, M., "A numerical model for predicting the fire resistance of reinforced concrete beams", *Cement and Concrete Composites*, 30(5), 431-443, 2008.
- [10] Campbell, T.I. and Kodur, V.K.R., "Deformation controlled nonlinear analysis of prestressed concrete continuous beams", *PCI Journal*, 42-55, 35(5), 1990.
- [11] American Society for Testing and Materials (ASTM), *ASTM E119: Standard test methods for fire tests of building construction and materials*, West Conshohocken, PA., 2007.
- [12] BS 476, "Method from determination of the fire resistance of elements of construction (general principles)", *Fire tests on building materials and structures*, London, UK, 1987.
- [13] European Committee for Standardization, "General rules - structural fire design", *Eurocode 2: Design of concrete structures*, Brussels, Belgium, 2004.
- [14] Lie, T.T., *Structural fire protection - ASCE Manuals and Reports of Engineering Practice 78*, American Society of Civil Engineering, New York, 1992.
- [15] Lie, T.T. and Irwin, R.J., "Method to calculate the fire resistance of reinforced concrete columns with rectangular cross section", *ACI Structural Journal*, 90(1), 52-60, 1993.
- [16] American Concrete Institute (ACI) Committee 440, *Guide for the design and construction of structural concrete reinforced with FRP bars*, ACI 440.1R-06, Farmington Hills, MI, 2006.
- [17] Mouritz, A.P. and Gibson, A.G., *Fire Properties of Polymer Composite Materials*, Springer Ltd, Dordrecht, the Netherlands, 2006.
- [18] Hashemi, S. and Al-Mahaidi, R., "Investigation of bond strength and flexural behaviour of FRP-strengthened reinforced concrete beams using cement-based adhesives", *Australian Journal of Structural Engineering*, 11(2), 129-139, 2010.
- [19] Nomura, S. and Ball, D.L., "Micromechanical formulation of effective thermal expansion coefficients of unidirectional fiber composites", *Advanced Composite Materials*, 3(2): 143-152, 1993.
- [20] Bowles, D.E. and Tompkins, S.S., "Prediction of coefficients of thermal expansion for unidirectional composites", *Journal of Composite Materials*, 23(4), 370-388, 1988.
- [21] International Organization for Standardization, *ISO 834: Fire resistance tests - elements of building construction*, Geneva, Switzerland, 2003.
- [22] GangaRao, H.V.S., Taly, N., and Vijay, P.V., *Reinforced concrete design with FRP composites*, CRC Press, Boca Raton, FL, 2007.
- [23] Bisby, L.A. *Fire behavior of fibre-reinforced polymer (FRP) reinforced or confined concrete*, Doctoral Thesis, Queen's University, Kingston, Canada, 2003.

HYBRID FIRE TESTING OF BUILDING STRUCTURES

Hossein Mostafaei

Research Officer, National Research Council Canada, Ottawa, Canada
e-mail: Hossein.Mostafaei@nrc-cnrc.gc.ca

Keywords: Hybrid Test, performance-based assessment, fire resistance, numerical analysis, fire test building in fire.

Abstract. A performance-based fire resistance evaluation method, called hybrid fire testing (HFT), was developed and carried out at the Fire Research Program of the National Research Council of Canada (NRC). HFT offers a more cost-effective approach to the assessment of the full structures performance in fire than that of a full-scale test and provides more reliable results than prescriptive single component testing. In the HFT method, the whole building is divided into two substructures; 1) the test specimen and 2) the model component. Then, fire performance of the whole structure is evaluated based on coupling the performance of the two substructures and by including their interactions in real time during the simulation. In this study, the HFT was applied for a 6-storey reinforced concrete building structure with a fire compartment scenario on the first floor. The test specimen was a worst-case scenario column in the compartment of fire origin in the building. The specimen was physically tested in a full-scale furnace, and the remaining of the building structure was modelled using numerical analysis software. In the HFT, the real time interactions between the two substructures are based not only on including the experimental results obtained from the test specimen into the numerical model component but most importantly also including feeding the output of the model component back into the test specimen environment (e.g. vertical and lateral loading changes). In other words, both equilibrium and compatibility conditions are satisfied between the test specimen and the model component. The results of this study show that the HFT is achievable and can be performed successfully for fire performance evaluation of a building structure.

1 INTRODUCTION

Traditional fire resistance testing evaluates the performance of individual building elements with no consideration given to the interaction with other parts of the building. On rare occasions, fire performance is assessed by constructing and testing an entire building, a very expensive approach. In the last few years an attempt was made at the Fire Research Program of the National Research Council of Canada (NRC) to explore solutions for such a gap by developing a performance-based approach called Hybrid Fire Testing (HFT).

HFT is based on performance simulation of the whole building using a sub-structuring approach. That is to split the whole structure into two substructures: 1) test specimen and 2) model component, as shown in figure 1. The test specimen is the structural element or assembly that is exposed directly to fire. The model component includes the remaining of the building structure, excluding the test specimen. The model component could include both elements exposed to fire and elements at ambient temperature, providing the analysis software has the capability of performing structural analysis at elevated temperatures.

Usually, in a building fire scenario, fire is expected to be confined in the fire compartment at the fire's origin. Therefore, compared to the total number of structural elements in a building, only a few of them are likely to be exposed to fire. Since more reliable models are available for structural analysis at ambient temperature than that at elevated temperatures; the test specimen should include all the elements exposed to fire, or at least the worst case scenario element/assembly, in the fire compartment. In this study, the column in the middle of the fire compartment, on the ground floor of the building, is selected as the test specimen, which is the only column exposed to fire. There are also four beams in the fire compartment, but they are simulated as part of the model component using SAFIR software [1]. SAFIR software has the capability of simulating structures at both ambient and elevated temperatures and therefore, it was selected for analysis of the model component of the HFT.

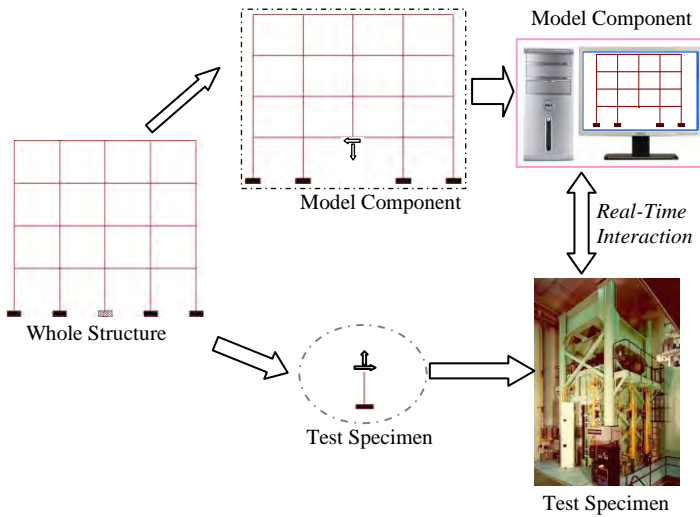


Figure 1. Division of a structure into test specimen and model component in the HFT.

One of the most important parts of the HFT process is the real-time interactions between the test specimen and the model component. That means, during the application of HFT, interface loads and deformations, between the test specimen and the model component, should be updated, at each interval time during the hybrid fire testing, to satisfy both compatibility and equilibrium conditions. The interactions could be performed using a controlled load or a deformation controlled method. For this study, the interface deformations on the model component were controlled by displacement of the test specimen and load on the column was controlled by the load obtained from the analysis of the model component. The detail of the HST methodology is provided by Mostafaei [2]. This paper provides only the results of the HFT application for the 6-storey building.

In the HFT described in this study, both the test specimen and the model component are exposed to an appropriate design fire. In other words, the temperature curve should be known before the test. In case of a real fire test, interactions must include temperature components in addition to the load and deformation. That is to measure temperatures for the test specimen and impose the model component to the same temperatures in the analysis.

The cost for application of HFT is very low, almost the same as that of the traditional prescriptive tests, however resulting in more reliable results than the prescriptive testing. Furthermore, the method is very flexible. Various building structural configurations and properties could be tested by building only the structural elements that are exposed to fire.

HFT can also be implemented remotely using different physical testing facilities and a simulation analysis from different locations anywhere in the world. This could be implemented by applying a proper communication technique between the software and physical testing facilities.

2 HFT METHODOLOGY

The HFT method conceptually was developed based on a sub-structuring analysis concept. In such an analysis, the whole structure is divided into two or more sub-structures by including force and deformation interactions amongst the sub-structures. The main purpose of sub-structuring analysis is to reduce the amount of analytical calculations by distributing them among different computers/processors. For instance, one of the main rules in structural decomposition is to have minimum interface nodes and have equal numbers of degree of freedom in the sub-structures. This would result in reduction of time and memory required for the analysis, since multiple processors will be used instead of one for the analysis [3]. However, for the HFT, the sub-structuring method is to divide the structure into two sub-structures, one being tested physically, the test specimen, and one being simulated numerically, the model component. Size of the test specimen substructure depends on the capacity of the test facility. For instance, in case of this study, the column furnace at the NRC could expose a full-scale column specimen. Therefore, the test specimen substructure consists of the worst case scenario column in the fire compartment. If a larger facility is accessible where the entire fire compartment can be simulated then the test specimen substructure includes all the elements of the fire compartment and the model component substructure includes the remaining of the structure, the elements at ambient temperature. Figure 2 shows the 6-storey building structure, for this study, with a fire compartment on the first floor. As shown in the figure, a column on the first floor is the column in the assumed fire compartment, which has been selected as the test specimen and the remaining of the 6-storey building is considered as the model component. In this study, symmetric conditions were assumed for the applied load and fire load. That means fire compartment was located symmetrically in the middle of the building on the first floor and the building was loaded uniformly under the typical dead load and live load, uniformly. This was done to simplify the first time implementation of the HFT. For application of HFT, in the case where the test specimen is located on upper floors or at a corner span, information is provided by Mostafaei [2].

Considering the above symmetric conditions, moments about the horizontal axes for beams next to the test specimen, the centre column on the first floor, will be the same but in the opposite directions. Therefore, no rotation is expected at the top end of the test specimen. Furthermore, fire compartment is assumed to be in the centre of the first floor. In this case, a symmetric distribution for thermal expansion of the floor is expected, resulting in zero lateral deformation in the centre of the floor where the test specimen is located, and a maximum lateral deformation at the edge of the floor. Therefore, the test specimen is not subjected to any lateral deformation at the floor level during the fire. In other words, the only interaction components between the test specimen and the model component are the vertical load, column's axial load, and the vertical deformation at the top end of the test specimen. Figure 3 shows the location of fire compartment in the building as well as the elevation and floor plan of the building.

Based on the above simplification, the HFT can be implemented, in the following simple steps:

Step 1: Run a structural analysis under the applied load for the whole structure, at ambient temperature and obtain the vertical load and vertical deformation at the top end of the test specimen, top of the first floor's centre column.

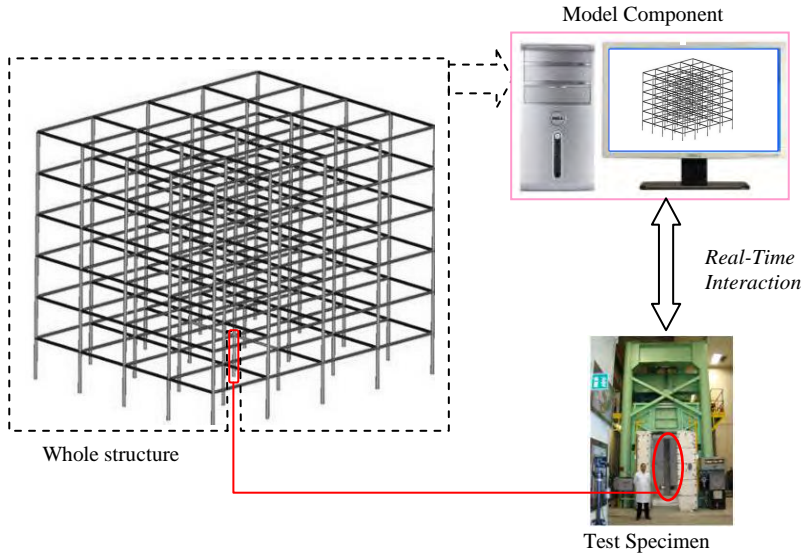


Figure 2. Division of a 3D 6-storey structure into Test Specimen and Model component in the HFT.

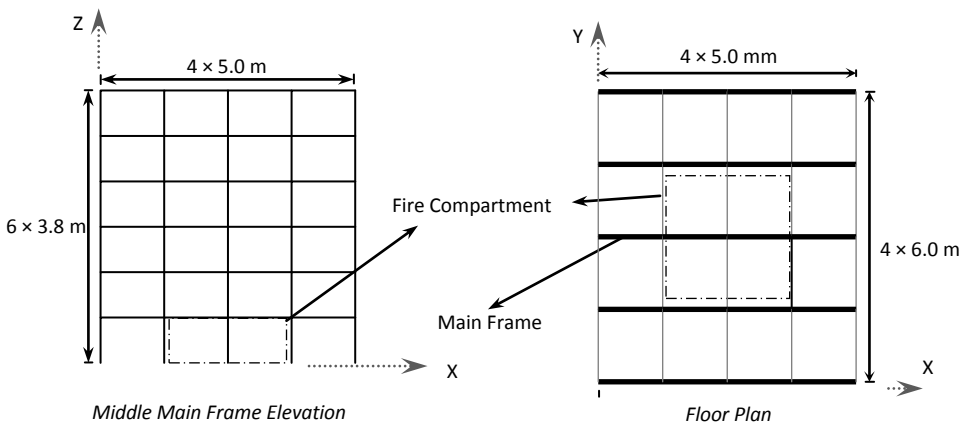


Figure 3. Elevation and floor plan of the building with location of the fire compartment.

Step 2: Run another structural analysis under the same applied loads but for the model component only, while the frame is subjected to the vertical deformation obtained in Step 1 for the top end of the test specimen. This will create a vertical constraint at the top end of the test specimen resulting in a vertical load reaction. Obtain the vertical load reaction. If the load reaction is different from the axial load obtained in Step 1, then an adjustment in deformation may be needed to minimize such a difference, as described in Mostafaei (2011). Normally the difference is very small and this can be ignored. The obtained axial load and vertical deformation in this step are considered as the initial values. The initial vertical load and initial vertical deformation for the top end of the test specimen of this study were 2000 kN and -0.00133 m respectively.

Step 3: Apply the initial vertical load, obtained from Steps 1 and 2, on the top of the test specimen, as the axial load of the column, gradually. Once the load is stabilized, the test is ready to start. Figure 4 shows the column specimen at this stage before the test.



Figure 4. Test specimen installed in the column furnace testing facility, just before the start of the fire.

Step 4: Start the fire in the furnace for the test specimen.

From here, all the steps will be repeated for each time increment, Δt .

Step 5: Read new vertical deformation of the test specimen, at the top end. Then run the analysis for the model component, while it is subjected to the previous applied load and to the new vertical deformation of the test specimen and obtain the new vertical load reaction.

Figure 5 shows the computer used for numerical simulation of the model component as well as the new digital controlling system of the column, used for the HFT.



Figure 5. The column furnace controlling system and the computer simulator used for application of the HFT.

Step 6: Adjust the vertical load of the test specimen, axial load of the column specimen in the furnace, with the new vertical load reaction obtained from the analysis in Step 5.

Step 7: Repeat steps 5 and 6 for each time increment, Δt , for the entire test including the cooling phase. Δt depends on the level of the acceptable error, e.g. acceptable variations of the vertical load and deformation between the test specimen and the model component. For this study, time increment was approximately every 5 minutes.

3 THE 6-STOREY BUILDING SPECIMEN

A 6-storey reinforced concrete building was designed as the whole structure specimen for this study. The design was based on the North American codes and standards. Details for the design of the 6-storey structure and information on the test specimen can be found in the original report [2]. Figure 6 shows the overall 3D structural frame configuration of the building.

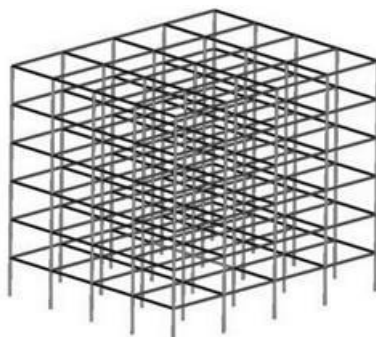


Figure 6. The 3D frame of the 6-storey reinforced concrete building designed for this study.

4 IMPLEMENTATION OF THE HFT

For implementation of HFT the NRC column furnace testing facility was used to perform fire test of the test specimen. The numerical analysis of the model component was simulated using a structural analysis software called SAFIR [1]. SAFIR has the capability of simulating the structures in fire; therefore, beams located in the fire compartment were simulated considering their fire exposure. The interactions between the test specimen and the model component was implemented manually during the test, by reading the test results and including them in the input file of SAFIR and after analysis, by reading the output file of SAFIR and posing the new vertical load on the test specimen. An interface software was developed to speed up the interaction process, which was being performed approximately every 5 minutes.

Mechanical properties of the concrete and steel reinforcement for all the cross sections were assumed identical to that of the column specimens. Beams and columns were simulated using fibre models and therefore shear responses of the elements were considered negligible. All the connections were considered moment resisting connections.

At the start of the test the measured ambient temperature was 23.4°C. The average temperatures in the fire compartment, both in the furnace and in the simulation, during the HFT, were controlled based on the CAN/ULC-S101 standard temperature-time curve [4].

5 HFT RESULTS

The HFT results include temperature distributions on the test specimen, driven from the furnace test, and all the elements, exposed to fire, in the model component, driven from the numerical analysis. Vertical load and deformation, as well as, deformation and the internal loads of the model component are determined and recorded at each time increment during the HFT. Therefore, comprehensive performance response information can be provided by the HFT for the whole structure.

As an example for the test specimen, Figure 7 illustrates temperatures in cover concrete and temperatures at the centre of the concrete cross section, compared with the average temperatures in the furnace, during the fire and the cooling phase.

As an example for the model component, Figure 8 illustrates deformation of the building at the time when the fire exposure stopped, at 4 hours. Figure 9 shows only half of the building in Figure 7, the rest of the building was hidden to better observe the structural response at the fire compartment location.

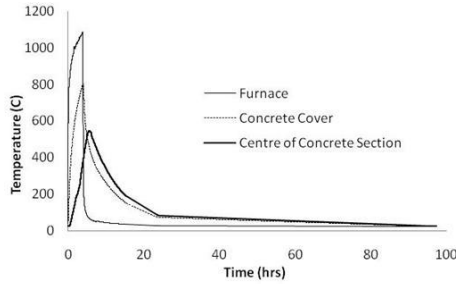


Figure 7. Temperatures in the furnace, cover concrete and centre of the concrete cross-section of the test specimen.

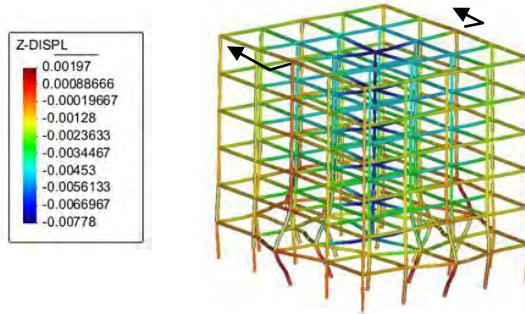


Figure 8. Vertical displacement response of the model component of the 6-storey building, after 4 hours fire exposure.

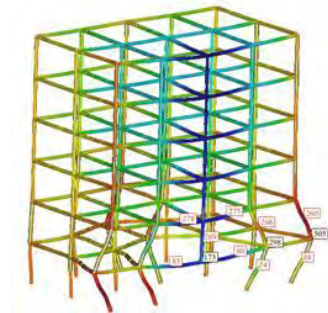


Figure 9. Section A-A of building in Figure 8.

The results of the numerical analysis include shear and axial load, moment, deformations and rotations for all the building elements and nodes as well as temperature distributions of the beams in the fire compartment. The main purpose of this study is to demonstrate that the HFT is achievable. Although, all the performance components for the building structure were calculated during the test, this study

focuses more on the application of the HFT. Therefore, only the overall results of structural performance of the building were provided in this paper.

6 VERIFICATION OF EQUILIBRIUM AND COMPATIBILITY CONDITIONS

For the HFT, equilibrium and compatibility conditions between the test specimen and the model component need to be satisfied. This is required to ensure that the interactions between the two substructures are adequately performed during the HFT and that the results of the two substructures could represent the results for the whole structure. The two main interaction components, in the case of the 6-storey building and the fire scenario in this study, are the vertical load and the vertical displacement at the interface of the two substructures. Therefore, the equilibrium condition will be evaluated by comparing vertical load of the test specimen and the model component. The compatibility condition will be assessed by comparing vertical displacement of the test specimen and the model component at their interface point. Figure 10 shows verification of the equilibrium condition and Figure 11 shows verification the compatibility condition. The results indicate that both equilibrium and compatibility conditions were satisfied during the HFT.

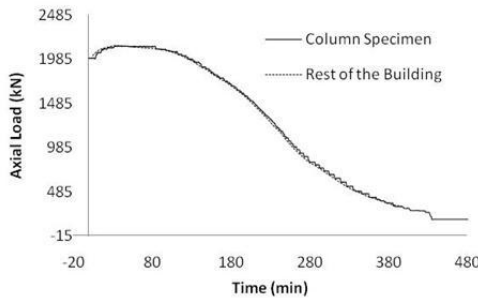


Figure 10. Equilibrium: vertical load at the interface of the test specimen and the model component.

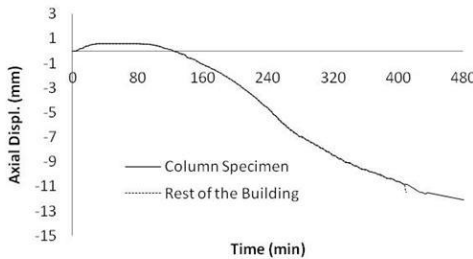


Figure 11. Compatibility: vertical displacement at the interface of the test specimen and the model component.

7 CONCLUSION

A new hybrid fire test (HFT) was implemented for the performance evaluation of a 6-storey building structure exposed to fire. Using the HFT, the whole structure was divided into two substructures: a) test specimen and b) model component. The test specimen was tested physically using the NRC column

furnace facility and the model component was simulated using numerical analysis software. Interaction components between the test specimen and the model component included load and deformations at the interface point. Both equilibrium and compatibility conditions were satisfied during the HFT performed for the 6-storey building. This study showed that application of a hybrid fire test for a typical structure, e.g. building, is achievable.

REFERENCES

- [1] SAFIR, Franssen J.-M., "A. Thermal/Structural Program Modelling Structures under Fire", *Engineering Journal*, A.I.S.C., Vol 42, No. 3, 143-158, 2005.
- [2] Mostafaei, H. "Hybrid Fire Testing for Performance Evaluation of Structures in Fire - Part 1 Methodology," Research Report No. RR-316, *National Research Council Canada*, pp.20, 2011.
- [3] Kaveh, A., Bahreininejad, A., Mostafaei, H. "Hybrid graph-neural method for domain decomposition," *International Journal Computers & Structures*, 70, pp. 667-674, 1999.
- [4] CAN/ULC-S101, "Fire Endurance Tests of Building Construction and Materials", *Underwriters' Laboratories of Canada*, Scarborough, ON

ULTRASONIC PULSE VELOCITY INVESTIGATIONS ON CONCRETE SUBJECTED TO HIGH TEMPERATURE WITH THE USE OF CYLINDRICAL AND EXPONENTIAL TRANSDUCERS

Izabela Hager* and H el ene Carr e**

* Cracow University of Technology, Institute of Building Material and Structures, Cracow, Poland
e-mail: ihager@pk.edu.pl

** University of Pau and Pays de l'Adour, SIAME, Anglet, France
e-mail: helene.carre@univ-pau.fr

Keywords: Concrete, UPV, Fire Damage, Assessment, High Temperature, Exponential and Cylindrical Transducers

Abstract. *The paper presents the results of a study on the impact of high temperature on compressive strength and ultrasonic pulse velocity in ordinary (OC) and high performance concrete (HPC). The relationship between concrete residual compressive strength (f_{cT}) and ultrasonic pulse velocity (V_T) was investigated and a regression curves $f_{cT}(V_T)$ having the similar logarithmic character was proposed. The basic curve proposed in the standard EN 12504-4 appears to be not appropriate in describing the dependency $f_{cT} = f(V_T)$ for heated concrete. Due to the basic curve limitation to ultrasonic pulse velocities ranging between 4.0 and 4.8 km/s, its practical implementation for heated concretes seems to be limited. In this study most of V_T values even for concrete samples heated to 200 °C were below the value of 4.0 km/s. In the paper the damage extent in thermally affected concrete element was also investigated with exponential transducers using point-by-point analyses on cored samples.*

1 INTRODUCTION

After a fire, concrete structure requires damage assessment. The aim of a post-fire investigation is to determine the extent of the damage and the thickness of the degraded concrete. As the duration of the actual fire is limited and concrete structures are usually not completely destroyed in a fire, according to [1] most of the fire affected structures can be efficiently repaired. However the assessment of condition and safety analysis of the structure after the fire is necessary to make the right decision on a strategy of repair, strengthening of the structure as an alternative to demolition. Most of the in situ techniques used to assess the condition of concrete after being exposed to fire are well-known methods, widely used to assess the properties of concrete in structures [1, 2, 3]. In case of fire damage, laboratory techniques are also used to examine concrete integrity. These tests require the sampling of material and laboratory testing.

The tests carried out on concrete core samples are designed to determine the residual mechanical properties of the damaged concrete (direct method) or else to estimate the temperature to which the concrete was exposed during the fire (indirect methods). Such tests include resonance frequency method, ultrasonic method, DTA, TGA, X-ray diffraction, scanning microscopy, thermoluminescence, chemical or petrographic analyses or colourimetry [4].

2 ULTRASONIC PULSE VELOCITY METHOD

2.1 Measurement principles and its applicability for heated concrete

The UPV measurements is the one of various non-destructive testing methods used to evaluate concrete quality and – more generally – the level of the damage to the material. In particular, the velocity of sound in concrete is a high-quality thermal damage indicator, due to its sensitivity to the Young's modulus changes. The elasticity change due to heating is progressive, quasi-linear decrease resulting from portlandite decomposition, CSH gel dehydration, but also due to the mismatch of deformations between the aggregates, which expand, and cement paste, which itself undergoes shrinkage. Moreover as it is widely admitted, the velocity of sound in concrete depends strongly from its moisture content. During heating, moisture is progressively removed from the material. The order in which water is removed from heated concrete depends on the energy that binds the water and the solid. Thus, free water evaporates first, followed by capillary water, and finally by physically bound water. The process of removing water that is chemically bound with cement hydrates is the last to be initiated. As the water presents in the porous structure of the material plays an important role on the measured V values thus, the water departure due to heating and dehydration will affects strongly the velocity of sound.

When concrete is heated under conditions of fire, the increase in temperature in the deeper layers of the material is progressive, but because this process is slow, significant temperature gradients are produced between the concrete member's surface and core. UPV techniques may be applied also to determine the inferior quality concrete layer by indirect techniques [3, 4] or by direct transmission on core material [4].

2.2 Ultrasonic measurement equipment and probes

In this research a PUNDIT plus - Portable Ultrasonic Non-destructive Digital Indicating Tester was used. The exponential and cylindrical transducers were applied for the concrete investigation. Both types of transducers were characterized by the nominal frequency of 54 kHz. The exponential transducers have exponentially curved tips witch acts to concentrate the ultrasonic energy to a small point. The concentrator tip end diameter of is of 6 mm, so it may be treated as the point source of spherical longitudinal wave. For this type of probes no acoustic coupling agent or polishing is required. Moreover, the application in case of curved surfaces, like core sample, or in case of rough spalled concrete elements is feasible. This type of probes provides relatively weak signals compared to conventional transducers. For this type of probes the preamplifier is indispensable in order to increase ultrasonic signal. The 20 dB preamplifier was used along with exponential probes.



Figure 1. PUNDIT plus ultrasonic test equipment.

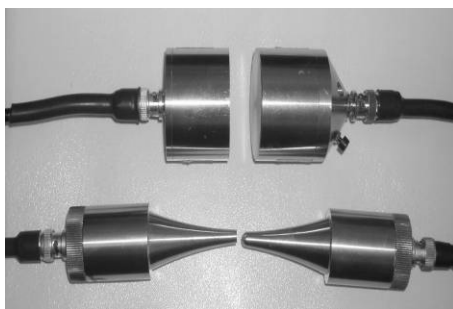


Figure 2. The cylindrical and exponential probes, frequency of 54 kHz.

The UPV measurement is very simple to perform, but initial calibration testing is required to interpret the results. An attempt to determine concrete strength (f_c) based on just the ultrasonic pulse velocity (V) cannot be regarded as reliable without correlating the velocity data with the results of destructive testing

of the affected material. Moreover, accordingly to EN 206-1 the possibility of the strength determination only on the basis of non-destructive testing is excluded. UPV tests should be treated as accompanying to the destructive core tests. The appropriate calibration procedures (direct correlation with cores, and calibration with cores for a limited strength range using an established relationship) are described by EN 13791 standard [5]. Following this standard recommendations, the scaling approximation is based on the basic curve derived from the formula:

$$f_c = 62.5 V^2 - 497.5 V + 990 \quad (1)$$

This formula is intended for concrete where the ultrasonic pulse velocity ranges between 4.0 and 4.8 km/s.

Without calibration, concrete quality can only be estimated by measuring the ultrasonic pulse velocity in accordance with the assumptions listed in Table 1. Studies carried out by [3, 6, 7, 8] demonstrated the validity of the ultrasonic method in assessing the uniformity of heated concrete. According to [7], the ultrasonic method can be successfully applied in both comparative and qualitative testing, such as fire damage assessment, but not in quantitative testing intended to determine strength.

3 OBJECTIVES AND SCOPE

The tests were performed on concrete samples heated to a temperature between 200 and 800 °C. The range was limited to 800°C because preliminary testing had shown that damage caused by temperature of 1000 °C was too important to allow compressive strength test realization.

The objective of this study was to identify the relationship between the results of non-destructive tests and changes in strength caused by heating. The results, given below, made possible the determination of correlations between residual compressive strength f_{cT} and ultrasonic pulse velocity V_T .

In this research two types of transducers were used, cylindrical and exponential, and the comparison of results obtained with the use of those two types of probes for two concrete was presented. Moreover, the results of the point-by-point analyses of concrete cores were performed on cores drilled from the concrete element where a gradient of temperature was achieved across the element section. By this mean the estimation of thickness of the inferior quality concrete layer was determined.

3.1 Tested materials

The tests were performed on ordinary (OC) and high performance (HPC) concretes. Both concretes were produced with the same components mixed in different proportions to achieve different properties. The compositions of the two concretes are summarised in Table 2. The content of the cement paste and mortar in both concrete mixes were constant, only the amount of water reducers varied in order to ensure appropriate consistency.

Table 1. Classification of concrete quality according to ultrasonic pulse velocity [8]

Ultrasonic pulse velocity V [km/s]	Concrete quality
> 4.5	Very good
3.5 – 4.5	Good
3.0 – 3.5	Dubious
2.0 – 3.0	Poor
< 2.0	Very poor

Table 2. Compositions tested ordinary OC and high performance HPC concretes

Concrete Component	Unit	OC	HPC
cement CEM II/A-V42.5R	kg/m ³	322	478
water	dm ³ /m ³	193	129
w/c ratio	-	0.6	0.27
riverbed aggregates			
- sand 0 - 2 mm	kg/m ³		623
- gravel 2 - 8 mm	kg/m ³		660
- gravel 8 - 16 mm	kg/m ³		550

3.2 Samples and heating method

All tests were performed on concrete cubes of side 0.15 m. Concrete age at the beginning of tests was of 120 days. The samples were heated in a programmable Nabertherm laboratory furnace at the heating rate of 0.5  C/min. Once, the set temperature T ($T = 200, 400, 500, 600, 800$   C) was reached, it was maintained for five hours to achieve a uniform temperature distribution across the sample. The samples were then cooled down in the oven at non-regulated rates. Once cooled down, the samples were stored for two months in laboratory conditions (at ca. 18  C and ca. 50% relative air humidity) prior to testing. This time interval between the heating up and testing was designed to represent real-life conditions where concrete diagnostics are not normally performed immediately after the fire.

As the surface of the heated samples showed no clear evidence of damage, cylindrical transducers were chosen for the measurements and located in the centre of opposite sides of the sample cubes. To avoid excessive energy loss on contact between the measuring head and the concrete surface, a coupling medium was used. Subsequently, the exponential transducers were used for the direct ultrasonic transmission measurements, also in this case probes were located in the centre of opposite sides of cubes. Compressive strength tests on both heated (two samples per temperature) and non-heated (three samples) concrete samples were performed when non-destructive tests were completed.

In order to verify if the damage assessment of the concrete elements, where the temperature and damage gradient is present, was possible the point-by-point analyses with use of exponential transducers were performed. HPC's concrete slab, size of 0.305 x 0.305 x 0.150 m, was heated mounted in the place of doorway of a laboratory furnace (Figure 3). In this way, a temperature gradient was achieved across the slab section, reflecting the real-life conditions during a fire. The furnace was programmed to heat the specimens with the maximum power in order to obtain a step temperature gradient leading to the damage gradient within the slab width. The heating gradient obtained within the specimens was of 43   C/cm. Type K thermocouples were embedded during slab casting in its centre at depths of 1, 3, 5, 7, 9 and 11 cm. The LUMEL KD7 data acquisition station was used and all signals were recorded at one-minute intervals. The specimen was heated until a surface temperature reaches 900   C, the Figure 3 shows temperature evolution within the slab. The continuous temperature measurement at the slab surface and the measurements taken at 1, 3, 5, 7, 9 and 11 cm allowed the reproduction of the temperature development in time. After heating the cores were drilled from the element and tested by the direct transmission.

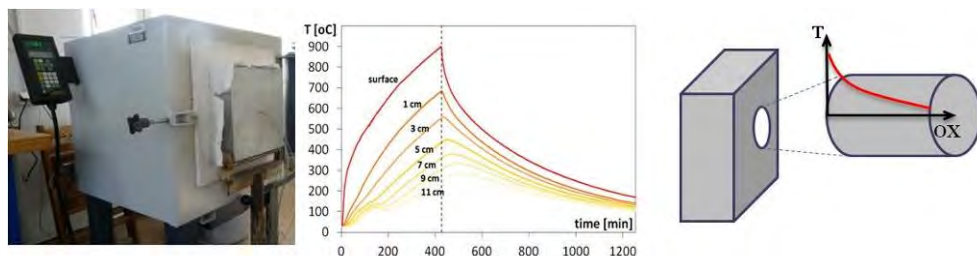


Figure 3. HPC's slab mounted in the place of doorway of the furnace - curve of temperature with time at several depths - scheme of the slab coring.

4 RESULTS ANALYSIS AND DISCUSSION

4.1 Results of uniformly heated cubic samples

For both ordinary and high performance concretes the gradual compressive strength decrease was observed with the temperature increase. This is primarily a consequence of progressive dehydration of the CSH gel, the breakdown of portlandite and the destruction of the contact zone between shrinking

cement paste and expanding aggregate. Figure 4 illustrates the change in residual compressive strength values as a function of temperature as determined using a destructive method.

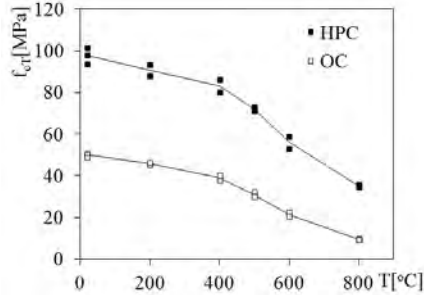


Figure 4. Impact of temperature on residual compressive strength (OC and HPC) [9].

For all samples the transit time of the ultrasonic wave was measured allowing the velocity determination. The results of ultrasonic pulse velocity measurements were obtained both by testing with the cylindrical and exponential probes (Figure 2). As the exponential transducers with the preamplifier were used, the measured velocities were significantly below those determined with the use of cylindrical ones. The difference between ultrasonic velocity readings obtained with cylindrical and exponential transducers was attributed to the erroneous assumptions concerning the distance measurement between exponential transducers (Figure 5). For all tests with exponential transducers, realized on uniformly damaged concrete cubes (side $a = 0.15$ m), the distance that should be considered was of AB (Figure 5). The real time of travel measured with PUNDIT device was of t_{AB} . That is the time of travel from side to side of concrete cube but also through two steel concentrator tips. In the construction of those transducers, cylindrical part containing piezoelectric crystals and stainless steel exponential wave concentrators can be distinguished. In order to evaluate the travel time error, the length of exponential concentrator tips was determined, and the correction of travel time δ was evaluated to be of $17.38 \mu\text{s}$. This correction was subsequently implemented in all measurement performed with exponential transducers.

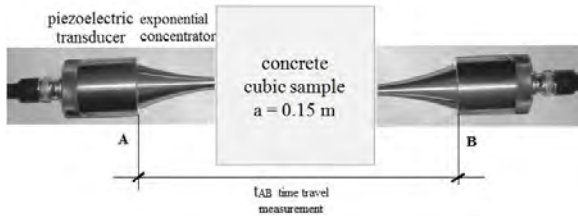


Figure 5. Real time of travel measurement using exponential transducers.

When the correction factor δ was taken into account a good agreement between cylindrical and with exponential transducer measurements was found. Figure 6 presents the results obtained in ordinary concrete (OC) and high performance concrete (HPC) for cylindrical and exponential probes. For non-heated concrete the ultrasonic pulse velocity was of 4.18 km/s in the OC and 4.87 km/s in the HPC. Similarly as in the case of compressive strength, heating caused a gradual reduction of the pulse velocity value V_T . In samples heated to the maximum temperature of 800°C , these velocities measured with cylindrical transducers were of 1.05 km/s and 1.67 km/s respectively.

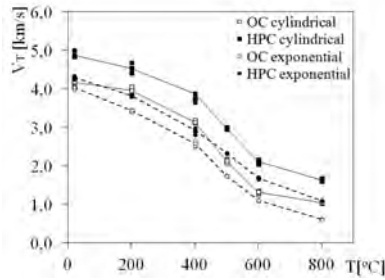


Figure 6. Impact of temperature on the ultrasonic pulse velocity (OC and HPC). Cylindrical and exponential transducers.

4.2 Decay factors

In Figure 7, the effect of temperature on compressive strength (D_{fc}) and ultrasonic pulse velocity (D_V) decay factors, both for heated OC and HPC concrete, are presented. Additionally, the UPV decay factors obtained with cylindrical and exponential transducers were compared. The decay factors (eq. 2 and eq. 3) evaluate the properties deterioration of the heated concrete samples, by comparing them with the parameters found in non-heated concrete:

$$D_{fc} = 1 - f_{cT}/f_{c20^{\circ}C} \tag{2}$$

$$D_V = 1 - V_T/V_{T20^{\circ}C} \tag{3}$$

These graphs show that the ultrasonic method, can serve as an effective tool for assessing qualitatively the damage caused by high temperature. When compared to the actual damage (D_{fc}) measured using a destructive method, the damage coefficient D_V identified with the ultrasonic method was slightly higher, with the exception of 800  C. From the engineering perspective the overestimated D_V results, both measured with cylindrical and exponential transducers, mean that the ultrasonic method allows for the safe assessment of the concrete deterioration.

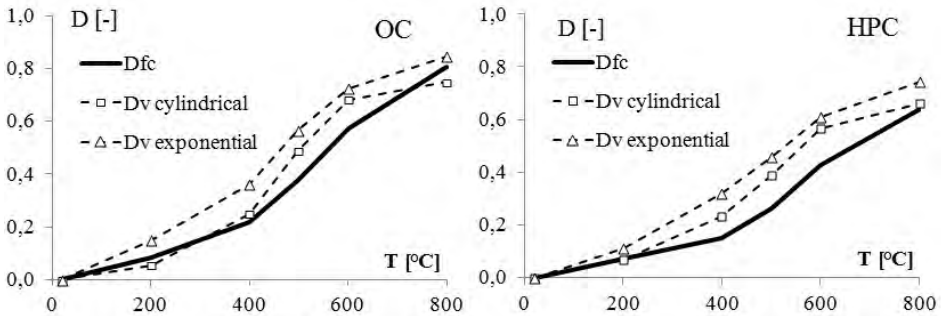


Figure 7. Compressive strength reduction coefficients (D_{fc}) and ultrasonic pulse velocity (D_V) as a function of temperature; a) ordinary concrete (OC), b) high performance concrete (HPC)

4.3 Regression curve

In both concretes the ultrasonic pulse velocity change curves in a function of temperature are almost identical in shape (Figure 6). This similarity can be found also in Figures 8 presenting the $f_{cT}(V_T)$ relationship for OC and HPC. A satisfactory agreement between measurements made with cylindrical and

exponential transducers may be observed, when the correction of travel time δ is applied. The best fitting line was determined by regression analysis on the data pairs that were obtained in the testing programme. The tests results were approximated using logarithmic functions. The equations of regression curves and determination coefficients, R^2 , describing their match to the results were also given in Figures 8.

The regression curve for exponential transducers were then corrected by adjusting the transit time by factor δ of $17.34 \mu\text{s}$. As the result, a corrected logarithmic curves were obtained (see Figure 8), described by the following equations:

$$f_{cV} = 44.86 \ln(V_T) + 25.15 \quad (4)$$

$$f_{cV} = 22.09 \ln(V_T) + 15.81 \quad (5)$$

A comparison of the test curves obtained and the basic curve prescribed in the EN 13791 [5] standard, shows an important mismatch (Figure 8). Indeed, only the non-heated samples (both concretes) and the high performance concrete samples heated to 200°C stayed within the velocity range of $4.0 - 4.8 \text{ km/s}$ required by the standard. The basic curve envisaged by the standard can therefore only be used for high quality concrete. However, after being heated to 400°C concrete samples still present 39.1 MPa for OC and 83.1 MPa for HPC. By the velocity range limitation, basic curve practical implementation for heated concretes is decidedly limited.

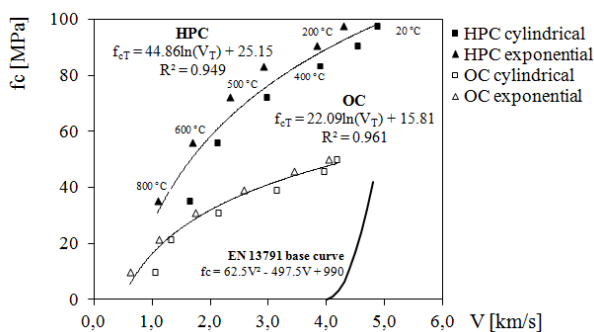


Figure 8. Regression curves for OC and HPC

According to the classification shown in Table 1, all concrete samples heated to more than 600°C and tested with the ultrasonic method showed poor or very poor quality. Ordinary concrete samples (OC), in accordance with the nomenclature proposed in [8], changed from good to dubious quality at as low a temperature as 400°C

5 POINT-BY-POINT ANALYSES OF CONCRETE CORES

Three cores of the diameter $\varnothing 0.08 \text{ m}$ and the length of 0.15 m were drilled from the element heated accordingly to the procedure presented in chapter 3.2. For each of cores the point-by-point measurements were taken following two axes with the step of 10 mm . When making the measurement, the probe tip was rocked on the surface of concrete sample until the minimum transit time was obtained. The results of direct transmission time are presented in Figure 9, and they are plotted as a function of the distance from heated surface.

The presence of the inferior quality layer of concrete was observed. Its thickness was of ca. 80 mm . That corresponds to the maximum temperature of 500°C . The temperature of $500 - 550^\circ\text{C}$ is the portlandite decomposition range ($\text{Ca}(\text{OH})_2 \rightarrow \text{CaO} + \text{H}_2\text{O}\uparrow$). The CaO created in this reaction makes the

elements made of Portland cement practically redundant after cooling. In particular when the CaO combines with water from the atmosphere a consequent expansion may lead to the supplementary material damage. More to the point, the 500 °C isotherm method of calculating the load-bearing capacity of reinforced concrete members subjected to fire, is based on the assumption that the section of concrete where the temperature had exceeded 500 °C is omitted from the calculations.

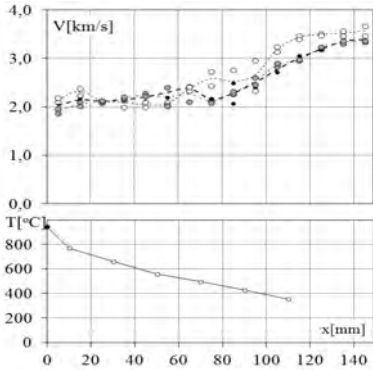


Figure 9. Point-by-point analyses of concrete on cores drilled from thermally damaged HPC's slab.

Figure 10. Cored specimen before and after compression test.

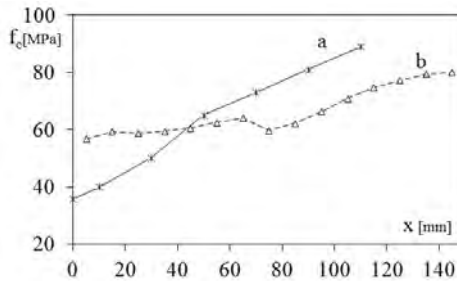


Figure 11. The local compressive strength values determined: a) on the basis of maximum temperature measured in the section, and $f_c(T)$ curve, b) with the UPV point-by-point exponential transducer measurements, and $f_c(V_T)$ regression curve.

The local velocity values, measured by point-by-point along the height of the core, were then determined on the basis of time of travel and sample diameter determination. Subsequently after the UPV tests, the surfaces of cores were grinded and then tested in compression. The average value of compressive strength obtained for tested cores (Figure 14) was of 34.6 MPa , and the results of particular test were of $f_{c1}=35.6$ MPa, $f_{c2}=32.2$ MPa and $f_{c3}=36.1$ MPa.

From the ultrasonic pulse velocity measurements, made with exponential transducers, the inferior quality layer presented the V_T of 2.0 km/s (Figure 9). For this layer the calculated compressive strength from calibration curve (Figure 11 b) was of ca. 60 MPa.

The value of local compressive strength in the depth of the slab was also designated on the basis of maximum temperature measured in the section. At the depth of 1 mm, the temperature of 770 °C was recorded which corresponds to a compressive strength value of 40 MPa. The evaluated f_c from the $f_{cT}(T)$ relationship is presented in Figure 11 a.

Eventually, both local compressive strength evaluation techniques described above gave an overestimated value of f_c , respectively 40 MPa and 60 MPa, compared with compressive strength determined on the core samples.

6 CONCLUSIONS

In view of the testing methods presented and their results the following conclusions seem justified:

- The temperature to which concrete is heated has a clear and straightforward influence on the measured ultrasonic pulse velocity and its compressive strength up to 800 C;
- Ultrasonic pulse velocities differ markedly between the ordinary and high performance concrete. However, the shape of the V_T curves as a function of temperature is similar for two tested concretes;
- The measurement of ultrasonic pulse velocity using the exponential transducers with the preamplifier gave repeatedly, lower values of V_T than those obtained with a cylindrical ones. Reason of this discrepancy was discussed. The correction of travel time δ need to be applied when the exponential transducers are in use;
- The basic curve proposed in the standard EN 12504-4 seem to be not appropriate in describing the dependency $f_{cT}(V_T)$ for heated concrete. Due to the basic curve limitation to ultrasonic pulse velocities ranging between 4.0 and 4.8 km/s, its practical implementation for heated concretes seem to be limited. This implies the use other empirical equations;
- The logarithmic regression curves for heated concretes were proposed for the UPV ranging between 1.0 and 4.8 km/s. A satisfactory agreement between measurements made with cylindrical and exponential transducers may be observed, when the correction of travel time δ is applied;
- The comparison of decay factors of compressive strength (D_{fc}) and ultrasonic pulse velocity (D_V) demonstrated that ultrasonic measurements may constitute an effective method of assessing the quality of concrete affected by high temperature. From the engineering perspective the overestimated decay results obtained by the mean of the ultrasonic method (cylindrical and exponential transducers) allows for the safe qualitative assessment of concrete degradation;
- With the point-by-point UPV measurements on cores drilled from thermally damaged slab, the layer of concrete with inferior quality was detected, corresponding to the maximum temperature of ca. 500  C. The application of exponential transducers on core allows the 500  C isotherm determination;
- Quantitative assessment using the exponential transducers give overestimated values of compressive strength compared with results obtained by destructive testing;

The scope of applicability of the dependencies determined in the study is restricted to concrete containing river aggregates and further research is needed to determine the $f_{cT}(V_T)$ relationship for concretes made with other types of aggregates.

The study was supported in part with the funds of the Polish Ministry of Higher Education (Grant N N506 045040).

REFERENCES

- [1] "Assessment, Design and Repair of Fire-Damaged Concrete Structures", Technical Report No. 68, The Concrete Society, London, United Kingdom, 2008.
- [2] "Fire design of concrete structures – structural behavior and assessment". State-of-art report prepared by Task Group 4.3, Fire design of concrete structures, FIB, July 2008, p. 209.

- [3] Felicetti, R., Colombo, M., New NDT techniques for the assessment of fire-damaged concrete structures, *Fire Safety Journal*, Vol. 42, Issues 6-7, Sept.-Oct. 2007, pp 461-472.
- [4] "Présentation des techniques de diagnostic de l'état d'un béton soumis à un incendie", Décembre 2005, n° 62, Laboratoire Central des Ponts et Chaussées, Paris, France, p. 114.
- [5] EN 13791:2007 Assessment of in-situ compressive strength in structures and precast concrete components.
- [6] Abraham, O., Dérobert, X., "Non-destructive testing of fired tunnel walls: the Mont-Blanc Tunnel case study", *NDT & E International*, Volume 36, Issue 6, September 2003, Pages 411–418
- [7] Stawiski, B. "Attempt to estimate fire damage to concrete building structure", *Archives of Civil and Mechanical Engineering*, 2006, Vol.VI, No 4, pp. 23-29
- [8] Whitehurst, E.A., "Evaluation of Concrete Properties from Sonic Tests", *ACI Monograph No. 2*, ACT, Detroit, MI, 1966
- [9] Hager, I. Compressive strength and ultrasonic pulse velocity in ordinary and high performance concretes subjected to high temperature (in polish), *Zeszyty Naukowe Politechniki Rzeszowskiej. Budownictwo i Inżynieria Środowiska*, Vol. 276, 2011, pp. 307-312.

FIRE ANALYSIS OF A NEW STEEL BRIDGE

Eric Tonicello*, Sylvain Desanghere **, Olivier Vassart***, Jean-Marc Franssen****

* MP Ingénieurs Conseils SA, Switzerland, ** Ligeron, France
eric.tonicello@ mp-ingenieurs.ch, sylvain.desanghere@ ligeron.com

*** ArcelorMittal, Luxemburg, **** University of Liège, Belgium
olivier.vassart@arcelormittal.com, jm.franssen@ulg.ac.be

Keywords: Fire, Structures, Bridge, CFD, F.E. analysis.

Abstract. *The new steel bridge “Hans-Wilsdorf” in Geneva is an exceptional steel structure that will drive general traffic through a main transportation axis. As the investment cost of the project is important, a structural fire analysis has been performed to study the sensitivity of the structure to a high temperature exposure, such as a truck in fire on the deck. This analysis will allow deciding whether a severe fire could be an unacceptable economical risk for the bridge.*

1 INTRODUCTION

Fire protection or fire analysis are rarely applied to bridges. When a new steel bridge is designed, fire is normally not an issue, especially if it crosses a river without navigation. But when a special project, donated to the City of Geneva by the Hans-Wilsdorf Foundation, is shaped like a “tunnel” of steel, the question may be asked: “And what about a fire on the bridge?”

This project is not a usual bridge. Its architecture is modern and spectacular. Carefully designed by *Brodbeck-Roulet* architects in Geneva and *Amsler&Bombelli* engineers in Lausanne, the main structure is made of several arches intersecting each other and the deck is made of a prestressed composite steel-concrete section. The 85m single span bridge weights 3000 tons.



Fig. 1 – Virtual image of the bridge (image © Brodbeck-Roulet SA)

The structural design and optimization of such a bridge is very complicated, even in normal “cold” ULS situation. So, when the fire resistance of the structure have been asked and investigated, many questions must find answers, and the use of advanced analysis methods and tools is necessary.

This fire design has been done by *MP Ingénieurs Conseils* in Crissier, and checked by S. Desanghere (FDS models and simulations), O. Vassart and J.-M. Franssen (SAFIR model).

2 STRUCTURE OF THE BRIDGE

The 85m single span bridge structure has been designed for the cold ULS situation, and led to the following structure:

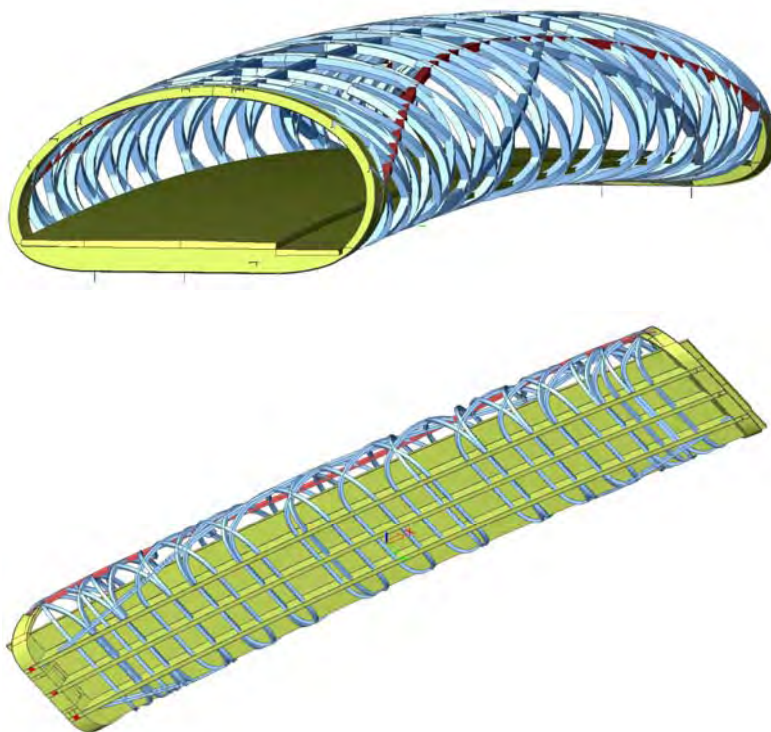


Fig. 2 - Different views of the SCIA Engineer design model

The deck is a prestressed RC composite slab, which is surrounded by a very complex 3D steel grid, made of welded steel sections.

The whole steel structure has been optimised and designed for optimum performance. Each truss member is a parallelepiped section (boxes size is about 400x400 mm), with continuously skewed sides and thicknesses varying from 25 till 100 mm, made of steel grade S355 or S460. The lower members, working a composite section with the concrete slab, are 1 000 mm height and 400 mm width.

The assembly of the bridge was made onsite, fully welded, for better quality and aesthetics. The bridge weights 3 000 tons, from which half is reinforced concrete and half is construction steel.

3 FIRE ANALYSIS

3.1 Normative thermal actions

To analyse the thermal actions, several fire curves were considered in preliminary investigations (fig. 2): ISO and hydrocarbon ones, besides a special artificial fire curve considering that the firemen could not be on site immediately. This assumption is done modifying an ISO curve where the temperature starts decreasing after 30 minutes, until reaching 20°C at 60 minutes.

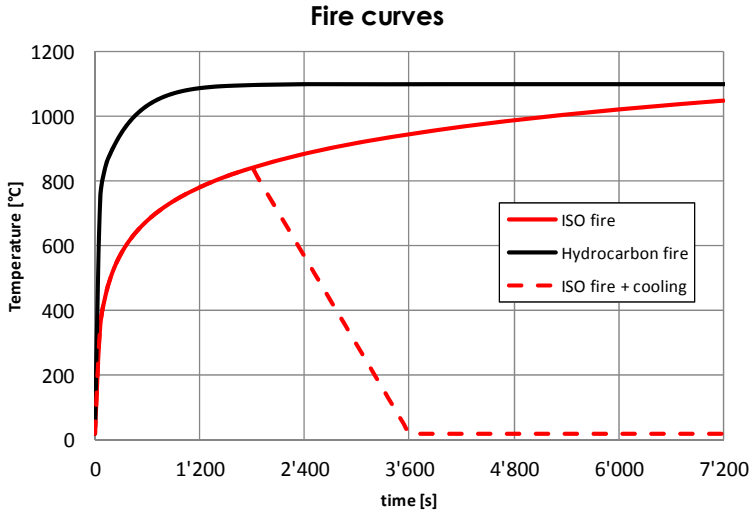


Fig. 2 - Fire curves used for the preliminary calculations

These first three scenarios should provide enough information about the thermal elevation sensitivity of the steel members. The first element to be heated with SAFIR software [1] is the arch section, made of a 400 mm side box with a plain round steel section, diameter 300 mm, inside.

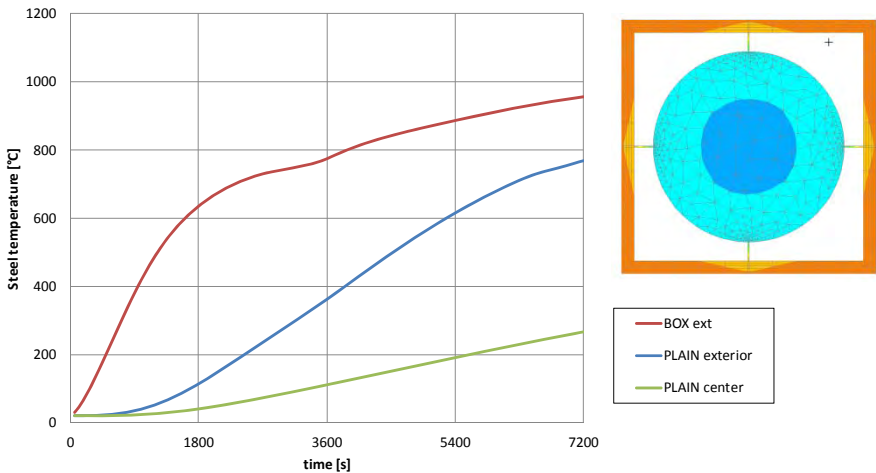


Fig. 3 - Arc section's steel temperature with ISO fire

We can observe that, if the inner plain section remains quite cold ($< 400\text{ }^{\circ}\text{C}$) after 1 hour of ISO fire exposure, the outer box heat rapidly, losing its bearing capacity. The engineers intuition is then confirmed: they added this plain section inside the arch box to reinforce the bridge, as well as offering a “little” fire resistance. This calculation shows that full resistance could be reached by this structural element; to be confirmed by the structural design later.

The hydrocarbon fire led to worse results, as expected, and the ISO + cooling scenario gave better results. The effect on the full bridge will be analysed later with the structural model.

3.2 CFD fires

After the standard fires calculations first results, and having in mind the architecture and the shape of the structure, the only realistic way is to run several CFD simulations, carried out with FDS [2] software and using several fire scenarios. These scenarios are mainly based on the recommendations issued by CETU in France [3], and others were discussed with the main engineering office.

To represent in a real way the modeled fire in a CFD model, we need to quantify the potentially energy that will be liberated during the fire. In our case, a normal car and a truck were available in the references we used [3]:

- Car $Q_{f,k} = 8\text{ [MW]}$
- Lorry $Q_{f,k} = 30\text{ [MW]}$
- Truck $Q_{f,k} = 100\text{ [MW]}$

The HRR diagrams are given in the CETU guide:

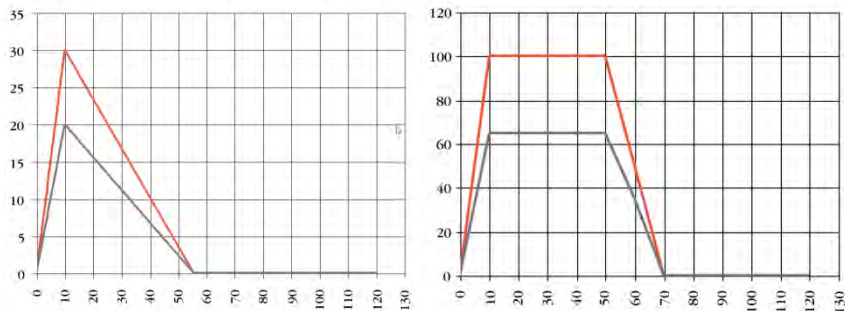


Fig. 4 - HRR diagram for a little truck (30 MW) and big (100 MW) truck in [MW and min] [3]

With these hypotheses, several scenarios were calculated using FDS software. Here we can see the truck scenario heating a simplified representation of the real structure, as in FDS version 5 mesh grid is only orthogonal. To get the adiabatic gas temperatures seen by the structure, a number of captors were set in the model.

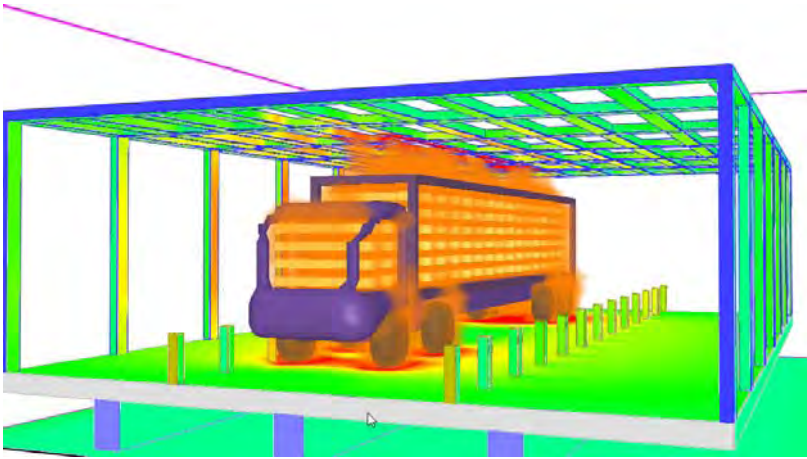


Fig. 5 – FDS simulation of a burning truck on a simplified geometry of the bridge's structure

The resulting adiabatic temperatures provided by FDS as input data in the structural model to analyse the section's heating and then the structural response of the bridge.

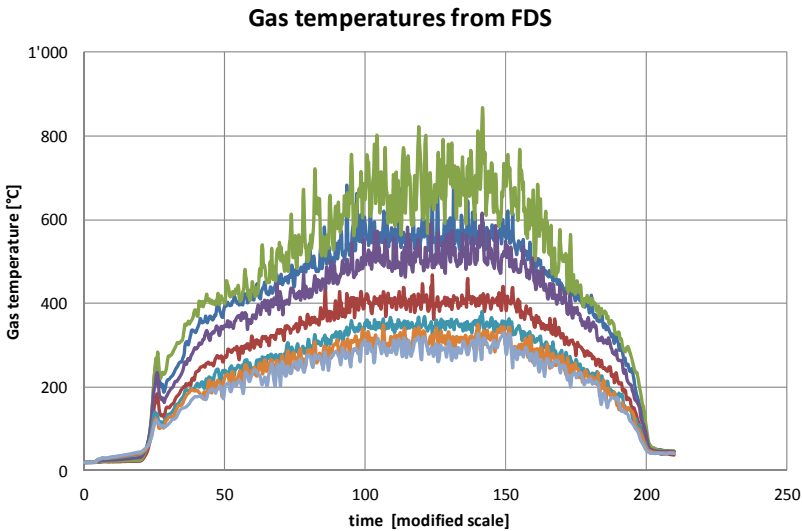


Fig. 6 – Adiabatic temperatures extracted from the FDS model

Figure 6 shows that the time scale has been modified. This has been done to reduce computational times. Indeed, FDS is used here only to compute thermal actions corresponding to a given heat release rate. Members' heating is not considered and we don't have to simulate the real fire curve in this first step.

In a second step, from these data, simplified fire curves were made, to be used as input in SAFIR 2D section heating calculation (as made with the ISO fire):

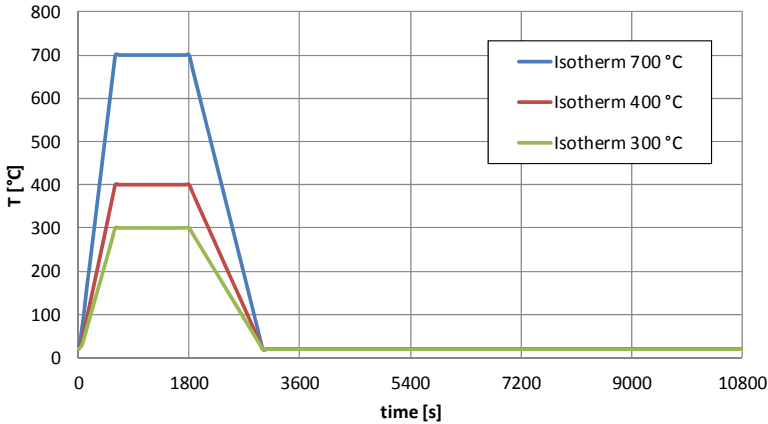


Fig. 7 - Simplified fire curve of a scenario used to heat steel elements

4 STRUCTURAL ANALYSIS

The whole bridge components were introduced into a SAFIR [2] 3D structural model, with BEAM elements for the arches and SHELL elements for the deck and the rigid connecting ring at both ends. As it can be seen in Fig 10, the resulting model is very complex.

In this model, the thermal actions were introduced in localized zones, as shown in the Fig 3 for a fire at mid span (heated BEAM Finite Elements in colours, cold ones in blue and orange):

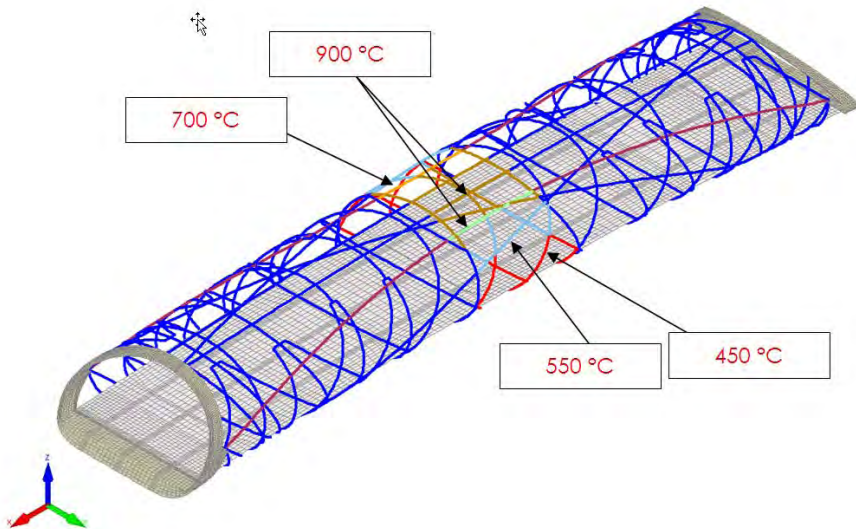


Fig. 8 – SAFIR 3D structural model with fire action at mid span

With the incremental (time dependent) non-linear structural calculation process of SAFIR software, the behaviour of the bridge can be predicted and analysed up to the eventual collapse, helping the engineer to understand and check the models and results.

After a cold calculation was performed to check the FEM model, the fire simulations were done with each scenario. We can see that, given the high mass of the steel bridge, the deformations are only localised over the fire, rarely determining for the whole bridge stability and security:

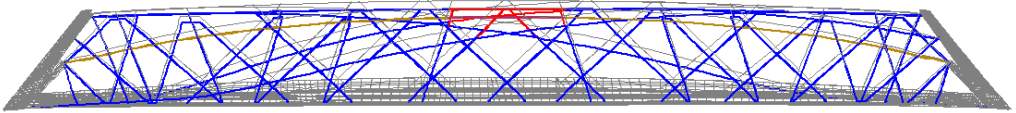


Fig. 9 - Deformation after 55 minutes of ISO fire : little influence (scale 1:1)

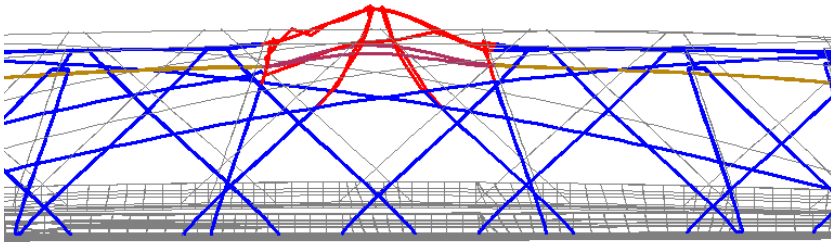


Fig 10 – Localised deformation with hydrocarbon fire (scale 1:5)

With natural fire (FDS) scenarios, we have in the first stage of the fire (with maximal temperatures) an elevation of the bridge due to the thermal expansion of the members, then an increasing deformation due to the readjustments of the heated then cooled structure:

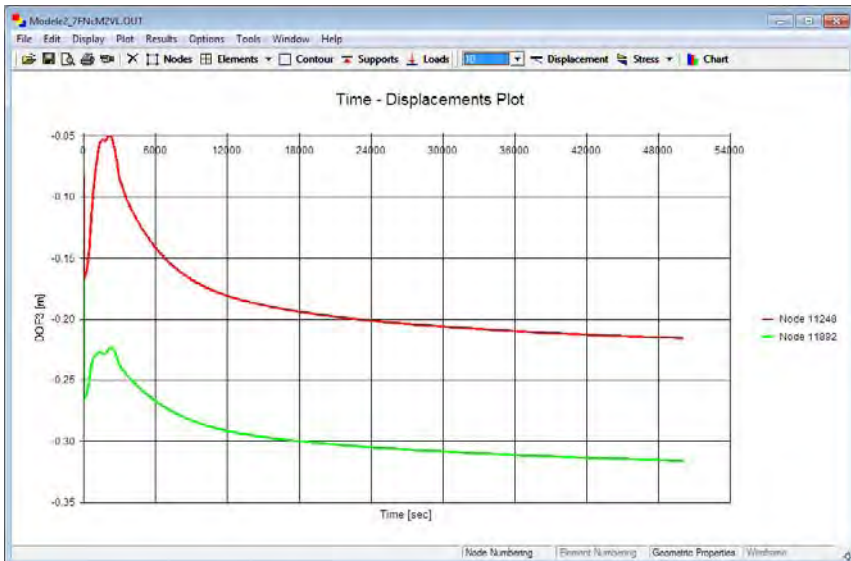


Fig. 11 – Mid-span deformation of the bridge under natural fire scenarios

5 RESULTS

The analysis realized showed that the «Hans-Wilsdorf Bridge» is to be considered safe for the studied fire situations, and numerical simulations showed a really satisfactory behavior.

This result is obtained partly because the different fire scenarios develop in open air (as opposed to tunnel fires for instance) and also because the massive steel arches are made of closed sections with thick walls, some having been reinforced to stand the fire situation.

The CFD analysis was very helpful and confirmed the assumed maximal temperature expected using simplified analytical models. Finite Elements structural analysis showed that the structural stability can be guaranteed, as well as the relatively low maximum deflection under fire situation.

The possibility to get adiabatic temperature values from the FDS model to be introduced into the SAFIR model was very helpful. A tool is currently being developed to simplify this step and allow to apply it on more sophisticated models, avoiding the simplifications we used in this case.

REFERENCES

- [1] J.-M. Franssen, “SAFIR. A Thermal/Structural Program Modelling Structures under Fire”, Engineering Journal, A.I.S.C., vol. 42, n° 3, pp. 143-158, 2005.
- [2] “FDS - Fire dynamic simulator - Technical reference”, NIST Special Publication 1018-5, NIST, 2007
- [3] “Guide Dossiers Sécurité - Les études spécifiques des dangers”, CETU, 2003

FIRE RESISTANCE OF SQUARE AND CIRCULAR CROSS-SECTION CONCRETE COLUMNS

João Paulo C. Rodrigues*, Luís M. dos Santos Laim* and Miguel C. Gonçalves**

* University of Coimbra, Coimbra, Portugal
e-mail: jpaulocr@dec.uc.pt, luislaim@hotmail.com

* University of Porto, Porto, Portugal
e-mails: miguelcg@fe.up.pt

Keywords: concrete, columns, fire, resistance, square, circular.

Abstract. *This paper reports an experimental research on the behaviour of reinforced concrete columns with restrained thermal elongation subjected to fire. Square and circular cross-section reinforced concrete columns were tested in order to know the influence of the cross-section shape on the behaviour of the columns in fire. The parameters tested were the load and restraint levels, the slenderness of the column and the longitudinal reinforcement ratio. The tests results showed that spalling phenomenon may occur even in square or circular columns. The restraint level to thermal elongation of the columns might not be much relevant in their fire resistance. The increasing of the load level lead to a reduction, while the increasing of the longitudinal reinforcement ratio or the decreasing of the slenderness of the columns lead to an increasing of the fire resistance.*

1 INTRODUCTION

The performance of a reinforced concrete (RC) building structure in fire depends particularly on the behaviour of the columns. These structural elements are of great importance on the structural integrity of the building because they contribute to its load carrying capacity and global stability. Fire can lead to severe consequences because the collapse of an essential column to the structure can lead to the progressive collapse of the whole building.

Common reinforced concrete structures under fire action have generally satisfactory behaviour. However, its performance could be much improved if it was well-known the effect of all parameters that influence the fire resistance of this type of structures. So the axial load ratio, fire exposure condition, axial and rotational restraint level, cross-sectional shape, longitudinal reinforcement ratio, slenderness, load eccentricity, concrete covering, spalling and concrete strength are several of the parameters that have recently been studied [1-11].

In the seventies a lot of fully restrained RC columns were tested at Braunschweig University, in Germany [1]. The columns had square cross-section and different distribution of reinforcement bars. They were tested columns with eccentricities equal the half, of the same value and higher than the length of the side of the column. Different applied load levels were also tested. In these tests it was observed that columns of higher eccentricities and smaller applied load levels led to higher fire resistances. Higher cross-sections and number of steel reinforcement bars, distributed along the side of the column, increased the fire resistance.

Lie and Lin [3], in 1985, presented a paper about the influence of a thermal restraint on the behaviour of reinforced concrete columns subjected to fire. Two experimental tests were carried out on fully restrained columns. The results obtained indicate that full restraint against the axial thermal elongation of reinforced concrete columns has little influence on their fire performance. The authors also indicate that

restraint on thermal elongation can be beneficial for the columns fire performance if the surrounding structure is able to redistribute part of the load.

Franssen and Dotreppe [6], in 2003, presented a paper reporting the results of fire resistance tests performed at the University of Liege on concrete columns. The tests were carried out to examine the influence of the circular shape on the behavior of the RC columns under fire conditions. This paper describes the test procedure, the observations made, and the values obtained for the fire resistance. The authors stated that the diameter of the longitudinal reinforcement had no significant influence on surface spalling and despite this phenomenon the values obtained for fire resistance were relatively high. The circular shape of the cross-section does not prevent the occurrence of spalling. An increase of the load level leads to a significant decrease of the fire resistance.

Ali et al. [11], in 2004, presented the results of an extensive experimental programme involving half-scale columns made of ordinary and high strength concrete. The experimental results were used in a parametric study to evaluate the influence of the axial restraint, loading level and heating rate on the performance of concrete columns subjected to high temperatures. In the study it was shown that increasing the loading level decreased the restraining forces and column's failure times. The increasing of the degree of axial restraint increased the generation of restraint forces and had a minor influence on the column's failure times. The low heating rate led to higher failure times of the columns. For normal strength concrete it was also observed that increasing the restraint degree increased the degree of spalling. The same was not observed for the high strength concrete contradicting the usual belief that this type of concrete is more susceptible to spalling. The addition of polypropylene fibres reduced the degree of concrete spalling.

Xu and Wu [9], in 2009, presented the results of experimental tests on reinforced concrete (RC) columns with L-, T- and +-shaped and square cross-sections. The effects of axial load ratio, fire exposure conditions, axial deformation and fire resistance of the columns, were analysed. The experimental results showed that when the axial load ratio is 0.55, the fire resistances of the columns with L-, T-, and +-shaped cross-sections subjected to fire on all sides were 60–73% that of the column with the square cross-section. In case of columns subjected to fire on all sides, its fire resistance with differently-shaped cross-sections increased in the following order: L-shaped cross-section, T-shaped cross-section and +-shaped cross-section. Load ratio and fire exposure had significant effects on the fire resistance of the columns.

In the wake of the previous studies, several fire resistance tests were carried out on square and circular concrete columns with restrained thermal elongation. These tests were carried out in the Laboratory of Testing Materials and Structures of the Department of Civil Engineering of the University of Coimbra [10, 11].

2 EXPERIMENTAL SYSTEM AND SPECIMENS

2.1 Test set-up

The experimental tests on reinforced concrete columns were conducted in the Laboratory of Testing Materials and Structures of the University of Coimbra, in Portugal. In Figure 1 the test set-up for fire resistance tests on columns with restrained thermal elongation, is illustrated. A two-dimensional reaction frame (1) consisted of two HEB500 columns and an HEB600 beam of S355 steel class was used to support a hydraulic jack (2) which applied a compression load to the columns. This hydraulic jack had a maximum capacity of 3 MN and was controlled by a servo hydraulic central unit W+B NSPA700/DIG2000. In addition, the stiffness of the surrounding structure of the columns under test was realized by a three-dimensional restraining frame with four HEB300 columns and four identical beams of S355 steel class, orthogonally arranged (3). The stiffness could be varied by changing the position of the columns or the height of the beams. During these experimental tests, only the position of the columns was changed. Additionally, above the specimen between the hydraulic jack and the beams of the three-dimensional restraining frame a compression load cell (4) was mounted in order to monitor the load during the whole test.



Figure 1. Experimental set-up for fire resistance tests on columns

The specimens were heated with a vertical electric furnace (5). This furnace was 1500 mm x 1500 mm x 2500 mm in internal dimensions and capable to heat up to 1200 °C and to follow fire curves with different heating rates.

The restraining forces generated in the column due to the heating were measured by a load cell of 3 MN located inside a void steel cylinder of high stiffness (6). This cylinder was rigidly connected to the restraining frame by means of M24 class 8.8 bolts as well as all connections between the elements in the experimental set-up. A massive steel cylinder, rigidly connected to the testing column, entered in a void steel cylinder and due to the thermal elongation of the column compressed the load cell.

The axial displacements and rotations on the top and bottom of the column were measured by displacements transducers, LVDT (7), orthogonally arranged in three different points, forming a deformation plan.

2.2 Test specimens

The tested columns were 3000 mm tall and square or circular cross-sections. The square cross-section columns had 160 mm x 160 mm and 250 mm x 250 mm and the circular cross-section ones had 250 mm and 300 mm in diameter (Fig. 2 and Table 1). Two steel plates, steel class S355, measuring 450 mm x 450 mm x 30 mm each, were still connected by welding to the longitudinal rebars. The circular columns had six longitudinal rebars, which were 12 or 20 mm and the square columns had four longitudinal rebars, which were 10, 16 or 25 mm, depending on the cases (Table 1). For each specimen the transversal reinforcement was performed by 6 mm or 8 mm diameter stirrups with a spacing of 100 mm until 700 mm from the supports, and a spacing of 150 mm in the central part (Fig. 2). It is noticed that the 6 mm diameter stirrups were used with the 12 mm diameter rebars in the circular columns and with the 10 or 16 mm diameter rebars in the square columns. The 8 mm diameter stirrups were used with the 20 mm diameter rebars in the circular columns and with the 25 mm diameter rebars in the square columns (Fig. 2). The concrete covering related to the stirrups for all tested columns was 30 mm.

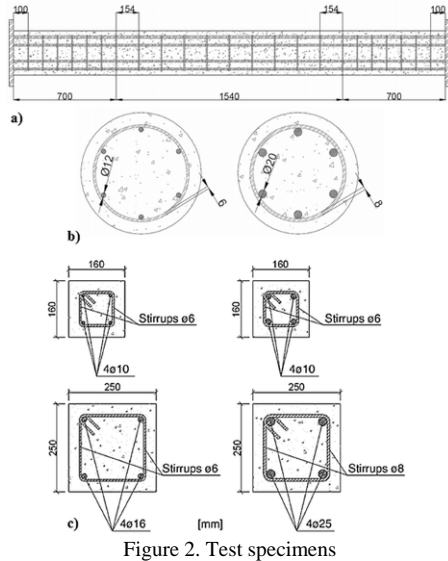


Figure 2. Test specimens

All specimens were fabricated with reinforcing bars of A500NR steel and calcareous aggregate concrete C20/25 according to EN 206-1 [12].

Figure 3 presents a scheme of the test columns with the position of temperature measuring points. The temperatures were measured in five cross-sections on the circular columns and in three cross-sections on the square columns (Fig. 3). In the square columns, T1 was attached to the longitudinal rebar, T2 to the stirrup, T3 was in the concrete near the surface, T5 in the centre of the cross-section and T4 at mid-distance between the last ones. In the circular columns, in cross-sections S1 and S5 it was placed only one thermocouple in the centre of cross-section, in cross-sections S2, S3 and S4, thermocouple T1 was attached to the longitudinal rebar, T2 was near the concrete surface, T4 in the centre of the cross-section and T3 at mid-distance between the last ones. Type K thermocouples were used to measure the temperatures on the specimen while probe thermocouples were used to measure the furnace temperatures.

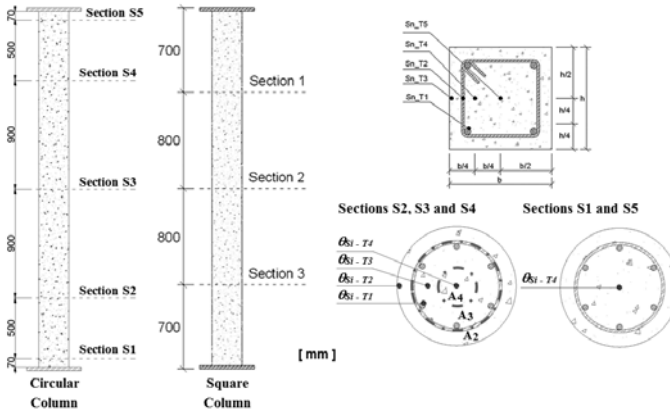


Figure 3. Test specimens and location of the thermocouples

2.3 Test Plan

The experimental programme consisted of 20 (10 circular + 10 square) fire resistance tests on concrete columns with restrained thermal elongation. However, in this paper are selected for presentation sixteen tests whose results are compared. The characteristics of the specimens tested are summarised in Table 1.

For the circular columns the reference C25-12re-70LL-13K corresponds to a 250 mm diameter circular column (C25) reinforced with 12 mm diameter longitudinal steel reinforcing bars (12re). The designation 13K indicates that the value of the axial stiffness of the surrounding structure was 13 kN/mm. The circular columns were tested for stiffness of the surrounding structure of 13 kN/mm and 128 kN/mm.

For the square columns the reference C16-10-k1 corresponds to a cross-section of 160 mm x 160 mm reinforced with 10 mm diameter longitudinal steel reinforcing bars. The designation k1 indicates 13 kN/mm and k2 indicates 45 kN/mm for the value of the axial stiffness of the surrounding structure. The square columns were tested for stiffness of the surrounding structure of 13 kN/mm and 45 kN/mm.

All the columns were axially loaded to 70% (referenced by 70LL in the circular columns) of the design value of buckling load at ambient temperature calculated according to EN 1992-1-1 [13]. These loading levels intended to simulate different serviceability load conditions of the columns when they are inserted in a real building structure.

Table 1. Characteristics of the tested columns

Column reference	Cross-section		Longitudinal reinforcement		Reinforcement ratio A_s/A_c (%)	Slenderness
	Diameter, d or h x b (mm)	Area, A_c (mm ²)	Number and diameter (mm)	Area, A_s (mm ²)		
C16-10-k1 C16-10-k2	160 x 160	25600	4 ϕ 10	314	1.23	77
C16-16-k1 C16-16-k2	160 x 160	25600	4 ϕ 16	804	3.14	77
C25-16-k1 C25-16-k2	250 x 250	62500	4 ϕ 16	804	1.27	49
C25-25-k1 C25-25-k2	250 x 250	62500	4 ϕ 25	1964	3.14	49
C25-12re-70LL-13K C25-12re-70LL-128K	250	49087	6 ϕ 12	679	1.38	58
C25-20re-70LL-13K C25-20re-70LL-128K	250	49087	6 ϕ 20	1885	3.84	58
C30-12re-70LL-13K C30-12re-70LL-128K	300	70686	6 ϕ 12	679	0.96	48
C30-20re-70LL-13K C30-20re-70LL-128K	300	70686	6 ϕ 20	1885	2.67	48

2.4 Test procedure

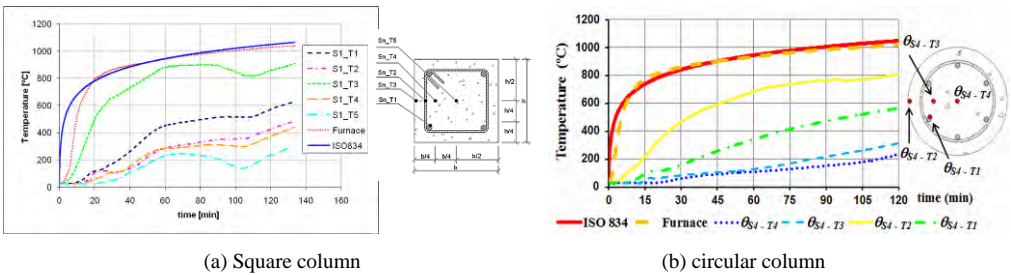
These fire resistance tests were performed in two stages. Firstly, the specimens were axially loaded up to the target force at a rate of 2.5 kN/s. The HEB300 beams of the three-dimensional retraining frame above the test specimen were not connected to the respective HEB300 columns, while the load was being applied. Then, when the loads reached the desired level, those connections were materialized by means of M24 class 8.8 threaded rods. Finally, at the second stage the test specimen was heated according to the standard fire curve ISO 834 [14]. It is noticed that the columns were only heated 2500 mm of their length, from 250 mm to 2750 mm height, because the columns had to be connected outside the furnace.

During the heating the load was kept constant and the test was considered terminated when the axial force of the specimen was lower than the initial applied load.

3 RESULTS

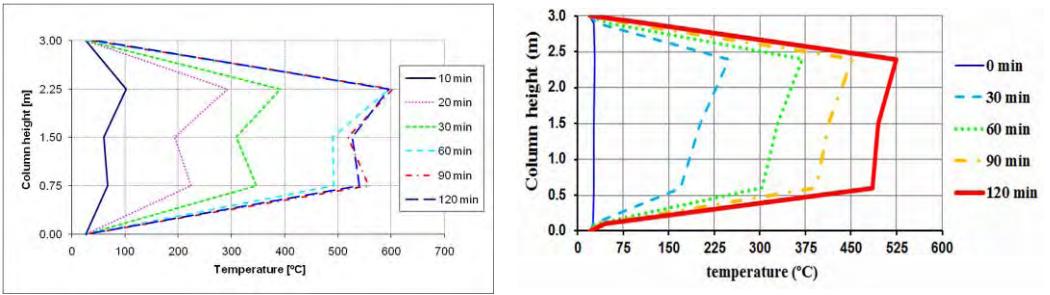
3.1 Temperatures

Figure 4 presents the distribution of temperatures on the cross-sections S1 for square columns (a) and S4 for circular columns (b). It could be observed that despite the beginning of the test, where a small delay between the set-point temperature and the real temperature of the furnace is registered, they are fairly close together. A great thermal gradient was observed along the column cross-section being the differences of temperatures between the surface and the centre of the cross-section of around 600°C after 120 min of test. These thermal gradients will induce internal cracks on the columns that are responsible by the collapse of the columns.



(a) Square column (b) circular column
Figure 4. Temperatures in the cross-sections of square and circular columns

Figure 5 presents the distribution of temperatures in height for square (a) and circular (b) columns. It could be observed a high thermal gradient in the direction of the column supports that increases in function of the time of test. This thermal gradient is visible in the first 0.5m of each end of the column because these parts are not directly exposed to the furnace radiation due to the attachment of the columns outside.



(a) Square column (b) circular column
Figure 5. Temperatures along the height of square and circular columns

3.2 Restraining forces

Figures 6 and 7 present the development of the restraining forces on square and circular cross-section columns in function of the time, respectively. In these figures it is observed the typical behaviour of columns with restraining thermal elongation and subjected to high temperatures. The restraining forces

started to increase up to a maximum and then decreased due to the degradation of the mechanical properties of the materials. In these graphs we will define the critical time (non-standard fire resistance) as the instant of time when the restraining forces reach again the initial applied load.

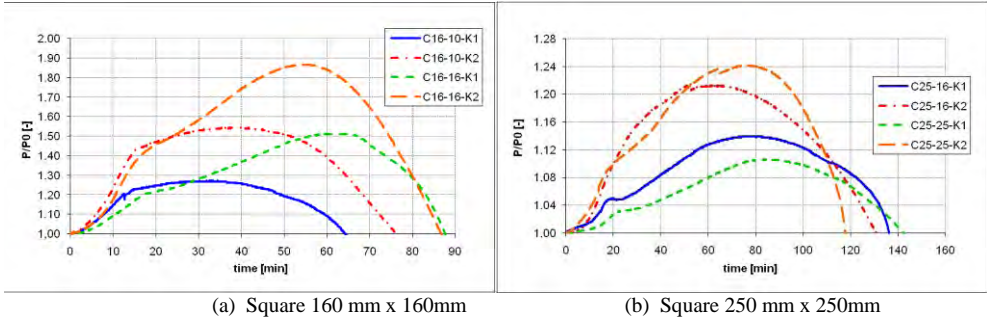


Figure 6. Restraining forces on square columns

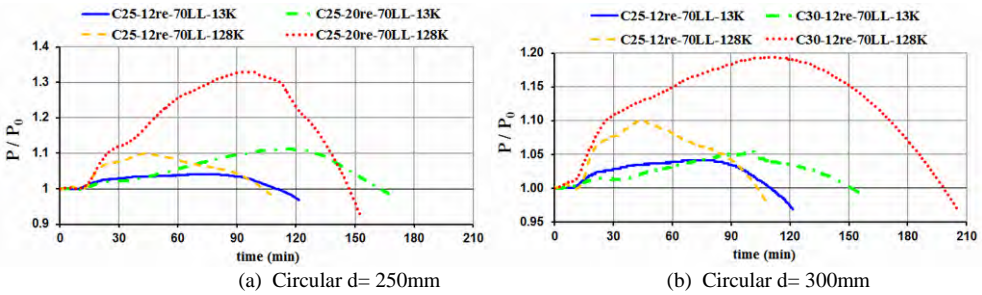


Figure 7. Restraining forces on circular columns

In Figures 6 and 7 it can be observed that higher stiffness of the surrounding structure higher the restraining forces. In Figure 6, for the square cross-section columns, increasing the cross-section dimensions increasing the critical time. The increasing of the longitudinal rebars diameter led also to an increasing of the critical times however this was more notorious for columns with cross-section 160 x 160 mm. For the columns 250 mm x 250 mm increasing the rebar diameter the critical time was practically the same. This may be explained that after a certain diameter of the rebar its lateral expansion can lead to concrete detachment leading to a reduction on the critical times.

Concerning to circular columns (Fig. 7) increasing the column diameter increasing the critical time. For columns of 250 mm diameter it was observed that increasing the diameter of the longitudinal rebars increasing the critical time (Fig. 7 a). The increasing of the stiffness of the surrounding structure seems not having influence on the critical times (Fig. 7 a and b).

Comparing the square columns 250 mm x 250mm (Fig. 6) with the circular columns of 250 mm diameter, no differences in the critical times was observed for the ones with small diameter rebars. However an interesting thing was observed that increasing the rebar diameter in the circular columns led to an increasing of the critical times and the same was not observed in square columns.

3.3 Results of restraining forces and critical times

Table 2 presents the results for square and circular columns in terms of the maximum value of the restraining forces, absolute and relative values of the restraining forces and critical times.

Table 2. Characteristics of the tested columns

Column reference	P_0 (kN)	P_{max} (kN)	P_{rest} (kN)	P_{max} / P_0	R (min)
C25-12re-70LL-13K	363	378	15	1.041	110
C25-12re-70LL-128K	363	400	37	1.102	104
C25-20re-70LL-13K	624	694	70	1.112	163
C25-20re-70LL-128K	624	829	205	1.328	147
C30-12re-70LL-13K	458	483	25	1.054	152
C30-12re-70LL-128K	458	547	89	1.194	198
C30-20re-70LL-13K	766	810	44	1.057	154
C30-20re-70LL-128K	766	975	209	1.273	185
C16-10-k1	144	183	39	1.274	65
C16-10-k2	152	236	84	1.548	77
C16-16-k1	181	274	93	1.512	88
C16-16-k2	185	345	160	1.866	87
C25-16-k1	495	564	69	1.139	136
C25-16-k2	507	616	109	1.214	132
C25-25-k1	656	726	69	1.106	144
C25-25-k2	675	838	163	1.241	118

3.3 Specimens after test

Figure 8 presents some circular columns after fire. It is visible some spalling having exposed the rebars to the heating. The spalling was not continuous along the height of the column and any relation of the column or rebar diameters with this phenomenon can be drawn.



C25-12re-70LL-13k

C25-20re-70LL-13k

C30-12re-70LL-13k

C30-12re-70LL-128k

C30-20re-70LL-13k

C30-20re-70LL-128k

Figure 8. Circular columns after fire

Figure 9 presents some square columns after fire. It is visible extensive spalling exposing the rebars to the heating. The spalling was more notorious on the edges and compressed zones of the columns. Columns of smaller diameter were more affected by spalling.

For column C25-25-K2 was observed buckling after test exposing completely the rebars. However it should be point out that this observation was only possible after taking the specimen out of the furnace. Due to the characteristics of the furnace, where nothing could be observed to inside during the test, it is difficult to predict when the different phenomena occurred.

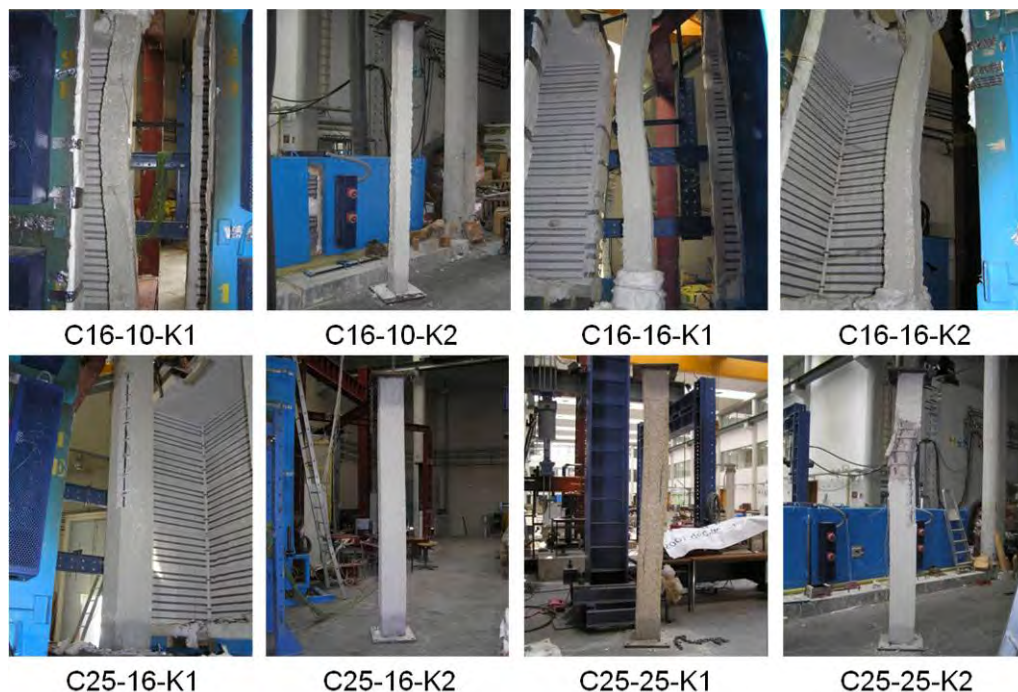


Figure 9. Square columns after fire

4 CONCLUSIONS

The results of this experimental research lead to the following conclusions about the effect of the tested parameters on the behavior of the columns subjected to fire:

- Increasing the longitudinal reinforcement ratio increases the fire resistance of RC columns, but that increase was more significant for columns with smaller cross-section. It was also confirmed that with an increase in the restraint level the positive effect of a higher reinforcement ratio is lessened.
- Increased slenderness leads to a significant reduction of fire resistance. That reduction was more significant for columns with lower reinforcement ratio.
- As expected, with an increase in the restraint level, higher restraining forces were generated. Thus, restraining RC columns against thermal elongation does not affect the performance of those members and so it would not be necessary to design them to cope with this parameter.
- The load level has a considerable influence on the performance of RC columns in fire. With an increase in the load level, a significant reduction of the fire resistance was observed. With a higher load level extensive spalling was observed.
- This study showed that spalling can occur in circular columns and even for low resistances of structural concrete.

ACKNOWLEDGEMENTS

The authors gratefully acknowledge to the Portuguese Foundation for Science and Technology – FCT (www.fct.mctes.pt) for their support under the framework of the research project PTDC ECM 65696-2006.

REFERENCES

- [1] Klingsch W, Haksever A, Walter R. Brandversuche an Stahlbetonstützen, Versuchsergebnisse und Numerische Analyse. Sonderforschungsbereich 148, Brandverhalten von Bauteilen, Arbeitsbericht, 1975-1977, teil I, T.U. Braunschweig, July 1977.
- [2] Lie, T.T., Lin, T.D., Allen, D.E., Abrams, M.S., Fire Resistance of Reinforced Concrete Columns, National Research Council of Canada, Division of Building Research, NRCC 23065, Ottawa, 1984, p. 55.
- [3] Lie, T.T., Lin, T.D., Influence of Restraint on Fire Performance of Reinforced Concrete Columns, Fire Safety Science – Proceedings of the First International Symposium, Gaithersburg, 9-11 October, 1985, p. 291-300.
- [4] Lin, T.D., Zwiers, R.I., Burg, R.G., Lie, T.T., McGrath, R.J., Fire Resistance of Reinforced Concrete Columns, Research and Development Bulletin RD101B, Portland Cement Association, 1992, p. 36.
- [5] Dotreppe J-C, Franssen J-M, Bruls A, Baus R, Vandeveld P, Minne R, Van Nieuwenburg D, Lambotte H. Experimental research on the determination of the main parameters affecting the behaviour of reinforced concrete columns under fire conditions. Magazine of Concrete Research 1997; 49 (179): 117-27.
- [6] Franssen J-M, Dotreppe J-C. Fire tests and calculation methods for circular concrete columns. Fire Technology 2003; 39: 89-97.
- [7] Kodur, V.K.R., Wang, T.C., Cheng, F.P., Predicting the fire resistance behaviour of high strength concrete columns, Cement & Concrete Composites 2004; 26: 141-153.
- [8] Ali, F., Nadjai, A., Silcock, G., Abu-Tair, A., Outcomes of a major research on fire resistance of concrete columns, Fire Safety Journal 2004; 39: 433-445.
- [9] Xu Y, Wu B. Fire resistance of reinforced concrete columns with L-,T- and '+'-shaped cross-sections. Fire Safety Journal 2009; 44: 869-880.
- [10] Martins AMB, Rodrigues JPC. Fire resistance of reinforced concrete columns with elastically restrained thermal elongation. Engineering Structures 2010; 32: 3330-3337.
- [11] Rodrigues JPC, Laím L, Correia AM. Behavior of fiber reinforced concrete columns in fire. Composite Structures 2010; 92: 1263-1268.
- [12] NP-EN 206-1 – Concrete. Specification, performance, production and conformity. European Standard (Portuguese version). CEN, Brussels; 2007.
- [13] EN 1992-1-1: Design of Concrete Structures - General rules and rules for buildings. CEN – Comité Européen de Normalisation, Brussels, 2004.
- [14] EN 1991-1-2: Actions on Structures Exposed to Fire. CEN – Comité Européen de Normalisation, Brussels, 2002.

AUTHORS LIST

AUTHORS LIST

Ab-Kadir, Mariyana A.	479	Dhima, Dhionis	367, 407
Abu, Anthony K.	23, 317, 397, 427, 679	Dong, Gang	499
Aguado, Jose V.	699	Dos Santos Laim, Luis M.	823
Ahmed, Shaikh F.U.	571	Elhami Khorasani, Negar	541
Ali, Faris	43, 75 275	Engelhardt, Michael D.	95, 175
Almeida, Saulo J.C.	55	Espinos, Ana	237, 699
Annerel, Emmanuel	561	Felicetti, Roberto	589
Ariyanayagam, Anthony D.	105	Ferraro, Anna	13
Audebert, Maxime	367, 407	Fike, Rustin	417
Aziz, Esam M.	225	Fischer, Erica C.	305
Baba, Shigeaki	629	Fontana, Mario	347
Baker, Gregory B.	23	Frangi, Andrea	347
Bamonte, Patrick	689	Franssen, Jean-Marc	155, 459, 815
Bénichou, Nouredine	619	Gales, John	659
Bhandari, N.M.	729	Gardoni, Paolo	541
Bhargava, Pradeep	479, 719, 729	Garlock, Maria E.	541
Bihina, Gisèle	295	Gavilán, Ana B.R.	285
Bijlaard, Frans S.K.	85	Gernay, Thomas	531
Bilotta, Antonio	649	Gillie, Martin	449, 479, 719
Bisby, Luke	659	Gonçalves, Miguel Carlos	285, 823
Bo, Zhou	747	Goodfellow, Nathan	275
Boström, Lars	581, 669	Green, Mark F.	619
Bouchair, Abdelhamid	295, 367, 407	Guo, Qianru	469
Boukhili, Rachid	509	Hager, Izabela	805
Buchanan, Andrew H.	317, 397, 427, 679	Hammoud, Rabah	509
Burgess, Ian W.	125, 135, 499	Hartmann, Stefan	439
Byström, Alexandra	185	Hauswaldt, Sebastian	439
Carradine, David M.	317, 397	Helwig, Todd A.	175
Carré, Hélène	805	Hirashima, Takeo	125, 135, 629
Caspele, Robby	775	Hollingshead, Kevin	619
Cefarelli, Giuseppe	13, 649	Hopkin, Danny	377
Chen, Cheng-Chih	267	Hospitaler, Antonio	237, 699
Chen, Chien-Jung	267	Houston, Brent	23
Chen, Ling-Zhu	257	Huang, Zhaohui	499
Chen, Xiaomei	767	Hugi, Erich	387
Choi, In-Rak	489	Ibañez, Carmen	237
Chung, Kyung-Soo	489	Jansson, Robert	581, 669
Collier, Peter C.R.	23	Jansze, Wim	709
Correia, António M.	65, 165	Jau, Wen-Chen	267
Cosenza, Edoardo	649	Jeffers, Ann E.	469
Cowez, Baptiste	155	Jensen, Elin A.	639
Del Prete, Iolanda	13	Jiang, Jian	479
Della Bella, Bruno	709	Jiang, Shou-Chao	257
Desanghere, Sylvain	815	Jiangtao, Yu	551
Devaney, Shaun	3	Joshi, Meenakshi	639
Dhakal, Rajesh P.	679	Just, Alar	337, 357

Kamada, Ryota	737	Petrou, Klelia	75
Kamath, Praveen	719, 729	Piloto, Paulo A.G.	285
Keerthan, Poologanathan	205	Pimienta, Pierre	589
Kequan, Yu	551	Py, Jean-Paul	709
Khaliq, Wasim	609	Qiang, Xuhong	85
Kim, Do-Hwan	489	Quinn, Michael	43
Kirsch, Thomas	115	Robert, Fabienne	709
Klein-Holte, Ronald	709	Rodrigues, João Paulo C.	55, 65, 165, 823
Klinzmann, Christoph	33	Rokugo, Keitetsu	737
Klippel, Michael	347	Romero, Manuel L.	237, 699
Kodur, Venkatesh K.R.	225, 417, 609, 785	Ruiz, Miguel Fernández	689
Kolstein, Henk	85	Sakamoto, Shigehiro	629
Korzen, Manfred	439	Sanghoon, Han	75
Kumar Sharma, Umesh	479, 719, 729	Sannino, Domenico	13
Kumar, Virendra	719	Scalliet, Matthieu	709
Lange, David	3, 669	Schaumann, Peter	115, 195
Lee, James	449	Schmid, Joachim	337, 357
Lee, Jinwoo	95	Schuel, Brittany L.	639
Li, Guo-Qiang	145, 257	Scullion, Tom	275
Lin, Jheng-Yi	267	Sedighi Gilani, Marjan	387
Lindström, Gösta	709	Selden, Kristi L.	305
Lo Monte, Francesco	589	Singh, Bhupinder	719
Mahendran, Mahen	105, 205	Singh, Yogendra	719
Maljaars, Johan	215	Sjöström, Johan	185, 669
Manfredi, Gaetano	13, 649	Soetens Frans	215
McParland, Tony	275	Spellman, Phillip M.	317, 427
Merk, Michael	327	Stein, James	417
Mesquita, Luis M.R.	285	Stein, René	327
Michikoshi, Shintaro	629	Stratford, Tim J.	659
Millard, Alain	531	Sun, Ruirui	499
Min, Jeong-Ki	679	Taazount, Mustapha	367, 407
Moliner, Vicente	237	Tabbador, Mahmood	417
Morimoto, Hiroaki	747	Tabeling, Florian	195
Morovat, Mohammed A.	95, 175	Taerwe, Luc	561, 775
Moss, Peter J.	317, 397, 427, 679	Taib, Mariati	125, 135
Mostafaei, Hossein	795	Taleff, Eric M.	95, 175
Muttoni Aurelio	689	Tan, Kang Hai	247, 599, 757
Nadjai, Ali	43, 75, 275	Tanibe, Toru	737
Naili, El-Hadi	75	Timmen, Florian	115
Neto, Jorge Munaiar	55	Tondini, Nicola	459
Nguyen, Truong Thang	599, 757	Tonicello, Eric	815
Nguyen, Tuan Trung	247	Torero, Jose	719
Nigro, Emidio	13, 649	Uchida, Yuichi	747
Nitsch, Andreas	709	Usmani, Asif S.	3, 479, 719, 729
O'Neill, James W.	427, 397	Van Acker, Arnold	709
Ortega, Javier	699	Van Coile, Ruben	775
Ozawa, Mitsuo	737, 747	van der Meulen, Ronald O.	215
Paliga, Karen	33	Varma, Amit H.	305
Pankaj, Pankaj	719	Vassart, Olivier	459, 815
Pascual, Ana	237	Veljkovic, Milan	185

Vila Real, Paulo	65
Vimonsatit, Vanissorn	571
Wang, Yong-Chang	145
Werther, Norman	327, 427
Wickström, Ulf	185
Winter, Stefan	327, 427
Wong, Bernice	125
Wu, Bo	521, 767
Wu, Yi-Chen	267
Xiong, Wei	521
Yahia, Ammar	509
Yu, Baolin	785
Zehfuss, Jochen	33
Zhang, Chao	145
Zhang, Jian	479
Zhao, Bin	295
Zhoudao, Lu	551

